https://ntrs.nasa.gov/search.jsp?R=19940031629 2020-06-16T10:43:44+00:00Z

NASA-CR-195744

P. 614

Lunar and Planetary Science XXV

(NASA-CR-195744) THE TWENTY-FIFTH LUNAR AND PLANETARY SCIENCE CONFERENCE. PART 2: H-O Abstracts Only (Lunar and Planetary Inst.) 614 p

N94-36136
--THRU--
N94-36174
Unclas

G3/91 0003602

Abstracts of papers submitted to the Twenty-fifth Lunar and Planetary Science Conference

PART 2 H - O

National Aeronautics and Space Administration

Lyndon B. Johnson Space Center
Houston, Texas

LPI / USRA

LUNAR AND PLANETARY INSTITUTE
UNIVERSITIES SPACE RESEARCH ASSOCIATION

LUNAR AND PLANETARY SCIENCE XXV

Abstracts of Papers Submitted to the

TWENTY-FIFTH LUNAR AND PLANETARY SCIENCE CONFERENCE

Sponsored by

National Aeronautics and Space Administration
Lunar and Planetary Institute
NASA Johnson Space Center

March 14–18, 1994

Part 2

Compiled by
Lunar and Planetary Institute
3600 Bay Area Boulevard
Houston TX 77058-1113

The Lunar and Planetary Institute is operated by the Universities Space Research Association under Contract No. NASW-4574 with the National Aeronautics and Space Administration.

Material in this volume may be copied without restraint for library, abstract service, educational, or personal research purposes; however, republication of any paper or portion thereof requires the written permission of the authors as well as appropriate acknowledgment of this publication.

Preface

This volume contains abstracts accepted by the Program Committee of the Twenty-Fifth Lunar and Planetary Science Conference.

The Program Committee was co-chaired by Douglas Blanchard (*NASA Johnson Space Center*) and David Black (*Lunar and Planetary Institute*); other members were Nadine Barlow (*Lunar and Planetary Institute*), James Bell (*NASA Ames Research Center*), Donald Bogard (*NASA Johnson Space Center*), Bruce Bohor (*U.S. Geological Survey, Denver*), Bruce Campbell (*Smithsonian Institution*), Mark Cintala (*NASA Johnson Space Center*), Tammy Dickinson (*NASA Headquarters*), Deborah Domingue (*Lunar and Planetary Institute*), Charles Hohenberg (*Washington University*), Walter Kiefer (*Lunar and Planetary Institute*), Marilyn Lindstrom (*NASA Johnson Space Center*), Glenn MacPherson (*Smithsonian Institution*), Renu Malhotra (*Lunar and Planetary Institute*), Scott Murchie (*Lunar and Planetary Institute*), Laurence Nyquist (*NASA Johnson Space Center*), Patricia Rogers (*NASA Headquarters*), Sue Smrekar (*Jet Propulsion Laboratory*), Allan Treiman (*Lunar and Planetary Institute*), Faith Vilas (*NASA Johnson Space Center*), Paul Warren (*University of California, Los Angeles*), and Michael Zolensky (*NASA Johnson Space Center*).

Papers are arranged alphabetically by the last name of the first author. There are four indexes: author, lunar sample number, meteorite, and keyword.

This abstract volume was compiled by the staff of the Publications and Program Services Department of the Lunar and Planetary Institute. Computer service support was provided by the LPI's Computer Center.

Logistics and administrative support for the conference was provided by the staff of the Publications and Program Services Department, Lunar and Planetary Institute.

CONTENTS

PRECEDING PAGE BLANK NOT FILMED

METEORITIC CONSTRAINTS ON THE 500 MA DISRUPTION OF THE L CHONDRITE PARENT BODY

H. Haack, Planetary Geosciences, SOEST, University of Hawaii, Honolulu, USA and Fysisk Institut, Odense Universitet, Odense, Denmark; K. Keil, E.R.D. Scott, M.D. Norman, Planetary Geosciences, SOEST, University of Hawaii, Honolulu, USA; and P. Farinella, Dipartimento di Matematica, Universitá di Pisa, Italy.

Abstract The high abundance of heavily shocked L chondrites (50%) with Ar-Ar ages of ≈ 500 My [1] suggests that the parent asteroid of these meteorites was catastrophically disrupted at that time [2]. The L chondrite Chico is a 105 kg meteorite containing approximately 60 % impact melt and 40 % host chondritic material [3]. The texture of Chico and other heavily shocked L chondrites indicates an origin close to the impact site and does thus provide clues to catastrophic fragmentation of asteroids. We have used data on the texture, post-impact thermal history, and exposure age of these meteorites to constrain their evolution. We suggest that after the 500 My event, the majority of these meteorites cooled relatively slowly (0.01-1°C/y) inside kilometer-sized fragments or rubble piles.

Introduction The study of cratering on asteroids and, in particular, catastrophic fragmentation suffers from a serious lack of physical data which can be used to constrain numerical models of the process. Some groups of meteorites which show evidence of catastrophic fragmentation may provide useful constraints [2]. The L chondrites are the most heavily shocked group of chondrites, with more than 50% of the samples having been shocked to more than 15 GPa [1] and all having Ar-Ar ages of ≈ 500 My. This is a higher fraction of shocked material than observed even within terrestrial impact craters [4] which suggests that the parent body was disrupted in the 500 My event [2,5]. The large proportion of impact melt observed in the L chondrite, Chico, and the occurrence of the melt as dikes intruded into the host chondrite, suggests that this meteorite was derived from a location close to the impact site. The thickness of kamacite rims in metal from the impact melt indicate post-impact cooling rates of 0.1°C/s at high temperatures (above 1150°C) and 0.01-1°C/y at low temperatures (700-500°C) [3]. The high temperature cooling rates are consistent with thermal equilibration of mixtures of melt and cold rocks with dimensions of decimeters. The slow low temperature cooling rates found in several heavily shocked L chondrites including Chico require a burial depth of at least several hundred meters if the rock was solid and less if it was fractured. Models of catastrophic fragmentation of asteroids suggest that the fragment size approaches zero near the impact site [6] which would suggest that these meteorites were derived from small fragments. On the other hand, studies of secondary craters on the Moon and Mars [7] and "megablocks" from the Ries crater suggest that kilometer-sized fragments can be ejected intact from impact craters.

We will discuss three scenarios that we considered to explain the formation of the features observed in L chondrites:

1. The L chondrite parent body was not catastrophically fragmented and Chico cooled at some depth under the crater floor.

If the high abundance of shocked L chondrites is a result of selective sampling of a crater floor on the parent body, then the thermal history of Chico could be the result of slow cooling at some depth under the crater floor. This would require a heated layer (≈ 1000°C) which was at least 1000 meters thick. Also, Chico must have cooled several hundred meters below the crater floor within the heated layer. In order to explain the high abundance of heavily shocked L chondrites, this scenario would require a later impact into the crater that delivered meter-sized fragments into Earth-crossing orbit. Exposure ages of L chondrites are diverse and all are younger than 500 Ma, indicating that such fragments experienced later impact stripping. Since the fraction of shocked material is very high, even if we assume that all of the L-chondrites were derived from the crater, this scenario also

implies that impacts outside the crater were unable to produce a significant amount of Earth-crossing fragments of unshocked L chondrite material.

2. The target material was broken into m-sized pieces and parts of it reaccreted into one or more rubble piles of kilometer size.

Experiments suggest that catastrophic fragmentation can produce "jets" of debris with small internal velocity differences [8], possibly resulting in loosely bound rubble pile bodies. This view is also supported by the relatively high abundance of terrestrial "doublet" craters [9] and of contact or nearly contact binary Earth-approaching asteroids (such as 4769 Castalia and 4179 Toutatis) which suggests that large fragments from asteroidal collisions can remain gravitationally bound. The fast low-temperature cooling rate of the heavily shocked L chondrite Ramsdorf (100°C/day) indicates a burial depth of ≈ 1m [10]. The fact that Ramsdorf survived to the present suggests that it was protected from space erosion by later accretion/rubble pile formation. A rubble pile scenario is thus consistent with the thermal histories of heavily shocked L chondrites and allows for small sizes of the fragments from which they were later derived. The lower thermal diffusivity of rubble would also allow for a smaller size of the rubble pile relative to a solid fragment. The slow post-impact cooling rate of Chico (0.01-1°C/y) is consistent with cooling in a rubble pile with a diameter of 100-1000 m or more, depending on the depth of burial.

3. A large fragment of the crater floor was dislodged from the parent body.

Although models of catastrophic fragmentation suggest that the material near the impact site is broken down to very small pieces, the intrinsic uncertainties are large, and evidence from large craters suggests that kilometer-sized fragments may be ejected from locations near the impact site. Studies of kilometer-sized "megablocks" from the Ries Crater [4] show abundant dikes with sizes similar to the ones observed in Chico. By assuming that Chico cooled in the center of a spherical fragment, a lower limit on the diameter of the fragment of 400-4000 m is obtained, which is similar to the size of the "megablocks". However, unlike the impact melt dikes in Chico, the "megablock" dikes are filled with brecciated material and the "megablocks" are also much less shocked than Chico.

Discussion We suggest that scenarios 2 and 3 are the most likely. Both of these would also be consistent with the survival of a large fraction of the parent body (i.e., a non-catastrophic impact), but for reasons discussed in [2] this may not have been the case. The only model which is consistent with the numerical models of catastrophic break-up and the cooling rate data from Chico is the second scenario. Unfortunately, very little is known about the formation of rubble piles. Therefore, although crater models predict too small a fragment size, we conclude that the abundant evidence for large fragments from large lunar and terrestrial impact craters makes an origin for Chico inside a kilometer-sized fragment the most likely scenario. The "megablocks" from the Ries crater could be analogs to these fragments (e.g. they have similar dike patterns and similar overall dimensions). Finally, the evidence for re-accretion from Ramsdorf suggests that some of the fragments from the catastrophic disruption of the L chondrite parent body 500 My ago may have re-accreted to form rubble piles.

References [1] Stöffler et al. (1992), *Meteoritics, 27*, 292-293. [2] Keil K., Haack H., and Scott E.R.D. (1994), Catastrophic fragmentation of asteroids: evidence from meteorites, Submitted to *Plan. Space Sci.* [3] Bogard et al. (1994), ^{39}Ar-^{40}Ar age and petrology of Chico: Large scale impact melting on the L chondrite parent body, Submitted to *GCA* [4] Stöffler D. and Ostertag R. (1983), *Fortschr. Miner., 61* No. 2, 71-116. [5] Turner G. (1988) In *Meteorites and the early solar system* , pp. 276-288. [6] Paolicchi et al. (1989) *Icarus ,77*, 187-212. [7] Vickery A.M. (1987) *GRL, 14*, 726-729 [8] Martelli et al. (1993) *Astron. Astrophys., 271*, 315-318. [9] Melosh H.J. and Stansberry J.A. (1991) *Icarus, 94*, 171-179. [10] Smith B.A. and Goldstein J.I. (1977) *GCA, 41*, 1061-1072.

X-RAY DIFFRACTION LINE BROADENING IN EXPERIMENTALLY SHOCKED ORTHOPYROXENES

K. Hackbarth[1], A. Deutsch[1] and D.Stöffler[2], [1]Inst. f. Planetologie, Wilhelm-Klemm-Str. 10, Westf. Wilhelms-Universität, D-48149 Münster, Germany, [2]Inst. f. Mineralogie u. Petrographie am Museum für Naturkunde, Humboldt-Universität, Invalidenstr. 43, D-10115 Berlin, Germany.

Introduction. Orthopyroxene (opx) is an important mineral in several meteorite groups and lunar rocks. Although experimental calibration data are not available so far, shock effects in opx can be used on an empirical basis for shock classification [1,2]. These shock effects include mechanical twinning, mosaicism, the formation of planar elements, reduction of birefringence, and at higher pressures, the transformation of opx into majorite [3,4] which has a garnet structure. The onset of this transformation could possibly serve as shock wave barometer. In order to calibrate these shock effects, we have started a series of shock recovery experiments on single crystal enstatite ($(Mg_{0.73}Fe_{0.27}Al_{0.05})Al_{0.06}Si_{0.94}O_3$) sampled from the Egersund Anorthositic Complex in SW-Norway.

Experimental methods. *Shock recovery experiments* were performed at room temperature on 0.5 mm thick disks (∅ 15 mm) with the shock wave travelling parallel to the (100)-plane of the enstatite. The experimental set-up with an high-explosive driven flyer plate was similar to that described by [5]. Peak pressure of 15, 30, 48, 72.5 and 118 GPa was reached by reverberation of the shock wave [6]. Due to this technique, the duration of the peak-pressure was short, being 0.75 μs for 15 GPa, 0.5 μs for 30 GPa, 0.4 μs for 48 and 72.5 GPa, and > 0.1 μs for 118 GPa.
The recovered samples were investigated by *microscopic*, *spindle stage*, and *X-ray diffraction techniques. X-ray measurements* were performed with a Guinier-Jagodzinski powder camera operating with monochromatic Cu-$K_{\alpha 1}$ radiation at 40kV and 30 mA. X-ray line intensity profiles were recorded with an automatic photometer. To obtain the pure diffraction pattern from the measured raw intensity profile, a Gaussian shape for each diffraction line was assumed [7]. For the shocked samples, the pure half-maximum breadth, β, of each line was then calculated by substracting the half-maximum breadth of the respective line in the unshocked reference sample, b, from the corresponding value in the shocked sample, B, as follows: $\beta^2 = B^2 - b^2$. According to [8], β is related to the mean crystallite size, L, and the lattice strain, ε, by the equation:

$$\frac{\beta^2 \cos^2\Theta}{\lambda^2} = \frac{1}{L^2} + 16\,\varepsilon^2 \frac{\sin^2\Theta}{\lambda^2}$$

Based on this relation, L and ε of the shocked sample can be evaluated in a plot of $\beta^2\cos^2\Theta/\lambda^2$ vs. $\sin^2\Theta/\lambda^2$. In this type of diagram, the slope of a regression line through data points for several orders of one lattice plane equals $16\,\varepsilon^2$, and the intercept corresponds to $1/L^2$ (Fig. 1).
Usually, for this type of analysis, the β values from at least 3 orders of reflection for one (hkl) plane are used. In the case of Guinier-Jagodzinski analysis of orthorhombic enstatite, however, such higher orders of reflection are missing in the recorded range of Bragg angles ($2\Theta \leq 68°$). For this work, therefore, β-values of all measured (hkl) planes were included in the analysis as suggested by [9] for shocked quartz.

Results. Compared to the unshocked reference enstatite, the shocked samples show with increasing shock pressure, undulary extinction and increasing fragmentation. Decrease of birefingence or the beginning of amorphization, however, could not be substantiated on the microscopic scale. In contrast, X-ray patterns allow a more detailed characterization of the shocked enstatite samples. With increasing pressure, diffraction lines broaden and peak intensities decline but a shift of peak positions was not detected. All peaks could be indexed and no indications of the presence of majorite was found.
Using the procedure described above, the change in L and ε was determined. As shown in Fig. 1 for the 48 GPa experiment, regression lines ($16\,\varepsilon^2$) have distinct positive slopes for all shocked samples. With higher pressure, the value for ε increases from 1.5 ‰ at 15 GPa to 4.3 ‰ at 118 GPa (Fig. 2). This increase in lattice strain is accompanied by a reduction of the crystallite size L. Our data indicate that L decreases continuously from 4770 Å for the unshocked reference material to 590 Å at 72.5 GPa (Fig. 2). For the sample shock-loaded at 118 GPa, a cristallite size of 360 Å was calculated.

X-RAY DIFFRACTION LINE BROADENING K. Hackbarth, A. Deutsch and D. Stöffler

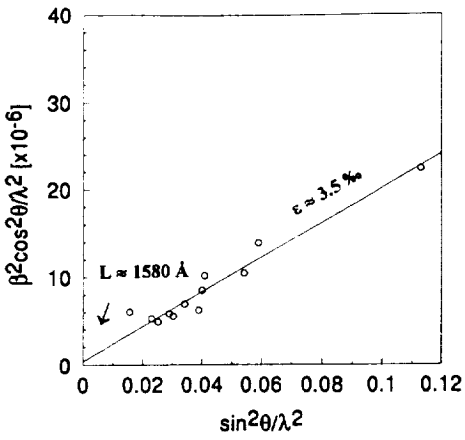

Fig. 1: Diagram for determination of the crystallite size L and the lattice strain ε. Points represent lattice planes (hkl); enstatite shocked experimentally at 48 GPa.

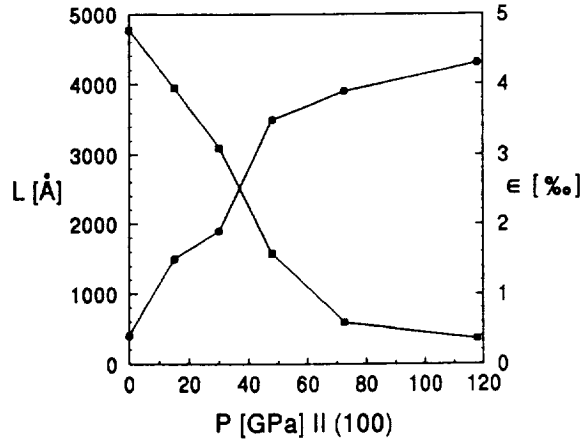

Fig. 2: Change of crystallite size L (squares) and lattice strain ε (circles) with shock pressure; experimentally shocked enstatite.

Discussion. Compared to the Debye-Scherrer method, as applied by [10], in the analysis of shocked silicates, the Guinier-Jagodzinski technique allows a quantitative analysis of line broadening. The new data for experimentally shocked enstatite suggest that a linear relation between internal grain size and shock pressure exists for opx in the range up to 72.5 GPa. Precise X-ray investigation of opx from natural impact lithologies may, therefore, yield a good estimate of the shock metamorphic overprint. As L and ε, however, are dependent of the pre-shock stage, such data can not serve as "absolute" shock barometer.

It is inherent in the reverberation method that the duration of the pressure pulse is short, in comparison to other experimental techniques, and that the post-shock temperature is low compared to the natural case. Therefore, shock recovery experiments carried out in this study are not directly applicable to defining the threshold pressure for the onset of shock-melting in opx, and for the shock-induced formation of majorite.

According to Hugoniot calculations by [11], the transition of opx into majorite should start at a shock pressure > 35 GPa. In static high pressure experiments, majorite begins to form at 15 GPa [4]. So far, the phase transition of enstatite into majorite has been reported only once [12] occuring in dynamic high pressure experiments between 35 and 50 GPa. On the basis of our X-ray analysis, however, this finding seems dubious, as the experiments were performed with the identical set-up, using shock wave reverberation. The short pressure impulse will hamper formation of high pressure polymorphs in all types of shock recovery experiments as long as total reorganization of the unit cell is required.

Acknowledgements. We are indebted to Dr. U. Hornemann (Ernst-Mach-Institut, Weil am Rhein) for performing the shock recovery experiments. This work was supported by DFG grant De 401/5.

References. [1] STÖFFLER, D et al. (1988) in KERRIDGE, J.F. & MATTHEWS, M.S. (eds.) *Meteorites and the Early Solar System*, 165-202. [2] STÖFFLER et al. (1991) *GCA*, **55**, 3845-3867. [3] SMITH, J.V. & MASON, B. (1970) *Science*, **168**, 832-833. [4] RINGWOOD, A.E. & MAJOR, A. (1971) *EPSL*, **12**, 411-418. [5] MÜLLER, W.F. & HORNEMANN, U. (1969) *EPSL*, **7**, 251-264. [6] RICE et al. (1959) in SEITZ, F. & TURNBULL, D. (eds.) *Solid State Physics*, 1-63. [7] KLUG, H.P. & ALEXANDER, L.E. (1974) *X-ray diffraction procedures*, 618-708. [8] MOROSIN, B. & GRAHAM, R.A. (1983) in ASAY, J.R., GRAHAM, R.A. & STRAUB, G.K. (eds.) *Shock waves in condensed matter*, 355-362. [9] LANGENHORST, F. (1993) *Hochtemperatur-Stoßwellenexperimente an Quarz-Einkristallen. Unpublished Ph. D. Thesis, Univ. Münster*, 126 pp. [10] HÖRZ, F. & QUAIDE, W.L. (1973) *The Moon*, **6**, 45-82. [11] AHRENS, T.J. & GAFFNEY, E.S. (1971) *J. Geophys. Res.*, **76**, 5504-5514. [12] JAKUBITH, M. & HORNEMANN, U. (1981) *Physics of the Earth and Planetary Interiors*, **27**, 95-99.

RESTORATION OF A PLANETARY GAMMA-RAY DATA MAP; E.L. Haines, Sunrise Research, Inc., Eugene, OR 97402; R.G. Radocinski, C. L. Lawson, and A. E. Metzger, Jet Propulsion Laboratory, Pasadena, CA 91109

An uncollimated gamma-ray spectrometer (GRS) in orbit above a planet counts gamma-rays from all surface points within its field of view. Mapping the count rates for a specific gamma-ray energy as the GRS moves about the planet yields a count rate map which, with sufficient statistics, will have a spatial resolution on the order of the altitude. Such maps are useful for deriving geochemical information on a large scale, but accuracy is reduced and much useful information about province boundaries is lost.

If the surface flux distribution or map, S, of the gamma-ray source and the response function, R, which describes how the GRS responds to all the factors which transform the surface flux, are both known, convolution of these two functions allows us to predict the count rate, Z_p, to be observed at altitude.

$$Z_p(x,y) = \int R(x-x', y-y') S(x',y') dx', dy'$$

However, the actual problem is inverted. The measured data provides a count rate map at altitude and we expect to derive the response function from basic principles and measurements of detector efficiency. We may recover the undistorted surface flux map, S, numerically by the least-squares method if we choose an assembly of data bins whose number exceeds that of model cells in the surface flux map.

With the same objective in mind a method of iterative convolution was developed and applied to selected regions of Apollo Gamma-Ray Spectrometer lunar data (Haines et al., 1978). An assumed surface distribution model was convolved with the response function for that experiment and the resultant image distribution at altitude compared with the actual data. Iteration proceeded until the agreement between prediction and observation could not be significantly improved. The method described here is a different approach employing direct deconvolution. Compared with the prior method, it is capable of application to the entire planetary surface rather than limited areas, is much less time consuming, and incorporates less human intervention.

The response function is the product of four parts which are largely independent of one another. These four parts are, 1) production or limb darkening, 2) geometry, 3) atmosphere and 4) GRS mass and detector anisotropy. Production treats the distribution with depth which depends on the mode of gamma-ray production as well as water content in the soil and results in limb darkening for gamma rays produced by some nuclear reactions. Geometry comprises the effects of relative distance, emission angle, and variations in elevation. An atmosphere, present at Mars but absent from the Moon and Mercury, collimates the gamma-ray flux since gamma rays arriving from

GAMMA-RAY DATA RESTORATION
Haines, E. L. et al.

points near the horizon must pass through a greater atmospheric mass then those from points near the nadir. Atmospheric thickness is strongly affected by local elevation and seasonal cycles. The mass of the GRS surrounding the detector further attenuates the gamma-ray flux. Anisotropies in thickness and composition must be factored in. Likewise, the efficiency of the gamma-ray detector is not isotropic but displays radial symmetry around the GRS axis. The total response function is the product of these four parts, expressed in nadir axis/azimuth coordinates.

The least-squares method for solving the convolution equation for the source map is based on minimizing the sum of the squares of differences between the observed count rate map and a predicted count rate map generated from the convolution integral by adjusting the values of the surface flux model cells. If the number of data bins into which count rate observations are collected is greater than the number of model pixels (areas over which the modeled gamma-ray flux is assumed to be constant), then a least-squares solution is possible.

To date we have operated the procedure with equal area (1^0x 1^0 equatorial) planet-wide data bins (~40,000) containing pseudo-data generated by the convolution of an assumed surface flux map and 3^0x3^0 model cells (~ 4400) . Before the introduction of statistical noise, the assumed source field has been regenerated with process noise of less than 1%. Statistical uncertainty in the count-rate map is propagated through the least-squares procedures and appears as uncertainties in and correlations between the surface flux values. This propagation is usually represented in least-squares problems by the product of the inverse normal matrix and the mean-square uncertainty. To truncate the problem we have chosen to calculate only the variances (diagonal elements) and ignore the covariances (off-diagonal elements).

We have taken advantage of several contemporary methods to reduce the extent of computation. As a technique to attempt to counter possible ill-conditioning in cases of significantly nonuniform distributions of data, we can augment the problem with a set of "restraint" equations which will smooth the solution by biasing it toward having spatial second derivatives of small magnitude in specified regions.

This numerical deconvolution process will convert maps of gamma-ray count rates recorded at altitude into maps of gamma-ray fluxes at the surface with an expected factor of 3-5 improvement in spatial resolution and more accurate fluxes than can be derived directly from the count rate data. While the method has been developed with the Mars Observer GRS experiment in mind, it can be applied to any gamma-ray spectrometer observing any planetary body from orbit.

THE GEOLOGY AND EVOLUTION OF HECATE CHASMA, VENUS, Victoria E. Hamilton, Department of Geology, Arizona State University, Tempe, AZ 85287; Ellen R. Stofan, Jet Propulsion Laboratory, California Institute of Technology, Pasadena, CA 91109.

Hecate Chasma is an 8000 km long approximately linear to sinuous zone of extensional deformation and volcanism extending from Atla Regio through Asteria Regio and ending at Beta Regio. Previous work has established that the development of a distinctive chain-like concentration of coronae associated with Hecate Chasma is closely linked to processes of the trough's formation [1-3]. Coronae in this chain do not display any clear age progression or systematic variation in topography and morphology, and are therefore not believed to be indicative of terrestrial-style hotspot activity [3]. We have examined the structural, morphologic, and spatial characteristics of the corona chain, associated coronae, the chasm, and regional volcanism in order to evaluate models of the formation of Hecate Chasma. We find that the predominance of features related to upwelling and extensional tectonism strongly favor an extensional/rifting origin for this region.

Regional setting. The geomorphic units surrounding Hecate Chasma appear to be mostly radar-dark volcanic flood plains with some mottled plains, both of which lie roughly 0.5 to 1 km above mean planetary radius (MPR). The source areas of both plains units are difficult to identify. Thousands of volcanic domes greater than 2 km in diameter may mark source vents for the plains units; additional material may have been supplied by corona-related volcanism or flows related to extensional tectonics. Twelve of the 17 impact craters in this region have been tectonically modified and two have been modified by volcanism [4, 5]. The number of modified craters indicates that there has been recent, significant geologic activity involving tectonism and less commonly, volcanism.

The sinuous southwest/northeast trending corona chain associated with Hecate Chasma is distinguished by a series of coronae partially linked by irregular fractures. Several deviations from this trend occur where peripheral "arms" of the chain diverge to the north, east, and southeast. The trace of the chain roughly corresponds to the trace of the trough defining Hecate Chasma. The density of complex fracturing along the chain and chasm decreases significantly 150-200 km away from the axis of the trough, indicating that fracture formation is closely related to trough-forming processes.

Volcanism. Volcanic activity in Hecate Chasma is represented by different types of plains units and edifices, including fracture-associated flows and large volcanic rises. Based on crosscutting relations, it is apparent that volcanism in the area has overlapped in time with tectonic activity as local volcanism may be younger or older than tectonic deformation. Flows associated with the linear fracture zones are generally digitate and flow down current topographic gradients, perpendicular to the local trend of deformation. As this type of flow and geometry is almost always present at known rift zones, the flows of Hecate Chasma are interpreted to indicate that a component of extensional tectonism is present. Three major volcanoes in the region are Ozza Mons in Atla Regio and two unnamed volcanoes in Asteria Regio. Ozza Mons marks a regional tectonic junction where several zones of linear deformation (Hecate, Parga, Ganis, and Dali Chasmata) terminate [14]. None of these fracture zones cuts completely across Ozza Mons. Both volcanoes in Asteria Regio are cut by regional normal faulting (some graben) and record a history of concurrent volcanism and tectonism.

Structures. Lineaments in the Hecate Chasma region are primarily associated with coronae and the trough. Graben, normal faults, and compressional fractures/wrinkle ridges are observed. Graben are usually associated with and trend parallel to the deepest portions of the chasm and also occur at volcanic centers. Diffuse sets of graben tend to occur on the flatter plains areas and at volcanic centers, while denser groupings are preferentially located in and along the chasm. Radially oriented graben sets are typically restricted to the interiors of coronae as predicted by models of corona formation [3, 6, 7, 11, 12], but may extend out beyond the corona annulus. Normal faults are found throughout the Hecate Chasma region, distinguished by radar-bright scarps. These faults are most prevalent near the volcanoes in Asteria Regio and Atla Regio, and in east-central Hecate near 18.5°N, 255°E. Compressional features occur preferentially at the annuli of coronae and at higher elevations associated with more intense deformation; they are more likely to be present further away from the trough than are graben. Compressional lineaments are almost always irregular and sinuous in planform, may anastomose, and tend to parallel the chasm, even when crossing/intersecting a corona.

Coronae. Coronae in the Hecate chain are typical of most coronae in that they are generally circular to elongate in planform, may be associated with extensive volcanism, and display tectonic features indicative of extension, compression, or both [3]. Coronae are generally between 200 and 350 km in diameter and display heavily fractured annuli of concentric or arcuate lineaments. Interiors may contain radial fractures, apparently random deformational features, or an absence of deformation (typically in flooded interiors). Additionally, many coronae are characterized by pervasive, throughgoing fractures that do not appear to be deflected by the coronae's deformation (or vice versa). In many cases, it is difficult to establish the temporal relation between these fractures and the associated coronae. Topographic profiles display considerable diversity ranging from domical features to plateaus with interior lows and annular moats. The distinctive topographic profiles, patterns of radial and

concentric fracturing, and other general characteristics of coronae suggest formation by mantle upwelling or mantle diapirs [3, 6-12]. Of the 51 coronae identified along the Hecate Chasma chain, 5 are interpreted to be fresh to intermediate in development, 9 are classified as intermediate, 15 are intermediate to degraded, and 22 are considered significantly degraded [3, 13]. The freshest/youngest coronae are randomly located throughout the area and do not appear to be spatially related.

Hecate Chasma. Magellan topography data show that the chasm is asymmetric with a reversal in the sense of asymmetry across a corona straddling the chasm at 16N, 252. To the southwest of this corona, the highest topography is on the northern side, and to the northeast of the corona it is on the southern side. The deepest portions of the chasm reach 3-4 km below MPR, and the rims of the trough reach elevations of up to 3-4 km above MPR: total relief in some localities is up to 6 km, often over relatively short horizontal distances. Profiles across the trough primarily display consistent patterns of inward facing, downward-stepping slopes consistent with normal faulting and extensional tectonism. Profiles of topography and emissivity are generally anti-correlated at high elevations as expected [15] except in two areas which show the base and the north side of the trough roughly correlating with emissivity. We are examining these areas to establish whether low emissivities at low elevations and high emissivities at high elevations can be related to geologically recent subsidence and volcanism, respectively.

Conclusions. Complex geologic processes have taken place in the Hecate Chasma region. We have found evidence for a variety of volcanic and tectonic activity, with dominant styles relating to upwelling and extension. Volcanism in the region includes flows emanating from fractures interpreted to have an extensional origin, and large volcanic edifices at the ends of the chasm. Extensive tectonism has resulted in a dominant pattern of fractures and a deep trough. Based on the unusual asymmetry of the chasm, the stair-stepped, inward-facing slopes, and associated graben, we believe the processes that have formed the trough to be extensional in nature. Coronae along Hecate Chasma are inferred to form due to processes of upwelling; most do not appear to be sites of subduction or retrograde migration [16-18] based on the continuity of radial and other features beyond the corona annului. Further studies of local variations in emissivity with topography may provide more insight into recent geologic processes along the trough. Continuing studies concentrate on constraining trough formation and the relationship of Hecate Chasma to Parga Chasma and similar trough/corona chains.

REFERENCES: [1] Hamilton, V.E. and E.R. Stofan, *LPSC XXIV*, 597, 1993; [2] E.R. Stofan et al., *LPSC XXIV*, 1361, 1993; [3] E.R. Stofan *et al., JGR*, **97**, 13,347, 1992; [4] G. Schaber *et al., JGR*, **97**, 13,257, 1992; [5] 2 of the 17 craters were not recognized as of the publication of [11].; [6] Stofan, E.R. and J.W. Head, *Icarus*, **83**, 216, 1990; [7] Pronin, A.A. and E.R. Stofan, *Icarus*, **87**, 452, 1990; [8] G. Schubert *et al., JGR*, **95**, 14,105, 1990; [9] E.R. Stofan *et al., LPSC XVIII*, 954, 1987; [10] E.R. Stofan *et al., JGR*, **96**, 20,933, 1991; [11] S.W. Squyres *et al., JGR*, **97**, 13,611, 1992; [12] D.M. Janes *et al., JGR*, **97**, 16,055, 1992; [13] Several coronae included here have been added to the corona database subsequent to the publication of [3].; [14] D.A. Senske *et al., JGR*, **97**, 13,395, 1992; [15] G.H. Pettengill *et al., JGR*, **97**, 13,091, 1992; [16] Sandwell, D.T. and G. Schubert, *Science*, **257**, 766, 1992; [17] Sandwell, D.T. and G. Schubert, *JGR*, **97**, 16,069, 1992; [18] Sandwell, D.T. and G. Schubert, *Eos, Trans. AGU*, 377, 1993.

ARE THERE CORRELATIONS BETWEEN EMISSIVITY, TOPOGRAPHY, AND AGE AT CORONAE ON VENUS?, Victoria E. Hamilton and Philip R. Christensen, Department of Geology, Arizona State University, Tempe, AZ 85287, Ellen R. Stofan, Jet Propulsion Laboratory, California Institute of Technology, Pasadena, CA 91109.

Coronae on Venus are proposed to be the surface expressions of mantle upwellings or diapirs [1-10]. The wide variation among coronae has led to a classification of these features based on their size and relative amounts and styles of volcanism and tectonism [4]. From this classification, a model was derived to describe the evolutionary sequence of corona features [3, 4]. Using this classification and model, further work provided a relative age for each corona on Venus [11]. This categorization does not include emissivities associated with each corona. Other workers [12, 13] have noted that above a "critical altitude", emissivity declines globally. This decline in emissivity is believed to be related to surface deposits of high dielectric constant, presumably pyrite, which form as a result of atmospheric weathering [12, 13]. We propose that coronae located at high altitudes and characterized by low values of emissivity may be older than high altitude coronae with "normal" or even high emissivity. By perfoming a global survey of corona altitudes versus emissivity we hope to establish what, if any, correlations exist between topography and emissivity. We will compare our relative "age" determinations with those of previous workers [11] and discuss assumptions and pitfalls affecting our method.

Sequence of corona formation and categorization. The three-stage sequence of corona formation [3] consists of 1) uplift, faulting, and volcanism, 2) formation of the annulus and trough and the initiation of topographic degradation, and 3) continued volcanism and topographic degradation [3]. These three stages are associated with the plume or diapir impinging on the base of the lithosphere, flattening and horizontal spreading of the plume head, and gravitational relaxation, respectively [3]. Further work has been aimed at an age categorization of every corona based on its morphological categorization and status/position in the evolutionary sequence. The results of this classification show that of the 359 coronae on Venus, 22 are fresh, 25 are fresh to intermediate, 93 are intermediate, 51 are intermediate to degraded, 159 are degraded, and 9 were uncertain [11].

Method. A global survey of coronae is being performed using Magellan CD-ROMS in order to establish the highest, lowest, and average elevation points of each corona and the emissivity of those points, yielding three pairs of points per corona. We will then examine the 3 sets of points for each corona by plotting emissivity versus elevation and look for any consistent trends. Any correlation (predicted or otherwise) will be examined carefully. If our prediction is confirmed by the data and we are able to determine that there are "young" or "old" coronae at high altitudes, we will then compare these relative ages to those based on morphology and topography [3, 11], paying special attention to any conflicting results (i.e., one scheme classifies a corona as "old" while the other classfies it as "young").

Problems with this method include variation in the "critical altitude" [12, 13] and poorer resolution of emissivity data at higher latitudes [12]. Average values of emissivity also tend to increase with altitude [12]. Additionally, it is important to note that the converse relationship between emissivity and elevation is not applicable at low altitudes, i.e., low altitudes are not necessarily expected to be characterized by abnormally high emissivities. This is due, in part, to the assumption that at low altitudes, surface catalysts dominate weathering reactions and are not predicted to produce pyrite [13].

Preliminary results. The initial part of this study consists of 360° of coverage from the north pole to 40°N latitude and coverage down to the equator between 240°E and 280°E. This preliminary survey area contains 84 coronae and examines topographic high points (only) along the rims of the coronae. Variations in altitude range from 6051.151 km to 6056.311 km and emissivities range from a minimum of 0.59 up to 0.92. In general, corona rims average elevations near 6052.4 km, and have emissivities averaging 0.87, both values near global averages [12]. The point of lowest emissivity (0.59) is correlated with the highest topographic point surveyed so far (6056.311 km). Looking at the 84 coronae as a group, however, no strongly defined correlations between emissivity and topography have yet been observed. Six

coronae are near or above an elevation of 6054.0 km, and of these, one is correlated to the lowest emissivity (see above), while four have emissivities of 0.82 or higher, and one has an emissivity of 0.71.

Continuing study. This survey is ongoing. It is hoped that by analyzing more points at each corona, and the rest of the corona population, that emissivity will be a useful parameter in characterizing corona stage of evolution. Atypical relationships between lava flows and emissivity have been noted at Theia Mons (24°N, 282°E)[14]. We will also examine correlations between emissivity and volcanic flows at coronae in order to determine if coronae are a source of unusual lava types.

REFERENCES: [1] Hamilton, V. E. and E.R. Stofan, *LPSC XXIV*, 597, 1993; [2] E.R. Stofan et al., *LPSC XXIV*, 1361, 1993; [3] E.R. Stofan *et al., JGR*, **97**, 13,347, 1992; [4] Stofan, E.R. and J.W. Head, *Icarus*, **83**, 216,1990; [5] Pronin A.A. and E.R. Stofan, *Icarus*, **87**, 452, 1990; [6] G. Schubert *et al., JGR*, **95**, 14,105, 1990; [7] E.R. Stofan *et al., LPSC XVIII*, 954, 1987; [8] E.R. Stofan *et al., JGR*, **96**, 20,933, 1991; [9] S.W. Squyres *et al., JGR*, **97**, 13,611, 1992; [10] D.M. Janes *et al., JGR*, **97**, 16,055, 1992; [11] E.R. Stofan, *EOS, Trans. AGU*, 1993; [12] G.H. Pettengill *et al., JGR*, **97**, 13,091, 1992; [13] K.B. Klose *et al., JGR*, **97**, 16,353, 1992; [14] J.J. Plaut, *LPSC XXIV*, 1151, 1993.

ELECTRON MICROPROBE ANALYSES OF LOW VANADIUM BASALT GLASSES;
B. Hanson and J. W. Delano, Department of Geological Sciences, State University of New York, Albany NY, 12222

The analysis of vanadium in trace abundances has typically been accomplished by means of INAA [e.g., 1], by SIMS [e.g., 2], or by XRF [e.g., 3]. This contribution details a technique with which accurate and precise analyses of vanadium in concentrations as low as 70 ppm can be obtained by the electron microprobe. Results of analyses using this technique on basaltic glasses produced during partial melting experiments performed on chondritic meteorites are presented elsewhere [4].

Vanadium analyses were performed on a JEOL 733 Superprobe equipped with 5 wavelength-dispersive spectrometers and on-line data reduction. The instrument was operated with an accelerating potential of 15 KeV and a specimen current of 100 nA and 250 nA.

Analysis of vanadium by electron microprobe is complicated by the interference of the titanium $K_{\beta 1}$ X-ray emission, having a wavelength of 2.59391 Å and an energy of 4.50486 KeV, on the vanadium $K_{\alpha 1}$ X-ray emission having a wavelength of 2.50356 Å and an energy of 4.95220 KeV. This interference can be corrected for by subtracting the X-ray counts derived from the titanium $K_{\beta 1}$ emission at the vanadium peak position from the total counts received at this position. The number of counts from the titanium $K_{\beta 1}$ peak measured at the vanadium peak position is a fixed percentage (Figure 1) of the counts above background measured at the titanium $K_{\alpha 1}$ peak position. This fixed percentage of the total titanium counts above background at the titanium $K_{\beta 1}$ peak position is a correction factor that can be applied to all analyses in which vanadium and titanium are both analyzed under identical conditions.

A correction factor was calculated by analyzing a series of vanadium-free basalt glasses with varying concentrations of TiO_2. These glasses were synthesized from reagent grade oxide powders and melted in a one atmosphere gas mixing furnace. The selected glasses span a wide range of basalt compositions (Table 1). The total counts/second/nA at both the titanium and vanadium peak positions corrected for backgrounds were determined using the same routine used in analysis of unknowns (see below). Since vanadium is not a component in these glasses, the number of counts received by the spectrometer at the vanadium peak position were contributed by the titanium $K_{\beta 1}$ peak. The correction factor was then calculated as simply the percent of the total counts/second/nA of the titanium $K_{\alpha 1}$ peak measured at the vanadium $K_{\alpha 1}$ peak position. Each glass was analyzed five times and an average correction factor was calculated. Figure 1 is a plot of the average correction factor calculated for each glass versus the total titanium abundance for each glass. These analyses were performed during two separate analysis sessions at different specimen currents (100 and 250 nA), and with two different spectrometer slit widths (500 and 300 μm). The correction factor is taken as an average of the correction factors determined for each of the glasses (0.5904 %). Figure 1 demonstrates that the correction factor is constant and does not vary with total titanium abundance, beam current, or spectrometer slit widths. Similar analyses on the primary rutile standard resulted in a much different correction factor (0.968 %) suggesting that the magnitude of the correction factor is sensitive to the matrix of the sample.

All analyses, including standards and unknowns, were analyzed using the same technique. In order to eliminate errors due to slight differences between the mechanics of different spectrometers, the same spectrometer (equipped with an LIF crystal) is used to measure counts at both the titanium and vanadium peak positions. Both titanium and vanadium were (a) measured under identical conditions for the same duration, and (b) backgrounds were collected during each analysis. Typical conditions were 250 nA beam current for 250 seconds and results were returned as counts/second/nA corrected for backgrounds. The beam current was decreased to 100 nA and count times increased for samples with high TiO_2 concentration in order to minimize error caused by detector dead time. Peak positions were determined by calibrating on a V_2O_5 oxide primary standard for vanadium and a rutile primary standard for titanium at the start of each analytical session. The measured peak positions of vanadium and titanium may vary slightly from one analytical session to another. In order to account for this source of error and to ensure highly accurate analyses, five well-characterized standard glasses were analyzed during each session (Table 1). From these analyses, a standard working curve was constructed (Figure 2) and the concentration of vanadium in the unknown samples were calculated. The origin was included as a regressed point for all working curves constructed. Included in this standard working curve (Figure 2) are the results of analysis of an Apollo 17 (74220) orange glass bead containing 9.1 weight percent TiO_2 and 120 ± 10 ppm V [5]. This point demonstrates that the analysis technique can be used to accurately analyze samples with high TiO_2 and low V concentration.

Approximately 550 counts (corrected for titanium interference) above a background of 4000 counts are obtained during a typical analysis at operating conditions of 250 nA beam current and counting for 250 seconds on a basalt glass containing 78 ppm V and 1.0 wt % TiO_2. The maximum analytical uncertainty of this technique wa*s estimated by replicate analysis on a single sample. The results of the five replicate analyses on

this glass analyzed for 250 seconds per analysis at 250 nA beam current yielded a one sigma uncertainty of 15 % total V. The results of five analyses on an Apollo 17 orange glass (74220) bead analyzed for 250 seconds per analysis at 200 nA beam current yielded a one sigma uncertainty of 13 % total V at the 120 ppm level.

A potential problem in analyzing trace elements with such high specimen currents and extended count times is the reduction of X-ray intensity due to the build up of contaminants on the surface of the specimen at the analysis point. This problem might be particularly acute when analyzing small samples with a narrow electron beam. In order to determine the effects of prolonged exposure, five replicate analyses were performed on the same spot on a 10 μm wide pool of glass from a partially melted sample of the Allende chondrite from the experiments performed by Jurewicz et al. [6]. There was no appreciable loss in X-ray intensity during 90 minutes of continuous exposure to a 5 μm electron beam with a current of 250 nA.

REFERENCES: [1] Hughes et al. (1988) GCA, 52, p. 2379-2391. [2] Shearer and Papike (1993) GCA, 57, p. 4785-4812. [3] Bender et al. (1984) J. Petrology, 25, p. 213-254. [4] Jones et al. (1994) This volume. [5] Hughes et al. (1989) PLPSC 19, p. 175-188. [6] Jurewicz et al. (1993) GCA, 57, p. 2123-2139.

TABLE 1
CHEMICAL COMPOSITION OF STANDARD GLASSES

	XV green (A)	XVII (74220)	Tamayo 975-2†	Tamayo D12-5†	MRG-1 ‡	A*	B*	C*	D**
SiO_2	45.5	38.5	46.3	49.7	39.32	48.79	44.6	39.6	54.49
TiO_2	0.38	9.1	2.00	1.28	3.69	0.83	3.78	12.6	2.00
Al_2O_3	7.75	5.8	15.9	15.5	8.26	17.50	9.06	7.36	-
FeO	19.7	22.9	8.78	9.43	8.63	8.19	21.7	24.6	-
MnO	0.26	0.27	-	0.15	0.17	0.00	0.22	0.35	-
MgO	17.2	14.9	9.57	8.53	13.49	9.50	10.3	8.06	18.13
CaO	8.65	7.40	11.8	12.3	14.77	12.87	9.68	6.68	25.38
Na_2O	0.14	0.37	5.16	2.42	0.71	2.13	0.35	0.37	-
K_2O	0.017	-	0.10	0.03	0.18	0.02	0.03	0.21	-
V (ppm)	168	120	353	287	520	-	-	-	-

† Major elements by electron microprobe, minor elements by XRF [4].
‡ Fused Mount Royal Gabbro MRG-1 (Canadian Certified Reference Materials Project).
* Synthetic vanadium-free glasses synthesized at 1 atmosphere at SUNY Albany Department of Geology.
** Diopside glass standard with 2.00 % TiO_2 (Di2Ti) from The Geophysical Lab, Carnegie Inst.

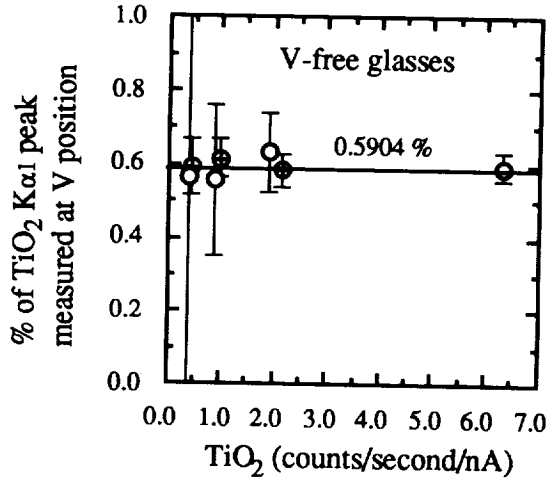

FIGURE 1
Correction factor calculated from analyses of V-free basalt glasses. Circles with crosses analyzed at 100 nA for 250 sec. with 500 μm slit. Open circles 200 nA, 100 sec., and 300 μm slit. Error bars std. dev. of 5 analyses

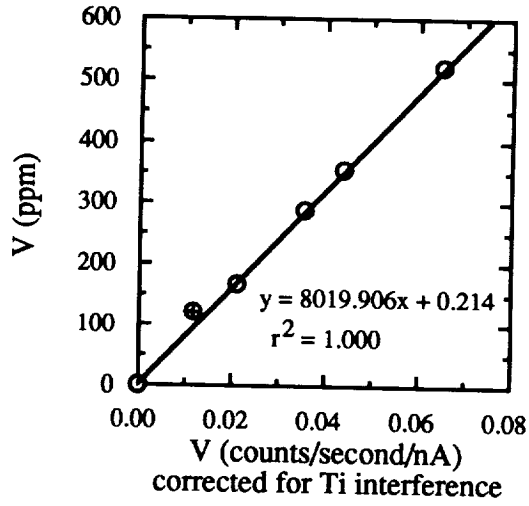

FIGURE 2
Example of a standard working curve constructed for every analytical session. Circle with cross is the XVII Orange Glass containing 9.1 wt % TiO_2 and 120 ppm V.

THE REFRACTIVE INDEX OF THE REGOLITH OF MERCURY; B. Hapke, Univ. of Pittsburgh.

The real parts of the average refractive indices of the regoliths of the Moon and Mercury in visible light can be estimated from the second Stokes vector using the method proposed in [1]. This method assumes that in the phase angle range between 30 and 70 degrees, all light internally scattered within regolith particles or multiply scattered between them is randomly polarized, so that the only contribution to the difference between absolute radiances polarized perpendicular and parallel to the scattering plane is Fresnel reflection from the grain surfaces. For dielectrics the angular Fresnel reflection coefficients depend only on the real part n of the index of refraction.

The analysis was carried out for two samples of Apollo fines and for integrated light from the Moon and Mercury. Laboratory measurements were used for the Lunar samples. For the Moon, polarization measurements [2,3] were combined with absolute photometric data [4,5] to deduce absolute polarized radiances. Similarly, polarization [2,6,7,8] and photometry [9,10, 11] were combined for Mercury.

The results of the analyses are given in table 1, along with typical values of n [12] for the most abundant minerals in the Lunar regolith. For the Moon the analysis gives n = 1.78±.03, in good agreement with the Apollo samples and with values expected from Lunar mineralogy. For Mercury the analysis gives n = 2.07±.08, significantly higher than the Lunar value. A possible reason for the larger n is the presence in the Mercurian regolith of metallic iron particles larger than the wavelength.

Because this technique has only been tested on a limited number of materials [1, 13], its general applicability has not yet been established. However, there may be significant compositional differences between the surfaces of Mercury and the Moon. This further demonstrates the importance of renewing the exploration of Mercury by spacecraft, such as the proposed Discovery-class Hermes Mercury Orbiter Mission.

Table 1. Real Refractive Indices

Object	n
Anorthite	1.6 - 1.8
Pyroxene	1.6 - 1.8
Olivine	1.6 - 1.9
Ilmenite	~ 2.7
Apollo 10084	1.68±.05
Apollo 12070	1.67±.04
Integrated Moon	1.78±.03
Integrated Mercury	2.07±.08

Refractive Index of Mercury; B. Hapke

REFERENCES: [1] Hapke B (1993), *Theory of Reflectance and Emittance Spectroscopy*; [2] Lyot B. (1929) NASA TTF-187; [3] Coyne G. & Pellicori S. (1970) Astron. J, 75, 54; [4] Lane A. & Irvine W. (1973) Astron. J, 78, 267; [5] Helfenstein P. & Veverka J. (1987) Icarus, 72, 342; [6] Dollfus A. (1957) NASA TTF-188; [7] Dollfus A and Auriere M. (1974) Icarus, 23, 465; [8] Gehrels T. et al. (1987) Icarus, 71, 386; [9] Danjon A. (1949) Bull. Astron., 14, 315; [10] De Vaucoulers G. (1964) Icarus, 3, 187; [11] Veverka J. et al. (1988) in *Mercury*, pp. 37; [12] Deer W. et al. (1975) *Introduction to the Rock Forming Minerals*; [13] McGuire A. (1993) *An Experimental Investigation of Light Scattering by Large, Irregular Particles*, Ph.D. thesis.

INVESTIGATIONS OF THE ^{182}Hf-^{182}W SYSTEMATICS; C. L. Harper Jr. & S. B. Jacobsen, Dpt. Earth & Planet. Sci., Harvard Univ., 20 Oxford St., Cambridge, MA 02138 USA

Introduction: The ^{182}Hf-^{182}W chronometer is likely to become a powerful tool in studies of the accretion and very early differentiation histories of planets. Careful investigation of the ^{182}Hf-^{182}W system is also important in astrophysics because a determination of the initial abundance of ^{182}Hf will provide a key constraint on models of the molecular cloud environment within which the sun formed. The 9 Ma half-life of ^{182}Hf provides an excellent timescale for studies of both star-forming and planet-building processes. Several geochemical aspects also make the ^{182}Hf-^{182}W systematics particularly well suited for dating planetary accretion-related (as opposed to nebular) processes. First, in contrast to the U/Pb, Rb/Sr, I/Xe and Pu/Xe parent/daughter pairs, both elements in the Hf/W parent/daughter pair are refractory. Therefore nebular fractionations involving episodes of volatile loss are unlikely to have modified the initial budgets of Hf and W in bulk planetary reservoirs (which are expected to have been present in chondritic proportions). Second, W is a moderately siderophile element, and its factor of 10-30 depletions in the silicate mantles of planets (Earth, Mars, Moon, eucrite parent body) is a consequence of the partitioning of W into planetary cores during core formation. In the case of the highly siderophile element chronometries, ^{187}Re-^{187}Os and ^{244}Pu-Ru,Pd [1], this relatively simple fractionation history is complicated by the likelihood that a significant part (up to >99%) of their silicate mantle budgets were supplied by a "late veneer" component of material accreted well after the epoch of core formation, and later admixed geodynamically. While this aspect of multistage complexity makes the ^{187}Re-^{187}Os and especially the ^{244}Pu-Ru,Pd systematics particularly attractive for studying early planetary geodynamics, any putative veneer contributions to W budgets in planetary silicate mantles are insignificant (<1%); consequently W isotopes should provide a clear window into the epoch of core formation. As we expect core formation to have been rate-limited by accretion during most of the major mass accumulation epochs of the silicate planets, ^{182}Hf-^{182}W provides an apparently unique source of potential information with which to test planetesimal coagulation models. Complexity arises in the context of large-scale giant-impact-type accretion events (mergers), in which planetary cores and mantles merge without chemically homogenizing (and thereby isotopically equilibrating). In the pure case of this mode of accretion, chronometric information in W isotopes in the final planetary silicate mantle approximates a mass-average over the differentiation histories of the pre-merged bodies, so the chronology of the late stages of hierarchical accretion series is not recorded. However, because giant impact events probably generate whole-mantle melting and mixing, the date of the last such event can in principle be constrained from the ^{146}Sm-^{142}Nd (silicate differentiation) chronometer (*cf.*, [2], & companion abstract by Jacobsen & Harper). In summary, W isotopes are capable of supplying information about the history of accretion (Fig. 1a,b) prior to any late stages of merger-type planet building.

^{182}W Measurements: W isotopic measurements by the negative thermal ionization mass spectrometry (NTIMS) method using WO_3^- beams were developed by Köppe (1989), Heumann *et al.* (1989) and Völkening *et al.* (1991) [3]. The first high precision W isotopic measurements of meteoritic W by NTIMS were reported by Harper *et al.* (1991) [4] as a comparison series of 12 runs each of standard tungsten and tungsten separated from the iron phase of the Toluca iron meteorite. Relative to a $^{183}W/^{184}W$ normalization, an apparent shift of -3.0±0.9 epsilon-units in $^{182}W/^{184}W$ was observed in the Toluca W relative to the standard (Fig. 2) with the $^{186}W/^{184}W$ ratio found to be normal within an uncertainty of ~±3 ε-units. After consideration of various possible sources of error (interferences and/or $^{18,17}O/^{16}O$ fractionation), the shift was concluded to be a real effect. It can be interpreted as a result of two possible processes: (i) neutron capture modification of the W isotopic composition during space exposure, or (ii) radiogenic growth of ^{182}W in the silicate portion of the Earth (= the high-Hf/W reservoir source of the standard) due to ^{182}Hf decay after removal of W to the Earth's core. In the latter case, Toluca W would approximate the non-radiogenic initial isotopic composition for $^{182}W/^{183}W$ in the solar system. In order to confirm the effect and study the fine structure of the non-radiogenic mass abundances of W from Toluca and other iron meteorites, we have developed a high precision multicollector technique for W isotopic measurements utilizing a 7-cup configuration allowing simultaneous monitoring of oxygen

INVESTIGATIONS OF THE ^{182}Hf-^{182}W SYSTEMATICS: Harper C. L. & Jacobsen S. B.

isotope fractionation and ReO_3^- interference (Figs. 3 & 4). Reproducibility for a suite of standard $^{182}W/^{183}W$ measurements normalized to $^{184}W/^{183}W$ is shown in Figure 5 and indicate an ~±1ε-unit level of precision. One measurement of Toluca W from a new separation is also shown. This measurement appears to confirm the finding of Harper *et al.* (1991) [3], but is imprecise due to a degradation of beam stability from impurity in the sample. Efforts are underway to obtain highest quality measurements with a new purified sample. **REFS:** [1] Harper C. L. Jr. (1993). *Meteoritics*, 28, 359; [2] Harper C. L. Jr. and Jacobsen S. B. (1992). *Nature*, 360: 728; [3] Köppe M. (1989). Ph. D. Chem. Thesis, Regensburg, F.R.G.; Heumann K. G. *et al.* (1989). *Proc. 37th ASMS Conf. Mass Spectrometry & Allied Topics*, p. 414; Völkening J. *et al.* (1991). *Int. J. Mass Spec. Ion Proc.*, 107: 361; [4] Harper C. L. *et al.* (1991). *LPS XXII:* 515.

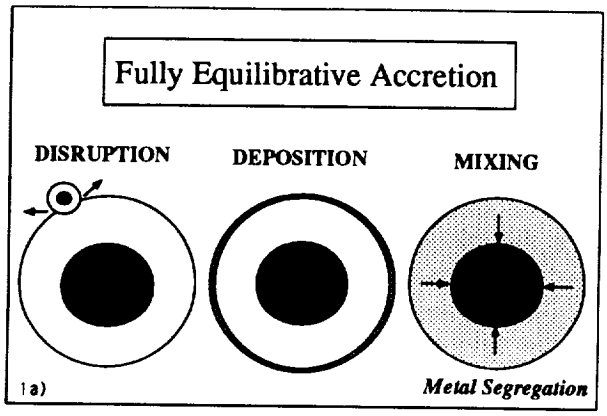

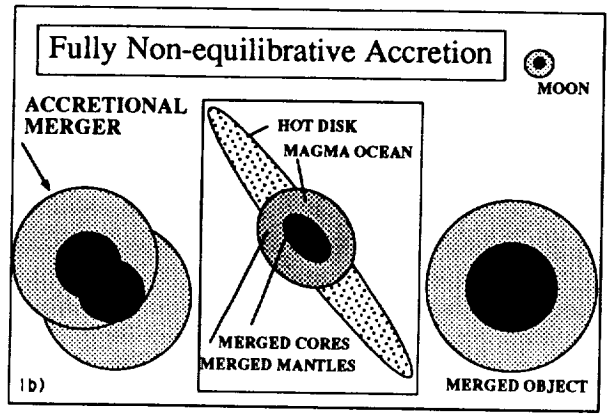

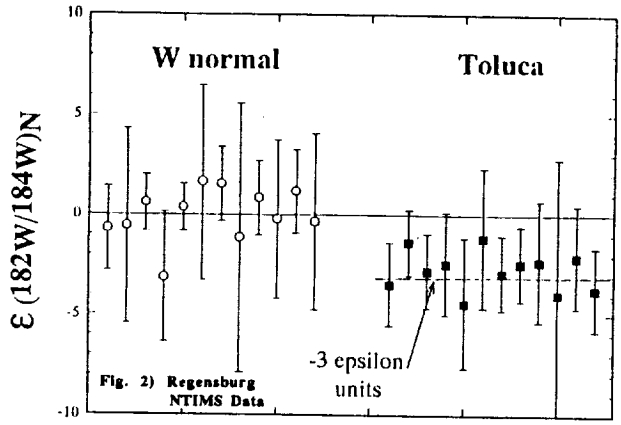

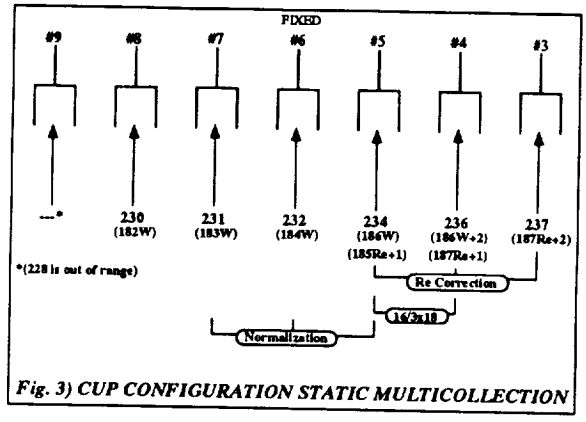

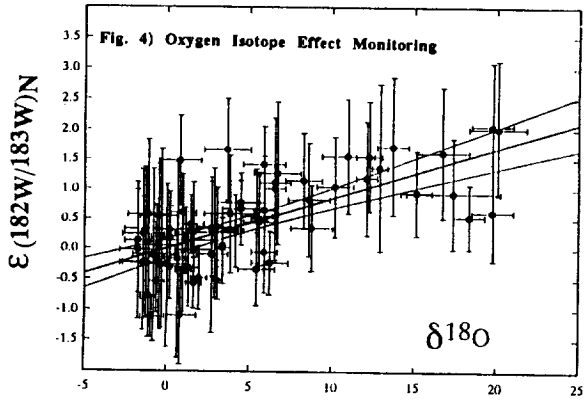

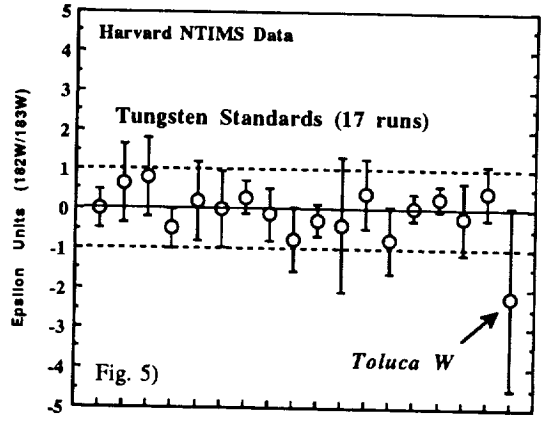

MARTIAN ATMOSPHERIC INTERACTION WITH BOLIDES: A TEST FOR AN ANCIENT DENSE MARTIAN ATMOSPHERE;

William K. Hartmann, PSI, Tucson AZ; Steffi Engel, Lunar and Planetary Lab, Univ. Ariz., Tucson AZ

The Magellan discovery of Venus' crater diameter distribution cutoff, due to atmospheric loss of small bolides, opens the door to using the size distribution of small Martian craters in ancient areas as a tool to search for the widely hypothesized, ancient, dense Martian atmosphere.

Melosh[1] looked at some aspects of this problem for the present Mars atmosphere, assuming ice, rock, and iron bolides. Under the assumptions of his calculations, he found that the smallest bolides to impact as effectively single bodies (making single or compound craters, instead of dispersed pits) were 66 to 24 m across, for a range of compositions from solid ice to iron, respectively. Thus, craters in dispersed clusters would be ≤ hundreds of meters across. However, this result assumed disruption of the bolide at 3 scale heights, and Melosh believes actual disruption for Mars would be much lower, meaning that dispersed clusters from these types of bolides would be much smaller, if visible at all (Melosh, private communication, 1994).

We have identified possible candidates for the fragmentation events in the form of isolated clusters of well-preserved craters. Individual pits in these clusters are typically hundreds of meters across and spread over 9 km (Fig. 1). These clusters have been noted previously by many workers (Barlow, Tanaka, private communications, 1993), but there has been little systematic study of them. They appear to have characteristics for breakup of very weak bodies, such as heavily fragmented, loosely bound icy cometary or carbonaceous bolides that have nearly zero tensile strength.

Existing work does not explain fully the variations in crater-cluster forms from planet to planet. Venus shows "cloverleaf" compound and misshapen craters; Earth shows quasi-elliptical fields of more isolated craters such as at Henbury; Mars shows tight clusters, rarely highly elliptical, according to our preliminary survey. The idea that Martian clusters might be limited to comet impacts presents an interesting opportunity to separate different types of impactors. At any rate, the existence of the Martian clusters encourages further application of Mars crater/atmosphere effects to problems of the planet itself.

The most important application is to use the crater size distribution to search for evidence of the widely hypothesized ancient dense Martian atmosphere, estimated by various workers at pressures as high as 100 or 1000 mb, or more.

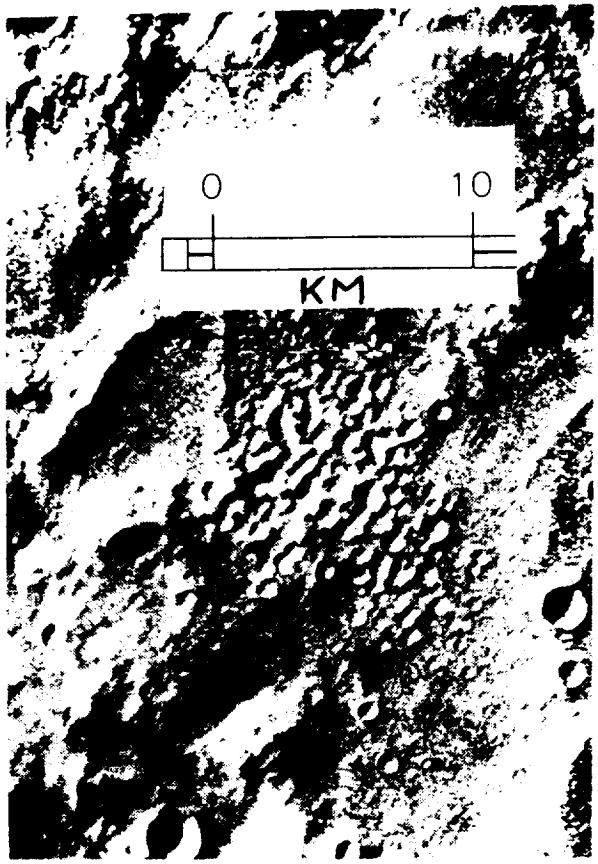

Fig. 1. Isolated crater cluster in the Ma'adim Vallis area of Mars. Such clusters may be signatures of atmospheric breakup of weak, cometary bolides.

MARTIAN ATMOSPHERIC INTERACTION: Hartmann, W.K. and Engel, S.

We have completed new, preliminary calculations of the minimum sizes of bolides that would penetrate hypothetical Martian atmospheres. We let surface pressures range from 6 to 1000 mb, and assumed projectiles of various strengths (icy comets; carbonaceous bodies; coherent chondrites; irons). The calculations are based on a program kindly provided by Chris Chyba, as published by Chyba *et al.*[2], and modified for Mars by one of us (SE). The results are used to estimate the position and shape of the turndowns in the crater size distribution, according to assumed fractions of bolides of different composition. Figure 2 shows the results, and predicts an important result at larger crater sizes than might have been expected.

As pressure rises from 6 mb to 100-300 mb, icy and carbonaceous bolides are lost, but because these may amount to < half the total population, the total downturn from these losses may be < a factor 2, hard to detect in view of Martian erosion effects and statistical uncertainties in the counts. However, for an atmosphere greater than a few hundred mb, stony bolides would also break up, and a unique offset by a factor 20-30 would develop in the crater diameter distribution at D ~ .5 to 4 km, due to loss of all but the rare iron bolides. This is shown in Fig. 2.

A careful search for this offset may allow us to detect evidence of a dense atmosphere during certain ancient time periods. This could put important constraints on some models of Martian history, such as models invoking ancient shorelines or global oceans in northern lowlands.

Subtraction of crater populations of younger areas from those of older areas would produce the diameter distributions created during specified early eras. Global detection of the predicted offset could establish the existence of a dense ancient atmosphere. Alternatively, failure to detect it could yield upper limits on the pressure of the atmosphere contemporaneous with the oldest surfaces. The main problem is to distinguish the predicted offset from erosional losses of ancient small craters; however the atmospheric effect would be global, while erosional losses could be local and variable; and the predicted offset is different in character than that predicted by Martian erosional models.

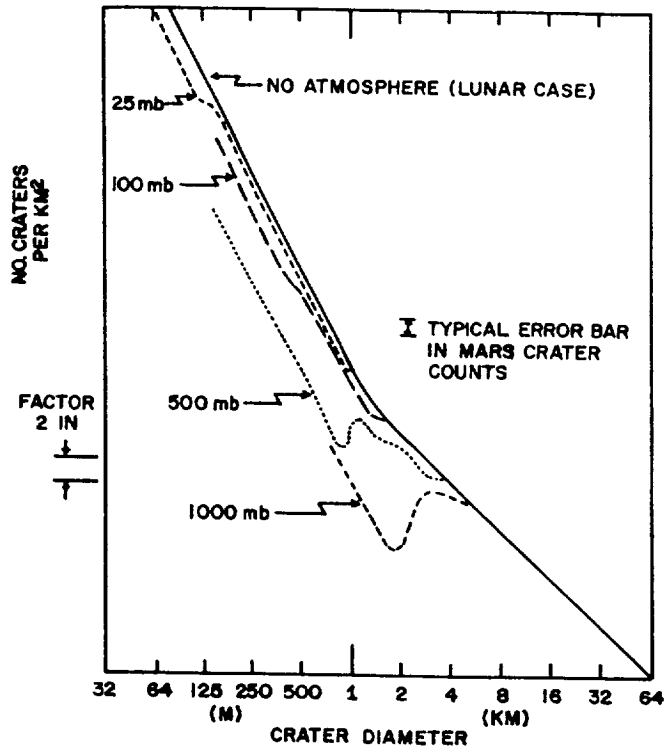

Fig. 2. Predicted shape of crater size distribution for different ancient Martian atmospheric surface pressures. A major kink appears at surface pressures > ~300 mb (see text).

We are currently seeking support to refine the calculations and conduct the necessary search in the cratering records.

References

[1]Chyba, C. and others (1993) *Nature*, **361**, 40.
[2]Melosh, H. J. (1989) *Impact Cratering* (NY: Oxford U. Press).

MELT INCLUSIONS IN PAT91501: EVIDENCE FOR CRYSTALLIZATION FROM AN L CHONDRITE IMPACT MELT. R. P. Harvey, Department of Geological Sciences, University of Tennessee, Knoxville, TN 37996-1410, E. Roedder, Department of Earth and Planetary Sciences, Harvard University, Cambridge, MA 02138.

The recently recovered Antarctic specimen PAT91501 (PAT) was originally classified as an L7 chondrite, based on mineral and oxygen isotope compositions and a macroscopic resemblance to the Shaw L7 chondrite [1]. Unlike Shaw, however, PAT is decidely igneous in texture, exhibiting both cumulate and poikilitic areas. In cumulate areas an equigranular contact-framework of nearly euhedral olivine grains surrounds interstitial spaces filled by plagioclase, pyroxenes, chrome spinel and several minor phases, while in poikilitic areas large orthopyroxene oikocrysts (rimmed with augite) surround olivine chadacrysts [2,3]. These textures strongly suggest that PAT crystallized from a melt. Further evidence suggests that this melt was of ordinary chondrite composition, and was probably impact-derived. PAT contains large (>1 cm) globular metal/sulfide inclusions, indicating that metal and sulfide liquids have segregated from an immiscible silicate liquid, as is seen in experimental melts of ordinary chondrite starting materials [4, 5]. The modal abundances of major minerals in PAT are similar to those expected during rapid, fractional crystallization from a melt of L-chondrite starting composition [6]. The compositions of spinel grains in PAT are distinct from those found in ordinary chondrites, but are identical to those that would crystallize from an L-chondrite melt [6].

Even given the evidence in favor of an origin for PAT as a crystallized product of an ordinary chondrite impact melt, the cumulate nature in PAT makes it difficult to directly assess the composition of the melt from which it crystallized. Luckily, olivine grains in PAT contain numerous inclusions that can be used to reconstruct the conditions present at the time of crystallization. Preliminary studies on the abundant inclusions in a large olivine grain from PAT (Fig. 1) show that two types are present; inclusions containing only vapor (primary vapor inclusions), and glassy inclusions containing the following major solid phases in varying proportions: high alkali glass; moderate alkali glass of high Si-Al composition; Fe-Ni metal; and Fe sulfide. Glass inclusions also contain small unanalysed solid daughter phases and a vapor bubble comprising 2-10 vol.%. These bubbles result from the combination of two processes on cooling: thermal contraction of the enclosed melt, and volume decrease on crystallization of olivine onto the inclusion walls, and hence are quite different in origin than the primary vapor inclusions. The latter require the existence of a vapor phase at the time of crystallization of the host olivine with a vapor pressure exceeding the sum of pressure from surface tension and depth of burial. The mm- to cm-sized vesicles in PAT were formed by larger volumes of the same vapor phase.

The microscope crushing stage [7] provides an estimate of the gas pressure now present in vapor bubbles within crystals. The vapor bubbles within the glass inclusions now contain a vacuum. We suggest that the vapor phase present at the time of formation, for both the primary vapor inclusions and the bubbles within glass inclusions, consisted of alkali vapors which then condensed to yield a vacuum. We cannot exclude the possibility that other condensable gases such as H_2O were present, or, as an unlikely alternative, a gas such as methane that is highly soluble in the immersion oil used on the crushing stage.

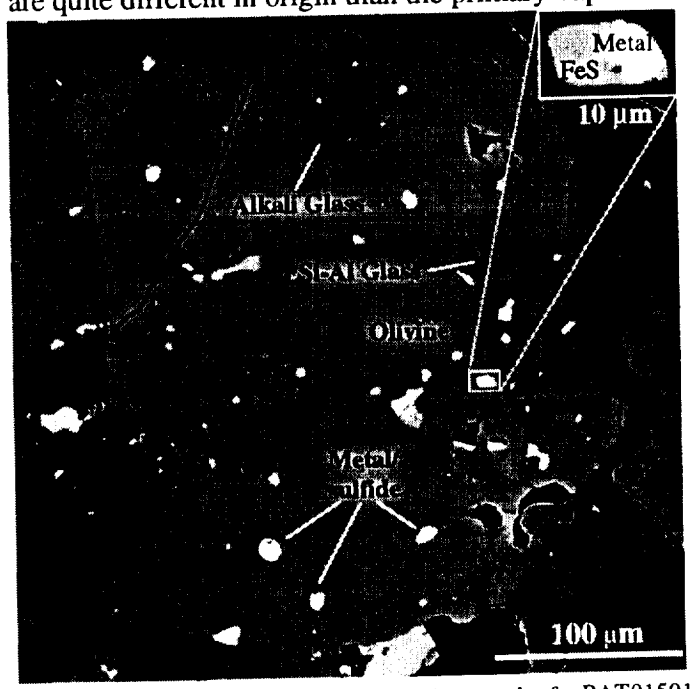

Figure 1. Backscattered electron photomicrograph of a PAT91501 olivine grain with abundant inclusions.

MELT INCLUSIONS IN PAT91501: Harvey R.P. and Roedder E.

We assume that some mixture of olivine (which plated out on the walls of the inclusion) and the four major inclusion phases (alkali-rich glass, Si-rich glass, metal and sulfide) will represent a parental magma for PAT. The minor phases, which combined account for <1% of the surface area of the grain studied, were not used in the model. Mass-balance calculations, following the methods of [8, 9], were used to calculate the parental magma composition. A system of mass-balance equations was constructed, including both exact and inexact constraints such as partition coefficients of major elements between olivine and coexisting liquid. These equations were weighted to give a high relative importance to the mass balance of the system and a low relative importance to the starting conditions (the modal abundances of the inclusion phases and the amount of admixed olivine).

Inclusion phase compositions and the results of the mass balance calculations are shown in Table 1. In general, the calculated parental magma compositions are very similar in bulk composition to an L chondrite, with a few distinctions. The PAT parental melt is slightly richer in FeO, SiO_2, Al_2O_3 and the alkalis (combined Na_2O and K_2O) than the bulk L chondrite composition, as might be expected for a magma generated by a high degree of partial melting. In addition, the PAT parental melt appears deficient in CaO, suggesting either that the minor inclusion phase apatite may have been under-represented in the model, or that crystallization of some Ca-rich phase preceded trapping. The phase relationships between the two presumbably coexisting, compositionally distinct Si-rich melts (as well as the pre-existing Si-poor chondritic melt) are unknown at this time.

The melt trapped during crystallization of the PAT olivine grain studied here supports the other evidence which suggests that this meteorite, and some related meteorite lithologies, are derived from a high degree of partial melting or total melting of ordinary chondrite material, presumably by impact processes[6]. The existence of lithologies like PAT suggest that phase segregation and differentiation may be relatively widespread at the surface of larger meteorite parent bodies, and can be invoked to explain the observed enhanced presence of olivine suggested by some asteroid reflectance spectra [6, 10].

Table 1. Composition of PAT91501 inclusion phases and calculated parental melt. Average L chondrite composition from [8].

	Major inclusion phases					Calculated	Avg. L
	Host olivine	Alk.-rich glass	Si-rich glass	FeS	Metal	PAT91501 melt	chondrite from [11]
Vol.% Incl.	63.2%	14.6%	8.9%	7.1%	6.2%	--	--
SiO_2	37.86	64.79	75.54	0.00	0.00	40.06	39.72
Al_2O_3	0.01	21.48	18.50	0.00	0.00	4.78	2.25
MgO	37.88	0.05	0.04	0.00	0.00	23.95	24.73
CaO	0.04	2.45	0.18	0.00	0.00	0.54	1.85
FeO	23.69	0.72	0.76	0.00	0.00	15.14	14.46
Na_2O	0.02	9.76	3.47	0.00	0.00	> 1.90*	1.06*
K_2O	0.00	0.63	0.74	0.00	0.00		
Fe	0.00	0.00	0.00	62.91	88.38	5.54	7.03
Ni	0.00	0.00	0.00	0.03	10.14	0.64	1.24
S	0.00	0.00	0.00	36.94	1.43	7.13	5.76
Total	99.50	99.88	99.23	99.88	99.95	99.68	98.10
Comp.	$Fa_{26.3}$	Or_4Ab_{85}				*Combined Na_2O, K_2O	

REFERENCES: [1] Mason B., Marlow R. and Score R. (1992) *Antarctic Meteorite Newsletter* **15(2)**, 30. [2] Mittlefehldt D. W., Lindstrom M. M. and Field S. W. (1993) *Meteoritics* **28**, 401-402. [3] Harvey R. P. and McSween H. Y. Jr. (1993) *Meteoritics* **28**, 360. [4] Takahashi, E. (1983) *Proc. 8th Symp. Ant. Met., Mem. NIPR Spec. Issue* **30**, 168-180.[5] Taylor J. G. (1992) *J. Geophys. Research* **97**, E14717-14726. [6] Harvey R.P. (1994) *Meteoritics*, submitted. [7] Roedder E. (1970) *Schweitz. Mineral. Petrog. Mitt.* **50(1)**, 41-58. [8] Harvey R.P. and McSween H.Y. Jr. (1992) *Earth Planet. Sci. Letters* **111**, 467-482. [9] Harvey R. P., Wadhwa M., McSween H.Y. Jr., and Crozaz G. (1993) *Geochim. Cosmochim. Acta* **57**, 4769-4784. [10] McSween H.Y. Jr., Bennett M.E. III and Jarosewich E. (1991) *Icarus* **90**, 107-116. [11] Jarosewich E. (1990) *Meteoritics* **25**, 323-337.
This work supported by NASA grant NAGW-3621 to H.Y. McSween, Jr.

SPECTRAL AND RADAR STUDIES OF THE SCHILLER-SCHICKARD REGION OF THE MOON; B. R. Hawke, D. T. Blewett, Planetary Geosciences/SOEST, Univ. of Hawaii, 2525 Correa Rd., Honolulu, HI 96822; B. A. Campbell, CEPS/National Air & Space Museum, Washington, DC 20560

We have been conducting a series of remote sensing studies of the Schiller-Schickard region. The major goals of the research are to determine the composition of geologic units, elucidate the geologic history of this complex area, and to examine the extent of local mixing induced by secondary cratering from Orientale. This report serves to present the most recent results of spectral and multispectral analysis, as well as to discuss preliminary findings of radar studies of the region. Data employed include near-IR reflectance spectra, multispectral images in the extended visible, and 3.8-cm, 70-cm, and 7.5-m radar images.

INTRODUCTION: The Schiller-Schickard (SS) region is located in the southwestern nearside highlands, south-southwest of the Humorum Basin and southeast of Orientale. A variety of interesting features are found in the region. Schickard (~44° S, 55° W) is a large (227 km diam.) pre-Imbrian crater whose floor contains mare basalt patches and a light plains unit [1]. Schiller crater (~52° S, 39° W) is elongated and is superimposed on an outer ring of the Schiller-Zucchius basin. The area around Schiller and Schickard contains a number of dark-halo impact craters (DHC's). Several previous studies have helped to decipher the complicated geologic history of the region. Near-infrared reflectance spectra were used [2, 3] to confirm the hypothesis [4] that DHC's formed when ancient mare basalts were excavated from beneath plains units with highlands affinities emplaced by the Orientale impact event. A buried mare deposit of this type is referred to as a cryptomare. Detailed spectral analysis [5] addressed the composition of regional highlands and light plains. The presence of a mare basalt component in the light plains within Schickard was confirmed, providing evidence for local mixing [6] by Orientale secondary-forming projectiles. Mixing model analysis of spectra and multispectral images [7, 8] determined that the proportion of mare basalt in the light plains is consistent with the ballistic erosion model of secondary cratering [6]. Additional information on the SS region has been provided by data from the Galileo spacecraft's first lunar encounter [9, 10]. A number of unresolved questions remain, including (1) the composition and nature of the plains units, (2) the role of secondary cratering in the formation of the distal deposits of the Orientale Basin, and (3) the origin of radar anomalies in the region.

DATA and ANALYSIS: Approximately 40 near-infrared reflectance spectra (0.6-2.5 μm) for a variety of features in the region have been collected and analyzed. The spectra were recorded with Planetary Geosciences instruments on University of Hawaii telescopes at Mauna Kea Observatory. Observational techniques and data reduction have been previously described [11]. Quantitative analysis of spectra was performed [12] to derive mineralogical information. Additionally, spectral endmembers were identified and mixing relationships studied by applying principal components analysis (PCA) [13]. Linear mixing of spectral endmembers was assumed [14].

In order to gain extended spatial coverage, multispectral images from a CCD imaging survey of the Moon [15] were utilized. The data set consists of two image cubes of the SS region, each with 12 spectral bands in the extended visible portion of the spectrum (0.4-0.99 μm). Interactive analysis of the image cubes was performed using the SIPS software [16]. Endmember areas within the scene were defined. Linear unmixing analysis produced endmember abundance and error images. The original images and endmember abundance images have been reprojected by defining tie points to the U. S. Geological Survey shaded relief airbrush map of the Moon.

The 3.8-cm radar data obtained by Zisk and coworkers [17], as well as 70-cm and 7.5-m radar images presented by Thompson [18, 19] were examined for this study. The data have been digitized and reprojected, and the 70-cm and 7.5-m images superimposed on the U. S. G. S. airbrush map for analysis.

RESULTS and DISCUSSION: The spectral, multispectral imaging, and radar findings are described below.

A. Spectral and Multispectral Imaging. Mapping of the spectra into principal components space revealed four endmember spectral types: fresh and mature highlands, and fresh and mature

mare basalt. Spectra of areas consisting of mixtures of these fall between the four endmembers in PC space. The distance of a spectrum from an endmember in PC space can be used to calculate the relative contribution of that endmember to the mixture. Mixing results indicate that spots on the Schickard light plains contain from ~40% to as much as 70% mare basalt. Two spectra for the Schiller Plains, a dark area west of Schiller [20], were analyzed with this technique. The model indicates that the proportion of mare basalt in the Schiller Plains is >80%, consistent with the interpretation [2] that the Plains are a post-Orientale mare surface which has received a small admixture of highlands material by lateral transport from nearby highlands craters. The interior of Schiller contains a light plains deposit. Mixing analysis on a spectrum of this floor material shows that ~70% mare basalt is present.

These findings have been confirmed and extended by mixing analysis conducted on the image cubes. The endmember images reveal that the Schickard light plains contain an average mare abundance of ~45%. The Schiller Plains have high mare contents, exceeding 75% in places, with an average of ~65%. Most of the floor of Schiller has a mare basalt contribution in the range 25-50%, though patches of higher mare content, up to 75%, do occur.

The amount of mare basalt in the Schickard light plains is a measure of the degree to which ejecta from Orientale affected the pre-existing terrain in the SS region. The ballistic erosion theory [21] allows the ratio of mass excavated by a secondary crater to the mass of the secondary-forming projectile to be calculated, given the secondary crater diameter, distance from the primary, and angle from the surface normal at which the secondary-forming fragment struck the surface. For typical Orientale secondaries near Schickard and assuming a 75° impact angle, this ratio is ~2, meaning that the fraction (excavated mass/(excavated mass + impactor mass)) is about 0.67. Thus ~67% local material should be expected. This is in reasonable agreement with our findings of 45% for the average proportion of basalt in the Schickard light plains. Considering that the pre-Orientale mare may have been thin and discontinuous, and that cratering efficiencies may be lower [22] than assumed in the Oberbeck model, we take this result as strongly supportive of the local mixing hypothesis.

B. Radar Studies. The Schiller-Schickard region exhibits a relatively uniform appearance in both the polarized and depolarized 3.8-cm radar images. No areas with anomalously low returns have been identified, and even the ponds of post-Orientale mare basalt are not distinct in the 3.8-cm data. The absence of low returns for the dark portions of the Schiller Plains appears to rule out the existence of a dark mantle of pyroclastic origin for this area [20]. The SS region contains several areas that exhibit low returns on the polarized and depolarized 70-cm radar images. The mare ponds in the region correlate with some of the areas with low backscatter. Other areas with anomalously low 70-cm returns are associated with certain portions of the SS cryptomare. In general, the northern portions of the cryptomare exhibit higher values while the low returns are concentrated in the south. In particular, low 70-cm backscatter values are associated with pre-Orientale mare deposits that contain Orientale secondary clusters. Much of the SS region exhibits low values in the 7.5-m radar data set. The lowest values are exhibited by mare and cryptomare units in Schickard and southwest of Schiller. However, much of the cryptomare surface has low 7.5-m returns. The presence of a substantial mare basalt component in the surface layers of the cryptomare may be, in part, responsible for the 70-cm and 7.5-m anomalies.

References: [1] T. Karlstrom (1974) U. S. Geol. Surv. Map I-823. [2] B. R. Hawke & J. F. Bell (1981) *Proc. LPSC 12th*, 665. [3] J. F. Bell & B. R. Hawke (1984) *J. Geophys. Res.* **89**, no. B8, 6899. [4] P. H. Schultz & P. D. Spudis (1979) *Proc. LPSC 10th*, 2899. [5] D. T. Blewett *et al.* (1992) *LPS XXIII*, 123. [6] V. Oberbeck (1975) *Rev. Geophys. Space Phys.* **13**, no. 2, 337. [7] D. T. Blewett *et al.* (1993) *LPS XXIV*, 133. [8] D. T. Blewett & B. R. Hawke (1993) *Meteoritics* **28**, no. 3, 325. [9] M. Belton *et al.* (1992) *Science* **255**, 570. [10] J. W. Head *et al.* (1993) *J. Geophys. Res.* **98**, no. E9, 17149. [11] T. B. McCord *et al.* (1981) *J. Geophys. Res.* **86**, no. B11, 10883. [12] P. G. Lucey *et al.* (1986) *Proc. LPSC 16th*, D344. [13] M. O. Smith *et al.* (1985) *Proc. LPSC 15th*, C797. [14] R. B. Singer & T. B. McCord (1979) *Proc. LPSC 10th*, 1835. [15] G. Neukum *et al.* (1991) *LPS XXII*, 971. [16] F. A. Kruse *et al.* (1993) *Rem. Sens. Environ.* **44**, 145. [17] S. Zisk *et al.* (1974) *Moon* **10**, 17. [18] T. Thompson (1987) *Earth, Moon, Planets* **37**, 59. [19] T. Thompson (1978) *Icarus* **36**, 174. [20] T. Offield (1971) U. S. Geol. Surv. Map I-690. [21] V. Oberbeck *et al.* (1975) *Moon* **12**, 19. [22] P. Schultz & D. Gault (1985) *J. Geophys. Res.* **90**, no. B5, 3701.

91-91 HR
3603

ATMOSPHERIC EFFECTS ON THE MAPPING OF MARTIAN THERMAL INERTIA AND THERMALLY DERIVED ALBEDO; J.N. Hayashi[1], B.M. Jakosky[1], R.M. Haberle[2]; [1]Laboratory for Atmospheric and Space Physics, University of Colorado, Boulder, CO 80309, [2]NASA/AMES Research Center, Moffet Field, CA 94035

The most widely used thermal inertia data for Mars assumes the atmospheric contribution is constant and equal to 2% of the maximum solar insolation [1,2,3]. In 1991, Haberle and Jakosky [4] investigated the effect of including a dusty CO_2 atmosphere and sensible heat exchange with the surface on thermal inertia. We recently [5] utilized Haberle and Jakosky's coupled surface-atmosphere model to investigate the effects of such an atmosphere on the thermally derived albedo. The thermally derived albedo is the albedo which, together with the thermal inertia, provides model surface temperatures which best match the observed temperatures. We present new maps of thermal inertia and thermally derived albedo which incorporate dust opacities derived from IRTM data.

We ran the coupled surface-atmosphere model for a series of latitudes, albedos, thermal inertias, pressures, and dust opacities to obtain minimum and maximum temperatures. Then, using the Palluconi and Kieffer [3] map of thermal inertias and thermally derived albedo, we ran a diurnal thermal model assuming a constant atmospheric contribution of 2% of the maximum solar insolation to obtain minimum and maximum temperatures. Pressure was obtained, to first order, from topographic maps. The dust opacity was approximated by averaging the dust opacities [6] for the period between Ls=345°-125°, which is the period used by Palluconi and Kieffer to obtain their thermal inertias and thermally derived albedos. The 2% minimum and maximum temperatures, pressure, and dust opacity were then used to do an interpolation and obtain the coupled model thermal inertias and thermally derived albedos.

The difference between the 2% model and the coupled model thermal inertias and thermally derived albedos are relatively small for most of the planet. The differences between the two models are largest in regions with either high dust opacities, such as Acidalia, Chryse, and Hellas Planitias, or significant topographic relief, such as Valles Marineris, Olympus Mons, and the Tharsis Volcanoes. It is interesting to note that some of the most geologically interesting regions as well as the two lander sites are located within the regions which show the largest difference between the two models.

Figure 1 is a two-dimensional histogram of the coupled model versus the 2% model thermal inertias. The larger the circle, the more map pixels which have the corresponding coupled model and 2% thermal inertias. The coupled model thermal inertias are slightly smaller than the 2% thermal inertias, with the mean difference between the two thermal inertias being approximately 40 $Wm^{-2}s^{1/2}K^{-1}$. This is in agreement with the results presented in [4] which indicated increasing dust opacity would lead to coupled model thermal inertias which are smaller than the 2% model thermal inertias.

Figure 2 is a two-dimensional histogram of the coupled model versus the 2% model thermally derived albedos. The albedos for the two models are very similar, although there is some excursion from a one-to-one relationship at low albedos. The effects which were included in the coupled model were insufficient to account for the differences between the 2% thermally derived albedo and the IRTM measured albedos.

References. [1] Kieffer H.H. et al. (1973) *JGR*, 78,4291. [2] Kieffer, H.H. et al. (1977) *JGR*, 82, 4249. [3] Palluconi F.D. and Kieffer H.H. (1981) *Icarus*, 45, 415. [4] Haberle R.M. and Jakosky B.M. (1991) *Icarus*, 90, 187. [5] Hayashi J.N. et al. (1993) *BAAS*, 25, 1039 (abstract). [6] Martin T.Z. and Richardson, M.I. (1993) *JGR*, 98, 10941.

Figure 1

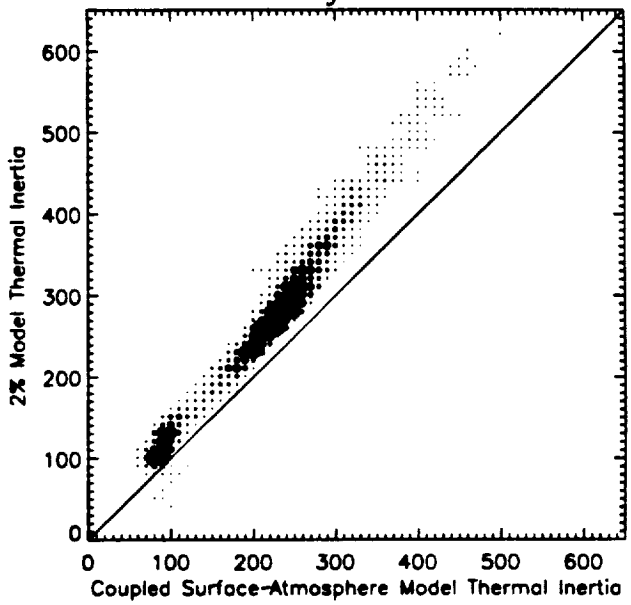

Figure 2

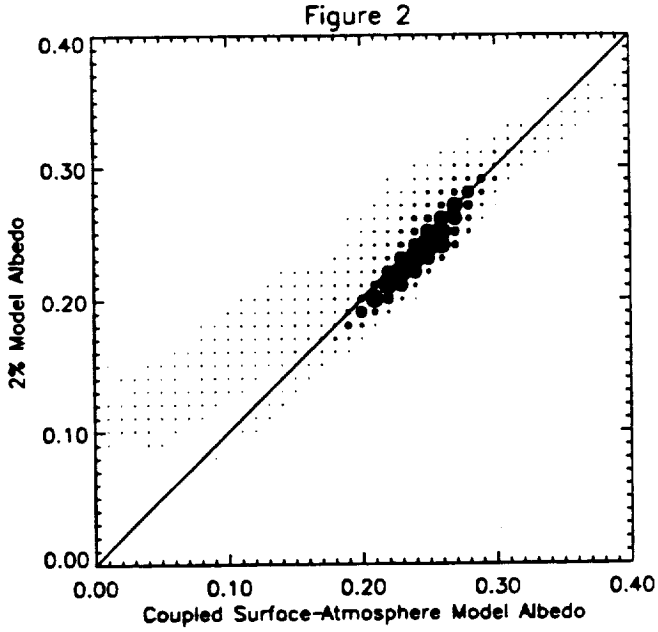

EFFECTS OF FINE PARTICLES (<25 μm) ON REFLECTANCE SPECTRA FROM 0.3 TO 25 μm. J. E. Hays and J. F. Mustard, Dept. Geol. Sci., Brown University, Providence RI, 02912

Introduction: One of the significant challenges to the use of visible-infrared spectroscopy for soil compositional analysis is separating the effects of particle size from composition. Weathering processes on most planetary bodies produce particulate surfaces where typical particle size distributions are dominated volumetrically by large particles but numerically by small particles. These fine particles dominate the spectral properties through increases in surface and volume scattering. Although there have been many studies documenting the effects of particle size on spectra (e.g. 1,2), there have been few studies to investigate the effects of very fine particles on reflectance spectra over the extended wavelength range from 0.3 to 25 μm. In this paper, we present the first results of a detailed investigation of the effects of particles <25 μm in size on the reflectance spectra of olivine over the wavelength range of 0.3 to 25 μm. Two fundamental results of this analysis are that the wavelength position of the transparency feature decreases as a function of decreasing particle size, and as the wavelength approaches the dominant particle size of each separate, the spectra exhibit a sharp decline in intensity.

Procedures: The sample used in this study is a fosteritic olivine (Fo 94) from Jackson County, North Carolina. The sample was first disaggregated and then the contaminants were removed by visual inspection. At this stage, many olivine grains possessed a thin rind of serpentine. This was removed through repeated light grinding and sieving until all the particles >100 μm were visually clean. The clean olivine was then ground to a fine powder with a mortar and pestle. A combination of dry and wet (ethanol) sieving procedures were utilized to acquire 18 grams of clean olivine with a particle size <25 μm. The 18 g of sample was professionally sieved by the Gilson Company into five particle size separates at 5 m intervals: 0-5, 5-10, 10-15, 15-20, and 20-25 μm. The actual size distribution for the separates were measured using an Elzone 280 PC Particle Size Analyzer (See Figure 1 for results). The spectra of each size separate was measured at the RELAB Facility at Brown University, from 0.3 to 2.6 μm with RELAB and from 0.9 to 25 μm with a Nicolet 740 FTIR Spectrometer. The Nicolet data was scaled and merged to the RELAB data at 1755 nanometers. These merged data are presented in Figure 2.

Results: The wavelength position of the spectral features related to compositional and structural properties of olivine were found to be largely invariant as a function of particle size. These include crystal field absorptions near 1.0 μm, the Christiansen feature and reststrahlen bands between 8.5 and 12.0 μm, and overtones and combinations of overtones of internal and lattice mode vibrations between 4 and 6 μm. This confirms the invariance of these primary diagnostic spectral features to the very finest particle size used in this analysis.

A small number of spectral features, however, do vary in wavelength as a function of particle size. The most notable of these is the transparency feature (3), near 13 μm. This feature exhibits a systematic shift in the position of the peak reflectance from 13.07 to 12.37 μm as particle size decreases (Figure 3). This shift in position was confirmed through repeated measurements with the biconical attachment on both on-axis and off-axis modes. In addition, the spectral contrast of the transparency feature changes with particle size. Initially, this feature increase in contrast as particle size decreases until a maximum contrast is reached at the 10-15 μm size range, then decreases again to the finest particle sizes (See Figure 2b).

Throughout the spectra shown in Figure 2, exists numerous changes in spectral contrast and intensity as particle size decreases. Most of these can be understood through basic principles of scattering and absorption (1, 2, 4). The two smallest size fractions (0-5 and 5-10 μm), however, exhibit unusual behavior in the near and mid infrared portion of the spectrum. The spectra of the 0-5 μm size fraction is the brightest in the visible and comparable to other spectra in the near infrared, until approximately 4 μm. At this wavelength, the intensity of the spectra begins to dramatically decrease, reaching a minimum shortwards of the Christiansen feature. The same behavior is observed for the 5-10 μm fraction, except the decrease in intensity occurs at a longer wavelength (6.5 μm). As the particle size of a surface becomes comparable to, and smaller than the wavelength of light, changes are expected in how particles and particulate surfaces scatter light. Mie theory provides a tool for determining the wavelength that this should occur for spherical

particles. Hapke (1993) calculated with Mie theory that extinction efficiency undergoes a rapid decrease when the parameter (n-1)X decreases to values less than approximately 2 (n is the index of refraction, and $X=(\pi D)/\lambda$, where D is particle diameter and λ is wavelength). Assuming a an index of refraction of 2.0 and the numeric mean for the particle size separates from the lab, we calculated the wavelength predicted by (n-1)X=2. We found that for the 0-5 μm separate, the expected wavelength is 4.4 μm, and for the 5-10 μm separate, the expected wavelength is 7.1 μm. These calculated diameters are comparable to wavelengths where we qualitatively identified the onset of rapid decrease in reflectance.

Conclusions: The narrow particle size separates for particles < 25 μm in size allows us to investigate the effects of decreasing particle size on reflectance spectra from 0.3 to 25 μm. The most useful observation is that the wavelength of the transparency feature is not constant as particle size becomes very small. Therefore the use of the wavelength position of the Christiansen and transparency features as diagnostic indicators of composition (e.g. 5, 7) may not apply to samples and natural systems dominated by small particles. We are continuing these investigations with other materials and to further understand the physical processes occurring in the spectra of very fine particle sizes.

References: (1) Salisbury et al (1992) Infrared (2.1-25 μm) Spectra of Mineral, Johns Hopkins University Press, Baltimore, Maryland; (2) Pieters (1983), JGR, 88, 9534-9544; (3) Salisbury and Wald (1992) Icarus, 96, 121-128; (4) Clark and Roush (1984), JGR, 89, 6329-6340; (5) Salisbury (1993) Remote Geochemical Analysis, Pieters and Englert ed., Cambridge University Press, Cambridge; (6) Hapke (1993), Theory of Reflectance and Emittance Spectroscopy, Cambridge University Press, Cambridge; (7) Salisbury and Walter, (1989) JGR, 94, 9192-9202.

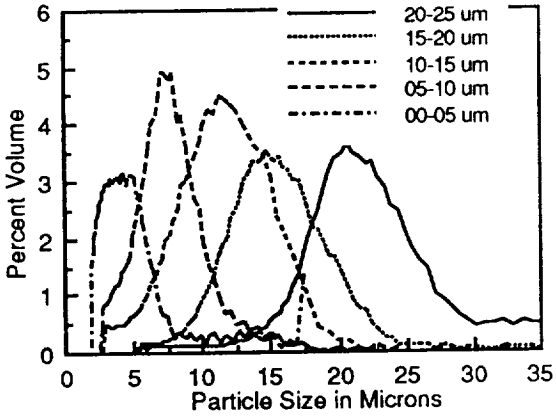

Figure 1. Distribution of particle size based on volumetric measuments.

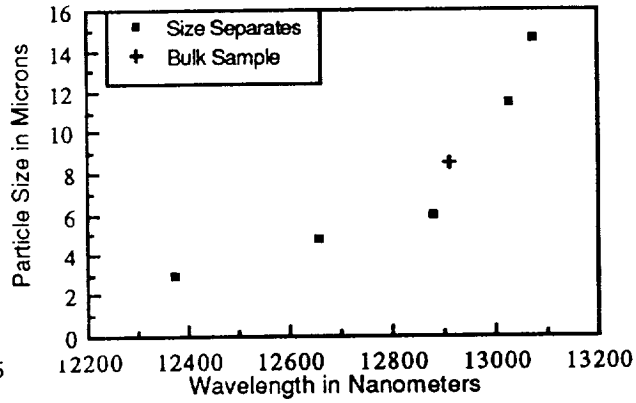

Figure 3. Wavelength position of peak reflectance of the transparency feature as a function of particle size.

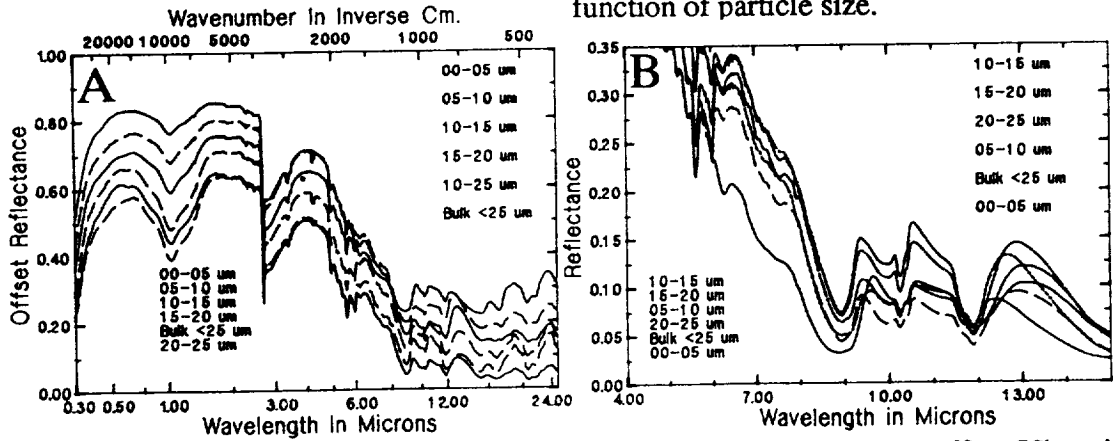

Figure 2. (a) Reflectance spectra of size separates and bulk sample. Spectra offset 5% veritically for clarity. (b) Detail of reflectance spectra in the mid infrared of size separates and bulk sample. Note the shift in postion of the transparency feature near 13μm with decreasing particle size.

LARGE IGNEOUS PROVINCES: A PLANETARY PERSPECTIVE: James W. Head, III, Department of Geological Sciences, Brown University, Providence, RI 02912 USA

Attention has recently been drawn to large igneous provinces on Earth, which are defined as regions characterized by transient large-scale intrusive and extrusive activity, including continental flood basalt (CFB) provinces (e.g., the Deccan Traps), volcanic passive margins (e.g., the Vøring Margin), oceanic plateaus (e.g., the Ontong Java Plateau), ocean basin flood basalts (e.g., the Carribean Flood Basalts), and large seamount chains (e.g., Hawaiian-Emperor) (1). Commonly analyzed separately in the past, recent studies (2, 3) have shown that there are important temporal, spatial, and compositional relationships among terrestrial large igneous provinces, informally referred to as LIPs.

These studies, and numerous others that document individual occurrences, show that the genesis and evolution of LIPs are closely linked to mantle dynamics, that LIPs represent major global events (large volumes of lava and associated intrusives are commonly produced in short episodes, and their emplacement had potentially major effects on the global environment), and that emplacement of some LIPs may be related to changes in rate and direction of plate motion. There is a possible episodicity in their formation but modification and destruction of older examples, and oceanic cover of others, makes this difficult to determine. Although several models have been proposed for the emplacement of LIPs (primarily associated with mantle plumes)(4,5,6), these models are not yet well constrained by observations. At present only a limited, but growing, amount of quantitative data is available to constrain associated mantle and crustal processes, to constrain LIP dimensions, durations, rates of emplacement, crustal structure, and relationship to tectonism, and to reliably predict environmental effects of LIP formation.

Large igneous provinces are also common on the terrestrial planets other than the Earth (7) and their presence, characteristics, and geologic and temporal settings offer a potentially important perspective for LIPs on Earth. For example, unlike the Earth, the majority of which is covered by water and virtually unknown at high resolution, *global imaging coverage* exists for the solid surface of the Moon and Mars, and Magellan has imaged over 98% of Venus at ~200 m resolution. In addition, *exposure and preservation* are excellent due primarily to fewer erosional agents, minimal erosional rates, and relatively stable lithospheres. Stable lithospheres also mean that *longer time intervals* are available for study. The age of two-thirds of the Earth's surface (the ocean basins) is less than 5% of the age of the planet; the majority of the surface of the Moon and Mars, however, dates to the first half of Solar System history. Terrestrial planetary bodies, by virtue of their number, offer *multiple examples* for study. Thus, LIPs might be studied in different places on one planet and between several planets. Similarly, the terrestrial planets provide an opportunity to assess how *different environmental conditions* (e.g., different crustal and thermal structure) might influence the formation and effects of large igneous provinces. Furthermore, the segmented, laterally moving, and constantly renewing terrestrial lithosphere both insulates and obscures the view of many mantle convection processes, and indeed is an active influence on these processes. The perspective offered by *one-plate planets* (8) such as the Moon, Mars, Mercury, and Venus can illustrate the long-term influences of mantle plumes and their variations under different thermal conditions in space and time. The multiple, well-exposed examples of LIPs on the planets can also help to reveal their *relation to tectonic structure*. For example, Venus has tens of thousands of km of exposed rift zones (9) which display a wide variety of igneous centers (9, 10), many of which are LIPs. Finally, the planetary record can be instructive in terms of the *chronology and episodicity* of large igneous events and provinces. The extended historical record permits an assessment of changes in the style of LIPs with time (potentially linked to thermal evolution, for example), and the frequency at any given time. Although there is a paucity of radiometric dates from the planetary record, clues from well-exposed deposit morphology can sometimes even be used to estimate single event duration (11). Finally, the planetary record can offer an *end-to-end perspective* on many processes associated with LIPs. For example, lateral plate movement on Earth in the case of the Hawaiian-Emperor seamount chain helps to illustrate many of the stages in the development of hot spots by spreading the signature out into a series of volcanic edifices; this same process, however, destroys the signature of the initial event in the

plume history. On the planets, particularly Venus, the end-to-end process of mantle plumes can be studied (e.g., the relation of thermal uplift, tectonics, and volcanism in a single example and from examples in different stages of formation) (12) and compared to Earth. In summary, the planetary record, in concert with the detailed examination of examples on Earth, should be of use in developing and testing models for the emplacement of LIPs, and in helping to distinguish plate tectonic influences from those linked to deeper interior (mantle and core) processes.

Examples of large igneous provinces from the terrestrial planets illustrate these points. On the Moon, the relatively low density anorthositic crust creates a density trap for rising basaltic magmas which collect in reservoirs at the base of the crust (13); shallow magma reservoirs and large shield volcanoes are not known (14). Reservoir overpressurization causes wall failure and dikes are propagated into the crust and toward the surface. The geometry is such that dikes sufficiently large to reach the surface are likely to result in large-volume, high effusion rate eruptions (15); indeed, single eruptive phases on the Moon are predicted and observed to be in the range of several hundred to over 10^3 km^3 (16-18). Indeed some *individual* eruptions may have been characterized by effusion rates of the order of 1.2×10^3 km^3 per year. This record may provide clues to the nature of similar terrestrial eruptions, a number of which combine together over short time periods to form LIPs such as the Columbia River Basalt.

On Mars, massive shield volcanoes are formed on the stable lithosphere over long-duration hot spots; shield heights are up to 25 km above the surrounding plains, which themselves are atop the 10 km high, several thousand km diameter Tharsis rise (19). Volumes of *single* edifices are of the order of 1.5×10^6 km^3, comparable to the volumes for the Columbia River, Karoo, Parana, Deccan and NAVP basalt provinces on Earth. The lower gravity on Mars causes dikes and vents to be wider and eruptions to be characterized by higher effusion rates; compositionally similar cooling-limited lava flows on Mars would be about six times longer than on Earth (20).

On Venus, the high atmospheric pressure influences gas exsolution, rock vesicularity and density, and the presence and distribution of neutral buoyancy zones (21). At low elevations, neutral buoyancy zones are not predicted, a situation favoring the direct ascent and outpouring of lavas, and low intrusion/extrusion ratios. Indeed, extremely large volcanic outflows are observed (22), covering areas of $1.8\text{-}3 \times 10^5$ km^2 (23), and some lava channels are in excess of several thousand km in length (24). In addition, the impact cratering record on Venus has been interpreted to mean that Venus underwent massive planet-wide volcanic resurfacing about 500 my ago (25), an event possibly related to the overturn of a depleted mantle layer resulting from the vertical accretion of a basaltic crust (26). This hypothesized event could be the equivalent of a "planet-wide" large igneous province.

REFERENCES: 1) M. Coffin and O. Eldholm, eds., *JOI/USSAC Workshop Rept.*, 1990. 2) M. Coffin and O. Eldholm, *Geol. Soc. London. SP 68*, 21, 1992. 3) M. Coffin and O. Eldholm, *Geology, 21*, 515, 1993. 4) R. White and D. McKenzie, *JGR, 94*, 7685, 1989. 5) R. Griffiths and I. Campbell, *JGR, 96*, 18295, 1991. 6) R. Larson, *Geology, 19*, 963, 1991. 7) Basaltic Volcanism Study Project, Pergamon, 1981. 8) S. Solomon, *PEPI, 15*, 135, 1977. 9) D. Senske *et al., JGR, 97*, 13395, 1992 10) K. Magee and J. Head, this volume. 11) J. Head and L. Wilson, *LPSC XI*, 426, 1980. 12) E. Stofan *et al., JGR, 97*, 13347, 1992. 13) S. Solomon, *PLSC VI*, 1021, 1975. 14) J. Head and L. Wilson, *GRL, 18*, 2121, 1991. 15) J. Head and L. Wilson, *G&CA, 56*, 2155, 1992. 16) G. Hulme, *Mod. Geol., 4*, 107, 1973. 17) G. Schaber, *PLSC IV*, 73, 1973. 18) A. Yingst and J. Head, this volume. 19) M. Carr, *JGR, 78*, 4049, 1973. 20) J. Head and L. Wilson, *RG*, in review. 21) J. Head and L. Wilson, *JGR, 97*, 3877, 1992. 22) J. Head *et al., JGR, 97*, 13153, 1992. 23) K. Magee Roberts *et al., JGR, 97*, 15911, 1992. 24) V. Baker *et al., JGR, 97*, 13421, 1992. 25) G. Schaber *et al., JGR, 97*, 13257, 1992. 26) E. Parmentier and P. Hess, *GRL, 19*, 2015, 1992.

LUNAR MARE DEPOSITS: MECHANISMS OF EMPLACEMENT, STRATIGRAPHY, AND IMPLICATIONS FOR THE NATURE AND EVOLUTION OF SOURCE REGIONS AND SECONDARY CRUSTS: James W. Head, Dept. Geol. Sci., Brown Univ., Providence, RI 02912 USA.

Introduction: The lunar maria represent an example of vertically accreting secondary crusts (those derived from partial melting of planetary mantles) (1) in which the total volume is sufficiently small (~1 x 10^7 km^3) (2) and the total area covered (~17% of the lunar surface) (2) is such that modes of formation, emplacement, and evolution of secondary crusts and their relationship to primary crusts (those formed as a result of accretional heating) can be well studied. We have been analyzing processes operating between mare basalt source regions and surface features (3) in order to understand surface features in terms of the geometry of the conduits delivering magma from the source to the surface (4). Using a basic theoretical framework for the ascent and eruption of magma on the Moon (3), we are assessing principles of reservoir development at neutral buoyancy zones at the base of the highlands crust or at rheological boundaries, the overpressurization of such reservoirs, and the general properties of dikes that would be propagated toward the surface (4, 5). Here we report on recent analyses of the mode of emplacement (Figs. 1, 2), stratigraphy, and implications for the nature of source regions.

Distribution and Range of Surface Morphologic Features: Lunar mare deposits occcur preferentially in topographic lows on the nearside, and display a wide range of volcanic landforms, many of which are associated with source vents (6, 7). These include lava flows, cones, domes, sinuous rilles, pits, crater chains, and collections of these features in volcanic complexes, such as the Marius Hills.

Source Regions: Fig. 1 shows a diagrammatic representation of a model for the emplacement of secondary crust through, and onto, the lower-density anorthositic crust (4, 8). At #1, early basaltic magmas rise diapirically to the density trap at the base of the crust. Those below topographic lows (thin crust) associated with lunar impact basins are in a favorable environment for dike propagation and extrusion of lavas to fill the basin interior. Diapirs reaching the base of the thicker crust on the farside and parts of the nearside (#2), stall and propagate dikes into the crust, most of which stall and solidify in the crust and do not reach the surface. Variations in regional and local compensation produce a favorable setting for emplacement of some lavas in craters and the largest basins on the farside (#3). With time, the lithosphere thickens (9) and ascending diapirs stall at a rheological boundary, building up excess pressure to propagate dikes toward the surface. At the same time, loading and flexure of the earlier mare deposits creates a stress environment which favors extrusion at the basin edge (#5) (10); lavas will preferentially emerge there, flowing into the subsiding basin interior. The latest eruptions are deepest and require high stress buildups and large volumes in order to reach the surface; thus, these tend to be characterized by high volume flows and sinuous rilles (#6). Ultimate deepening of source regions and cooling of the Moon causes activity to diminish and eventually to cease (11).

Mode of Emplacement: This configuration (Fig. 1) has important implications for the mode of emplacement of mare basalts and the interpretation of surface morphological features. For example, shallow magma reservoirs are difficult to produce because overpressurization events are likely to be widely separated in time, during which time dikes will solidify in the crust. Indeed there is little evidence for shallow reservoirs and the large shield volcanoes that would be produced from them (6, 12). Volcanic landforms indicate that many eruptions were of high volume (13). Dikes that establish pathways completely to the surface on the nearside should have very high volumes, comparable to the volumes associated with many observed flows and sinuous rilles (Fig. 2, right). An abundance of dikes should exist in the lower crust of the Moon, many more than those feeding surface eruptions (Fig. 2, left). The presence and abundance of such dike swarms have important implications for the interpretation of the average composition of the lunar crust and the composition of basin and crater ejecta. A small percentage of dikes should penetrate to the vicinity of the surface (Fig. 2, middle), and our analyses suggest that they should form a variety of surface structures, including linear rilles caused by near-surface stresses related to dike emplacement. Volatile exsolution from magma in the cooling dikes can cause explosive (vulcanian) eruptions, pyroclastic activity, and chains of collapse craters (Fig. 2, middle).

Stratigraphy: Analysis of returned samples and photogeologic and remote sensing studies (summarized in 6, 7) show that mare volcanism began prior to the end of heavy bombardment (the period of cryptomare formation), in pre-Nectarian times, and continued until the Copernican Period, a total duration approaching 3.5-4 Ga. Recent analyses have increased the surface area known to contain cryptomaria, and shown that there were several widespread mare regions during that period comparable in area to presently exposed maria such as Humorum and Serenitatis (14-16). Detailed analyses and synthesis of lunar mare stratigraphy is revealing the range of volumes typical of individual eruptions (17) and the compositional affinities and volumes of units in individual basins and regions.

Flux: These stratigraphic analyses show that the mare volcanic flux was not constant, but peaked in early lunar history during the Imbrian Period. Average *global* volcanic output rate during this peak period was about

10^{-2} km^3/a, comparable to the present *local* output rates for individual volcanoes on Earth such as Kilauea, Hawai'i. Some eruptions associated with sinuous rilles may have lasted about a year and emplaced 10^3 km^3 of lava; a single such eruption would represent the equivalent in one year of about 70,000 years at the average flux. The flux was variable in space and time during this period, and the patterns revealed by the stratigraphy show evidence for regional concentrations of sources and compositional affinities. These patterns are the basic input data to defining the configuration, size, and density of mantle source regions (Fig. 1) throughout the period of mare basalt emplacement.

Implications for Source Regions: The nearside-farside mare deposit asymmetry can be readily explained by differences in crustal thickness. Magma ascending from the mantle or from a buoyancy trap at the base of the crust should preferentially extrude to the surface on the nearside, but should generally stall and cool in dikes in the farside crust, extruding only in the deepest basins. Therefore, the nearside-farside dichotomy is unlikely to represent first-order differences in mantle source region characteristics. The nearside record provides considerable evidence for patterns in the scale, location, composition, and duration of source regions, and these data are presently being compard to models for mare basalt petrogenesis (18, 19).

Formation of Secondary Crusts: Lunar mare deposits provide an example of the transition from primary crusts to secondary crusts and illustrate the significance of several factors in the evolution of secondary crusts, such as crustal density, variations in crustal thickness, presence of impact basins, state and magnitude of stress in the lithosphere, and general thermal evolution. These factors are also responsible for the extremely low volcanic flux, even during periods of peak extrusion.

References: 1) S. Taylor, *Tectonophysics, 161*, 147, 1989. 2) J. Head, *Origins of Mare Basalts*, LPI, 66, 1975. 3) L. Wilson and J. Head, *JGR, 86*, 2971, 1981. 4) J. Head and L. Wilson, *G&CA, 56*, 2155, 1992. 5) J. Head and L. Wilson *PSS*, in press, 1994. 6) D. Wilhelms, *USGS PP-1348*, 302 pp., 1987. 7) BVSP, Pergamon, 1981; J. Head, *RGSP, 14*, 265, 1976. 8) S. Solomon, *PLSC 6th* , 1021, 1975. 9) S. Solomon and J. Chaiken, *PLSC 7th* , 3229, 1976. 10) S. Solomon and J. Head, *JGR, 84*, 1667, 1979. 11) R. Kirk and D. Stevenson, *JGR, 95*, 12133, 1989. 12) J. Head and L. Wilson, *GRL, 18*, 2121, 1991. 13) G. Schaber, *PLSC 4th* , 73, 1973. 14) J. Head *et al.*, *JGR, 98*, 17149, 1993. 15) R. Greeley *et al.*, *JGR, 98*, 17183, 1993. 16) B. Hawke *et al.*, *GRL, 20*, 419, 1993; I. Antonenko and J. Head, this volume; J. Mustard *et al.*, this volume. 17) A. Yingst and J. Head, this volume. 18) J. Longhi, *G&CA, 56*, 2235, 1992; C. Neal and L. Taylor, *G&CA, 56*, 2177, 1992. 19) P. Hess and E. M. Parmentier, *LPSC XXIV*, 651, 1993.

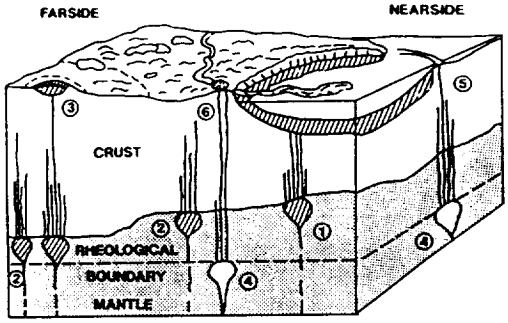

Figure 1

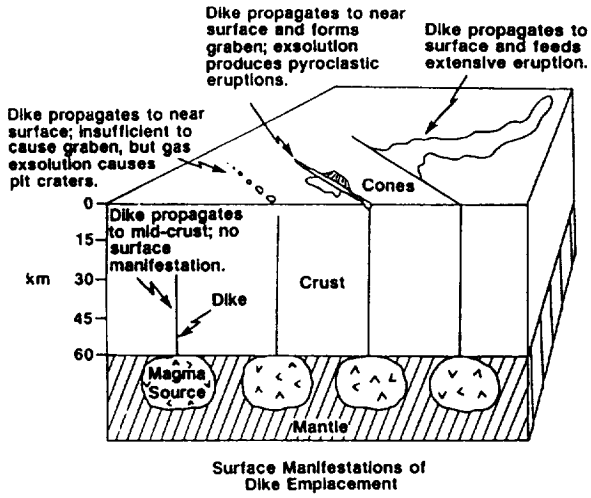

Figure 2

NOAH: A PROGRAM TO VISUALIZE LAVA FLOODING OF THE VENUS CRUST;
James W. Head and Paul Haggerty, Department of Geological Sciences, Brown Univ., Providence RI 02912 USA.

Volcanism is a fundamental contributor to the formation and evolution of the crust of Venus (1). Although it is known that over 80% of the Venus surface consists of volcanic plains, the mode of emplacement and history of these vast plains units is as yet not understood. The issue of the mode of emplacement of the Venus plains is crucial in addressing some of the most critical questions in the understanding of Venus. For example, the present distribution of impact craters on Venus (2,3) permits several alternate scenarios for the style of volcanic resurfacing. Discussions are underway in the literature addressing these issues (1-3), and testable hypotheses have been proposed, but a clear consensus has not yet emerged. Several lines of evidence have led to the hypothesis that Venus was catastrophically volcanically resurfaced on the order of 500 million years ago and that volcanism has been local and of minimal volumetric importance since that time (2). This scenario predicts that the earliest deposits should be extremely voluminous and widespread and that later deposits should be of lower volume and localized. Perspectives on the formation of secondary planetary crusts (derived from partial melting of the mantle) show that Venus is an important part of the picture (4). Lunar maria represent initial stages of secondary crust development (5), while the Earth's oceanic crust represents a young and highly laterally mobile secondary crust with a thin and constantly recycled depleted mantle layer. Venus appears to represent a vertically accreting crust with a potentially significant underlying accumulation of depleted mantle. The evolution of the depleted mantle layer may ultimately result in instabilities and the periodic and catastrophic overturning of the layer leading to several predicted styles of large-scale volcanic resurfacing (6). At the present time, there is insufficient understanding of the nature of the plains to test these and other hypotheses.

In order to understand further the formation and evolution of the plains and to test these hypotheses, we seek to use altimetric data to perform several flooding experiments on existing topography in order to assess the patterns of emplacement and their volume and pattern implications. The strategy of the experiment follows approaches that we have developed for the Moon (7) in which we utilize a preexisting topographic datum and successively flood several typical regions (cratered terrain, basin interiors, etc.) tracking areal extent and accumulated volume. Additional products of this approach are isopach maps which illustrate the areal distribution of thicknesses and are useful in geophysical analyses of loading and flexure, as well as in the understanding of the emplacement of plains.

Here we describe the initial development and testing of the program in which the user defines an area of interest and tracks flow emplacement through a series of thickness and volume steps. The program continues tracking the flooding until all preexisting topography has been obscured. The distribution of map patterns (i.e., kipukas or regions of embayed but unflooded topography) at various stages in these examples provides an important frame of reference for the examination and mapping of plains units on Venus. The volume - thickness - area plots and the isopach maps from this analysis are then contributions to the understanding of plains unit emplacement, and in loading and flexure studies.

The NOAH terrain flooding program is designed to accept Magellan VICAR images (Fig. 1). The left window is used to display the SAR imagery and the underlying topography image, and shows the area chosen for flooding and the graphic results of the flooding operations. The Message Window maintains a constant report of the lat/lon and elevation of the point under the cursor tip. The Plots Window displays topography and image histograms of selected areas. If the user places the cursor on the histogram, the program responds by printing the DN or topo level and the number of points at that level. Also given are the min, max, mean, and standard deviation of the values, and for topography, the range. This window also displays in the plots mode the area/depth and volume/depth graphs (Fig. 2). Each time the user performs a flooding operation, the depth, area flooded, and volume flooded are stored and displayed (Fig. 2); by placing the cursor on any of the squares, the user obtains a readout of the depth and area/volume at that point.

The Flooding Information Window (Fig. 3) reports the current elevation at which flooding will be performed and the step value for changing the flood elevation. At the bottom of the window are three statistics calculated from the flooding operation. At the top the program displays the min/max values for the topography. The user can type in any elevation in the flood level box. By clicking on the flood button, the user initiates the flooding operation which will update the main window by blacking out any pixels that fall below the flood level, thus giving a visual display of the patterns of flooding on the surface of Venus. By pressing the step button, the current flood elevation is changed by the amount shown in the step box. The last three items in the window reflect the status of the current flooding operation (total area selected; total area flooded by the last operation; total volume flooded by the last operation).

The user moves the cursor into the main window and clicks the mouse button to outline the area of interest for analysis, which can be any shape; a final outline of the area will appear on the screen. The File menu has three functions: 1) Load Image. 2) Perform Auto Flood (user selects interval and min/max elevations and the flooding steps are done automatically). 3) Quit. The Views menu has three functions: 1) Show Image/Show Topo (switches

display between SAR image and topography. 2) Show Overlay/Hide Overlay. 3) Clear Flood Graphics (erases all flooding graphics within area of interest). The Graphs menu has seven functions: 1) Image Histogram. 2) Topography Histogram. 3) Thickness vs Area. 4) Thickness vs Volume. 5) Reset Graphs. 6) Save Graphs to Disk. 7) Save Histograms to Disk. The Options Menu has four functions: 1) Choose Contour Style/Choose Flood Style. 2) Specify Contour Width. 3) Set Image Histogram Limits. 4) Set Topo Histogram Limits.

Shown in Fig. 4 is an example from an intermediate step in a flooding program for Lavinia Planitia. An outgrowth of this analysis will be the determination of the typical size of topographically closed basins on Venus. The statistics of basin size and geometry will be one way of determining the potential for regional plains development from individual sources. One of the products of this will be a set of templates which represent sequential flooding of real Venus topography and the associated volume, thickness and areal coverage data. These templates will then be compared to several areas of Venus plains to estimate their stage of burial and evolution. Following the completion of initial testing the program will be released to users for Venus and other planetary applications. For information on how to obtain a final copy contact head@pggipl.geo.brown.edu.

REFERENCES: 1) J. Head *et al.* (1992) *JGR, 97*, 13,153; 2) G. Schaber *et al.* (1992) *JGR, 97*, 13,257; 3) R. Phillips *et al.* (1992) *JGR, 97*, 15923; 4) J. Head (1990) *Earth, Moon Planets, 50/51*, 25; 5) J. Head and L. Wilson (1992) *G&C A, 56*, 2155; 6) Parmentier and Hess (1992) *GRL, 19*, 2015; 7) J. Head (1982) *Moon and Planets, 26*, 61.

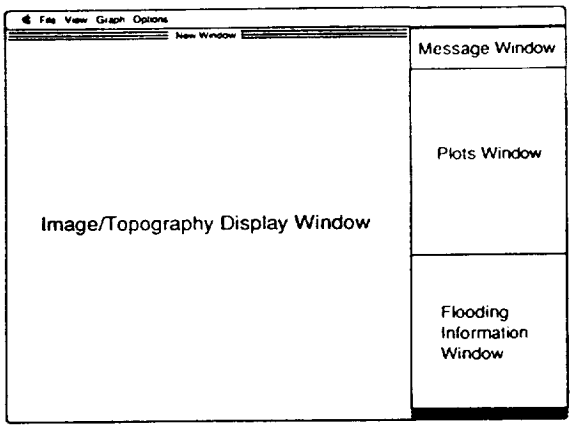

Fig. 1. Layout of Terrain Flooding Windows

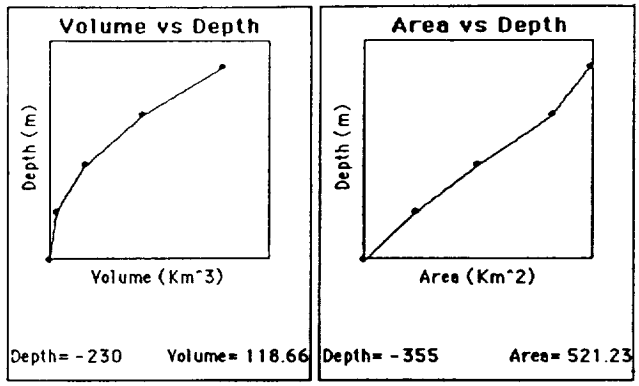

Fig. 2. The Plotting Window in Plots Mode

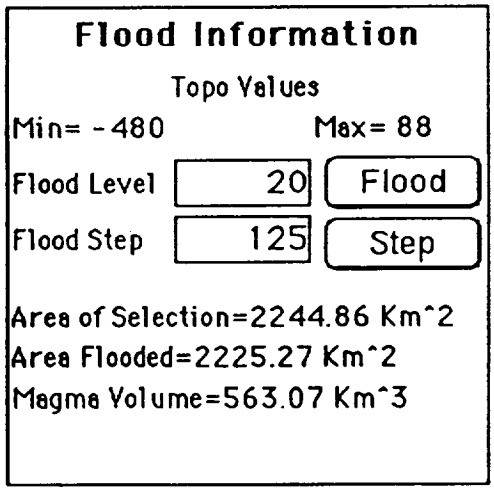

Fig. 3. The Flood Information Window

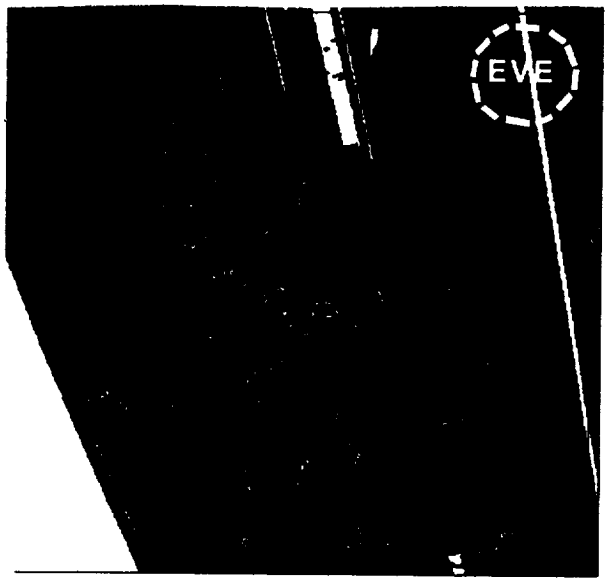

Fig. 4. Display of partial flooding of Lavinia Planitia. Black area represents region flooded from present topography up to a depth of -900 m below MPR. Outlined in the upper right corner is the 330 km diameter Eve corona.

MARS: FORMATION AND EVOLUTION OF MAGMA RESERVOIRS; James W. Head[1] and Lionel Wilson[1,2], [1]Dept. Geol. Sci., Brown Univ., Providence, RI 02912 USA, [2]Environ. Sci. Div., Lancaster Univ., Lancaster LA14YQ, UK.

We have undertaken a theoretical analysis of the formation and evolution of magma reservoirs on Mars and a comparison to observed edifices and features. Here we report on a preliminary analysis of magma reservoir formation and evolution.

Ascent of Magma and Formation of Reservoirs. Primary magma source reservoirs will form above zones of partial melting in the upper parts of mantle plumes or other instabilities as melt segregation occurs. Buoyant melt bodies of various sizes will ascend as equant diapirs or as dike-like bodies until they encounter the surface or some kind of trap. Equant diapiric bodies, rising by deforming the surrounding rocks in a plastic fashion, are most likely to be trapped at rheological boundaries at depths, dictated by the thermal structure of the lithosphere. Buoyant dikes, penetrating the surrounding rocks by elastic fracture mechanisms, may be halted by thermal losses if they are sufficiently narrow, but otherwise penetrate to the surface unless they encounter a neutrally buoyant level. Neutral buoyancy levels may exist wherever there is a profile of significantly increasing country rock density with depth, such that the density of ascending magma lies within the country rock density range. Such crustal density profiles will be influenced by fracturing of near-surface rocks by impact cratering events and also the compaction, during progressive burial, of surface materials deposited in a loosely packed state. Such materials could be sediments or volcanic materials accumulating *in situ* from successive eruptions.

Squyres *et al.* (1) summarize models of self-compaction in which surface porosities of 20% to 50% are assumed. These models adopt an exponential decline of porosity with depth, for which a decay constant of 6.5 km is found to be appropriate to the martian gravity. Head and Wilson (2) proposed an analogous model of the self-compaction of volcanic sediments. If martian magmas contain volatile contents similar within a factor of 2 to 3 to those of magmas on Earth, secondary, shallower reservoirs are likely to form in growing edifices at levels of neutral buoyancy at depths between about 6 and 15 km, with a concentration near 8 to 12 km.

Magmas which are not buoyant in the overlying rocks may still ascend in dikes from a melt source region if a sufficient excess pressure exists in the source region. Excess pressures on the order of a few to a few tens of MPa, are likely to be present in any partial melt produced at a great enough rate that the surrounding rocks cannot accommodate the volume changes by plastic flow. Such pressures are quite adequate to compensate for the negative buoyancies of mafic melts ascending for 100 to 200 km through the anorthositic lunar highland rocks (3). Magma ascending in a long, continuous dike from an overpressured source at great depth is very much less sensitive to the density and stress structure of the lithosphere through which it passes than magma rising in an isolated, buoyant body. Dense magmas rising in this way may erupt at the surface or, if there is insufficient excess pressure to allow the dike tip to reach the surface, may form intrusions. When eruptions occur, it is likely that they will take place at high effusion rates, since dikes which penetrate great vertical distances through the lithosphere will be driven by high excess pressures and induced stress fields which ensure that they are relatively wide and have relatively great horizontal extents (3). There is little reason to expect successive intrusive events of this sort to concentrate magma in a small region, or over a small range of depths, to begin to form a reservoir. Thus, discrete volcanic edifices showing evidence of a central, shallow magma reservoir are most likely to be associated with the less vigorous rise of buoyant magma.

Evolution of Reservoirs and Edifices. The lateral and vertical sizes of magma reservoirs will evolve in response to several factors: the episodic injection of new magma from deeper primary reservoirs, causing the reservoir to expand elastically and increase its internal pressure to accommodate the new volume (4); the intermittent loss of magma into vertical and lateral intrusions (which may or may not lead to surface eruptions) when the reservoir walls fail due to the accumulated stresses; and the continuous cooling of magma against the reservoir walls.

Parfitt *et al.* (5) point out that intrusions which do not lead to eruptions essentially represent extensions of the reservoir until such time as they solidify. If many intrusions occur within a short space of time from the same part of a reservoir wall, the accumulated heating of the country rocks reduces the rate at which the later intrusions cool. Provided enough events occur within a short enough time, the reservoir wall migrates outwards in a stochastic manner. The relative amounts of lateral and vertical growth of a reservoir therefore depend on the relative frequencies, and these depend in turn on the relative ease with which the walls will fail as a function of position around the reservoir edge. Parfitt *et al.* (5) show that, as a reservoir grows, initially with equal probability in all directions, it requires an ever larger internal excess pressure in the magma to cause failure at the top (and bottom) of the reservoir relative to the excess pressure needed to cause failure around the center-line. Vertical growth must essentially stop

when the difference between these two excess pressures, ΔPB, becomes too great. Let σ be the stress required to cause wall failure (by overcoming either the tensile strength or the fracture toughness of the wall rocks); then equations (2a), (3a) and (6) in Parfitt *et al.* (5) can be combined to show that the magma excess pressure PB required to cause wall failure at a depth h below the roof of a reservoir whose top is a distance D below the surface is $PB = \sigma + \rho c\, g\, (D + h) - \rho m\, g\, h$, where g is acceleration due to gravity, ρm is density of the magma and ρc is density of the country rocks. The difference between excess pressures required at the top of the reservoir and at its center-line is the difference between the values of the above expression evaluated at $h = 0$ and $h = R$, where R is the half-height of the reservoir, i.e., $\Delta PB = g\, R\, (\rho c - \rho m)$. ΔPB can depend only on the mechanical and thermal properties of the magma reservoir wall rocks and, to the extent that these are likely to be similar for all mafic silicates, will be the same for reservoirs on all planets. The implication is thus that the maximum vertical size to which a mafic reservoir is likely to grow is inversely proportional to the density contrast between the magma and host rocks and also inversely proportional to the planetary gravity. Rock densities and density contrasts in mafic environments are not likely to vary systematically between Mars and Earth, but the gravities differ by a factor of about 2.6. Thus, magma reservoir vertical sizes of 3 to 4 km which typify the hawaiian volcanoes on Earth would imply martian equivalents in the 8 to 10 km range.

There is no obvious equivalent constraint on the likely maximum lateral size of a growing magma reservoir. The lateral extent is most likely to reflect the average rate of injection of new magma into the reservoir (5), since this in turn determines the rate of stress accumulation, the average interval between lateral dike injection events, and consequently the time interval available for cooling between events. Although no detailed models have yet been published, the controlling parameters are clearly likely to be the elastic and thermal properties of the rocks involved, implying that there will be no strong dependence of reservoir horizontal dimensions on planetary gravity.

Edifices grow as a result of the accumulation of the products of explosive and effusive eruptions from vents distributed near the summit and around the flanks. These vents could be fed by dikes extending down to primary reservoirs in the mantle; however, it is more likely that the vast majority of eruptions taking place on a shield are fed from its shallow reservoir. The overall morphology depends on the volume of magma erupted in each event, the area over which it is dispersed, the frequency with which eruptions occur as a function of distance from the summit, and the azimuthal distribution of vents, strongly controlled on Earth by the presence or absence of rift zones.

Blake (4) developed a model of the elastic response of the rocks surrounding a shallow reservoir to the addition and removal of magma and showed that, if the wall response remained elastic, only a few percent of the volume of the reservoir was likely to be removed in a single eruptive or intrusive event. Even if part of the response of the surrounding rocks is inelastic, the melt fraction capable of being removed only increases a few %. However, the likely large volumes of martian magma reservoirs (at least up to 2000 km^3) imply that individual eruptions could involve magma volumes up to 200 km^3, consistent with the volumes of some of the larger flows on the Tharsis volcanoes which have lengths up to 300 km (6).

A further aspect in this simple relationship occurs when one considers lateral magma transport in dikes from a central reservoir to a flank eruption. Unless magma is being fed to the reservoir from the mantle at a high enough rate during the activity to buffer the reservoir pressure, only a finite volume of magma can be withdrawn from the reservoir before its elastic relaxation reduces the dike driving pressure to the point where intrusion must cease. By analogy with an analysis of this process for intrusions on Earth and Venus (7), individual lateral dike segments would probably extend for no more than ~10 km from the reservoir in unbuffered conditions. However, the existence of dike swarms extending for at least 1000 km from identifiable source areas on both these planets implies that buffering by such high mantle supply rate episodes does occur. Not enough is yet understood about the mantle conditions allowing such events to infer if they should have been common on Mars, but the existence of martian rift zones with lengths in excess of 200 km cannot currently be explained by any other mechanism. By analogy, volcanoes which do not possess major rift zones could nevertheless have had vents capable of delivering large volumes of melt to the surface distributed widely over their flanks - certainly out to distances up to 200 km.

References. 1) S. Squyres *et al.*, *Mars*, U AZ Press, 523, 1992; 2) J. Head and L. Wilson, *JGR*, *97*, 3877, 1992; L. Wilson and J. Head, Mars: Review of volcanic eruption condition theory and relationship to observed landforms, in review, *Reviews of Geophysics*, 1993; 3) J. Head and L. Wilson, *G&CA*, *55*, 2155, 1992; 4) S.Blake, *Nature*, *289*, 783, 1981; 5) E. Parfitt *et al.*, *JVGR*, *55*, 1, 1993; 6) P. Cattermole, *JGR*, *92*, E553, 1987; 7) E. Parfitt and J. Head, *EMP*, *61*, 249, 1993.

GEOLOGY OF THE LAVINIA PLANITIA AREA, VENUS; James Head, Kari Magee, Susan Keddie, Martha Gilmore, and Aileen Yingst, Department of Geological Sciences, Brown University, Providence RI 02912 USA

BACKGROUND: The Lavinia Planitia area is one of the several large relatively equidimensional lowland areas of Venus and as such is an important region for study in the analysis of processes of lowland formation and volcanic flooding. Prior to Magellan it was known to be a lowland area (1) surrounded by several corona-like features and rift-like fractures parallel to the basin margin to the east and south (2,3). Arecibo data showed that the interior was populated with complex patterns of ridge-belt like deformational features and volcanic plains, and several regions along the margins were seen to be the sources for extensive outpourings of digitate lava flows into the interior (2,3). Early Magellan results showed that the ridge belts were composed of complex deformational structures of both extensional and compressional origin (4) and that the complex lava flows (fluctus) along the margins (5) emanated from a variety of sources ranging from volcanoes to coronae (6). In addition, Lavinia Planitia is an area deficient in the distribution of distinctive volcanic sources and corona-like features (7). Indeed, the characteristics and configuration of Lavinia Planitia have been cited as evidence for the region being the site of large-scale mantle downwelling (8). Thus, this region is a laboratory for the study of the formation of lowlands, the emplacement of volcanic plains, the formation of associated tectonic features, and the relationship of these to mantle processes. We have begun mapping the V55 Lavinia Planitia Quadrangle with these goals in mind. Summarized below are the results from our initial analyses, including a model for the regional stratigraphy (Fig. 1).

REGIONAL SETTING: The Lavinia Planitia Quadrangle consists of a centralized deformed lowland surrounded by Dione Regio to the west, Alpha Regio tessera and Eve corona to the northeast, an extensive rift zone and coronae belt to the east and south, Mylitta Fluctus to the south, and Helen Planitia to the southwest.

PLAINS: There are several plains types and they include mottled plains, dark plains, and digitate flows. Mottled Plains are characterized by abundant superposed ridges, locally large numbers of shields; sometimtes radar dark, sometimes radar bright, but brighter is usually the older member and contains the shields. Dark Plains have fewer superposed wrinkle ridges and commonly occur as small patches adjacent to or within fracture belts. Digitate Flows are clearly younger than most deformation and only locally have wrinkle ridges. Sources for these latter flows are localized around the margins of the basin (5,6).

STRUCTURE: Deformation belts consist of ridge belts which are similar in morphology to the wrinkle ridges in plains and in general are topographically lower than fracture belts, which generally deform mottled plains but not dark plains; digitate plains always embay them (4). Components of fracture belts are similar in morphology to grooves in the plains, but are more concentrated. Wrinkle ridges form on all units throughout the plains sequence, even in the youngest digitate plains, but are much less abundant in the youngest units; orientations are distinctive regionally and therefore do not seem to have changed much with time. Grooves, oriented orthogonal to wrinkle ridges, appear to be younger than mottled and dark plains, but do not cut digitate plains. Not all the structures are contemporaneous. There is a significant variability between belts, and between individual deformation belts and plains. Many ridge belts are parallel to wrinkle ridge orientation in plains, and the same is true for groove belts; there are cases where one belt turns into another where it changes orientation. Some individual ridges and grooves within deformation belts grade into ridges and grooves in ridged or fractured plains. Central Lavinia is characterized by lowland plains which generally overlie highly deformed tectonic ridge and groove belts. There are two distinctive directions of background deformation; these are at high angles to one another and are clearly superimposed (ENE first, and NNW second). The initial ENE deformation is predominantly extensional in the NW area, but then appears to be compressional as one works toward the SE and down into Lavinia Planitia (4).

STRATIGRAPHIC SEQUENCE: The stratigraphic sequence according to our preliminary mapping is as follows: the youngest units are the Dark Haloed craters; older craters are observed but none of them in the quadrangle are embayed by lava. Younger plains include the fluctus, which appear as floods with few domes, and mostly emerge from sources in the adjacent rift and coronae belt to the east and south (5,6). Medial plains include many distributed domes and are commonly mottled. Older plains are cut by NNW trending graben. The oldest unit, tessera, is well developed in Alpha Regio and may underlie larger parts of the quadrangle, but definitive exposures and thus evidence of its presence is lacking over most of the quadrangle.

INTERPRETED GEOLOGIC HISTORY: Volcanism prior to downwelling produced background plains which were deformed by subsidence of the basin. Ridge belts are interpreted to be fold belts that formed by buckling of strong upper crust in response to ridge-normal compression. Subsequent volcanism produced extensive volcanic plains between and among the deformation belts apparently from sources within the basin. The latest volcanism issued from centers located along the edge of the basin (associated primarily with the extensive rift zone extending for 6000 km along the western and southern margin of Lavinia Planitia) and flowed into the basin, but intrabasin sources at this time are not obvious (5,6). We believe that these structural features and this stratigraphic sequence supports models which suggest that mantle downwelling first produces a topographic low and deforms crust into ridges. Late-stage marginal rifting and volcanism may be related to upwelling counterflow linked to the general downwelling. The lack of abundant evidence of features that might be linked to small-scale mantle instabilities (e.g., coronae, large volcanoes) in central Lavinia (7) appears to support the general downwelling model (8).

REFERENCES: 1) G. Pettengill *et al.* (1980) *JGR, 85*, 8261; 2) D. Senske *et al.* (1991) *Earth, Moon, Planets, 55*, 97; 3) D. Campbell *et al.* (1991) *Science, 251*, 180; 4) S. Squyres *et al.* (1992) *JGR, 97*, 13579; 5) K. Magee Roberts *et al.* (1992) *JGR, 97*, 15991; 6) K. Magee and J. Head (1992) Role of rifting in the generation of melt: Implications for the origin and evolution of Lada Terra-Lavinia Planitia region of Venus, *JGR*, in review; 7) L. Crumpler *et al.* (1993) *Science, 261*, 591; 8) D. Bindschadler *et al.* (1992) *JGR, 97*, 13495.

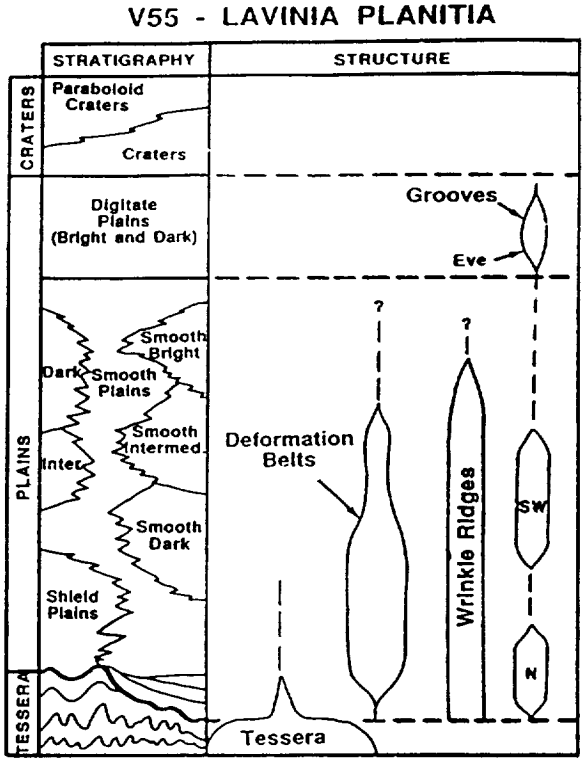

Figure 1

KAWELU PLANITIA, VENUS: GEOLOGY AND MECHANISMS FOR THE FORMATION OF A MAJOR VOLCANIC REGION, Michael B. Helgerud, Carleton College, Northfield, MN 55057, Dave Senske, Jet Propulsion Laboratory, Pasadena, CA 91109.

Mantle upwelling is interpreted to be a major process in the formation of large volcanic centers on Venus [1,2,3]. Kawelu Planitia possesses characteristics similar to other parts of Venus interpreted to have formed in association with mantle plumes, namely large volcanic centers, narrow belts of rifting, and extensive flows emplaced by apparent lava flooding [4,5]. To better understand the geologic history of this area and to link the surface geology to processes in the interior, we have mapped it in detail and modeled gravity data for several Magellan Cycle 4 orbits.

Kawelu Planitia, centered near 45° N, 244° E, is a relatively flat low land dominated by the volcano Sekmet Mons and three lobate regions interpreted to be lava flow fields. Within the area studied here, C1-MIDR45N244 (Fig.1), 9 units are identified, the oldest of which is complex ridged terrain (CRT), a highly deformed unit containing multiple directions of deformation. Embaying this unit are regionally extensive homogeneous plains that contain few lobate features. Superimposed on these two oldest units are numerous flow fields, Coronae, troughs, lineaments, radar-dark diffuse patches, and impact craters with associated ejecta. Due to a lack of contacts, age relations between many of the younger units are difficult to ascertain. In several locations, troughs have clearly controlled the emplacement of some the major lava flows, representing deformation that occurred prior to major episodes of volcanism but after the emplacement of the plains.

Three lava flow complexes dominate Kawelu Planitia. Stratigraphic relations suggest that volcanism may have progressed in a north to south direction. One of the major flow complexes originates at Sekmet Mons, a volcano superposed on complex ridged terrain (CRT). The majority of the volcanic material from Sekmet has been emplaced to the north and east. Numerous lineations superimposed on the volcano are unambiguously identified as troughs. The truncation of many of these structures by summit flows implies that at least two episodes of eruption occurred separated by a period of rifting. Lineations arrayed roughly radially on the SW flank of Sekmet Mons cross lava flow boundaries and define the NE segment of an elongate topographic depression, suggesting the occurrence of subsidence Two other major flow complexes, an Eastern Flow Field and a Western Flow Field (Fig. 1), are associated with clusters of volcanic domes. Both appear to be at least partially located within depressions. One of the flows (42.6° N, 243.2° E), originating from the Eastern Flow Field, is channelized in a trough that cuts across the distal flows of Sekmet. Initial lava emplacement from Sekmet Mons thus occurred prior to rifting and the flow associated with the dome cluster. Lineaments in the southeastern portion of Eastern Flow Field border a topographic low and are part of a system of graben that formed after lava emplacement. A northern lobe from the Western Flow Field superposes a flow from the Eastern Flow Field, suggesting that at least a portion of the western unit is younger. The complicated history of lava emplacement and the ambiguity of contacts between units prevents this statement from being made about the two flow fields as a whole.

During its fourth mapping cycle, Magellan obtained line-of-sight (LOS) acceleration data over Kawelu Planitia (orbits 7115-7189). To obtain a general understanding of the relationship between the surface geology and processes responsible for the formation of the volcanic features, we examined simple two dimensional models in the LOS geometry using the program ORBSIM [6]. In this model, the gravitational attraction due to topography as well as that due to a corresponding compensating mass at depth is determined. The results from the modeling indicate that a single depth of compensation cannot account for features observed in the gravity data. For three orbits 7146, 7152 (Fig. 2) and 7156, a positive anomaly of 4 mgal is centered near the depression associated with a dome cluster and a major lava flow field (40.5° N, 246° E). Modeling provides a good fit to the structure of this anomaly for a depth of 150 to 200 km. The northern part of the gravity profile, however, is better fit with an apparent compensation depth (ADC) of approximately 50 km. For orbits greater than 7156, those where the sub-spacecraft crosses regional plains units and CRT, ADC's range from 50 to 100 km.

The geologic history of Kawelu Planitia is characterized by early episodes of regionally extensive lava flooding followed by rifting and later the production of volcanic centers associated with major flow fields and clusters of volcanic domes. In several locations, the uphill trend of lava deposits suggests post emplacement subsidence. The correspondence of gravity data, surface features, and ADC's shows a trend with the largest values centered on areas of large-scale volcanism. On the basis of the presence of large-scale volcanic features, rifting, and large compensation depths, this region is interpreted to be associated with a region of mantle upwelling. In other areas, parts of the plains and the CRT, the relatively shallow depths suggest that these regions are most likely crustally compensated.

REFERENCES. [1] Senske, D. A., et. al., J. Geophys. Res., 97, 13395-13420, 1992. [2] Phillips, R. J., et al., Science, 252, 651- 658, 1991. [3] Grimm, R. E. and R. J. Phillips, J. Geophys. Res., 97, 16035-16054, 1992. [4] Helgerud, M. B. and J. R. Zimbelman, LPSC XXIV, 637-638, 1992. [5] Zimbelman, J. R., Eos Transactions, 74, 379, 1993. [6] Phillips, R. J. et al., J. Geophys. Res., 85, 5455-5465, 1978.

KAWELU PLANITIA: HELGERUD M. B. AND SENSKE D. A.

Figure 1

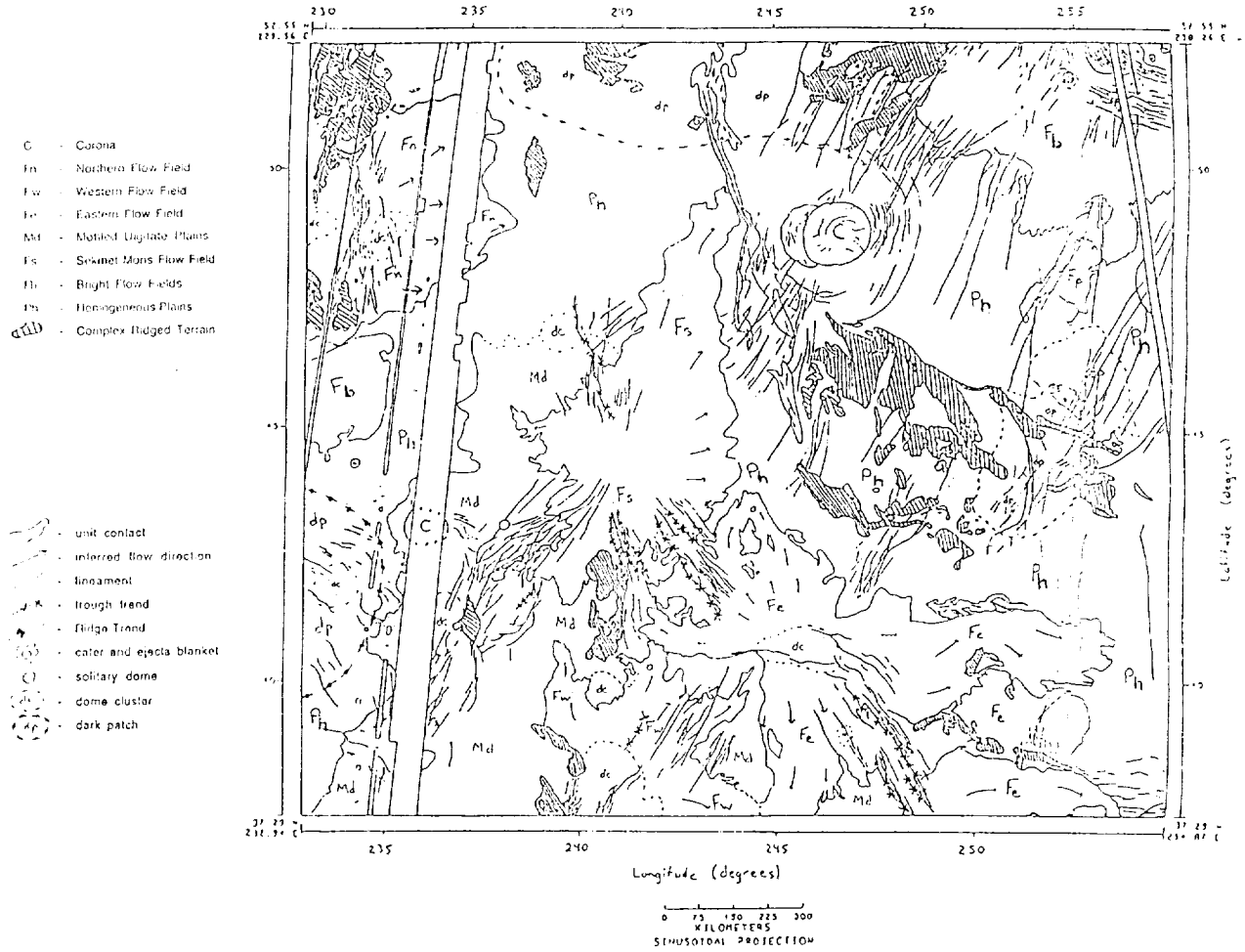

Figure 2

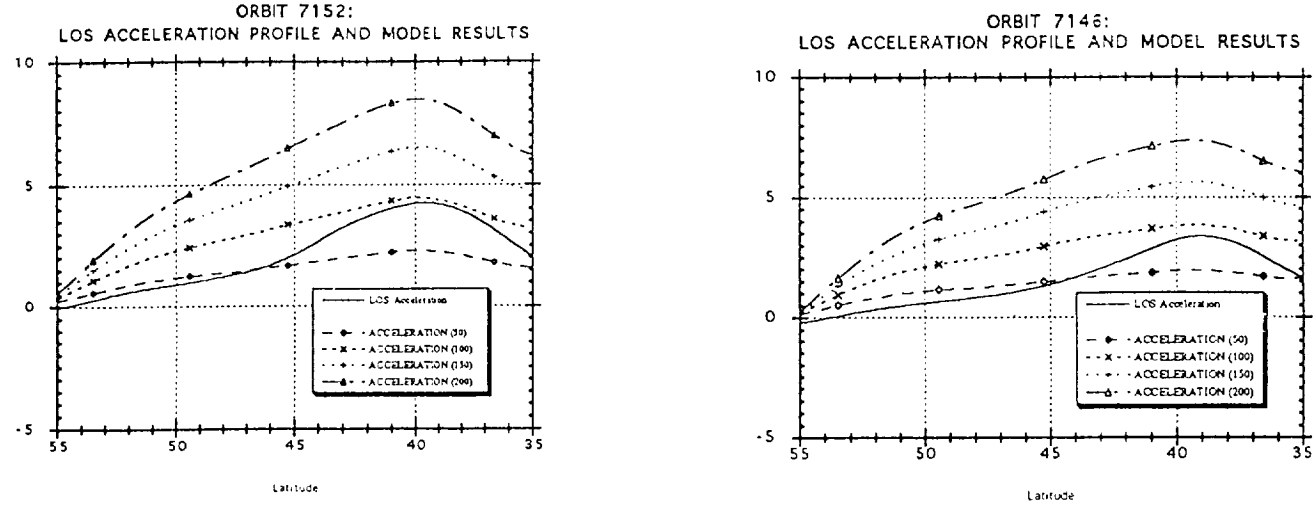

NEW LABORATORY MEASUREMENTS OF MID-IR EMISSION SPECTRA OF SIMULATED REMOTE PLANETARY SURFACES; B. G. Henderson*, P. G. Lucey†, and B. M. Jakosky*. *Laboratory for Atmospheric and Space Physics, University of Colorado; †Planetary Geosciences, University of Hawaii.

Introduction: Thermal-infrared energy emitted from a particulate planetary surface is produced in the top few hundred microns of the material. On airless bodies, radiative cooling to space can create significant thermal gradients in this thin near-surface layer due to the importance of radiation relative to solid and gas conduction. The effects of a near-surface thermal gradient will show up in an emission spectrum due to the wavelength variation in the opacity and its relationship to the depth dependence of the temperature. We have measured emission spectra of particulate materials in conditions simulating that of remote planetary objects using an environment chamber at the University of Hawaii's spectroscopy lab. Our experiment parallels that of Logan et al. (1973) but is different in that the samples in our experiment were heated from below by a temperature-controlled substrate rather than from above by a simulated solar source.

Experiment Description: The emission measurements reported here were made using a scanning grating monochromator hooked up to a HgCdTe detector at the spectroscopy lab at the University of Hawaii . This particular setup allows spectral emission measurements to be made from 7-13 μm. The lab is equipped with a recently modified environment chamber in which the user can control the temperature of the substrate (77 K to 500 K), the radiation shield surrounding the mineral sample (77 K or 273 K), and the internal atmospheric pressure (10^{-5} to 760 torr). The main objective in this experiment was to look for spectral features due to a near-surface thermal gradient brought about by infrared radiative cooling of the near surface. The temperature of the radiation shield was therefore maintained at 77 K to simulate as closely as possible a cold-space background. Initial measurements were made in near-vacuum conditions in order to maximize any potential thermal gradient. Subsequent measurements were made at different pressures by adding dry N_2 to the chamber. Quartz was selected as the candidate sample and was prepared by sifting the powder through a 0-50 μm sieve directly into a 3 mm sample cup. The substrate temperature was maintained at $\approx$ 500 K in all trials. Spectra were obtained as emission of the sample relative to a hot reference blackbody. An estimated blackbody temperature was used to convert the relative emission spectrum to spectral radiance of the sample which was converted to an "effective emissivity" by assuming unit emissivity at the spectral location with the maximum brightness temperature.

Results: Figure 1 shows effective emissivity spectra of granulated quartz sitting on a 500 K substrate. Spectrum a was measured at an atmospheric pressure of 10^{-3} torr. The prominent emission feature at 7.35 μm is located at the wavelength of the principal Christiansen frequency and is interpreted as the result of a thermal gradient in the uppermost layer of the material. At the Christiansen frequency, the index of refraction of the material approaches unity and scattering is thus minimized. The material is more transparent, allowing increased emission from the warmer material at depth. The spectra labeled b and c were taken of the same sample but with 410 torr and 5 torr of dry N_2 added to the chamber, respectively. These data show reduced spectral contrast presumably due to a lesser thermal gradient brought about gas conduction in the pore spaces. However, the 410 torr spectrum shows more contrast than the 5 torr spectrum, counter to intuition. It is plausible that the effect of the gas at higher pressures is harder to predict since it is in contact with the 77 K radiation shield. The band near 12.5 μm is also a Christiansen-type feature and is evident in all three plots. Note that the 9-μm quartz doublet is more evident in the gas spectra than in the vacuum spectrum. Another interesting aspect which occurs in these spectra is that there is

virtually no discernable shift in the wavelength location of the emission maxima which was so notable in the measurements of Logan et al. (1973).

Conclusion: We measured emission spectra of particulate quartz heated from below in an environment chamber designed to simulate the conditions of remote planetary surfaces. Our results show that the spectra of particulate materials on the surface of warm airless bodies display prominent emission features due to the existence of near-surface thermal gradients. Increasing the gas pressure tends to decrease the magnitude of the thermal gradient, thus decreasing the spectral contrast. Our spectra are in general consistent with the measurements of Logan et al. (1973). However, our spectra do not show the shift in the wavelength location of the emission maxima with changes in gas pressure that occurred in their measurements. Since the samples in the Logan et al. (1973) experiment were heated from above with a solar lamp, it seems reasonable to conclude that the shifts seen in their spectra are due to differences in solar versus infrared absorption length scales. This result suggests that these wavelength shifts can be understood with further modeling and experimental measurements, and the emission features can be used to determine surface composition of airless bodies.

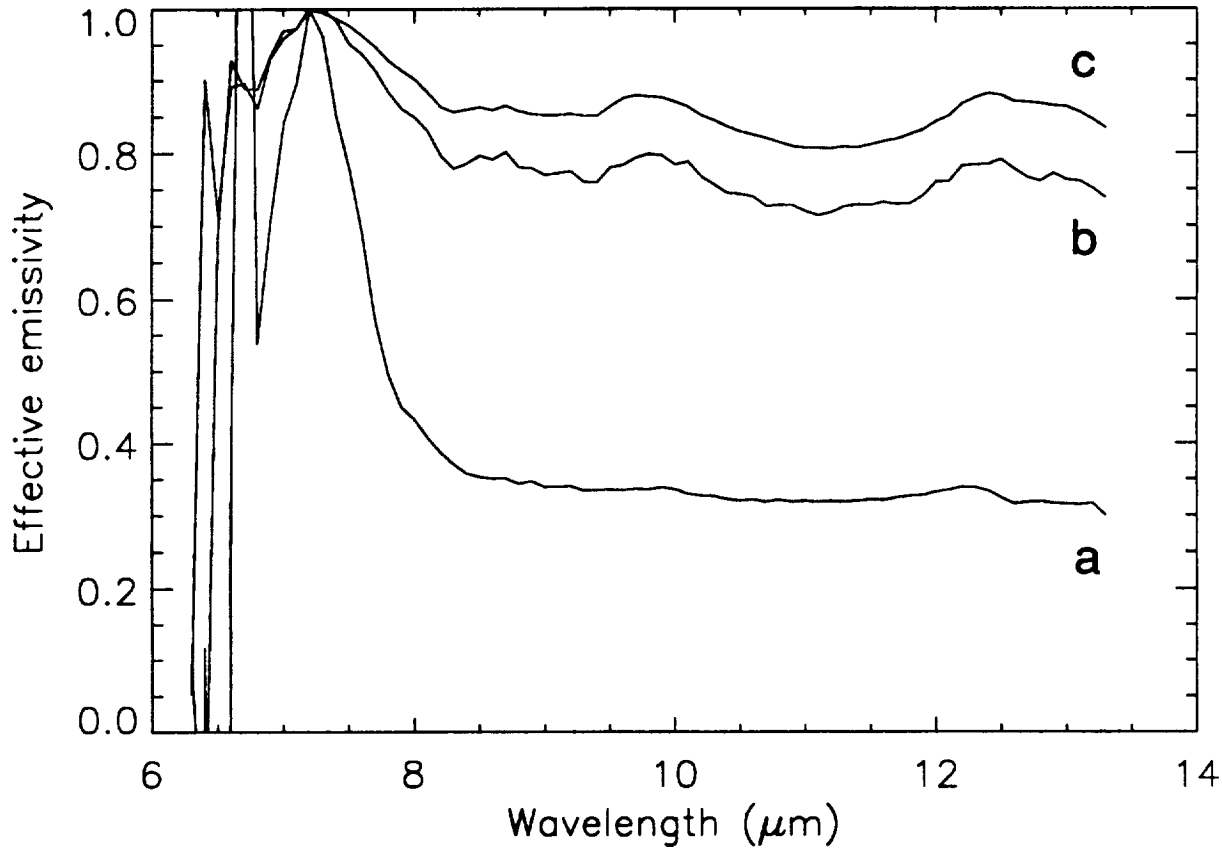

Figure 1: Effective emissivity spectra of granulated quartz measured at 3 different pressures: 10^{-3} torr (a), 410 torr (b), and 5 torr (c).

REFERENCES: Logan, L. M. et al., *J. Geophys. Res.* **78**, 4983-5003, 1973.

GEOLOGIC MAP OF THE MTM -85280 QUADRANGLE, MARS; K. E. Herkenhoff, Jet Propulsion Laboratory, California Institute of Technology

The geologic map presented here covers the portion of Mars between latitudes 82.5°S to 87.5°S, longitudes 260-300°W. The Viking Orbiter 2 images used to construct the photomosaic base used for mapping were taken during the southern summer of 1977, with resolutions no better than 180 meters/pixel. A digital mosaic of Mariner 9 images was also constructed to aid in mapping. The Mariner 9 images were taken during the southern summer of 1971-72, and have resolutions as high as 90 meters/pixel. However, usefulness of the Mariner 9 mosaic is limited by incomplete coverage and atmospheric dust opacity.

The most common bedrock unit in this quadrangle is the polar layered deposits, first described by Murray *et al.* [1] and Cutts [2]. The layered deposits are characterized by smooth morphology and gently sloping, asymmetrical troughs. Visibility of layers is limited by the resolution of available images of the map area, but layering in this area appears similar to that in other parts of the layered deposits in terms of topographic expression, dip, and thickness [3]. An unusually steep, irregular scarp in the layered deposits has been found at 83.3°S, 297°W, near the upper edge of the flank of a low-relief trough. Unlike the steep scarps in the north polar layered deposits [4], this scarp does not appear to be the source of dark, saltating material. The scarp is barely resolved in a 91 m/pixel Mariner 9 image, and appears to be fluted with individual flutes up to 1 km across. Other trough flanks in this area have low-albedo streaks extending from flat areas of layered deposits down the shallow slopes of the trough flanks. These streaks are interpreted as areas of layered deposits that have been exposed by saltation of dark material and removal of the dust mantle. Only two possible impact craters have been recognized in the layered deposits on this map, one of which was noted by Plaut *et al.* [5]. Their modeling suggests that the layered deposits are at least 120 million years old, and the mapping presented here is consistent with their results.

The layered deposits appear to have been eroded to form Chasma Australe and expose the upper member of the Dorsa Argentea formation along the northeast side of the map. Tanaka and Scott [6] used Viking Orbiter images to recognize flow fronts in areas outside this map in the Hesperian-age Dorsa Argentea Formation, and interpreted the member as volcanic in origin. They and others recognized braided and sinuous ridges in the member that have been variously interpreted as volcanic, aeolian, tectonic, fluvial or glacial features [7]. None of these hypotheses for the origin of these ridges can be ruled out completely using observations of the few ridges in this map area. Better understanding of these features will require higher-resolution imaging from future spacecraft.

Two nonvolatile surface units overlying the layered deposits are also mapped here. These units were first recognized and mapped by Herkenhoff and Murray [8] at 1:2,000,000 scale using a color mosaic of Viking Orbiter images. This mosaic and an additional Viking color mosaic were used to confirm the identification of three color/albedo units within this quadrangle: bright red dust mantle (unit Am), darker, less red layered deposits (unit Ald), and dark, neutrally colored saltating material (unit Ad). The colors and albedos of these units are presented in Table 1, where Lambert albedos were derived by dividing the observed reflectance (corrected for atmospheric scattering) by the cosine of the incidence angle. Because the resolution of the color mosaics is not sufficient to map these units in detail at 1:500,000 scale, contacts between them were recognized and mapped using higher resolution (black and white) Viking and Mariner 9 images.

The bright, red dust mantle (unit Am) does not appear to obscure topography, and is therefore probably no more than a few meters thick, and perhaps much less. The extent of the dust mantle changed in some areas during the 3 Mars years between the Mariner 9 and Viking missions, indicating that it is ephemeral. A new Viking Orbiter 2 color mosaic of the study area, taken during orbit 358, was constructed using controlled images provided by T. Becker of the U. S. Geological Survey in Flagstaff. Analysis of this color mosaic indicates that the bright red unit extends beyond the layered deposits, supporting my previous interpretation of this unit as a dust mantle. This interpretation is also consistent with thermal inertia models of

GEOLOGIC MAP OF THE MTM -85280 QUADRANGLE, MARS: K. E. Herkenhoff

Viking IRTM data that show that the thermal inertia of the surface of the layered terrain is very low [9].

The location of dark, neutrally colored material (unit Ad) in topographic depressions here and elsewhere in the south polar region indicates that it is transported by saltation [8]. It may be composed of sand-sized particles or low-density aggregates of dust grains, and is more abundant in other parts of the layered terrain outside of this map area. Unit Ad is found only on exposed layered deposits, suggesting that saltation of dark particles strips away the dust mantle. Local saltation of the dark particles in unit Ad would also be expected to eject dust grains into suspension, or allow them to trickle down between dark particles and out of sight. This unit may have been deposited recently, perhaps with particle motion continuing until the present. Image resolution is insufficient to resolve dune forms, and there is no evidence of temporal variations in the extent or location of the dark material.

With the exception of areas covered by perennial frost, the south polar layered deposits appear to have undergone net erosion in the recent geologic past. Solar heating of the deposits causes sublimation of the water ice within them [10,11], probably forming a lag deposit of non-volatile material. Such a nonvolatile layer would protect underlying water ice from further sublimation. Herkenhoff [12] proposed that minor amounts of dark, magnetic dust exist in the layered deposits along with the bright, red dust (unit Am) that covers much of the Martian surface. The magnetic dust may preferentially form filamentary sublimation residue particles [13] that eventually erode and saltate, ejecting the remaining dust into suspension. Dark, low-density particles less than 1 mm in size will continue to saltate until trapped by an obstacle or in a depression, forming isolated patches of unit Ad. Eventual destruction of such particles could allow the dark dust to be recycled back into new layered deposits via atmospheric suspension.

The above scenario is consistent with the color, albedo, and geology of the units mapped here. The thin dust mantle appears to be a temporary feature, perhaps deposited during a major global dust storm such as that observed in 1971. Where it has been removed by winds, the water ice in the layered deposits is protected from further sublimation by a weathering rind of dust and residue particles. Layers may be currently forming where frost remains on the surface throughout the year [8].

REFERENCES

[1] Murray, B. C. *et al.*, *Icarus* **17**, 328-345 (1972).
[2] Cutts, J. A., *J. Geophys. Res.* **78**, 4211-4221 (1973).
[3] Condit, C. D. and Soderblom, L. A., U. S. Geological Survey Miscellaneous Investigations Series Map I-1076 (1978).
[4] Thomas, P. C., and Weitz, C., *Icarus* **81**, 185-215 (1989).
[5] Plaut, J. J. *et al.*, *Icarus* **75**, 357-377 (1988).
[6] Tanaka, K. L., and Scott, D. H., U. S. Geological Survey Miscellaneous Investigations Series Map I-1802-C (1987).
[7] Kargel, J. S., *Lunar and Planetary Science* **XXIV**, 753-754 (1993).
[8] Herkenhoff, K. E., and Murray, B. C., *J. Geophys. Res.* **95**, 1343-1358 (1990).
[9] Paige, D. A. and Keegan, K.D., *J. Geophys. Res.*, in press (1994).
[10] Toon, O. B., *et al.*, *Icarus* **44**, 552-607 (1980).
[11] Hofstadter, M. D. and Murray, B. C., *Icarus* **84**, 352-361 (1990).
[12] Herkenhoff, K. E., *Lunar and Planetary Science* **XXI**, 495-496 (1990).
[13] Storrs, A. D., *et al.*, *Icarus* **76**, 493-512 (1988).

Unit	Interpretation	Violet	Red	R/V
Am	dust mantle	0.04-0.05	0.14-0.18	3.2-3.8
Ald	layered deposits	0.03-0.05	0.10-0.13	2.5-3.2
Ad	dark material	0.02-0.05	0.04-0.10	1.8-2.1

TABLE 1. Lambert albedos and colors of surface units

GRAVITY ANALYSIS OF IMPACT BASINS AT SPACECRAFT ALTITUDES: LESSONS FROM CHICXULUB;

R. R. Herrick and V. L. Sharpton, Lunar and Planetary Institute, 3600 Bay Area Blvd., Houston, TX 77058

We have upwardly continued gravity data from the buried Chicxulub impact basin on Earth to typical orbiting spacecraft altitudes. The signal is negligible above 100 km, indicating that orbital line-of-sight (LOS) gravity will give no information about the subsurface structure of impact basins on the terrestrial planets unless the basin is extremely large (> 1000 km diameter). The gravity signal of the subsurface structure of an impact basin has most of its energy at shorter wavelengths than the structure itself, and shorter wavelength signals are preferentially decreased by upward continuation. Forward modeling of the signature caused by the Mead impact basin on Venus indicates that its topography should produce about a 20 mgal anomaly at Magellan altitude, but that only about 5 mgals of the anomaly would be clearly distinguishable from the signature of the regional field. Preliminary analysis of the Magellan LOS data over and around Mead indicate that this is the case.

INTRODUCTION. The Chicxulub structure on Earth is the only impact basin for which gravity data has been collected at high resolution and at an elevation of a few hundred meters above the structure. Here we use this data set to evaluate the gravitational signature at satellite altitudes for impact basins on other planets, particularly the Mead impact basin on Venus observed with LOS gravity data collected by the Magellan orbiter (~180 km altitude for Cycle 4 data).

Based on drill-core and gravity analysis, the Chicxulub structure is estimated to have a diameter of ~280 km and a multi-ring morphology [1]. Preburial depth varies from ~700 m near the rim to ~1.3 km in the center. Because the Chicxulub basin is filled with sediments similar to the upper target lithologies the majority of the observed gravity signature is due to the original subsurface structure of the basin rather than crater topography. The impact itself was into sedimentary rocks extending to 2 km depth, underlain by crystalline rocks. Mead basin has a diameter of 270 km, and a maximum depth of ~1 km. Thus, Mead and Chicxulub are similar-sized features. The near-surface density structure of Venus is unknown, but it is unlikely that density changes with depth more rapidly than on Earth.

The surface gravity signature at Chicxulub [Fig. 1] is negative compared to the surrounding terrain, with a a maximum anomaly ~30 mgals below regional values. Although there is a positive signature associated with uplifted deep basement the overall signature is negative due to brecciation of material in and around the transient cavity. If Chicxulub was not buried, the free-air anomaly associated with the topography would be roughly -120 mgals. Thus, the surface free-air anomaly of an intact 300 km impact basin should be negative, and a substantial fraction of this siganl is due to the subsurface structure.

Figure 1 shows the Chicxulub gravity data upwardly continued to different altitudes, and the signal is negligible at Magellan altitude. Figure 2 shows that the upward continued signal of a simple topographic model of a Chicxulub-sized basin produces a 16 mgal anomaly at Magellan altitude. Consequently, the total free-air basin signal at Magellan space craft altitudes is almost entirely due to the contribution from crater topography. Upward continuation multiplies the amplitude of the signal by $e^{-h/\lambda}$ where h is altitude and λ is wavelength. The Chicxulub data indicate that the gravity signature due to substructure is concentrated at wavelengths that are roughly one fourth those associated with the topography of an unburied basin. Thus, at Magellan altitude the signature due to the topography of Mead should be reduced by a factor of about 6 and the subsurface signature is below detection.

The width of the topographic model's signal [Fig. 2] at Magellan altitude is substantially larger than the surface feature, making it likely that much of the signal will be difficult to separate from regional gravity signatures. In fact, when the gravity is calculated due to the topography in a 1000 x 1000 km grid surrounding Mead [Fig. 3], simple techniques for removing a regional gravity signature (such as a planar fit to the regional field) leave only about a 5 mgal anomaly that can be directly associated with the crater. This corresponds closely with the observed signal we obtained from inspection of the Magellan LOS

gravity profiles over and around Mead.

In summary, as a rule of thumb, we suggest that useful information about the subsurface structure of impact basins cannot be gained at spacecraft altitudes greater than about 1/10 the diameter of the basin. At altitudes approaching the basin's diameter even the signature associated with the topography of a basin may be difficult to separate from surrounding structures.

REFERENCES. [1] Sharpton V.L. et al. (1993) *Science, 261,* 1564.

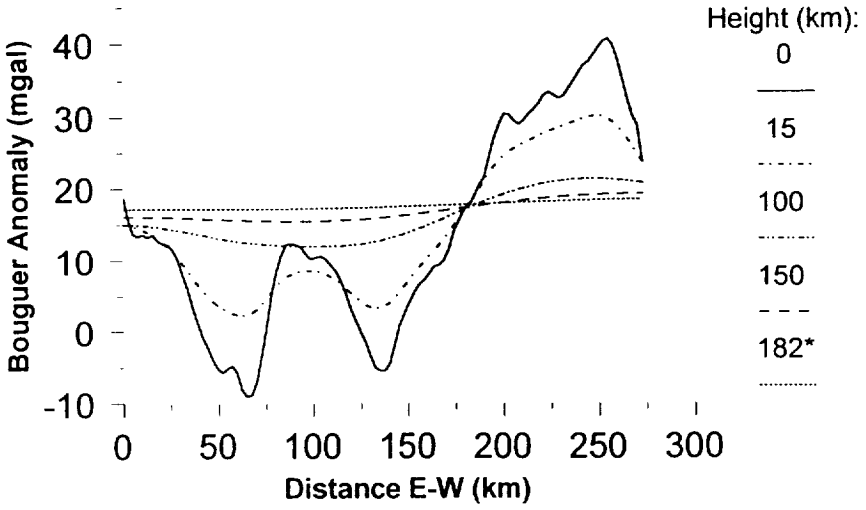

*Magellan Space Craft Altitude over Mead Impact Basin

Figure 1. Chicxulub gravity data upward continued to various elevations. At Magellan altitude the signal is negligible.

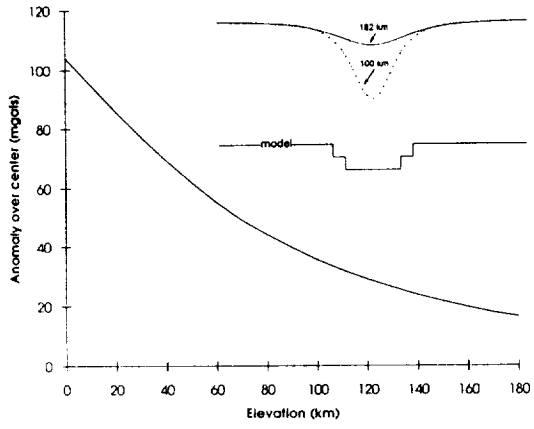

Figure 2. Gravity signal at different altitudes directly over a simple topographic model of an impact basin (crustal density of 2500 kg m^{-3} used). Inset shows shape of the anomaly at two different elevations.

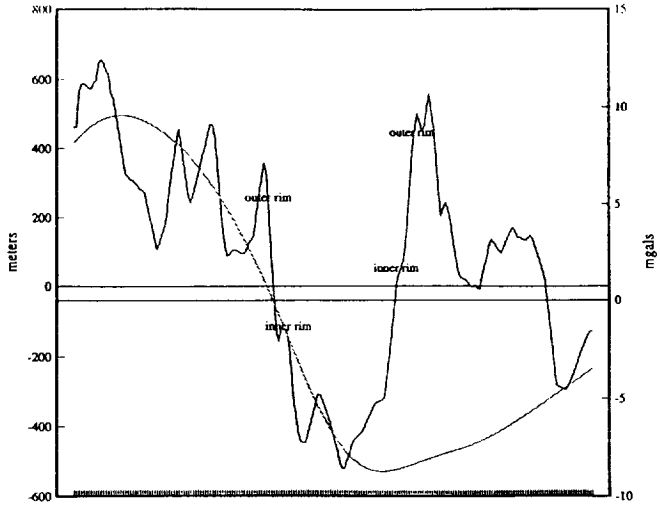

Figure 3. Topographic profile across Mead impact basin and corresponding gravity signal produced by the regional topography. Profile is 1000 km across.

^{26}Al, ^{10}Be, AND Mg ISOTOPES IN THE GRANT IRON METEORITE; G.F. Herzog[1], A.E. Souzis[2], S. Xue[1], J. Klein[3], and R. Middleton[3]. 1) Dept. Chemistry, Rutgers Univ., New Brunswick, NJ 08903; 2) US Army Research Lab., EPSD, Fort Monmouth, NJ 07703-5601; 3) Dept. Physics, Univ. Pennsylvania, Philadelphia, PA 19104.

Introduction. During the exposure of iron meteorites to cosmic rays, similar nuclear reactions of the target elements iron and nickel produce the three stable isotopes of magnesium, ^{24}Mg, ^{25}Mg, and ^{26}Mg, and the cosmogenic radionuclide ^{26}Al ($t_{1/2}$=0.71 My). When the cosmic-ray bombardment lasts 50 My or more, a lower limit typical for many irons, ^{26}Al activities reach limiting values and most of the ^{26}Al produced has time to decay to stable ^{26}Mg. Under these conditions a ^{26}Mg/^{26}Al exposure age, t_{26}, can be calculated from the relation $t_{26}(\mathrm{Gy}) = \frac{44.1 \times {}^{26}Mg(ppb)/{}^{26}Al(dpm/kg)}{[1 + P({}^{26}Mg)/P({}^{26}Al)]}$, provided that the production rate ratio P(^{26}Mg)/P(^{26}Al) is independently known. The degree to which this ratio is independent of shielding will help determine whether ^{26}Mg/^{26}Al exposure ages turn out to have general usefulness. We present here an examination of a proxy for P(^{26}Mg)/P(^{26}Al), namely the cosmogenic ^{26}Mg/^{26}Al ratio in several samples of the Grant (IIIA) iron meteorite.

Experimental Methods. Courtesy of R.S. Clarke, Jr., we obtained four samples of Grant from a documented slab kept at the Smithsonian Inst. (Washington, D.C.). The locations of the samples in the slab are indicated by the information given in Table 1 and Figure 1 of [1]. The shielding characterizations of column 3 are based on the ^{26}Al activities and ^{4}He/^{21}Ne ratios of nearby specimens [1]. Specifically, we assume comparable shielding for the following locations (This Work/Ref. [1]): O+10/N+10; K-306/J-325; K-47/Avg. {F-44, J-47}; G-223/F-223.

The isotopic composition of magnesium was determined by glow discharge mass spectrometry. The VG 9000 spectrometer used gives ppt detection limits and high mass resolution (>4000). As in [2], samples were first cut to size (20 mm × 2 mm × 2 mm) with a diamond saw and then loaded in the spectrometer and sputtered for about 1 h to remove surface contamination before data acquisition began. In this work, however, we looked at the mass range from 24 to 26 AMU only and broke an analysis time that was increased to ~ 8 h into three or more runs for each sample. Some material (0.1-0.3 g) was taken from each specimen of Grant for the separate analysis of ^{26}Al and other cosmogenic radionuclides by accelerator mass spectrometry [3].

Results and Discussion. Table 1 summarizes the results of the magnesium analyses. In the course of replicate runs we collected a total of about 250 counts attributable to ^{26}Mg for each sample, out of which ~10% were background. Counts were converted to ppb by mass by using a relative sensitivity factor supplied by instrument manufacturer. Average ^{24}Mg concentrations in the four samples vary by a factor of 20, from 0.17 to 3.3 ppb. At worst, the 1-σ uncertainties of the individual values are about 30%. As did [4], we conclude that large, local variations of the Mg concentrations occur in Grant.

Table 1. Average Mg isotopic abundances in four samples of Grant

Sample	Location		Shielding	n	^{26}Mg	^{25}Mg/^{24}Mg	^{26}Mg/^{24}Mg
	Bar	Range (mm)			ppb	ppb/ppb	
O+10	O	0 to 21	Low	6	0.21±0.04	0.34±0.05	0.36±0.09
K-306	K	-295 to -317	Med. low	4	0.122±0.005	0.48±0.04	0.35±0.01
K-47	K	-35 to -59	Med. high	6	0.118±0.025	0.78±0.25	0.70±0.09
				4	0.110±0.010	0.68±0.07	0.62±0.02
G-223	G	-213 to -234	High	3	0.54±0.02	0.17±0.02	0.16±0.01

C-2

Figure 1 shows the measured Mg isotopic ratios. To separate cosmogenic and primordial components values for the isotopic ratios of cosmogenic magnesium are needed. In [2] we chose $(^{24}Mg/^{26}Mg)_c$ =0.831 and $(^{25}Mg/^{26}Mg)_c$ = 0.914 (mass/mass) by rough analogy with results for stable neon isotopes in iron meteorites. Inspection of Figure 1 suggests that these adoptive ratios may have to be changed. Pending further work, however, we retain these values here. For terrestrial Mg abundances (by mass) we take ^{24}Mg = 77.95%, ^{25}Mg = 10.28%, and ^{26}Mg = 11.77% [5].

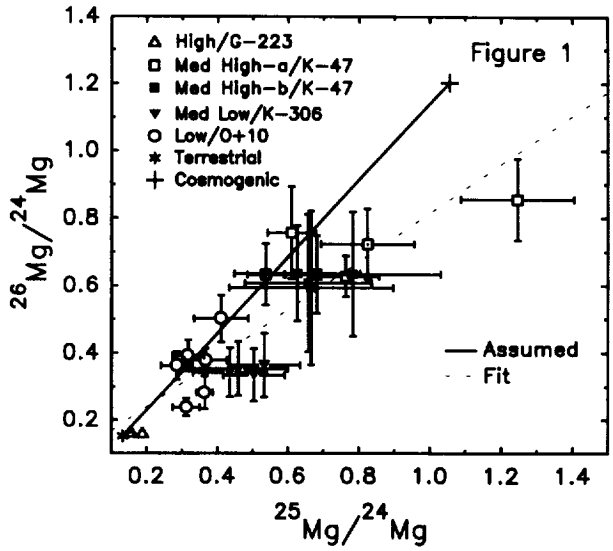

Cosmogenic ^{26}Mg and primordial ^{24}Mg $(^{24}Mg)_p$ concentrations appear in Table 2. In three of the four samples, more than 50% of the ^{26}Mg is cosmogenic. Where the average absolute deviation of $^{26}Mg_c$ is more than 20% larger than the standard deviation, we quote the former as the uncertainty; otherwise we give the latter. Also shown are the ^{26}Al and ^{10}Be activities, which agree well with the results of [1]. The measurements of ^{26}Al and ^{10}Be were more precise than usual judging from various measures of accelerator stability, the consistency of the ^{10}Be/^{26}Al ratios, and the strong linearity of a plot of ^{26}Al *vs* ^{4}He/^{21}Ne (not shown). Accordingly, we assign errors of ±4% to the measured activities.

Table 2. Cosmogenic nuclides and primordial ^{24}Mg in Grant

Sample	$^{24}Mg_p$ ppb	^{10}Be dpm/kg	^{26}Al dpm/kg	$^{26}Mg_c$ ppb	$^{26}Mg_c/^{26}$Al (10^3 atom/atom)
O+10	0.5±0.3	3.87	2.90	0.13±0.02	1.9±0.2
K-306	0.29±0.02	3.10	2.40	0.079±0.03	1.4±0.4
K-47	0.09±0.02	2.90	2.26	0.10±0.02	1.9±0.2
G-223	3.3±0.1	2.60	2.01	0.04±0.04	0.9±0.9

Concentrations of cosmogenic ^{26}Mg and ^{26}Al in the samples correlate, as one would expect from shielding systematics. The $^{26}Mg_c/^{26}$Al ratios of all four samples agree within experimental error although the result for G-223 (high shielding) is not meaningful because of a large primordial correction to ^{26}Mg (see Fig. 1). The average $^{26}Mg_c/^{26}$Al ratio, weighted inversely as the square of the uncertainties, is 1.86± 0.12. Assuming P(^{26}Mg)/P(^{26}Al) = 1.79 [2] and neglecting the terrestrial age of Grant, we obtain t_{26} = 0.68±0.05 Gy, which may be compared with the ^{40}K/K age of 0.695±0.065 Gy [6]. A terrestrial age for Grant of <50 ky (see [7]) would decrease t_{26} by <50 ky. The ^{40}K/K age agrees better with t_{26} than expected; normally exposure ages based on short-lived radionuclides are smaller than those based on potassium isotopes (see [8]). More work is needed to confirm the relative sensitivity factor of Mg, to establish the isotopic ratios of cosmogenic magnesium and to determine the production rate ratio P(^{26}Mg)/P(^{26}Al). The latter parameter may best be determined by a modern calculation.

References. **[1]** Graf Th. et al. (1987) *Nucl. Instrum. Meth. Phys. Res. B29*, 262-265. **[2]** Herzog G.F. et al. (1993) *Lunar Planet. Sci. XXIV*, 647-648. **[3]** Middleton R. and Klein J. (1987) *Phil. Trans. Roy. Soc. London A323*, 121-143. **[4]** Shimamura T., Nagai H. and Honda M. (1986) *Lunar Planet. Sci. XVII*, 795-796 .**[5]** Browne E. and Firestone R.B. (1986) *Table of Radioactive Isotopes.* John Wiley & Sons. **[6]** Voshage H. and Feldmann H. (1979) *Earth Planet. Sci. Lett. 45*, 293-308. **[7]** Vogt S. et al. (1991) *Meteoritics 26*, 403-404. **[8]** Aylmer D. et al. (1988) *Earth Planet. Sci. Lett. 88*, 107-118.

OVERTURN OF MAGMA OCEAN ILMENITE CUMULATE LAYER (II): IMPLICATIONS FOR LUNAR THERMAL AND MAGMATIC EVOLUTION.

P.C. Hess and E.M. Parmentier, Department of Geological Sciences, Brown University, Providence, RI, 02912

Inferred source depths greater than 400-500 km (1,4) as well as the ages (3.9-3.1 Gyr) of high and low-Ti mare basalt volcanism (5) provide important constraints on mechanisms of lunar internal evolution. We continue to explore a model for the evolution of the lunar interior that explains the origin and evolution of lunar magmatism (2). We assume that a magma ocean differentiated into the anorthositic crust and chemically stratified cumulate mantle. For example, an 800 km deep magma ocean would create 60 km of anorthosite crust, 40 km of an ilmenite enriched residuum beneath the crust, a 700 km cumulate pile of relatively dense (low Mg*) orthopyroxene-olivine layers near the top and less dense dunite (high Mg*) layers at the base, all overlying about 940 km of primitive moon. A calculated intrinsic (chemical) density distribution is shown in Fig. 1. The cumulate mantle is gravitationally unstable with dense ilmenite cumulate layers overlying olivine-orthopyroxene cumulates with Fe/Mg that decreases with depth. Primitive lunar mantle rises to its level of neutral buoyancy in the cumulate pile and the dense ilmenite rich layer sinks to the center, forming a core (2,3). The resulting density distribution is also shown in Fig 1.

For concentration of incompatible heat producing elements 3-10 times that of the bulk moon, the ilmenite core heats the overlying orthopyroxene-bearing cumulates. A thermal boundary layer at the core-mantle boundary that thickens by conduction becomes unstable when the Rayleigh number based on the boundary layer thickness exceeds a critical value Ra_c (~1000) generating plumes that rise into the overlying chemically layered mantle. To explore the subsequent thermal and magmatic evolution, we make several simple, but reasonable assumptions. 1) Plumes with the average temperature in the marginally stable thermal boundary layer rise to a height above the core-mantle boundary (CMB) where the positive thermal and negative chemical buoyancy balance. 2) The plumes cause overturn and mixing, thus chemically homogenizing a mantle layer equal to the plume rise height. The evolution of this mixed layer thickness z* and the mean temperature within it are calculated from a simple energy balance: the change of thermal energy over a given small increment of time is a consequence of heat added by thermal boundary layer instability and entrainment of cooler overlying mantle into the mixed layer. The core temperature is determined by balancing secular and radioactive heating with heat loss to the overlying mantle. Since substantial melting of the ilmenite-rich core occurs, the heat of melting is also included. These energy balances are formulated in a spherical geometry.

We explore predictions of this model for a range of mantle viscosity (10^{18} to 10^{20} Pa-s) and core radioactivity (3 to 10 times bulk earth) values with an initial core and mantle temperature of 1100°C. An example of the calculated thermal structure as a function of time is shown in Fig 2. Temperature increases with height in thermal boundary layer above the CMB and remains uniform through the mixed layer. Melting of the mantle first occurs just above the CMB. Shallower melting later occurs as the temperature at the top of the thickening mixed layer intercepts the peridotite solidus. Fig. 3 shows the mixed layer thickness as a function to time for the above range of parameters. The beginning of melting at the CMB and later at the top of the mixed layer are shown by symbols. Mantle viscosity affects the times of melting but not the mixed layer thickness.

This model has important implications for both the timing and chemical characteristics of lunar magmatism. Once a dense, ilmenite-rich residual layer crystallizes at the top of the magma ocean, the overturn depicted in Fig. 1 should occur in less than one Myr. Decompression melting of primitive lunar mantle during this overturn may explain early Mg-rich magmatism. As seen in Fig. 3, melting, representing the beginning of mare basalt volcanism, occurs only after a time

LUNAR THERMAL AND MAGMATIC EVOLUTION

P.C. Hess and E.M. Parmentier

interval that depends on the mantle viscosity and radioactive heat content of ilmenite cumulate. The onset of mare volcanism will also depend on whether melt generated at the core-mantle boundary is buoyant relative to overlying mantle (4) and can rise to the surface. This melt could mix with the already molten ilmenite core creating TiO_2-rich volcanics. Later volcanism from melting at the top of the mixed layer would be lower in TiO_2,thus explaining an observed trend in lunar volcanism.

References: (1) Hess, P.C., GRL 18, 2069, 1991. (2) Hess. P.C., and E.M. Parmentier, LPSC 26, 651, 1993. (3) Herbert, F., Proc. 11th Lunar Planet. Sci. Conf., 2015, 1980. (4) Delano, J.W., Proc. 20th Lunar Planet. Sci. Conf., 3, 1990. (5) Nyquist, L.E., and C.-Y. Shih, Geochim. Cosmochim. Acta 56, 2213, 1992.

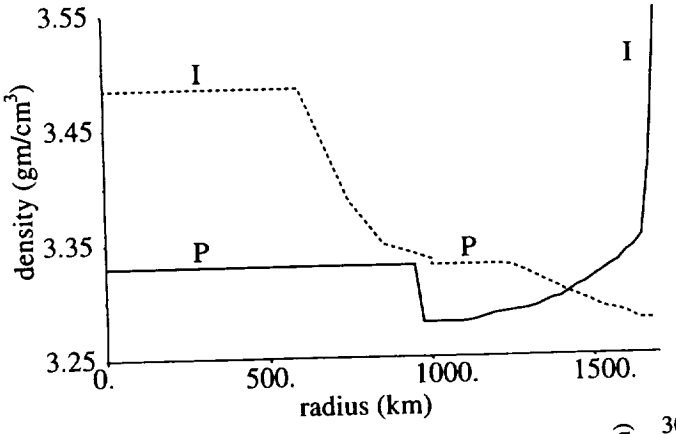

Figure 1. Intrinsic (chemical) density distribution as a function of radius before (solid) and after (dashed) overturn. We assume that buoyancy forces in the original unstable configuration result in a rearrangement of mantle layers so that density decreases monotonically with radius. I and P identify ilmenite cumulate and primitive moon, respectively.

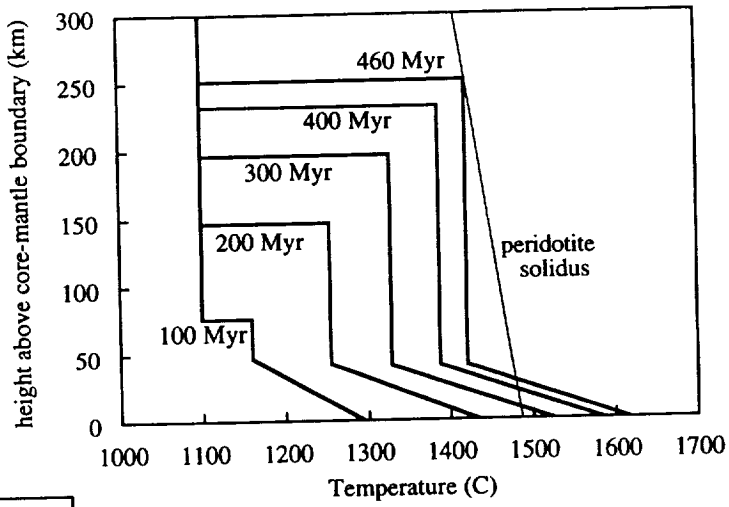

Figure 2. Calculated thermal structure as a function of time for a 10^{19} Pa-s mantle viscosity, core radioactivity 3 times bulk earth, and initial core and mantle temperature of 1100°C.

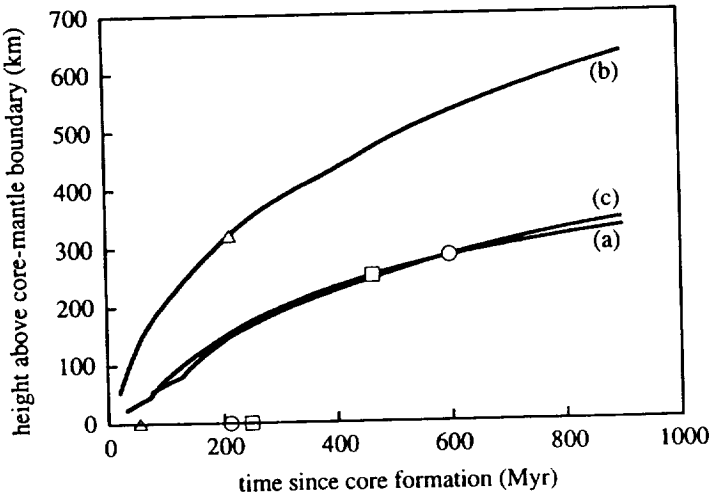

Figure 3. Mixed layer thickness as a function of time for mantle viscosities and core radioactivity values of (a) 10^{18} Pa-s and 3 x bulk earth mantle; (b) 10^{18} Pa-s and 10 x bulk earth; (c) 10^{19} Pa-s and 3 x bulk earth mantle. Symbols mark times of the beginning melting, first at the core mantle boundary and then at the top of the mixed layer.

POSSIBLE ORIGIN OF SI-BEARING METAL IN CHONDRITES. R.H. Hewins[1], B. Zanda[2], H.C. Connolly Jr.[1] and M. Bourot-Denise[2] 1. Geological Sciences, Rutgers University, P.O. Box 1179, Piscataway, N.J. 08855-1179, U.S.A. 2. Laboratoire de Minéralogie, Muséum National D'Histoire Naturelle, 61 rue Buffon, 75005 Paris,and Institut d'Astrophysique Spatiale, Orsay, France

Si-bearing metal is characteristic of enstatite chondrites (ECs), but also fairly common in the other classes of chondrites [1]. In primitive ordinary and carbonaceous chondrites (OCs and CCs), Si in metal can be found in reduced form (up to 0.2 wt% in some metal grains of Semarkona) or as round silica inclusions probably formed as an emulsion in the metallic melt during chondrule cooling [1]. Si-bearing metal grains are restricted to highly reduced chondrules (Fig. 1) and they exhibit a constant concentration within each of these chondrules, and significant differences from chondrule to chondrule. The fO2s that can be derived derived from Si concentration in metal and the Fo (or En) contents of silicates are in good agreement, which suggests integration of Si in metal during chondrule formation [1]. It is the purpose of the present paper to discuss a possible way to integrate Si in metal during chondrule formation and discuss the applicability of such a scheme to the case of enstatite chondrites.

Si has been reduced in metal in a number of experiments involving C [e.g. 2]. By introducing C-bearing phases (graphite, diamond and silicon carbide) into the precursor assemblage of synthetic chondrules, we have produced metal grains containing silica droplets exactly similar to those observed in chondritic metal. It is likely that CO-CO2 is evolved at high temperature reducing the molten charge, whereas ambiant furnace gases reassert control of the redox state of the charge during cooling, allowing the reintroduction of oxygen. By introduction of a reducing agent in the charge, we have thus been able in the laboratory to induce successive reduction and oxidation of silicon, as in chondrule formation, confirming the conclusions of [1] concerning the origin of Si-bearing metal in OCs and CCs.

The variable amounts of Si in OC and CC chondrules may be explained by varying amounts of C-bearing reducing agents in the chondrule precursors. Could a similar explanation hold for the origin of ECs? Two observations tend to suggest integration of Si into metal during chondrule formation as well: (i) Metal grains from Parsa exhibit significant chondrule to chondrule differences with respect to their Si content (Table 1). (ii) Si in the metal grains from Galim (E3) is not present in reduced form but as silica inclusions, which suggests early oxidation of Si out of metal (not due to metamorphism, as Si still is in metal in Saint-Sauveur, E4) possibly as a result of chondrule formation. However, the normal silicates in ECs (and notably Parsa) are not more reduced than those of many type I chondrules from OCs or CCs such as Semarkona and Renazzo, although accompanied by very Si-rich metal with which they clearly are not in equilibrium (Fig. 1).

The highly reduced EC mineral assemblages require unusual conditions, either high gas pressures (3), formation from a gas of high C/O ratio (4), or formation high above the nebular mid-plane (5). A key feature of EC unexplained by any of these models is that the silicates, though reduced, are not as reduced as metal in the same chondrules. Chondrules are typically not in redox equilibrium with nebular gas, either because oxygen fugacity was significantly enhanced by partial evaporation of precursor minerals and perhaps ice during chondrule heating (6), or because the low pressure gas is unable to react completely with the chondrules in the short time they are molten and they are essentially self-buffered (7). Different amounts of C-bearing phases such as organics glueing silicate precursors together, would clearly lead to different redox states in self-buffered chondrules and there must have been more C in the EC chondrite precursors to reduce more Si to metal. Similarly evaporation during heating of C-rich precursor material would generate a lower oxygen fugacity than in other regions. This might permit slight reoxidation of the silicate melt leading to FeO-bearing silicates without generally oxidising the Si to SiO2, except in the case of Galim.

This explanation requires a localised high abundance of C-rich material, which is abundant in the interstellar medium and meets an uncertain fate in the protoplanetary disk. Interstellar dust is usually assumed to be thoroughly mixed, but there are signs of imperfect mixing. The chondritic reservoirs differ chemically in non-systematic ways which are difficult to explain by nebular processes but might be inherited from inhomogeneous interstellar material. The striking N anomalies in CR chondrites (8) are due to some specific organic carrier (9) which must be heterogeneously distributed and much less abundant elsewhere. A modest enhancement of the abundance of C-bearing material in the EC reservoir would explain the reduced mineral assemblages, whereas the specific combination of reducing agents within the chondrules and a more oxidising low pressure gas outside would explain the sequence of oxidation and reduction experienced by many OC and CC chondrules.

REFERENCES

1. Zanda B., Bourot-Denise M., Perron C. and Hewins, R.H. *Science*, revised (1993).
2. T.L. Dickinson, G.E. Lofgren, I. Casanova, *Lunar Planet. Sci.* XXIII, 309 (1992).
3. Herndon, J.M. and Suess, H.E. *Geochim. Cosmochim. Acta* 40, 395 (1976).
4. Larimer, J.W. *Geochim. Cosmochim. Acta* 39, 389-392 (1975).
5. Ikeda Y. *Proc. NIPR Symp. Antarct. Meteorites* 2, 147-165 (1989).
6. Wood, J.A. *Protostars & Planets II* Black and Matthews U. Arizona, 687-702 (1985).
7. Larimer, J.W. *Geochim. Cosmochim. Acta* **32**, 1187-1207 (1968).
8. Grady, M.M. and Pillinger, C.T., *Earth Planet. Sci. Lett.* 116, 165-180 (1993).
9. Ash, R.D., Morse, A.D., and Pillinger, C.T. *Meteoritics* 28, 318-319 (1993).

Table 1 Si in metal of Parsa chondrules

Chondrule	no. of analyses	wt.% Si
C1	4	2.02 +/- 0.06
C2	14	2.28 +/- 0.10
C3	3	0.49 - 1.86
C4	4	0.26 - 1.97
C5	2	1.65 +/- 0.00
C9	2	1.55 +/- 0.02
C7*	7 periphery	1.99+/- 0.03
	2 interior	1.82 +/- 0.02
C17	1	0**
C13	1	1.98
C14	1	1.98

*"Sulfide" chondrule containing metal beads and surrounded by metal

**After correction from fluorescence from adjoining silicates, based on Mg abundance.

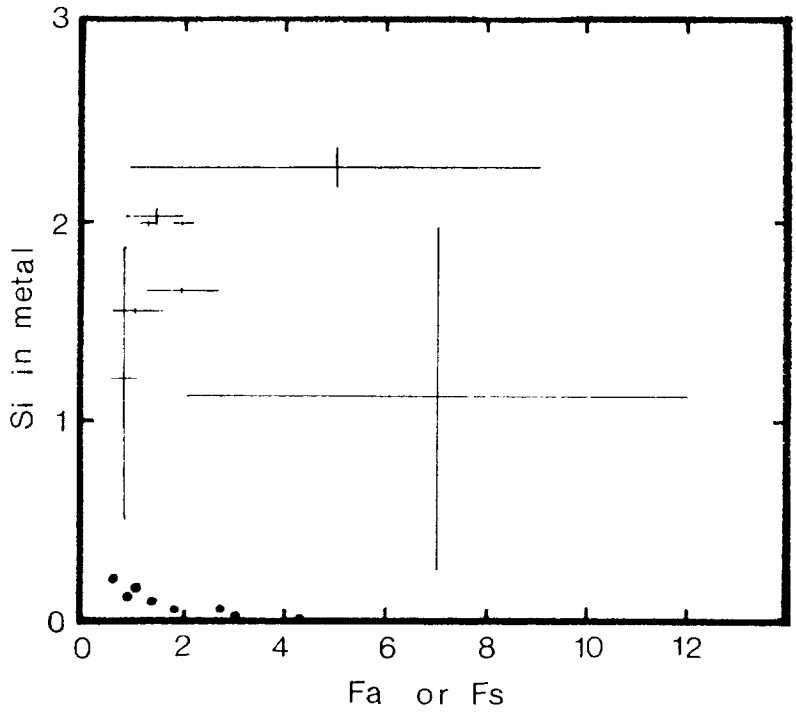

Figure 1 Si in metal versus Fa or Fs in silicates for chondrules. Metal and silicates in Renazzo and Semarkona (dots) are in redox equilibrium with Si increasing as FeO decreases. By contrast, in Parsa (crosses) there is disequilibrium, an excess of Si or of FeO, and no negative correlation.

SEARCH FOR EXTRACTABLE FULLERENES IN CLAYS FROM K/T BOUNDARIES OF NEW ZEALAND. D. Heymann[1], L.P.F. Chibante[1], W.S. Wolbach[2], and R.E. Smalley[1]. [1] Departments of Geology and Geophysics and of Chemistry, Rice University. Houston TX 77251-1892, USA. (713) 527-4890. [2]Department of Chemistry. Illinois Wesleyan University. Bloomington IL 61702-2900, USA..

The occurrence of substantial amounts of soot from wildfires at K/T boundaries worldwide (1) and the recent discovery that small amounts of C_{60} and C_{70} are formed in the free burning of hydrocarbons in air (2) suggest that fullerenes may be associated with the K/T soots, hence may become tracers in the geological record for specific processes of their formation in nature.

Samples of clays from the K/T boundaries at Woodside Creek (WC) and Flaxbourne River (FR), New Zealand (3) were treated with toluene. Also treated were shale partings from the Tertiary limestone above the boundary at Woodside Creek. The filtered fluids were analyzed by High Pressure Liquid Chromatography as described elsewhere in this volume (4). Procedural blanks (PB) and Instrumental Blanks (IB) were done.

Fig. 1 shows the chromatogram of a typical IB. Fig. 2 shows the chromatogram of the extract of one of the WC samples. The area of this peak is one order of magnitude greater than the areas under the average "zig-zag" of figure 1. The peak "rides" on the tail of a hydrocarbon peak. The retention time of C_{60} is 4.44 minutes.

Fig. 3 shows from top to bottom: A: the series of measurements of IB's, PB's, shale parting (SH) and K/T boundary clay (KTB) from the WC site. The numbers along the horizontal axis represent the exact sequence of injections of this series. The vertical axis represents the integrated peak area at the retention time of C_{60}; B: the series of measurements of IB's, PB's, SH and KTB samples from a second WC sample; and C: the series of measurements of IB's, PB's and KTB samples from the second WC sample (repeat) and from the FR sample.

RESULTS: 1) the average peak area of all IB's and PB's was 75 AUS; 2) only boundary clays have peak areas significantly larger than average IB+PB; 3) the extracts from SH contain hydrocarbons, but no significant peak at the retention time of C_{60}; 4) no significant signals above background were found for C_{70} in the samples from the boundary clays; and 5) the spectrum in the range 310-430 nm at 4.44 min is dominated by the hydrocarbon "tail", hence no acceptable C_{60} spectrum was obtained. Larger amounts of boundary clay are needed for a firm spectral proof that the signals at 4.44 min are due to C_{60}. Assuming that the extracts from the boundary clays contain C_{60}, the quantitative results are summarized in the table.

TABLE 1

Sample	C_{60} weight (ng)	C_{60} (ppm)*	C_{60} (ng/cm^2)**
(WC)KTBa	7.6 ± 1.0	0.17 ± 0.03	2.4 ± 0.3
(WC)KTBb	9.1 ± 1.5	0.17 ± 0.03	3.6 ± 0.5
(FR)KTB	1.1 ± 0.3	0.10 ± 0.03	2.5 ± 0.8

* based on the weight of the C-rich residue after demineralization. ** based on g/cm^2 of the clay seams and the weights of the pristine clay samples.

REFERENCES: (1) Anders E., Wolbach, W.S., and Lewis, R.S. (1986) *Science* 234, 261-264; (2) Chibante, L.P.F., Alford, M.A., Diener, M.D., and R.E. Smalley (1993) Personal Communication; (3) we are indebted to Dr. R.R. Brooks of Massey University, Palmerston North, New Zealand for donating the K/T boundary samples; (4) Chibante, L.P.F., Wolbach, W.S., and Heymann, D. (1993) "Determination of nanogram amounts of C_{60} by High Pressure Liquid Chromatography" In: these abstracts.

This work was supported by grants from the NSF and the Welch Foundation.

C_{60} AT THE K/T BOUNDARY. D. Heymann *et al.*

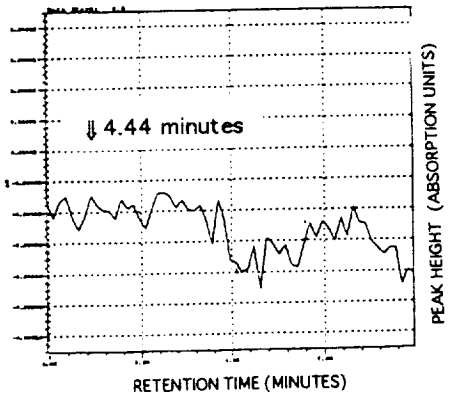

⇐FIGURE 1

CHROMATOGRAM OF AN INSTRUMENTAL BLANK INJECTION OF CLEAN TOLUENE

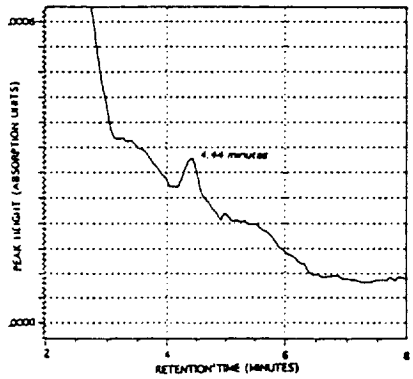

⇑ FIGURE 2

CHROMATOGRAM OF SAMPLE (WC)KTBb

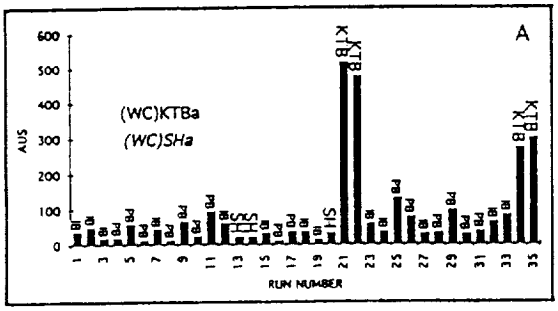

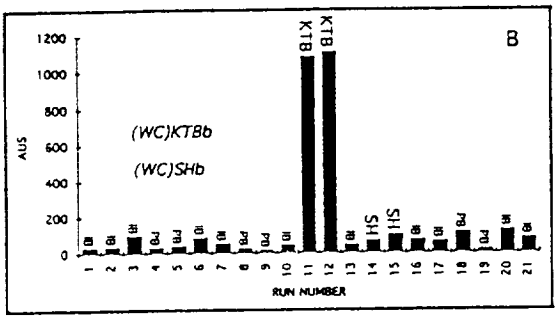

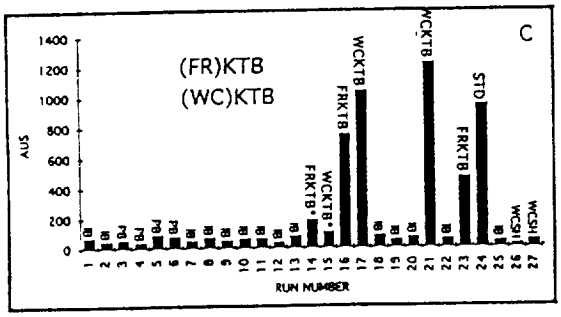

⇐FIGURE 3

RUNS OF SAMPLES AND BLANKS

PETROGRAPHIC CHARACTERIZATION OF LUNAR SOILS: APPLICATION OF X-RAY DIGITAL-IMAGING TO QUANTITATIVE AND AUTOMATED ANALYSIS. Stefan J. HIGGINS, Allan PATCHEN, John G. CHAMBERS, Lawrence A. TAYLOR, Planetary Geosciences Institute, Dept. of Geol. Sci., Univ. of Tennessee, Knoxville, TN 37996; and David S. McKAY, Mission Sci. & Tech. Office, Code SN14, Johnson Space Center, Houston, TX 77058.

The rocks and soils of the Moon will be the raw materials for various engineering needs at a lunar base, such as sources of hydrogen, oxygen, metals, etc. The material of choice for most of the bulk needs is the regolith and its < 1 cm fraction, the soil. For specific mineral resources it may be necessary to concentrate minerals from either rocks or soils. Therefore, quantitative characterizations of these rocks and soils are necessary in order to better define their mineral resource potential. However, using standard point-counting microscopic procedures, it is difficult to quantitatively determine mineral abundances and virtually impossible to obtain data on mineral distributions within grains. As a start to fulfilling these needs, Taylor et al. [1] and Chambers et al. [2] have developed a procedure for characterization of crushed lunar rocks using x-ray digital-imaging. In this paper, we describe the development of a similar digital-imaging procedure for lunar soils as obtained from an Oxford Instruments, Inc. Energy-Dispersive-Spectrometer unit (EDS) attached to a Cameca SX-50 EMP.

SOIL FORMATION AND CONSTITUENTS: Lunar soil was formed by three processes: 1) **comminution** - the disaggregation of rocks and minerals into smaller particles by micrometeorites; 2) **agglutination** - the welding of mineral and rock fragments together as a result of melts derived from micrometeorite impacts; 3) **spallation and implantation** - the addition of important elements derived from solar winds (including H_2, ^4He, ^3He, and CO) to the soil [3, 4].

These soils contain monomineralic (clean) particles and fragments of basaltic and highland rocks (multimineralic), melt rocks, microbreccias, impact glasses, pyroclastic glasses (beads), and agglutinates. Of these different soil grains, the unique constituents are the **agglutinates.** Agglutinates contain a myriad of single-domain (40-300 Å in size) and larger native iron (Fe^0) spheres formed as a product of the extreme reducing environment imposed on the silicate melt by the presence of solar-wind implanted H_2 and C [5]. In addition, release of the solar-wind implanted volatiles during this melting process creates abundant vesicles. The abundance of tiny Fe^0 spheres and the presence of vesicles serve as a means of petrographically distinguishing

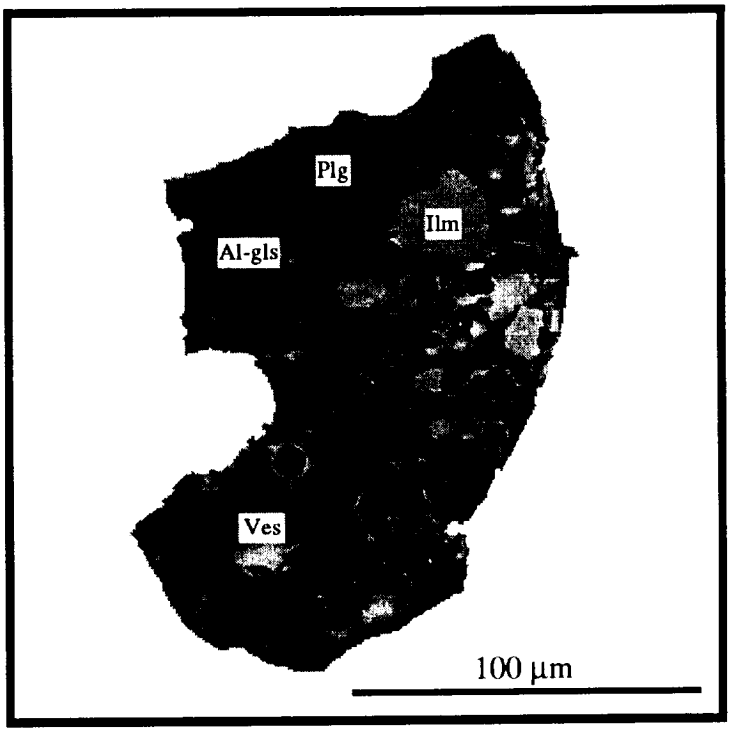

Figure 1. Digital image of a typical agglutinate from lunar soil 10084, 74-150 µm size fraction.

agglutinates from other impact products [6].

DIGITAL IMAGING OF LUNAR SOILS: In order to determine the phases and grains present in lunar soils by x-ray mapping, qualifying chemical and petrographic data were established through an iterative process involving traditional microscope techniques and EMP image analysis. The *Featurescan* software utilizes user-defined chemical and physical criteria to identify phases (e.g., hi-Ca and hi-Al are indicative of plagioclase), and because of the differences in rock and soil types amoung the two regions of the Moon (i.e., the highland and mare), the same criteria can not be used all over. In this study, user-defined criteria are established for a mare basalt soil, 10084, because such soils have greater potential for resource utilization [4].

APPLICATION: The "imaging soil petrography" technique of this study was developed using various size fractions and magnetic splits of a hi-Ti, mature mare soil, 10084. This soil was chosen because of its petrologic complexity and vast array of petrographic constituents (i.e., from agglutinates to clean mineral fragments to pyroclastic glass beads). A secondary backscatter electron (BSE) digital image of a typical agglutinate from 10084 (74-150 μm size fraction) is shown in figure 1. Note the distinct holes (vesicles) and high glass content, both criteria used for classification. Table 1 compares data for the 44-74 μm fraction of 10084 acquired from this study with petrographic particle-count data obtained by Taylor and Oder [4]. The minor differences in the data are attributed to the subjectiveness of the defining criteria. The table is broken into four groups: (I) particles containing glass, (II) monomineralic fragments, (III) basalts, and (IV) iron sulfides.

Table 1. Digital-imaging obtained particle percentage data for lunar soil 10084, 44-74 μm, as compared with microscopic data of Taylor and Oder [4].

	particle	this study	Taylor and Oder
	agglutinate	45.31	47.1
	microbreccia	6.75	0.9
(I)	melt rocks	17.38	14.9
	impact glass	6.62	5.9
	beads	0.52	3.8
	ilmenite	5.84	7.0
(II)	plagioclase	2.89	6.6
	pyroxene/olivine	1.12	1.6
(III)	basalt	13.38	11.6
(IV)	Fe/FeS	0.20	0.2

Group I soil grains, with the exception of agglutinates, are defined entirely on glass content. Morphology is used as an additional criteria for defining agglutinates. Therefore, fragments classified as agglutinates contain > 15% glass and have vesicles. Microbreccias, melt rocks, impact glasses, and beads contain 10-30%, 30-80%, 80-100%, and 80-100% glass, respectively. Beads are distinguished from impact glasses on the basis of texture (i.e., they are round). Except for ilmenite grains, particles containing 80-100% of one mineral (e.g. pyroxene, plagioclase) are placed in Group II. In this classification, fragments containing 40% ilmenite are considered (as per Taylor and Oder [4]) monomineralic. Group III (basalts) consists of soil grains that contain two or more major phases (e.g., pyroxene and plagioclase). Particles classified in Group IV (Fe/FeS) are defined according to chemistry (i.e., fragments containing low Ti and Al, and high Fe and S).

CONCLUSIONS: Essentially, the procedures outlined in this paper using digital-imaging analysis should be useful in quantitatively characterizing lunar soils for scientific purposes as well as for evaluations of potential resource utilization.

REFERENCES: [1] Taylor et. al., 1993, LPSC XXIV, 1409-10. [2] Chambers et. al., 1994, Space 94, ASCE, in press. [3] Taylor and McKay, 1992, Space 92, ASCE, 1058-1068. [4] Taylor and Oder, 1990, Space 90, 143-152. [5] Taylor, 1988, Space 88, ASCE, 67-77.

TEKTITES FOUND IN THE RUINS OF THE MAYA CITY OF TIKAL, GUATEMALA; A.R. Hildebrand, Geological Survey of Canada, 1 Observatory Crescent, Bldg. 3, Ottawa, ON, Canada K1A 0Y3; H. Moholy-Nagy, Museum of Anthropology, University of Michigan, Ann Arbor, MI, USA 48109; C. Koeberl, Institute of Geochemistry, University of Vienna, Dr.-Karl-Lueger-Ring 1, A-1010, Vienna, Austria; L. May, Department of Chemistry, Catholic University, Washington, D.C., USA, 20064; F. Senftle, A.N. Thorpe, Department of Physics and Astronomy, Howard University, Washington, D.C., USA, 20059; P.E. Smith, D. York, Department of Physics, University of Toronto, Toronto, ON, Canada, M5S 1A7

Tektites are natural glasses quenched from superheated melts produced, and ejected at relatively large velocities, by impacts on the surface of the Earth. Some of their most obvious petrologic characteristics (e.g. reduction, volatile depletion, and lack of crystallites) are a consequence of this superheating. To date, tektites have been reported from 5 strewnfields, in some cases associated with known source craters, but tektites are probably produced in all sufficiently large terrestrial impacts. Unusual glass nodules discovered by archeological studies in the Maya city of Tikal, Guatemala show petrologic signatures characteristic of tektites and may represent products of an as yet unknown impact.

Provenance: During sorting and classification of glass artifacts found in excavation of the Maya ruins at Tikal, Guatemala, 11 unworked glass nodules were separated on the basis of their shape, size (See Figure 1) and colour (clear brownish green) from the commonly found obsidian artifacts (1). The nodules were found in general excavations widely scattered through the city, mostly in small structure groups that are presumed to have been residences. We assume that the nodules were collected at points unknown and transported by the Maya to the city of Tikal; no other similar nodules have yet been reported from other Maya archeological sites.

Petrography: The 3 nodules studied to date are composed of clear glass lacking any phenocrysts, microlites or schlieren visible to optical or SE microscopes. On this basis a possible impact origin had been previously suggested (2). Spherical vesicles ranging up to ~0.5 mm occur similar in abundance and size to those found in philippinites. Although the nodules' surfaces are pitted from presumed dissolution, no surficial alteration rims were obvious in cross section.

Composition: The tektites' composition has been studied by electron microprobe, INAA, ICP-MS and XRF. All 3 samples yield similar compositions of major, minor and trace elements and results are consistent with previous work (2). The silica abundance is ~62%, a value lower than those exhibited by most tektites excepting those of Cretaceous/Tertiary (K/T) age. Indeed, the major and minor element abundances are similar to those of the K/T tektites causing us to speculate that the Tikal tektites might have been transported from K/T boundary sections that outcrop near Tikal. However, trace elements, such as the REE, revealed patterns distinct from those displayed by the K/T tektites (3,4). In general, all lithophile incompatible elements are depleted relative to abundances found in the other four tektite groups consistent with the depletion in Si although an upper crustal affinity is evidenced.

Water Content: Tektites are depleted in all volatiles relative to other natural glasses; water contents are of the order of 100 ppm which is more than an order of magnitude less than found in the driest volcanic glasses (5). The water content of the 3 samples was studied using IR spectrometry yielding water contents of 60 to 80 ppm, values typical of tektites.

Fe^{+3}/Fe^{+2} ratio: Because of superheating, tektites display reduced chemistry such as Fe^{+3}/Fe^{+2} ratios approaching zero in contrast to terrestrial volcanic glasses that exhibit ratios of near unity or above. Mossbauer studies of one of the samples detected no Fe^{+3} consistent with extreme reduction. Magnetic studies of all 3 samples reveal magnetic susceptibilities, magnetizations and Curie constants generally consistent with reduction levels as found in other tektites (6). The temperature-independent susceptibility is higher than that of most tektites, but is similar to those of Haitian K/T tektites. The Curie constants are also similar to those of the Haitian glasses.

Age: The age of the tektites was expected to be 10 to 100 million years so an Ar-Ar study was planned with an irradiation optimized for an age of this order. However, a much younger age of

800,000 ± 100,000 years (2σ) was found based on an isochron defined by the 3 samples. This experiment will be repeated with an irradiation optimized for this younger age and larger samples to provide more radiogenic ^{40}Ar.

Conclusions: The Tikal nodules are of impact origin based on their petrologic character and represent fusion of an upper crustal target of intermediate composition. No natural occurrences of tektites are known in the region excepting the potential occurrence of tektites produced by the Chicxulub impact of K/T boundary age or from the North American tektite strewn field of Late Eocene age. Both of these tektite producing events are excluded as possible sources for the Tikal tektites because of their greater ages. The remaining possibilities are that these tektites represent transported individuals (of unusual composition) from 1 of the 2 youngest tektite strewnfields (Ivory Coast or Australasian) or are products from an as yet unknown impact in the region. The former is regarded as unlikely based on available compositional constraints but the preliminary age datum does overlap the age of the Australasian strewn field which also exhibits considerable compositional variation (7). Additional studies will discriminate between these possibilities.

Acknowledgements: We are grateful to M. Thompson (Dept. of Planetary Sciences, Univ. of Arizona) for help with INAA studies, Dr. A. Beran (Institute of Mineralogy, Univ. of Vienna) for help with the IR water measurements and the Analytical Chemistry Laboratories of the GSC.

References: (1) Moholy-Nagy, H. & Nelson, F.W. (1990) *Ancient Mesoamerica, 1*, 71; (2) Essene, E.J. et al. (1987) *Eos, 68*, 462; (3) Koeberl, C. & Sigurdsson, H. (1992) *GCA, 56*, 2113; (4) Hildebrand et al. (1993) *XXIV LPSC*, 657; (5) Koeberl, C. & Beran, A. (1988), *Proc. 18th LPSC*, 403; (6) Thorpe, A.N. & Senftle, F.E. (1964) *GCA, 28*, 981; (7) Chapman, D.R. & Scheiber, L.C. (1969) *JGR, 74*, 6737.

Figure 1: Six of the irregular nodules recovered from archeological excavations at Tikal, Guatemala. The nodules range from 1.3 to 3.0 cm in greatest dimension. The nodules' shapes are apparently the result of pitting and spalling from originally comparatively equant to teardrop shapes (Courtesy of Tikal Project, University Museum).

HIGH PRESSURE AND TEMPERATURE METAL-SILICATE PARTITIONING BEHAVIOR OF MODERATELY SIDEROPHILE ELEMENTS: IMPLICATIONS FOR THE EARLY HISTORY OF THE EARTH

Valerie J. Hillgren[1], Michael J. Drake[1], and David C. Rubie[2]. [1]Lunar and Planetary Laboratory, University of Arizona, Tucson, Arizona 85721; [2]Bayerisches Geoinstitut, Universität Bayreuth, D-95440 Bayreuth, GERMANY

Introduction. It has been known for some time that siderophile element abundances in the Earth's mantle are too high for metal to have been in equilibrium with silicate [e.g., 1], particularly if equilibrium was established at low pressures and temperatures near the surface of the accreting Earth. Although many hypotheses have been proposed to account for this apparent disequilibrium, none has been entirely satisfactory [2]. Murthy [3] proposed that the problem may be reconciled if metal-silicate equilibrium was established at high pressures and temperatures. We have performed experiments on the distribution of siderophile elements between liquid metal and liquid silicate at 100 kbars and 2000 °C. These experiments demonstrate that it is unlikely that siderophile element abundances were established by simple metal-silicate equilibrium at any combination of temperature and pressure, and that core formation in the Earth was probably a mixture of complex physical and chemical processes.

Experimental Techniques. Experiments were conducted in the 1200 ton multianvil apparatus at the Bayerisches Geoinstitut. The sample was contained in either MgO or Al_2O_3 capsules which were surrounded by a MgO sleeve contained within a cylindrical $LaCrO_3$ heater with a geometry designed to minimize thermal gradients across the sample [4]. The sample assembly consisted of a MgO (+5 wt.% Cr_2O_3) octahedron with an edge length of 18 mm. Temperature was monitored with a 0.25 mm diameter W3%Re/W25%Re thermocouple in contact with the sample capsule.

The starting material consisted of a synthetic basalt prepared by mixing together reagent grade oxides in the following proportions: 50 wt. % SiO_2, 19 wt. % FeO, 13 wt. % Al_2O_3, 11 wt. % CaO, and 7 wt. % MgO. This synthetic basalt was doped with 1.5 wt. % each of NiO and CoO, or MoO_2 and WO_2, or V_2O_3, Cr_2O_3, and MnO. These mixtures were melted and quenched to a glass and then ground back to a powder. This glass powder and Fe metal filings were mixed together in an approximately 50-50 ratio by mass.

The samples were first brought to a pressure of 100 kbars, and then were heated to 1600 °C and held at that temperature for 45-60 minutes to sinter the capsule material in order to minimize its subsequent chemical interaction with the sample. The temperature was then raised to 2000 °C and held there for 3 minutes. At this temperature and pressure, both metal and silicate are liquids. The charges were quenched rapidly (to less than 300 °C in 1 second) by turning off the power to the $LaCrO_3$ furnace.

Experimental results. The samples were analyzed with a Cameca SX50 electron microprobe. The initially homogeneously distributed metal filings had largely segregated into a single spheroid in the center of the charge. The silicate liquid did not quench to a glass but segregated into two phases with a dendritic texture. Thus to determine the composition of the silicate liquid prior to quenching the electron beam was rastered over an area approximately 20 μm on a side, and 30 to 40 analyses were taken and averaged together. For the metal a point beam was used. For major elements a beam current of 30 nanoamps and a counting time of 15 seconds were used. For the trace elements beam currents between 125 and 250 nanoamps and counting times of up to 10 minutes were used.

The metal-silicate partition coefficients we determined for Ni, Co, Mo, W, Fe, V, Cr, and Mn are shown in Table 1 along with their one sigma uncertainties and an estimated oxygen fugacity relative to the iron-wüstite buffer. Molybdenum and W were both below analytic detection in the silicate glass, thus lower limits for their metal/silicate partition coefficients are reported. Our results for Ni and Fe agree well with those of Walker *et al.* [5].

Discussion. In Figure 1, we compare our partition coefficients that were approximately 1.6 log units below the iron-wüstite buffer to 1260 °C, 1 bar data that were in a similar redox state. This Figure shows that the Ni and Co metal-silicate partition coefficients decrease with

increasing temperature and pressure. Although the W partition coefficient measured in this study is only a lower limit, it is larger than its lower temperature and pressure counterpart indicating that W becomes more siderophile with increasing temperature and pressure. This result is contrary to the prediction of [3]. The Mo partition coefficient is also a lower limit. It is presently unclear whether Mo becomes less siderophile or more siderophile with increasing temperature and pressure. Because of the large variability of the lower temperature and pressure V, Cr, and Mn data, it is difficult to say what trends are present.

Although we are working under the assumption that temperature has a stronger influence on partitioning behavior than pressure, with this limited data set, we can not say for certain which variable is more important. There is evidence that pressure may play a significant role in the partitioning of siderophile elements [6].

The partition coefficients reported above may be used to evaluate whether simple high temperature equilibrium between metal and silicate during accretion of and core formation in the Earth can account for the abundances of Ni, Co, W, Mo, V, Cr, and Mn in the upper mantle of the Earth. In particular, the approximately equal abundances of Ni, Co, and W constitute a powerful test. Simple mass balance between the core and the mantle of the Earth may be used to calculate what metal-silicate partition coefficients are necessary to produce the observed abundances of these elements in the mantle. Calculated metal-silicate partition coefficients are given in Table 1. To first order, mean core-mantle partition coefficients for Ni, Co, and W need to be 40 ± 5. Inspection of Figure 1 indicates that this condition is not satisfied in the pressure range of 1 bar to 100 kbars and temperature range of 1260 °C to 2000 °C. Extrapolation of these results to higher temperatures and pressures is very uncertain, but there is little evidence that the metal-silicate partition coefficients for Ni, Co and W will ever converge on a value of 40 ± 5 for Ni, Co, and W, especially if the trends observed in Figure 1 continue.

This work was supported by NASA Grant NAGW 3348.

References: [1] A. E. Ringwood (1966) GCA 30, pp.41-104. [2] H. E. Newsom and K. W. W. Sims (1991) Science 252, pp. 926-933. [3] V. R. Murthy (1991) Science 253, pp.303-306. [4] D.C. Rubie, C. R. Ross II, M. R. Carroll, and S. C. Elphick (1993) Amer. Mineral. 78, pp.574-582. [5] D. Walker, L. Norby, and J. H. Jones (1993) Science 262, pp.1858-1861. [6] H. Keppler and D. C. Rubie (1993) Nature 364. [7] J. H. Jones and M. J. Drake (1986) Nature 322,pp.221-228. [8] M. J. Drake, H. E. Newsom, and C. J. Capobianco (1989) GCA 53, pp. 2101-2111.

Figure 1: Comparison of 1260 °C, 1 bar parition coeffcients to the ones measured in this study. One bar data from [7] and [8].

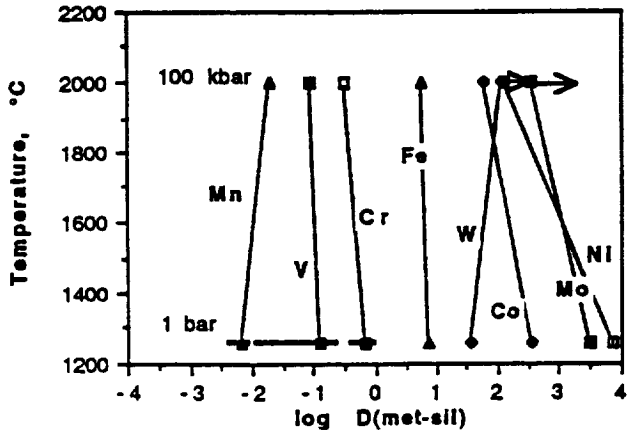

Expt.	capsule material	ΔIW	Fe	Ni	Co	W	Mo	V	Cr	Mn
888	Al_2O_3	-1.6	6.2±0.2	135±15	60±3	*	*	*	*	*
891	MgO	-2.3	12.4±0.4	247±44	106±16	*	*	*	*	*
895	Al_2O_3	-1.6	6.0±0.1	*	*	>123	>360	*	*	*
912	Al_2O_3	-1.6	6.5±0.5	*	*	*	*	0.09±0.01	0.32±0.03	0.016±0.002
$D_{(met/sil)}$ required for core/mantle equilibrium			16	45	40	35	160	4	5	13

* = not present in charge

POSSIBLE SPINEL ABSORPTION BANDS IN S-ASTEROID VISIBLE REFLECTANCE SPECTRA: T. Hiroi and F. Vilas, SN3, NASA Johnson Space Center, Houston, TX 77058; J. M. Sunshine, SETS Technology, Inc., 300 Kahelu Avenue., Mililani, HI 96789.

Minor absorption bands in the 0.55-0.7 μm wavelength range of reflectance spectra of 10 S asteroids [1] have been found and compared with those of spinel-group minerals using the Modified Gaussian Model [2]. Most of these S asteroids are consistently shown to have two absorption bands around 0.6 and 0.67 μm. Of the spinel-group minerals examined in this study, the 0.6 and 0.67 μm bands are most consistent with those seen in chromite. Recently, the existence of spinels has also been detected from the absorption-band features around 1 and 2 μm of two S-asteroid reflectance spectra [3], and chromite has been found in a primitive achondrite as its major phase [4]. These new findings suggest a possible common existence of spinel-group minerals in the solar system.

Reflectance spectra of the 10 S asteroids were measured using a CCD spectrograph [1]. Reflectance spectra of spinel-group minerals were measured using the RELAB bidirectional spectrometer at 30° incidence and 0° emergence angles [5]. A spectrum of chromite (<25 μm) from Nye, Montana was measured at every 1 nm from 0.4 to 1.1 μm [6]. A spectrum of spinel-rich CAI in the Allende meteorite was measured at every 10 nm from 0.35 to 2.6 μm by [3,7]. An absorbance spectrum of a spinel ($Mg_{0.82}Fe_{0.22}Cr_{0.92}Al_{1.05}O_4$) from Lesotho was taken from [8] and digitized at every 5 nm.

Each measured reflectance spectrum was converted to the approximate absorbance spectrum by taking its natural logarithm, which was then deconvolved into a background (linear to energy) and a series of modified Gaussians according to the Modified Gaussian Model [2]. Two parameters of the background and three parameters (band center, half width, and strength) of each absorption band were optimized for the best fit with each asteroid spectrum. For this study, the initial values of the background parameters were chosen so that the background is in contact with the measured spectrum at as many data points as possible. After deconvolving each asteroid spectrum, artificial random noise was added to the solution spectrum as a simulation of the noise introduced during asteroid observations. These simulated spectra were then deconvolved to estimate the error ranges for the band parameters.

Some of the results of the deconvolutions of reflectance spectra of the S asteroids and spinel-group minerals are shown in Fig. 1. The measured spectrum, background, fitted spectrum, and the residual errors are shown for each plot in Fig. 1. These asteroids have two broad bands and one small, narrow band in the 0.55-0.7 μm region. The small and narrow bands are, however, well within the noise and are thus deemed to be unreliable. The spinel-group minerals have three absorptions in the 0.55-0.7 μm region, which have similarities to those found in the S asteroids. However, both the Nye chromite and the Allende CAI spectra have a strong absorption band around 0.75 μm which is absent in the S asteroids. In a noisy asteroid spectrum, the 0.75 μm absorption in the Nye chromite may not be detectable, but instead be merged with the 0.66 and 0.68 μm bands to form a single absorption band around 0.68 μm. The 0.75 μm band in the Allende CAI, if present in asteroid spectra, is however, expected to be distinguishable from the 0.65 μm band.

The band centers and half widths of the major absorptions in the S asteroids and spinel-group minerals are plotted in Fig. 2. The S asteroid points are shown as filled squares with the estimated standard deviations as error bars. Points for spinel-group minerals are shown as three different markers. The uncertainty of the points for spinel-group minerals should be much smaller than the asteroid points. Asteroid 483 Seppina has no absorption bands and was well fit using only the background continuum. This suggests that a linearly tangent background is appropriate for modeling S asteroids in the 0.55-0.7 μm region. Reflectance spectra of 692 Hippodamia and 1368 Numidia are so noisy that existence of their absorption bands is highly unreliable. The absorption bands of 152 Atala overlap significantly making their band parameters uncertain. However, the band parameters of the other two absorption bands are very consistent among the asteroids and are likely to be reliable. If the 0.6 and 0.67 μm bands in the asteroid spectra are due to a single mineral phase, Nye chromite (open circle) may be a good analogue. However, further study is necessary to better confine the mineral candidates responsible for these two absorptions.

ACKNOWLEDGMENTS: We thank Drs. C. M. Pieters and M. J. Gaffey for reflectance spectra of Nye chromite and Allende spinel-rich CAI, respectively. We thank S. F. Pratt for the measurements. RELAB is a multiuser facility operated under NASA grant NAGW-748. F. V. was a visiting astronomer, CTIO, NOAO. T. H. and F. V.

are supported by NASA Planetary Astronomy Program. This work was done while T. H. held a National Research Council-NASA/JSC Research Associateship.

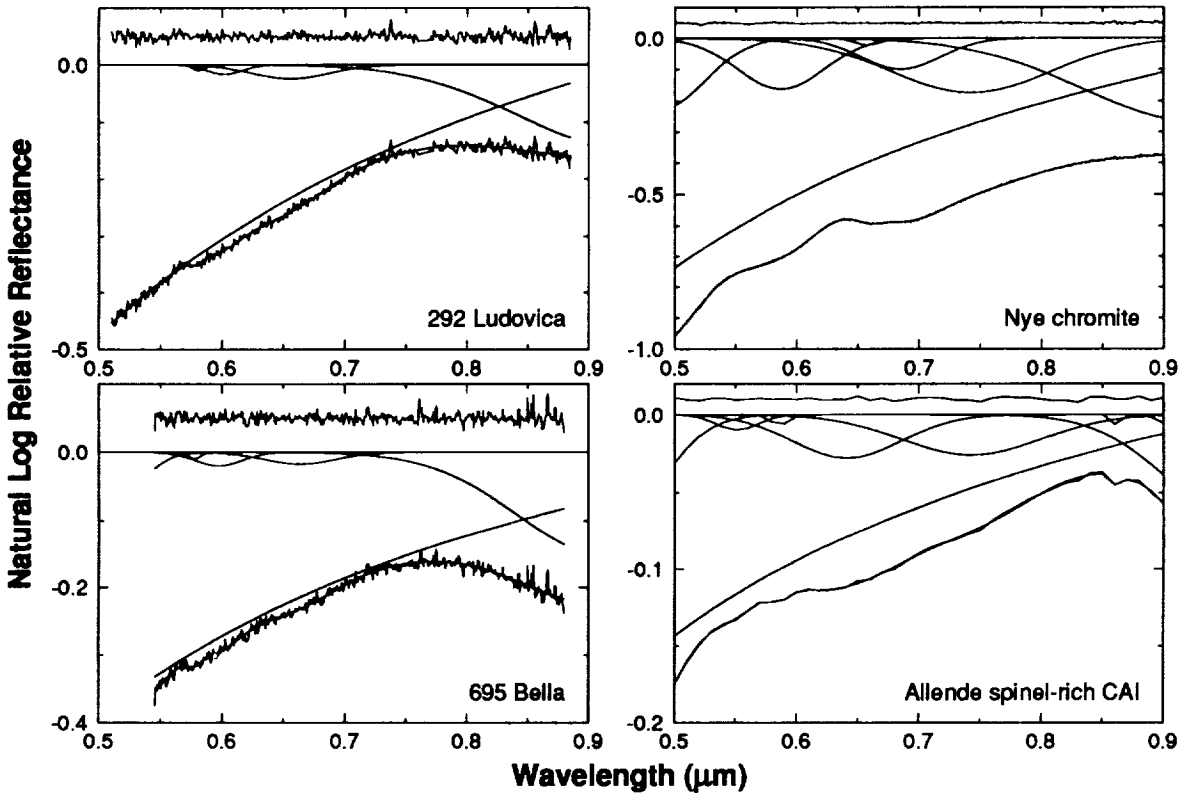

Fig. 1. Modified Gaussian Model [2] deconvolutions of reflectance spectra of two S asteroids and spinel-group minerals. The residual errors are offset for clarity.

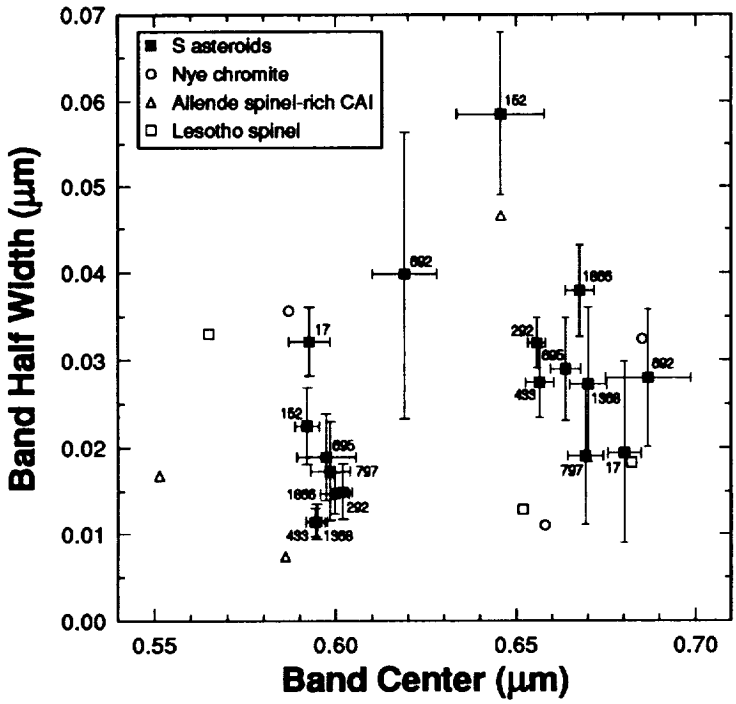

Fig. 2. A plot of the major absorption band centers and half widths of the S asteroids and spinel-group minerals.

REFERENCES: [1] Vilas F. and Smith B. A. (1985) *Icarus, 64*, 503; Vilas F. and McFadden L. A. (1992) *Icarus, 100*, 85. [2] Sunshine J. M. et al. (1990) *JGR, 95*, 6955. [3] Burbine T. H. et al. (1992) *Meteoritics, 27*, 424. [4] Takeda H. et al. (1993) *Lunar Planet. Sci., 24*, 1395. [5] Pieters C. M. (1983) *JGR, 88*, 9534. [6] Pieters C. M. (1993) Personal communications. [7] Gaffey M. J. (1993) Personal communications. [8] Mao H. K. and Bell P. M. (1974) *Carnegie Inst. Washington Yearbook, 73*, 332.

THE AMMONIA-WATER PHASE DIAGRAM AND PHASE VOLUMES TO 4 KBARS;

D.L. Hogenboom[1], J.S. Kargel[2], T.C. Holden[1], and J. Ganasan[1], [1] Department of Physics, Lafayette College, Easton, PA 18042, [2] USGS-Flagstaff

Overview. As part of a continuing study [1] we have measured the densities of liquids and placed limits on the densities of solids in the ammonia-water system under conditions corresponding to the interiors of icy satellites. Our goal is to determine the high-pressure phase diagram of the NH_3-H_2O system and the densities of the equilibrium phases so as to constrain models of cryomagmatic processes. The apparatus and techniques have been described at previous conferences [1], and recent modifications are explained below. Our results for the thermal expansion of ammonia-water liquids agree with the measurements by Croft et al. at 1 atm [2]. Our preliminary pressure-melting curves of ammonia dihydrate and ammonia monohydrate are consistent with the Clapeyron equation's predictions. Boone and Nicol's [3] measured monohydrate melting curve agrees with ours but their dihydrate melting curve does not and its slope is thermodynamically inconsistent. We observe that (1) the peritectic melting point at low pressures shifts to more water-rich compositions with increasing pressure (at least to 2 kbars), (2) the melting behavior of ammonia dihydrate changes from incongruent to congruent melting at P ~200 bars, and (3) the peritectic/eutectic liquid is slightly less dense than the compositionally equivalent solid along the pressure-melting curve to ~2 kbars; above this pressure, where ice II becomes stable, the eutectic solid is much denser than the liquid. The small density contrast at pressures < 2 kbars suggests that there should be a tendency toward igneous intrusion of NH_3-H_2O liquids in icy satellites and that fractional crystallization should not be as important in NH_3-H_2O magmas in icy satellites as this process is in silicate magmas in Earth.

Recent modifications to the experiment. A newly fabricated pressure vessel uses a miniature silicon diode thermometer that extends into the middle of the sample. This system has a much faster thermal response than our old thermometer, thus improving the accuracy of measured transition temperatures and enabling us to distinguish easily between exothermic and endothermic reactions.

We recently fabricated sample capsules that remain flexible below the ammonia-water freezing point, but they are slightly permeable to the pressure-transmitting fluid we want to use. When perfected, these capsules should allow us to measure the densities and phase transitions in completely solidified samples.

Phase equilibria. Figure 1 shows isobaric phase boundaries in the ammonia-water system at pressures of 1 atm, 1000 bars, 2000 bars, and 3000 bars. Ammonia dihydrate melts congruently above 200 bars and incongruently at lower pressures. The low-pressure peritectic (X = 32.6 wt % NH_3, T = 176.16 K, P = 1 atm) shifts at higher pressures to a more water-rich eutectic (*e.g.*, X = 28.6% NH_3, T = 176.95 K, P = 1800 bars). The ammonia monohydrate liquidus is still preliminary, but our data suggests that at pressures above about 1200 bars the stable eutectic melting point may occur between monohydrate and water ice.

The temperature-pressure curves of eutectic/peritectic melting in ice-bearing NH_3-H_2O mixtures are shown in Figure 2. The slope of the melting curve of pure ammonia dihydrate and of dihydrate-ice mixtures is consistent with the Clapeyron equation, especially when compressibility is considered (Fig. 3). Our observations and the predictions of the Clapeyron equation are inconsistent with an earlier determination of the melting curve of dihydrate [3]. The slope of their dihydrate melting curve corresponds nicely with the slope of the melting curve of ammonia monohydrate reported by those researchers and as calculated from the Clapeyron equation. Hence, we suggest that they may have mistaken ammonia monohydrate for the dihydrate. However, unlike Boone and Nicol [3], who examined compositions as ammonia-rich as the monohydrate, we have not yet explored the region to the ammonia-rich side of the dihydrate composition, so our phase diagrams and interpretations are still preliminary.

Density relationships and planetological implications. Density measurements on ammonia-water liquids at low pressures (20-50 bars) confirm the measurements of thermal expansivity made by Croft et al. [2]. We have not yet succeeded in obtaining densities for the solid phases in the ammonia-water system, although the signs of the density differentials of the solids with respect to their equilibrium liquids are consistent with the known densities of these phases at 1 atm. We have used our volume data for the liquids and the volume data and models of solid densities from [2] to compile a figure showing some important density relations along the eutectic/peritectic melting curve from 1 to 1800 bars (Fig. 4). The densities are not actually expected to fall along straight lines, but for simplicity they were calculated as such. Throughout this pressure range there is no qualitative change in the calculated relative densities of the phases. However, the apparent change of slope from positive to negative in the pressure-melting curve of dihydrate (Fig. 2) implies that the densities of dihydrate and its congruent liquid cross at this pressure; we consider this a tentative result until we obtain more data.

Figure 4 shows that the eutectic liquid has a density that is consistently less than that of its own solid at any given pressure up to ~ 2 kbars. Above approximately this pressure, ice changes to ice II, so that the solid-liquid density contrast increases further. These relationships indicate that gravitationally driven volcanic extrusion of ammonia-water liquid can occur through a crust of the same composition.

AMMONIA-WATER SYSTEM: D.L. Hogenboom et al.

The maximum density differential of any of the solid phases or of the eutectic solid mixture with respect to the eutectic liquid is ≤ 0.02 g cm^{-3} (Fig. 4). As noted by [2], extrusion of liquid could be inhibited by this small density contrast of there exists a few percent porosity in the upper crust; hence, there may be a tendency toward plutonic intrusion in the crusts of ammonia-rich icy satellites. Interestingly, Schenk and Jackson [4] interpreted the cantaloupe terrain of Triton as a product of solid-state diapirism involving ammonia hydrates; this terrain just as well could represent multiple intrusions of massive ammonia-water plutons. The small density differentials between solid phases and the eutectic liquid also suggests that fractional crystallization and development of layered plutons is less likely than in the case of mafic silicate plutons on Earth.

References. [1] Hogenboom, D.L., and Kargel, J.S., 1990, Lun. Planet. Sci. Conf. XXI, p. 522-523. [2] Croft, S.K., Lunine, J.I., and Kargel, J.S., 1988, Icarus, v. 73, p. 279-293. [3] Boone, S. and Nicol, M., 1991, Proc. Lun. Planet. Sci. Conf., v. 21, p. 603-612. [4] Schenk, P., and Jackson, M.P.A., 1993, Geology, v. 21, p. 299-302.

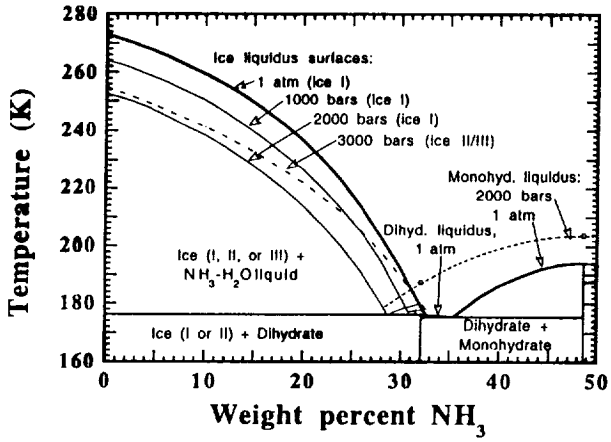

Figure 1. Phase diagram of the water-rich portion of the ammonia-water system.

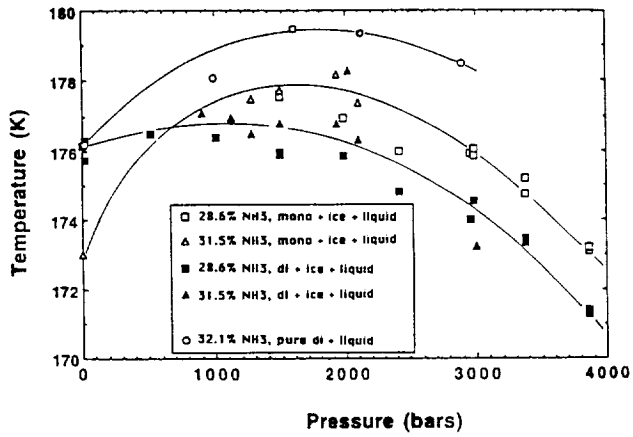

Figure 2. Melting temperature as functions of pressure in ice-bearing mixtures of ammonia-water.

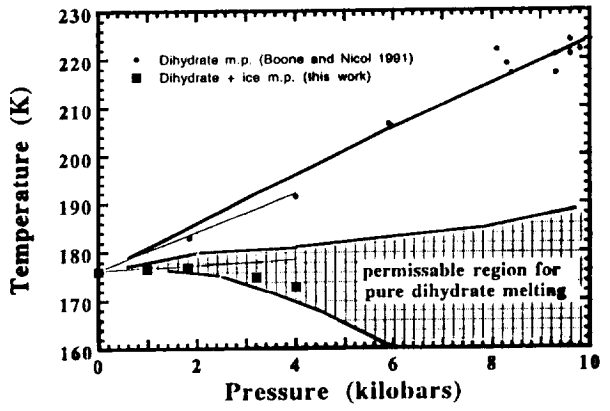

Figure 3. Melting curve of ammonia dihydrate and of dihydrate mixed with water ices. Thin lines give the Clapeyron slope of the dihydrate melting curve at the limit of zero pressure. The "permissable region" refers to the bounds of possible pressure-melting of dihydrate when compressibilities of liquid and solid are considered (from [2]). The upper bold line and dots show the melting curve of dihydrate as determined by [3]; this curve is thermodynamically inconsistent with dihydrate melting, but it is consistent with the melting curve calculated for monohydrate.

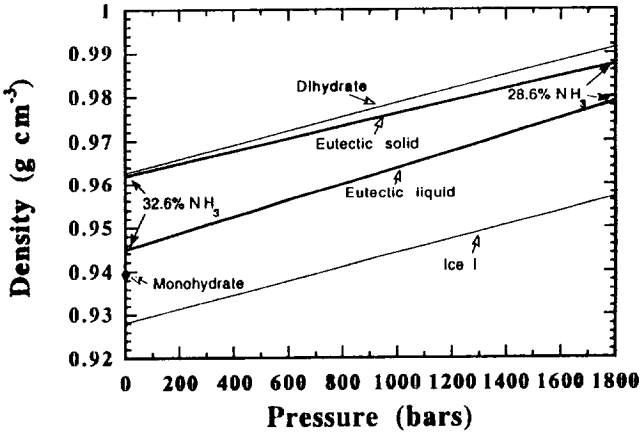

Figure 4. Densities of solids and liquids in the ammonia-water system as functions of pressure. Note that the eutectic/peritectic compositions and temperatures shift with pressure (Figs. 1, 2). The densities at 1 atm of ammonia hydrates are from [2]; their densities at elevated pressures were calculated on the assumption that, like water ice, they are about half as compressibile as their corresponding liquids. The dihydrate density is uncertain by at least +0.010, -0.013 g cm^{-3}; this uncertainty does not include uncertainty in compressibility, but it is known that dihydrate is slightly denser than its equivalent liquid at least to 1200 bars; the small density differential decreases at higher pressures.

AN EXPERIMENTAL STUDY OF KREEP BASALT EVOLUTION B. Holmberg and M.J. Rutherford, Dept. of Geological Sciences, Brown University, Providence, RI, 02912.

Introduction: The relationship of the various KREEP-rich lunar lithologies, such as lunar granites and quartz monzodiorite (QMD), to one another and to some original "ur-"KREEP component has been the subject of numerous studies (*ie.* [1],[2],[3]). It has been proposed that KREEP or urKREEP is the residuum formed by extreme fractionation of the lunar magma ocean; KREEP basalts such as 15386 have an mg* which is much too high for such a residual melt [4]. Emphasizing this point, Warren (1987) has suggested that the more evolved QMD may be used to represent urKREEP. However, the petrogenisis of QMD and lunar granite are not well established. Earlier work indicated that fractionation of a KREEP basalt composition at 1 atm produces a QMD composition residual melt just before becoming immiscible [5]. It is generally accepted that immiscibility was involved in the genisis of lunar granites in the near-surface environment; it has not been established whether immiscibility is stable at the base of the lunar crust (3 kbar). We investigate the crystallization of A15 KREEP basalt at 1 atm and 3 kbar in order to determine what melt compositions may be produced at near-surface conditions, and at the base of the lunar crust. Can QMD-like compositions be produced at the base of the crust, and can immiscibility occur at this depth?

Methods and Results: A series of experiments were performed to map out the phase equilibria and residual liquid changes during crystallization of KREEP basalt at near-surface (~1 atm) conditions. An oxide powder of KREEP basalt 15386 composition was prepared (Table 1; REE were neglected and are assumed to follow P_2O_5), and reduced to fO_2~1 log unit below the M/W buffer. To prevent oxidation, the synthesis was contained in Mo-foil in an evacuated silica glass tube and sealed. The Mo/MoO_3 buffer maintained the fO_2. The charge was suspended in a furnace and held at near liquidus temperature (1180-1200°C) for several hours to fuse the powder, dropped at ~3°C/hr to the experimental temperature, held for 48-230 hrs. (longer for lower T), then removed and quenched in water. Experiments were conducted over a temperature range from 1185°C (super-liquidus) to 1026°C (near-solidus), and were controlled to ±1-2°C. The charges were thin sectioned and examined by optical microscope and electron microprobe to determine phases present and composition of the residual glass. Microprobe examination indicates the Mo did not detectably contaminate any of the mineral or glass phases, nor did it deplete the melt in any elements to form spinels.

The liquidus temperature of 15386 is fairly tightly constrained by experiments run at 1185°, 1180°, and 1175°C, all of which produced glass only. Just sub-liquidus, at 1172°C, the melt (mg*=55) is apparently multisaturated, containing crystals of low-Ca pyroxene ($En_{68}Fs_{24}Wo_8$), plagioclase (An_{95-97}) and olivine (Fo_{79-80}). At 1140°C, with ~11% crystallization, the only crystals in contact with the melt are px+plag, though a core of ol is found in one pyroxene. From 1140° to 1080°C, the phases found are low-Ca px+plag+glass, and melt mg* drops from 47 to 34. Ilmenite saturation is reached at 1064°C (Table 1), when the melt is 55-60% crystallized (though minute ilmenite crystals occur in a couple of the higher temperature experiments, they appear to be quench crystals). Ti and Fe contents in the residual melt drop accordingly. At 1039°C, with approximately 70% crystallization and mg*=19, the melt becomes immiscible (Table 1), separating into high-FeO and high-SiO_2 compositions [1,6]. The 1039°C charge contains large (up to 100μ), euhedral tridymite crystals, in addition to px+plag+il+liquids. An experiment at 1026°C produced the same phases, plus a phosphate; the mafic glass showed greater compositional variation, presumably due to a lack of melt communication or different degrees of immiscible melt separation in this crystal-choked charge.

Preliminary results from similar experiments carried out at 3 kbar pressure (analogous to conditions at the base of the lunar crust) indicate some interesting differences. These experiments were performed using an internally heated pressure vessel, with Ar gas as the pressure medium. Chips of low-pressure experimental charges were surrounded by graphite powder (using the C/CO_2 buffer to regulate fO_2) and held at temperatures 20-35°C higher than they experienced at 1 atm in order to reach approximately the same degree of crystallization. The same general sequence of phases crystallize at 3 kbar and 1 atm: first plag+px, joined by ilmenite as crystallinity increases. Subjecting a chip of material with immiscible liquids (from 1039°C, 1 atm) to 1060°C at 3 kbar resulted in the elimination of immiscibility, while retaining ~70% crystallization; a silica polymorph is still stable. Melt compositions in this charge vary considerably, depending on the local phases in contact with the melt (Table 1 for representative extremes).

KREEP BASALT EVOLUTION: Holmberg, B. and Rutherford, M.J.

Discussion and Conclusions: The presence of olivine on the low pressure liquidus of the 15386 composition, followed closely by low-Ca pyroxene (in reaction) and plagioclase, has not previously been recognized. This indicates that olivine could have been present in the source region. However, increased pressure will reduce the size of the olivine field in the An-Fo-SiO_2 phase diagram: at some depth, olivine would not crystallize from 15386 KREEP basalt composition. We continue to investigate the possibility of an olivine-bearing KREEP source at the base of the lunar crust. At near-surface conditions, our experiments demonstrate that fractionation of 15386-type KREEP basalt follows the path: (1) initial olivine crystallization, (2) crystallization of low-Ca pyroxene+plagioclase (and reacting out of olivine) producing FeO-enriched residual melts with little SiO_2 build-up, (3) ilmenite crystallization at ~1064°C, resulting in moderate SiO_2 enrichment, and (4) liquid immiscibility producing FeO-rich basaltic and granitic melts at T<1040°C (Table 1). At base-of-the-crust pressure (3 kbar), the 15386 melt follows a similar crystal fractionation path. However, while px+plag+il crystallization produce a range of QMD-like, silica-bearing melts at 1060°C, there is no liquid immiscibility. The increased pressure apparently results in a greater increase of the solidus T than of the critical point of the miscibility gap.

Our experiments have shown that within the range of pressures of the lunar crust, a liquid of KREEP basalt composition may be evolved through crystallization to form QMD and granite. Functionally, then, KREEP basalt can satisfy this most pressing constraint for an ur-KREEP. KREEP basalt is generally considered a derivative of ur-KREEP, however, because the relatively high mg* is incompatible with calculations which suggest urKREEP was close to mg*=0 [3,4]. Recent models of overturn in the cooling lunar magmasphere due to gravitational instability [7] may provide the means for increasing the mg* of ur-KREEP through interaction with more Mg-rich materials brought up from depth. Model ages for KREEP-rich lithologies indicate that KREEP lithologies, including many lunar granites and KREEP basalts, may have existed as early as 4.3 Ga [8,9], constraining these processes to a time early in lunar history.

References: [1] Rutherford, M.J., et al (1974) *Proc. Lunar Planet. Sci. Conf.*, **5**, 569-583; [2] Ryder G. (1976) *Earth Planet. Sci. Lett.*, **29**, 255-268.; [3] Warren P.H. (1987)*Proc. Lunar Planet. Sci. Conf.*, **18**, 233-245; [4] Gromet, L.P., et al (1981) *Proc. Lunar Planet. Sci. Conf.*, **12B**, 903-913; [5] Hess P.C., et al (1975) *Proc. Lunar Sci. Conf.*, **6**, 895-909; [6] Hess P.C. (1989) In *Workshop on Moon in Transition: Apollo 14, KREEP, and Evolved Lunar Rocks*, LPI Tech. Report 89-03, p.46-52; [7] Parmentier, E.M. (1993) *LPSC XXIV*, 1119-1120; [8] Carlson, RW and Lugmair, GW (1979) *Earth and Planet. Sci. Lett.*, **45**, 123-132; [9] Shih, C-Y, et al (1993)*Geochim. Cosmochim. Acta*, **57**, 4827-4841; [10] Irving A.J. (1977) *Proc. Lunar Planet. Sci. Conf.*, **8**, 2433-2448.

TABLE 1: Compositions of glasses produced in equilibrium crystallization experiements on KREEP basalt 15386 composition (this work) and comparison KREEP-rich lithology bulk compositions

wt%	15386 experimental initial	15386 1064°C 1atm glass	15386 1039°C 1 atm. glass A	15386 1039°C 1 atm. glass B	15405,12 Granite [2]	15386 1060°C 3 kbar glass	15386 1060°C 3 kbar glass	A15 QMD [10]
SiO_2	50.8	50.54	50.77	67.49	68.08	52.90	60.96	57.4
TiO_2	2.27	4.68	3.49	1.92	0.90	3.34	2.37	1.1
Al_2O_3	14.01	10.71	10.09	11.44	10.15	11.30	11.76	13.2
FeO	11.4	15.40	18.38	7.86	6.99	16.52	10.85	11.2
MgO	7.76	3.32	2.47	1.01	1.53	2.21	1.36	3.4
CaO	10.14	10.18	10.03	4.71	4.89	8.57	6.13	9.0
Na_2O	0.98	0.90	0.81	1.23	0.79	0.95	1.26	1.0
K_2O	0.66	1.43	1.56	3.88	3.39	2.30	3.52	1.9
P_2O_5	1.04	2.41	3.41	0.91	0.52	2.87	0.99	0.4
mg*	55	28	19	19	28	19	18	35
phases	–	px+plag+il	px+plag+il+silica		–	px+plag+il+silica		–

RECIPES FOR IMPACT CRATERING; K.A. Holsapple, University of Washington, FS-10, Seattle, WA 98195

Knowledge of the relations between the sizes of craters and the impactor that caused them are now to where reasonable estimates can now be given for lunar, terrestrial and other craters, over the entirety of observed sizes and simple and complex morphologies. Here complete dimensionless and dimensional forms are presented for these relations in a concise form.

The results are a consequence of a variety of assumptions and analyses, most importantly:

1. The final size of terrestrial craters smaller than a few tens of meters diameter is determined by the strength of the surface ("strength" regime), while the size of substantially larger craters is determined by the surface gravity ("gravity" regime). The crater diameter for the transition between these regimes scales as the inverse of the surface gravity for rocky bodies. Thus, all kilometer-sized lunar craters are in the gravity regime.
2. Craters smaller than about *3 km* diameter (terrestrial) or about *15 km* (lunar) have the classical "bowl-shapes" of laboratory and explosion field craters ("simple craters"). Larger craters first form as a bowl-shaped transient crater, undergo some elastic rebound to pass through an equivalent simple shape, then undergo some poorly understood later-stage process (probably involving massive rim-wall slump) to the final shapes seen for the larger "complex" craters. This simple to complex transition size also varies as the inverse of the surface gravity.
3. The transformation from the equivalent simple morphology to the final complex morphology is volume conserving.
4. Simple craters have a scaling consistent with the point-source assumption of energy and momentum deposition (Holsapple and Schmidt [1]), and according to that determined for laboratory and field impact and explosive craters (e.g. Schmidt et al. [2]). A consequence is that all in a given geology are geometrically similar.
5. The morphometry for the simple and complex lunar craters is as given by Pike [3].

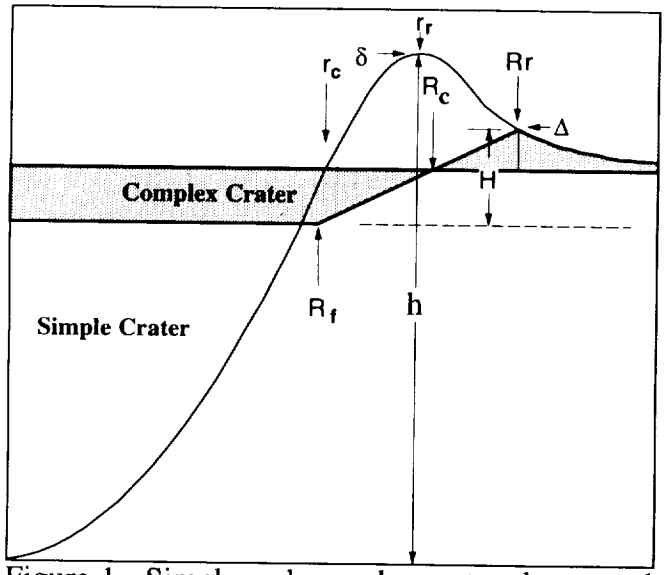

Figure 1. Simple and complex crater shapes and notation. The complex crater forms as a constant volume redistribution of material to the radius R_r, a point on the profile of the simple crater.

An analysis of the relations between an earlier simple crater and a final complex crater was given by Holsapple [4]. It was shown that the complex lunar crater measurements given by Pike are sufficient to derive the complete profile of the outer rim and ejecta blanket of an earlier simple crater, and other geometric relations. The analysis constructs a prior simple crater in very good agreement with the measured laboratory simple craters. Figure 1 shows a typical simple and the resulting complex crater and some of the notation.

Many additional analyses of the relations between simple and complex craters have been made with the purpose of ascertaining the stability of the results to small changes in the inputs. Based on a number of calculations, a final form was derived. It gave a transition radius $R_* = 6.5\ km$ for the Moon. The extension to terrestrial and other craters has been made, based on invariant dimensionless forms. The simple to complex transformation for lunar, terrestrial and general crater rim radius R_r larger than about two times the complex transition radius R_*, satisfies $R_r/r_r = 1.021(R_r/R_*)^{0.075}$. Using the existing scaling for simple craters for a non-porous body [5], and assuming a rocky impactor (but there is little effect of the impactor composition) gives the results in following tables.

RECIPES FOR IMPACT CRATERING; Holsapple, K.A.

Quantity	**General dimensionless form, rim radius $r_r \le R_*$**	**Terrestrial Craters, ≤ 3 *km* diameter**	**Lunar Craters, $\le$ *15 km* diameter**
Crater volume V_c below the original surface	$\frac{\rho V_c}{m} = 0.13 \left[\frac{g}{U^2} \left(\frac{m}{\rho} \right)^{1/3} \right]^{-0.65}$	$V_c = 4.4\ 10^{-10}\ m^{0.78} U^{1.3}$	$V_c = 1.4\ 10^{-9}\ m^{0.78} U^{1.3}$
Crater volume V_r below the rim top	$\frac{V_r}{V_c} = 1.68$	$V_r = 7.4\ 10^{-10}\ m^{0.78} U^{1.3}$	$V_r = 2.4\ 10^{-9}\ m^{0.78} U^{1.3}$
Rim radius r_r	$\frac{r_r}{V_c^{1/3}} = 1.59$	$r_r = 1.21\ 10^{-3}\ m^{0.26} U^{0.43}$	$r_r = 1.81\ 10^{-3}\ m^{0.26} U^{0.43}$
Radius r_c at ground surface	$\frac{r_c}{r_r} = 0.81$	$r_c = 9.8\ 10^{-4}\ m^{0.26} U^{0.43}$	$r_c = 1.47\ 10^{-3}\ m^{0.26} U^{0.43}$
Depth h of crater floor below rim	$\frac{h}{r_r} = 0.40$	$h = 4.8\ 10^{-4}\ m^{0.26} U^{0.43}$	$h = 7.2\ 10^{-4}\ m^{0.26} U^{0.43}$
Height δ of rim above original surface	$\frac{\delta}{r_r} = 0.07$	$\delta = 8.5\ 10^{-5}\ m^{0.26} U^{0.43}$	$\delta = 1.27\ 10^{-4}\ m^{0.26} U^{0.43}$

Table 1. Dimensionless forms for crater sizes and shapes in the gravity regime for simple craters. Dimensional forms use units of *km, sec, kg.*

Quantity	**General dimensionless form, rim radius $R_r \le 2\ R_*$**	**Terrestrial Craters, ≥ 6 *km* diameter**	**Lunar Craters, ≥ 30 *km* diameter**
Rim radius, R_r	$\frac{R_r}{R_*} = 0.89 \left[\frac{m^{1/3}}{\rho^{1/3} R_*} \right]^{1.08} \left[\frac{g}{U^2} \left(\frac{m}{\rho} \right)^{1/3} \right]^{-0.2}$	$R_r = 6.95\ 10^{-4}\ m^{0.28} U^{0.47}$	$R_r = 9.5\ 10^{-4}\ m^{0.28} U^{0.47}$
Radius at original surface, R_c	$\frac{R_c}{R_r} = 0.78 \left(\frac{R_r}{R_*} \right)^{0.056}$	$R_c = 0.76\ R_r^{1.056}$	$R_c = 0.70\ R_r^{1.056}$
Crater volume V_c below the original surface	$\frac{V_c}{R_r^3} = 0.23 \left(\frac{R_r}{R_*} \right)^{-0.47}$	$V_c = 0.28\ R_r^{2.53}$	$V_c = 0.55\ R_r^{2.53}$
Crater volume V_r below the rim top	$\frac{V_r}{R_r^3} = 0.45 \left(\frac{R_r}{R_*} \right)^{-0.49}$	$V_r = 0.55\ R_r^{2.51}$	$V_r = 1.12\ R_r^{2.51}$
Depth of crater below rim, H	$\frac{H}{R_r} = 0.35 \left(\frac{R_r}{R_*} \right)^{-0.70}$	$H = 0.47\ R_r^{0.30}$	$H = 1.3\ R_r^{0.30}$
Height of rim above original surface, Δ	$\frac{\Delta}{R_r} = 0.10 \left(\frac{R_r}{R_*} \right)^{-0.60}$	$\Delta = 0.13\ R_r^{0.40}$	$\Delta = 0.31\ R_r^{0.40}$

Table 2. Results in the gravity regime for complex craters with diameters greater than two times the transition radius R_*. Dimensional forms use units of *km, sec, kg.* It uses R_*=*1.5* for the Earth, R_*=*6.5* for the Moon.

References:
[1] Holsapple, K.A. and R.M. Schmidt, *J. Geophys. Res., Vol. 92, No. B7*, 6350-6376, 1987.
[2] Schmidt R.M., Housen K.R. and K.A. Holsapple, DNA-TR-86-182, *Defense Nuclear Agency*, Wash D.C., 1988.
[3] Pike, R.J. , in Impact and Explosive Cratering, ed by Roddy, D.J. and others, Pergamon Press, New York, 1977.
[4] Holsapple, K.A. "The Size of Complex Craters", *Lunar and Planetary Science XXIV*, 1993
[5] Holsapple, K.A., *Annual Reviews of Earth and Planetary Sciences* **21** pp333-373, 1993.

GALILEO MAGNETIC FIELD SIGNATURE: NO EVIDENCE THAT GASPRA IS DIFFERENTIATED; Lon L. Hood and Charles P. Sonett, Lunar and Planetary Laboratory, University of Arizona, Tucson, Arizona 85721.

As summarized in ref. 1, the asteroid 951 Gaspra is a relatively small, elongated body with a mean radius of about 7 km orbiting near the inner edge of the main asteroid belt (2.2 a.u.). Gaspra has spectral properties that put it in the S taxonomic class with an inferred surface composition of olivine, pyroxene, and iron-nickel metal. The major unresolved issue relating to S-type asteroids is whether they are parent bodies of ordinary chondrite meteorites or of the stony-iron meteorites. In the former case, they are undifferentiated and have relatively little metal while in the latter case they have been differentiated into metal and silicate components during an early heating event. Ground-based spectra of Gaspra show it to be unusually red and olivine-rich suggesting that it may be differentiated.

The Galileo flyby of Gaspra occurred on October 29, 1991 at a distance of 1600 km (200 - 300 Gaspra "radii"). Analyses of the resulting images suggest that it is a fragment or combination of fragments from the collisional disruption of one or more precursor asteroids and is covered with regolith (1,2). But the question remains of whether its composition is more like that of the ordinary chondrites or like that of stony-iron meteorites. Unfortunately, an accurate determination of Gaspra's mass (and hence density) was not possible due to the distance of the flyby. However, as described by Kivelson et al. (3), the Galileo magnetometer did detect a change in direction of the interplanetary magnetic field near the time of closest approach to Gaspra. The magnetic field apparently rotated toward Gaspra beginning one minute before closest approach and rotated back toward its original orientation two minutes after closest approach. According to the analysis by Kivelson et al., the field signature can be interpreted as evidence for "draping" of the solar wind magnetic field around a "magnetospheric" obstacle. Under this interpretation, Kivelson et al. estimate a magnetic dipole moment for Gaspra of between 6×10^{15} and 2×10^{17} Gauss-cm^3. Assuming a mass density of 4 gm cm^{-3}, the corresponding limits on the magnetic dipole moment per unit mass are 0.001 and 0.03 G-cm^3 gm^{-1}.

Accepting the above estimated limits on the magnetic dipole moment of Gaspra and assuming that the moment is due to intrinsic bulk magnetization, one may compare the inferred magnetization levels to those characteristic of ordinary chondrites and stony iron meteorites. Kivelson et al. (3) have concluded that the inferred magnetization limits are "in the range observed for iron meteorites and highly magnetized chondrites." Such a conclusion would suggest a stony iron composition. However, this result is based on a comparison with a relatively small sample of meteorite magnetization intensities (4) (see Figure 4 of ref. 3). Here, we compare the inferred magnetization limits of Kivelson et al. with a sample of 200 natural magnetic remanence (NRM) values previously studied by Sonett (5) and compiled from original measurements by Russian investigators, primarily Gus'kova, Pochtarev, and Gorshkov (6). The sample population contains 8 achondrites, 70 L ordinary chondrites, 35 H chondrites, 11 stony-irons (pallasites and mesosiderites), and 76 iron meteorites excluding the anomalous irons. As seen in Figure 1, the bulk magnetization limit estimates of Kivelson et al. tend to bracket the measured values for H and L ordinary chondrites. Only 2 of 11 stony-iron samples have measured NRM values within the inferred range for Gaspra. Only 21 of 76 iron meteorites have measured

NRM values within the inferred range. Thus, while a stony-iron composition may not be excluded, the inferred magnetization limits are most consistent with an ordinary chondrite composition.

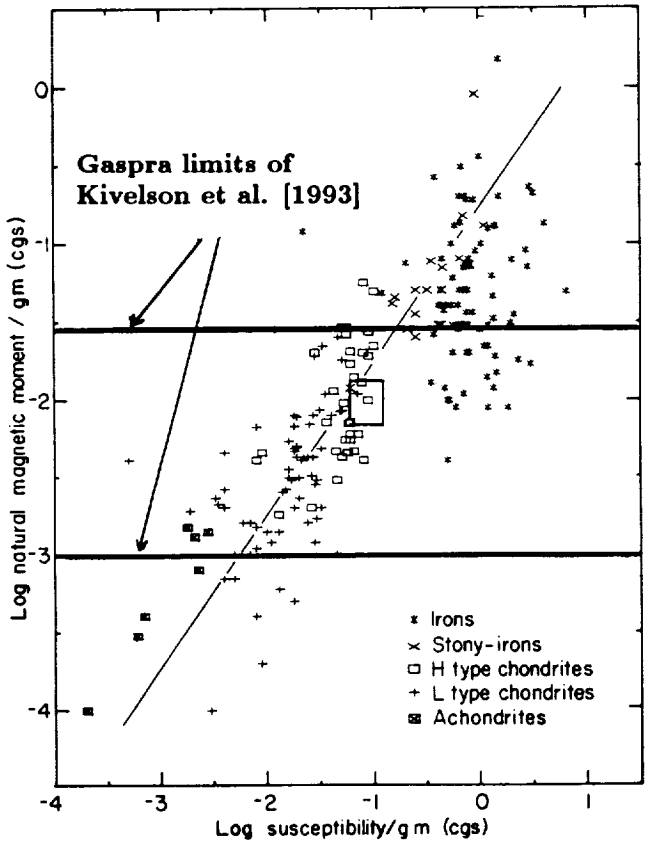

Figure 1. Comparison of meteorite NRM data from Sonett (5) with limits on Gaspra's magnetic moment per unit mass from Kivelson et al. (3). The meteorite NRM data are plotted versus magnetic susceptibility. The rectangular box indicates one-sigma values for 38 subsamples of the meteorite Pultusk.

REFERENCES: (1) Belton, M.J.S. et al., *Science, 257*, 1647-1652, 1992; (2) Greenberg, R. et al., in *Lunar Planet. Sci. XXIV*, p. 571-572, 1993; (3) Kivelson, M. et al., *Science, 261*, 331-334, 1993; (4) Sugiura, N. and D. W. Strangway, in *Meteorites and the Early Solar System*, J. F. Kerridge and M. S. Matthews, Eds. (U. of Arizona Press, Tucson, 1988), p. 595-615, 1988; (5) Sonett, C. P. *Geophys. Res. Lett., 5*, 151-154, 1978; (6) Herndon, J. M. et al. *Meteoritics, 3*, 263-274, 1972.

EVIDENCE FOR AN INTERSTELLAR NITRIDE GRAIN WITH HIGHLY ANOMALOUS ISOTOPIC COMPOSITIONS OF C, N AND Si; P. Hoppe, R. Strebel, and P. Eberhardt, Physikalisches Institut der Universität Bern, Sidlerstr.5, CH-3012 Bern, Switzerland; S. Amari, McDonnell Center for the Space Sciences and Physics Department, Washington University, St. Louis, MO 63130-4899, USA; R. S. Lewis, Enrico Fermi Institute, University of Chicago, Chicago, IL 60637-1433, USA.

We have analyzed the C-, N- and Si-isotopic compositions of 795 individual grains from the Murchison SiC separate KJE (average size 1.14 μm [1]) with the University of Bern ion microprobe. Results for a subset of these grains have been reported previously [2]. Subsequent analyses revealed one grain that contained only little carbon with an atomic abundance ratio of C/Si ~ 0.006. Its CN^-/C^- ratio, a qualitative measure for the nitrogen content, is very high, ~ 30x higher than that of a typical SiC grain (cf. Fig. 4), suggesting that this grain is a refractory nitrogen-bearing mineral. The isotopic compositions of C, N and Si are highly anomalous and similar to those of the very rare SiC component grains X [3].

Silicon nitride (Si_3N_4) and silicon oxynitride (Si_2N_2O) are silicon- and nitrogen-rich minerals. Both minerals are known to occur in meteorites. Silicon nitride has been identified in ordinary as well as in enstatite chondrites [4, 5, 6], and silicon oxynitride has been found in enstatite chondrites [7, 8]. Since we do not have information on the detailed mineralogy of our silicon- and nitrogen-rich grain we measured the elemental ratios of C, N and Si in synthetic Si_3N_4 and synthetic Si_2N_2O that contained carbon in varying small amounts. As nitrogen is measured as CN^- the CN^-/Si^- ratio strongly depends on the C^-/Si^- ratio and on the mineralogy (Fig. 1). Unfortunately, the CN^-/Si^- and C^-/Si^- ratios of our silicon- and nitrogen-rich grain (KJE853) plot in a region where the correlation lines found for synthetic Si_3N_4 and Si_2N_2O do not allow a differentiation between these two minerals. However, regardless of the presence of oxygen, in grain KJE853 nitrogen is a major element and carbon is a minor constituent.

The isotopic properties of grain KJE853 are shown in Figs. 2 and 3. It is characterized by light C ($^{12}C/^{13}C = 157\pm33$), heavy N ($^{14}N/^{15}N = 18\pm1$) and light Si ($\delta^{29}Si = -43\pm56$ ‰, $\delta^{30}Si = -271\pm50$‰). Such an isotopic pattern is the signature of the rare SiC component called grains X [3]. As grain KJE853 is isotopically related to grains X the same type of stellar source, namely, type II supernovae is suggested. The formation of silicon nitride or silicon oxynitride requires a nitrogen-rich environment such as the H-burning shell of pre-supernova stars. While the ^{15}N enrichment could originate from explosive nucleosynthesis in this layer, the isotopic signatures of C and more significantly Si require admixture of material from underlying layers, namely, the He-burning shell (rich in ^{12}C) and the O-burning shell (rich in ^{28}Si).

Five of the SiC grains X found in separate KJE have a very high nitrogen content, ~ 5x higher than that of a typical SiC grain from KJE (Fig. 4). The fact that the Al-concentration of interstellar SiC roughly correlates with the N-concentration led Zinner et al. [9] to suggest that nitrogen is present as AlN. However, as grain KJE853 is isotopically related to grains X it appears not unrealistic that the very high nitrogen content of some grains X can be attributed to silicon nitride or silicon oxynitride that is present either as subgrains (such as TiC found within interstellar graphite grains [10]) or in solid solution with SiC.

While the Murchison grain KJE853 resembles isotopically the rare SiC grains X, it has a distinctive chemistry and is a further indication of the variety of stardust that can be found.

This work was supported by the Swiss National Science Foundation and by NASA.

INTERSTELLAR NITRIDE GRAIN: Hoppe P. et al.

REFERENCES: [1] Amari S. et al. (1993) *Geochim. Cosmochim. Acta*, in press. [2] Hoppe P. et al. (1993) *Meteoritics* **28**, 363-364. [3] Amari S. et al. (1992) *Astrophys. J.* **394**, L43-L46. [4] Lee M. R. et al. (1992) *Meteoritcs* **27**, 248-249. [5] Stone J. et al. (1991) *Earth Planet. Sci. Lett.* **107**, 570-586. [6] Alexander C. M. O'D. et al. (1991) *Lunar Planet. Sci.* **22**, 5-6. [7] Andersen C. A. et al. (1964) *Science* **146**, 256-257. [8] Keil K. and Andersen C. A. (1965) *Nature* **207**, 745. [9] Zinner E. et al. (1991) *Nature* **349**, 51-54. [10] Bernatowics T. et al. (1991) *Astrophys. J.* **373**, L73-L76.

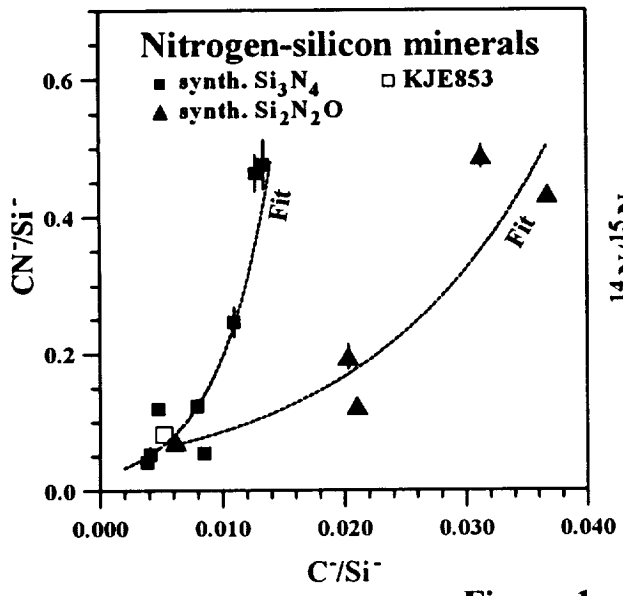

Figure 1

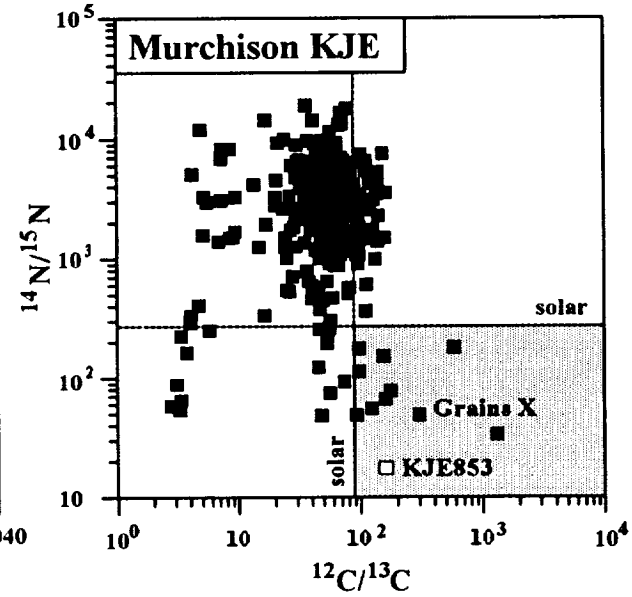

Figure 2

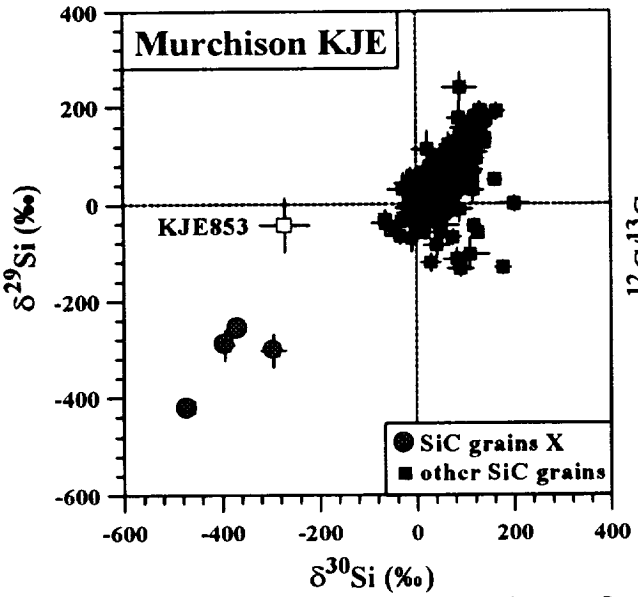

Figure 3

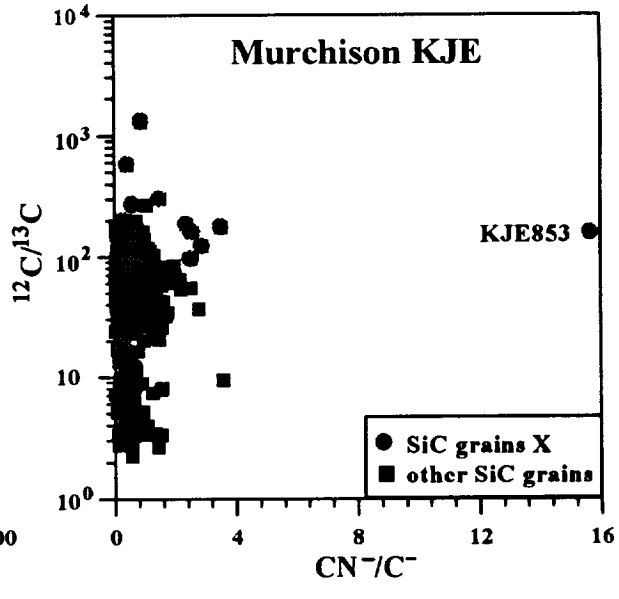

Figure 4

SHOCKED MATERIALS FROM THE DUTCH PEAK DIAMICTITE, UTAH; F. Hörz[1], T.E. Bunch[2], and V.R. Oberbeck[2], [1]NASA Johnson Space Center, Houston, TX. 77058, [2]NASA Ames Research Center, Moffett Field, CA 94035,

INTRODUCTION: Comparative planetology established that large-scale impact bombardment affected the crustal evolution of planets, including Earth. It is also established that the Earth-Moon system suffered an early period of intense bombardment, yet impact events producing the Sudbury and Vredefordt craters, or the events at the KT boundary demonstrate that "large" scale impacts did occur throughout Earth history, which is also consistent with modern astronomical observations about the flux of Earth-crossing asteroids [1,2]. These considerations lead to the search for evidence of impacts in the early terrestrial record and we suggested that some of the highly polymict, clastic deposits previously mapped as glacial tillites or diamictites may indeed be the continuous ejecta deposits of large-scale impacts [3]. Evidence of shock-metamorphism in such a deposit would provide a powerful argument for their association with impact processes, because impact is the only geologic process capable of producing the prerequisite shock waves. We report here the first evidence of shock metamorphism in the Dutch Peak diamictite, S-Utah.

THE DUTCH PEAK FORMATION: The Dutch Peak diamictite in the Sheeprock Mountains, Utah, is of Proterozoic age and a minor part of the Dutch Peak Formation [4]. The diamictite occurs at the base of a sequence of geosynclinal sediments that rest on continental, crustal rocks; these sediments formed in response to a late Precambrian continental breakup event [5]. This structural setting is similar to that for other diamictites at continental breakup margins where they formed as some of the first sediments in the geosyncline and frequently interfinger with, or directly underlie basalts [5].

One of us (T.B.) collected specimen A250, a shocked sample, during a brief visit of the Harker Canyon area of the Sheeprock Mts, Utah. Some 62 granitic and quartzite samples were collected as pebble- or cobble-sized inclusions from float that was obviously from local sources. Of the many inclusions observed, only A250 appeared to be weathered and/or deuterically altered. It is the only shocked sample in the current collection. However, a few quartz grains in the clastic matrix of other thin sections from this diamictite reveal some basal deformation lamellae that may or may not be shock produced.

SHOCKED SAMPLE A250: This sample consists of equant, anhedral grains of quartz, K-feldspar and plagioclase, the latter heavily altered and weathered (*i.e.*, only few remnants of actual fedspar remain). The dominant quartz seems heavily recrystallized and annealed; undulatory extinction is rare, yet individual quartz grains are typically made up of a few ($n < 10$) discrete, slightly misoriented domains that have exceptionally sharp and crisp boundaries. Minor accessory minerals include chlorite, Mn-rich ilmenite, sphene and carbonate. Shock-produced planar elements in quartz are illustrated in Figure 1. They are all of the decorated type, their typical appearance in highly annealed hosts [6]. Most quartz grains contain at least 1 set of lamellae; 2 or 3 lamellae systems are common with 4 sets being the maximum number of sets observed in individual grains. Evidence for shock is thus pervasive in this specific sample. Figure 1 was taken with partially crossed polarizers, and illustrates the annealed domains alluded to above. These domains do not seem unusual or important per se, but they very much affect the precision

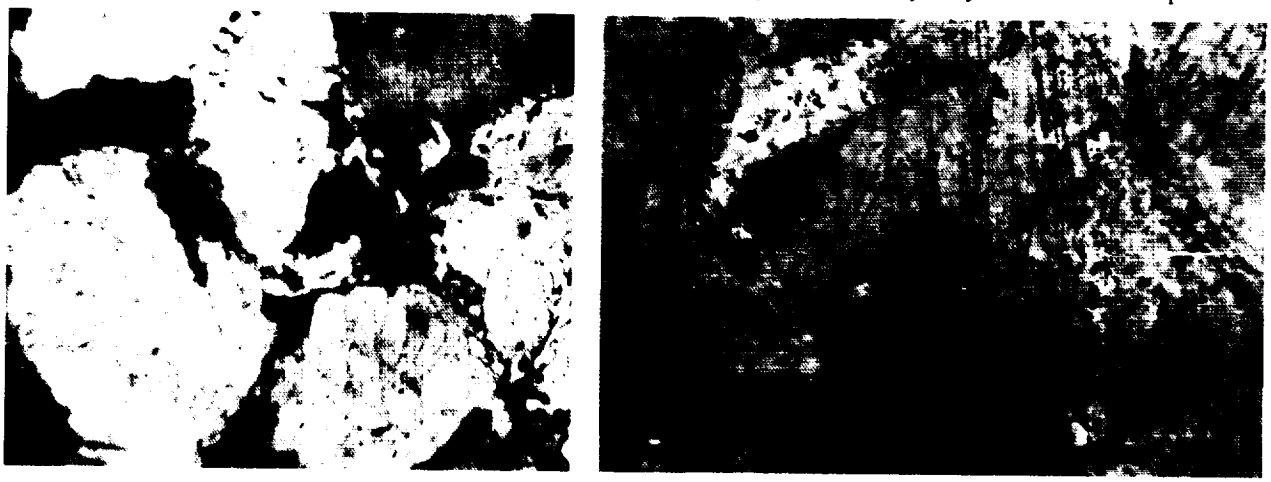

Figure 1. Overview of A250 (left; FOV = 2.5 mm) and multiple sets of shock lamellae (right; FOV = 0.3 mm).

with which the optical axis may be identified and measured, which in turn feeds into the accuracy with which the crystallographic orientation(s) of individual lamellae systems may be determined with optical (U-stage) methods. Obviously, this accuracy was not very good for sample A250.

Nevertheless, we measured the crystallographic orientation of 244 lamellae systems in 106 grains. Figure 2 illustrates the angle of the planar element normal to the optical axis for all measurements. Two broad maxima occur around 0 degrees (basal plane;{0001}) and around 22°, which coincides with the {10$\bar{1}$3} rational lattice plane of quartz. The stereographic projections (Figure 3) of select data demonstrate that {10$\bar{1}$2} orientations are present as well, although the latter orientation is not very prominent in Figure 2. The imprecision with which the optical axis could be measured in these samples leads to a relatively broad maximum between≅20° and 34° in Figure 2. Figure 3a is a stereoplot of the crystallographic orientation of 28 grains, each containing 3 sets of lamellae, while 3b summarizes 10 grains, each containing 4 lamellae sets. Note that some 75% of all systems follow rational lattice planes. These observations and crystallographically controlled deformations are consistent with shock [6,7,8].

CONCLUSION: We report on the first evidence of shock processes in materials associated with diamictite. It is presently difficult to evaluate the significance of this single specimen. Without additional and substantial field-work, and petrographic characterization of this formation, a number of scenarios for the presence of a shocked clast and the emplacement of the entire formation remain viable.

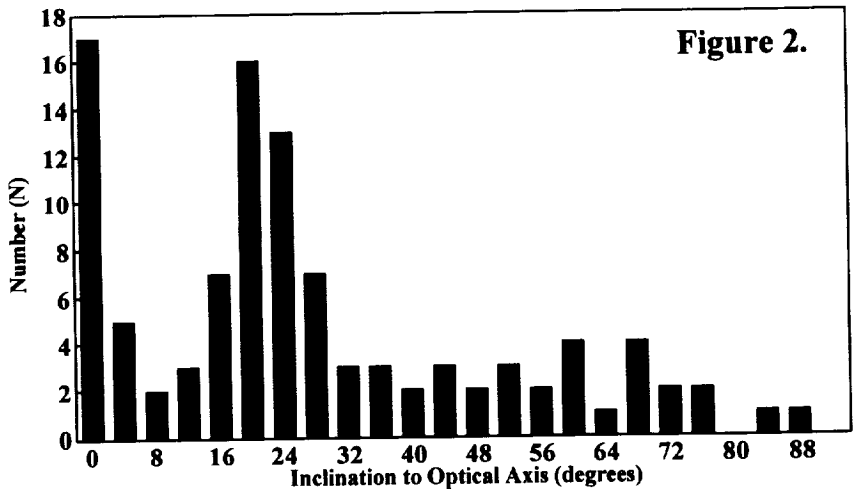

Figure 2.

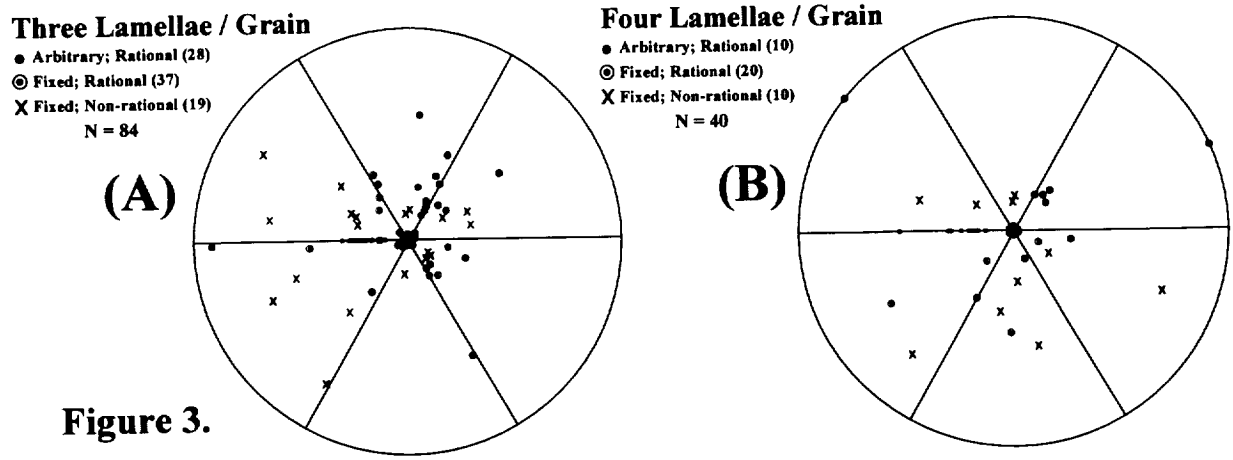

Figure 3.

REFERENCES: [1] Wetherill, G. W. and Shoemaker, E.M.(1981) *Geol. Soc. Am. Spec. Pap. 190*, 1-14; [2] Grieve, R.A.F. and Pesonen L.J. (1992), *Tectonophysics, 216*, 1-30; [3] Oberbeck , V.R. *et al.* (1993), *J. Geology, 101*, 1-19; [4] Blick, N. (1981), *Earth's Pre-Pleistocene Glacial Record*, Cambridge University Press, London, p.740-744; [5] Stewart. J.H. (1972), *Geol. Soc. Amer., 83*, 1345-1360; [6] Engelhardt, W.v. *et al.* (1968), in *Shock Metamorphism of Natural Materials*, Mono Book Baltimore, p. 475-482; [7] Hörz, F. (1968), in *Shock Metamorphism of Natural Materials*, Mono Book, Baltimore, p. 243-254; [8] Alexopoulos, J.S. *et al.* (1988), *Geology, 16*, 796-799.

EXPERIMENTAL IMPACTS INTO TEFLON TARGETS AND LDEF THERMAL BLANKETS; F. Hörz[1], M.J. Cintala[1], M.E. Zolensky[1], R.P. Bernhard[2], and T.H. See[2], [1]NASA Johnson Space Center, SN4, Houston, TX 77058, [2]Lockheed-ESC, C23, 2400 NASA Road. 1, Houston, TX 77058.

INTRODUCTION: The Long Duration Exposure Facility (LDEF) exposed ~20 m^2 of identical thermal protective blankets, predominantly on the Ultra-Heavy Cosmic Ray Experiment (UHCRE; [1]). Approximately 700 penetration holes >300 μm in diameter were individually documented, while thousands of smaller penetrations and craters occurred in these blankets [2]. As a result of their 5.7 year exposure and because they pointed into a variety of different directions relative to the orbital motion of the non-spinning LDEF platform, these blankets can reveal important dynamic aspects of the hypervelocity particle environment in near-Earth orbit (*e.g.*, [3,4,5]). The blankets were composed of an outer teflon layer (~125 μm thick), followed by a vapor-deposited rear mirror of silver (<1000 Å thick), that was backed with an organic binder and a thermal protective paint (~50-75 μm thick), resulting in a cumulative thickness (T) of ~175-200 μm for the entire blanket [6]. Many penetrations resulted in highly variable delaminations of the teflon/metal or metal/organic binder interfaces that manifest themselves as "dark" halos or rings, because of the subsequent oxidation of the exposed silver-mirror [6]. The variety of these dark albedo features is bewildering, ranging from totally absent, to broad halos, to sharp single or multiple rings [2,6].

We previously reported [7] on the behavior of pure Teflon^{FEP} using ~6 km/s soda-lime projectiles. Over the past year we have conducted similar experiments over a wide range of velocities (*i.e.*, 1-7 km/s) to address velocity dependent aspects of cratering and penetrations of teflon targets. In addition, we experimented with real LDEF thermal blankets to hopefully duplicate the LDEF delaminations and to investigate a possible relationship of initial impact conditions on the wide variety of dark halo and ring features.

CRATERING EXPERIMENTS: Craters in massive Teflon targets are characterized by frayed, fibrous, highly irregular crater bottoms and walls that form a poorly defined central cavity, which is surrounded by a relatively large, well defined spall zone (see [7]). Figure 1 illustrates the velocity dependence of crater diameter (D_c; measured at the original target surface) and of the spall zone (D_s; average diameter of highly scalloped failure surface). All experiments utilized soda-lime glass projectiles 3175 μm in diameter; experiments requiring projectile velocities >3 km/s were performed with a 5 mm light-gas gun, while a powder-propellant gun was utilized for lower velocity projectiles. For comparison, we include the general cratering equations by Watts *et al.* [8]. The agreement is fair as the crater diameter data of [8] lies between our D_c and D_s measurements; this discrepancy may -- in large part -- result from operator-dependent idiosyncrasies in the definition of D_c. In any case, a linear regression line through the experimental data yields a slope/exponent of 0.441 for the velocity dependence of crater-size in Teflon^{FEP} targets.

PENETRATION EXPERIMENTS: Penetrations of teflon are characterized by the formation of substantial spall zones at the target's front and back side, with the latter always being the larger, especially for "massive" ($T > D_p$) targets. The prominent spallation from the target's rear leads to the unusual situation, albeit over a limited D_p/T range, that the penetration hole can actually be larger in diameter than the corresponding crater in infinite half-space targets [7]. Figure 2 illustrates penetration-hole diameters (D_h) in teflon targets of variable thickness (T) using the 3175 μm soda-lime glass at systematically different velocities of 2.3, 4.0, 6.3 and 7.0 km/s. The format of this plot (see [7]) is such that one may solve for the unknown parameter D_p from the measurement of hole diameter (D_h) and target thickness (T) on space-exposed surfaces, assuming some modeled velocity. Unfortunately, the circumstance that the hole diameter can be larger than the crater diameter causes the curves to be somewhat wavy, unlike aluminum [7], yet this effect becomes progressively less pronounced as velocity increases. Note that the velocity dependence for massive targets is substantial. At any fixed D_h/T, diameter D_p systematically decreases with increasing impact velocity. In contrast, for very thin films this velocity dependence diminishes and essentially vanishes at $D_p/T > 50$ (*i.e.*, approaching the condition of $D_h/D_p = 1$). The point: velocity matters a lot with massive targets, yet little to nothing when ultra-thin foils are being penetrated.

Having ranged from infinite half-space to penetrated targets also yielded the ballistic-limit thickness (T_{BL}) for penetrations of teflon at specific velocities; at 2.3 km/s this limit was reached at $D_p/T = 0.29$, whereas it is at $D_p/T = 0.15$ for the 7 km/s case. Although T_{BL} of the intermediate velocities would nicely comply with a linear regression defined by the above velocity endmembers, such a linear extrapolation to cosmic velocities is almost certainly incorrect, because the regression would be strongly affected by modest velocity (<4 km/s) data that do not reflect expected high velocity behavior [9].

EXPERIMENTS WITH LDEF BLANKETS: We intially experimented with pristine, unexposed samples of LDEF blankets, and were unsuccessful in duplicating the dark-albedo delamination features, despite extensive efforts

at different projectile velocities (1-7 km/s), projectile sizes (50 to 3175 μm) and projectile densities (from 1 to 8 g/cm^3; nylon, glass, aluminum, alumina, brass, steel). We had no problem in producing faint rings as reported by [10], yet these features are quite different from the dark-albedo features of the space-exposed LDEF blankets. We concur with [6] that space exposure must have "pre-conditioned" and somehow weakened the teflon/Ag bonding (without specifying the actual mechanism to accomplish this). Therefore, many of the above experiments were repeated utilizing target specimens cut from space-exposed, and supposedly "preconditioned" LDEF blankets. Unfortunately, we still could not duplicate the concentric dark-albedo features. Assuming that temperature might have played some role, we conducted experiments with pristine and exposed foils cooled to -80° C at the time of impact, none of which yielded the desired delaminations. We are currently preparing to perform similar experiments at "elevated" temperatures. The nature of the dark-albedo features on the LDEF teflon thermal blankets remains enigmatic, at present.

Nevertheless, most of these blanket experiments also served as "calibration" experiments to test the assumed equivalence of pure Teflon^{FEP} and the composite LDEF thermal blankets. Absolute and relative dimensions of the LDEF blanket penetrations are indistinguishable from those of pure Teflon^{FEP}.

REFERENCES: (1) O'Sullivan, D. *et al.* (1992), *LDEF 1st Post Retrieval Symp., NASA-CP 3134,* 367-377; (2) See, T.H. *et al.* (1990) *NASA JSC Publication # 24608,* 586 pp.; (3) Zook, H.A. (1992), *LDEF 1st Post Retrieval Symp., NASA-CP 3134,* 569-581; (4) Kessler, D.E. *et al.* (1988), *NASA TM-100-47* and *LDEF 2nd Post Retrieval Symp., NASA-CP 3194,* 585-594; (5) Coombs, C. *et al.* (1993), *LDEF 2nd Post Retrieval Symp., NASA-CP 3194,* 619-664; (6) Allbrooks, M and Atkinson, D. (1992), *NASA Contractor Report NCR-188258,* 83 pp; (7) Hörz, F. *et al.* (1993), *Int. J. Impact Engng., 14,* 347-358; (8) Watts, A. *et al.* (1992) *NASA Contractor Report NCR 188259,* 92 pp; (9) Schmidt, R.M. *et al.* (1994) *Int. J. Impact Engng.,* submitted; also Holsapple, *Int. J. Impact Engng., 14,* 335-345; (10) Schneider, E. *et al.* (1993) *Int. J. Impact Engng., 14,* 631-636.

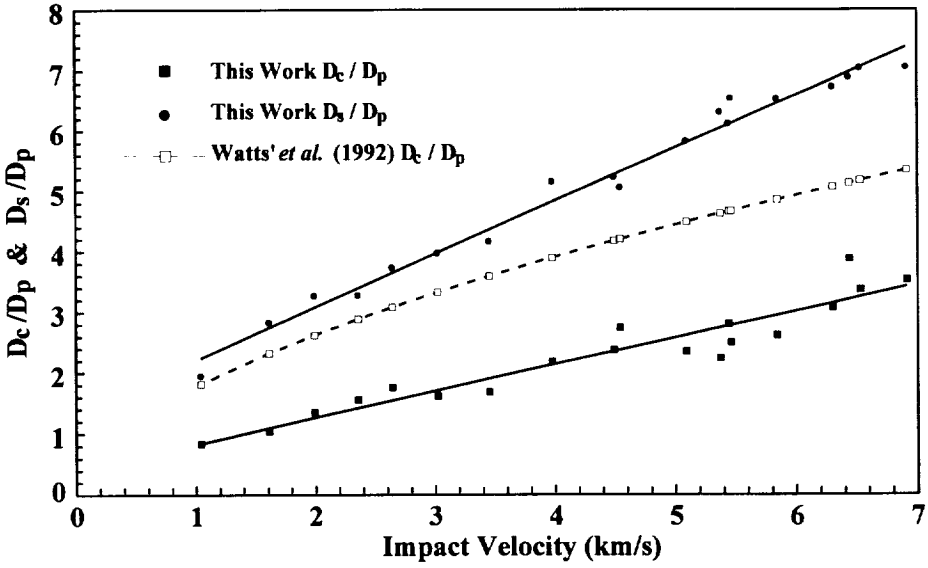

Figure 1.

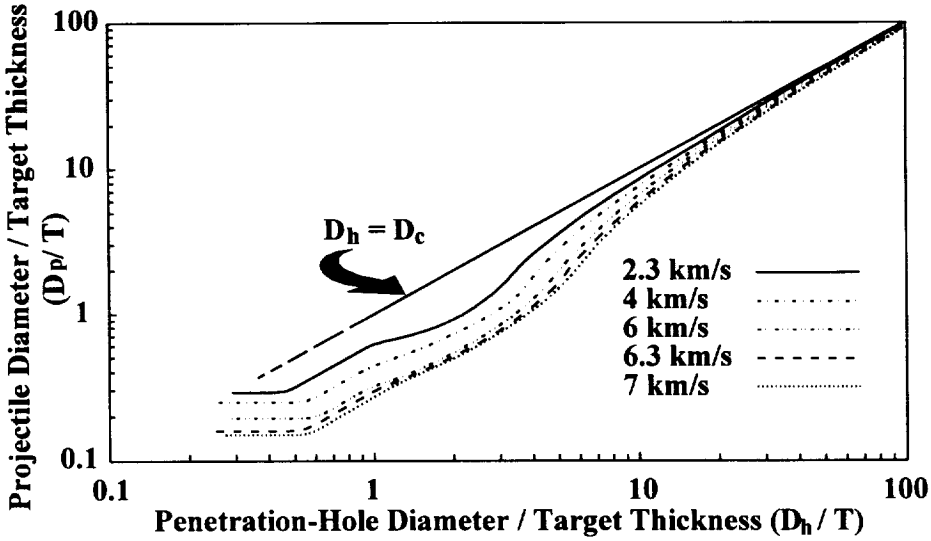

Figure 2.

SIMULATION OF GRAVITY-DOMINATED COLLISIONS

Kevin Housen, Shock Physics Group, The Boeing Company MS 87-60, Seattle, WA, 98124.

Collisonal fragmentation experiments have been limited to target sizes of several cm or less, and have therefore been restricted to a regime in which the outcome of the collision is determined by the strength of the target material. This contrasts with asteroid or satellite fragmentation events, which may be dominated by self-gravity rather than strength. A partial solution to this problem was obtained by performing fragmentation experiments in a pressurized environment (Housen *et al.* 1991). Gas overpressure was used to simulate the average lithostatic confining pressure that exists within an asteroid of a given size of interest. For reasons of practicality, shallowly-buried explosive charges were used to fragment the targets. The present study presents an improved technique, which allows impacts to be conducted at elevated pressure, thereby removing the uncertainties associated with the use of explosive charges to simulate impacts.

EXPERIMENTAL APPARATUS

The explosive fragmentation experiments were conducted in a cylindrical chamber, rated to a working pressure of 6000 psi. The same chamber was used in the present study, but was modified to provide a small opening in the top of the chamber. The opening is just large enough to accept the end of the barrel of a two-stage light-gas gun. A thin (76μ) mylar film diaphragm over the opening allows the chamber to be pressurized. Upon firing the gun, the projectile ruptures the mylar and enters the pressurized chamber. An O-ring seal between the chamber and the barrel prevents loss of pressure after the diaphragm is ruptured. The velocity of the projectile is determined from two gates of breakwires that the projectile passes through.

An experiment was conducted with a spherical target made of the weakly-cemented basalt described by Housen *et al.* (1991). The target was 14.7 cm in diameter and had a mass of 4427 g. Static strength measurements were made on cylindrical specimens at the time the experiment was conducted. Two cylinders exhibited compressive strengths of 92 and 119 psi (0.63 and 0.82 MPa) respectively. Two additional cylinders exhibited tensile strengths of 15.0 and 27.8 psi (0.10 and 0.19 MPa).

The chamber was lined with foam rubber to minimize breakage of any fragments striking the walls. After placing the target in the chamber, the chamber was pressurized with nitrogen to 76 psi.

The impactor was an aluminum cylinder with length and diameter of 0.632 cm, a mass of 0.535 gm and a velocity of 3.6 km/s.

RESULTS

The impact produced a significant crater, but left the bulk of the target intact. Only 7% of the target mass was removed, thereby leaving a largest "fragment" which was 93% of the original target mass. Therefore, the specific energy of this collision was well below the value requred for catastrophic fragmentation.

The result of this test contrasts markedly with previous impacts conducted without an applied overpressure (see Figure 1). Housen (1993) reported three collisional fragmentation tests under conditions identical to those described here, except that the earlier events were conducted at ambient atmospheric pressure. Three tests were performed to estimate experimental reproducibility Each resulted in significant fragmentation, with the largest remaining fragment ranging from 21% to 32% of the original target mass. These results support the conclusion from explosive simulations that the ambient overpressure has a strong affect on the outcome of a fragmentation event.

Figure 1 compares the results for impacts with those for explosions. At zero overpressure, the impact events resulted in more severe fragmentation than did the explosions, suggesting that the

GRAVITY-DOMINATED COLLISIONS; K. Housen

explosives should have been buried slightly deeper to provide an equivalence with impact. At present, it is difficult to tell if this same trend occurs at elevated pressure. If so, the specific energy for catastrophic fragmentation of large bodies may be somewhat lower than that estimated by Housen *et al* (1991). This will be addressed in further impact tests at elevated pressure.

The overpressure used here (76 psi) corresponds to the volume-averaged lithostatic compressive stress for a 72 km diameter body. On this basis, the effects of gravitational self-compression are expected to significantly affect the fragmentation of a 72 km-diameter body, as long as the body is composed of a material whose strength is comparable to, or less than, that of the material used here.

Weakly cemented basalt was designed to simulate the strength of rock at large scales, i.e. rock samples whose strength is degraded by numerous naturally occurring joints and cracks. Centrifuge simulations with this material have shown that it's strength (i.e. the strength measure which governs crater size) is comparable to that of terrestrial basalt flows in the sense that a centrifuge simulation of the SAILOR HAT field cratering test (500 tons of TNT in basalt) provided a reasonable match of the field crater profile. If the material comprising rocky asteroids has a strength comparable to, or less than, terrestrial basalts, then gravitational effects should be important in the fragmentation of rocky bodies with diameters of several tens of km. Additional tests will provide a better estimate of the strength/gravity transition and the specific energy required for fragmentation in the gravity-dominated regime.

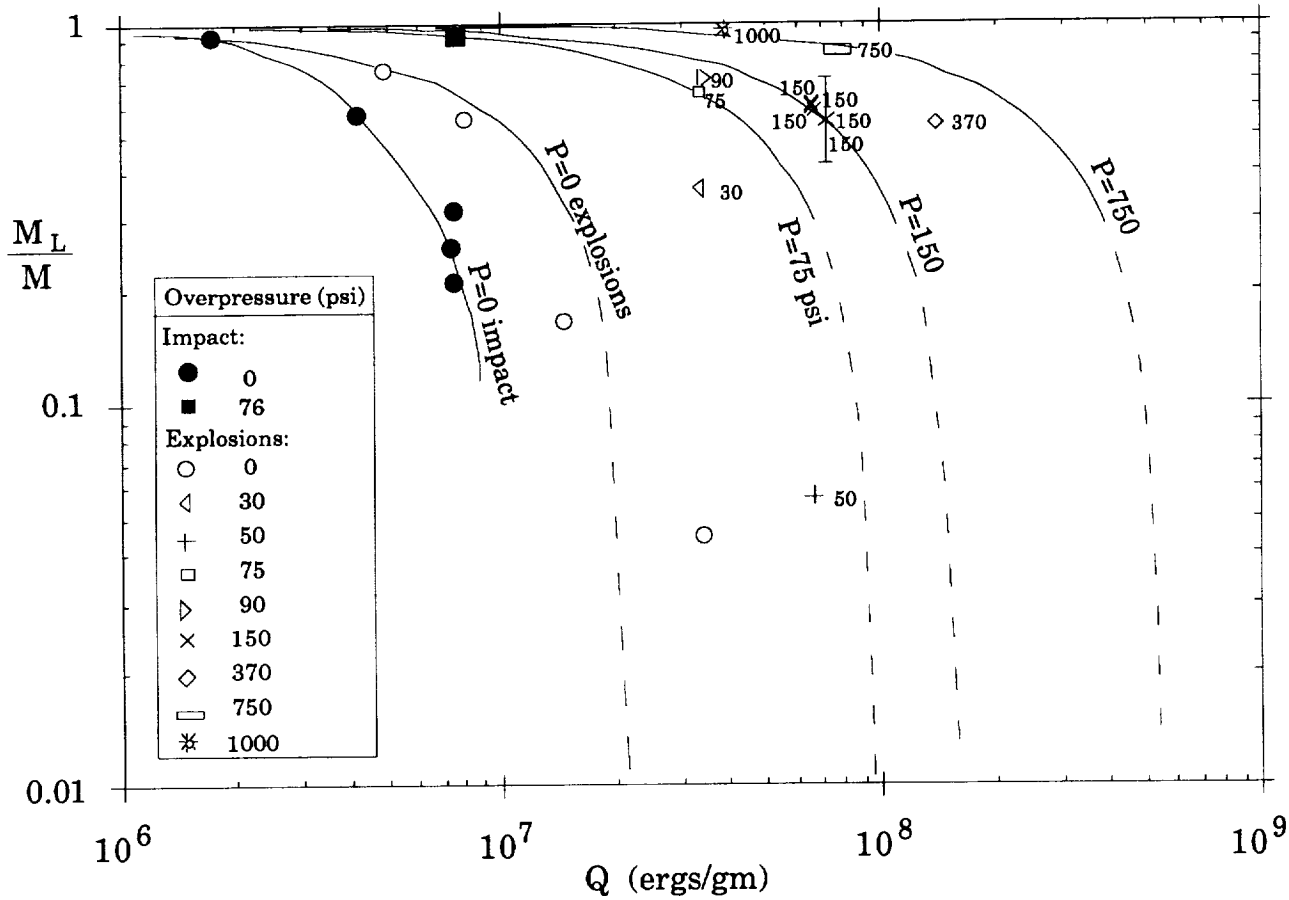

Figure 1. The mass of the largest remaining fragment, normalized by the target mass, for explosions (Housen et al., 1991) and for impacts.

References: (1) Housen *et al.* (1991) *ICARUS* **94** 180-190. (2) Housen K.R. (1993) *LPSC XXIV* 675-676.

ON THE FORMATION OF ENSTATITE IN UNEQUILIBRATED ENSTATITE CHONDRITES. Weibiao Hsu and Ghislaine Crozaz. Dept of Earth and Planetary Sciences and McDonnell Center for the Space Sciences, Washington Univ., One Brookings Drive, St. Louis, MO 63130.

The highly reduced enstatite chondrites are generally believed to have formed in a region of the solar nebula with a much higher than average C/O ratio. Their major mineral, enstatite, is essentially Fe-free and, under electron bombardment, shows either red or blue cathodoluminescence (CL) that, according to some [1], is associated with the concentrations of minor elements such as Mn and Cr. Unequilibrated enstatite chondrites (UECs) also contain some more oxidized "Fe-rich" (>3% FeO) low-Ca pyroxenes (e.g., [2,3]). Weisberg *et al.* [4] suggested, on the basis of petrological and chemical data, that some of the red enstatite may be the product of reduction of this Fe-rich pyroxene and that the blue enstatite rims on these crystals grew by direct nebular condensation. Last year, we reported REE concentrations in UEC enstatites [5] and showed that the REE patterns tend to be mirror images of those in the major REE carrier, oldhamite, either relatively flat or with modest HREE enrichments. Eu and Yb anomalies, when present in enstatite, are negative. We have since confirmed that all the enstatite grains we had measured had a red CL. To better understand the relationship between red and blue enstatite and their respective origins, we have measured trace element concentrations in blue enstatite of the most unequilibrated enstatite chondrite, Qingzhen (EH3).

As in other UECs, most of the enstatite in Qingzhen has a red CL. Both red and blue enstatite occur as single grains or in chondrules (most often porphyritic) that usually include mixtures of red and blue enstatite. We found some blue enstatite completely surrounded by a thin rim of red enstatite (but not the opposite as reported by [4]) and also analyzed a barred blue enstatite chondrule. Since enstatite is not the major REE carrier in UECs, a relatively large primary ion beam was used (~15nA) and special attention was paid to the possibility of contamination by oldhamite (CaS) by monitoring the Ca and S signals throughout the analysis.

McKinley *et al.* [6] have previously observed that the CL color of enstatite is not uniquely correlated with its composition. With the exception of the bright blue enstatite, which has much lower minor element concentrations, red and blue enstatite were found to have a considerable overlap in composition. The present study confirms (and extends to trace elements) these observations; there are no REE patterns or abundances that uniquely characterize either type of enstatite. Figure 1 reports data for oldhamite, red, and blue enstatite from the same porphyritic chondrule. The REE pattern of red enstatite has a small depletion of the LREEs as well as negative Eu and Yb anomalies that seems to be mirrored in the oldhamite REE pattern. REE concentrations in blue enstatite are much lower (~0.01xC1) and, considering the large associated errors, consistent with those in red enstatite. REE patterns for a blue enstatite grain (2 analyses) and an adjacent red enstatite are also very similar (Figure 2). The two analyses of red enstatite are in excellent agreement but REE concentrations are lower in red than in blue enstatite. Four analyses of a single blue barred chondrule with thin red enstatite bars (not shown) yielded 4 similar REE patterns (also characterized by negative Eu and Yb anomalies) but with different REE concentrations. The range of concentrations is attributed to the presence (in different amount in each analysis) of small (typically ~1μm) trapped melt inclusions of sulfide and albitic compositions which are common in enstatite [7]. These inclusions, which are hard to avoid even in an electron microprobe analysis, probably contributed to the overlap in red and blue enstatite compositions observed by [6].

We believe that the REE patterns of both red and blue enstatite are controlled by the composition of the melts they trapped during their rapid crystallization. The similarity of REE patterns measured in adjacent crystals of both types implies that red and blue enstatites have a common origin. The data, therefore, do not confirm the model advocated by Weisberg *et al.* [4] in

FORMATION OF ENSTATITE IN UEC: Hsu W. and Crozaz G.

which red and blue enstatites had independent modes of formation. The relatively flat REE patterns observed in enstatite are compatible with an igneous origin despite the fact that REE equilibrium partition coefficients (e.g., [8]) for pyroxene indicate that this mineral strongly favors the incorporation of the HREEs over that of the LREEs. When the chondrules formed by rapid cooling, equilibrium could not be maintained and small amounts of melt were trapped in the growing crystals. Although the trapped melt is volumetrically insignificant, its essentially flat chondrite-normalized REE composition dominates the REE pattern of enstatite, a mineral in which REEs are otherwise strongly incompatible elements. In support of this explanation, the same effect has actually been observed in an experiment simulating the formation of chondrules [9]. The data for the barred chondrule indicate that it has the largest amount of trapped melt, an observation that is consistent with its very high cooling rate (greater than for porphyritic chondrules) as implied by dynamic crystallization experiments [10]. Because Eu and Yb are the most volatile REEs under reducing conditions [11], their depletions in enstatite is attributed to evaporative loss during chondrule formation. The complementarity of oldhamite and enstatite REE patterns noted by [5] suggests that the REE-rich oldhamite did not form by condensation from an otherwise solar gas with a C/O ratio>1 (as concluded by [11]) but rather was a byproduct of the igneous process that led to the formation of the enstatite.

REFERENCES: [1] Leitch and Smith (1982) *GCA* ,**46**, 2083-2097. [2] Rambaldi et al. (1984) *Nature*, **311**, 138-140. [3] Lusby et al. (1987) *Proc. LPSC* **17th**, E679-E695. [4] Weisberg et al. (1993) *LPSC* **XXIV**, 1501-1502. [5] Crozaz and Hsu (1993) *LPSC* **XXIV**, 357-358. [6] McKinley et al. (1984) *Proc. LPSC* **14th**, B567-B572. [7] Smith (1983) *LPSC* **XIV**, 710-711. [8] Colson et al. (1988) *GCA*, **52**, 539-553. [9] Kennedy et al. (1993) *EPSL*, **115**, 177-195. [10] Lofgren (1989) *GCA*, **53**, 461-470. [11] Lodders and Fegley (1993) *EPSL*, **117**, 125-145.

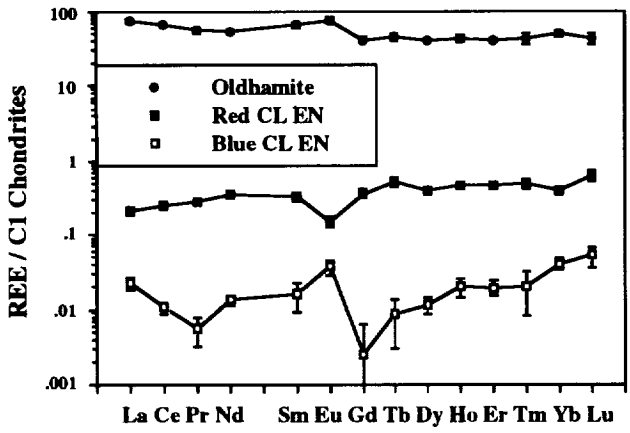

Fig.1 REE patterns for oldhamite and enstatites in a porphyritic chondrule

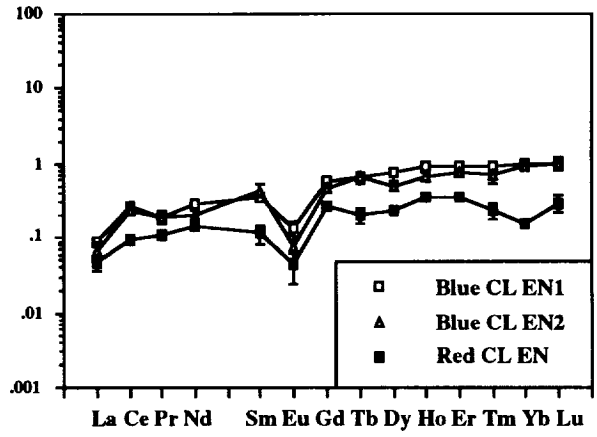

Fig. 2 REE patterns for red and blue CL enstatites

GROUP A5 CHONDRULES IN ORDINARY CHONDRITES: THEIR FORMATION AND METAMORPHISM. Shaoxiong Huang, Paul H. Benoit and Derek W. G. Sears. Cosmochemistry Group, Department of Chemistry and Biochemistry, University of Arkansas, Fayetteville, Arkansas 72701, USA.

The group A5 chondrules in type 3 ordinary chondrites are those containing oligoclase-normative mesostasis and olivine and/or pyroxene with more than a few percent FeO (1,2). With respect to these major properties, they resemble the chondrules in equilibrated chondrites and they represent a distinct chondrule group from the group A1 and B1 (roughly equivalent to the type I and type II chondrules in Semarkona) normally discussed (3,4). About 5% by number of the chondrules in Semarkona (type 3.0) are group A5, and this number increases steadily with increasing petrologic type until all the chondrules in type 5 chondrites are group A5 (1,2). In the present paper we compare group A5 chondrules from low petrologic type 3 ordinary chondrites with A5 chondrules in equilibrated chondrites. We discuss both their formation - arguing for lower peak temperatures during formation than group A1 chondrules and slower cooling following formation than group B1 chondrules - and we discuss the complex changes this chondrule group underwent during metamorphism.

The CaO and FeO of the olivine in the A5 chondrules of several LL chondrites are shown in Fig. 1, with the compositional fields of the other chondrule groups. The A5 chondrules show a decrease in CaO and an increase in FeO with increasing metamorphism, but much less than for the other groups, and the heterogeneity (expressed as the coefficient of variation of FeO in olivine, $\sigma/\bar{x}$) increases from 5-20% in Semarkona (3.0) and Krymka (3.1) to 5-50% in ALHA 77214 (3.4), then decreases to <5% in Dhajala (3.8) and <2% in types 4-6. The pyroxenes show similar behavior to the olivine except that the CaO reaches an equilibrium value of 0.8-1.0% and pyroxene lags behind olivine as the metamorphic changes occur. Mesostasis compositions (Fig. 2) are very similar in all A5 chondrules, which are essentially Na-rich feldspar-normative, with few readily delineated metamorphic trends.

We suggest that there are two processes occurring during metamorphism which are driving these compositional trends. First, chondrules which formed originally with mean mesostasis compositions close to the equilibrated values underwent simple internal homogenization as essentially closed systems and olivine/pyroxene in these chondrules migrated to the equilibrated state by losing CaO and gaining FeO. Second, chondrules with mesostasis and olivine/pyroxene compositions far removed from the equilibrated values (the A1 or B1 chondrules) underwent element exchange with other meteorite components during open-system metamorphism to become A5 chondrules. This process can apparently be observed directly in ALHA 77214 (type 3.4) where many chondrules are B3 in their central region and A5 in their outer region (2).

The rate at which equilibration occurred depended on the original chondrule class, group A1-4 chondrules equilibrating faster than group B1-3 chondrules. This difference in rate of equilibration is due to considerable differences in the diffusion rate of olivine and pyroxene and of mesostases of various compositions. Volume diffusion rates in calcic glasses are greater than those of sodic or quartz-normative glasses (5), but more importantly, there are major differences in friability and crystallization rates for glasses of different composition (6) and grain boundary and vapor phase diffusion are thus facilitated. The pyroxenes do not fully achieve their equilibrated compositions until petrologic type 5 (2).

The changes in compositional heterogeneity observed among the olivines and pyroxenes of group A5 chondrules suggest that the group A5 chondrules in Semarkona were not metamorphosed prior to emplacement in the meteorite, and the presence of A5 chondrules in Semarkona is not due to brecciation. Rather, it indicates that the chondrule-forming process was capable of producing chondrules with mineral phase compositions resembling those of chondrules in equilibrated chondrites. There are several lines of evidence, summarized by refs. 3 and 7, which suggest that group A1 chondrules experienced higher temperatures during formation than other chondrules. We have previously argued that this also resulted in their volatile-poor and highly reduced compositions (8,9). Conversely, the volatile-rich, oxidized group B1 chondrules apparently experienced lower peak temperatures during formation. The composition of the mesostasis relative to the olivine/ pyroxene grains infers supercooling in the case of group B chondrules (4,10) but not for group A chondrules (3), including A5. We suggest that the three chondrule groups in Semarkona represent three very different thermal histories; reducing, relatively high temperatures of formation and fast cooling (group A1), oxidizing, low temperatures of formation and fast cooling (group B1) and low temperatures of formation and slow cooling (group A5). The peak temperature experienced during chondrule formation is determined by the intensity of the thermal pulse responsible for the chondrule, but the cooling history must be independent of the heating pulse and depends on the gas and dust density around the chondrule. Lewis *et al.* (11) have found experimental evidence for recondensation of Na into chondrules during

chondrule formation, and that the Na content of chondrules depends on not only Na vapor pressure, but the cooling rate. This may be the case for the formation of group A5 chondrules, whose bulk Na concentrations are often higher than those of bulk chondrites. Zoned mesostasis and sulfide and metal rich rims around group A chondrules might imply an environment suitable for recondensation of volatiles for group A (12,13,14).

Apparently, the conditions and processes associated with chondrule formation showed considerable variation, as did the responses of the various primary chondrule groups to metamorphism. Clearly, chondrule history is very complicated and diverse and much of the literature discussion of the topic has been oversimplified.

1, Sears D. W. G. *et al.* (1992) *Nature* 357, 207-210. 2, DeHart J. M. *et al.* (1992) *Geochim. Cosmochim. Acta* 56, 3791-3807. 3, Jones R. H. and Scott R.H. (1989) *19th Lunar Planet. Sci. Conf.* 523-536. 4, Jones R. H. (1991) *Geochim. Cosmochim. Acta* 54, 1785-1802. 5, Schairer J. F. and Bowen N. L. (1956) *Amer. J. Sci.* 254, 129-195. 6, Sears D. W. G. and DeHart J. M. (1989) *Meteoritics* 24, 325. 7, Hewins R. H. and Radomsky P. M. (1990) *Meteoritics* 25, 309-318. 8, Lu J. *et al.* (1991) *Lunar Planet. Sci.* XX 720-721. 9, Huang S. *et al.* (1993) *Lunar Planet Sci. Conf.* XXIV, 681-682. 10, DeHart J. M. (1989) *PhD thesis.* University of Arkansas.11, Lewis *et al.* (1993) *Meteoritics* 28, 622-628. 12, Huang S. *et al.* (1993) *Meteoritics* 28, 367-368. 13, Matsunami S. *et al.* (1993) *Geochim. Cosmochim. Acta* 57, 2101-2110. 14, Ikeda Y. and Kimura M. (1985) *Meteoritics* 20, 670-671. Supported by NASA grant NAGW-3519.

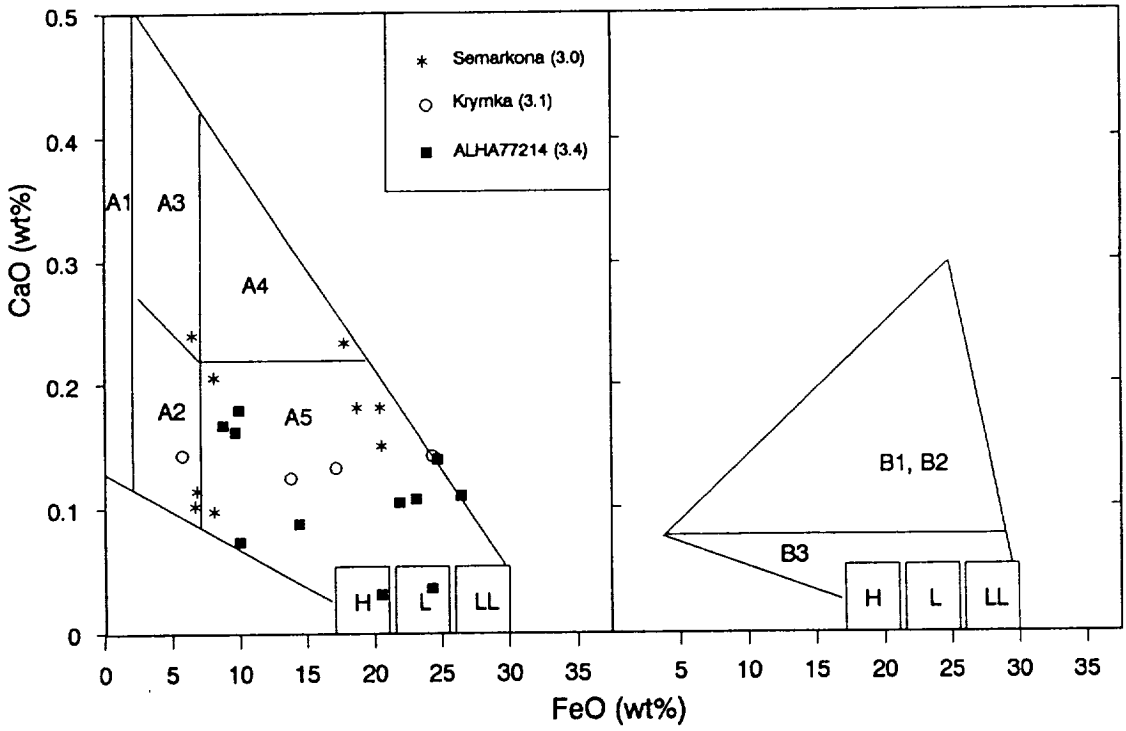

Fig. 1. CaO vs FeO in chondrule olivines with the chondrule class boundaries indicated (After ref. 1,2 with minor simplifications).

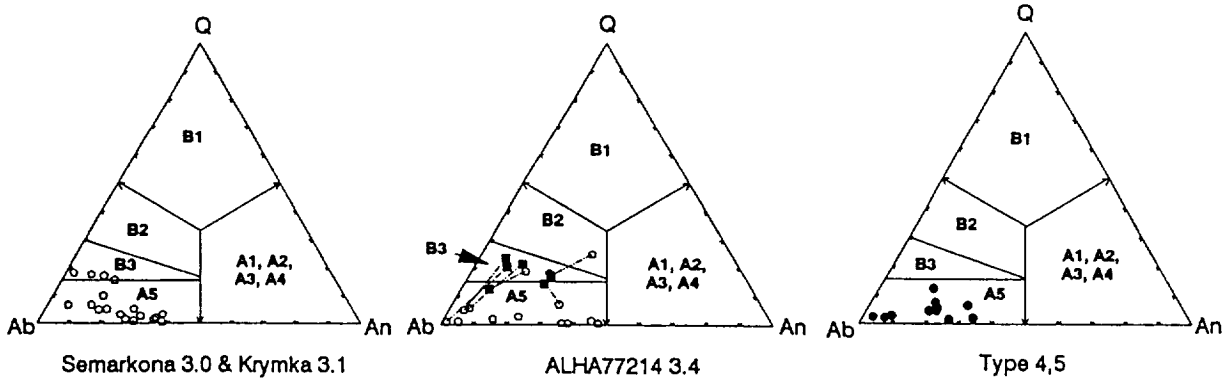

Fig. 2. Quartz-albite-anorthite ternary (normative compositions) for mesostasis compositions with chondrule class boundaries indicated (refs. 1,2). In all cases, data for group A5 chondrules are indicated.

NIMS SCIENCE OBJECTIVES AND OBSERVATIONAL PLANS FOR GANYMEDE DURING THE GALILEO TOUR John Hui (Jet Propulsion Laboratory, California Institute of Technology, Pasadena, CA 91109), Hugh H. Kieffer (U.S. Geological Survey, Flagstaff, AZ 86001), and the NIMS team.

This paper discusses the observational plans for Ganymede by the Galileo NIMS instrument during the tour beginning in 1996. A brief description of the instrument capabilities and the science objectives of NIMS are given. Observational plans for Ganymede include, for example determination of the Galileo Regio and Marius Regio regions are targetted for special high resolution studies.

The Near Infrared Mapping Spectrometer (NIMS) is a remote sensing instrument on the Galileo spacecraft on its way to Jupiter. NIMS has the unique capability to image and take spectra the same time. This allows mapping of regional features while simultaneously giving spectral information on their composition and mineralogy, thus providing data for geological studies of the Galilean satellite surfaces. NIMS spectral range is from 0.7 to 5.2 μm, which includes two parts, the surface reflected light and the emitted thermal radiation. This spectral range was chosen because known and anticipated minerals on the Galilean satellites surface have spectral signatures at these wavelengths.

Our main science objective at Ganymede is to determine the chemical components in the various surface composition units. To further understanding of these units in a global context, it is desirable to map their distribution over the surface of the satellite. The dark regions are thought to represent darker material mixed with the more common water-ice crust of Ganymede. The dark materials could be silicates, containing olivines, pyroxenes, or iron-bearing minerals which have spectral features in the NIMS spectral range. Or, they could be organic materials, like those found on some asteroids, and might have C-H features, e.g., near 3.5 μm, detectable by NIMS. Another explanation for these materials is the implantation of reactive chemicals into the water-ice crust to modify Ganymede's surface; for example sulfur from the magnetosphere implanted on the surface and reactive with water-ice to form sulfur-monoxide.

A study of the mineralogy relating to the morphology of the grooved terrains will give information on the causal processes (e.g. tectonic and/or tidal heating). These terrains appear to be similar to the linear markings on Europa. Craters of various types and ages will also be studied, from palimpsests to dark-rayed craters. The composition of the exposed materials may reveal the nature of the subsurface materials. Ejecta may show compositional correlations with size, age, latitude, terrain type, or longitude that would provide insight into their nature and origin. Volatile species may be found cold-trapped in Ganymede's polar caps. Such information would provide some insight into the processes of frost deposition at high latitude, but not at low latitudes. An additional objective is to search for the presence of an atmosphere on Ganymede having components such as oxygen.

Galileo's two-year tour around Jupiter consists of eleven orbits; five of the orbits will involve close encounters with Ganymede. In order to identify the compositional units, high spectral resolution observations will be made of the different types of surfaces. In order to put them in context, global map observations of Ganymede's surfaces will be obtained. With the given geometry of the tour and telemetry constraints, only 60% (90% if telemetry improves) of the surface can be mapped. These global observations will be acquired with moderate spectral resolution, due to telemetry constraints. To achieve the rest of the science objectives, regional observations with moderate/high spatial and spectral resolutions are made on the appropriate target areas, e.g. different grooved terrains and craters. The north and south poles will be observed, and observations across high latitudes will be made to understand the frost deposition variation. Limb scans will be used to search for an atmosphere around Ganymede.

CHARACTERIZATION OF LAVA-FLOW SURFACE TEXTURES IN DIFFERENT ERUPTIVE ENVIRONMENTS ON VENUS; L.K. Hultgrien, Department of Earth and Planetary Sciences, Johns Hopkins University, Baltimore, MD 21218; and L.R. Gaddis, U.S. Geological Survey, 2255 N. Gemini Drive, Flagstaff, AZ 86001

Overview: We have compiled a comprehensive database of morphologic and material properties of more than 300 effusive volcanic units on Venus and the relationships of these characteristics to geologic setting, tectonic environment, and elevation. In addition to morphologic data from SAR images, we used Magellan imaging radar, altimetry (reflectivity, roughness, topography), and emissivity data to document and classify surface textural and backscatter characteristics of the effusive volcanic units. Preliminary analyses of the database indicate the presence of basaltic lava flows with surface textures included within the full pahoehoe-transitional-aa range of terrestrial flow types. Even the highest rms slope values observed for these lava flows (~6° to 8°) are consistent with textures comparable only with those of the roughest terrestrial pahoehoe flows. A major aspect of our future analysis of this database will be to assess the relative importance of primary (emplacement) and secondary (weathering) influences on the observed lava-flow morphologies and backscatter characteristics.

A direct correlation between flow types and textures on Venus and Earth is not expected due to the high Venusian atmospheric density, pressure, and temperature. However, theoretical studies [1,2] suggest that many of the lava-flow structures observed on Earth are also likely to occur on Venus. We have begun a series of detailed morphometric and surface-roughness studies of Venusian lava flows in an effort to (1) determine the types of flow textures and features (channels, levees, and tubes); (2) interpret eruptive styles and emplacement histories; (3) compare the roles of both formational (primary) and degradational (secondary; e.g., [3]) processes in the creation and preservation of observed flow characteristics; and (4) assess the influence of elevation factors (related to both atmospheric pressure and edifice height) and tectonic setting on flow morphologies. These analyses of flow forms and surface textures will provide a basis for (1) discrimination between impact-triggered volcanic deposits and impact-induced melt units, (2) identification of transitional flow types and those of chemically more evolved lavas [4], and (3) characterization of flow types suggestive of magma source regions enriched in volatiles.

The format and some of the basic information in our lava-flow database were adapted from the Magellan Volcanic and Magmatic Feature Catalog of Crumpler et al. ([5], version 6/93). The Magellan left-looking Cycle 1 imaging radar data (84% coverage of Venus) were the primary data used. Where available, right-looking Cycle 2 SAR data (50% coverage) and left-looking Cycle 3 stereo coverage (~35% coverage) were also used. The morphologies of selected lava flows as they appear in Magellan SAR images were documented, with particular attention to the following: presence of channels, levees, and other structural features; nature and location of surface-brightness changes; and flow-margin geometries. Geologic context was established for each site, including observations of superposition, transection, and other possible age relations; associated vent types (where preserved); possible topographic influences; and overall surface textures. Analyses of these measurements will enable us to characterize and compare flow rheologies and emplacement styles associated with different types of volcanic eruptive centers on Venus and on Earth. These data will be made available on request.

For these analyses we selected more than 300 effusive volcanic flows from the Magellan SAR images . Lava flows in three primary volcanic/tectonic associations are included: flow complexes (~100-1000 km long) commonly associated with rifts and fractures and located in and adjacent to lowlands [6,7]; radially distributed flows within and near coronae, volcano-tectonic features ~100-700 km in diameter (coronae are possibly associated with mantle diapirs [8] and are located at intermediate elevations); and shields (~10-1000 km in diameter, with radial flows) that are associated with mantle plumes and/or hotspots and are located at higher elevations [6]. The primary criterion for selection of these effusive volcanic sites was the presence of numerous,

PRECEDING PAGE BLANK NOT FILMED

clearly identifiable lava flows with a range of forms and a variety of backscatter properties. Additional desirable characteristics were identifiable source vents, internal flow structures, and both unponded and ponded flows. Detailed morphologic characterization of lava flows associated with each of these types of volcanic features should enable us to establish a sequence of development of their eruptive styles and products and to evaluate the relative importance of local and regional tectonic influences and elevation effects on flow morphologies.

We have made preliminary analyses of this lava-flow database. Most dielectric-constant values (~2.5 to ~7) extracted from the Magellan emissivity data are consistent with basaltic compositions for the flows. Normalized backscatter cross-sections (σ°, dB) at the Magellan S-band wavelength range from -22 to -3 dB; these values suggest that the Venusian flow textures are included within the full pahoehoe-transitional-aa range of terrestrial flow types [9]: ~80% are like pahoehoe, ~5% are transitional, and ~15% are like aa. These backscatter data are consistent with results obtained from analysis of the rms-slope characteristics of the flows: rms-slope values range from ~0° to ~8°, and ~80% of the flows are "smooth" [10]. Even the highest rms-slope values observed (~6° to 8°) are consistent with only the roughest terrestrial pahoehoe flows [11]. The possible dominance of smooth, pahoehoe-like lavas on Venus can be interpreted as due either to primary (emplacement) or to secondary (weathering) processes. We are currently examining the relative importance of these primary and secondary influences on the observed lava flow morphologies and backscatter characteristics. For example, it is expected that the predominance of primary factors on flow morphology will be reflected in the presence of lava channels, inferred tubes, and pahoehoe-like flow fields with multiple, relatively short flows. The influence of possible weathering processes on flow surface textures can be studied by using flow fractal-margin analysis techniques [12]. The existence of lava flows with aa-like margins and pahoehoe-like backscatter characteristics will provide important clues to post-emplacement, flow-surface modification processes.

Questions to be addressed next in our analysis of this database include the following: Can specific types of lava flows be related to source vent types, proposed magma sources, and/or the nature and stage of development of eruptive centers? What are the scales of lava flows and associated structures (channels, levees, tubes)? How do lava flows associated with volcanic edifices/vents compare with those associated with coronae/novae, and with crater outflow deposits? Do the extensive lowland plains on Venus consist of voluminous lava flows? The answers to these questions may reveal consistent patterns among lava-flow characteristics and may help us to understand the extent to which we can interpret those patterns from our terrestrial experience and use them to recognize behaviors that are unique to Venus.

References: [1] Head, J.W. and Wilson, L. (1986) *JGR, 91*, 9407. [2] Head, J.W. and Wilson, L. (1992) *JGR, 97*, 3877. [3] Arvidson, R.E. et al. (1992) *JGR, 97*, 13303. [4] Hess, P.C. and Head, J.W. (1990) *Earth, Moon, and Planets, 50/51*, 57. [5] Crumpler, L.S. et al. (1993), Special Paper submitted to GSA. [6] Head, J.W. et al. (1992) *JGR, 97*, 13153. [7] Moore, H.J. et al. (1992) *JGR, 97*, 13479. [8] Stofan, E.R. et al. (1992) *JGR, 97*, 13347. [9] Gaddis, L.R. (1992) *GSA Bull., 104*, 695. [10] Bindshadler, D.L. and Head, J.W. (1988) *EM&P, 42*, 133. [11] Campbell, B.A. (1992) *LPSC XXIII*, 201. [12] Bruno, B.J. et al. (1992) *LPSC XXIII*, 171.

THE NON-TERRESTRIAL ORIGIN OF THE MOON; Munir Humayun[1] and Robert N. Clayton[1,2]; [1]Dept. of the Geophysical Sciences, [2]Enrico Fermi Institute and Dept. of Chemistry, The University of Chicago, Chicago, IL 60637, USA.

The chemical constraints on the origin of the Moon indicate two possible solutions: a) lunar origin from the Earth's (or planetary) mantle followed by loss of volatiles, or b) derivation from the mantle of an impactor planet, already depleted in volatiles more severely than the Earth. We present K isotopic results that can distinguish between these hypotheses. The loss of volatiles by the distillation of condensed matter necessarily occurs in a mass-dependent manner. We have obtained a "bulk lunar" $\Delta^{41}K_{Moon\text{-}Earth} = +0.2 \pm 0.4$ ‰ that indicates no evidence of mass-dependent fractionation, and argue that this constitutes *prima facie* evidence for the derivation of lunar material from the impactor mantle, with little or no subsequent chemical modification. The distinct lunar volatile element abundances provide an independent chemical argument for a non-terrestrial origin of the Moon, supporting the giant impact theory [1, 2].

Two significant observations on the chemistry of lunar material returned by the Apollo missions have been made: the severe depletion of the lunar composition in volatile elements [3, 4, 5] relative to C1 chondrites (e.g. K about 30x) or to Earth's mantle (e.g. K about 4-5x), and the low siderophile element concentrations of mare basalts and pristine highlands rocks [4, 5, 6]. Most discussion of the volatile element depletion is non-unique, in that every lunar formation scenario involves intense heating and vaporization of protolunar material. Thus, it is uncertain as to whether volatile elements were lost prior to Moon formation (by mechanisms responsible for the depletion of volatiles in the Earth, SNC parent body, and eucrite parent bodies [4]), or during Moon formation by volatile loss from a hot, protolunar disk of largely vaporized silicate material [e.g. 5]. We have proposed a simple test for the determination of loss of volatiles during evaporative processes, by measuring changes in the isotopic composition of potassium [7] brought about by distillation of the vapor as it escapes to space. We report here the results of our investigations on 18 lunar samples. The analytical methods are slightly modified from [7], with the addition of oxalic acid to complex Ti, Al, Fe, etc. We still obtain impurities of Cr and Al in some glasses, for which small corrections are applied. We report our individual analyses relative to an in-house laboratory standard, Suprapur® KNO_3, and we report the lunar mean relative to the mean of 17 representative terrestrial samples, as follows:

$$\delta^{41}K = 1000 \cdot (R_x / R_{std} - 1) \quad \pm \quad 2\sigma_m$$

$$\Delta^{41}K = \delta^{41}K_{Moon} - \delta^{41}K_{Earth} \quad \pm \quad \{(3\sigma_{Moon})^2 + (3\sigma_{Earth})^2\}^{1/2}$$

where $R = {}^{41}K/{}^{39}K$. Our analyses are shown in the attached figures. Replicate measurements on two new aliquots of vesicular basalt 15556 show no evidence of isotopic fractionation [cf. 7], and we take this to represent the true value of the sample. Anorthosite 60015 is apparently light, and this is not easy to understand. No obvious source of laboratory error can be discerned, but the sample has a low K content, and we consider the analysis suspect until redetermined. All other rock samples (excluding lithified soil 15505) are unfractionated relative to the terrestrial mean. No dependence of isotopic composition on vesicularity, or chemical properties, can be discerned. We include only pristine [8] lunar samples in our calculation of the mean, even though the three impact melted glassy coatings on A16 anorthosites are unfractionated. We have analyzed four samples previously analyzed for K isotopic composition by Garner et al. [9] and two soils analyzed by Church et al. [10]. We obtain good agreement with data on rocks, including fractionated sample 15505, while data on soils show several permil differences, probably due to sample heterogeneity. In general, we confirm their findings, indicating accuracy of the previous studies. Our analyses allow the definition of a "bulk lunar" $\Delta^{41}K = +0.2 \pm 0.4$ ‰, in agreement with the data of [9], but do not support the findings of Hinton et al. [11] of an isotopically light Moon. Doubtlessly, the potassium in the feldspars analyzed by [11] was derived from highly evolved KREEP melts, and if such melts are isotopically distinct from pristine KREEP 15386, this is a local effect with no consequences for lunar origin.

LUNAR POTASSIUM ISOTOPES: Humayun M. and Clayton R. N.

Implications for Lunar Origin: The low lunar abundances of elements more volatile than Mg/Si can be considered to be either 1) a primordial abundance acquired during condensation of the solar nebula, or 2) a measure of the volatile loss during intense heating of protolunar matter (presumably) during lunar formation. In the earlier case, the depletion in volatile elements is an inherited feature, and its origin must be considered within the context of the formation of terrestrial planets and differentiated meteorites. Cameron's [12] suggestion that the volatiles are added from a few unvaporized "particles" mechanically transported to several Earth radii, is indistinguishable. In the second case, the volatile loss is from the protolunar disk, and takes place in a mass-dependent manner with striking isotopic effects in the affected elements. We find no evidence for a resolved isotopic effect in potassium at the 3 σ confidence limit. Loss of material during peak temperatures in the disk should result in large fractionations of light vs. heavy species, and the most sensitive measure of this is the Li/Yb ratio which is similar between Earth, Moon, and C3 chondrites [13]. In their treatment of early disk evolution, Thompson and Stevenson [14] find mass loss of vapor to be negligible. As emphasized by Taylor [15], the lunar chemical data require loss of volatiles progressively as a function of condensation temperature, after condensation of refractory elements and Mg/Fe silicates. Conceivably, in the later stages of condensation of the protolunar disk or after disk fragmentation into small, largely molten, moonlets (a stage in need of physical modelling), some loss of K and other volatile elements may take place. Our data constrain this to be in the form of **bulk** loss of (volatile-rich) gas, but this scenario does not explain the progressive depletion of the Moon. From this, we conclude that loss of potassium from a vaporized protolunar disk as the result of a giant impact is excluded, unless a mechanism of volatile loss can be found that does not induce isotopic fractionation. We, therefore, conclude that the volatile element abundances of the Moon were inherited from the impactor, and that vapor fractionation during the impact process was negligible. This corroborates the impact theory, which derives the bulk of lunar material from the impactor [1, 2].

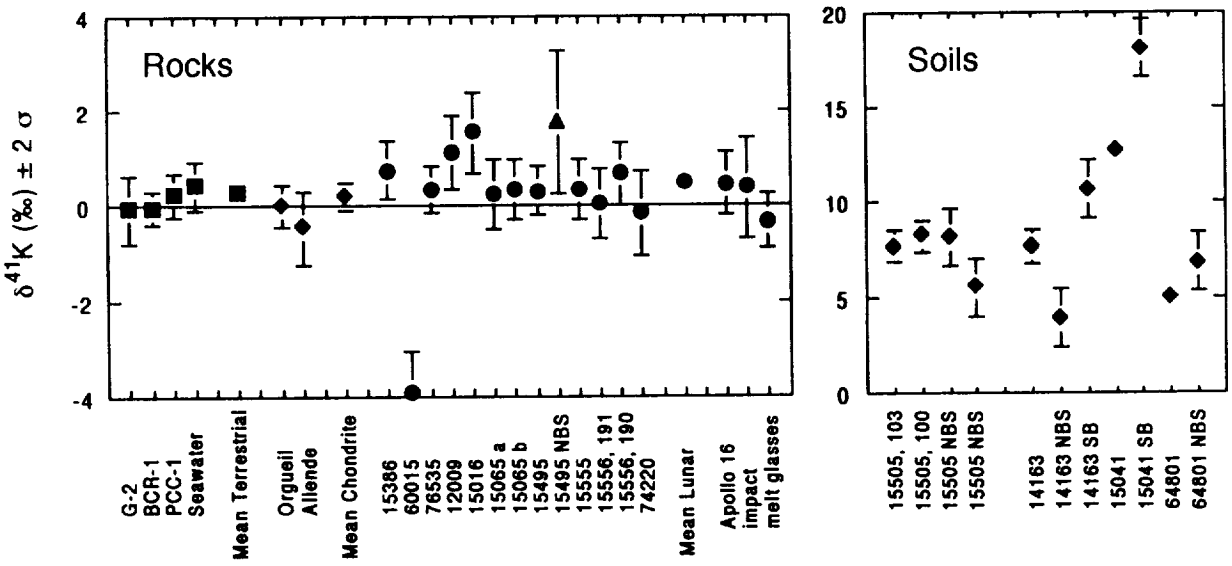

REFERENCES: [1] Benz et al. (1989) Icarus 81, 113. [2] Melosh HJ (1989) Impact Cratering: A Geologic Process, Oxford, 245 pp. [3] Wänke *et al.* (1977) Phil. Trans. R. Soc. Lond. A 285, 41. [4] Wolf R and Anders E (1980) GCA 44, 2111. [5] Ringwood AE (1970) Earth Planet. Sci. Lett. 8, 131; *ibid.* 111, 537; Nature 322, 323. [6] Newsom HE and Taylor SR (1989) Nature 338, 29. [7] Humayun M and Clayton RN (1993) LPS XXIV, 685. [8] Warren PH and Wasson JT (1977) PLSC 8, 2215. [9] Garner *et al.* (1975) PLSC 6, 1845. [10] Church *et al.* (1976) PLSC 7, 423. [11] Hinton *et al.* (1988) LPS XIX, 497. [12] Cameron AGW (1993) LPS XXIV, 245. [13] Norman MD and Taylor SR (1992) GCA 56, 1013. [14] Thompson C and Stevenson DJ (1988) Ap. J. 333, 452. [15] Taylor SR (1987) GCA 51, 1297.

POTASSIUM ISOTOPIC COMPOSITION OF SOME AUSTRALASIAN TEKTITES; Munir Humayun[1], Robert N. Clayton[1,2], and Christian Koeberl[3], [1]Dept. of the Geophysical Sciences, [2]Enrico Fermi Institute and Dept. of Chemistry, Univ. of Chicago, Chicago, IL 60637, USA; [3]Institute of Geochemistry, Univ. of Vienna, Dr.-Karl-Lueger-Ring 1, A-1010 Vienna, Austria.

We have analyzed the potassium isotopic composition of four tektites from the Australasian strewn field, spanning a wide diversity of thermal histories, inferred from textures and volatile contents. Our results indicate no isotopic differences between tektites and terrestrial rocks, placing stringent limits of ≤ 2 % loss of potassium during the brief duration of high temperature experienced by these samples. This indicates that the chemical composition of tektites is entirely a reflection of source rocks and has not been modified by the tektite-forming process for elements less volatile then potassium. Losses of more volatile components, e.g. halogens and water, are not precluded by the present data.

Tektites are natural glasses occurring in four large strewn fields on Earth [1,2]. It is generally agreed that these are associated with large impact events on Earth, and that chemical composition indicates derivation from surface sedimentary rocks. Tektites have experienced severe heating, with temperatures in excess of 2000°C, but the role of selective chemical changes due to volatility has been contentious. This can be evaluated by comparing the isotopic composition of various elements with their source rocks, and data are available for $\delta^{18}O$, $\delta^{30}Si$, and $\Delta^{25}Mg$ [3,4,5]. $\Delta^{25}Mg$ indicates less than 20% vaporization of tektite material [5]. The more sensitive elements (O, Si) show variations that cannot unambiguously be assigned to volatilization, because of variability in source rock composition. The $\delta^{30}Si$ effects are small [4], but $\delta^{18}O$ data have a large range, generally lighter than source rock sediments by several permil [3]. The lowering of $\delta^{18}O$ correlated with SiO_2 can be understood in terms of meteoric porewaters present in sandy sedimentary rocks at the time of impact melting [6], which provides a better explanation than vapor fractionation [7].

We have applied potassium isotopic techniques to investigate the role of volatilization in determining the composition of Australasian tektites. Potassium is determined with precision and accuracy sufficient to recognize even a few percent losses of K, and terrestrial rocks of every kind thus far determined have identical $\delta^{41}K$, eliminating the uncertainties of source rock isotopic values [8]. This allows us to determine the existence of kinetic isotope effects produced by the partial loss of potassium by distillation during high temperature processes, e.g. impact melting. Fresh interior chips were dissolved in HF-HCl-HNO_3, dried, taken up in 0.1 M oxalic acid, and added to an ion exchange column (ID= 11 mm) filled with 12 ml of AG 50W-X8 resin. The potassium was eluted with 0.5 N HNO_3, quantitatively recovered in the 80-250 ml fraction, with adequate separation from Na, Mg, Ca, and other potential interferences. The separated K was converted to 2% K Ba borate glass and analyzed against our in-house standard, Merck Suprapur® KNO_3, using the Chicago AEI IM-20 ion microprobe [8]. Analyses of the tektites, several terrestrial rocks and lunar soils, and the terrestrial mean, are given in Table 1. None of the tektite analyses deviate from the terrestrial composition within errors. We can calculate the maximum degree of loss permitted by the errors, assuming Rayleigh distillation of single K atoms (the dominant species observed experimentally), and these are tabulated as well. This sets stringent limits to the permissible losses of potassium, and taken in conjunction with isotopic

data on other elements, implies that selective distillation is small to non-existent for all major elements, and for trace elements more refractory than potassium. Taylor [1] and Blum et al. [9] present convincing arguments against the significant loss of more volatile alkalis, Rb and Cs. Certain elements, e.g. water and halogens, do show marked depletions relative to sedimentary rocks [10], but such elements may have been lost at temperatures even below the glass transition.

There are two consequences of our observation that tektites are not chemically modified by the impact melting process. From studies of lunar soils, we observe large $\delta^{41}K$ enrichments for less than 15% chemical depletions of K/U ratios, e.g. 14163 is chemically indistinguishable from KREEP but has $\delta^{41}K = 7.8 \pm 0.8$ ‰. Thus, the absence of isotopic enrichments in potassium indicates chemical modifications too small to affect any discussion of the geochemistry of tektites, which must entirely reflect source composition (exceptions previously noted). The absence of significant losses of volatiles from hot, molten spheres, exposed to vacuum (or very low pressures) places constraints on the cooling rates of these liquid spheres. The net loss, for a given surface area, is a function of vapor pressure and cooling rate, and is determined from the isotopic constraints given to be, $P^{K}_{v}.t = 0.003$ atm. seconds, where P^{K}_{v} is the vapor pressure of potassium (in atm) over a melt of tektite composition, and t is the cooling time from peak temperature to the glass transition temperature. We note that for such brief heating events very viscous glasses such as tektites are not likely to be well mixed, and that chemical losses may be restricted to an external rind, which may not be well represented in our analyses. That will not affect our conclusions regarding the absence of a distillation effect on the bulk composition of tektite glasses.

TABLE 1. Potassium isotopic composition of Australasian tektites.

Sample	# points	$\delta^{41}K \pm 2\,\sigma_m$ (in ‰)	% K volatilized
MN X-103, Muong Nong	22	- 0.1 ± 0.6 ‰	≤ 2.0 %
AUS 9301, Australite	27	+ 0.0 ± 0.5 ‰	≤ 2.0 %
T 9201, Thailandite	14	+ 0.4 ± 0.8 ‰	≤ 4.6 %
P 9201, Philippinite	26	- 0.1 ± 0.5 ‰	≤ 1.6 %
USGS G-2, Westerly granite	20	- 0.1 ± 0.7 ‰	
USGS BCR-1	82	+ 0.0 ± 0.3 ‰	
Average Terrestrial (n=17)	414	+ 0.3 ± 0.2 ‰	
14163, lunar soil	14	+ 7.8 ± 0.8 ‰	≈ 10 %

REFERENCES: [1] Taylor SR (1973) Earth Sci. Rev. 9, 101. [2] Koeberl C (1986) Ann. Rev. Earth Planet. Sci. 14, 323. [3] Taylor HP and Epstein S (1962) JGR 67, 4485. [4] Molini-Velsko *et al.* (1982) Meteoritics 17, 255. [5] Esat TM and Taylor SR (1987) LPS XVIII, 267. [6] Engelhardt W v. *et al.* (1987) GCA 51, 1425. [7] Walter LS and Clayton RN (1967) Science 156, 1357. [8] Humayun M and Clayton RN (1993) LPS XXIV, 685. [9] Blum JD *et al.* (1992) GCA 56, 483. [10] Koeberl C (1992) GCA 56, 1033.

PRESOLAR Al_2O_3 WITH A LARGE EXCESS OF ^{17}O AND DEPLETED ^{18}O. Gary R. Huss[1], Albert J. Fahey[1], Roberto Gallino[1,2] and G. J. Wasserburg[1], [1]Lunatic Asylum, Division of Geological and Planetary Sciences, California Institute of Technology, Pasadena, CA 91125; [2]Istituto di Fisica Generale dell'Università, Via P. Giuria 1, 10125 Torino, Italy.

Carbon-rich presolar grains (diamond, SiC, and graphite) have been known in meteorites for several years [1–3]. Oxygen-rich presolar Al_2O_3 has been recognized only recently [4–7], even though astronomical observations show that oxygen-rich grains dominate interstellar dust [8]. It has been difficult to isolate oxygen-rich presolar material primarily because local solar-system material, which is also oxygen-rich, is so overwhelmingly dominant in meteorites. We have been using the ion microprobe to examine refractory oxide minerals from acid residues of primitive chondrites, looking for isotopic signatures indicative of a presolar origin. Initial work in Orgueil (CI) yielded one Al_2O_3 grain with oxygen enriched by a factor of two in ^{17}O relative to the solar composition and a large excesses of ^{26}Mg, presumably from decay of ^{26}Al, indicating an initial $^{26}Al/^{27}Al$ ratio 18 times the canonical solar-system value [4,6,7]. Here we report the discovery of another presolar Al_2O_3 grain, B39 from Bishunpur. The oxygen in B39 is enriched in ^{17}O by a factor of 5.7 ($^{16}O/^{17}O = 385 \pm 9$) and is depleted in ^{18}O by a factor of 2 ($^{16}O/^{18}O = 854 \pm 25$) relative to solar-system values ($^{16}O/^{17}O = 2610$; $^{16}O/^{18}O = 499$). The oxygen composition of this grain is consistent with an origin in a star that has experienced first dredge-up.

Figure 1 shows the oxygen compositions of 28 Al_2O_3 grains (●), 12 spinels (◇) ($MgAl_2O_4$), 14 hibonites (○) ($CaAl_{12}O_{19}$), and one TiO_2 grain (□) from our Bishunpur SiC-spinel separate, which was prepared for a study of abundances of presolar grains [9]. The compositions of two previously reported presolar Al_2O_3 grains [5-7] and the mean of our Allende spinel analyses and standard mean ocean water (SMOW) are also shown. All but one of the measured grains fall within the range previously observed for solar-system processed materials (inset Fig. 1). The hibonite and spinel grains fall along the ^{16}O mixing line observed in minerals from CAI from carbonaceous chondrites [10], and span essentially the same range as observed by previous workers [e.g., 11]. These grains are most likely part of a small CAI component known to be present in ordinary chondrites [12]. The Al_2O_3 grains show somewhat more scatter. Among the Al_2O_3 grains measured in Bishunpur, only B39 has an oxygen composition significantly outside the range exhibited by solar-system materials (Fig. 1). This extreme composition clearly shows that B39 formed outside the solar system in a stellar environment where C/O > 1. B39 is a roughly spherical, 3 μm diameter grain with a 'platy' surface texture similar to SiC grains. The abundance of presolar corundum in Bishunpur is roughly comparable to that of rare 'X' SiC grains, about 5 ppb of Bishunpur.

The composition of grain B39 is remarkably similar to both spectroscopic observations [13] and theoretical expectations [14] for atmospheres of mass-losing red giants that have undergone the first dredge-up, where the ashes of partial hydrogen burning in inner zones are mixed outward to the surface by deep convection. Calculations show that the resulting envelope compositions should be enriched in ^{17}O by factors of up to 30 and depleted in ^{18}O by up to 30%, while ^{16}O remains unchanged [14]. The uncertainties on predicted compositions are relatively large, particularly for ^{17}O, due to poorly known reaction rates. When the highest choice for the reaction rate for $^{17}O(p,\alpha)^{14}N$ [15] is used to reproduce the observed $^{16}O/^{17}O$ ratios in stellar envelopes [14], the predicted $^{16}O/^{17}O$ ratios as a function of stellar mass match grain B39 in stars of 1–2 $M_\odot$ and 8–12 $M_\odot$. The prediction for the lower mass range is relatively robust and is probably more reliable than observations from individual stars; on the other hand, predictions for $M > 3\ M_\odot$ depend strongly on the rates chosen [14] and observations may be a more reliable guide. $^{16}O/^{18}O$ is only weakly dependent on mass and thus does not really constrain the mass of the parent star. A more important constraint may be the stellar mass-loss rates which, particularly for the low-mass stars, increase along the Asymptotic Giant Branch (AGB) as the envelope of the

star becomes ^{12}C-rich and oxygen remains basically unchanged [8]. Mass-loss rates for 1-3 $M_\odot$ stars on the early AGB are only a few x 10^{-7} $M_\odot$ yr^{-1}, which would seem to be insufficient to allow growth of 3 μm grains like B39, but mass-loss rates of a few x 10^{-6} $M_\odot$ yr^{-1} are observed in the late AGB and rates of 10^{-5} $M_\odot$ yr^{-1} are estimated for the planetary nebula phase.

The isotopic composition of B39 is broadly consistent with formation in almost any star that has undergone first dredge-up. Even the envelope of a type II supernova is a possible source, if the supernova explosion does not mix the massive envelope with the products of explosive nucleosynthesis. Interestingly, the measured $^{16}O/^{18}O$ in B39 is slightly higher than most ratios observed in envelopes of giant stars [13], although the errors on the stellar observations are large. Thus the composition of grain B39 might indicate a need to re-evaluate uncertainties in the stellar observations and the calculations that use them for calibration. On the other hand, two previously reported presolar Al_2O_3 grains [4-7] have smaller ^{18}O depletions (Fig. 1) and fall in the middle of the range of spectroscopic observations, so the ratio in B39 could reflect an unusual origin.

A longstanding problem in meteoritics is to understand the source of the variations in oxygen composition in solar system materials [e.g., 10, 11]. One possible explanation is that the solids in the sun's parent molecular cloud carry a variety of oxygen compositions, with refractory ^{16}O-rich 'carrier' grains producing the oxygen variations [11], although a chemical origin is also possible [16]. It is strikingly clear from Fig. 1 that the presolar Al_2O_3 grains found to date are not the carriers of ^{16}O needed to explain the solar-system oxygen data.

[1] Lewis R. S. *et al.* (1987) *Nature* **326**, 160. [2] Bernatowicz T. *et al.* (1987) *Nature* **330**, 728. [3] Amari S. *et al.* (1990) *Nature* **348**, 715. [4] Huss G. R. *et al.* (1992) *LPSC* **23**, 563. [5] Nittler L. R. *et al.* (1993) *LPSC* **24**, 1087. [6] Huss G. R. *et al.* (1993) *Meteoritics* **28**, 369. [7] Hutcheon I. D. *et al.* (1994) Ap. J. submitted. [8] Gehrz R. D. (1989) In Interstellar Dust (eds. L. J. Allamandola & A. G. C. M. Tielens, IAU), 445. [9] Huss G. R. *et al.* (1994) GCA submitted. [10] Clayton R. N. *et al.* (1977) *EPSL* **34**, 209. [11] Fahey A. J. *et al.* (1987) *Ap. J.* **323**, L91. [12] Bischoff A. and Keil K. (1983) *Nature* **303**, 588. [13] Smith V. V. and Lambert D. L. (1990) *Ap. J.* **72**, 387. [14] Dearborn D. S. P. (1992) *Physics Reports* **210**, 367. [15] Caughlan G. R. and Fowler W. A. (1988) *Atomic Data Nuclear Data Tables* **40**, 283. [16] Thiemens. M. H. and Heidenreich III, J. E. (1983) Science **219**, 1073. Division contribution 5358 (833); NASA NAGW-3297, NAGW-3040.

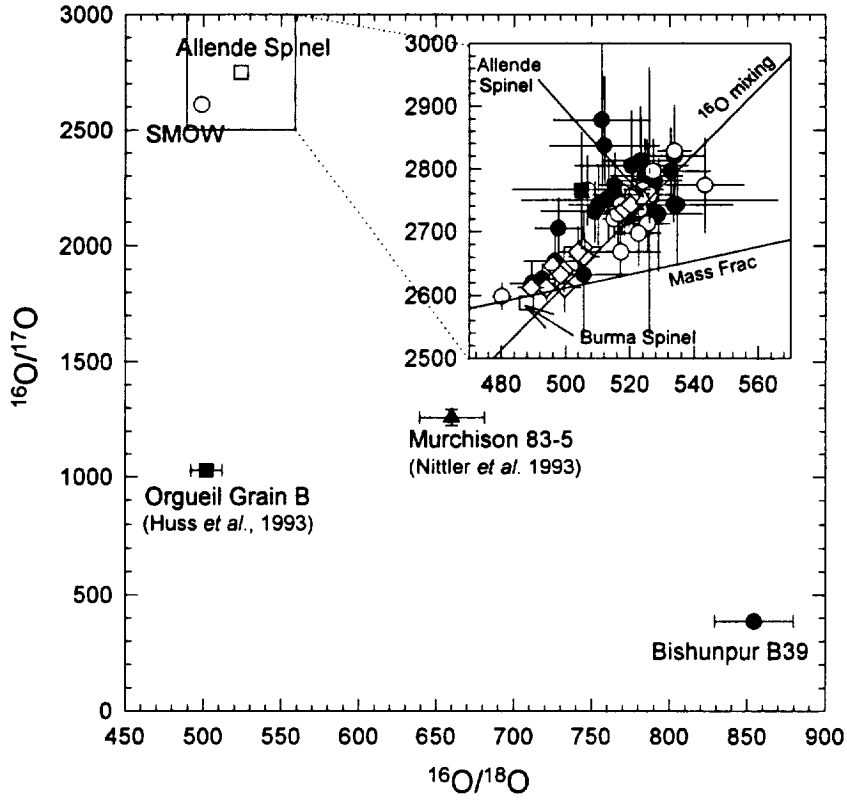

SILICON CARBIDE IN UNEQUILIBRATED ORDINARY CHONDRITES. Gary R. Huss, Albert J. Fahey and G. J. Wasserburg, Lunatic Asylum, Division of Geological and Planetary Sciences, California Institute of Technology, Pasadena, CA 91125

Presolar SiC has been found in the most primitive members of all classes of chondritic meteorites [1–3]. Isotopic studies of bulk SiC samples [4,5] and of individual SiC grains [6–14] have revealed a remarkable isotopic diversity indicating that meteoritic SiC was derived from a number of stellar sources. Important outstanding questions include: 1) is the same mixture of grains from different sources present in all meteorites; and 2) if the mixtures are different, were the differences inherited from the nebula or produced in the meteorite. Ne-E(H) and Xe-S abundances in acid residues suggest that all classes sampled the same mixture of SiC, although this mixture may have been modified during the subsequent history of the meteorites [3]. Single-grain work on Murchison K-series SiC [9,11,12] and SiC from Orgueil [7,13,14] indicates that the mixtures in these meteorites are the same, and an initial study of SiC in UOCs suggests these meteorites also contain the same SiC mixture [10]. On the other hand, Murchison L-series SiC exhibits unique isotopic systematics [8], and SiC grains from Indarch (EH3-4) and Inman (LL3.3), meteorites that have been metamorphozed, seem to have a more restricted range of isotopic compositions [7,10]. We have begun an ion-probe study of SiC in various classes of chondritic meteorites. In this abstract we report Si and C isotopic data for 33 individual SiC grains from Semarkona (LL3.0) and 23 grains from Bishunpur (LL3.1) and show that SiC from these meteorites has the same range of isotopic characteristics as Orgueil (CI) SiC and Murchison (CM2) K-series SiC.

Silicon isotopic data are shown in Figure 1. All of the Semarkona grains and 20 of 23 Bishunpur grains fall along single arrays on Si 3-isotope plots. The arrays for these meteorites are indistinguishable from those exhibited by SiC from Murchison [11,12] and Orgueil [13,14]. (Figure 1 is a ratio plot so the slope of the array differs from that on a delta plot (~1.34) by the factor 0.0505331/0.033464, the ratio of the Si isotope ratios). No groupings are evident in the UOC data, consistent with observations from Murchison K-series and Orgueil [11–14]. Carbon isotopic data for SiC from Semarkona, Bishunpur, are compared with Orgueil SiC [14] in Figure 2a–c. SiC for all three meteorites shows essentially the same distribution of $^{12}C/^{13}C$, which peaks between 40 and 75. Carbon isotopes are generally uncorrelated with Si isotopes.

In Bishunpur, two grains were found which are highly enriched in ^{28}Si (Fig. 1b, inset) and ^{12}C ($^{12}C/^{13}C$ = 160, 373) compared to most SiC. Such grains have been called 'X' grains and are believed to come from supernovae [9]. Another Bishunpur grain is depleted in ^{29}Si and enriched in ^{30}Si, falling well to the right of the main Si array and far below the terrestrial fractionation line (Fig. 1b). Its carbon ($^{12}C/^{13}C$ = 59) falls in the middle of the range for 'mainstream' grains. Such grains have been called 'Z' grains [10] and their origin is not understood. One Semarkona SiC is enriched in ^{12}C ($^{12}C/^{13}C$ = 122) and on Figure 1a falls below the terrestrial fractionation line and slightly to the right of the main Si array. Similar grains with $^{12}C/^{13}C > 150$ have been called 'Y' grains [9,12]. Although the Semarkona grain has a lower $^{12}C/^{13}C$, it exhibits the isotopic signatures of He-burning characteristic of 'Y' grains.

The Si and C isotopic compositions of SiC grains from Semarkona (LL3.0) and Bishunpur (LL3.1) display basically the same ranges and distributions observed in Murchison (CM2) K-series grains and SiC from Orgueil (CI). Our SiC grains were 0.9 to 4 μm in diameter, with an average of ~1.7 μm, most similar to Murchison KJE and KJF grains (mean grain sizes 1.14 and 1.86 μm) [11]. (The smaller size of our grains is probably not a true size difference between meteorites but rather is due to the low abundance of SiC, and therefore of large SiC, relative to spinel, etc. in the residues.) Smaller grains tend to have a wider range of isotopic compositions and a somewhat higher percentage of highly anomalous grains than do larger grains [8, 11, 12]. The number of grains with extreme carbon compositions and the relative abundances of 'X' (2 of

55), 'Y' (1 of 55), and 'Z' (1 of 55) grains in Semarkona and Bishunpur are very similar to those of Murchison KJE and KJF [11]. Nothing in our data so far points to differences between SiC from Semarkona and Bishunpur and that from Murchison (K-series) or Orgueil.

The number of stellar sources responsible for 'mainstream' SiC grains is still unknown, but multiple sources are suggested, and 'X', 'Y', and 'Z' grains almost certainly require independent sources [9–12]. Fig. 2d shows carbon compositions for red giant and AGB carbon stars [15]. Sampling is reasonably representative of carbon stars in the galaxy. The distribution of carbon stars looks remarkably like those of SiC grains (Figs. 2a-c). This similarity suggests that SiC in meteorites comes from a cross section of carbon stars and roughly reflects the relative abundances of different types of such stars. An alternative explanation, that a single star with C/O > 1 passes through all of the stages represented by Fig. 2d seems untenable. Although typical low-mass stars progress from oxygen-rich M stars with $^{12}C/^{13}C$ of 10–30 to carbon stars with $^{12}C/^{13}C$ of 30–80, this evolution follows a track on a $^{12}C/^{16}O$ vs $^{12}C/^{13}C$ diagram that is much steeper than the carbon star array [15], indicating that each star reaches the carbon-star array at a different point. In addition, standard AGB models cannot explain carbon stars with $^{12}C/^{13}C < 20$ and CJ stars are particularly problematic [15]. These considerations coupled with the similarity in distributions of $^{12}C/^{13}C$ values in stars and SiC grains indicate that a cross-section of carbon stars supplied the SiC to the solar system.

[1] Huss G. R. (1990) *Nature* **347**, 159. [2] Alexander C. M. O'D.*et al.* (1990) *EPSL* **99**, 220. [3] Huss G. R. and Lewis R. S. (1993) *GCA* submitted. [4] Lewis R. S. *et al.* (1990) *Nature* **348**, 293. [5] Ott U. and Begemann F. (1990) *Ap. J.* **353**, L57. [6] Zinner *et al.* (1989) *GCA* **53**, 3273. [7] Stone J. *et al.* (1990) *EPSL* **107**, 570. [8] Virag A. *et al.* (1992) *GCA* **56**, 1715. [9] Amari *et al.* (1992) *Ap. J.* **394**, L43. [10] Alexander C. M. O'D. (1993) *GCA* **57**, 2869. [11] Hoppe P. *et al.* (1993) *Meteoritics* **28**, 363. [12] Hoppe P. *et al.* (1994) *Ap. J.* in press. [13] Huss *et al.* (1993a) *LPSC* XXIV, 687. [14] Huss *et al.* (1993b) *Meteoritics* **28**, 368. [15] Smith V. V. and Lambert D. L. (1990) *Ap. J. Supp.* **72**, 387. Division Contribution 5357 (832); NASA NAGW-3297.

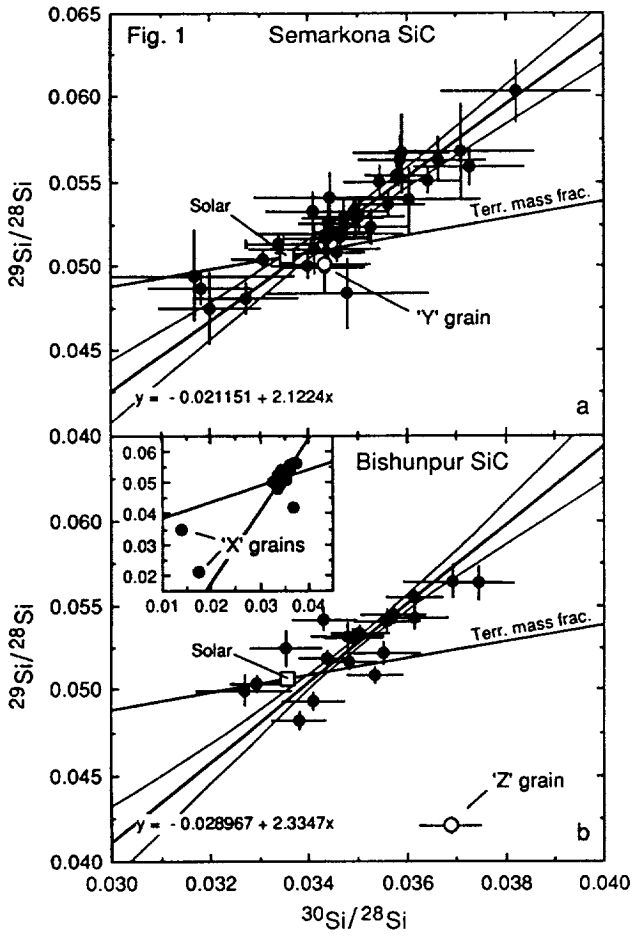

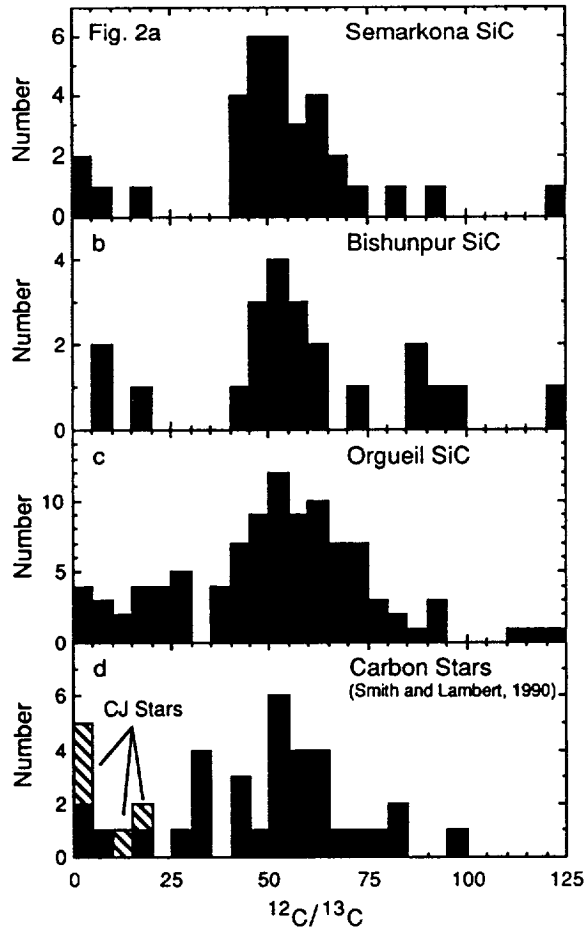

A SEARCH FOR ^{26}AL IN CHONDRITES: CHONDRULE FORMATION TIME SCALES; I.D. Hutcheon[1,2], G.R. Huss[1],and G.J. Wasserburg[1], [1]The Lunatic Asylum, Division of Geological and Planetary Sciences, Caltech, Pasadena, CA 91125; [2] Nuclear Chemistry Division, Lawrence Livermore Laboratory, Livermore, CA 94551

Models of solar nebula accretion and evolution predict rapid coagulation of solids to form meter-size bodies on a time scale of ~0.01 Ma and the growth of asteroid-size planetesimals within 1 Ma [1,2]. No astrophysically viable models yield an extended period of nebular evolution approaching 10 Ma. If this short time scale is representative and if ^{26}Al was uniformly distributed at the canonical initial ^{26}Al/^{27}Al ratio of ~5 x 10^{-5}, observable levels of radiogenic ^{26}Mg* from the decay of ^{26}Al ($\tau_{1/2}$ = 0.72 Ma) should not be confined to CAI but should also be present in Al-rich, Mg-poor phases in chondrules and "old" igneous rocks. Most searches for ^{26}Mg* outside CAI have, however, been unsuccessful. Evidence of ^{26}Mg* in non-refractory objects has been reported in only three ordinary chondrites and the inferred ^{26}Al/^{27}Al ratios fall below the canonical $5x10^{-5}$ value by factors of between ~7 and 250 [3-5]. Attempts to identify ^{26}Mg* in differentiated meteorites have also been unsuccessful [6-8]. We report here a new search for evidence of ^{26}Mg* in plagioclase-bearing chondrules and igneous rock fragments in seven ordinary chondrites. The absence of ^{26}Mg* in these samples and, more generally, the paucity of ^{26}Al in chondritic material has important implications for an absolute chronology of the early solar system. It appears either (1) ^{26}Al was not uniformly distributed and an initial ^{26}Al/^{27}Al ratio of < $1x10^{-6}$ is more representative of chondritic material; (2) the predicted evolutionary time scale is too short and the initial formation of solids in the nebula extended over several Ma; or (3) many chondrules and rock fragments are not primary objects but represent material recycled through multiple episodes of evaporation and recondensation, mixing and partial melting, and gas-dust fractionation.

Using PANURGE, we determined the Mg isotope composition of plagioclase in (1) a ~3 mm chondrule in Bovedy (L3) consisting of orthopyroxene laths with interstitial clinopyroxene and plagioclase, (2) a 3x2 mm inclusion in Los Martinez (L6) consisting of a highly zoned,single plagioclase crystal containing abundant, exsolved Cr-rich spinel [9], (3) a 1x1.5 mm barred chondrule in Manych (L3) consisting of olivine laths with interstitial pyroxene and plagioclase, (4) a 1.5x1 mm chondrule in Ragland (LL3) consisting of intergrown pyroxene and olivine with interstitial plagioclase surrounded by pyroxene laths containing poikilitic olivine, (5) a 1.2x1.5 cm basaltic pebble in Barwell (L6) with H-chondrite chemistry [10], consisting of coarse-grained olivine and turbid, brown plagioclase laths, interstitial to the olivine and overgrown by a granular mosaic of clear plagioclase; the inclusion has an ^{40}Ar-^{39}Ar age of 4.44±0.08 Ga and an ^{129}Xe-^{129}I age of -3.7±1.3 Ma relative to Bjurbole, (6) a 0.25 mm spherical chondrule in Ikhrarene (L4) consisting of reversely-zoned plagioclase laths with interstitial olivine, and (7) a 0.5 mm ameboid CAI in Clovis (H3) [11] consisting of irregular patches of anorthite and fassaite with euhedral spinel set in a cryptocrystalline feldspathoid core; a diopside rim surrounds the core. These samples were chosen because they contained plagioclase crystals large enough (> 10 μm) to analyze; no other selection criteria were applied.

This study reveals isotopically normal Mg in all objects examined; no evidence of intrinsic mass-dependent fractionation, $|F_{Mg}| < 4$ ‰/amu, or radiogenic ^{26}Mg* was found in any plagioclase. We calculate upper limits to the ^{26}Mg*/^{27}Al ratios of between $1.1x10^{-5}$ and $1.2 x 10^{-7}$ (Table 1). These data demonstrate that ^{26}Al was much less abundant during crystallization of most plagioclase-bearing objects found in ordinary chondrites than during CAI formation. If this low abundance is due to decay of ^{26}Al from an initial ^{26}Al/^{27}Al ratio of 5 x 10^{-5}, the minimum interval between CAI and chondrule formation is 1.6 - 6.3 Ma. Qualitatively, this scenario appears self-consistent. CAI formed early, at high temperature by partial melting of

isotopically anomalous, refractory precursors containing live ^{26}Al. Chondrules most plausibly formed by very similar processes but at a later time, after ^{26}Al decay. The difficulty with this chronological interpretation arises with the need to reconcile the ^{26}Al time scale with the dynamical time scales for condensation, grain aggregation and planetesimal formation; the predicted time scales are one to two orders of magnitude shorter [1,2].

We consider three plausible resolutions of this dilemma. (1) The distribution of ^{26}Al in the solar nebula was not homogeneous and an initial ^{26}Al/^{27}Al ratio of ~5x10^{-5} is characteristic only for CAI. The ^{26}Mg-^{26}Al system then has little chronological significance and the ^{26}Mg*-deficient objects studied here may have formed concurrently with CAI but in a region of the nebula depleted in ^{26}Al. (2) The dynamical time scales for condensation, grain aggregation and planetesimal formation are unrealistically compressed. While there may be little reason *a priori* to question the evolutionary time scale, the formation of kilometer-size planetesimals within 0.1 Ma is very difficult to reconcile with both meteorite chronology and astronomical observations. Differences in initial ^{87}Sr/^{88}Sr ratios and Pb-Pb ages, for example, strongly suggest the eucrite parent body formed > 11 Ma after CAI [8], while astronomical evidence indicates that disk lifetime varies systematically with parent star mass and may be as long as 10 Ma for a one solar mass star [13]. (3) Chondrule formation is a multi-step process involving a repeated sequence of mixing and partial melting, evaporation and recondensation over an extended time scale of several Ma.. Chondrule precursors may have formed contemporaneously with CAI but reprocessing and interaction with a locally dense (gaseous) environment continued until ^{26}Al was no longer extant. Similar reprocessing may have also have affected CAI and may provide an explanation for the low abundance of ^{26}Mg* in some CAI.

With the exception of the Semarkona noritic fragment (^{26}Al/^{27}Al~8x10^{-6}) [3] there is no evidence for high ^{26}Al in chondritic material. It now appears unlikely ^{26}Al was an important heat source for early planetary differentiation and was present only at a very low level during chondrule formation. We suggest chondrule formation was an ongoing process extending over several Ma and the absence of ^{26}Al reflects late formation rather than nebular heterogeneity. Resolution of this question must await high precision Pb-Pb, ^{87}Sr/^{88}Sr and Mg-Al isotope studies on individual chondrules and planetary fragments. Contrib. 5356 (831); NASA NAGW-3297.

References: [1] S.J. Weidenschilling (1988) in Meteorites and the Early Solar System, 348; [2] J.A. Wood and G.E. Morfill (1988) ibid, 329; [3] I.D. Hutcheon and R. Hutchison (1989) Nature 337, 238; [4] I.D. Hutcheon et al. (1989) LPS XX, 434; [5] E. Zinner and C. Gopel (1993) Meteoritics 28, 311; [6] D.N. Schramm et al. (1970) EPSL 10, 44; [7] M.T. Bernius et al. (1991) LPS XXII, 93; [8] G.W. Lugmair and S.J.G. Galer (1992) GCA 56, 1673; [9] A.J. Brearley et al. (1991) Meteoritics 26, 287; [10] R. Hutchison et al. (1988) EPSL 90, 105; [11] A.F. Noonan (1975) Meteoritics 10, 51; [12] S. Niemeyer (1988) GCA 52, 309; [13] L.A. Hillenbrand et al. (1992) Ap J 397, 613; [14] A.K. Kennedy et al. (1992) EPSL 113, 191.

METEORITE		An (mole %)	^{26}Mg*/^{27}Al (x10^{6})	ΔT[1] (Ma)
Los Martinez	(L6)	55-18	< 11	>1.6
Ragland	(LL3)	80-77	< 10	>1.7
Manych	(L3)	80	< 1.9	>3.4
Clovis	(H3)	96-84	<1.8	>3.5
Ikhrarene	(L4)	?	< 1.3	>3.8
Barwell	(L6)	74-42	< 0.55	>4.7
Bovedy 1971,1	(L3)	77	< 0.12	>6.3
Parnallee	(LL3)	75-70	< 4, [14]	>2.6
Semarkona	(LL3)	100	7.7±2.1, [3]	1.9±0.2
Bovedy GB-1	(L3)	85	0.25±0.10, [4]	5.5±0.4
Ste. Marguerite	(H4)	?	0.20±0.06, [5]	5.7±0.3

[1] Time interval to obtain observed ^{26}Mg*/^{27}Al from (^{26}Al/^{27}Al)$_0$ = 5x10^{-5}.

GRAIN CHARGING AND PLASMA POTENTIALS IN A DUSTY PLASMA WITH A DUST GRAIN SIZE DISTRIBUTION; T.W. Hyde and L.A. Bringol, Department of Physics, Baylor University, Waco, TX 76798-7316.

Dusty plasmas are found in planetary rings, comet tails and the protoplanetary nebula. Dust grains immersed in a plasma become charged. This charge will affect the motion of the grain in the electromagnetic field of a planetary magnetosphere and is involved in both the formation of the spokes in Saturn's rings and the erosion of the rings by micrometeorites. Additionally, the charge on the grain affects the coagulation rate of the dust into planetesimals in the protoplanetary nebula. We have solved the system of nonlinear charging equations using a modified Powell hybrid algorithm and a finite-difference approximation to the Jacobian. We show results using our method for a 1 eV hydrogen plasma which agree well with an earlier paper (1).

The charge on a grain is determined by plasma characteristics, secondary and photoemission from the grain, and a variety of other charging mechanisms. Grain equilibrium is attained when the sum of the currents to the grain is zero and there is an overall charge balance in the dusty plasma. Employing the standard equations (1) in cgs units, the charge balance for a dust cloud with a size distribution embedded in a plasma with the length scale of the dust cloud much longer than the Debye length of the plasma is given by

$$en_e - en_i - U\int_{r_{min}}^{r_{max}} r_d dn(r_d) = 0 \qquad (1)$$

where $n_{e,i}$ are the electron and ion number densities, respectively, U is the potential of the dust surface (dust minus plasma cloud), and $dn(r_d)$ is a distribution for the dust size.

The current balance to the grain is given by

$$I_e + I_i + I_{ph} + I_{se} + I_t = 0 \qquad (2)$$

Secondary electron currents and tunneling currents are generally only significant at T above tens of eV. If the plasma is assumed to be thermalized (Boltzmann distribution) and composed of hydrogen ions and electrons, (and with sticking coefficients $S_e = S_i = 1$) the currents are given to be

$$I_e = -e\pi a^2 \left(\frac{8kT}{\pi m_e}\right)^{1/2} n_e \exp\left(\frac{eU}{kT}\right), \quad U \le 0 \qquad (3)$$

$$I_e = -e\pi a^2 \left(\frac{8kT}{\pi m_e}\right)^{1/2} n_e \left(1 + \frac{eU}{kT}\right), \quad U \ge 0 \qquad (4)$$

$$I_i = e\pi a^2 \left(\frac{8kT}{\pi m_i}\right)^{1/2} n_i \left(1 - \frac{eU}{kT}\right), \quad U \le 0 \qquad (5)$$

$$I_i = e\pi a^2 \left(\frac{8kT}{\pi m_i}\right)^{1/2} n_i \exp\left(-\frac{eU}{kT}\right), \quad U \ge 0 \qquad (6)$$

$$I_{ph} = e\pi a^2 \Gamma_{ph} \qquad (7)$$

where Γ_{ph} is the photoelectric flux off of the dust grain per square centimeter.

The plasma densities are given by

$$n_e = n_{eo} \exp\left(\frac{eV}{kT}\right) \qquad (8)$$

$$n_i = n_{io} \exp\left(\frac{-eV}{kT}\right) \qquad (9)$$

where V is the plasma cloud potential.

Substituting (8) and (9) into (1), we get

$$\exp(\tfrac{eV}{kT}) - \exp(\tfrac{-eV}{kT}) - P(\tfrac{eU}{kT}) = 0 \qquad (10)$$

where

$$P = 6.95\times10^{6}\, n_{e0}^{-1} T_{eV} \int_{r_{min}}^{r_{max}} r_d dn(r_d) \qquad (11)$$

P is a function of the dust size distribution, $dn(r_d)$. Usually a power law is assumed of the form

$$dn_d(r_d) = c_j r_d^{-s} dr_d \qquad (12)$$

where c_j is a constant. Once the temperature regime is chosen, the appropriate currents from (3) to (7) can be substituted into (2). The system of nonlinear equations generated may then be solved using a modified Powell hybrid algorithm and a finite-difference approximation to the Jacobian for U and V and for a range of P and R values.

As a test of the method, we now assume a 1 eV hydrogen plasma. Substituting the ion, electron and photoelectron current equations into (2), we get

$$-\exp(\tfrac{eU+eV}{kT}) + 2.334\times10^{-2}\exp(-\tfrac{eV}{kT}) - P(\tfrac{eU}{kT}) = 0 \qquad (13)$$

The results from solving equations (10) and (13) with R values ranging from 0 to 0.9 are shown in Fig. 1 and agree well with an earlier paper (1). Results assuming a non-thermalized plasma (Lorentzian distribution) will be reported in a forthcoming paper.

References: (1) Havnes, O. T.K. Aanesen and F. Melandso, JGR Vol. 95, No. A5, pp. 6581-6585, 1990.

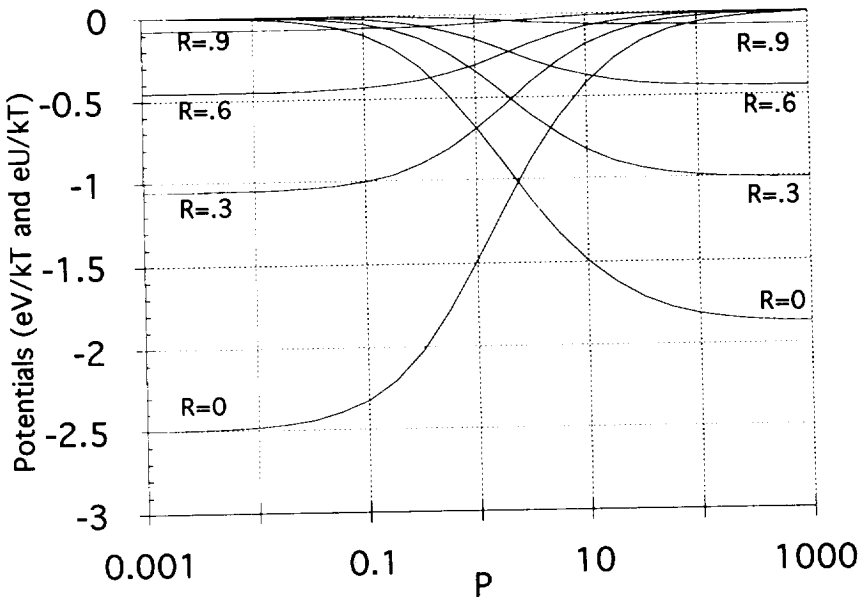

Figure 1

EXTENDED GRAIN LATTICE FORMATION WITHIN A DUSTY PLASMA; T.W. Hyde and W.M. Richter, Department of Physics, Baylor University, Waco, TX 76798-7316.

There are still open questions in theories concerning the origin of planetary systems. Many of these questions are centered around the problem of planetesimal formation by dust grain coagulation processes. Most current theories simply start with the planetesimals already in existence as an initial condition. There are also unanswered questions concerning the existence of the tenuous rings in our own solar system which are linked to grain coagulation. One promising mechanism suggested in the literature (1) which allows for grain coagulation while avoiding the problems of sticking coefficients, grain fragmentation, settling by gravitational instability, etc. examines a dusty plasma as a coupled system. It has been suggested (2) that the Uranian ring system (and perhaps the protoplanetary disk) might be examples of coupled systems. If the dusty plasma comprising a thin ring could be described in such a manner it might provide for the formation of a "Coulomb lattice" with the dust grains ordered along a solid-state lattice style structure or collapsed to a "solid" in the center of an extended mass-loaded plasma.

The coupling between the dust grains and the plasma is strongly dependent upon both the charge on the grains in the ensemble as well as the plasma Debye length. Both of these are also dependent upon the interaction between the dust grain ensemble and the plasma. As a result, the manner in which an extended grain ensemble charges within a plasma must be examined. The plasma particle depletion which occurs when a large dust grain ensemble is embedded in a plasma (especially a tenuous or limited plasma) or any sort of dust grain production mechanism produced by the plasma moving over the larger ring particles such as that suggested by Sheridan and Goree (3) should enhance many of the well known collective effects which occur due to the interaction of the plasma with the grain ensemble. In addition, a dust source or plasma particle sink will alter the plasma particle distribution function in a non-linear manner affecting grain charging as well as the plasma Debye length.

The standard method for calculating the charge on a dust grain ensemble is to attempt a solution of the Poisson equation under appropriate conditions. This is customarily accomplished by a linearization of the Poisson equation (usually by assuming a Maxwell-Boltzmann distribution of the plasma) and then solving by means of a Green's function approach. Although the Green's function approach can still be used, the approximation which allows a linearization of the Poisson equation is not applicable to the problem at hand since the plasma distribution function will be strongly non-linear due to the interaction of the plasma with the dust grain ensemble. In this case, the problem of determining the plasma distribution in the vicinity of the grain ensemble (which in turn allows for a calculation of the charge on the grains and determines the local plasma Debye length) demands the simultaneous solution of the Boltzmann-Vlasov transport equation and the Poisson equation. This can be accomplished numerically as shown by Hyde and Richter (4) using a modified 2-D particle-particle algorithm. This approach provides a method for studying the charging of a grain lattice immersed in a plasma while including the collective effects caused by the interaction of the lattice with the plasma and the interparticle effects (both of the grains within the lattice and the particles which comprise the plasma). Figure 1 shows the equilibrium charge (in electrons) on individual grains positioned in a two-dimensional (9 by 9) square dust grain lattice immersed in a plasma. The grains have a 5μ radius and are immersed in a 10 eV plasma with an initially random distribution of plasma particles (with a Maxwellian velocity distribution) and an initial plasma density around 100 electrons per cubic centimeter. The outermost grains in the lattice charge to the highest values while the grains farther into the lattice charge to lower values. Grains at the very center of the lattice obtain a charge slightly higher than their nearest neighbors. Figure 2 shows the radial electron distribution where the origin represents the center of the grain lattice. Their is an electron "pile-up" at the outer edge of the grain lattice and then a sharp drop past the lattice boundary. The electron distribution begins to climb before dropping again past the next lattice layer. The electron distribution falls to a minimum near the center of the grain lattice. Figure 3 shows individual grain potential as a function of time (again for grains arranged along a 9 by 9 square dust grain lattice).

It is seen from the above that an extended mass-loaded plasma will cause a decrease in the charge on inner lattice grains and also decrease their coupling parameters. However, the decrease in the radial electron distribution will at the same time change the plasma Debye length and may allow coupling of the grain lattice as a whole (especially for extended lattices) to remain fairly large. If a mechanism for continual mass-loading of the plasma is included (for example, the one suggested by Sheridan and Goree mentioned above) the interaction of the charged lattice grains with the plasma becomes more pronounced. Dense grain packing causes the charge on the inner grains of the lattice to become much smaller than that on the outer lattice grains. In addition, the interaction of the grain lattice with the plasma creates a significant decrease in the radial electron distribution which in turn increases the Debye shielding length to the point that the grains are no longer shielded from each other by the plasma (even for relatively dense plasmas). This allows for long-range Coulomb interactions in the grain lattice since lattice grains on the outer boundary of the lattice will no longer be shielded (necessarily) from the grains on the opposite side of the lattice (perhaps even for lattices which are tens of meters wide). Also, toward the center of the lattice, the grains will be at a lower charge which may enable them to collapse to a quasi-solid while the outer grains (being at a larger

charge and intergrain displacement) remain in equilibrium. This would create an extended grain lattice in which the outer layers of the lattice remain in a quasi-stable equilibrium while the inner layers collapse to a densely packed, low charge configuration. This densely packed collection of grains should have a relatively high probability for coagulation. An attempt to quantify the necessary stability conditions as well as determine coagulation rates at the center of this grain configuration is presently underway.

References: (1) Michel, F.C., Geophys. Res. Lett.,Vol. 13, pp. 442, 1986. (2) Goertz, C.K., Reviews of Geophysics, 27, 2 pp. 271-292, 1989. (3) Sheridan, T.E. and J. Goree, Journal of Geophysical Research, Vol. 97, No. A3, pp. 2935-2942, 1992. (4) Hyde, T.W. and W.M. Richter, Adv. Space Res. 13, No. 10, 1993.

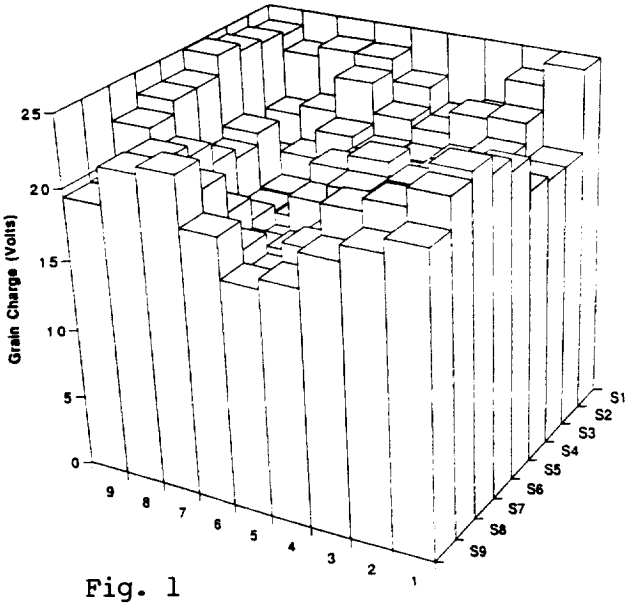

Fig. 1

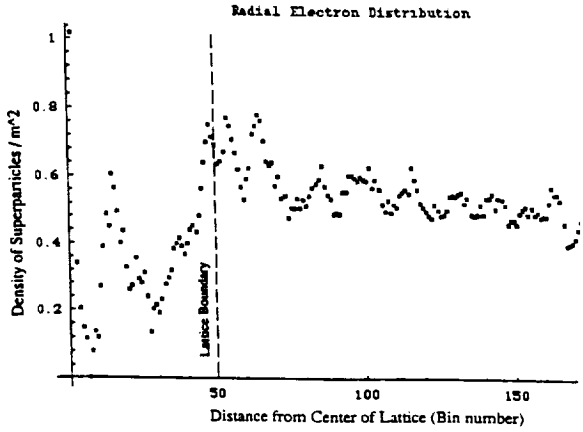

Fig. 2

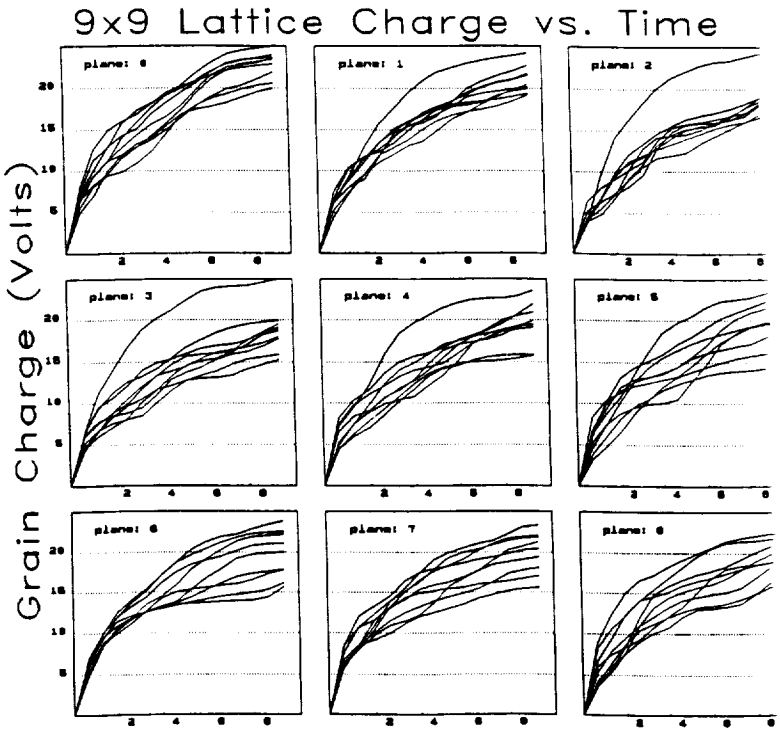

Fig 3

DYNAMICS OF TWO INTERACTING OBJECTS ORBITING THE SUN

S.I. Ipatov. *Institute of Applied Mathematics, Moscow, Russia*

The investigations of orbits of two gravitationally interacting objects moving around the Sun in one plane were made basing on the results of numerical integration of the equations of motion of the planar three-body problem. Regions of initial data corresponding to different types of evolution were considered.

Several types of evolution of orbital elements of two interacting close planets are known [1–6]. Below these types are denoted by letters *N*, *M*, *A*, *C*, and *P*. For *N*– and *M*–types, graphs of the time dependence of the semimajor axes are "*N*" and "*M*"–shaped, respectively. If one of the axes of synodic coordinates coincides with the direction from the Sun to the first object, then for these types we have tadpole and horseshoe synodic orbits of the second object. One triangular point of libration is inside the synodic orbit for *N*–type, and two triangular points are inside this orbit for *M*–type. Close encounters of objects and their collisions can take place only for *A*–type. Semimajor axes of objects cross each other during the evolution. Orbits of objects often become resonant for a rather long time if the mass of the larger object exceeds that of the Earth [1]. Variations in orbital elements are chaotic for *A*– and *C*–types, but for *C*–type there are no close encounters and semimajor axes are not crossing. *P*–type corresponds to such periodic variations in orbital elements when the Sun is inside the synodic orbit.

The aim of our investigations was to determine regions of $\varepsilon=|a_2^\circ-a_1^\circ|/a_1^\circ$ and $\varphi_\circ$ corresponding to various types, where a_1° and a_2° are initial values of semimajor axes of objects and $\varphi_\circ$ is the initial value of the angle φ with the apice in the Sun between directions to the objects. For one series of computer runs we have $\mu_1=\mu_2$, and $\mu_2=0.01\mu_1$ for another series of runs, where μ_1 and μ_2 are the mass ratios of the two objects to the Sun ($10^{-9}\le\mu_1\le 10^{-3}$). The considered time span N_c exceeds 25,000 revolutions of objects around the Sun. Let α, β, γ, δ be the values of ε corresponding to boundaries between *N*–, *M*–, *A*–, *C*–, and *P*–regions, respectively. The case of initially circular orbits is considered below. Earlier it was obtained that $\delta=2.1\mu^{1/3}$ at $\varphi_\circ=0$ [2], $\delta=2.4\mu^{1/3}$ at $\varphi_\circ=180^\circ$ [3,4], and $\gamma=1.49\mu^{2/7}$ [5], where $\mu=\mu_1+\mu_2$. The values of $\alpha^*=\alpha/\mu^{1/2}$, $\beta^*=\beta/\mu^{1/3}$, $\gamma^*=\gamma/\mu^{1/3}$, and $\delta^*=\delta/\mu^{2/7}$ obtained by us are presented in Figs. *a–d*. The values of δ at $\varphi_\circ=60^\circ$ are, as a rule, greater than those at $\varphi_\circ=0$ and $\varphi_\circ=180^\circ$ (Fig. *d*). For most of runs at $\varphi_\circ=60^\circ$ and $\mu\le 2\cdot10^{-4}$, we obtained that $\alpha^*\approx1.63$–1.64, $\beta^*\approx0.77$–0.81, $\gamma^*\approx2.1$–2.45, and $\delta^*\approx1.45$–1.64. For the considered time spans, a small *P*–region usually was obtained inside the *C*–region and several small *C*–regions might be located inside the *A*–region. The value of $\varphi_\circ$ corresponding to the boundary between *M*– and *A*–regions at $a_2^\circ=a_1^\circ$ is denoted by φ_M. The values of $\varphi_M^*=\varphi_M/\mu^{1/3}\approx3.9$–$4.4$ are presented in Fig. *e*. If $\mu_1\gg\mu_2$

DYNAMICS OF TWO INTERACTING OBJECTS ORBITING THE SUN

Ipatov S.I.

than $\varepsilon^2 \approx \varepsilon_*^2 - \frac{8}{3}\mu\{(1-\cos\varphi)+[2(1-\cos\varphi)]^{-1/2}-1.5\}$, where ε_* is the value of ε at $\varphi=60°$ [1]. By analyzing this equation we obtained that α^* is maximum at $\varphi=60°$ and this maximum value is equal to $\sqrt{8/3}\approx 1.633$. This value is presented in Fig. *a* by a solid line. The dashed and solid lines in Fig. *e* correspond to the values of φ_M^* obtained from the above equation for $\varepsilon_*=0.8\mu^{1/3}$ and for the values of $\varepsilon_*=\beta$ presented in Fig. *b*, respectively. If $\mu_1 \le 10^{-5}$, then $e_M=e_{max}/\mu_1^{1/3}$ usually does not exceed 7–8 at $\mu_1 \gg \mu_2$ and 4–6 at $\mu_1=\mu_2$ for *A*–type, and 4–6 at $\mu_1 \gg \mu_2$ and 4 at $\mu_1=\mu_2$ for *C*–type, where e_{max} is the maximum eccentricity during the evolution. For *A*– and *C*–types and $a_2^\circ > a_1^\circ$, the values of $\Delta r_\delta=(\max\{r\}-a_1^\circ)/a_1^\circ\delta$ are about 3, 6.5, 2, and 3.5 at $\mu_1=10^{-9} \gg \mu_2$, $\mu_1=10^{-5} \gg \mu_2$, $\mu_1=\mu_2=10^{-9}$, and $\mu_1=\mu_2=10^{-5}$, respectively, where $\max\{r\}$ is the maximum value of the distance r from the Sun to the second object. For *C*–type and $\mu_1 \gg \mu_2$, it is obtained that $\min\{r\}-a_1^\circ \approx 0.4\gamma a_1^\circ$. For three objects orbiting the Sun e_{max} can be several tens times larger than that for two objects [7]. For initially eccentric orbits, the values of α and β are smaller and the values of δ and γ may be considerably larger than those obtained for initially circular orbits. The values of e_{max} are greater for greater initial eccentricities.

This work was supported in part by National Science Foundation under Grant No. PHY89–04035 in 1992 and by Russian Fund of Fundamental Investigations under Grant 93–02–17035 in 1993.

References: [1] Ipatov, S.I. (1981) *Sov. Astron.*, **25(58)**, *N* 3, 352–357. [2] Gladman, B., Duncan, M. (1990) *Astron. J.* **100**, 1680–1693. [3] Birn, J. (1973) *Astron. Astrophys.*, **24**, 283–293. [4] Gladman, B. (1993) *Icarus, in press.* [5] Duncan, M., Quinn, T., Tremaine, S. (1989) *Icarus.* **82**, 402–418. [6] Dermott, S.F., Murray, C.D. (1981) *Icarus*, **48**, 1–11. [7] Ipatov, S.I. (1988) *Kinematics Phys. Celest. Bodies*, **4**, *N* 6, 76–82.

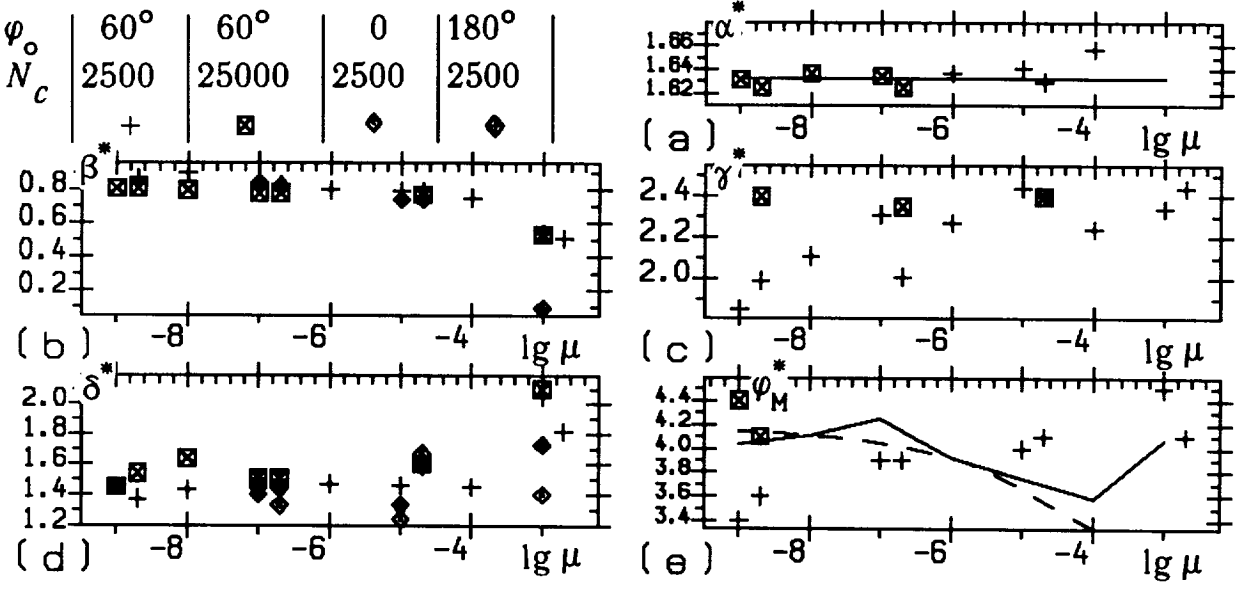

NEW PHOSPHIDES IN THE KAIDUN METEORITE A.V. Ivanov[1], M.E. Zolensky[2], G.J. MacPherson[3], S.V. Yang[4], and N.N. Kononkova[1]. [1]Vernadsky Institute of Geochemistry and Analytical Chemistry, Russian Acad. Sci., Moscow 117975, Russia; [2]SN2, NASA Johnson Space Center, Houston, TX 77058; [3]Department of Mineral Sciences, Smithsonian Institution, Washington DC 20560, USA; [4]Lockheed Engineering and Science Co., Houston, TX 77058.

Abstract: Two grains containing the phosphides TiFeP, $Fe_4Cr_2P_3$, and Fe_5CrP_3 were found in a fragment of the Kaidun chondrite breccia. We propose that the phosphide formation involved the remelting of a selected phase assemblage from enstatite chondrite material, followed by aqueous alteration.

Two elongate grains (grains 1 and 2, respectively measuring 190x90 μm and 300x90 μm) containing unusual phosphides were found during SEM study of a polished section of a fragment (#53.10) of the Kaidun chondritic breccia; the main part of the fragment is extremely brecciated C and E chondrite material, displaying varying stages of alteration, and has not yet been well characterized. Grains 1&2 contain numerous laths of Fe-Cr-phosphides, measuring up to 1.0-1.5 μm in width and up to 5 μm in length. The laths often form extended chains up to 100 μm length. Grain 1 also contains equant to lozenge-shaped crystals of a Fe-Ti-phosphide with a maximum dimension of 14 μm.

Chemical compositions Electron microprobe analyses of all phases were obtained, with the use of the most appropriate standards available; these were troilite, Ni-Cr-Fe metal and schreibersite. Average compositions of the matrix of grains 1&2 and the enclosed phosphides are given in Tables 1 and 2, respectively. Matrix and Fe-Ti-phosphide grains were analyzed directly. However, the Fe-Cr phosphides were too small to permit single phase analyses by microprobe. Accordingly, the compositions of Fe-Cr-phosphides were calculated by subtraction of matrix compositions (from immediately adjacent regions) from the multiphase microprobe analyses. We recognize the inherent dangers in this approach.

Table 1. The chemical composition of the grain matrix (wt.%)

	FeO	NiO	CoO	Cr2O3	P2O5	S	SiO2	Al2O3	MgO	Na2O	Sum
Grain 1	39.41	12.00	1.53	0.82	0.33	6.55	17.99	1.00	2.34	0.52	82.99
Grain 2	41.11	7.05	1.48	4.94	0.64	6.87	11.34	0.51	2.30	2.65	78.89

TiO2, CaO and V2O5 contents <0.1wt.% in both grains.

Table 2. The chemical composition of phosphides (wt.%)

		Fe	Ni	Co	Ti	Cr	V	P	Si	Sum
1	Grain 1	41.32	5.17	0.55	30.82	0.76	0.81	22.10	0.28	101.81
2	Grain 1	58.5	7.0	0.5	<0.1	8.6	1.9	20.7	1.9	99.1
3	Grain 2	49.8	4.4	0.5	3.1	16.7	2.0	20.7	1.1	98.3

The phosphide compositions can be approximated by formulas:

1 $(Ti,V,Cr)_{0.95}(Fe,Ni,Co)_{1.05}P_1$ (direct analysis)

2 $(Fe,Ni,Co)_{4.8}(Cr,V)_1(P,SI)_3$ (after matrix subtraction)

3 $(Fe,Ni,Co)_{4.1}(Cr,V,Ti)_2(P,SI)_3$ (after matrix subtraction)

NEW PHOSPHIDES IN KAIDUN: Ivanov et al.

Fe-Cr-phosphides have already been reported in the ALH85085 "CH" chondrite [1&2]. The phosphides in ALH85085 are close in composition to the phosphide phase reported here from grain 2. The other two phosphides reported here have not been reported previously in nature.

Discussion Chemical compositions of the matrix of host grains 1&2 (Table 1) are very similar to the observed products of aqueous alteration of Fe-Ni metal-containing material in the Kaidun III EH5 sample [3&4] and in some other Kaidun samples that we studied, and we suggest that the matrix here has experienced similar alteration. The precursor to the matrix in these host grains could be an impure metal, or a ferromagnesian silicate with metallic inclusions. The bulk composition of the host grain matrix, low totals, and comparisons to other Kaidun materials we have observed suggests that it now consists of an Fe-rich serpentine phase (such as greenalite) with sub-micrometer sized sulfide grains (principally pentlandite). The observed difference in the average matrix composition of the grains in Kaidun could reflect different precursor phases, or local variations in the alteration process.

Synthetic TiFeP is fairly well known to steel makers, and is one of the ternary Co_2P-type phosphides, which crystallize with the *anti*-$PbCl_2$-type structure [5]. In the synthetic systems it is common to find Zr, Nb and Ta substituting for Ti, rather than the V and Cr here, but the latter substitutions are logical. Substitution of Co and Ni for Fe has been observed in the synthetic TiFeP. The formation of the unusual phosphides in Kaidun can be explained by the remelting of typical opaque assemblages observed for EH chondrites (Fe-Ni metal + sulfides + osbornite + schreibersite). The regular distribution of the Fe-Cr-phosphides in the Kaidun host grains suggests an exsolution process occurring during cooling. Both inferred processes - remelting (and subsequent exsolution) and aqueous alteration - are plausibly connected with shock events. The remelting (impact) process could have occurred during the "meeting" of the two E chondrite Kaidun lithologies (EL and EH). The alteration of the phosphide-containing grains occurred later, possibly during final accumulation of the Kaidun parent body. The varying degree of aqueous alteration exhibited by the various Kaidun clasts testifies to the complex nature of the final accumulation and alteration history of this meteorite's parent body

AVI was supported by RFFI Grant 93-05-9222 and NASA Grant 152-11-40-23 to MEZ.

References: [1] M. Kimura and A. El Goresy (1989) *Meteoritics, 24*, 286; [2] B. Zanda (1992) *LPSC XXIII*, 1569-1570; [3] A.V. Ivanov et al. (1992) *LPSC XXIII*, 571-572; [4] A.V. Ivanov et al. (1993) *Geochemistry Intern. 30*, 11-19; [5] S. Rundqvist and P.C. Nawapong (1966) *Acta Chemica Scand., 20*, 2250-2254.

Figure 1 The phosphide-containing grain 1 from Kaidun. The grain matrix is gray, TiFeP grains (white) are indicated by arrows, other phosphides are present as white linear arrays throughout the matrix. A dark electron beam contamination spot is present at upper right.

DYNAMIC FRAGMENTATION OF A COMET IN THE JOVIAN ATMOSPHERE. B. A. Ivanov, Institute for Dynamics of Geospheres, Moscow, 117939 and H. J. Melosh, Lunar and Planetary Lab, University of Arizona, Tucson, AZ 85721.

The expected impact of comet Shoemaker-Levy IX (SLIX) on Jupiter in late July 1994 is simulated with 2D hydrocode to study the dynamic fragmentation of a body during its flight through the Jovian atmosphere. Preliminary results predict the disruption of a 10-km ice sphere into fragments with dimensions of 250 to 500 m at a depth of approximately 70 km below 1 bar pressure level.

Introduction. The expected collision of the Comet Shoemaker-Levy IX with Jupiter [1] has generated a great deal of interest since it may be possible to observe the event [2,3]. The effects of the impact on Jupiter's atmosphere depend strongly on the energy transfer from the incoming comet to the atmosphere, which in turn depends on the comet's deformation during its flight through the atmosphere.

We used the SALE code [4] modified by Melosh et al. [5] to compute the history of dynamic fragmentation of SLIX cometary fragments during their flight through the Jovian atmosphere. To try to bracket the uncertainties in the SLIX composition [3] we simulated the collision of both basalt and ice bodies. The same parameters as in [6] were used in both the equation of state and in the Grady-Kipp model of dynamic fragmentation.

Initial model parameters. We assume initially spherical basalt and ice projectiles with diameters of 10 km. The initial velocity is 60 km/s. The angle of entry is 45 degrees, so the projectile's height decreases at a rate of 42.4 km/s.

To describe our results we use "geographical" coordinates: a spherical projectile has a "south pole" at the center of the leading edge and a "north pole" at the center of the trailing edge. The atmospheric flow moves from "south" to "north" with respect to the projectile.

In these preliminary computations the atmospheric gas flow around the projectile is not simulated directly by the hydrocode. The external pressure is defined at the projectile surface according to a theoretical formula: the stagnation pressure, P_{stag}, at the "south pole" decreases as P_{stag}*SIN(LATITUDE). At the "equator" the pressure falls to zero. Zero pressure is applied to the entire "northern" hemisphere. The standard ideal gas equation describes the value of the stagnation pressure: P_{stag} is proportional to the density of the ambient atmosphere and the square of the descent velocity at a given instant of time.

The height, h, is measured from the 1 bar pressure level, which we take to be positive above and negative below this level. We use a simplified model of the Jovian atmosphere that includes an isothermic atmosphere above the 1 bar level with a scale height H1=23.66 km, and an isentropic atmosphere below with a scale height H2=77.44 km. A density of 0.17 kg/m^3 at h=0 gives a rather good fit to more realistic models of the Jovian atmosphere. Thus the atmospheric density, ρ_a, is described as

$$\rho_a = 0.17 \exp(-h/H1) \qquad 0<h<400 \text{ km}$$

$$\rho_a = 0.17 (1-h/H2)^{2.27} \qquad h<0.$$

Calculations begin at the height of 400 km, where P_{stag} is low enough to produce only elastic strain in the body.

Ice projectile. The first manifestation of disruption occurs at 5 sec at a height of 190 km, where P_{stag} is about 0.5 bar. The velocity of bulk sound waves in the model ice is about 2.9 km/s, so the time for an acoustic pulse reverberation is about 7 sec. This means that disruption begins under non-equilibrium conditions--the acoustic waves are not fast enough to adjust the body's entire volume to the increasing external pressure on the leading hemisphere.

Disruption begins at the body's surface between 30°S and 60°S and propagates into the body as a series of cracks. The azimuthal tensile stress is the maximum, so the first cracks seem to be radial ones which "slice" the body into "orange sections". A natural drawback of an axisymmetric hydrocode is that is gives a poor representation of such a crack, so the following results have a qualitative character.

Using the statistical approach developed in [5,6], the characteristic dimension of the first "sections" is estimated as 350 m, which is comparable with the size of a computational cell (about 500 m).

The full disruption of the ice body is achieved around 11 sec at the height of -70 km (P_{stag} is around 3 GPa). The size of the most probable fragment varies from 500 to 250 m. The internal motion of the deforming body has a maximum velocity of 500 m/s. Most of the projectile is disrupted by tension; only several cells failed by shear in compression.

Due to full disruption and an increased ambient atmospheric density the body begins to deform faster after 11 s. The computationwas halted at 15 sec (h=-240 km) when the Lagrangian grid failed to describe the body deformation. A non-Lagrangian grid may be needed in the future to describe the final deceleration and explosion of the body.

DYNAMIC FRAGMENTATION OF A COMET: Ivanov, B. A. and Melosh, H. J.

Basaltic projectile. Being much stronger, a basaltic projectile begins to disrupt at 9 sec at a height of 18 km. The bulk sound speed for basalt is around 4.3 km/s, and the reverberation time is around 4.6 s. So before disruption begins stress waves can travel twice from the "south" to "north" pole and back. The result is a closer approach to equilibrium conditions inside the body in comparison with ice. In the "southern" hemisphere the external pressure creates compressive stresses that prevent tensile disruption. The first "cracks" appear close to surface in the "northern" hemisphere (latitude around 45N).

Several code runs reveal a correlation between the point where the disruption begins and the Poison ratio of the projectile material. This point needs to be elaborated further; our first impression is that a low Poison ratio shifts the position of the first crack toward the "equator". As with ice, the first cracks in a basalt sphere are meridional. The size of the "sections" are computed to be around 3 km, which is larger than a cell dimension (~ 500 m), so an axisymmetric 2D hydrocode fails to describe quantitatively the further disruption ("orange sections" may be intact inside while all the ring cells are fully damaged in the computational grid). In the future this fault may be partially compensated with a more sophisticated damage description. A 3D code would be a better solution of the problem.

Quantitatively, a range of fragments sizes from 100 m to 3 km has been calculated. The body is fully disrupted at 16 s at height of -300 km, where stagnation pressure is about 30 GPa. Only the "northern" hemisphere is disrupted in tension, while the material in the "southern" hemisphere fails by shear in compression above the shear strength limit (about 1 GPa in the first model run).

The calculation was halted at 17 sec, when the body diameter increased approximately by a factor of two. The relative internal motion had a maximum velocity of 1 km/s.

Venus test. The impact crater population on Venus allows us to test the model of dynamic disruption described above. According to [7] the minimal projectile diameter which strikes the Venusian surface as a single body is about 0.8 km for a vertical impact. Using the same code as for Jupiter (except the atmospheric model) we calculated the vertical flight of a basaltic sphere with a diameter of 1 km through the Venusian atmosphere with an initial velocity 20 km/s. The disruption pattern demonstrates that a 1-km basaltic body is very close to the actual limiting diameter. Smaller bodies seem to strike the surface as a cluster of separated fragments. In the future multiple craters on Venus may be used to calibrate the dynamic fragmentation model.

Possible role of acoustic vibrations. In several test runs with a decreased damping of numerical instabilities in the code, we observed an avalanche growth of damage initiated by internal "waves". This qualitative result presents an interesting possibility for the real event. If a real body is not an ideal sphere, the gas flow around the rough body surface may generate noise (well known to all air passengers). The tension phase of a sound wave may locally accelerate fracture growth, increasing the damage. A change in bearing capacity may result in the localization of deformation, further accelerating the damage growth at a given point. The acoustic "noise" field may thus increase the level of damage in comparison with previous estimates.

Possible role of structural inhomogeneities. If the projectile has some initial damage (for example, from previous impacts or tidal disruption) the disruption may be governed by this pre-damage structure. In this case weak planes may localize the new accumulated deformations. At the qualitative level it may increase the fragment size. Future simulations with statistically distributed pre-damaged zone may give quantitative estimates.

Conclusion. Numerical simulation of the SLIX comet's fragmentation in the Jovian atmosphere may produce better constraints for impact energy release, which are important for the observational predictions of the event.

References:

[1] Chapman, C.R. (1993) Nature **363**: 492-493. [2] Sekanina, Z. (1993) Science, **262**,382. [3] Zahnle, K., M.-M. Mac Low, and C.F.Chyba (1993) Some consequences of the collision of a comet and Jupiter, submitted to Icarus. [4] Amsden, A.A., H.M.Ruppel, and C.W.Hirt (1980) Rep. LA-8095, Los Alamos Nat. Lab., Los Alamos, N.M. [5] Melosh H.J., E.V.Ryan, and E.Asphaug (1992) J. Geophys. Res. **97**: 14,735-14,759. [6] Asphaug E., and H.J.Melosh (1993) Icarus **101**: 144-164. .[7] Ivanov B.A. and 5 others (1992) J. Geophys. Res. **97**: 16,167-16,181.

DYNAMICS OF FLUIDIZED EJECTA BLANKETS ON MARS; B.A.Ivanov[1], B.C.Murray[2] and A.S.Yen[2]; [1]Institute for Dynamics of Geospheres, Russian Academy of Sciences, Moscow, 117979, [2]California Institute of Technology, 170-25, Pasadena, 91125.

We report the preliminary results of a study of fluidized ejecta blankets (FEBs) with rampart or convex termini around Martian impact craters. A numerical model was developed which suggests "dynamic" and "quasi-static" stages of ejecta emplacement. Turbulent versus laminar flow regimes are discussed. Viking Orbiter images were used to constrain ejecta flow velocities and subsequently to estimate cohesion and viscosity using a Bingham model. Comparisons between Martian ejecta flows and terrestrial rock avalanches and lahars are described. The final goal of the project is to better constrain the volatile content in the upper layers of the Martian crust.

The primary deposition process. The general scenario of ejecta depositing around an impact crater is formulated using the well-known Z-model of cratering [1,2]. The ejected debris flies along ballistic trajectories forming a "plume" in the shape of an inverted cone; this debris moves as a cloud of particles, not as a continuous sheet. The slowest particles are the first to be deposited on the uplifted rim of the crater, and the collective motion of the ejecta layer begins only after deposition of the material. The falling particles may disrupt the target surface and involve some of the ground material in the collective motion [3].

Flow models. We have evaluated several analytical and numerical models of the FEB's motion. The final radial extent of the FEB in our models is controlled by dissipation of the initial kinetic energy of the blanket (just after deposition). The dissipation mechanisms tested were turbulent and linear viscosity as well as finite cohesion. All of the ejecta is assumed to be at the surface when the outward flow begins, and the initial velocity is assumed to be the horizontal velocity of ejecta near the crater rim: $v_0 \approx \mathrm{sqrt}\{(2/15)*g*R\}$. For craters from 5 to 50 km in diameter, the initial flow velocity is approximately 30 to 100 m/s, respectively.

The linear viscosity model. The MAC numerical code [5], which calculates flows of Newtonian viscous fluids, was used to evaluate flow characteristics. The ejecta blanket is assumed to be an annular ring with a thickness that decreases as the inverse cube of the distance from the crater center. Although this model cannot calculate the final radius of the FEB (a viscous fluid in a gravity field will spread to infinity), it does reveal two distinct stages of the flow: (1) The dynamic stage where the inertia of the material is very important and (2) the late quasi-static stage where the flow spreads like a volcanic lava flow. The FEB for a 5-km crater has a model derived viscosity of 20 m^2/s and flows in the dynamic regime to a diameter of 15 km over several minutes. During the subsequent quasi-static stage, it takes ≈5 hours to increase the diameter from 15 to 20 km (velocity is a function of flow thickness). The material parameters may change over this long time period; models with time dependent material properties will be considered in the future. Further study will also indicate whether we can distinguish between dynamic and quasi-static deposits.

These MAC calculations also show that in the dynamic regime of a purely laminar flow, it is difficult to achieve a ratio of Rej (the final outer FEB radius) to R (the crater radius) larger than 3. For a laminar, dynamic flow, Rej/R is proportional to (viscosity)**(-1/8) for a constant R, therefore, an increase of Rej/R from 2 to 3.5 implies a two order of magnitude reduction in viscosity. For larger Rej/R values in the dynamic regime, the viscosity may be low enough to have a turbulent flow just after ejecta deposition.

The Bingham model. The final radius of the FEB is derived from the Bingham mechanical model: Plastic behavior under some threshold shear stress and a viscous fluid above the threshold (e.g., [4]). Bingham parameters have been estimated for avalanches and lahars on the slopes of Mount St. Helens [6], and we've constructed a similar model for the FEBs. In contrast to [6], FEBs flow on a horizontal surface, using the initial kinetic energy and the potential energy derived

from its thickness. In our analytical model, the fluidized ejecta flow is a flat disk of constant volume spreading out from the crater rim, and the dissipation factors used in [6] are included. Some of the resulting parameters indicate that the FEB's flow is turbulent. In a strict sense, however, the term "turbulent flow" is only valid for continuous media. The ejecta from impacts is a collection of fragments with some size-frequency distribution and may contain some volatiles (Mars and Earth). The so-called Bagnold debris flow [7] may mimic the turbulent fluid flow: In both cases the shear stress is proportional to the square of the shear strain rate [8]. Depending on the chosen parameters, the model shows that the flow will have different velocity decays with distance. Constraints from Viking Orbiter images have been used to refine the model parameters.

Observations from Viking Orbiter images I. We have found and analyzed 15 situations in the Viking Orbiter images where the ejecta flow either overran or did not overrun older craters. The estimated heights of these obstacles were used to derive lower or upper limits of the flow velocities. The resulting model values of cohesion (2000 to 10,000 Pa) and viscosity (1 to 100 m^2/s) have been compared with the same parameters for Mount St. Helens (MSH) rock avalanches and lahars calculated in [6]. This comparison shows that model derived cohesion and viscosity range between values derived in [6] for MSH rock avalanches (10,000 Pa, 200 m^2/s) and lahars (500 to 1000 Pa, about 1.5 m^2/s). Longer flows ($Rej/R \approx 6$) have parameters close to terrestrial lahars while shorter runouts are more like rock avalanches. Values of these parameters are model dependent and may change for more sophisticated models.

Observations from Viking Orbiter images II. Another source of observational constraints is from the morphology of the FEBs surfaces. A subset of multiple-lobe FEBs exhibit radial striations extending from the crater rim to at least the edge of the inner ejecta lobe. A lahar-like flow could be responsible for this morphology. We discuss two possible scenarios: (1) The inner lobe may be deposited within the turbulent zone close to the rim; eddies help to sort the fragments, and the finer debris flows out to form the outer lobe. In this case, the striations are regions of shear and form when the flow in the inner lobe becomes laminar before the motion ceases. (2) The outer lobe flows over the earlier inner lobe deposits [9]; large rocks and boulders can be carried by the lower viscosity lahar-like flow thus creating the radial striations on the inner lobe. Further investigations will yield additional observational constraints on the FEB's deposition mode.

Conclusions

- Fluidized ejecta blankets may be formed as a dynamic, laminar flow only if $Rej/R < \sim 3$; this regime operates over several minutes. An alternative is slow viscous spreading to $Rej/R >> 3$ over the course of several hours.
- For $Rej/R > \sim 3$, turbulent flow is predicted by our model.
- The preliminary dynamic model results for $4 < Rej/R < 6$ show that in terms of effective cohesion and viscosity, Martian FEBs may be similar to some terrestrial lahars.
- In future work, we hope to be able to distinguish between deposits of turbulent and laminar flows in Martian FEBs. A better understanding of the radial striations may help constrain the FEB's mode of emplacement.

References

[1] Maxwell, D.E. (1977) In "Impact and Explosion Cratering", Pergamon Press, 983-1002.
[2] Ivanov B.A. and Comissarova L.I. (1977) Lunar Science VIII, 499-501.
[3] Oberbeck V.R. (1975) Rev. Geoph. and Space Phys., V.13, 337-362.
[4] Gault D.E. and Greeley R. (1978) Icarus, V. 34, 486-495.
[5] Welsh J.E., et. al. (1966) Los Alamos Scientific Laboratory Report TID-4500, 146 pp.
[6] McEwen and Malin (1989). J. Volcanology and Geothermal Res. 37: 205-231.
[7] Bagnold, R.A. (1954) Proc. R. Soc.London Ser. A 225: 49-63.
[8] Campbell, C.S. (1990) Annu. Rev. Fluid Mech. 22: 57-92.
[9] Mouginis-Mark, P.J. (1981) Icarus 45: 60-76.

INDUCED THERMOLUMINESCENCE STUDY OF EXPERIMENTALLY SHOCK-LOADED QUARTZ

A.I. Ivliev, L.L. Kashkarov, and D.D. Badjukov
V.I. Vernadsky Institute of Geochemistry and Analytical Chemistry, Russian Academy of Sciences, Moscow, Russia

There are a number of shock "geobarometers" that can have an application of a study of impactites. The base of "geobarometer" is using a shock-induced disorder in some minerals, especially such as a quartz [1-4].

The TL of minerals is very sensitive to detect defects in mineral lattice and in principle can be used for a study of shock effects. In has been reported [5-6], that TL of plagioclases changed essentially in shocked samples. However the shocked quartz is studied insufficiently in spite of broad investigations of shock metamorphism of quartz. For this reason we studied TL of quartz samples experimentally shocked to pressures of 8.4, 9.0, 12.2, 20.0, 24.0, 27.0, 31.5, 34.0 and 49.0 GPa respectively. We studied artificial TL that was caused by ^{137}Cs gamma-ray source. The method of shock loading of the quartz samples has been reported earlier [4]. For TL measurements the material was crushed up to powder fraction less than 60 μm and aliquots of samples of 2 mg were placed in cups of 6 mm in diameter. The cups were made of Ni foil. Data of two equal sets of the TL measurements show difference in values of +/-10%.

We carried out two different sets of measurements of TL glow curves, which were conditioned by different ways of the irradiation. The first set is characterized by the successive TL measurements after each step of the irradiation. A dose of irradiation after the step was about 100 krad. It was carried out seven cycles of the TL measurements and the irradiations consequently for the all samples of shocked quartz. The processing of TL data demonstrated changes of maximum temperature of glow curves, a full width on half of a peak high and intensity of TL for all samples. Observed peculiarities of artificial TL can be due to an alteration of a crystal lattice of shocked quartz, that can be formed as a result of a sample irradiation and/or as a result of heating up to 500 °C during the TL measurements (a rate of the heating of the samples was 14°C s^{-1}). Considering the irradiation as main reason of a difference of the TL patterns, we should analyse a dependence of a TL sensitivity on a total dose accumulated in the samples. (The TL sensitivity is an area of glow curve for temperature interval of 100-380 °C per one unit of the irradiation dose and sample weight.) The curves of the TL sensitivity versus the dose of the irradiation demonstrate changes of the TL sensitivity for all samples and the changes depend on a value of shock pressure. The curves can be divided into two groups (see Fig.). The first group includes the samples loaded less than 20 GPa. The changes in TL sensitivity in this group are rather chaotic and have a maximum of the TL sensitivity by different values of a summary dose. It can be seen that for the samples shocked by 9 and 20 GPa respectively the values of the maximum of the TL sensitivities are 1.3 and 2.0 times as higher than the same value for unshocked quartz.

The second group of the samples shocked to 20 GPa and higher demonstrates monotonous decreasing of the TL sensitivity up to five steps of the irradiation by a total dose of 517 krad (Fig.b). At shock pressure of 34 GPa after a first step of irradiation the value of the TL sensitivity is eight times higher than that in the unshocked sample. The same increasing of the TL sensitivity has been reported for shocked plagioclase [5,6].
The aim of the second set of the TL measurements is a study of dependence of TL saturation on shock pressure. The measurements were made after irradiation of samples by increasing doses of the gamma-rays. The doses were 300, 650, and 1000 krad. The data show that the TL saturation in low-temperature interval (100-250 °C) by irradiation dose of about 1 Mrad is reached for the samples loaded by pressures less than 34 GPa. For the samples shocked to 34 GPa and higher there is the simultaneous and approximately equal TL saturation both in low temperature and high temperature (250-380 °C) intervals. Following TL measurements after irradiation by dose of 260 krad show an increasing of TL sensitivities for the all samples, which approach to the maximum recorded values (see Fig.).

The study of the TL for shocked quartz samples display high sensitivity of the method for registration of lattice defects formed by shock loading. The used method of TL measurements after different doses of irradiation gives a possibility to determine in impactites three intervals of shock pressures, which are 0-20, 20-34 and 34-49 GPa respectively.

References [1] Horz F., (1968) /in: French, B.M., and Short, N.M., eds., Shock metamorphism of natural materials: Baltimore, Mono Book Corp.,/ p. 243. [2] Stoffler D., (1974) Fortshr. Miner. **51**, p. 256. [3] Stoffler D., (1984) J. Non-Cryst. Solids, **67**, p. 465. [4] Badjukov D.D. (1986) Meteoritika, **45**, p. 122. [5] Ivliev A.I. et al. (1992) LPS XXIII, p. 589. [6] Ivliev A.I., Kashkarov L.L., Badjukov D.D. (1993) LPS XXIV, p. 699.

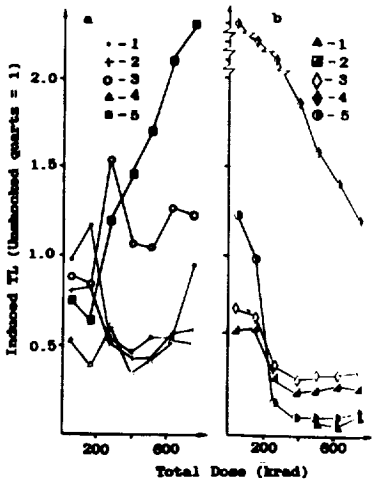

Fig. TL sensitivity of shock-loaded quartz versus the dose of gamma-irradiation. a) 1-0; 2-8.4; 3-9.0; 4-12.2; 5-20.0 GPa. b) 1-24.0; 2-27.0; 3-31.5; 4-34.0; 5-49.0 GPa respectively.

SHOCK-THERMAL HISTORY OF EREVAN HOWARDITE MATTER ON DATA OF THERMOLUMINESCENCE ANALYSIS OF SILICATE MINERALS

A.I. Ivliev[1], L.L. Kashkarov[1], and Yu.Yu. Korotkova[2]
[1]) V.I. Vernadsky Institute of Geochemistry and Analytical Chemistry, Russian Academy of Sciences, Moscow, Russia.
[2])Moscow State University, Faculty of Geology, Moscow, Russia

Earlier studies [1] of thermoluminescence (TL) of Kapoeta howardite have shown that this method allows to obtain the important information about the microstructure peculiarities of individual silicate mineral grains reflecting their shock-thermal history during the regolith stage that preceded the burial of meteorite matter into the parent body volume. The TL measurements of Erevan howardite were carried out for the further investigation the problem and a comparison with TL-parameters of meteorites having the similar formation history and distinguishing by unequal radiation-thermal processing in the regolith environment. The Erevan howardite is a relatively poorly studied complex polymict breccia of impact origin [2] containing some types of clasts [3]. Unlike the Kapoeta howardite, the Erevan bulk matter is characterized, according to noble gas data, by significantly lower irradiation degree by low-energy solar cosmic rays (SCR) and solar wind ions on the unshielded surface of parent body regolith. So the ^{4}He content is up to 10 times lower as compared to the Kapoeta dark portion, and the ratio values of $^{20}Ne/^{22}Ne$ in Erevan and Kapoeta are equal to 7.2 and 12.9 respectively. The track data are in accord with these characteristics: so the observed by us in the Kapoeta silicate minerals maximum track density value due to SCR VH-nuclei reaches ~ $3 \cdot 10^{8}$ cm^{-2} while this value for Erevan is about 30 times lower [4].

The grains (size up to ~ 200 μm) of two mineral fractions were handpicked under binocular from Erevan bulk sample for TL measurements. 1) Pyroxenes represented by pigeonite and orthopyroxene that are related by their chemical compositions either to Fe-rich (FM=Fe/(Fe+Mg)=60-62%) pyroxenes (that is characteristic of equilibrated eucrites) or to the pyroxenes with FM=44-46% connected with a melt [3]. 2) Plagioclases represented by An within interval of 72-98%.

The results of Erevan TL measurements were considered in comparison with TL data for Kapoeta [1]. The natural TL in bulk samples did not reveal noticeable differences, and this value for separated OPx and Pl fractions with unequal FM and An ratios is characterized by the presence of high-temperature TL in the region of 250-350 °C. The most part of studied samples (~ 70%) of Erevan meteorite showed the natural TL that is close to the background one. The TL induced by ^{137}Cs radioactive source gamma-rays allowed to distinguish in the Kapoeta and Erevan meteorites five and four shapes of glow curves respectively that are not connected with the chemical composition of the samples under study (see Fig. in the given paper and Fig.in [1]). These groups of glow curves are distinguished both by the

presence of different amount of TL peaks and a change of TL intensity either in low-temperature (< 200 °C) or in high-temperature (> 200 °C) spectrum regions. The repeat measurements of TL induced by gamma-radiation showed the appreciable changes in the glow curve of Kapoeta and the absence of similar changes in studied Erevan meteorite fractions. The obtained data allow to suppose that the revealed variety of glow curve shapes and their changes after repeat gamma-irradiation reflect the microstructure peculiarities in Kapoeta howardite orthopyroxnes caused by the different shock-thermal histories of individual grains at the early stage of this meteorite formation. From this point of view orthopyroxene from Erevan must have been undergone more "soft" and uniform shock-thermal history.

Our investigation of TL induced by X-ray radiation in Erevan meteorite bulk samples heated previously at 500 °C for 6 hours confirms this conclusion. The comparison of TL characteristics between the unannealed and annealed samples showed that the annealed ones are characterized as follows: a) the 2-5 times increase in total TL intensity; b) the appearance of more low-temperature peak at 110 °C along with the 170 °C peak; c) the decrease in TL intensity by (50-100)% in the temperature range of (300-400) °C. Such noticeable changes of TL parameters allow to suggest that, firstly, the most part of Erevan howardite matter was not undergone the shock-thermal influence at temperature up to 500 °C during regolith processing. Secondly, during its all the subsequent history this matter was not also heated up to temperature of about 500 °C that could induce the similar microstructure changes.

References

1. Ivliev A.I., Kashkarov L.L., Korotkova Yu.Yu. (1993) LPS XXIV, p. 701. 2. Kvasha L.G. et al. (1978) Meteoritica (Russia), **37**, p. 80. 3. Nazarov M.A. et al. (1993) LPS XXIV, p. 4. Kashkarov L.L., Korotkova N.N. (1994) LPS XXV.

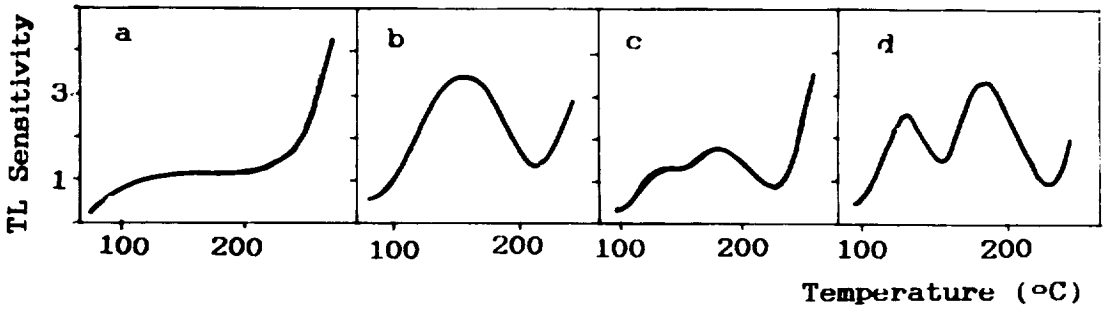

Fig. Induced TL glow curves from Erevan howardite

RELATIONSHIPS AMONG RADAR BACKSCATTER, MICROWAVE EMISSIVITY, ALTITUDE, AND GEOLOGY IN OVDA REGIO, VENUS. Noam R Izenberg, and Raymond E. Arvidson, Dept. Earth and Planetary Sciences, McDonnell Center for the Space Sciences, Washington University, St. Louis MO 63130

Analyses of Magellan multiple cycle radar images, emissivity, and altimetry data show that the transition from low emissivity (<0.7), high radar backscatter to "normal" emissivity (>.8) and backscatter in the highest altitudes (>6056.6 km radius) of Ovda Regio is dependent on elevation alone, i.e., it is independent of geology. Further, the transition is abrupt, occurring over ~200 m of elevation, compared to the transition of "normal" emissivity to low emissivity from lowlands to highlands over 1-2 km elevation [1; 2].

METHOD: Two digital elevation maps (DEMs) of the highest altitude regions in Ovda Regio (Figure 1a) were constructed using the Vexcel software package Magellan Stereo Toolkit (Figure 1d,g). Each DEM was constructed using two sub-areas from Magellan cycle 1 and cycle 3 full resolution mosaic image data records (F-MIDRs f05s098.1, and f05s099.301). These sub-areas were run through the Vexcel software, an automated stereo imaging system and DEM utility described in [3]. The DEMs have a relative accuracy of ~70 m and an absolute accuracy of ~200-500 m. The coregistered orthographic Magellan SAR images from Cycle 1 are shown next to the DEMs in Figures 1c,f. Corresponding emissivity from Magellan cycle 1 Global Emissivity Data Record (GEDR) are shown in Figures 1e,h.

OBSERVATIONS: Figure 1b shows the general area of the highest elevations in Ovda Regio. The two most striking features in the image are the high backscatter lava flow or flows in the southwest quadrant, and the low backscatter feature in the central-southern part of the image. Note that the interior of the high backscatter flow (8-9 dB) is 5 dB (a factor of 3) lower than the flow margins. Altimetry data indicate that the interior of the flow is also ~1 km lower than the northern flow margins (~6055.5 km). Figure 1c is covered mostly by the thick (~1 km) lava flow or set of flows. The image shows that the flow boundaries do not correspond to the abrupt change in radar backscatter. This decrease corresponds to an increase in elevation of ~200 m (Figure 1d), and an emissivity increase from ~.6 to ~.8. The decrease in backscatter in the northwest corner of the image is coincident with the interior of the lava flow seen in Figure 1b, and lower elevations in Figure 1d. Fractures and rifts are present in several places, and the southern part of the image shows deeply cut valleys with flat floors and evidence of mass wasting. Figure 1f shows fringes of the lava flow in the northwest corner, but the image is dominated by mountainous tessera terrain. Several flat-floored valleys are also visible. In both sub-areas, the change from low emissivity to "normal" emissivity is abrupt and accompanied by an overall change in radar backscatter from high to low. The changes are not due to geologic unit boundaries; in Figure 1c, there are no flow boundaries visible in the transition zone; in Figure 1f, tessera lies both above and below the transition. Note also that where the valley floors in Figure 1c lie above the transition altitude, radar backscatter is low, whereas lower floors show high backscatter. The emissivity image, at a resolution of 5x5 km pixels is too coarse to show these features.

IMPLICATIONS: The relationships imply that emissivity in this region is dependent only on elevation, not on geology. "Normal" emissivities are ubiquitous at the highest elevations, while lower emissivities are present in the rest of the highlands. The uniformity of geologic types both above and below the change in emissivity, implies that there is no fundamental difference in base materials going from low to high emissivity. Either some component of surface materials behaves differently at different elevations (i.e. ferroelectric materials [2]), some process is weathering materials differently at different elevations independent of bedrock type [4; 5; 6], or some process is transporting and concentrating materials of different radiometric properties in the highlands [7], yet maintaining the sharp boundaries we see in emissivity.

FIGURE 1. (Next Page) Images of the highest areas of Ovda Regio. a) Ovda Regio (45° to -45° lat, 53° to 127° lon) from c314s060; b) Enlargement of the central box of 1a. Parts of F-MIDRs f05s098 and f05s093 (-3.27° to -7.63° lat, 94.52° to 98.92° lon). The smaller rectangle is ~25 km wide; c,d,e) Orthographic SAR, DEM, and emissivity images of the smaller sub-area (-6.04° to -7.48° lat, 95.77° to 96.02° lon). Note the gradual change in backscatter and emissivity as elevation increases. These images are ~25 km across; f,g,h) Orthographic SAR, DEM, and emissivity images of the larger sub-area (-5.54° to -7.48° lat, 96.85° to 97.12° lon). These images are the same scale as c,d,e. The two grey-scales are altitude (DEM) and emissivity (EMI). The transition altitude from high to low backscatter and low to high emissivity is 6056.6 ± 0.1 km, and is shown on the grey-scale.

REFERENCES: [1] Klose et al. (1992) JGR 97, 16353. [2] Shepard et al. (this volume). [3] Leberl et al. (1992) JGR 97, 13675. [4] Pettengill et al. (1992) JGR 97 13091. [5] Tryka and Muhleman (1992) JGR 97, 13379. [6] Fegley et al. (1992) Proc. LPSC 22, 3. [7] Brackett et al. (this volume).

FIGURE 1.

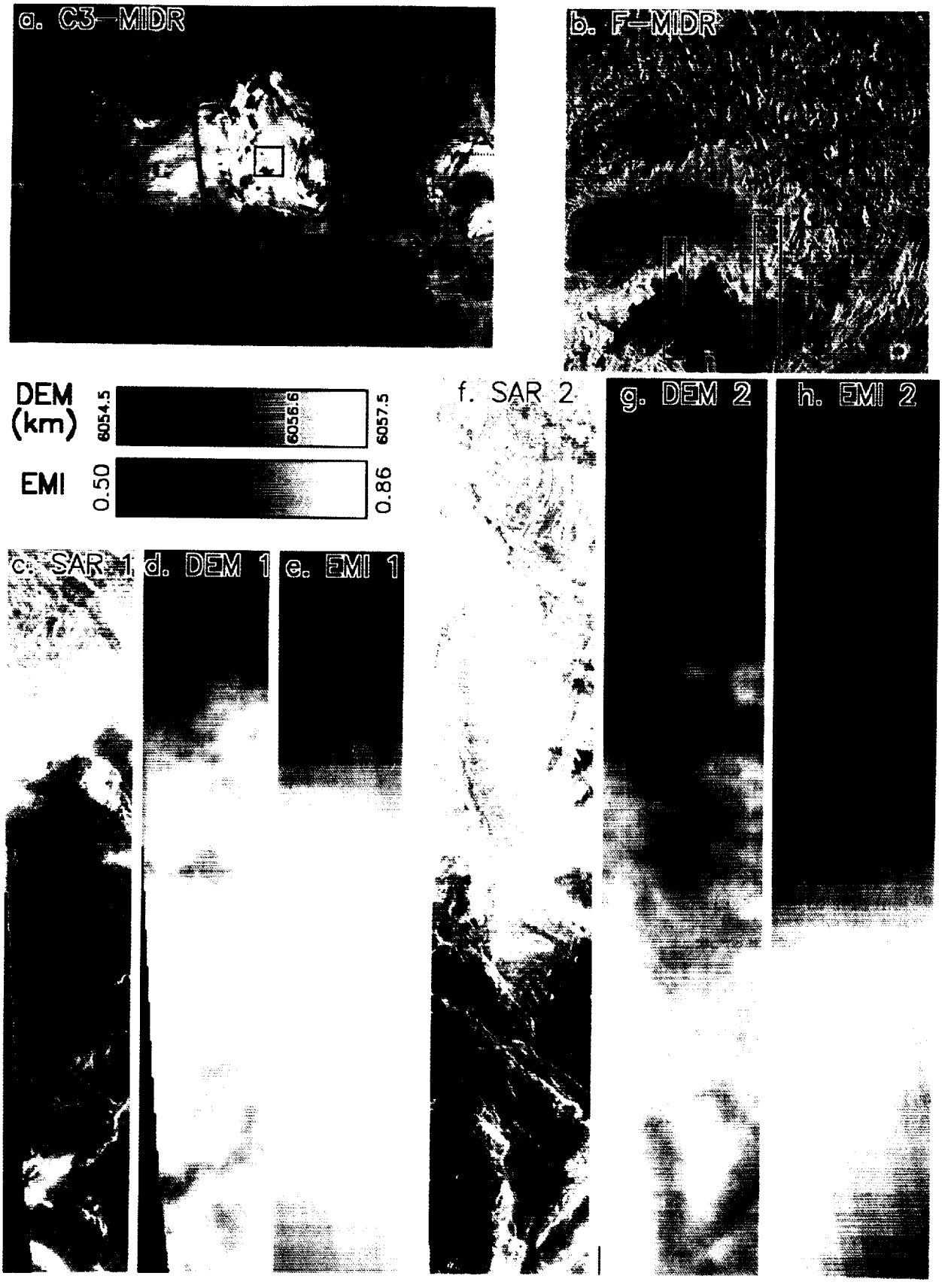
a. C3-MIDR
b. F-MIDR
DEM (km)
6054.5
6056.6
6057.5
EMI
0.50
0.86
c. SAR 1
d. DEM 1
e. EMI 1
f. SAR 2
g. DEM 2
h. EMI 2

SIZE AND DISTRIBUTION OF SHOCKED MINERAL GRAINS IN THE PIERRE SHALE (LATE CRETACEOUS) OF SOUTH DAKOTA RELATED TO THE MANSON, IOWA, IMPACT EVENT

G.A. Izett and W.A. Cobban, U.S. Geological Survey, Denver Federal Center, Denver, CO 80225

Recent $^{40}Ar/^{39}Ar$ dating [1] of sanidine masses in the high-temperature melt-matrix breccia of the Manson, Iowa, impact structure (MIS) indicates that it formed 73.8 ± 0.3 Ma and that it is not coincident with the Cretaceous-Tertiary (K-T) boundary dated at 64.6 ± 0.1 Ma [2] (both ages relative to MMhb-1 513.9 Ma). The MIS sanidine is 9 m.y. older than $^{40}Ar/^{39}Ar$ age spectra of MIS shock-metamorphosed microcline and melt-matrix breccia interpreted by Kunk and colleagues [3, 4] to be 64-65 Ma. The new $^{40}Ar/^{39}Ar$ age of 73.8 ± 0.3 Ma indicates that the extraterrestrial object that formed the Manson structure struck an area probably covered by shallow waters of the Western Interior Cretaceous seaway. Our prediction [1] that a physical record of the Manson impact, including tsunami deposits and shocked mineral grains, might be found in the Pierre Shale in eastern South Dakota at a stratigraphic horizon commensurate with our proposed age for the Manson impact structure was confirmed by Izett and colleagues [1]. Large grains (0.4-2.3 mm) of shocked quartz, quartzite, and feldspar are present in Late Campanian age rocks of the Pierre Shale at eight sites in southeastern South Dakota.

In most of southeastern South Dakota, the lower part of the Pierre Shale consists typically of 55 m of marine shale. The reason for the abrupt appearance of a thin marl 2-3 m thick and underlying basal sandy unit 15-20 cm thick (Crow Creek Member) within the shale-dominated Pierre has intrigued geologists for more than 40 years. The basal sandy unit is pervasively crossbedded siltstone and contains rip-up Cretaceous shale clasts (Sharon Springs Member) as large as 4.5 cm. At a locality southwest of Chamberlain, the remains of a large palm frond were found in the basal crossbedded siltstone. These features suggest that the basal sandy unit may be a reworked tsunami deposit that formed in the Western Cretaceous seaway following the Manson impact event.

Mineralogic evidence diagnostic of an impact was found in the basal Crow Creek Member at eight places in southeastern South Dakota (fig. 1): (1) in Black Dog Township, Lyman County; (2) several sites near Chamberlain; (3) near the Gregory Pumped Storage core hole , Gregory County; (4) near DeGrey in Hughes County, Mount Vernon in Davison County, and along Crow Creek in Buffalo County; and (5) two sites in Yankton County (Yankton limestone quarry and House of Mary Shrine). The acid-insoluble residue of samples from the basal Crow Creek from these sites consists chiefly of quartz and minor feldspar and mica. A few percent of the

MAXIMUM SIZE OF SHOCKED MINERALS IN PIERRE SHALE: G.A. Izett and W.A. Cobban

quartz and feldspar (microcline and plagioclase) grains contain multiple intersecting sets of planar lamellae identical to those in shocked mineral grains from rocks at known impact structures. Some of the shocked quartz grains lack strictly planar lamellae but instead contain irregular, widely spaced fractures indicative of low-level shock.

A map showing the sizes of the largest shocked grains recovered from samples at the eight sites is shown on figure 1. The largest shocked grains are at the two Yankton County sites (2.3 mm and 1.7 mm) and at the site near Mount Vernon (2.2 mm). These sites are about 250 km from the Manson structure in Iowa. In contrast, the largest shocked mineral grains from the basal sandstone of the Crow Creek in Lyman County, at DeGrey in Hughes County, and near Chamberlain are only 0.4-0.7 mm. The large size of the shocked mineral grains in Yankton County and near Mount Vernon implies that they came from a nearby source, such as the Manson impact structure.

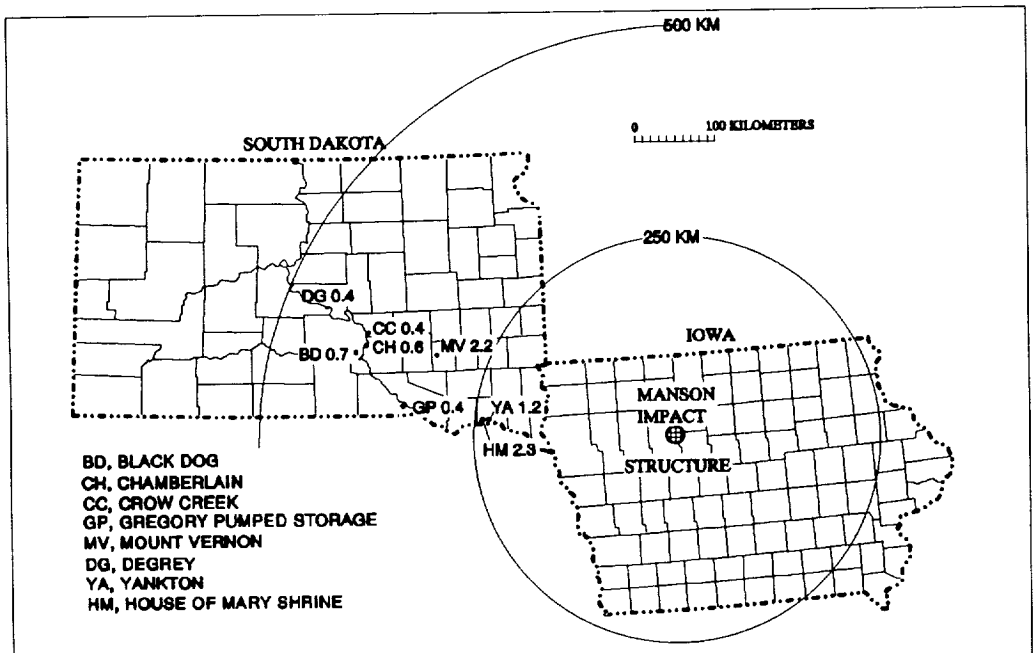

FIG. 1 MAXIMUM SIZE (MM) OF SHOCKED MINERAL GRAINS IN CROW CREEK MEMBER OF PIERRE SHALE

REFERENCES: [1] Izett, G.A., Cobban, W.A., Obradovich, J.D., and Kunk, M.J., 1993, Science, 262, 729; [2] Dalrymple, G.B., Izett, G.A., Snee, L.W., and Obradovich, J.D., 1993; U.S. Geol. Surv., Bull. 2065, 20 p.; [3] Kunk, M.J., Izett, G.A., Haugerud, R.A., and Sutter, J.F., 1989; Science 424, 1565; [4] Kunk, M.J., Snee, L.W., French, B.M., and Harlan, S.S., 1993, LPS, 24, 815.

Dust Evolution from Comets and Asteroids: Their Velocites at Earth Orbit Intersection

A. A. Jackson, Lockheed Engineering and Science Co., Houston, Texas
H. A. Zook, NASA Johnson Spacecraft Center, Houston, Texas

We have revised and updated the study published by Jackson and Zook in Icarus [1] on the evolution of dust particles from comets and asteroids. In our previous study the planets only moved in simple two-body orbits. In the study we report here, the effects of accurate many-body planetary motion on the gravitational perturbations of the dust grains are computed.

In a computer simulation, dust grains of radius 10, 30, and 100 μm were released at perihelion passage from each of 36 different celestial bodies: 16 main belt asteroids, 15 short period comets with perihelion greater than 1 AU, and 5 short period comets with perihelion less than 1 AU. (There has been one asteroid added to the model since the last study.) The evolving orbit of each of the 108 released dust grains was then continuously computed with the Everhart numerical integrator until the dust particle orbital aphelion passed inside of 0.387 AU, or the dust grain had been ejected from the solar system. The forces due to the gravitational fields of the Sun and the planets as well as radiation pressure, Poynting-Robertson drag, and solar wind drag were all included in these numerical simulations.

Table I displays the orbital elements when the dust crosses the Earth's orbit at a node. When compared to the same table in our Icarus paper we note there is little change in the evolved orbital characteristics. The only slight exception being that the magnitude of the intercept speed at the Earth's orbit for 10 micron particles is about one km/sec higher. This gives us confidence that the original simplified analysis we simulated is accurate.

It is found that when dust grains evolve to intersection with the Earth's orbit, they nearly always retain orbital characteristics indicative of their origins; grains from main belt asteroids differ significantly in orbital characteristics, especially in orbital eccentricity, from grains that evolve from comets. In reference 1 we plotted eccentricity versus orbital crossing speed as method of separating asteroids from comets. We present a new method that examines velocity components versus the magnitude of velocity. These velocity components are the radial, tangential and normal ones of the grain velocity in a coordinate frame fixed to the earth.

In figure 1 we plot the radial velocity versus the magnitude of the velocity. We see a very marked separation in the velocity magnitude between the asteroidal and cometary particles. The higher eccentricities and inclinations of the cometary particles preserve their position in the higher velocity regions on this plot. The asteroidal particle that is in the approximate 12 km/sec velocity region is from asteroid Hungaria which has an inclination of 22.5 degrees so that this particle's crossing speed has a higher normal-to-the-plane component. In fig. 1 even the lowest velocity components are almost a factor of 2 greater than the velocity of the great majority of asteroidal particles. It appears that a velocity sensor in earth orbit should genearally be able to distinguish between the dust grains from asteroids and comets.

We will address the issue of using these velocity data to specify what accuracy a velocity measurement must meet in order to distinguish between asteroidal and cometary particles captured by an instrument in earth orbit.

[1] Jackson, A. A. and Zook, H.A. (1992). Orbital Evolution of Dust Particles from Comets and Asteroids, Icarus, 97, 70-84.

DUST EVLOUTION: JACKSON,ZOOK

Table I Summary of particle orbital elements and velocites as they cross at the ascending node and descending node of their orbits at the Earth's orbit. <e> is the average eccentritity, σ is its standard deviation, e is its minimum, and e is its maximum. Simililarly for the inclination, i, and the magnitude of the relative velocity ,u, at crossing.

	Asteroids			Comets(q>1 AU)			Comets(q<1 AU)		
	10μ	30μ	100μ	10μ	30μ	100μ	10μ	30μ	100μ
<e>	.091	.157	.128	.509	.405	.407	.583	.580	.583
σ	.042	.077	.056	.218	.200	.175	.088	.115	.131
e_{min}	.005	.003	.043	.110	.075	.125	.131	.305	.255
e_{max}	.198	.328	.282	.854	.998	.999	.998	.926	.998
<i> (deg)	9.12	8.95	11.53	16.4	12.29	16.3	14.50	21.7	14.5
σ	5.593	5.94	3.78	6.62	4.38	9.24	8.1	12.9	8.13
i_{min}	.451	1.59	.659	.1.28	2.65	6.32	3.72	1.37	3.72
i_{max}	23.2	21.0	18.4	37.5	32.77	107.2	54.4	63.4	54.4
<u> (km/sec)	5.38	6.50	6.84	14.3	10.67	11.9	13.94	16.4	13.9
σ	2.81	2.71	1.60	3.21	3.22	5.28	4.90	6.12	4.90
u_{min}	0.41	2.06	2.75	9.79	4.77	7.04	9.33	11.6	9.3
u_{max}	12.53	13.91	10.6	29.8	21.76	58.3	33.0	36.4	33.0

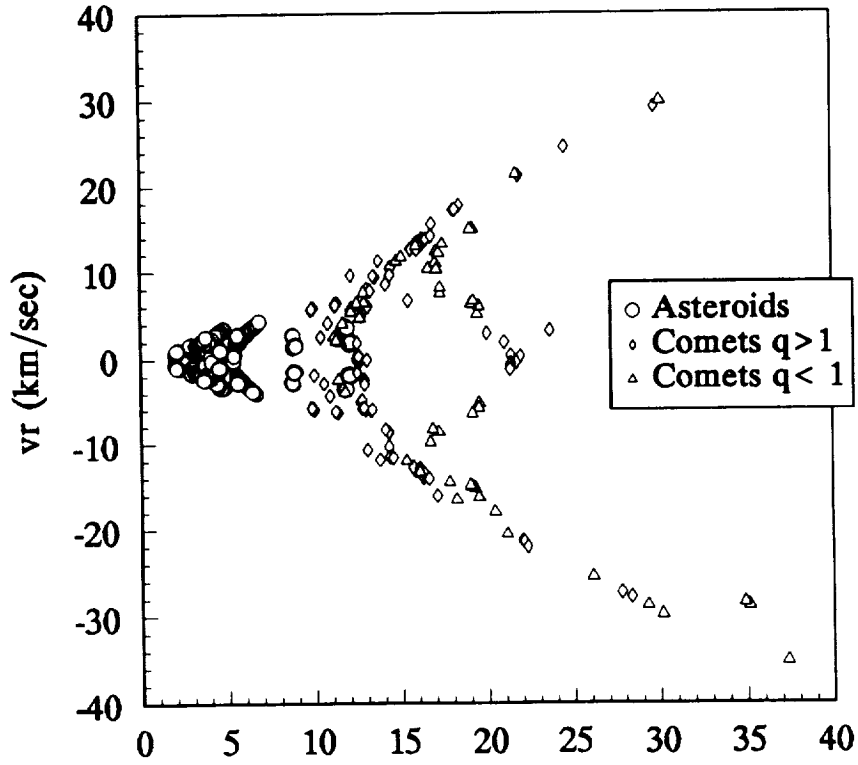

Fig. 1

NEW SULFUR ISOTOPIC MEASUREMENTS OF METEORITES AND POSSIBLE NEBULAR RELATIONS;

T. JACKSON, S. G. BOBIAS AND M.H. THIEMENS, DEPARTMENT OF CHEMISTRY, 0356, UCSD, LA JOLLA, CALIFORNIA. 92093-0356

With recent advances in the precision of sulfur isotopic measurements it has become possible to search for small systematic differences between meteoritic classes (Gao and Thiemens, 1991, 1993a,b). Recently published data have shown that there exists a clear isotopic distinction in $\delta^{34}S$ between enstatite, ordinary and carbonaceous chondrites. The enstatite chondrites possess the lightest isotopic composition, ranging in $\delta^{34}S$ from -0.4 to -0.2 (Gao and Thiemens, 1993b). The ordinary chondrites range in $\delta^{34}S$ from -.08 to 0.07 and carbonaceous chondrites from 0.1 to 0.6 (Gao and Thiemens, 1993a,b). The observation that a bulk isotopic group distinction may exist suggests a similarity to oxygen, for which defined isotopic grouping exists (Clayton, 1993). If this is the case then it could reflect the initial process by which sulfur is acquired from the nebula and nebular compositions in general. This might derive from nebular heterogeneity as for oxygen. In order to pursue this question we have performed high precision isotope ratio measurements on achondritic meteorites for which there is either limited or no sulfur isotopic data, with choice of meteorites guided by the oxygen isotopes.

The observed range in sulfur isotopic compositions is quite small, less than approximately 1.4 per mil for $\delta^{34}S$ for bulk samples. To insure high purity, the SF_6 from the fluorination process is submitted to a series of cryogenic, then gas chromatographic purification procedures (Gao and Thiemens, 1993 a,b). This is particularly crucial for the ^{36}S isotopic measurements which are restricted by the low natural abundance (0.017%). The present measurements were performed on our new multi-collector Finnigan MAT 252 mass spectrometer. Along with the meteoritic data reported we routinely analyze Canon Diablo troilite for standardization. Standards of commercial silver sulfide are routinely fluorinated and analyzed isotopically as a further procedural check. The meteoritic sulfur isotopic data for all three stable isotope ratios is given in the Table. All values are reported with respect to Canyon Diablo Troilite (CDT). Included in the analysis are representative bulk samples from two aubrites, a howardite and ureilite. There are several significant and new observations to be made from the present observations.

First, the two aubrites, Norton County and Cumberland Falls, have similar isotopic compositions, -0.256 and -0.329, respectively for $\delta^{34}S$. As recently discussed by Clayton (1993) the aubrites are of special interest with regard to the oxygen isotopes as they are the only achondrites with an oxygen isotopic composition the same as a chondrite group. Watters and Prinz (1979), Wilson and Keil (1991) and recently Lodders et al (1993) have discussed the origin of the aubrite parent body and its possible relation to the enstatite chondrites based upon mineralogical, petrographic and trace element considerations. The present sulfur isotopic measurements demonstrate that the bulk sulfur isotopic composition is precisely within the bulk enstatite chondrites, which are isotopically distinct from any other meteoritic class. The present observations thus track with the oxygen isotopes and are consistent with the hypothesis that there is a genetic association between the two classes.This also suggests that careful future isotopic analysis of oldhamite separates are good candidates for searches for nucleosynthetic anomalies. Lodders and Palme (1990) and Lodders et al (1993) have argued that the high observed rare earth element abundances in aubritic oldhamite derives from uptake into oldhamite during condensation, thus suggesting oldhamite is a relict phase.

The ureilite ALHA 81101.35 possesses several interesting features. First, the $\delta^{34}S = 0.35$ is unusual, it is isotopically heavier than any other non-carbonaceous chondrite. Clayton and Mayeda (1988) have demonstrated that the ureilites possess a strikingly unusual isotopic

pattern. The bulk values fall on a ^{16}O mixing line which is in part co-linear with the compositional line defined by CAI inclusions from C3 meteorites (Clayton, 1993). It is noted that the sulfur isotopic composition also falls within that observed for C3 meteorites (Hulston and Thode, 1965; Kaplan and Hulston, 1966; Gao and Thiemens, 1993a) again suggestive of a possible relation. A second possibly interesting feature is observed in the $\delta^{33}S/\delta^{34}S$ ratio. The deviation from mass fractionation is approximately 0.1 per mil. The error associated with the entire technique is approximately 0.05 per mil for both ratios (Gao and Thiemens, 1993a). The present observation clearly may not statistically be claimed to be an anomaly, however, given that 1) a ^{33}S anomaly was reported in Allende (Rees and Thode, 1977) and 2) the oxygen isotopes possess heterogeneous mixtures of carbonaceous chondritic components, future analysis of ureilites and their mineralogical components will be of importance and is warranted. The howardite, EET 87503 possesses an isotopic composition that is heavier than any of the ordinary chondrites (Gao and Thiemens, 1993b) and lighter than most carbonaceous chondrites or ALHA 81101. It is premature to derive any conclusions regarding this composition, future analysis of other howardites will determine whether this is a representative isotopic value.

In conclusion, the present sulfur isotopic observations appear to reflect a similarity to meteoritic oxygen isotopes. The aubrites possess an isotopic composition which lies within the unique enstatite chondritic range, suggesting an association. The isotopic association also suggests that future analysis of oldhamite may be important, as it is suggested as being primitive condensate material. The ureilite ALHA 81101 possesses a unique isotopic composition for a non-chondrite and is within the range of C3 meteorites, as is the case for oxygen. There is also a hint of a ^{33}S anomaly. The present and previous observations suggest similarities to oxygen and, given that sulfur is relatively abundant it is possible that, like oxygen, it reflects primary nebular features observable at the bulk level. Future high precision sulfur isotopic analysis at the bulk and mineralogical level will provide further insight into these processes.

REFERENCES. [1] Clayton R.N. and Mayeda T.K. (1988). *Geochim. Cosmochim. Acta 52*, 1313. [2] Clayton R.N. (1993) *Annual. Rev. Earth and Planet. Sci. 21*, 115. [3] Gao X. and Thiemens M.H. (1991) *Geochim. Cosmochim. Acta 55*, 2671. [4] Gao X. and Thiemens M.H. (1993a) *Geochim. Cosmochim. Acta 57*, 3159. [5] Gao X. andThiemens M.H. (1993b) *Geochim. Cosmochim. Acta 57*, 3171. [6] Hulston J.R. and Thode H.G. (1965). *J. Geophys. Res. 70*, 3475. [7] Kaplan I.R. andHulston J.R. (1966). *Geochim. Cosmochim. Acta 30*, 474. [8] Lodders, K. and Palme H. (1990) *Lunar and Planet. Sci.. 21*, 710. [9] Lodders K. Palme H. and Wlotzka F. (1993) *Meteoritics 28*, 538. [10] Rees,C.E. and Thode H.G. (1977). *Geochim. Cosmochim. Acta 41*, 1679. [11] Watters T.R. and Prinz M. (1979) *Proc. Lunar and Planet. Sci. Conf. 10th*, 1073. [12] Wilson L. and Keil K. (1991) *Earth and Planet. Sci. 104*, 505.

TABLE 1. Sulfur isotopic composition of meteorites with respect to CDT.

METEORITE	$\delta^{33}S$	$\delta^{34}S$	$\delta^{36}S$
NORTON COUNTY	-0.11	-0.26	-0.1
ALHA 81101 (UREILITE)	0.28	0.35	0.6
CUMBERLAND FALLS	-0.14	-0.33	-0.2
EET 87503 (HOWARDITE)	0.17	0.24	0.4

DATING THE GIANT MOON-FORMING IMPACT WITH ^{146}Sm-^{142}Nd SYSTEMATICS;

S. B. Jacobsen & C. L. Harper Jr., Department of Earth & Planetary Sciences, Harvard University, 20 Oxford St., Cambridge, MA 02138 USA

Introduction: Chronology is a key part of efforts to evaluate the giant impact model of the origin of the Moon. A giant impact event sufficient to form the Moon will very likely have caused re-homogenization of any pre-existing Sm/Nd-fractionated reservoirs in the Earth, whether mineral systems in rocks or large-scale differentiated reservoirs. The timing of such an event therefore will limit the age of the oldest differentiated reservoirs in both the Earth and Moon from which isotopic vestiges might have survived as small shifts in $^{142}Nd/^{144}Nd$. The oldest ages potentially seen by the ^{146}Sm-^{142}Nd system will approximate the age of the giant impact event itself to the degree that the durations of any planetary magma ocean cooling phases are short.

The state of preservation of the most ancient "primordial" crustal materials of planets varies with their tectonic-geodynamic histories. The Moon preserves a crustal "highlands" province containing a high proportion of fragments of what is thought to have been a magma ocean flotation crust. The Earth has experienced a long complex history of erosion and tectonic recycling and no crustal materials older than ~4.2 Ga have been found thus far. The terrestrial protocrust appears to have been destroyed *in toto*. Efforts to date the earliest epoch of terrestrial differentiation are therefore constrained to the isotopic record preserved in the *source reservoirs* of later-formed melts or their sedimentary relicts. A similar strategy can be pursued for mantle reservoirs on the Moon to provide differentiation ages for stages in freeze-up of the lunar magma ocean (LMO).

Relevant Results for the Earth: We have presented evidence for a +0.33±0.04 ε-unit shift in $^{142}Nd/^{144}Nd$ in an Isua metasediment (715-28) with an apparent mantle extraction age of 3.81 Ga and initial ε_{143Nd} of ~+4 at that time [1]. The simplest interpretation of this datum is formation of its source reservoir prior to 4.44 Ga. However an older mantle extraction age and more highly depleted (higher ε_{143Nd}) source is plausible and would allow a younger differentiation age of the source. Our continued studies of Nd in the Earth's oldest rocks and those of other groups [2] have not found any further samples with resolvable ^{142}Nd shifts relative to standards. Isua samples we have studied (Fig. 1) also do not fit a simple two-stage fractionation model for formation of variable Sm/Nd-fractionated sources at 4.47 Ga, (generating the range of apparent initial ε_{143Nd} values inferred for the samples at 3.81 Ga). Geodynamic mixing may have wiped out most of the earliest depleted mantle regions, so a preserved record of primordial differentiation may be a rare exception in the early Archean rock record. More work will be needed before the early mantle differentiation story will yield evidence for or against a giant impact of lunar age.

Relevant Results for the Moon: The anorthositic lunar protocrust survives to the present day as the high-albedo highlands covering a large part of the lunar surface. In the Apollo and lunar meteorite sample records, this ancient component is observed as a population of plagioclase crystals and plagioclase-rich ferroan anorthosite microclasts in multiply shocked and recrystallized breccias. Dating this component correctly is a nontrivial exercise. Ar-Ar studies have indicated plagioclase closure to Ar loss from Hi-T sites by 4.51±~0.03 Ga [3]. A distinctly younger age of 4.44±0.02 Ga was obtained by ^{147}Sm-^{143}Nd mineral systematics of plagioclase and mafic minerals in ferroan anorthosite 60025 [4], but these minerals were separated from a bulk breccia sampling and likely do not give reliable age information if the mafic minerals came from a different younger protolith as suggested on the basis of REE studies of [5]. An older precise ^{147}Sm-^{143}Nd mineral isochron age of 4.54±~0.06 Ga was obtained for a ferroan noritic anorthosite clast [6]. The most important ^{146}Sm-^{142}Nd reservoir constraints are for two ~3.9 Ga old KREEP basalts [7]. Nd in these samples is thought to have been assimilated from a global residual liquid "KREEP" reservoir ponded under the plagioclase flotation crust after freeze-up of the LMO. Because the Sm/Nd ratio of this reservoir is thought to be precisely and accurately represented by the measured Sm/Nd in the samples themselves [8], it is possible to determine precise CHUR-referenced model ages for the formation of the KREEP source reservoir. A two-stage model age interpretation of these data is shown in Figure 2 and suggests freeze-up of the LMO by 4.56±0.06 Ga [7]. The isotopic shifts upon which this age is based, however, are small and require careful confirmation (work in progress on recently received sample allocations).

DATING THE GIANT MOON-FORMING IMPACT...: S. B. Jacobsen & C. L. Harper Jr.

Summary: High precision studies of $^{142}Nd/^{144}Nd$ in KREEP basalts offer exciting prospects for precisely constraining the time of formation of the Moon, with existing data suggestive of an "old" ≥4.50 Ga age. Our results for Isua 715-28 are consistent with an episode of mantle differentiation on Earth at 4.47(+0.07/-0.03) Ga, but could be interpreted for differentiation as late as 4.40 Ga.

^{142}Nd Effects in Young Rocks Tapping Old Reservoirs: There appears to be some confusion surrounding certain basic concepts in the use of ^{146}Sm-^{142}Nd chronometry applied to planetery-scale reservoirs. Some salient conceptual points are the following: (i) Reservoirs (like rocks) can be dated by isotopic systematics. (ii) Old reservoirs can be sampled by melts extracted from them at later times with preservation of the isotopic information carrying the differentiation age of the source. (iii) Early-formed mantle reservoirs in non-recycling planets necessarily have $^{142}Nd/^{144}Nd$ shifts. (iv) Some domains of ancient mantle reservoirs in tectonically dynamic planets may have survived processes that destroyed crustal records (for example if isolated from geodynamic remixing), and may have been sampled by old melt extraction episodes. (v) The present day rock record of such reservoir-tapping melts may or may not be rare on the surface of a planet. (vi) If the isotopic record is carried in $^{142}Nd/^{144}Nd$, and if ^{146}Sm decayed *in situ* in the source reservoir, then no chemical effects can change the content of information preserved in the isotopes so long as a closed system holds for the information-carrying element. Neither melt transport, nor erosion, nor redeposition, nor metamorphism will have any effect on the information content of a closed system sub-reservoir. (vii) The precise interpretation of $^{142}Nd/^{144}Nd$ involves model-dependent assumptions. However, powerful age constraints can be derived simply from the existence of an effect at a given level, because of rapid early ^{146}Sm decay.

Uniform Initial ^{146}Sm in the Earth, Moon and Meteorites: A further significant point involves the question of whether or not live ^{146}Sm was present initially in the Earth and Moon. A common misperception seems to be that some radionuclides are exotic and belong in meteorites but not in planets. While it is true that there *may* have been variations in initial $^{146}Sm/^{144}Sm$ in different large-scale material reservoirs in the solar system, we believe this possibility to be unlikely because ^{146}Sm in the solar system is probably a due to *p*-process contributions by many supernovae during ~300 Ma of presolar history. These should have become well mixed with respect to the older ~7 Ga galactic mix of supernova contributions of stable *p*-process ^{144}Sm in the presolar molecular cloud complex. Also, large variations in initial $^{146}Sm/^{144}Sm$ would lead to large isotopic effects that are not observed. If the Earth had $^{146}Sm/^{144}Sm = 0$ at 4.57 Ga, a 2.8 ε-unit deficit would be present in ^{142}Nd in bulk Earth Nd relative to meteorite samples with unfractionated Sm/Nd. Young basalts have $^{142}Nd/^{144}Nd$ within ≤0.2 ε-units of meteorite samples with unfractionated Sm/Nd. This clearly implies that $(^{146}Sm/^{144}Sm)_{4.57\ Ga}$ ~0.008±1 holds for both meteorites and the Earth/Moon system, as expected from numerous evidences for isotopic homogeneity in heavy element compositions down to the sub-%-level for large-scale nebular reservoirs.

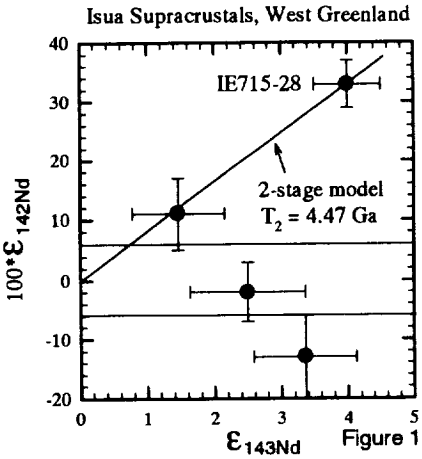

Figure 1

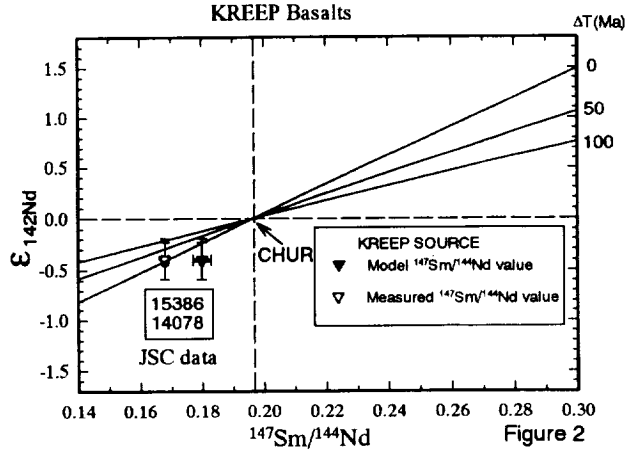

Figure 2

REFERENCES: [1] Harper C. L. Jr. & Jacobsen S. B. (1992). *Nature*, 360: 728; [2] McCulloch M. T. & Bennett V. C. (1993). *Lithos*, 30: 237, and references therein; [3] Huneke J. C. & Wasserburg G. J. (1979). *LPS X*, 598; [4] Carlson R. W. & Lugmair G. W. (1988). *EPSL*, 90: 119; [5] James, O., Lindstrom M. M. & McGee J. J. (1991). *PLPSC 21st:* 63; [6] Norman M. D., Alibert C. & McCulloch M. T. (1993). *LPS XXIV*, 1089; [7] Harper C. L. Jr., Nyquist L. E., Bansal B., Wiesmann H. & Shih C.-Y., *submitted* ; [8] Lugmair G. W. & Carlson R. W. (1978). *PLPSC 9th*, 689.

S7-91 1663 157
3607

MARS ATMOSPHERIC ESCAPE AND ISOTOPIC FRACTIONATION: SYNTHESIS OF DATA AND MODELS. Bruce M. Jakosky (1), Janet G. Luhmann (2), and John H. Jones (3). (1) Univ. of Colorado, Boulder, CO 80309-0392; (2) IGPP/UCLA, Los Angeles, CA 90024, (3) NASA/JSC, Houston, TX 77058.

The present Mars atmosphere is relatively thin and cold. It is not at all like that which is presumed to have been responsible for the formation of valley networks and the heavy erosion of craters during the earliest epochs of martian history. An important goal of Mars exploration is to try to understand the properties of the early atmosphere, the initial inventory of volatiles at the planet's surface, the processes by which the atmosphere and climate have evolved over time, and the current location of volatiles presumed to have been in the atmosphere in the earlier times. We describe the current status of our understanding of the escape of volatiles to space over geologic time and the resulting fractionation of isotopes of stable atoms remaining in the atmosphere, and we construct a scenario for volatile abundance and evolution that is consistent with the available information on the escape and fractionation of each species. In particular, we examine the evolution of hydrogen, carbon, oxygen, and nitrogen, as contained in atmospheric (and non-atmospheric) water, carbon dioxide, and molecular nitrogen.

The following arguments and conclusions are based on the available models and measurements pertaining to the present and past atmosphere:

(1) The enrichment of $^{15}N/^{14}N$ and $^{38}Ar/^{36}Ar$ in the present atmosphere appears to be a unique indicator of loss of volatiles to space and the resulting isotopic fractionation. The argon isotopes indicate the occurrence of sputtering loss, while the nitrogen fractionation results from both sputtering and photochemical loss.

(2) The enrichment of D/H indicates the loss of a large fraction of the hydrogen, and hence water, in the system. Watson suggests that her recent measurements of D/H in SNC meteorites are most consistent with the observed fractionation occurring over geologic time rather than on formation of the planet.

(3) The apparent lack of enrichment of $^{13}C/^{12}C$, despite abundant loss mechanisms, indicates the loss of less than about half of the C, derived from CO_2, in the system.

(4) The apparent lack of enrichment of $^{18}O/^{16}O$, also despite abundant loss mechanisms, indicates the loss of less than about half of the O in the system. Here, O is most likely derived from either CO_2 or H_2O, but may be buffered instead by interaction with silicates in hydrothermal groundwater systems.

(5) Estimates of the total loss of C integrated over geologic time, due to both pick-up-ion and hot-O sputtering, are equivalent to the loss of about 0.5 bars of CO_2. This then requires the present existence of a non-atmospheric reservoir also containing at least 0.5 bars CO_2.

(6) Estimates of the total loss of O integrated over geologic time, due to both sputtering and photochemical loss, are equivalent to the loss of either 1.5 bars CO_2 or 30 m

water (as a global equivalent layer). Again, this then requires the present existence of a non-atmospheric reservoir of comparable or greater size.

(7) The regolith is incapable of holding enough CO_2 as adsorbed gas to account for the non-atmospheric reservoir of C. However, CO_2 is stable at the poles as long as it is confined beneath an overlying layer of water ice only a few tens of centimeters to meters thick; this is the case even at the north, where CO_2 is not stable at the surface. Thus, the polar ice deposits may contain sufficient CO_2 to account for this reservoir. This CO2 could be released at the highest obliquities.

(8) The size of the required oxygen buffer could be accommodated by polar water ice, polar CO_2 ice, or some combination of the two. Non-polar H_2O or CO_2 is probably not as likely to be exchangeable in the required abundances.

If this scenario is correct, then the polar deposits are primarily CO_2 ice, and there is relatively little exchangeable water in the system (perhaps only a layer of water ice 100 m thick at the north pole). Clearly, there is much more water than this in the martian environment. The C and O isotopic evidence suggests that any excess water is rapidly removed from the exchangeable system; for instance, much of the water from the outflow channels would have to have been frozen out and trapped in the northern lowlands without becoming a part of the atmosphere-polar cap-regolith system.

Unlike previous descriptions of the evolution of martian volatiles from a geochemical perspective, the scenario we present appears to be consistent with the geomorphological evidence for climate change. That is, our model is consistent with the existence of about a bar of CO_2 in the martian environment during the earliest epochs, with half of that being lost to space and half being sequestered into a polar reservoir; the timescales for the occurrence of these events are consistent with the requirement for a thicker early atmosphere to allow formation of valley networks and degradation of craters.

SIDEROPHILE AND VOLATILE ELEMENTS IN APOLLO 17 IMPACT MELT ROCKS: Odette B. James, 959 National Center, US Geological Survey, Reston, VA 22092

Introduction: Most Apollo 17 impact melt rocks fall into two groups. One ("poikilitic") consists of rocks from boulders at Stations 6 and 7 and Boulder 2 at Station 2. These are clast poor and have fine- to medium-grained poikilitic melt-derived groundmasses of similar compositions and roughly constant ratios of siderophile elements. The second group ("aphanitic") consists of rocks from Station 3 and Boulder 1 at Station 2. Most are clast rich and heterogeneous in texture, clast population, and siderophile-element ratios. They have very fine grained melt-derived groundmasses with higher Al_2O_3 and lower TiO_2 contents than those in the poikilitic rocks. The poikilitic rocks are thought to be melt generated in the Serenitatis impact [1-3]. Some authors [4-6] have proposed that the aphanitic rocks represent a different facies of Serenitatis melt, whereas others [3,7] have suggested that some aphanitic rocks are melt formed in a different impact. Some of the evidence for the latter view is based on the assumption that siderophile elements in an impact melt are almost entirely derived from the impacting body, so that variation of siderophile-element ratios indicates genesis in different impacts. To reevaluate the relations among the melt rocks and the hypothesis that siderophile-element ratios are diagnostic of specific impacts, I am reexamining previously published radiochemical neutron activation analysis data for siderophile and volatile elements in these rocks.

Method: Most of the data used thus far in this study are from the laboratory headed by Edward Anders [7-12], so that interlaboratory bias is minimized. In this work, the most useful plots are normalized abundance patterns like those used for rare-earth elements. Two different normalizing compositions are used herein. For comparisons with meteorites, the data are normalized to the composition of C1 chondrites [13]. For comparisons with lunar rocks, the data are normalized to the composition of one type of aphanitic melt rock (average 73215 black aphanite). The relative abundance patterns fall into numerous groups, and only those judged to be the most important are discussed herein.

Geochemical behavior of elements: In the relative abundance patterns (Fig. 1), the elements Ir-Tl are arranged, from left to right, roughly in order of increasing volatility. The elements Ir-Pd ("siderophiles") are primarily siderophile, but Ni can also be chalcophile and lithophile. The elements Sb-Tl ("volatiles") are primarily chalcophile, except that Sb and Ge can also be siderophile, Br is lithophile, and Zn, Cd and Tl can also be lithophile. The elements Rb-U ("lithophiles") are lithophile.

Endogenous lunar rocks: To determine the composition of meteoritic components in the melt rocks, it is necessary to know the composition of endogenous lunar components. Many Apollo 17 endogenous rocks show similar relative abundance patterns (Fig. 1a): the increasingly refractory siderophiles are increasingly depleted relative to chondrites; and the volatiles are less depleted and show patterns with pronounced "humps" and "troughs." KREEP basalt shows a distinctive peak at Sb-Ge.

Aphanitic melt rocks: Black aphanites from 73215 and 73255 show patterns (Fig. 1b) of siderophile and volatile elements that are little fractionated relative to C1 chondrites, whereas most other aphanites show more complex patterns. Most samples from Boulder 1 at Station 2 show one of two patterns (Figs. 1c,d). The patterns differ for the siderophile elements and Ge: Group I (Fig. 1c) has high Ir; and Group II (Fig. 1d) has low Au and high Ge. Both patterns are similar for most volatile elements and are typified by "troughs" at Bi, Te and Tl and "humps" at Zn-Cd and Br.

Poikilitic melt rocks: Typical relative abundance patterns for these rocks are shown in Fig. 1e. The volatiles are like those in Group I and II aphanites, but the siderophiles are like those in 73215-73255 black aphanites.

Granulitic breccias: Granulitic breccias are the most abundant siderophile-element-rich clasts in the Apollo 17 impact melt rocks; they are especially abundant in the aphanitic melt rocks. Many of the granulitic breccias fall into three groups. In Groups A and B (Fig. 1f), the siderophile-element patterns suggest that the samples in each group contain metals of the same bulk composition but that the amount of metal varies considerably; in Group B, relative abundances of Ir and Re are similar, and in Group A, Ir is enriched. Group C (Fig. 1g) consists of samples that have similar patterns for most volatile elements.

Discussion: The endogenous lunar rocks considered herein (Fig. 1a) show elemental abundances that are fractionated relative to chondrites. The most striking features of the volatile-element patterns are relative enrichments in Ag, Br, Zn, and Cd and relative depletions in Te, Bi, and Tl; Ge and Sb enrichment of the KREEP basalt is noteworthy.

The 73215-55 black aphanites are clast-poor, rapidly crystallized variants of aphanitic melt rock. Because the elemental abundances in these rocks are little fractionated relative to chondrites (Fig. 1b), both the siderophiles and volatiles in these rocks may be largely derived from the impacting body. The relative abundances of the elements Ir-Sb are identical with those in EH chondrites (Fig. 1h); thus, the impacting body (probably the Serenitatis projectile) may have been a variant of enstatite chondrite.

The Boulder 1 aphanites are much richer in unmelted clasts than the 73215-55 black aphanites, suggesting that contamination by clasts is the reason for the variable relative abundance patterns in these rocks (Fig. 1c,d). The patterns for the Group I aphanites from Boulder 1 (Fig. 1c) suggest that these samples contain large amounts of high-Ir (Group A) granulitic breccia and small amounts of KREEP basalt. A quantitative test of this hypothesis is shown in Fig. 1i. The components used are: 3% 72275 KREEP basalt; 76% metal-poor granulitic breccia, in which volatile- and lithophile-element abundances are the average shown in Fig. 1g and siderophile-element abundances are 30% of those in 72235,37 (see Fig. 1f); and 21% metal-rich black aphanite (average of 73215-55 black aphanite, with siderophile-element abundances doubled). Using these components, the average siderophile- and volatile-element composition of the Group I aphanites is closely approximated, but a good match was not possible without varying the metal content of the melt and granulitic-breccia lithologies. The lithophile elements could not be matched without an additional component (probably lunar granite, a common clast type in these rocks). The Group II aphanites from Boulder 1 (Fig. 1d) appear to show contamination by the KREEP basalt that is a common clast type in this boulder, in that they have very low Bi and Tl contents and relatively high Ge, Br, Zn and Cd contents. Calculations like those done for the Group I aphanites show, however, that adding KREEP basalt alone will not duplicate the Group II siderophile-element patterns; a good match also requires changing the granulitic-breccia component to one having a composition like that of 77135,50 (see Fig. 1g), but only 80% of the siderophiles.

The relative abundance patterns for poikilitic melt rocks indicate that there is no more variability between these rocks and the aphanitic melt rocks than there is within the group of aphanites as a whole. In fact, aphanitic melt rock 72215,40 (Fig. 1c) is virtually identical in all elements, except Ir, to poikilitic rock 76015 (Fig. 1e). The flat siderophile-element patterns in the

SIDEROPHILE AND VOLATILE ELEMENTS IN APOLLO 17 MELT ROCKS: Odette B. James

poikilitic rocks suggest that the metals in these rocks have the same composition as those in the black aphanites.

Conclusions: This study suggests that siderophile-element compositions of analyzed melt-rock samples do not always relate to the composition of the impacting body in a simple way, and the assumption that data such as Ir-Au ratios alone are diagnostic of the impacting body is probably not correct. The variations in siderophile-element ratios in the aphanitic melt rocks from Boulder 1 at Station 2 can probably be explained by variations in content of clasts in the analyzed samples. The similarity of volatile-element patterns in endogenous rocks, Type C granulitic breccias and Types I and II aphanitic melt rocks suggest that the volatiles in all these rocks are dominated by a similar endogenous component. Noteworthy is the fact that rocks showing similar volatile-element patterns can show different siderophile-element patterns, and vice versa, suggesting decoupling of the siderophile and volatile components. The data for all the aphanitic and poikilitic melt rocks show no persuasive evidence for more than one impact, and all could have formed in a single impact.

References: [1] Simonds C.H. et al. (1976) PLSC7, 2509. [2] Simonds C.H. (1975) PLSC6, 641. [3] Spudis P.D. and Ryder G. (1981) in Multi-Ring Basins, GCA Suppl. 15, 133. [4] Wilhelms D.E. (1987) USGS Prof. Paper 1348. [5] Wolfe E.W. et al. (1981) USGS Prof. Paper 1080. [6] James O.B. et al. (1987) PLPSC9, 789. [7] Higuchi H. and Morgan J.W. (1975) PLSC6, 1625. [8] Morgan J.W. et al. (1974) PLSC5, 1703. [9] Morgan J.W. et al. (1976) PLSC7, 2189. [10] Gros J. et al. (1976) PLSC7, 2403. [11] Hertogen J. et al. (1977) PLSC8, 17. [12] Morgan J.W. and Petrie R.K. (1979) PLPSC10, 789. [13] Wasson J.T. (1985) Meteorites: Their Record of Early Solar-System History, W.H. Freeman, NY. [14] Hertogen J. et al. (1983) GCA47, 2241.

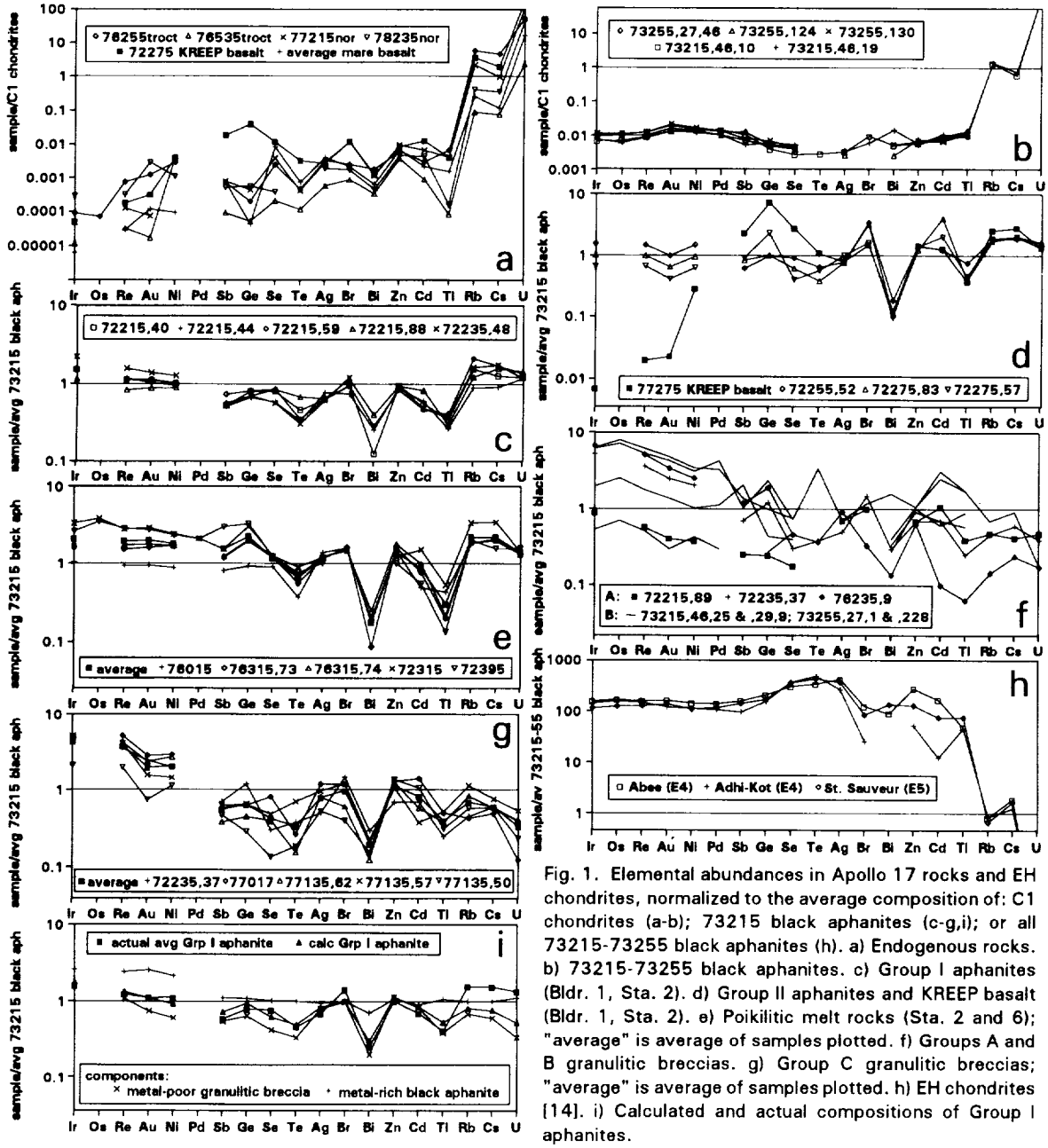

Fig. 1. Elemental abundances in Apollo 17 rocks and EH chondrites, normalized to the average composition of: C1 chondrites (a-b); 73215 black aphanites (c-g,i); or all 73215-73255 black aphanites (h). a) Endogenous rocks. b) 73215-73255 black aphanites. c) Group I aphanites (Bldr. 1, Sta. 2). d) Group II aphanites and KREEP basalt (Bldr. 1, Sta. 2). e) Poikilitic melt rocks (Sta. 2 and 6); "average" is average of samples plotted. f) Groups A and B granulitic breccias. g) Group C granulitic breccias; "average" is average of samples plotted. h) EH chondrites [14]. i) Calculated and actual compositions of Group I aphanites.

LIFE CYCLE OF VENUSIAN CORONAE Daniel M. Janes and Steven W. Squyres, Center for Radiophysics and Space Research, Cornell University, Ithaca, NY 14853

Coronae are large circular topographic and tectonic features on the surface of Venus. They are believed to result from the uplift of the surface over a rising mantle diapir and the subsequent relaxation of the raised topography [1,2]. To date modeling of the formation and evolution of these features has involved many simplifying assumptions which may result in inadequate representation of all the forces and dynamics involved. For example, models of uplift have assumed either a purely viscous rheology [3] or have modeled the dynamics of the diapir rise by examining static models of the diapir at some depth [2]. Similarly, models of the relaxation phase have assumed that the complexities of a stratified, visco-elastic, non-Newtonian rheology can be modeled using linearized viscous modeling [2,3]. We address these simplifications by developing two models. The first includes an elastic lithosphere and follows the deformation of the diapir as it rises through the mantle and interacts with the overlying lithosphere. The second treats the relaxation of the upraised topography and includes non-Newtonian viscosity, as well as elastic and isostatic support.

In the diapir uplift model, the diapir is treated as a swarm of point masses, spread uniformly through the volume of the diapir, the mantle as a constant viscosity fluid, and the lithosphere as an elastic shell. We then use mantle velocity formulations [4] to determine the distance moved by points within both the diapir and the mantle over some small timescale and reposition the points that constitute the diapir accordingly. Examples of results from this model are shown below. Fig. 1a shows a 100-km radius diapir at a depth of 1100 km below the base of the lithosphere and the flow field that it sets up in the mantle. Our results indicate that a spherical diapir of this size rising from depth under these conditions will begin to spread laterally at a depth of approximately 800 km. In the example shown, the mantle has a Newtonian viscosity of 10^{21} Pa s and the diapir is 60 kg/m less dense than the mantle. Fig. 1b shows changes in the topography of the surface of a 5 km thick lithosphere overlying the diapir as the diapir rises. Uplift becomes higher and more narrowly concentrated with time, reaching its maximum height after approximately 100 My. At later times, the uplift becomes broader and somewhat less pronounced as the diapir flattens out against the base of the lithosphere. These results also show that a depression begins to form outboard of the central uplift at about the time of maximum central uplift because mantle and diapir material flows out and down as the diapir flattens. Formation of the moat surrounding most coronae, therefore, may be partly a consequence of initial uplift rather than being entirely due to later relaxation. The timescale for the diapir to rise from this depth and flatten out against the underside of the lithosphere is approximately 100 My. One important finding of our work to date is that only a relatively limited set of model parameters appear capable of fitting the topography and tectonics associated with the resulting radially-fractured domes [5].

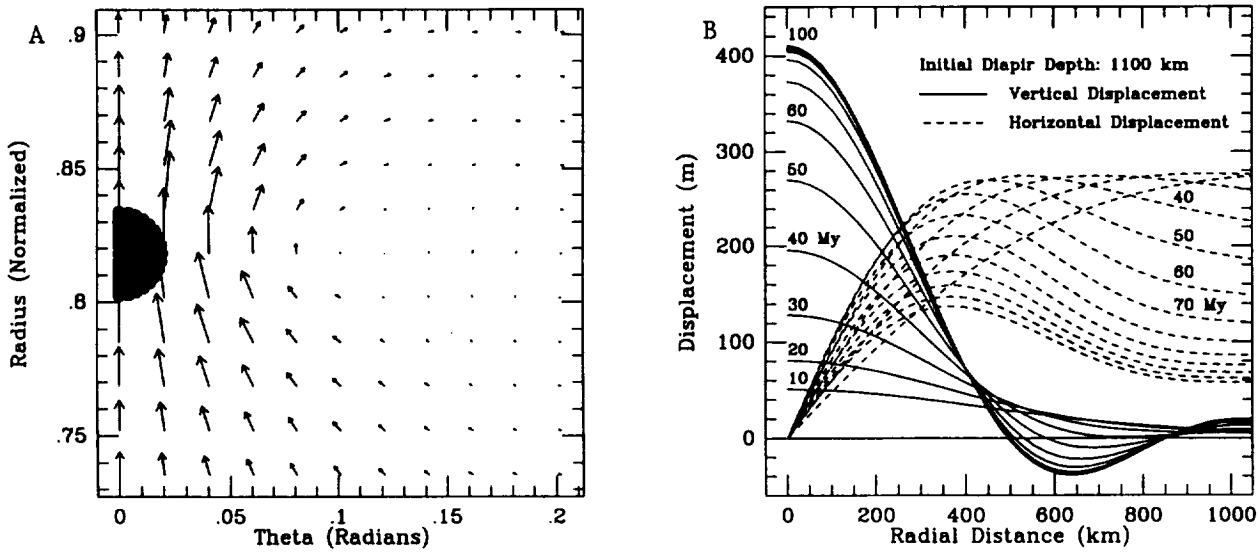

Fig. 1. a) Flow field in the mantle due to a 100 km radius diapir at a depth of 1100 km. b) Surface displacements through time as the diapir rises.

LIFE CYCLE OF CORONAE: Janes, D.M. and Squyres, S.W.

We examine the relaxation of topographic highs from diapiric uplift using the finite element code TECTON, which permits a significantly more detailed treatment of the relaxation problem than is afforded by analytical modeling. Our modeling includes an estimate of the initial stresses present in the mantle, crust and load, eliminating the unrealistic elastic deformation present in many applications of TECTON. We have also developed a protocol for the application of restoring forces. For thick crusts and steep geothermal gradients, the lower portion of the crust can behave as a viscous fluid over relatively short timescales. This requires that buoyancy forces be applied not at the mantle/crust boundary, but rather at the viscous/elastic boundaries in both the crust and mantle. We extend the finite element grid to sufficient depth and width that mantle flow during relaxation is fully accounted for and elastic edge effects are eliminated.

An example of the results from this modeling is shown in Fig. 2. The case shown is for a 1 km high plateau load on a 5 km thick crust. The near surface temperature gradient is 15K/km. The plateau relaxes to produce the central elevated basin, the high standing rim, and the peripheral moat that are seen in a typical corona. For stress dependent, non-Newtonian rheologies, relaxation occurs at a very rapid rate initially, with most of the relaxation taking place in as little as 10,000 to 100,000 years. This timescale is much shorter than the expected cooling time for the diapir [3] so that the relaxation time will be governed by cooling and loss of thermal buoyancy rather than by the viscosity of the mantle or crust. The end state of the relaxation model occurs when the topography is in equilibrium, supported by any residual thermal or compositional buoyancy of the diapir, isostatic forces, and elastic stresses. No further relaxation will occur and, in the absence of erosion or constructional volcanism (especially flows filling the peripheral moat), the topography will remain unchanged.

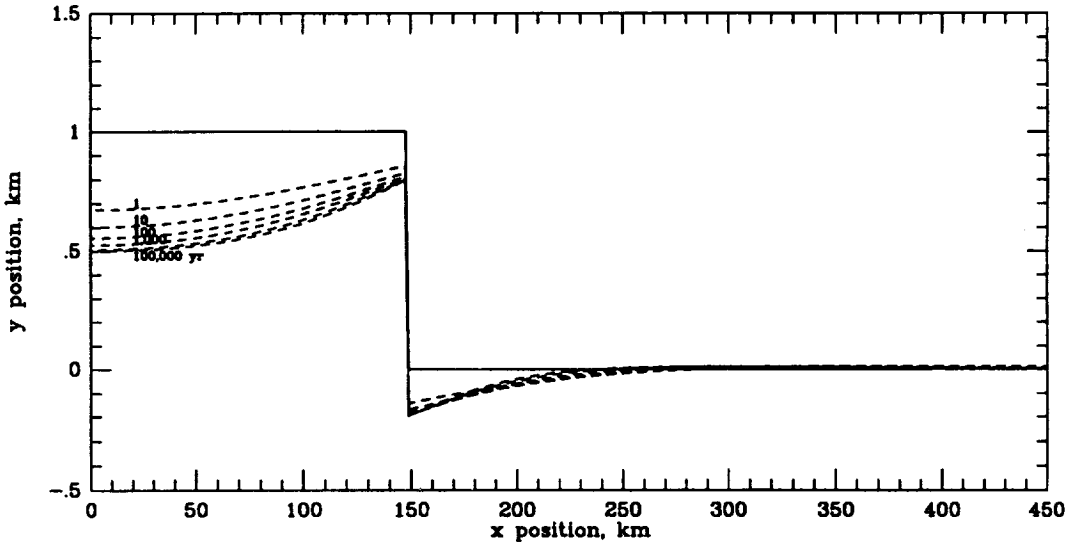

Fig. 2. Topographic profiles through time of a relaxing plateau-shaped load.

The results of the two models indicate that most of the life cycle of coronae should be taken up by the rise of the diapir through the mantle and by the static end state of equilibrium. The transition from an uplifted radially fractured dome and a relaxed corona should occur rapidly with the total time for relaxation dependent on the time needed for the diapir to cool and lose buoyancy. During most of the diapir rise time, surface manifestations are minimal so that continuous formation of coronae over the last several 100 My should result in a current surface marked by a few recently formed radially fractured domes with many more coronae which have relaxed to equilibrium as was observed by Magellan [6].

References 1) Barsukov, V.L., et al., *J. Geophys. Res.*, 91, D378–D398, 1984. 2) Janes, D.M., et al., *J. Geophys. Res.*, 97, 16055–16067, 1992. 3) Stofan, E.R., et al., *J. Geophys. Res.*, 96, 20933–20946, 1991. 4) Janes, D.M. and H.J. Melosh, *J. Geophys. Res.*, 93, 3127–3143, 1988. 5) Janes, D.M. and S.W. Squyres, *GRL*, in press. 6) Stofan, E.R., et al., *J. Geophys. Res.*, 97, 13347–13378, 1992.

N94-36144

THE STRUCTURAL CHANGES OF WATER ICE I DURING WARMUP.

Peter Jenniskens and David F. Blake, NASA/Ames Research Center, Space Science Electron Microscopy Lab, Mail-stop 239-4, Moffett Field, CA 94035-1000.

ABSTRACT. We have mapped the polymorph transitions of vapor deposited water ice I during warmup from 15 K to 210 K by means of Selected Area Electron Diffraction. The polymorph transitions account for many phenomena observed in laboratory analog studies of cometary outgassing and radical diffusion in UV photolysed interstellar ices.

Vapor-deposited water ice, and mixtures containing water ice, are often studied in laboratory experiments in the context of the production of solid organic matter in interstellar space and the outgassing properties of comets. These experiments usually monitor gas release [1,2], infrared absorption bands [3,4], or heat release [5,6] during gradual warmup of ice layers. Although they address structural changes of the ice, all these methods are indirect. We have used Selected Area Electron Diffraction (SAED) in an instrumental configuration that allows dynamic observations of the ice structure during warmup and have mapped the polymorph transitions of water I [7].

Our results show distinct changes in the electron diffraction patterns due to a series of polymorph transitions [8]. Below 30K the vapor deposited ice is in a high density amorphous polymorph (I_ah). A sluggish transition to a low density amorphous polymorph (I_al) occurs between 45 K and 65 K (vapor deposition at 15 K at a rate of 18 micron/hr and subsequent warmup at 1-3 K/min). We have obtained the first structural evidence for a third amorphous polymorph of water with an on-set at 131-142 K (depending on annealing time). We refer to this polymorph as I_ac. I_ac persists when the ice crystallizes to a cubic I_c phase at 142-161K and only crystallizes into a hexagonal I_h crystalline phase at a temperature of about 225 K [9,10].

In dense interstellar clouds water mantles on dust grains are photolysed and recombination of the photolysis products results in small refractory molecules that are further processed by UV photons and cosmic rays into a poorly ordered hydrogenated amorphous carbon [11]. By comparing the transition regions found from our diffraction studies with studies reported in the literature, we find that radical diffusion and recombination occurs in the amorphous to amorphous transitions [8]. This probably accounts for the relatively high efficiency of residue formation in laboratory studies [11] and suggests that organic residue can form under astrophysical conditions in which temperature fluctuations below the sublimation limit occur together with amorphitisation by UV photons and electrons. This may also have implications for organic molecules that are thought to be formed on icy surfaces of some of the outer planets and their satellites.

Comets are thought to be the most primitive objects in the solar system, possibly containing pristine interstellar matter [12]. For both the study of planet formation and the study of comet formation and evolution, it is important to determine at what temperatures the cometary ice releases impurities and ulitmately volatilizes. By comparing the transition regions found above with the outgrassing studies reported in the literature [1,2], we find that it is mostly the amorphous to crystalline transition that accounts for outgassing [8]. Small volumes of gas release can, however,

STRUCTURAL CHANGES OF WATER I ICE: Jenniskens P., Blake D.F.

be associated with the amorphous to amorphous transitions.

These results apply to water dominated ices. However, cometary ices, for example, have been shown to contain 3-5 % methanol [13]. Seven percent methanol in a water ice matrix is enough to produce Type II clathrates above 130 K. In this case, clathrate formation is relevant to cometary outgassing phenomena [14].

REFERENCES. [1] A. Bar-Nun, G. Herman, D. Laufer (1985) ICARUS 63, 317. [2] A. Kouchi, T. Kuroda, (1990) Proc. 24th ESLAB Symp. on the formation of stars and planets, vol SP-315, 193. [3] E. Mayer, R. Plezer (1984) J. Chem Phys. 80, 2939. [4] B. Rowland, M. Fisher, J.P. Devlin (1991) J. Chem Phys. 95, 1378. [5] J.A. Ghormley, (1968) J. Chem Phys. 48, 503. [6] A. Hallbrucker, E. Mayer, G.P. Johari (1989) J. Phys. Chem. 93. [7] D.F. Blake and G. Palmer (1991) Proc. 26th MAS, 293-298. [8] P. Jenniskens, D. F. Blake (1994) Science (submitted). [9] Dowell L.G., Rinfret A.P., (1960) Nature 188, 1144. [10] Hallbrucker A., Mayer E. (1991) ICARUS 90, 176. [11] P. Jenniskens, G.A. Baratta, A. Kouchi, M.S. de Groot, J.M. Greenberg, G. Strazzulla, (1993) Astron. Astrophys. 273, 583. [12] P. Jenniskens (1992) Proc. 30th Liege International Astrophysical Colloguium (A. Brahic, J. Surdej eds.), p. 335. [13] D. Bockelee-Morvan, P. Colom, J. Crovisier, D. despois, G. Paubert (1991) Nature 350, 318. [14] D.F. Blake, L. Allaman- dola, S. Sandford, D. Hudgins, F. Freund (1991) Science 254, 548. *This work was supported in part by a National Research Council Associate Award to one of us (PJ).*

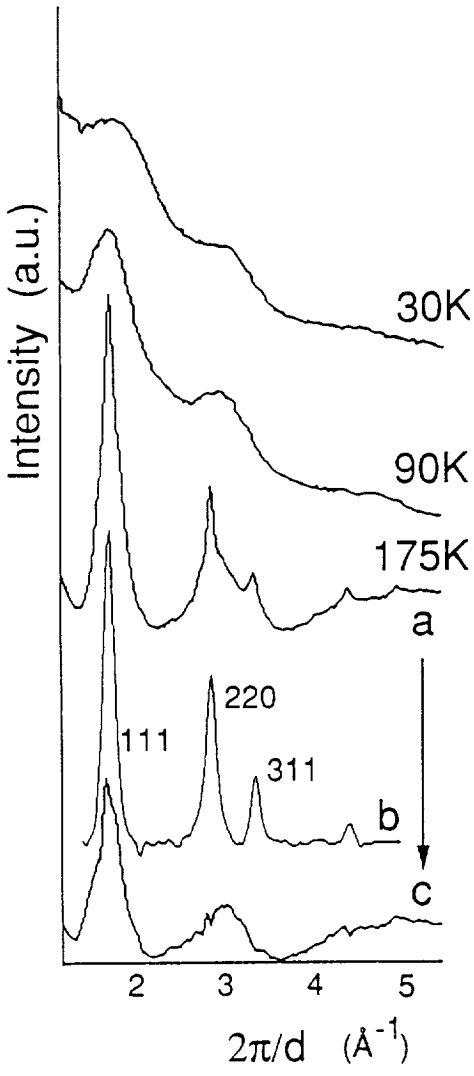

FIGURE. Examples of typical diffraction patterns obtained with Selected Area Electron Diffraction. The pattern taken at T=30 K is of polymorph I_ah, the one at T= 90 K is I_al, and the one at T=175 K contains both crystalline diffraction lines (b) of cubic I_c and an amorphous component (c) to which we refer as I_ac.

9017 70 P645

BUOYANT MANTLE FLOW AND RIFT ASSOCIATED VOLCANISM: APPLICATION TO VENUS.
K. Jha and E.M. Parmentier, Department of Geological Sciences, Brown University, Providence, RI 02912

Globally distributed rifts on Venus [1] have average widths on the order of a few hundred km and total extension limited to about 25% [2]. Rift-associated volcanism occurs in varying amounts in different rifts; most rifts have associated volcanism. Volcanism occurs simultaneously with rifting: faults cut volcanic structures, and some faulting is covered by lava flows [3]. The presence of lava flows that cover faults indicates that melt generation continues after rift extension is complete. Volcanism is non-uniformly distributed along rifts. Volcanic centers such as coronae and flowfields occur along rifts with a regular spacing that varies from rift to rift over a range of 300-600 km [4]. In this study, two (2D) and three (3D) dimensional numerical models of mantle flow beneath rifts that include both passive upwelling due to extension and buoyant upwelling due to melting are used to assess the amount of magma generation and its temporal and spatial distribution.

Mantle-depletion and melt-retention buoyancy arise due to the extraction of basaltic melt and the presence of low density melt in the mantle respectively. Passive extensional velocities arise from thinning the lithosphere within the rift zone by pure shear. Decompression melting occurs if temperatures based on the advection and diffusion of heat exceed a typical peridotite solidus, accounting for the latent heat of melting. The amount of melt present in the mantle depends on the rates of melt generation and migration. We assume melt migration by porous flow [5]. The flow calculations are performed using the finite difference method [6].

Using 2D models we first examine the dependence of temporal variation of magma generation on lithosphere thickness, the presence of a depleted mantle layer, the rate and duration of extension, the temperature of the interior mantle, and the mantle viscosity. The initial mantle temperature distribution is a horizontally uniform error function with depth. With the base of the thermal lithosphere defined as 1100°C, thicknesses (z_l) of 100 and 200 km are considered. If Venus has been conductively cooling for 500 My, the lithosphere may be as thick as 300 km [7]. The thickness of an initially depleted mantle layer is determined by the depth at which the initial temperature distribution intersects the solidus. The temperature distribution in the depleted layer is derived from a prescribed depletion distribution. Extension rates (U) between 0.1 and 10 cm/yr are considered. The duration of extension is determined by a total extension of 25% and the prescribed extension rate. Interior mantle temperature, T_m, is inferred from parameterized convection studies to be ≈1500-1600°C [8,9]. Mantle viscosity (μ) is varied between 10^{18}-10^{22} Pa-s.

Figure 1 shows the effect of extension rate on the duration and extent of melt generation. Melt volume is expressed as change in isostatically compensated rift floor elevation assuming that crust generated is spread uniformly within the rift. At the slowest rate (0.1 cm/yr) melting occurs in pulses due to the accumulation of depleted mantle beneath the rift. Buoyant mantle upwelling in the region of melting results in adjacent regions of downward flow. This effect, combined with the slow advection of depleted mantle away from the rift relative to its creation, results in the formation of roots of depleted mantle adjacent to the melt region whose buoyancy acts to oppose upwelling beneath the rift axis. In this case, melting does not resume before extension ceases since at this extension rate there is not enough time to advect away the accumulated depleted mantle. At higher rifting rates, the rate of advection of depleted mantle is increasingly comparable with its rate of generation, allowing melt generation to become continuous. The smaller accumulation of depleted mantle also results in increased melt production and higher melt-retention buoyancy, allowing melt production to continue longer after rift extension stops.

Figure 2 considers cases with a 200 km thick lithosphere. For 25% total extension and a 1500°C interior mantle temperature, the lithosphere does not thin enough to generate melt. When the mantle temperatures is raised to 1600°C, extension occurs amagmatically until the upwelling mantle first reaches the solidus. Once melting begins, the higher mantle temperature increases the magnitude of buoyant upwelling and post-extension melt production continues longer than corresponding cases in Figure 1.

BUOYANT MANTLE FLOW AND RIFT ASSOCIATED VOLCANISM: APPLICATION TO VENUS
K. Jha and E.M. Parmentier

Figure 3 shows the effect of mantle viscosity on the duration and magnitude of melt generation. For high mantle viscosity ($\geq 10^{21}$ Pa-s), passive flow is more important than buoyant flow and melt production stops rapidly after extension ceases. At lower mantle viscosities stronger buoyant upwelling causes melting to continues longer after extension stops.

Using 3D models, we examine the spatial distribution of melt generation. A stability analysis shows that along-rift buoyant instabilities are expected to develop but only for sufficiently low mantle viscosity and extension rates [10]. Therefore the existence of along-rift variations in volcanic activity could have important implications for these parameters. In our models, finite amplitude three dimensional flow, consisting of centers of buoyant upwelling and melt production, develops rapidly within the period of extension for low values of mantle viscosity. Along-rift wavelengths on the order of 300 km occur for a mantle in which viscosity is independent of depth. This wavelength should be proportional to the height of the melting column. Therefore, varying lithosphere thickness or mantle temperature may explain observed variations in along-rift wavelengths.

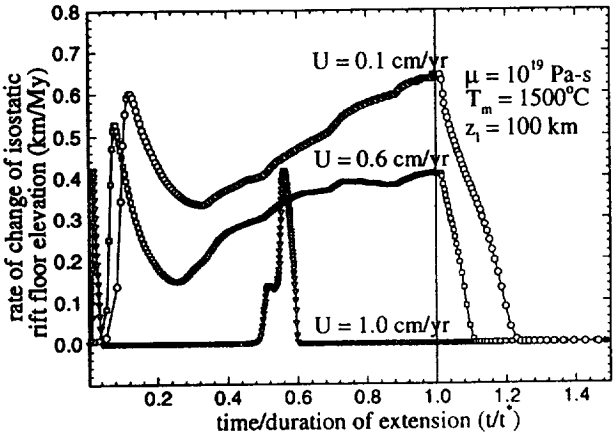

Figure 1

References: [1] Crumpler L.S. et al. (1993) *Science*, 261, 591. [2] Solomon et al. (1992) *JGR*, 97, 13199. [3] Magee Roberts, K. and J.W. Head (1993), *GRL*, 20, 1111. [4] Magee K. and J.W. Head (1994), *this volume*. [5] Ahern and Turcotte (1979), *Earth Planet. Sci. Lett.*, 45, 115. [6] Parmentier E.M. and J. Phipps Morgan (1990), *Nature*, 348, 325. [7] Turcotte D.L. (1993) *EOS Trans. AGU*, 74, 187. [8] Turcotte D.L. et al. (1979), *Proc. LPSC*, 10, 2375. [9] Schubert et al. (1979), *Icarus*, 38, 192. [10] Parmentier, E.M. (1988), *LPSC Proc.*, 19,907.

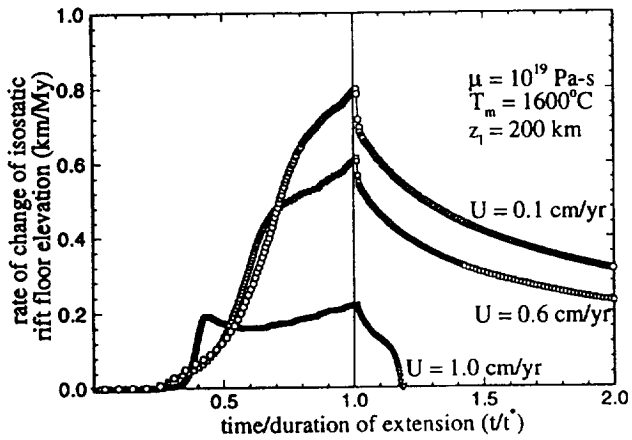

Figure 2

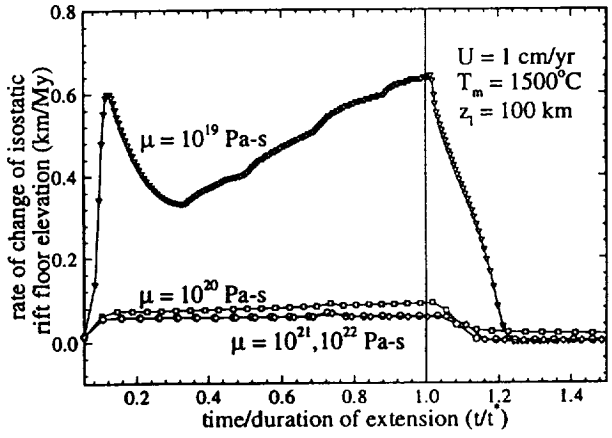

Figure 3

RESOLUTION ANALYSIS OF MAGELLAN CYCLE 5 GRAVITY DATA;

C. L. Johnson & D. T. Sandwell, Scripps Institution of Oceanography, La Jolla, CA 92093-0208

Introduction

Magellan altimetry, radar and Cycle 4 gravity data have raised important questions concerning the nature of support of topographic features on Venus. Distinguishing between static and dynamic support of some of the shorter wavelength topographic features requires exceedingly careful analysis of the gravity data, in terms of understanding the shortest wavelengths which are resolvable. For example, models of flexural support of topographic features predict a gravity / topography transfer function which has a shape determined in part by the elastic plate thickness. Gravity observations in the wavelength band 200-800 km are required to investigate elastic plate thicknesses in the range 10-40 km. A "rule of thumb" estimate for the maximum horizontal resolution of the gravity data is 2-4 times the spacecraft altitude (400-800 km near periapsis for Cycle 5 data). We present some resolution analyses, using Cycle 5 gravity data, in order to determine the maximum spatial resolution of the data in specific regions. This type of analysis can then be used to design filters to isolate certain wavelengths in the gravity signal.

Gravity data from the Magellan spacecraft was first available whilst the spacecraft was still in an elliptical orbit around Venus (Cycle 4 data). Earth-based tracking of the spacecraft produces Doppler velocity residuals which can be processed to obtain line-of-site (LOS) gravitational accelerations and/or a spherical harmonic representation of the global gravity field [1, 2]. High resolution regional gravity studies have been performed using the inversion package GASP, which uses an orbit simulation procedure to model LOS accelerations [3].

One of the major limitations of both of the methods described above is the problem of establishing the maximum spatial resolution of the gravity data. This varies considerably for the Cycle 4 data, due to the elliptical spacecraft orbit, and in fact spherical harmonic solutions based on Cycle 4 data alone are only useful in the latitude band 30°S - 50°N. Magellan is currently in a more nearly circular orbit (200-600 km) and thus the Cycle 5 data will yield a much improved estimate of the high latitude gravity field. The amplitude of the shortest wavelength resolvable features depends upon several factors including the noise level and the viewing geometry. The maximum resolution available from spherical harmonic gravity solutions is determined by the cut-off level in the expansion and any regularization imposed during the inversion (Kaula's rule). Current regional inversions use LOS accelerations computed from smoothed (splined) Doppler residuals, and the smoothing may affect the true spatial resolution of the models.

Resolution analysis procedure and some preliminary results

We have taken 8 sequential Cycle 5 X-band orbits over a test area (Figure 1, white tracks). This region is not ideal for the type of analysis we present, because although some short

RESOLUTION OF MAGELLAN GRAVITY DATA: Johnson C. L. & Sandwell D. T.

wavelength topographic features are present, they are of low amplitude and do not have a strong associated gravity signal. The region was selected purely on the basis of accessibility of Cycle 5 data at the time of writing and we intend to extend this study as further Cycle 5 data becomes available. The cross track spacing of adjacent orbits (~10 km) is much less than the shortest wavelength that we expect to resolve so the individual tracks should show common short wavelength features. Raw Doppler residuals for each of these orbits are plotted against time in Figure 2, where the zero time corresponds to 60°N and the sampling frequency is 0.5. Gaps in the Doppler residual records were filled by linear interpolation and the resulting records were padded to a length of 256. The resulting records were stacked end-to-end to produce two time series: the first series contained the first (N-1) orbits, the second series contained the second (N-1) orbits. A joint spectral analysis of these two series was performed: this type of analysis yields the power spectra, cross-spectra, transfer functions, coherence and phase between the two time series. Resolvable wavelengths in the gravity data should have a coherence >~ 0.5 and the phase should vary smoothly as a function of wavenumber. Preliminary results, using the data shown give a coherence of > 0.9 for wavelengths longer than 800 km, about 4 times the spacecraft altitude in this region. We expect that this is a minimum estimate of the spatial resolution of the gravity data for such spacecraft altitudes, because of the lack of strong short wavelength signals in our test area. Coherence analyses from other areas, e.g. over proposed flexural signatures will be presented.

Figure 1: Topography + Orbit Tracks

[Orbit tracks (white), data gaps (black)]

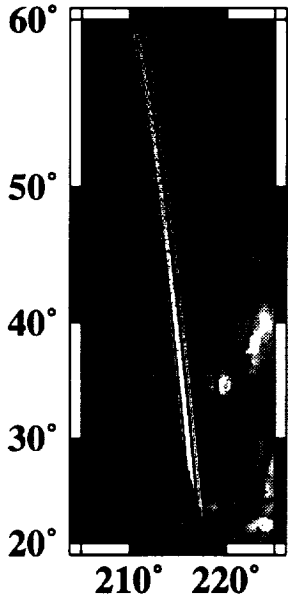

Figure 2: Doppler Residuals

[MGN40E removed]

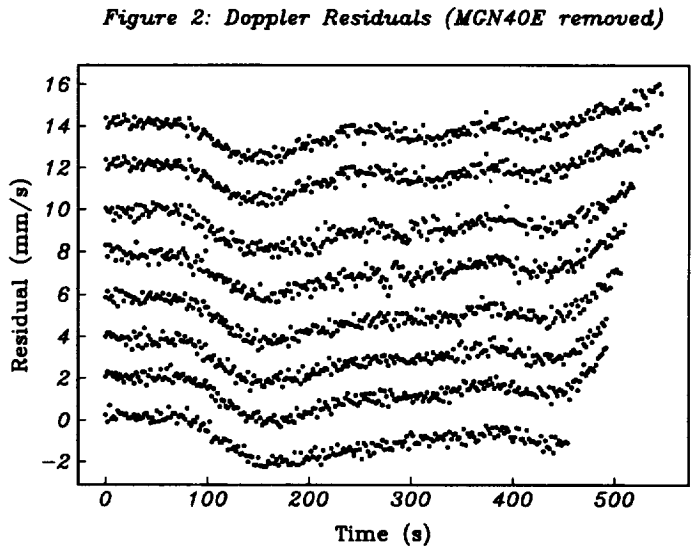

References: [1] Konopliv et al., Geophys. Res. Lett., 20, 2403-2406, 1993; [2] Nerem et al., Geophys. Res. Lett., 20, 599-602, 1993; [3] Phillips et al., J. Geophys. Res., 83, 5455-5465, 1978

BACKSCATTER CROSS SECTIONS OF VENUSIAN FEB CRATER DEPOSITS ;

J.R. Johnson and V.R. Baker, Lunar and Planetary Laboratory and Department of Geosciences, Space Sciences Bldg., University of Arizona, Tucson, AZ, 85721.

Specific radar cross sections (σ_0) of ejecta deposits and surrounding plains associated with three fluidized ejecta blanket (FEB) craters (Addams, Isabella and Markham) are part of a comprehensive multiple-cycle study of FEB crater surface properties using Magellan data **[1,2]**. Using digital unit mapping techniques, σ_0 values for morphologically defined ejecta units were obtained from Cycle 1 and 2 SAR imagery. Comparison of these backscatter curves (Figure 1) to those for terrestrial lava surfaces and standard scattering functions **[3]** constrains estimates of relative surface roughness and/or compositional effects.

Units. FEB flow, ballistic, and transitional material units are used here. FEB flow materials are radar-bright, fluvial-like materials emanating from or near the crater rim and exhibit streamlined features **[e.g., 4,5]**. Ballistic ejecta are intermediate to radar-bright hummocky materials extending radially from the crater rim, possibly with lobate margins, and may occur as dispersed materials overlying the plains. Transitional ejecta are very radar-bright, hummocky materials forming gradational contacts with ballistic and/or FEB flow materials (similar to the "proximal" unit of **[4]**). Simulated S-band AIRSAR data for sites in the Lunar Crater volcanic field are also shown in Figure 1 **[6]**. The young Blackrock a'a flow shows a slightly flatter but higher return backscatter curve than the mantled flow, which has been smoothed by aolian fill. The degraded flow has undergone additional weathering to preferentially remove small-scale structures and so exhibits the steepest, lowest return terrestrial curve. This is similar to the Venus planetary average (Muhleman) curve and higher than the Hagfors scattering curve.

Addams. The σ_0 curve for the Addams plains units falls well below the average curve and exhibits the steepest slope, consistent with the plains being smoother (at wavelength scales) than the other surfaces shown. The curve for the FEB flow falls along the planetary average, while the ballistic and transitional ejecta fall above the average and show increasingly flatter curves respectively. The transitional ejecta thus appear roughest at this scale, although the overlap of the σ_0 standard deviations might suggest greater parity between ejecta roughnesses.

Isabella. The low σ_0 values of the plains show the steepest slope and fall closest to the Hagfors curve, while the ballistic ejecta fall below the Muhleman average curve and have a more shallow slope. The inclusion of intervening plains materials within the mapped ballistic ejecta is responsible for its relatively low σ_0 values. The transitional ejecta fall above the average curve and have a steeper slope than all but the plains. The FEB flow appears anomalous since it has lower σ_0 values but an evidently rougher surface (flatter σ_0 curve) than the higher σ_0-valued transitional ejecta. It may be that while the heavily channelized northern FEB section is responsible for the flat (rough) curve, the southern, parabola-mantled FEB **[2]** suppresses the overall strength of the σ_0 values. This occurs in much the same fashion for the terrestrial mantled flow where the σ_0 values have been suppressed relative to the Blackrock a'a flow without substantially altering the slope of the scattering curve.

Markham. Here the plains again fall below the average Muhleman curve and exhibit the steepest slope. The FEB flow shows the flattest curve (roughest surface), followed by the transitional ejecta and the ballistic ejecta, respectively. The transitional ejecta show slightly higher σ_0 values, while the FEB flow and ballistic ejecta σ_0 averages appear to undergo a "contrast reversal" suggesting that the FEB flow probably has greater wavelength-scale roughness and that the ballistic ejecta are slightly more quasi-specular scattering **[3]**.

ACKNOWLEDGEMENTS: We thank J. Plaut (JPL) and N. Stacy (DSDO) for assistance with use and reduction of SAR image data.

REFERENCES: **[1]** Johnson, J.R., and Baker, V.R., submitted manuscript, 1994, *Icarus*; **[2]** Johnson, J.R. and Baker, V.R., Longitudinal Surface Property Variations Along Venusian Feb Flows: Isabella, this volume; **[3]** Plaut, J.J., and R.E. Arvidson, 1992, *JGR.*, **97**, 16279-16291; **[4]** Chadwick, D.J., and Schaber, G.G., 1993, *JGR*, **98**, 20891-20902; **[5]** Asimow, P.D., and J.A. Wood, 1992, *JGR.*, **97**, 13643-13665; **[6]** Arvidson, R.E., et al., 1992, *JGR.*, **97**, 13303-13317.

BACKSCATTER OF VENUSIAN FEB CRATERS: Johnson J.R. and Baker V.R.

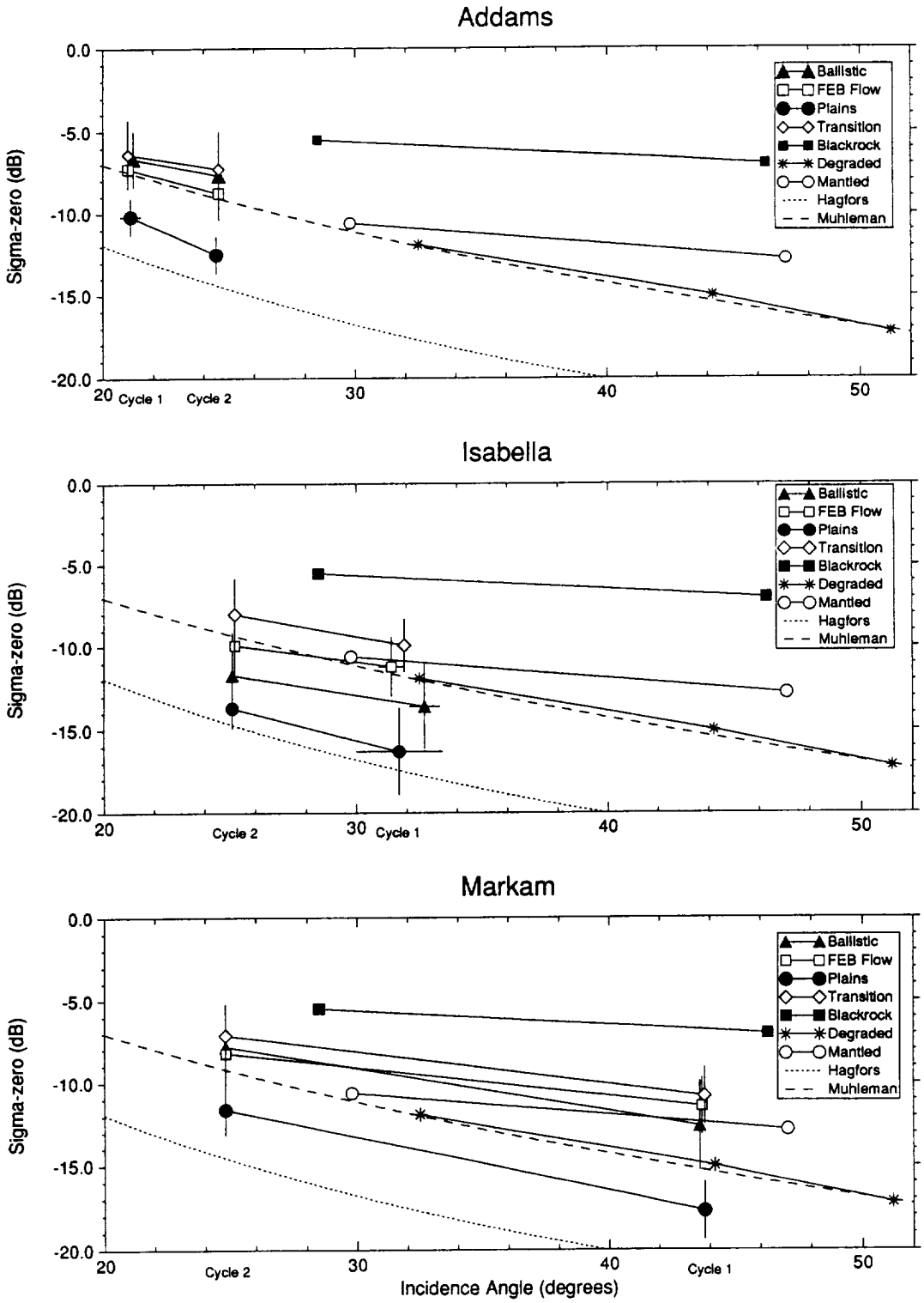

Figure 1. Specific backscatter cross section curves (σ_0) for ejecta and plains units associated with FEB craters Addams, Isabella, and Markham from Cycle 1 and 2 SAR image data. Error bars represent standard deviations about the mean σ_0 values and incidence angles for the entire unit as derived from the unit mapping procedure [1]. Blackrock, Mantled, Degraded represent terrestrial lava surfaces from the Lunar Vocanic field [6]. Also shown are the planetary average (Muhleman) curve and a representative Hagfors function (derived using an uncorrected Fresnel reflection coefficient of 0.109 and rms slope of 2.77°) [3].

LONGITUDINAL SURFACE PROPERTY VARIATIONS ALONG VENUSIAN FEB FLOWS: ISABELLA

J.R. Johnson and V.R. Baker, Lunar and Planetary Laboratory and Department of Geosciences, Space Sciences Bldg., University of Arizona, Tucson, AZ, 85721.

Magellan Cycle 1 and 2 altimetry, radiometry, and SAR imagery of fluidized ejecta blankets (FEBs) associated with venusian impact craters reveal down-flow variations in surface properties that provide insight to their emplacement styles. Traverses have been made along the flow lobes and surrounding plains using images of radar parameters constructed by subjecting orbital footprint dimensions and data values to polygon-filling algorithms. Results are presented here for two FEB flows of the crater Isabella (175 km; -29.7°, 204.1° **[cf. 1,2]**). The longitudinal variations in surface roughness are related to changes in the FEB surface textures and the effects of mantling by subsequent Cohn crater (20.5 km; -33.2°, 208.1°) ejecta.

Method. ARCDRs were used in combination with modified MGMDQE software (P. Ford, MIT) and polygon-filling algorithms to construct raster-based images of topography, rms slopes, corrected reflectivity, its diffuse component, and emissivity **[3]**. This process excludes interpolated image data (as found in GxDRs) and flagged "problem" footprints. Specific radar cross section (σ_0) values were obtained from the SAR images **[4]**. For each parameter image, traverses were taken along FEB flow lobes southeast (C-C*) and south (E-E*) of Isabella (Figures 1,2).

Observations and Discussion. Comparison of several multiple cycle radar property data sets allows estimates of roughness and/or dielectric variations down-flow. For example, positive correlations between emissivity, the diffuse component of corrected reflectivity, and/or σ_0 values suggest that wavelength-scale roughness effects dominate radar properties. Similar trends in rms slopes values suggest roughness dominance at meter or larger scales. Flow styles may be inferred from down-flow roughness variations. Increased roughness down-flow suggests a lava/melt-like flow while roughness decreases are more consistent with a pyroclastic/debris-like flow **[e.g., 6]**. Alternatively, emissivity and reflectivity trends (though not expected to be strictly complementary in Magellan viewing geometries **[e.g., 5]**) may positively correlate in regions where dielectric effects dominate the radar properties.

Topography varies along traverse C-C*, possibly due to large channelized portions of the FEB, but is sloped southward only ~0.0002. Values of σ_0 vary by 7-8 dB over the northern channelized FEB flows. These become more constant where parabola deposits from the nearby crater Cohn begin to mantle the FEB flow at about the 160 km mark. Emissivity, slope, and diffuse component values peak near the center of the northern FEB elbow, suggesting that central rougher areas grade to smoother areas nearer the margins, which is more consistent with a pyroclastic/debris flow. After the 80-90 km these parameters all increase again, indicative of a lava/melt flow nature for the southern FEB lobe. The steady decrease and lesser correlation of these data sets after ~180 km may be more indicative of Cohn deposit mantling effects than of true variations in flow properties.

The slope of the northern leg of traverse E-E* is ~0.002 , while the southern branch is nearly flat overall (~0.0003). A steady increase in emissivity and σ_0 data indicative of a lava/melt flow occurs until ~100 km. From there a large dip in emissivity, diffuse component, and σ_0 data occurs that is anticorrelated with reflectivity. This reflects a roughness decrease potentially due to the mantling effects of radar-dark Cohn parabola deposits. The distal (> 150 km) increase in the emissivity and diffuse component is inferred to result from roughness associated with a more lava/melt-like flow.

ACKNOWLEDGEMENTS: We thank P. Ford (MIT), R. Simpson (Stanford), J. Plaut (JPL), and R. Kirk (USGS) for assistance with use and interpretation of the altimetry, radiometry, and SAR image data.

REFERENCES: **[1]** Schaber G.G. et al. (1992) *JGR, 97*, 13257; **[2]** Asimow P.D. and Wood J.A. (1992) *JGR, 97*, 13643; **[3]** Johnson, J.R., and Baker, V.R., submitted manuscript, *Icarus* , 1994; **[4]** Johnson, J.R., and Baker, V.R., Backscatter cross sections of venusian FEB crater deposits, this volume; **[5]** Tryka, K.A., and D.O. Muhleman, 1992 *JGR*, **97**, 13379-13394; **[6]** Johnson, A.M., Physical Processes in Geology, 1970, Ch. 12-14, Freeman, Cooper & Co.

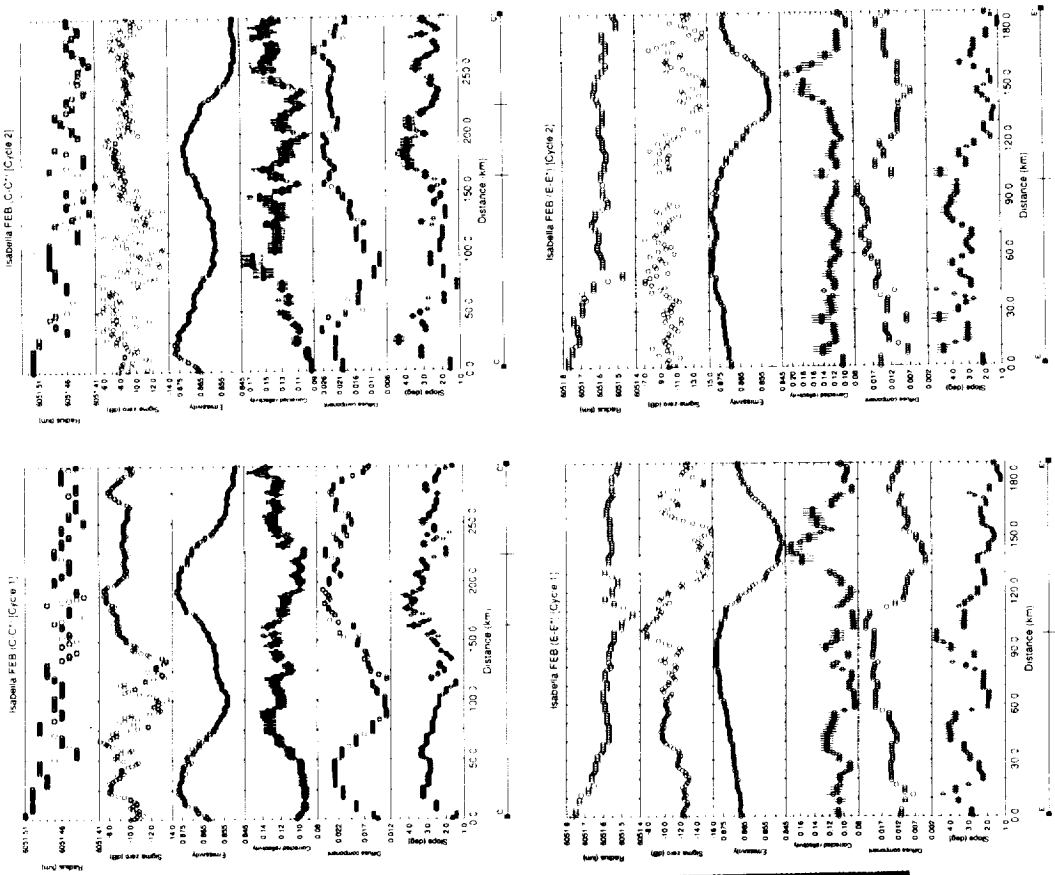

Figure 2. Cycle 1 and 2 traverses of (top to bottom) radius, σ_o, emissivity, corrected reflectivity (and formal errors), its diffuse component, and rms slope (and formal errors). Ticks along baseline show bends in traverse lines.

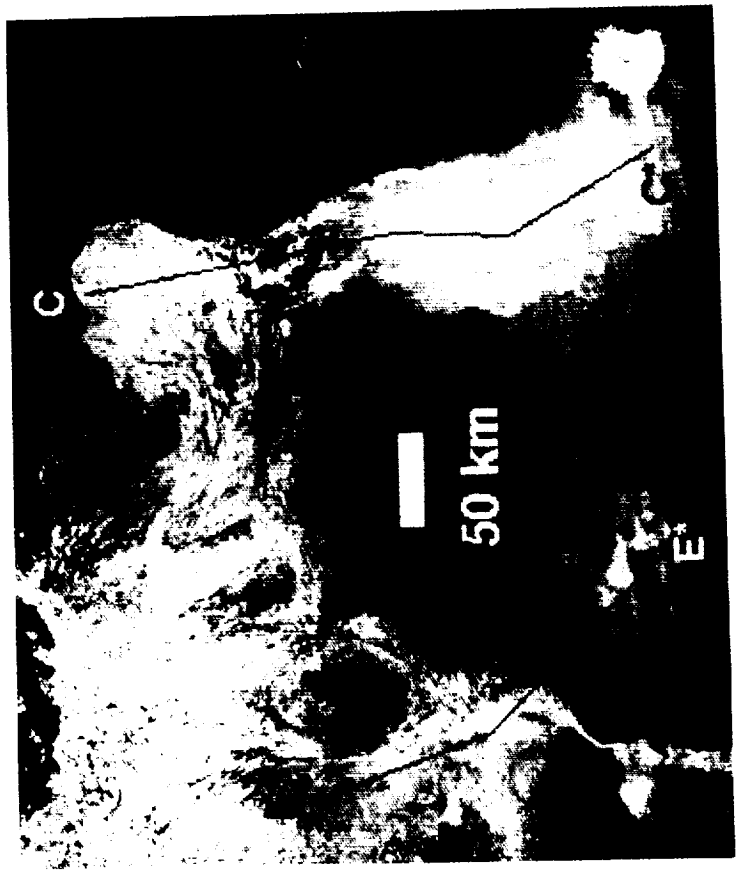

Figure 1. Location map for traverses C-C* and E-E* along Isabella crater FEB flows. Southern edge of Isabella crater visible in upper left. Crater Cohn (20.5 km) visible in lower right.

C-3

PRELIMINARY GEOLOGIC MAPPING OF VENUS QUADRANGLE V59 (BARRYMORE)

J.R. Johnson, G. Komatsu, and V.R. Baker, Lunar and Planetary Laboratory and Department of Geosciences, Space Sciences Bldg., Univ. of Arizona, Tucson, AZ, 85721.

As part of the Venus Geologic Mapping Program, preliminary 1:5 million geologic mapping is underway for the Barrymore quadrangle (V59; 50-75° S, 180-240°). This predominantly plains region south of Imdr Regio provides a potentially ideal geologic setting for deciphering the history of regional and/or local plains deformation. A high concentration of canali-type channels occurs in the northwest portion of the map area, including the eastern portion of a 3000 km long canali system. At least three instances of channel bifurcation from N-S to E-W orientations occur in this region. A N-S oriented, 1300 km linear ridge belt dominates the central map region. The southern tip of this feature interacts with a similarly extensive E-W trending curvilinear chain of elevated ridges and disrupted corona-like, volcanic/tectonic arcuate depressions and rises. Extended deposits associated with impact crater materials exhibit severe contrast reversals between Cycle 1 and 2 resulting potentially from asymmetrically oriented dune faces.

Crater Deposits. Twenty-seven impact craters have been found in the map area. The largest is Sayer (90 km; -67.5°, 230°) which exhibits a radar dark flooded floor and a fluidized ejecta blanket (FEB) with several diffuse outflow lobes of intermediate radar brightness. The crater Guan Daosheng (46 km; -61.05°, 181.8°) exhibits a radar bright floor and very bright FEB lobe. Both this crater and Eudocia (28 km; -59.05°, 201.8°) are associated with peculiar extended deposits (parabolas) that exhibit severe contrast reversals in SAR backscatter between Cycles 1 and 2 **[1,2]**. These may result from preferentially oriented facets associated with aolian deposits, or from an actual change in the distribution of surface materials/fines between Cycles **[2]**. Lack of Cycle 3 coverage in the map area prevents additional testing of the latter hypothesis.

Channels. The canali-type channels in the northwest portion of the map area exhibit distinct bifurcations between N-S and E-W orientations (Figure 1). These canali are heavily disrupted by later tectonism (e.g., ridge belts, wrinkle ridges--see **[3]**). The location of the canali bifurcations appears to coincide with the western edge of an irregularly shaped, > 1000 km wide and 1 km deep basin. This suggests a possible link between the canali formation and basin subsidence.

Ridge Belts. The N-S oriented, elevated central ridge system exhibits a complex association of smooth ridges and wrinkle ridges along its entire length, suggestive of a dominantly compressional origin. Topography shows elevated regions extending beyond the limits of the compressional features. Deep troughs surround some of the highest and narrowest ridge belts, suggestive of moat-like crustal depressions similar to those found around some coronae **[e.g., 4]**. Less elevated, arcuate, smooth ridges occur intermittently throughout the map area, potentially marking sites of failed corona development.

Corona chains. All corona-like features along the southern E-W chain are disrupted by later compressional (and/or extensional?) tectonism. The intersection of this chain and the N-S ridge belt is a complicated region marked by volcanic cone fields, flooded terrain, and disrupted steep-sided domes. As such, this region provides several potential stratigraphic markers. Curvilinear smooth ridges and troughs of nearly constant ~50 km width occur in the southern portion of the map area, often bounded or cross-cut by wrinkle ridges, and appear to be the southern manifestation of the ridge belt system and/or the corona chain.

Future work. Continued mapping efforts will concentrate on the intersection of the central ridge belt and corona chain. Wrinkle ridge patterns may be useful as additional chronostratigraphic tools **[5]**. Radiophysical properties and multiple-cycle SAR backscatter measurements of the extended deposits will be used to further refine interpretations of these surficial features. Altimeter-derived properties such as reflectivity and rms slopes appear partially contaminated by artifacts in this particular map area, however, which limits their usefulness **[1]**.

ACKNOWLEDGEMENTS: We thank the USGS (Flagstaff) for providing the map bases for this quadrangle.

REFERENCES: **[1]** Plaut et al., 1992, in *Papers Pres. Int. Coll. Venus*, LPI Cont. No. 789, p. 92-93; **[2]** Farr, T.G., 1993, Chapter 5, in *Guide to Magellan Image Interpretation, JPL Publication 93-24*, 45-56; **[3]** Komatsu,

G., and V.R. Baker, Longitudinal profiles of plains channels on Venus, this volume; [4] Stofan, E.R., et al., 1992, *JGR.*, 97, 13347-13378; [5] McGill, G.E., 1993, *GRL*, 20, 2407-2410.

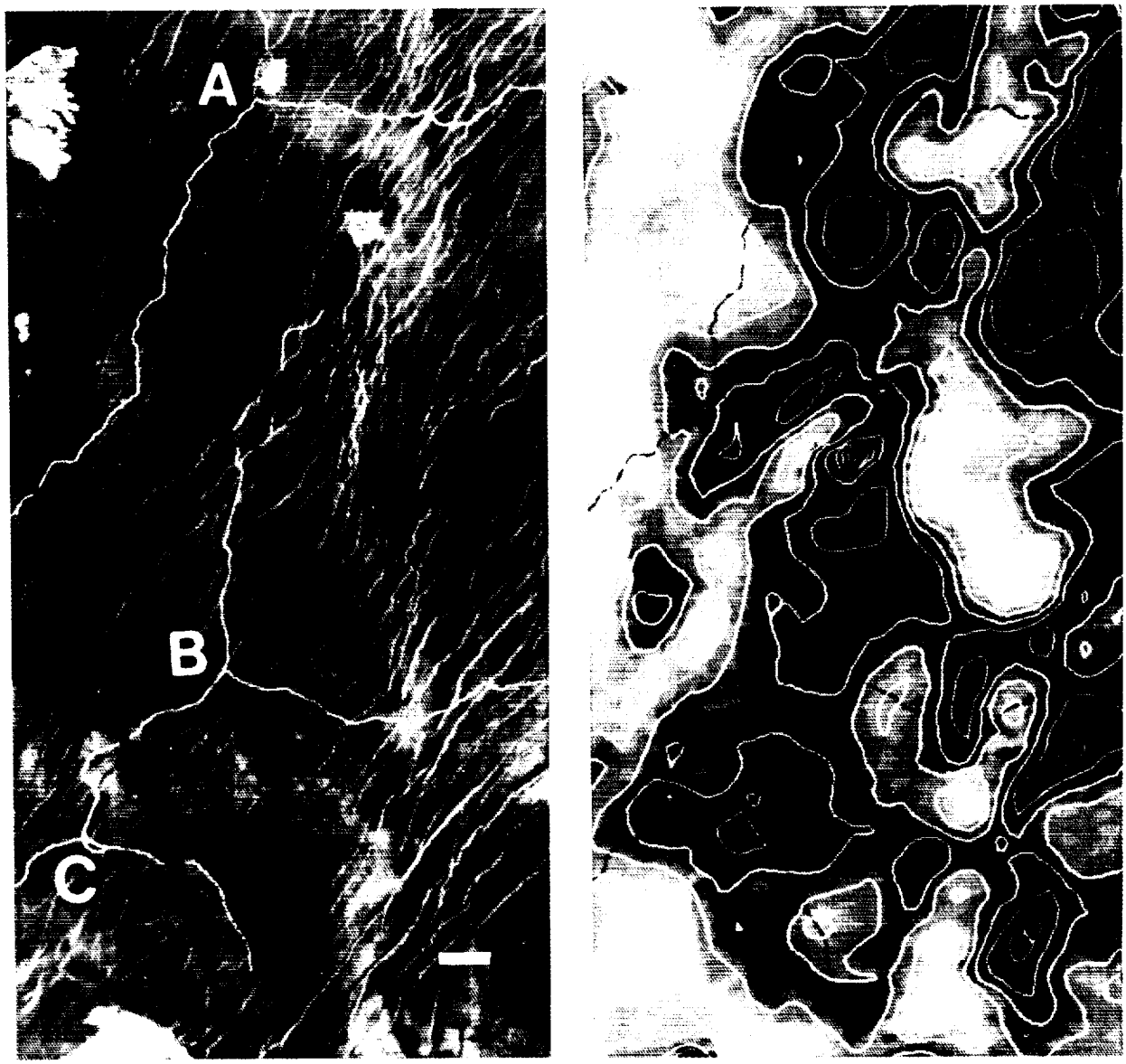

Figure 1. Magellan Cycle 1 SAR image (left) and corresponding topography (right; 250 meter contours) of northwestern portion of map area centered at -55°, 183°. Scale bar is 50 km. Overlain on both are tracings of canali-type channels showing three bifurcation points (labeled A,B,C) in which orientations change from predominantly N-S to E-W directions. These occur on the western edge of basin complex, suggesting a possible relation between basin formation and channel flow directions.

SEARCHING FOR RARE HIGHLAND IGNEOUS ROCKS AT APOLLO 14: FRAGMENTS OF MAGNESIAN-SUITE ASSEMBLAGES. BRADLEY L. JOLLIFF, DEPARTMENT OF EARTH AND PLANETARY SCIENCES & MCDONNELL CENTER FOR THE SPACE SCIENCES, WASHINGTON UNIVERSITY, ST. LOUIS, MO 63130.

Most of the rocks returned from the Apollo 14 landing site were impact melt breccias. A statistical survey of lithic fragments in an Apollo 14 soil revealed only some 8% or less to be pieces of monomict lithologies [1]. Many of these have relatively alkaline mineral assemblages characterized by plagioclase An contents less than 80–85% and a few percent or more of modal K-feldspar. From the Apollo 14 sample collection, only about 20 subsamples, mainly clasts extracted from impact breccias, have been characterized as igneous, monomict, magnesian-suite rocks [2]. In this abstract, modal mineralogy and mineral compositions are given for four possibly pristine, monomict samples for which only the bulk compositions as determined by INAA, and in one case, phosphate compositions, have been previously reported [1,3]. The four assemblages are 14161,7037 norite, 14161,7076 gabbronorite, 14161,7080 norite, and 14161,7350 magnesian anorthosite. Three of the four have elevated REE concentrations due to accessory whitlockite, but other incompatible trace elements are not in proportionately high concentrations relative to Apollo 14 KREEP (impact-melt breccias [1,4]). Mineral compositions within each of the four samples are quite uniform, indicating that they are monomict; all except ,7076 were listed in the compilation of [2] as possibly pristine. Sample 14161,7037 has an unusual mineral assemblage in that it contains a trace of sphene (cf. [5]) mantling troilite, vanadian rutile, and regions of silica-K-feldspar granophyre and pyroxene-plagioclase vermicular intergrowths. The residual melt of this assemblage appears to have reached the field of silicate-liquid immiscibility after some 98% crystallization, yet the bulk assemblage has low incompatible-trace-element (ITE) concentrations. An unanswered question is whether igneous rocks from the Apollo 14 site come from mantle-derived intrusions into the crust or from the differentiation of early, thick, basin-impact melt sheets. Ages for most of the igneous samples, where determined, exceed 4.0 billion years, so they predate the major known basins. The samples described in this abstract have significantly different mineral assemblages and compositions from one another, and they have incompatible-element enrichments different from those of "Apollo 14 KREEP" [1,4]. Thus, it appears likely that they derive from mutually unrelated, endogenous intrusions into the pre-basin upper crust of the Moon.

Descriptions of textures. Sample 14161,7037 is a monomict breccia with a fragmental matrix. It has a cataclastic texture dominated by orthopyroxene and plagioclase clasts typically ranging up to ~300 μm, but one mass of nearly monomineralic orthopyroxene spans 2 mm and constitutes about a third of the thin section. Orthopyroxene contains thin, oriented (exsolved) chromite needles. Scattered in several different locations are 100–200 μm silica–K-feldspar granophyric intergrowths and clinopyroxene-plagioclase-silica vermicular intergrowths. Compositions of plagioclase and pyroxene suggest that these intergrowths belong to the noritic assemblage, but resulted from crystallization of late-stage residual liquid as that liquid reached a field of immiscibility. Troilite occurs in several small grains in the thin section; in one, it is mantled by sphene (Table 6), possibly a result of late-stage sulfidization and replacement of ilmenite (?). Other accessory minerals include chromite and vanadian rutile.

Sample 14161,7076 is also a cataclastic, monomict breccia, consisting mainly of hypersthene, augite, plagioclase, and accessory olivine, ilmenite, troilite, and zircon. Neither alkali feldspar nor whitlockite were found in thin section, but the bulk Ba concentration of 725 ppm and REE concentrations of ~100 × chondrites [1] indicate that they were present in the sample. Plagioclase and pyroxene form clasts and monomineralic "stringers" up to ~0.75 mm, but generally, they are finely crushed. Thin exsolution lamellae are observed in pyroxenes. This sample bears compositional similarities to magnesian alkali-gabbronorite [6] from sample 67975.

Sample 14161,7080 norite has been highly shocked such that all of its feldspars are maskelynite (isotropic). Low-Ca pyroxene constitutes about half of the mode (Table 1) and occurs in heavily fractured masses up to about 0.8 mm across. Only a few grains of augite occur in the thin section, and K-feldspar glass occurs as thin wisps in plagioclase glass and in one separate 50 μm mass. Whitlockite forms cataclastic masses reaching ~100 μm across; no apatite was found in the section. The sample contains a trace of troilite and Fe-Ni metal.

Sample 14161,7350 is a highly magnesian, olivine-bearing anorthositic assemblage. The thin section consists mostly of coarse, highly fractured plagioclase split by an ~300 μm zone of crushed olivine, low-Ca pyroxene, and diopside. Bulk REE concentrations of ~100–300 × chondrites are due to a composite apatite-whitlockite grain several hundred μm across [3].

Table 1. Modal mineralogy of magnesian-suite lithic fragments from sample 14161 (weight percent).

	,7037	,7076	,7080	,7350
mass (mg)	20.7	10.3	15.6	11.8
Plagioclase	36.9	57.5	42.0	87.9
Low-Ca Pyroxene	59.4	28.2	49.4	0.5
High-Ca Pyroxene	1.7	14.2	6.0	1.0
Total Pyroxene	61.1	42.4	55.4	1.5
Olivine		0.5		7.7
Apatite	tr			1.0
Whitlockite		tr	0.5	0.9
Ilmenite		tr		
K-feldspar	1.0	tr	2.0	1.0
silica	0.5			
zircon		tr		tr
spinel	tr			
sphene	tr			
troilite	tr	tr	tr	

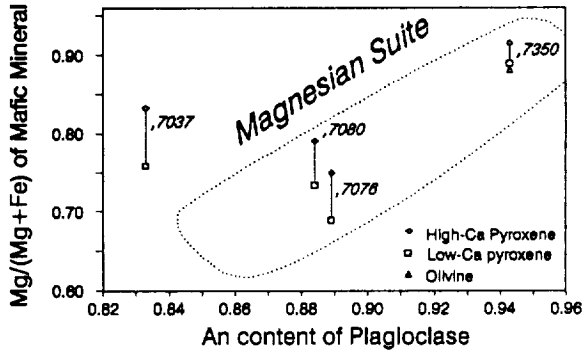

IGNEOUS SAMPLES FROM APOLLO 14: JOLLIFF B. L.

Through surveys of lithic fragments in soil samples, which are polymict materials, we continue to find new samples of rare lunar rock types that allow us to effectively sample broad areas of the Moon and better understand its lithologic diversity. Developments in micro-analytical techniques such as the ion microprobe and mass-spectrometry of plugs removed from thin sections by micro drill make small, monomict samples such as those identified and characterized by our INAA survey a scientifically valuable part of the lunar sample collection.

Acknowledgments. Funding for this work was through NASA grant NAGW-3343.

Table 2. Feldspar compositions of magnesian-suite igneous lithic fragments from sample 14161.

	,7037 Plag coarse n=6	,7037 Plag fine n=2	,7037 Plag late* n=2	,7037 K-feld Avg n=2	,7076 Plag Avg n=7	,7080 Maskel Avg n=8	,7080 K-feldspar Gls 1 n=1	,7080 K-feldspar Gls 2 n=3**	,7350 Plag Avg n=8
				Chemical Composition (Weight Percent)					
SiO2	46.55	47.10	53.30	62.26	45.97	45.76	65.26	62.73	44.19
Al2O3	33.68	33.01	29.62	19.02	35.32	34.63	19.02	19.77	35.11
FeO	0.14	0.26	0.05	0.04	0.16	0.21	0.08	0.32	0.04
MgO	0.03	0.04	0.05	0.02	0.12	0.04	0.00	0.00	0.05
CaO	16.94	16.32	12.60	0.11	17.64	17.72	0.69	0.20	19.20
BaO	0.00	0.00	0.06	3.81	0.03	0.03	1.57	3.65	0.03
Na2O	1.78	2.01	3.87	0.19	1.17	1.15	1.00	0.99	0.61
K2O	0.13	0.16	0.36	14.09	0.07	0.18	13.32	12.35	0.04
Total	99.26	98.90	99.90	99.54	100.48	99.73	100.94	100.0	99.27
				Cation Formula based on 8 Oxygens					
Si	2.155	2.186	2.415	2.947	2.104	2.114	2.983	2.932	2.058
Al(IV)	1.838	1.806	1.581	1.061	1.905	1.885	1.025	1.089	1.927
Sum	3.993	3.992	3.996	4.008	4.009	3.998	4.007	4.021	3.985
Fe(2+)	0.005	0.010	0.002	0.002	0.006	0.008	0.003	0.013	0.002
Mg	0.002	0.003	0.003	0.002	0.008	0.003	0.000	0.000	0.003
Ca	0.841	0.811	0.611	0.006	0.865	0.877	0.034	0.010	0.958
Ba	0.000	0.000	0.001	0.071	0.001	0.001	0.028	0.067	0.001
Na	0.160	0.181	0.340	0.017	0.103	0.103	0.089	0.089	0.055
K	0.008	0.010	0.021	0.851	0.004	0.011	0.777	0.736	0.002
Sum	1.016	1.014	0.979	0.948	0.988	1.003	0.930	0.915	1.021
				Molecular Proportions of Anorthite (An), Albite, Orthoclase (Or), and Celsian (Cs)					
An	83.3	81.0	62.8	0.6	88.9	88.4	3.6	1.1	94.3
Ab	15.9	18.0	34.9	1.8	10.6	10.4	9.6	9.9	5.4
Or	0.8	0.9	2.2	90.1	0.41	1.1	83.8	81.6	0.2
Cn	0.0	0.0	0.10	7.5	0.06	0.06	3.0	7.4	0.1

* In vermicular intergrowth with pyroxene and adjacent silica-K-feldspar granophyre.
** Oxide sums exceded 100 by several percent, so each was normalized before averaging.

Table 3. Pyroxene compositions of magnesian-suite igneous lithic fragments from sample 14161.

	14161,7037 OPX n=5	14161,7037 Aug n=3	14161,7076 OPX n=5	14161,7076 Aug n=5	14161,7080 OPX n=17	14161,7080 Aug n=3	14161,7350 OPX n=1	14161,7350 Diop n=4
				Chemical Composition (Weight Percent)				
SiO2	53.93	53.60	52.67	51.75	53.18	51.76	56.51	52.67
TiO2	0.70	0.50	0.76	1.32	0.93	1.26	0.51	1.10
Al2O3	0.45	0.61	0.75	1.78	1.05	1.46	0.82	1.57
Cr2O3	0.62	0.42	0.28	0.68	0.46	0.57	0.40	0.56
FeO	15.43	5.68	19.26	9.30	16.58	7.63	7.32	2.92
MnO	0.21	0.10	0.27	0.26	0.23	0.15	0.16	0.07
MgO	27.17	15.95	23.94	15.55	25.75	16.16	33.23	17.56
CaO	1.17	22.22	1.84	19.68	1.88	20.95	1.37	23.07
Na2O	0.01	0.15	0.00	0.16	0.01	0.16	0.00	0.11
Total	99.69	99.24	99.78	100.48	100.07	100.10	100.32	99.62
				Cation Formula Based on 6 Oxygens				
Si	1.958	1.984	1.949	1.918	1.938	1.918	1.960	1.928
Al(IV)	0.019	0.016	0.033	0.078	0.045	0.064	0.034	0.068
Sum T-site	1.977	2.000	1.982	1.996	1.983	1.982	1.994	1.996
Al(VI)	0.000	0.011	0.000	0.000	0.000	0.000	0.000	0.000
Ti	0.019	0.014	0.021	0.037	0.025	0.035	0.013	0.030
Cr	0.018	0.012	0.008	0.020	0.013	0.017	0.011	0.016
Fe(2+)	0.468	0.176	0.596	0.288	0.505	0.236	0.212	0.089
Mn	0.007	0.003	0.008	0.008	0.007	0.005	0.005	0.002
Mg	1.470	0.880	1.321	0.859	1.399	0.893	1.718	0.958
Ca	0.045	0.881	0.073	0.782	0.073	0.832	0.051	0.905
Na	0.001	0.011	0.000	0.011	0.001	0.011	0.000	0.008
Sum M1,M2	2.028	1.988	2.028	2.006	2.024	2.029	2.011	2.008
				Cation Ratio Mg/(Mg+Fe) and Molecular Proportions of Wollastonite (Wo), Enstatite (En), and Ferrosilite (Fs)*				
Mg/(Fe+Mg)	0.76	0.83	0.69	0.75	0.73	0.79	0.89	0.91
Wo	2.2	43.4	3.7	38.1	4.1	40.8	2.9	44.4
En	74.2	47.1	66.3	46.4	70.4	46.8	86.4	50.8
Fs	23.6	9.4	29.9	15.5	25.4	12.4	10.7	4.7

* corrected for "others" (<2%)

Table 4. Phosphate Compositions.

	,7037 Apat n=1	,7350 Apat n=17	,7080 Whit n=6	,7350 Whit n=6
	Chemical Composition (Weight Percent)			
P2O5	41.1	41.55	43.66	43.17
SiO2	0.30	0.28	0.06	0.24
Al2O3	0.04	<0.02	0.17	0.00
FeO	0.22	0.04	0.85	0.17
MnO	0.04	<0.01	0.01	0.02
MgO	0.08	0.10	3.36	3.60
CaO	55.69	54.98	41.90	39.52
Na2O	0.02	0.01	0.59	0.23
Y2O3	0.10	0.14	2.04	3.09
La2O3	<0.02	0.06	0.83	1.14
Ce2O3	0.04	0.16	2.10	3.16
Nd2O3			1.35	1.96
Yb2O3			0.09	0.17
Other REE	0.06	0.13	1.69	2.31
F	2.97	3.32		
Cl	0.80	0.71		
Total	101.42	101.50	98.72	98.75
- O = F	1.25	1.40		
- O = Cl	0.18	0.16		
Total	99.99	99.94	98.72	98.75
	Apatite Formula based on 12.5 Ox		Whitlockite based on 56 Oxygens	
P	2.942	2.973	13.901	13.918
Si	0.025	0.024	0.021	0.091
Sum(Tet)	2.967	2.997	13.923	14.010
Al	0.004	0.000	0.077	0.000
Fe(2+)	0.016	0.003	0.266	0.054
Mn	0.003	0.001	0.005	0.006
Mg	0.010	0.013	1.886	2.041
Ca	5.049	4.978	16.886	16.126
Na	0.003	0.001	0.434	0.166
Y+Ln(3+)	0.007	0.017	1.218	1.807
Sum Other	5.092	5.012	20.772	20.201
F	0.796	0.887		
Cl	0.114	0.102		
sum F,Cl	0.910	0.989		
Mg/(Fe+Mg)	0.39	0.82	0.88	0.97

Notes: (1) Apatite ,7037 "other REE" estimated from Y, Ce.
(2) Apatite ,7350 REE determined by ion microprobe [3].
(3) Whitlockite ,7080 "other REE" estimated from Y, La, Ce, Yb.
(4) Whitlockite ,7350 REE determined by ion microprobe [3].

Table 5. Olivine in 14161,7350.

	Oliv n=2
Composition (Wt. %)	
SiO2	39.91
TiO2	0.02
Al2O3	0.01
Cr2O3	0.04
FeO	11.55
MnO	0.13
MgO	48.04
CaO	0.05
Na2O	0.00
Total	99.76
Cation Formula Based on 4 Oxygens	
Si	0.989
Ti	0.000
Cr	0.001
Fe(2+)	0.240
Mn	0.003
Mg	1.775
Ca	0.001
Na	0.000
Sum Oct.	2.021
Mg/(Fe+Mg)	0.881
Molecular Proportions	
Fayalite	11.9
Forsterite	88.0
Ca2SiO4	0.1

Table 6. Spinel and chromite compositions in 14161,7037.

	Sphene n=2	Chromite n=1
SiO2	30.06	0.05
TiO2	38.99	2.20
Al2O3	0.64	6.24
Cr2O3	0.54	57.04
FeO	0.47	30.62
MnO	0.09	0.32
MgO	0.09	2.86
CaO	27.47	0.06
Na2O	0.01	0.00
Total	98.36	99.39
Cation formula based on:	5 Ox.	4 Ox.
Si	0.998	0.002
Al(VI)	0.025	0.262
Ti	0.974	0.059
Cr	0.014	1.606
Fe(2+)	0.013	0.912
Mn	0.002	0.010
Mg	0.005	0.152
Ca	0.977	0.002
Na	0.001	0.000
Sum Other	2.011	3.003
Mg/(Fe+Mg)	0.255	0.143

References [1] Jolliff B.L. et al. (1991) *PLPS* 21, 193-219. [2] Warren P.H. (1993) *Am. Min.* 78, 360-376. [3] Jolliff B.L. et al. (1993) *Geochim. Cosmochim. Acta* 57, 4069-4094. [4] Warren P.H. (1989) in *Workshop on Moon in Transition: Apollo 14, KREEP, and evolved Lunar Rocks*, 153. [5] Grieve R. et al. (1972) in *LSC III*, 300-302. [6] James O.B. et al. (1987) *PLPSC 17th*, E314-E330.

EVIDENCE FOR THE NATURE OF THE IGNEOUS PRECURSOR OF FERROAN PLUTONIC ROCKS FROM NORTH RAY CRATER, APOLLO 16. BRADLEY L. JOLLIFF AND LARRY A. HASKIN, DEPARTMENT OF EARTH AND PLANETARY SCIENCES & MCDONNELL CENTER FOR THE SPACE SCIENCES, WASHINGTON UNIVERSITY, ST. LOUIS, MO 63130.

A set of rocks from the southern rim of North Ray Crater constitutes a geochemically and petrogenetically related group that derived from a ferroan-anorthositic, plutonic igneous rock body. A subset of lithic fragments from sample 67513 forms a coherent geochemical group with mineral assemblages ranging from anorthositic to gabbronoritic. Polymict breccias, including mixtures of melt-matrix and fragmental-matrix breccias, have compositions that lie along a correlation line that has igneous-textured plagioclase-rich and pyroxene-rich end members (Fig. 1). Bulk trace-element concentrations and mineral compositions relate the polymict and igneous samples (e.g., Fig. 2). We interpret this suite of samples as having formed from an igneous body of noritic-anorthosite bulk composition wherein the mafic component resulted from solidification of intercumulus melt of cotectic composition within a plagioclase suspension cumulate (Fig. 3). Plagioclase-rich samples form three compositional groups distinguished by their plagiophile-element concentrations, for example, Na_2O (wt.%): 0.27-0.32, 0.35-0.38, and 0.42-0.45; and Eu (ppm): 0.71-0.72, 0.77-0.80, and 0.84-0.86 (Fig. 4). Results of geochemical modeling and calculations involving mass-balance of sodium suggest that either some re-equilibration occurred between cumulus plagioclase and intercumulus melt during solidification or that original cumulus plagioclase compositions spanned a range of Na concentrations such as we observe in the samples now. The possibility that re-equilibration involving Na was associated with plagioclase recrystallization during prolonged cooling is not supported by our observation that domains of coarsely recrystallized plagioclase maintain the same Na concentration as primary plagioclase. There is, however, evidence for the loss of mafic components from cumulus plagioclase by the clearing of mafic inclusions in primary plagioclase during recrystallization. The Mg' values of mafic silicates coexisting with cumulus plagioclase appear to be governed by intercumulus pyroxene as opposed to mafic components exsolved from plagioclase.

We take the bulk composition of the precursor igneous system to be that of the mass-weighted average of 148 lithic fragments from sample 67513; this composition has ~30 wt.% Al_2O_3, 4% FeO, 3% MgO, and Mg' of 0.56. Many individual lithic fragments contain similar impact melt components ranging from about the same to slightly more mafic than the inferred bulk system (Al_2O_3: 27-31%, FeO: 3.8-8.5%), suggesting that on a large scale, there was some variability in proportions of cumulus plagioclase and intercumulus melt, but that the mafic material and cumulus plagioclase were present in a single rock formation and did not form separate layers or intrusions.

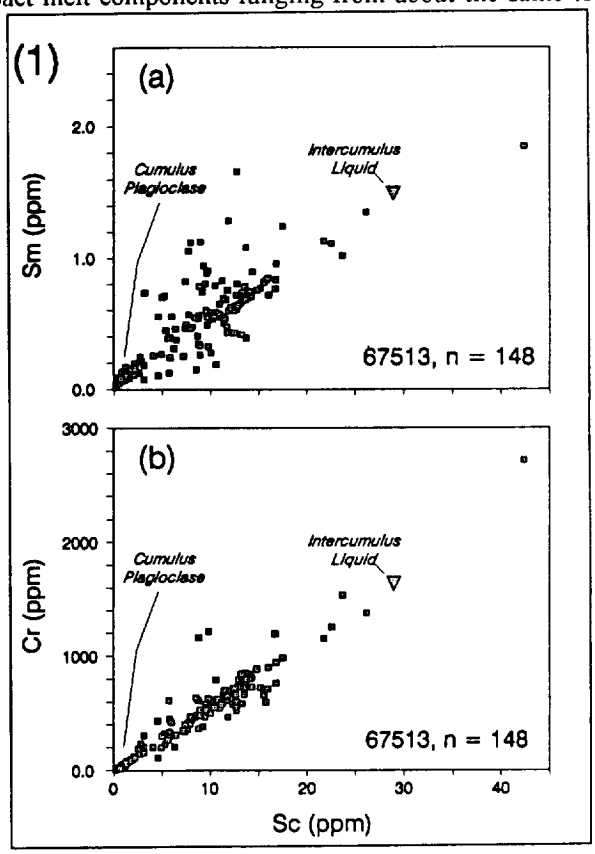

The inferred bulk composition of the system corresponds to a mixture of some 70 wt.% cumulus plagioclase and 30% intercumulus material (Fig. 3). We calculated the intercumulus melt composition by mass balance given the 30:70 ratio, the bulk system composition, and an average cumulus plagioclase composition. Cumulus plagioclase compositions span a range of Na_2O concentrations (Fig. 4), and an average Na_2O concen-tration of 0.37 leaves the intercumulus melt with a low enough Na_2O concentration to produce orthocumulus plagioclase as calcic as that observed (Fig. 2).

From our geochemical modeling [1], we conclude that solidification of the igneous system was dominated by equilibrium crystallization of intercumulus melt once the cumulus plagioclase - intercumulus melt system became isolated from other parts of the parent magmatic system. Scatter about the correlation line of Fig. 1a is consistent with some migration of intercumulus melt during

FERROAN PLUTONIC ROCKS FROM NORTH RAY CRATER: Jolliff B. L. and Haskin L. A.

solidification, such as in tension fractures due to shrinkage, leaving compositionally less evolved (lower incompatible element concentrations) assemblages in some locations and more evolved assemblages elsewhere. However, the strength of correlations such as those shown in Fig. 1 and the limited range of mineral compositions (Fig. 2) indicate that such migration and/or fractional crystallization was minimal. Although the number of data points is low, there is some indication in Fig. 2 for the existence of two separate mineral compositional trends. Perhaps infiltration of late-stage residual melt into the most calcic regions of cumulus plagioclase (e.g., Gp. A, Fig. 4) produced the steeper trend at high An content (cf. model of [2]. All of the 67513 fragments plotted in the high-An trend are samples with Gp. A plagioclase.

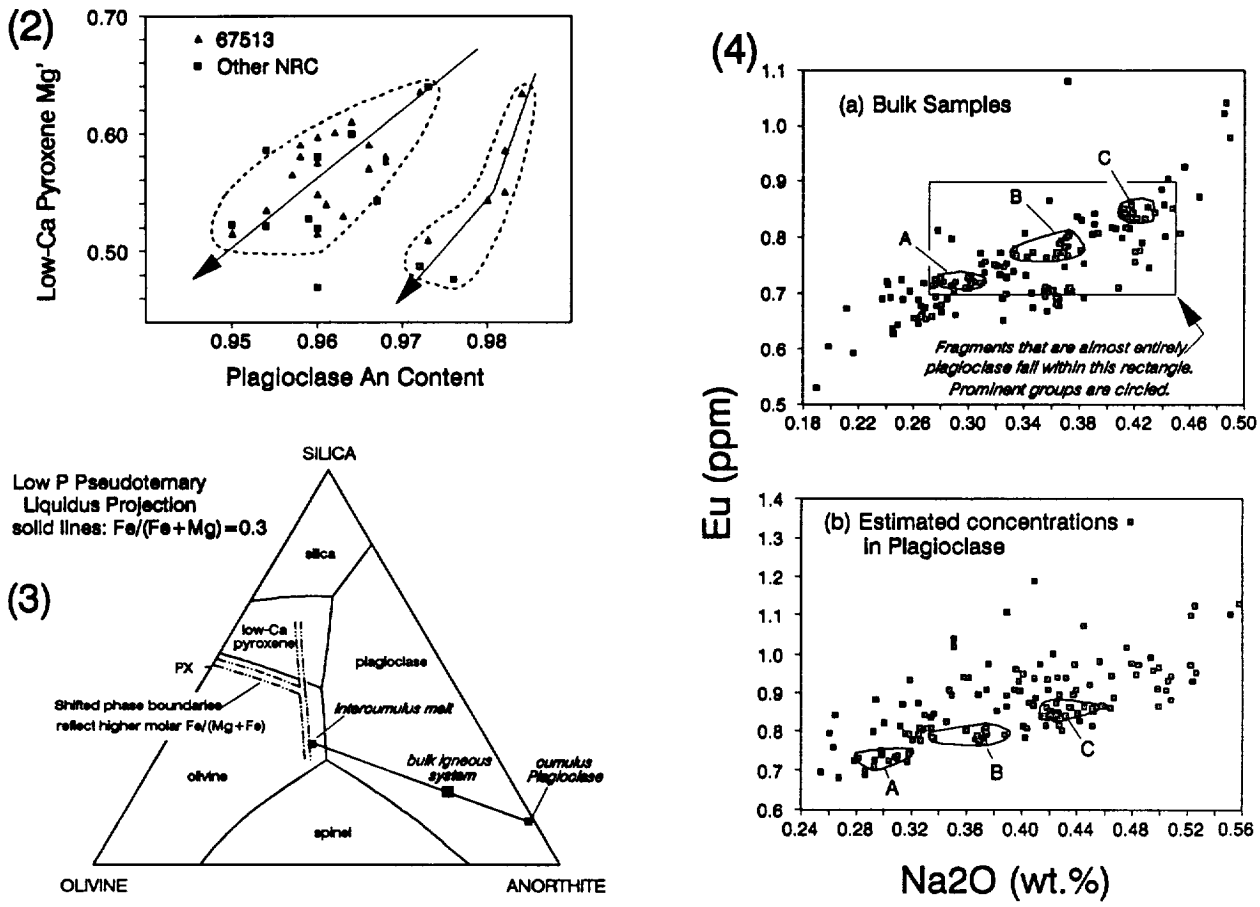

The separation of the plagioclase-intercumulus melt mush from any cogenetic mafic parts of the system may have resulted from physical separation of the plagioclase-rich system as a diapir (cf. [3]), or simply when the residual porosity of the plagioclase cumulus mesh was sufficiently low as to prevent further chemical exchange with a larger body of contemporary magma. In either event, the eventual separation occurred on a large scale because we find no evidence of more mafic cumulates or rock products of a large body of contemporary melt such as gabbro or impact melt of gabbroic composition among the sample suite from North Ray Crater. Ferroan igneous rocks such as those exhumed from North Ray Crater would be expected as part of magma ocean plagioclase-rich suspension cumulates; in fact, in analogy with similar anorthositic rocks from the terrestrial Stillwater Complex, we should expect to find large bodies of noritic or gabbroic anorthosite (89-90% plagioclase) rather than anorthosite *sensu stricto* (90-100% plagioclase). We envision, however, not a horizontally-layered magma body such as the Stillwater layered mafic intrusion, but instead, a body remotely separated from any corresponding mafic cumulates, such as terrestrial massif anorthositic bodies.

Acknowledgments. Funding for this work was through NASA grant NAGW-3343.

References [1] Jolliff B.L. and Haskin L.A. (1994) Igneous differentiation of ferroan plutonic rocks from North Ray Crater, Apollo 16. submitted to *Geochim. Cosmochim. Acta*. [2] Raedeke L.D. and McCallum I.S. (1980) *Proc. Conf. Lunar Highlands Crust*, 135-153. [3] Longhi J. and Ashwal L.D. (1985) *PLPSC 15th*, C571-C584..

SAMPLING THE APOLLO 17 HIGHLANDS USING SOILS AND LITHIC FRAGMENTS. BRADLEY L. JOLLIFF, KAYLYNN M. ROCKOW, RANDY L. KOROTEV, AND LARRY A. HASKIN, DEPARTMENT OF EARTH AND PLANETARY SCIENCES & MCDONNELL CENTER FOR THE SPACE SCIENCES, WASHINGTON UNIVERSITY, ST. LOUIS, MO 63130.

What would we know about the rock types and geology of the Apollo 17 highlands if all we had were samples of the soils and small lithic fragments contained therein? As a precursor to future automated rover or other sampling or reconnaissance missions, we must determine how best to sample an area and what can or should be learned from different kinds of samples. The Apollo 17 landing site is ideal for comparing different kinds of sampling, including remote sensing, soils, and hand-sample-size rocks because of the diversity of rock types present and the complex geology of the site. In the present abstract, we consider compositional and petrographic information obtained on 2–4 mm lithic fragments and compare that to what we can discern from bulk soil samples, large-rock samples, and remotely-sensed data. The diversity of lithologic information contained in the lithic fragments of some soils nearly equals that found among large rock samples, and most information bearing on petrographic relationships is maintained, even in such small samples. Given a small number of large samples for "petrologic ground truth," small lithic fragments contained in soil "scoop" samples can provide the basis for interpreting photogeologic units and their compositions.

Recent remote-sensing studies [e.g., 1,2] have focused on relatively small areas (e.g., 1 km "footprint") and spectral reflectance data have been used to characterize regions of highlands as anorthositic (>90% plagioclase), noritic or gabbroic (low- or high-Ca pyroxene-rich, respectively), troctolitic (olivine-bearing), or some mixture. These average characterizations are, however, for areas that may be large relative to individual, subsurface geologic rock formations. Information pertaining to important details of composition and petrologic history are lacking, for example, (1) are the rocks of alkaline, magnesian, or ferroan geochemical character, (2) what is the range of rock types, (3) are they breccias, igneous rocks, or soils, and (4) do they form related rock series? Analyses of fresh rock surfaces such as central peak slopes or crater walls may yield information on bedrock, but the makeup of regions bearing a veneer of regolith is obscured and, at best, averaged. Near-IR reflectance spectra of North and South Massifs, and other similar-appearing locations on the rim of the Serenitatis basin indicate that the mineralogical makeup of the rocks is generally that of anorthositic norite [1]. Indeed, the average composition of a mixture of Serenitatis-related impact melt breccia, relatively anorthositic granulitic breccias, and a variety of igneous rocks including dunite, norite, and gabbro, is that of anorthositic norite. There are, however, few large-rock specimens of actual anorthositic norite (e.g., 78255 - 48g [3,4]; Lunar sample information catalog, 1973). It is difficult to infer the subregolith or sub-megaregolith basement geology from the average remotely-sensed surface composition. Data from specific rocks samples are required.

From careful sampling by the Apollo 17 astronauts along traverses totaling 31 km and return of some 102 kg of rock samples, the major rock types present in the area are known. The site is at the join of a bay of the basaltic maria and uplifted blocks of highlands material. Samples from the valley floor are dominated by high-Ti mare basalts, and those from the highlands are dominated by impact-melt breccia of approximately "noritic" composition. Subordinate to the high-Ti basalts are orange pyroclastic debris and subordinate to the noritic impact breccias are igneous lithologies including anorthositic gabbro, dunite, troctolite, and norite proper [4-7]. The geochemical diversity of the large-rock samples is well represented on plots of CaO vs. FeO and Sc vs. Sm concentrations (see figures).

Bulk soil samples collected at each of the sampling stations by the astronauts also show a diversity of compositions. These can be interpreted generally in terms of the geology and known rock types of the site, but their compositions indicate somewhat different proportions for their precursor rocks than are found among the large samples. Also, mass-balance models suggest that several compositional components are present which are not easily defined in terms of known rock types (see [8] for a recent summary).

We focus on the 2–4 mm size range because (1) there is a statistically significant number of such fragments in most returned soil samples, typically 2–3%, corresponding to ~250 fragments in a five-gram split of 2–4 mm particles (but only 50 or less in a five-gram split of 4–10 mm particles; (2) they are large enough to provide a good bulk composition or petrographic representation of rock lithologies (as opposed to individual mineral fragments, which are far more common in the 1–2 mm range); (3) local vertical and lateral mixing from small meteorite impacts has increased the variety of rock types that may be represented in a single sample.

In the figures, we also show the distribution of compositions of lithic fragments in the 2–4 mm range from North and South Massif soils. Sample 76503 is from a submature soil [9] and contains a wide diversity of rock types, including several variants of high-Ti basalt fragments thrown up by local deposits from the valley floor. The samples from South Massif are from mature soils, but come from the light mantle, a relatively recent surge deposit resulting from a secondary impact near the top of the massif [10]. Their lithologic diversity is restricted to noritic

impact melt breccia and lithic clasts contained therein. In a companion abstract [11], we compare what is known about local rock types at the Apollo 17 site to what we have learned from the 2–4 mm lithic fragments of the soils.

Acknowledgments. Funding for this work was through NASA grant NAGW-3343.

References [1] Hawke B.R. et al. (1992) in *Workshop on Geology of the Apollo 17 Landing Site. LPI Tech. Rpt. 92-09*, p. 14–15. [2] Pieters C.M. and Taylor G.J. (1989) *PLPSC 19th*, 115-125. [3] Warren P.H. and Wasson J.T. (1978) *PLPSC 9th*, 185-217. [4] Lunar Receiving Laboratory (1973) *Lunar Sample Information Catalog, Apollo 17*, NASA JSC, MSC 03211, 447p. [5] Ryder G. (1993) *Catalog of Apollo 17 Rocks, Vol. 1*, NASA JSC #26088, 411p. [6] Neal C.R. and Taylor L.A. (1993) *Catalog of Apollo 17 Rocks, Vol. 2*, NASA JSC #26088, 522p. [7] Wolfe E. and others (1981) *USGS Prof. Paper 1080*, p. 125. [8] Korotev R.L. and Kremser D.T. (1992) *PLPS* 22, 275-301. [9] Morris R.V. (1983) *Handbook of Lunar Soils*. [10] Luchitta B. (1992) in *Workshop on Geology of the Apollo 17 Landing Site*. LPI Tech. Rpt. 92-09, p.31. [11] Rockow K.M. et al. (1994) this Vol.

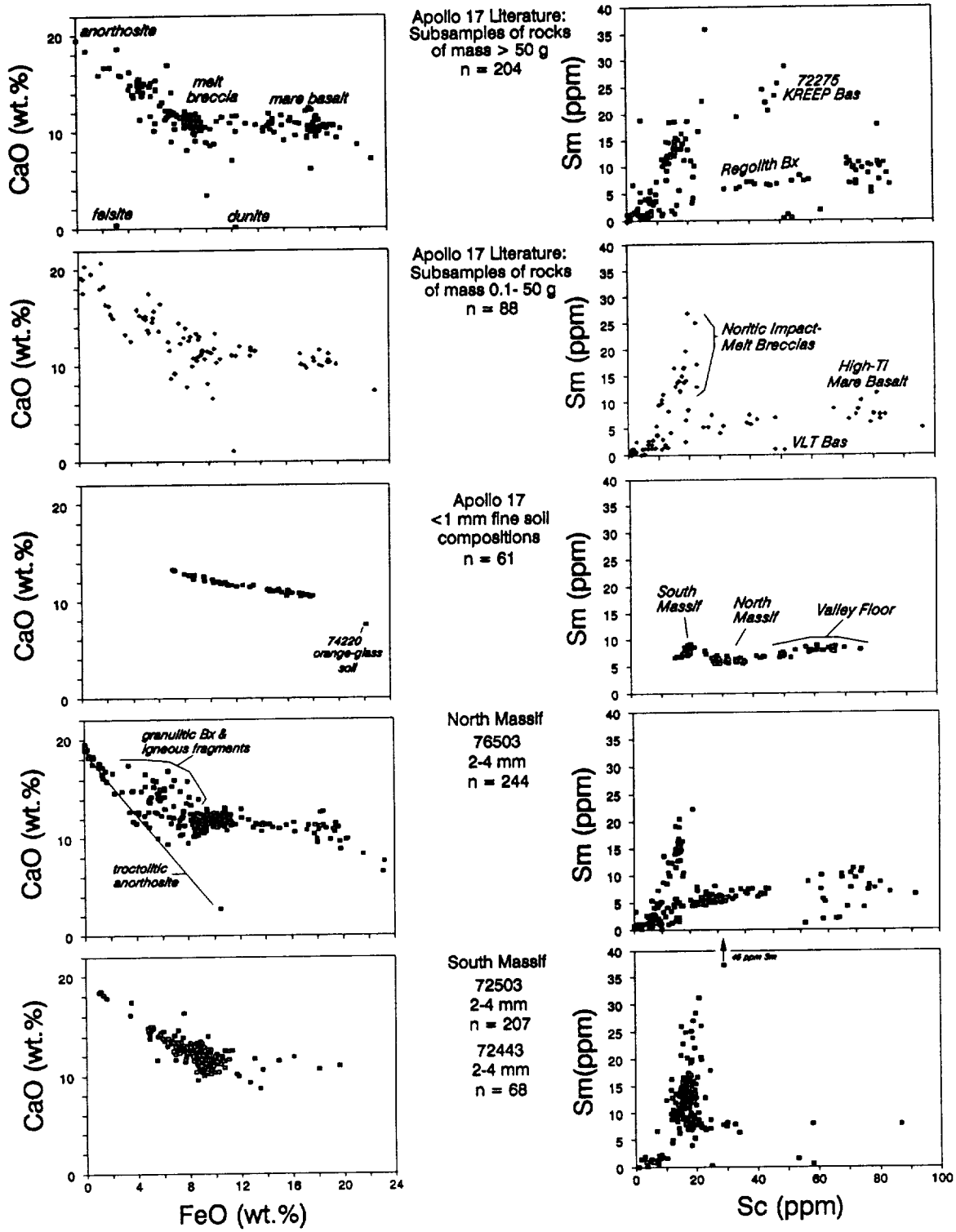

THE COMPOSITIONAL SIMILARITY BETWEEN SIOUX COUNTY AND EXPERIMENTALLY PRODUCED PARTIAL MELTS OF THE MURCHISON CHONDRITE FAVORS A PARTIAL MELTING ORIGIN FOR PRIMITIVE EUCRITES. J.H. Jones*, B.Z. Hanson‡, G.A. McKay*, A.J.G. Jurewicz†, J.W. Delano‡, and D.W. Mittlefehldt†. *SN4, NASA/JSC, Houston, TX 77058; ‡Dept. of Geology, SUNY Albany, Albany, NY 12222; †C23, Lockheed Engineering and Sciences Co., 2400 NASA Road 1, Houston, TX 77058.

Introduction. There has been a long-standing debate over the origin of the eucrites, a suite of basaltic achondrites [1,2]. High temperature experiments on eucrites and carbonaceous chondrites have, on balance, supported the viewpoint that primitive eucrites such as Sioux County are simple partial melts [1,3,4]. However, the intimate association of eucrites with cumulate pyroxenites (diogenites) in meteoritic breccias (howardites) argues that the eucrites formed after extensive fractional crystallization of orthopyroxene, which accumulated to form diogenites [2, 5].

This divergence of opinion is unfortunate. Eucrites are presumably very simple basalts, and their asteroidal origin seems well established [6]. Thus, it appears that neither high pressure (> 1 kbar) perturbations of phase relations nor volatile element fluxing have contributed to eucrite petrogenesis. Consequently, considering the relative simplicity of asteroidal basalts, it is disquieting that quite different petrogenetic models have successfully competed for over a decade. If we cannot understand the origins of simple basalts, the implications for understanding the petrogenesis of terrestrial, lunar and martian basalts are not reassuring.

Only minor variation is observed in the major element compositions of typical ("main group") eucrites [4] and the majority of their lithophile refractory trace elements have flat, chondrite-normalized abundances, ~10X CI [e.g., 3]. However, Sc, Cr and V are exceptions to this rule [3]. These elements are depleted in eucrites relative to other refractory lithophile elements by factors that are presumably related to their compatibility in mafic silicates and spinel. Of this trinity, only Sc is easily modeled [3], since the V/Cr ratio of a magma will be extremely sensitive to the amount of spinel present in the residuum. Regardless, it is clear that it should be of great importance to understand the process(es) that produced the signature depletions of Cr, Sc and V.

Partial melts of Murchison. In a previous study on the partial melting of the Murchison (CM) chondrite [4], we found that our experimental melts (1170-1200°C; fo_2 = IW-1) were nearly indistinguishable in their refractory, lithophile element abundances from those of eucrites. Specifically, Si, Ti, Al, Cr, Fe, Mg, and Ca concentrations were nearly identical to those of Sioux County, a primitive eucrite [4; and Table 1]. Only Mn, which is somewhat volatile, was depleted relative to eucrites. This was presumably because Murchison itself is depleted in Mn compared to the Eucrite Parent Body (EPB). We deemed this compositional agreement between Sioux County and our experimental glasses to be significant because the liquidus temperature of the Sioux County eucrite had already been determined to be within the range of our experiments [1].

Consequently, it appeared to us that another way to model the abundances of some elements in eucrites was not to perform calculations, but to perform experiments. If major element concentrations of experimental glasses produced from chondrites were sufficiently close to those of eucrites, then trace elements (especially Sc and V) should be analyzed as well.

Analytical. We have analyzed our 1170, 1180 and 1200°C Murchison experiments for V using the JEOL electron microprobe at the Rensselaer Polytechnic Institute and have made corrections for contributions from the Ti $K\beta$ to the V $K\alpha$. More analytical details are given in an accompanying abstract [8]. Abundances of Cr and Ti were also measured and were similar to those reported earlier [4]. For comparison, selected glasses from Allende and St. Severin experiments performed in the same temperature range as Murchison were also analyzed. In addition, we have also attempted to measure the Sc contents of our 1180°C Murchison glass using the JSC Cameca electron microprobe and the trace element analysis technique of [7]. Corrections for the large contribution to the Sc $K\alpha$ from the Ca $K\beta$ were made by analyzing a Sc-free glass having a CaO content similar to that of Sioux County.

Results and Discussion. Table 1 compares analyses of our 1180°C Murchison glass to those of Sioux County. The comparison is striking, and it seems to us that such close agreement is unlikely to be fortuitous. In our experiments, the abundance levels of these elements are

established by partial melting, not by fractional crystallization. Thus, by analogy, our results favor the partial melting model over the fractional crystallization model. We envision an EPB that is similar to an anhydrous CM or CO chondrite, but which is enriched in Mn relative to the refractory lithophile elements. We also envision that primitive eucrites such as Sioux County are simple partial melts.

The V and TiO_2 abundances of our experimental glasses are clearly distinguished from those eucrites that are believed to substantially differ from Sioux County in their petrogenetic history, either in their degree of partial melting (e.g., Stannern and Bouvante) or by experiencing significant amounts of fractional crystallization (e.g., Nuevo Laredo and Lakangaon). Partial melts of Allende and St. Severin also show significant differences from those of Murchison. Thus, the fact that Cr, Sc and V are at near-Sioux County concentration levels in Murchison melts distinguishes Murchison melts both from partial melts of other chondrites and from eucrites with different petrogenetic histories than Sioux County.

Vanadium/Cr ratios of silicate liquids in spinel-saturated systems are strong functions of the bulk Cr concentration, as well as of temperature and fo_2 [9]. Thus, the agreement in Cr and V contents between our spinel-saturated glasses and natural eucrites further boosts our confidence in Murchison as a reasonable starting material. Initially influenced by the work of Stolper [1], we chose the temperature and fo_2 of our experiments to be 1200-1170°C and IW-1, respectively, and these choices also seem validated.

The error on our Sc measurement is quite large and is mainly attributable to an interference from a satellite Ca $K\beta$ peak. Our measured concentration of Sc may be compared to a calculated concentration, using $D_{Sc}^{ol/liq}$ and $D_{Sc}^{pyx/liq}$ [10], a bulk Sc concentration [11], and observed modal abundances [4]. Correcting for 16% volatile loss [12], 9% metal precipitation [4], 18% partial melting [4], and partitioning [4, 10], we calculate that our 1180°C melt should have a Sc content of 26 ppm. A similar calculation for La yields a liquid concentration of 2.3 ppm. Literature values for Sc and La in Sioux County are 29 ppm and 2.4 ppm, respectively ([13]; Table 1). Thus, it seems that our Sc may be slightly low compared to what would be expected, but only by about 10%.

Still, because Sc, Cr and V are all much more compatible in orthopyroxene than La, we infer that the similarity between the Sc/La, Cr/La, and V/La ratios of Sioux County and our 1180°C Murchison melt should be difficult to maintain if Sioux County had been produced by extensive orthopyroxene fractionation from a more primitive magma. Consequently, based on our partial melting experiments, we favor a partial melting origin for primitive eucrites such as Sioux County. Thus, the relationship, if any, between eucrites and diogenites remains obscure, and the MnO abundance of the EPB (and Mars? [14]) remains a problem.

Table 1
Comparison of a Murchison Experimental Glass to Sioux County

	wt.%							ppm		
	SiO_2	TiO_2	Al_2O_3	Cr_2O_3	FeO	MgO	CaO	V	Sc	La
Sioux Co.†	49.5	0.60	13.4	0.32	18.8	7.2	10.3	89±12	28.9±0.6	2.4±0.2
Murchison 1180°C‡	49.2	0.60	13.3	0.33	18.0	7.0	10.2	90±8	25±5	2.3*
Nuevo Laredo†	49.5	0.89	12.1	0.26	19.8	5.5	10.3	64±2	38±1.5	3.9±0.1
Bouvante†	50.2	1.02	11.1	0.31	19.7	6.7	10.4	51±2	30.7±0.3	6.1±0.2

†From [13]. ‡From [4] and this work. *Calculated.

References: [1] Stolper E.M. (1977) *G.C.A.* **41**, 587-611. [2] Mason B. (1962) *Meteorites*. Wiley. [3] Jones J.H. (1984) *G.C.A.* **48**, 641-648. [4] Jurewicz A.J.G. et al. (1993) *G.C.A.* **57**, 2123-2139. [5] Warren P.H. (1985) *G.C.A.* **49**, 577-586. [6] Binzel R.P. and Xu S. (1993) *Science* **260**, 186-191. [7] McKay G.A. et al. (1986) *Proc. Lunar Planet. Sci. 16th.*, D229-D237. [8] Hanson B.Z. and Delano J.W. (1994) *Lunar Planet. Sci. XXV*, this volume. [9] Hanson B.Z. and Delano J.W. (1992) *Lunar Planet. Sci. XXIII*, 481-482. [10] Paslick C.R. et al. (1990)*Lunar Planet. Sci. XXI*, 936-937. [11] Kallemeyn G.W. and Wasson J.T. (1981) *G.C.A.* **45**, 1217-1230. [12] Jarosewich E. (1971) *Meteoritics* **6**, 49-52. [13] Mittlefehldt D.W., unpublished compilation. [14] Laul et al. (1989) *G.C.A.* **50**, 909-926.

REDUCED, PLAGIOCLASE-RICH CHONDRULES IN THE LANCÉ AND KAINSAZ CO3 CHONDRITES. Rhian H. Jones and Adrian J. Brearley, Institute of Meteoritics, Department of Earth and Planetary Sciences, University of New Mexico, Albuquerque, NM 87131.

Summary. Recent observations of fractionated, igneous inclusions in chondrites have raised important questions concerning the timing of melting of the parental melts relative to chondrite accretion, and the mechanism by which mixing of chondritic and basaltic components is achieved. Kurat and Kracher (1980) reported the occurrence of several pyroxene-plagioclase, basaltic inclusions in Lancé and suggested that they were derived from differentiated melts. We have studied a further three, similar inclusions in Lancé, and one in Kainsaz, in order to reexamine the genesis of such objects. Based on preliminary electron microprobe data, we suggest that these inclusions are better described as Al-rich chondrules. Metasomatic introduction of Fe, Na and K into the inclusions altered silica to ferrosalite and plagioclase to nepheline. This process may have taken place in the nebula before chondrite accretion.

Introduction. Three basaltic inclusions in the Lancé CO3 chondrite have been described previously [1]. These authors suggested that the inclusions are differentiated melts, possibly formed by impact melting, and that a secondary metasomatic event introduced Fe, Na and K into the system in a water-free environment. Several questions remain to be answered, including the nature and origin of the basaltic melts, and the timing and location of Na and Fe mestasomatism. It is also important to assess how widespread the occurrence of such inclusions may be, by searching for similar objects in other CO3 chondrites.

Observations. In this study we found three further, similar inclusions in Lancé (LB1, LB2, LB3) in a search of 3 thin sections. We also searched a total of 9 thin sections of other CO3 chondrites (ALH A77307, ALH A77003, Kainsaz, Ornans, Isna, Warrenton) and found only one similar, plagioclase-bearing object in Kainsaz (KB1). These four inclusions are 250-350 μm in size and have several properties in common. Three are strikingly round in thin section, and the fourth (LB2) has a rounded, pear-shaped morphology. LB1 has a clearly defined, fine-grained, complete rim and the other inclusions have partial rims. All the inclusions were clearly identified in an optical microscope, by the presence of laths of plagioclase occurring in an ophitic texture with pyroxene phenocrysts.

Mineralogy. The predominant phenocryst assemblage in all four inclusions consists of an intergrowth of low-Ca orthopyroxene (Wo_{3-9}), augite and plagioclase. Augite commonly occurs as rims on orthopyroxene. In LB1 and LB2, assemblages of clinoenstatite (Wo_{1-2}) are present with small olivine chadocrysts enclosed, and these are located near the edges of the inclusions. LB3 contains abundant olivine but no clinoenstatite, and neither of these minerals is present in KB1. Mean compositions of olivines and pyroxenes are shown in Fig. 1. Clinoenstatite, orthopyroxene and augite are all extremely low in FeO (Fs<2). Minor element concentrations (Ti, Al, Mn, Cr) are high, similar to those reported by [1]. Olivine is strongly zoned (Fa_{3-42} in LB1), with Fe enrichments at grain edges and around cracks. Mean olivine compositions are correspondingly higher in FeO than the associated pyroxenes (Fa_{15-31}). Plagioclase grains are altered to varying extents by a Na-rich phase that we infer to be nepheline (Fig. 2). Nepheline occurs as thin (<1μm) parallel lamellae that propagate through the crystal, suggesting that replacement is crystallographically controlled by the host plagioclase. Unaltered plagioclase compositions are in the range An_{80}-An_{90}. The Na/(Na+K) ratio of the nepheline is around 0.93 in Lancé and 0.98 in Kainsaz. Alteration is considerably less pronounced in KB1 than in the Lancé inclusions (Fig. 2). Fe,Ni metal and Fe sulfide blebs are present as a minor component in all the inclusions. The groundmass of the inclusions consists of a fine-grained intergrowth of several phases, including an FeO-poor Ca-rich pyroxene and an FeO-rich, Ca-rich pyroxene. The latter was described previously by [1], and termed ferrosalite. Compositions of this phase in LB2 and KB1 are included in Fig. 1. In KB1, the ferrosalite is present as a lacy network surrounding islands of silica, and appears to be a reaction product of Fe and primary SiO_2. This texture is not as well defined in any of the Lancé inclusions studied, where the reaction appears to be nearer completion. The primary assemblage is evidently silica-bearing, which was not noted by [1].

Discussion. Several features of the inclusions suggest that they formed by a process similar to that which formed ferromagnesian chondrules. These include their round shapes, the presence of rims, and their clearly igneous textures. Rapid cooling rates are indicated by the presence of twinned clinoenstatite. The presence of both olivine and silica indicates disequilibrium conditions. The primary assemblage crystallized in a reducing environment, as indicated by the Mg-rich compositions of the silicates and the presence of Fe,Ni

PLAGIOCLASE-RICH CHONDRULES: Jones R.H. and Brearley A.J.

metal. We suggest that these inclusions are more closely related to Al-rich chondrules [2] than to differentiated melts formed by igneous processes. The apparently high concentration of these inclusions in Lancé relative to the other CO3 chondrites indicates that formation of these objects was rather localized.

The presence of nepheline replacing plagioclase, and ferrosalite replacing silica, shows that these inclusions have experienced secondary alteration in which Na, K and Fe were added to the system, as suggested by [1]. Two different environments for this process are possible: 1) reaction with Fe-Na-K-rich vapors in the nebula, after crystallization, and 2) solid-state exchange during parent body metamorphism. The CO3 chondrites appear to have experienced an episode of metamorphism after accretion [3], so that any earlier alteration may be partially overprinted by this later event. The major characteristic of parent body alteration is elemental exchange of Fe and Mg between chondrules and matrix, but there is little evidence for major redistribution of alkalis. The style of alteration involving alkalis and Fe observed in the inclusions is very similar to that commonly observed in CAIs in CV3 and CO3 meteorites [4]. In these cases, alteration is attributed to low-temperature gas-solid exchange, probably in a nebular environment, and nepheline is a common replacement mineral. Several observations in our study lead us to believe that the principal characteristics of the inclusions were established during a period of metasomatism prior to accretion, and that the effect of parent body metamorphism is relatively minor. A similar history has been proposed for CAI in Ornans [5]. These observations include: i) The FeO enrichment in olivines in the Lancé inclusions (means Fa_{15-31}) is more pronounced than enrichments observed in comparable primary Mg-rich olivine from type I chondrules in the same chondrite (mean Fa_5, [3]), ii) The Fe/Mg ratio of the pyroxene produced by reaction with silica in KB1 is considerably higher than that expected in a chondrite of subtype 3.1, iii) There is no evidence that other chondrules or matrix in Lancé or Kainsaz have been affected by alkali metasomatism, although Lancé matrix has been incipiently altered by aqueous fluids [6], iv) The low Na abundance in bulk chondritic CO3 compositions appears to preclude the internal generation and transport of Na-rich fluids which could cause the observed style of alteration. We suggest that these Al-rich inclusions have been affected by similar pre-accretionary processes to CAI in the same chondrites.

This preliminary study shows that the Kainsaz inclusion, KB1, is less altered than any of the Lancé inclusions. This difference may be associated with parent body metamorphism, because Kainsaz (subtype 3.1) is less equilibrated than Lancé (subtype 3.4). However, it is not clear to what extent metasomatism and metamorphism are related, on the basis of the limited number of inclusions studied.

References. [1] Kurat G. and Kracher A. (1980) Z. Naturforsch. 35a, 180-190. [2] Bischoff A. and Keil K. (1984) GCA 48, 693-709. [3] Scott E.R.D. and Jones R.H. (1990) GCA 54, 2485-2502. [4] McPherson G.J. (1988) et al. Meteorites and the Early Solar System, 746-807. [5] Davis A.M. (1985) LPSC XVI, 165-166. [6] Keller L.P. and Buseck P.R. (1990) GCA 54, 1155-1163.

Acknowledgments. This work was supported by NASA grant NAGW-3347 (J.J. Papike, P.I.).

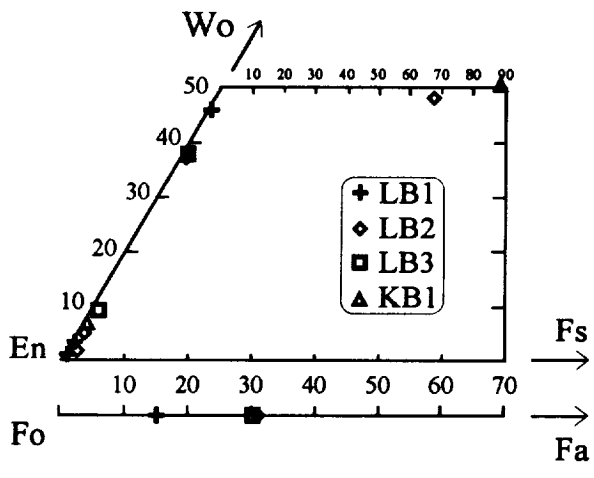

Fig.1. Mean pyroxene and olivine compositions in the four inclusions studied.

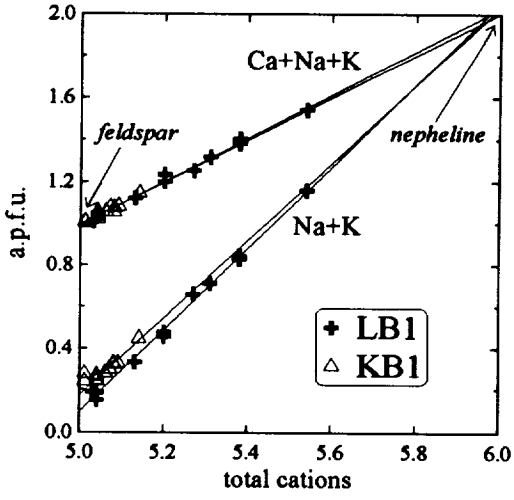

Fig. 2. Analyses of altered feldspar in LB1 and KB1, 10 μm electron beam. Alteration product appears to be nepheline.

AN ADDITIONAL ALBA PATERA - STRUCTURE IN TEMPE TERRA, MARS ?

Heinz - Peter Jöns, Technische Universität, Clausthal, Geol. Inst. Leibnizstr. 10, 38678 Clausthal-Zellerfeld, Germany

A morphologic investigation of the relief of the Tempe Terra uplands on Mars reveals the possibility that an additional Alba Patera - like feature exists in that area.

The Alba Patera - system on Mars is characterized by its countless lava flows, its central complex caldera which both together form a central shield volcano which is surrounded by a complex fracture system (countless shallow grabens). The whole system is nested in a larger fracture system, the Ceraunius Fossae which probably indicate a (fossil?) embryonic spreading system (1,2,3, 4). The diameter of the central part of the much larger general structure is appr. 400km.

Detailed investigations of the Tharsis Sutur in the area of the Tempe Terra uplands reveal a similar but much smaller structure in that area which is still unnamed. In the latter case a small volcano with numerous individual flows but without a caldera is nested in a set of countless grabens of the Tharsis Sutur which roughly surround the western half of the volcano. Its eastern flank is surrounded by numerous small arcuate lineations (very narrow grabens and fractures) which cut the grabens of the Tharsis Sutur (arrows 1-3). Hence, the activity which led to the origin of thoses smaller grabens and fractures has been younger then the last tectonic activity of the Tharsis Sutur.

Both features, the Alba Patera - system as well as the Tempe Terra - volcano, are remarcably flat. Alba Patera is roughly 7 000m high, whereas the unnamed Tempe Terra - volcano is not detectable in the pattern of the 1 000m contour lines of the U.S.G.S. maps. That fact seems to be very important because martian shield volcanoes normally reach elevations between 18 000m and 27 000m. The central part of the Tempe Terra - structure has a diametre of roughly 100km; see Fig. 1.

It should be pointed out that the features mentioned above show many similarities with venusian coronae with many respects. Venusian coronae are very flat features with or without a flat volcano in their centre as well. In many cases they are surrounded by numerous concentric features (grabens and/or fractures). Hence, there might be a relation between martian and venusian concentric features which probably have been affected by endogenic forces (upwelling mantle plume?,5); whereas similar features have not jet been identified on Earth.

AN ADDITIONAL ALBA PATERA - STRUCTURE ON MARS? H.-P. JÖNS

Fig. 1
Alba Patera - like volcano (V) with surrounding large grabens of the Tharsis Sutur and with smaller, younger grabens and fractures (arrows 1 - 3); North at top.

References:
1) Cattermole,P. (1990), Icarus, 83, 453 - 493.
2) Raitala, J (1988), Earth, Moon, and Planets, 42, 277 - 291.
3) Jöns, H.-P. (1989), Lun. and Plan. Sci. XX, Abstr., 486 - 487.
4) Jöns, H.-P. (1991), Lun. and Plan. Sci.XXII, Abst., 663 - 664.
5) Janle, P. and Ercul, E. (1991), Earth, Moon, and Planets, Vol. 53, 217 - 232.

TEXTURAL CONSTRAINTS ON THE FORMATION OF ALTERATION PHASES IN CM CHONDRITES

L. H. Joseph[1], L. B. Browning[2], M. E. Zolensky[3], [1]Department of Geological Sciences, University of Rochester, Rochester, NY 14627, [2]Department of Geological Sciences, University of Tennessee, Knoxville, TN 37996-1410, [3]Solar System Exploration Division, NASA Johnson Space Center, Houston, TX 77058.

Although it is generally believed that the secondary alteration phases observed in CM chondrites resulted from parent body reactions [1], the influence of nebular processing can not yet be dismissed [2]. We have analyzed 5 CM falls using optical and electron microscopy to construct a comprehensive pictorial reference set of textural and mineralogical associations bearing on the origin of alteration products in these meteorites. Our analyses support pervasive aqueous alteration on the CM parent body, but do not exclude the possibility of minor nebular alteration.

Most isolated anhydrous silicates display extensive embayments with phyllosilicate infillings that branch into the surrounding matrix (Figure 1). Gradational compositional boundaries between the remnant crystals, adjacent phyllosilicates and surrounding matrix support the production of phyllosilicates by in situ reactions between anhydrous matrix phases and fluid. Isolated anhydrous silicates are also, in general, more extensively embayed than chondrule phases, which supports the infiltration of fluids in a parent body setting because the high permeability of the fine-grained matrix, and high surface-to-volume ratios of the individual crystals would result in preferential alteration of isolated matrix crystals. However, a few fractured chondrules maintain relatively sharp boundaries between chondrule phyllosilicates and surrounding matrix. This distinction between chondrule and matrix phyllosilicates suggests the mechanical mixing of partially altered chondrules with fine-grained matrix. Alternatively, some brecciation may have continued after alteration was complete.

Phyllosilicate- and carbonate-filled veins have been observed in CI chondrites and demonstrate aqueous alteration in a parent body setting [3,4]. We observe phylosilicate veins extending from chondrules into the matrices of several CM chondrules. Vein phyllosilicates typically have a larger grain size than the surrounding alteration products and are oriented with their long dimensions roughly perpendicular to the vein walls. Veins are filled with Mg-rich serpentines, which is also consistent with previously noted trends from Fe to Mg-rich phyllosilicates with progressive alteration [5,6]. Late-stage vein formation which cross-cuts all CM textural components is consistent with fluid flow in a parent body setting.

It is generally believed that the carbonates in CM chondrites probably precipitated from an evolved fluid on the CM parent body because the partial pressure of CO_2 within the solar nebula was probably not high enough to permit the formation of carbonates prior to the accretion of the parent body [4]. We observe phyllosicate rimming calcite crystals, which suggests that

phyllosilicates may also have formed on the parent body. Also, embayed anhedral calcite crystals imply in situ dissolution or formation rather than nebular processing.

We observe many fragile features in CM chondrites. Veins, extensions from chondrules, ponded phyllosilicates and other delicate textural components are suggestive of in-situ alteration because it does not seem probable that these fragile products of aqueous alteration would be preserved throughout the rigorous accretion and lithification processes associated with parent body formation.

Although features such as sharp boundaries between isolated olivine crystals and the surrounding matrix suggest that at least some aqueous reactions may have occurred in the solar nebula, the common occurrence of carbonates, veins, degraded remnant matrix silicates and fragile alteration products supports the predominance of parent body alteration.

References: [1] Zolensky, M. E. and McSween H. Y. Jr. (1988) in Meteorites and the Early Solar System (eds. J. F. Kerridge and M. S. Matthews), University of Arizona Press, 114-143, [2] Metzler K. et al. (1992) Geochim. Cosmochim. Acta **56**, 2873-2897, [3] Richardson S. M. (1978) Meteoritics **13**, 141-159, [4] Armstrong J. T. et al. (1982) Geochim. Cosmochim. Acta **46**, 575-596, [5] Browning L., McSween H. Y. Jr., Zolensky M. (1993) LPSC XXIV, [6] Bunch T. E. and Chang S. (1980) Geochim. Cosmochim. Acta **44**, 1543-1577.

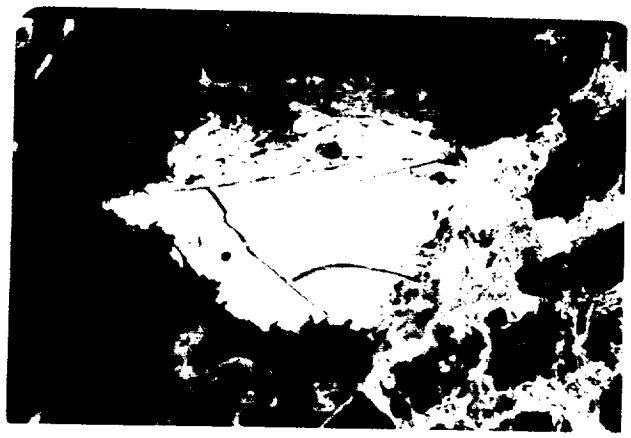

Figure 1: Isolated matrix olivine in Murchison being replaced by phyllosilicates.

^{14}C TERRESTRIAL AGES OF ACHONDRITES FROM VICTORIA LAND, ANTARCTICA;

A. J. T. Jull, E. Cielaszyk, S. T. Brown and D. J. Donahue, NSF Arizona Accelerator Mass Spectrometry Facility, University of Arizona, Tucson, AZ 85721, USA.

Achondrites are meteorites which draw more interest than ordinary chondrites, due to their probable origin in planetary-sized objects. As such, their terrestrial age or residence time on the Earth's surface is an important parameter in determining their recent history. Terrestrial age can be determined using several radioisotopes, predominantly ^{14}C [1,2] and ^{36}Cl [3]. Terrestrial ^{36}Cl [3] and ^{81}Kr ages [4] established that the meteorites collected from the main icefield at Allan Hills were generally over 100,000 years, beyond the range of ^{14}C dating. The old ages are generally thought to be due to burial and transport of meteorites in the ice. An important exception to this rule are a number of achondrites, including ALHA 81005 (Lunar), ALHA 77256 (Diogenite), and three ureilites, the ^{14}C ages for which are listed in table 1. One ordinary chondrite from the main icefield (ALHA 77262, H4) has a short terrestrial age [5]. We suggest that these meteorites of low terrestrial age must have fallen directly onto the ice and cannot have been transported appreciable distances. For the Allan Hills Far Western Icefield, younger terrestrial ages, almost all of which are <40kA are observed [3,6]. We have determined over 50 ^{14}C ages on all types of meteorites from this icefield [6], of which five new results on achondrites are listed in table 1. ^{14}C is extracted from meteorite samples by melting 0.2-0.5g of crushed sample with an iron flux, in a flow of oxygen. Evolved gases are passed through an MnO_2 trap to remove sulfur compounds, and then trhough CuO/Pt at 450°C, converting all carbonaceous gases to CO_2. The CO_2 is collected and its volume measured. The CO_2 is then converted to graphite for accelerator mass spectrometry. Procedures are discussed in detail in earlier papers [1,2]. In this paper, we report on some new ^{14}C terretrial age measurements on interesting ureilites, basaltic achondrites and SNC meteorites.

Ureilites: We have studied the ^{14}C ages of a number of ureilites. The ages of the meteorites from three different location show groupings of ages at around 7-8, 11-13 and 22-24 kA. There is a ureilite from the main icefield, ALHA 77257 which has a long terrestrial age of >44kA by ^{14}C, and which was determined by Nishiizumi to have a ^{36}Cl age of 360 ± 90 kA [3]. From the ^{14}C content, it is difficult to assume that ALH 82106 and ALH 82130 are necessarily paired, as suggested by compositional data [7]. Our data suggests that all these meteorites may represent different falls.

SNC Meteorites: We now have ^{14}C ages on three meteorites, EETA 79001 which has an age of about 11-12 kA [8], ALH 84001 which is about 6.5 kA and LEW 88516 having an age of about 21 kA. ALHA 77005, which was the first shergottite discovered in Antarctica has a long terrestrial age of 200 ± 80 kA [3]. Again, available evidence from physical locations, differences in composition and exposure and terrestrial ages argues against any pairing.

Eucrites and diogenites: In general, ^{14}C ages of eucrites from Antarctica tend to be at the limit of ^{14}C dating [1,5]. Eucrites ALHA76005, ALHA78132, ALHA81011, EETA 79004, EETA 79005, EET 83235, PCA 82502, diogenite EETA 79002 [5] all have limit ages (>40kA) for ^{14}C. The terrestrial ages of some of these meteorites have been measured using ^{36}Cl or ^{81}Kr, specifically ALHA 78132 (120 ± 50 kA), EETA 79004 (250 ± 40 kA), EETA 79005 (180 ± 30 kA) and PCA 82502 (310 ± 30 kA) [3,4]. Few of these basaltic achondrites seem to show low terrestrial ages. The exceptions are ALH 85001, LEW 86001 and LEW 87295, reported below and ALHA 77256 (10.5 kA) [5].

It is not clear why there should be such a difference in terrestrial age distribution between different groups of achondrites. Although the statistics of small numbers makes any comparisons weak, there does seem to be a trend. Some of these differences may be due to the lack of resistance to weathering, which must be a problem for the SNC meteorites in particular. The composition and physical characteristics of eucrites and diogenites must make them more resistant to destruction by weathering. This hypothesis creates a problem, however, if the terrestrial ages of the SNC meteorites are compared to the 10 Antarctic meteorites of lunar composition, only one of which has an apparently young terrestrial age, 18kA for ALHA 81005, and a second, EET 87521 which is between 44-60 kA [3]. If more SNC meteorites had been destroyed by weathering, then there must have been a greater flux of SNC meteorites at the earth's surface than for lunar meteorites. This seems unlikely, as if SNC meteorites come from Mars, it would be expected that there should be one or a very few events producing the meteorites and secondly,

fewer meteorites should reach the earth. This suggests that the young terrestrial ages of the three SNC meteorites, especially when combined with their low exposure ages, are due to the timing of the breakup of some larger object, which allowed the meteorites to arrive in a geologically brief time span of 6 to 22 kA. If we assume that the transit times for these meteorites in space are brief, this puts a serious constraint on the timing of either the breakup of a larger heterogenous SNC parent meteoroid. If the meteorites were ejected independently from Mars, their arrival in this relatively short time span is a similar constraint.

References: [1] Jull A. J. T. et al (1989), GCA, **53**, 2095-2099. [2] Jull A. J. T. et al (1993), Meteoritics, 28, 188-195. [3] Nishiizumi K. et al (1989), EPSL, **93**, 299-313. [4] Freundel et al (1986), GCA, **50**, 2663. [5] Jull, A. J. T. et al. (1989), Lunar Planet. Sci. XX, 488-489. [6] Jull, A. J. T. et al. (1993), Meteoritics, 28, 376. [7] Delaney, J. S. and Prinz, M. (1989) Smithson. Contrib. Earth Sci., 28, 65-86. [8] Jull, A. J. T. and Donahue, D. J. (1988), GCA, 52, 1309-1311.

Table 1: ^{14}C terrestrial ages of some achondrites from Victoria Land.

Meteorite	Class	^{14}C (dpm/kg)	Terrestrial Age (kA)
		Allan Hills Main Icefield	
ALHA77257	Urei	<0.25	>44[1]
ALHA78019	Urei	13.1 ± 0.9	12.0 ± 1.3
ALHA81101	Urei	21.8 ± 0.3	7.3 ± 1.3
		Far Western Icefield	
ALH 82106	Urei	22.4 ± 1.5	7.1 ± 1.4
ALH 82130	Urei	11.7 ± 0.2	13.0 ± 1.3
ALH 84136	Urei	14.5 ± 0.9	10.7 ± 1.4
ALH 84001	SNC	27.9 ± 0.5	6.5 ± 1.3[2]
ALH 85001	Euc.	44.9 ± 0.6	2.5 ± 1.3
		Elephant Moraine	
EET 87517	Urei	4.22 ± 0.16	21.4 ± 1.3
EET 83225	Urei	18.5 ± 0.4	8.7 ± 1.3
EET 87720	Urei	3.1 ± 0.6	23.8 ± 2.0
		Lewis Cliff	
LEW 88516	SNC	4.51 ± 0.24	21.5 ± 1.4
LEW 87295	Euc.	4.5 ± 0.2	25.0 ± 1.5
		Pecora Escarpment	
PCA 82506	Urei	13.2 ± 1.0	11.5 ± 1.0[1]

[1] Jull et al. [5]. [2] A value of 11 ± 1 kA was reported earlier [5].

EVIDENCE FOR AN IMPLANTED SOLAR COMPONENT OF ^{14}C IN LUNAR SAMPLES; A. J. T. Jull[1], D. Lal[2] and D. J. Donahue[1]. [1]NSF Arizona Accelerator Mass Spectrometry Facility, The University of Arizona, Tucson, AZ 85721. [2]Geophysical Research Division, Scripps Institution of Oceanography, University of California, San Diego, La Jolla, CA 92093.

We present evidence that suggests an implanted ^{14}C component in the very surfaces of lunar samples. It has been known since the first Apollo 11 soils were analyzed [1] that lunar soils contain large amounts of solar gases. Begemann et al [2] observed high surface values of 72 ± 11 dpm/kg ^{14}C in lunar rock 12053, a similar result for rock 12002 was found by Boeckl [3]. Begemann et al [2] suggested this could be due to a solar-implanted ^{14}C component, although Boeckl's interpretation was of an enhanced solar-cosmic-ray (SCR) flux producing the ^{14}C. Measurements of SCR ^{14}C in lunar rock 68815 support an SCR explanation for most of these effects, but it is possible that some implanted ^{14}C was removed during the pretreatment procedure of Jull et al [4]. Fireman (1978) showed evidence for some enhanced ^{14}C in surface soils 73221 and 10084. In this new series of experiments, we improve on the stepwise-heating experiment of Fireman [5,6], using an acid-etching technique, smaller samples and accelerator mass spectrometry to measure ^{14}C, as well as to investigate the possibility of separating the various ^{14}C components. Wieler et al. [7] and Rao et al. [8] have used selective-etching for rare-gas studies. With this information we can set upper limits to the amount of ^{14}C which can originate from implanted ions from solar-wind or suprathermal events [7], or solar-flare implantation [7,8]. Using a weak HF etching technique, we present evidence for implanted ^{14}C in rock 68815, and in surface soils 73221 and 10084.

Samples of lunar soil (0.17-0.2g) are loaded into a teflon container, which is placed inside a stainless steel vacuum bomb. In each case, frozen HF solutions had previously been added to the container. The sample is then pumped and carrier gases of CO and CO_2 added. For the first etchings, 5-6cm^3 0.06M HF was used. The vessel is closed off with a specially-designed teflon valve, and heated to 80°C for 24 hr. After this time, the carrier gases are recovered. A second experiment is then performed by recovering the residual lunar soil, and adding it to a second teflon container, this time with stronger HF. This procedure is repeated up to 5 times. In each case, the carrier gases are recovered. All HF solutions were recovered for ICP elemental analysis. The gases are covered to graphite and analyzed by accelerator mass spectrometry (AMS).

Lunar soils 73221, 73241 and 73261 were studied, which come from the Apollo 17 trench sequence at station 3 site, an area covered with light highland soils from the adjacent South Massif [8]. Soil 73221 comes from a depth of 0 to 0.5cm, and 73241 from a depth of about 5cm, and 73261 from a depth of 5-10cm [8]. Soil 10084 was a large surface sample from roughly 0-5cm collected during Apollo 11 [9]. We have also studied a sample of surface scrapings of rock patina and chips from 68815 [4].

The ^{14}C contents of the CO and CO_2 resulting from the HF etching studies are given in figure 1. Sequential etching of increasing strength from 0.06M to 8.4M HF, or 50% (26M) HF for 73221, were used. An interesting observation is that the bulk of the cosmogenic ^{14}C is released in the fourth and fifth etching steps. Samples 73241 and 73261, which were recovered from locations where there should be no SCR or implanted ^{14}C components confirm this. A large amount of ^{14}C not related to dissolution of much sample (see figure 1), is released in the third etching step in sample 73221, using 6cm^3 of 0.16M HF. Also, the amount of ^{14}C/g Si is by far the highest for step 3, and is over ten times higher than for the adjacent samples. It is far too high to be explained by SCR effects [4,10]. We estimate the etching depth to be about 4-7u. We do not expect ^{14}C/dpm/kg soil in excess of about 70 dpm/kg for even the most surface samples from SCR effects combined with the GCR-produced ^{14}C. In the case in 73241 and 73261, where most of the ^{14}C is released in the later steps, there is no significant enhancement in the third etching step, and amounts of ^{14}C are more uniform, though some smaller variations are apparent. This depth is much deeper than the 300-500A (0.03-0.05u) expected for solar-wind implantation. Similar results to that found for 73221 were also found for soil 10084. The surface sample of rock 68815 was subjected to a similar, but milder series of etching experiments. In contrast to the soil samples, the scraping samples from 68815 are from a surface of known position and orientation. The first three successive treatments of 0.0003 moles HF should have removed less than about 6.2mg (5.7%) of the material, which is estimated to be about 2.7×10^{-3} cm^3, but released at least 38 dpm/kg ^{14}C, over 40% of all the ^{14}C in the sample. We estimate the first three etchings would have removed about 9 microns of rock, in contrast to the 3 microns for the soil etchings. This depth is similar to that at which

Rao et al. [8] observed implanted solar He. The total ^{14}C results from the second and subsequent etchings of 68815, 297 fit very well with our previous estimates of SCR produced ^{14}C (approx 25 dpm/kg) and GCR (25 dpm/kg). The remaining surface excess of 38 dpm/kg (1.65 X 10^8 ^{14}C/g) at an estimated depth of 9u is ascribed to an implanted component. We can estimate the magnitude of this implanted ^{14}C using the surface-area estimate of about 26 cm^2/g for this sample, which gives us 6.35 X 10^6 ^{14}C, or a rate of 2.46 X 10^{-5} $^{14}C/cm^2/s$. The $^{14}C/H$ ratio of this implanted component would be 1.23 X 10^{-13}. This is an important confirmation of the previous proposed ^{14}C solar component [1,5,6].

References: [1.] F. Begemann, et al. (1972), Proc. Lunar Sci. Conf. 3rd, 1693-1702. [2.] P. Eberhardt, et al. (1970) Proc. Apollo 11 Lunar Sci. Conf., 1037-1070. [3.] R. S. Boeckl (1972), Earth Planet. Sci. Lett., 16, 269-272. [4.] A. J. T. Jull, D. J. Donahue and R. C. Reedy (1992) ^{14}C depth profile in lunar rock 68815. Lunar Planet. Sci. XXIII, 639-640. [5.] E. L. Fireman (1977) Proc. Lunar Sci. Conf. 8th, 3749-3754. [6.] E. L. Fireman (1978) Proc. Lunar Planet. Sci. Conf. 9th, 1647-1654. [7.] R. Wieler et al. (1986), Geochim. Cosmochim. Acta, 50, 1997-2017. [8.] M. N. Rao, et al. (1993), J. Geophys. Res. 98, 7827-7835. [9.] W. R. Muehlberger et al. (1973) Preliminary geologic investigation of the Apollo 17 landing site., NASA SP-330, p. 6-1 [10.] M. N. Rao et al. (1993) Geochim. Cosmochim. Acta, submitted.

Figure: ^{14}C (dpm/kg metals) released from sequential etching experiments of Apollo 17 trench soils.

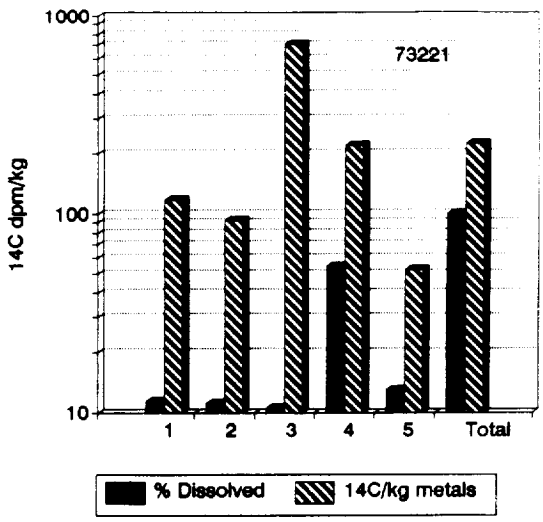

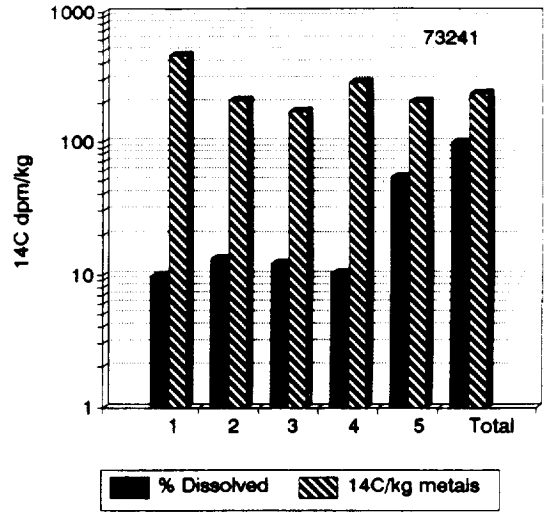

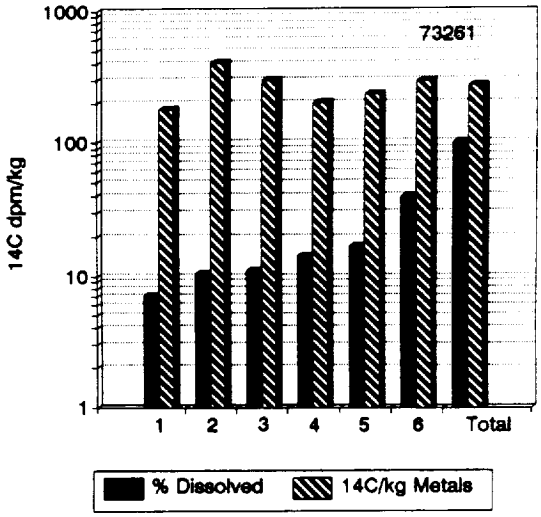

3612

PARTIAL MELTING OF THE ST. SEVERIN (LL) AND LOST CITY (H) ORDINARY CHONDRITES: ONE STEP BACKWARDS AND TWO STEPS FORWARD; A.J.G. Jurewicz, J. H. Jones+, D.W. Mittlefehldt: Mail Code C23, LESC, PO Box 58561, Houston, TX 77258; +SN4 NASA/Johnson Space Center, Houston TX 77058

This study looks at partial melting in H and LL chondrites at near one atmosphere total pressure as part of a continuing study of the origins of basaltic achondrites. Previously, melting experiments on anhydrous CM and CV chondrites showed that, near its solidus, the CM chondrite produced melts having major element chemistries similar to the Sioux County eucrite; but that pyroxenes in the residuum were too iron-rich to form diogenites *[1]*. Our preliminary results from melting experiments on ordinary (H, LL) chondrites suggested that, although the melts did not look like any known eucrites, pyroxenes from these charges bracketed the compositional range of pyroxenes found in diogenites *[2]*. We had used the Fe/Mg exchange coefficients calculated for olivine, pyroxene and melt in these charges to evaluate the approach to equilibrium, which appeared to be excellent. Unfortunately, mass balance calculations later indicated to us that, unlike our CM and CV charges, the LL and H experimental charges had lost significant amounts of iron to their (Pt or PtRh) supports. Apparently, pyroxene stability in chondritic systems is quite sensitive to the amount of FeO, and it was this unrecognized change in the bulk iron content which had stabilized the high temperature, highly magnesian pyroxenes of *[2]*. Accordingly, this work re-investigates of the phase equilibria of ordinary chondrites, eliminating iron and nickel loss, and reports significant differences from *[2]*. It also looks closely at how the iron and sodium in the bulk charge affect the stability of pyroxene, and comments on how these new results apply to the problems of diogenite and eucrite petrogenesis.

Experimental: Powdered, chemically-characterized silicate separates of Lost City (H) and St. Severin (LL) chondrites were obtained from E. Jarosewich (Smithsonian Inst., NMNH). A synthetic metal fraction, comprised of fine Ni and Fe powders using the composition of *[3]*, was mixed with the silicate to complete our starting material.

Pressed pellets of starting material (~110 mg) were "spot-welded" onto Pt or Pt-40%Rh loops. These loops had previously been doped with iron and nickel by equilibrating them with a simulated H-chondrite at high temperatures for 4-7 days. The charge was then run isothermally, under a controlled oxygen fugacity (fO_2), for between 3-5 days and, finally, drop-quenched into de-ionized water.

The furnace fO_2 was set at IW-1 (one log unit below the iron-wüstite buffer) using appropriately mixed flowing CO/CO_2 gas. Target temperatures were between 1170° and 1350°C. Since the charges were open to the gas stream, volatiles were lost. Rapid loss of the volatiles early in the run reduced the volatile-content of each charge to a low, metastable value, so that the final concentration of volatile elements depended primarily on the initial charge composition and run temperature, not run duration. Details for this technique are given in *[1]*.

Results: All charges contained melt, olivine, and metal, ±low calcium pyroxene, ±chromite, and ±sulfide. Melts plotted near the Ol-Py-Pl peritectic point used by *[4]* to describe eucritic melts. Even at the lowest temperature, 1170°C, charges contained 10-15% melt, and neither plagioclase nor a high-calcium pyroxene was observed. Figure 1 gives the calculated abundances for each silicate phase and metal as a function of temperature.

Several of the lower temperature charges retained a significant amount of sodium (melts having 1-2 wt% Na_2O; open circles in Figure 1). Melts from these charges were all consistently more plagioclase and pyroxene normative than their corresponding low-sodium counterparts, being more siliceous and having lower CaO/Al_2O_3 ratios. Consequently, the modal abundance of pyroxene in these charges was smaller (c.f., *[5] and Figure 1*). The other volatile showing significant variability, sulfur, did not measurably affect the silicate phase equilibria.

The effect of bulk iron on these systems can be seen in part in Table 1, which compares results from 1275°C and 1325°C Lost City charges *[this study, 2]*. Because bulk iron was not lost during this study, Mg#s for melt, olivine and pyroxene in the new charges were generally lower than previously reported *[2]*. In general, the differences were in (1) the phase abundances observed at each temperature and (2) the pyroxene disappearance temperature. Specifically, an increase in the bulk iron corresponded with a decrease in the amount of pyroxene, a corresponding increase in the amount of olivine, and a slight increase in the amount of metal in the residue; however, the amount of melt observed was basically unchanged. In *[2]*, pyroxene was present at all temperatures, persisting even at 1325°C. In contrast, in this study, pyroxene disappeared at lower temperatures: at ~1220°C in Lost City ($Wo_2\ En_{66}\ Fs_{32}$); just above 1328°C in St. Severin ($Wo_1\ En_{75}\ Fs_{24}$).

Implications for Eucrite and Diogenite Petrogenesis: Although the conclusions of *[2]* need to be revised slightly, the gist of the arguments remain intact. Melting of CM, CV, H and, by inference, CO chondrites leaves a residue that is dominated by olivine, making these chondrites poor candidates for the parent material of diogenites.

However, our 1180°C Murchison partial melts had major element contents within 3% of those measured for Sioux County, and melts of Allende at 1180°C were similarly close to Ibitira *[1]*. Conversely, the LL chondrites may have sufficient pyroxene in the residuum to produce diogenites and, above ~1200°C, St. Severin pyroxenes have CaO and Al_2O_3 abundances (0.5-2 wt% CaO; 0.5-1 wt% Al_2O_3) which overlap those in diogenitic pyroxenes *[7]*. However, their low temperature melts do not closely resemble any of the main group eucrites.

Thus, the long-standing problem of relating diogenites and eucrites remains unresolved. Currently, CO or CM chondrites appear to be the best choices for producing eucrites *[6]*, but a more siliceous composition (e.g., LL chondrites) seems necessary for the production of diogenites. The CaO and Al_2O_3 abundances in St. Severin pyroxenes reinforce the idea that the diogenites crystallized from a parent with chondritic relative abundances of these elements *[9]*; and the LL pyroxenes which have Mg#s approaching that of the average diogenitic pyroxene (~74) also have an appropriate CaO content (~1.0-1.5 wt% *vs.* ~1.2 wt% for diogenites). However, the match in Mg# is tenuous. Since the Mg# of ~74 for diogenitic pyroxene is an *average* value, and since only our highest temperature pyroxenes have Mg#s ~74-75, then the average Mg# for the entire suite of experimental pyroxenes (~70-71) is too low to produce diogenites. One way to attain a higher overall Mg# is to remove FeO from the silicate system by increasing the amount of Fe^0; e.g., by lowering the fO_2. This could mean that the diogenite parent was similar to an LL chondrite, but slightly more reduced than in our experiments (~IW-1.5 *vs.* ~IW-1).

Regardless, we have yet to demonstrate that one natural chondrite composition can produce both eucrites and diogenites in a single petrogenetic scenario that elegantly conforms to all of the geochemical constraints. The lack of a unifying model is worrisome, as there is physical evidence that both lithologies coexist on a single, small body.

References: *[1]* Jurewicz *et al.* (1993) *GCA* **57** 2123-2139;*[2]* Jurewicz *et al.* (1993) *LPSC* **XXIV** 739-740 (abst.); *[3]* Jarosewich (1990) *Meteoritics* **25** 323-337; *[4]* Stolper (1977) *GCA* **41** 587-611; *[5]* McGuire *et al.* (1994) *LPSC* **XXV**, *this volume*; *[6]* Jones *et al.* (1994) *LPSC* **XXV**, *this volume*; *[7]* Mittlefehldt (1994) *GCA*, *in press*; *[9]* Jurewicz *et al.* (1994) *in preparation.*

Figure 1. Calculated modal abundances for silicates and metal in St. Severin and Lost City. Data from 1325°C charges which gained or lost FeO, and from charges which retained more than 1 wt% Na_2O in the melt, are given as open symbols.

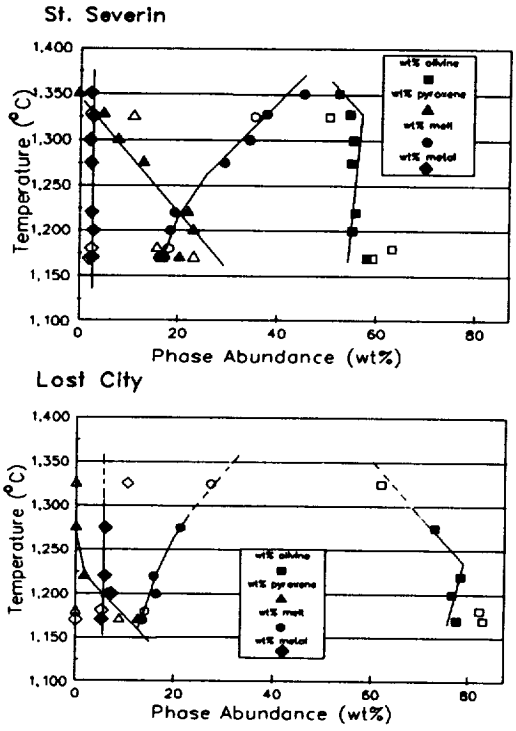

Table 1. Melt compositions, Mg#, and the silicate phase assemblages for pairs of Lost City charges (one low bulk iron; one relatively unchanged) at two temperatures. Note: decreased FeO stabilizes pyroxene.

Temperature	1325	1325	1275	1275
Status of Bulk Fe*	small iron gain (~6%)	iron loss (~40%)	no measurable loss or gain	iron loss (~35%)
Silicate phase assemblage	ol-melt	ol-melt-low calcium pyroxene	ol-melt	ol-melt-low calcium pyroxene
SiO_2	44.92	50.94	47.18	50.79
TiO_2	0.26	0.27	0.31	0.39
Al_2O_3	7.00	7.25	8.30	11.02
FeO	31.06	20.36	28.24	17.33
MnO	0.37	0.46	0.35	0.42
MgO	11.24	13.72	9.52	11.27
CaO	5.42	5.83	6.34	8.07
Na_2O	0.03	0.01	0.01	0.06
Cr_2O_3	0.74	0.79	0.67	0.67
Total	101.05	99.65	101.04	100.05
Mg#	39.21	54.56	37.54	53.69
CaO/Al_2O_3	1.41	1.46	1.39	1.33
$^{ol/m}K_{D\ Fe/Mg}$	0.34	0.35	0.35	0.37
$^{px/m}K_{D\ Fe/Mg}$	–	.29	–	.33

*all iron as FeO.

3613

Preliminary Results of Sulfide Melt/Silicate Wetting Experiments in a Partially Melted Ordinary Chondrite. Stephen R. Jurewicz and John H. Jones, Mail Code SN4, NASA-Johnson Space Center, Houston, Texas 77058

Recently, mechanisms for core formation in planetary bodies have received considerable attention. Most current theories emphasize the need for large degrees of silicate partial melting (40-50 vol.%) to facilitate the coalescence and sinking of sulfide-metal liquid blebs through a low strength semi-crystalline silicate mush, e.g. [1, 2]. This scenario is based upon observations that sulfide-metal liquid tends to form circular blebs in partially molten meteorites during laboratory experiments [3, 4]. However, recent experimental work by Herpfer and Larimer [5] indicates that for some sulfide-Fe liquids (particularly eutectic Fe-S liquid) have wetting angles at and slightly below 60° in an olivine aggregate, implying an interconnected melt structure at any melt fraction. Such melt interconnectivity provides a means for gravitational compaction and extraction of the majority of a sulfide liquid phase in small planetary bodies without invoking large degrees of silicate partial melting. Because of the important ramifications of these results, we conducted a series of experiments using H-chondrite starting material in order to evaluate sulfide-liquid/silicate wetting behavior in a more complex natural system.

Experimental: An ordinary H-chondrite was selected as a starting material for several reasons: 1) high metal and sulfur contents, 2) a simple mineralogy comprised predominantly of olivine and pyroxene, and 3) its common nature suggests that it is a likely starting material for many asteroids. A two gram sample of the Benld (H6) chondrite was obtained from the Chicago Field Museum of Natural History. Benld is a typical H6 chondrite composed of olivine, pyroxene, plagioclase and substantial metal and sulfide [6]. The sample was pulverized and then ground under acetone in an agate mortar to a very fine powder. The silicate and sulfide fractions have an estimated average grain size less than 10 microns while the Fe-Ni metal particles were approximately 100 microns. An extremely fine powder increases the surface area (and subsequently the surface energy) and lowers the diffusion distance that atoms must travel to get to a grain boundary, thus reducing the time needed to attain textural equilibrium [7].

The experiments were run in a piston cylinder apparatus at 10 kb pressure and temperatures of 1000°C, 1100°C, and 1150°C. Sample containers were made of either crushable MgO or fired pyrophyllite. A standard piston cylinder assembly was used with the thermocouple located 1mm from the top of the capsule. The temperature gradient over the sample is estimated to be no more than 10°C. Fourteen day run durations were used in an effort to approach textural equilibrium. After each run the charge was sectioned, mounted, and polished for analysis. Electron probe analyses were performed to check mineralogy, and high resolution SEM photographs were used for wetting angle measurements. Angle measurements were made from photographs using a very precise goniometer.

Results: The microstructure obtained from the 1000°C experiment is illustrated in Figure 1. As is apparent from the scale bar in the figure, even after two weeks at 1000°C the grain size of the silicate matrix was so small that it was very difficult to measure wetting angles with any degree of accuracy. However, 91 measurements were made from the photographs. Because of the difficultly in making these measurements, it was not possible to accurately separate the angles for different silicate phases. The angle measurements indicate that the median sulfide melt/silicate wetting angle from all phases is approximately 77°. However, examination of the frequency distribution for this experiment shows at least two potential peaks: one around 60 degrees and a second around 80 degrees. Given the complex mineralogy of the charge, multiple peaks are a possibility. The predominant silicate phases were determined to be olivine, two pyroxenes, and plagioclase. Silicate phases were categorized during angle measurements based on grey tone variations. This does not allow for accurate phase determinations (e.g. cpx vs. opx) and may be the primary cause for multiple peaks. However, it is also possible that the charge was not completely texturally equilibrated. The solid Fe-Ni metal in the charges remained as large grains and the silicate phases contacting them developed a rounded texture.

The 1000°C run was the only run made in a crushable MgO capsule. During the initial stages of the run, some of the sulfide liquid rapidly infiltrated the grain edge porosity of the capsule. This infiltrating behavior led to thermocouple contamination in the higher temperature runs, so fired pyrophyllite was subsequently used as the sample container.

The microstructure of the 1100°C experiment is illustrated in Figure 2. In contrast to the 1000°C run, the silicates in the 1100°C experiment underwent substantial grain growth. The larger grain size facilitated making angle measurements for specific phase contacts. However, the problem of determining mineralogy from grey tone

variations on the photographs still leads to multiple or ill-defined angle peaks on the frequency distribution. Approximately 60 measurements each were made for olivine/sulfide-liquid, olivine/pyroxene/sulfide-liquid, and pyroxene/pyroxene/sulfide-liquid wetting angles. As in the previous experiment there appears to some tendency for multiple angle peaks. The olivine/olivine/sulfide contacts appear to have several angle peaks with a median angle around 78°. The pyroxene/olivine/sulfide angles show a broad peak with a median angle of 73° and the pyroxene/pyroxene/sulfide-liquid angles have a median of 65°. The Solid Fe-Ni metal decreased in abundance but texturally appeared similar to the previous experiment.

The 1150°C experiment was similar to the 1100°C experiment in general texture but the silicate grain size had increased still further. Between 30 and 60 angle measurements were made for each silicate phase/sulfide-liquid combination with the same phase determination problems. The apparent olivine/olivine/sulfide-liquid, olivine/pyroxene/sulfide-liquid, and pyroxene/pyroxene/sulfide-liquid median angles were 99°, 83°, and 82°, respectively.

Discussion: The important result from our experiments is that the sulfide-liquid wetting angles vary in a relatively small range between 60 and 100 degrees. Although the complex silicate mineralogy of our ordinary chondrite system prevents an accurate assigning of specific sulfide-liquid contact angles to silicate mineral combinations, this range of angles suggests that it is highly unlikely that complete sulfide melt interconnectivity could be maintained at liquid fractions below 1 or 2 vol. % [8]. Conversely, it also implies that there will be at least some sulfide liquid interconnectivity with only a few volume percent of melt. Such interconnectivity could provide a pathway for gravitational segregation of a least a portion of the sulfide metal liquid. However, the complete segregation of both metal and sulfide from a silicate matrix is a complex process in which wetting behavior is only one part.

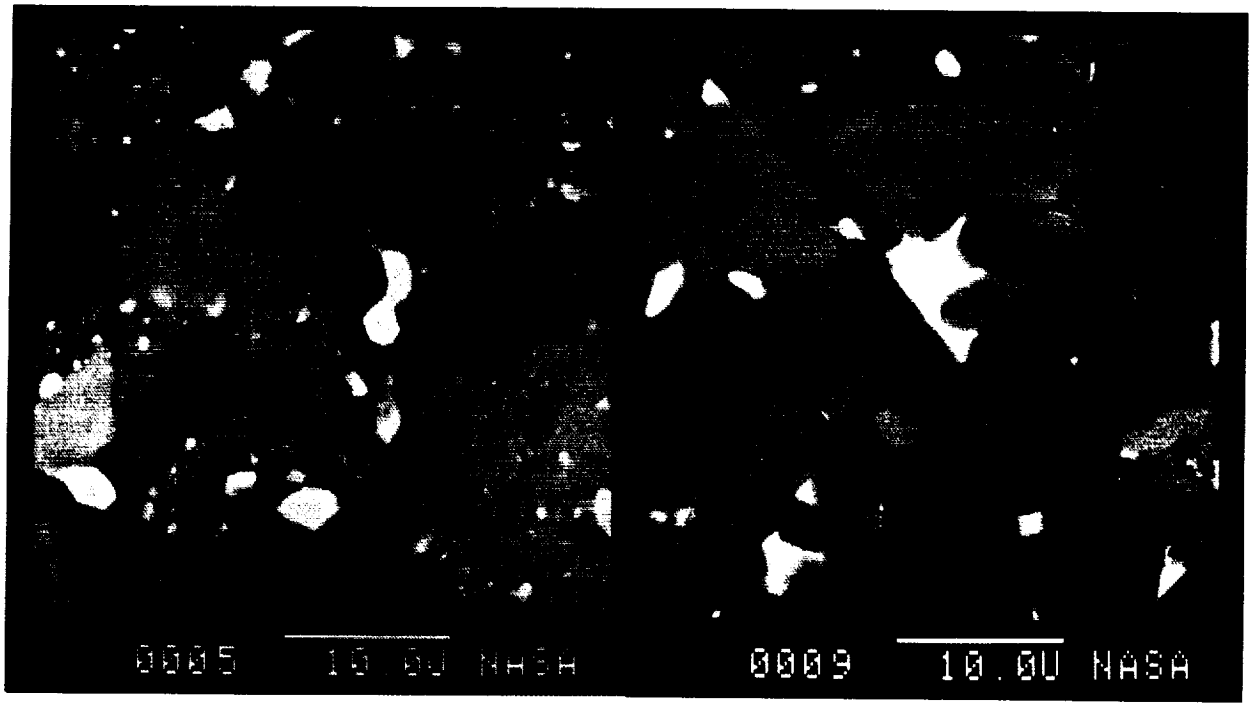

Fig. 1 **Fig. 2**

References: [1] Stevenson D.J.(1990) In Origin of the Earth, 231-249. [2] Taylor G.J. (1992) *J. Geophys. Res.* **97**, 14717-14726. [3] Takahasi E. (1983) *Mem. Nal. Inst. Polar Res. Spec. Issue Jpn.* **30**, 168-180. [4] Walker D. and Agee C.B. (1988) *Meteoritics*, **23**, 81-91. [5] Herpfer M.A. and Larimer J.W. (1993) *Meteoritics* **28**, 362. [6] Mason B. (1963) *Geochim. et Cosmochim. Acta* **27**, 1011-1017. [7] Lifshitz I.M. and Slyozov V.V. (1961) *J. Phys. Chem. Solids*, **19**, 35-50 [8] von Bargen N. and Waff H. (1986) *J. Geophys. Res.* **91**, 9277-9282

RADAR IMAGING OF "OVERSPREAD" BODIES USING COHERENT FREQUENCY HOPPING; R. Jurgens, L. Robinett, M. Slade, D. Strobert; Jet Propulsion Laboratory; B. Flores; University of Texas at El Paso

The quest for higher quality radar images of planets, moons, and asteroids and comets using ground-based radar has been satisfied primarily by moving to shorter wave lengths where greater antenna gain is possible for a given collecting area. Higher transmitter power and lower receiver system temperatures have also helped, but larger and more precise antenna systems provide the greatest possible improvement. Shorter wavelengths, however, have the a draw back in that the bodies to be imaged become increasingly "overspread", i.e, the product of the Doppler frequency width and the range depth is a number greater than unity. Conventional delay-Doppler processing leads to serious aliases that render the image more or less useless depending upon how large this product is. The planet Mars presents the worst case where the overspread factor is about 600 at 3.5cm wavelength.

Recently Sulzer [1] and Hagfors and Kofman [2] have demonstrated that full disk imaging of overspread targets is possible using random modulation. In this technique, a matched processing filter is formed for each delay and Doppler pixel required in the image. Harmon et al. [3,4] have demonstrated that full disk imaging of Mars and Mercury is possible using random binary phase modulation. With this approach, a given pixel in the image results from a response to a specific region on the planet, and to all side-lobes of the resolving filter responding to other places on the planet. Thus the image is contaminated by "self-noise" as well as the usual the thermal background noise. The randomization of the coding results in a statistical side-lobe pattern that tends to average to a uniform background thus permitting the desired pixel to be seen.

We have studied the use of random frequency hop coding as a technique that provides some further advantages in that out-of-band interference is less than for binary phase encoding, and the level of the side-lobes can be controlled as discussed below. The implementation of this technique is easily accomplished with programmable digital oscillators that are being used for tuning the radar receiver system. Currently these oscillators can be coherently up-dated 1000 times a second, and modifications are planned to reach 10,000. The resolution and side-lobe level depend upon the modulation bandwidth, B, the number of frequency hop states, N, the baud period, T, and the number of coherently processed bauds, M. The number of hop states is a new additional parameter that can be adjusted to optimize the image quality. The product MT controls the frequency resolution, and B and T control the range resolution depending upon the selection of the BT product. The average side-lobe level depends upon all of the

parameters in a fairly complicated manner. We are exploring this parameter space to optimize the imaging of Mercury, Mars, and the Galilean satellites.

We have calculated the variance of the side-lobes along the zero frequency axis considering N equally spaced hop frequencies from -B/2 to B/2. Each state is selected randomly from a uniform distribution. There are values of B for which the set of frequencies is orthogonal in the period T. These frequencies drive the variance to zero, however, this holds only along the zero frequency axis. Figure 1 shows a plot of the side-lobe level relative to the main peak plotted against B for three values of N, and with M set to 16 segments. The baud period is set to 1ms, and the coherence period MT is then 16ms corresponding to 62.5 Hz resolution. B_j is the modulation bandwidth, and the σ^2 correspond to values of N equal to 2, 4, and 8 hop states. We have not yet explored controlling the side-lobe structure off the zero frequency axis by use of non-uniformly weighted Fourier transforms, however, this is easily accomplished in the signal processing. The zero delay axis shows the usual $(\sin(x)/x)^2$ behavior.

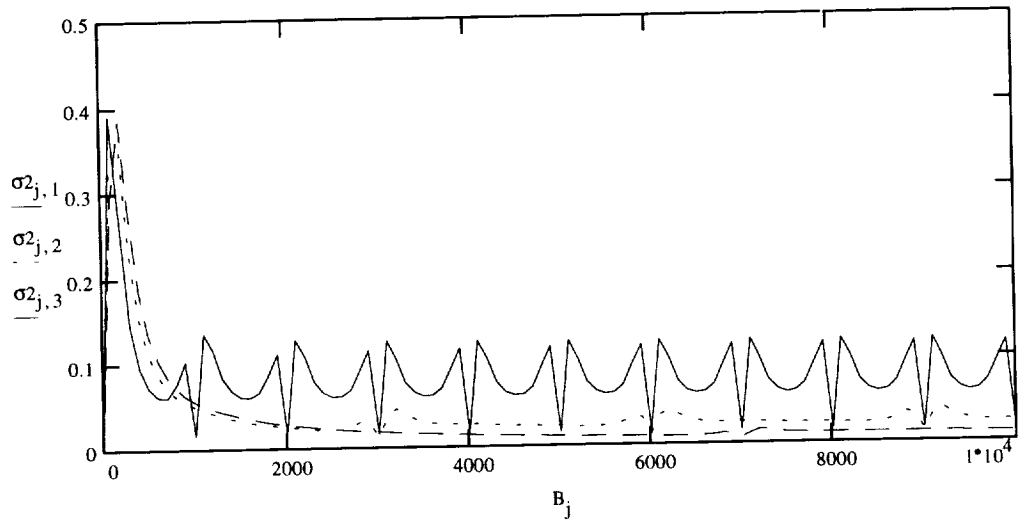

Figure 1

Relative side-lobe or variance for an unmatched frequency hop code using random uniformly distributed frequency hopping 2, 4, and 8 hop states. Other fixed parameters are: T = 1ms, and M = 16 coherently processed segments.

References:(1) Sulzer, M., Radio Science, 21, 1033-1040, 1986. (2) Hagfors, T, and W. Kofman, Radio Science, 26, 403-416, 1991. (3) Harmon, J.K., M.P. Sulzer, and P.J. Perillat, Icarus, 95, 153-156, 1992. (4) Harmon, J.K. and M.A. Slade, Science, 258, 640-643, 1992.

THE EFFECT OF OXYGEN FUGACITY ON THE PARTITIONING OF NICKEL AND COBALT BETWEEN MELT AND METAL:Arnold A.Kadik, *V.I.Vernadsky Institute of Geochemistry and Analytical Chemistry,RAS,Kosigin St.19,Moscow V 334,Russia*

Partitioning of nickel,cobalt and between metal and silicate phase has been determined in the system diopside -albite-anorthite at 1350 °C and 1 atm over the oxygen fugacity (fO_2) $10^{-5.5}$-10^{-12} atm. This range of fO_2 from Nickel-Nickel oxide (NNO) to two log units below the Iron-Quatz-Fayalite (IQF-2) buffers,span the range relevant for crystal/liqud processes in terrestrial planets. Correlations between logfO_2 and the log of the partition coefficients were observed. The unusual slops in the log D_{Ni} vs. logfO_2 correlation at high NiO concentration in melt can be explained by a strong dependence of the NiO activity in the liquid silicate composition.

METHOD: All experiments were conducted in CO_2-H_2 gas mixing furnaces. Silicate starting materials were close to albite-anorthite-diopside composition.A bead of molten sample held on a hook ,made from 1mm of thin Ni,Co wires. Gold and diopside were used as temperature calibrant and NiNiO,CoCoO as fO_2 calibrants [1]. Samples were equilibrated at constant temperature (1350 °C) and run duration between 17-24 hours. Samples were quenched by withdrawal from furnace. After separation from the loops glass were analyzed by electron microprobe.The homogeneity of Ni,Co distribution in glasses and reversed experiments with initially high NiO content in mix confirmed the attainment of equilibrium .

RESULTS: In Fig 1 the metal/silicate partition coefficients *(Dm/s)* of Ni and Co (Table) are plotted *vs* the logarithm of oxygen fugacity.The data can be fitted by straight lines: $log\ D_{m/s} = A + n*logfO_2$ (1). The slopes of *log Dm/s vs. logfO*$_2$ for Co and Ni at $logfO_2$ between NNO-2 and IQF-2 and low NiO content in melt are close to 0.5-0.6 (Co=0.570+0.03,Ni=0.68+0.04).The slop of *log Dm/s vs. logfO*$_2$ for Ni at $logfO_2$ between NNO and NNO-2 and high NiO content in melt is close to 0.2 (0.21+0.08). The similar slop (0.21) for Ni was found by Schmitt at al [2] for the metal-basalt equilibrium.According to [2,3]: $logD_{m/s}=-logK_{Me}-log(vMe/vMe_{x/y})-(y/x)*logfO_2$ (2) where K_{Me}- equilibrium constant, $vMeO_{y/x}$- the coefficient of activity of the oxide $MeO_{y/x}$ in the silicate and vMe- the coefficient of activity of element *Me* in metal. For a constant of $(vMe/vMe_{x/y})$ ratio we have $n=dlog\ D_{m/s}/dlogfO_2 = -(x/y)$ (3)In this case the slope of the correlation, *n* (Eqn.1) is a measure of the number of oxygen molecules to metal atoms of the considered element in silicate liquid (Rammensee et al.,1983).The slop of the linear correlation,*n*,(Eqn.1) can comply with another condition,namely, $dlog(vMe/vMe_{x/y})/dlogfO_2=constant=b$. In this case $n=dlogD_{m/s}/dlogfO_2=-(x/y)-b$ (4) and *n* of the linear regression don't equal to (x/y) directly. The measured values of *n* may be higher or less than the values of (x/y).It means that the formal valency-states of the various species in the silicate melt,calculated according Eqn(3),may be higher (b>0) or less (b>0),than those expected.

*DISCUSSIAN.*The calculated valences for Ni and Co at *log fO*$_2$ from NNO-2 to IQF-2 agree reasonably well with those expected (2.52 for Ni and 2.28 for Co).There is no doubt that at *log fO*$_2$ from NNO to NNO-2 and high NiO content in melt (1-20 % wt.) Ni occurs in the divalent states. The calculated valency of about one (0.85) most likely reflects variations of activity coefficients with melt composition.Thus a estimation of Ni valency in melt,based on correlation of (1) may therefore be difficult. A dependence of the Ni partition coefficient on the melt composition might be expected, as it was proposed by [2].

ACKNOWLEDGMENTS: This research is supported by grant N 9305-9856 of Russian Fond of Fundamental Investigations

THE EFFECT OF OXYGEN FUGACITY ON PARTITIONING OF NICKEL AND COBALT:A.A.Kadik

REFERENCE: [1] Biggar,G.(1978) Progress in experimental petrolgy,118-120; [2] Scmitt,W at al (1989) GCA 53,173-185; [3] Rammensse, W. et al (1983) LPSC XIV,628-629; [4] Kadik ,A.A. and Holloway,J.R.(1989) LPSC XX,494-495;

Table 1. Experimental results of solubility of Ni, Co and Fe in silicate melts and calculated metal/liquid silicate partition coefficients at T=1350°C and variable oxygen fugacities.

Ni				Co		
$logfO_2$	NiO mix [% wt]	NiO in glass [% wt]	D(m/s) Ni	$logfO_2$	CoO in glass [% wt]	D(m/s) Co
- 6.2	10.0	9.52-+0.2	10.5	-8.02	29.11-+0.1	3.43
-6.2	5.2	9.10-+0.1	11.1	-8.55	18.08-+0.06	5.35
-6.2	2.2	8.87-+0.3	11.3	-8.93	7.39-+0.07	13.53
-6.2	0.0	10.12-+0.2	9.9	-9.45	6.78-+0.02	14.75
-6.7	10.0	6.92-+0.02	14.4	-10.35	1.77-+0.15	56.50
-6.7	2.2	7.06-+0.06	14.2	-11.45	0.47-+0.01	212.7
-6.7	0.0	7.18-+0.01	13.9	-12.00	0.13-+0.01	787.0
-7.4	2.2	5.93-+0.04	18.8			
-7.4	0.0	5.79-+0.09	17.3			
-8.1	2.2	3.41-+0.01	29.3			
-8.1	0.0	3.46-+0.01	28.9			
-8.6	0.0	0.88-+0.03	113.6			
-9.4	0.0	0.48-+0.02	208.3			
-11.4	0.0	0.23-+0.01	434.5			

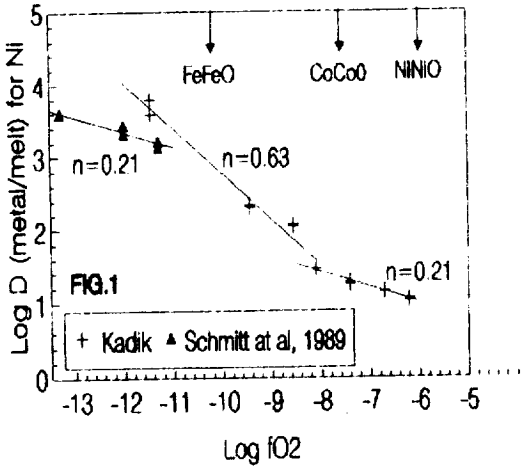

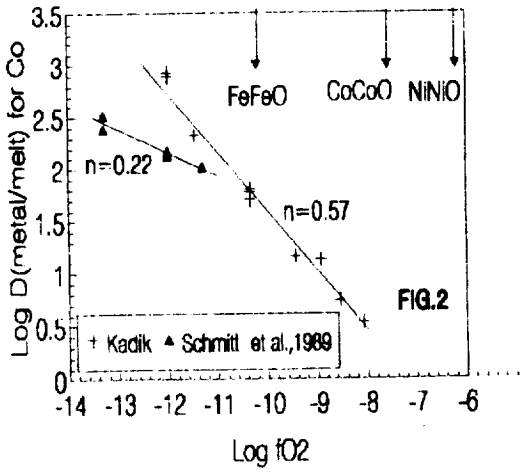

THE CO_2 FORMATION IN TERRESTRIAL MAGMAS DURING THE FLUID-ABSENT MELTING OF CARBON-BEARING ROCKS. **A.A. Kadik and S.N.Shilobreeva,** *V.I.Vernadsky Institute of Geochemistry and Analytical Chemistry,RAS,Kosigin St.19,Moscow V 334,Russia*

The experiments were made on *C(graphite)-melt-crystals equilibria for C + basaltic melt, C + basaltic melt + CPx* at 15-30 kbar and 1350-1400°C and on *C +Mg_2SiO_4, C + Mg_2SiO_4 + melt, C + (CO-CO_2) vapor+melt* for $CaMgSi_2O_6$-Mg_2SiO_4 composition at 25-40 kbar, 1400-1700°C. Experiments show, that carbon may be soluble in forsterite and pyroxene on concentration of 10-100 *ppm* and reactions with graphite lead to formation in melt 400-4000 *ppm* of CO_2. The coefficient of distribution *D* = (*C* in melt/*C* in crystal) equals about 10-100. It is shown, that fluid-abcent melting of the carbon-bearing peridotites leads to the formation of the carbon species in melts in amount of 300-1200 *ppm*.

PROBLEMS. There is general agreement that carbon dioxide plays an important role in the evolution the terrestrial basalts, but there is considerable uncertainty about the reactions, that lead to formation volatile components. It should be expected, that interaction between primary native carbon and production of partial melting of the upper mantle [1, 2]: $C(graphite) + O^{2-}(melt) + O_2 = CO_3^{2-}(melt)$ (1) may play important role in formation of CO_3^{2-}(carbonate ion) in melt. Eq.(1) shows, that the carbonate ion or the carbon dioxide content in melt in equilibrium with graphite is a function of oxygen fugacity. Next mechanism, that may control the presence of free carbon and the formation of *C*-bearing components in magmas, is the carbon solubility in minerals under mantle conditions by participating in point defect equilibria [3, 4].

EXPERIMENTS. The solubility of carbon in crystals and silicate melts was determined by registration of the beta activity from ^{14}C [5] and by the infrared determinations of species in glasses. Fig.1 shows results of experimental examinations of solubility carbon in basaltic melt with initial amount of H_2O = 0.1 % and 1.1 % wt. at 1 - 30 kbar and 1250 - 1400°C. It was found that structural sites of dissolved carbon is determined by formation of carbonate ionic complex CO_3^{2-}. The reaction between graphite and basaltic melt leads to the formation of 0.04-0.40 % *wt.* CO_2 in melt at high pressure (15 - 30 kbar, 1350 - 1700°C). In the presence of (*CO*, CO_2) vapor at low pressure (1 - 5 kbar, 1250°C.) the reactions between graphite and basaltic melt lead to formation of 0.01 - 0.03 *wt.*% CO_2. It was found influence of dissolved H_2O on the carbon concentration in melt. It increases with increasing of H_2O content in system (Fig.1). We expect reaction between carbon and melt species relating with molecular water, hydroxil and carbonate groups: $C(graphite) + 2OH^-(melt) + 2O = H_2O(melt) + CO_3^{2-}(melt)$ (2), where *O* represent a distinguishable reactive oxygen species e.g. bridging, non-bridging or free. According to Eqn.(2) melt with higher ratio of species OH^- to molecular water would have a higher concentration of carbonate ion in melt.

Beta track experiments at 20 - 40 kbar and 1400 - 1700°C on *C +* Mg_2SiO_4), *C + (*CO_2, *CO) vapor +* Mg_2SiO_4 *+ melt* equilibrium for $CaMgSi_2O_6$(60%) - Mg_2SiO)(40%) composition and on *C+basalt+ CPx* equilibrium at 30 kbar and 1400°C show, that *C* may be soluble in forsterite and pyroxene in concentration of 10 - 100 *ppm* and *D* (coefficient of distribution) = (*C in melt/C in crystal*) equals about 10 - 100. Thus carbon is incompatible element in the melt + crystals equilibria and during the fluid-absent partial melting magma will be enriched in carbon in comparison with crystalline rest .

DISCUSSION. It may be suggested, that the carbon-melt-crystal reactions during *1*) fluid - absent melting in presence some amount of free carbon (*carbon saturated equilibrium of*

THE CO_2 FORMATION IN TERRESTRIAL MAGMAS DURING FLUID-ABSENT MELTING: A.A. Kadik and S.N.Shilobreeva

melt+crystals+graphite) and *2*) fluid- absent melting of carbon-bearing minerals (*carbon unsaturated equilibrium of melt+carbon-bearing minerals*) may be reason of the carbon-species formation in basaltic magmas. The reaction between graphite and basaltic melt in th presence some amount H_2O may lead to formation in magma 0.1 - 0.5 % *wt.* CO_2, observed generally in basaltic glasses (*first case*). And CO_2 content in melt during partial melting of carbon-bearing minerals in the absent of the free carbon (*second case*) may be enough high (several hundreds *ppm*) (Fig.2). At the same time we see, that the melting must have depleted the concentration of the carbon in the crystalline rest.

ACKNOWLEDGMENTS: This research is supported by grant N 9305-9856 of Russian Fond of Fundamental Investigations.

REFERENCES: [1] Holloway, J.R et al. (1992) Eur.J.Mineral, v 4, N 1, 105-114; [2] Kadik,A.A.(1990) Proc.Indian Acad.Sci.(Earh Planet.Sci.), v 99, N 1, 141-152; [3] Freund,F. (1981) Contrib.Mineral.Petrol, v 76, N 4, 474-482; [4] Watson, E.B (1986) Geophys.Res.Letters, v 13, N 6, 529-532; [5] Senin,V.V. et al. (1991) Nucleonika, v 36, N1-12, 45-58.

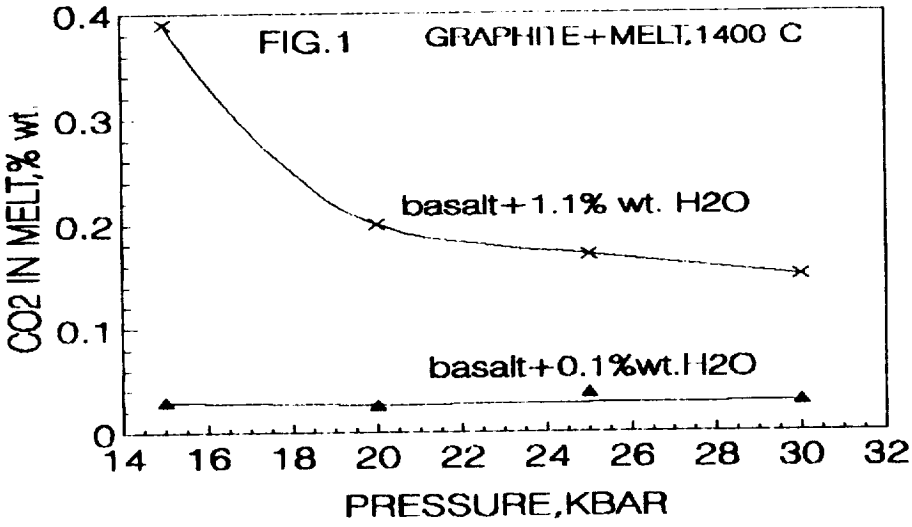

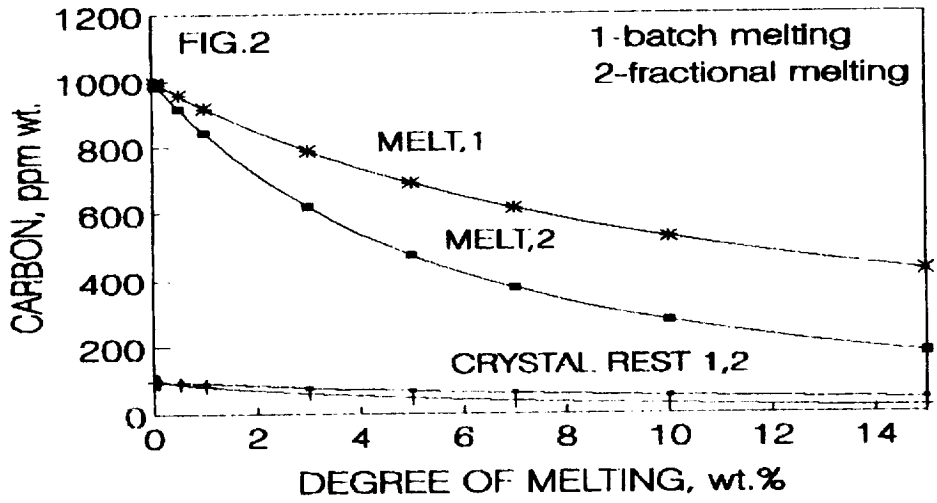

COMPOSITIONAL SIMILARITIES BETWEEN UNGROUPED LOONGANA 001 AND CV4 COOLIDGE; G. W. Kallemeyn, Institute of Geophysics and Planetary Physics, University of California, Los Angeles, CA 90024

Loongana 001 was initially determined to be a carbonaceous chondrite, possibly related to CR chondrites or ALH85085, due to its low abundance of moderately volatile elements. But it has a significantly lower abundance of Fe than ALH85085, and its olivine Fa and pyroxene Fs compositions are more Fe-rich than typical CR values. New INAA data suggest a close compositional relationship to the CV4 carbonaceous chondrite. Coolidge, although the abundance pattern of Loongana 001 was apparently disturbed by terrestrial contamination of some elements.

The Loongana 001 meteorite was found in 1990 in the Nullarbor area of Western Australia. The meteorite is weathered, with all original metal now oxidized. An initial study by Spettel et al. [1] concluded that it was a carbonaceous chondrite based on the presence of Ca,Al-rich inclusions and its relatively high matrix/chondrule ratio. They suggested that its low abundance of moderately volatile elements indicated a relationship to CR chondrites or the ungrouped ALH85085. Olivine in Loongana 001 is equilibrated with a mean composition of ~Fa11, while pyroxene is somewhat less equilibrated with a mean composition ~Fs6-7 [2,3]. This is in contrast to typical CR chondrites in which olivine compositions peak at Fa <2 and pyroxene values peak at Fs<3.

Coolidge was classified as a CV4 chondrite by Van Schmus and Wood [4]. Olivine and pyroxene compositions are Fa14 and Fs11, respectively [5]. McSween [6] further classified Coolidge as a 'reduced group' subtype of the CV chondrites, having metal more abundant than magnetite and having a relatively low matrix/chondrule ratio. He noted that a significant amount of metal was oxidized due to terrestrial weathering. Kallemeyn and Wasson [7] performed INAA analysis of Coolidge. They found refractory lithophile abundances similar to those in CV chondrites, but that abundances of moderately volatile elements were significantly lower. They concluded that Coolidge had an initial formation history similar to typical CV chondrites, but lost its volatiles during open-system metamorphism on the parent body.

Preliminary INAA data show that Loongana 001 is compositionally similar to Coolidge. Refractory lithophile element abundances (CI, Mg-normalized), excepting the REE, are similar and in the range of CV chondrites (~1.35× CI). These abundances in mean CR chondrites are much lower (~CI). The REE in Loongana 001 show a fractionated pattern, with the light-REE enriched relative to the heavy-REE and to mean CV, suggesting contamination by a terrestrial source. Moderately volatile lithophile element abundances are nearly identical to Coolidge, significantly lower than both mean CR or CV chondrite values.

Refractory siderophile element abundances in Loongana 001 are similar to Coolidge and mean CV values, but higher than mean CR values. Loongana 001 and Coolidge have similar patterns of moderately volatile siderophile and chalcophile element abundances. Two notable exceptions

are a lower abundance of Fe in Coolidge and a very high abundance of Br in Loongana 001. The Fe content of our Coolidge sample was probably atypically low due to weathering. An XRF study of another Coolidge [8] sample gives an Fe/Mg ratio very similar to our Loongana 001 ratio. The high Br in Loongana is likely due to terrestrial contamination. The abundances of moderately volatile elements in both Coolidge and Loongana 001 are significantly lower than those of either mean CR or CV chondrites.

In Fig. 1 Zn/Mn vs. Al/Mn ratios are plotted for Coolidge and Loongana 001, along with the carbonaceous chondrite groups (except CI which plots off scale to the upper left) and several ungrouped chondrites. The established chondrite groups form distinct clusters on such a diagram. Coolidge and Loongana 001 plot near each other and far from the other grouped and ungrouped chondrites.

It would appear that Loongana 001 and Coolidge are related compositionally. They are probably members of the CV clan, but whether or not they should both be classified as CV4 or as members of a new grouplet is unclear. In recent years, some 'former' CV chondrites were reclassified into the CK group. Further petrographic studies of both are needed to confirm their relationship to one another, and to help settle the question of group membership.

References: [1] Spettel B., Palme H., Wlotzka F. and Bischoff A. (1992) *Meteoritics* 27, 290-291. [2] Wlotzka F. (1992) *Meteoritics* 27, 482. [3] A. Rubin, unpublished data [4] Van Schmus W. R. and Wood J. A. (1967) *GCA* 31, 747-765. [5] Van Schmus W. R. (1969) In *Meteorite Research*, 480-491. [6] McSween H. Y. (1977) *GCA* 41, 1777-1790. [7] Kallemeyn G. W. and Wasson J. T. (1982) *GCA* 46, 2217-2228. [8] McCarthy T. and Ahrens L. *EPSL* 14, 97-102.

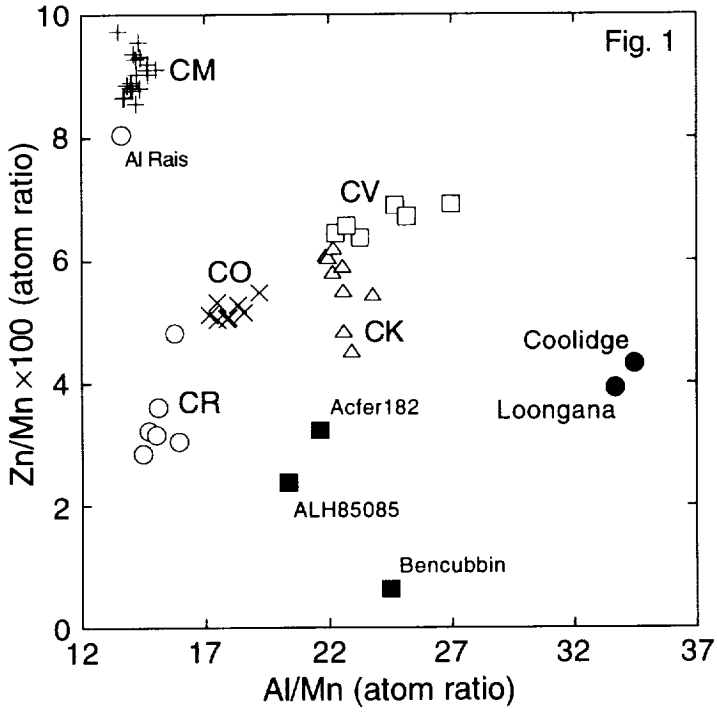

GEOCHEMISTRY OF LEW88774 AND TWO OTHER UNUSUAL UREILITES

GREGORY W. KALLEMEYN AND PAUL H. WARREN
Institute of Geophysics and Planetary Physics, UCLA, Los Angeles, CA 90024-1567

Précis: Ureilites are a large class of igneously differentiated meteorites, most likely formed as mantle partial melt residues on C-rich asteroids. A newly analyzed ureilite, LEW88774, is remarkably enriched in Al, Sc, Ca, V, Ga , rare earth elements (REE), and especially Cr (4.3 wt%), compared to all previously known ureilites. These enrichments might have been inherited from a refractory-enriched carbonaceous chondritic precursor material, or reflect trapping of a small amount of basaltic matter, or reflect local accumulation of Cr-spinel and pyroxene within a relatively melt-rich region undergoing partial melting.

We have used INAA to determine the bulk composition of LEW88774 [1,2] along with two other unusual ureilites: EET87511, which is unusually rich in orthopyroxene [3], and contains minor augite [4]; and Y791538, which is among the most magnesian ($Fo_{91.2}$) of ureilites [5]. Results (Table 1) are generally unremarkable in the case of Y791538. The EET87511 composition is more unusual, with unprecedentedly low concentrations of the four most volatile siderophile elements determined: Ni, Co, Au and Se (Fig 1; volatility increases to the right). The correlation with volatility is not necessarily as significant as the correlation with "siderophility." However, volatile lithophile elements K, Na and Ga are also extremely low in EET87511.

Results for LEW88774 are bizarre, even by ureilite standards. The Cr content, 4.3 wt%, is high, but modal recombination of microprobe data [2] similarly implies roughly 3-4 wt%. Several other elements are also greatly enriched compared to all previous ureilite data: Al, Sc, Ca, V, and Ga (and to a lesser degree, Na). REE are also at uncommonly high levels (Fig. 2). Among possibly monomict ureilites, only FRO90054 [3] appears similar. However, FRO90054 (reportedly 60% augite) is so C-poor that Grady et al. [7] have doubts as to whether it is truly a ureilite. Plots of Cr vs. Al and vs. V (Fig. 3) provide some perspective on the magnitude of these enrichments, showing them in relation to the limited dispersion amongst previously analyzed ureilites.

Several possible scenarios may be envisaged to engender the strange composition of LEW88774. Most of the enriched elements are refractory (vs. nebula gas; Figs. 1-2), so conceivably LEW88774 simply inherited its strangeness from a strange variety of chondritic precursor. On a plot of Ca vs. Sc (Fig. 4), ureilites form a trend that parallels the trend of carbonaceous chondrites, with both trends extending towards LEW88774. Chromium is seldom refractory, but Cr valences are so complex that conceivably, under temporary (and local) oxidizing conditions it might become refractory. Still, it is hard to rationalize the enrichment of Ga this way. Spitz [8] suggested that ureilites divide into two distinct groups, one of which trends toward CI chondrites, on a plot of Ga vs. Ir. However, a few of Spitz's [1992] ICP-MS Ga data seem spuriously high. An up-to-date literature compilation, including most of her data (but not for PCA82506, as her Ga is 2× higher than three literature analyses, including one by Spitz and Boynton [9]), shows no significant clustering within the ureilites, and no coherent trend in the direction of LEW88774 or CI (Fig. 5).

Some of the enriched elements (Al, Ca, Na, Ga) are plagiophile, and the REE might correlate, assuming that LEW88774 has retained slightly more basaltic matter than other ureilites (which are remarkably depleted in Al). However, Cr, V and Sc are neither plagiophile nor incompatible. Another possibility is that the weird composition was engendered by accumulation of a Cr-spinel and pyroxene in the presence of melt. Such an accumulation process requires the proportion of melt to be (locally) unusually high, at least in comparison to the general ureilite formation conditions, so that crystals move about, as opposed to being locked in a rigid crystal framework that limits them to interacting with tiny pockets of interstitial melt. This model should not be mistaken for an appeal to the venerable, but probably incorrect, cumulate model for ureilite genesis [10]. No layered intrusion is implied, only a slight degree of localized heterogeneity (one out of 40(+) partial melt residues significantly affected) at the end of the partial melting process. This model, too, has a notable drawback. Siderophile elements in LEW88774 show the classic ureilite pattern of high CI-normalized Os, Ir and Ru, in comparison to Ni, Co, Au, As, Sb and Se, and a low Ni/Co ratio. The near-chondritic siderophile abundance levels in ureilites distinguish them from most other ultramafic igneous rocks [5], and LEW88774 is especially siderophile-rich. In a ureilite that has interacted with an uncommonly high proportion of melt, siderophiles should be depleted by segregation into sinking blobs of metal.

Conceivably, all three of these models are partially correct. LEW88774 greatly extends the range of ureilite composition, and it may have formed by a process that was unusual, even by ureilite standards.

Table 1. Bulk-rock compositions of ureilites determined by INAA.

	Na mg/g	Mg mg/g	Al mg/g	K µg/g	Ca mg/g	Sc µg/g	V µg/g	Cr mg/g	Mn mg/g	Fe mg/g	Co µg/g	Ni µg/g	Zn µg/g	Ga µg/g	As µg/g	Se µg/g	Ru ng/g	La ng/g	Sm ng/g	Eu ng/g	Yb ng/g	Lu ng/g	Hf ng/g	Os ng/g	Ir ng/g	Au ng/g
EET87511	0.28	198	3.1	3.9	7.5	7.9	99	4.80	3.14	99	26.5	276	227	1.42	<0.18	*0.24*	<160	<51	*10*	<11	*37*	*9*	<47	*105*	93	5.3
LEW88774	2.70	142	13.0	121	33.4	21.5	430	43.0	3.83	147	146	1690	301	28.7	*0.43*	1.48	*570*	168	146	40	380	*62*	80	*480*	480	34
Y791538	0.27	190	2.7	*22*	12.8	11.2	100	4.33	3.10	75	103	1280	243	2.54	*0.32*	*0.60*	*360*	<70	*16*	<12	*104*	*18*	<51	*250*	230	32

References: [1] Satterwhite C. et al. (1993) *Antarctic Meteorite Newsl.* 16(1), 15. [2] Warren P. H. and Kallemeyn G. W. (1994) *LPS XXV*, this volume. [3] Berkley J. L. (1990) *LPS XXI*, 69-70. [4] Score et al. (1988) *Antarctic Meteorite Newsl.* 11(2), 18. [5] Goodrich C. A. (1992) *Meteoritics* 27, 327-352. [6] Boynton W. V. and Hill D. H. (1993) *LPS XXIV*, 167-168. [7] Grady M. M. and Pillinger C. T. (1993) *LPS XXIV*, 551-552. [8] Spitz A. H. (1992) *LPS XXIII*, 1339-1340. [9]. Spitz A. H. and Boynton W. V. (1991) *Geochim. Cosmochim. Acta* 55, 3417-3430. [10] Berkley J. L. et al. (1980) *Geochim. Cosmochim. Acta* 44, 1579-1597.

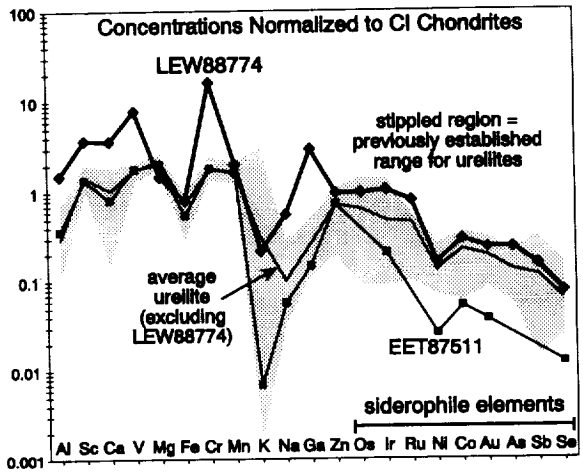

Fig. 1

Fig. 2

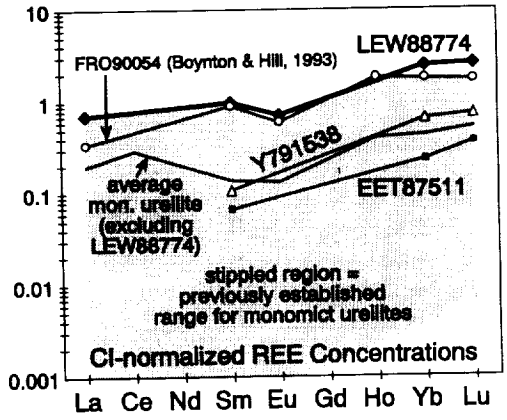

Fig. 3

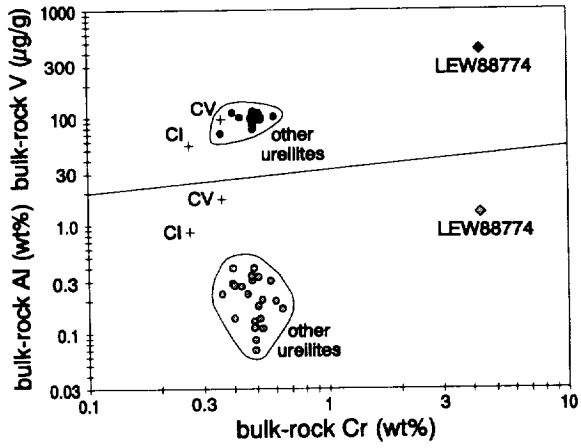

Fig. 4

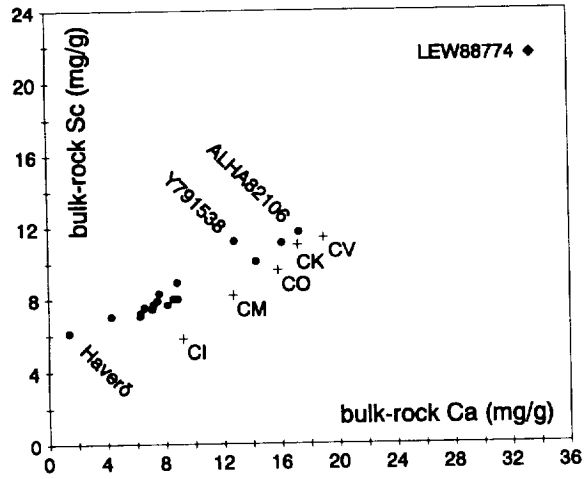

Fig. 5

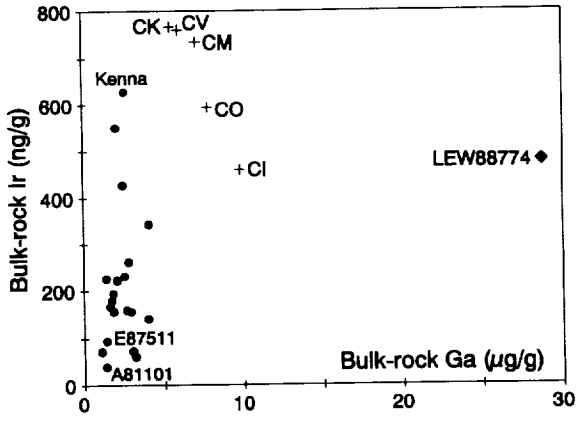

ISOTOPIC, CHEMICAL AND TEXTURAL PROPERTIES OF ACID RESIDUES FROM VARIOUS METEORITES

N. Kano, K. Yamakoshi and H. Matsuzaki
Institute for Cosmic Ray research, University of Tokyo, Tanashi, Tokyo 188, Japan

Detail analysis of acid residues from various meteorites has been continued for study of the evolution of the solar system and information on processes of nucleosynthesis in the pre-solar stage. Last year we reported the results of chemical compositions of acid residues from three meteorites [Canyon Diablo (IA), Allende (CV3), Nuevo Mercurio (H5)] and the preliminary results of Ru isotopic compositions[1]. In these samples, Cr isotopic analyses were also performed to investigate 1) ^{54}Cr(neutron-rich e-process) anomaly and 2) the effect of extinct radioactive nuclide (^{53}Mn→^{53}Cr). The following progress report deals with the chemical and textural properties of acid residues from Murchison(CM2), La Criolla(L6), Qingzhen(E3) and Cr isotopic compositions measured so far.

Major element compositions in acid residues of Murchison, La Criolla, Qingzhen are shown in Table1 along with the fraction of these acid residues. Representative SEM photographs with EDS spectra of the aliquants of acid residues of them are shown in Fig. 1. It is known that spinel, hibonite, chromite etc. as well as carbonaceous matter are present in Murchison residues [e.g. 2], and in our sample, these minerals may be included. But high S content indicates that it contains much S-bearing particles and/or organic matter or something. On the other hand, acid residues of La Criolla consist of chromite for the most part judging from abundant Cr and Fe contents by INAA and Cr:Fe ratios of about 2:1 in the EDS spectra. Ti and V are also much enriched (Ti: 1.51%; 35 times/CI; V: 0.445%; 79 times/CI) in La Criolla residues. In acid residues of Qingzhen, Cr content is relatively low than that of other meteoritic residues. It is consistent with the fact that enstatite chondrite contain no chromite[3]; and Cr:Fe ratios of about 2:1 in the EDS spectra and fairly abundant S content show that daubreelite may be present in Qingzhen residues. In addition, enrichment of refractory siderophiles is characteristics of acid residues for any kind of meteorites. We are now analyzing TEM bright field images and SAD(selected area diffraction) patterns of these acid residues to idetify minerals therein definitely.

The samples (HCl/HF residues) were decomposed in sealed teflon vessels by a microwave dissolution method with several mixed acids and Cr was separated by precipitation and anion exchange method[4]. In mass spectrometric techniques of Cr, the zone-refined (99.995%) outgassed V-shaped Re single filament with silica gel and boric acid was employed. Isotopic analyses were performed by a VG 354 thermal ionization mass spectrometer.

Preliminary Cr isotopic analyses were carried out for acid residues of Allende, Nuevo Mercurio and La Criolla so far. Remarkable isotopic anomalies far beyond experimental errors could not be detected for both ^{53}Cr/^{52}Cr and ^{54}Cr/^{52}Cr, but in acid residues of Allende, ^{54}Cr/^{52}Cr are slightly enriched relative to normal values though errors are rather large. In recent paper, Rotaru et al. [5] suggested that Cr isotopic composition of the Solar System results from the mixing of several major components with distinct isotopic compositions, and that particularly C1 and C2 chondrites keep, at least partially, the memory of their initial isotopic diversity. We expect such heterogenities could be detected in our various kind of samples. Isotope abundance studies in acid residues, concentrating on more specific mineral phases by means of stepwise dissolution method, are currently underway.

Aknowledgements -- We thank Y. Suzuki of Yamagata University for analyses of samples by TEM/SEM-EDS.

References : [1] Kano, N. et al. (1993) LPS(Abstracts), **24**, 749 [2] Alaerts, D. N. et al. (1980): GCA, **44**,189 [3] Srinivasan, K. et al. (1977): JGR, **48**, 2567. [4] Lee, T. and Tera, F. (1986): GCA, **50**, 199. [5] Rotaru et al. (1992): Nature, **26**, 29-36.

Table 1 Major element contents in acid residues of three meteorites

Sample	Acid residues fraction (wt.%)	combustion method(%) C*	H*	N*	S*	INAA# (%) Cr	Fe	Ni	Al	Mg
Murchison(CM2) HCl/HF residue	3.12	34.6	2.10	1.48	46.5	1.14	0.694	0.240	0.958	0.943
HCl/HF-HNO_3 residue	1.30	29.5	1.71	2.56	27.5	1.75	3.50	0.191	1.13	2.15
La Criolla(L6) HCl/HF residue	0.83	1.20	0.16	---	12.8	35.6	18.8	0.424	2.76	2.75
Qingzhen (E3) HCl/HF residue	0.65	6.26	2.05	0.71	7.27	0.409	0.800	0.0216	0.673	7.92

*) We are indebted to T. Seki of Tokyo University for determing C,H,N,S.contents of samples.

#) Errors of INAA data are below 5% except Ni in Qingzhen(~10%). Neutron irradiations and use of the counter facilities were carried out at the Inst. for Atom. Energy Res. in Rikkyo University.

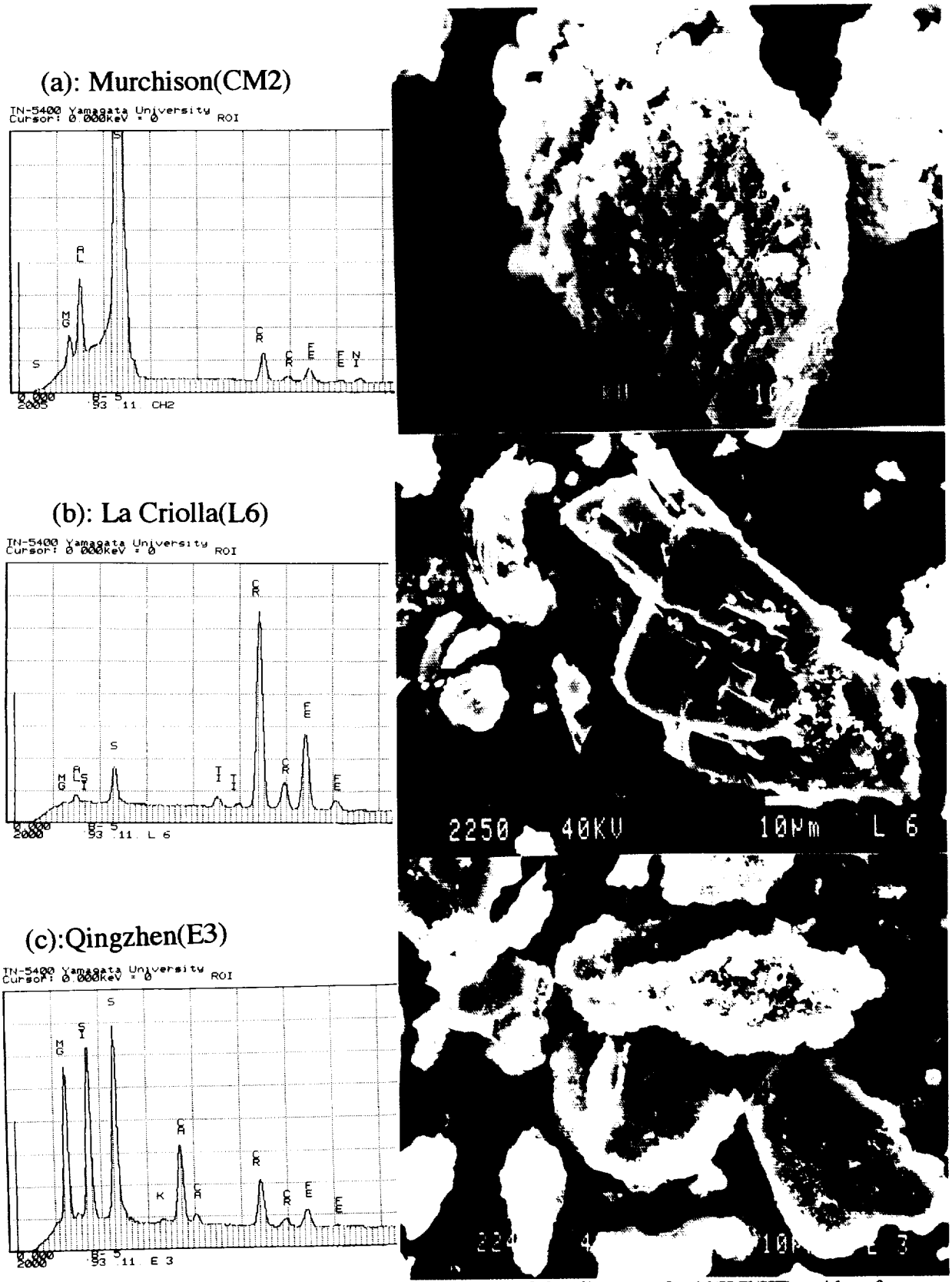

Fig. 1 Reprentative SEM pictures with EDS spectra of the aliquants of acid(HCl/HF) residues from three meteorites((a): Murchison(CM2), (b): La Criolla(L6), (c):Qingzhen(E3)).

AN ALLUVIAL DEPOSITIONAL ANALOG FOR SOME VOLCANIC PLAINS ON VENUS;

J.S. Kargel, U.S. Geol. Survey, 2255 N. Gemini Dr., Flagstaff, AZ 86001

Overview. Many types of landforms that are commonly associated with basaltic volcanism on Earth are widespread on the Venusian lowlands [1]. Geochemical evidence supports a dominance of mafic silicate volcanism on Venus [2-3]. The interpretation of some uniquely Venusian landforms, especially canali, is less certain. Canali are volcanic channels that resemble terrestrial river channels more than any known volcanic features on Earth, Moon, or Mars (Fig. 1). Canali are long and sinuous and have shallow cross sections (depth:width ~0.01-0.04). Any given canale maintains a fairly constant width for hundreds to thousands of kilometers. Hildr is over 6800 km long, the longest known channel of any type in the Solar System [4]. Some canali are leveed, whereas others apparently are not so at available radar image resolutions. Some canali possess features that indicate a history of meander migration, including meander cutoffs (oxbows) and meander scrolls (Fig. 1), whereas other canali appear to have had fairly stable courses. To be sure, canali are not dried river channels, because many have volcanic sources and terminal lava flows. Peculiar circumstances seem to be implied in the origin of canali, perhaps involving a chemically exotic lava [3, 4-7] or an ordinary silicate lava erupted under other extraordinary conditions [8]. The model presented below, based on an alluvial analog, suggests that canali-forming lavas had physical properties that allowed them to mimic the hydraulic and sedimentologic behavior of terrestrial rivers. As discussed below, carbonate lavas are most consistent in this regard, but highly fluid silicate lavas might have eroded canali under certain unusual circumstances.

Geomorphic analogs. The closest known volcanic analogs of canali are lunar-type sinuous rilles, which occur on the Moon, Mars, and Venus, and similar but much smaller lava channels on Earth [9-10]. Compared with canali, lunar-type sinuous rilles are relatively short (1 - 500 km), and terrestrial lava channels are shorter still (100 m to 50 km, [9-10]). However, canali do not appear to be simply large versions of lunar-type sinuous rilles, because canali are distinguished by many morphologic aspects besides length. Unlike canali, lunar-type sinuous rilles and terrestrial lava channels are comparatively deep (depth:width generally ~0.05-0.3), and they tend to become narrower and shallower downstream. The meander habits of canali and lunar-type sinuous rilles are distinctly different, apparently reflecting different formational mechanisms (Fig. 2).

Some terrestrial river channels are better morphologic analogs for many canali than known volcanic channels. The meander habits, relatively constant widths, and low depth:width ratios of canali resemble these aspects of terrestrial river channels in aggrading, low-gradient alluvial plains. Evidence for extensive meander migration, a hallmark of many rivers, is exhibited by some canali, but not by lunar-type sinuous rilles. One canale even has a terminal lava delta that resembles some fluvial deltas. The morphologic resemblance of canali to river channels suggests that fluvial processes on low-gradient alluvial plains may approximate the hydraulic regimes of canali-forming flows better than do processes involving silicate lava rivers. The thermal regimes of canali-forming flows also may have been comparable with those of rivers (i.e., rates of cooling and crystallization may have been similar -- zero for many rivers; very low for canali-forming flows).

The river channel analog: Implications for processes and lava compositions. River channels acquire their morphologic attributes partly as a result of continual adjustments of the hydraulic flow regimes, sediment loads, and bed shapes of streams to variations in water input. The physical properties of water (especially viscosity, density, and freezing point in relation to ambient surface temperature) critically affect the forms of river channels and help distinguish them from silicate lava channels. Rivers commonly are near the threshold between mechanical erosion and sediment deposition [11]. The spatial patterns and temporal cycles of erosion and deposition cause gradual lateral migration of river meanders; over periods of 100-1000 years, meanders of alluvial rivers commonly relocate over distance scales of about one meander wavelength.

The alluvial model of canali and their plains deposits implies that the surface rocks in these areas are in lateral and vertical accretion sequences comparable with those of terrestrial flood plains. If this analog is strictly correct, then the principal type of sediment should be preexisting plains material and/or sediment eroded from the source area. However, on Venus we are dealing with a lava of some type, so that a large fraction of sediment could be crystalline precipitates of the lava itself.

The dynamic balance between erosion and deposition, as implied by the alluvial analog, may indicate extremely low viscosities of the lava, probably lower than the viscosity of basalt (10^2-10^3 p). Several types of silicate lava have viscosities much lower than that of basalt [4-5], including strongly silica-undersaturated, mafic alkaline lava, lunar-type Fe-Ti basalt, picrite, and komatiite. Even less viscous are carbonate lavas, which have viscosities of just a few centipoises, comparable with the viscosity of water (~2 cp) [12].

The ability of canali lavas to flow thousands of kilometers in shallow, low-gradient channels whose depth and width remain fairly constant suggests not only a low viscosity, but also a low rate of crystallization (hence, probably a low melting temperature). Many canali have associated lava flows, so that the liquidus (and probably solidus) temperature of the lava was greater than Venusian ambient conditions (475^{O} C). If the liquidus

VENUSIAN VOLCANIC PLAINS: J.S. Kargel

temperature was only slightly greater, then this property could help explain the dimensional characteristics of canali. A liquidus temperature like those of fluid types of silicate lavas (~1200°-1500° C) probably would have caused rapid cooling and large downstream increases in lava viscosity and depletion of liquid, thus shallowing and narrowing the lava channel. The high temperature of Venus' surface compared with Earth's and the Moon's is a negligible factor if the Venusian lavas are silicate; this is because the T^4 dependence of radiative heat loss means that the high Venusian surface temperature causes only about a 7% reduction in heat loss rates of a basaltic flow compared with basalt flows on Earth or the Moon, if other factors are held constant. (In fact, convective cooling may have caused flows to cool faster on Venus because of its dense atmosphere.) Therefore, if the canali-forming lavas are silicates, then a factor other than Venus' warm surface must have been responsible for the extraordinary characteristics of canali. On the other hand, the warm Venusian surface could cause a carbonate lava (with a liquidus temperature as low as 510° C) to cool 10 to 100 times more slowly than a terrestrial basalt flow.

In sum, canali-forming lavas may have had silicate or nonsilicate compositions. However, to the extent that the alluvial analog of canali and associated plains may be correct, a "waterlike" lava, such as carbonatite, could be indicated. The compositions of Venus' atmosphere and rocks, so far as they are known, are consistent with large amounts of carbonates on the surface [3,13] and with widespread carbonate volcanism.

[1] Head, J.W., L.S. Crumpler, J.C. Aubele, J.E. Guest, and R.S. Saunders, 1992. *J. Geophys. Res.* **97**, 13,153-13,198. [2] Barsukov, V.L. 1992. In: V.L. Barsukov, A.T. Basilevsky, V.P. Volkov, and V.N. Zharkov, *Venus Geology, Geochemistry, and Geophysics*, Univ. Arizona Press, 165-176. [3] Kargel, J.S., G. Komatsu, V.R. Baker, and R.G. Strom, 1993. *Icarus* **103**, 253-275. [4] Arvidson, R.E., V.R. Baker, C. Elachi, R.S. Saunders, and J.A. Wood, 1992. *Science* **252**, 270-275. [5] Kargel, J.S., G. Komatsu, V.R. Baker, J.S. Lewis, and R.G. Strom, 1991. *Lunar Planet. Sci. Conf.* **XXII**, 685-686. [6] Baker, V.R., G. Komatsu, T.J. Parker, V.C. Gulick, J.S. Kargel, and J.S. Lewis, 1992. *J. Geophys. Res.* **97**, 13,421-13,444. [7] Komatsu, G., J.S. Kargel, and V.R. Baker, 1992. *Geophys. Res. Lett.* **19**, 1415-1418. [8] Gregg, T.K.P., and R. Greeley, 1993. *J. Geophys. Res.* **98**, 10,873-10,882. [9] Cruikshank, D.P., and C.A. Wood, 1972. *The Moon* **3**, 412-447. [10] Greeley, R., 1987. *U.S.G.S. Prof. Pap.* **1350**, 1589-1602. [11] Hickin, E.J., 1974. *Amer. J. Sci.* **274**, 414-442. [12] Treiman, A.H. 1989. In: K. Bell, *Carbonatites: Genesis and Evolution*, Unwin-Hyman, London. 89-104. [13] Fegley, B., Jr., A.H. Treiman, and V.L. Sharpton, 1992. *Proc. Lunar Planet. Sci. Conf.* **22**, 3-19.

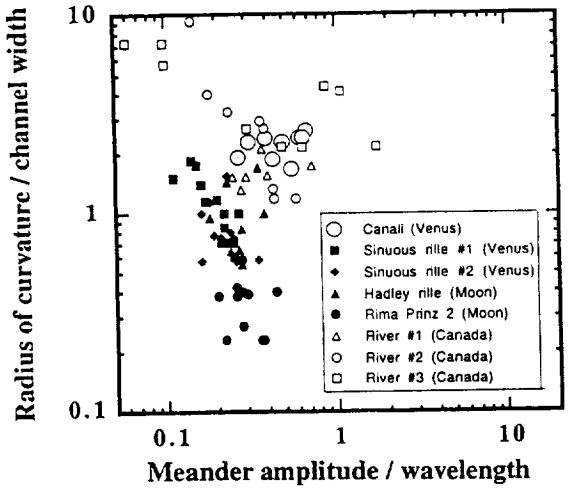

Fig. 2. Meander characteristics of canali, lunar-type sinuous rilles on Venus and the Moon, and river channels on Earth.

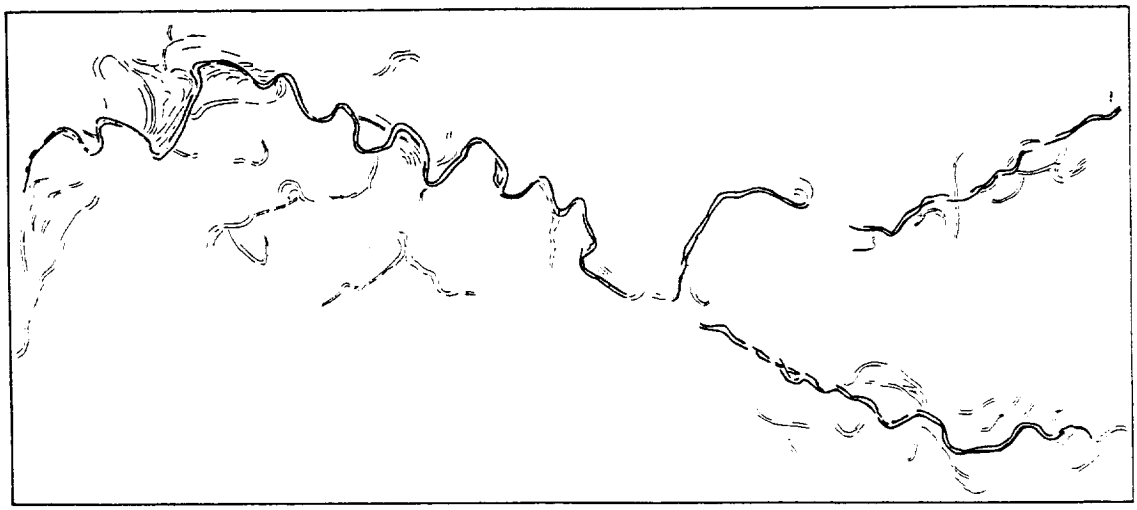

Figure 1. Map of meandering canali (bold lines) and features interpreted as meander scars (thin lines), including cutoff meanders and meander scrolls. Center near lat 33.5° S., long 158.5°. Mapped from Magellan SAR mosaic F-MIDRP. 35 S 157;1. Map spans 289 km from left to right (west to east).

COSMIC-RAY EXPOSURE HISTORY OF THE EREVAN HOWARDITE MATTER BY TRACK DATA. *L.L.Kashkarov, N.N.Korotkova.* V.I.Vernadsky Institute of Geochim. and Analyt. Chemistry, Russian Academy of Sciences.

Achondrites are one of the most important meteorite types whose matter retained the traces of shock-thermal and radiation influence in regolith environments on their parent body surfaces [1]. Study of tracks of solar (SCR) and galactic cosmic rays (GCR)- in silicate minerals of poorly studied Erevan howardite [2] has been carried out aimed at further investigation the radiation-thermal conditions of formation of these meteorites. The meteorite was found in ~ 1911 [2] as an individual stone ~500 g by weight partially covered with fusion crust. It is an impact polymict breccia having the K-Ar age of 4.0 10^9 years. The estimated meteorite effective exposure age (T_{RAD}) based on its ^{21}Ne content [3] and ^{21}Ne production rate in howardites [4] is equal to 32.10^6 years. The significantly lower value of T_{RAD} = 22.10^6 years has been obtained on the basis of ^3He content [2]. The great discrepancy in T_{RAD} values can be caused by greater losses of ^3He produced at regolith stage as compared to those of ^{21}Ne.

116 grains of plagioclase (Pl) and 94 grains of pyroxene (Px) handpicked from the Erevan howardite crushed bulk sample (N 15199 in meteorite Committee collection of RAN) have been studied. The mounted in epoxy and polished crystals were etched in following conditions: Pl in boiling solution, $NaOH:H_2O$=3:4, 15 min and Px in boiling solution, $NaOH:H_2O$=3:2, 90-100 min. The measurements of track density (ρ,cm^{-2}) and track length projections (l,μm) observed on the etched crystal surfaces have been made by means of optical microscope. The VH-nuclei galactic cosmic ray (GCR) tracks having ρ values within (1-10) 10^6 cm^{-2} were found in all the Pl and Px crystals under study (see Fig.1 a,b). The mean $\bar{\rho}$ values for Pl and Px grains are equal to (4,3±0,4) 10^6 cm^{-2} and (2,5±0,3) 10^6 cm^{-2} respectively, and the difference is due to unequal efficiency of registration of VH-nuclei by given minerals. In 17 Pl grains two track generations were revealed: (I)-very short ($l \lesssim 2$ μm) tracks naving ρ_I=(9.6±0.5) 10^6 cm^{-2} and (II)-tracks having ρ_{II}=(5,5±0,5) 10^6 cm^{-2} and practically unannealed lengths ($l \simeq 5$-6 μm). The part of a Pl crystal containing such tracks is presented in Fig.2 microphotograph. As it is seen in Fig.1c, the ρ value distribution in these crystals is bimodal and their $\bar{\rho}$ mean values are beyond the scope of 3σ. On this base and the appreciable difference in track lengths we can suggest that the tracks of the I-st and II-nd generations were formed at different stages of Erevan howardite evolution. The I-st group tracks can be caused by earlier "surface" radiation by SCR and the II-nd group tracks were produced by GCR VH-nuclei at later regolith stage when the crystals were buried at the depth more at least several centimeters, and during irradiation of the meteoroid body in cosmic space. The shortening of I-st group tracks can be due to their longer and more complex history.

The ρ distribution in the volume of each Pl and Px crystal under study is uniform. The ρ value gradient from the crystal

COSMIC-RAY EXPOSURE HISTORY... Kashkarov L.L., Korotkova N.N.

surface to its depth was found only in about 2% of Pl grains. The flat shape of gradients can be explained by partial shielding of crystals with thin layer of substance (thickness about some microns) during their exposure on the regolith surface.

The obtained data indicate that the Erevan howardite matter has been undergone the relatively moderate processing in the environments of parent body regolith. This conclusion was drawn on the ground of comparison of obtained track parameters with those for highly irradiated Kapoeta howardite [1] and also Pesyanoe [5] and Norton County [6] achondrites having quite different radiation histories.

References .[1] Goswami J.N., Lal D., Wilkening L.L.(1984) Space Sci.Rev.,37,p.111. [2] Kvasha L.G., Skripnik A.Ya. et al. (1978) Meteoritika, v.37, p.80. [3] Levskij L.K., Fedorova I.V. et al.(1971) Geochimiya, N 5, p.515. [4] Cressy P.J., Bogard D.D. (1976), Geochim.Cosmochim.Acta. 40, p.749. [5] Kashkarov L.L., Genaeva L.I. (1993) Meteoritika, v.50, p.95. [6] Genaeva L.I., Kashkarov L.I., Perelygin V.p. (1985), v.44, p.100.

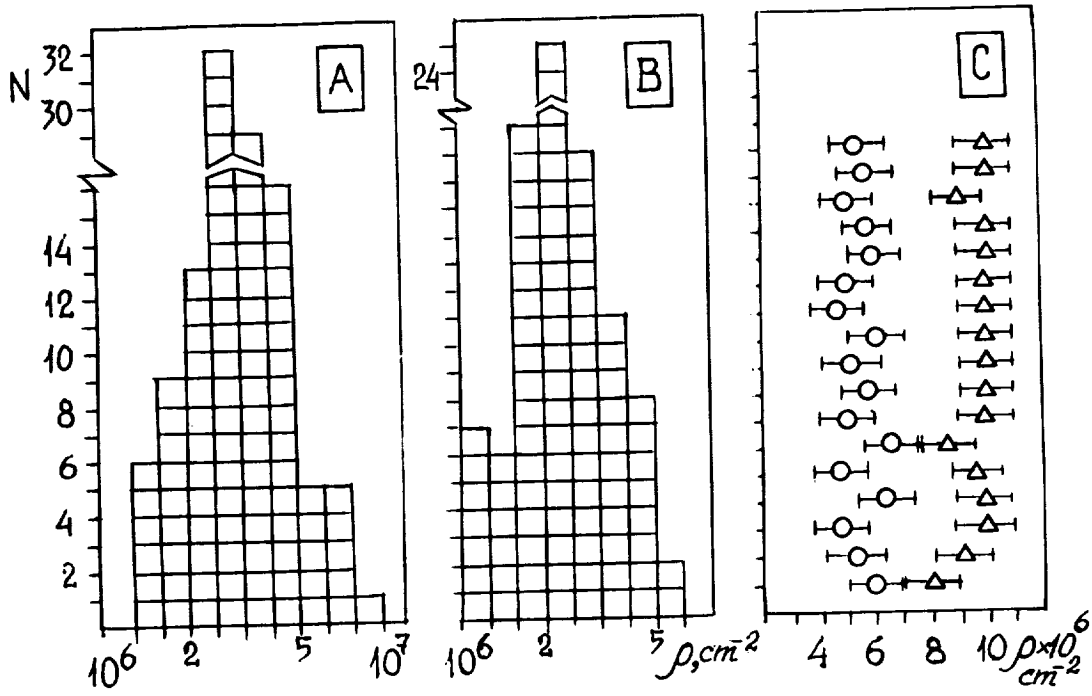

Fig.1

Fig.2

SOME GENERAL CHARACTERISTICS OF THE EARLY RADIATION-THERMAL HISTORY OF CARBONACEOUS AND ORDINARY CHONDRITE MATTER ON DATA OF TRACK STUDIES. *L.L.Kashkarov, N.N.Korotkova, G.V.Kalinina.*
V.I.Vernadsky Institute of Geochim. and Analyt. Chemistry, Russian Academy of Sciences.

Investigations of cosmic ray VH-nuclei tracks in silicate minerals of some carbonaceous (CC) (Allende CV3 [1], Kainsaz CO3 [2], Kaidun CR2 [3]) and ordinary (OC) (Saratov L4, Ochansk H4, Doroninsk H6 et al. [4-6]) chondrites suggest an uniformity of the radiation-thermal processes accompanied the formation of the primary parent bodies of these meteorites at the pre-accretion stages. The main conclusion is in the great similarity of the statistic distribution of silicate mineral grains depending on the observed track densities (ρ) and the similarity of other track parameters [7] for both CC and OC which did not suffer the intensive exogenic treatment in regolith environments. The data given in Table and the histograms of distribution of silicate mineral grains depending on their ρ for a number of chondrites are characterized as follows: 1) the rather broad (10^3 -10^7 cm^{-2}) total range of ρ values; 2) the very low values of ρ_{min}= (10^3 -10^4) cm^{-2} for the most representative part of crystals that depend both on the depth of their occurrence in the preatmospheric meteorite body and on the exposure age (T_{RAD}); 3) the relatively low values of $\rho_{max} \lesssim 10^7$ cm^{-2} which are tens-hundreds times lower than those for OCs irradiated by solar cosmic ray (SCR) VH-nuclei in the upper regolith layer; 4) the very low percentage (0-2%) of individual mineral grains with gradient ρ that is at least by an order of magnitude lower than that for OCs rich in solar gases [8] irradiated by SCR VH-nuclei.

The statistical distribution of glass inclusions from Kaidun anomaleous CC [9] depending on their track parameters is of a particular interest. There are at least two track groups among them distinguished by the values: ρ_I=(2,7+-1,7) 10^5 cm^{-2} and ρ_{II} within (3,1 - 3,7) 10^6 cm^{-2} The detailed analysis of the relation between the ρ value and uranium concentration in each glass inclusion [10] leads us to the conclusion that about 10% of them retained tracks due to pre-accretion irradiation which are not connected with fission fragment tracks of extinct ^{244}Pu.

The data stated above allow to suppose the identity as a whole of the radiation thermal history of OCs and CCs at the early pre-accretion stage of Solar system matter formation. The meteorites that did not suffer the intensive processing in the parent body regoliths retained many common irradiation features. Therefore, by analogy with the OCs [11], one of the possible source of VH-nuclei having energies $E \lesssim 100$ MeV/nucleon for the CCs can be considered the accelerated locally multi-charged SW ions from the thermalized gas of protoplanet gas-dust nebula. This was possible at the earliest stages of nebula evolution preceded the termination of gas dissipation process out of nebula region where the parent bodies of these meteorites were formed.

References: [1] Lavrukhina A.K., Kashkarov L.L., Korotkova N.N., et al.(1984) LPS XV,p.471. [2] Kashkarov L.L., Kalinina G.V.

(1993) LPS XXIV, p.759. [3] Kashkarov L.L., Korotkova N.N.,et al. (1993) LPS XXIV, p.761.[4] Kashkarov L.L., Korotkova N.N., et al. (1989) Meteoritics, **24**, p.284. [5] Kashkarov L.L., Kalinina G.V. (1990) LPS XXI, p.601. [6] Kashkarov L.L., Kalinina G.V. (1991) LPS XXII, p.691. [7] Kashkarov L.L., Kalinina G.V. (1990) In Particle Tracks in Solids XV, p.72. [8] Kashkarov L.L., Genaeva L.I., et al. (1983) JGR, **88**, p. A765. [9] Kashkarov L.L., Korotkova N.N., et al. (1990) LPS XXI, p.611. [10] Kashkarov L.L., Korotkova N.N., et al. (1993) Meteoritika, **50**, p.105. [11] Kashkarov L.L. (1988) Izv. Acad. Nauk USSR, ser. phys., **52**, p.2321.

Table. Statistical track parameters in silicate minerals of carbonaceous and ordinary chondrites containing no solar gases.

Meteorite	Number of cryst.	ρmin 10^4 cm^{-2}	ρmed 10^4 cm^{-2}	ρmax 10^7 cm^{-2}	$\frac{N_{irr}}{N}$	$\frac{N_H}{N}$	$\frac{N_{grad}}{N}$
Allende CV3	1187	1	1	6	0.06	0.06	0.013
Kainsaz CO3	570	0.3	1.5	2	0.10	0.005	0.02
Kaidun CR2	79	1	0.2-80	0.06-1	0.1-0.4	0.06-0.2	n.o.
Chainpur LL3	125	1	6	0.1	0.48	0.04	n.o.
Saratov LL4	164	1	1	0.7	0.20	0.06	0.007
Nikolskoe L4-5	413	1	1	3	0.1	0.09	n.o
Ochansk H4	238	1	3	2	0.20	0.01	n.o.
Borodino H5	102	1	8	0.3	0.41	0.1	n.o.
Doroninsk H5	226	1	1	1	0.04	0.01	0.0004

Notes (*)The intervals of track parameter values observed in Ol,Px and Pl are indicated. (**)Nirr-the number of crystals with $\rho \gtrsim 10^5$ cm^{-2}. (***) NH-the number of crystals with $\rho \gtrsim 10^6$ cm^{-2}.

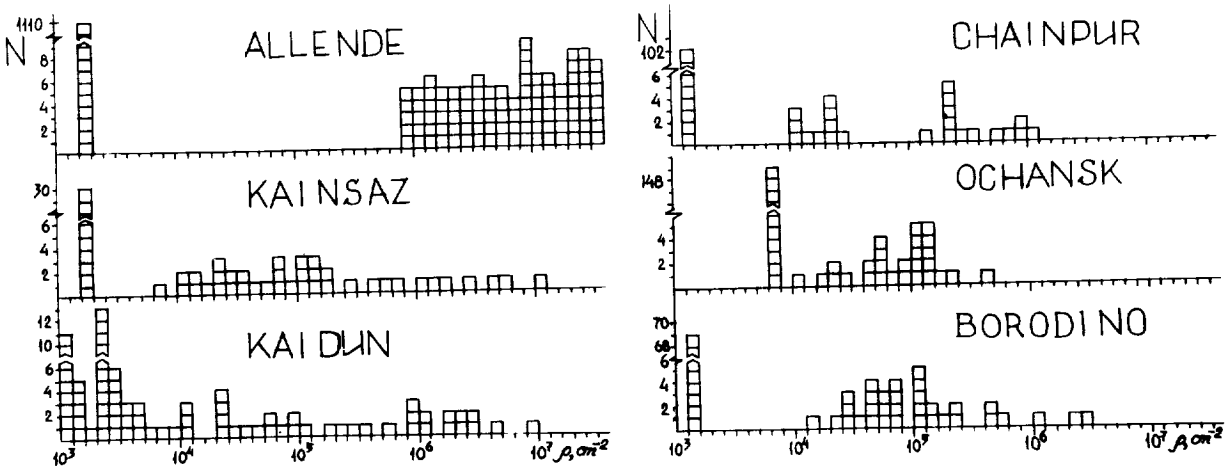

STRUCTURAL CHARACTERISTICS AND CLASSIFICATION OF DOUBLE-TYPE CORONAE AND CORONA-LIKE FEATURES ON VENUS. K. Kauhanen and T. Törmänen. Department of Astronomy, University of Oulu, 90570 Oulu, Finland.

Introduction. Coronae on Venus are generally circular, elongate or complex structures where the annulus is defined by compressional and/or extensional features surrounding a less deformed central plains area. A three-stage model has been developed to explain the formation of the coronae [1]. An upwelling mantle diapir impinges the lithosphere, forming a bulge which extends due to flattening of the diapir and relaxes due to volcanic load and disappearing dynamic uplift. A variety of corona morphologies shows that the model works only as an ideal case. To understand the corona formation we need to study individual structures.

Although coronae tend to form clusters and chains, no evidence is found supporting their formation by movement of the lithosphere over a mantle plume [2]. However, many of the individual coronae show movements of tectonic and volcanic activity with time. These trends may reveal changes in the ascent of the diapir through the lithosphere. One interesting type of coronae possibly showing these trends is characterized by two interconnecting parts.

We have identified 40 coronae and corona-like features exhibiting double structure with varying amount and nature of connectivity [3]. The observations were not restricted to coronae recognized in other surveys [2, 4] only, but were extended to cover also other corona-like volcanotectonic patterns. Observations were made from Magellan cycle 1, 2 and 3 radar images.

Classification of double-type features is based on the morphology of the annular rim and the associated concentric ridges and/or fractures. The rim is defined either by topographic trough or rise or structures on the inner and outer edge of the rim. Four morphological classes were found in the feature population.

Class A consists of features where two adjacent parts have a common section of feature annulus between them. In Class B features there is no common section but two distinct parts surrounded by an annular rim. Some of the features in this class were elongated or pear-shaped. Class C includes features, where younger feature overlaps an older one or two close-by features with touching rims. Class D features have either a class A or B type of pattern, which is broken by a smaller feature in the center, or a complex pattern of lineaments disrupting the center. Only two features of this type were found. An example of each class is presented in Figure 1.

General structures. A and B class features seemed to form small groups [3] with somewhat similar type of annulus. Structural patterns depend on the size of the feature: for example, lithospheric flexure and ridges confining the rim were associated with larger features, which may have experienced larger amount of volcanism and gravitational relaxation (Fig.1, B). Wrinkle ridges commonly postdate the formation of the features, and their density seems to depend on the strength and orientation of regional wrinkle ridge patterns. Ridges avoid larger structures perhaps due to the strength profile acting like a positive relief [5]. Radial fractures and graben tend to be associated with larger coronae and corona-like features. Fractures originating from the rim usually concentrate as belts and emerge into a few directions from the corona. Some of these fractures extend towards nearby volcanic features. They can be divided into several sets of different age indicating successive and repeated phases of uplift and relaxation.

Volcanism. Volcanic features associated with double coronae and corona-like features include lava flows and channels, small shields and steep-sided domes. Usually the patterns of volcanism within the two parts of the corona are different from each other, due to differences during the late volcanic stages. The appearance of lava flows varies from digitate to flood like patterns. The youngest deposits seem to be on the bottom and just outside the margin.

Conclusions. Differences between the components of double-type features consist mainly of differing number and characteristics of tectonic features, and more degraded appearance of one of the parts. Most of the tectonic features seem to follow larger scale structural patterns on the plains, i.e. ridge systems and deformation belts. In the absence of a strong controlling tectonic pattern a few minor patterns can emerge. Formation of the two parts must have occurred close in time for most of these double-type features.

DOUBLE-TYPE CORONA-LIKE FEATURES: Kauhanen K. and Törmänen T.

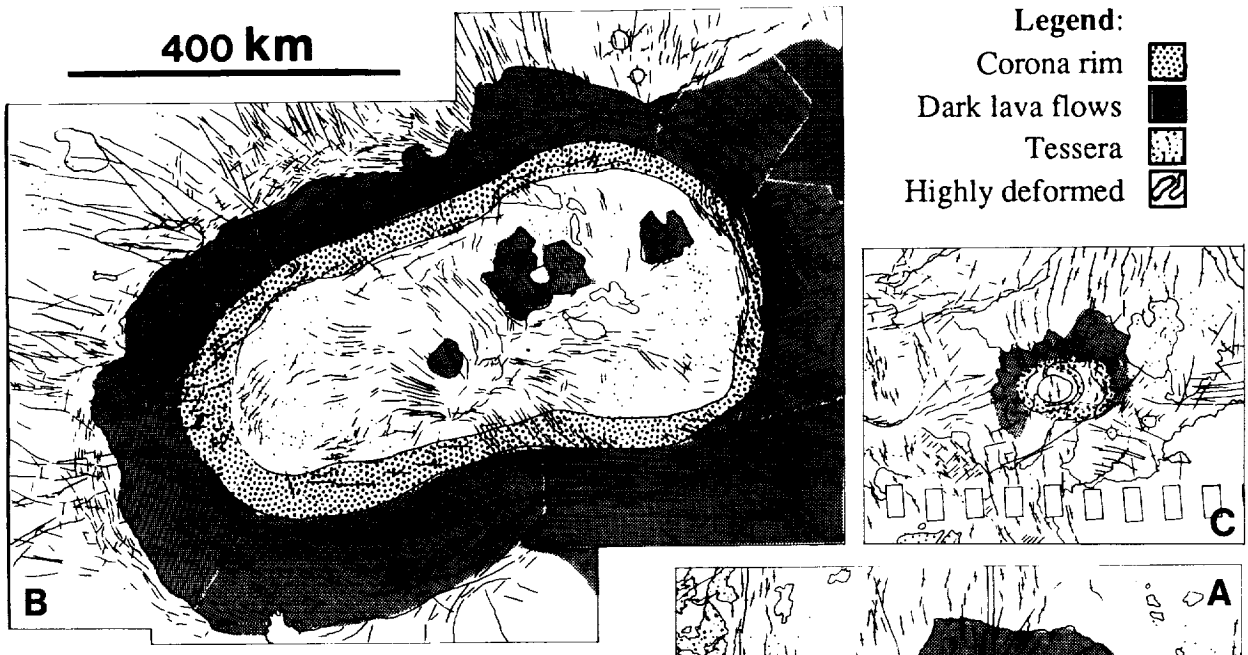

Figure 1. Geologic sketch maps. Examples of different classes of double-type coronae and coronae-like features. A) Cassatt Patera (66N206.5) is located in the northern ridge belt area. Earlier radial fractures have been embayed by flood lavas. The bottom of the western part is filled with lavas from late-stage activity. Note a linear trend of domes. The eastern part seems to be younger. B) Demeter Corona (54N295) is a large feature with a deep trough outside the rim. Earlier flexural fractures have been covered by young lava flood. Markings of young radial fracturing are visible in the center and some fractures extend beyond the trough. Notice weak linear belts extending outside from the rim. C) An unnamed feature (16.5N202.5) is an example of a feature overlying an older one. This small feature does not possess any strong resistance against regional tectonic patterns. Notice a ridge pattern converging towards the center of the feature. D) Hatshepshut Patera (28N65) is divided by a high linear fracture/fold belt resulting in a very different outlook of the parts. Digitate lava flows extend to both sides of the belt.

References:
[1] Squyres et. al. (1992) JGR, 97, 13611. [2] Stofan et. al. (1992) JGR, 97, 13347. [3]Törmänen T. and Kauhanen K. (1994) LPSC XXV, this volume. [4]Head J. W. et. al. (1992) JGR, 97, 13153. [5]McGill G. E. (1993) GRL, vol. 20 no. 12, 2407.

DIONE REGIO VENUS: A COMPARISON TO OTHER REGIONAL HIGHLANDS: S.T. Keddie and J.W. Head, Dept. Geological Sci., Brown University, Providence, RI, 02912

Abstract: Dione Regio (20°-45°S, 315°-340°) is found to exhibit many characteristics that are observed at other regional highlands, including locally elevated topography, large-scale volcanism, and rift zone formation. Like Western Eistla Regio, Dione is relatively small and low, has few remnants of tessera, and limited rifting. It differs, however, in the domination of centralized volcanism over coronae and the presence of significant small scale volcanism (in the form of small shields). We interpret Dione to be a region of mantle upwelling, similar to Western Eistla and Bell, and differing from the other, larger-scale upwellings observed at Beta and Atla Regiones.

Introduction: Several volcanic rises, defined by their locally elevated topography, extensive volcanism, and development of rift zones have often been interpreted to be related to mantle upwellings or mantle plumes [1,2]. Western Eistla, Bell, Beta, and Atla Regiones are all located in the equatorial region of Venus and have many common characteristics [1,2]. In this paper, we outline the characteristics of Dione Regio [3,4], a fourth rise imaged at the end of the Magellan mission and compare it with the other four.

Description: Dione Regio is located mid-way between Phoebe and Alpha Regiones, on the NW edge of the lowlands of Lavinia Planitia. It covers an area of approximately 5 x 10^6 km^2, from 20°-45°S and 315°-340°. It is an oval-shaped, local topographic rise, 2700 km N-S x 1200 km E-W which connects to the west with the rise associated with Themis Regio. Superposed on this broad rise is an irregular-shaped region of higher topography (mean elevation 6052 km) that is elongated N-S with a cross-like E-W projection. Four local topographic highs (1.1-2.4 km above the adjacent highland plains) correlate with four large volcanic edifices. Ushas, Innini, and Hathor Montes (each about 500-600 km diameter) are oriented from N to S along the main portion of the rise, and an unnamed volcano (250 km diameter) is located on the western projection An elongate, local low NW of Innini may be a flexural moat but there is no evidence that flows have ponded here.

The geology of Dione Regio is complex [3] (see also their Figure 1). The oldest units are tessera and tectonized plains that were flooded by extensive plains, leaving only small inliers. At some later point these regional plains were deformed, resulting in narrow, sinous ridges. SE of Innini the ridges in the plains rotate and become circumferential to the local topography, suggesting that in at least one location the high topography developed before the period of ridging. Superposed on the ridged plains are four small corona and many smaller patches of younger plains, including regions of plains that are covered in hundreds of small shields. Although there is some evidence of earlier centralized volcanism [3], the majority of the volcanoes appear to post-date the plains. In addition to the four major volcanoes, there are four minor volcanoes: two on the flanks of Hathor , one covering early eruptions but deflecting later eruptions from Innini, and one in the plains SW of Ushas.

Late stage fracturing has influenced all four of the major volcanoes to different degrees. Fracturing at Ushas Mons forms a radial pattern to the north and south of the edifice. This radial pattern and the association of lava flows with several of these fractures suggests that the fracturing is likely related to lateral dike emplacement. There is limited fracturing of undetermined origin on the south flanks of Innini. Lava flows on the SE flanks of the unnamed volcano have been captured by fractures which merge into the well-developed rift zone NW of Hathor. This rift zone dissects the small volcano on the flanks of Hathor and extends up towards the summit. On Hathor's SE flanks the rift zone continues but it is not as strongly developed: although many lineaments and, in some cases, fractures are observed, there is not the strong graben development that is seen to the NW. There is also limited fracturing on the SW flanks which produces the appearance of a triple junction at the summit of Hathor. Fractures are not observed at the summit but they may have been buried by volcanic deposits.

Although the small number of impact craters in total on Venus precludes determinations of unit ages, it is possible to assess the density of craters of the region as a whole and thus get an estimate of the age of the region. There are 11 impact craters, ranging in diameter from 5-49 km, in the area mapped in Figure 1 of [3]. Nine are located on the ridged plains, one on shielded plains, and one on tectonized plains near the Hathor rift. These

locations suggest that most of the craters likely post-date the development of the rise. In contrast to craters at other rises, none of the Dione craters are clearly embayed by volcanism, although a crater N of Ushas is cut by radial fractures associated with the volcano. The density of all these craters is 2.19 craters per 10^6 km^2, similar to the planetary average of 2.0 craters per 10^6 km^2 [5].

Discussion: Dione Regio is similar in many ways to other volcanic rises on Venus. All rises are characterized by broad-scale elevated topography, wide-spread, significant volcanism (in the form of large volcanoes and corona), and the development of rift zones in association with volcanoes. There are, however, significant differences between the rises in the amount and distribution of the volcanism, the degree of rifting, and the aerial expanse of old, tessera terrain (Table 1). In addition, Dione is unique among these rises in that it has a large amount of small scale volcanism in the form of hundreds of small shields that occur predominantly at the crest of the high south of Ushas Mons, on the flanks to the SW and NE of Ushas, and at the summit and to the NW of the unnamed volcano. These shields superpose the ridged plains (suggesting that they are syn- or post-uplift) and some are embayed by Ushas lavas. In addition, relatively more of the volcanism at Dione occurs as large volcanoes than as corona. Although there is one 'major' rift zone at Hathor Mons, it is only well-developed on the NW flanks of the volcano. It is 100 km wide and extends for roughly 300 km, which is small in comparison to Guor Linea at Eistla Regio (100-150 km wide and more than 700 km long). In contrast to Atla Regio, where the topographic asymmetry is parallel to the rift zones, at Dione the rift cuts across the elongation of the topography at an angle of approximately 45°.

Conclusions: Dione Regio appears to be a region that originally was dominated by plains that were uplifted and ridged, covered to a large extent with volcanic deposits of various forms, and finally slightly rifted. It exhibits many of the characteristics that are common to other volcanic rises on Venus. All rises, however, differ in the details of the distribution or degree of development of these features. With its small size, lower topography, and limited rifting, Dione most closely resembles Western Eistla and Bell. In contrast to other rises, large volcanoes are the dominant form of volcanism and none of the impact craters are embayed by lavas. [1] and [2] interpreted the highlands they studied to be associated with mantle plumes or regions of mantle upwelling. We suggest a similar source for the high topography, extensive volcanism, and rifting observed at Dione Regio. The differences between the regions are likely related to pre-upwelling geology and the geometry of the upwelling.

References: [1] Senske, D.A., et al., 1992, *Jour. Geophys. Res.* 97, pp. 13395-13420; [2] Binschadler. D.L., et al., 19992, *Jour. Geophys. Res.*, 97, pp. 13495-135532; [3] Keddie, S.T., and Head, J.W., 1994, *LPSC XXV*, this volume; [4] Senske, D.A. et al., 1991, *Earth Moon Planet.*, 55, pp. 97-161; [5] Schaber, G.G., et al., 1992, *Jour. Geophys. Res.* 97, pp. 13257-13301.

Table 1: Characteristics of 4 regional highlands

	Dione	**Bell**	**W. Eistla***	**Beta***	**Atla***
Area (km^2)	5 x 10^6	2 x 10^6	3 x 10^6	13 x 10^6	11 x 10^6
Craters/10^6 km^2	2.19	1.8	2.1	1.8	2.4
Elevation of major rise	6051-6052	6052-6053	6051-6052	6053-6054	6053-6054
Major volcanoes (minor) volcanoes	4 (4)	3	2	3 (1)	3 (2)
No. corona	4	1	8	12	10
Location of corona	1 on crest, 3 on E flanks of high	N part of high	linear trend across the high	around N lower flanks	to E off crest of high
Tessera	minor, scattered	minor, scattered	minor, low flanks	dominant	minor, low flanks
Rifts	1 major	1 very minor	1 major, 1 minor	3 major (junction) 2 minor	5 major (junction)

* Most of this data compiled from [1].

THE GEOLOGY AND STRATIGRAPHY OF DIONE REGIO, VENUS. S.T. Keddie and J.W. Head, Dept. Geological Sci., Brown University, Providence, RI, 02912.

Abstract: Detailed regional mapping of the Magellan gap (20°-45°S, 315°-340°) missed on Cycles 1 and 2 has been completed and reveals that Dione Regio is an area that experienced early tectonic activity in the form of tessera and tectonized plains. Only small inliers of this old terrain remain today, having been flooded by several periods of plains formation. Late stage volcanism at several volcanoes and limited rifting completes the regional stratigraphic sequence. The stratigraphy determined here is similar to that identified elsewhere on the planet.

Introduction: In the fall of 1992 Magellan imaged the final, large portion of the planet. Dione Regio is located in the southern hemisphere (20°-45°S, 315°-340°) and separates the lowland plains of Lavinia Planitia from the rifted and volcanic regions of Phoebe and Themis Regiones. Preliminary mapping of a portion of this region confirmed the observations from Arecibo data [1]: Dione Regio is a regional highland with extensive volcanism. During the past year, regional mapping of the entire thermal gap-fill and its surroundings has been performed. In this paper we outline the geology and stratigraphy of Dione Regio. Elsewhere we discuss the characteristics of this rise in relation to other volcanic rises on the planet [2].

Observations: Dione Regio is an irregular-shaped topographic high that is elongate in a north-south direction. The mean elevation of the high is approximately 6052 km and superposed on this are several local highs (6053.6-6054.4 km) which correlate with volcanic constructs. Superposed on the high and the plains immediately surrounding it (Figure 1) are 11 impact craters ranging in size from approximately 5 km diameter to 49 km (Danilova, one of two of the craters from the 'crater farm' mapped in this study). The craters have a density of 2.19 craters per 10^6 km^2, a value similar to the planetary average of 2.0 craters per 10^6 km^2 [3]. We have identified nine major units (including six plains subdivisions). On the basis of embayment and superposition relationships, their stratigraphic sequence has also been determined and is shown in the legend for Figure 1.

Tessera (t): This highly tectonized unit occurs in small (few-10's km across), isolated patches generally peripheral to the rise and predominantly in the northern half of the region. At least two directions of deformation are observed and no or little internal patches of undeformed plains are visible.

Tectonized plains (p_t): In contrast to the tessera, there is evidence for the preservation of small, internal patches of undeformed plains, which are uniformly brighter than the surrounding, embaying plains. In many cases only one direction of deformation occurs in these plains. The ridge belt in the SE is included within this unit.

Ridged plains (p_r): The most common unit, particularly in the south, are relatively dark plains which are mottled in large patches (few hundred km) but which were then uniformly deformed. The narrow, sinuous ridges that characterize these plains are spaced about 15-20 km apart (though the density is not constant) and frequently turn gradually and become concentric to the local high topography. The ridging of early stages of eruption from an unnamed volcano to the south of Hathor Mons suggests that centralized volcanism and plains formation were contemporaneous in at least one location and that the ridges were formed slightly after emplacement of the plains.

Other plains (smooth: p_s; dark: p_d; shielded p_{sh}; and fractured: p_f): Following what seems to be a fairly regional resurfacing by the p_r, there were many episodes of smaller patches (few hundred km) of resurfacing which, because of their separation in space, cannot be more tightly stratigraphically constrained. The most abundant of these are the shielded plains which are characterized by hundreds of small shields (most with central pits). Although in very few cases is it possible to trace a flow to one of these shields, there are clear contact relationships

surrounding concentrations of shields which suggests that resurfacing by flows as well as shield construction occurred.

Corona (c): Several small (and now quite degraded) corona formed at approximately the same time as many of these young plains units. They are quite small (50 -100 km diameter), with well-developed tectonic annuli and limited volcanism.

Volcanic edifices (v): The most recent event in the region (along with cratering) is the emplacement and rifting of large volcanic centers. Four major and four minor volcanoes are located in the region. Ushas, Innini, and Hathor Montes (described in detail in [1]) dominate the rise and another large volcano is located on an extension of the rise, 900 km WNW of Innini. Smaller volcanoes occur to the SW of Hathor, the NW of Hathor (cut by rifting), west of Innini, and SW of Ushas. Hathor has a well-developed rift zone, cutting the lower flanks of the volcano on a NW-SE trend, fracturing south of Innini is of limited extent, and radial fracturing at Ushas is likely related to dike emplacement.

Conclusions: Dione Regio and its surrounding plains show a complex history of tectonic activity, followed by areally significant flooding and, most recently, extensive centralized volcanism with limited rifting. The stratigraphy detailed here is similar to the general stratigraphic sequence identified at 36 locations around the planet [4].

References: [1] Keddie, S.T., 1993, *LPSC XXIV*, pp. 771-772. [2] Keddie, S.T., and Head, J.W., 1994, *LPSC XXV*, this volume. [3] Schaber, G.G., et al., 1992, *Jour. Geophys. Res.*, 97, pp. 13257-13301. [4] Basilevsky, A.T., and Head, J.W., 1993, *EOS Trans AGU*, v. 74 no. 43, p.378.

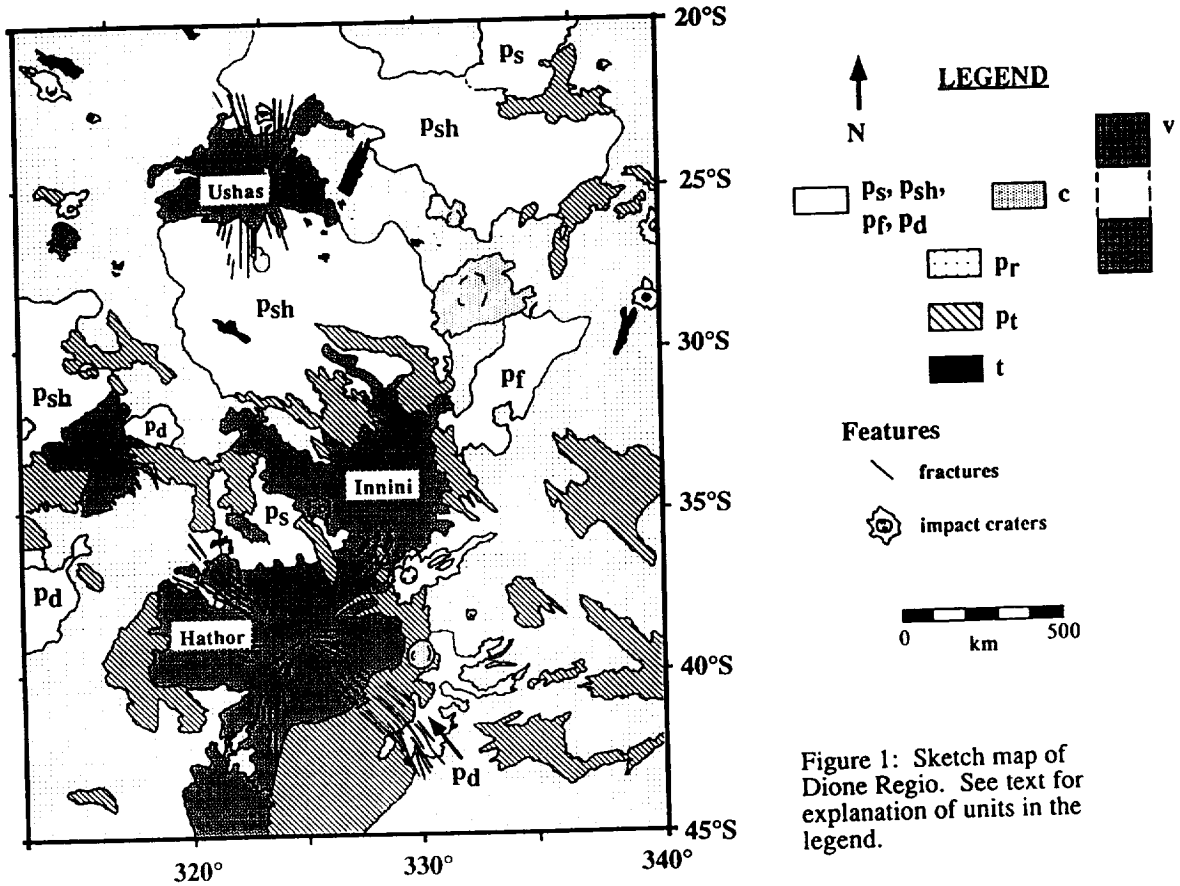

Figure 1: Sketch map of Dione Regio. See text for explanation of units in the legend.

SAPAS MONS: EVOLUTION OF A TYPE-SHIELD VOLCANO ON VENUS: S.T. Keddie and J.W. Head, Dept. Geological Sci., Brown University, Providence, RI, 02912.

Introduction: Sapas Mons is a large (600 km diameter) volcano located in Atla Regio, about 1000 km to the west of Ganis Chasma. The lava flows are very well-preserved and the apparent total exposure suggests that it may be possible to determine the full sequence of development at this volcano. Previous mapping of Sapas Mons [1] identified 6 flow units with distinctive properties. In this paper we briefly review the characteristics of Sapas Mons and then examine some of the implications these observations have for magma chamber size and evolution, magma supply, and the general history of the volcano.

Characteristics: In comparison to a well-known shield volcano on the Earth (eg. Mauna Loa), Sapas Mons has a low height (2.4 km above the surrounding plains) and long flows (10's-100's of km). The estimated volume of 8.8 x 10^4 km^3 for Sapas is more voluminous than the largest Hawaiian shield (Mauna Loa, 42.5 x 10^3 km^3), but it is much less than an estimated volume for the entire Hawaiian-Emperor (H-E) chain of 1.08 x 10^6 km^3 [2]. There is an asymmetrical distribution of both lava flows and radial fractures and small shields on the flanks of Sapas Mons. The lava flow distribution is likely the result of original topography (local highs to the SW and NE restricted flows, and local lows to the NW and SE enhanced flow distances). The fractures and shields, which are dominantly early-stage, are predominantly observed where flows are relatively scarce, suggesting that there may have been an original radial pattern that was partly preferentially buried to the NW and SE. The Magellan data permit the identification of 6 stratigraphic flow units (from oldest to youngest these are identified as units 1 through 6 respectively). Although there are distinct differences between the flow units [1], in general they can be divided into two types. Type 1 flows (units 1-5) are similar to each other in that the flows are long (10's of km), narrow (1-5 km), with very little evidence for breakouts, extensive fingering, or channeling. The majority of type 1 flows appear to be cooling limited [3] and radial to a single point that is near the topographic summit of the volcano. On the basis of their simple outlines [4] and radar backscatter cross-sections [5], the majority of these flows likely have pahoehoe surfaces. There is a systematic decrease in lava flow distances with younger age. Estimates of the volumes of type 1 flow units are remarkably similar: the average volume is 5720 km^3 (except for unit 2 flows, which are somewhat more than three times the volume). In contrast, type 2 flows (unit 6) are short and broad, with steep flow fronts, small volumes, hummocky radar-texture, and possibly an a'a surface texture. In addition, type 2 flows are closely associated (and seem to source from) the two summit scalloped margin domes (SMDs)

Discussion: The above observations provide important constraints on the magma reservoir characteristics and magma flux with time. *Magma Reservoir*: Using Blake's [6] relationship which suggests that in a closed or buffered system the volume of material erupted is proportional to (about 1% of) the volume of the chamber, the average volume for the flow units implies a spherical chamber of approximately 100 km in diameter. Although this chamber is huge by terrestrial standards, there is additional evidence to suggest a large chamber under Sapas. It is frequently argued (eg. [7]) that the size of collapse at the summit is a good approximation of the size of the chamber at depth. Near the summit of Sapas is a discontinuous ring of fractures and graben that is 75-100 km in diameter. We suggest that this region represents an area of collapse over a chamber, similar to the sag depression observed at Pavonis Mons on Mars [8]. A chain of pits on the outer edge of the graben appears to be a source for some lava flows, suggesting a connection at depth to a source of magma. Although the radial fractures are observed on the upper flanks of the volcano, none are observed within the ring of graben, consistent with an origin for these fractures as the surface expression of dikes propagated laterally from a chamber. And finally, at the elevation of Sapas Mons, magma chambers are predicted to form, to be relatively large, and relatively shallow, but likely not within the edifice itself [9]. *Magma Flux*: The systematic decrease in lava flow distances suggests a decrease in eruption rate and/or duration with time. The similar volumes for four of the five type 1 flows, however, suggests that the volume of material supplied to the chamber from depth was relatively constant. The three-fold increase in volume associated with unit 2 flows may indicate a period of enhanced magma supply. The distinctive morphological change to type 2

flows and the construction of the SMDs suggests that supply waned or ceased, allowing volatile exsolution and/or chemical evolution of the magma remaining in the chamber to produce flows of apparently greater viscosity.

Conclusions: *Reservoir evolution*: These observations and inferences allow us to characterize the reservoir beneath Sapas Mons as one in which we interpret the following conditions to have prevailed: buffered conditions for the majority of eruptions, producing flows of similar volumes but decreasing flow lengths; unbuffered conditions during the eruption of the voluminous unit 2 flows and possibly the emplacement of many of the lateral dikes and small shields; final chemical evolution producing the morphologically distinct unit 6 flows and final summit asymmetry (two SMDs). This suggests that the majority of eruptions at Sapas were triggered by the episodic influx from depth of similar volumes of magma into the chamber and the resulting overpressure of that chamber. A period of enhanced supply led to sustained eruptions during emplacement of unit 2 flows. As supply from depth waned or ceased, the latest eruptions were likely caused by chemical evolution and pressure increase by volatile exsolution.

Sapas as a type volcano The similar properties of large volumes of magma over the total history of the volcano as well as a prolonged period of magma supply from depth with an episode of enhanced flux and gradual waning are consistent with an origin as a mantle plume or hot spot. This type of magma source has been proposed for many large volcanoes on Venus, particularly those associated with rift zones. Preliminary observations of other large volcanoes on Venus confirm that they share many important characteristics and could be classified as shield volcanoes, similar to those seen associated with hotspots on the Earth. We would argue, therefore, that the following characteristics make Sapas Mons a "type" shield volcano on Venus: low heights and broad diameter; large volume; long, narrow, overlapping radial flows (that can often be grouped into units); close association on the flanks and surrounding plains of small shields; circumferential summit structure (a sag depression at Sapas, but calderas are observed elsewhere); and presence of radial fractures. A few characteristics are unique to Sapas including the absence of complex flow morphologies (channels, breakouts etc.), the presence of the summit SMDs, and the concentration of the radial fractures and shields into two zones (although this may be an artifact caused by the asymmetric flow distribution).

Comparison to Earth: This typical shield volcano on Venus differs from hotspot volcanism on the Earth in several important ways. These differences, however, can generally be understood when considered in the context of the Venus environment. The low heights and long flow distances observed at Sapas and other Venus volcanoes can be attributed to a variety of factors including high surface temperature, predicted large volumes of chambers, and, possibly, low viscosity magmas [9, 10, 11, 12]. The absence of well-developed flanking rift zones on Venus may be a result of the low heights achieved by Venus volcanoes; finite element modelling of volcanoes suggests that the preferential migration of magma laterally rather than vertically within an edifice only happens when a certain edifice height is achieved [13]. The lack of repetition of stages of development that are seen in individual volcanoes along the H-E chain is likely the result of the absence of significant plate motion on Venus; these stages at Hawaii may be related to the need to penetrate 'fresh' lithosphere between successive volcanoes. The smaller volume (compared to the total for the H-E chain) and absence of broad-scale topographic swell observed at Sapas may be indicating the presence of a relatively smaller plume at Sapas; other volcanoes on Venus (eg. Theia Mons) are more voluminous and associated with large topographic swells.

References: [1] Keddie, S.T., and Head, J.W., 1992, *LPSC XXIII*, pp. 669-670. [2] Bargar, K.E., and Jackson, E.D., 1974, *Jour. Res. U.S.G.S.*, 2, pp. 545-550.. [3] Wilson, L., et al., 1993, *LPSC XXIV*, 1527-1528. [4] Bruno, B.C., et al., 1992, *GRL*, 19, pp. 305-308. [5] Campbell, B.A., and Campbell, D.B., 1992, *Jour. Geophys. Res.*, 97, pp. 16293-16314. [6] Blake, S., 1981, *Nature*, 289, pp. 783-785. [7] Zuber, M.T., and Mouginis-Mark, P.J., 1992, *Jour. Geophys. Res.*, 97, pp. 18285-18307. [8] Crumpler, L.S., and Aubele, J.C., 1978, *Icarus*, 34, pp. 496-511. [9] Head, J.W., and Wilson, L., 1992, *Jour. Geophys. Res.*,97, pp. 3877-3903. [10] Schaber, G.G., 1991, *PLPSC,XXI*,.pp. 3-11. [11] Head, J.W., and Wilson, L., 1986, *Jour. Geophys. Res.*, 91, pp. 9407-9446. [12] Hess, P.C., and Head, J.W., 1990, *Earth Moon Planet.*, 50/51, pp. 57-80. [13] McGovern, P.J., and Solomon, S.C., "State of stress, faulting, and eruption characteristics of large volcanoes on Mars", submitted to *Jour. Geophys. Res.*.

STRUCTURAL EVOLUTION OF DANU MONTES, VENUS: DEFORMATION AROUND A CURVED BOUNDARY; M. Keep and V. L. Hansen, Department of Geological Sciences, Southern Methodist University, Dallas, Texas, 75275

Summary. Four sets of structures are mapped along the Danu Montes/Vesta Rupes deformation belt. Contractional ridges change orientation with curvature around Lakshmi Planum, from NE-trending at the eastern, Danu, end of the belt to NW-trending at western Vesta Rupes. Extensional graben and fractures also parallel the Lakshmi boundary, occupying original valleys between ridges, and are interpreted in terms of extensional collapse of the original contractional belt. Temporally coeval, to later, extensional graben and fractures trend normal to the Lakshmi boundary, and accommodate curvature of the deformation belt. Post-deformational volcanic activity, producing volcanic pits and chains, may have used pre-existing structures. The proposed deformation history is compatible with early contraction and extensional collapse around the Lakshmi margin, with contemporaneous to later margin-normal extension accommodating belt curvature. The orientation and spatial distribution of structures around the Lakshmi margin are suggestive of a boundary effect, perhaps related to a fundamental boundary at depth between Lakshmi Planum to the north and the plains to the south.

Introduction. At 5 km above MPR, the Danu Montes/Vesta Rupes deformation belt parallels the curving southern margin of Lakshmi Planum. Belt orientation varies from northeast-trending at the eastern, Danu Montes, end of the belt, to northwest-trending at the western end of Vesta Rupes. The main deformation belt is approximately 50 km wide, immediately adjacent to Lakshmi Planum, although parallel structural trends are observed up to ~250 km outboard of Danu Montes. Along Vesta Rupes, two small areas of deformed crust, separated from Vesta Rupes by wide (~50 km) bands of radar-smooth and -dark material also preserve structures parallel to those of the deformation belt. Structures continue uninterrupted from Danu Montes westward to Vesta Rupes. The long, narrow shape and high aspect ratio of the belt are unlike other deformation belts surrounding Lakshmi Planum. This work addresses the structural history of the Danu Montes/Vesta Rupes deformation belt and proposes a model for Danu/Vesta deformation.

Observations. Three structural suites are observed on Danu Montes/Vesta Rupes. These include ridges, graben and fractures, and volcanic features. **1. Ridges:** Ridges, which vary in length from ~15 to 100 km and have an average spacing of 6 km, change orientation with belt curvature from NE-trending in the east (60N, 338E), through ENE-, W-, and NW-trending along the Danu/Vesta transition (59N, 331E), to NNW-trending at the western end of Vesta Rupes (60N, 318E). Ridges in eastern Danu are observed outboard as far as ~58N, 339E, where they are short (<15 km) and wispy. Ridges anastomose increasingly toward western Vesta Rupes. **2. Graben and fractures:** Interpreted as extensional structures, both graben and fractures are oriented both parallel to and normal to the deformed belt. **a. Belt-parallel:** Graben and fractures that parallel the belt change orientation from NE-trending on Danu, to NW-trending along Vesta Rupes. Graben are short, paired, parallel lineaments, with an average width <5 km. Graben length varies from 10-30 km. Fractures are sharp, singular lineaments that vary in length from ~20-30 km. Belt-parallel graben and fractures also parallel the ridges described above. Along western Vesta Rupes, belt-parallel graben and fractures become oriented at an acute angle to the deformation belt, and are thus neither belt-normal nor belt-parallel. These orientations are discussed further below. **b. Belt normal:** On Danu, NW-striking belt normal graben and fractures are ~20 km long, with close spacing (~5 km). Graben are narrow, <5 km wide, and both graben and fractures crosscut ridges. Along Vesta Rupes (e.g., 59.5N, 325E) NE-striking graben and fractures are short (<10 km), with spacing <5 km. These structures are concentrated on the highest parts of the belt, along ridges adjacent to Lakshmi Planum. Graben and fractures are confined to individual ridges, with parallel sets on adjacent ridges; graben and fractures decrease in number with decreasing belt topography to the northwest. Outboard of

these ridge-bounded graben and fractures, closely spaced wispy fractures and narrow graben become sigmoidal, oriented ~20° to the belt (NNW). Original belt-parallel and belt-normal structures parallel this NNW orientation (e.g., 60N, 323E). At the westernmost end of Vesta Rupes, long (>50 km) ridges and graben parallel each other, trend NNW, and are cut by wispy ENE-striking fractures and narrow graben. These structural relations are mimicked in two regions outboard of Vesta Rupes, both of which are separated from the main deformation belt by 50 km wide bands of radar-dark and -smooth material. Both of these regions preserve sigmoidal, generally NNE-trending, ridges and graben, which are cut by NE- and ENE-striking graben (e.g., 58N, 327E and 58N, 324E). **3. Volcanic features:** Small (<3 km diameter), circular, radar-dark pits are observed throughout Danu Montes and Vesta Rupes, generally in the deformation belt adjacent to Lakshmi Planum. At westernmost Vesta Rupes and easternmost Danu Montes the pits are closely spatially associated with long, linear, volcanic features, some of which are lobate at one end. The lobate nature of the lineaments is reminiscent of coalesced pits, and many single pits occur at the termination of a single volcanic lineament (e.g., 61N, 319E, 61.5N, 339E). These lineaments all have a NNW orientation and span the transition from the smooth plains of Lakshmi Planum to the deformation belt. In most cases the lineaments become increasingly lobate to the southeast, although the opposite is true locally. All of the volcanic lineaments cross cut the deformation belt. These lineaments have been interpreted as extensional volcanic collapse pit chains [1], although their mode of origin is not clearly understood. Similar volcanic features oriented east-west across Danu (60.5N, 339E) also cross cut the deformation belt and may have a similar origin. Two impact craters, Magnani (58.5N, 337E), and an unnamed crater (57.7N, 333E) also occur in close proximity to Danu Montes. Magnani, the larger of the two craters, is fresh and undeformed, in contrast to the second crater, which is deformed.

Interpretation. Interpreted extensional structures form the dominant structural fabric of the Danu Montes/Vesta Rupes deformation belt. Belt-normal extensional structures are everywhere observed to cross cut the ridges, and, less clearly, the belt-parallel extensional structures, and they are therefore interpreted to be younger than the ridges and belt-parallel extension. Belt parallel extensional structures are interpreted to be slightly younger than the ridges they parallel, as the extensional structures occupy original valleys between ridges. The volcanic pits and chains crosscut all of the deformation structures, and are therefore interpreted to be post-deformational. Similarly, the crater Magnani is interpreted to be post-deformational, although the smaller, unnamed crater, which records deformation, is interpreted as pre-deformational. The relative order of structure formation is therefore: i) ridges; ii) belt-parallel graben and fractures; iii) belt normal graben and fractures; iv) small impact crater (sometime during i, ii, and iii); v) volcanic collapse pits and chains and impact crater Magnani.

The above structural sequence is compatible with a progressive strain regime in which initial crustal contraction perpendicular to the Lakshmi Planum margin was followed by margin-parallel extensional collapse of shortened crust. Later margin-normal extension helped to accommodate belt curvature; the two extensional episodes may have overlapped in time. The final volcanic activity may be related to reactivation of existing crustal weaknesses resulting from deformation. This scenario requires two directions of crustal contraction, northwest-directed shortening on Danu Montes, and northeast-directed shortening along Vesta Rupes, reflecting the curved nature of the boundary. Interaction of these two shortening regimes would result in the changing structural orientations seen around the Lakshmi margin. The orientation and spatial distribution of structures around Lakshmi Planum suggest that deformation is a boundary effect related to the Lakshmi margin, perhaps reflecting a fundamental boundary at depth between Lakshmi Planun to the north and the plains to the south.

References. [1]. S.E. Smrekar and S.C. Solomon (1992) JGR **97**, 16,121.

XENON ISOTOPIC MEASUREMENTS IN SHALLOWATER: IN SITU PULSED LASER VOLATILIZATION AND THE SEARCH FOR THE CARRIER OF RADIOGENIC ^{129}XE: K. Kehm, C.M. Hohenberg and R.H. Nichols, Jr., McDonnell Center for the Space Sciences, Washington University, St. Louis, MO 63130 USA.

Introduction. The present measurements of Xe in Shallowater, a unique enstatite achondrite [1], represent our maiden attempt at *in situ* noble gas laser volatilization. Conventional bulk analyses of Shallowater have shown the presence of large amounts of radiogenic ^{129}Xe (^{129}Xe* from the decay of extinct ^{129}I), which is enriched by a factor of ~3 times the normal trapped ^{129}Xe and is thought to be carried in the enstatite [2]. This enrichment is present in fixed proportion to the amount of I in the bulk meteorite, providing a relatively precise I-Xe age ($\pm 10^5$yrs.) for Shallowater, but offering very little insight into what closure event(s) the I-Xe clock is dating. Much of this ambiguity can, in principle, be eliminated if the carrier phase(s) of the ^{129}Xe* can be determined, thereby associating a bulk I-Xe age with Xe closure in specific mineral phases. Apparent I-Xe ages of enstatite meteorites, unlike other meteorite types, seem to correlate with petrologic type in these objects [cf. 2]. While the Xe-retentive iodine hosts may be largely secondary minerals in most meteorites (and thus the I-Xe age reflects *secondary* processes), the host in enstatite meteorites may be enstatite itself (typically 80% of the bulk) or small inclusions within the enstatite. By selectively excavating Xe from various mineral phases in a Shallowater thick-section, we have tried to identify the carrier phase of ^{129}Xe* in order to provide more insight into the relationship between the bulk I-Xe age determination for Shallowater and its ^{129}Xe* carrier phase. While the carrier phase of radiogenic Xe in Acapulco, for example, has been determined via the analysis of individual mineral grains [3], selective *in situ* laser excavation of noble gases possesses an advantage over bulk and single grain techniques in that it can potentially link noble gas signatures with specific mineral phases in meteorites without the need for mineral disaggregation.

Technique. A polished thick section of Shallowater, approximately 2 mm thick and 1 cm^2 area, was mounted on an Al SEM stub for SEM analysis and subsequent laser volatilization. A back scattered SEM mosaic clearly delineated the primary mineral assemblages discussed by Keil et al. [1] including large ortho-enstatite crystals (~80% by volume), metallic Fe/Ni, and troilite. The section was subsequently loaded into the laser extraction cell of a low-blank noble gas mass spectrometer [4]. The extraction cell is fitted with a Pyrex viewport through which an acoustically pulsed 200 W Nd:YAG laser can be focused on the sample in vacuum. In addition, the cell was mounted on a high-precision (sub-micron resolution), computer controlled XY stage. During laser volatilization, the stage is programmed for side to side movements allowing the sample area to be "rastered" at a strictly controlled rate providing relatively uniform excavation depths (typically, 3×10^{-6} cm^3). Optimum pulse frequency and laser output power were determined to be 600 Hz and ~70 W on the basis of preliminary studies on a Springwater thick section.

Results. Data shown in Fig. 1 indicate that pure enstatite crystals (closed circles) or small inclusions within the enstatite carry most of the ^{129}Xe*. (In both Figs. 1 and 2 values for the bulk meteorite are given by the dashed lines.) No ^{129}Xe* was detected in the two metal phases for

which upper limits are given. The concentrations of $^{129}Xe^*$ in one troilite and one Fe/Ni metal phase (indicated by the open and closed squares, respectively) were at least an order of magnitude below the highest concentrations measured in enstatite. The presence of $^{129}Xe^*$ in these shots may be due solely to the heating or vaporization of nearby enstatite during the excavation of the metal phases. In addition, the analysis of an area of enstatite heavily veined with Fe/Ni metal (open circle) yielded a relatively low concentration of $^{129}Xe^*$, suggesting that I may not be sited along enstatite/metal grain boundaries. The result that enstatite or inclusions within the enstatite carry the $^{129}Xe^*$ is consistent with previous measurements on enstatite meteorites [5,6].

Neon isotopic measurements were also performed so that an independent determination of the excavation volumes could be computed from the cosmogenic ^{21}Ne abundances. The ($^{129}Xe^*/^{21}Ne_{cos}$) ratios in the enstatite (Fig. 2) may thus provide an insight into whether the $^{129}Xe^*$ is carried within the volume of the enstatite or within small inclusions contained within the enstatite. If $^{129}Xe^*$ is derived from the enstatite lattice, then the ratio should plausibly be constant. If, on the other hand, the $^{129}Xe^*$ is carried by small inclusions, then the ratio may vary. However, in this preliminary study, the two highest $^{129}Xe^*$ concentrations for enstatite shots have the two lowest ($^{129}Xe^*/^{21}Ne_{cos}$) ratios to first order, contrary to what we would expect. At the present time we do not fully understand the whole story. Work currently in progress will hopefully provide data that will elucidate some of these problems.

References. [1] Keil *et al.* (1989) *GCA* **53**, 3291-3307. [2] Kehm *et al.* (1993) *LPSC* **24**, 777-778. [3] Nichols *et al.* (1994) *GCA* **58**, in press. [4] Hohenberg (1980) *Rev. Sci. Instr.* **51**, 1075-1082. [5] Crabb and Anders (1982) *GCA* **46**, 2511-2526. [6] Wacker and Marti (1983) *EPSL* **62**, 147-158.

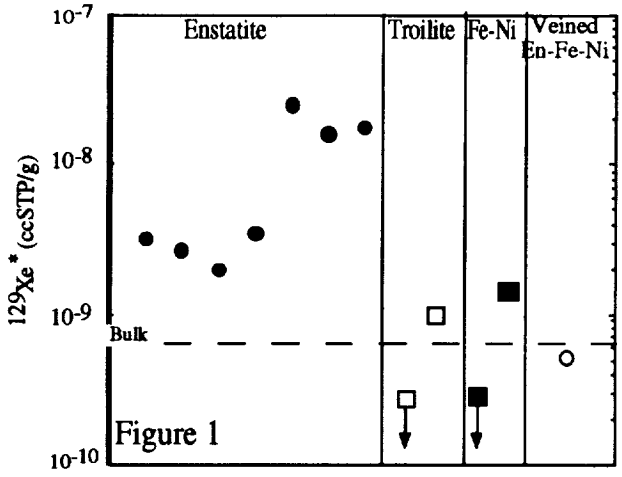

Figure 1

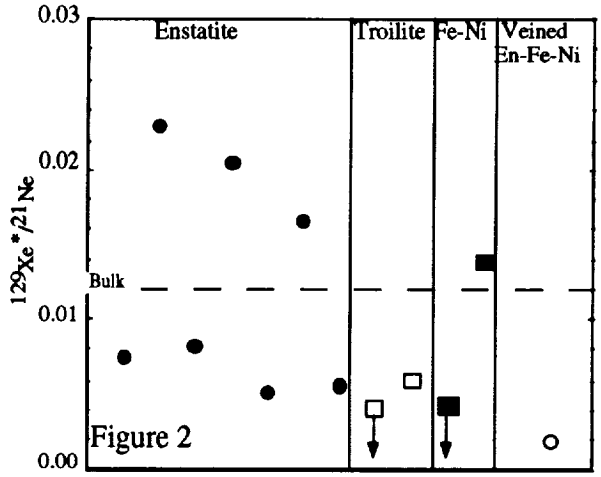

Figure 2

THE NATURE OF AGGLUTINITIC GLASS IN THE FINE-SIZE FRACTION OF LUNAR SOIL 10084.
Lindsay P. Keller[1] and David S. McKay[2], [1]MVA Inc., 5500 Oakbrook Parkway, Suite 200, Norcross, GA 30093 and [2]SN, NASA-JSC, Houston, TX 77058.

Introduction. Agglutinitic glass contains much of the reduced Fe in lunar soils [1], and contributes to the modification of reflectance spectra from lunar soils [2]. Previous work has shown that agglutinitic glass can be compositionally heterogeneous [e.g. 3-5], but the scale of these heterogeneities is not well known. In addition, few data are available on the characterisitics of the inclusions in agglutinitic glass. Here we report on our preliminary transmission electron microscope (TEM) examination of agglutinitic glass fragments from the Apollo 11 soil 10084.

Methods. Aliquots of the <20 μm size fraction of 10084 were embedded in low viscosity epoxy and specimens were prepared for electron microscope examination by ultramicrotomy. In the ultramicrotomed thin sections (80- to 100-nm thick), random fragments of agglutinitic glass free of lithic fragments were analyzed using a TEM equipped with an energy-dispersive x-ray (EDX) spectrometer. We analyzed 13 fragments of agglutinitic glass and collected 5 to 10 random analyses from each fragment (97 total analyses) using a probe size of ~100 nm. Thin-film EDX analyses were collected so that counting statistics for major elements were ~1%; experimental k-factors have relative errors of <5%. The size distribution of submicroscopic Fe metal was determined for each analyzed area.

Results and Discussion. Agglutinitic glass in our samples shows large variations in composition and texture. To assess the heterogeneity within *individual* fragments, we plotted all the analyses from different regions within each fragment in plots of MgO/SiO_2 (wt.%) versus Al_2O_3/SiO_2 (wt.%). From these plots, three broad patterns are observed. **Group I**. The smallest group (3 of 13 fragments) random analyses within each fragment are tightly clustered about the composition of the <10 μm fraction of the bulk soil (Fig. 1a). These compositions are highly homogeneous over distances of several micrometers, and the size distribution and number density of Fe inclusions is very similar among fragments of this group. Group 1 fragments represent well-mixed, total melts. **Group II**. This group contains 5 of the 13 fragments and is characterized by linear mixing trends in x-y scatter plots (Fig. 1b). The mixing trends extend between an anorthite-rich component and a mafic component. These melts are not well-mixed. **Group III**. Agglutinitic glass in this group shows strong compositional and textural gradients on a scale of <0.1 μm. The compositional variations are large and are not systematic. In only a few fragments have we identified domains within the agglutinitic glass that correspond to melts of individual minerals (5 regions of anorthite-composition glass and 1 region of augite glass were observed). Textural differences include the presence or absence of vesicles (and the number density of vesicles), the types of opaque inclusions, the size distribution of opaques, and the spatial distribution of opaques.

In agreement with previous studies, the average composition of our agglutinitic glass approaches that of the finest size fraction (Fig. 1e). We have however, observed that S is enriched by a factor of ~3 in agglutinitic glass relative to the bulk soil. Similar enrichments in S are observed in vapor-deposited coatings on mineral grains in the same soil [6], and so we believe that the S enrichment observed in agglutinitic glass is the preserved signature of the precursor materials, i.e. fine-grained soil grains with vapor coatings.

Opaque inclusions are typically spherical although most of the larger grains have begun to assume more euhedral shapes, including grains with octahedral faces and cubic forms. The number density of metal inclusions varies significantly among and within individual fragments of agglutinitic glass, however, the size distributions appear similar. Our results show that averaged over all analyzed agglutinitic glass fragments, the sizes of the metal inclusions follow a log-normal distribution (Fig. 1f) with a geometric mean grain size of 6.4 nm (the geometric standard deviation $\sigma_g = 1.81$). The measured size range of Fe grains closely corresponds to the proposed size range for the reduced metal that is known to be responsible for the ferromagnetic resonance (FMR) absorption used to estimate soil maturity [1]. The FMR data suggest a size range of ~4- to 33-nm for the metal grains produced by the exposure-induced reduction of Fe^{2+} [1].

Conclusions. 1) Agglutinitic glass shows compositional and textural heterogeneities at the 0.1 μm scale. 2) The glass fragments preserve a component of vapor deposited material. 3) The number density of Fe inclusions in agglutinitic glass is highly variable, but in general the size distributions tend to be similar and follow a log-normal distribution. 4) The actual size range of Fe grains in agglutinitic glass is similar to that estimated by FMR.

References. [1] Morris, R. V. (1980) *PLPSC* **11**, 1697. [2] Pieters, C. M. *et al.* (1993) *JGR* **98**, 20817. [3] Hu, H-N and Taylor, L. A. (1978) *Mare Crisium: The View from Luna 24*, 291-302. [4] Walker, R. J. and Papike, J. J. (1981) *PLPSC* **12B**, 421. [5] Basu, A. and McKay, D. S. (1985) *JGR* **90**, D87. [6] Keller, L. P. and McKay, D. S. (1993) *Science* **261**, 1305.

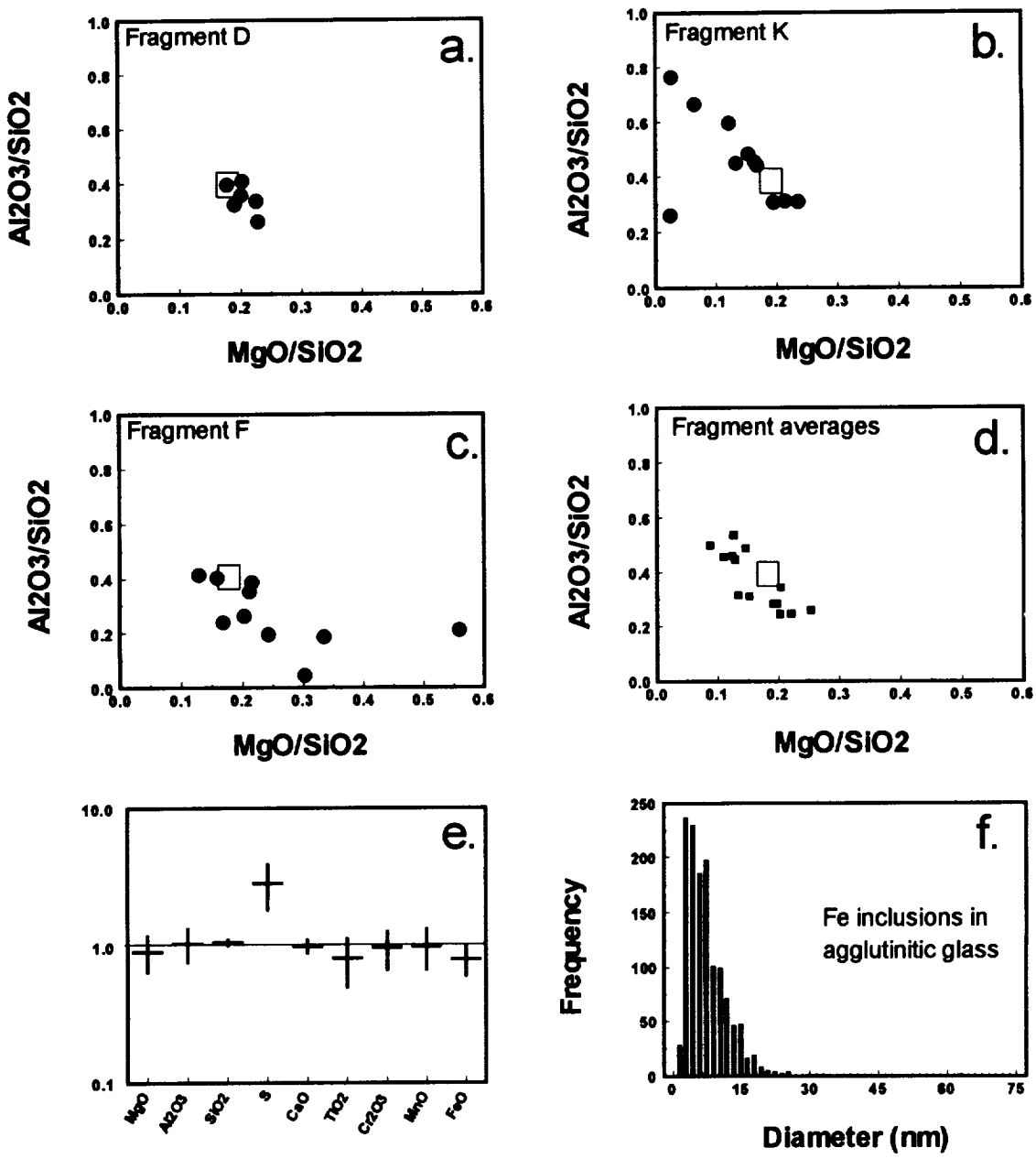

Figure 1a-1c. Plots of MgO/SiO_2 (wt.%) versus Al_2O_3/SiO_2 (wt.%) for individual fragments of agglutinitic glass showing a.) Group I, b.) Group II, and c.) Group III patterns (open square is the ratio for the >10 μm size fraction (from [4]), see text for details. Figure 1d shows the composition of each individual fragment obtained by combining the analyses from different regions within the same fragment to obtain an average. Figure 1e. The average composition of analyzed agglutinitic glass fragments relative to the bulk composition of the >10 μm size fraction (from [4]) of 10084. Figure 1f. A plot of the average size distribution of Fe grains in the analyzed agglutinitic glass fragments.

ELECTRON ENERGY-LOSS SPECTROSCOPY OF CARBON IN INTERPLANETARY DUST PARTICLES. Lindsay P. Keller[1], John P. Bradley[1], Kathie L. Thomas[2], and David S. McKay[3], [1]MVA, Inc., 5500 Oakbrook Parkway, Norcross, GA 30093, [2]C23, Lockheed, NASA/JSC, Houston, TX 77058, and [3]SN, NASA/JSC, Houston, TX 77058

Introduction. The nature of the carbon-bearing phases in IDPs provides information regarding the chemical and physical processes involved in the formation and evolution of the early solar system. Several carbon-bearing materials have been observed in IDPs [e.g. 1], but details of their nature, abundance, and distribution are still poorly known. A knowledge of the abundance and nature of carbon in IDPs is useful in constraining the sources of IDPs and for comparisons with other chondritic materials. Estimates of carbon abundance in anhydrous and hydrated IDPs indicate that most of these particles have significantly higher carbon than the carbonaceous chondrites [2,3]. Mineralogical analyses show that carbonates are only a minor component of most hydrated IDPs, and so the high carbon abundances in this group of IDPs indicates that other carbon-bearing phases are present in significant concentrations [3]. Using the technique of electron energy-loss spectroscopy (EELS), we have identified two forms of carbon in a hydrated IDP, oxidized carbon (carbonates) and amorphous elemental carbon.

Methods. EELS spectra were obtained using a JEOL 2010 TEM equipped with a GATAN parallel EELS detector. Carbonate standards were finely ground and dispersed onto SiO thin films for the EELS analysis. Ultramicrotome thin sections(~80 nm thick) of IDPs were placed on holey carbon films and only those regions of the thin sections that were over holes in the film were analyzed. EELS spectra were acquired at 0.2 eV/channel, with an analysis time of 1 second/scan. The scanned spectra were summed until more than 50K photodiode counts in the carbon K-absorption edge were accumulated.

Carbon Near-edge structure. In amorphous carbon, the excitation of a 1s electron to the first empty band (the π^* conduction band) results in the onset of the carbon K-edge at ~284 eV. The broad peak in the EELS spectra at ~292 eV corresponds to transitions from 1s to the σ^* conduction band. In graphite, the π^* peak involves the pz orbitals (the weak bonds between planes of carbon atoms in the graphite structure), while the sigma* peak results from sp2 hybrid bonds between coplanar carbon atoms. Structural variations (i.e. the degree of graphitization) can be estimated by comparing the relative proportions of π^* and σ^* bonding in the high-loss region [4,5].

There is a distinct energy shift in the onset of the carbon K-edge in carbonates relative to amorphous carbon. In carbonates, the onset of the carbon K-edge occurs at ~290 eV with a second broader peak centered at ~302 eV [6].

Results and Discussion. EELS spectra were collected from several regions (~0.5 μm in diameter) in thin sections of L2006G1, a hydrated IDP that contains 20 wt.% C [3]. L2006G1 consists of abundant Mg-rich saponite that coexists with fine-grained Fe-Ni sulfides. Distinct grains of Mg-Fe carbonates are observed in the thin section. This IDP shows no mineralogical evidence of strong heating (e.g. a magnetite rim) even though the diameter of the particle is ~25 μm.

Typical EELS spectra from L2006G1 are shown in Figure 1. Spectra obtained from the carbonate grains show the characteristic doublet structure for oxidized carbon, however, they also exhibit a slight contribution from indigenous amorphous carbon (the small peak with an onset at 284 eV). EELS spectra from other areas in the thin sections (e.g. phyllosilicate-dominated regions) have carbon K-edges that are typical of amorphous carbon. Comparisons with the edge structure of the carbon support film suggest that the amorphous carbon in L2006G1 is more disordered than the holey carbon film.

Conclusions. The analysis of the carbon near-edge structure in the EELS spectra from a hydrated interplanetary dust particle shows that carbonates and amorphous elemental carbon are the major carbon-bearing phases. The carbonates occur as discrete grains in the IDP whereas the amorphous carbon is associated with the fine-grained phyllosilicates. Electron energy-loss spectroscopy in the TEM provides a means of mapping the chemical state of carbon in IDPs with high spatial resolution

Acknowledgements. This work was supported by NASA RTOPs 152-17-40-23 and 199-52-11-02, and MVA, Inc.

References. **[1]** Bradley, J. P. *et al.* (1988) Interplanetary Dust Particles. In *Meterorites and the Early Solar System*, 861-898. **[2]** Thomas, K. L., G. E. Blanford, L. P. Keller, W. Klöck and D. S. McKay (1993) *Geochimica et Cosmochimica Acta* **57**, 1551-1566. **[3]** Keller, L. P., Thomas, K. L., and McKay, D. S. (1993) *LPSC XXIV*, 785-786. **[4]** Miner, B. (1988) *Poorly Graphitized Kerogens: A High-Resolution TEM Study*. Ph.D Dissertation, Arizona State University. **[5]** Katrinak, K., Rez, P., and Buseck, P. R. (1992) *Environmental Science and Technology*, 26, 1967-1976. **[6]** Smith, D. A., Clarke, D. R., Chisholm, M. F., Batson, P. E., and Olsson, E. (1990) *Proc. XII Intl. Cong. Electron Microscopy*, 32-33.

Figure 1. Electron energy-loss spectra of the main carbon-bearing phases in L2006G1.

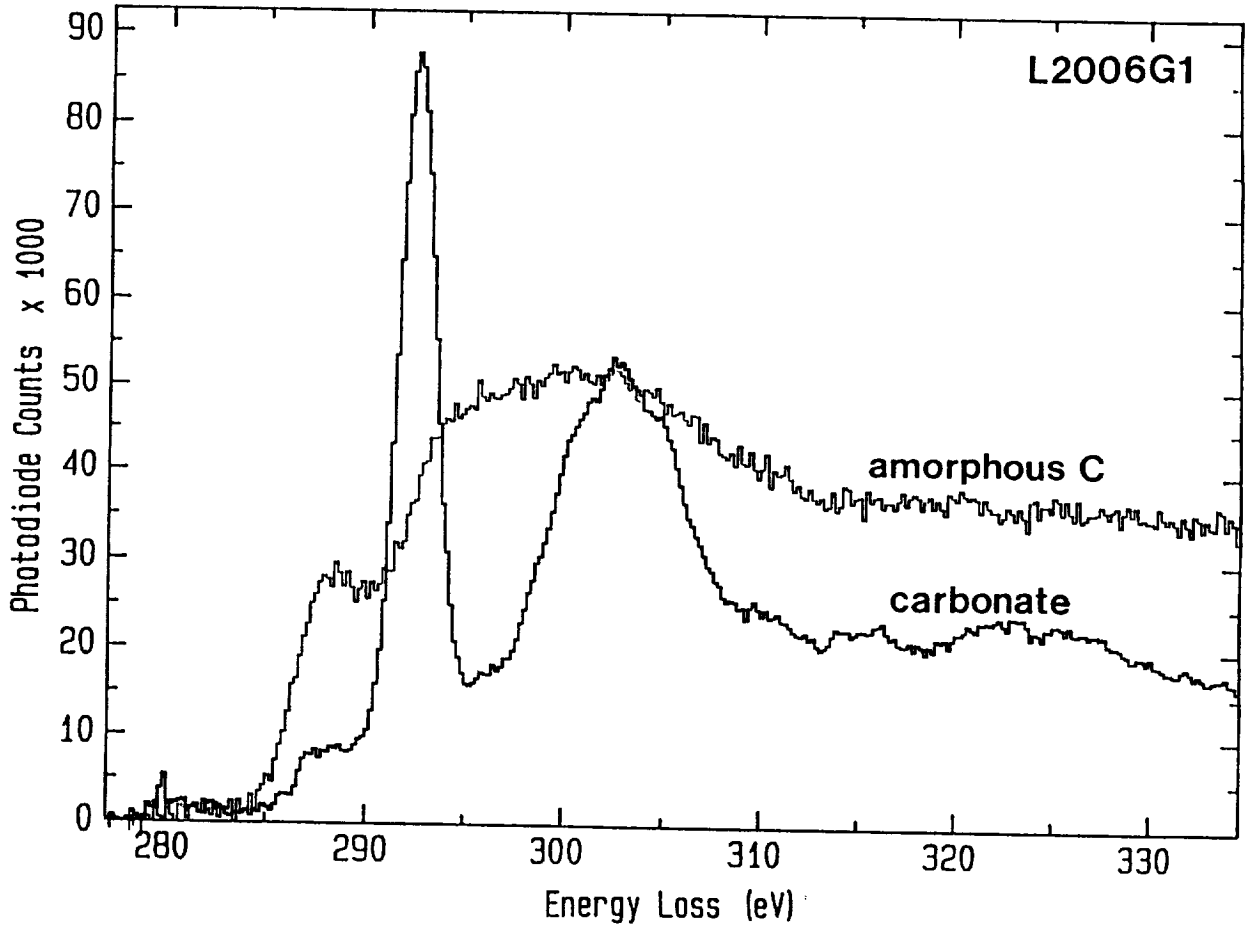

SHIFT TO P 739

COMPOSITIONAL EVIDENCE IN FAVOR OF A GENETIC LINK BETWEEN THE NYSA AND HERTHA ASTEROID FAMILIES; M. S. Kelley and M. J. Gaffey, Dept. of Earth & Env. Sci., Rensselaer Polytechnic Institute, Troy, NY 12180-3590; J.G. Williams, Jet Propulsion Laboratory, California Institute of Technology, Pasadena, CA 91109

High resolution spectral data has been obtained for 135 Hertha using the 52-channel double CVF (0.8-2.5μm) system at the Infrared Telescope Facility on Mauna Kea. The spectrum of Hertha exhibits a narrow, weak feature centered near 0.9μm indicating the presence of at least a small amount of silicate material on its surface. To date, this spectral feature has not been seen in published spectra of other M-types. 44 Nysa also exhibits a similar narrow absorption feature near 0.9μm [1] which is not seen in the high resolution spectra of other E-type asteroids (e.g. 3103 [2]). This distinct spectral feature, indicating a unique pyroxene composition, makes both these asteroids anomalous within their taxonomic classes. This distinctive feature also provides the genetic link in their mineralogy. Probable compositions of Nysa and Hertha can be reconciled with plausible compositions of F-types in this region and with extensive igneous processing of a parent body with E-chondrite starting composition.

Previously, several investigators have suggested a possible connection between the Nysa and Hertha families. Zellner, et al. [3] suggested that 44 Nysa is the largest surviving fragment of a silicate crust, broken away from the iron-core body 135 Hertha. However, they were unable to volumetrically reconcile these two objects with an enstatite-chondrite starting composition for the parent body. Gradie, et al. [4] also favored a connection and suggested ways to resolve the volumetric considerations. Williams [5] considered these to be separate families, but admitted that the close location of Nysa and Hertha suggests a connection.

Other investigators have argued against a common origin for these families. Bell [6] considered Nysa to be an interloper in its own family and Hertha and its family to be completely unrelated. These conclusions were primarily based on taxonomic classifications of family members. Chapman, et al. [7] and Granahan and Bell [8] reached the same conclusions again based almost solely on taxonomic classifications.

Recent additions of higher numbered objects to the previously identified [9] Nysa and Hertha families show a definite structure in the distribution of objects in this region. With a diameter of 57 kilometers, 142 Polana is the largest known F-type asteroid in this region, and it is second in size to 44 Nysa (73 kilometers) in the Nysa family. At least two distinct cratering events off of 142 Polana are identifiable. One of these cratering events has yielded a string of objects extending from Polana to the 3:1 Jupiter resonance. All of the objects in this structure that have been taxonomically identified are F-types. Spectral data (primarily ECAS) available for these objects show no obvious inconsistencies. However, the similarity between some asteroids (e.g. Nysa and Hertha) only becomes apparent in the subtle features of high resolution data.

Taxonomy-based studies [3-8,10] are an important first step in making general statements about asteroid families and they often point out intriguing directions for one to explore. For instance, part of the interest in the Nysa-Hertha region is the high concentration of F-asteroids relative to the background population, and their apparently odd association with M- and E-types. However, considering the mineralogical variability that exists within just one class of asteroids, the S-types [11], use of taxonomy is generally inadequate for testing genetic relationships between potential members of asteroid families. Therefore, arguments against the genetic reality of asteroid families based on their apparent inconsistencies between taxonomy of members may be invalid. The only rigorous test of the genetic reality of an asteroid family is one based on mineralogical characterization of the proposed family members and development of plausible thermal history and differentiation models to support or rule out membership.

GENETIC LINK BETWEEN THE NYSA AND HERTHA ASTEROID FAMILIES: Kelley, M. S., et al.

If the Nysa and Hertha families originated from a common parent body, that body must have been heated sufficiently to allow a core (Hertha) to separate from silicate mantle (Nysa) material. During the differentiation process, it is reasonable to expect that partial melts (basalts) would be extruded onto the surface of the body. To date no basaltic objects have been identified in the Nysa-Hertha region. Therefore, this material has either been lost, or it is somehow going undetected. It has been suggested that this material could have been lost to space by energetic eruptions during differentiation of the parent body [12,13]. At the high temperature required to melt a body of E-chondrite composition abundant CO would have been produced. CO produced in magma at depth in the parent body would have been converted to CO_2 at lower pressure as the gas migrated toward the surface. This may have resulted in the deposition of carbon in the cooler, primitive material near the surface. Subsequent disruption of the parent body would have yielded M- (core), E- (mantle), and F-type (carbon-darkened, E- or F-chondrite) objects.

In order to resolve this issue, rotational spectral coverage and visible and thermal infrared lightcurves need to be obtained for 44 Nysa, 135 Hertha and 142 Polana. This level of detail is required to distinguish spectral variations due to body shape from those due to lithologic variations on the asteroid surfaces. Understanding the arrangement of family member surface lithologies allows one to constrain the internal compositional structure of the parent body. In addition, high resolution spectral data in the visible to near infrared are needed to characterize several F-type objects inside and outside the Nysa-Hertha region.

ACKNOWLEDGMENTS: Portions of this work were supported by NSF Solar System Astronomy grant AST-9012180, NASA Planetary Geology and Geophysics grant NAGW-642, and an Ernest F. Fullam Award from The Dudley Observatory. M. J. Gaffey and M. S. Kelley are Visiting Astronomers at the Infrared Telescope Facility which is operated by the University of Hawaii under contract to the National Aeronautics and Space Administration. Thanks to Pranoti M. Asher for the use of a portable computer.

REFERENCES: [1] Gaffey M.J., Bell J.F. and Keil K. (in preparation). [2] Gaffey M.J., Reed K.L. and Kelley M.S. (1992) *Icarus*, **100**, 95-109. [3] Zellner B., Leake M., Morrison D. and Williams J.G. (1977) *Geochim. Cosmochem. Acta*, **41**, 1759-1767. [4] Gradie J.C., Chapman C.R. and Williams J.G. (1979) in *Asteroids*, U. Arizona Press, pp. 359-390. [5] Williams J.G. (1992) *Icarus*, **96**, 251-280. [6] Bell J.F. (1989) *Icarus*, **78**, 426-440. [7] Chapman C.R., Paolicchi P., Zappala V., Binzel R.P. and Bell J.F. (1989) in *Asteroids II*, pp. 386-415. [8] Granahan J.C. and Bell J.F. (1993) *Icarus* (submitted). [9] Williams J.G. (1989) in *Asteroids II*, pp. 1034-1072. [10] Gradie J.C. (1978) Ph.D. dissertation, Univ. of Arizona [11] Gaffey M.J., Bell J.F., Brown R.H., Burbine T.H., Piatek J.L., Reed K.L. and Chaky D.A. (1993) *Icarus* (in press). [12] Wilson L. and Keil K. (1991) *Earth and Planet. Sci. Let.*, **104**, 505-512. [13] Wilson L. and Keil K. (1991) *Lunar and Planet. Sci. XXII*, 1515-1516.

MODELLING LAVA FLOW COOLING USING A FINITE-DIFFERENCE NUMERICAL APPROXIMATION; R. M. Kent, and H. Pinkerton, Environmental Science Division, Lancaster University, Lancaster, LA1 4YQ, U.K.

The flow of lava is influenced by several factors, including the rheology and initial temperature of the lava, and the pressure gradient that drives the flow, [1]. The rheology of lava at sub-liquidus temperatures is often approximated by a Bingham model with a yield strength and plastic viscosity, [2], [3], two parameters that are highly temperature dependent. Therefore, to accurately model the movement of lava flows it is very important to understand the way in which they lose heat. As a first step in this process, lava flow cooling models have been developed using finite-difference techniques. Similar models have previously been developed, [4], [5], but they assume a fixed temperature of 0 °C at the upper surface of the lava flow.

While analytical solutions are available for many flow and heat transfer problems, a numerical approach offers greater flexibility, allowing complex geometry's to be considered, and also permitting time-dependent boundary conditions and temperature dependent material properties. The problem of lava flow cooling has been examined, initially for a stationary body, using a simple finite-difference approximation to the one-dimensional heat conduction equation, [6]

$$v_m^+ = v_m + \frac{\kappa\tau}{h^2}\left(v_{m+1} - 2v_m + v_{m-1}\right) \qquad (1)$$

where v_m^+ represents the temperature at the mesh m and at time $t+\tau$, v_m is the temperature at time t, and the subscripts $m+1$ and $m-1$ show the temperatures at the meshes adjacent to the mesh m. The mesh size is h and κ is the thermal diffusivity.

At the free surface of the lava flow the heat flux into the atmosphere due to radiation and convection can be included as a boundary condition. If there is an imbalance between the heat lost to the atmosphere and the heat that can be conducted through the body of lava, the surface temperature will change. The heat flux at any point in the lava flow is described by the heat conduction equation, of which a suitable finite-difference approximation for the surface mesh, $m=0$, is

$$F_s = \frac{K}{2h}\left(v_1 - v_{-1}\right) \qquad (2)$$

where v_{-1} is the temperature at an imaginary mesh, the centre of which is situated at a height h/2 above the free surface, (Schmidt's method, [7]) and K is the thermal conductivity. Eliminating v_{-1} from equations 1 and 2 gives an expression for the surface temperature which includes the heat flux boundary condition.

$$v_0^+ = v_0 + \frac{\kappa\tau}{h^2}\left[2\left(v_1 - v_0\right) - \frac{2hF_s}{K}\right] \qquad (3)$$

The surface heat flux term can then take the form

$$F_{SR} = \varepsilon\sigma\left(v_0^4 - v_A^4\right) \qquad (4)$$

for radiative heat transfer, where ε is the emisivity, σ is the Stefan-Boltzman constant, and v_A is the atmospheric temperature. Alternatively, or in addition, the heat loss through convection can be modelled using the expression, [8]

LAVA FLOW MODELLING: **Kent, R.M., and Pinkerton, H.**

$$F_{SC} = \frac{NuK_A(v_0 - v_A)}{L} \qquad (5)$$

where L is the typical horizontal length scale of the problem, K_A is the thermal conductivity of the air, and Nu is the Nusselt number.

Figure 1 shows the decrease in surface temperature with time for the finite-difference approach compared with the analytical model of Head and Wilson, [8]. The surface heat flux included the radiative flux term plus either a forced convection or a natural convection term. At each time step the greater of the two convection terms is included in the surface heat flux, and the smaller term is ignored. The forced convection calculation in this example was based on a mean wind speed of 5 $m.s^{-1}$. The flow is 10m thick and it is assumed to have been emplaced instantaneously on Earth. Figure 2 shows typical temperature profiles through the flow and the country-rock at different times, given in days. The initial temperature of the lava for both the figures was 1273 K.

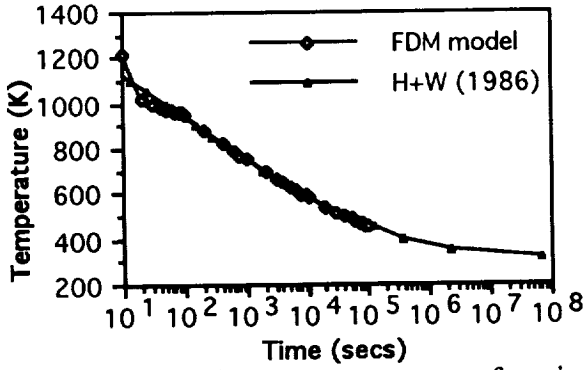

Figure 1. Surface temperature as a function of time for the model of Head and Wilson (H+W), and the finite-difference approximation, (FDM), for a 10m thick flow losing heat by radiation and convection at the upper surface.

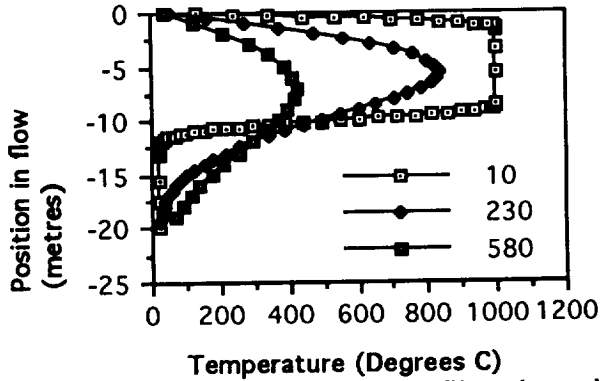

Figure 2. Temperature profiles through a 10m flow. Depth=0 represents the upper surface of the flow, and Depth= -10 is the lava country rock contact. Time is given in days.

The finite-difference approach can be extended to include the effects of a broken crust, where heat is lost directly from the lava flow interior as well as from the surface, [9]. Extending to two-dimensions also allows the influence of advection to be considered. Planetary flows can be modelled by changing the appropriate variables in the surface heat flux terms to account for varying atmospheric conditions.

References: [1] Griffiths, R. W., Fink, J. H., Jour. Fluid. Mech., vol. 252, p.667-702, 1993 [2] Pinkerton, H., Wilson, L., Bull. Volc., *in press* [3] Dragoni, M., *et. el.*, Jour. Volc. Geoth. Res., vol. 52, p.247-254, 1992 [4] Long, P. E., Wood, B. J., Geol. Soc. Am. Bull., vol.97, p.1144-1155, 1986 [5] Manley, C. R., Jour. Volc. Geoth. Res., vol. 53, p.27-46 [6] Carslaw, H. S., Jaeger, J. C., (1959), Conduction of Heat in Solids, Oxford Univ. Press, New York, pp510, [7] Jaeger, (1950), Proc. Camb. Phil. Soc., Vol. 46, p.634-641, [8] Head, J. W., Wilson, L., Jour. Geoph. Res., Vol. 91, p.9407-9446, [9] Crisp, J., Baloga, S., Jour. Geoph. Res., Vol. 95, p.1255-1270

MODELLING THE FLOW AND HEAT TRANSFER OF MAGMA IN DIKES USING COMPUTATIONAL FLUID DYNAMICS

R. M. Kent, and H. Pinkerton, Environmental Science Division, Lancaster University, Lancaster, LA1 4YQ, U.K.

Understanding the movement of magma in dikes is important on the terrestrial planets, where dikes can feed large lava flow fields, [1], [2]. There are many models which describe the heat loss from a magma filled dike, including solutions for stationary bodies of magma, [3], [4], [5], and models which include the effects of advection, [6], [7], [8]. Analytical solutions produce accurate results where approximations to geometry and material properties can be made, but, if a model describing a dike of changing dimensions and a magma with temperature-dependent properties is required then a numerical approach is necessary, [8]. The problem of magma flow in dikes was considered using the techniques of computational fluid dynamics (CFD), which in this case used a Galerkin formulation of the finite-element method to solve simultaneously the momentum and mass conservation equations of the system. The inclusion of an energy conservation equation is also required if heat transfer processes are important. In addition to modelling simple dike shapes, we have analysed heat loss from the Pu'u 'O'o feeder dike in the East Rift Zone of Kilauea Volcano, Hawaii.

Probably the greatest advantage of a numerical solution to magma flow problems is the ease with which temperature, strain-rate, and species dependent rheology models can be included. A simple exponential temperature dependency was used in the present analysis, [9], but the method also permits the effects of suspended crystals and bubbles, [10], temperature dependent yield strengths, [11], and strain-rate dependent viscosities, [12], to be included.

Transient analyses allow the growth of the solidifying layer of magma at the dike walls, and the subsequent changes in flow dynamics, to be examined. The heat added to the system at the melt/solid interface can be included as an enthalpy term or as direct latent heat release. In common with all the other material properties the amount of energy liberated is temperature dependent. The influence of the viscous dissipation term will depend on the dike geometry, the driving pressure, and the size of the viscosity/temperature dependency. In some cases the effects will be negligible, but it has been shown to be important for some dike systems, [8]. Under extreme conditions there is also the possibility of thermal runaway, which will rapidly promote conduit blocking, or melt back regimes, [7]. This positive feedback system can produce extreme instabilities in the numerical approach.

The method was used to investigate the flow of magma that fed the 1984 eruptions of Pu'u `O'o in the Eastern Rift Zone of Kilauea Volcano, Hawaii. Using known dimensions of the feeder dike, [13], and driving pressure gradients derived from summit tilt recordings, [14], the CFD simulation was set up using the commercial package FIDAP to model the initial start-up of the magma in the conduit and the developing flow profile. The decreasing driving pressure, which in part determines the duration of the eruption, was included as a time dependent boundary condition. The dike was assumed to be 18 km long, the first 16 km of which are parallel sided and 3 m wide, with the last 2 km necking to 30 cm wide at the eruption site. The vertical dimension of the dike is assumed to be great enough that it can be ignored, reducing the problem to two-dimensions, and so the effects of gravity and buoyancy can also be omitted. Figure 1 shows the start-up of the magma in the Pu'u `O'o feeder dike for episode 25 of the 1983-1986 eruption, which is initially at rest before the required driving pressure is applied at the dike inlet. The inlet temperature is assumed to be 1473 K. Figure 2 shows the velocity profile across the dike outlet 10 minutes after the start of the eruption. The centreline of the dike is at *0.0 m* and the solidified region can be seen at the dike wall between *0.11527 m* and *0.14409 m*. The velocities at the outlet are an order of magnitude higher than those at the inlet due to the decrease in dike width. Figure 3 shows the temperature profile across the outlet from the centreline to the dike wall and *0.3 m* into the country rock, after 10 minutes.

It has been suggested that the development of a yield strength in the narrow section of the Pu'u `O'o feeder dike due to preferential cooling controls the cessation of an eruption, and not

MAGMA FLOW IN DIKES: Kent, R. M., Pinkerton, H.

necessarily just the drop in driving pressure to zero, [13]. The present work will therefore be extended to include magmas with temperature dependent yield strengths, and the dynamics at the end of eruptions will be investigated.

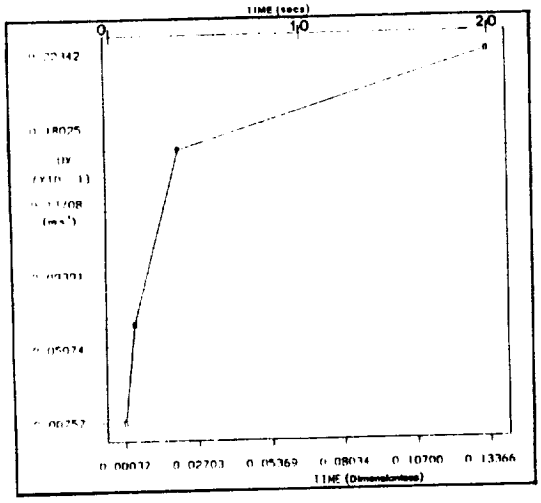

Figure 1

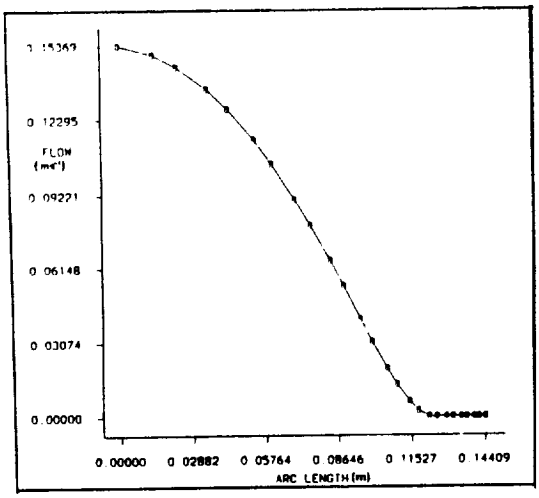

Figure 2

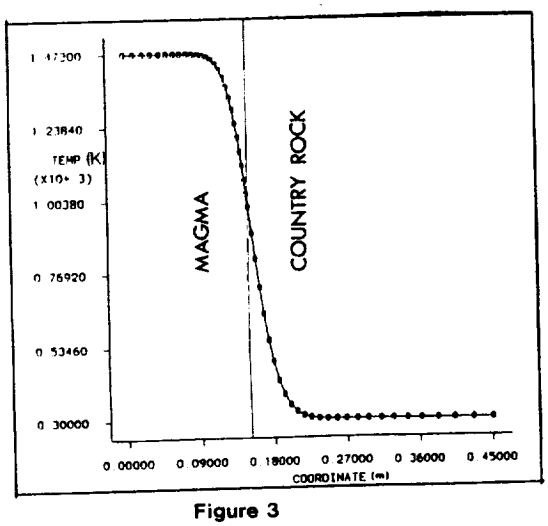

Figure 3

References: [1] Head, J. W., *et. al*, Jour. Geoph. Res., vol. 97, no. E8, p.13153-13197, 1992 [2] Magee Roberts, K. *et. al.*, Jour. Geoph. Res., vol. 97, no. E10, p.15991-16015,1992 [1] Jaeger, J. C., in Basalts: The Poldervaart Treatise on Rocks of Basaltic Composition, eds. Hess, H. H., Poldervaart, A., Interscience, New York, p.503-536, 1968. [3]Jaeger, J. C., Am. Jour. Sci., vol.255, p.306-318, 1957. [5] Jaeger, J. C., Am. Jour. Sci., vol. 257, p.44-54, 1959. [6] Delaney, P. T., Pollard, D. D., Am. Jour. Sci., vol. 282, p.856-885, 1982. [7] Bruce, P. M., Huppert, H. E., in Magma Transport and Storage, ed. Ryan, M. P., John Wiley and Sons, p.87-101, 1990. [8] Carrigan C. R. *et. al.*, Jour. Geoph. Res., vol. 97, no. B12, p.17377-17392, 1992. [9] Shaw, H. R. *et. al.*, Am. Jour. Sci., vol. 266, p.255-264, 1968. [10] Pinkerton, H., Stevenson, R. J., Jour. Volcanol. Geotherm. Res., vol. 53, p.47-66, 1992. [11] Dragoni, M., Bull. Volc., vol. 51, p.88-95, 1989. [12] Norton, G., Pinkerton, H., LPS XXIV, p.1149-1150, 1993[13] Parfitt , E. A., Wilson, L., Jour. Volc. Geoth. Res, *.in press*. [14] Parfitt, E. A., *personal communication*, 1993.

PRODUCTION OF SUPERPARAMAGNETIC FE^0 ON THE LUNAR SURFACE

John F.Kerridge, Dept.Chemistry & California Space Inst., UCSD, La Jolla, CA 92093-0317

Inclusions of Fe^0, some tens of nm in size, are formed in the amorphous rims of lunar regolith grains from solar-wind-reduced indigenous Fe^{++}, by either radiation-induced lattice rearrangement, or micrometeorite-induced vaporisation and recondensation, or both. This leads to surface correlation of the resulting FMR signal. Subsequent regolith maturation transfers that metal into agglutinitic glass, generating a volume-correlated FMR component. Typical lunar regolith contains a mixture of both components.

Even before the Apollo 11 landing, it was recognised that solar-wind irradiation probably leads to chemical reduction of the lunar surface [1,2,3]. Subsequent analysis of Apollo regolith samples confirmed this prediction [4,5]. Furthermore, it was found that agglutinates in the lunar regolith contain very fine metallic Fe particles [6] and that at least a fraction of these are single-domain, superparamagnetic grains, i.e., <30nm in diameter, thereby yielding a characteristic ferromagnetic resonance (FMR) signal [7]. As the proportion of agglutinates builds up during maturation of the regolith, the FMR intensity, I_S, increases, the parameter I_S/FeO being an excellent quantitative measure of regolith maturity [7]. Microscopically visible metal grains, and presumably also submicroscopic grains, are concentrated in the glass that binds each agglutinate together [8]. It has been generally accepted that such grains are produced during melting of precursor regolith minerals by micrometeorite impact, with reduction of lunar Fe^{++} being effected by solar-wind H previously implanted in the mineral surfaces [7,8]. However, the exact sequence of events involved in the production of superparamagnetic Fe^0 has not been clear. In particular, it was found [9] that in some immature soils the superparamagnetic Fe^0 was apparently surface correlated, Fig. 1, leading to speculation that in some way micrometeorite impact initially caused either the proportion of agglutinitic glass, or the density of fine-grained metal in that glass, or both, to vary inversely with regolith particle size [9]. The physical basis of this scenario seems questionable, even though the distribution of maturity-dependent properties among different grain-size fractions is not well established, but a plausible alternative has been lacking. However, observations [10,11] of 10-200nm-sized inclusions of Fe^0 in the amorphous rims of mineral grains from the lunar regolith provide an explanation for this phenomenon.

Previous studies of the amorphous rims that characterise most lunar regolith grains have concluded that those rims result solely from the intense radiation damage that the solar wind inflicts on the outermost lunar surface [12]. Thus, the rims were regarded as being effectively glass with the same chemical composition as the underlying grain interiors [13]. However, results of Auger and ESCA spectroscopy suggested that the surfaces of lunar regolith grains are enriched in Si and Fe, with some of the excess Fe being in the metallic state [14]. Furthermore, it was established that regolith S is surface correlated [15,16], and from isotope systematics it was possible to infer that regolith grain surfaces are depleted in O, i.e., reduced [17]. Consequently, although reduction of Fe^{++} to Fe^0, by solar-wind-induced sputter ejection of O [18], was consistent with a purely solar-wind radiation-damage origin for the amorphous rims, enrichment of those rims in S, Si and possibly Fe^{++} appeared to require either an additional or an alternative process, such as condensation from impact-generated vapor [10,19,20]. Direct analyses of such rims in silicate [10] and ilmenite [11] grains have recently confirmed the enrichments in S and Si (though revealing depletion of Fe^{++}); however the Ti contents of the ilmenite rims demonstrate that the rims are not solely produced by vapor deposition but result from a combination of vapor deposition and radiation damage [11]. Whether vapor deposition is involved in the reduction of

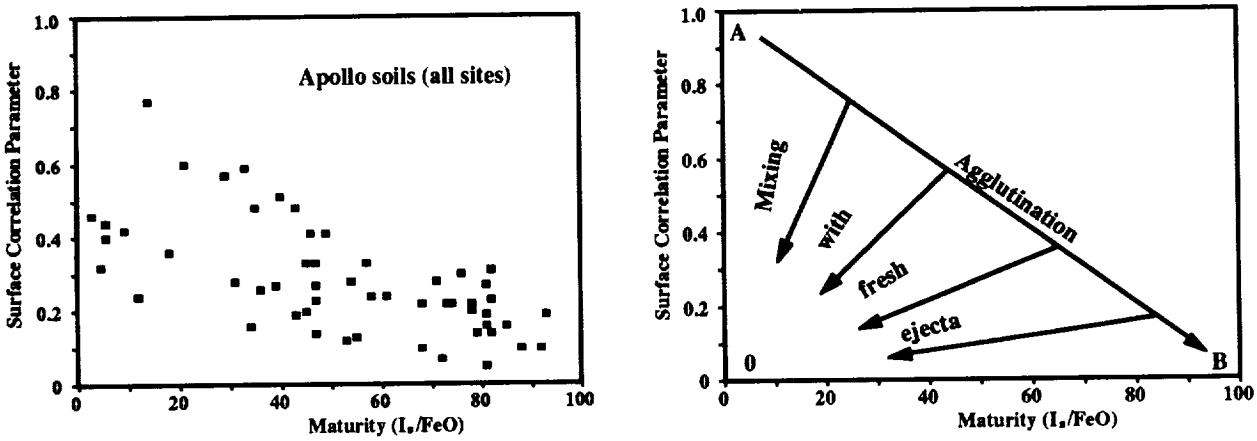

Fig.1 (left). Surface correlation parameter for intensity of ferromagnetic resonance, I_S, as a function of maturity for lunar soils. The surface correlation parameter is the negative of the slope of a log-log plot of I_S *vs.* grain size. A value of 1 connotes a pure surficial component; a value of 0 a pure volume component. After [9]. Fig. 2 (right). Schematic representation of evolution of the surface correlation parameter with increasing regolith maturity.

Fe^{++} to Fe^0 is presently unknown.

Despite uncertainty concerning the possible role of vapor deposition in their production, the observation of ultrafine Fe^0 inclusions in the rims of regolith mineral grains leads to the following semi-quantitative model to explain the data in Fig. 1. This is illustrated by means of Fig. 2.

Solar-wind sputtering of surfaces of Fe^{++}-bearing mineral grains leads to production of Fe^0 which generally remains as isolated atoms or small clusters within the increasingly metamict mineral lattice. Such material would plot at the origin in Fig. 2. Aggregation of Fe^0 clusters into inclusions tens of nm in size then occurs within the amorphous rims, either as a result of further irradiation damage (possibly involving higher-energy solar particles) leading to substantial rearrangement of the atoms comprising the rim, or as a result of micrometeorite-induced vaporisation of reduced surficial material and recondensation onto surfaces of neighboring mineral grains, or both. Regolith at this stage would plot at point A in Fig. 2. Subsequent impacts further modify this material in two ways: fusing of fine lithic grains into agglutinitic glass, and mixing with pristine rock. These two effects lead to trends towards points B and O, respectively, in Fig. 2. Production of the melt that forms the agglutinitic glass probably results in further reduction of Fe^{++} by solar-wind H liberated during fusion, and further aggregation into superparamagnetic Fe^0. However, the earlier stages will continue to operate throughout the process so that which stage dominates in production of superparamagnetic Fe^0 is not yet clear.

[1] Hapke,B.W., in:*The Lunar Surface Layer*, 323 (1964). [2] Gold,T., in:*The Lunar Surface Layer*, 345 (1964). [3] Rosenberg,D.L. & Wehner,G.K. *JGR* 69,3307 (1964). [4] Hapke,B.W. et al. *PLSC Apollo 11*, 2199 (1970). [5] Gold,T. et al. *PLSC Apollo 11*, 2149 (1970). [6] Housley, R.M. et al. *PLSC3*, 1065 (1972). [7] Morris,R.V. *PLSC7*, 315 (1976). [8] Housley,R.M. et al. *PLSC4*, 2737 (1973). [9] Morris,R.V. *PLSC8*, 3719 (1977). [10] Keller,L.P. & McKay,D.S. *Science* 261, 1305 (1993). [11] Bernatowicz,T. et al., *LPSXXV*, this volume (1994). [12] Borg,J. et al. *PLSC2*, 2027 (1971). [13] Borg,J. et al., in:*The Ancient Sun*, 431 (1980). [14] Baron,R.L. et al. *EPSL* 37, 263 (1977). [15] Rees,C.E. & Thode,H.G. *PLSC5*, 1963 (1974). [16] Kerridge,J.F. et al. *PLSC6*, 2151 (1975). [17] Taylor,H.P. & Epstein,S. *PLSC4*, 1657 (1973). [18] Yin,L.I. et al. *JGR* 77, 1360 (1972). [19] Kerridge,J.F. & Kaplan,I.R. *PLPSC9*, 1687 (1978). [20] Kerridge,J.F. *PLPSC21*, 301 (1991).

Formation of Venusian Crustal Plateaus over Mantle Downwellings; J.G. Kidder, R.J. Phillips, Dept. of Earth and Planetary Sciences, Washington University, St. Louis, MO 63130.

Introduction. It has been proposed that formation of Venusian crustal plateaus such as Ovda, Thetis, and Tellus Regiones is due to the presence of mantle downwellings ("coldspots"), which lead to large amounts of crustal flow, and ultimately to crustal thickening [1, 2, 3]. We have performed a finite element analysis of crustal thickening over a mantle downwelling using the finite element code TECTON [4], a Lagrangian finite element formulation capable of solving problems of visco-elastic deformation for materials with Newtonian or power law rheologies, and temperature dependent viscosities. A finite element solution of this problem may be more realistic than an analytical solution in that conservation of mass is assured without any assumption of layers of infinite horizontal dimensions. In this abstract we conclude that under a variety of conditions the topographic uplift produced over a mantle downwelling never exceeds one kilometer in one billion years of simulation.

Models. We have carried out a series of model runs with different boundary conditions, geometries, and flow laws to test the feasibility of formation of large crustal plateaus over mantle downwellings in a geologically reasonable period of time. Our reference model consisted of a 20-km-thick diabase crust overlying a 30-km-thick dunite mantle (50 km being chosen as the thickness of the Venusian mechanical lithosphere). Power law rheologies were used with the diabase flow law of Caristan [5] and the dunite flow law of Chopra and Patterson [6]. The model is 6000 km wide and the boundary conditions are as follows: the left side is fixed in the x-dimension (a symmetry boundary condition), but free to move in the y-dimension, the right side and top are free boundaries, and the base is a free boundary, with a downwelling force imposed by a gaussian-shaped load (σ = 700 km and maximum magnitude such that the initial isostatic depression is 1 km at the surface) applied over the first 2000 km. The temperature distribution was calculated using the error function equation of Zuber and Parmentier [7], with the surface temperature 740 K, the asymptotic temperature 1510 K, and the temperature gradient at the surface 15 K/km. This gave a temperature at the base of our reference model of 1331 K. We ran the model through approximately 1 billion years, and achieved only 863 m of positive topography at the surface (see Figure 1A).

We have tested the effect of (i) varying the width of the model, (ii) a fixed vs. free side boundary condition, and (iii) using the diabase flow law of Mackwell et al. [8] to model the crust. Using the new flow law dramatically reduced the amount of crustal thickening in the model: after 1 billion years, the surface was still depressed 996 m (see Figure 1B).

Conclusions. None of the model runs produced the high topography associated with large Venusian crustal plateaus such as Ovda Regio. Bindschadler and Parmentier [1] show a non-dimensional uplift ratio of four or greater, but for our models this quantity is never greater than unity after a billion years of simulation. The amount of topography generated is greatly affected by using realistic horizontal dimensions of material and by the use of the diabase flow law of Mackwell et al. [8]. Our ongoing investigations are examining the effects of changing the crustal thickness, the temperature gradient, the mantle flow law [9], and the depth of the perturbing source. We are also studying the effect of an axisymmetric vs. a plane strain

VENUSIAN CRUSTAL PLATEAUS: Kidder, J.G., and Phillips, R.J.

geometry, and are applying a velocity boundary condition at the base of the crust to better simulate the shear forces caused by a convecting mantle. We will also take into account the effects of the thickening crust on mantle convection itself.

References. [1] Bindschadler D.L. and Parmentier M. (1990) *JGR, 95,* 21329; [2] Lenardic A. et al. (1991) *GRL, 18,* 2209; [3] Bindschadler D.L. et al. (1992) *JGR, 97,* 13495; [4] Melosh H.J. and Raefsky A. (1980) *Geophysical Journal of the Royal Astronomical Society, 60,* 333; [5] Caristan Y. (1982) *JGR, 87,* 6781; [6] Chopra P.N. and Paterson M.S. (1984) *JGR, 89,* 7861; [7] Zuber M.T. and Parmentier E.M. (1990) *Icarus, 85,* 290; [8] Mackwell S.J. et. al. (1993) *EOS, 74,* 378; [9] Karato S. and Wu P. (1993) *Science, 260,* 771.

FIGURE 1A

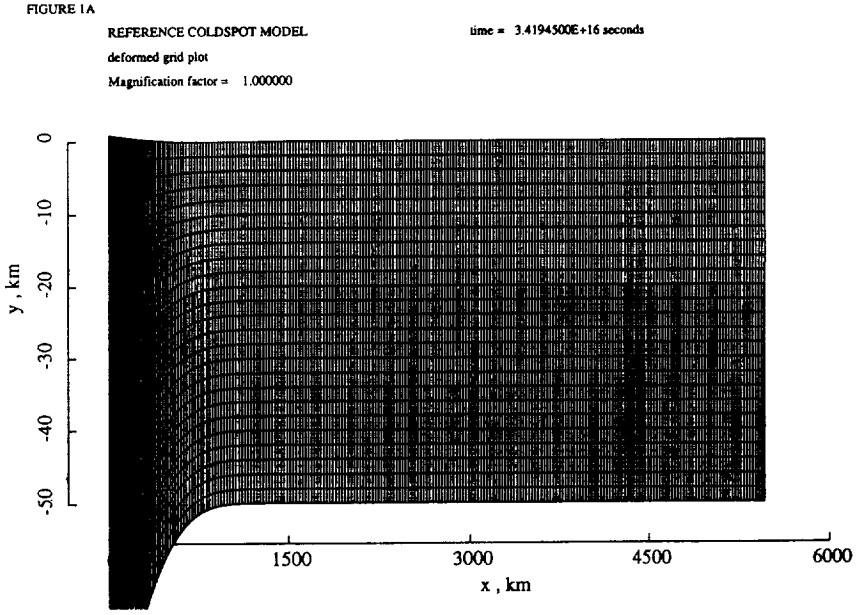

FIGURE 1B

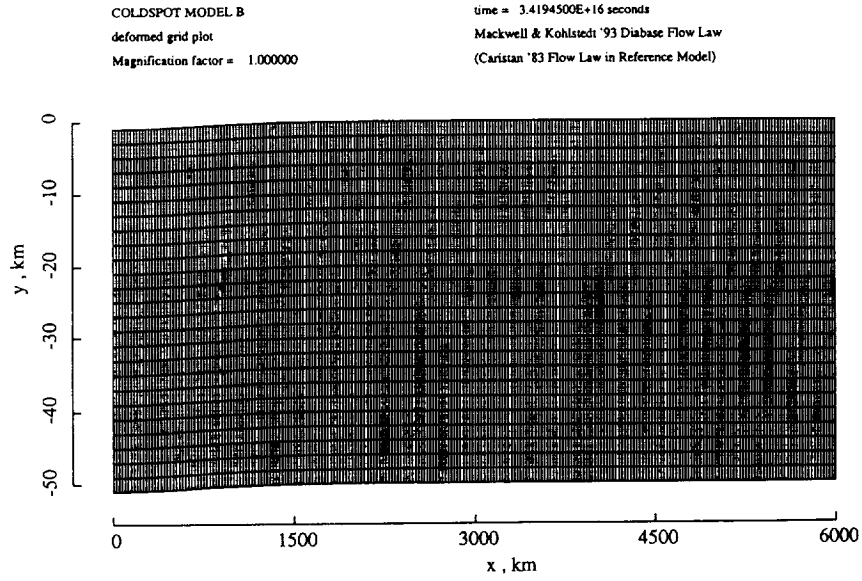

MANTLE PLUMES ON VENUS: NEW HIGH RAYLEIGH NUMBER MODELS AND APPLICATIONS TO MAGELLAN OBSERVATIONS

Walter S. Kiefer, Lunar and Planetary Institute, 3600 Bay Area Blvd., Houston TX 77058
(713) 486-2110; Fax (713) 486-2162; kiefer@lpi3.jsc.nasa.gov

New finite element simulations of axisymmetric mantle plumes are presented which extend earlier work to a thermal Rayleigh number of 10^7. These results verify earlier predictions based on power-law extrapolations and can explain observations of the geoid and topography of Atla and Beta Regiones if Venus lacks a low-viscosity zone in its upper mantle. Decreasing the aspect ratio of a convection cell decreases the width of the surface uplift and decreases the amplitudes of the uplift and of the geoid anomaly; such models can account for the geoid and topography of western Eistla Regio and Bell Regio. Contrary to a recent assertion in the literature, these results demonstrate that high Rayleigh number mantle convection can be an important contributor to the geoid and topography of Venus.

New High Rayleigh Number Models

Kiefer and Hager [1,2] developed a series of finite element mantle plume simulations and applied them to observations of geoid anomalies and topography of the Equatorial Highlands of Venus. They showed that a range of models can account for the observations, with the Rayleigh number and the mantle's viscosity stratification trading off against one another. Specifically, they found that a model with a thermal Rayleigh number of 10^6 and an upper mantle viscosity of 0.1 times the lower mantle viscosity and a model with thermal Ra between 1 and $3 \cdot 10^7$ and an isoviscous mantle could both explain geoid and topography observations of Beta and Atla Regiones. In that work [1], the geoid and topography for $Ra > 10^6$ were based on power-law extrapolations of lower Ra finite element results. The physical basis for such extrapolations is that the geoid and topography reflect the details of the internal temperature distribution, which is dominated by thermal boundary layers that are well-known to have a power-law dependence on Ra. Thus, the observation that geoid anomalies and topography are also power-law functions of Ra [2] was not surprising.

Nevertheless, it is desirable to verify the results of these predictions by finite element modeling. This has now been done for Ra up to 10^7 for viscosity models 1 and 2 of [1]. The finite element results for viscosity model 1 (high viscosity surface layer + isoviscous mantle) agree with the power-law projections to within 2.5 meters of geoid and 200 meters of topography. The finite element results for viscosity model 2 (high viscosity surface layer and an upper mantle viscosity of 0.1 times lower mantle viscosity) are weakly time-dependent at $Ra > 10^6$, with the mean amplitudes agreeing with the power-law projections to within 5 meters of geoid and 250 meters of topography. These new results therefore validate the earlier discussion [1, Table 2] concerning trade-offs in the allowed Rayleigh number and mantle viscosity structure that can explain observations of geoid anomalies and topography at Beta and Atla. This is illustrated graphically in Figure 1. The dashed lines have $Ra = 10^6$ and an order of magnitude increase in viscosity between the upper and lower mantles (viscosity model 2). This was the model in [1] which best fit observations of Beta and Atla. The solid lines are for an isoviscous mantle (viscosity model 1) and $Ra = 10^7$. The two sets of model results are virtually identical, and either model can account for most of the observed geoid and topography at Beta and Atla. Turcotte's recent assertion [3] that convection can contribute significantly to the geoid and topography of Venus only at $Ra \leq 3 \cdot 10^5$ is incorrect.

What is the Role of a Low Viscosity Zone on Venus?

Figure 1 shows that mantle plumes can produce geoid and topography amplitudes similar to those observed on Venus, provided that the viscosity contrast between upper and lower mantles is small. The absence of a pronounced low viscosity zone is unlike Earth, and the canonical explanation for this has been that Venus's mantle is much drier than Earth's mantle [e.g., 1]. Turcotte [3] has recently argued that this mechanism cannot prevent the existence of a low viscosity layer, because raising the

asthenosphere's viscosity due to a lack of water will cause the asthenosphere to heat up, thus lowering the viscosity again. However, this temperature increase will also affect the deeper mantle, lowering the viscosity there as well. The self-regulation argument must be applied to the mantle as a whole rather than to individual layers of the mantle, and thus can not be used to require the existence of a low viscosity zone on Venus. Indeed, one can easily construct a suite of models which transport the same amount of heat but which have different viscosity stratifications and hence very different geoid and topography signatures.

Effects of Variable Aspect Ratio

The results in Figure 1 and [1] are for plumes with an aspect ratio of 1, which for whole mantle convection gives horizontal scales of topographic uplift comparable to that observed at Beta and Atla Regiones. Features with smaller horizontal scales, such as western Eistla Regio and Bell Regio, are also believed to be related to mantle plumes [1,4,5]. These features vary in horizontal scale by about a factor of 2. Terrestrial hotspot swells also vary in diameter by about a factor of 2 [6], although the larger terrestrial swells are similar in size to the smaller Venus swells.

For terrestrial hotspot swells, there is a positive correlation between swell diameter and the amplitudes of both geoid anomalies and topographic uplift [6]. Similarly, on Venus, Bell and western Eistla have smaller amplitude topography and gravity anomalies than do Beta and Atla. The difference in horizontal scales suggest that the plumes which underlie Bell and western Eistla may be narrower than those beneath Atla and Beta, possibly due to a smaller aspect ratio of the convective structure. A finite element model with an aspect ratio of 0.5 but with conditions otherwise identical to those of the dashed line model in Figure 1 produces a geoid anomaly of 29 meters, a free-air gravity anomaly of 90 mgals, and a dynamic uplift of 1.9 km at the center of the upwelling. These results are roughly comparable with values observed at Bell and western Eistla.

Applications to Magellan Observations

The prior generation of plume models [1] was compared with Pioneer Venus Orbiter observations, which had a horizontal resolution of 60 km (topography) to 2000 km (gravity anomalies). In contrast, Magellan has made observations with a horizontal resolution of 10 km (topography, [7]) to 600 km (gravity anomalies, [8]). The improved resolution of these observations allows more detailed testing of mantle plume models. Detailed comparisons between the models described here and Magellan observations are currently being performed.

[1] Kiefer and Hager, JGR 96, 20947, 1991. [2] Kiefer and Hager, Geophys. J. Int. 108, 198, 1992. [3] Turcotte, JGR 98, 17061, 1993. [4] Smrekar and Phillips, EPSL 107, 582, 1991. [5] Grimm and Phillips, JGR 97, 16035, 1992. [6] Monnereau and Cazenave, JGR 95, 15429, 1990. [7] Ford and Pettengill, JGR 97, 13103, 1992. [8] Konopliv et al., GRL 20, 2403, 1993.

Figure 1. Geoid anomalies and dynamic topography versus distance from the center of upwelling for 2 finite element models. Solid lines are for $Ra = 10^7$, a high viscosity surface layer, and a uniform viscosity mantle. Dashed lines are for $Ra = 10^6$, a high viscosity surface layer, and an upper mantle viscosity a factor of 10 less than the lower mantle viscosity. Scaling constants from [1].

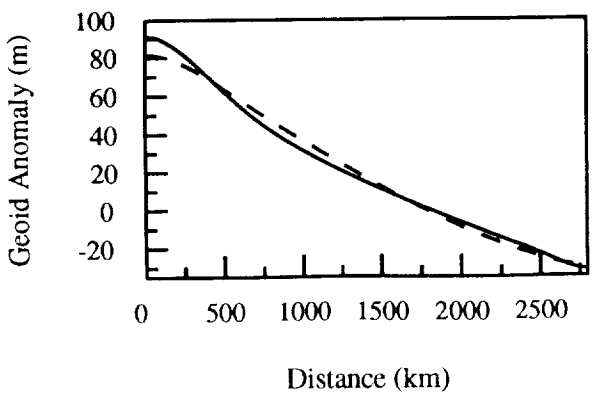

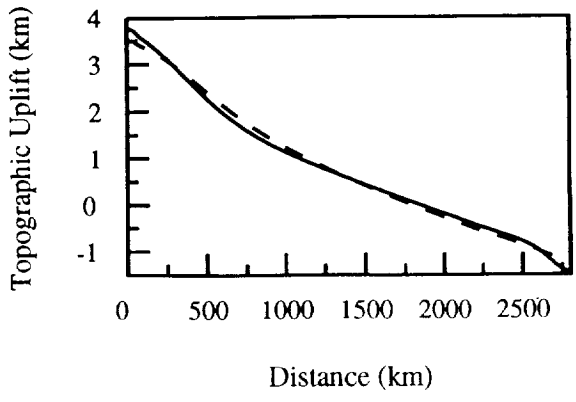

ISOLATION OF COSMIC-RAY-PRODUCED NITROGEN IN METEORITIC SILICATES AND SOME IMPLICATIONS; J. S. Kim, Y. Kim, and K. Marti, Dept. of Chemistry 0317, University of California at San Diego, 9500 Gilman Dr., La Jolla, CA 92093-0317.

Abstract: We measured nitrogen isotopic signatures in meteoritic silicate separates of Enon, Brenham, and Forest Vale. Enon and Forest Vale silicates reveal almost pure cosmic-ray-produced nitrogen. Nitrogen in Brenham silicates is an isotopically equilibrated mixture of cosmogenic and trapped components. We used spallation nitrogen as a monitor for volume diffusion properties and found that trapped nitrogen in chondritic silicates sited in minor carrier phases rather than in the silicate lattice.

Recently, several studies of the nitrogen distribution and of nitrogen isotopic signatures in different meteorites played an important role in the understanding of the evolution of parent bodies and their genetic relationships, supplementing information provided by oxygen isotope signatures. However, sometimes cosmogenic stable isotopes mask information on the trapped components and it is necessary to correct the spallation component. Although the distribution of trapped noble gas has been constrained [1], the carbon-rich carrier phase does not account for all the gases. As part of our general study of carriers and of distribution of noble gases and of nitrogen in meteorites, we selected Enon (ungrouped), Brenham (pallasite), and Forest Vale (H4), because of their long cosmic exposure ages in an attempt to use the spallation component that is sited in silicate lattice as monitor for volume diffusion. We used metal and silicate separates and measured N and Xe isotopic signatures of gas extracted by a combination of combustion and pyrolysis steps.

The ratio of ^{14}N and ^{15}N are very different in trapped and cosmogenic components. We measure $^{14}N^{14}N$, $^{14}N^{15}N$, and $^{15}N^{15}N$ molecules rather than atomic species. The isotopic exchange reaction between labeled N_2 molecules was observed with the use of catalysts [2]. Also, when mixtures of several distinct components are analyzed by mass spectrometry, the nitrogen molecules are dissociated and equilibrated isotopically [3, 4]. In our work on mineral separates, we considered three components (trapped, cosmogenic, and adsorbed air nitrogen). The trapped indigenous component is isotopically similar to air N but differs from cosmogenic N. Cosmogenic nitrogen is produced from oxygen in silicates. Therefore, the site of cosmogenic nitrogen is in the lattice of silicates. If two nitrogen components are released differentially from distinct carriers by stepwise extraction, it has to be expected that nitrogen is isotopically disequilibrated. As mentioned in [4], from the $^{29}N_2/^{28}N_2$ ratios of mechanical mixture and isotopic equilibrium, we can obtain isotopic signature for 2nd components, which is the mixture between cosmogenic and trapped nitrogen in the silicate lattice. This is a useful tool to measure very small amounts of trapped nitrogen. Hashizume and Sugiura [4] hypothesized that nitrogen released from bulk ordinary chondrite at high temperature steps was not isotopically equilibrated for trapped and cosmogenic N based on the time dependent changes in 29/28 ratio and mass 30 peak. However, Murty [5] criticized their hypothesis stating that cosmogenic N is produced in atomic form in the lattice of silicate, therefore, it is expected that N will isotopically exchange with trapped N in ordinary chondrite silicates.

Experimental: In nitrogen measurement, the main mass interference is from CO^+ ions. By monitoring mass 30, we can correct CO^+ contributions. Usually >50% of the mass 30 peak is due to CO^+, but $\delta^{15}N$ corrections are <5‰. Occasionally NO^+ interference is observed, that can cause a rapid decay of the mass 30 peak. In the melting step of Enon silicate, we observed mass 29 increased while mass 30 decreased with time in the mass spectrometer as shown in Fig. 1. We find isotopically disequilibrated molecular nitrogen in the following observations: 1) The magnitude of mass 30 intensity loss equals 50% of the gain of mass 29 peak. 2) The ratio 30/31 and its time dependence reflect the decay of $^{15}N^{15}N$. Other possible interferences (CO, NO and hydrocarbons) can be eliminated. An isotopic exchange reaction does not occur during our clean-up procedure. On the other hand, we extracted nitrogen from bulk Enon and did not observe isotopic disequilibrium. It is not clear how N isotopic equilibrium is achieved in the bulk sample. A possible mechanism is the catalytic reaction by metal or else nitrogen is released in different molecular form, but not only as N_2.

Results: Enon is an ungrouped meteorite which contains silicates of chondritic composition with more than 50% metal. It shows a undisturbed old K-Ar age and a cosmic ray exposure age of ~80My [6]. We measured N and Xe in bulk Enon, in metal and in silicates. The bulk sample reveals very low Xe concentrations (< 2.4 $\times 10^{-12}$cc/g) and low N (0.3ppm) and the spallation component is visible in melting step ($\delta^{15}N$=228‰). The metal separate yields δ15N=5‰ and [N]=0.8ppm. We found almost pure cosmogenic nitrogen in Enon silicates. The measured high $\delta^{15}N$ >1500‰ in the melting step shows isotopic disequilibrium. From the $^{29}N_2/^{28}N_2$ ratios in the mechanical mixture, and after isotopic equilibrium we obtained cosmogenic nitrogen component with

$(^{15}N/^{14}N)_C > 0.87$. Since the theoretical value for $(^{15}N/^{14}N)_C$ is ≥ 1, the cosmogenic nitrogen in Enon silicates may have in part exchanged with either trapped, blank or adsorbed nitrogen during the extraction process.

An earlier nitrogen study [7] of Brenham revealed 21ppm of N with $\delta^{15}N$=-66‰ in metal and below the detection limit in silicate. We measured nitrogen to obtain the isotopic signature of trapped N from metal and the cosmogenic [$^{15}N_C$] from olivine separates. Our data revealed 69ppm N in the metal with $\delta^{15}N$=-73‰, and 0.83ppm N in the olivine with $\delta^{15}N$=+47‰. The Brenham olivine data showed that cosmogenic nitrogen was isotopically equilibrated with trapped nitrogen. The Brenham olivine obiously contains trapped nitrogen in the silicate lattice which possibly was incoporated during metamorphism.

In the H-chondrite Forest Vale, we studied N and Xe isotopic signatures in silicates. Most of the silicates represent broken chondrules. Cosmogenic nitrogen was released above 1050°C, mostly in the melting step, and revealed isotopic disequilibrium corresponding to $(^{15}N/^{14}N)_C > 0.45$. On the other hand, trapped nitrogen was released in all temperature steps yielding a total [N]= 2.1ppm. Comparing Forest Vale, Enon and Brenham silicates, we note that chondritic silicates have a different carrier that contains most of the trapped nitrogen, but the silicate lattice itself may actually contain little trapped nitrogen. It is interesting to note that trapped Xe was released before the melting step (1200°C), while a considerable fraction of radiogenic $129Xe_r$ was released on the melting step (1500°C). The different release patterns of cosmogenic nitrogen and of trapped and radiogenic Xe again reveal different sites in the silicates. In fact, microscopic inclusions are typically observed in silicates.

Conclusions: The evidence for nitrogen isotopic disequilibrium in meteoritic silicates may depend on the trapped nitrogen in the silicates lattice. Enon silicates are extremely depleted in volatile and the nitrogen disequilibrium is seen in cosmogenic nitrogen. Brenham is not depleted in nitrogen, and silicates release isotopically equilibrated N_2 of trapped and cosmogenic nitrogen. The record in Forest Vale suggests that the observed disequilibrium may indicate that the silicate lattice carries little trapped nitrogen. Enon is an excellent sample for studies of volatile cosmogenic nuclides. We have identified the signature of cosmogenic nitrogen $(^{15}N/^{14}N)_C > 0.87$ in Enon silicates.

We acknowledge Drs. C. Perron and P. Pellas for supplying the Enon and Forest Vale silicates.

References. [1] Lewis R. S. et al. (1975) *Science 190*, 1251. [2] Kummer J. T. and Emmett P. H. (1951) *J. Phys. Chem. 19*, 289. [3] Wiens R. C. and Pepin R. O. (1988) *GCA 52*, 295. [4] Hashizume K. and Sugiura N. (1992) *GCA 56*, 1625. [5] Murty S. V. S. (1992) *GCA 57*, 1353. [6] Niemeyer S. (1983) *GCA 47*, 1007. [7] Prombo C. A. and Clayton R. N. (1993) *GCA 57*, 3749.

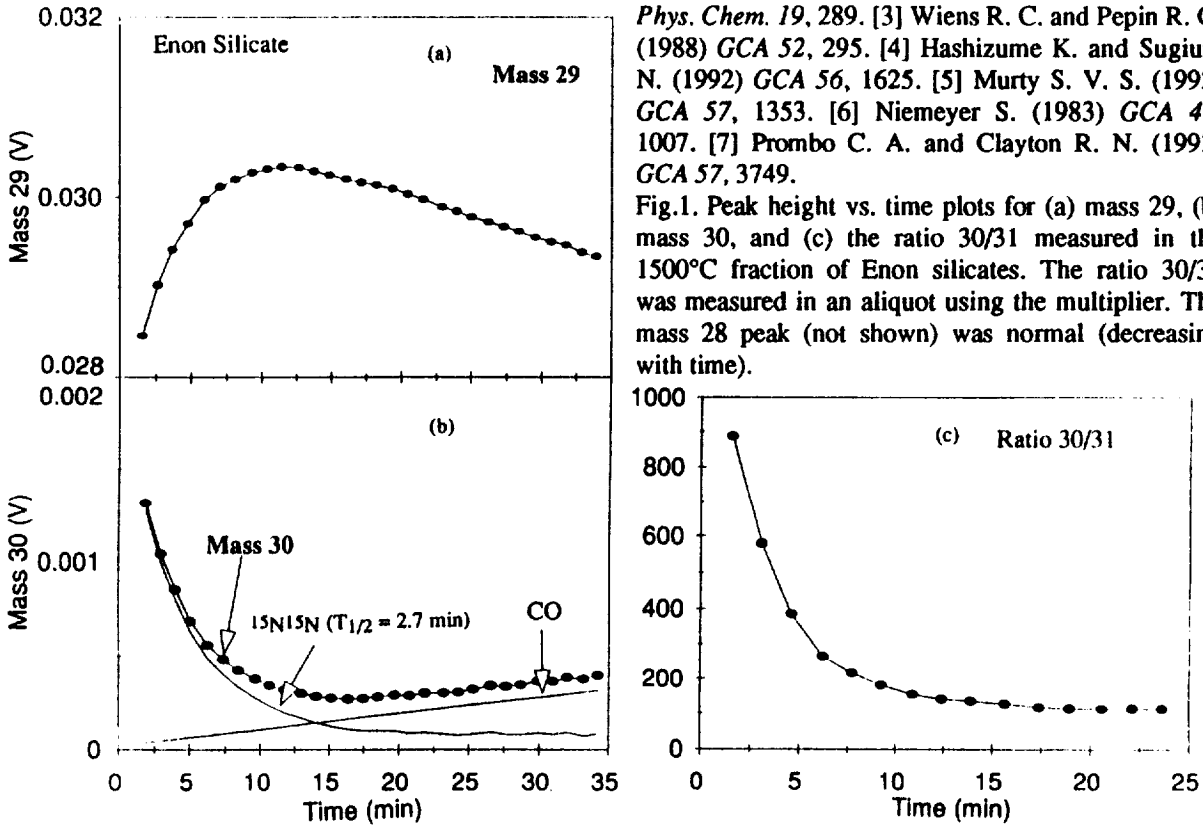

Fig.1. Peak height vs. time plots for (a) mass 29, (b) mass 30, and (c) the ratio 30/31 measured in the 1500°C fraction of Enon silicates. The ratio 30/31 was measured in an aliquot using the multiplier. The mass 28 peak (not shown) was normal (decreasing with time).

GENETIC RELATIONSHIP OF ACAPULCOITES AND LODRANITES? A STUDY OF NITROGEN AND XENON ISOTOPIC SIGNATURES; Yoosook Kim and Kurt Marti, Dept. of Chemistry 0317, University of California at San Diego, La Jolla, CA 92093-0317.

Abstract: Nitrogen and xenon isotopic signatures in mineral separates of acapulcoites and lodranites further constrain a genetic relationship implied by the oxygen isotopes. While the nitrogen signatures differ for Acapulco silicates, metal and chromite, only one signature is observed in the lodranites EET84302 and FRO90011. The ^{129}Xe isotopic abundance is uniformly evolved in both types relative to OC-Xe and the major Xe carrier was identified as the "magnetic" silicates.

Introduction: Primitive achondrites possibly represent a transitional state between chondrites and differentiated achondrites (1). The available chronological data on Acapulco reveal an old age of its parent body (2,3) but the time of system closure for ^{129}Xe in Acapulco phosphates postdates that of at least some chondrites (4), and apparently dates secondary processes on its parent body. Acapulcoites and lodranites were considered to have close genetic relationships, and to possibly originate from a single parent body (5). The FRO90011 and EET84302 meteorite are both classified as lodranites (6) and the latter was considered to provide a clue for the understanding of S-type asteroids, since the metal-rich primitive achondrites appear to match the observed reflectance spectra (7).

We report new isotopic signatures which bear on the genetic relationship between acapulcoites and lodranites. Previous nitrogen isotopic studies of Acapulco revealed the existence of nitrogen isotopic disequilibrium (8,9), because of the very light nitrogen component of metal ($\delta^{15}N \leq -150‰$) which contrasts to those of silicates ($\delta^{15}N$ +15‰) (9). The Acapulco silicates display uniform nitrogen isotopic signatures. The light nitrogen component was also found in the cores of "magnetic" silicates (9) and in chromite [Figure 1], documenting the isotopic disequilibrium among mineral phases. Recent work (10) shows that Acapulco metal has graphite inclusions which have very light nitrogen and each grain shows variation in nitrogen and carbon isotopic signatures. This isotopic disequilibrium occurs on a microscale. It is not clear yet how much of the light nitrogen is carried by the graphite in Acapulco, but it indicates that the nitrogen carriers in Acapulco have not lost their primordial isotopic heterogeneity. Acapulco also reveals relatively large concentrations of trapped noble gases, comparable to those of type 4 ordinary chondrites (11,9), and at least two different carriers of radiogenic ^{129}Xe (9).

Nitrogen: Nitrogen isotopic abundance in mineral separates of the two lodranites EET84302 and FRO90011, shows similarities. Their metals reveal low nitrogen abundance ($\leq$ 1ppm) with similar isotopic signatures ($\delta^{15}N$ +2 to +14‰). These signatures may be compared to those of silicates ($\delta^{15}N$ ~0 to +30‰) and to bulk Lodran ($\delta^{15}N$ +3 to +9‰) (12). Moreover, "magnetic" silicate and chromite of EET84302 are also depleted in nitrogen (<1ppm) without any evidence for the light nitrogen signatures. It appears that nitrogen isotopic equilibration was achieved in lodranites. These results contrast with the metal of Acapulco which has higher nitrogen concentration (13±3ppm) (9) and a very light nitrogen signature.

Xenon: Trapped Xe in Acapulco is mostly carried by "magnetic" silicates (9) (silicate with swarms of metallic inclusions) and its isotopic composition is consistent with OC-Xe (13), except for a higher $^{129}Xe/^{132}Xe$ ratio (1.065±0.005) presumably due to radiogenic $^{129}Xe_r$. Our results suggests that trapped Xe is carried in the "cores", since a "magnetic core-concentrate" shows an enrichment (9) with constant isotopic composition. The uniform OC-Xe composition with a

higher $^{129}Xe/^{132}Xe$ ratio in "magnetic" silicate indicates that ^{129}Xe excesses probably are signatures of the trapped phase, not produced in situ. EET84302-bulk shows a large concentration of trapped Xe (1170×10^{-12} STP cm^3g^{-1}), comparable to that observed in Lodran (1330×10^{-12} STP cm^3g^{-1}) (14). The distribution of trapped Xe, in many respects is very similar to that of Acapulco since a high concentration is found in "magnetic" silicates (9180×10^{-12} STP cm^3g^{-1}), together with the OC-Xe signatures and including the high $^{129}Xe/^{132}Xe$ ratio (1.065± 0.004). However, in EET84302 bulk we found no visible evidence for in situ produced $^{129}Xe_r$ components which are prominent in Acapulco. In the latter one of these resides in phosphates and the other carrier is an minor "interstitial" phase on metal surfaces (9) which released $^{129}Xe_r$ at very low temperatures. Our ~50mg sample of FRO90011 did not reveal a "magnetic" silicate phase and the separates (silicates, the nonmagnetic fraction and acid-etched metal concentrate) all show low abundance of trapped Xe ($\leq110\times10^{-12}$ STP cm^3g^{-1}), in agreement with data on trapped Ar in FRO90011 bulk (14) which is lower by a factor of 20 compared to Lodran. The nonmagnetic fraction of FRO90011 shows a significant ^{129}Xe excess (70×10^{-12} STP cm^3g^{-1}).

Conclusion: The nitrogen isotopic signatures help to constrain the genetic relationship between Acapulco and two lodranites, EET84302 and FRO90011. The low nitrogen concentration in metal and in the chromite of EET84302 together with the evidence for isotopic equilibration in lodranites does not conflict with the evidence for high-temperature metamorphism. The presence of large concentrations of trapped Xe, carried by "magnetic" silicates, with uniform relative enrichment of ^{129}Xe in Acapulco and EET84302 supports a genetic relationship between these two samples. High-temperature metamorphism may have achieved complete homogenization of volatile gases in lodranites. However, a process capable of depleting and equilibrating the nitrogen in "magnetic" silicate of EET84302 and simultaneously enriching trapped Xe is called for. This may require a later formation time of "magnetic" silicates, since $^{129}Xe_r$ is slightly evolved. The loss of nitrogen and noble gases in FRO90011, together with a clear $^{129}Xe_r$ excess in the nonmagnetic separate requires an early evolution, before ^{129}I had decayed.

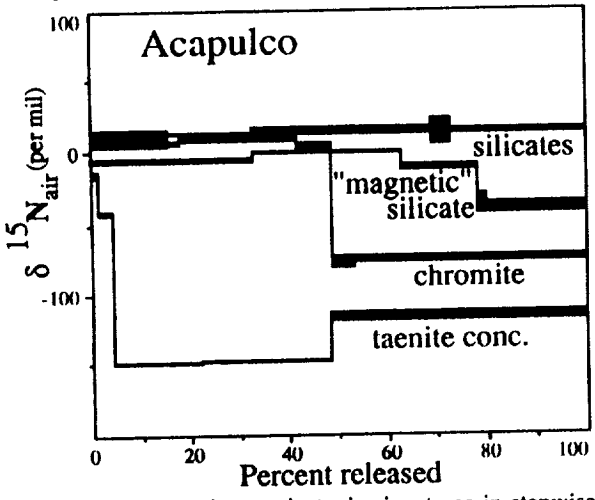

Fig. 1 The nitrogen isotopic signatures in stepwise release are shown for Acapulco silicates, "magnetic" silicate, chromite and taenite concentrates.

Reference: (1) Zipfel, J. and Palme H. (1993) Meteoritics 28, 469. (2) Prinzhofer A. (1990) Lunar Planet. Sci. XXI, 981. (3) Göpel Ch. et al. (1992) Meteoritics 27, 226. (4) Nichols R. H. Jr. et al. (1993) Geochim. Cosmochim. Acta, submitted. (5) McCoy T. J. et al. (1992) Lunar and Planet. Science XXIII, 871-872. (6) McCoy T. J. et al. (1993) Lunar and Planet. Science XXIV, 945-946. (7) Takeda H. et al. (1993) Lunar and Planet. Science XXIV, 1395-1396. (8) Sturgeon G. and Marti K. (1991) Proc. Lunar Planet. Sci. 21th, 523. (9) Kim Y. and Marti K. (1993) Lunar and Plante. Science XXIV, 801-802. (10) El Goresy A.et al. (1994) Lunar and Plante. Science XV, this volume. (11) Palme H. et al. (1981) Geochim. Cosmochim. Acta 45, 727-752. (12) Grady M. M. et al. (1993) Meteoritics 28, 355-356. (13) Lavielle B. and Marti K. (1992) J. Geophys. Res. 97, E12: 21,875-21,881. (14) Eugster O. and Weigel A. (1993) Lunar and Planet. Science XXIV, 453-454.

SPLOTCHES ON VENUS: DISTRIBUTION, PROPERTIES, AND CLASSIFICATION.

R. L. Kirk and D. J. Chadwick, U.S. Geological Survey, Flagstaff, AZ.

Introduction

"Splotches," the diffuse, roughly circular features discovered in the Magellan images of Venus and attributed to the disintegration of small impacting bodies in the atmosphere [1], are of interest for several reasons. First, we would like to understand their physical properties and the processes by which they form. Such an understanding is especially desirable because splotches are probably the simplest and easiest to understand of a wide variety of Venusian features formed by impactor-atmosphere interactions. (Other such features are halo craters, parabolic crater deposits, and "butterfly" ejecta patterns.) Second, although the splotches do not shape the landscape in a major way, they are part of the stratigraphic record. Unless they are ephemeral (which has yet to be determined), they will contribute to our understanding of Venus' resurfacing history in the same way as craters [2,3]. Third, unlike craters, splotches appear to be nonuniformly distributed , and splotches of similar types seem to cluster. The distribution of splotches may therefore tell us something about the properties of the surfaces on which they form. Finally, it is possible that a close study of the properties of both splotches and crater halos will reveal patterns that distinguish asteroidal from cometary impactors. This information would tie the cratering records of the terrestrial planets more firmly to the observed numbers of asteroids and comets, improving the absolute accuracy of the cratering timescale.

Splotch Database

Because splotches have yet to be studied systematically in any detail, we expect that considerable insight can be gained by starting with empirical, statistical studies of splotch properties and distributions. We have therefore focused initially on building a splotch database. Schaber et al. [2] described a basic database containing splotch positions, a preliminary classification based on the pattern of concentric dark (D) and light (L) rings outward from the center as well as a possible central "impact" feature (I), and the radii of these rings. We have continually updated this database as new Magellan images have been released; it now contains 401 splotches in 11 different classes. More importantly, we have added considerable information. First, we identified the Magellan image mosaics (C1-MIDRs) in which each splotch occurs and which of the several incidence-angle profiles were used to image the splotch. (We examined the mosaics, many of which contain parts having no data, to be sure that the splotches had actually been imaged in a given mode.) Second, we extracted data values from the Magellan global datasets for altimetry (GTDR), emissivity (GEDR), reflectivity (GREDR), and surface slopes (GSDR), as well as the image data resampled to the same resolution. We recorded the average value within the splotch (out to the outermost radius) and the average in an annulus of equal area surrounding the splotch, converting the data numbers to physical units. The software developed to extract data values from the GxDRs has obvious applications to the study of features other than splotches, and it will be released as part of the Planetary Image Cartography System (PICS).

Spatial and Physical-Properties Distributions

Several types of statistical investigation are possible with the database just described. Our first approach was to analyze the uniformity of the splotch distribution, both spatially and with respect to background values of elevation, emissivity, and so on. One way to do this is to plot the cumulative probability distribution of a property for the set of splotches versus the equivalent distribution for the whole planet (e.g., plot at 1/360 the fraction of splotches between longitudes 0° and 1° , at 2/360 the fraction between 0° and 2°, and so on, or plot the fraction of splotches below a given elevation versus the fraction of the planet's area below that elevation). The resulting plot will be a diagonal line if the chosen parameter does not influence splotch formation; departures from the diagonal are readily visible and their significance can be quantified by powerful statistical tests [4]. We have found that splotches are distributed nonuniformly with respect to all the parameters in our database. To look for patterns in this nonuniformity, we have converted the cumulative plots to a relative density of splotches as a function of the dimensional data values. For example, the density of splotches decreases almost monotonically with elevation (Fig. 1). This trend is not related to Venus having more lowlands than highlands; the uneven distribution of elevations for the planet as a whole has been taken into account in this plot. The other datasets show that splotches are nonuniformly distributed in latitude and longitude and that they prefer intermediate emissivities (0.79 to 0.87); intermediate reflectivities (0.08 to 0.18); intermediate backscatter cross-sections (-3 to 9 db relative to Muhleman's law, peaking at 2 db); and low but not the very lowest slopes (density decreases monotonically with slope except for surfaces with slopes less than 2°, where almost no splotches are present). Slope is the only parameter for which the distributions within and outside the splotches differ (the splotches are typically smoother than the surround). Splotch/surround differences would be expected for backscatter cross-section (the splotches are visible in the backscatter images), but the differences are probably suppressed because we combined all splotch classes and averaged backscatter over all rings out to the outermost radius. We plan to analyze splotch backscatter properties in much more detail by using the C1- MIDRs, which have a resolution 20 times better than the resampled mosaic used here.

An immediate question is whether these trends are interrelated. After all, emissivity varies roughly oppositely with reflectivity, the Venusian highlands tend to be rough and to have high backscatter cross

sections and low emissivities, and so on. Perhaps (for example) splotches do not form readily on the highlands, or they are harder to detect in rugged highland terrain. We have tested such hypotheses by comparing maps of the predicted density of splotches based on each dataset individually. The highlands appear as low-density areas in all the maps, supporting the idea that all trends reflect a single cause there. In the lowlands, however, there is little correspondence between the maps, suggesting that the variables have separate and competing effects on the likelihood of splotch formation. The nature of these effects is not yet clear, except that the near-monotonic trend with elevation strongly suggests that splotch formation is favored by high atmospheric pressure. We are currently performing Monte Carlo simulations of splotch distribution to explore the possible correlation between different controlling variables. Another obvious extension of this work will be to examine the dependence of splotch density on geologic unit type, but a global, digital geologic map of Venus is unfortunately not yet available.

Allometry and Classification

A second important area for statistical investigation is the refinement of the initial system of splotch classification, starting with a search for relations between the classes of splotches as initially defined. We are interested in comparing splotch properties and distributions both to discriminate between asteroidal and cometary impactors and to study the effects of different surface properties on splotch formation. These studies are frustrated by the large number of possible combinations of splotch classes and physical parameters, and also because most classes have very few splotches, resulting in poor statistics. A preliminary comparison of the allometry of the splotches (both the statistical distribution of the radius of each ring and the joint distributions of multiple radii) suggests that the rings in different classes can be identified with one another, as shown in Table 1. We hope, ultimately, to understand the processes that create the different light and dark rings.

With this tentative idea of the relations between splotch classes, we have begun to group the classes in different ways and to study the distributions of the groups. For example, splotches with impact scars (classes 5, 6, 11) are biased toward surfaces with lower backscatter crosssection than than those without (classes 1, 2, 10). Splotches with (I)DL rings (classes 1, 6) do not show any such bias in comparison with the corresponding classes (2 and 5) with (I)D only. Had we found the reverse, we might have dismissed a greater abundance of (say) DL splotches on dark terrains as a selection effect having to do with the backscatter contrast between splotch and background. The preference of I splotches for dark terrain is clearly a clue to the conditions that influence the formation of splotches. The task of gathering and understanding all such clues is daunting, but the analyses that we have begun show great promise for increasing our understanding of both the splotch-formation process and the surface properties of Venus.

References Cited
[1] Phillips, R. J., et al. 1991. *Science* **252**, 288-297; Soderblom, L. A., et al. 1992. *Lunar Planet. Sci.* **XXIII**, 1329-1330; Zahnle, K. J. 1992. *J. Geophys. Res.* **97**, 10,243-10,255. [2] Schaber, G. G., et al. 1992. *J. Geophys. Res.* **97**, 13,257-13,301. [3] Phillips, R. J., et al. 1992. 97*J. Geophys. Res.* **97**, 15,923-15,948. [4] D'Agostino, R. B., and Stephens, M. A., eds. 1986. Goodness of Fit Techniques. Statistics: Textbooks and Mongraphs, v. 68, Marcel Dekker, New York and Basel, 560 pp.

Table 1. Conjectured Relations Between Rings of Different Splotch Classes

Ring	I	L1	D1	L2	D2	L3	
Mean Radius (km)	5	11	25	37	55	105	
% of Splotches w/Ring	15.2	3.7	67.6	5.0	33.4	70.8	
Class							% in Class
1			D			L	54.6
2					D		18.2
3						L	4.0
4		L			D		0.5
5	I				D		7.0
6	I		D			L	8.0
7			D	L	D		3.0
8			D	L	D	L	1.5
9		L	D	L	D		0.5
10		L			D	L	2.5
11	I	L			D	L	0.25

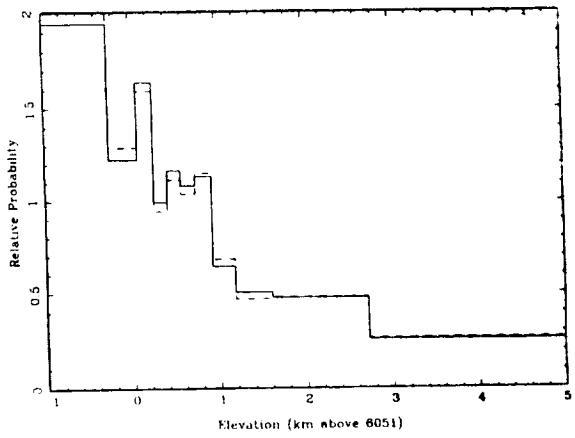

Figure 1. Relative density of Venus' splotches as a function of elevation. Effect of preponderance of area at low elevations has been removed. Data are binned unequally in elevation so that each bin contains an equal number of splotches. Solid line: elevation just outside splotch. Dashed line: elevation within splotches. (Because splotches have no relief, difference between curves reflects errors in measurement.)

^{57}Fe MÖSSBAUER STUDIES OF THE KINETICS OF PYRITE DECOMPOSITION ON THE SURFACE OF VENUS, G. Klingelhöfer[1], B. Fegley, Jr.[2,3], and K. Lodders[2] (1) Institut für Kernphysik, Technische Hochschule, 64289 Darmstadt, Germany, (2) Dept. of Earth & Planetary Sciences, and (3) McDonnell Center for the Space Sciences, Washington University, St. Louis, MO 63130-4899 USA.

Introduction. After the Pioneer Venus mission, pyrite was suggested to be present in high radar reflectivity regions at high altitudes on Venus. This led us to determine experimentally whether or not pyrite is stable on the surface of Venus. Fegley and coworkers [1-4] showed that pyrite decomposes to pyrrhotite in CO_2, CO_2-CO, CO_2-SO_2, and in CO_2-CO-SO_2 gas mixtures at temperatures of ~ 660 to 1120 K, which spans the range of surface temperatures (~ 660 to 760 K) on Venus. The experiments were done by isothermally heating cut slices of natural pyrite crystals in controlled gas mixtures at about one atmosphere total pressure for different time periods. The pyrite decomposition rate was determined by measuring the weight losses of the heated samples. Here we present Mössbauer data for samples heated along three isotherms (689±4 K, 742±3 K, and 804±3 K) in CO_2 and in a CO_2-CO-SO_2 gas mixture. The Mössbauer data and the gravimetric data for the amount of pyrite reacted as a function of time give consistent results for the pyrite decomposition kinetics.

Mössbauer Method. Mössbauer spectroscopy (MS) is a nuclear technique, which measures for a Mössbauer isotope the resonance absorption of recoil free emitted gamma quanta. The absorption rate is measured as a function of the energy shift of the Mössbauer quanta, which is obtained by moving the Mössbauer source (or the absorber) with a periodically changing doppler velocity v. Due to electric and magnetic hyperfine interaction (HFI), the nuclear levels are shifted (isomer shift) and/or split and resonance absorption occurs at different velocities. For ^{57}Fe two and six resonance lines appear in the Mössbauer spectrum for pure electric quadrupole and magnetic HFI respectively. If both electric quadrupole and magnetic HFI are absent, a single resonance line is observed. The HFI values are characteristic for a particular Fe compound. Therefore MS determines the different Fe bearing phases in the sample as well as their relative intensities, given by the area of the subspectrum, which is proportional to the relative amount of the Fe phase and its Debye Waller factor f [5]. From this the weight percentage of each Fe component can be calculated taking into account the stoichiometric factor S. The elemental abundance of Fe in the sample cannot be determined by MS. We have measured the Mössbauer spectra in transmission geometry at room temperature. A ^{57}Co/Rh source was used with an activity of about 70 mCi and a line width of about 0.16 mm/s. The experimental setup consists of a loudspeaker type drive running in constant acceleration mode, and a Si Pin-diode for the detection of the 14.4 keV Mössbauer radiation. The absorber thickness was about 20 mg cm^{-2}. Typical recording times are 2-4 days for one spectrum. The data have been fitted by a sum of 9 subspectra. This was necessary because the reacted samples contain residual pyrite (1 doublet) which is contaminated by minor amounts of chloritoid (1 doublet), and the reaction products pyrrhotite (3 to 4 sextets), hematite (1 sextet) and magnetite (2 sextets). The iron oxides are not present in all samples. Figure 1 shows the spectra for three samples (R12, R32, R41) heated in pure CO_2 at three different temperatures.

Results. The weight loss and Mössbauer data for the % pyrite in the reacted samples are given in Table 1. There is generally good agreement between the two independent methods. The weight loss data underestimate the small amounts (< 3%) of pyrite left in heavily reacted samples which are predominantly pyrrhotite (e.g., R41-43, R73). The disagreement for R45 is probably due to heterogeneous sampling because the MB work is done on a portion of the entire sample. Fig. 2 shows graphically the good agreement between the two methods. The temperature dependence of the MB rate data along these three isotherms gives an activation energy of 151±17 kJ mole^{-1}, in good agreement with the values of 153±19 kJ mole^{-1} reported by [3] from weight loss data along five isotherms, and of 142 kJ mole^{-1} reported by [1] from weight loss data over the 739-1118 K range.

Summary. The Mössbauer results confirm the pyrite decomposition rates and activation energy determined from weight loss measurements. These kinetic data show that pyrite rapidly decomposes on the surface of Venus. Furthermore, this study also demonstrates the potential utility of Mössbauer spectroscopy for chemical analyses of the surface of Venus using a Mössbauer spectrometer which is being developed for the Russian Mars-96 mission [6-7].

References. [1] B. Fegley, Jr. & A.H. Treiman 1992 in AGU Monograph No. 66, pp. 7-71; [2] B. Fegley, Jr. & K. Lodders *Lunar Planet. Sci.* **XXIV**, pp. 467-468; [3]B. Fegley, Jr. & K. Lodders 1993 *EOS Trans. AGU* **74**, 190; [4] B. Fegley, Jr., K. Lodders, and G. Klingelhöfer 1993 *Bull. Amer. Astron. Soc.* **25**, 1080; [5] W. Meisel, P. Griesbach, H.J. Grabke, P. Gütlich 1990 *Hyperfine Interactions* **57**, 2001; [6] G. Klingelhöfer, J. Foh, P. Held, H. Jäger, E. Kankeleit, R. Teucher 1992 *Hyperfine Interactions* **71**, 1449; [7] G. Klingelhöfer et al 1992 *Lunar*

Planet. Sci. **XXIII**, pp. 695-696. **Acknowledgments**. The work at St. Louis was supported by grants from the NASA Planetary Atmospheres and VDAP Programs. We thank D. Kremser and R. Poli for technical assistance.

Table 1 Experimental results for samples studied by Mössbauer spectroscopy.

Run No.	Temp. (K)	Duration (Hours)	Wt. % Pyrite WL*	MB*	Run No.	Temp (K)	Duration (Hours)	Wt. % Pyrite WL*	MB*
8[a]	740	24	83.4	83.3	43[a]	806	65	0	0.1
9[a]	738	65	58.9	59.4	44[a]	802	5	68.2	67.6
11[a]	741	41	79.2	79.4	45[a]	805	16	12.1	1.1
12[a]	685	96	87.4	91	47[a]	803	2.5	84.4	79.2
14[a]	686	161	66.2	62.4	49[a]	806	8	53	58.2
18[a]	686	233	55	60.2	61[b]	690	24.7	93.1	90.5
32[a]	739	187	33.2	41.3	62[b]	740	21	80.7	81.4
33[a]	745	329	34.1	27.8	63[b]	739	1.1	99	96.8
38[a]	694	140	82.6	85.7	65[b]	741	142.8	17.5	10.7
41[a]	807	97.5	0	0.1	66[b]	691	211	70.7	82.4
42[a]	798	43	0	0.5	73[b,c]	745	94	0	2.7

Notes: *WL = weight loss and MB = Mössbauer spectroscopy, [a]Run done in CO_2 (Coleman Instrument Grade, 99.99% pure), [b]Run done in CO_2(97%)-CO(1.5%)-SO_2(1.5%), [c]R73 fell out of the sample holder at an unknown time during the run which lasted for 94 hours.

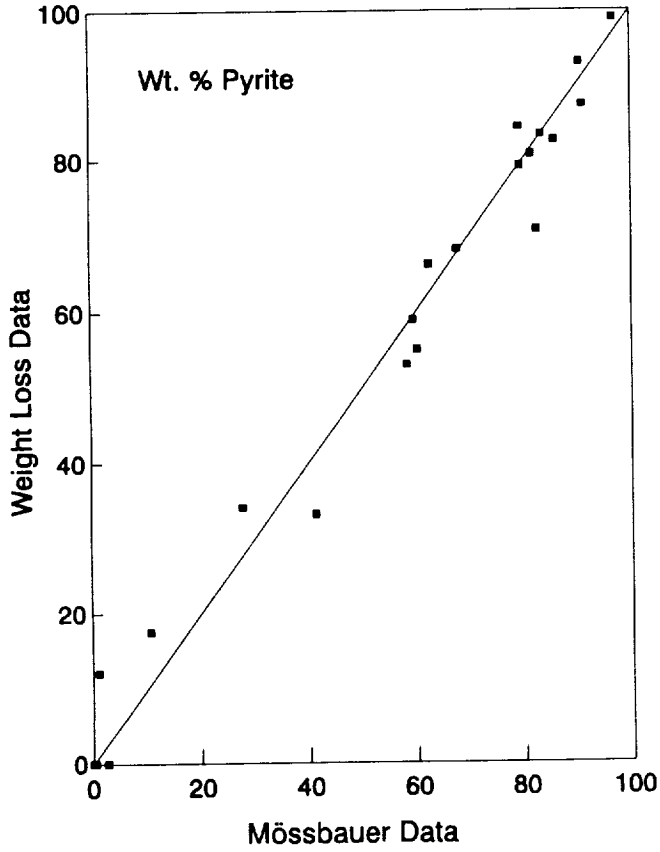

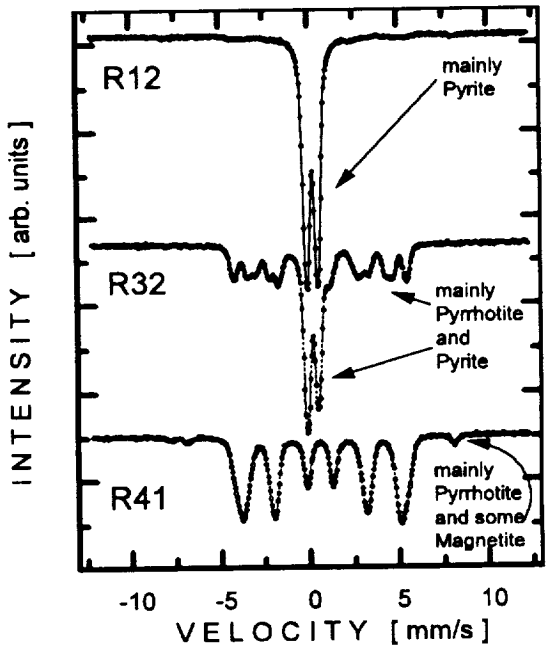

Fig. 1 (above) Mössbauer spectra of samples R12, R32, and R41. The data are normalized to the individual background count rate. Fig. 2 (left) A comparison of weight loss and Mössbauer data for the amount of pyrite left in the reacted samples.

OPTIMIZATION OF THE MINIATURIZED BACKSCATTERING MÖSSBAUER SPECTROMETER *MIMOS* G. Klingelhöfer, P. Held, J. Foh, F. Schlichting, R. Teucher, E. Kankeleit, Inst. f. Kernphysik, TH Darmstadt, Schlossgartenstr. 9, 64289 Darmstadt, Germany; E.N. Evlanov, O.F. Prilutski, G.V. Veselova, E.A. Duzheva, Space Research Institute (IKI), Moscow, Russia.

Introduction. A Mössbauer spectrometer for the mineralogical analysis of the Mars surface is under development [1,2,3]. This instrument will be installed on a Mars-Rover, which is part of the Russian Mars-96 mission [4]. The MB experiment will be positioned by a robotic arm to take spectra from the fine soil on the surface, from rocks and from deeper layers of the soil, which will be accessible by a drilling device. The use of permanent magnets similar to the magnet array which is included in the US MESUR Pathfinder mission [5], in combination with the MB instrument will allow a magnetic separation of the magnetic phase in the Martian dust [6]. The electromechanical drive and the electronic components have been miniaturized. Solid state detectors (PIN-diodes) are used for γ- and x-ray detection in backscattering geometry. In this paper we will discuss especially the detector system, the temperature behaviour and the shielding of the radioactive ^{57}Co Mössbauer source.

Method. The MB backscattering technique, which needs no sample preparation, is highly suitable for a rover mission with the possibility for selecting samples. The main disadvantage of backscattering is the secondary radiation caused by the 122 keV transition. For a reduction of the background at 14.4 keV and the 6.4 keV x-ray line, good energy resolution of the detector system is required but also high count-rate capabilities with the strong sources to be used. For this reason Si-PIN-diodes were chosen as detectors. The general setup of our "**MI**niaturized **MO**essbauer backscattering Spectrometer" (MIMOS) is shown in fig. 1.

Mössbauer Source Shielding. The ^{57}Co source mounted on the small drive is surrounded by a graded shield. Collimated radiation passes through a Be window and the reemitted radiation is detected by a ringlike array of PIN-diodes behind the same Be window. Most important is an effective shielding of the PIN diodes from direct and cascade radiation. The 8 mm inner diameter graded shield consists of concentric tubes of 0.5 mm thick brass, 1 mm U, 1 mm W and another 0.5 mm brass. In fig. 2 the spectrum of the backscattered radiation, measured with one of the PIN diodes of the detector system (see fig. 1) is shown. No direct 122 keV radiation is seen in the detectors, only the 122 keV radiation scattered by the sample is detected. This shielding acts also as collimator, limiting the maximum emission angle to 25° and reducing the cosine smearing to a level that still allows a reasonable separation of the outer lines of γ- and α-Fe_2O_3.

Detector System. For a backscatter geometry a detector system covering a large solid angle is needed to minimize data acquisition time. The detector system consists of Silicon-PIN-diodes with 5 x 5 mm^2 or 10 x 10 mm^2 active area in an array arrangement as indicated in two options in fig.1. A thickness of about 400 μm is a good choice according to our experience.
Spectra of ^{57}Co/Rh radiation backscattered from a Stainless Steel (SS) plate, measured in- and off resonance, which are equal in recording time, are shown in fig. 2. A continuum is seen above 122 keV resulting from the few 692 keV γ quanta which are not completely absorbed in the shielding. No photo peak appears at 122 keV. But this radiation shows up in a broad compton distribution. A second compton distribution originates in the detector itself as seen in the rising slope starting below 40 keV. On top of these we see a peak at 22.1 keV due to the Ag backing of the detector. Below that in SS at zero velocity the 14.4 keV MB resonance line and also the 6.4 keV x-ray line dominate.

The temperature dependence of the parameters of the source similar to the one which will be used for the Mars-96 MB-experiment has been investigated experimentally in order to check its performance. The ^{57}Co source had the following characteristics: rhodium matrix, Ø 4 mm, thickness 6 μm, activity 122 mCi, linewidth 0.172 mm/s. The measurements were made in a temperature interval from 79 K to 295 K in transmission geometry using a liquid nitrogen cryostat. The Mössbauer absorber (SNP) was driven with sinusoidal velocity waveform. No splitting of the source lines in the studied temperature interval was found and the linewidth remains constant. As expected, a change in isomeric shift of 0.015 mm/s due to the relativistic second-order Doppler shift and a variation of the resonance yield according to the temperature dependence of the Debye-Waller factor were found for the temperature interval on the Mars surface. From this results we conclude that this type of sources can be used for our experiment.

Computer simulations. The statistical significance of the measured data will depend strongly on the background radiation seen by the detectors. It depends for instance on the intensity of direct radiation from the ^{57}Co source,

the radiation from other nearby devices with radioactive sources (especially the radioisotope thermal electric generator (RTG) with 8.5 W thermal power), the compton backscattering of high-energy radiation of our source by the Martian surface, the electronic noise of the detectors and so on. Of importance is the proper design of the radiation shield. Some of the background characteristics can be measured easily in laboratory experiments (see above) but for other parameters this is difficult. Therefore a Monte Carlo computer program was developed to simulate the radiation background in order to optimize details of the design. It allows the evaluation of the properties of the radiation shield, the estimation of the influence of the high-energy γ-rays from our ^{57}Co source and from the RTG, as well as the calculation of the radiation spectrum produced by photon interaction with the device structure and the Martian soil. The real geometry and elemental composition of the critical experiment parts (especially the shield) are therefore considered in the calculation. Preliminary results of these simulations are: (i) the main source of background radiation will be due to scattering by the Martian surface, (ii) the direct radiation from the source can be decreased below the necessary limits by using a radiation shield having a sufficiently small mass of less than 30 grams, (iii) the background produced by the RTG will be smaller than the background due to scattering. With some additions this program will be used later on for the evaluation of Mössbauer spectra from the Martian surface.

Summary and Outlook. MB spectroscopy is now widely accepted as a new tool for space research. Besides the Russian Mars-96 mission, in the European MARSNET proposal, a network of fixed stations on the surface of Mars, Mössbauer spectroscopy is also included. Recently a proposal for a more powerful European Mars Rover was presented to ESA, also having a MB spectrometer on board. Besides the development of an instrument, which is currently done also by another group [7], a number of laboratories have started programs on so-called Mars Sample Analogs, which are studied not only by MB technique. Correlations of the MB results to magnetic properties, reflectance spectroscopic data etc. are most important.

Acknowledgements. This experiment is performed in cooperation with the Mössbauer group at the University of Copenhagen, Denmark, and C.N.R.S.-U.P.S., Toulouse, France. We appreciate very much the help of CYCLOTRON enterprise (Obninsk, Russia) in the source production and temperature measurements. This work is supported by DARA, Bonn.

[1] G. Klingelhöfer et. al., in B. Fegley and H. Wänke, eds., LPI Tech. Rpt. 92-07 Part 1; [2] E. Kankeleit et. al., Hyp. Int. 1994, in press; [3] E.N.Evlanov et. al., LPSC XXII (1991) 361; [4] Mars-94, Space Research Inst., Vernadsky Inst., Russian Academy of sciences, Babakin Center, Russia; [5] M.B. Madsen et. al., LPSC XXIV, (1993) 917; [6] J.M.Knudsen et. al., Hyp. Int. 68 (1992) 83; [7] G. Agresti et. al., Hyp. Int. 72 (1992) 285-298.

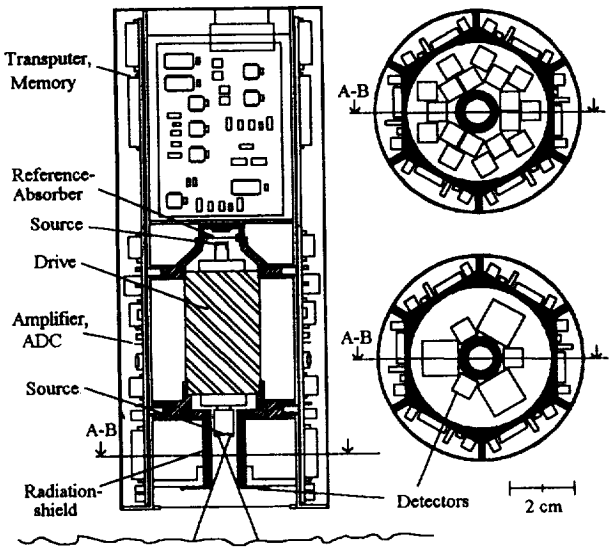

Fig. 1 Mössbauer spectrometer MIMOS for backscattering geometry. The system has the size of a soft drink can, a weight of less than 500 g and a power consumption of less than 3 W.

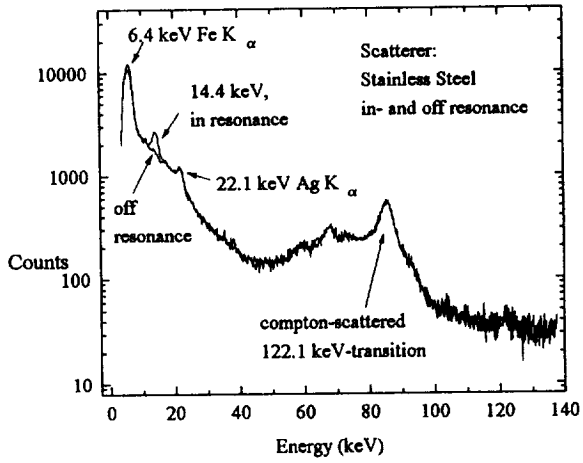

Fig. 2 Energy spectra of backscattered ^{57}Co/Rh radiation, using a prototype of the MIMOS spectrometer.

GEOCHEMICAL AND MINERALOGICAL CONSTRAINTS ON THE PARENT OBJECTS OF MICROMETEORITES:

W.Klöck[1], T.Presper[2], [1]Institut für Planetologie, Wilhelm-Klemm-Str.10, 48149 Münster, Germany, [2]Max-Planck-Institut für Chemie, Saarstraße 23, 55122 Mainz, Germany.

The majority of extraterrestrial matter recovered from Earth´s surface is most likely debris from asteroidal parent objects (1). Dusty matter, like stratospheric interplanetary dust particles (IDPs) or cosmic spherules (CSs) and micrometeorites (MMs) provides the main extraterrestrial mass influx onto Earth. In contrast to meteorite-falls, which are dominated by ordinary chondritic material, dust particle composition is closely related to carbonaceous chondrites. Three possibilities may explain the predominance of carbonaceous matter: (a) selection bias during sample preparation, (b) orbital parameters allowing carbonaceous matter to enter Earth´s atmosphere without becoming vaporized, and (c) a true predominance of carbonaceous chondrite-like parent bodies which produce dust.

Cosmic spherules and micrometeorites used in our study were collected by M. Maurette in Greenland and Antarctica, and kindly put at our disposal. Trace element abundances were obtained by neutron-activation techniques. One unmelted (phyllosilicate) particle (W17) of 39.4 μg was large enough to trust its weight within 5%. Abundances of refractory, moderately volatile and siderophile elements of this micrometeorite, normalized to CI-chondrite abundances are given in Fig.1. Refractories are close to chondritic values. Ca-depletion is characteristic for phyllosilicate micrometeorites (2). Iron is depleted by about 30%. Volatile elements, such as Na, Zn, Br and Se are lost to even higher degrees. 95% of Ni and 98.5% of Ir are lost compared to CI-chondrite levels. The Ni/Ir ratio of particle W17 is unlike those seen in most other phyllosilicate particles, which are characterized by low Ni/Ir ratios compared to CI-chondrite (Fig.2). Relative low Ni contents of unmelted particles are generally explained by weathering of Ni-bearing sulfides or sulfates in Antarctica (3). Among a set of 62 cosmic spheres, approximately 50% have chondritic Ni/Ir ratios, those having lower Ni/Ir ratios suffered Ni loss either by entry heating or, less likely, by aqueous alteration in the ice (Fig.3) (4).

Phyllosilicate particles are remarkably close to the CI-chondrite Sc/Cr ratio (Fig.4). On the contrary, Sc/Cr ratios of cosmic spheres, seem to support the presence of at least two populations (Fig.5). One with chondritic Sc/Cr and one with high Sc/Cr. About 50% of all cosmic spheres with high Sc/Cr ratios (> 1E-2), are low in siderophile elements. In the table below Sc/Cr ratios, Ni,Co and Ir abundances of this group of cosmic spheres and possible source materials are compiled:

	Sc/Cr	Ni (ppm)	Co (ppm)	Ir (ppb)
cosmic spherules	3E-2(1-7E-2)	250(5-550)	29(9-81)	23(<2-70)
SNCs	1-4E-2	120	46	0.05-3.5
Eucrites	1.3-1.5E-2	13-60	2-10	20
lunar meteorites	1.1E-2	280(80-700)	21	8(4-17)
Aubrites	1.3E-2	160	5	50
terrestrial basalts	1E-1-5E-2	150(100-400)	45	<< 1

Only future petrographic or isotopic studies will reveal if achondrite material is present among the low-Cr cosmic spheres. The Na/Fe versus Zn/Fe diagram (Fig.6) of phyllosilicate particles, shows that Na is, on average, compared to CI, depleted by a factor of 2-3, whereas Zn depletions are more prominent. Some of these particles were already studied petrographically and confirm that less thermally processed particles have higher Zn/Fe ratios compared to strongly heated particles (scoriaceous particles).

According to atmospheric entry heating calculations (5), 100 μm-sized cosmic dust particles, at an entry velocity of 12 km/s, suffer maximum temperatures of 900°C-1500°C, depending on their entry angle. It was shown experimentally that 100 μm fragments of meteorites lost 30% and 90% of their Zn inventory, within 20s and 60s at 1200°C (6). It appears that the calculated entry temperatures, experimentally determined volatile element losses and trace element analyses of micrometeorites are reasonably compatible. The moderate Zn losses of the phyllosilicate micrometeorites argue in favour of an asteroidal origin of these dust particles. Relative percentages of phyllosilicate particles among unmelted micrometeorites range from 70% to 90% in different sets of micrometeorites (7). Crystalline micrometeorites are far less frequent at about 10-30%. Striking is the lack of non-carbonaceous MMs. One reason for that may be simply that during sample preparation predomantly dark dust particles were selected because they are with a higher probability of extraterrestrial heritage. But it seems more likely, that this lack reflects the real frequency of micrometeorite types. We can conclude, that carbonaceous dust is able to

enter Earth's atmosphere without becoming vaporized. These dust particles must have low velocitiy and low inclination orbits, and should therefore come from the asteroid belt. Non-carbonaceous dust should also exist in interplanetary space. Either orbital parameters of this dust population do not allow low-velocity entry into Earth's atmosphere or these particles are too large in size to allow intact collection after atmospheric entry

References: (1) Dermott et al., Workshop on the Analysis of Interplanetary Dust, May 15-17, 1993, Lunar and Planetary Institute, Houston, Texas. (2) Beckerling W. et al., (1992) Meteoritics 27, 200-201. (3) T. Presper et al., (1993) LPSC 24, 1177-1178. (4) Presper T. and Palme H. (1991) Meteoritics 26, p.386. (5) Love S.G. and Brownlee D.E. (1991) Icarus 89, 26-43. (6) Klöck W. et al., (1994) LPSC 25, (this volume). (7) Presper T. (1993) Ph.D. thesis, Johannes Gutenberg-Universität, Mainz, and personal data.

Fig.1 Antarctic micrometeorite W17

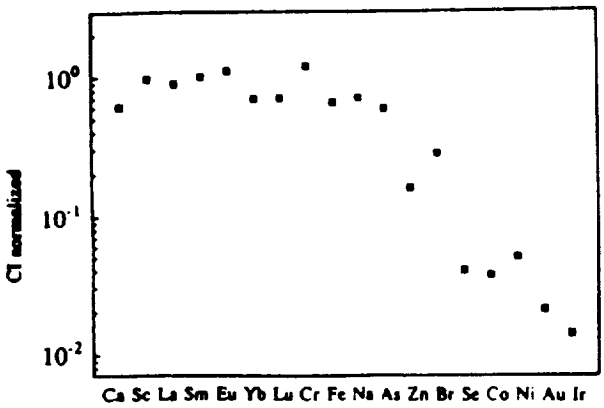

Fig.2 Phyllosilicate micrometeorites

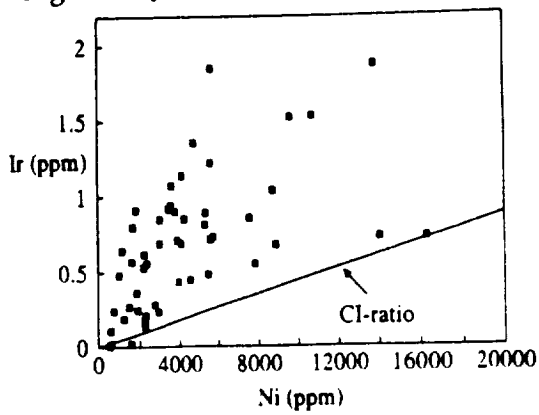

Fig.3 Cosmic spherules

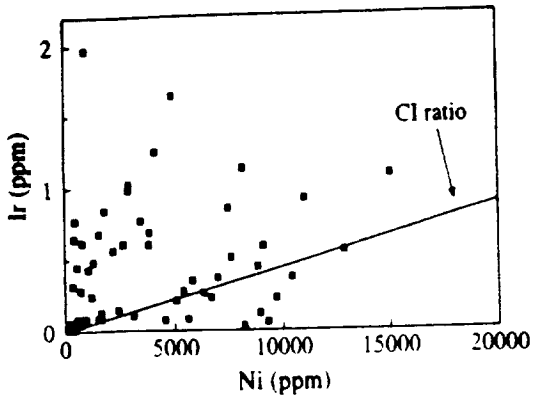

Fig.4 Phyllosilicate micrometeorites

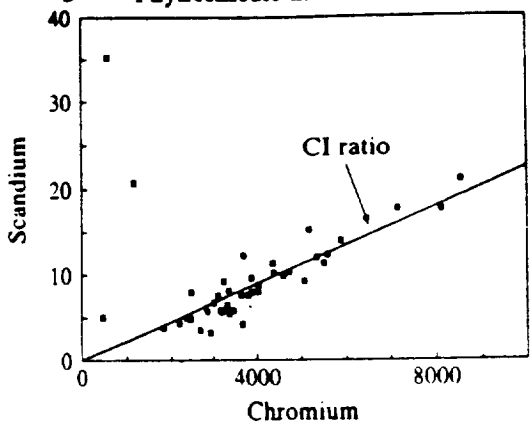

Fig.5 Cosmic spherules

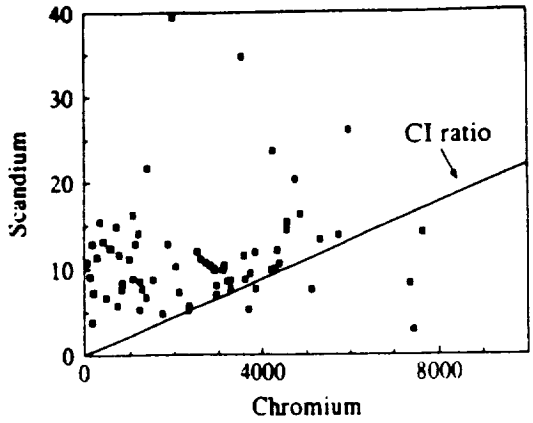

Fig.6 Phyllosilicate micrometeorites

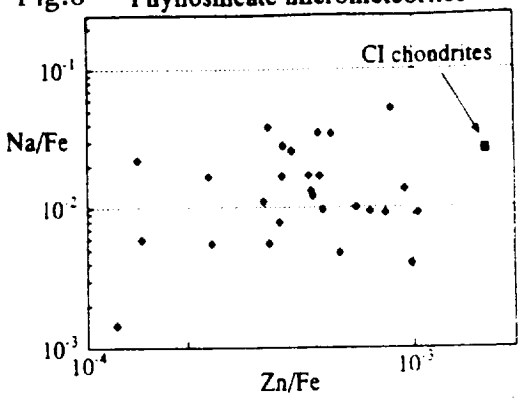

HEATING EXPERIMENTS SIMULATING ATMOSPHERIC ENTRY OF MICRO-METEORITES; W. Klöck[1], G.J. Flynn[2], S.R. Sutton[3,4], Sasa Bajt[3,4] and K.Neuking[5], [1]Institut für Planetologie, Wilhelm-Klemm-Str. 10, 48149 Münster, Germany, [2]Dept. of Physics, SUNY-Plattsburgh, Plattsburgh, NY 12901, USA, [3]Dept. of the Geophysical Sciences, The University of Chicago, Chicago IL 60637, USA, [4]Dept. of Applied Science, Brookhaven National Laboratory, Upton, NY 11973, USA, [5]Institut für Metallforschung, Wilhelm-Klemm-Str.10, 48149 Münster, Germany.

On average, cometary particles are heated to higher temperatures compared to asteroidal particles during atmospheric entry (1,2). A calibration of chemical and mineralogical thermal indicators is necessary to distinguish between these two types of extraterrestrial material. Our experiments demonstrate that volatile elements are lost from 100 μm sized meteorite particles on time scales comparable to the duration of the entry heating pulse experienced by micrometeorites. The Zn-loss temperature is at 1000°C and 1200°C, depending strongly on the duration of the heating event. Mineralogical changes occur already at lower temperatures. Combining the information from trace element abundances, rare gas data and mineralogy of individual IDPs with experimental data, helps to make reasonable estimates about the thermal history of these dust particles.

On entering Earth´s atmosphere interplanetary dust particles(IDPs) and micrometeorites are heated to high temperatures depending mainly on their entry velocity and size (1,2). The availability of a thermometer for this heating event would allow the inference of sources, main-belt asteroids or comets, for many IDPs (1). From the work of Flynn (1) and Love and Brownlee (2), it appears that cometary particles and asteroidal particles suffer, on average, different degrees of atmospheric entry heating. Thermal indicators could therefore help to distinguish cometary from asteroidal material. Recently it was demonstrated that we can distinguish already IDPs having chondritic abundances of volatile elements and particles depleted in volatile elements (3). A depletion of Zn is most prominent. This Zn-loss is correlated with the appearance of magnetite rims on the surfaces of dust particles (4,5). In addition, it was shown that some of these particles have experienced ^{4}He loss in support of atmospheric heating (6). Zn depletions and magnetite rim formation are therefore chemical and mineralogical indicators, demonstrating severe heating of dust particles. However, the Zn-loss and magnetite formation kinetics are poorly constrained. The purposes of our heating experiments were to (1) determine the time scales of volatile element losses, (2) establish a volatility scale for this process, and (3) to correlate chemical and mineralogical thermal indicators.

For this study phyllosilicate fragments about 100 μm in size of the Orgueil and Alais CI-chondrites were heated in evacuated quartz capillaries (0.2 mbar of air). They were heated for 20 and 60 seconds and immediately cooled in water. The individual fragments were analyzed by Synchroton X-Ray Fluorescence (SXRF) for volatile elements before and after the heating experiments. Ratios of volatile elements in heated samples divided by the unheated samples are given in the table. The SXRF data were computed assuming the CI iron abundance (18.5 wt%). Precision of the analyses varies from a few percent for Ni to about 20% for Se. Some of the "after heating" concentrations are higher than the "before heating". We think this is a heterogeneity effect (x-ray beam smaller than the fragments) that will be circumvented with studies of smaller fragments. There is evidence that the two meteorites behave differently when heated, i.e., the 800°C/60s data, both in volatility and mineralogy. This observation has important implications for any thermometer and needs to be confirmed in future work. It also demonstrates the importance of future heating experiments on IDPs, rather than meteorite analogs, since the host phases of particular volatile trace elements could be different in the IDPs.

We have demonstrated that Zn is lost from 100 μm sized particles in times comparable to the duration of the entry heating pulse experienced by micrometeorites. The Zn-loss temperature in our experiments is at a temperature of 1000°C and 1200°C, depending strongly on the duration of the heating event. Earlier heating experiments with carbonaceous chondrites over several days time showed loss of Zn starting at 700°C (7,8) and major depletion of Zn at 1050°C and 1150°C at reducing condi-

tions (log fO_2 <-10)(9). The Zn losses occuring in our experiments seem to be reasonably consistent with the Zn-depletions observed by (9) considering the huge difference in time scale (60s compared to $3x10^5$ s). According to (9) Zn is not volatile under oxidizing conditions. The observed Zn loss in our experiments might be caused by self-buffering of our samples in the range of the Ni/NiO buffer, due to the presence of carbonaceous material and/or carbonates in Orgueil and Alais fragments. At an oxygen fugacity of log -10 at 1000°C and 1200°C Ga should not be volatile (9). We cannot rule out that loss of Ga (and possibly of Ge as well) could partly be due to the high solubility of Ga and Ge in quartz (9). Heated IDPs typically show greater Zn depletion than Ga or Ge depletion (3). Ga and Ge loss are however consistent with meteorite heating experiments summarized by Lipschutz and Woolum (7).

A measurable loss of Zn occurs only at high temperatures in our experiments. Mineralogical transformations seem to be more sensitive to flash heating, even at lower temperatures. Phyllosilicates react to a finegrained mixture of olivines and pyroxenes already within 20 s at 800°C. At 1000°C all hydrated phases are destroyed. The grain sizes of the newly formed Mg-Fe silicates increase with increasing temperature and time. Fe-Mg diffusion under our experimental condition is fast enough to permit the formation of almost equilibrated olivines and pyroxenes within 20 s at 1200°C from the breakdown of phyllosilicates. No evidence of magnetite formation was observed in any of the fragments perhaps because atmospheric conditions were insufficiently simulated by the environmental conditions of these experiments. Mineral textures observed e.g. in CI-chondrite samples heated to 1000°C are almost identical to mineral textures found in IDPs L2005A8, L2005H50 and L2006A24 (which are fragments of larger particles). The individual particles are characterized by Zn depletions and high ^4He release temperatures (10). Their textures suggest that the original micrometeorite was heated to at least 1000°C for about 20 seconds. By combining trace element contents, rare gases and mineralogy of dust particles with experimental results, we should be able to make reasonable estimates about the extent of thermal processing of IDPs and micrometeorites in the Earth´s atmosphere.

References: (1) Flynn G.J.(1989) Icarus 77, 287-310. (2) Love S.G. and Brownlee D.S.(1991) Icarus 89, 26-43. (3) Flynn G.J. et al., (1993) Meteoritics 28, 349-350. (4) Thomas K.L. et al., (1992) LPSC 23, 1427-1428. (5) Flynn G.J. et al., (1993) LPSC 24, 497-498. (6) Brownlee D.E. et al., (1993) Meteoritics 28, 332. (7) Lipschutz M.E. and Woolum D.S. (1988) in: Meteorites and the early solar system, The University of Arizona Press, 462-487. (8) Ikkramuddin M., Binz C.M. and Lipschutz M.E. (1977) GCA 41, 393-401. (9) Wulf A.-V. (1990) Ph.D. thesis, Johannes Gutenberg-Universität, Mainz. (10) Klöck W. et al., (1992) Meteoritics 27, 243-244.

Sample and experiment condition	Ni	Cu	Zn	Ga	Ge	Se	mineralogical observation after heating experiment
Orgueil 6; 600°C/60s							all phyllosilicates intact
ratio heated/unheated	1.24	1.26	1.9	1.2	1.7	0.8	
Orgueil 1, 800°C/20s							about 50% of phyllosilicates converted into anhydrous Mg-Fe silicates, grain sizes of anhydrous silicates are 10-30 nm.
ratio heated/unheated	0.91	0.8	1.0	0.7	1.0	0.7	
Orgueil 4, 800°C/60s							phyllosilicates are all replaced by olivines and pyroxenes having grain sizes <20 nm.
ratio heated/unheated	0.46	0.4	0.5	0.9	0.7	1.2	
Alais 6, 800°C/60s							some phyllosilicates still intact, but the majority is converted into olivines and pyroxenes < 20 nm in size.
ratio heated/unheated	0.94	0.9	1.1	0.5	1.0	1.0	
Orgueil 7, 1000°C/20s							all phyllosilicates transformed into olivines and pyroxenes, sizes of Mg-Fe-silicates range from 10-30 nm.
ratio heated/unheated	1.0	1.1	1.2	1.2	1.1	1.2	
Alais 2,1000°C/60s							all phyllosilicates reacted to olivines and pyroxenes, grain sizes of Mg-Fe-silicates range from 40-80 nm
ratio heated/unheated	1.14	2.0	0.6	0.5	0.7	0.8	
Orgueil 3, 1200°C/5s							sample lost after chemical analysis
ratio heated/unheated	0.94	1.7	1.0	0.4	0.2	1.5	
Alais 4, 1200°C/20s							sample consists of olivines and pyroxenes (size 100-200 nm) embedded in a silica matrix, Fa content of olivines:36±3
ratio heated/unheated	1.06	2.6	0.7	0.2	0.3	0.8	
Alais 8, 1200°C/60s							sample consists of olivines and pyroxenes, in the size range 0.3 to 1μm, iron content of silicates: Fa 40 ± 4, Fs 31±3
ratio heated/unheated	1.0	1.7	0.1	0.05	0.3	1.0	

WAVE TECTONICS ON THE MOON AND SYMMETRIES-ANTISYMMETRIES OF MARE ORIENTALE REGION; G.G.Kochemasov,IGEM of the Russian Academy of Sciences,35,Staromonetny,Moscow,109017,Russia.

- Wave tectonics on the Moon is imprinted in three classes of ring structures related to three kinds of cyclic motion of the satellite (in galaxy,about the Sun and the Earth) and represented respectivly by the Ocean,the Marea and large craters. -

Wave tectonics in the solar system bodies shows itself in regularity (rhythms) of phenomena and structures and in symmetry-antisymmetry combinations caused by interference of planetary waves (lithospheric,atmospheric &others) of various directions and lengths/1,2/.On the Moon the Mare Orientale region draws attention by clear regularly spaced rings/3/,their "polygonality" and sectoral pattern of the Mare and its frame.In the Mare superstructure/4,5/ symmetrically about its NE diameter are disposed:1)craters Schickard(a) & Hertzsprung(b) being 1250km away from the Mare centre;2)clusters of radial disjunctive structures-crater chains at NW and radial vallies at SE(i.g.,Inghirami,Baade,Bouvar)(fig.1).Craters Grimaldi(d) and Brouwer(i) being ~950 km away from the Mare centre are symmetrical about its NW diam. These craters are parts of symmetric linear zones long ~ 600 to 650km. The first,submeridional,includes craters Rocca(c),Grimaldi(d),Lohrmann(e),Hevelius(f),Cavalerius(g);the second,sublatitudinal,includes craters Blackett(h),Brouwer(i),Langmuir(j),Chebyshev(k),Kleymenov(l).Order in lay-out of these craters tied to tectonic zones could speak in favour of their endogenous origin. Antisymmetry in superstructure of the Mare Orientale shows itself in heterogeneity of lithosphere.For example,in its SE half unlike the NW one thickness of the crust is diminished what is shown in relatively increased role of mare basalts in craters of this region.The "Galileo" NIMS & SSI results (dec.1990) also show a stronger mafic,maria like signature in Schickard area/6, 7/. "Regularities" seen in basin and mare superstructures one can extend.In /8/ is shown that most marea and big craters (Ø>200km) are arranged in limits of two perpendicular diagonal belts and along equator and meridians ±90°.This network does not contradict a periodic system of ring structures of lithospheres formed by interference of lithospheric waves of 4 directions (ortho-& diagonal)/1,2/.The interference table is scale invariant and infinite. General morphotectonic make-up of planets and satellites is linked to interference of waves long more than a body radius(extra-long) /9/.Against background of known W-E and S-N asymmetries of the Moon/i.g., 10/morphotectonically different sectors are clearly distinguished:opposite differently subsided sectors of

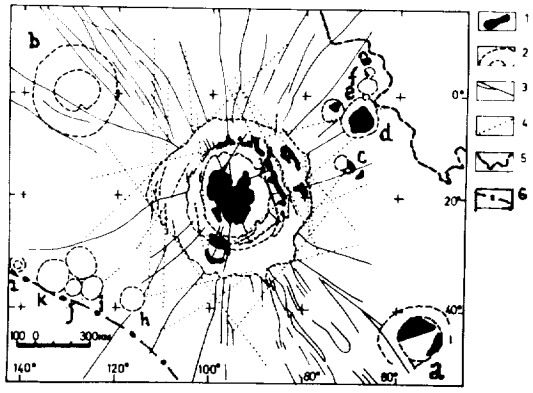

Fig.1.Superstructure of Mare Orientale. 1.Mare basalts;2.Craters,ring faults;3.-4.Weakness zones:radial(3),tangential (4);5.Ocean Procellarum limit;6.South Pole-Aitken b.

WAVE TECTONICS ON THE MOON..... Kochemasov G.G.

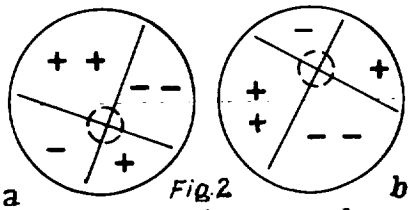

Fig.2

the Ocean Procellarum(--) and the South Pole-Aitken Basin(-) and separating them uplifted sectors(++,+)(Fig.2a).Area west of the Ocean is the most elevated and cratered on the Moon/10/.Four planetary sectors of the Earth's eastern hemisphere are comparable to the lunar ones in respect of relative sizes and evolution tendencies: two opposite variously elevated-Asian(+) and Afro-Mediterranean(++),and two opposite variously lowered-Eurasian(-) and Indoceanic(--)/9/(Fig.2b).Fundamentality of such sector division at the Earth is substantiated by relief,crust and lithosphere thicknesses,geoid anomalies. In /10,11 & others/ is shown that such deep relations exist on the Moon too.Similarity of planetary sectors at the Earth and its satellite is no accident as the Earth-Moon system jointly rotates in galaxy and around the Sun.

Position of the Earth and Moon in one solar orbit determines equal relative length of their superstructure waves-πR/4/2/. At the Earth these waves specifically form superstructures of the Archean cratons. On the Moon them correspond superstructures of marea (but not of the Ocean !) and large craters and thalassoids multi-ring character of which and presence of outer rings with large diameters are discussed in /3/. The Moon rotates also around the Earth. Monthly rotations around it are comparable with rotation of photosphere of the Sun where supergranules are formed with characteristic wave-length πR/(48-60) /12/. On the Moon derivatives of such waves should be "superstructures" with diameters of some tens to 80-100 km. They should be found among important craters saturating highlands and observed on marea.

So,proceeding from position peculiarities of the Moon in space and the wave model of ring structure formation,it is possible to predict on it three basic populations of multi-ring "polygonal" endogeneous structures. One,tied to wave-length πR (superstructures of I order -Ocean Procellarum and South Pole-Aitken Basin),second,tied to wave-length πR/4 (superstructures of II order),third,tied to wave-length πR/(48-60) (superstructures of III order). All populations occur on the Moon where they are masked by numerous(?) impact structures.

References:/1/Kochemasov G.G.(1991)Astronom.circular,n1550, 35-36 (in russian);/2/Kochemasov G.G.(1992)LPS XXIII,703-704; /3/Pike R.J.,Spudis P.D.(1987)Earth,Moon,and Planets,v.39,n 2, 129-194;/4/Kochemasov G.G.(1986)Astronomical circular,n 1440,5-7;/5/Kochemasov G.G.(1988)LPS XIX,621-622; /6/McCord T.B. et al. (1991)EoS,v.72,n 17 sup.,182; /7/Head J.W. et al.(1991)EoS,v.72, n 17 sup.,182; /8/Lipsky Yu.N.,Rodionova Zh.F.(1975)In:"Cosmochemistry of the Moon and planets",Moscow,Nauka,pp.764; /9/Kochemasov G.G.(1991)Astronomical circular,n 1550,37-38 (in russian); /10/Rodionova Zh.F.et al.(1988)LPS XIX,992-993; /11/Rodionova Zh. F. et al.(1991)14th Sov.-Americ.microsymposium on planetology, Moscow,Vernadsky Inst.,Abstracts,76-77; /12/Kochemasov G.G. (1992)16th Russ.-Americ.microsymposium on planetology,Abstracts, Moscow,Vernadsky Inst. (GEOKHI),36-37.

NI-RICH CR SPINELS IN SPHERULE BEDS FROM THE BARBERTON MOUNTAIN LAND (SOUTH AFRICA) ARE OF TERRESTRIAL ORIGIN: EVIDENCE AGAINST IMPACT ORIGIN OF SPHERULE LAYERS.

Christian Koeberl[1] and Wolf Uwe Reimold[2]. [1]*Institute of Geochemistry, University of Vienna, Dr.-Karl-Lueger-Ring 1, A-1010 Vienna, Austria (a8631dab@vm.univie.ac.at);* [2]*Economic Geology Research Unit, Department of Geology, University of the Witwatersrand, Johannesburg 2050, South Africa (065wur@witsvma.wits.ac.za).*

INTRODUCTION AND SUMMARY. A number of distinct spherule layers have been found in the Barberton Greenstone Belt, Eastern Transvaal, South Africa. These spherule layers have been interpreted by Lowe and co-workers [1-3] as deposits resulting from large-scale Precambrian impacts, about 3.2 Ga ago. Their arguments were largely based on petrological and geochemical analyses, showing quench textures and high abundances of siderophile elements (of which some show chondritic proportions). A recent detailed mineralogical, petrological, and geochemical study [4] pointed out that there are numerous difficulties with the impact model for the Barberton spherule beds. Nevertheless, Byerly and Lowe [5] described unusual Ni-chromites from some of the Barberton spherules, which they regard as being derived from the impacting bolide and thus interpreted as further proof of an impact origin of the spherule beds. We have found similar Ni-rich Cr-spinels in samples from several other spherule bed localities. Some of our analyses show also high Ni contents and compositions similar to those found by [5]. However, calculations of the Fe^{3+}/Fe(total) ratio based on spinel stoichiometry, following the method used by Robin et al. [6] for cosmic and terrestrial spinels, yield low ratios. The ratios vary between about 28 and 65, with a maximum between 40 and 55. Practically all spinels derived from extraterrestrial matter have ratios larger than 65; spinels found at the K-T boundary typically have ratios between 80 and 99. The low Fe^{3+}/Fe(total) ratios observed in the Barberton Cr-spinels are more typical for spinels formed in magmatic processes [6] and can therefore not be used to support an impact model for the Barberton spherule layers.

SAMPLE DESCRIPTIONS. For [4,7] and for this study, drill core specimens from Princeton and Mount Morgan mines and hand specimens from underground exposures at the Princeton and Sheba gold mines, all near Barberton, and two samples from the type surface exposure [2] were analyzed in order to compare specimens from heavily sulfide- (and gold-) mineralized settings in gold mines with samples from a less mineralized locality. The samples are thought to represent either the S2 (BA-2,3,4 from Sheba mine) and S3 or S4 (Princeton, Mt.Morgan mines) spherule beds [2]. In the present study, we concentrated on samples from the Sheba locality. Sheba sample BA-2 originates from Fig Tree metasediments just south of the Birthday Anticline, while samples BA-3 and -4 were associated with tightly infolded Onverwacht strata oriented parallel to the Sheba Fault in crosscut 6 in Sheba Mine, to the west of the Birthday Anticline. The Sheba samples most likely represent the S2 layer at the contact between Fig Tree and Moodies Group. All our samples are completely converted to assemblages of secondary minerals, the products of hydrothermal alteration. Major mineral constituents are quartz, siderite, sericite, and pyrite. Underground, drillcore and surface samples all have similar mineralogical compositions. Individual samples from the Sheba gold mine and from the surface exposure contain more silica in the matrix between spherules - at the expense of siderite and sericite proportions. Some of these samples are heavily transected by chert bands. Minor minerals are sphalerite, occasionally baryte, chalcopyrite, and apatite, as well as some clay minerals (biotite, muscovite or montmorillonite). Important trace minerals are gersdorffite that was observed nearly in every sample, less abundant chrome-spinel, a Zn-Cu-Sb-sulfide (probably a Fahlore mineral, such as Zn-rich tetrahedrite), and occasionally arsenopyrite and rutile.

CHEMISTRY OF NI-RICH CR-SPINEL. The occurrence of unusual Ni-chromites in Barberton spherule samples was first described Byerly and Lowe [5]. They concluded that the high Ni contents resulted mainly from the impacting bolide and were further evidence for an impact origin of the spherule beds. We have also found some Ni-rich chromites in various samples from different spherule bed localities. Detailed electron microprobe analyses were performed (see, e.g., Table 1 for some typical results; more analyses are given in [7]) and have shown that their compositions are, in general, similar to those reported by [5] (see also Table 1). However, besides Ni-rich chromite, other spinel phases with Zn and Ni, or Zn and Fe are present in these samples. This leads to the question whether these chromites represent primary or secondary phases. We have repeatedly observed intergrowths of chromite and gersdorffite, with or without chalcopyrite. These phases

occur not only in spherules, but also in the matrix of spherule beds. Furthermore, we have recalculated the Fe^{3+}/Fe(total) ratios in the spinels from stoichiometry, following the method of Robin et al. [6]. These authors presented a detailed study of spinel chemistry and oxidation state of terrestrial and extraterrestrial spinels and found that all extraterrestrial spinels have Fe^{3+}/Fe(total) ratios larger than about 65 (Fig. 1), while terrestrial spinels have, in general, much lower ratios. Using the same procedure as [6], we find that the Barberton spinels have low ratios (Fig. 1), inconsistent with an extraterrestrial origin. Their low modal abundance and the low Fe^{3+}/Fe(total) ratios are more characteristic of conditions typical of magmatic processes.

ACKNOWLEDGEMENTS: We are grateful to E. Robin (CEA-CNRS, Orsay, France) for help with the calculations and detailed discussions; and to Anglovaal Ltd. (Barberton) for samples and logistical support.

REFERENCES: [1] Lowe, D.R., and Byerly, G.R. (1986) Geology **14**, 83-86. [2] Lowe, D.R., Byerly, G.R., Asaro, F., and Kyte, F.T. (1989) Science **245**, 959-962. [3] Kyte, F.T., Zhou, L., and Lowe, D.R. (1992) Geochim. Cosmochim. Acta **56**, 1365-1372. [4] Koeberl, C., Reimold, W.U., and Boer, R.H. (1993) Earth Planet. Sci. Lett. **119**, 441-452. [5] Byerly, G.R., and Lowe, D.R. (1992) Lunar Planet. Sci. **XXIII**, 193-194. [6] Robin, E., Bonté, P., Froget, L., Jéhanno, C., and Rocchia, R. (1992) Earth Planet. Sci. Lett. **108**, 181-190. [7] Koeberl, C., and Reimold, W.U. (1994) Precambr. Res., submitted.

TABLE 1. SELECTED ELECTRON MICROPROBE ANALYSES OF NI-RICH CR-SPINELS FROM VARIOUS BARBERTON SPHERULE SAMPLES AND STOICHIOMETRICALLY CALCULATED Fe^{3+}/Fe(TOTAL) RATIOS.

	BA2Cr1	BA2Cr7	BA2Cr9	BA2Cr10	BA3Cr1	BA3Cr2	BA3Cr3	BA3Cr4	105-12-R*	294-1-C*	294-1-C*
Weight(%)											
MgO	0.42	2.89	1.03	2.18	0.87	0.87	0.82	0.85	0.37	1.56	1.58
Al_2O_3	1.32	7.24	6.14	6.29	0.45	0.47	0.43	0.45	1.24	0.17	2.16
TiO_2	0.10	0.60	0.32	1.03	0.08	0.10	0.09	0.10	0.06	0.09	0.12
Cr_2O_3	34.00	39.04	37.67	39.90	51.22	50.34	49.76	48.95	50.56	53.11	48.17
MnO	0.04	0.10	0.03	0.01	0.04	0.07	0.08	0.09	0.44	2.01	1.69
FeO	40.84	32.04	35.52	29.56	28.87	29.17	30.21	30.57	27.67	25.87	23.62
Co	0.31	0.28	0.29	0.31	0.34	0.33	0.31	0.36	0.23	0.30	0.243
NiO	15.45	0.40	14.59	1.13	13.73	12.97	13.04	12.21	10.40	12.02	11.24
Total	92.47	82.59	95.60	80.41	95.59	94.31	94.73	93.57	90.97	95.13	88.82
Fe^{3+}	0.984	0.327	0.655	0.245	0.441	0.446	0.476	0.483	0.334	0.390	0.352
Fe^{2+}	0.534	0.845	0.545	0.868	0.543	0.562	0.567	0.586	0.644	0.487	0.492
$Fe^{3+}/Fe(t)$	64.812	27.891	54.555	22.041	44.830	44.267	45.641	45.195	34.179	44.440	41.667

*Wt%-analyses taken, for comparison, from Byerly and Lowe [5]; sample numbers are theirs.

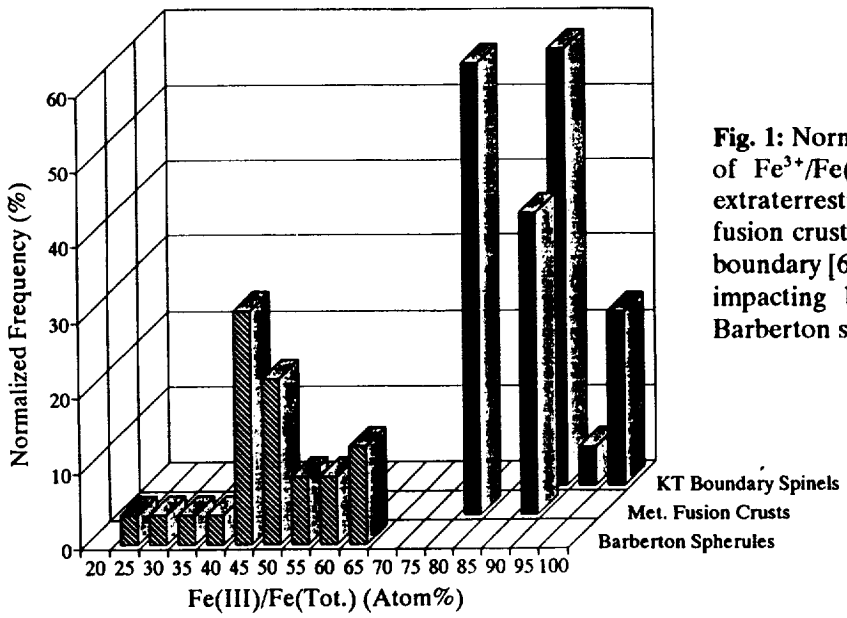

Fig. 1: Normalized frequency (to 100%) of Fe^{3+}/Fe(total) ratios in spinels of extraterrestrial origin (from meteorite fusion crusts [6]), spinels from the K-T boundary [6] (which originated from the impacting bolide), and spinels from Barberton spherule samples.

MINERALOGICAL, PETROLOGICAL, AND GEOCHEMICAL STUDIES OF DRILL CORES FROM THE MANSON IMPACT STRUCTURE: A PROGRESS REPORT.

Christian Koeberl[1,4], Raymond R. Anderson[2], Rudolf H. Boer[3], Joel D. Blum[4], C. Page Chamberlain[4], Alfred Kracher[5], Wolf Uwe Reimold[3], Barbara Träxler[1], and Andreas Vormaier[1]. *[1]Institute of Geochemistry, University of Vienna, Dr.-Karl-Lueger-Ring 1, A-1010 Vienna, Austria (a8631dab@vm.univie.ac.at); [2]Iowa DNR Geological Survey Bureau, Iowa City, IA 52242-1319, USA; [3]Economic Geology Research Unit, Department of Geology, University of the Witwatersrand, Johannesburg 2050, South Africa; [4]Dept. of Earth Sciences, Dartmouth College, Hanover, NH 03855, USA; [5]Dept. Earth Sciences, Iowa State University, Ames, IA 50011, USA.*

INTRODUCTION AND SUMMARY. A core drilling program at the Manson Impact Structure, initiated and supported by the Iowa DNR Geological Survey Bureau and the U.S. Geological Survey, led to the recovery of 12 cores totaling over 1200 m (e.g., [1-3]). All these cores (M1 through M11 and M2A, plus two cores from 1953, 1A and 2A) have been sampled for the present project [4]. Four main impact rock types were encountered and were classified by, e.g., [1-3] according to their main rock components as: (1) Sedimentary Clast Breccia (SCB), (2) Crystalline Clast Breccia with Sandy Matrix (CCB-S) and Melt Rock Matrix (CCB-M), (3) Central Peak Igneous and Metamorphic Rocks (CP), and (4) an overturned flap of Impact Ejecta (IE). The SCB is dominated by clasts of Cretaceous marine shale and mudstone, with subordinate Cretaceous sandstones, Paleozoic carbonates, minor Proterozoic Red Clastics, and rare crystalline rock and impact melt-rock clasts in a medium gray, calcareous, sandy, silty, shale matrix. We have selected 136 samples, representing all major units in all drill cores, for a complete major and trace element study, and a subset of the 136 samples for petrography, microprobe analyses, fluid inclusion study, and $\delta^{18}O$, Rb-Sr, Sm-Nd, and Re-Os isotope analyses. The aim of our studies is a complete characterization of all major target rock, breccia, and impact melt units.

PETROGRAPHY OF M-1 CORE SAMPLES. The M1 core was drilled on the eastern edge of the central uplift to a depth of 214.3 m. It contains abundant impact breccias ([4-6]). Polished thin sections of twenty-eight samples from drillcore M1, covering the interval between 81.8 and 205.2 m (268.5 and 673.2 ft) depth, were studied petrographically. This sample suite consisted of fragmental breccia (to 98.8 m [324.2 ft]), impact melt (103.1 - 147.0 m [338.4-482.2 ft]), fragmental breccia and suevite alternating between 153.2 and 192.3 m (502.7-631 ft), and fragmental breccia till 205.2 m (673.3 ft) depth. Several larger clasts were also sampled. Aspects investigated include nature of breccia matrices, shock effects in clasts, alteration effects, and ore mineral petrography. In every section throughout this drillcore interval at least a few strongly shocked (≥3 sets of PDFs per grain) quartz or feldspar clasts were observed (see also Fig. 1). Microcline frequently shows shock-induced twinning and PDFs, as well as local melting. Plagioclase often displays PDFs oriented either near-perpendicular or parallel to twin lamellae. Partial or complete isotropization of quartz, and to a lesser extent, feldspar was recognized. Isotropization is clearly more important in the impact melt zone than in under- and overlying fragmental and suevitic breccias. In the lower part of the impact melt layer isotropic crystals with melt veinlets were observed, and clast recrystallization and annealing is very prominent. Mafic minerals rarely show shock deformation, besides the ubiquitous kinkbanding of mica. Amphibole is frequently strongly fractured, generally parallel to normal cleavage orientations. Some grains were seen to be locally brecciated, but no characteristic shock metamorphic effects were recorded in this mineral. In the 86.5 m (283.8 ft) specimen some zircon crystals with PDFs parallel to (001) were noticed, and 180.1 m (591.0 ft) contains sphene with PDFs. In agreement with macroscopic observations, we find that the clast population is variable from sample to sample, with regard to proportions of different lithologies (granite, gneiss of granitic to dioritic composition, amphibolite, quartzite, sandstone, shale or mudstone). Sedimentary clasts are important in the population of fragmental breccia from the upper zone, but are very rare and often completely absent in the lower section where crystalline basement-derived material forms the bulk amount of the clast component.

GEOCHEMICAL STUDIES. 136 samples from all 12 new and the two 1953 drill cores were prepared for complete major (XRF) and trace (INAA, XRF, AAS, DCP) element analyses. We have completed the major element analyses, and most of the trace element analyses. A subset of these samples (incorporating most compact rocks, but not shales) was selected for petrographic, mineralogical, and electron microprobe studies. We have been trying to locate pristine impact glass, which is extremely rare but was found in a sample from the M7 core. However, most glass is devitrified (Fig. 2). Quartz samples of clearly post-impact origin were selected for fluid inclusion studies (classical, and mass spectrometrical), attempting to determine the composition of a possible post-impact (impact-induced) hydrothermal fluid. These studies are in progress. Table 1 gives an example of major element data from suevitic and fragmental breccia samples from the 192.3 to 214.1 m depth interval of the M1 core. For three of the samples in Table 1, plus a clast sample, Fig. 3 shows the rare earth element (REE) patterns. The Rb-Sr, Sm-Nd, and oxygen isotopic compositions of a variety of samples have been measured, adding to earlier data [7,8].

ACKNOWLEDGEMENTS: We thank the Iowa Geol.Survey Bureau for samples. Supported by Austrian FWF Project P08794-GEO.

REFERENCES: [1] Anderson, R.R., Witzke, B.J., Hartung, J.B., Shoemaker, E.M., and Roddy, D.J. (1993) LPS **XXIV**, 35-36. [2] Shoemaker, E.M., Roddy, D.J., and Anderson, R.R. (1993) LPS **XXIV**, 1301-1302. [3] Anderson, R.R., Witzke, B.J., and Hartung, J.B. (1993) Meteoritics **28**, 317. [4] Koeberl, C., Anderson, R.R., Hartung, J.B., and Reimold, W.U. (1993) LPS **XXIV**, 811-812. [5] Bell, M.S., Reagan, M.K., Anderson, R.R., and Foster, C.T. (1993) LPS **XXIV**, 87-88. [6] Bell, M.S., Reagan, M.K., Anderson, R.R., and Foster, C.T. (1993) Meteoritics **28**, 321-322. [7] Blum, J.D., Chamberlain, C.P., Hingston, M.P., and Koeberl, C. (1993)

LPS XXIV, 135-136. [8] Blum, J.D., et al. (1993) Nature 364, 325-327.

Fig. 1: Multiple sets of PDFs in quartz from breccia (2A core, depth 109.8 m); crossed nicols, image width: 1.1 mm. **Fig. 2:** Spherulitic devitrification of completely melted, originally probably granodioritic clast in impact melt rock (M7 core, 65.6 m depth); crossed nicols, image width: 1.75 mm.

Table 1: Major element composition (XRF) of 2 suevitic breccias (Suev), one fragmental breccia (FrBre), and matrix from a fragmental breccia, all from M1 core; sample numbers are depths in feet. Data in wt%.

	630.9 Suev	631.0 Suev	647.0 FrBre	702.5B Matr
SiO_2	59.41	60.00	60.69	59.42
TiO_2	0.93	0.90	0.85	0.89
Al_2O_3	15.62	15.32	14.67	15.01
Fe_2O_3	7.04	7.18	6.90	6.53
MnO	0.113	0.113	0.127	0.089
MgO	3.80	3.92	4.70	3.49
CaO	5.36	5.33	4.56	5.48
K_2O	4.51	4.85	4.43	5.41
Na_2O	1.94	2.06	1.80	2.26
P_2O_5	0.211	0.189	0.219	0.214
L.O.I.	0.83	0.80	1.42	1.47
Total	99.77	100.65	100.36	100.26

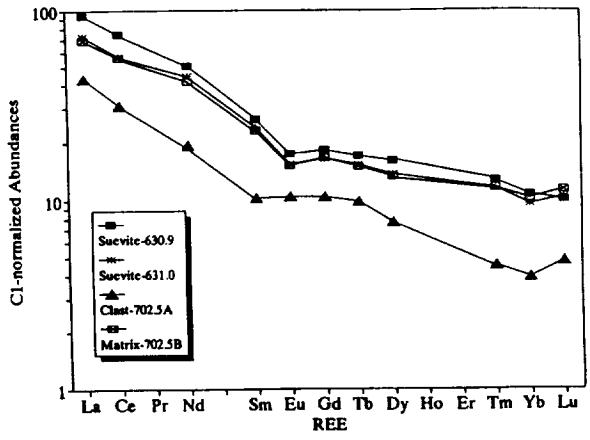

Fig. 3: C1-normalized REE abundance patterns in two suevitic breccias (Table 1), and of a large pegmatite-granite clast and matrix (Table 1) of a fragmental breccia, from M1 (sample numbers are depth in feet).

AMES STRUCTURE, OKLAHOMA: AN ECONOMICALLY IMPORTANT IMPACT CRATER.

Christian Koeberl[1], Wolf Uwe Reimold[2], and Robert A. Powell[3]. [1]*Institute of Geochemistry, University of Vienna, Dr.-Karl-Lueger-Ring 1, A-1010 Vienna, Austria (a8631dab@vm.univie.ac.at);* [2]*Economic Geology Research Unit, Department of Geology, University of the Witwatersrand, Johannesburg 2050, South Africa (065wur@witsvma.wits.ac.za);* [3]*Universal Resources Corp., Oil Center East, 2601 Northwest Expressway, Oklahoma City, OK 73112, U.S.A..*

INTRODUCTION AND SUMMARY. The Ames structure is situated in northwestern Oklahoma near the town of Ames in southeastern Major County. Structural disturbances in several horizons drew attention to the existence of an unusual feature. Mapping of the top of the Upper Ordovician Sylvan shale showed the presence of a relatively circular, concentric, structural depression with a minimum diameter of about 15 km (Fig. 1). The whole structure is set in Cambro-Ordovician Arbuckle dolomite. Structural studies showed the presence of two concentric rims, an outer rim, which is about 1.5 to 3 km wide, and an inner "rim". The rocks of the outer rim consist mainly of fractured and brecciated Arbuckle dolomite. The rocks of the inner "ring" structure, which seems to be the remnant of a structural uplift within a central depression, are comprised of brecciated Precambrian age granite and Arbuckle dolomite. The structure is sealed by Middle Ordovician Oil Creek shale, which overlies the Arbuckle dolomite. Wells from both the crater rim and the central uplift are oil- and gas-producing, making Ames one of the more economically important impact structures. The whole feature is buried beneath almost 3000 m of sedimentary cover, making an exploration difficult. However, some rocks recovered from the central uplift were reported to shows quartz grains with shock-diagnostic planar deformation features [1], indicating an impact origin for the structure. We have started a more detailed mineralogical, petrological, and geochemical study of rocks recovered from various drill cores and report here preliminary data from the Bland #1-33 well at the eastern side of the uplift.

GEOLOGY AND SAMPLES. Oil exploration in northwestern Oklahoma led to the discovery of a structural anomaly with a diameter of about 15 km. Geophysical studies and drill-core analyses led to the suggestion that this structure could be a buried impact crater (e.g., [1-3]). The feature has morphological characteristics, such as a central uplift surrounded by a circular depression and an outer ring (Figs. 1-3), which are typical of those of complex impact craters. The central uplift is about 5 km in diameter and is collapsed or eroded in the center. Although the interpretation of the Ames "Hole" as an impact structure has been challenged in favor of a volcanic origin (e.g., [4,5]), the reported discovery of some shocked quartz is evidence in favor of an impact origin. We have begun detailed studies of samples from several drill-cores, in the hope of confirming the presence of shock-diagnostic mineralogical features, and to provide a thorough geochemical and mineralogical description of the crater units. The first core to be studied is from the URC Bland #1-33 well which was drilled to a total depth of 2885 m and produces more than 300 barrel of oil per day. A core was taken from 2801 to 2803 m, and drill cuttings are available from 2743 to 2885 m. Thin sections of 10 basement granite samples, of 8 specimens of carbonate-rich fragmental breccia with abundant quartzite-derived clasts, and of several finer-grained breccia or carbonate rocks with fine-grained quartz clasts were studied optically. All samples are from the drill core.

RESULTS AND IMPLICATIONS. Several, up to 1 cm wide, granitic clasts, as well as feldspar clasts in fragmental breccia, display significant deformation in the form of local cataclasis of quartz or feldspar minerals and of localized annealing, particularly along grain margins (Fig. 4). It is possible that this local recrystallization could be the result of frictional heating. However, despite careful search at high microscope magnification, no unequivocal evidence for shock metamorphism could be identified in any of our samples. However, studies of some sidewall cores and other drill cores (including the D&J James #1-20 core), which were reported to have shocked quartz, are in progress. Some first results from our geochemical analyses of the various rock types encountered in the drill cores are given in Table 1. Samples include Arbuckle dolomite, Precambrian granite, and breccias with various proportions of mainly dolomite and granite. This crater is of interest for several reasons. If confirmed as an impact structure, it will add to our understanding of buried craters (in comparison to, e.g., Manson). In addition, the abundance of natural gas and oil at this crater will allow the study of impact craters as hydrocarbon traps.

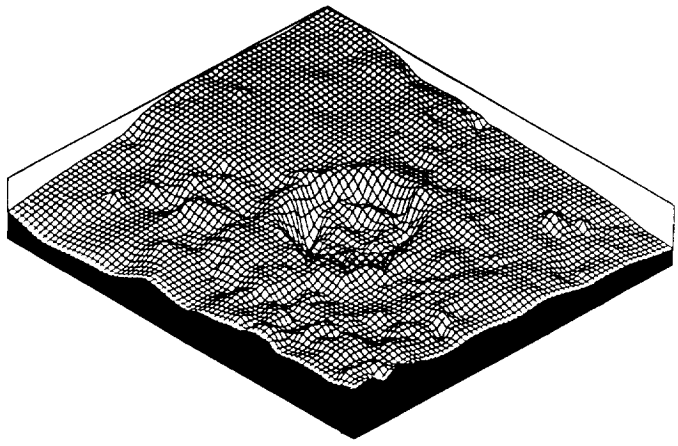

Fig. 1. Surface of Sylvan shale, showing the Ames structure. Vertical exaggeration 16x.

ACKNOWLEDGEMENTS: We thank Universal Resources Corp., D&J Oil Comp., and Continental Resources Corp. for samples and data. Supported by Austrian FWF Project P08794-GEO (to CK).

REFERENCES: [1] Carpenter, B.N., and Carlson, R. (1992) Oklahoma Geol. Notes **52**, 208-223. [2] Roberts, C., and Sandridge, B. (1992) Okl. Shale Shaker **42**, 118-121. [3] Hamm, H., and Olsen, R.E. (1992) Oil & Gas Jour. **90(16)**, 113-116. [4] Roemer, C.D., Roemer, C., and Williams, K. (1992) Oil & Gas Jour. **90(26)** 75-80. [5] Coughlon, J., and Denney, P. (1993) Okl. Shale Shaker **43**, 44-58.

Table 1: Major element composition (XRF) of selected samples from the Bland #1-33 drill core; data in wt%.

	9189.0 br	9189.1 dol	9193.4 br	9194.0 br	9189.1 gra	9193.8 gra
SiO_2	7.60	9.59	52.83	63.73	73.30	75.92
TiO_2	0.07	0.09	0.17	0.22	0.22	0.20
Al_2O_3	1.65	1.67	8.33	9.71	11.20	12.91
Fe_2O_3	1.99	4.41	2.32	1.93	1.43	0.76
MnO	0.418	0.427	0.197	0.119	0.051	0.017
MgO	18.60	17.23	5.78	3.19	0.85	0.01
CaO	27.27	25.16	9.13	5.23	1.75	0.27
K_2O	0.34	0.48	2.72	3.42	3.52	4.16
Na_2O	0.28	0.34	3.22	3.60	4.40	5.09
P_2O_5	0.001	0.015	0.014	0.028	0.024	0.031
L.O.I.	41.15	37.37	14.56	8.55	2.93	0.54
Total	99.37	96.78	99.27	99.71	99.68	99.89

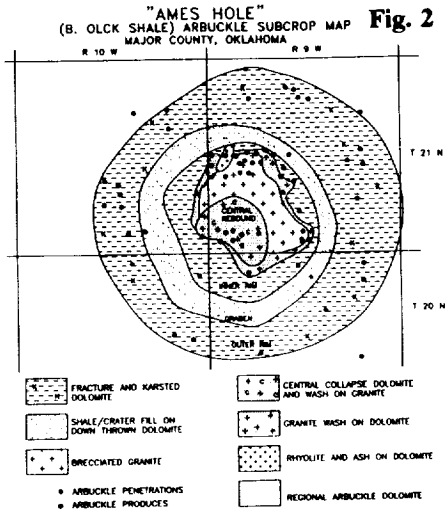

Fig. 2

Fig. 4

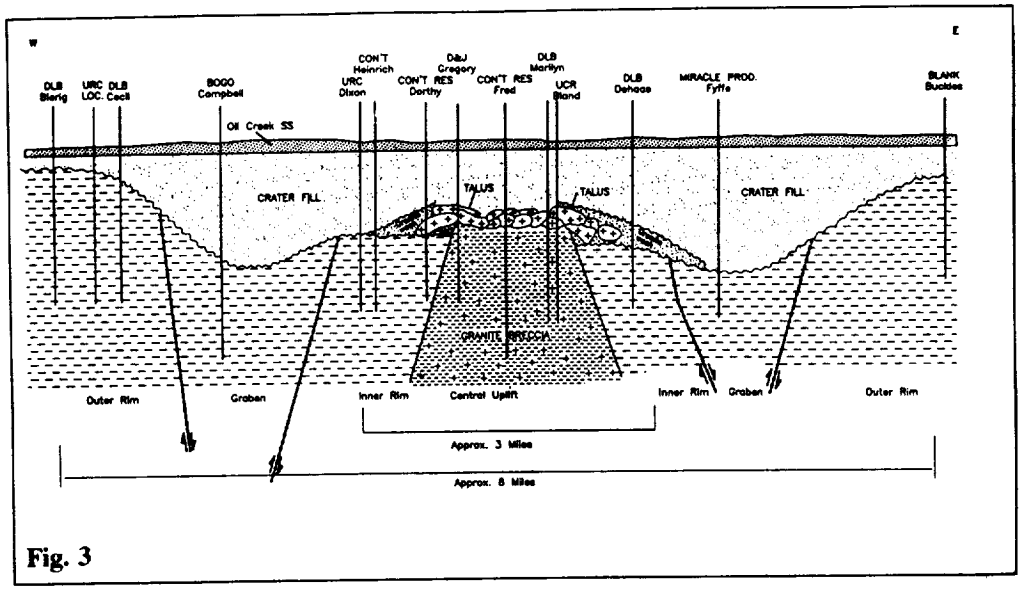

Fig. 3

Fig. 2: General geological layout of the Ames structure, showing the localities of oil and gas wells.
Fig. 3: Schematical cross section of Ames structure; not to scale (vertically exaggerated); showing location of URC Bland #1-33 and other wells.
Fig. 4: Thin section microphotograph of breccia sample 9189.1-br (from 2800.8 m depth; Bland #1-33 well). Cataclasis and marginal melting in granite clast in carbonate-rich fragmental breccia. Image 1.75 mm wide.

C-4.

MAGNESIUM ISOTOPIC FRACTIONATION IN THE OLIVINES FROM ALLENDE CHONDRULES AND ISOLATED GRAINS

A. KOGA[1], H. NAGAHARA[1], H. YURIMOTO[2], AND O. KOIKE[2], (1)Geol. Inst., Univ. Tokyo, Hongo, Tokyo 113, Japan, (2) Inst. Geosci, Univ. Tsukuba, Tsukuba, Ibaraki 305, Japan.

Evaporation experiments have shown that isotopic fractionation takes place when solid silicates are heated at high temperatures in vacuum, and the maximum degree of isotopic fractionation from solid is estimated to be several to ten per mill [1]. Much larger isotopic fractionation has been reported for a molten silicate [2]. Although isotopic fractionation in CAIs has been intensively studied [summarized in 3], very few studies have been made for chondrules except for silicon isotopes [3]. Kinsey *et al.* [4] and Esat and Taylor [5] investigated Mg isotopic compositions of chondrules from Bjurbole, Murchison, and Semarkona, but did not find evidence for isotopic fractionation. Because heating temperatures and cooling rate for formation of chondrules and type B1 CAIs are similar [6], there is a possibility that chondrules possess records of isotopic fractionation induced by partial evaporation during chondrule formation.

In order to search isotopic fractionation in chondrules, we have studied isolated olivine grains and chondrules in Allende. A polished thin section was newly prepared. Detailed petrographic work with an SEM-EDS was done before SIMS work, and all the objects larger than 40 μm were studied. The thin section contains 113 objects excluding CAIs and amoeboid olivine inclusions, which consists of 13 isolated grains, 66 porphyritic chondrules, 29 granular chondrules, and 5 barred to radial olivine chondrules. Isolated grains are olivine with sizes ranging from 50 to 250 μm; three of them have irregular outline and two have partly straight crystallographic surface. They are Fo>93 showing iron enrichment in thin outermost layer of grains and along cracks. Porphyritic chondrules range from 100 to 1620 μm; 9 of them contain almost pure forsterite (Fo>99), and most of them contain 99>Fo>(95-85) olivine. They are characterized by the presence of opaque phases and plagioclase. Granular chondrules consist mainly of anhedral olivine, and range from 100 to 930 μm. 13 out of 29 have Fo>99 olivine and 3 are of type II (Fo<70). They are characterized by the coexistence of clinoenstatite and minor abundance of opaque phases and plagioclase. Barred to radial olivine chondrules contain clean to devitrified glass and often have thick rim. They are magnesian having Fo>95 olivine.

Magnesium isotopic compositions of olivine grains, particularly forsteritic olivine, of those four different occurrences were measured with a Cameca IMS-3f ion-microprobe at the University of Tsukuba with the analytical method described by Koike *et al.* [7]. Masses 24, 25, and 26, were measured but 27 was not measured. Because the instrumental mass fractionation changes depending on many factors, we have analyzed olivine from San Carlos as a reference sample of which isotopic composition has been known [8]. After one day, the instrument got very static, and the instrumental mass fractionation for the reference and the same unknown grain was nearly constant. Therefore, the results are plotted without any correction (Fig. 1). The cross in the box represents average value of the reference and the box is 1σ of four reference measurements made at the beginning and the end of a series of analysis. Error bars of unknown samples are 1σ of each analysis which is made of 90 cycles. The results are normalized against the reference sample, which locates at the original point of the graph. In this plot, a slope for fractionation incudes instrumental mass fractionation, and therefore, it does not necessarily be 1/2.

There was neither systematic isotopic difference among olivines with different occurrence, nor heterogeneity within grains in spite that the Fo value varies from highly magnesian (Fo>99) to less magnesian (Fo<95). These results show that the isotopic composition of olivines in chondrules and isolated grains had been achieved before crystallization of chondrules, which should have been established at least at the highest temperature stage of chondrule formation or before that. The results form a nearly straight line, suggesting that the

effect of instrumental mass fractionation is constant through the analyses and there is no excess ^{26}Mg derived from decay of radioisotopic ^{26}Al. An interesting result is that most data are located at the upper right portion along the line; that is, almost all olivine have heavier isotopic compositions than the reference. Heavy isotopic composition suggests that the olivines are either evaporation residues or higher temperature condensates. The latter possibility, however, seems to be incompatible with recent low temperature solar nebular models. Thus, the evaporation residue origin may be plausible for the isotopically heavy olivines. The maximum degree of fractionation for the olivines is about 10‰, which well coincides with the value estimated for isotopic fractionation formed through evaporation of solid material in vacuum with the evaporation degree of more than 80% [1]. Alternatively, isotopic fractionation up to 10 ‰ could be achieved if molten silicates evaporated at a smaller degree [2]. Although the present results cannot be directly compared to the experimental results because the experiments were carried out with single crystals and because natural chondrules might possess records of precursors, melting and crystallization, this is the first report that chondrules and isolated olivine grains show magnesium isotopic fractionation which could have generated during heating event in the solar nebula.

REFERENCES: [1] Nagahara, H. (1994) This volume, [2] Davis, A. *et al.* (1990) *Nature* **347** 655-657, [3] Clayton, R. N. *et al.* (1985) in Protostars and Planets II, 755-771, [4] Kinsey, A. E., Esat, T. M. and Taylor, S. R. (1988) *LPSC* **XIX** 603-604, [5] Esat, T. M. and Taylor, S. R. (1990) *LPSC* **XXI** 333-334, [6] Nagahara, H. (1987) *LPSC* **XVIII** 692-693, [7] Koike, O. *et al.*. (1993) *Proc. NIPR Symp. Antarct. Meteorites* **6** 357-363, [8] Catanzaro, E. J. *et al.* (1966) *J. Res. Nat. Bur. Stand.* **70a** 453-458.

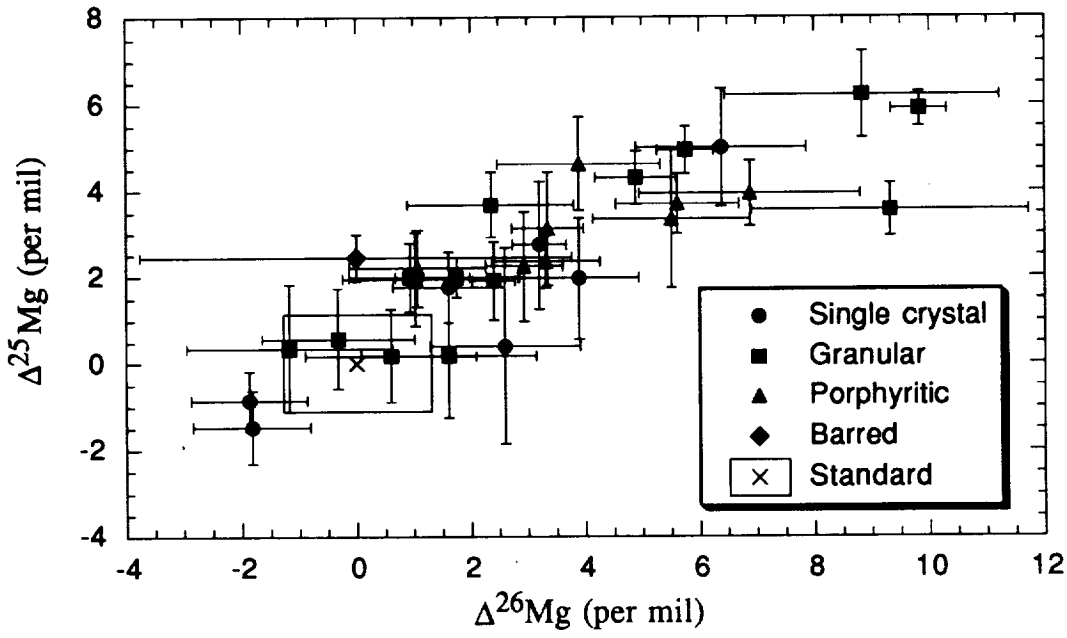

Fig. 1. Magnesium isotopic compositions of forsteritic olivine in Allende isolated grains and chondrules with three different textures. The cross and box is the average and 1σ of four standard measurements made at the beginning and the end of a series of unknown measurements. The error bars are 1σ of 90 cycles for one analysis.

$$\Delta^{25}Mg=1000*[\frac{(^{25}Mg^{+}/^{24}Mg^{+})_{MEAS}}{(^{25}Mg/^{24}Mg)_{REF}} - 1] \text{ and } \Delta^{26}Mg=1000*[\frac{(^{26}Mg^{+}/^{24}Mg^{+})_{MEAS}}{(^{26}Mg/^{24}Mg)_{REF}} - 1].$$

Al-Mg isotopic and REE clues to the formation of a Type B1 CAI from Allende meteorite; Osamu Koike[1], Hisayoshi Yurimoto[1] and Hiroshi Nagasawa[2] ,[1]Institute of Geoscience, University of Tsukuba, Tsukuba, Ibaraki 305, Japan, [2]Department of Chemistry, Gakushuin University, Mejiro, Tokyo, 171, Japan.

CALCIUM-ALUMINUM-RICH INCLUSIONS(CAIs) in carbonaceous chondrites are generally believed to be the first solids to have formed in the solar nebula and must record many clues to the formation of itself:for example, isotopic, petrologic and chemical signatures. Therefore, in order to make the formation revealed, we have measured the distribution of Mg isotopes and rare earth element(REE) abundances in a Type B1 CAI of Allende meteorite.

Sample and Experimental Method: The sample used in this study was two polished thin sections (HN3-1c and b) from Allende HN3-1 Type B1 CAI. Petrologic characteristics of this inclusion was described by elsewhere[1]. The surface of polished thin sections was coated by gold film. In-situ Magnesium isotopic and REE analyses were performed by CAMECA IMS-3F SIMS instrument equipped with electrostatic peak switching system of University of Tsukuba.

All Mg isotopic measurements were made at a sufficient high mass resolution to exclude any interferences from MgH^+ as well as other possible molecular and doubly-charged ions. A mass resolution power was ~4000. Measurement were made by cycling through the mass sequences 24, 25, 26, and 27 in automatic magnetic peak jumping mode. After the magnetic peak jumping mode, a precise peak centering of each mass was made by electrostatic peak switching mode [2]. Primary beam currents from 0.5 to 2 nA were used depending on the Mg concentration. The beam size was 10-20μm in diameter. The energy slit was set to select an energy window of 50eV. A run consisted of 90 cycles. Several runs were usually made on a given spot. Terrestrial mineral standards of spinel, clinopyroxene, and anorthite and synthetic glass standard of melilite composition were prepared to determine the relative sensitivity factors of Mg^+ and Al^+ and to check on the deadtime of the pulse-counting system and the normal Mg isotopic ratios. $^{27}Al^+ / ^{24}Mg^+$ intensity ratios of some anorthite spots became systematically increased during analysis because the sample surface was slightly charging electrostatically with sputtering. In order to confirm the $^{27}Al / ^{24}Mg$ ratios, the same point of all anorthite spots was measured again under energy filtering mode. $^{27}Al / ^{24}Mg$ calculated from energy filtering mode was equal to that from high mass resolution mode except for the drift data. Such charging effects were not observed on the other minerals except for anorthite.

Rare earth elements were measured with energy window of 20eV, offset voltage of -70V and mass resolution power of 300 by means of energy filtering. This condition is efficient in eliminating molecular-ion interferences of REE isotopes except for EuO^+ at the mass 169 for anorthite and melilite. Sensitivity factors of each REE between secondary ion intensity and concentration were determined by using of the augite single-crystal of which REE contents were well determined by INAA analysis [3].

Results and Discussion: The results of the ^{26}Al - ^{26}Mg analyses are given in Fig. 1. In the figure, the fractionation-corrected excess ^{26}Mg in permil is given relative to the normal ratio ($^{26}Mg / ^{24}Mg$)=0.13932 [4]. Different symbols for anorthite denote different crystals in the HN3-1 CAI.

Al-Mg and REE clues to the formation of CAI in Allende: Koike et al.

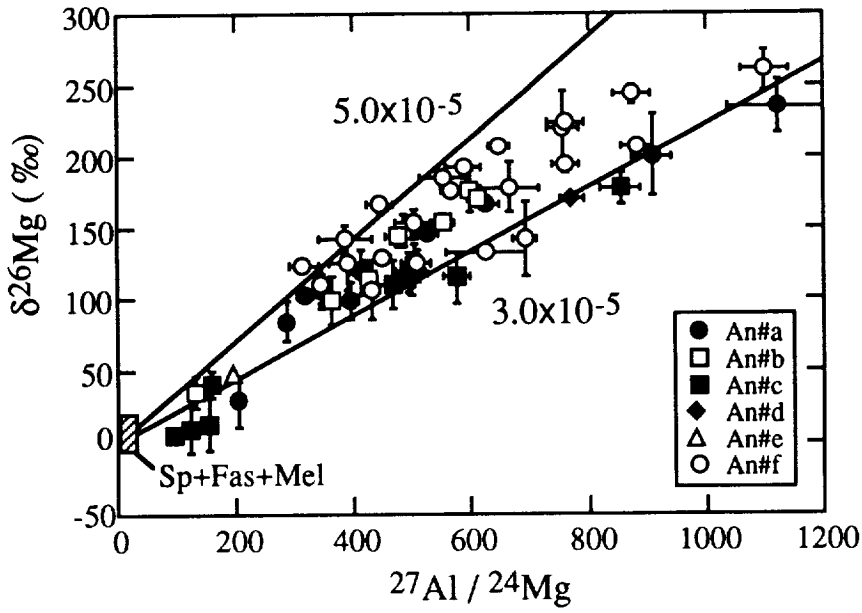

Fig. 1. ^{26}Al-^{26}Mg plot for measurements in individual mineral grains of Allende HN3-1 Type B1 CAI. Each anorthite single crystals were numbered by An#a, #b, #c, #d, #e, and #f. The rectangle area indicating "Sp+Fas+Mel" near the origin is the region of spinel, fassaite, and melilite data points. Most anorthite data points scatter between the line of $3.0x10^{-5}$ and the line of $5.0x10^{-5}$. The error bars are $\pm 2\sigma$.

Most anorthite data points, particularly the data points of An#f, scatter between the slopes of $3.0x10^{-5}$ and of $5.0x10^{-5}$. There was no clear relationship between petrologic features and scattering of $\delta^{26}Mg$. So we concluded that the scatter in ^{26}Al -^{26}Mg systematics in six anorthite crystal in this CAI reflected the heterogeneous ^{26}Al distribution in CAI melt before the anorthite crystallized.

The representative REE patterns for melilite are shown in Fig. 2. Melilite had a fractionated REE pattern with a large positive Eu anomaly and the REE abundance had a tendency to decrease slightly as the akermanite content increases, which was consistent with the results of the model prediction of simple fractional crystallization from melt. But, The considerable decrease of HREE concentration with akermanite content is difficult to describe by the simple fractional crystallization of melilite.

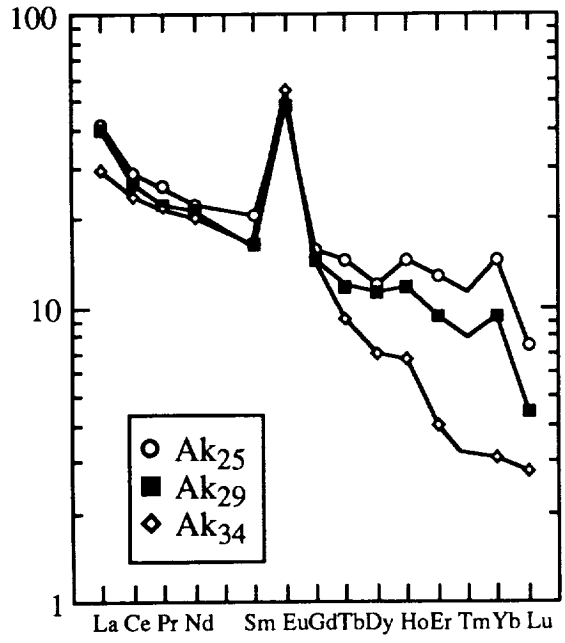

Fig. 2. Representative REE patterns for mantle melilite.

References: [1] Nagahara, H., Nagasawa, H.,Nakamura, N., and Matsui, T. (1987) *Lunar Planet. Sci.* **XVIII**, 694-695. [2] Koike, O., Yurimoto, H., Nagasawa, H., and Sueno, S. (1993) *Proc. NIPR Symp. Antarct. Meteorite*, **6**, 357-363. [3] Onuma, N., -iguchi, H. and Nagasawa, H. (1968) *Earth Planet. Sci. Lett.*, **5** 47-51. [4] Catanzaro, E. J., Murphy, T. J., Carner, E. L. and Shields W. R. (1966) *J. Res. Nat. Bur. Stand.*, **70a**, 453-458.

LONGITUDINAL PROFILES OF PLAINS CHANNELS ON VENUS; G. Komatsu and V. R. Baker, Lunar and Planetary Laboratory, University of Arizona, Tucson, AZ 85721

The long channels (> 500 km) in plains regions are canali-type channels [1]. Preliminary studies indicate that the longitudinal profiles of these channels show tectonic deformation [2][3]. We extend these studies by using a more precise measurement technique and by increasing the number of channels analyzed.

We measured longitudinal profiles of channels using the MGMDQE program developed by P. Ford's group at MIT. This program enables us to display an image, and ARCDR altimetric footprints overlapped on top of it. Because of the relatively large footprint size (about 10x20 km) compared with canali widths (up to 4 km), and because of the shallow depths of channels, the derived altitude generally represents that of the surrounding plains. The size of the footprints is about the same as the sampling interval. The range of error associated with each sample is between 2 and 14 m, but this is small compared with the range of altitudes.

The longest channel occurs west of the Atla Regio (Figs. 2a). The channel (Fig. 2b) is highly deformed. The channel deformation occurs at multiple wavelengths indicating that deformation is hierarchical. Since channels are sinuous, wavelengths of the profile undulations do not exactly correlate with characteristic scales of tectonic deformation. Nevertheless, at least two wavelengths (300-400 km and about 3000 km) are observed, and these probably represent characteristic modes of tectonic deformation in the plains regions (Figs. 2b and c). The long wavelengths correspond to basin structures and short wavelengths correspond mostly to belts of compressional ridges. These tectonic activities postdate the emplacement of at least the uppermost plains materials as represented by the canali-type channel. Highlands probably already existed at the time of channel formation because the channel seems to avoid the northern arms of Atla Regio (Figs. 2a). This channel is postdated by lava flows, impact cratering and various episodes of tectonic deformation. The inferred temporal sequence of various activities is summarized in Figure 1. The second longest channel occurs in eastern Aino Planitia (Fig. 3a). The profiles also (Fig. 3b) show multiple wavelengths. The long wavelength does not have an obvious corresponding geologic feature in the SAR image. This concave undulation corresponds to a longitudinal basin. The short wavelength undulations correspond to belts of compressional ridges parallel to the longer axes of the basin (Fig. 3c). The north-trending lineaments in Figure 3a are wrinkle ridges (average spacing 20-40 km). These do not appear in the topographic profile because of the large spacing of altimetric sampling. Some of these wrinkle ridges may have formed concurrently with canali, as suggested by the diverted channel path (T. Parker, personal communication). The possible interpretations of the tectonism include downwarping of the basin concurrently with the formation of compressive ridge belts and wrinkle ridges.

B. Janes (Cornell) provided advice during production of the synthetic perspective images, which were created using vart ray-tracing software supplied by P. Averkamp (Tech. Univ. Munich) which runs under the Khoros workspace environment (Univ. N. Mex.)

REFERENCES: [1] Komatsu, G. et al. (1992) *Icarus,* **102**, 1-25. [2] Parker, T.J. et al. (1992) *LPSC* **XXIII**, 1035-1036. [3] Baker, V.R. et al. (1992) *J. Geophys. Res.*, **97**, 13,421-13,444.

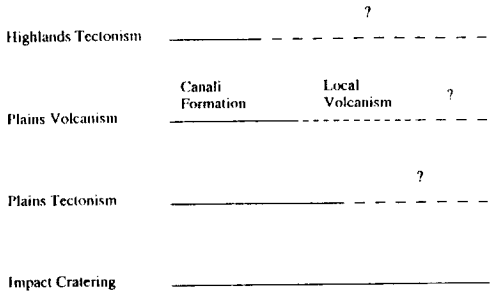

Fig. 1 Time sequence of various geologic activities.

LONGITUDINAL PROFILES OF VENUSIAN CHANNELS: G. Komatsu and V.R. Baker

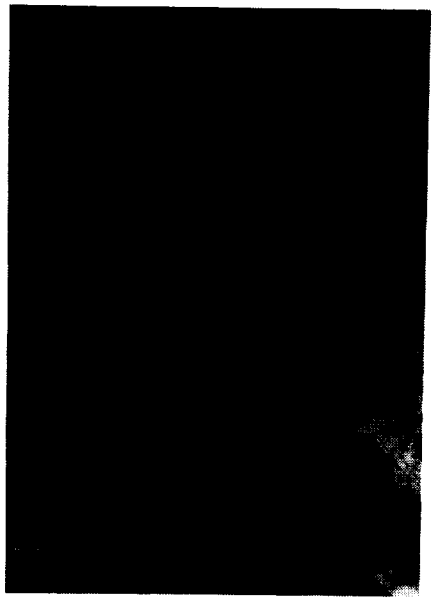

Fig. 2a Atla Regio, plains and longest channel (highlighted). Longitudinal topographic profile was derived between A and A'.

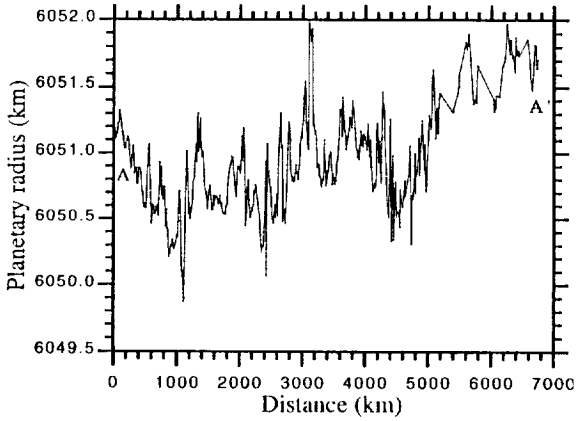

Fig. 2b Longitudinal topographic profile of longest channel. At least two wavelengths (300-400 km and about 3000 km) are observed.

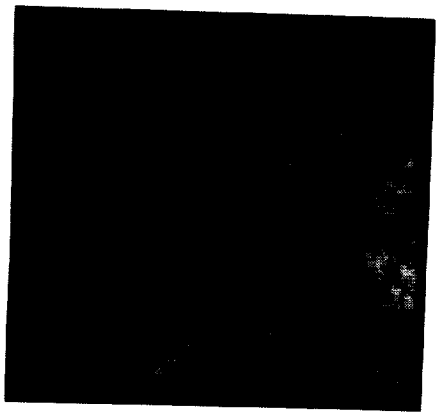

Fig. 2c 3-dimensional perspective of Atla Regio and plains and longest channel (highlighted).

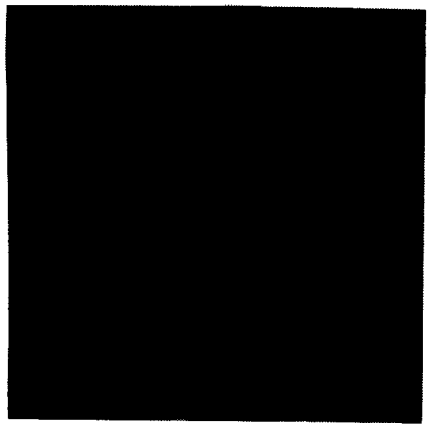

Fig. 3a A canali-type channel in the eastern Aino Planitia (highlighted). Longitudinal topographic profile was derived between A and A'.

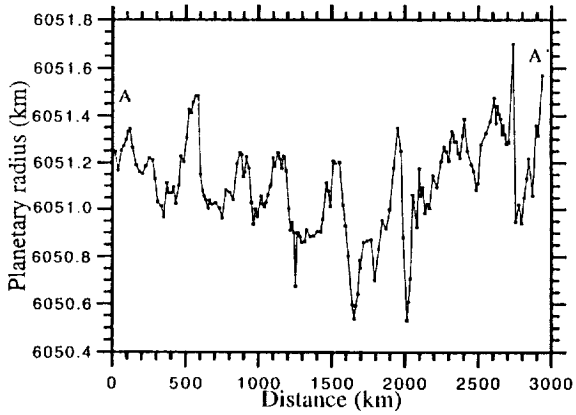

Fig. 3b Longitudinal topographic profile of the canali-type channel in the eastern Aino Planitia. At least two wavelengths (300-400 km and about 3000 km) are observed.

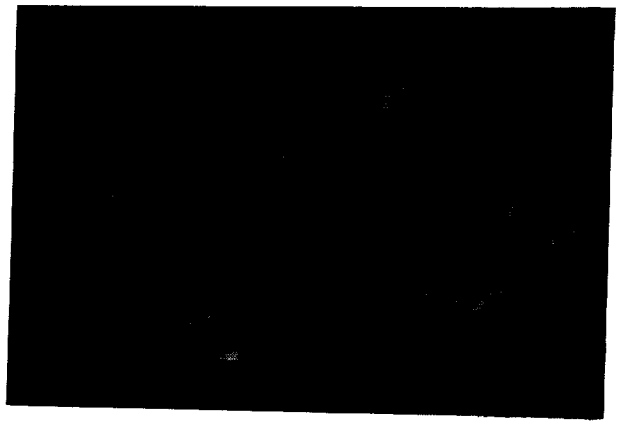

Fig. 3c 3-dimensional perspective of eastern Aino Planitia and a canali-type channel (highlighted).

GEOCHEMICAL COMPARISON OF FOUR CORES FROM THE MANSON IMPACT STRUCTURE;
RANDY L. KOROTEV, KAYLYNN M. ROCKOW, BRADLEY L. JOLLIFF, and LARRY A. HASKIN, Department of Earth & Planetary Sciences, Washington University, St. Louis, MO 63130 and *PETER MCCARVILLE and LAURA J. CROSSEY,* Department of Earth & Planetary Sciences, University of New Mexico, Albuquerque, NM 87131

Samples of impact melt breccia taken through the 130-foot-thick CCB-MM unit (crystalline-clast breccia, melt matrix) of the M-1 core of the Manson Impact Structure (MIS) are all similar in composition to each other and different from samples from the overlying SCB units (sedimentary-clast breccia) and underlying CCB-SM units (crystalline clast breccia, sandy matrix) [1]. Our new analyses indicate that samples from the CCB-MM units of the M-7, M-8, and M-10 cores are generally similar in composition to each other and to the CCB-MM samples of M-1 (Fig. 1); however, some striking, systematic differences exist. The CCB-MM unit of M-1 has Cs concentrations consistently 2.5 times that of the melt-breccia units of the other cores and has a slight relative enrichment in heavy REE (rare earth elements) compared to other units in the M-1 core and to CCB-MM units in the other cores (Fig. 2). Other minor differences exist among the melt-breccia units and, in detail, melt-breccia samples from the M-1 core are distinguishable from melt-breccia samples from the other cores. For example, the CCB-MM unit of the M-10 core is richer in Fe, Sc, and Co than the corresponding unit in M-1 and appears compositionally to contain a greater component of the biotite or hornblende gneiss of the central peak crystalline (CPC) rocks, such as the unit sampled at the bottom of the M-7 core (Fig. 1). These various differences may result from differences in abundance of some components of the melt mixtures, differences in clast distribution, or to some post-impact processes; in any case, we have not yet identified the components and/or processes. Among CCB-MM units, that from the M-1 core is texturally unique in having low porosity, few clasts, and a fine-grained matrix, thus some of the observed differences may simply result in variable clast content. Preliminary mass-balance calculations indicate that the CCB-MM *breccias* (melt plus clasts) contain more than 50% crystalline components (biotite/hornblende gneiss and a granitic component); this contrasts with estimates that the *melt* consists primarily of sedimentary components [3].

The units of sedimentary-clast breccia (SCB) are compositionally distinct, compared to other units, in having low concentrations of Na, K, Sc, Fe, and Ba, as well as high concentrations of Ca and, particularly, As and Sb. These differences reflect the high proportion of clastic limestone and shale.

The five samples analyzed from the CPC unit (central peak crystalline) of the M-7 core are remarkably uniform in composition and are compositionally most similar to clasts of biotite gneiss and hornblende-plagioclase gneiss or amphibolite extracted from the CCB-SM units of cores M-1 and M-7. The CPC rocks are more mafic than the CCB-MM units (melt breccia) and have distinctly different relative abundances of REE, particularly Eu (Fig. 2b). The CCB-SM units are not as compositionally uniform as are the CCB-MM units, and some particularly anomalous samples occur among samples from CCB-SM units. The SM breccias contain large clasts, appear more porous than the MM breccias (at least in M-1), and have been affected strongly by hydrothermal alteration [4]; any or all of these factors may lead to the compositional variability. Nevertheless, the mean compositions of the CCB-SM units in the three cores in which this unit was sampled are all similar. Compared to the CCB-MM units, the CCB-SM units are richer in elements associated with mafic silicates (Ca, Fe, Sc, Cr, Co, Ni) and have different relative REE abundances (Fig. 2b). The CCB-SM units appear to contain a component of CPC rocks in excess of that contained in the CCB-MM units.

REFERENCES. [1] Korotev R. L., Jolliff B. L., Rockow K. M., Haskin L. A., and Crossey L. J. (1993) *Meteoritics* **28**, 383-384 (abstr.); [2] Anderson R. R., Witzke B. J., Hartung J. B., Shoemaker E. M., & Roddy D. J. (1993) In *Lunar and Planetary Science XXIV*, pp. 35–36 (abstr.). [3] Anderson R. R. and Hartung J. B. (1992) *PLPSC22*, 101-110; [4] Crossey L. J. and McCarville P. (1993) In *Lunar and Planetary Science XXIV*, pp. 351–352 (abstr.).

Manson Cores: *Korotev R. L., Rockow K. M., Jolliff B. L., Haskin L. A., McCarville P. & Crossey L. J.*

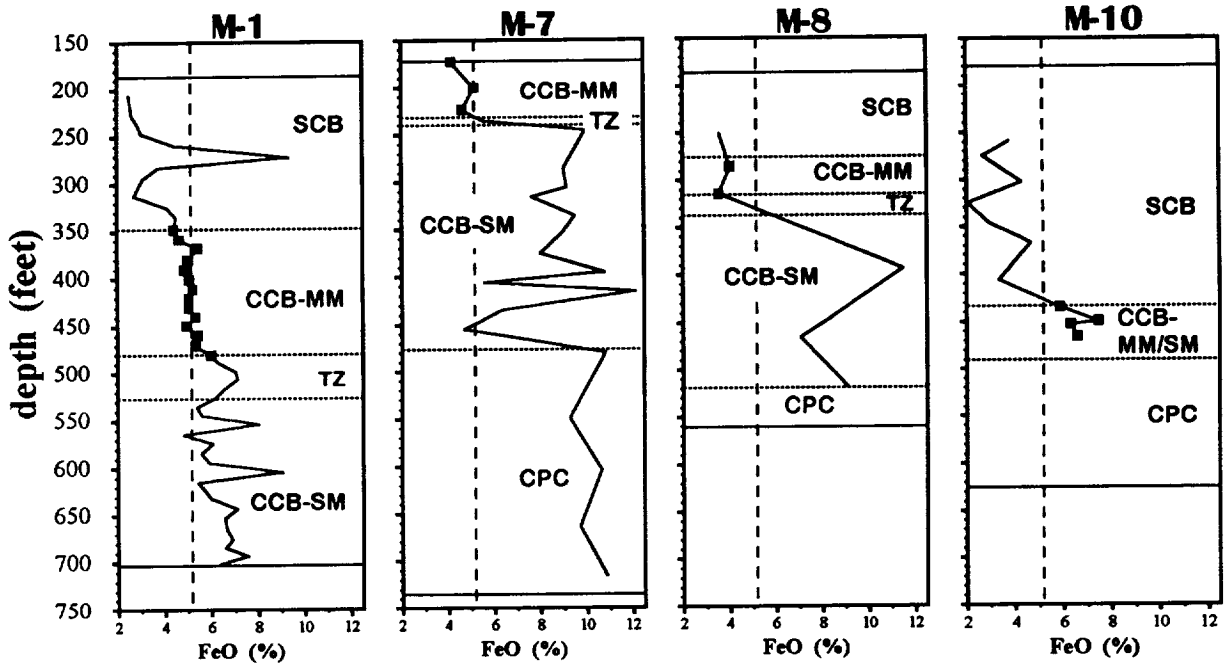

Fig. 1. Profile of Fe concentrations (total Fe as FeO) in four cores into the MIS. The solid points represent samples from units of impact melt breccia (CCB-MM = crystalline-clast breccia, melt matrix). For reference, the mean composition of melt breccia in core M-1 is reresented by the vertical dashed line in each profile. Other units are indicated: SCB = sedimentary-clast breccia, TZ = transition zone; CCB-SM = crystalline-clast breccia, sandy matrix, CPC = central peak crystalline. See [2].

Fig. 2. Mean concentrationsof rare earth elements in some MIS units normalized to the mean concentration of samples from the CCB-MM unit of the M-1 core.

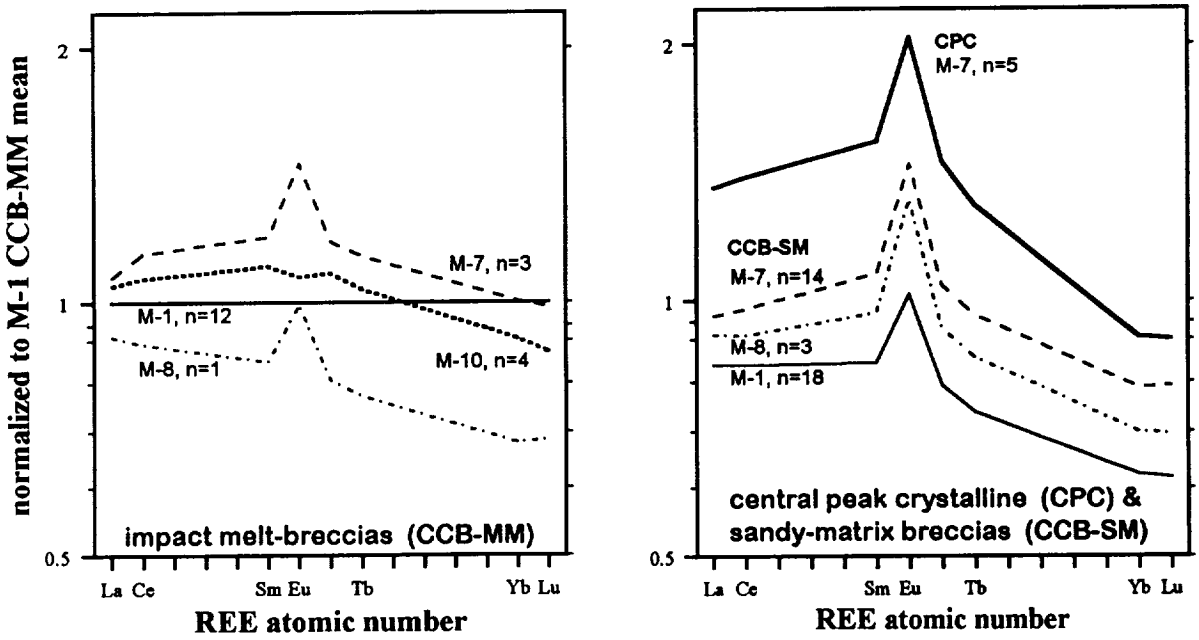

THE IONIZED LUMINOUS COLUMN CREATED DURING THE FLIGHT OF A COMET THROUGH JOVIAN ATMOSPHERE

Kosarev I.B., Nemtchinov I.V. (Institute for Dynamics of Geospheres, Russian Academy of Sciences, 38 Leninskii Prospekt, build.6, Moscow, 117979, Russia)

A comet or an asteroid penetrating the atmosphere of a planet creates a bow shock wave. If the velocity of the body and the temperature behind the shock wave are high enough, a large amount of energy may be irradiated from the shock front. The expansion of an ionized column in the magnetic field of a planet can create a magnetic impulse into the ionosphere and magnetosphere - up to the radiation belts. The radiation impulse and magnetohydrodynamic disturbances may be used to detect the impact of a cosmic body and to estimate its size and other properties. The size of the wake and the density in it substantially determines the process of the ejection of the plasma plume from fireball created after the explosion of the body in the dense layers of the atmosphere. We shall try to estimate the characteristics of the ionized and luminous column created by a Shoemaker - Levy 9 comet during its flight through the dense layers of Jovian atmosphere.

The equation of state of Jovian atmosphere have been calculated for a wide range of densities (10^{-1}-10^{-8} g/cm^3) and temperatures (T = 10^2-10^5 K). For densities lower than 10^{-9}g/cm^3 the assumption of local thermodynamic equilibrium is not valid, temperatures higher than $5\cdot10^4$ K can not be achieved for the velocities of 60-70 km/sec. The processes of ionization, dissociation and excitation of molecules, atoms and ions have been taken into account. The initial composion in mole fractions of the Jovian atmosphere has been assumed: 0.89 H_2 and 0.11 He, $1.1\cdot10^{-3}$ H_2O, $6.3\cdot10^{-4}$ CH_4, $1.5\cdot10^{-4}$ NH_3, $2.9\cdot10^{-5}$ H_2S [1].

Using this EOS and the Hugoniot relations at the hydrodynamic discontinuity the temperature at the shock front T_s, specific internal energy e_s, effective adiabatic exponent $\gamma_s=1 + P_s/\rho_s e_s$, where P_s is the pressure and ρ_s is the density be hind the shock wave the degree of ionization α_e, and the velocities of particles U, km/sec for different densities ρ_a in front of the shock wave have been determined. As an example these data are given for $\rho_s = 10^{-5}$ g/cm^3 at Table. In cold Jovian atmosphere because of negligible photoabsorption of H_2 molecules in spectral range 1200 - 6000 A the main role in the absorption belongs to H_2O, CH_4, NH_3, H_2S. Photodissociation continuums in A and B bands of water give mean free paths of photons in range 1200-1800 A for density 10^{-7} g/cm^3 changing from 0.1 to 1 km. Increasing of precursor temperature to some kK due to thermal flux from shock front rises the absorption due to

THE IONIZED LUMINOUS COLUMN: Kosarev I.B., Nemtchinov I.V.

quasi-molecular continuum in collisions of two H atoms and after further temperature increasing due to photoabsorption by H^-. The calculated spectral opacities of the shock-heated and ionized Jovian aimosphere make possible to conduct 1D, 2D, and even 3D radiation hydrogynamic numerical simulations to predict fluxes of emitted radiation, and to describe the process of propagation of the ballistic shock wave and the expansion of luminous and ionized column behind the shock front.

The preliminary results show that the shock wave at the velocity of 60 km/sec is supercritical ($\sigma T^4 > 1/2\rho_a U_s^3$) at the altitudes where ρ_a is about 10^{-7} g/cm^2 or lower. At the height where $\rho_a = 10^{-5}$ g/cm^3 the radiation flux from the shock front near the blunt nose is about 10 MW/cm^2 and is falling to 0.1 MW/cm^2 when the velocity is decreasing to 10 km/sec (when the diameter of the column is approximately 12 km for a 1 km diameter body). At this distance the shock wave breaks away from the cooling wave of the quasicylindrical "fireball" and the effective radiation temperature is approximately 10 kK. The final diameter of the heated and luminous column is approximately 50 km and the radiation at this stage is dominated by the emission of the ablated comet.

Due to radiation losses behind the supercritical shock wave the density in the wake becomes higher and its size becomes smaller than in the case when the radiation losses are neglected. For $\rho_a = 10^{-8}$ g/cm^{-3} the radiation flux at the blunt nose is falling to about 1 MW/cm^2. At higher altitudes the shock wave becomes transparent and the radiation flux falls approximately $\rho_a^{-1/2}$ and the radiation losses becomes negligible.

T_s, 10^3K	e_s, MJ/g	γ	α_e	U_s, km/s
3.98	0.11	1.20	$0.75\cdot10^{-7}$	14.67
5.01	0.16	1.21	$0.28\cdot10^{-5}$	17.89
6.31	0.17	1.26	$0.90\cdot10^{-4}$	18.49
7.94	0.18	1.32	$0.14\cdot10^{-2}$	18.67
10.00	0.20	1.36	$0.13\cdot10^{-1}$	19.83
12.57	0.31	1.29	$0.75\cdot10^{-1}$	25.05
15.85	0.59	1.22	0.37	34.45
20.00	1.05	1.19	0.91	45.74
25.12	1.52	1.20	1.42	55.05
31.62	1.85	1.23	1.68	60.89
39.81	2.11	1.26	1.79	64.97

References: 1. West R.A, Strobel D.F. and Tomasko M.G. (1986) Glouds, aerosols and photochemistry. Icarus **65**, 161-217.

LUNAR AND PLANETARY MISSION SCENARIO FOR H-II LAUNCH VEHICLE

H.Koshiishi[1],R.Kouda[2],K.Matushima[3],and A.Takano[4]

1.Remote Sensing Technology Center of Japan. Roppongi, Tokyo, Japan

2.Geological Survey of Japan. Tukubashi,Ibaragi-ken, Japan

3.National Aerospace Laboratory. Chohu, Tokyo, Japan

4.National Space Development Agency,Tukubashi, Ibaragi-ken, Japan

Abstract

Remote Sensing Technology Center of Japan (RESTEC) was entrusted from NASDA with mission study of Lunar and Planetary development and utilization, and organized a committee composed of researchers from governmental institutes, universities, and space industlies to do this studies. NASDA has settled a scenario for the Lunar and Mars development and utilization missions by H-II launch vehicle based on the mission studies. Here are described an outline of the scenario and Phobos-Deimos exploration mission.

The committee

The committee has two sub working groups for Lunar exploration and Mars exploration. These groups mainly conduct the study of respective mission and other members of the committee do studies of other Planetary missions including Phobos-Deimos mission, Asteroid mission and so on. Particulary, study of Phobos-Deimos mission are conducted energitically.

The outline of Lunar and Planetary development and utilization scenario

NASDA has settled a scenario for development and utilization of Lunar and Mars based on the committee's studies.

A) The scenario of Lunar development and utilization: this scenario is comprized of five steps. That is (1) remote sensing by LPO, (2) in situ exploration by rovers,(3) fixed point experiment by unmanned system, (4) mannned experiments and short term staying, and (5) long term staying in Lunar base.

(1) Remote sensing by LPO: detailed mapping of Lunar surface, exploration of Lunar resources, and soft landing experiment (option).

(2) In situ experiment by rovers:in situ detailed exploration of large area by multiple rovers. Descriptions of the first rover mission will be presented in this 25th LPI Science Conference by chair person of Lu-

LUNAR AND PLANETARY MISSION FOR H-II LAUNCH VEHICLE ; H.Koshiishi

nar exploration group of the committee.

(3) Fixed point experiment by unmanned system: detailed analysis of Lunar resources, processing experiment of Lunar resources, verification of unmanned operation, sample return, astronomical observatory, and other scientific explorations including boring.

(4) Manned experiments and short term staying:life science experiment, verification of dwelling technologies including ECLSS and operation technologies.

(5) Long term staying in Lunar base: construction of Lunar base and staying long term in the base.

B) Scenario of Planetary development and utilization: this scenario is comprized of five steps. That is (1) remote sensing by Mars observer,(2) fixed or multiple points observations by Mars landers, (3)in situ exploration by Mars rovers,(4) sample return and detailed analysis, and (5) construction of Mars base.

Outline of the first Lunar rover

(1) launching time is around 2000, (2) mission term is more than 2 years, (3) weight is 450kg including 50kg instruments, (4) exploration distance is more than 1000km, (5) maximum climbing inclination is 30° and maximum step difference is 30cm.

Phobos and Deimos exploration mission

Phobos-Deimos is selected on following reasons: (1) easily accessible, (2) precurser mission to asteroid, (3) fairly good information, (4)suitable for H-II launch vehicle. A midway result of the system study was presented in 24th LPI Conference. Fig.1 shows the imaging experiment using Phobos model.

Fig.1 Phobos model image taken at M=120°

References

1) NASDA Mission Study Report, Vol.3, 1991,Vol.4, 1992, and Vol.5,1993 (in Japanese), RESTEC. 2) A Mission Concept of Phobos/Deimos Exploration, K. Matushima, et al,24th LPI Conference

TOWARDS FORMATION OF SHELLS AND RAYS IN COMETARY IONOSPHERE

Nikolay Ya. Kotsarenko, Olga P. Verkhoglyadova (Space Physics Lab., Astronomy Dept., Kiev University, Vladimirskaya 64, Kiev 252017, Ukraine)

It follows from numerous observations that cometary shells and rays are probably formed due to the common physical mechanism which affects the cometary ionosphere as a whole [1]. It is likely that interaction between the cometary plasma and the solar wind stream results in this phenomenon. We assume that electromagnetic plasma-beam instabilities are responsible for stratification of the cometary plasma into shells or layers and their extension downstream to the ray system. We consider filamentation instability as one of the possible mechanisms [2]. The study is carried out within framework of paraboloidal geometry, namely the streamlines and fieldlines are directed along the surfaces of two sets of orthogonal paraboloids of revolution in the region of interaction. The results of MHD-modeling of the cometary ionosphere are in favor of this assumption [3]. We study the problem in terms of MHD-equations for 4 components, i.e. protons and electrons of the solar wind stream and ions and electrons of the cometary plasma, with taking into account a collision frequency of electrons [4]. The origin of these collisions may be the quasilinear scattering of the electrons on the plasma waves [2]. The stream velocities of the cometary plasma components are neglected in comparison with those of the solar wind stream components. The bow shock effects are not taken into account.

We consider the development of the above instability which results in separation of the background plasma to shells or layers due to the interaction between the solar wind and the cometary ionosphere. With standard mathematical technique the set of the MHD-equations is represented in the curvilinear geometry. Undisturbed magnetic field lines and plasma streamlines are oriented along the surfaces of the $x_2 = const$ and the system is symmetrical relative to rotation around the Sun - cometary nuclei direction. We consider stratification along $x_1 = const$, thus only partial derivatives by x_2 are taken into account. Variable x_1 acts as a parameter.

We consider the widest shells and do not take into account the thermal effects that affect on the thinnest ones [2]. The Fourier transformation on time variable is used, namely small disturbances of the physical values are proportional to $exp(i\omega t)$, where ω is the frequency of the wave process. For aperiodic filamentation instability $Re\omega \simeq 0$ and $Im\omega \neq 0$ that results in "pure" stratification of the plasma without oscillatory part.

Using standard technique [4] we obtain the set of equations for three components of the electrical field. In order to solve the problem analytically we use the assumption that typical scales of the shells and rays are smaller sufficiently than the cometsheath' thickness. One obtains that

$$n \sim \frac{\partial P_0(a,z)}{\partial z},$$

where n is disturbed plasma density and $P_0(a,z)$ is a Coulomb wave function of the zero order [5],

which is a solution of the following equation:

$$\frac{\partial^2 w}{\partial z^2} + (a + \frac{2}{z})w = 0,$$

$$z = \frac{x_1^2 x_2^2 k^2}{8}, \; a = \frac{16}{x_1^4 k^2}.$$

Here k is a parameter defined from the dispersion equation [2] and which acts as a wave number. Further we consider k that corresponds to the fastest growing wave mode. Let analyze the solution using asymptotic expansions of the function $P_0(a, z)$.

Near the cometary head $P_0(a, z) \sim z j_0(z\sqrt{a})$, where j_0 is the spherical Bessel function of the zero order, and $n \sim cos(z\sqrt{a})$. Therefore instability development gives rise to formation of separate condensations along the curve of $x_1 = const$. Their boundaries are determined by the expression:

$$x_2 = \frac{\pi(1 + 2r)}{k}, \; r \epsilon \mathbf{N}$$

For different surfaces $x_1 = const$ these condensations creates a set of paraboloidal shells.

Moving along the cometary tail and using another expansion of the function $P_0(a, z)$ one can obtain the system of quasiparallel rays directed along the tail axis. The latter case has been already studied in the problem with cylindrical geometry.

Sums up the above results we conclude that plasma stratification may be a result of electromagnetic filamentation instability of the plasma streams in the cometary ionosphere. The instability development results in formation of separate shells in the cometary head, which extend to a straight ray system in the plasma tail. The influences of an asymmetry of the cometary ionosphere, weak plasma flow towards the tail axis and initial inhomogeneity of the cometary plasma are the lines of the further investigation of the proposed mechanism.

References

[1] Bonev T. and Jockers K. (1993) *MPAE-W-12-93-23, Max-Planck-Institut für Aeronomie, FRG.*

[2] Verkhoglyadova O.P., Kotsarenko N.Ya., Pasko V.P., Churyumov K.I. (1993) *Sov. Astron. Lett.*, 19(9), 823.

[3] Schmidt H.U. and Wegmann R.(1991) In *Cometary plasma processes, (A.D. Johnstone ed.), Geophysical Monograph 61, AGU*, 49.

[4] Akhiezer A.I. et al. (1975) *Plasma electrodynamics*, Pergamon Press, Oxford, New York.

[5] Curtis A.R. (1964) *Coulomb wave functions, Cambridge College Press.*

ASPECT OF LUNAR RESOURCES EXPLORATION

Ryoichi Kouda[1] and Hajime Koshiishi[2]

1: Geological Survey of Japan, 1-3, Higashi 1-chome, Tsukuba, Ibaraki 305, Japan
2: Remote Sensing Technology Center, 7-15-17, Roppongi, Minatoku, Tokyo 106 Japan

ABSTRACT

Major purposes of the exploration and development of lunar resources are to assist the earth resources supply especially for the nuclear fusion energy, to supply energy and materials to construct the lunar and other planetary development base and the operation, and to supply energy and materials for properties for the space base and the industries. The reduction of energy cost of material extraction is required for the resource development. The integrated exploration method is proposed using the precise digital mapping by remote spectral sensors and the following in-situ measurement of elements, minerals, and the material characteristics by semi-automated rover vehicle investigation on near-mountainous regions of Lunar surface. The mission will be launched early soon in the next century[1].

The solar wind directly affects the lunar surface, so that some amounts of light elements concentrate or implanted in the surface materials, regolith for example. The lunar surface contains up to hundred ppm of hydrogen, nitrogen, carbon, and noble gases mostly in the lunar regolith[2]. Helium(He) concentrates in several ten's ppm with ^{3}He, the isotope, which amount is about one-twentieth to two- thousandth of total He[2]. If the second stage of the nuclear fusion energy is available, ^{3}He is the suitable source to obtain the nuclear fusion process. All the elements on the moon other than ^{3}He may be costly to take and transport to the earth surface in the present technological phase.

Future space industries will need the cosmic resources. We will not be able to launch all the materials and the energy from the earth used for the space activities when the space industry develops for the communication networks, for the space factory to produce materials with micro gravity environment, for the observations of the outer space and of the earth, for the space sightseeing and so on. One of the important source of the space materials and the energy is from the Lunar resources.

To date, we supply all the energy and materials to keep the operation of satellites and the launching systems, the cost of which have been very expensive. We need much more energy and materials for space construction and maintenance when we need more space industries. We can supply the energy using solar battery cell in the space, though the costs of launching larger solar battery cell will increase more. In order to decrease the cost for the various space industries, we will need to develop the lunar surface where the gravity is about one-sixth lower than on the earth and very low atmospheric pressure.

The first step to develop the lunar resources, we need to bring much amount of materials and energy from the earth. After the construction of Moon base and the transportation pass, we can extract the lunar resources. Oxygen, hydrogen, nitrogen, carbon, and other light elements can be extracted from the regolith. Almost all the lunar materials are lack of water nor

hydrogen. Consequently we may extract the hydrogen using the similar process of helium. Oxygen can be extracted from the lunar silicate or oxide costly.

Metals and non-metal elements can also be extracted from regolith and rocks. On the earth, we usually extract metals from sulfide or oxide because of the cost of energy. The metal compounds have their bond energy so that we must consume the proper amount of energy to separate and concentrate the metals from the earth's materials. The energy cost to form the silicate minerals is generally very large, and the silicate minerals usually melt in higher temperature. Extraction of metals from the silicate minerals on the moon needs much amount of energy. The energy cost to form sulfide or oxide is relatively lower than silicate, and the melting or vaporized temperature is relatively lower. The concentration of sulfide and oxide are of the common resources on the earth but not common on the lunar surface.

The cost of energy to extract metals and compounds from the mixture of common materials on the moon will be too high to keep the lunar resource development as a beneficial industry. In order to decrease the energy cost, we need to search the significant concentration of materials with the low cost process to extract elements from them. Lunar surface is almost lack of air pressure that is sometimes favorable for the smelting process, though the heat conduction or cooling in lunar condition is another problem.

The lunar regolith and rocks can be available to build the lunar base or to use the lunar materials to construct or to maintain the large satellite base. This procedure is resemble to the construction process on the earth. The definite difference is the low gravity and low atmospheric pressure. We do not need to consider the large gravity loading or water problem. The problem is how to bind the materials to keep the appropriate strength. Melting the lunar materials is a possible answer that needs high energy and temperature. The binder material is another answer that needs the transportation cost of it from the earth. If the nuclear fusion energy is available on the lunar surface, the cost of energy can be low cost with benefit. The solar battery cell on the lunar surface can supply more effective electric energy than on the earth.

In order to obtain resources with lower cost, we first explore the unknown but significant lunar surface to get the detailed information of material distribution, surface structures, and material chracteristics[3]. The lunar-base will be developed in the proper place to supply energy and materials to the space industry[4]. The technological development of low energy smelting and other process is needed. We may furthermore utilize the lunar base as the multipurpose observation and the relay stations for farther space development.

REFERENCES

[1] National Space Development Agency of Japan(NASDA) (1992) TK-SS 0438, 145p.)
[2] G. Heiken et al. (1991) Lunar Source Book. Cambridge University Press, 736p.
[3] R. Kouda et al. (1993) Proceedings of First International Conference on Processing Materials for Properties(PMP'93), 483-486.
[4] R. Kouda (1993) DJIT, No.279, 28-34.

3616

MERCURY: MID-INFRARED (7.3 - 13.5 μm) SPECTROSCOPIC OBSERVATIONS SHOWING FEATURES CHARACTERISTIC OF PLAGIOCLASE. R.W.H. Kozlowski[1,2], A.L. Sprague[1], F.C. Witteborn[3], D.P. Cruikshank[3], D. Wooden[3], and K.D. Snyder[2]: (1) Lunar and Planetary Lab, U. Arizona, Tucson, AZ 85721 (2) Physics Dept. Susquehanna U., Selinsgrove, PA 17870 (3) NASA Ames R.C., Moffett Field, CA 94035

Mid-infrared spectroscopic observations of the surface of Mercury are reported for the wavelength range 7.3 to 13.5 μm. The observed spectral radiance emanated from equatorial and low latitude regions between 110-130° Mercurian longitude. The area is primarily an intercrater plain. The spectra show distinct and recognizable features, the principal Christiansen emission peak being the most prominent. The Christiansen feature strongly suggests the presence of plagioclase (Ca,Na)(Al,Si)$AlSi_2O_8$, (in particular labradorite: $Ab_{(50)}$ - $Ab_{(30)}$). In addition we have studied the effects of thermal gradients to gain insight into the effects of thermal conditions on the spectral radiance of rock samples. This simulates the thermophysical effects as the rotating surface of Mercury is alternately heated and cooled. The spectral features of the samples are retained, however the relative and absolute amplitudes vary as illustrated by laboratory reflectance and emittance spectra from quartzite.

Figure 2 shows a solid, whole rock sample of quartzite that was measured for both reflectance and emittance. Spectral emittance (E1) is high when the rock is initially removed from an oven (530K). After some cooling (E2) the peak of the Planck function moves to longer wavelength and the ratio of the cooler rock to the same blackbody cavity shows decreased emissivity at short wavelengths. Spectra obtained from a cold sample immediately after illumination (R1), and after steady illumination for two minutes (R2) are shown. It can be seen in figure 2 that the effect of rock warming with time was to change the slope of the overall spectrum. The values at the short wavelength end of the spectrum are raised because of the additional flux contributed by warming the rock. Spectral features are well-correlated among all four spectra. The characteristic fundamental and overtone Si-O stretching modes are clearly seen although the emission spectra show less overall spectral contrast than those in reflectance.

OBSERVATION - INSTRUMENTATION

Mercury observations were made at the NASA Infrared Telescope Facility (IRTF) 3.0 m telescope on Mauna Kea, Hawaii. The thermal IR spectra were obtained July 12, 1992 using the High Resolution Grating Spectrometer (HIFOGS) Witteborn *et al.* [1]. HIFOGS has cryogenically cooled aperture and filter wheels, grating, and a linear array of 120 Bi-doped Si detectors. To increase the spectral range slightly, and to increase the resolution (decrease the wavelength sampling increment), all standard stars and Mercury were measured at two grating settings. The first grating setting spanning wavelengths of 7.22 to 13.02 μm and the second 7.61 to 13.30 μm. The individual spectra have an average resolution of 0.048 μm. After the spectra from the two grating settings are interleaved, the spectral resolution is improved to 0.025 μm. Telluric absorptions were corrected for by using alpha Boo. All ratioed spectra were then corrected for the spectral shape of alpha Boo (K2 II) using a spectrum generated from several observations of alpha Boo from Kuiper Airborne Observatory, the IRTF, and the NASA 1.5 m telescope at Mt. Lemmon (Cohen *et al.* [2]; Cohen *et al.* [3]). The spectra were smoothed with a five point smoothing function and normalized to unity at the maximum in emissivity.

References: [1] Witteborn F.C., et al. Astro. Soc. Pacific Conf. Series Astro. IR Spec. Conf. 365-372 (1993). [2] Cohen et al. Astro. J. 104, 5, 2030-2044 (1992). [3] Cohen et al. Astro. J. 104, 5, 2045-2052 (1992).

MERCURY: MID-INFRARED SPECTROSCOPY. Kozlowski, R.W.H. *et al.*

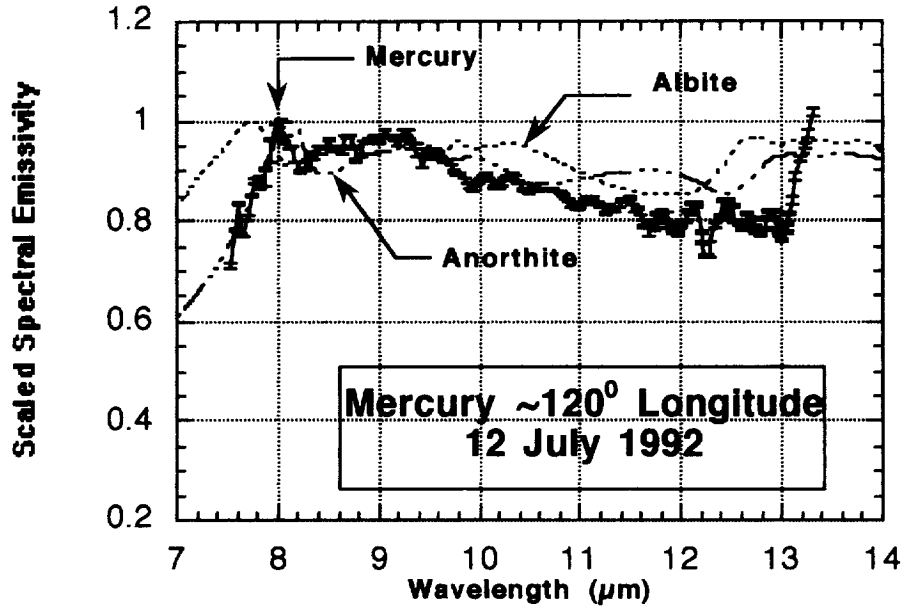

Figure 1. The Mercury spectrum is plotted with spectra of the end members of the plagioclase series: albite ($NaAlSi_3O_8$) and anorthite ($CaAl_2Si_2O_8$). Note the Christiansen features at 7.7 and 8.2 μm respectively. The Mercury Christiansen feature is at 8.0 μm. Assuming a linear mixing model, this corresponds to 40% albite and 60% anorthite, i.e. labradorite. Labradorite is characteristic of igneous rocks of gabbroic composition and of anorthosites.

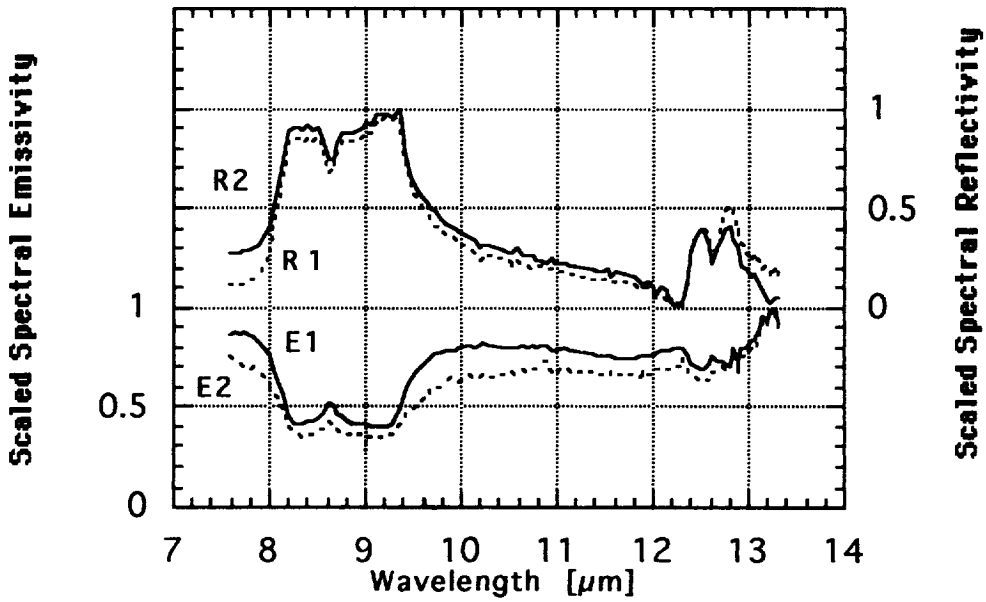

Figure 2. Plotted above are spectra of quartzite obtained with HIFOGS at the same spectral resolution used to observe Mercury. The top two spectra (R1 and R2) are reflectance spectra from an illuminated, cold sample. The bottom two spectra (E1 and E2) are emittance spectra obtained from the same sample after heating to 530 K. Spectra were ratioed to the spectrum of a blackbody cavity at 347 K. Heating and cooling effects are described in the text.

FATE OF HALOGENS AT THE SURFACE OF TEKTITES; U. Krähenbühl and M. Langenauer, Laboratorium für Radiochemie, University of Bern, Switzerland.

For years the investigation of the relation of the composition of tektites, the possible target material and of the projectile causing their formation was of main interest of the scientific community active in this field [1,2]. Lately, more detailed studies were performed with the goal to gain information regarding formation, alteration during transport or ejection and weathering of tektites [3,4,5]. In this respect the study of the halogen distribution is of great importance for the investigation of volatilisation processes during impacts, because the 4 elements forming the group of halogens demonstrate quite different volatility. They change their behaviour in the presence of oxidation reagents (e.g., oxygen partial pressure). Iodine shows the highest mobility under oxidising conditions. Meisel et al. [6] have presented results of the halogens in tektites and in impact glasses.
After the investigation of the depth distribution of halogens in Antarctic meteorites [7] it was interesting for us to start a similar study for tektites. A goal of this study was to look for answers for a more detailed understanding of the formation and the transport of these objects. Is it possible to deduce maximum temperatures reached during the formation? What about the duration of the high temperature regime? Can we predict if the tektites were and for which period in a environment with reduced external pressure?

We analysed the following samples of tektites the first by our normal investigation procedure, the stepwise mechanical removal of layers from the outside to the interior. From the second tektite individual parts were characterised: flange, top of tektite (in flight direction) and opposite side.

(1) Thai tektite from an area about 150 km in radius around Khon Kaen.
(2) Tektite from the Nullarbor Plain in Western Australia (exact location not known).

In contrast to ordinary chondrites both tektites were very hard for drilling. So it was very difficult to produce the necessary fine material from thin layers for the analysis of the chemical composition by stepwise drilling.
The halogens were separated from the matrix after irradiation with thermal neutrons by hydropyrolytic decomposition of the material in presence of V_2O_5 as strong oxidising agent [8]. The investigation of the distribution of halogens in tektites from the surface to the interior was the goal of this investigation. For an additional chemical characterisation of the aliquots from the Nullarbor Plain tektite the material was submitted to instrumental neutron activation analysis.
Table 1 presents the results of the determination of the halogens, Table 2 the concentrations of minor and trace elements in the investigated fractions of the Nullarbor Plain tektite.

Discussion: The volume concentrations for the halogens of the two investigated tektites show less than 10% variation (exception Br). Compared to our earlier measurements they are most similar to the halogen pattern of Ivory Coast Tektites [6] . With the exception of Br all the exterior fractions show higher concentrations for the halogens than the one measured for the volume. This can be the result of contamination by material embedding the tektites at the recovering site and/or the alteration from the atmosphere (e.g., sea spray). The different enrichment of F, Cl and I over the volume concentrations for the two tektites reflect in our opinion either the variable degree of halogens disposal at the collecting site and/or different duration of the contamination processes. The weathering of the tektites has certainly also influenced the concentrations of halogens in these objects.
From our results we can only deduce limited information regarding the indicated goals, since the observed contamination on halogens covers any mobilisation of the investigated elements during formation or transport of tektites.

Table 1. Halogens in tektites (ppm). Errors 1s: F and Cl = 5%, Br and I = 10%.

		F	Cl	Br	I
Thai	surface - 0.2 mm	21	34	0.49	0.059
	0.2 - 0.4 mm	24	32	0.15	0.045
	volume	13	1.9	0.18	0.008
Nullarbor	'hot zone' (top)	62	102	0.15	0.059
	'cold zone' (opposite side)	42	88	0.19	0.070
	'molten zone' (flange)	27	6.1	0.38	0.019
	volume	14	2.1	0.47	0.005

Table 2. Minor and trace elements.

		Na (%)	K (%)	Fe (%)	Cr (ppm)	Co (ppm)	Sc (ppm)
Nullarbor	'hot zone' (top)	0.97	2.00	3.7	780	66	10.4
	'cold zone' (opposite side)	0.89	2.00	3.8	1060	53	10.0
	'molten zone' (flange)	0.97	2.25	3.4	67	13	10.6
	volume	1.10	2.08	4.2	54	17	12.7

Acknowledgement: This work was supported by the Swiss National Science Foundation. The Thai tektite was given by Darryl Futrell and the sample from the Nullarbor Plains originate from the collection of Natural History Museum at Bern (B. Hofmann).

REFERENCES: [1] C. Koeberl and K. Fredriksson (1986) Earth Planet. Sci. Lett., 78, p. 80-88. [2] D. Matthies and C. Koeberl (1991) Meteoritics, 26, p. 41-45. [3] O. Müller and W. Gentner (1973) Meteoritics, 8, p. 414-415. [4] G.S. Ridenour (1986) Meteoritics, 21, p. 271-281. [5] J.W. Delano, Y.G. Liu, R.A. Schmitt (1993) Lunar Planet. Sci., XXIV, p. 397-398. [6] T. Meisel, M. Langenauer, U. Krähenbühl (1992) Meteoritics, 27, p. 576-579. [7] M. Langenauer and U. Krähenbühl (1993) Earth Planet. Sci. Lett., 120, p. 431-442. [8] M. Langenauer, U. Krähenbühl, U. Furrer, A. Wyttenbach (1992) Geostand. Newslett., 16, p. 41-44.

SMALL GRAINS WITH HIGH LEAD CONCENTRATION IN CHAINPUR;

J.L.A.M. Kramer, A.C. Kik and R.D. Vis, Department of Physics and Astronomy, Free University Amsterdam.

Using Particle Induced X-ray Emission (PIXE) [1], a small spot with an extremely high concentration of lead has been found in a Chainpur chondrule. This spot is about 70 micrometer in diameter with a maximum lead concentration of 5 wt. percent. An electron probe measurement revealed that the spot was consisted of even smaller grains, ranging in size from 1 up to 5 micrometer with lead concentrations of about 50 wt. percent. The grains are surrounded by enstatite. The isotopic ratios of these lead grains, determined with SIMS, fall on the Pb-Pb isochron with an age of 4.55 Gyr. According to the simple one-stage model we find for $\mu = {}^{204}Pb/{}^{238}U$ a value of about 6.5, whereas the PIXE measurements showed a maximum uranium concentration of only 5 ppm. If contamination is ruled out, it is likely that a recent metamorphic event separated the lead from its source region. Other spots in the same sample have been found with the same chemical composition for lead compound.

Introduction. PIXE is a very powerful method for measuring trace element concentrations in situ on micrometer scale. Minimum detection limits of several ppm for elements of $Z = 20$ and higher are easily reached with a lateral resolution down to 4 micrometer [2]. Determining volatile trace elements like zinc in unequilibrated ordinary chondrites is our main goal of research. A Chainpur (LL3.4) chondrule has been studied for this reason [3]. The studied chondrule has a fine rim with some troilite and metal grains in it. Easy to recognize is a strange spot in the centre, which is embedded in mainly enstatite minerals together with some small pigeonite crystals. Rather high lead concentrations have been found in this region. Besides the PIXE measurements also one SIMS and one electron probe measurement have been performed. More spots with high lead concentration have been found in the same Chainpur sample but have not yet been studied extensively.

Measurements and results. To study this chondrule it has been scanned from one edge to the other in a PIXE measurement with a broad beam of about 8 by 20 micrometer. Protons with an energy of about 3.5 MeV were used, which produce detectable X-rays for lead down to roughly 30 micrometer deep in an average matrix. The very distinct spot of about 70 micrometer in diameter in the middle of the chondrule shows a maximum lead concentration of 5 wt. percent. The bulk concentration of lead in ordinary chondrites is around 1.0 ppm [4]. Also an electron probe measurement on the same spot has been performed to check the PIXE results. From the backscattered electron image in figure 1, it can be seen that lead is actually concentrated in small grains of a size of about 1 to 5 micrometers in diameter with even much higher lead concentrations. Results of both PIXE and EPMA measurements on one of these grains are shown in table 1. Galena (PbS) is one possible mineral for these small grains. However, since the M X-ray lines of lead interfere with the K lines from sulphur, it is not possible to determine sulphur with PIXE. In the gamma-ray spectrum, produced by Coulomb excitation of nuclei by 3.5 MeV protons, some sulphur was found on this spot but it was hard to quantify. Also one SIMS measurement was done and the results are depicted in a ${}^{207}Pb/{}^{204}Pb$ vs. ${}^{206}Pb/{}^{204}Pb$ diagram in figure 2. In spite of the rather large error bars, the measurement seems to fall on the isochron together with other chondrites. Assuming the single stage model to be correct, a μ of about 6.5 was found. PIXE showed much lower lead uranium ratios: an upper limit of uranium of 5 ppm and thorium of 18 ppm was measured (see table 1). Other PIXE measurements in the same sample showed more of this kind of spots, with roughly the same distribution of elements. Very apparent is the coincidence with zirconium. To assure the sample has not been spoiled by terrestrial lead, we also looked for traces of antimony, because this element generally occurs in industrial lead (6 wt. percent Sb), but it was not found at all in these grains.

Discussion. If the lead will be found in galena, the possibility of contamination from laboratory origin can be excluded. The grains were too small to be easily identified as galena under a microscope, although they were recognized with the help of the backscattered electron image. The SIMS measurement shows that the lead in the grain is quite normal radiogenic. The absences or low concentrations of uranium and thorium together with the high concentration of lead and a μ of roughly 6.5, indicates that the lead has been recently separated from its source. One might speculate about different events, but it seems most likely that it happened during a major collision which broke up the parent body, taking into account the low gas retention ages of chondrites of all groups [5].

Outlook. A new sample of Chainpur is being prepared for more measurements. In addition to measurements on this new sample, more electron probe and SIMS measurements will be performed on the other spots found in the original sample. It is important to find out what kind of mineral is involved, and to determine the isotopic ratios with higher accuracy on the other spots.

Table 1: **PIXE and EPMA results.**
*) PIXE measurement

lead spot		nearby mineral	
Si	17.0%	MgO	35.6 %
Fe	0.7%	SiO_2	57.6 %
Pb	49.9%	FeO	4.5 %
Zn	58.7 ppm*	CaO	2.0 %
Rb	6.0 ppm*	MnO	0.28%
Sr	22.4 ppm*		
Zr	267.0 ppm*		
Th	<18.0 ppm*		
U	< 5.0 ppm*		

figure 1. Backscattered electron image.

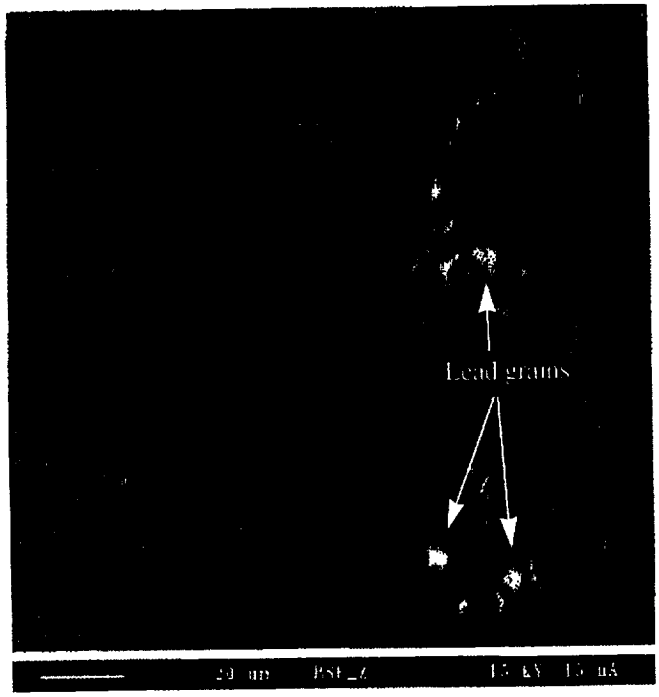

figure 2. $^{207}Pb/^{204}Pb$ vs. $^{206}Pb/^{204}Pb$ diagram. [4]

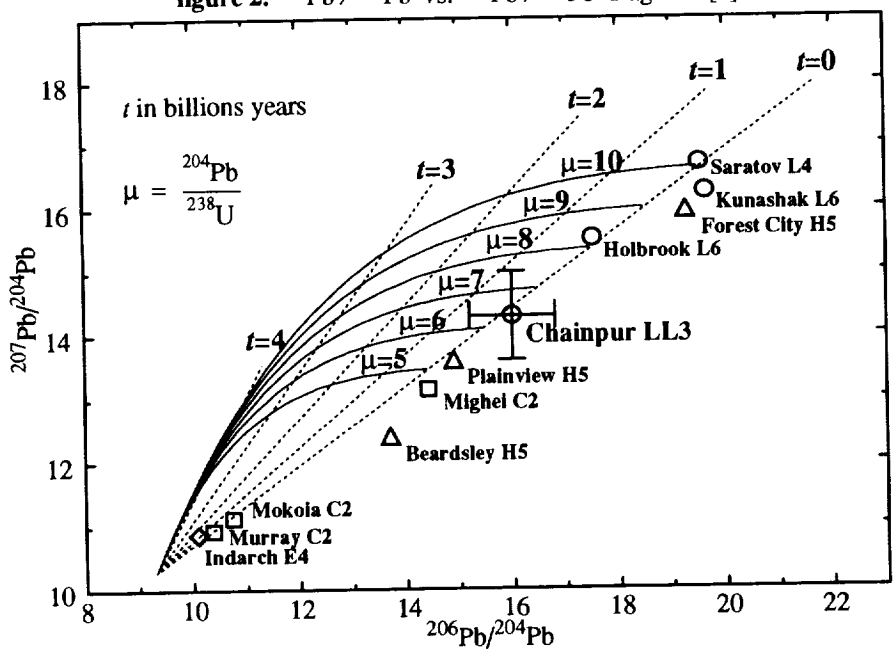

Acknowledgements. We thank D. Heymann for making it possible to do the necessarily electron probe measurements at Rice University, Houston. From the Shell laboratory in Amsterdam, we thank W. Koot and in particular C. van der Spek for doing the SIMS measurements.

References. [1] S.A.E. Johansson and T.B. Johansson (1976), *Nucl. Instr. Meth.* **137** 473-516. [2] K. Ishii and S. Morita (1988), *Nucl. Instr. Meth.* **B34** 209-216. [3] J.N. Grossman and J. Wasson (1982), *Geochim. Cosmochim. Acta* **46**, 1081-1099. [4] B. Mason, ed. (1971), *Handbook of Elemental Abundances in Meteorites*, Gordon & Breach Sci. Publ. [5] D. Heymann (1967), *Icarus* **6**, 189-221.

3617

UNIQUENESS OF A SOLUTION OF A STEADY-STATE PHOTOCHEMICAL PROBLEM: APPLICATIONS TO MARS; V. A. Krasnopolsky, NASA/Goddard SFC, Greenbelt, MD 20771

Based on conservation of chemical element in chemical reactions, a rule is proved that the number of boundary conditions given by densities and/or non-zero velocities should not be less than the number of chemical elements in the system, and the components given by densities and velocities should include all elements in the system. Applications of this rule to Mars are considered. It is proved that a problem of CO_2-H_2O chemistry in the lower and middle atmosphere of Mars, say, in the range of 0-80 km does not have an unique solution, if only CO_2 and H_2O densities are given at the lower boundary, while all other boundary conditions are fluxes. Two models of this type are discussed. These models fit the same boundary conditions, are balanced with a relative uncertainty of 10^{-4} for H_2 (and much better for other species), and predict the O_2, CO, and H_2 mixing ratios which differ by orders of magnitude. One more species density, e. g. that of O_2, should be specified at the boundary to obtain the unique solution. The situation is better if the upper boundary is extended to the exobase where thermal escape velocities of H and H_2 can be specified. However in this case either oxygen nonthermal escape rate (and hence the total hydrogen escape rate) or the O_2 (or other species) density at the surface should be given as the boundary condition. Two models of Mars' photochemistry, with and without nitrogen chemistry, are considered. The oxygen nonthermal escape rate of 1.2×10^8 $cm^{-2}s^{-1}$ is given at 240 km and is balanced with the total hydrogen escape rate within uncertainty of 1% for both models. Both models fit the measured O_2 and CO mixing ratios, the O_3 line absorption at 9.6 μm and the O_2 1.27 μm dayglow within the uncertainties of the measured values, though the model without nitrogen chemistry fits better. The importance of nitrogen chemistry in the lower and middle atmosphere of Mars depends on a fine balance between productions of NO and N in the upper atmosphere which is not known within the required accuracy.

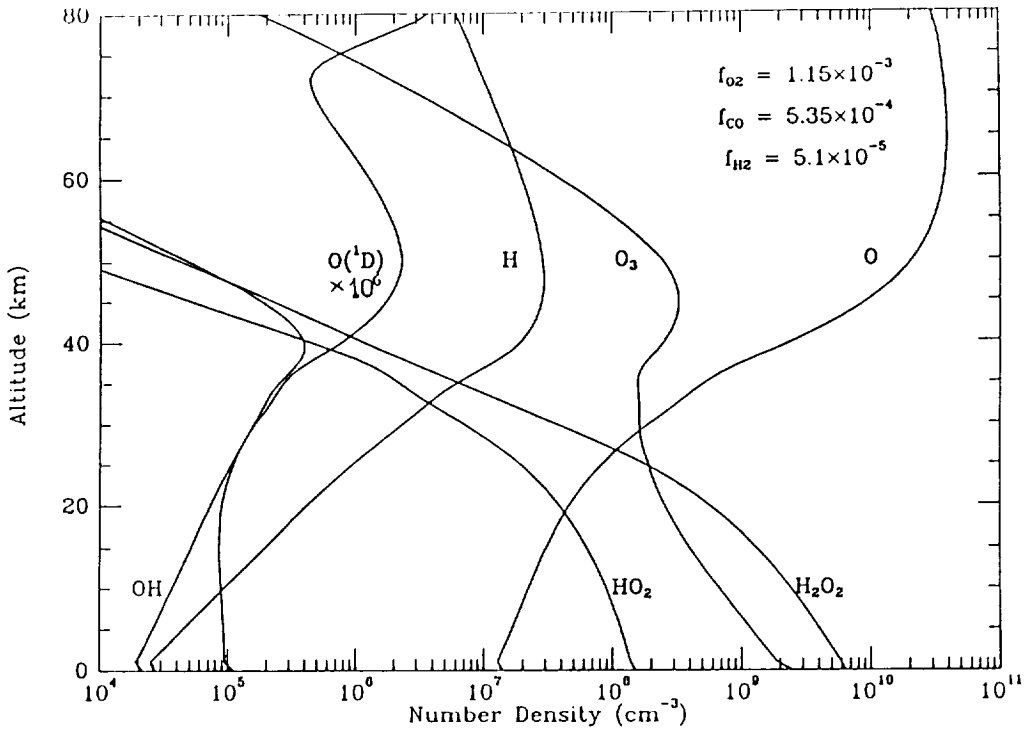

Model of Mars' photochemistry without nitrogen chemistry. The effective absorbing O_3 abundance is equal to 0.44 μm, and the O_2 1.27 μm dayglow intensity is equal to 3.2 MR (the measured values are 0.54±0.15 μm and 3±1 MR, respectively).

S16-71
3613

H_2O-H_2SO_4 SYSTEM IN VENUS' CLOUDS AND OCS, CO, AND H_2SO_4 PROFILES IN VENUS' TROPOSPHERE;

V. A. Krasnopolsky, NASA/Goddard SFC, Greenbelt, MD 20771
J. B. Pollack, NASA/Ames RC, Moffett Field, CA 94035

A coupled problem of diffusion and condensation is solved for the H_2SO_4-H_2O system in Venus' cloud layer. The position of the lower cloud boundary, profiles of the H_2O and H_2SO_4 vapor mixing ratios and of the H_2O/H_2SO_4 ratio of sulfuric acid aerosol and its flux are calculated as functions of the column photochemical production rate of sulfuric acid, Φ_{H2SO4}. Variations of the lower cloud boundary are considered. Our basic model, which is constrained to yield f_{H2O}(30 km) = 30 ppm [1], predicts the position of the lower cloud boundary at 48.4 km coinciding with the mean Pioneer Venus value, the peak H_2SO_4 mixing ratio of 5.4 ppm, and the H_2SO_4 production rate $\Phi_{H2SO4} = 2.2\times10^{12}$ $cm^{-2}s^{-1}$. The sulfur to sulfuric acid mass flux ratio in the clouds is 1:27 in this model, and the mass loading ratio may be larger than this value if sulfur particles are smaller than those of sulfuric acid. The model suggests that extinction coefficient of sulfuric acid particles with radii of 3.7 μm (mode 3) is equal to 0.3 km^{-1} in the middle cloud layer. The downward flux of CO is equal to 1.7×10^{12} $cm^{-2}s^{-1}$ in this model. Our second model, which is constrained to yield f_{H2SO4} = 10 ppm at the lower cloud boundary, close to that measured by the Magellan X-band radiooccultation [2], predicts the position of this boundary at 46.5 km, f_{H2O}(30 km)= 90 ppm close to the Venera 11-14 data [3] at this altitude, $\Phi_{H2SO4} = 6.4\times10^{12}$ $cm^{-2}s^{-1}$ and $\Phi_{CO} = 4.2\times10^{12}$ $cm^{-2}s^{-1}$. The S/H_2SO_4 flux mass ratio is 1:18, and extinction coefficient of the mode 3 sulfuric acid particles is equal to 0.9 km^{-1} in the middle cloud layer. A strong gradient of the H_2SO_4 vapor mixing ratio near the bottom of the cloud layer drives a large upward flux of H_2SO_4 which condenses and forms the excessive downward flux of liquid sulfuric acid. This flux is larger by a factor of 4-7 than the flux in the middle cloud layer. This is the mechanism of formation of the lower cloud layer. Variations of the lower cloud layer are discussed. Our modeling of the OCS and CO profiles measured in the lower atmosphere [1] provides a reasonable explanation of these data and shows that the rate coefficient of the reaction SO_3 + CO → CO_2 + SO_2 is equal to 10^{-11}exp(-(13100±1000)/T) cm^3/s. The main channel of the reaction between SO_3 and OCS is CO_2 + $(SO)_2$, and its rate coefficient is equal to 10^{-11}exp(-(8900±300)/T) cm^3/s. In the conditions of Venus' lower atmosphere $(SO)_2$ is removed by the reaction $(SO)_2$ + OCS → CO + S_2 + SO_2. The model predicts a OCS mixing ratio of 28 ppm near the surface.

[1] Pollack J. B. et al. (1993) *Icarus, 103*, 1; [2] Jenkins J. M. et al. (1994) *Icarus* (submitted); [3] Moroz V. I. et al. (1983) *Cosmic Res., 21*, 246.

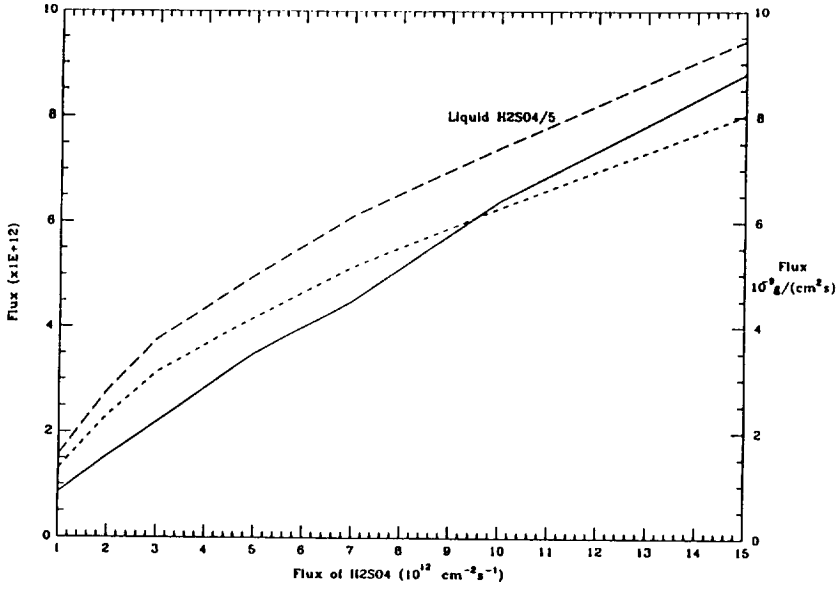

Fig. 1. Fluxes of CO (solid) and of liquid H_2SO_4 (reduced by a factor of 5 to be on scale, long dashes), and flux of sulfuric acid aerosol (the right scale, short dashes) as functions of the column photochemical production of H_2SO_4. All fluxes are given at the lower cloud boundary.

PRECEDING PAGE BLANK NOT FILMED

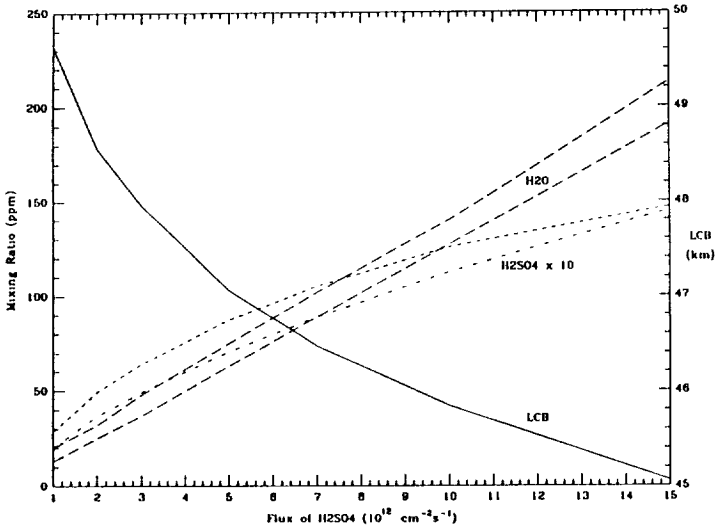

Fig. 2. H_2O mixing ratios at 30 km which meet the requirement f_{H2O}(62-65 km)=1-10 ppm, the position of the lower cloud boundary and the H_2SO_4 mixing ratio at this boundary (short dashes) and at 45 km (dot-dashes) as functions of the column photochemical production of H_2SO_4.

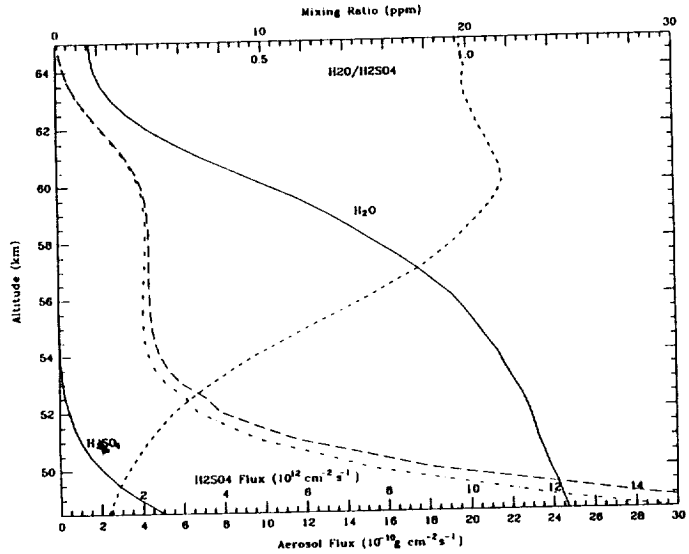

Fig. 3. Model 1 results: H_2O and H_2SO_4 mixing ratios (solids), H_2O/H_2SO_4 ratio in the cloud particles (short dashes), the downward flux of H_2SO_4 in the liquid phase (long dashes), and the downward flux of sulfuric acid droplets (dot-dashes).

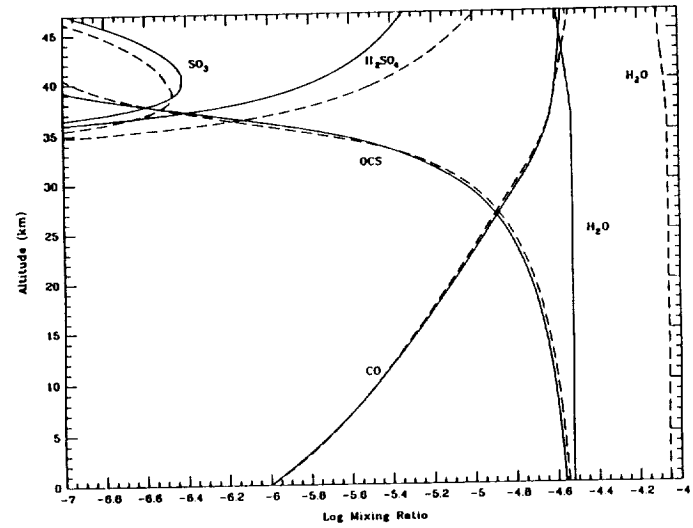

Fig. 4. Profiles of OCS, CO, H_2SO_4, SO_3, and H_2O calculated for Model 1 (solids) and Model 2 (dashes).

FIRST MEASUREMENT OF HELIUM ON MARS: IMPLICATIONS FOR THE PROBLEM OF RADIOGENIC GASES ON THE TERRESTRIAL PLANETS;

V.A. Krasnopolsky, NASA/Goddard SFC, Code 693, Greenbelt, MD 20771
S. Bowyer, Center for EUV Astrophysics, University of California, Berkeley, CA 94720
S. Chakrabarti, Center for Space Physics, Boston University
G. R. Gladstone, Southwest Research Institute, San Antonio, Texas
J. S. McDonald, Department of Astronomy, San Diego State University

108 photons of the Martian He 584 Å airglow detected by the Extreme Ultraviolet Explorer satellite during a two-day exposure (January 22-23, 1993) correspond to the effective disk average intensity of 43±10 Rayleigh. Radiative transfer calculations, using a model atmosphere appropriate to the conditions of the observation and having an exospheric temperature of 210±20 K, result in a He mixing ratio of 1.1±0.4 ppm in the lower atmosphere. Nonthermal escape of helium is due to electron impact ionization and pickup of He^+ by the solar wind, to collisions with hot oxygen atoms, and to charge exchange with molecular species with corresponding column loss rates of 1.4×10^5, 3×10^4, and 7×10^3 $cm^{-2}\,s^{-1}$, respectively. The lifetime of helium on Mars is 5×10^4 yr. The He outgassing rate, coupled with the ^{40}Ar atmospheric abundance and with the K:U:Th ratio measured in the surface rocks, is used as input to a simple two-reservoir degassing model which presumes the loss of all argon accumulated in the atmosphere during the first Byr by large-scale impacts. The model results in total planet mass ratios of 10^{-5} g/g for K, 2.3×10^{-9} g/g for U, 8.5×10^{-9} g/g for Th, 4×10^{-10} g/g for He, and 1.5×10^{-9} g/g for ^{40}Ar. The predicted radiogenic heat flux is 2 erg cm^{-2} s^{-1}. Similar modeling for Venus results in total planet mass ratios of 4.7×10^{-5} g/g for K, 6.7×10^{-9} g/g for U, 2.2×10^{-8} g/g for Th, 1.3×10^{-9} g/g for He, 6.7×10^{-9} g/g for ^{40}Ar, and a radiogenic heat flux of 15 erg cm^{-2} s^{-1}. The implications of these results are discussed. The modeling shows that the radioactive elements were not distributed uniformly in the protoplanetary nebula, and their relative abundances differ very much in the terrestrial planets.

Comparison of the Earth, Venus, and Mars

Parameter	Earth	Venus	Mars
U and Th	1	0.3	0.1
K	1	0.17	0.04
Rad. Heat Flux, erg/cm²/s	63	15	2
Surface enrichment	100	100	250
Degassing time, Byr	9	5	5
$k = aR^2/\tau$	1	2	1/2
T(surface, K)	280	730	200

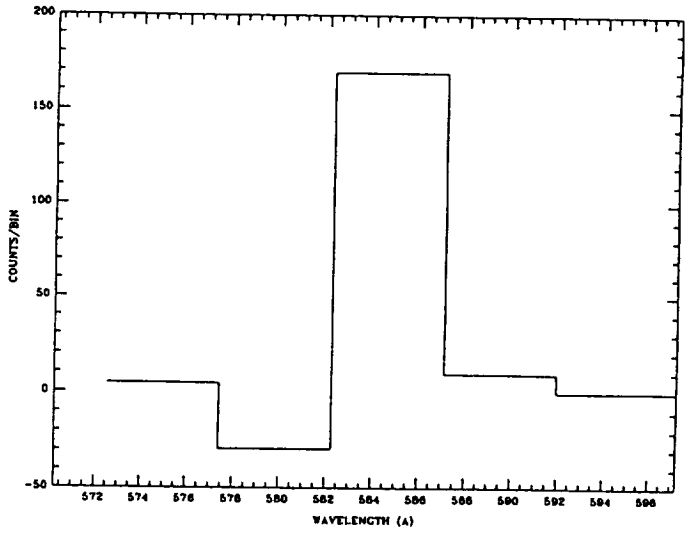

Fig. 1. Spectrum of Mars in vicinity of the He 584.3 Å line

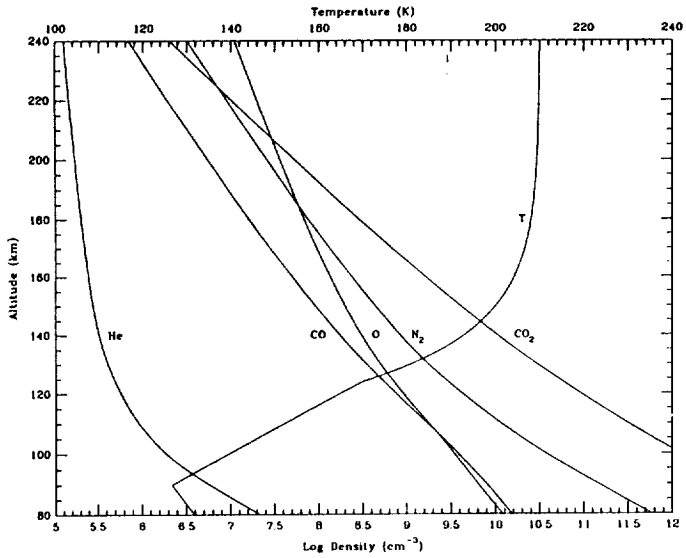

Fig. 2. The Mars model atmosphere appropriate to the conditions of the EUVE observation

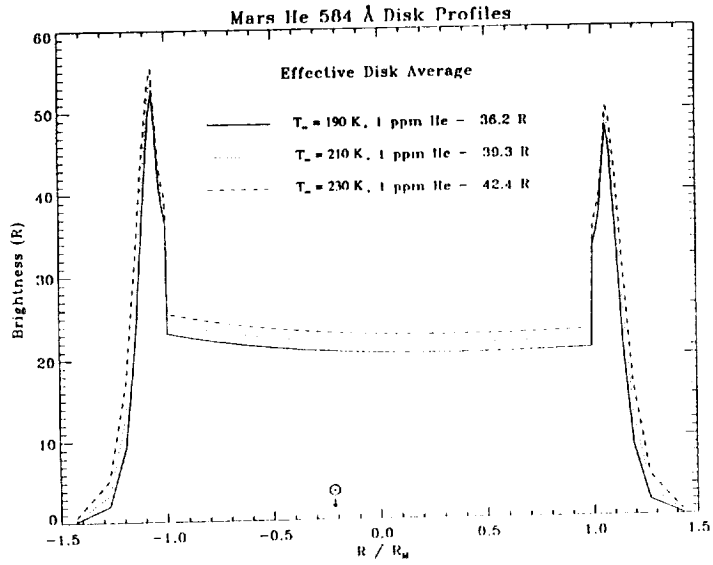

Fig. 3. The calculated He 584 Å brightness profiles across the mid-section of Mars for three models of the atmosphere with T_∞ = 190 K, 210 K, and 230 K

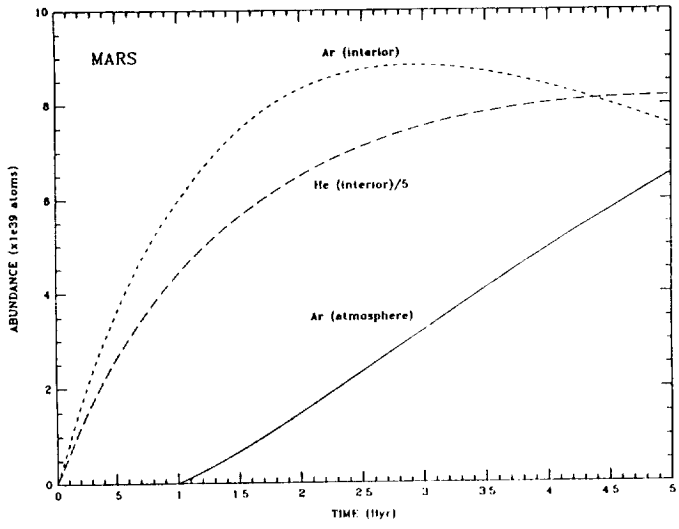

Fig. 4. Abundances of ^{4}He in the interior and ^{40}Ar in the atmosphere and the interior of Mars during its history

Omit to p. 791

MODEL FOR ASCENDING OF MANTLE DIAPIRS FORMING CORONAE ON VENUS;

Mikhail A. Kreslavsky Astronomical observatory of Kharkov University Sumskaya 35, 310022 Kharkov Ukraine

Coronae on Venus are usually treated as a surface manifestation of overheated bodies (diapirs) ascending in the mantle. Model considered describes quantitatively rate of ascending, rate of enlargement, and changing of thermal excess of the diapir with ascending. Application of the model to venusian corona population leads to following conclusions: (1) sources of diapirs forming coronae on Venus are at different depths in the mantle; (2) if sources of the diapirs are located at some fixed levels in the mantle (e.g. core-mantle boundary and probable phase transition at the bottom of upper mantle), then effective viscosity and/or thermal gradient in upper mantle is varied spatially and/or with time; (3) effective viscosity of upper mantle is relatively low.

Introduction. Coronae are wide-spread circular features of hundreds to a thousand km in diameter on Venusian surface. They are usually treated as surface manifestations of mantle diapirs or plume heads, i.e., with rising of overheated buoyant bodies from mantle depth (e.g., [1,2,3]). Some coronae, especially small ones, are of perfect circular form, that show their source to be relatively compact and/or deep. Possible source of such diapirs or plumes could be any instability in the mantle. In intensively convecting mantle conditions for plume or diapir formation could be achieved only in thermal boundary layers.

Griffiths and Campbell [4] proposed a model for ascending of mantle plume heads from core - mantle boundary. Li Yinting and Janle [5] applied this model for venusian conditions. The result was that only large coronae could be generated with this mechanism. To generate smaller coronae more shallow source of overheated material is needed. An instability in thermal boundary layers related with phase transition in the mantle could be such a source [5]. Thus existence of small coronae indicates presence of such layers that gives an evidence that convection of venusian mantle is layered (e.g., [6]) at least somewhere and in some periods of recent geological history.

Possible presence of small superadiabatic thermal gradient (STG) in the mantle leads to sufficient changes in law of overheated body ascending. Modification of the model by Griffiths and Campbell [4] presented here accounts for the influence of STG.

Model. Diapir rises due to its buoyancy and solid-state ductility of surrounding mantle material. Material inside the hot diapir body is stirring due to relatively low effective viscosity. A layer of surrounding material is heated conductively and involved into stirring. Total buoyancy of the diapir is increased due to superadiabatic thermal gradient (STG) when diapir rises. Following Griffiths and Campbell [4] the diapir ascending speed was estimated according to Stokes law for a relatively inviscid spherical drop. Rate of entrainment of ambient material into the diapir body was estimated semiempirically [4].

Diapir body is described with its diameter D and effective thermal excess ΔT. Volume balance and thermal balance lead to differential equations for D and ΔT. Following parameters are used in the equations: effective viscosity η, density ρ, acceleration due to gravity g, thermal conductivity χ, thermal expansion coefficient α, STG γ. Changing of mantle material parameters leads only to rescaling: distances are scaled as $(\rho g)^{-1/3} \eta^{1/3} \chi^{1/3}$; time is scaled as $(\rho g)^{-2/3} \eta^{2/3} \chi^{-1/3}$; temperature is scaled as α^{-1}.

In the frame of the model a style of diapir behavior depends on two dimensionless parameters. One of them is Rayleigh number $R = D^3 \Delta T \alpha \rho g \gamma \eta^{-1} \chi^{-1}$. Diapir exists only when R is sufficiently greater than critical value $R_c \sim 200$. In opposite case the thermal excess dissipates almost without prominent vertical displacement of the overheated body and the model actually cannot be applied.

As pointed out in [2] size frequency distribution of coronae is close to a power law bounded at small sizes with diameter of about 100 km. Coronae are usually supposed to be of diameter twice larger then the diapir because diapir flattening near the surface (e.g. [4,5]). So, diapirs forming smallest coronae should be of $D \sim 50$ km. Most of smallest coronae have wide depression in their central part. If this depression was formed

DIAPIRS FORMING CORONAE ON VENUS. Kreslavsky M. A.

due to thermal shortening of cooled diapir material, then initial thermal excess should be of order of 100 K. Many small coronae have very poor set of associated volcanic features if any, so at least for this coronae initial thermal excess should not sufficiently exceed this estimation. This assessment allows to estimate R for smallest coronae. To provide diapir motion $R > 2000$ is needed. It demands effective viscosity of upper mantle not to be higher then 10^{20} g.cm^{-1}s^{-1}, if common values of other upper mantle material parameters are adopted. Reliability of this estimation is reduced by the fact that R strongly depends on degree of diapir flattening.

Parameter $\Xi = \gamma^2 D^5 \Delta T^1 \alpha \rho g \gamma \eta^{-1} \chi^{-1} = R (\gamma D / \Delta T)^2$ indicates how strong STG influenced diapir motion. At very small Ξ ($\Xi << \Xi_c \sim 200$) effect of STG is negligible; R does not change with time unless mantle material parameters do not change; ΔT decreases due to involving of cold surrounding material into diapir body; ascending velocity decreases; Ξ, however, increases with time. For higher values of Ξ cooling surrounding material while ascending slows decreasing of ΔT, R increases with time. When $\Xi = \Xi_m = 0.16\ \Xi_c$ cooling of diapir body is entirely compensated by decreasing of surrounding temperature when rising; at $\Xi > \Xi_m$ ΔT increases with time. Ξ increases with time until $\Xi = \Xi_c$. If $\Xi > \Xi_c$ Ξ decreases. Actually regime with $\Xi > \Xi_c$ is not interesting because in this case ΔT grows so rapidly that inner temperature exceeds melting point before diapir moves significantly.

If mantle material parameters are treated to be uniform, the set of differential equations for ΔT and D can be solved analytically. It allows to overview the solution at different values of parameters.

Evaluation of the solution shows following. Let diapirs start from some level within the mantle with the same ΔT and different R. When diapirs reach the upper boundary of the mantle, range of R usually become much narrower than initial one. This narrowing of the range of R is weaker when STG is prominent and some diapirs from the range get Ξ of about Ξ_m at some stage of ascending. If source of diapirs is a thermal boundary layer in the mantle, initial ΔT are about superadiabatic temperature drop across the layer and initial R are about layer depth. Thus single shallow thermal boundary layer would produce narrow distribution of coronae size. Power-low-like size distribution of coronae points that either sources of diapirs are scattered over the whole mantle or mantle conditions are widely varied. Effective viscosity and STG are only parameters that could vary in a wide range.

Conclusion and future study.

● *Ascending of diapirs from single level under uniform superadiabatic thermal gradient could not fit the whole corona size range*. Diapirs probably rose from different depths and/or STG varied over the surface and/or with time.

Are there local families of coronae of similar origin? Preliminary overview of whole population of coronae hints that coronae of similar morphology tend to cluster. From other hand calculations showed that there is no prominent correlation between size of nearest coronae. An advanced study of size and location distribution of coronae of different morphology accompanied by assessment of their relative age might clarify the problem.

● *Population of small coronae could be formed only from relatively shallow source* (in agreement with [5]), *and, probably, under prominent superadiabatic thermal gradient.*

● *Existence of small coronae demands low effective viscosity of upper mantle.*

To obtain reliable quantitative constrains for diapir source depth, value of STG and effective mantle viscosity more intricate model is needed, including simulation of diapir behavior beneath the lithosphere. It might clarify relation of corona morphology with diapir parameters.

References.

[1] Pronin A.A. and Stofan E.R.,(1990) *Icarus, 87,* 1990, 327 - 338.
[2] Stofan E.R *et al.* (1992) *J. Geophys.Res., 97,* 13347 - 13378.
[3] Squyers S.W *et al.* (1992) *J. Geophys.Res., 97,* 136111 - 13634
[4] Griffiths R.W. and Campbell I.H. (1991) *Earth Planet. Sci. Let., 99,* 66 - 78
[5] Li Yinting and Janle P. (1993) *Planet. Space Sci.* In print.
[6] Zharkov V.N. and Solomatov V.S. (1992) In:*Venus Geology, Geochemistry, and Geophysics.* Univ. of Arizona Press, Tucson, 280-320.

SILICA- AND MERRIHUEITE/ROEDDERITE-BEARING CHONDRULES AND CLASTS IN ORDINARY CHONDRITES: NEW OCCURRENCES AND POSSIBLE ORIGIN.

Krot A.N.[1,2] and Wasson J.T. [1] [1]Institute of Geophysics and Planetary Physics, University of California, Los Angeles, 405 Hilgard Ave., CA 90024, USA; [2]Vernadsky Institute of Geochemistry and Analytical Chemistry, Russian Academy of Sciences, Kosygin 19, Moscow 117975, Russia.

Merrihueite $(K,Na)_2(Fe,Mg)_5Si_{12}O_{30}$ ($na<0.5$, $fe>0.5$, where na = Na/(Na+K), fe = Fe/(Fe+Mg)), is a rare mineral previously described only in several chondrules and irregularly-shaped fragments in the Mezö-Madaras L3 chondrite breccia [1,2]. Roedderite $((Na,K)_2(Mg,Fe)_5Si_{12}O_{30}$ ($na>0.5$, $fe<0.5$) was reported previously only in enstatite chondrites and in silicate inclusions in IAB irons [3-5]. We describe two additional silica- and roedderite-bearing clasts in L3.5 ALHA77011 and LL3.7 ALHA77278 and a silica- and merrihueite-bearing chondrule in L3.5 ALHA77115. We suggest that the silica- and merrihueite/roedderite-bearing clasts and chondrules experienced a complex evolution including: (a) fractional condensation in the solar nebula to produce Si-rich and Al-poor precursors, (b) melting of nebular solids resulting in formation of silica-pyroxene chondrules, (c) fragmentation in the solar nebula or on a parent body, (d) reaction of silica with alkali-rich gas to form merrihueite/roedderite on a parent body, (e) formation of fayalitic olivine and ferrosilite-rich pyroxene due to reaction of silica with oxidized iron on a parent body, and (f) minor thermal metamorphism, possibly generated by impacts.

Merrihueite in Mezö-Madaras chondrules always coexists with ferroan olivine (Fa_{50-90}) and magnesian pyroxene (Fs_{0-10}). Dodd et al. [6] suggested that the merrihueite-bearing chondrules (MBC) formed by melting K,Na-bearing precursors undersaturated in Al; fayalitic olivine formed by reaction between the silicon-rich MBC and oxidized Fe in the solar nebula. Wood and Holmberg [2] suggested that the MBC formed in the solar nebula by partial evaporation of solids, recondensation of silica-rich and Al-poor vapors, then melting and reaction with alkali and Fe-rich vapor in an oxidizing environment during chondrule formation. According to this model these events took place during a brief period near the nebular midplane; rapid formation was followed by aggregation into a parent body.

The silica- and merrihueite-bearing chondrule in L3.5 ALHA77115, 700x900 μm in size, has an ellipsoidal shape and porphyritic texture. It consists of subhedral porphyritic low-Ca pyroxene (Fs_{13-49} $Wo_{0.6-0.3}$) and silica grains; accessory phases include plagioclase mesostasis, ferroan olivine ($Fa_{57.5-86.9}$), ferroan pyroxene ($Fs_{84.9}$ $Wo_{2.2}$), merrihueite (fe = 0.56, na = 0.32) and troilite. Merrihueite occurs as thin veins within one of the silica grains that is surrounded by plagioclase mesostasis. Fayalitic olivine and ferrosilite-rich pyroxene are associated with merrihueite and occur as thin veins in silica that transect through the merrihueite veins.

The silica- and roedderite-bearing clast in ALHA77011 is an irregularly-shaped fragment, 1.8x2.5 mm in size, that has a coarse-grained igneous texture. It conists of low-Ca pyroxene ($Fs_{7.7-42.8}$ $Wo_{0.3-2.1}$), silica, roedderite (fe = 0.42-0.43, na = 0.52) and troilite. Low-Ca pyroxene occurs as anhedral and subhedral grains partially resorbed by the surrounding roedderite. Silica occurs as subhedral inclusions in pyroxene and as anhedral grains within roedderite. The silica grains are corroded by roedderite and contain thin veins of ferrosilite-rich pyroxene ($Fs_{62.7}$ $Wo_{3.6}$) with tiny regions of fayalitic olivine. Abundant troilite occurs as veins in pyroxene grains and as tiny inclusions in roedderite.

The silica- and roedderite-bearing clast in ALHA77278 is an irregularly-shaped fragment, 1.9x1.9 mm in size, that has a coarse-grained igneous texture. It consists of low-Ca pyroxene $Fs_{9.8-22.3}$ $Wo_{0.4-2.4}$, high-Ca pyroxene ($Fs_{9.3-12.4}$ $Wo_{42.3-43.3}$), silica and roedderite (fe = 0.16, na = 0.50). Low-Ca pyroxene occurs as porphyritic grains in silica and in high-Ca pyroxene. Silica forms

SILICA- AND MERRIHUEITE-BEARING CHONDDRULES **Krot A.N. and Wasson J.T.**

compact areas scattered throughout the clast. High-Ca pyroxene fills the interstitial areas between silica and low-Ca pyroxene. Roedderite forms reactional intergrowths with silica. Olivine ($Fa_{30.2}$) occurs in the outer zone of the
clast where it substitutes for silica. The clast is enriched in troilite which forms tiny spheroids mainly in high-Ca pyroxene.

Based on the igneous textures of the clasts and chondrules and the normal igneous zoning of low-Ca pyroxene grains and petrographic observations we suggest that the pyroxene and silica in the objects described above crystallized from melts. The ALHA77278 clast contains a significant amount of Ca-rich pyroxene that crystallized after the low-Ca pyroxene and silica. Merrihueite/roedderite is in reactional relationships with silica in all three objects and with low-Ca pyroxene in the ALHA772728 clast, indicating that the merrihueite/roedderite formed after crystallization of silica and low-Ca pyroxene. According to the experimental data for the system K_2O-MgO-SiO_2 [7], silica and merrihueite should crystallize along the cotectic curve in contradiction to our petrographic observations. The reactional relationships between silica and merrihueite/roedderite possibly indicate that silica and merrihueite crystallized in disequilibrium or, more likely, that merrihueite/roedderite did not crystallize from the melts but it is a secondary phase formed by reaction of silica and alkali-rich fluid. Fayalitic olivine and ferrosilite-rich pyroxene are the late crystallizing phases substituting for silica. These ferroan phases are in disequilibrium with the relatively magnesian pyroxenes of the host objects and are similar in texture and composition to the fayalitic olivines and ferrosilite pyroxenes in silica-fayalite-bearing chondrules in ordinary chondrites [8]. The ferroan olivine and pyroxene in the silica-bearing chondrules as well as in the silica- and merrihueite/roedderite-bearing chondrules and clasts formed by reaction of silica with oxidized iron. The presence of abundant troilite in the ALHA77011 and ALHA77278 clasts indicates that these clasts experienced shock metamorphism after solidification.

We suggest that silica- and merrihueite/roedderite-bearing chondrules and clasts (SMBC) experienced a complex history of formation: (1) In the solar nebula, fractional condensation or partial evaporation and recondensation resulted in the formation of Si-rich and Al-poor precursor. (2) These materials were melted during chondrule formation events, resulting in the formation of silica-pyroxene chondrules. (3) Agglomeration and accretion led to incorporation of the silica-pyroxene chondrules into the parent bodies. (4) Impact heating produced alkali-rich vapors which reacted with SiO_2 to form merrihueite-roedderite. (5) During mild metamorphism, possibly induced by the same impact heating event, reaction of silica with oxidized iron led to the formation of fayalitic olivine and ferrosilite-rich pyroxene. (6) Thermal metamorphism resulted in partial equilibration of the fayalitic olivine with preexisting mafic minerals. (7) Shock metamorphism introduced abundant troilite into some of the silica- and merrihueite/roedderite-bearing chondrules and clasts.

References: [1] Dodd et al. (1965) Science 149, 972-974. [2] Wood J.A. and Holmberg B.B. (1993) Icarus (in press). [3] Fuchs L.H. (1966) Amer. Mineral. 51, 949-955. [4] Rambaldi et al. (1983) LPS 14, 661-662. [5] Olsen E. (1967) Amer. Mineral. 52, 1519-1523. [6] Dodd et al. (1966) Amer. Mineral. 51, 1177-1191. [7] Roedder E. (1951) Amer. J. Sci. 249, 81-130. [8] Wasson J.T. and Krot A.N. (1994) EPSL (submitted).

AB INITIO CALCULATIONS OF THERMODYNAMICS AND KINETICS OF GAS-PHASE REACTIONS RELEVANT TO THE EARLY SOLAR NEBULA;

J. D. Kubicki, J. R. Beckett, G. A. Blake and E. M. Stolper, Division of Geological and Planetary Sciences, California Institute of Technology, 170-25 Pasadena, CA 91125

Abstract. Calculations based on molecular orbital (MO) theory using the program Gaussian 92 [1] and G2 theory [2] have been used to study the reactions $MgO \rightarrow Mg + O$ and $SiO_2 + H_2 \rightarrow SiO + H_2O$. We demonstrate that MO calculations can reproduce structures and vibrational spectra of gas-phase molecules accurately with the MP2/6-311+G** basis set. We can also calculate accurate molecular dissociation energies, D_e, if G2 corrections are made to account for limitations of the basis set in describing electron orbitals. Consequently, MO calculations can act as a check on experimental thermodynamic values where the uncertainty is high (e. g., $D_e(MgO)$; [3]) or where activation energies, ΔE_a, do not exist (e. g., $MgO + H_2 \rightarrow H_2O + Mg$). Furthermore, the lowest energy reaction pathways may be followed between reactants and products to obtain predictions of mechanisms of gas-phase reactions.

Introduction. Molecular dynamics (MD) simulations of free evaporation in crystalline and molten forsterite (Mg_2SiO_4) have been performed previously [4] to investigate possible speciation of gas-phase molecules leaving the condensed phase surface and better understand the isotopic fractionation results of [5-7]. Species such as $SiO_2(g)$, MgO(g) and larger molecular units were observed leaving the crystal and melt surfaces in our simulations. Two limitations of our previous modeling have led us to study the gas-phase of this process with high level, ab initio calculations. First, the MD simulations were limited to an ionic description of the atoms since the interatomic potential was taken from a semi-empirical fit of Leinenweber and Navrotsky [8] to crystal data in the system Mg-Si-O. Second, the MD simulations did not include hydrogen because there is no interatomic potential available for hydrogen compatible with the Leinenweber and Navrotsky [8] parameters. We have chosen to model the gas-phase reactions separately from the surface evaporation process at this point because of these limitations, although we note that hydrogen at the surface of the condensed phase may play a role in the chemical and isotopic fractionations associated with evaporation in the early solar nebula [6].

Methodology. Molecular structure optimizations were made with the MP2/6-311+G** basis set because theoretical gas-phase geometries reproduce experimental values fairly accurately at this level (Table 1; [2]). (For an explanation of basis set codes see [1].) Molecular structures were optimized by solving for the lowest energy structure for a given molecule or dimer. The first and second derivatives of the molecular energy with respect to movement of the nucleii are used to move the atoms into lower energy positions following the Berny algorithm [1]. We have tested the dynamic stability of each stationary point by performing force constant analyses of the optimized molecular configurations. At an equilibrium configuration, the first derivatives of the energy with respect to atomic motions $dV/dq_{ij} = 0$ and all the second derivatives $dV^2/dq_{ij}^2 > 0$. Hence, calculation of the second derivative matrix at an equilibrium configuration results in eigenvalues (i. e., force constants) that are all positive.

Reaction pathways were also calculated between the stable configurations of products and reactants. Structural optimizations were made for molecular configurations along the reaction pathway with one parameter constrained and the others allowed to optimize. For $SiO_2 + H_2 \rightarrow SiO + H_2O$, one O---H distance was constrained starting at the optimized dimer geometry (Fig. 1) and then decreasing to the transition state (i. e., the highest energy point along the reaction path). After formation of SiO and H_2O, the constrained parameter was the Si---OH_2 distance. For MgO dissociation, the constrained parameter was the Mg-O distance. Energetics of reactions can be significantly in error even with the relatively large MP2/6-311+G** basis set. Theoretical energies of reactions are inaccurate because only a basis set of infinite size with full configuration interaction can predict exact molecular energies. For this reason, Pople and co-workers have devised a method, G2 theory, that generally reproduces reaction energies within ± 10 kJ/mol [2]. We have used G2 theory to calculate the reaction energetics of interest.

Results and Discussion. Calculated structures and vibrational frequencies of gas-phase molecules are listed and compared to experiment in Table 1. Bond distances are within ± 0.02 Å, and vibrational frequencies generally < 7% higher than the observed frequencies with the MP2/6-311+G** basis set indicating that this level of theory reproduces molecular structures and vibrational spectra. Calculated dissociation energies, D_e, in Table 1 are generally close to the experimental dissociation energies. The MgO molecule has the largest error with 35% underestimation of experiment.

The calculated energy change of SiO + H_2O forming from SiO_2 and H_2 using the G2 corrections is -57 kJ/mol at 0 K compared to the experimental ΔH of -85 kJ/mol at 300 K. Such a close approximation of experimental

reaction energies allows us to calculate the activation energy of the reaction accurately following the same methodology. Figure 1 pictures the rearrangement of the SiO_2 + H_2 and SiO + H_2O molecules as the SiO_2 + H_2 → SiO + H_2O reaction occurs. H_2 orients itself at an angle of ≈ 144° relative to the SiO_2 molecule as it approaches with the O---H-H angle nearly 180°. This geometry optimizes the interaction between one electron lone pair on the oxygen and one of the hydrogen atoms. The transition state in Fig. 1b gives an energy ≈ 180 kJ/mol higher in energy than the SiO_2---H_2 dimer in Fig. 1a. This energy difference is an estimate for ΔE_a of this reaction and is comparable to activation energies for diffusion in silicate melts. Hence, the conversion of SiO_2 to SiO should be rapid at the elevated temperatures of the early solar nebula. On the other hand, our predicted activation energy for the dissociation of MgO into isolated atoms is ≈ 500 kJ/mol and the reaction is ≈ 250 kJ/mol endothermic, so MgO could be a long-lived metastable species if evaporated from a crystal or melt. However, the MgO + H_2 → Mg + H_2O reaction is ≈ 235 kJ/mol exothermic, and further study of this reaction will be necessary to evaluate the validity of this conclusion in the presence of H_2.

Table 1 - Calculated dissociation energies, D_e, structures and vibrational frequencies (MP2/6-311+G**) of various molecules compared to experiment (in parentheses).

Molecule	De (kJ/mol)	Bond Length (Å)	Frequencies (cm^{-1})
H_2	442 (436)	0.74 (0.74)	4531 (4401)
H_2O	494 (498)	0.96 (0.96)	1627, 3888, 4008 (1648, 3832, 3943)
SiO	790 (799)	1.54 (1.55)	1182 (1122)
SiO_2	427 (481)	1.53 (1.55)	267, 974, 1441 (370, 980, 1430)
MgO	248 (381)	1.76 (1.75)	997 (785)

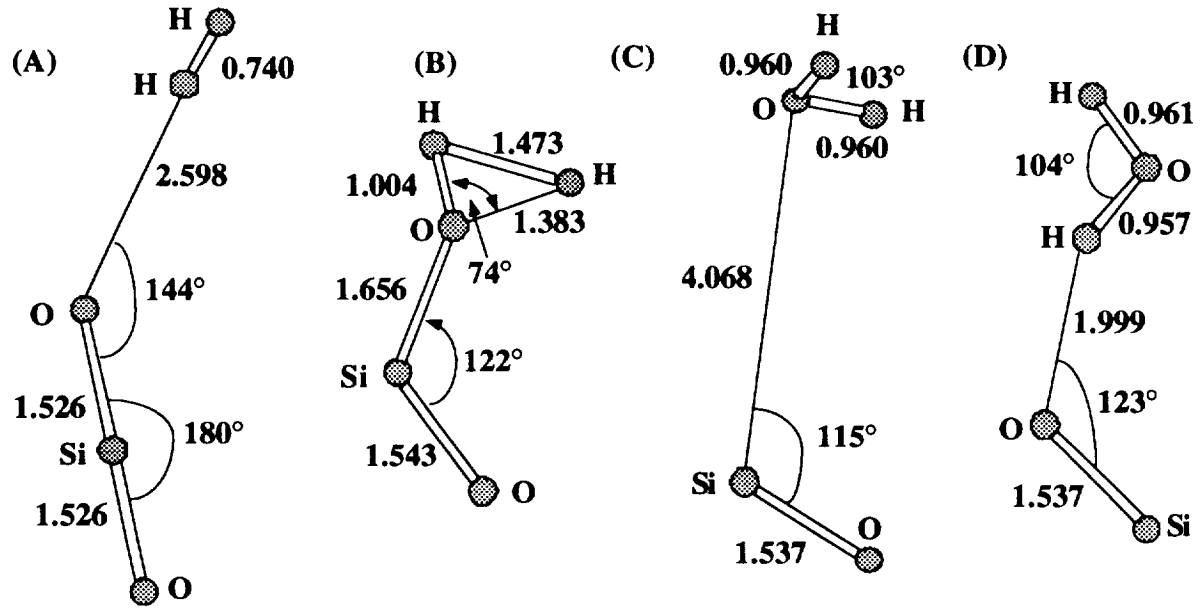

Figure 1 - (A) Optimized dimers of SiO_2---H_2, (B) optimized transition state structure, (C) and (D) optimized SiO-H_2O in two different configurations. (D) is lower in energy and thus more stable than (C).

References [1] Frisch MJ et al. (1992) Gaussian 92. Revision C, Gaussian, Inc., Pittsburgh PA. [2] Curtiss LA, K Raghavachari, GW Trucks and JA Pople, 1991, *J. Chem. Phys.* 94, 7221-7230. Huber KP and G Herzberg, 1979, Molecular Spectra and Molecular Structure. IV. Constants of Diatomic Molecules. Van Nostrand Reinhold Co. New York, 716p. [4] Kubicki JD and EM Stolper, 1993, *Lunar and Planetary Sci.* **XXIV**, 829-830. [5] Hashimoto A, 1990, *Nature*, **347**, 53-55. [6] Davis AM, A Hashimoto, RN Clayton, and TK Mayeda, 1990, *Nature*, **347**, 655-658. [7] Uyeda C., A Tsuchiyama, and J Okano, 1991, *Earth Planet. Sci. Lett.*, 107, 138-147. [8] Leinenweber K and A Navrotsky, 1988, *Phys. Chem. Min.* **15**, 588-596.

ISOSTASY MODELS AND CORRELATIONS OF GEOID AND TOPOGRAPHY DATA FOR CHARACTERISTIC HIGHLANDS ON VENUS; A.B. Kucinskas, Jet Propulsion Laboratory/California Institute of Technology, Pasadena, CA 91109; D.L. Turcotte, Department of Geological Sciences, Cornell University, Ithaca, NY 14853.

We have used the newest solution for the Venus geopotential, incorporating tracking data from the circularized orbit (cycle 5) of Magellan, along with global Venus topography data to study correlations of geoid and topography variations (N and h) in several regions characteristic of the principal classes of highlands found on Venus. For each region, mean values of N and h data were compared to theoretical correlations for Pratt, Airy, and thermal isostasy. We find strong coherence in the regional correlations of this data and the topography is substantially compensated. Although there are large variations in model parameters for the regional fits, h and N data correlations in the chosen sample areas can be explained by isostatic compensation models involving variations in crustal (Airy) and/or lithospheric (thermal) thicknesses provided a thick zero-elevation thermal lithosphere is assumed for Venus.

Following the success of the aerobraking experiment, the orbit of the Magellan spacecraft has been quasi circularized. From the preliminary cycle 5 Doppler tracking data, a new 60x60 degree and order Venus geopotential spherical harmonic solution has been produced (1) which features lower uncertainties than previous cycle 4 models and higher resolution gravity data at high latitudes for part of the planet (eg Western Ishtar Terra). We used this new geopotential model along with a global 120 x 120 spherical harmonic model for Venus topography (2,3) to obtain 5° x 5° mean values of observed geoid and topography anomalies for six 30° x 30° regions most representative of the three principal classes of highlands (4) found on Venus. Our chosen samples include an area in Western Ishtar Terra, in the Northern latitudes, namely the high plateau of Lakshmi Planum surrounded by mountain ranges on all sides (5). Also included are five samples in the equatorial zone, namely: the topographic swells of Beta and Atla Regiones, the plateau-shaped areas of Ovda and Thetis Regiones and one sample region in the central part of Aphrodite Terra, in the so-called Chasmata area. The latter is in a class of its own, presenting a series of elongated ridges and linear to arcuate throughs (4).

For each of the 30° x 30° areas considered in this study we performed a least-squares fit of the observed geoid anomaly versus elevation data values to Pratt, Airy, and thermal theoretical correlations of N and h. For these models, isostatic compensation and support of high topography is achieved by horizontal variations in density, low density crustal roots, and thinning of the thermal lithosphere (thermal boundary layer) by basal heating, respectively. Geoid anomalies are non-zero in isostatically compensated regions and are thus preferred over gravity anomalies to determine the dependency of density with depth and study the mechanism of compensation in the lithosphere. Indeed, for a shallow source (density distribution) and in the long-wavelength approximation, the isostatic geoid anomaly is directly proportional to the dipole moment of the density-depth distribution (6,7). This so-called HOT formula was used to obtain the theoretical h, N relationships for the isostasy models considered in this work.

For a given region, fitting of the models to the data yields the following model parameter values: the geoid to topography ratio (GTR), or the slope of the best fitting correlation line, and the corresponding depth of compensation W for the Pratt mechanism; for the Airy correlation the zero-elevation crustal thickness H and, for a given regional elevation h, the total crustal thickness $T(h) = H + b(h)$ with b(h) the corresponding root; finally, for the thermal thinning model the thickness of the unperturbed (ie corresponding to zero elevation) thermal lithosphere Y_{Lo} and, for a given thermal elevation of h, the thickness of the thinned lithosphere $Y_L(h)$. For each of our sample regions we also define a degree of compensation C (8) as the slope of the regression line fitted to the regional 5° x 5° data values of $\Delta g^u - \Delta g$ plotted against Δg^u, with Δg^u the Bougher gravity anomaly for an uncompensated topography and Δg the observed gravity anomaly.

ISOSTASY MODELS AND CORRELATIONS OF GEOID AND TOPOGRAPHY: Kucinskas, A.B. and Turcotte, D.L.

From the results of the fits listed in Table 1 we first note that the degree of compensation is high for all samples and that the correlation of the h, N data presents strong coherence. For all three models considered there are large variations in model parameters between the regional fits. Also, for the Pratt and Airy model correlations there is a grouping into classes depending on model parameter values. These are relatively small for Ovda and Lakshmi and large for the Beta, Atla, and Chasmata area samples. The Thetis sample has somewhat intermediate values. These observations hint towards the application of different compensation mechanisms for the various areas considered. This seems particularly true for Aphrodite Terra which shows an increase in GTR, W and H from West to East thus confirming with the Magellan data a tendency previously noted by other authors (9, 10, 11) in studies using lower resolution PVO data. In the case of the thermal correlations, however, it must be noted that the theoretical model barely manages to reproduce the Thetis data (ie the highest elevations) and completely fails for Ovda Regio and Lakshmi Planum. For the other regions a thermal thinning model can account for the observed regional topography and geoid though it is reasonable to assume that the thermal component may vary in strength depending on the sample considered.

Thus it appears that isostatic compensation models can explain the geoid-topography correlations observed in the highland areas considered in this work. However, a thick unperturbed thermal lithosphere is required, with Y_{Lo} ~300 km. One way to obtain such a thick lithosphere would be conductive cooling during the past ~500 My, as suggested by Turcotte (12). Based on these premises, compensation mechanisms could be distributed among our sample regions as follows: mainly Airy isostasy for Ovda Regio and Lakshmi Planum. For Thetis Regio: Airy with perhaps a thermal component. And a very strong thermal component for Atla, Beta, and the Chasmata area since the large values of H obtained for these regions are unrealistic even with a 300 km lithosphere.

References: **(1) Sjogren, W.L., and A.S. Konopliv, Trans. Am. Geophys. Un. 74, Supple., 43, 374. (2) Konopliv, A.S. et al, GRL 20, 2403-2406, 1993. (3) Kucinskas, A.B., N. J. Borderies, and D.L. Turcotte, Lunar Planet. Sci. XXIV, 831-832, 1993. (4) Solomon, S.C., et al, JGR 97, 13199-13255, 1992. (5) Ford, P.G., and G.H. Pettengill, JGR 97, 13103-13114, 1992. (6) Ockendon, J.R., and D.L. Turcotte, Geophys. J. Roy. Astron. Soc., 48, 479-492, 1977. (7) Haxby, W.F., and D.L. Turcotte, JGR 83, 5473-5478, 1978. (8) Turcotte, D.L., R.J. Willemann, W.F. Haxby, and J. Norberry, JGR 86, 3951-3959, 1981. (9) Herrick, R.R., B.G. Bills, and S. A. Hall, GRL 16, 543-546, 1989. (10) Black, M.T., M.T. Zuber, and D.C. McAdoo, JGR 96, 301-315, 1991. (11) Smrekar, S.E., and R.J. Phillips, Earth and Planet. Sci. Letters 107, 582-597, 1991. (12) Turcotte, D.L., JGR 98, 17061-17068, 1993.**

TABLE 1. Parameters for Regional Model Fits

Region	Cx100	h	GTR	W	σ_{Pratt}	H	T(h)	σ_{Airy}	Y_{Lo}	Y_L	σ_{th}
	%	km	m/km	km		km	km		km	km	
Lakshmi	89.0	4.7	10.4	134	9.3	62.0	96.0	9.7	NA	NA	NA
Beta	67.8	2.8	33.3	426	13.8	235	255	13.7	357	102	16.8
Ovda	92.8	4.0	9.1	117	6.4	53.8	82.8	6.5	NA	NA	NA
Thetis	85.5	3.2	19.4	248	10.6	129	153	11.0	292	0.2	8.6
Chasmata	80.2	1.2	21.9	280	5.5	157	166	5.4	209	99.2	5.7
Atla	64.4	4.0	23.7	304	13.0	158	187	13.3	369	4.3	13.0

MARS, A CARBON RICH PLANET?—BEHAVIOR OF H AND C DURING EARLY CORE FORMATION—; Kiyoshi Kuramoto and Takafumi Matsui, Department of Earth and Planetary Physics, University of Tokyo, Bunkyo-ku, Tokyo 113, Japan.

In this paper we try to estimate initial abundance and chemical forms of H- and C-bearing species in proto-atmosphere and -mantle of Mars. Fe rich core is a potential reservoir of the accreted H and C [1,2]. Several lines of evidence suggest that the martian core was formed during or just after the accretion [3]. It is likely that impacts of large planetesimals induce widespread (but not global) melting of proto-Mars and trigger segregation of metal [4]. Analysis of SNC meteorites suggests that building stones of Mars contain a significant amount of volatiles including H and C [5]. When a planetesimal size is large enough to generate a molten region (magma pond) at impact, a substantial portion of H and C contained in the planetesimal is expected to be buried in a magma pond. Of course some portion is subjected to an impact-induced degassing [6]. A portion of buried H and C may be partitioned to metallic iron and eventually transported to a planetary core. One of the factors controlling this process is the solubility of H and C in liquid form of metallic iron. On the other hand, the composition of degassed gas species depends on oxygen fugacity, which is controlled by the redox reaction with metallic iron and silicate. This can be evaluated using a thermodynamic model based on experimental data. Accreted amount of H and C as well as S-content in the core are important for this issue. We estimated them according to the two component model by Dreibus and Wänke [5].

C as much as approximately 5 wt% dissolves in liquid metallic iron at 1 bar and 1873K [8]. Because volume change with dissolution is small, its solubility does not change significantly even at high pressures at least $\sim$ 10GPa. Incorporation of S in liquid metallic iron substantially decreases the C solubility [8]. Since the martian core may contain $\sim$14 wt% of S [5], the saturated C content is estimated to be as low as 2$\sim$3 wt%, which is slightly dependent on temperature and pressure (Fig. 1). On the other hand, the accreted C content is estimated to be 6.2 wt% relative to the core mass. This suggests that more than half of the accreted C remain in the proto-atmosphere or mantle mainly as CO gas or graphite just after the metal segregation. Since the oxygen fugacity is estimated to be about 1 order of magnitude smaller than the IW buffer before the segregation of metal, CO is the dominant gas species compared to CO_2. Furthermore, amount of CO_2 dissolved in silicate melt plays negligible role in C budget in proto-mantle because of its low oxygen fugacity.

H buried in planetary interior is partitioned between silicate melt and liquid metallic iron during silicate-metal segregation in the magma pond. Because of the large solubility of H_2O into silicate melt, a substantial fraction of H is expected to be partitioned to the silicate melt as H_2O. Since existence of S and C decreases the solubility of H in liquid metallic iron, H may be partitioned largely to the proto-martian mantle.

MARS, A CARBON RICH PLANET ?: Kuramoto, K., and Matsui, T.

Graphite and CO in proto-mantle and proto-atmosphere are considered to be eventually reacted with H_2O. Therefore a large amount of CO_2 is generated, and there also occurs vigorous degassing of H_2 from proto-mantle and escape of H_2 from atmosphere to space. The amount of H_2O decomposed by this reaction may reach 1~2% martian mass for the CO dominated case and 2~4 % for the graphite dominated case, while the accreted H_2O is estimated to be 3.4%. This means that a significant portion of the accreted H_2O may be lost due to oxidation of such reduced C-bearing species. In extreme case, H_2O might be entirely lost by this mechanism. Whether or not this occurs depends on the ratio of CO/graphite, which is dependent on the impact degassing efficiency at each impact event. Such an extensive loss of H_2O might be consistent with the high D/H ratio of both martian atmosphere [8] and the hydrous mineral inclusion in SNC meteorite [9].

Since the present martian mantle is relatively oxidized, initial abundance of H_2O may be larger than that enough for its complete decomposition. In such a case, the proto-mantle is oxidized through H_2O degassing. Production of CO_2 or CO_3^{2-} in the interior region might be also possible, if such oxidized silicates are mixed with the graphite-bearing region of proto-martian mantle due to convention. This might induce SiO_2 poor volcanism, which appears to be consistent with the martian crustal formation [10].

REFERENCES [1] Fukai, Y., *Nature*, **308**, 174–175, 1984. [2] Abe, Y., in *Proc. 21st ISAS Lunar and Plant. Symp.*, Inst. Space Astronaut. Sci., Sagamihara, pp.238–244, 1988. [3] Schubert, G. et al., in *Mars*, Eds. H. H. Kieffer et al., Univ. of Arizona Press, Tucson, pp. 147–183, 1992. [4] Tonks, W. B. and Melosh, H. J., *Icarus*, **100**, 326–346, 1992. [5] Dreibus, G. and Wänke, H., *Icarus*, **71**, 225–240, 1987. [6] Ahrens, T., et al., in *Origin and Evolution of Planetary and Satellite Atmospheres*, Eds. S. K. Atreya et al., Univ. of Arizona Press, Tucson, pp. 328–385, 1989. [7] Wang et al., *ISIJ inter.*, **31**, 1292–1299, 1991. [8] Owen, T., in *Mars*, Eds. H. H. Kieffer et al., Univ. of Arizona Press, Tucson, pp. 818–834, 1992. [9] Watson, L. L., et al., in *Lunar and Planet. Sci. XXIV*, 1493–1494, 1993. [10] Longhi et al., in *Mars*, Eds. H. H. Kieffer et al., Univ. of Arizona Press, Tucson, pp. 184–208, 1992. [11] Ogino, K. et al., *J. Japan Inst. Metals*, **48**, 1004–1010, 1984.

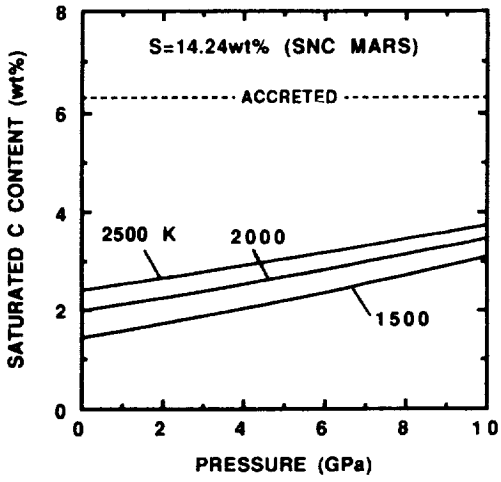

Fig. 1. Estimated saturated C content in Fe-S alloy (S=14.24wt%). Estimation is based on thermodynamic parameterization of Fe-S-C ternary system at 1 bar [7] and the partial molar volume of C in liquid metallic iron [11].

FRACTIONATED TRACE ELEMENT ABUNDANCES IN MICROMETEORITES FROM ANTARCTICA; Gero Kurat, Naturhistorsiches Museum, Postfach 417, A-1014 Vienna, Austria, Christian Koeberl, Institut für Geochemie, Universität Wien, Dr.-Karl-Lueger-Ring 1, A-1010 Vienna, Austria, Michel Maurette, Centre de Spectrometrie Nucleaire et de Spectrometrie de Masse, Batiment 108, F-91405 Orsay, France.

Major and trace element contents of two unmelted, three scoriaceous micrometeorites (MMs) and one cosmic spherule are presented. The data confirm previous observations which showed that MMs have bulk compositions similar to those of hydrated carbonaceous chondrites but have experienced some alterations which led to depletions and enrichments of certain elements as compared to chondritic abundances. The new data also show various degrees of depletions of MMs in Na, Rb, Zn, Ni, Co, Au, and Se and enrichments in K, Br, Fe, Au, As, and Sb. Correlations between the degree of melting and some elemental depletions (Na, Zn, Au, Se) suggest elemental loss by volatilization, presumably during atmospheric entry. Depletions in Ni and Co could be due to leaching of soluble salts from the MMs. However, because the cosmic spherule shows a Ni,Co-depletion similar to that of the MMs, another mechanism causing the depletion must exist. We tentatively suggest that preferential loss of Ni,Co-bearing sulfates by decrepitation during the atmospheric heating event is responsible for the depletion. All enrichments of MMs in volatile elements are believed to be the result of re-condensation of meteoritic vapors onto and into the MMs in the high atmosphere. Unusual enrichments of our MMs in refractory lithophile elements could be due to (unknown) contents of refractory minerals.

SAMPLES and METHODS. Indivudual particles were selected from the 100-400 μm size fraction of the dust collection made on January 15, 1991, from the blue ice near the French Antarctic station Dumont d'Urville [1]. The particles we report on here were selected because of their irregular shape and dark color, with the expectation that some of them will be unmelted micrometeorites. Particle masses ranged from 2.5 to 5 μg. In addition, one large (mass 59 μg), irregular cosmic spherule covered by COPS [2,3] was selected. Particles were analyzed by INAA following the procedure outlined in [4]. The samples are now being sectioned for petrographic and mineral chemical analyses.

RESULTS. Preliminary trace element data are given in the Table and normalized abundance patterns are shown in the Figure. Refractory lithophile elements have unfractionated chondritic abundances only in the cosmic spherule 5M1. The scoriaceous MMs (5M2, 5M5, 5M8) and unmelted MMs (5M3, 5M10) have fractionated refractory lithophile element contents, three of them (5M2, 5M10, 5M3) at super-chondritic abundances. The moderately volatile elements Na, K and the volatile element Zn are depleted in the spherule and in some scoriaceous MMs. Potassium is enriched in one unmelted, Rb in one scoriaceous, and Br in all MMs. Also the spherule has a chondritic Br content. The siderophile elements show a peculiar pattern which is similar in all samples. Osmium and Ir have chondritic to super-chondritic abundances and are unfractionated. Nickel and Co are depleted with respect to Os and Ir. The abundance pattern always follows the sequence Ni < Co < Fe. The Au abundance of the MMs is highly variable and ranges from about chondritic to enriched (~20xCI). The spherule is strongly depleted in Au. All MMs are strongly enriched in As and Sb, their average Se abundance is chondritic. The spherule has a similar pattern at a considerably lower abundance level.

DISCUSSION. The largest sample, spherule 5M1, has refractory trace element abundances between 1 and 2xCI. The depletions in elements more volatile than Cr must be the result of volatilization during melting in the upper atmosphere [6,7]. However, many elements, which are more volatile than Na or Au, are not depleted in spherule 5M1. Because it is covered by large amounts of COPS, we may speculate that the most volatile elements reside in this phase. Consequently, they were added to the spherule after it was formed in the high atmosphere. Similar enrichments of volatile elements in micrometeorites must have a similar cause [4,7,8] although these elements apparently do not reside in an identifyable phase. Similar enrichments observed in stratospheric IDPs (interplanetary dust particles) have also been shown to be likely of terrestrial [9] rather than primordial [10] origin. Depletions of MMs in non-volatile elements such as Ni and Co have been interpreted as indicating loss of Ni,Co-bearing salts from the MMs by dissolution in water [7,8]. However, the fact that spherule 5M1 shows a Ni/Ir fractionation identical to that of the MMs requires an additional mechanism, involving similar compounds such as Ni,Co-bearing sulfates. A possible - speculative - way could be a preferential loss of such phases by decrepitation during the heating event in the high atmosphere. The fractionated REE patterns displayed by most of our MMs are unusual. Such patterns have not been observed before [e.g., 4,6,7,11] except for a CAI-bearing

MM described by [12]. Some refractory grains might be present in these MMs which, however, we have not yet been able to identify.

ACKNOWLEDGEMENTS. This work was financially supported by FWF in Austria (project no. P8125-GEO) and by IN2P3 and the European Community SCIENCE (Twinning and Operations) Programme (contract no. SCI-CT91-0618, SSM) in France. We thank Ljuba Kerschhofer and Thomas Presper for help with INAA and Elke Wäsch for help with the SEM catalogue.

REFERENCES. [1] Maurette M. et al.(1992) Meteoritics, 27, 473. [2] Perreau M. et al.(1992) Meteoritics, 26, 274. [3] Engrand C. et al.(1993) LPSC, XXIV, 441. [4] Koeberl C. et al.(1992) LPSC, XXIII, 709. [5] Anders and Grevesse N.(1989) GCA. 53, 197. [6] Koeberl C. and Hagen E.H.(1989) GCA, 53, 937. Volatile depletion in spherules. [7] Presper T. et al.(1993) LPSC, XXIV, 1177. [8] Kurat G. et al.(1992) Meteoritics, 27, 246. [9] Jessberger E. et al.(1992) EPSL, 112, 91. [10] Flynn G.J. and Sutton S.R.(1992) LPSC, XXIII, 373. [11] Kurat G. et al.(1993) 18th Symp. Antarct. Meteorites, NIPR, Tokyo, 153. [12] Kurat G. et al.(1994) this volume.

Figure: Orgueil-normalized [5] abundances of selected elements in unmelted (5M3, 5M10) and scoriaceous (5M2, 5M5, 5M8) MMs and cosmic spherule 5M1.

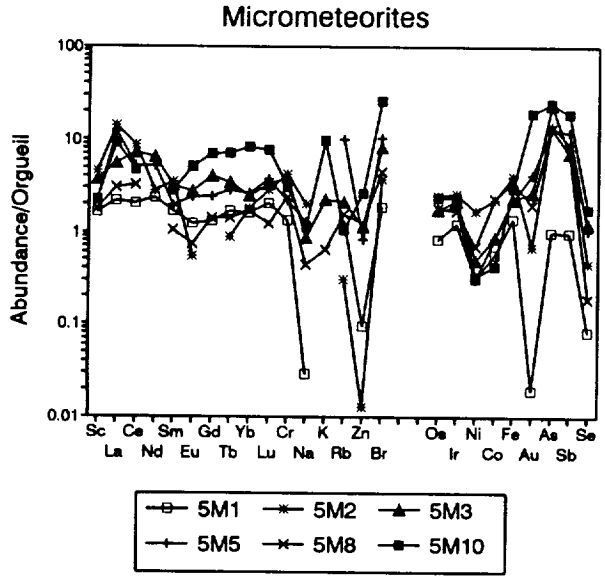

Table: INAA of Antarctic micrometeorites (ppm)

	5M1	5M2	5M3	5M5	5M8	5M10
Mass	59	2.7	5	3	5	2.5
Na(%)	0.014	0.98	0.425	0.627	0.213	0.543
K(%)	<1	<1	0.126	<1.8	0.036	0.55
Sc	9.51	27	21.7	12.8	10.3	13
Cr	3580	11390	10340	5700	6350	8210
Fe(%)	25.1	74.2	41.8	40.8	66.2	54.5
Co	285	1140	438	430	1165	213
Ni	3458	18800	5370	3390	7550	3570
Zn	29.4	4	352	258	383	816
Ga	60	20	1	5	1	2
As	1.84	26.7	43.5	24	25	46
Se	1.5	8.25	22.4	18.9	3.4	32
Br	6.5	13	29	37	15.9	92.8
Rb	3.1	0.7	4.9	22.9	3.6	2.4
Sr	19	15	75	117	110	45
Zr	4	<10	5	40	15	80
Ru	0.81	2.7	2.3	4.5	0.52	3
Sb	0.13	1.2	0.94	1.6	0.94	2.5
Cs	<0.14	0.07	0.64	0.12	<0.83	<0.7
Ba	4.1	<20	<50	<40	5	8
La	0.51	3.3	1.3	2.9	0.72	2.2
Ce	1.26	5.4	4.5	3.2	2	2.9
Nd	1.08	1.3	3	2.4	<2.4	<6.3
Sm	0.248	0.5	0.45	0.28	0.15	0.4
Eu	0.068	0.03	0.15	0.13	0.04	0.28
Gd	0.26	<0.2	0.8	0.48	0.28	1.4
Tb	0.06	0.03	0.12	0.1	0.05	0.25
Tm	0.06	<0.1	<0.18	<0.27	<0.28	<0.74
Yb	0.267	0.3	0.41	0.44	0.28	1.38
Lu	0.05	0.07	0.06	0.09	0.03	0.19
Hf	0.34	<0.06	0.41	0.08	0.4	0.55
Ta	0.01	0.02	0.03	0.02	0.03	0.03
Os(ppb)	402	1190	830	810	875	1140
Ir(ppb)	574	1230	1030	870	805	1100
Au(ppb)	2.8	98	390	610	260	2770
Th	0.067	0.35	0.46	0.6	0.48	0.7
U	0.004	<0.1	<0.05	0.02	0.02	<0.1

PRELIMINARY REPORT ON SPINEL-RICH CAIs IN AN ANTARCTIC MICROMETEORITE;Gero Kurat, Naturhistorisches Museum,Postfach 417, A-1040 Vienna, Austria, Peter Hoppe, Physikalisches Institut, Universität Bern, Sidlerstraße 5, CH-3012 Bern, Switzerland, Michel Maurette, Centre de Spectrometrie Nucleaire et de Spectrometrie de Masse, Batiment 108, F-91405 Orsay, France

A large (ca. 330 μm) micrometeorite (MM) in a polished mount of unmelted Antarctic MMs (92/15, particle 23) consists of a metamorphosed phyllosilicate matrix which includes numerous spinel-rich Ca-Al-rich inclusions and one large chromite grain.The matrix has a clastic texture of Fe-and/or S-rich angular clasts of fine-grained dehydrated phyllosilicates (and others) set into a more Mg,Si-rich matrix. Both major and trace element contents of the MM's matrix, as determined by ASEM, EMP, and SIMS techniques, are chondritic but with depletions in Na, Ca, and Ni, and enrichment in Ba. The spinel-rich CAIs consist of Mg,Al-spinel, which occasionally includes some tiny (<1 μm) perovskite grains, rimmed by an Fe-rich phase whose composition is that of a (probably dehydrated) Fe-rich phyllosilicate. In places, this rim is covered by a Ti-,Al-bearing Ca-rich pyroxene which is fairly Fe-poor (7.8 wt% FeO). Bulk trace element contents of the CAIs are comparable to those of group II CAIs from carbonaceous chondrites. However, some deviations from common group II patterns could indicate more oxidizing conditions during the formation of 92/15-23 CAIs as compared to carbonaceous chondrite CAIs.

SAMPLE and METHODS. During January 1991 tens of thousands of dust particles were collected from about 260 t of ice melt-water [1]. Dark colored angular, apparently unmelted, particles were selected from the grain-size fraction 100 - 500 μm, mounted in epoxy, and polished. The collection on polished mount 92/15 contains a large number of partially melted chondritic MMs (scoriaceous MMs), many oxide particles (terrestrial), and also a surprisingly large number of unmelted MMs. The latter comprise mainly coarse-grained crystalline MMs and some phyllosilicate-type MMs. One of these contains abundant CAIs. Because such a micrometeorite was not observed before, it was selected for this study in which we utilized optical microscopy, analytical scanning electron microscopy (ASEM), electron microprobe analysis (EMPA), and secondary ion mass spectrometry (SIMS, modified procedure after [2]).

RESULTS. Particle #23 of the mount 92/15 is angular, cut by some cracks and about 330 μm long. The main mass consists of a fine-grained matrix-like material with an inhomogeneous microbreccia texture (Fig. 1). The matrix is Si,Mg-rich (Table 1, 1st analysis) as compared to the lighter-colored clasts, which are Fe- and/or S-rich. The high totals of matrix analyses indicate that it is probably a dehydrated former phyllosilicate matrix. Some very small olivines are present within the matrix as well as some low-Ca pyroxene. The chromite has an aluminous composition. Spinel-rich CAIs are abundant in 92/15-23 (dark grey in Fig. 1). They form round and elongated rounded objects which are mostly continuously covered by a rim (light grey). The rim apparently consists of a single Fe-rich silicate phase whose composition does not correspond to that of olivine. The cation/oxygen ratio (0.7 - 0.73) rather suggests a phyllosilicate but which probably is also dehydrated. On top of the Fe-rich rim there is a discontinuous rim of a Ti,Al-bearing clinopyroxene with a high Mg/Fe ratio . The surface of the particle is covered by a very thin discontinuous magnetite rim (well visible in Fig. 1).

The trace element content of the particle's matrix (Table 2, Fig. 2) is chondritic for all, refractory and volatile, elements. However, all trace elements have somewhat elevated abundances as compared to CI and CM chondrites and Ba is over-abundant by about an order of magnitude. The trace element pattern of the spinel-rich CAI is fractionated among both, the refractory and moderately volatile elements, resembling a group II CAI pattern [4].

DISCUSSION. The main mass influx of extraterrestrial matter on the earth consists mainly of dust particles in the size-range 50 - 1000 μm [5]. Of that matter a surprisingly large proportion survives atmospheric entry without melting [6]. Such micrometeorites not only comprise coarse-grained crystalline and anhydrous but also phyllosilicate-dominated lithologies. The latter resemble CI-, CM-, and CR-type mineral-associations [7-10]. Bulk major and trace element abundances in MMs are consistent with that view [11,12] and differences between micrometeorite and chondrite elemental abundances could be shown to be mainly of terrestrial origin(s). The bulk composition of 92/15-23 typically fits that picture. Most elements have abundances comparable to those in CI and CM carbonaceous chondrites. Depletions in MMs in Ni, Ca, and Na are probably due to leaching of soluble phases from the MMs in the terrestrial environment and the enrichment in Ba could be due to atmospheric contamination (compare [11-14]). A similar situation holds for the much smaller IDPs (interplanetary dust particles [13]). Refractory inclusions are characteristic constituents of carbonaceous chondrites. Among MMs such inclusions are apparently rare. Only one fine-grained CAI has been reported so far [16] which has a group I trace element pattern but whose mineralogy is not known. A few CAIs are known from IDPs [17-19]. However, refractory minerals have been reported from many MMs and IDPs.

The spinel-rich CAIs in MM 92/15-23 are the first CAIs from extraterresterial dust with a group II pattern. Group II CAIs are quite common in CM chondrites [20], a fact which underlines the previously recognized relationship between MMs

and CM chondrites. However, the 92/15-23 CAI has elemental abundances which differ somewhat from those of carbonaceous chondrite CAIs (e.g., [21,22]). Contents of Th, Sc, and V are high in the 93/15-23 CAI (by factors 2, 2, and 10, respectively), and those of Ce and Cr are low. The low abundance of Sr could be a crystal-chemical effect (our CAI is almost pure spinel). All other deviations could indicate a formation of the 92/15-23 CAI in a more oxidizing environment as compared to that of the carbonaceous chondrite CAI formation site. This view is consistent with the higher abundance of pyroxenes and Fe-containing olivines in MMs as compared to carbonaceous chondrites.

ACKNOWLEDGEMENTS: This work was financially supported by FWF in Austria (project no. P8125-GEO), the Schweizerische Nationalfonds zur Förderung der wissenschaftlichen Forschung in Switzerland, and by IN2P3 and the European Community SCIENCE (Twinning and Operations) Programme (Contract no. SCI-CT91-0618,SSM) in France. We thank Thomas Presper and Franz Brandstätter for performing some of the EDS and EMP analyses.

REFERENCES. [1] Maurette M. et al. (1992) Meteoritics, 27, 473. [2] Zinner E. and Crozaz G. (1986) Intl. J. Mass Spectr. Ion Processes, 69, 17. [3] Anders E. and Grevesse N. (1989) GCA, 53, 197. [4] Martin P.M. and Maason B. (1974) Nature, 249, 333. [5] Hughes D. W. (1978) In: McDonnell J. A. M. (ed) Cosmic Dust, Wiley, 123. [6] Maurette M. et al. (1991) Nature, 351, 44. [7] Kurat G. et al. (1992) LPSC, XXIII, 747. [8] Christophe Michel-Levy M. and Bourot-Denise M. (1992) Meteoritics, 27, 73. [9] Presper T. et al. (1992) Meteoritics, 27, 278. [10] Brandstätter et al. (1991) Eur. J. Mineral. Beih., 3/1, 40. [11] Koeberl C. et al. (1992) LPSC, XXIII, 709. [12] Kurat G. et al. (1992) Meteortitics, 27, 246. [13] Jessberger E. K. et al. (1992) EPSL, 112, 91. [14] Presper T. et al. (1993) LPSCL XXXIV, 1177. [15] Kurat G. et al. (1993) 18th Symp. Antarct. Meteorites, NIPR, Tokyo. [16] Lindstrom D. J. and Klöck A. O. (1992) Meteoritics, 27, 243. [17] Zolensky M. E. (1987) Science, 237, 1466. [18] McKeegan K. D. (1987) Science, 237, 1468. [19] Stadermann F. J. (1991) LPSC, XXII, 1311. [20] Ekambaram V. et al. (1984) GCA, 48, 2089. [21] Kornacki A. S. and Fegley B. (1986) EPSL, 79, 217. [22] Wark D. A. (1986) EPSL, 77, 129.

Figure 1: BSE image of spinel-rich CAIs.

Figure 2: Orgueil-normalized [3] SIMS data.

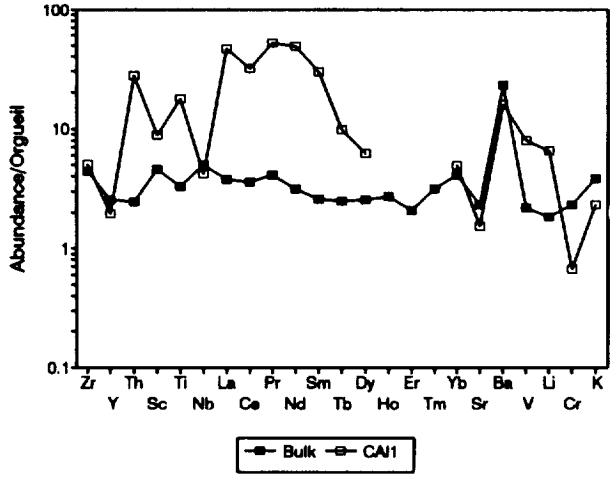

Table 2: MM92/15-23 Ion Probe Data

ppm	Bulk	error	CAI1	error
Li	2.71	0.05	9.8	0.18
K	2175.51	4.57	1313.23	5.81
Sc	26.89	0.24	51.7	0.66
Ti	1429.08	8.03	7754.04	37.38
V	120.67	0.72	445.32	2.73
Cr	6130.64	9.91	1783.09	6.81
Co	1517.9	5.21	302.17	4.24
Sr	18.15	0.3	11.78	0.47
Y	3.91	0.13	2.96	0.23
Zr	17.54	0.48	20	1.01
Nb	1.23	0.12	1.03	0.21
Ba	53.58	0.86	37.27	1.4
Th	0.07	0.04	0.8	0.26
La	0.89	0.08	11.01	0.58
Ce	2.2	0.14	19.56	0.84
Pr	0.37	0.05	4.64	0.37
Nd	1.45	0.11	22.82	0.86
Sm	0.37	0.09	4.3	0.56
Eu	0.08	0.05	0.13	0.1
Gd	0.25	0.13	0.5	0.8
Tb	0.09	0.03	0.35	0.15
Dy	0.62	0.08	1.52	0.29
Ho	0.15	0.04	0.09	0.06
Er	0.33	0.06	0.22	0.12
Tm	0.07	0.02	0.2	0.06
Yb	0.68	0.09	0.82	0.18
Lu	0.05	0.03	0.12	0.09

Table 1 MM93/15-23 Phase Compositions (wt%); *:EDXA normalized to 100%.

	Mx	Mx	Mx	Chr	Px	Sp-rich CAI Sp	Phyl*	Phyl*	Phyl*	Cpx*
SiO2	35.30	21.20	24.90	1.14	55.30	0.21	36.10	27.10	30.20	48.90
TiO2	0.17	0.18	0.09	0.97	0.13	0.09	0.29	0.35		0.63
Al2O3	2.10	3.80	5.50	15.80	1.90	70.30	3.40	10.00	4.70	2.56
Cr2O3	0.56	0.20	0.20	46.40	0.50	0.11	0.43	0.10		0.14
FeO	29.60	42.10	47.20	26.20	12.20	0.83	36.50	46.60	51.30	8.00
MnO	0.57	0.54	0.17	0.31	0.20		0.34	0.69	0.50	0.26
MgO	21.50	13.10	15.20	5.30	29.50	26.00	18.30	14.40	13.10	18.10
NiO	1.39	0.91	0.47				0.43	0.66		
CaO	0.31	0.17	0.07	0.03	0.15		4.20	0.10	0.30	21.40
Na2O			0.22							
SO3	6.70	17.30	3.40							
Total	98.20	99.50	97.42	98.15	99.88	97.54	99.99	100.00	100.10	99.99

Mx:matrix; Chr:chromite; Px:pyroxene; Sp:spinel;
Phyl: phyllosilicate; Cpx: clinopyroxene

NON-STEADY MODELING OF COMET'S WAKE IN THE RAREFIED LAYERS OF THE JOVIAN ATMOSPHERE

Kuzmitcheva M.Ju.,Popova O.P. (Institute for Dynamics of Geospheres, Russian Academy of Sciences, 38 Leninskii Prospekt, build.6, Moscow, 117979, Russia)

At high altitudes wake behind the comet must be considered with involving of non-equilibrium processes such as dissociation, ionization and radiation. The wake which is produced by flight of meteor with radius R and velocity V, can be modeled by motion of a cylindric piston with velocity V during time $t \sim R/V$.

The processes of ionization and dissociation are very essential for energy balance. Precise description of radiation requires to solve the equation of radiation transfer, but radiative energy losses can be considered as volume losses when the shock compressed layer is optically thin. Energy losses due to line radiation can be taken into account as volume losses when the next non-equality holds

$$C_{21}N_e / (A_{21}\theta + C_{21}N_e) << 1 \qquad (1)$$

where N_e is the electron density, $C_{21} \cdot N_e$ is the collision decay velocity of upper energy level of line, A_{21} is the velocity of radiative decay and θ is the escape factor, which permits to take into account a reabsorption of radiation and corresponds to photon probability to escape the volume. This condition means that the main manner of upper level deexcitation is radiative decay. The escape factor $\theta \sim (kR)^{-1.5}$ in a cylindrical case for Doppler shape of line. Here k is the absorption coefficient in the line center and R is radius of the cylinder. This condition allows to use volume energy losses for lower altitudes, when the shock becomes optically thick.

We modeled wake which will be formed by penetration of Shoemaker-Levi comet into Jovian atmosphere with initial velocity 60 km/s [1]. The method of solving is described in [2] and includes ionic dynamics into hydrodynamics code. Jovian atmosphere is assumed to consist of pure hydrogen. Cylindrical shock wave increases temperature Ti of heavy particles and leads to dissociation of molecules. For $Ti \approx 4$ eV the degree of dissociation is about 1 and the dissociation time is about 10^{-3} s, so the atomic hydrogen atmosphere was considered. Condition (1) permits to use volume energy losses approximation in Jovian atmosphere for thickness of compressed layer $R \sim 100 - 1000$ m at altitudes $H \sim 300 - 600$ km, depending on initial electron density.

Ionization processes strongly depend on initial electron density and electron temperature. Density of atmosphere is about 10^{-11} g/cm^3 and particle density is about $6 \cdot 10^{12}$ cm^{-3} at height H=440 km. Electron-heavy particle energy exchange time is about

NON-STEADY MODELING OF WAKE: Kuzmitcheva M.Ju., Popova O.P.

10^{-3} s for electron temperature about 0.5 - 2 eV. Ionization time τ is about 10^5 - 10^3 s for initial average charge $Z \sim 10^{-2}$ and electron temperature Te~ 1-2 eV, and τ is about $1\text{-}10^{-2}$s for average charge $Z \sim 10^{-2}$. On Fig.1 distributions of electron and ion temperatures Te and Ti and gas velocity v over radius r are represented for time t=0.15 s. Dashed and solid curves correspond to different initial electron densities ($6\cdot10^7$ and $6\cdot10^{10}$cm^{-3}). Electron excitation of Ly-α line increases radiation losses to 25% for 0.07 s in the latter case. So the shock velocity decreases on 2 km/s and Te and Ti fall too. A radius of the wake diminishes. The decreasing of the wake due to radiation losses is able to change essentially a pattern of gasdynamics flow of final explosion ejecta.

All dissociative, ionic and radiative processes in shocks are non-stationary for these heights (> 400 km) in Jovian atmosphere, so attempts to model the meteor wake with help of state equations rather than doubtful.

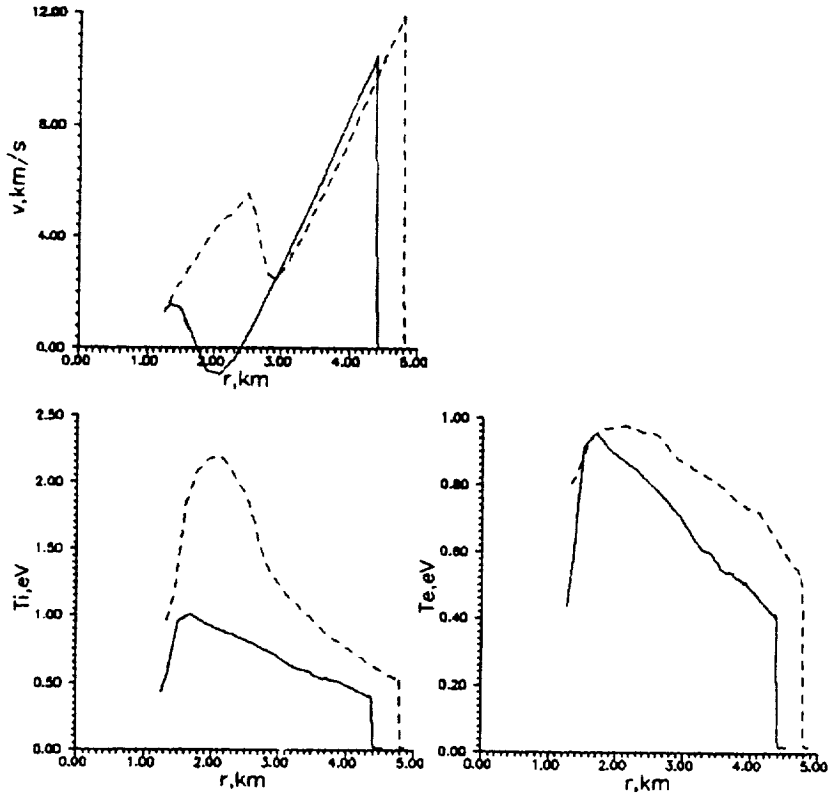

Fig. 1

References: 1. Chapmen C.R. (1993) Comet on target for Jupiter. Nature, **363**, 492-493. 2. Kosarev I.B., Kuz'micheva M.Yu., Popova O.P. (1993) Modeling of gasdynamics in multi-charged Khimicheskaya fizika, 12, 626-635.

VOLCANISM AND TECTONISM IN RUSALKA PLANITIA AND ATLA REGIO, VENUS; M. G. Lancaster and J. E. Guest (University of London Observatory, University College London, London, NW7 2QS, U. K.).

In order to investigate the relationships between volcanism and tectonism in Rusalka Planitia and Atla Regio, the geology of four adjacent Cycle 1 Magellan C1MIDRs has been mapped (C100N180, C115N180, C115N197, and C100N197). These cover nearly 12 x 10^6 km^2 between latitudes 7.6 S and 22.6 N, and longitudes 171.4 to 206.2 E. This region was chosen because it contains nearly all the types of volcanic and tectonic features observed on Venus, and covers plains as well as highlands.

The western half of the region comprises most of the volcanic plains of Rusalka Planitia, which are characterized by a large-scale pervasive fabric of NW-SE trending sinuous ridges that resemble lunar and martian wrinkle ridges [1]. A NW-SE to N-S trending deformation belt occupies the SW corner of C100N180, and contains several coronae including Eigin Corona (5.0 S, 175.0 E). The belt is the source for large, radar-bright, plains forming, flood lava flow fields. A similar collection of corona-like centers and deformation belts composed largely of ridges, is found in the NE corner of C115N197, where an extensive collection of lava flow fields is also present. Other smaller regions of radar-bright lava lie scattered across the plains. A number of N-S to NNW-SSE trending ridge belts occupy the north-central part of these plains.

The eastern half of the area is cut by a major rift-zone, which includes Ganis Chasma in the north, and several smaller rifts. The large volcano Ozza Mons (4.6 N, 201 E) lies at the southern end of Ganis Chasma, and has an extensive flow apron. A wide rift-zone runs SW from Ozza Mons, and the large volcano Maat Mons (0.5 N, 194.4 E) lies off the ridge axis to the SW of Ozza Mons. Many other lava flow fields lie to the south, west, and east of the Maat and Ozza Flow aprons, including a fissure-fed sub-parallel complex of flow fields to the SE of Ozza Mons. A large volcano is centered on Ganis Chasma at 17 N, 194 E, and has been dissected by intense faulting. The large volcano Sapas Mons lies at the center of the region at 9.5 N, 187.5 E, and a large volcano at 14.2 N, 204.7 E is comprised of a corona-like center surrounded by an extensive flow apron.

A region of elevated terrain known as Nokomis Montes is located in the north central part of the region at the north-eastern extremity of Ganis Chasma. Nokomis is composed of blocks of tessera which have been extensively rifted, and in this respect is very similar to Rhea Mons in Beta Regio [2]. An extensive outcrop of un-rifted tessera is found to the SE of Nokomis Montes, where it has been embayed by plains forming lavas to form large, irregular islands. The least common unit identified in the region is that of textured terrain [3], which is embayed by the ubiquitous radar-dark plains, and possesses a fine-scale structural grain which is similar in some respects to the tessera. As well as sinuous-ridges, and apart from the tectonic belts and zones, the plains contain abundant radar-bright lineaments of extensional origin. These features include swarms of en-echelon faults, straight and curvilinear lineaments which are thousands of kilometers in length, and graben. The lineaments belong to regional trends which are usually radial to tectono-volcanic centers, or normal to the deformation belts and rift-zones. A number of impact features are also scattered throughout the region.

The region has been subjected to a long and varied geologic history, composed of numerous episodes of deformation and volcanism. The tessera is the oldest unit in the region, and records a long history of extensional and compressional deformation that is generally not related to the adjacent tectonic structure on the plains which embay it. Outcrop patterns suggest it may form a basement underlying large areas of plains on C115N197. The textured terrain is also embayed by the plains, and is commonly associated with the ridge belts which deform it. The relationship between the tessera and the textured terrain is unclear, but they share a similar stratigraphic position and may be related in origin. The plains themselves are the most extensive unit, and are undoubtedly composed of numerous, superposed, flood-type lava flow fields, as well as many fields of small volcanos [4]. By virtue of their similar radar properties, most of these lava flow fields are indistinguishable from each other, although many fields with higher and contrasting backscatter to the rest of the plains have been distinguished and mapped. As elsewhere on Venus, the plains have evidently had a long and spatially variable history of formation in this region.

RUSALKA PLANITIA AND ATLA REGIO: Lancaster, M. G., and J. E. Guest.

The plains of Rusalka have been subject to widespread areal compressive deformation in the form of NW-SE wrinkle ridges, which form structurally coherent patterns over thousands of kilometers. In C115N180 the plains have been deformed into ridge belts, which have the same orientations as the adjacent sinuous ridges. Indeed, some of the wider sections of ridge belt appear to be merely concentrations of these ridges, suggesting that both these features were the result of the same, generally NE-SW compressive stress field. Magellan altimetry reveals the presence of other elevated belts which coincide with concentrations of sinuous ridges, which are not otherwise obvious as ridge belts within the SAR images.

Broad deformation belts in the SW and NW corners of the region are also marked by elevated topography and concentrations of sinuous ridges. However they also contain several coronae and corona-like features. Eigin Corona (5.0 S, 175.0 E) is defined by an annulus of ridges which in places both constitute, and elsewhere are crosscut by, ridges of the deformation belt itself. These structures, and the sinuous ridges on Rusalka Planitia, deform extensive radar-bright lava flow fields, whose source regions are the corona-like tectono-volcanic centers. Thus the emplacement of these fields has largely preceded the most recent deformation in the area.

Ganis Chasma and associated rifts in northern Atla Regio, cut the plains with a swarm of normal faults, fractures and graben. The flow apron of Ozza Mons both covers and is crosscut by the structures of the rift. The flow aprons of Maat and Ozza lie on older, rift related flow fields, and Maat Mons is one of the most recent volcanic centers in the area [5], superposing the flow apron of Ozza Mons. Several cross-cutting swarms of radar-bright lineaments, generally older than the flow aprons of Maat and Ozza Mons, radiate out from those volcanic centers, cross-cutting older flow fields and plains. Sinuous ridges are largely absent in the area of these large volcanos, the region of C100N197 being dominated by extensional deformation. The relative timing of rifting in Atla Regio and sinuous ridge and ridge belt formation elsewhere is unclear, and it is almost impossible to establish stratigraphic relations between features spaced more than a few hundred kilometers apart in the Magellan images. The NW extension of Ganis Chasma cuts an older, "banded terrain" which is interpreted as an old, degraded deformation belt. Each subparallel "band" is formed by a pair of parallel ridges with a shallow trough in between them. The whole belt has a mottled appearance and is embayed by plains in the north.

A number of fields of small volcanos are scattered across the region, and are commonly associated with swarms of radar-bright lineaments. The lineaments are presumed to be faults, and the extensional environment of the fault swarms may have favored the formation of these small volcanos. This is evidenced by the fact that many of them are aligned in chains along the lineament trends.

The volcanic and tectonic history of this region has been both varied and complex. However the overall sequence of plains deformation is broadly similar to that of other areas of Venus, such as Eistla Regio/Guinevere Planitia [6] and Lavinia Planitia [3]. Hence widely separated regions of the planet appear to have undergone the same general sequence of events.

REFERENCES: [1] Solomon, et al., (1992), *J. Geophys. Res.*, 97, 13,199-13,255, [2] Senske, et al., (1991), *Geophys. Res. Lett.*, 18, 1159-1162, 1991, [3] Squyres et al., (1992), *J. Geophys. Res.*, 97, 13,579-13,599, [4] Guest et al., (1992), *J. Geophys. Res.*, 97, 15,949-15,966, [5] Senske, et al., (1992), *J. Geophys. Res.*, 97, 13,395-13,420, [6] McGill, et al., (1991), *LPSC XXII*, 877-878.

STRATIGRAPHIC ASSESSMENT OF GUSEV CRATER AS AN EXOBIOLOGY LANDING SITE; Ragnhild Landheim, *Departments of Botany and Geology, Arizona State University, Tempe, AZ,* Nathalie A. Cabrol, *Observatoire de Meudon, France,* Ronald Greeley, *Department of Geology, Arizona State University, Tempe, AZ,* Jack D. Farmer, *NASA Ames Research Center, Moffett Field, CA*

SUMMARY An exobiology goal is to identify sites on Mars that exhibit a variety of sediments, including those which have the potential for preserving organic compounds and fossils. Gusev crater, a candidate site to meet these objectives, was a major depo center for Ma'adim Vallis. Terraces within Gusev crater suggest former standing water that may have functioned as a local base level for the channel; multiple terraces along Ma'adim Vallis provide evidence for episodicity in stream flow.

This study involves regional geologic mapping using Viking data for the area of 5° to 30°S and 175° to 190°W. Local mapping was performed for the Gusev crater area (12.4° to 17.6°S, 180° to 190°W) at a scale of 1:500K.

REGIONAL GEOLOGY Gusev crater is ~160 km in diameter and located within highlands, near the border with the northern lowlands. The areas SE and SW of the crater are ancient Noachian terrain that has been extensively modified by fluvial [1,2,3] and tectonic processes. The fluvial valleys here are more subdued than the surface adjacent to the central and northern areas east of Gusev. This appearance might be due to resurfacing by flooding from Ma'adim Vallis.

STRATIGRAPHY The oldest features near the Ma'adim Vallis outlet are Gusev and two 30 km craters [Fig. 1]. Prior to the incision of Ma'adim Vallis into these craters they acted as a dam, preventing water from flowing further north [4] and causing water to pond locally and to serve as a temporary base level. Terraces within Ma'adim Vallis might have formed in response to base level fluctuations determined by long-term variations in stream discharge. Terrace formation probably corresponds to the deposition of two flood units [Fd1 and Fd2] in Gusev crater by overtopping of the southwest and east crater rims and subsequent channelization of the flows. Similarly, the three youngest terraces [T9-T11] may correlate to three stratigraphic units [Ch9-Ch11] in Gusev crater.

The oldest unit, Fd1, occupies the eastern 1/4 of Gusev crater where it forms a rugged terrain; this may reflect removal of fines by wind, or erosion to the level of underlying impact ejecta. The unit lies ~100 m above the next youngest unit, Fd2. Unit Fd1 is believed to have originally covered the entire floor of Gusev and was subsequently eroded. Fd2 covers the western 3/4 of the crater floor, and exhibits smooth plains which are ridged in the northern part. Fd2 appears to have been deposited during overflooding of the SW rim of Gusev crater. Unit Ch9 corresponds to the third depositional episode in the crater. The unit forms plateaus interpreted to be the remnants of an ancient delta. The fourth depositional episode within Gusev crater is recorded by unit Ch10, recognized as an elongate, SE/NW patch of low albedo that projects across the crater floor north of Ma'adim Vallis. Flow from the channel apparently drained north following the main slope of the crater floor, but stopped short of the northwestern rim.

The final outflow event through Ma'adim Vallis is recorded by unit Ch11. This unit includes high albedo material extending 50 km beyond the outlet of Ma'adim Vallis, and is interpreted to be reworked material derived from unit Ch9. Furthermore, unit Fd1 is covered locally by delta deposits [Dd], representing fluvially transported material derived from areas east of Gusev. It is difficult to assess the age relations of the Dd unit relative to Fd2, Ch9, Ch10, and Ch11.

The floor of Gusev crater is extensively modified by aeolian activity: high albedo wind streaks oriented SE-NW are present in the lee of craters beyond unit Ch9. These streaks are interpreted as aeolian deposits derived from unit Ch11; their orientation is consistent with the inferred wind direction based on dunes at 12.8°S, 181.9°W, as well as predictions from models of atmospheric circulation [5].

RELEVANCE TO EXOBIOLOGY Gusev crater exhibits at least eleven episodes of fluvial deposition, punctuated by periods of lacustrine sedimentation. Our analysis suggests prolonged hydrological activity and sediment deposition within Gusev crater, which make it a high priority for exobiology [6, 7, 8, 9]. Calculations of terrace relief based on shadow measurements suggest a minimum thickness of 500 m for fluvial sediments exposed in Ma'adim Vallis, and 900 m including the upper levels of the adjacent plateau. Fine-grained delta and lacustrine sediments are prime targets to sample for organic compounds on Mars, especially if they have low permeability and are cemented, which could protect organic materials against subsequent oxidation [6,10]. Furthermore, sediments exposed in channel walls along the southern margin of Gusev crater and the distal reaches of Ma'adim Vallis constitute important targets for future robotic missions designed to search for a fossil record and for high resolution imaging during orbital missions. High resolution images could allow more detailed analysis for planning surface missions, as well as give insight into stratigraphic relations to further evaluate our interpretations of long-term depositional processes and cycles in the Gusev crater region.

REFERENCES CITED [1] Schneeberger D.M. (1989) *LPSC XX abstracts,* 964-965. [2] Brakenridge G.R. (1990) *JGR, 95,* 17, 289-17,308. [3] Cabrol N.A. et al. (1993) *LPSC XXIV abstracts,* 241-242. [4] Cabrol N.A. et al. (1994) *LPSC XXV abstracts,* XX-xx. [5] Greeley R. et al. (1993) *JGR, 98,* 3183-3196. [6] Farmer J.D. and Des Marais D.J. (in press) *Case for Mars V proceedings,* XX-xx. [7] Farmer J. et al. (in press) in *Mars Landing Site*

Catalog (Sec. Ed.), NASA Refr. Pub. #1238, R. Greeley (ed), XX-xx. [8] Landheim R. et al. (1993) *LPSC XXIV abstracts,* 845-846, 1993. [9] Landheim R. et al. (in press) *Case for Mars V proceedings,* XX-xx. [10] Farmer J.D. and Des Marais D. J. (in press) *Case for Mars V proceedings,* XX-xx.

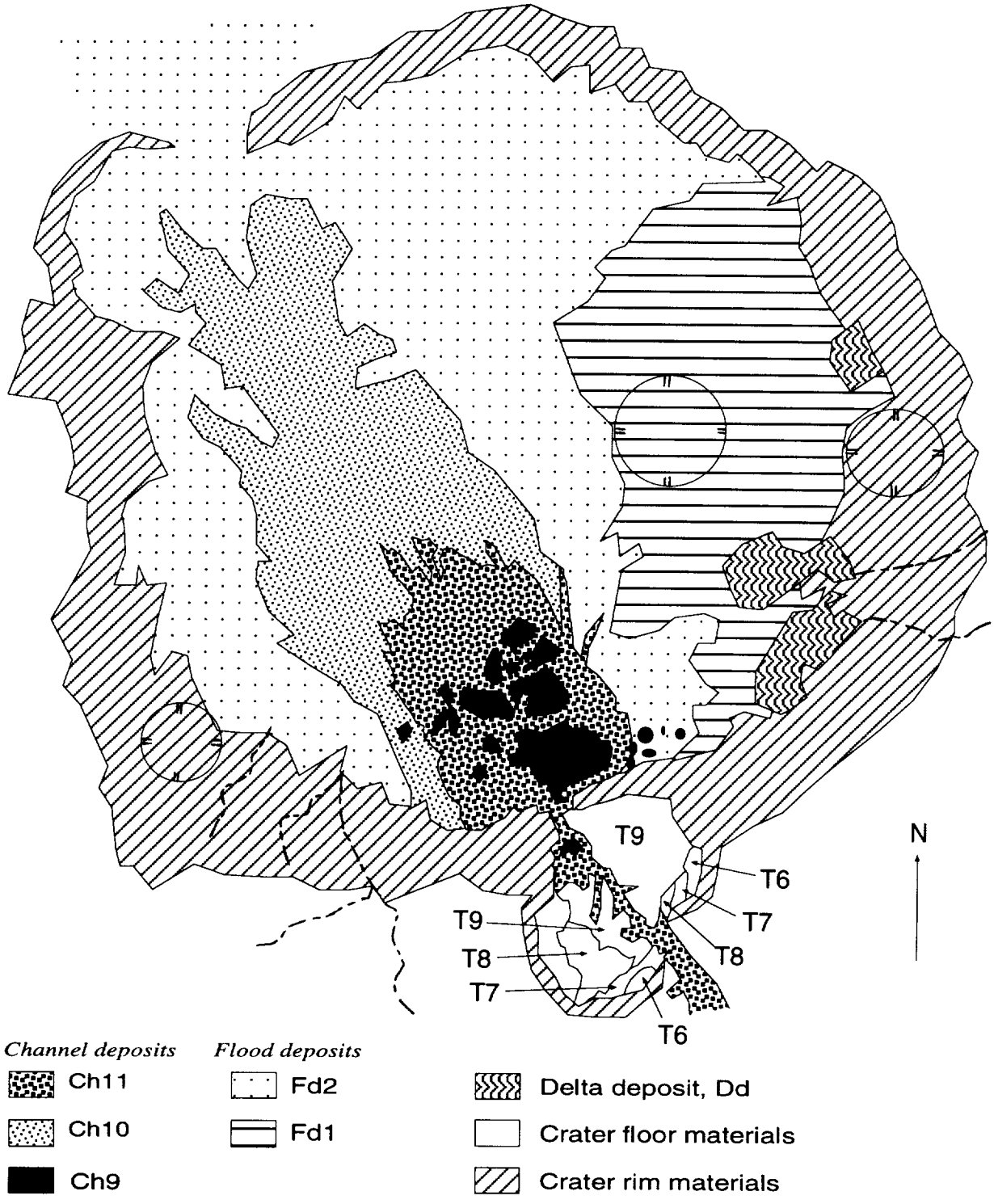

Figure 1. A geologic sketch map of Gusev crater.

MOSSBAUER AND SPECTRAL (VISIBLE AND NEAR-IR) DATA FOR Fe^{3+}-SUBSTITUTED RUTILE; H. V. Lauer Jr. (LESC, Houston, Tx 77058), R. V. Morris (NASA/JSC, Houston, Tx 77058), and R. K. Vempati (Lamar University, Beaumont, Tx)

INTRODUCTION: Titanohematite and rutile containing some Fe^{3+} are possible highly oxidized weathering products of ilmenite and titanomagnetites. We report here Mossbauer and reflectivity data (visible and near-IR) for Fe^{3+}-substituted rutile as a part of our continuing studies of ferric-substituted minerals that might have bearing on the interpretation of Martian spectral data.

SAMPLE PREPARATION: Appropriate amounts of titanous chloride and ferric chloride were mixed together in a polyethylene beaker. To 25 - 30 ml of this solution, 100 ml of 7M sodium hydroxide was added while constantly stirring. After the entire NaOH solution was added, the entire contents of the beaker (brown precipitate + supernate) was aerated by pouring it back and forth between two beakers several times. The solution was then allowed to incubate for an hour. After washing the precipitate several times in deionized water, the supernate was poured off and the precipitate was dialyzed against deionized water for three weeks. Several times a day the dialysis water was changed and the dialysis bag was washed off and rotated to stir its contents. With time the precipitate slowly changed color to a light yellow tan. Once the contents of the dialysis bag appeared to be uniform in color and no more color changed was observed, the contents of the bag was washed and transferred back to a 1 L polyethylene beaker. The volume of the solution was increased to 500 ml using 0.3M NaOH. The beaker was covered with a watch glass and incubated at 70 C in a convection oven for 48 hrs. After cooling the resulting precipitate was again dialyzed against deionized water for a week. The dialyzed material was freeze dried and then calcined in air for 40 hrs at 500, 650, 800, 1000 C. The only polymorph of TiO_2 stable above 700 C is rutile.

RESULTS AND DISCUSSION: We will discuss result for five of the samples heated to 1000 C. They will be referred to as RuF(i)/1000 with i = 1 - 5 referring to the starting sample ID. The iron content in the sample increases with i (i = 0 is undoped). Fig. 1 shows the reflectivity spectra for RuF0/1000 through RuF5/1000. Their room-temperature Mossbauer spectra were all ferric doublets in octahedrally coordinated sites (IS ~ 0.36 mm/s).

Comparing the reflectivity spectrum of RuF0/1000 to those of RuF(1 - 5)/1000 shows that the increased depth of the spectral features is consistent with increasing Fe^{3+} content in each successive sample. Also, the reflectivity spectra of RuF(1,2,3) are similar, and RuF(4,5) are similar. This same grouping is also found in the quadrupole splittings, with the first group having distinctly lower quadrupole splittings (0.36 versus 0.60 mm/s). The reason for the difference is not clear, but the local environment of ferric iron clearly changes between the RuF3/1000 and RuF4/1000 samples. It may be that the pair transiton shifts to lower energies and thus obscures the band minima at ~875 nm ($^6A_1 \rightarrow {}^4T_{2g}$) and 475 nm ($^6A_1 \rightarrow {}^4E, {}^4A$).

FIGURE 1

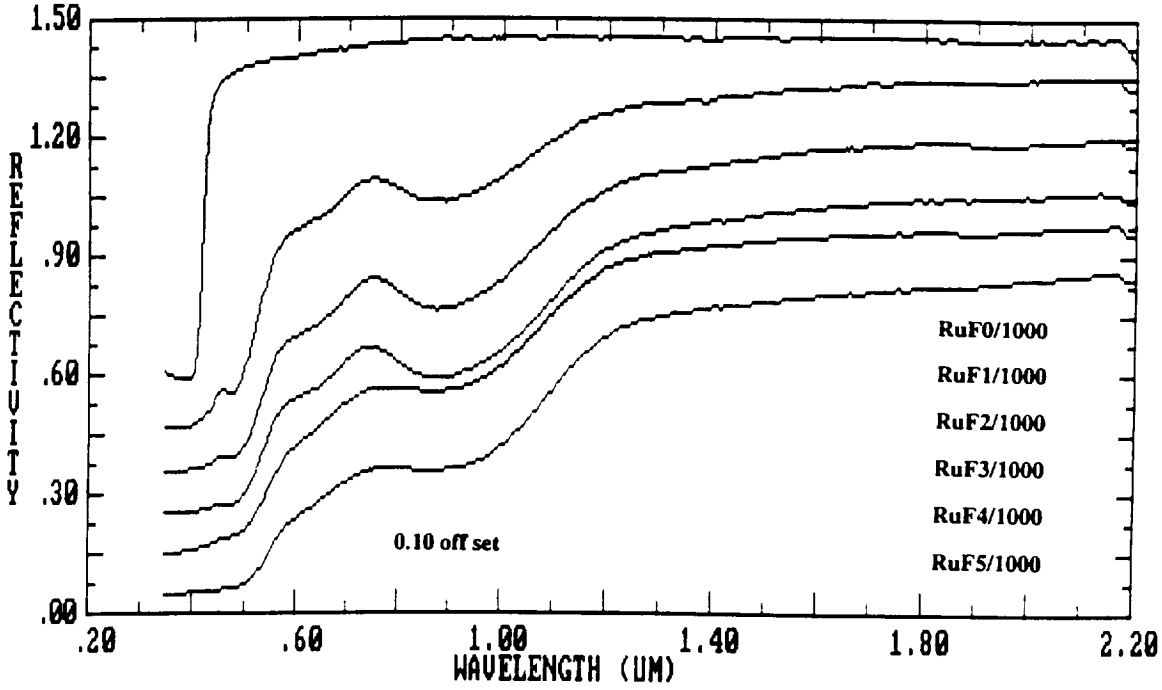

AN EXPERIMENTAL STUDY OF IRON SULFIDE FORMATION KINETICS IN H_2-H_2S GAS MIXTURES AND APPLICATION TO IRON SULFIDE CONDENSATION IN THE SOLAR NEBULA, D. Lauretta[1] and B. Fegley, Jr.[1,2] (1) Dept. of Earth & Planetary Sciences, and (2) McDonnell Center for the Space Sciences, Washington University, St. Louis, MO 63130-4899 USA.

Introduction. Troilite (FeS) is the most common sulfur-bearing mineral in meteorites. Furthermore, FeS, which is the dominant sulfur-bearing condensate in solar gas, was presumably an important sulfur-bearing phase accreted by the terrestrial planets. It is generally believed that troilite is the only iron sulfide to form in a solar composition gas [1,2]. Recently it was suggested that pyrrhotite ($Fe_{0.875}S$) would condense before troilite [3]. Thermochemical equilibrium calculations were done for stoichiometric FeS and pyrrhotites ranging from $Fe_{0.98}S$ to $Fe_{0.875}S$ (see Figure 1). These show that FeS forms at the pressure independent temperature of 719 K in a solar composition gas via the net thermochemical reaction $H_2S(g) + Fe(metal) = FeS(solid) + H_2(g)$. The calculations show that FeS forms 56° before $Fe_{0.875}S$. This is in agreement with [1] and [2] but contrary to [3]. Using thermodynamic data from [4] and [5] the uncertainty in the condensation temperatures is ±20K. Fegley [6-8] presented theoretical models of troilite formation kinetics which predict that FeS formation is rapid relative to the estimated nebular lifetime of 10^{13} seconds. However, prior to this study no experimental data were available on the kinetics of troilite formation in the solar nebula. Here we present experimental results which show that the reaction rate is indeed very rapid.

Experimental Methods. The above reaction was studied by suspending iron foil (Johnson Mathey Puratronic grade, 99.9975%), of known weight and surface area in a Deltech vertical tube furnace within an H_2S /H_2 gas mixture (868 ppm H_2S ±2%) for varying time periods and at temperatures of 500-650 °C with an uncertainty in the temperature of ±5K. These conditions fall within the troilite stability field (see Fig. 1). Standard techniques were used to control gas flow rates and temperature. The reaction rate was determined by measuring the weight change of the reacted samples after removal from the furnace.

Results. Figure 1 shows condensation temperatures of FeS and pyrrhotites ($Fe_{0.98}S$, $Fe_{0.90}S$, $Fe_{0.89}S$, $Fe_{0.875}S$) at different H_2/H_2S ratios calculated from thermochemical data presented in [4]. The diagram predicts that either troilite or $Fe_{0.98}S$ is the first iron sulfide to condense from a solar composition gas. However, X-ray diffraction of several experimental samples shows only troilite and no detectable pyrrhotite. Once troilite forms in a solar gas, pyrrhotites are unstable and do not condense. The solid circles in Figure 1 represent the location of the runs that reacted to produce troilite. The open circle represents run 1, which did not react over 43 hours, indicating that it lies in the stability field for iron metal. The condensation temperatures for the iron sulfides at the solar H_2/H_2S ratio ($H_2S/H_2 \sim 3.69 \times 10^{-5}$) are listed in Table 1. The reaction rates for each run are presented in Table 2. The samples that were exposed to the gas for relatively longer periods of time show the lowest reaction rates, even though these samples were kept at higher temperatures. This is possibly due to diffusion control and to the rate dependence on T and f_{S2} which varies as $\exp[2 \log_{10}(f_{H2S}/f_{H2})-1.740-3388.6/T]$.

Applications to the Solar Nebula. The sulfurization of Fe-alloy grains is widely acknowledged to have been responsible for the incorporation of sulfur into solid material in the solar nebula. This assumes that the rate of FeS formation is rapid relative to the lifetime of the solar nebula. The kinetics of this reaction are important for understanding FeS accretion by the terrestrial planets, the origin of troilite in meteorites, and gas-grain chemistry in protostellar accretion disks. However, the only available kinetic data on iron sulfurization reactions to date were obtained by materials scientists working at pressure, temperature, and compositional conditions which do not apply to the solar nebula. This study is the beginning of a larger research project designed to increase the amount of information available on gas-solid reaction kinetics under solar nebula conditions. This study shows that the retention of sulfur by troilite formation is a relatively rapid process at the H_2/H_2S ratio under consideration. Future experiments are being planned to measure these rates under conditions much closer to those estimated to occur in the solar nebula ($\log_{10}(P_{H2}/P_{H2S}) \sim 4.4$).

Summary. Thermodynamic calculations show that troilite is the most likely candidate for the iron sulfide phase responsible for the retention of sulfur in the solar nebula. This requires that the reaction rate be fast enough for the reaction to occur within the lifetime of the solar nebula. The thermodynamic and kinetic results presented in this abstract strongly suggest that troilite is the only stable iron sulfide in the solar nebula and that troilite formation occurred within the lifetime of the solar nebula.

Acknowledgments. This work was supported by grants from the NASA Origins of Solar Systems and Planetary Atmospheres Program to Washington University (B. Fegley, Jr., P.I.). We acknowledge advice from K. Lodders and technical assistance from D. Kremser and R. Poli.

PRECEDING PAGE BLANK NOT FILMED

TROILITE FORMATION KINETICS: D. Lauretta and B. Fegley Jr.

References. [1] J.S. Lewis 1972 Earth Planet. Sci. Lett. 15, 286-290; [2] J.W. Larimer 1967 Geochim. Cosmochim. Acta 31, 1215-1238; [3] J.A. Wood and A. Hashimoto 1993 Geochim. Cosmochim. Acta 57, 2377-2388; [4] F. Gronvold and S. Stolen 1992 J. Chem. Thermodynamics 24, 913-936; [5] JANAF Thermochemical Tables third edition 1985, Jour. Phys. Chem. Ref. Data 14; [6] B. Fegley, Jr. 1988 in Workshop on the Origins of Solar Systems, LPI Tech. Rept. No. 88-04, pp. 51-60; [7] B. Fegley, Jr. and R.G. Prinn 1989 in The Formation and Evolution of Planetary Systems, ed. H.A. Weaver and L. Danly, Cambridge Univ. Press, pp. 171-211; [8] B. Fegley, Jr. 1993 in *Chemistry of Life's Origins*, edited by M. Greenberg and V. Pirronello, Kluwer Academic Publishers, Dordrecht, Netherlands.

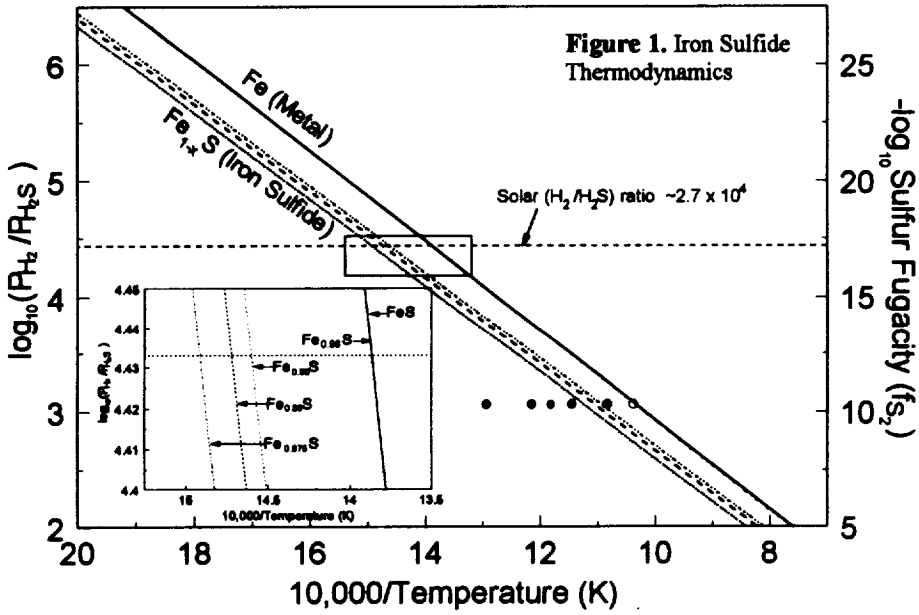

Figure 1. Iron Sulfide Thermodynamics

Table 1. Condensation temperatures for Fe sulfides at the solar H_2/H_2S ratio

Sulfide	$T_{Condense}$ (K)
FeS	719.3
$Fe_{0.98}S$	718.9
$Fe_{0.90}S$	678
$Fe_{0.89}S$	672
$Fe_{0.875}S$	663

Figure 2. Photograph of a cross-section of reacted sample R2. Note the iron sulfide layer surrounding the metallic iron core. The scale bar equals 0.17mm. The iron foil had an initial thickness of 0.25 mm.

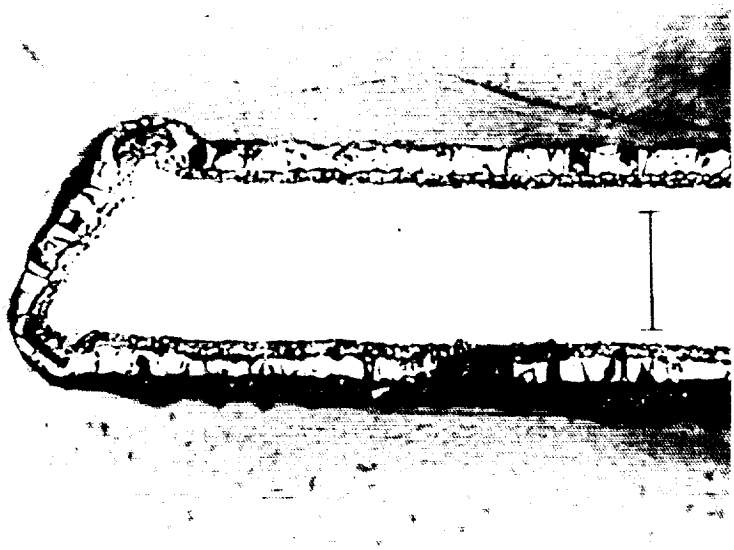

Table 2. Rate data

Run Number	Temperature (K)	Duration (min)	Rate x 10^{16} (atoms S /cm^2 min)
1	963	2,575	0
2	923	2,810	5.02
3	823	2,963	4.69
4	873	872	8.53
5	776	731	6.72
6	848	456	12.86

THE MASSIVE O,B STAR OF SECOND GENERATION MAY BE SOURCE OF INTERSTELLAR DIAMOND, SiC AND GRAPHITE IN CHONDRITES.
A.K.Lavrukhina and A.V.Fisenko. *V.I.Vernadsky Institute of Geochemistry and Analytical Chemistry, Russian Academy of Sciences, Moscow. Russia*

The analysis of properties and isotopic anomalies of interstellar diamond, SiC and graphite grains in chondrites shows possibility of formation of these grains and their isotopic compositions during various evolution stages of alone massive O,B star of second generation.

The interstellar grains of diamond, SiC and graphite in primitive chondrites have their typical peculiarities. They differ one from another by structures, granulometric composition, isotopic compositions of H, C, N, O, Si and by presence of products of various nuclear reactions (r, p or s process) [1]. Hence these relic phase were formed in different astrophysical conditions. Unlike from many investigators, who have proposed several sources of their formation (novae, supernovae, AGB and WR stars), we propose the scenario of processes in alone massive O,B star of second generation passed stages of WR star and supernova. It is establish on examination of nuclear reactions on all evolution stages of such star [2,3]. They have lead to anomalous isotopic composition of elements during condensation of diamond, SiC and graphite grains. Main peculiarity of WR star is intensive interactions of powerful stellar wind with the matter of circular nebula, which is formed at the expense of H shell escape after He burning beginning in star core. This have lead to great varieties of chemical and isotopic compositions of grains, C/O ratios, P,T parameters in different parts of nebula.

Most of SiC grains were condensed in stellar wind regions, corresponding to He burning beginning, when they contain many products of CNO and Mg-Al cycles, and C/O > 1 [4]. About that witness high values of ^{13}C and ^{14}N contents ($^{12}C/^{13}C \geq 4$ and $^{14}N/^{15}N \leq 5000$) and of $^{26}Al/^{27}Al$ ratios [5] in SiC grains. For them have taken place the $^{26}Al/^{27}Al$ - $^{12}C/^{13}C$ correlations. Graphite grains were condensed in nebula regions, where predominates a stellar wind, consisting of products of H burning beginning in WR star shell. In these conditions $^{12}C/^{13}C$ ratio reacts to equilibrium value, but ^{14}N is not still accumulated. This wind mixes with wind, consisting of products of He burning during a transition of WN stage to WC stage. It is accompanied by nuclear reactions, which have lead to ^{18}O excess [6], $^{12}C/^{13}C$ increase and $^{14}N/^{15}N$ decrease.

THE MASSIVE O,B STAR... Lavrukhina A.K. & Fisenko A.V.

The great differences of isotopic anomalies of diamond from the same of SiC and graphite witness that it was not formed in circular nebula during H burning in core and WR stage. The anomalous Xe-HL, inherent only to diamond, was formed in r and p processes in He shell during supernova [7]. Therefore the most probably source of diamond formation is a discharge region behind shock wave front from supernova. We propose a model, based on assumption, that diamond condensation have taken place in mixed layer of He and H shells. It was formed by turbulent mixing of shells during supernova explosion. This mixing have lead to observed isotopic compositions of C($^{12}C/^{13}C \approx 90$) and N ($^{14}N/^{15}N \approx 370$) [8]. The simultaneous implantation of Xe-HL and great amounts of He and Ne in diamond grains [8] had taken place only in that mixed layer. The enrichment of diamond in H (10-40 atom %) [9] also witnesses about its formation in hydrogen environment. Very small sizes of diamond grains (average 26 Å) and data of X-ray and differential thermal analysis [10] of diamond fraction from Efremovka CV chondrite indicate that diamond grains very likely were formed by means of fast non-equilibrium processes from carbon atoms in gas phase. Ultrasmall grains of diamond were rapid carried out from He and H layer by shock waves and were mixed with circular nebula matter. The enrichment of diamond in D (δD=245-342‰) [8] is consequence of ion-molecular reactions at low temperatures in cooled supernova remnant. Because of very great surface of diamond grains this effect can be considerable.

References: [1] Lavrukhina A.K., Fisenko A.V. (1993) Geochimia, in press. [2] Lavrukhina A.K. (1993) LPS XXIV,853. [3] Lavrukhina A.K. (1993) Geochimia (Russian), N3, 309. [4] Prantzos N. (1985) Preprint. [5] Amari S. et al. (1992) LPS XXIII, 27. [6] Hoppe P. et al. (1992) Meteoritics, 27, 198. [7] Lavrukhina A.K. (1986) Geochimia (Russian), N2, 131. [8] Anders E. (1988) In: Meteorites and the early solar System, 927. [9] Vigar A. et al. (1989) LPS XX, 1158. [10] Fisenko A.V. et al. (1992) Geochimia (Russian), N1, 155.

ON FORMING Mg-26 AND Cr-53 ANOMALIES IN SOME METEORITIC MINERALS; A.K.Lavrukhina and G.K.Ustinova, Institute of Geochemistry and Analytical Chemistry, RAS, Moscow 117334, Russia

Formation of Mg-26 and Cr-53 anomalies due to decay of the radioactive nuclides Al-26 and Mn-53, respectively, which were produced by accelerated particles with a variable energy spectrum in some refractory minerals of the protosolar nebula in the conditions of shock wave propagation is considered.

A new possible mechanism of forming isotopic anomalies in the protosolar nebula has been revealed in our previous works /1-3/. It is caused by changing energy spectrum of accelerated particles in the conditions of strong shock wave propagation /4/ (e.g., due to a supernova explosion), so that small-scale isotopic heterogeneity of all the nuclides whose excitation functions are sensitive to the form of the energy spectrum of particles inevitably arises. In /5-7/ the formation of isotopic anomalies of Mg-26 and Cr-53 is considered, with their radioactive progenitors Al-26 and Mn-53, respectively, being assumed to be produced in the gaseous phase of the protosolar nebula during the strong shock wave propagation, and further, after solidifying minerals to decay in situ. However, some relic grains of the refractory dust could exist in the nebula and survive the extreme PT-conditions at the formation of the solar system. Therefore, the radioactive progenitors could be produced directly in the mineral grains irradiated by the accelerated particles. In the work such a model of generation of Mg-26 anomalies in corundum, hibonite, melilite, spinel and silicon carbide grains as well as of Cr-53 anomalies in olivine, troilite, metallic FeNi, alabandite, pyroxene, Fe and Mn orthophosphate, chromite and daubreelite minerals, irradiated by the accelerated particles with the variable energy spectrum is calculated. As follows from Fig.1a, the Al-26/Al-27 ratio formed in the considered minerals under the same irradiation conditions proved to be about equal except for

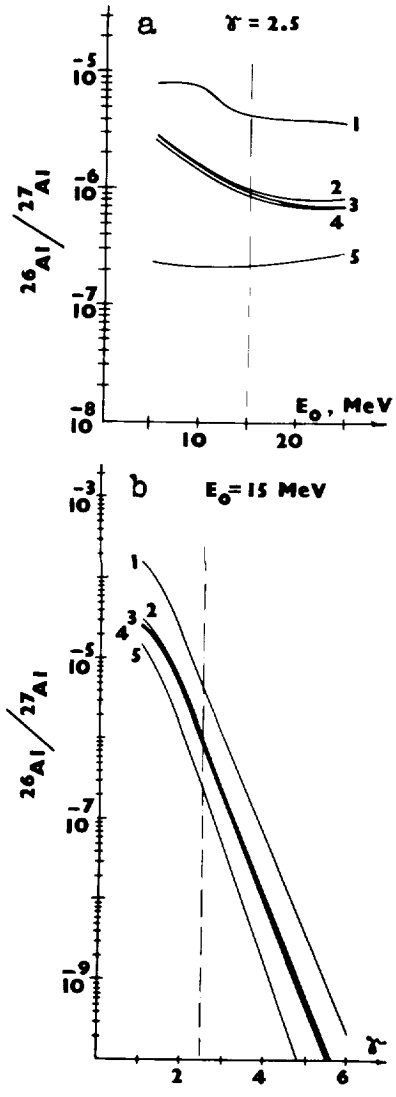

Fig.1- Al-26/Al-27 ratios formed in the mineral grains in dependence on: /a/ the cut-off energy E_0 of the average spectrum (γ = 2.5) of accelerated particles; and /b/ the spectral index γ of the spectrum above the average cut-off energy E_0=15 MeV (1 -in gaseous phase; 2,3,4 and 5 -in grains of melilite, spinel, corundum (similar to hibonite) and SiC, successively)

Mg-26 AND Cr-53 ANOMALIES: Lavrukhina A.K. and Ustinova G.K.

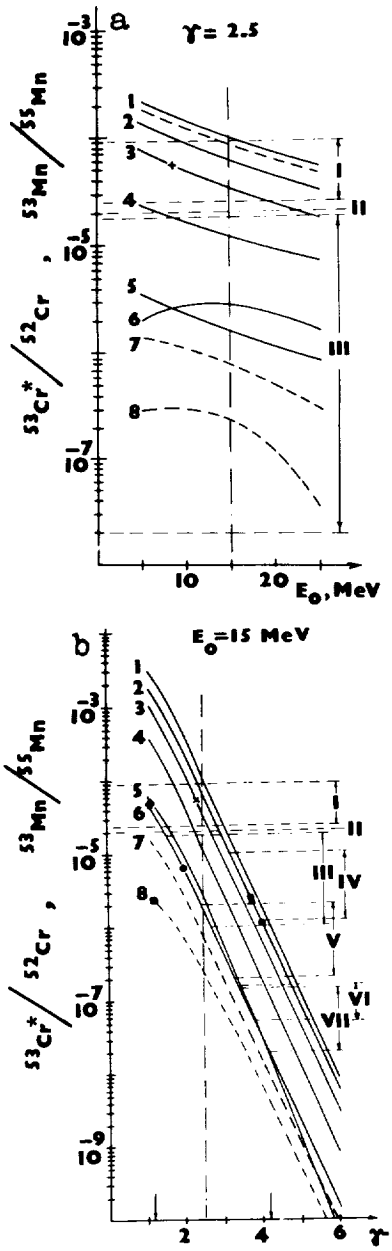

Fig.2- Mn-53/Mn-55 (solid curves) and Cr-53/Cr-52 (dashed curves) formed in the minerals in dependence on E_0 /a/ and γ /b/ (1- in gaseous phase; from 2 to 8, successively,- in olivine, troilite, FeNi, $Fe_3(PO_4)_2$, MnS(similar to $Mn_3(PO_4)_2$ and pyroxene), Cr_2FeS_4 and Cr_2O_3; I -CAI Allende; II- Orgueil; III- differentiated meteorites in /a/ and graftonites of IIIAB irons in /b/; IV- olivines of angrites; V and VI- alabandites and sphalerites of EL3-chondrites, respect.; VII- MnS of IAB irons; x- Acapulco; ♦-Wiley; • -Indarch; ■ -Eagle Station; exp.data are from /8-13/)

5 times lower that in SiC. On the other hand, the Al-26/Al-27 ratios formed directly in irradiated minerals are 5 times lower than those generated in the gaseous phase and captured by minerals during condensation. The range of possible Mn-53/Mn-55 ratios in the considered minerals irradiated in the same conditions accounts for more than two orders of magnitude (see Fig.2a). The highest Mn-53/Mn-55 ratios, $(0.1\text{-}0.6)\cdot10^{-4}$, i.e., only slightly lower than in the gaseous phase ($1.0\cdot10^{-4}$), are produced in olivine, troilite and FeNi; they total $(2\text{-}3)\cdot10^{-6}$ in Fe and Mn orthophosphate, alabandite and pyroxene; and Cr-53/Cr-52 ratios account for $(3\text{-}8)\cdot10^{-7}$ in daubreelite and chromite.

In the conditions of shock wave propagation the Al-26/Al-27 as well as Mn-53/Mn-55 and Cr-53/Cr-52 ratios can vary by 6-7 orders of magnitude that well exceeds the above indicated differences between the minerals (see Figs.1b and 2b). The observed variations of these ratios in meteorites, even being smoothed by diverse secondary processes resulted in redistribution of elements, conform, on the whole, to the calculated range, e.g., the measured Al-26/Al-27 diapason in hibonites of different meteorites totals 10^{-8}-10^{-3}. It testifies to a strong incident heterogeneity of distribution of the extinct radionuclides in the protosolar nebula, in partcular, among the condensation reservoirs of minerals that should be remembered in using ones as cosmochronometers of meteorite matter.

References. [1] Lavrukhina A., Ustinova G., LPS XXIII (1992)761. [2] Lavrukhina A., Ustinova G., Doklady RAN, 326(1992)166. [3] Lavrukhina A., Ustinova G., Astron.Vestnik, 26(1992)62. [4] Ellison D., Eichler D. Ap.J., 286(1984)691. [5] Ustinova G., Lavrukhina A., LPS XXIII (1992) 1461. [6] Lavrukhina A., Ustinova G., Geokhimia 3(1993)320. [7] Lavrukhina A., Ustinova G., LPS XXIV (1993)855. [8] Birck J., Allegre C., Nature 331(1988)579. [9] Harper C.et al., LPS XXIII (1992)489;491. [10] Hutcheon I.et al., ibid.565. [11] Lugmair G.et al., ibid.823. [12] Goresy A.et al., ibid.331. [13] Rotaru M.et al., LPS XXI (1990)1037.

Characterizing Image Errors Using the Spectral Mixture Framework

M.E. Lawler and J.B. Adams, Geological Remote Sensing, Univ. of Washington, Seattle, WA 98195

Summary

Spectral mixture analysis (SMA) has been used to analyze multispectral images from a variety of instruments such as the Phobos 2 Infrared Spectrometer (ISM), Galileo Solid State Imager (SSI), and Landsat Thematic Mapper. We report here on a new approach within the SMA framework for estimating the residual errors in an image's encoded radiance (DN values) and then computing the errors in the estimated fractions of reference endmembers. Error analysis is an essential step for quantifying thresholds of detectability of scene components and for determining the reliability of classifications based on fractions of endmembers.

Introduction

SMA has been applied to images of Mars, the Moon, many environments on Earth, and even galaxies. (A few selections from the SMA literature are given in [1–5].) The SMA approach deals with the problems of sub-pixel spectral mixing, terrain illumination, and calibration by linearly transforming DN values from each pixel into fractions of reference endmembers. The reference endmembers correspond to materials important to an observer in the field, e.g. minerals, rocks, soils, vegetation, etc., each of which has a characteristic reflectance spectrum.

The SMA framework assumes that each pixel in the scene comprises mixtures of endmembers, and that in each spectral band the radiances from these endmembers add linearly. If we know the spectrum of each likely endmember, then by inversion we can find the fractions of each endmember in each pixel. The method requires the analyst to have a good knowledge of the likely scene characteristics, so that reasonable endmembers are selected. From the mixtures of reference endmembers yielded by SMA, an analyst can make classifications that correspond to useful geological or ecological field units.

Error Analysis Framework

Before being analyzed by SMA or any other method, a raw image should be corrected to the fullest extent possible to remove geometric distortion, to co-register all band images to each other, to linearize detector response, and to remove other unwanted instrumental effects. Some residual errors will remain in the DN values even after such correction.

It is particularly important to quantify fraction errors when we are trying to extract information at the edges of the reliability of the data. This is especially true in threshold detection, where insufficient signal to noise may render a particular endmember statistically undetectable [6]. Moreover, relatively small errors in some bands' DN values can create relatively large errors in fractions of some endmembers.

Residual errors can have serious effects on the reliability of the classifications. The classification method in SMA relies upon dividing up endmember space into domains that represent classes of interest. For example, if a pixel has less than X% of endmember A and more than Y% of endmember B, it may be assigned to a certain class. However, if there are significant residual errors in the estimated endmember fractions, then pixels with fractions near the boundaries of X% and Y%, respectively, may be assigned to the wrong class. Conversely, the reliability of our classifications could be characterized if we knew the likely errors in endmember fractions.

In SMA the endmember fractions are derived as linear functions of the DNs. The errors in endmember fractions are therefore also linear functions of the errors in the DNs. Namely, for each pixel, the covariance matrices are related as

$$(\mathrm{cov}_{\text{endmember fraction}}) = \mathrm{P}(\mathrm{cov}_{\text{DN values}})\mathrm{P}^{\mathrm{T}}$$

P is the matrix that yields the vector of endmember fractions when multiplied by the DN vector.

Thus if we can estimate the covariance matrix of the DNs for each pixel, then the problem can be solved. The approach we have developed is to estimate the DN errors due to every possible source in an instrument, sum them statistically, and then apply the above equation. Important error

sources in most instruments are misregistration between different band images, optical aberrations and imperfections, electronic and quantization noise, and detector nonlinearities and biases.

Principal Error Sources

In every imaging system each pixel in the detector is "contaminated" to some degree by radiation from nearby pixels. The extent of the contamination can be estimated if we know the instrument's modulation transfer function (MTF) [7] and the underlying spatial frequency properties of the scene down to scales of multiple cycles per pixel. As an example, in the Galileo SSI instrument [8] an average of 43% of the signal from each pixel is contributed by portions of the scene outside that pixel. While this effect will average out across an image, it reduces our certainty in classifying any particular pixel.

Any residual misregistration that remains after applying standard registration algorithms will limit the accuracy of endmember fractions and classification. For example, a Galileo SSI pixel misregistered by 20% of a pixel width in one band with respect to the other bands will have roughly 5% more contamination than if all bands were perfectly registered. Each band has its own MTF, so the error contribution of misregistration will differ accordingly in different bands. Because the MTF will be lower at longer wavelengths (the point spread function is broader), there will be larger errors in estimated fractions of endmembers that are highly reflective at long wavelengths.

Fourier image analysis can be used to assess the errors arising from both the MTF and misregistration. The following is done in each band. First a Fourier transform is developed that represents the underlying sub-pixel spatial frequency properties of the scene, based upon any available or hypothetical knowledge of the properties of the scene. Add to this the Fourier transform of the DN image, divided by the MTF (including corrections for optical distortion). Take the inverse transform of this sum, and resample the new image according to how the bands are misregistered, if this is known. This new image should be an approximation of the original, perfectly registered scene, at least in terms of its spatial frequency components and registration. Compare it to the original DN image to generate a DN covariance matrix that represents the DN errors for an average pixel.

Other possibly important error sources are quantization of the DN values, data roundoff errors, and biases and non-linearities that remain after standard corrections to the raw image. Smearing due to movement of the target during the exposure or between exposures with sequential filters will add further errors to the DNs. The Fourier domain may be the best way to handle this problem much as is done for misregistration. When each likely significant error source has been characterized by a DN covariance matrix, the covariances can be statistically added and the covariance matrix for the endmember fractions computed.

Conclusions

The SMA method provides a useful framework to quantify errors in spectral image analysis. By characterizing these errors, it is possible to determine whether detection requirements can be met. It also becomes possible to evaluate classifications, and to make them more robust to the effects of errors. It may ultimately be possible to improve registration between band images by iterating on different fits between band images until the residual errors are minimized. This work also illustrates that, if the most effective use is to be made of future multispectral imaging instruments, then before flight the MTFs should be measured in all bands to spatial frequencies into the range of multiple cyles per pixel.

References

[1] Adams, J.B. et al. (1993) in *Topics in Remote Sensing 4: Remote Geochemical Analysis*, Pieters and Englert, Eds., Cambridge University Press, p. 145; **[2]** Adams, J.B. et al. (1986) *JGR* **91**, No. B8, 8098; **[3]** Smith, M.O. et al. (1990) *Remote Sens. Env.* **31**, 1; **[4]** Gillespie, A.R. et al. (1990) *Proc. Airborne Sci. Workshop: AVIRIS*, JPL, CA, June 1990; **[5]** Head, J.W. et al. (1993) *JGR* **98**, No. E9, 17,149; **[6]** Sabol, D.E. et al. (1992) *JGR* **97**, No. E2, 2659; **[7]** William, C.S. and Becklund, O.A. (1989) *Introduction to the Optical Transfer Function*, John Wiley & Sons, New York; **[8]** Klaasen, K. (1993) *Galileo Solid-State Imaging Subsystem Calibration Report: Part 2*, JPL, CA.

IMPACT-RELATED LOW-EMISSIVITY ANOMALIES ON VENUS S. L. Lawson[1] and J. J. Plaut[2]; [1]University of Colorado, Department of Astrophysical, Planetary, and Atmospheric Sciences, Boulder, CO 80309; [2]Jet Propulsion Laboratory, MS 230-225, 4800 Oak Grove Dr., Pasadena, CA 91109.

Magellan radiothermal emissivity data were analyzed to find low-emissivity impact-related areas on the surface of Venus. Although low-emissivity parabolic crater-related features have been previously reported [1, 2], it was the goal of this study to conduct an independent detailed examination of low-emissivity areas and investigate the relationship between these areas and impact craters. In addition, while the previous investigations incorporated only Magellan Cycle 1 data, this work analyzed data from the first three Magellan data acquisition cycles. The reduced emissivity data used here had an absolute error of 0.02, with 0.005 variations detectable [3].

The Venus surface was divided into 34 subsections which were individually analyzed. Large low-emissivity regions were defined as totaling approximately half of each subsection. In addition, small lower-emissivity regions were subjectively defined as being the relative lowest-emissivity areas on each subsection. Up to four large and thirteen small areas were defined on each subsection. Plotted over these low-emissivity areas were 919 craters from Schaber et al. [4] and their additional unpublished data, and a few craters independently found from Magellan Cycle 3 SAR images. The low-emissivity areas were arranged into four categories: 1) clearly associated with impact craters; 2) likely associated with impact craters; 3) possibly associated with impact craters; and, 4) not associated with impact craters. The categorization of the areas was subjective, but required the agreement of both authors. Areas were generally considered to be clearly associated with an impact crater if the crater was in or to the east of the low-emissivity area; often the low-emissivity areas were related to more than one impact crater. Although the crater thought to be the primary cause of the low-emissivity area could often be easily identified, sometimes the relationship between the craters and the areas was ambiguous, with perhaps more than one crater being the cause of the anomalous emissivities. High elevation areas and crater floors, which are also known to have anomalously low emissivities, were not categorized.

The average difference between the clearly crater-related emissivity lows and the emissivity of the surrounding terrain was 0.04. The largest value of this difference was 0.09, while the smallest was 0.01. The diameters of the craters clearly associated with the low-emissivity areas ranged in size from 2.5 km to 150 km; see Table 1 for a detailed listing of craters. The total number of craters clearly associated with anomalous low-emissivity areas is 88, with an additional 34 craters likely related to emissivity lows. These numbers include craters that lie within the defined low-emissivity areas, but perhaps were not the cause of them. It was found that not all the anomalous low-emissivity areas are parabolic shaped and neither do they all have corresponding SAR parabolas. Campbell et al. [2] reported finding eight craters associated with emissivity parabolas.

The identification of over 60 low-emissivity features clearly or likely associated with impact craters indicates that these surfaces are more common and perhaps longer-lived than previously thought. When combined with extended ejecta deposits observable in SAR data [5], the fraction of craters that retain such signatures comprises a majority of the crater population. Impact events are clearly the dominant source of low-elevation low-emissivity anomalies; in many plains regions >50% of the surface has emissivities lowered by impact-related features. Enhanced dielectric constants appear to be the most likely cause of the low emissivity values [6]. The precise physical mechanisms producing higher dielectric constants (compositional and/or density differences), and their implications for impact processes and target properties remain to be determined.

REFERENCES [1] Arvidson, R. E. et al. (1991). *Science* **252**, 270-275. [2] Campbell, D. B. et al. (1992). *JGR* **97**, 16,249-16,277. [3] Pettengill, G. H. et al. (1992). *JGR* **97**, 13,091-13,102. [4] Schaber, G. G. et al. (1992). *JGR* **97**, 13,257-13,301. [5] Izenberg, N. R. et al. (1992). Proc. Lunar Planet. Sci. Conf. XXIV, 703-704. [6] Plaut, J. J. and R. E. Arvidson (1992). *JGR* **97**, 16,279-16,291.

IMPACT-RELATED LOW-EMISSIVITY ANOMALIES

Lawson S. L. and J. J. Plaut

TABLE 1. Low-emissivity areas clearly associated with impact craters

Crater	Latitude (°N)	Longitude (°E)	Diameter (km)
MAGNADI	58.60	337.00	26.6
Kartini	57.80	333.00	24.8
RUTH	43.29	19.90	18.0
Prichard	44.00	11.50	22.1
FEDORETS	59.65	65.15	54.0
ZHILOVA	66.53	125.50	56.0
TSVETAYEVA	64.65	146.90	40.0
YABLOCHKINA	48.27	195.15	63.0
unnamed	48.30	191.40	5.0
ANYA	39.50	297.80	20.0
Lenore	38.70	292.30	15.5
UNNAMED	6.00	331.85	12.6
UNNAMED	0.90	338.75	10.8
UNNAMED	10.60	346.30	12.8
Rhoda	11.50	347.70	13.0
NADINE	7.80	359.10	19.0
Hellman	4.75	356.30	35.0
unnamed	9.30	358.00	10.0
UNNAMED	2.90	4.95	6.0
unnamed	4.30	3.65	5.0
Piaf	0.80	5.25	43.0
UNNAMED	36.70	1.70	12.5
unnamed	36.75	3.60	2.5
EDGEWORTH	32.20	22.75	30.5
Noreen	33.45	22.70	19.5
unnamed	34.40	18.90	10.0
unnamed	28.40	14.50	7.5
UNNAMED	21.95	37.20	7.5
MIRIAM	36.50	48.20	15.0
RILEY	14.05	72.30	24.0
ADIVAR	8.95	76.10	31.0
unnamed	7.95	74.00	3.5
Naomi	6.00	70.10	18.0
MERIT PTAH	11.30	115.65	18.5
unnamed	13.25	112.80	4.0
HIMIKO	19.00	124.17	36.5
BAN ZHAO	17.20	146.90	42.0
GREENAWAY	22.95	145.00	92.0
Marie Celeste	23.45	140.20	95.0
DU CHATELET	21.50	164.95	18.5
unnamed	23.55	165.35	8.5
CACCINI	17.40	170.40	38.0
CORPMAN	0.35	151.85	52.0
BOLEYN	24.40	219.90	69.0

Crater	Latitude (°N)	Longitude (°E)	Diameter (km)
DE WITT	-6.50	275.60	21.0
unnamed	25.11	285.28	12.0
ROSE	-35.15	248.20	15.0
Moore	-30.30	248.30	21.0
unnamed	-30.30	249.40	10.0
Kanik	-32.60	249.80	16.0
UNNAMED	-13.00	328.00	35.0
CARSON	-24.20	344.10	41.0
Danilova	-26.40	337.25	49.0
Aglaonice	-26.50	339.95	65.0
Saskia	-28.60	337.15	37.0
FRANK	-13.10	12.90	23.0
unnamed	-6.00	6.00	75.0
Xantippe	-10.80	11.75	40.0
unnamed	-11.20	13.50	7.2
BATHSHEBA	-15.10	49.35	36.0
Gillian	-15.20	49.95	15.5
BASSI	-18.95	64.70	33.0
BOULANGER	-26.55	99.30	62.0
Simonenko	-26.80	97.55	34.0
VON SHUURMAN	-5.00	190.95	29.0
Trollope	-54.80	246.40	26.0
Godiva	-56.10	251.60	32.0
Delilah	-57.85	250.50	18.0
unnamed	-58.70	252.25	22.0
ABINGTON	-47.75	277.80	22.5
unnamed	-49.00	275.80	11.0
MEITNER	-55.60	321.60	150.0
SARTIKA	-63.40	67.10	28.0
unnamed	-61.90	70.90	12.0
Lucia	-62.10	67.80	17.0
unnamed	-61.00	53.50	6.0
Berggolts	-63.40	53.00	31.0
Danute	-63.50	56.50	14.0
Rand	-63.75	59.50	27.0
GUAN DAOSHENG	-61.50	181.80	46.0
unnamed	-62.20	178.30	9.0
Bryce	-62.55	197.10	24.5
Vacarescu	-63.00	199.60	29.5
EUDOCIA	-59.05	201.80	27.5
Barrymore	-52.30	195.55	50.0
unnamed	-53.20	198.50	6.0
STOWE	-43.20	233.00	82.0
RUSLANOVA	84.00	16.50	45.0

Craters are separated into groups corresponding to a single low-emissivity area. Craters in upper case are believed to be the primary cause of the associated low-emissivity area, while the craters in lower case may be additionally responsible. In some areas, there is believed to be more than one primary crater, while in other areas the primary crater is not easily identified.

PROJECT ARTIST: INTEGRATING ASTRONOMY AND PLANETARY SCIENCES INTO THE ELEMENTARY AND MIDDLE SCHOOL CURRICULUM; Larry A. Lebofsky, Lunar and Planetary Laboratory, University of Arizona 85721 and Nancy R. Lebofsky, Steward Observatory, University of Arizona, Tucson, Arizona 85721

Scientists from the University of Arizona and teachers from southern Arizona are collaborating on ways to make astronomy and planetary science ("space science") accessible and interesting to children from diverse backgrounds at both the elementary and middle school levels. Programs which offer instruction in space science through hands-on experiences, integrated curriculum, and translated materials are described below and will be presented in the session.

In elementary school, science is a subject that is often neglected by teachers for a variety of reasons. In particular, the demands of the basic "reading, writing, and arithmetic" can consume the entire school day leaving little or no time for science. Therefore, in order to teach science, science must be integrated into the existing school curriculum.

Space science can be used to introduce students to the natural world which is a part of their lives. Even children in an urban environment are aware of such phenomena as day and night, shadows, and the seasons. It is a science that transcends cultures, has been prominent in the news in recent years, and can generate excitement in young minds as no other science can. Space science also provides a useful tool for understanding other sciences and mathematics, and for developing problem solving skills which are important in our technological world.

Over the past 4 years we have been conducting a series of workshops for elementary and middle school teachers from Southern Arizona. Our workshops have included 1-day workshops for bilingual teachers, 2-day aerospace workshops, and 2- and 4-week workshops in space sciences.

Our current program is **Project ARTIST** (Astronomy-Related Teacher Inservice Training), which started out as a 2-week pilot workshop in 1990. Project ARTIST is now a four-year program of workshops and materials development funded by the National Science Foundation Teacher Enhancement program. ARTIST provided a four-week workshop (June 1993) for 24 teachers of grades 1–8 from schools throughout Pima County. The workshop stressed hands-on activities and experiments, while providing instruction in space science content and concepts. ARTIST also encouraged the use of space science materials across the curriculum. In fact, several teacher "teams" attended the workshop. Two more summer workshops will accommodate 24 teachers each in 1994 and 1995.

ARTIST staff members were assisted in both the planning and presentation of the workshop by 11 facilitators, i.e., classroom teachers who had attended the 1990 ARTIST pilot workshop and had been using space science materials in their classes for the intervening three years. A TUSD curriculum specialist was added to the team during the planning stages, and amateur astronomer David Levy was added to the staff in 1993. Of the 39 ARTIST participants and facilitators 25 are women, 11 are Hispanic, 15 teach in

schools with large minority populations, 10 teach in bilingual or limited English proficiency classrooms, 1 is a bilingual special education teacher, and 1 teaches at a Bureau of Indian Affairs boarding school. Therefore, the students affected by these teachers' new skills and knowledge is very broadbased, including students from groups traditionally underrepresented in the sciences.

Project ARTIST seems to work well because of its partnership approach. Research scientists provide *content*, planetarium personnel emphasize *concepts*, and facilitators put activities in the *context* of the classroom. Primary, intermediate, and middle school teachers bring a diversity of experiences and methodology to the program, enhanced by the special insights of bilingual, ESL, gifted, and special ed teachers. Amateur astronomers and guest staff provide unique experiences in observational astronomy and planetary surfaces. Mutual respect by each component for the professionalism of every other component allows everyone involved to learn from each other.

Project ARTIST provided funds for 3 facilitators to attend the National Science Teachers Association convention in Kansas City (April 1993). A local school district provided funds for a fourth ARTIST facilitator. The facilitators assisted project staff in presenting a one-hour hands-on workshop. In October 1993, a group of 11 facilitators and 1993 workshop participants attended the Arizona Science Teachers Association convention, presenting several hands-on activities during a one-hour workshop attended by nearly 100 teachers.

In addition to providing the audiences with information and activities, the ARTIST teachers benefitted from peer interaction, the empowering experience of being a leader, and, for many, their first attendance at a state or national conference.

Of the four facilitators who attended the Kansas City meeting, one was chosen to attend the American Association for the Advancement of Science 1993 Forum for School Science (In Pursuit of Excellence and Equity: Models for Effective Science Teaching), and one was honored by her district's governing board for her science teaching at the elementary level. Two have moved from self-contained elementary classrooms to middle school science positions. The students, schools, peers, and district have all benefitted from the experiences of these teachers.

At this meeting we will present a variety of materials from the workshops, activities developed by the workshop participants, and materials produced by the students of the workshop participants. This presentation will stress the integration of science with language arts, fine arts, math, and social studies.

THE NATURE OF LOW ALBEDO ASTEROIDS FROM 3-μm SPECTROPHOTOMETRY Larry A. Lebofsky*, Daniel T. Britt*, Ellen S. Howell*, and Andrew S. Rivkin*, Lunar and Planetary Laboratory, University of Arizona, Tucson, Arizona 85721

Over the past decade, our group has been investigating the nature and distribution of water (thought to be in the form of hydrated silicates) on the surfaces of asteroids. Our early spectrophotometric observations (3-μm spectral region) of low-albedo main-belt C-class asteroids showed little or no correlation between solar distance and hydration state (1). In our more recent work (2, 3, 4) we expanded our observations to include other low-albedo classes of asteroids (F-, P-, D-, and T-class asteroids), asteroids that range from the outer asteroid belt (>2.5 AU) to the Trojan region at 5.2 AU. Because of their greater solar distances and their low albedos ($\leq$15%) these asteroids should have experienced lower temperatures and thus should have higher volatile content than the Cs.

The 3-μm absorption feature in hydrated silicates is the only diagnostic feature observable in the dark, volatile rich CI and CM meteorites and has been used to determine the presence of hydrated silicates on asteroids (1–4; see Fig. 1). However, visual and near-IR high resolution observations of dark asteroids by Vilas (5,6) show that other, weak, though diagnostic, spectral features do exist that indicate aqueous alteration products

Our observations showed that while many of the C asteroids closer to the Sun contain hydrous minerals, the asteroids in the colder, more remote regions of the asteroid belt do not. These observations seemed to imply that in the outer part of the asteroid belt the kinetics of the nebula-solid reactions were too slow for chemical equilibrium to be attained. Under these conditions, the asteroid belt started out as a mixture of ice and anhydrous rock. Asteroids in the inner part of the belt may have undergone moderate heating, resulting in the melting of some of this ice and subsequent aqueous alteration; those in the outer belt were not so heated, and instead lost their water to gradual sublimation over the age of the solar system. This scenario is consistent with the observed chemical nature of the CI meteorites, the spectra of the C versus P and D asteroids, and with our understanding of sublimation rates versus heliocentric distance.

To date, we have observed about 70 asteroids in the 3-μm spectral region. Approximately 60% of the C-class asteroids show evidence of the water of hydration feature. There appears to be no correlation of hydration state with solar distance. Our most recent work (7), implies that water in some form may also exist on the surfaces of asteroids that are considered to have high-temperature surface materials—the E- and M-class asteroids. These results clearly imply that the processes involved in the aqueous alteration of asteroid surfaces are complex and as yet not well-understood. These results also bring into question the relationship between asteroid class and our previous assumptions relating to surface mineralogy. We will discuss our present understanding of the these surface alteration processes and attempt to explain the distribution of compositions that we see (for the primative bodies) in the asteroid belt.

---

* Visiting astronomer at the Infrared Telescope Facility which is operated by the University of Hawaii under contract to the NASA

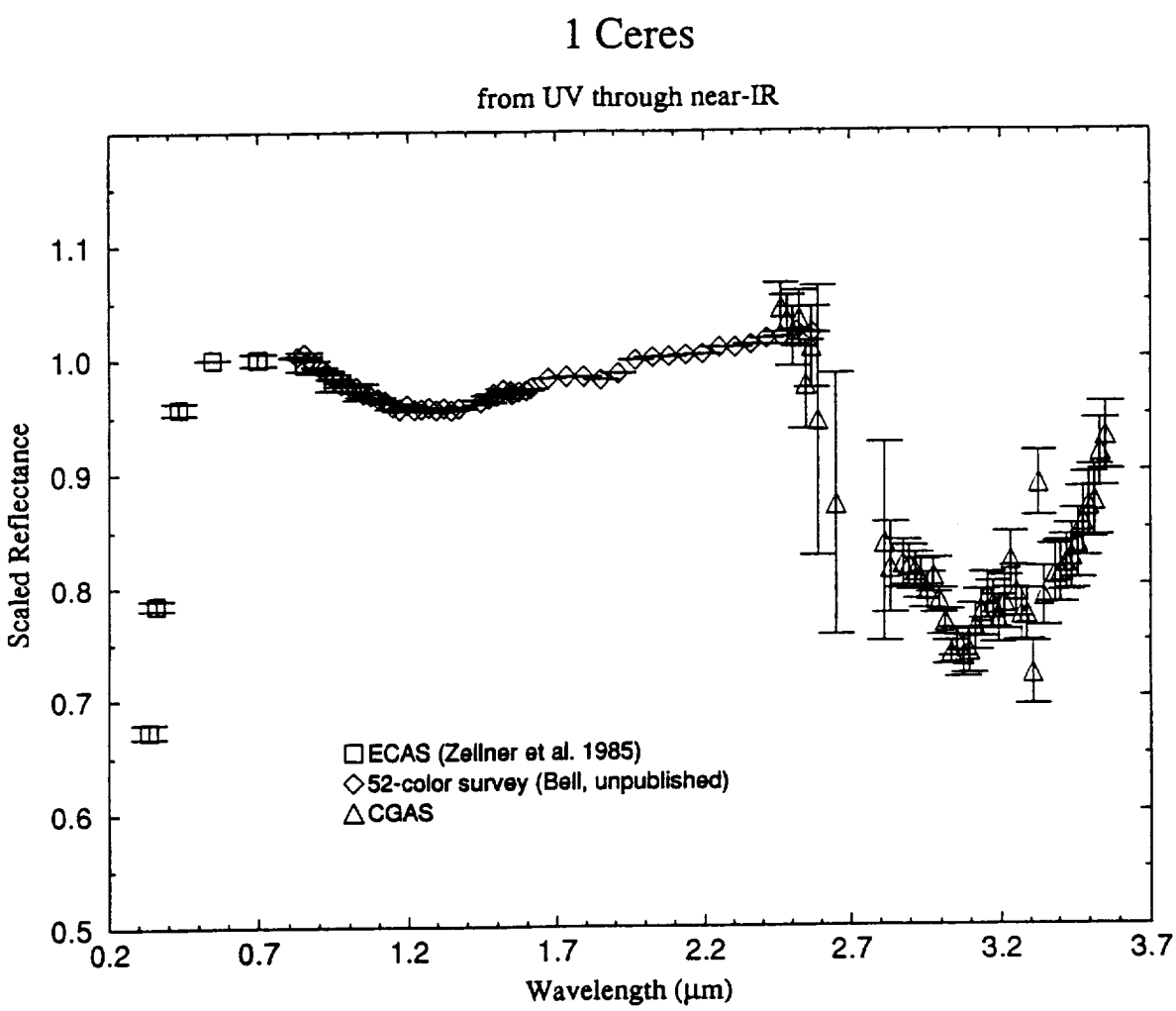

Fig. 1: Relative reflectance spectra (0.3 to 3.5 μm) of asteroid 1 Ceres, which shows the distinctive 3-μm feature indicative of water of hydration.

Acknowledgements:

This work was supported by NASA Grants NAGW-1975 and NAGW-1146.

References:

(1) FEIERBERG, M. A., L. A. LEBOFSKY, AND D. J. THOLEN (1985). *Icarus* **63**, 183–191. (3) LEBOFSKY, L. A., T. D. JONES, P. D. OWENSBY, M. F. FEIERBERG, AND G. J. CONSOLMAGNO (1990). *Icarus* **83**, 16–26. (4) JONES, T. D., L. A. LEBOFSKY, J. S. LEWIS, AND M. S. MARLEY (1990). *Icarus* **88**, 172–192. (5) VILAS, F., AND L. A. MCFADDEN (1992). *Icarus* **100**, 85–94. (6) VILAS, F., S. M. LARSON, E. C. HATCH, AND K. S. JARVIS (1993). *Icarus* **105**, 67–78. (7) RIVKIN, A. S., E. S. HOWELL, D. T. BRITT, AND L. A. LEBOFSKY (1993). *BAAS* **25**, 1134.

MAPPING REGOLITH AND BLOCKS ON ASTEROID 243 IDA: THE EFFECTS OF PHOTOMETRIC VIEWING GEOMETRY.

Pascal Lee[1], Joseph Veverka[1], Michael J. S. Belton[2], Peter C. Thomas[1], Brian T. Carcich[1], Ronald Greeley[3], Robert Sullivan[3], Robert Pappalardo[3], and the Galileo SSI Team. [1]Department of Astronomy, Cornell University, Ithaca, N.Y. 14853. [2]Kitt Peak National Observatory, NOAO, Tucson, AZ 85719. [3]Department of Geology, Arizona State University, Tempe, AZ 85287.

We mapped the distribution of ejecta blocks on asteroid 243 Ida both "conservatively" and "liberally", and find that it may be significantly biased by photometric viewing geometry. Most observed blocks occur under relatively small emission angles where block visibility is understandably enhanced. Most blocks also appear to be associated with large (Ø > 2 km) or fresh-looking craters. While few blocks are seen where the viewing geometry is unfavorable, there are at least two broad areas on Ida where blocks are rare *in spite of* favorable viewing conditions. The subdued topography in these areas suggests that they might possess a thicker regolith cover than elsewhere. We find no clear indication that the distribution of blocks on Ida presents any systematic asteroid-wide asymmetry.

With the recent flybys of 951 Gaspra and 243 Ida by the Galileo spacecraft, disk-resolved images of the surfaces of main-belt asteroids have become available. As suspected from earlier (indirect) evidence, impact cratering appears to be the principal geological process currently at work on these objects. While *direct* evidence for the existence of the finer-grained fraction of a regolith is generally lacking for small bodies, high-resolution spacecraft imaging data provide such evidence for the coarser fraction of their regolith: several discrete and localized positive relief features (PRFs), meters to tens of meters in size, have been identified on the surfaces of Phobos and Deimos [1], and now possibly many are seen on 243 Ida, most of which likely represent individual ejecta blocks. The size of the largest blocks observed on Ida, about 150 m, is consistent with the relationship between maximum ejecta block size and crater diameter found for the Moon, Phobos and Deimos [1].

In light of these observations, attempts are currently underway to map the distribution of ejecta blocks on Ida. The maps will hopefully provide clues to the mechanisms by which ejecta is produced and emplaced on small bodies, and lead to a better understanding of their evolution and of the impact cratering process. In constructing the maps however, several shortcomings become apparent. These may be observational (limited spatial resolution, varying photometric viewing geometry, albedo contrasts or lack thereof, etc.), or intrinsic (partial to complete burial of ejecta blocks, block fragmentation in response to varying material strengths, etc.). On Ida, block identification is indeed first challenged by the spatial resolution limit (31 to 38 m/px for the mosaic currently available) ; then, because regolith depths of order several tens of meters or more are conceivable on Ida, partial or even complete burial of all but the largest ejecta blocks is possible. While interesting in themselves, such caveats clearly would affect the observed distribution of blocks and must be taken into account.

In an attempt to measure more specifically the possible effects of varying photometric viewing geometry on the observed distribution of blocks on Ida, we determined the angles of incidence i and emission e under which each PRF is observed, using the latest numerical shape model available for the asteroid. Two approaches were adopted: a "conservative" one, in which only the PRFs that were deemed most likely to be individual blocks were included in the count - 29 were found ; and a more "liberal" one, in which virtually all discrete PRFs were taken into account, so long as there was reasonable doubt as to what the features might actually be (an ejecta block indeed, or merely a raised crater rim or protruding bedrock) - 185 were found. In both approaches, the locations of the PRFs were mapped against Ida's shape model (Figures 1 and 2). We find that the observed blocks have a tendency to occur in greater numbers very near, and often within, large (Ø > 2 km) craters or in the close vicinity of fresh-looking, smaller craters. While larger craters might constitute efficient traps for blocks ejected ballistically from other areas on Ida and fresher craters have better-exposed ejecta, the rougher topography found in the immediate vicinity of all craters probably also enhances block visibility and might thus bias their mapping. We note also that there are two distinct areas on Ida (R_A and R_B in Fig.2) where very few blocks are visible in spite of favorable viewing circumstances.

MAPPING BLOCKS ON 243 IDA
Lee, P. et al.

While the distribution of blocks on Ida may not be uniform, the subdued topography in these areas suggests that the regolith cover could be thicker there than elsewhere and have buried even the largest blocks. The thickness of the regolith might thus vary regionally on Ida. The observed distribution of blocks shows otherwise no clear indication of an asteroid-wide asymmetry, such as a rotational leading side/trailing side dichotomy as might be expected from a non-uniform "sweep-up" of ejected blocks by the rotating asteroid [2].

The photometric viewing geometry under which our two populations of blocks were observed (in the conservative and liberal approaches) is presented in Figures 3 and 4, where $\mu_0 = \cos i$ is plotted against $\mu = \cos e$. Because the current shape model is still coarse and the shape of the asteroid itself is such that not all photometric geometries occur with equal frequency, the observed distributions must be interpreted with caution. (Note also that some combinations of μ and μ_0 are not represented in the original mosaic. The excluded domain, however, is very limited.) Figures 3 and 4 show how the observed block distribution may be affected significantly by differences in photometric viewing geometry. Most PRFs appear to be clustered in the large μ region, likely because foreshortening is minimal at small emission angles, optimizing viewing. Very few PRFs are visible near the limb (the "y" axis) where e becomes large. Meanwhile, several PRFs also occur at intermediate incidence and emission angles where shadows are reasonably well-developped and open to view. More surprizing, however, is the apparent lack of blocks at large incidence angles (small μ_0) and intermediate emission angles ($\mu \sim 0.6$). Blocks viewed under this geometry would be conspicuous. Perhaps they are absent or lie hidden from view.

REFERENCES: [1] Lee S.W. et al. (1986) *Icarus* 68, 77-86. [2] Geissler, P., personal communication.

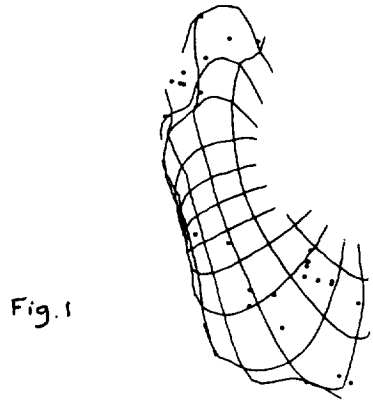

Fig. 1

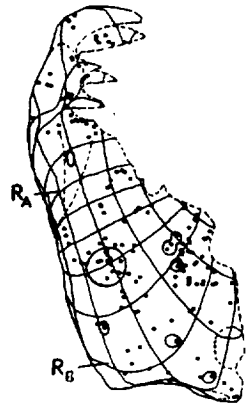

Fig. 2

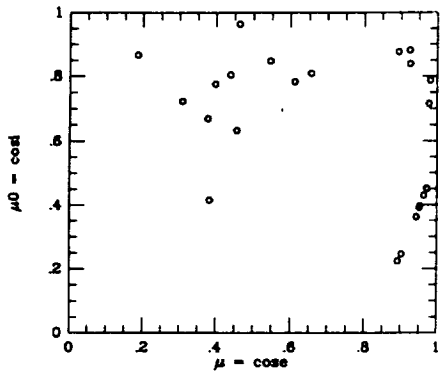

Fig. 3

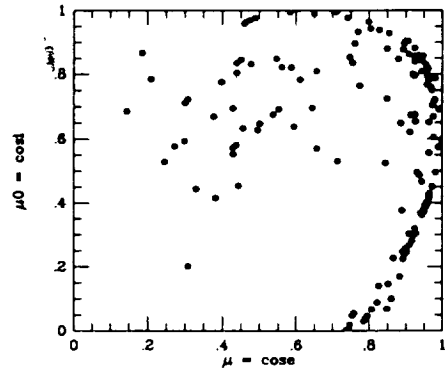

Fig 4

Fig.1: Distribution of PRFs on asteroid 243 Ida mapped on best available shape model drawn with an 18° grid spacing: "conservative" approach (see text), yielding 29 possible ejecta blocks.
Fig.2: Distribution of PRFs on asteroid 243 Ida mapped on the same shape model as in Fig.1: "liberal" approach (see text), yielding ~185 possible ejecta blocks. Major geological features are outlined, along with areas R_A and R_B.
Fig.3 and Fig.4: Photometric viewing geometry of the blocks shown in Figures 1 and 2, respectively.

PROGRESS IN THE DEVELOPMENT OF THE GMM-2 GRAVITY FIELD MODEL FOR MARS; *F.G. Lemoine[1,2], D.E. Smith[1], F.J. Lerch[1], M.T. Zuber[3,1]* and *G.B. Patel[4]*, [1]Laboratory for Terrestrial Physics, NASA/Goddard Space Flight Center, Greenbelt, MD 20771, [2]Astronomy Department, University of Maryland, College Park, MD 20742, [3]Dept. of Earth and Planetary Sciences, Johns Hopkins University, Baltimore, MD 21218, [4]Hughes-STX Corp., Lanham, MD 20706.

Last year we published the GMM-1 (Goddard Mars Model-1) gravity model for Mars [1]. This new model makes several improvements: it extends the size of the field in degree and order, moves the calculations to the 1991 IAU reference frame[2], takes into account the effects of Phobos and Deimos, introduces new atmospheric corrections to the tracking data[3], and applies an elevation cut-off of 10 degrees to the tracking data to reduce contamination by Earth troposphere and ionosphere effects. New station coordinates were introduced, and the effect of plate motions, ocean loading and pole tide on the station coordinates were accounted for. Where appropriate, the antenna corrections defined by Moyer[4] were applied. In anticipation of the arrival of Mars Observer at Mars, we used the new DE-234 set of planetary ephemerides and associated constants[5]. The switch to the new reference system changed the reference radius for the gravity field from 3394.2 km to 3397.0 km as recommended by the IAU[2]. Finally, where the Culp and Stewart Mars atmospheric drag model was used in GMM-1[6], we applied the newer Stewart drag model in GMM-2 [7].

We have completely re-analyzed the Viking and Mariner 9 tracking data in the development of the new field, designated GMM-2. The model is complete to degree and order 70. Many orbital issues which were unresolved in GMM-1 have been accounted for in GMM-2. Our present solution includes 282 arcs, compared to 270 in GMM-1. Arcs which had inexplicably high RMS of fit, or which overlapped the periods of the Viking Bistatic Radar Experiment[3] were divided into smaller segments. Six additional arcs of high altitude, Viking-1 1500 km periapse height data were added to the solution. These data spanned the period from orbit insertion on June 20, 1976 through July 23, 1976. Although the elevation cutoff criterion of 10 degrees deleted approximately one to three percent of the data, depending on the satellite and periapse altitude, the number of observations in GMM-2 is greater than in GMM-1 (232,322 Doppler observations in GMM-1 vs. 233,814 Doppler observations in GMM-2).

We anticipated that some of the larger anomalies, such as those associated with the Tharsis bulge, would be larger because of the higher resolution, but this does not appear to have been the case. We assume that the large size of the new field and the improved modeling have extracted almost all the available gravity information from the tracking data. We find that the estimate of supporting parameters, including those associated with solar radiation pressure and atmospheric drag, are more stable in the new solution.

The introduction of *a priori* constraints on the drag coefficients dramatically improves the RMS of fit to the low altitude periapse (300 km) data. The RMS of fit to the high altitude periapse (1500 km and 800 km) remains essentially unchanged. However, to prevent spurious artifacts from appearing in the anomaly maps, once per revolution acceleration parameters have been estimated for each Viking-1 and Viking-2 300 km arc. This slight change in the method of solution enhances the power of the coefficients in GMM-2 compared to GMM-1. We attribute the improvement to better separability between the drag parameters and gravity coefficients. The impacts of the changes in the solution methodology continue to be investigated. In the latest solution, the location of the gravity anomaly low associated with the Hellas basin correlates more closely with the topographic low than in GMM-1 (see Figure 1).

References: [1]Smith, D.E., et al., (1993), *JGR-Planets,* 98, 20871. [2]Davies, M.E., et al., (1992)*Cel. Mech. and Dyn. Astron.*, 53, 377. [3] Lemoine, F.G. (1992), Mars:*The Dynamics of Orbiting Satellites and Gravity Model Development,*, Ph.D. Thesis, Univ. of Colorado, Boulder. [4] Moyer, T.D. (1971), *JPL Tech. Rep. 32-1527.* [5] Standish, E. M. Jr., (1991), *JPL IOM 314.6-1348.* [6] Culp R.D. and A.I. Stewart (1984), *J. Astronaut. Sci.*, 32, 329. [7] Stewart, A.I. (1987), *JPL PO NQ-802429.* [1]Wu S.S.C., et al., (1986), *NASA Tech. Memo. 88383,* 614.

Figure 1. Free air gravity anomalies computed from the preliminary solution for GMM-2. The contour interval is 50 mGals. The anomalies are plotted relative to a reference ellipsoid with an inverse flattening of 191.1372. The line contours in the plot represent a 50 x 50 spherical harmonic expansion of the Mars DEM [8], with topographic values referred to the GMM-2 geoid. The contour interval is 1 km.

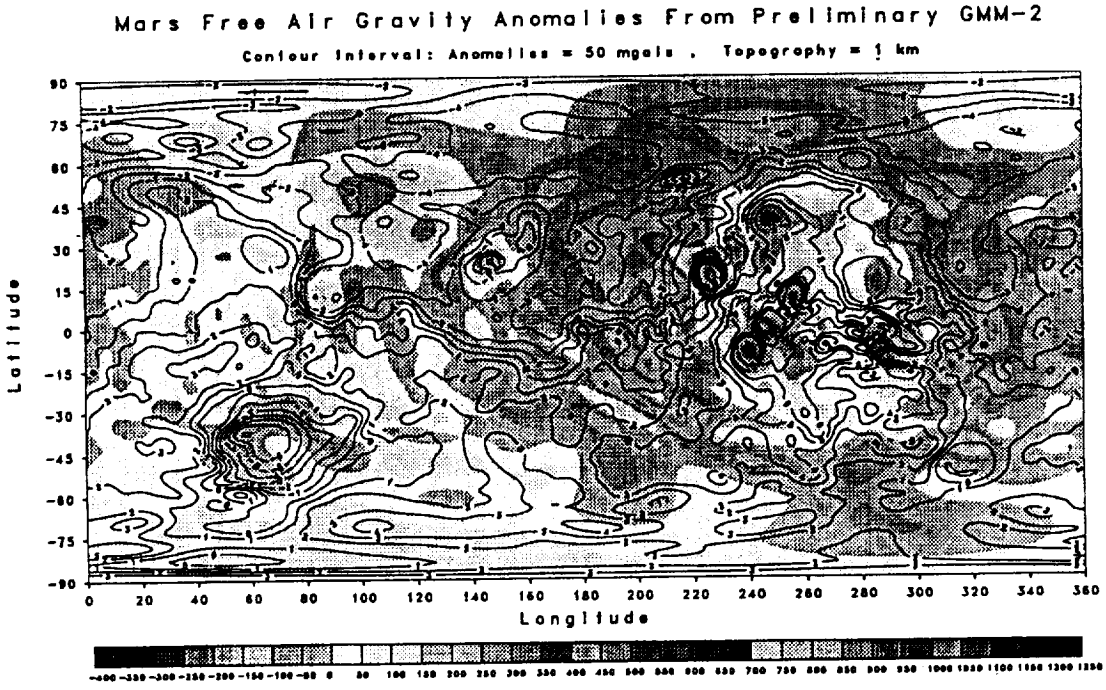

PRELIMINARY SOLUTIONS FOR THE LUNAR GRAVITY FIELD FROM ANALYSIS OF LUNAR ORBITER TRACKING DATA; *F. G. Lemoine*[1,2], *D.E. Smith*[1], *M.T.Zuber*[3,1], *D.D. Rowlands*[1], and *S. K. Fricke*[4], [1]Laboratory for Terrestrial Physics, NASA/Goddard Space Flight Center, Greenbelt, MD 20771, [2]Astronomy Department, University of Maryland, College Park, MD 20742, [3]Department of Earth and Planetary Sciences, Johns Hopkins University, Baltimore, MD 21218, [4]RMS Technologies Inc., Landover, MD 20706.

Knowledge of the gravitational field, in combination with surface topography, provides one of the principal means of inferring the internal structure of a planetary body. Previous analyses [1-11] of the lunar gravitational field have been based on data from the Lunar Orbiters, the Apollo subsatellites, and the low altitude passes of the Apollo spacecraft. Recently, Konopliv et al. [12] have reanalyzed all available Lunar Orbiter and Apollo subsatellite tracking data, producing a 60th degree and order solution.

In preparation for the Clementine mission to the Moon, we have also initiated a re-analysis of the Lunar Orbiter and Apollo substellite data. We have attempted solutions of 60th and 70th degree and order, which correspond to a spatial resoltutions of 160 to 180 km where the data permit. Our reanalysis takes advantage of advanced force and measurement modeling techniques as well as modern computational faciilities. We applied the least squares collocation technique which stabilizes the behaviour of the solution at high degree and order [13]. The extension of the size of the field reduces the aliasing coming from the omitted portion of the graviational field. This is especially important for the analysis of the tracking data from the Lunar Orbiters, as the periapse heights frequently ranged from 50 to 100 km.

While analysis of available data continues, our preliminary solutions are based on 80 orbital arcs from S-Band tracking of the Lunar Orbiters 2, 4 and 5 by the Deep Space Network (DSN) between November 1966, and January 1968. So far, 170,000 observations have been included in the solutions. The data were processed using the GEODYN/SOLVE orbit determination programs, which previously have been used in the derivation of the Goddard Earth Models (GEM) [14], as well as GVM-1, and GMM-1 gravity models for Venus and Mars [15,16].

The gravitational potential, V_M, at the spacecraft altitude is represented in spherical harmonic form as:

$$V_M(r) = (GM/r) \sum_{l=0}^{N} \sum_{m=0}^{l} \left[a_e/r \right]^l P_{lm}(\sin\phi) \left[C_{lm} \cos m\lambda + S_{lm} \sin m\lambda \right] \quad (1.1)$$

where r is the radial distance from the center of mass of the Moon to the spacecraft, θ and λ are the selenocentric latitude and longitude of the spacecraft, a_e is the mean radius of the reference ellipsoid of the Moon, taken to be 1738 km in our analyses, GM is the gravitational constant for the Moon, P_{lm}

are the normalized associated Legendre functions of degree *l* and order *m*, C_{lm} *and* S_{lm} are the normalized spherical harmonic coefficients which are estimated from the tracking data, and *N* is the maximum degree representing the size of the field.

To determine the solutions, the data were processed in arcs of 1 to 34 days. The Lunar Orbiter spacecraft possessed an uncoupled attitude control system which introduces accelerations during each sequence of attitude maneuvers. These maneuvers were modeled as finite accelerations, since the times and durations of these maneuvers are tabulated. One day arcs were used for the primary phase of each Lunar Orbiter mission, corresponding to the first few weeks in orbit when maneuvers were most numerous. Longer arcs are possible during the extended mission phases when the attitude changes were less frequent. For each arc, we estimate a state vector, a solar radiation pressure coefficient, Doppler tracking biases, and 3-axis accelerations for each batch of attitude maneuvers. The gravitational field was then found by adding together the information equations for each arc and solving the resulting linear system. We found that constraining the magnitudes of the maneuvers strengthened the gravity field solutions.

References: [1]Muller, P.M., and W. L. Sjogren (1968) *Science,* 161, 680. [2]Lorell, J. and W.L. Sjogren (1968)*Science*, 159, 625. [3] Liu, A.S, and P. Laing (1971), *Science*, 173, 1017. [4] Michael Jr., and Blackshear (1972), *The Moon,*, 3, 388. [5] Ferrari, A. (1977), *JGR*, 82, 3065. [6] Bills, B. and A. Ferrari (1980), *JGR,* 85, 1013. [7] Ferrari et al. (1980), *JGR*. [8]Sjogren, W. L.et al. (1972), *Science*, 175, 165. [9] Muller, P. et al. (1974), *The Moon*, 10, 195. [10] Sjogren, W.L. et al. (1974), *The Moon*, 11, 35. [11] Sjogren et al. (1974), 11, 41. [12] Konopliv, A.S. et al. (1993), *1993 AAS Astrodynamics Conf.,* Paper 93-622. [13] Schwartz, K.P. (1976), *Geod. Sci.*, 35, 309. [14] Lerch et al. (1979), *JGR*, 84, 3987. [15]Nerem et al. (1993), *GRL*, 20, 599. [16] Smith et al., (1993), *JGR*--Planets, 98, 20871.

Precision noble gas measurements on presolar diamonds from the Murchison meteorite

Roy S. Lewis; Enrico Fermi Institute, University of Chicago, Chicago IL 60637

Presolar micro diamonds have been identified as the carrier of isotopically anomalous Xe-HL & associated isotopic components of He, Ne, Ar, Kr, & N (1 – 7). These diamonds also contain 2 other noble gas components, P3 and P6: all three components are extensively discussed in (8). P3, ~ solar in isotopic compositions of He – Xe, is found in the lowest petrologic types of meteorites, including Murchison. P6 & HL are isotopically distinct from all other known exotic or local components (8,9) although P6 may be roughly similar to the local solar system composition (10). Graphite and silicon carbide, the other two types of identified presolar grains that have been extensively studied, have yielded a plethora of isotopic anomalies for the whole periodic table, as well as correlations amongst various physical & chemical properties such as grain size & ease of destruction and isotopic ratios & elemental abundances (11 and refs. therein). Diamonds, on the other hand, have yielded little outside the noble gases. Hydregen and nitrogen are the only other elements distinctly different from solar, even carbon is within the range of normal solar materials (4,5,7,12). Perhaps not surprising, other elements are at very low abundance (13), but where measured (Ba & Sr) these other elements have only meager isotopic variations (14). There is no a priori reason to expect less variation amongst the individual presolar diamond crystals than amongst the graphite and silicon carbide. However, the small size of the diamonds, ≈20Å (15), which makes their separation from the rest of the meteorite relatively easy, makes any further separation extremely difficult. The noble gas components P3, P6 & HL and their separation from each other and from the isotopically distinct nitrogen by sequential metamorphic destruction of their carriers and also by their separate release temperatures in the laboratory (4,16) imply distinct carriers in some sense. While some attempts have been made to understand the possible nucleosynthetic origins of the Xe-HL in these diamonds (17,18) little progress has been made in understanding the complete set of 5 noble gases plus carbon and nitrogen, nor in understanding the origins of the P3 and P6 components. Clearly, obfuscation will likely rule if the best samples are mixtures of diamonds from widely different sources. The small size of the diamond grains precludes isotopic measurements on single grains, a technique which has successfully demonstrated the wide heterogeneity of the graphite and the silicon carbide grains (refs. in 11). Our hope is that the origins of the different diamond carriers correlate with some of their physical properties, and that by employing the correct techniques (still to be determined) significant enrichments and depletions can be obtained. I present some results of my ongoing effort to implement enrichments or depletions of the distinct carriers by a variety of techniques.

A separated and repurified sample of Murchison diamonds, LD1 was used (19). A portion was used for noble gas measurements by stepped combustion. A major portion of LD1 was used in a titration experiment, finding it similar to separated Allende diamond (20). This portion was then separated by the speed with which it would become colloidal while the acidified flocs settled through a pH gradient . Specifically, the sample was suspended in low ionic strength base and then acidified to pH~2.6; upon ageing most of the diamonds flocked together. These flocs were then transferred to the top of a citric acid pH gradient, pH3 to pH7 (top to bottom) with a moderate excess of buffering capacity compared to that of the diamonds themselves, but with excess base below as well as excess acid above the sample. The whole column was stabilized with an isopropanol-water density gradient. This was then centrifuged at 100xg for 90', settled (1xg) for 7 days, then centrifuged at 200xg for 40', then 1000xg for 120'. As the flocs slowly settled through the column, the diamonds would eventually become ionized and separate into the colloidal phase. Once separated, the small size and high charge density makes these diamonds stable against further settling for laboratory time scales at <4000xg. Visible layers of diamond were evident and were separated one from another. Noble gases where measured by stepped pyrolysis in portions of 4 of the separated fractions, LDA(not flocked at pH~2.6), LD3 (pH~5.4–5.6), LD4 (pH~5.6–6.7), and LD7 (>pH~7). This is just a test of the process as a single pass is unlikely to generate pure samples: surviving flocs will mechanically retain (& entrain) some of the ionized grains. Slight abundance variations in the components are indeed found. These large samples also provide high precision noble gas measurements. Data acquisition and reduction are largely as indicated in (21). It should be added that the nominal blanks have been subtracted, and that these have negligible effects (typically <<1%) for all but the smallest extraction steps, but that the procedural blanks immediately following large fractions are substantially larger, resemble the large fractions, and amount to an effective blurring of the separations obtained by stepped extraction. This effect has been ignored in the Ne, Kr and Xe data tabulated herein.

As reported in (10), where calculation details are explained, the ratio of ^{132}Xe-P3/^{132}Xe-HL varies from 2.00 to 2.37 from Murchison LD3 to LD7. Similarly the model calculation of ^{132}Xe-P3 in Cζ, its carrier, runs from (66±4 to 218±34) x 10-8 cc/g from Murchison LDA to LD7. Evidently this separation procedure is partially effective. I note that the release sequence of P3, HL, then P6 is the same in the 4 pyrolysis samples as in the parent LD1 run by combustion: To first order the data imply that for each component Ne, Kr, & Xe are released together in both pyrolysis and combustion. The combustion sample LD1 has most of its noble gases release correlated with the production of CO_2, as measured with an on line pressure gauge (250–1001°C: 0.7, 4, 9, 2x, 4x, 5x, 7, <0.4, <0.3, <0.2, <0.2, 0.04, 0.03, 0.04 μg of C, where the 3 largest fractions are not well determined due to saturation of the 0 – 0.100 Torr pressure gauge). This combustion temperature is less than that reported by (4), possibly due to a higher oxygen pressure. The combustion sample does show Ne-E, Kr-s, and Xe-s in the highest temperature fractions, in proportions consistent with sub-μm SiC, although at ~100x higher concentration than found in coarser bulk samples of SiC (21), based on the quantity of CO_2 produced. If this higher concentration is due to a special population of SiC, or is due to a new carrier (diamond?) must be left open at this time, especially as the CO_2 quantification has not been confirmed or calibrated. However, the 700, 800, & 900 °C fractions appear to be at most a few tenths of a microgram of C, or <800ppm of SiC, not far from the measured Si abundance as 600ppm SiC!. The separation process may have depleted the SiC from the fractions LDA, LD3, LD4, & LD7. If not then the pyrolysis did not separate the SiC release from the larger amounts of HL, P3 & P6 carried in the diamonds, consistent with the oxidation & pyrolysis behavior of C and SiC. That P3, HL, P6 remain in sequence & that all 3 are mostly released simultaneously with the largest production of CO_2 is consistent with all 3 being carried in diamonds of slightly varying properties.

Refs: (1) Lewis *et al.* (1975) *Science* 190 1251. (2) Lewis *et al.* (1987) *Nature* 326 160. (3) Tang & Anders (1988) *GCA* 52 1235. (4) Verchovsky *et al.* (1993) *LPSC* 24, 1461. (5) Verchovsky *et al.* (1993) *Meteoritics* 28 452. (6) Frick (1977) Proc. *LPSC* 8 273. (7) Ash *et al.* (1987) *Meteoritics* 22 319. (8) Lewis & Anders (1988) *LPSC* 19 679. (9) Verchovsky (1991) *Meteoritics* 26 402. (10) Huss & Lewis (1994) *Meteoritics*, #1 in press. (11) Anders & Zinner (1993) *Meteoritics* 28 490. (12) Russell *et al.* (1991) *Nature* 254 1188 (13) Lewis *et al.* (1991) *Meteoritcs* 26 363. (14) Lewis *et al.* (1991) *LPSC* 22 807. (15) Fraundorf *et al.* (1989) *Ultramicroscopy* 27 401. (16) Huss & Lewis (1984) *Meteoritics*, #2 in press. (17) Clayton (1989) *Astrophys. J.* 340 613. (18) Heymann and Dziczkzniec (1980) *Proc. LPSC* 11 1179 (19) Amari *et al.* (1994) *Geochim. Cosmochim. Acta*, in press. (20) Lewis *et al.* (1989) *Nature* 339 117. (21) Lewis *et al.* (1994) *Geochim. Cosmochim. Acta*, in press.

Acknowledgments: We thank Sachiko Amari for providing the original diamond separate, leading to LD1 and subsequent daughter fractions, from Murchison. Support was provided by NASA grants, currently NAGW-3342.

PRECISION NOBLE GAS MEASUREMENTS ON PRESOLAR DIAMONDS: Lewis R.S.

Sample Temp.°C	22 E-8 cc / g	Neon 20/22	err 20	21/22	err 21	84 E-8 cc / g	Krypton 78/84	err 78	80/84	err 80	82/84	err 82	83/84	err 83	86/84	err 86
LDA Murchison diamond separate (7.75%), pH<2.6; 0.371 mg; Pyrolysis																
600	21	9.003	0.007	0.02882	0.00017	10.09	0.00640	0.00020	0.03986	0.00011	0.2028	0.0002	0.2032	0.0003	0.3113	0.0006
800	108	8.879	0.019	0.02876	0.00002	46.71	0.00628	0.00006	0.03965	0.00004	0.2025	0.0001	0.2035	0.0001	0.3125	0.0003
1000	84	8.783	0.015	0.03014	0.00005	13.77	0.00642	0.00015	0.03950	0.00011	0.2018	0.0001	0.2037	0.0003	0.3135	0.0005
1200	91	8.695	0.016	0.03142	0.00005	2.33	0.00620	0.00089	0.03854	0.00027	0.1989	0.0007	0.2034	0.0012	0.3162	0.0017
1400	152	8.610	0.026	0.03298	0.00002	1.11	0.00643	0.00174	0.03494	0.00046	0.1862	0.0012	0.1992	0.0020	0.3311	0.0033
1600	410	8.542	0.013	0.03520	0.00007	6.08	0.00538	0.00035	0.03428	0.00011	0.1831	0.0003	0.1996	0.0005	0.3338	0.0007
1800	130	8.362	0.021	0.03734	0.00004	6.34	0.00562	0.00031	0.03616	0.00014	0.1893	0.0003	0.2018	0.0005	0.3295	0.0008
2000	13	7.808	0.008	0.03281	0.00013	0.79	0.00603	0.00248	0.03704	0.00057	0.1908	0.0018	0.2006	0.0027	0.3262	0.0045
2200	18	7.180	0.010	0.02480	0.00012	0.24	0.00582	0.00779	0.03430	0.00166	0.2014	0.0060	0.1932	0.0084	0.3110	0.0131
LD3 Murchison diamond separate (13.68%), pH5.4–5.6; 0.373mg; Pyrolysis																
600	40	8.931	0.010	0.02923	0.00007	24.99	0.00628	0.00010	0.03974	0.00005	0.2028	0.0001	0.2036	0.0002	0.3121	0.0003
800	88	8.818	0.018	0.02920	0.00005	42.97	0.00626	0.00005	0.03971	0.00008	0.2025	0.0001	0.2036	0.0002	0.3131	0.0002
1000	87	8.695	0.015	0.03089	0.00005	13.42	0.00625	0.00015	0.03941	0.00012	0.2017	0.0003	0.2035	0.0004	0.3138	0.0006
1200	128	8.614	0.022	0.03258	0.00004	2.20	0.00663	0.00090	0.03771	0.00022	0.1962	0.0007	0.2025	0.0012	0.3211	0.0017
1400	254	8.618	0.044	0.03418	0.00010	2.23	0.00560	0.00088	0.03448	0.00028	0.1837	0.0007	0.2000	0.0011	0.3327	0.0017
1600	320	8.540	0.055	0.03596	0.00007	7.08	0.00545	0.00028	0.03531	0.00011	0.1860	0.0002	0.2014	0.0005	0.3312	0.0007
1800	150	8.398	0.025	0.03791	0.00013	6.35	0.00563	0.00032	0.03549	0.00013	0.1866	0.0003	0.2020	0.0005	0.3302	0.0008
2000	11	8.102	0.007	0.03965	0.00013	0.77	0.00590	0.00253	0.03587	0.00089	0.1890	0.0019	0.1998	0.0028	0.3268	0.0046
2200	3	8.602	0.020	0.03518	0.00028	0.19	0.00849	0.00982	0.03515	0.00204	0.1866	0.0071	0.2012	0.0110	0.3322	0.0176
LD4 Murchison diamond separate (34.03%), pH 5.6–6.7; 0.467mg; Pyrolysis																
600	2	9.161	0.027	0.02917	0.00040	0.91	0.00707	0.00173	0.04014	0.00042	0.2036	0.0014	0.2029	0.0021	0.3104	0.0032
800	105	8.873	0.024	0.02911	0.00014	61.36	0.00628	0.00005	0.03971	0.00004	0.2026	0.0001	0.2097	0.0002	0.3128	0.0003
1000	86	8.746	0.019	0.03040	0.00010	19.98	0.00632	0.00008	0.03948	0.00006	0.2022	0.0001	0.2036	0.0002	0.3135	0.0003
1200	82	8.657	0.018	0.03512	0.00016	2.70	0.00633	0.00058	0.03860	0.00021	0.1991	0.0005	0.2034	0.0007	0.3162	0.0012
1400	162	8.624	0.035	0.03354	0.00006	1.30	0.00563	0.00122	0.03530	0.00037	0.1866	0.0009	0.1996	0.0015	0.3297	0.0022
1600	148	8.603	0.032	0.03465	0.00011	1.48	0.00571	0.00109	0.03449	0.00029	0.1838	0.0008	0.1993	0.0012	0.3308	0.0022
1800	149	8.575	0.032	0.03560	0.00012	2.48	0.00584	0.00068	0.03492	0.00019	0.1856	0.0005	0.2015	0.0009	0.3313	0.0013
2000	328	8.442	0.069	0.03714	0.00007	11.09	0.00609	0.00015	0.03558	0.00007	0.1866	0.0001	0.2015	0.0002	0.3316	0.0004
2200	6	8.185	0.008	0.03851	0.00015	0.61	0.00657	0.00254	0.03707	0.00070	0.1901	0.0019	0.2026	0.0029	0.3277	0.0045
LD7 Murchison diamond separate (15.24%), pH >7; 0.336mg; Pyrolysis																
600	5	8.875	0.015	0.02933	0.00007	41.41	0.00634	0.00019	0.03969	0.00005	0.2027	0.0001	0.2033	0.0002	0.3124	0.0003
800	79	8.791	0.018	0.02961	0.00003	51.24	0.00621	0.00006	0.03958	0.00004	0.2023	0.0001	0.2035	0.0002	0.3131	0.0003
1000	85	8.637	0.015	0.03147	0.00004	15.73	0.00644	0.00014	0.03951	0.00007	0.2019	0.0002	0.2040	0.0003	0.3133	0.0004
1200	114	8.573	0.021	0.03274	0.00003	2.40	0.00626	0.00091	0.03797	0.00024	0.1976	0.0008	0.2019	0.0011	0.3184	0.0018
1400	258	8.567	0.011	0.03426	0.00011	2.18	0.00561	0.00104	0.03491	0.00029	0.1859	0.0007	0.1997	0.0012	0.3291	0.0018
1600	390	8.522	0.010	0.03588	0.00011	8.33	0.00541	0.00029	0.03559	0.00010	0.1872	0.0003	0.2011	0.0004	0.3298	0.0007
1800	209	8.327	0.009	0.03772	0.00014	9.55	0.00566	0.00025	0.03611	0.00009	0.1884	0.0002	0.2014	0.0003	0.3296	0.0006
2000	11	7.203	0.008	0.03259	0.00013	0.97	0.00621	0.00222	0.03678	0.00056	0.1929	0.0017	0.2003	0.0025	0.3246	0.0040
2200	5	7.009	0.018	0.02830	0.00022	0.29	0.00517	0.00732	0.03697	0.00159	0.1963	0.0054	0.1993	0.0078	0.3162	0.0123
2300	2	8.503	0.015	0.03407	0.00032	0.20	0.00666	0.00998	0.03740	0.00217	0.1982	0.0077	0.2048	0.0111	0.3255	0.0178
LD1 Murchison purified diamond (=100%), 1.219mg; Combustion																
200	1.48	9.004	0.045	0.0302	0.0002	0.786	0.00627	0.00043	0.03999	0.00031	0.2034	0.0004	0.2036	0.0004	0.3107	0.0004
250	5.25	8.977	0.045	0.0299	0.0001	3.219	0.00614	0.00013	0.03991	0.00008	0.2027	0.0002	0.2034	0.0003	0.3110	0.0003
298	14.97	8.896	0.044	0.0300	0.0001	9.186	0.00623	0.00005	0.03973	0.00004	0.2026	0.0002	0.2035	0.0001	0.3110	0.0003
350	37.57	8.777	0.044	0.0299	0.0001	19.721	0.00624	0.00006	0.03963	0.00003	0.2027	0.0001	0.2035	0.0001	0.3117	0.0002
400	106.54	8.710	0.044	0.0314	0.0002	32.858	0.00619	0.00004	0.03945	0.00008	0.2021	0.0002	0.2035	0.0002	0.3127	0.0003
450	357.08	8.572	0.043	0.0334	0.0002	37.730	0.00603	0.00003	0.03877	0.00008	0.1995	0.0002	0.2032	0.0002	0.3157	0.0003
475	458.10	8.427	0.042	0.0359	0.0002	10.674	0.00546	0.00004	0.03530	0.00006	0.1858	0.0001	0.2015	0.0001	0.3315	0.0002
500	13.19	7.819	0.039	0.0419	0.0002	0.162	0.00439	0.00214	0.03179	0.00038	0.1708	0.0009	0.1931	0.0010	0.3482	0.0011
550	0.52	7.765	0.039	0.0393	0.0004	0.014	0.02010	0.01787	0.04070	0.00168	0.1921	0.0032	0.1956	0.0047	0.3249	0.0038
600	0.62	7.867	0.039	0.0346	0.0005	0.010	0.00680	0.02276	0.04050	0.00169	0.1940	0.0043	0.1968	0.0028	0.3195	0.0071
700	1.08	6.779	0.036	0.0257	0.0002	0.012	0.00580	0.01617	0.03940	0.00195	0.2098	0.0032	0.1935	0.0029	0.2935	0.0065
800	0.79	5.491	0.067	0.0246	0.0003	0.011	-0.00245	0.02029	0.04310	0.00282	0.2151	0.0041	0.1928	0.0048	0.3062	0.0031
900	0.20	4.562	0.216	0.0247	0.0011	0.008	0.01250	0.01999	0.04260	0.00296	0.2125	0.0049	0.1909	0.0039	0.2982	0.0057
1000	0.08	3.017	0.497	0.0239	0.0029	0.006	-0.00250	0.03288	0.04650	0.00357	0.2070	0.0060	0.1970	0.0050	0.3020	0.0090
1000	0.14	9.354	0.104	0.0311	0.0015	0.010	0.01840	0.02136	0.04060	0.00244	0.2100	0.0030	0.1920	0.0050	0.3060	0.0040

Sample Temp.°C	132 E-8 cc / g	Xenon 124/132	err124	126/132	err126	128/132	err128	129/132	err129	130/132	err130	131/132	err131	134/132	err134	136/132	err136
LDA Murchison diamond separate (7.75%), pH<2.6; 0.371 mg; Pyrolysis																	
600	2.9554	0.00467	0.00020	0.00412	0.00004	0.0813	0.0002	1.0720	0.0007	0.16013	0.00023	0.8248	0.0004	0.3834	0.0003	0.3219	0.0006
800	18.1634	0.00466	0.00001	0.00409	0.00001	0.0804	0.0001	1.0574	0.0006	0.15936	0.00007	0.8240	0.0004	0.3822	0.0003	0.3201	0.0003
1000	5.9134	0.00474	0.00002	0.00412	0.00002	0.0808	0.0001	1.0396	0.0004	0.15912	0.00015	0.8238	0.0004	0.3904	0.0003	0.3323	0.0004
1200	1.3348	0.00542	0.00005	0.00444	0.00004	0.0836	0.0002	1.0261	0.0018	0.16050	0.00027	0.8222	0.0013	0.4498	0.0008	0.4215	0.0013
1400	1.0888	0.00734	0.00007	0.00522	0.00006	0.0877	0.0003	1.0215	0.0016	0.15850	0.00033	0.8295	0.0012	0.5757	0.0014	0.6079	0.0011
1600	6.6593	0.00773	0.00003	0.00537	0.00001	0.0887	0.0001	1.0447	0.0005	0.15805	0.00013	0.8376	0.0004	0.5943	0.0005	0.6418	0.0005
1800	7.3478	0.00723	0.00003	0.00530	0.00003	0.0881	0.0001	1.0569	0.0004	0.15668	0.00008	0.8362	0.0005	0.5505	0.0004	0.5848	0.0008
2000	1.5775	0.00665	0.00007	0.00515	0.00004	0.0882	0.0003	1.0556	0.0012	0.15880	0.00036	0.8318	0.0016	0.5176	0.0010	0.5389	0.0008
2200	0.5648	0.00601	0.00005	0.00459	0.00011	0.0866	0.0004	0.9647	0.0023	0.18360	0.00039	0.7762	0.0030	0.4807	0.0019	0.4965	0.0012
LD3 Murchison diamond separate (13.68%), pH5.4–5.6; 0.373mg; Pyrolysis																	
600	8.0108	0.00467	0.00002	0.00410	0.00002	0.0810	0.0001	1.0701	0.0008	0.15985	0.00012	0.8239	0.0005	0.3822	0.0003	0.3202	0.0007
800	17.4512	0.00465	0.00002	0.00410	0.00001	0.0803	0.0000	1.0522	0.0005	0.15887	0.00010	0.8246	0.0004	0.3832	0.0001	0.3207	0.0003
1000	5.5963	0.00481	0.00001	0.00417	0.00002	0.0806	0.0002	1.0399	0.0012	0.15844	0.00010	0.8260	0.0006	0.3950	0.0004	0.3386	0.0005
1200	1.4822	0.00621	0.00006	0.00486	0.00005	0.0840	0.0003	1.0341	0.0016	0.15664	0.00032	0.8323	0.0007	0.4992	0.0012	0.4934	0.0008
1400	2.1508	0.00774	0.00005	0.00528	0.00006	0.0877	0.0002	1.0358	0.0014	0.15508	0.00034	0.8394	0.0012	0.6019	0.0010	0.6445	0.0011
1600	7.1547	0.00766	0.00004	0.00537	0.00002	0.0882	0.0002	1.0490	0.0005	0.15549	0.00014	0.8379	0.0006	0.5884	0.0005	0.6326	0.0005
1800	8.2303	0.00728	0.00003	0.00530	0.00002	0.0881	0.0001	1.0602	0.0006	0.15646	0.00014	0.8372	0.0004	0.5529	0.0003	0.5878	0.0006
2000	1.6898	0.00690	0.00008	0.00522	0.00004	0.0878	0.0002	1.0575	0.0013	0.15706	0.00024	0.8337	0.0011	0.5278	0.0012	0.5563	0.0013
2200	0.4257	0.00725	0.00011	0.00523	0.00010	0.0879	0.0006	1.0471	0.0030	0.15560	0.00060	0.8366	0.0022	0.5564	0.0021	0.5848	0.0017
LD4 Murchison diamond separate (34.03%), pH 5.6–6.7; 0.467mg; Pyrolysis																	
600	0.2506	0.00467	0.00005	0.00410	0.00014	0.0815	0.0004	1.0790	0.0040	0.16110	0.00050	0.8237	0.0021	0.3849	0.0016	0.3223	0.0013
800	22.8849	0.00468	0.00002	0.00408	0.00001	0.0804	0.0001	1.0590	0.0005	0.15924	0.00010	0.8249	0.0003	0.3828	0.0002	0.3201	0.0003
1000	8.5199	0.00477	0.00001	0.00413	0.00002	0.0803	0.0001	1.0405	0.0008	0.15882	0.00010	0.8250	0.0004	0.3897	0.0002	0.3309	0.0004
1200	1.4548	0.00557	0.00007	0.00445	0.00004	0.0825	0.0002	1.0368	0.0015	0.15739	0.00023	0.8299	0.0008	0.4473	0.0009	0.4172	0.0010
1400	1.2445	0.00728	0.00004	0.00522	0.00004	0.0867	0.0002	1.0338	0.0015	0.15523	0.00021	0.8358	0.0014	0.5767	0.0011	0.6086	0.0013
1600	1.4110	0.00774	0.00007	0.00533	0.00004	0.0879	0.0003	1.0384	0.0011	0.15534	0.00026	0.8392	0.0009	0.6035	0.0011	0.6471	0.0007
1800	2.3312	0.00772	0.00005	0.00540	0.00004	0.0882	0.0002	1.0431	0.0010	0.15532	0.00023	0.8394	0.0011	0.5979	0.0008	0.6413	0.0008
2000	13.3948	0.00737	0.00002	0.00530	0.00002	0.0882	0.0001	1.0563	0.0007	0.15620	0.00011	0.8387	0.0004	0.5828	0.0002	0.6011	0.0007
2200	1.3759	0.00688	0.00003	0.00508	0.00004	0.0877	0.0002	1.0588	0.0009	0.15702	0.00027	0.8352	0.0011	0.5307	0.0008	0.5542	0.0009
LD7 Murchison diamond separate ((15.24%), pH >7; 0.336mg; Pyrolysis																	
600	14.1081	0.00463	0.00001	0.00408	0.00001	0.0806	0.0001	1.0674	0.0006	0.15943	0.00008	0.8250	0.0005	0.3809	0.0002	0.3167	0.0003
800	21.3982	0.00462	0.00001	0.00407	0.00001	0.0802	0.0001	1.0500	0.0005	0.15871	0.00008	0.8247	0.0003	0.3819	0.0002	0.3194	0.0003
1000	6.6877	0.00479	0.00003	0.00415	0.00002	0.0808	0.0002	1.0414	0.0007	0.15852	0.00021	0.8255	0.0007	0.3924	0.0002	0.3344	0.0004
1200	1.5396	0.00597	0.00006	0.00460	0.00006	0.0839	0.0003	1.0339	0.0014	0.15810	0.00040	0.8289	0.0015	0.4820	0.0011	0.4685	0.0011
1400	1.9855	0.00744	0.00004	0.00523	0.00004	0.0883	0.0003	1.0346	0.0013	0.15761	0.00022	0.8331	0.0013	0.5985	0.0009	0.6254	0.0010
1600	7.5503	0.00758	0.00003	0.00531	0.00002	0.0882	0.0001	1.0475	0.0007	0.15573	0.00012	0.8369	0.0005	0.5829	0.0004	0.6253	0.0008
1800	11.6832	0.00720	0.00002	0.00522	0.00002	0.0880	0.0001	1.0575	0.0008	0.15679	0.00009	0.8368	0.0003	0.5458	0.0004	0.5785	0.0006
2000	2.1682	0.00677	0.00004	0.00503	0.00005	0.0889	0.0002	1.0475	0.0008	0.16070	0.00030	0.8291	0.0010	0.5209	0.0007	0.5444	0.0012
2200	0.5152	0.00662	0.00012	0.00462	0.00009	0.0927	0.0004	1.0148	0.0035	0.17060	0.00070	0.8046	0.0021	0.5083	0.0015	0.5288	0.0017
LD1 Murchison purified diamond (=100%), 1.219mg; Combustion																	
250	0.8574	0.00471	0.00005	0.00415	0.00003	0.0817	0.0002	1.0690	0.0010	0.15964	0.00020	0.8239	0.0010	0.3899	0.0004	0.3309	0.0007
298	2.5415	0.00479	0.00003	0.00411	0.00002	0.0813	0.0002	1.0681	0.0010	0.15982	0.00010	0.8247	0.0005	0.3903	0.0003	0.3323	0.0004
350	6.2169	0.00479	0.00001	0.00417	0.00002	0.0810	0.0001	1.0611	0.0003	0.15948	0.00009	0.8244	0.0002	0.3932	0.0002	0.3358	0.0004
400	13.2754	0.00499	0.00001	0.00420	0.00001	0.0810	0.0001	1.0514	0.0005	0.15850	0.00013	0.8251	0.0002	0.4073	0.0002	0.3563	0.0004
450	22.4071	0.00567	0.00001	0.00451	0.00001	0.0824	0.0001	1.0449	0.0002	0.15709	0.00021	0.8289	0.0003	0.4553	0.0004	0.4293	0.0004
475	13.2420	0.00719	0.00001	0.00523	0.00000	0.0875	0.0001	1.0593	0.0004	0.15590	0.00012	0.8362	0.0002	0.5493	0.0003	0.5822	0.0005
500	0.5012	0.00687	0.00008	0.00524	0.00006	0.0908	0.0004	1.0810	0.0020	0.16127	0.00030	0.8352	0.0010	0.5013	0.0006	0.5408	0.0009
550	0.0299	0.00640	0.00020	0.00490	0.00020	0.0912	0.0013	1.0790	0.0060	0.16400	0.00190	0.8340	0.0040	0.4760	0.0030	0.5080	0.0030
600	0.0185	0.00600	0.00020	0.00430	0.00020	0.0917	0.0018	1.0550	0.0110	0.16460	0.00190	0.8210	0.0040	0.4730	0.0030	0.4830	0.0050
700	0.0177	0.00480	0.00020	0.00410	0.00030	0.1084	0.0014	0.9260	0.0100	0.20590	0.00220	0.7490	0.0080	0.3920	0.0020	0.3920	0.0020
800	0.0227	0.00470	0.00020	0.00380	0.00020	0.1060	0.0019	0.9080	0.0060	0.20650	0.00190	0.7290	0.0050	0.3930	0.0040	0.4020	0.0060
900	0.0088	0.00420	0.00030	0.00400	0.00040	0.1066	0.0032	0.9010	0.0080	0.23200	0.00200	0.7500	0.0080	0.3990	0.0070	0.3910	0.0060
1000	0.0028	0.00470	0.00110	0.00440	0.00060	0.0870	0.0070	0.8790	0.0200	0.21300	0.00800	0.7200	0.0400	0.4100	0.1800	0.3820	0.1500
1001	0.0023	0.00700	0.00200	0.00400	0.00100	0.0940	0.0030	0.9620	0.0170	0.18300	0.00500	0.7910	0.0170	0.4390	0.0110	0.4120	0.0100

EXPLORING METEORITE MYSTERIES: A TEACHERS' GUIDE WITH ACTIVITIES .
M. Lindstrom (SN2/NASA JSC, Houston TX 77058), J. Allen (DUAL), A. Treiman (Lockheed), J. Burch (Pearland ISD), K. Crowell, K. Stocco, B. Swaby (Pasadena ISD), R. Luksch, K.Tobola (Alvin ISD).

In 1991 two boys in Noblesville, Indiana watched a rock fall out of the sky. Their curiosity led them to ask questions about what it was and what it meant. They learned that it was a meteorite. Scientists told them that meteorites reveal clues to many of the mysteries of the solar system, such as: how the solar system formed; what the asteroids, Moon and Mars are like; how life began; or how the dinosaurs died. EXPLORING METEORITE MYSTERIES is a teachers' guide with activities that allows other students to share the boys' experience and to investigate many of the mysteries of the solar system.

EXPLORING METEORITE MYSTERIES was developed at JSC by a team of planetary scientists and teachers from grades 4-12 with funding and guidance from the NASA Office of Education. It is currently being tested and evaluated in classrooms in Houston for revision and publication in 1994. It will be available through education offices at all NASA centers or through the JSC Office of the Curator. The teachers' guide will be available separately, with audio-visual materials (currently a slide set; a video or CD are planned), or packaged with a lucite disk containing chips of six different types of meteorites. EXPLORING METEORITE MYSTERIES teaches basic science concepts and techniques together with math, reading, writing and social implications. It is consistent with national goals for the reform of science education. The lessons include a variety of different teaching styles that are either hands-on or heads-on and emphasize observation, experimentation and critical thinking. The activities are designed for upper elementary through high school; most of the lessons can be easily modified for different grade levels. The interdisciplinary approach is ideal for the Middle School team format. Meteorites are a natural subject for interdisciplinary teaching because their study involves all fields of science (math, physics, chemistry, earth science, astronomy, biology) and offers fascinating historical accounts and possibilities for creative expression.

The EXPLORING METEORITE MYSTERIES teachers' guide contains three main parts: 1) Background information for the teacher or advanced student; 2) Classroom activities and 3) Narrative for the accompanying slides. The outline for the lessons is given below. The lessons begin with the story of the two boys witnessing the Noblesville fall. Students are asked to put themselves in the boys' place and brainstorm on how the boys felt, what they did, and what they wanted to know. This student involvement sets the stage for the following lessons that attempt to answer the questions: Where did they come from? What are they? How did they form? How do they affect people? and How can I use them? The concluding lessons are an activity on careers and teamwork and a meteoroid tabloid.

EXPLORING METEORITE MYSTERIES provides teachers with information, activities and visual aids to use meteorites to teach the interdisciplinary science of the solar system. It also provides planetary scientists with activities to take to local schools and ideas for sharing their knowledge with their communities.

EXPLORING METEORITE MYSTERIES Outline: Lindstrom M. et al.

PART 1 BACKGROUND INFORMATION

PART 2 CLASSROOM ACTIVITIES

Lesson #	Topic	Activity type/Objective	Subject
1	Noblesville Fall	brainstorm	English
2	Follow the falling meteorite	triangulate, plot data	math
3	Searching for meteorites	experiment, control variables	earth science
4	Orbits in the solar system	plot trajectories, predict	math, physics
5	Looking at asteroids	observe, experiment	astronomy, physics
6	Making impact craters	experiment, observe, predict	earth, physics
7	Crater hunters	map, observe, predict	earth science
8	Edible rocks	observe, describe, teamwork	science, English
9	Classifying meteorites	observe, compare	chemistry
10	Building blocks of planets	demonstrate, experiment	astronomy, chem
11	Changes inside planets	demonstrate, experiment	earth, chemistry
12	Building blocks of life	critical thinking, experiment	biology, chemistry
13	Noblesville meteorite	observe, describe, classify	chemistry, earth
14	Meteorite explorers' game	critical thinking	astronomy, earth
15	Historical meteorite falls	read, critical thinking	English, history
16	Near miss - impacts	role play, plan	social studies
17	Direct hit - K/T crater	analyze, experiment, write	bio, chem, Eng.
18	Asteroid resources	sim[illegible] experiment, plan	astronomy, social
19	Antarctic meteorite teams	tea[illegible] careers	science, social
20	Meteoroid tabloid, epilogue	ev	English, science

PART 3 NARRATIVE FOR SLIDE SET

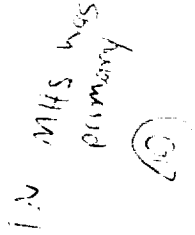

S21-90 AC
2423

PIGEONHOLING PLANETARY METEORITES: THE LESSONS OF MISCLASSIFICATION OF EET87521 AND ALH84001.

M.M. Lindstrom[1], A.H. Treiman[2] and D.W. Mittlefehldt[3]. 1) SN2 NASA-JSC, 2)Lunar and Planetary Institute, 3) C23 Lockheed, Houston TX 77058.

The last few years have provided two noteworthy examples of misclassifications of achondritic meteorites because the samples were **new kinds** of meteorites from **planetary** rather than asteroidal parent bodies. Basaltic lunar meteorite EET87521 was misclassified as a eucrite [1,2] and SNC (martian) orthopyroxenite ALH84001 was misclassified as a diogenite [3]. (Here a *planetary body* is one that remained internally active for a significant period of geologic time. The term *planetary bodies* includes the Moon, while *the planets* does not.) In classifying meteorites **we find what we expect:** we pigeonhole meteorites into known categories most of which were derived from the more common asteroidal meteorites. But the examples of EET87521 and ALH84001 remind us that planets are more complex than asteroids and exhibit a wider variety of rock types. We should **expect variety** in planetary meteorites and we need to know how to **recognize them when we have them.**

Lunar meteorites were unknown and unexpected in 1982 when ALHA81005 was found in Antarctica. But the comparison of this anorthositic breccia with returned lunar samples left no doubt as to its parent body. As the number of lunar meteorites grew to 7, our knowledge that 17% of the lunar surface was covered by mare basalts should have led us to anticipate a basaltic lunar meteorite. Nonetheless EET87521 was classified as a eucrite because it almost fit in that pigeonhole. Its real parentage was soon discovered by investigators [1,2] and within a year three more basaltic lunar meteorites were identified (two reclassified and one a new meteorite). In 1991, with the lunar highlands and mare well represented by meteorites, the discovery of Calcalong Creek, a KREEP-rich lunar breccia [4], was surprising only as the first non-Antarctic lunar meteorite. Table 1 lists generalized lithologies of meteorite parent bodies and planets. The lithologic types and abundances for Earth and Moon were determined by studies of surface rocks, while those of the asteroids and other planets were inferred from meteorites and remote geology. The current suite of lunar meteorites represents the three most common lithologies on the lunar surface.

The study of martian meteorites has also been hampered by pigeonholing. ALHA77005 was originally classified as a unique achondrite with similarities to several types of achondrites. Research established a petrogenetic link to shergottites and subsequently ALHA77005 (and later LEW88516) was classified as a shergottite, a basalt pigeonhole that does not really fit its ultramafic character (10 % plagioclase). ALH84001 was also pigeonholed, as a diogenite, where it remained little-studied for 8 years before its SNC affinities were revealed [3]. By the mid-1980s SNC achondrites were assumed to be martian meteorites [5, 6] by all but the most diehard skeptics. Should we not have expected a wider variety in basalts and ultramafic rocks from the planet Mars than are seen in the HED meteorite suite from an asteroid? Yet we continued to try to squeeze all martian meteorites into one of the three S-N-C pigeonholes. If we had opened our minds to a wider variety of martian igneous rocks, might we have discovered ALH84001 sooner?

Our intent here is to show that our asteroidal perspective is inappropriate for planetary meteorites, not to criticize curators for misclassifications. The initial descriptions and classifications are deliberately cursory so as not to impinge on detailed research, yet they noted unusual features in both EET87521 and ALH84001 which should have been clues that further study was needed. Table 2 lists some characteristics of basalts (and ultramafic rocks) from various bodies in the solar system. Some are determined in the initial classification, but others should be measured in the first round of scientific analysis. Many of these characteristics have been used before to distinguish planetary from asteroidal meteorites, especially Fe/Mn and oxygen isotopes, but they are tabulated together here for the whole suite of basalts. Many other characteristics are also useful. No single characteristic can clearly identify the parent body because the values overlap (Fe/Mn HED=Mars, Earth~Moon; O isotopes: HED=Angrites, Earth=Moon), but two or more characteristics together may be definitive, even without the canonical oxygen isotope analysis. Use of these characteristics should make it possible to identify planetary igneous rocks within the first year of study and prevent the recurrence of the long delay in discovery of ALH84001.

Several of the characteristics in Table 2 appear to be dependent on the size of the parent body: oxidation state, volatile content, and ages of volcanism. The smaller bodies, the Moon and the differentiated asteroids, are volatile-poor and more reduced than the planets which are volatile-rich and oxidized. Duration of volcanism is shorter on smaller bodies. Other correlations with the size of the parent body include the variety and fractionation of igneous rocks [7, 8]. The differences in volatiles, duration, variety and fractionation are reflected in Table 1.

Sedimentary rocks are not expected on the Moon and asteroids because they are volatile-depleted and lack an atmosphere, but should be common on the terrestrial planets (except Mercury). Fractionation on the Moon was early and global and led to anorthosites, while igneous processes on Earth were complex and produced granites. Mars is likely to be intermediate between Earth and Moon and Venus to be more Earth-like.

In comparing the current suite of martian meteorites to the expected lithologies, we see that they represent only mafic igneous rocks. We have no felsic rocks, sediments or impact breccias. Furthermore, they represent only the young volcanic province, and not the older martian highlands. The characteristics listed in Table 2 may serve as a starting point in evaluating likely mineralogies and compositions of sediments and felsic igneous rocks, but the values will be modified by fractionation and sedimentary processes. However, we must first find the meteorites before we can identify their parent bodies. Would we recognize martian sediments or felsic rocks as meteorites if we found them in Antarctica? Probably not, because they would look too much like Earth rocks. The case is even worse for recognizing possible Earth or Venus meteorites [9]. As long as we look at all meteorites from an asteroidal rather than planetary perspective, we may be missing some of the most interesting meteorites .

TABLE 1. KNOWN AND LIKELY LITHOLOGIES OF DIFFERENTIATED METEORITE PARENT BODIES AND PLANETS. [CAPS: known based on field geology and surface samples. **bold**: known as meteorites. under: very likely, based on remote geology or inferred from collected meteorites. *italics*: likely, based on remote geology or inferred from collected meteorites. Refs. 5-12]

Lithologies	HED	Angrites	Moon	Earth	Mars	Venus
Igneous						
basaltic	common	**common**	COMMON	COMMON	common	common
ultramafic	present	**present**	RARE	RARE	**common**	*rare*
anorthositic	none	none	COMMON	RARE	*possible*	*rare*
granitic	none	none	RARE	COMMON	*possible*	*probable*
Sedimentary						
chemical/clastic	none	none	NONE	COMMON	common	common
Impact						
breccias	common	*possible*	COMMON	RARE	*possible*	*rare*
Metamorphic						
meta igneous	present	*possible*	PRESENT	PRESENT	*possible*	*possible*
meta sediment	none	none	NONE	PRESENT	*rare*	*possible*
meta impact	*possible*	*possible*	PRESENT	RARE	*rare*	*rare*

TABLE 2. CHARACTERISTICS OF SOLAR SYSTEM BASALTS. [normal: approximate measurements in surface samples for Earth & Moon, in meteorites for Mars, HED and Angrites and remote sensing for Venus. *italics*: inferred from remote measurements and geology for Venus. Refs. 5-7, 10-13]

Characteristics	HED	Angrites	Moon	Earth	Mars	Venus
Mineral Composition						
Fe/Mn (px)	35	90	70	60	35	*55*
Plagioclase	An90	An99	An92	An50	An50	--
Oxidation: Fe3+ ox, px	N	Y (ox)	N	Y	Y	Y
iron metal	Y	N	Y	N	N	*N*
sulfide	Troilite	Troilite	Troilite	Pyrrh.	Pyrrh.	*Pyrrh.*
Secondary Alteration Minerals	none	none	none	Hydrous CO_3, SO_4	Hydrous CO_3, SO_4	*Anhydrous* CO_3, SO_4
Bulk Composition						
Fe/Mn	28-40	80-95	60-80	50-70	35-50	55±30
K/U	2,000	150	1,700	12,500	15,000	12,500
K/La (xCI)	0.03	0.002-0.03	0.03	0.15	0.2	*0.1-0.2*
Rb/La (xCI)	0.002-0.02	0.001	0.016	0.09	0.3	*0.1*
Isotopic Composition						
$\Delta^{17}O$	-0.2	-0.2	0.00	0.00	+0.3	*0.0-0.3*
Age of Volcanism	4.6-4.5 Ga	4.6 Ga	4.3 - 3 ? Ga	4 Ga - 0 a	4 ? Ga - 180 ? Ma	*4 Ga- 0 a*

References: [1] Delaney (1989) Nature 342, 889-890. [2] Warren and Kallemeyn (1989) GCA 53, 3323-3330. [3] Mittlefehldt (1994) Meteoritics., in press. [4] Hill et al (1991) Science 352, 614-617. [5] McSween (1985) Rev. Geophys. 23, 391-416. [6] Treiman et al (1986) GCA 50, 1071-1091. [7] BVSP (1981) Basaltic Volcanism on the Terrestrial Planets, Pergamon, 1286 pp. [8] Walker et al (1979) PLPSC 10, 1995-2015. [9] Melosh and Tonks (1993) Meteoritics 28, 398. [10] Keiffer et al, ed (1992) Mars, U.Az, 1498 pp. [11] Barsikov, ed (1992) Venus Geology, Geochemistry and Geophysics, U.Az, 421 pp. [12] Mittlefelhdt & Lindstrom (1990) GCA 54, 3209-3218. [13] Clayton & Mayeda (1983) EPSL 62, 1-6.

THUMBPRINT TERRAIN IN ISIDIS PLANITIA: FORMED IN A GLACIAL PALEOLAKE ENVIRONMENT?

J. F. Lockwood (Sahuaro H. S., Tucson, AZ.), J. S. Kargel, (USGS-Flagstaff)

INTRODUCTION- Much controversy surrounds the nature of the thumbprint terrain (hereafter "TT") of the northern plains of Mars. Otherwise known as "striped ground"[1] or whorl patterned terrain[2], these areas of curvilinear, parallel ridges, are found overlying millions of square kilometers between 30 and 70° N , although a very large area (Isidis Planitia), centered at 13° N, 272° lies near the equator. Occupying topographic basins primarily at elevations between 0 and -2 km. relative to the Martian datum, 22 areas of TT exist, ranging in size from 5,000 to 420,000 km^2. Some ridges are continuous in nature, but many have a beaded or knobby structure. Each area of TT is associated with anastomosing ridge systems or solitary long sinuous ridges that are typical of eskers on earth.[3] The tops of many of the knobby thumbprint hills appear to be indented along their top surface to some degree. Single ridges can be composed of up to thirty of these knobby hills connected together via shallow undulating valleys, making some ridges over 30 km. in length. Other ridge systems appear to be reduced to isolated beads with several hundred meter gaps separating them. Several explanations have been proposed for the genesis of TT, among them recessional moraines[1], ice-pushed ridges[5], linear ice-cored ridges[6], products of the breakdown of surface material by subsurface ice, ice-shoved glaciotectonic ridges[2], or paleoshore features. The largest area of TT, Isidis Planitia, will be discussed in detail. Our interpretation is that TT represents moraines formed in a glaciolacustrine environment.

OBSERVATIONS - The shape of Isidis Planitia is fairly circular, and follows the basin contours. Ridges are absent in the center of the basin in an area approximately 100 km in radius (see Fig. 1). The parallel ridges to the east, southwest, and northeast of the center of Isidis tend to form crudely concentric or arcuate patterns.

In some of the Isidis TT areas, the ridges are reduced to the previously mentioned "beaded" hills. These hills are remarkably uniform in size, ranging from 300 to 800 m. long, with the vast majority 400 m. in length and 300 m. in width (N = 193). In some regions the hills, whether connected or separated, line up in parallel rows, and have an average separation of between 2 and 4.0 km. (See Table 1, VO frame 146S23). In other regions the ridges, and the knobs that make them up, degenerate into a more chaotic pattern (See VO frame 146 S17).

Several esker-like ridges stretch in a parallel fashion between 274 and 279°, at 18° N. In fact, many of the other areas of TT in the Northern Plains have these same type of structures associated with them, and often occur on the outer margins of the TT region. In the case of Isidis Planitia TT, esker-like ridges and associated tunnel valley type structures ring the basin, with the majority of them along the northern most edge near 18 to 19° N. Their orientation appears to be uniformly downslope and all of them align radially with the area in the center of the basin (13° N, 272°) that is bereft of TT, like the spokes of a wheel (See fig. 1). Similar features, also interpreted as eskers and tunnel channels, occur with other possible glacial landforms in other large basins, such as Argyre and Hellas Planitia and elsewhere in the northern plains.[3]

INTERPRETATIONS - We propose that TT of the Isidis Planitia has a glaciolacustrine origin. Rogen and De Geer moraines appear of fit the parameters of TT to a large degree, except TT ridges are larger. Rogen moraine, explained as an underwater glacial push moraine, give an irregular ribbed appearance to the landscape[7]. In Quebec, individual ridges range from 10 to 30 meters high, are over 1 km. long, and have crests between 100 and 300 meters apart. The ridges are "gently arcuate, and slightly concave upglacier".[8] De Geer moraines are smaller features, seldom reaching 15 m. in height and their separations can reach 300 m. De Geer moraines may form some distance behind the margin of an ice sheet which floats in a sea or lake[9], but their origin is a matter of conjecture. Sublacustrine recessional moraine ridges have been discovered by soundings off the coast of Norway in over 400 m of water. These moraines are more than 1 km long and are up to 30 m high. They appear to be directly deposited by glacier ice in at least 400 m of water[10]. Other such large moraines have been detected in other shelf areas,[11] in the Gulf of Bothnia under 150 m of water, and off the coast of Labrador[12]. Martian TT, in its fully developed ridge form or in its knobby form, is almost an order of magnitude larger than these terrestrial examples.

Thumbprint terrain may well be a much too general term for several different types of ridges found in Isidis. Three separate types of TT exist in the Isidis Planitia system: a lobate, arcuate uniform ridge form; a beaded, pearl necklace like, somewhat discontinuous, yet parallel form; and a seemingly eroded, dappled linear form. In the Isidis Planitia basin, all three types occur along with other evidence that can be interpreted in terms of a lake and glacier environment. R plots and cumulative frequency measurements by elevation, show a distinct decrease in small craters in lower areas all across the northern plains[13], which suggests an agent of deposition in these regions. The pattern of esker-like features, all radially situated to the center of the basin, lends support to the hypothesis that a disconnected ice sheet once covered this region at some time in the past. In an era of a warmer climate on Mars, this ice sheet may have overlain a 500 to 1000 m deep lake. The total or partial freezing of this water layer, the grounding of all or part of the ice sheet, and its subsequent ablation in a dry climate could account for many of the TT/moraine features mapped in the basin. TT may be a combination of end or recessional moraines, push moraine, and De Geer type moraine all deposited at different stages in the evolution of such a marine ice sheet. The final disintegration of the glacial lobes may produce, towards the center of such a receding and disintegrating glacier, glacial karst topography. [14] Possible glacial Karst is seen in the center of Isidis.

CONCLUSIONS - The existing TT pattern in Isidis Planitia could be explained by the solidification of a large (400,000 km^2) paleosea in the Isidis basin, perhaps part of Oceanus Borealis[15] or a separate entity similar to the proposed Elysium Paleolake.[16] It is hypothesized that the Isidis paleolake gradually froze, the ice eventually grounded, and the frozen lake then behaved as a glacial ice sheet, until the glacier sublimated under cold, dry conditions. Further study is

THUMBPRINT TERRAIN J.F. Lockwood, J. S. Kargel

necessary to ascertain whether the types of TT found on the edges of the basin are fundamentally different from the TT found closer to the center, or are gradations of same depositional phenomena.

References: [1]Carr, M. H., Shaber, G. G., 1977, *J. G. R., v. 82*, pp. 4039-4065. [2]Scott, D. H., Underwood, J. R., 1982, *J. G. R., v.* [3]Kargel, J. S., Strom, R. G., 1991, Geology, v. 20, p.3-7, [4] Scott, D. H., Underwood, J. R., 1991, *Proc. Lunar and Pl. Conf. XXI, LPI*, pp. 627-634., [5]Rossenbacher, L. A., Judson, S., 1981, *Icarus, v. 45*, pp. 39-59. [6]Kupsch, W. O., 1962, *Jour. Geol., v. 70*, pp 582-594., [7]Cowan, W. R., 1968, *Can. Jour. Earth Sci., v. 5*, pp 1145-59., [8]Hughes, O. C., 1964, *Bull. Geol. Surv. Canada, v. 106*, pp 2-22., [9]Andrews, J. T., 1975, *Glacial Systems*, Duxbury, pp. 147-170., [10]Holtedahl, H., Sellevoll, M., 1972, in Andrews, 1975, p. 159., [11]Winterhalter, B., 1972, *Fin. Geol. Survey Bull., v 258*, 66 pages., [12]Fillon, R. H., 1975, *Nature-London, v. 253*, pp. 429-31., [13]Lockwood, J. F., *LPSC XIV*, pp. 1099-1101., [14]Clayton, K. M., 1964, *Jour. of Glac., v. 5*, pp. 107-112., [15]Baker, V. R., Strom, R. G., et. al., 1991, *Nature, v. 352*, pp. 588-596., [16]Scott, D. H., Underwood, M. G., 1991, *Proc. of the Lunar and Pl. Conf. XXI, LPI*, pp. 669-634.

Table 1 - Measurements of Thumbprint Ridge Beads and Ridge Separations (Wavelengths)

Part I - "Bead" Characteristics

Parameter	Value (km)
Bead length (max)	.80
Bead length (min)	.20
Bead length (mean)	.43 ± .10
Bead length (median)	.40
Bead width	.20 to .40 ± .10
Sample Size = 193	

Part II - Ridge Separations ("Wavelengths")

Wavelength (max)	8.4
Wavelength (min)	2.0
Wavelength (mean)	4.1 ± .3
Sample Size = 95	

Part III - Thumbprint Ridge Separations (or wavelengths)

Bin (km.)	# wavelengths in bin
2 to 4.0	58
4.1 to 6.0	25
6.1 to 8.0	10
> 8.0	2
Sample Size = 95	

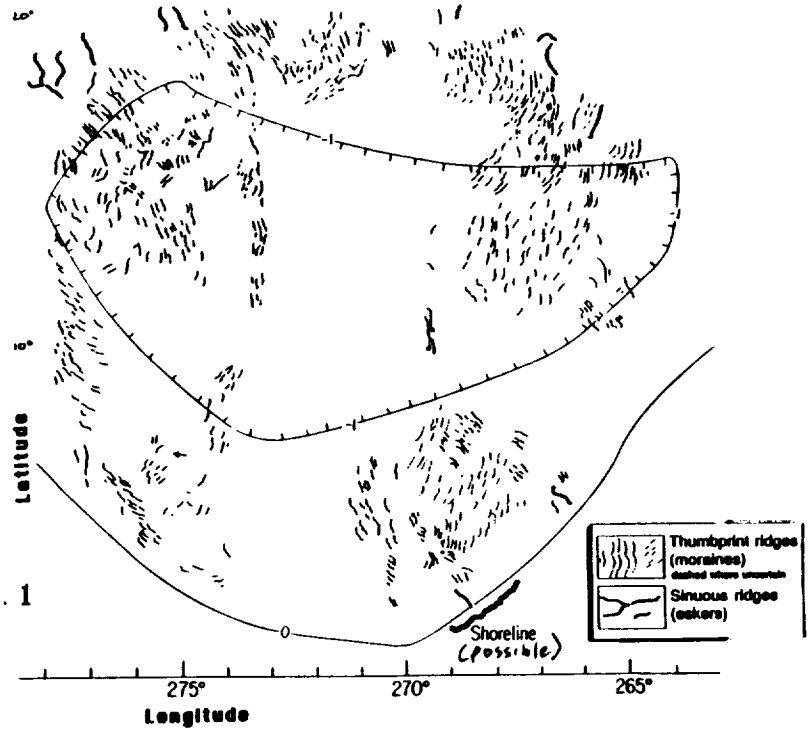

Fig. 1

ON THE ORIGIN OF ENSTATITE CHONDRITE CHONDRULES BASED ON THEIR PETROGRAPHY AND COMPARISON WITH EXPERIMENTALLY PRODUCED CHONDRULES;

G.E. Lofgren, SN-4, NASA-JSC, Houston, TX 77058, J.M. DeHart, 1914 Amherst Ave., Casper, WY 82601, and P.J. Burkett, code 7431 NRL, Stennis Space Center, MS 39529.

The recent discovery of several types 3 and 4 enstatite chondrites (EC) in the Antarctic collection [1] increases greatly the ability to compare unaltered, naturally-formed EC chondrules with chondrules produced experimentally from melts of enstatite chondrule composition [2]. Because these discoveries are so recent we have undertaken the task of characterizing these chondrules for purposes of comparison. Two E3 chondrites have already been examined carefully, Yamato-691 and Qingzhen, and these will be compared as well. EC chondrules are similar in the range of textures to the ordinary chondrite (OC), pyroxene-rich chondrules. Porphyritic textures are most common followed by the fine grained radial textures. Two kinds of radially textured objects are found, the droplet or almost perfectly spherical chondrules and angular fragments. The experimental studies [2] that have duplicated these textures suggest a long and complex formation history for EC chondrules. The presence of sharply defined, radial chondrules in E5 and E5 chondrules suggests that they do not represent metamorphosed E3 and E4 chondrites.

The most extensive study of EH3 chondrite chondrule textures has been on EH3 Yamato-691. Ikeda [3] found that radial pyroxene (RP) textures dominate. Their textures ranged from excentro-, to centro-, to multiradial pyroxene; some with olivine, but most without. Prophyritic textures were also common with textures ranging form porphyritic pyroxene/olivine (POP) to porphyritic pyroxene (PP) to equigranular to microporphyritic (MP). Other less common types include barred pyroxene/olivine, cryptocrystalline (spherulitic or massive), and pure SiO_2. Grossman et al. [4] studied whole chondrules extracted from EH3 Qingzhen. Of the 15 chondrules they studied 4 were PP, 5 were POP, 5 were RP and one was a dendritic olivine and pyroxene mixture.

OBSERVATIONS: We have looked at several new Antarctic E3 chondrites (EH-3's: ALH-84170 and PCA-91020; EL3's: ALH-77156, ALH-7295, LEW-87223, and MAC-88136) and Qingzhen. They all have numerous chondrules with well defined outlines and readily identifiable textures. All have mostly porphyritic chondrules (PP and POP), but there are differences in the size and kinds of textures. RP (both the classic spherical radial and the more common angular fragments), barred/dendritic px, and cryptocrystalline chondrules are present in differing amounts with one exception noted below.

PCA-91020: Mostly PP & POP, olivine is a minor phase when present usually as an inclusion. Phenocrysts s range from euhedral to subhedral, elongate skeletal to equant euhedral to granular. Textures show a large variation and range from microporphrytic. to porphyritic to granular to seriate. Barred/dendritic pyroxene occurs as fragments, usually elongate and are rare. Classic spherical RP chondrules are rare, radial fragments are more common and range from coarsely radial to cryptocrystalline.

ALH-77156: Chondrules are more uniform in character and size and smaller on average than other E3's. Most are microporphyritic, phenocrysts are equant euhedral to subhedral. Classic RP chondrules are absent; a few cryptocrystalline and barred to dendrite fragments are present.

ALH-77295: This meteorite is paired with ALH-77156 and though the chondrule assemblage varies somewhat with a larger range in chondrule size and texture, it is far more similar to 77156 that any other E3.

LEW-87223: The most distinctive feature of this meteorite is the lack of dark, fine-grained matrix. Chondrules are mostly PP with some POP, olivine usually present as inclusions in pyroxene and as relicts. There is a large variation in chondrule size and porphyritic texture. Some PP have granular rims that appear to be a later feature, not observed in other E3's, and there is one quite large granular fragment. Classic and fragmental RP, barred/dendritic, and cryptocrystalline chondrules are present mostly as fragments. The Fe-metal is coarse grained more like what would be expected in an E6 not E3 chondrite texture.

MAC-88136: Mostly PP & POP with numerous MP chondrules. There is a large size range; most MP chondrules are smaller. There are a few granular PP. There is only one classic RP chondrule and some radial textured fragments. There are also very few barred/dendritic, and a couple large cryptocrystalline fragments; the largest fragment is cryptocrystalline.

ALH-84170: There is very little dark, matrix material, almost like 87223. Chondrules are mostly PP & POP; the MP chondrules are smaller; The larger PP's are porphyritic with large En phenocrysts, some with olivine

inclusions; some have a granular texture. There is one classic RP, one coarse RP fragment, and cryptocrystalline fragments

Qingzhen: Mostly PP & POP chondrules with a large size range. The smaller ones are mostly MP with skeletal to equant euhedral phenocrysts. The larger En phenocrysts often have olivine inclusions (probably not relict); there are some olivine phenocrysts (skeletal, primary and rounded, relict??) set in a pyroxene matrix. A few granular pyroxene, a single classic RP, barred/dendritic, and cryptocrystalline chondrules are present.

The chondrules in the E4 chondrites from the Antarctic collection that have been examined and they resemble the E3 chondrites closely except for the slightly increased degree of alteration. The E5 and E6 chondrites examined have distinctly different textures. Chondrules are barely distinguishable, but each of them has a few sharply defined ones. In TIL-91714 (E5), there are 2 sharply defined, coarsely radial fragments and 1 coarse, barred fragment. In RKP-80259 there is 1 very sharply defined, coarsely excentroradial chondrule and 2 radial fragments. In ALH-81021 (E6) there is 1 coarsely radial fragment and in LEW-88180 (E6) there are 2 sharply defined, excentroradial chondrules and several radial fragments (in fact there are enough sharply defined chondrules that we question its classification as an E6)

COMPARISON WITH EXPERIMENTS: Comparison of the textures observed in the chondrules with dynamic crystallization experiments [2] presents some insight into the EC chondrule forming process. The complex array of PP and POP textures suggests multiple melting of heterogeneously agglomerated precursor material at varying temperatures. The MP chondrules, however, mostly likely formed from even grained, relatively homogeneous precursor material. Melting occurred near the liquidus and cooling was relatively rapid. The more complexly porphyritic, larger chondrules with seriate or bimodal phenocryst textures most likely had more heterogeneous precursor material, especially grain size. The presence of olivine in these chondrules can be explained partly by the complex nucleation kinetics in this system. The peritectic relationship that has olivine on the liquidus of the EC chondrule composition requires that pyroxene nuclei be present at the initiation of cooling in any chondrule melts that are ultimately to crystallize pyroxene. The presence of olivine with shapes from equant to skeletal to barred is the result of a paucity of pyroxene nuclei, and the relative ease of olivine nucleation. Early formed olivines are also found as inclusions in pyroxene phenocrysts in the experiments and thus are not relict, but part of the melting, nucleation and growth process. Similar olivine inclusions observed in natural EC chondrules must be interpreted with care.

The radially textured, often angular fragments are clearly crystallized melt. It is not so clear that they were chondrules, but because radially textures are common in chondrules, it is a logical conclusion. If that is true, they are very large chondrules. Some fragments of radial material have round edges that represent part of the original chondrule outline. Projection of this outline in such fragments suggests the unbroken chondrules have diameters of 2 to 4 mm. Significant superheating of the precursor melts would be required to produce such textures. The range of complex EC chondrule textures suggests a long and complicated event or events.

The presence of clearly defined radial chondrules and radial and barred fragments in E5 and E6 chondrites and the virtual absence of others kinds of sharply defined chondrules suggests to us that it would be difficult to produce the E5 and E6 chondrite by simple metamorphism of E3 and E4 chondrites. Porphyritic chondrules are more difficult to distinguish in the metamorphically altered chondrites partly because the blend with the pyroxene fragments in the matrix readily. The radial textures stand out more readily, but they are also more disequilibrim features that should be more susceptible to alteration than the prophyritic chondrules. The presence of sharply defined, radial chondrules and fragments suggests that the E5 and E6 chondrites are assembled from slightly different material perhaps some of which is already altered before the chondrites are aggregated (see discussion of this topic in Dodd, 1981 chapter 5 [5]).

CONCLUSIONS: The EC chondrule forming event is complex and the precursor material is quite variable. There is a suggestion based only on the analysis of the textures of the chondrites and their chondrules that the E5 and E6 chondrites are not metamorphosed E3 and E4 chondrites.

REFERENCES CITED: [1] Keil, K (1989) Meteoritics **24**, 195-208. [2] Lofgren, GE and AB Lanier (1991) Meteoritics **26**, 366-367. [3] Ikeda, Y (1989) Proc. NIPR **2**, 75-108. [4] Grossman, JN et al. (1985) GCA **49**, 1781-1795. [5] Dodd, R. (1981) Meteorites, Cambridge Univ. press, 368pp.

LIQUIDUS EQUILIBRIA OF LUNAR ANALOGS IN THE GARNET STABILITY FIELD.

J. Longhi, Lamont-Doherty Earth Observatory, Palisades, NY 10964

New melting experiments have been performed in the range of 28 to 30 kbar on partially crystallized synthetic glasses in order to refine parameterizations of liquidus boundaries and crystal/liquid partition coefficients employed in polybaric fractional fusion (PFF) calculations (1,2). Results confirm that PFF of a low-Al_2O_3 (< 1.5 wt%), low-Mg' (~0.80) source may yield composite melts similar in composition to the picritic green volcanic glasses (3): a) if pressure-release melting (~1%/kbar) begins very deep within the Moon (1200 km, ~40 kbar), b) if ~60% of the available melt effectively separates after each 1-2 % melting, and c) if there is some means of aggregating the melt produced over a range of depths. New results from high Mg' compositions also agree with predictions (4) that the clinopyroxene(cpx) coexisting with olivine(ol) + orthopyroxene(opx) ± garnet(gar) on the solidus of anhydrous planetary mantles in the garnet stability field is not only low in CaO (5-8 wt%), but is also supercritical.

Volcanic glasses with picritic compositions (3) have posed a thorny problem for petrologists: their compositions are multiply-saturated with olivine and orthopyroxene at pressures of 17.5 to 25 kbar (cf. 5) and traditionally the pressure of multiple saturation is interpreted as the minimum pressure of melt segregation, yet on the Moon these pressures translate to depths of 350 to more than 500 km.. The physics of transporting melt these distances through cracks without altering the melt composition have been modeled (6) and the possibility of such transport seems remote at a time in lunar history when the thickness of the elastic lithosphere was on the order of 50 to 100 km (7). Thus polybaric melting models analogous to those proposed for terrestrial midocean ridge basalts (8) provide attractive alternatives. Algorithms in the polybaric melting model proposed by the author (1) depended upon several extrapolations of phase equilibria and crystal/liquid partitioning from experiments at lower pressures on terrestrial compositions, so a series of melting experiments was initiated to provide data at high pressure with which to test and refine the model. The first round of experiments [(2) - partial results in Fig. 1a] produced melts with Mg' (0.40-0.45) lower than that appropriate for the green glasses. The new experiments (Fig. 1b and c) have multi-saturated melts with Mg' ranging from 0.50 to 0.78 — the lower end of the range are more appropriate to green glass source regions, whereas the higher values are appropriate to proposed bulk Moon compositions that are similar to the Earth's upper mantle (e.g., 9)

The new experiments also provide relevant data on partitioning and phase equilibria. There are dramatic increases in the molar partition coefficients (D*) for Al_2O_3 for opx/liq and aug/liq from average values of ~0.1 and ~0.2, respectively, at low pressure to values of ~0.5 and ~0.7 at 30 to 40 kbar (Fig. 2). Although in both cases the strongest correlating factor is P/T, the aug/liq coefficient has several statistically significant compositional dependences including the wollastonite fraction in pyroxene (WoPx). So an independent expression for WoPx, appropriate for augite at low pressures and supercritical cpx at high pressures, was obtained by linear regression (Fig. 2). The original model (1) employed constant values of D* for opx/liq (0.35) and cpx/liq (0.44) at high pressure that are now obviously too low for pressures in the range of 30 to 40 kbar. A consequence of using a pressure-dependent D* for Al is that now it is more difficult to deplete the source in Al_2O_3 at high pressure and extraction of melt at each pressure must, therefore, be more efficient to produce a polybaric pooled melt with green glass composition. Consequently, permissible melt extraction efficiency is now more than 60% as compared to 40% originally.

Fig. 1 shows the approximate location of liquidus boundaries (dashed curves) projected from the olivine component at 30 kbar for low (a) and intermediate Mg' liquids (b) and at 28 kbar for high Mg' liquids (c). Experimental liquid compositions are shown as squares, crystal compositions as circles. Filled symbols indicate olivine and liquid coexisting with two other solid phases, open symbols indicate one other solid phase. Fig. 3a contrasts liquidus boundaries at 1 bar (light solid lines) and 30 kbar (dashed lines) for Mg' appropriate for mare basalts. Opx is not stable at 1 bar, but has a relatively large stability field at 30 kbar; the cpx that coexists with opx, gar, and ol is constrained to be low in CaO; minimum melts of garnet peridotite assemblages are tholeiitic; and the psuedoinvariant point is a peritectic with opx in reaction with liquid. The 30 kbar topology in Fig. 3b, which is appropriate to picritic compositions, is similar to that in 3a: the data here fix the position of the ol + opx + cpx liquidus boundary and definitively show opx in reaction with liquid. The bulk composition of the green glass source region used in the polybaric melting calculations (1) is shown as a cross. Because the cross is lower in Al than the pyroxenes coexisting with gar and liq, garnet is not stable on the solidus. The coverage of data in Figs. 3a and b is ambiguous as to whether both low- and high-Ca pyx are stable as separate phases. However, the data in Fig. 3c show that cpx solid solution is continuous in petrologically relevant compositions as predicted by Bertka and Holloway (4). Liquidus boundaries in Fig. 3c are shifted to higher Al than those in Figs. 3a and b. This shift is the result of higher Mg' and alkalies. The projection of primitive terrestrial upper mantle compositions (PUM - depleted and undepleted (9)) shows that

garnet is on the solidus of terrestrial-like bulk Moon compositions (8). The considerable difference in Al contents between the PUM and model green glass source regions is not likely to be the result of differing degrees of basalt extraction — pyroxene accumulation seems to be essential to produce the low Al contents of the green glass source.

REFERENCES

(1) Longhi J. (1992) *Proc. Lunar Planet. Sci. 22*, 343-353. (2) Longhi J. (1993) *Lunar Planet. Sci. XXIV*, 895-896. (3) Delano J.W. (1986) *J. Geophys. Res. 91*, D201-D213. (4) Bertke C. M. and Holloway J. R. (1993) *J. Geophys. Res. 98*, 19,755-19,767. (5) Longhi J. (1992) *Geochim. Cosmochim. Acta, 56*, 2235-2251. (6) Spera F. J. (1992) *Geochim. Cosmochim. Acta, 56*, 2253-2265. (7) Solomon S.C. and Head J.W. (1979) *J. Geophys. Res. 84*, 1667-1682. (8) Klein E.M. and Langmuir C.H. (1987) *J. Geophys. Res. 92*, 8089-8115. (9) Warren P. W. (1986) in *Origin of the Moon*, pp.279-310, The Lunar and Planetary Institute, Houston.

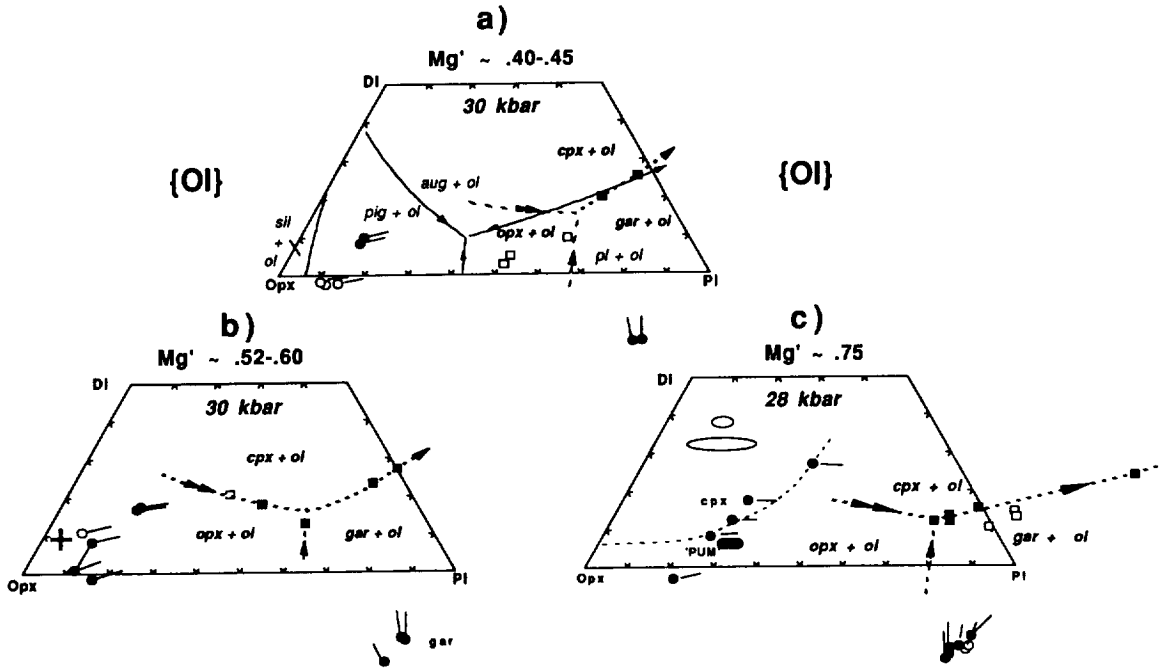

Fig. 1 Projections from Olivine component {Ol} onto a portion of the Wollastonite(Wo) - Orthopyroxene(Opx) - Plagioclase(Pl) plane. Symbols described in text. Arrows show direction of decreasing temperature; double arrows show reaction boundaries. Olivine coexists with all phases: a) fo_{67-72}, b) fo_{75-80}, c) fo_{87-91}. Large ellipses in c) show range in composition of liquid analyses (~30 micron raster of quench crystals); smaller ellipses show compositional ranges of pyroxene analyses (spot).

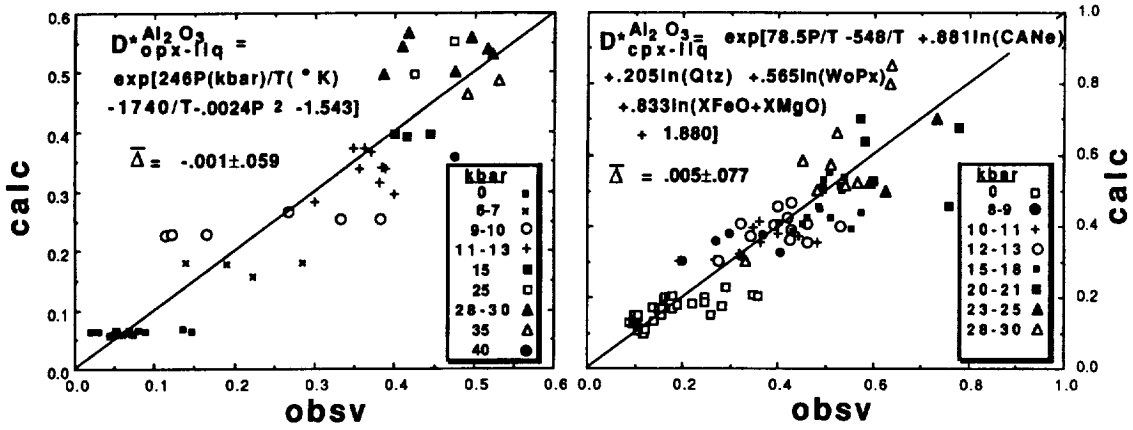

Fig. 2 Comparison of observed and calculated molar Al_2O_3 partition coefficients (D*) for aug/liq and opx/liq.

A MODEL FOR FORECASTING LAVA FLOW LENGTHS Rosaly Lopes-Gautier (Jet Propulsion Laboratory, California Institute of Technology, Pasadena, CA 91109) and Christopher R. J. Kilburn (Environmental Sciences Division, University of Lancaster, Bailrigg, Lancaster LA1 4YQ, England).

Models which relate lava flow dimensions (such as final length and width) to emplacement parameters (such as discharge rate and duration) are of prime importance for the interpretation of extra terrestrial lavas. For example, the flow field growth model of Kilburn and Lopes (1) has been used to infer eruption conditions of martian flows using final flow dimensions and topography (2, 3). The same approach can be used for terrestrial lavas but, more commonly, the driving emphasis for using such models on Earth is hazard assessment. In order to do this, the reverse approach is necessary: eruption parameters have to be used to predict final flow dimensions. Here we present a method for estimating final flow lengths of single aa flows.

Final flow length is usually the key dimension needed for assessing the hazard from an effusive eruption. A first-order model for the emplacement of aa lavas (1, 4) shows that the final length of a single flow (L) is related to mean discharge rate (Q) by:

$$L = (2/3)^{1/2} [(h/k) \sin a]^{1/2} Q^{1/2} \quad (1)$$

where h is the mean frontal thickness in metres, *a* is the angle of ground slope in degrees, k is the lava's thermal diffusivity (4×10^{-7} m^2 s^{-1}), L is length in metres and Q is discharge rate in m^3 s^{-1}.

In the case of single aa flows from Mount Etna, (h sin *a*) lies between 0.1 and 1 (5). Thus minimum and maximum values of length can be obtained from equation 1. For the purpose of forecasting maximum flow lengths (assuming $(h \sin a)_{max} = 1$), equation 1 becomes:

$$L_{max} = 1300\ Q^{1/2} \quad (2)$$

This shows good agreement with data from Mount Etna (4) and Puu O'o. This relation has also been used to forecast the lengths of small flows approaching the town of Zafferana, on Etna, in 1992.

Such promising results show that this model has great potential for hazard reduction from effusive eruptions. However, some limitations must be stressed: firstly, the model is not applicable to pahoehoe lavas (1, 4). Secondly, some modifications to the model may be needed before it can be applied to blocky lavas such as those of Colima (Mexico) and Arenal (Costa Rica), because of:

(i) different bulk rheology compared to typical aa flows;

(ii) increased development of rubble talus ahead of the flow front which may increase frontal resistance;

(iii) possible differences on how Q varies with time.

Although the model appears to be consistent with provisional blocky lava data, more detailed measurements are needed for a comprehensive test of the model's general applicability to these lavas. In particular, actual field measurements of frontal thickness and corresponding angles of slope of blocky lavas are needed. In addition, measurements of lengths and discharge rates made during eruptions of blocky lava flows would be invaluable to test the applicability of the model.

REFERENCES: (1) Kilburn, C.R.J. and Lopes, R.M.C. (1991): *J. Geophys. Res.* 96, 19,721-19,732. **(2)** Lopes, R.M.C. and Kilburn, C.R.J. (1990): *J. Geophys. Res.* 95, B9, 14,383-14,397. **(3)** Lopes-Gautier *et. al.* (1993): *LPSC XXIV*, pp. 899-900. **(4)** Kilburn, C.R.J. (1993): Lava crusts, aa flow lengthening and the pahoehoe-aa transition. In: Kilburn, C.R.J. and Luongo, G. (eds): *Active Lavas: Monitoring and Control*. London: UCL Press, pp. 263-280. **(5)** Walker, G.P.L. (1967): *Nature*, 213, 484-485.

GALILEO'S NEAR INFRARED MAPPING SPECTROMETER (NIMS) SCIENCE OBJECTIVES AND OBSERVATIONAL PLANS FOR IO R. Lopes-Gautier, R. Carlson, W. Smythe (Jet Propulsion Laboratory, California Institute of Technology, Pasadena, CA 91109), L. Soderblom (U.S. Geological Survey Branch of Astrogeology, Flagstaff, Arizona) and the Galileo NIMS Team.

One of the primary objectives of the Galileo mission is to investigate the nature of Io's dynamic volcanism. The Near Infrared Mapping Spectrometer (NIMS) is a remote sensing instrument aboard Galileo which combines imaging and spectral capabilities and will be used to map the composition and temperature of Io's surface and plumes. The NIMS observing plan for Io and selected observation designs will be presented.

NIMS has the unique capability to image and obtain spectral data simultaneously and is the first instrument of its kind to be flown in a planetary mission. The spectral range of NIMS is from 0.7 to 5.2 microns, which spans two regions: surface reflected light and emitted thermal radiation. NIMS will investigate both the surface mineralogy and the temperature of Io's surface features, as well as search for selected atmospheric species.

The main NIMS science objectives at Io include: (i) determining the composition of the surface units 50 km or larger on one hemisphere; (ii) determining the composition of selected surface units less than 10 km in size; (iii) characterizing the composition and temperature of flows and plumes; (iv) setting limits on the density of atmospheric SO2; (v) measuring cooling of hot spots during eclipses; (vi) mapping shifts in surface composition and temperature with time.

Galileo's best opportunities for observing Io will take place during Jupiter orbit insertion (JOI), during which the spacecraft will fly by Io at a range of 1,000 km. NIMS's priorities during this period will be (i) to obtain high spatial resolution samples of selected areas at high spatial resolution (a few km) and medium spectral resolutions (50 to 204 wavelengths); (ii) to obtain global coverage at moderate spatial resolutions (around 50 km) and high spectral resolutions (204 to 408 wavelengths); and (iii) to map part of Io's darkside and the Loki plume using NIMS's thermal channels together with Galileo's photopolarimeter radiometer (PPR).

During the subsequent eleven orbits over a period of two years, NIMS observations will focus on monitoring changes in surface composition (such as SO2 distribution) and temperature with time, using mainly moderate spectral resolutions (50 to 204 wavelengths). Observations of both the dayside and nightside will be made and will cover most longitudes at spatial resolutions ranging from about 100 to 1000 km. Additional observing opportunities during the tour will be provided by eclipses of Io by Jupiter, which will allow NIMS to investigate hot spots down to about 200K.

MORPHOLOGY OF METEOROID AND SPACE DEBRIS CRATERS ON LDEF METAL TARGETS

S. G. Love, D. E. Brownlee, and N. L. King, Dep't. of Astronomy FM-20, Univ. of Washington, Seattle, WA 98195; and F. Hörz, Solar System Exploration Division SN4, NASA Johnson Space Center Houston, TX 77058

We measured the depths, average diameters, and circularity indices of over 600 micrometeoroid and space debris craters on various metal surfaces exposed to space on the Long Duration Exposure Facility (LDEF) satellite, as a test of some of the formalisms used to convert the diameters of craters on space-exposed surfaces into penetration depths for the purpose of calculating impactor sizes or masses [1, 2, 3, 4, 5]. The crater depth-diameter ratio (P/D) may depend on projectile diameter, mass, and speed, and on projectile and target density and strength [6, 7, 8, 9]. We find the average P/D of craters formed in aluminum targets by normal impacts to be 0.56-0.60, significantly higher than the canonical value of 0.50. P/D does not change with crater size, with target Brinell hardness for values between 40 and 90, or with average impact velocity above 5 km/s. P/D varies roughly as target density to the 0.1 power. Less than 10% of the craters examined had major-to-minor axis ratios higher than 1.5, consistent with the production of shallow, elongated craters exclusively by oblique impacts. The natural width of the P/D distribution of non-oblique craters probably stems from variation in projectile shapes.

Target Materials and Orientation Surfaces examined in this work included panels of 1.6 mm thick 6061-T6 aluminum from the space-facing end of LDEF, plus smaller surfaces ("flanges") facing each row of the LDEF cylinder. Two of these faced 8° off the apex (leading) and antapex (trailing) directions respectively. Other surfaces came from the Chemistry of Micrometeoroids Experiment (CME) which exposed sheets of >99.99% Au and >99.9% Al facing different directions, allowing investigation of the effects of target density and Brinell hardness.

Crater Measurements and Sample Populations Craters were measured to an accuracy of 3% with an optical microscope coupled to a CCD camera and video printer. For each measurement, the microscope was focused on the flat target surface surrounding the crater, and diameters were measured along the crater's longest and shortest dimensions. The "diameter" we refer to is the average of the two measurements, and the circularity index is the long:short axis ratio.

Crater depths were measured by moving the motor-driven vertical focusing mechanism downward until the lowest point in the crater floor was in focus. The height difference between this point and the original surface plane was recorded as the crater depth. Most of these measurements were performed using an objective lens with a 3 μm depth of focus, yielding depths accurate to better than 5% for most craters.

Effects of Oblique Impacts P/D for the 552 craters on the two best-examined space-end panels is 0.528±0.104. This sample included relatively shallow, elongated craters, probably produced by impacts at angles greater than 70° from normal [10]. Very elongated craters formed a very small part of the sample. Less than 10% of impacts on zenith-pointing surfaces in LEO occur at such oblique angles [11], so the scarcity of elongated craters in our sample is understandable.

To address P/D independent of oblique impacts, we selected against them by excluding craters with circularity index > 1.05. The remaining group of circular craters had P/D = 0.574±0.069 (N=241), significantly larger than the value of 0.5 usually adopted for normal incidence craters in aluminum [1]. We also selected nearly-circular craters when comparing surfaces with different orientations (which experience impacts from different distributions of angles) to minimize the effect of varying proportions of oblique impacts on the P/D distributions.

We also chose craters with circularity index ≤ 1.05 when comparing the depth-diameter ratios of crater populations with very different average diameter, even on surfaces with identical orientation. Our definition of average diameter allows rare, highly elongated craters (formed by uncharacteristically small projectiles) to be included in any given size-selected crater population. At projectile sizes above 200 μm, the steepening impactor size distribution slope [12, 13]. means that, for a given resulting crater size, the proportion of rare oblique impacts of smaller particles becomes higher in comparison to the reduced flux of large particles at more normal incidence. Choosing circular craters decreases the importance of this effect in the P/D data.

Effects of Projectile Velocity To investigate velocity effects, we examined the apex (highest

PRECEDING PAGE BLANK NOT FILMED

impact speed) and antapex (lowest speed) flanges. Mean encounter speeds for natural meteoroids are 21.1 and 13.4 km/s for the leading and trailing edges respectively [14]. Mean impact velocities for man-made debris are 7.8 and 1.8 km/s for the leading and trailing edges respectively [15]. Because the relative numbers of artificial versus natural impactors is not known, a mean velocity for all the cratering events is difficult to define. P/D is 0.589±0.063 (N=16) for the apex, and 0.581±0.034 (N=12) for the antapex. The z-ratio of 1.22 suggests that the two populations are statistically similar, indicating that relative crater shape is invariant above some velocity threshold value. In support of this conclusion, craters recently produced at 1 to 7 km/s at the JSC Experimental Impact Laboratory, employing aluminum targets and glass projectiles, seem to approach a constant P/D value near 0.55 at speeds above 5 km/s.

Effects of Crater Size We obtained P/D data for the 30 smallest (~80 μm diam.) and the 30 largest (~700 μm diam.) circular craters measured in this study. P/D is 0.556±0.070 for the smallest craters, and 0.560±0.042 for the largest craters. The z ratio of 0.27 shows that there is no significant difference between the distributions.

Effects of Target Hardness Brinell hardness (H) can be used to describe the penetration behavior of metals [1, 10]. To isolate its effects, we compared surfaces of 6061-T6 and 1100 aluminum surfaces, differing only in Brinell hardness, exposed to identical bombardment conditions. P/D is 0.586±0.076 (N=25) for 6061-T6 alloy (H=90), and 0.585±0.078 (N=28) for the 1100 alloy (H=40). There is no statistical difference between the distributions.

Effects of Target Density The surfaces available for this study included pure Au. The Brinell hardness of Au is 30, similar to that of the 1100 Al. Since the latter's P/D distribution was identical to that of the 6061-T6 aluminum with the same orientation, comparison of crater shapes from the gold targets with those from the identically-exposed 6061-T6 flange should reflect the effects of target density only. P/D is 0.581±0.033 (N=15) for aluminum (2.7 g/cc), and 0.476±0.050 (N=20) for gold (19.3 g/cc). This difference is significant (z=7.4), but P/D varies only as roughly the 0.1 power of target density.

Effects of Projectile Properties The range of P/D for circular craters probably results from variable projectile density and shape. If the range of P/D were attributed to projectile density alone, the dominant range of the P/D distribution should correspond to the dominant range of impactor densities. A study of ~100 stratospheric micrometeorites found that most had densities of 1.0 to 5 g/cc [16] which would imply that P/D varies as density to the 0.2 power. An 8 g/cc (Fe-Ni) projectile can be associated with the deepest LDEF craters with P/D = 0.8 On the other hand, the scarcity of shallow craters (P/D < 0.4) rules out large numbers of projectiles densities <1 g/cc. A multi-peaked P/D distribution has been reported for craters on glassy lunar spherules [17] possibly indicating a meteoroid population with distinct density components. We find no analogous structure in our data.

Alternatively, the natural width of the P/D distribution for circular craters may depend on projectile shape. We refer to rod penetrator studies [18, 19, 20] to constrain projectile shape. Typically, the rod length to diameter ratio (l/d) controls relative penetration depth. For $l/d = 0.5$, penetration depth (at 5 km/s) is typically only 20% shallower than for l/d=1. The shallowest circular craters observed on LDEF may correspond to flat disks of $l/d < 0.3$, while the deepest craters would correspond to projectiles of $l/d > 2$. Because projectiles need not be substantially elongated or flattened to affect crater shape, we attribute the range in P/D to projectile shape.

REFERENCES [1] Cour-Palais B. G. (1987) *Int. J. Impact Engng* **5**, 221. [2] Humes D. H. (1991) NASA CP-3134, 399. [3] McDonnell J. A. M. and Sullivan K. (1992) in *Hypervelocity Impacts in Space* (ed. J. A. M. McDonnell), University of Kent, 39. [4] Coombs C. *et al.*, (1993) NASA CP-3194, 619. [5] Bernhard R. P. *et al.* (1993). NASA CP-3194, 551. [6] Gault D. E. (1973) *Moon* **6**, 32. [7] Herrmann W. and Wilbeck, J. S. (1987) *Int. J. Impact Engng* **5**, 307. [8] Holsapple K. A. and Schmidt R. M. (1987) *J. Geophys. Res.* **92**, 6350. [9] Watts A. *et al.* (1993) NASA NCR-188259. [10] Christiansen E. L. (1992) AIAA # 92-1462. [11] Peterson R. B. (1990) Presented at *CDCF Open Forum, 1990.* [12] Grün E. *et al.* (1985) *Icarus* **62**, 244. [13] Love S. G. and Brownlee D. E. (1993) *Science* **262**, 550. [14] Zook H. A. (1991) NASA CP-3134, 569. [15] Kessler D. J. (1993) NASA CP-3194, 585. [16] Love S. G. *et al.* (1993) *Lunar Planet Sci XXIV*, 901. [17] Smith D. *et al.* (1974) *Nature* **252**, 101. [18] Orphal D. L. *et al.* (1990). 12th Int'l Symp. Ballistics, San Antonio, TX, Oct. 1990. [19] Hohler V. and Stilp A. J. (1987) *Int. J. Impact Engng* **5**, 323. [20] Charters A. C. *et al.* (1990) *Int. J. Impact Engng* **10**, 93.

OMIT TO P. 879

SCARP HEIGHTS OF MARTIAN CHANNELS FROM SHADOW MEASUREMENTS: B.K. Lucchitta and J. Dembosky, U.S. Geological Survey, Flagstaff, Arizona 86001

The volume of water and sediments transported through the outflow channels remains one of the major outstanding questions on Mars. This volume is not only important to assess the planet's water inventory [1], it is also needed to shed light on the events that shaped the northern plains and affected the atmosphere. To determine channel volumes, channel widths and depths have to be established. The widths can be readily measured on available maps, but the depths remain unknown for most channel reaches. Most contours on topographic maps are in 1-km ±1 km increments [2], and thus they are not definitive for small channel features. The photoclinometric method of deriving topographic profiles requires areas of uniform albedo and has other constraints that make the available images unusable for measurements in many places. Shadow measurements give fairly accurate height determinations where illumination is adequate, and the method has been tried for many individual localities [1, 3-6]. The present study is an attempt to measure systematically the shadows on scarps along and within all channels where adequate images exist.

To implement the study, we devised latitude and longitude blocks containing all major channels on Mars. Then we conducted a computer search and inspected all images within these blocks that meet the following parameters: resolution less than 250 m/pixel, incidence angle of 60°-75°, emission angle of 0°-30°, moderate to good quality, clear or red filters. After inspection, we compiled a final list.

Images in the final list were processed on the computer to level-1 quality (labels were added, reseaux marks and noise were removed, and the radiometry was corrected). Then a computer program (TVPHOTOST in PICS system) was run that permits the interactive measurements of shadows: a line giving the down-sun direction was plotted on each image, the pixels at the beginning and end point of each shadow were registered, and the height of the scarp corresponding to the measured shadow was calculated by using the appropriate trigonometric functions. Variations of the sun-angle and camera geometry within individual images were taken into account.

Obtaining shadow measurements on level-1 images by computer is better than obtaining shadows on hard-copy prints, because it is easier to establish that the shadows are real and not produced by grazing light that mimics shadows on scarps. Criteria used to establish true shadows are (1) high density contrast between the area in shadow and its surroundings, (2) persistent low-density (dark) values within the shadow, and (3) whether the feature and its shadow have the same shape. Shadows cast onto undulate terrain were not used. For most measured shadows, the contrast is sharp and the edge of the shadow could be determined to within 1 pixel. Shadows whose ends could not be determined to within 3 pixels were flagged as unreliable. At a 3-pixel uncertainty, errors would be as below. Error values between these end members would vary accordingly.

Resolution	Incidence Angle	
m/pixel	60°	75°
250	±220m	±100m
20	±20m	±10m

We investigated Ares, Al-Quahira, Ma'adim, Nanedi, Nirgal, Shalbatana, Tiu, Uzboi, Kasei, Maja, Mamers, and Mangala Valles. Several other, small channels do not have adequate images, and no measurements were obtained. We looked at 326 images, of which only about two-thirds contain shadows that could be measured. The most significant results of our measurements (about 1,000) follow.

Ares Valles (20 images, 62 measurements): The trunk channel arises from chaotic terrain and has a fan-shaped, grooved intake area. Many tributary channels look like the main channel. The channel walls descend gradually through a series of scarps. The floors are marked by irregular grooves and small streamlined islands. Upper channel-wall scarps generally do not exceed 800 m in height, and most wall scarps are about 200 m high. Channel islands are 200 to 500 m high. Grooves on channel floors are mostly less than 100 m deep. It is difficult to establish the total channel depth because the gradually descending walls are unsuitable for shadow measurements.

Al-Quahira Vallis (8 images, 23 measurements): The channel, a modified graben, traverses highlands with many old craters. Channel depth is generally 500 to 800 m, but it ranges unsystematically because of the irregular topography of the surface.

Ma'adim Valles (21 images, about 60 measurements): Beginning where tributaries merge, the channel increases gradually in width and depth and debouches into an old crater near the highland boundary. For most of its length it has a well-defined trunk with only minor tributaries. The walls are steep and locally have

scarps; the floor is generally flat but has terraces in places. The upper part of the channel is 300 to 500 m deep, the main part, 1500 to 2000 m deep. Terraces on the channel floor and on a dissected mesa at the channel mouth inside the crater are 100 to 300 m above the floor.

Nanedi Vallis (7 images, 14 measurements): The channel has two merging branches, which are deeply entrenched, flat floored, and meandering. The shape of widened sections appears to follow exhumed small craters. The steep channel scarps measure less than 200 m high in the V-shaped upper reaches and are about 300 m high throughout most of the flat-floored reaches.

Nirgal Vallis (9 images, 21 measurements): The meandering channel is deeply entrenched and has dendritic tributaries similar to channels on Earth. An upper V-shaped section gives way to a lower flat-floored section. The gradual increase in width is accompanied by a gradual increase in depth from about 400 m to 800 m.

Shalbatana and Simud Valles (4 images, 23 measurements): Shalbatana has two distributaries: one is entrenched and flat floored in its wider sections and lacks meanders; the other merges with a chaotic section of Simud Vallis. The scarps in the entrenched section are 1300 to 1400 m high. The mesas and knobs in the chaotic section of Simud Vallis gradually decrease in height from over 1000 m in the south to less than 500 m in the north, toward the channel mouth.

Tiu Vallis (13 images, 90 measurements): The channel originates in chaotic terrain. It has chaotic sections like Simud Vallis and grooved and scarped sections like Ares Vallis. The channel-wall height also decreases northward. Scarps facing the chaotic terrains or located nearby are over 2000 m high in places. Channel walls in the upper reaches measure 1600 to 1800 m high, but in the main part of the channel the walls are generally 800 to 1000 m high and decrease gradually to as little as 400 m (on interior-mesa scarps in the north near the channel mouth).

We have compiled the measurements of the remaining major channels on 1:500 000-scale maps and, for Mamers Vallis where no such maps exist, on a mosaic compiled from images. We are in the process of analyzing these channels in more detail. Eventually we will combine height and width measurements to arrive at cross sectional areas of the channels and volumes of water or ice that may have moved through them.

References: [1] Carr, M.H., Wu, S.S.C., Jordan, Raymond, and Schafer, F.J., 1987, Volumes of channels, canyons and chaos in the circum-Chryse region of Mars, in Abstracts of papers submitted to the Eighteenth Lunar and Planetary Science Conference, pt. 1, Houston, March 16-20, 1987: Houston, LPI, 155-156. [2] U.S. Geological Survey, Topographic maps of the polar, western, and eastern regions of Mars: U.S. Geol. Surv. Misc. Inves. Series Map I-2160. [3] Chapman, M.G., and Scott, D.H., 1989, Geology and hydrology of the north Kasei Valles area, Mars, in Lunar and Planet. Sci. Conf., 19th, Houston March 14-18, 1988, Proc.: Cambridge University Press and Lunar and Planet. Inst., 367-375. [4] Lucchitta, B.K., 1982, Ice sculpture in the Martian outflow channels: J. Geophys. Res. 87, no. B12, 951-9973. [5] Lucchitta, B.K., 1984, Ice and debris in the fretted terrain, in Proceedings of the Fourteenth Lunar and Planet. Sci. Conf., pt. 2, J. Geophys. Res., 89, Suppl., B409-B418. [6] Robinson, M.S., and Tanaka, K.L., 1990, Magnitude of a catastrophic flood event at Kasei Valles, Mars: Geology, 18, 902-905.

C-5

SMALL TIME DIFFERENCES IN DIFFERENTIATED METEORITES RECORDED BY THE ^{53}MN - ^{53}CR CHRONOMETER: G. W. Lugmair, Ch. MacIsaac, and A. Shukolyukov*, Scripps Inst. of Ocean., Univ. of Calif. San Diego, La Jolla, CA 92093-0212. * Now at the Max Planck Institute in Mainz.

We have recently presented evidence for the decay of live ^{53}Mn ($T_{\frac{1}{2}}$ = 3.7 My) in the angrites LEW 86010 (LEW) and Angra dos Reis [1]. Here we offer new ^{53}Cr/^{52}Cr and ^{55}Mn/^{52}Cr results obtained on mineral separates and bulk samples from the eucrite Chervony Kut (CK) for which evidence for the decay of live ^{60}Fe has recently been reported [2]. The problems we seek to resolve with these continuing studies of the ^{53}Mn–^{53}Cr system in differentiated meteorites are manifold. Some primary questions include: Was ^{53}Mn still alive when these meteorites cooled from a magma? If so, can we determine the ^{53}Mn/^{55}Mn ratio at that time? Can we resolve small differences in cooling times between meteorites, particularly in those where other chronometers do not offer the required resolution (*e.g.* ^{146}Sm–^{142}Nd) or where other isotopic systems are disturbed by secondary effects? Can we map the relative ^{53}Mn–^{53}Cr chronometer onto an absolute time scale using the precise Pb-Pb ages of the angrites? Can we estimate the time of core formation in planetesimals using the initial ^{53}Cr/^{52}Cr ratios? Using this 'absolute' time scale can we estimate the ^{60}Fe/^{56}Fe ratio in the solar nebula and at the time of planet formation? And what are the implications for the Rb-Sr evolution in angrites *vs.* eucrites? Our newest results will hopefully lead us closer to an answer for at least some of these questions.

We have measured ^{53}Cr/^{52}Cr, and Mn and Cr concentrations in two bulk rocks (TR-1, and TR-5), chromite (Chr), pyroxene (Px), and plagioclase (Pl) from the eucrite Chervony Kut. The Cr isotopic compositions were measured by single-collector TIMS. For each sample 10 to 16 repeat measurements were performed and the results were averaged. The sample loading procedure for Cr was further refined from [1]. Residual mass fractionation effects from the application of a strict exponential law and small mass discrimination effects, which most likely are caused by minor residual and stray magnetic fields in the low energy region of the ion source, were observed. These were corrected by utilizing the strongly correlated variations of ^{53}Cr/^{52}Cr *vs.* ^{54}Cr/^{52}Cr from 40 Cr standard measurements made during the same time period. The estimated precision for the averaged meteorite ^{53}Cr/^{52}Cr data ranges from 10 to 12 ppm. The Cr and Mn concentrations were determined by repeat measurements using graphite furnace AA on small splits of the original solutions. The estimated precision of the ^{55}Mn/^{52}Cr ratios is ≤ 5%.

The ^{53}Cr/^{52}Cr ratios, expressed in ε notation (deviations from the standard in parts in 10^4) and ^{55}Mn/^{52}Cr ratios obtained from bulk samples and mineral separates from CK are shown in the Figure. Although the ranges in both the ^{53}Cr/^{52}Cr and ^{55}Mn/^{52}Cr ratios are very small when compared to the LEW data [1] (*i.e.* lack of olivine), a clear variation of ^{53}Cr/^{52}Cr with ^{55}Mn/^{52}Cr is evident. This variation shows that ^{53}Mn was still extant when CK cooled on the eucrite parent body. Further, the data also show a good linear relationship. From the slope of the best fit line through this correlated data set we can derive a reasonably precise ^{53}Mn/^{55}Mn ratio of $(3.6\pm0.5)\times10^{-6}$ for the time when CK cooled below the closure temperature of the ^{53}Mn–^{53}Cr isotope system.

For comparison, the dashed line in the Figure corresponds to the significantly lower ^{53}Mn/^{55}Mn ratio of $(1.29\pm0.07)\times10^{-6}$ which we have previously obtained for LEW [1]. If we assume that ^{53}Mn was homogeneously distributed in

the early solar system, at least where the parent planetesimals of these meteorites were formed, then these $^{53}Mn/^{55}Mn$ data indicate that the eucrite CK solidified (5.5±0.7)x10^6 years before the angrite LEW. This is a surprisingly large time difference. However, the initial $^{53}Cr/^{52}Cr$ ratios for both meteorites, ε_I^{LEW} = 0.75±0.07 and ε_I^{CK} = 0.65±0.09, appear to be the same within error, which implies that the Mn/Cr ratios in their source magmas were established at similar times.

Since no precise absolute age is yet available for CK we now attempt to map the CK data onto an absolute time scale by using the Pb-Pb age of 4.5578 ±0.0005 Ga obtained for the angrites [3]. The absolute age of CK then becomes 4.5633±0.0010 Ga. This age is considerably older than all precise absolute ages obtained for other eucrites. If this age is true then combined with the Pb-Pb ages of Allende CAI (4.566±0.002 Ga) [4] this implies that it may have taken less than 6 my to accrete and fully differentiate the eucrite parent body. If the ^{60}Fe-^{60}Ni and ^{53}Mn-^{53}Cr systems have closed contemporaneously then this higher age would suggest that less ^{60}Fe was present at the time of accretion than previous estimates have indicated [2] and that planet heating due to its decay was much less significant.

References: [1] Lugmair G. W., MacIsaac Ch., Shukolyukov A. (1992), LPSC XXIII, 823. [2] Shukolyukov A., Lugmair G. W. (1993), Science **259**, 1138. [3] Lugmair G. W., Galer S. J. G. (1992), GCA **56**, 1673. [4] Göpel Ch. *et al.*, (1991), Abstr. 54th Meteor. Soc., 73.

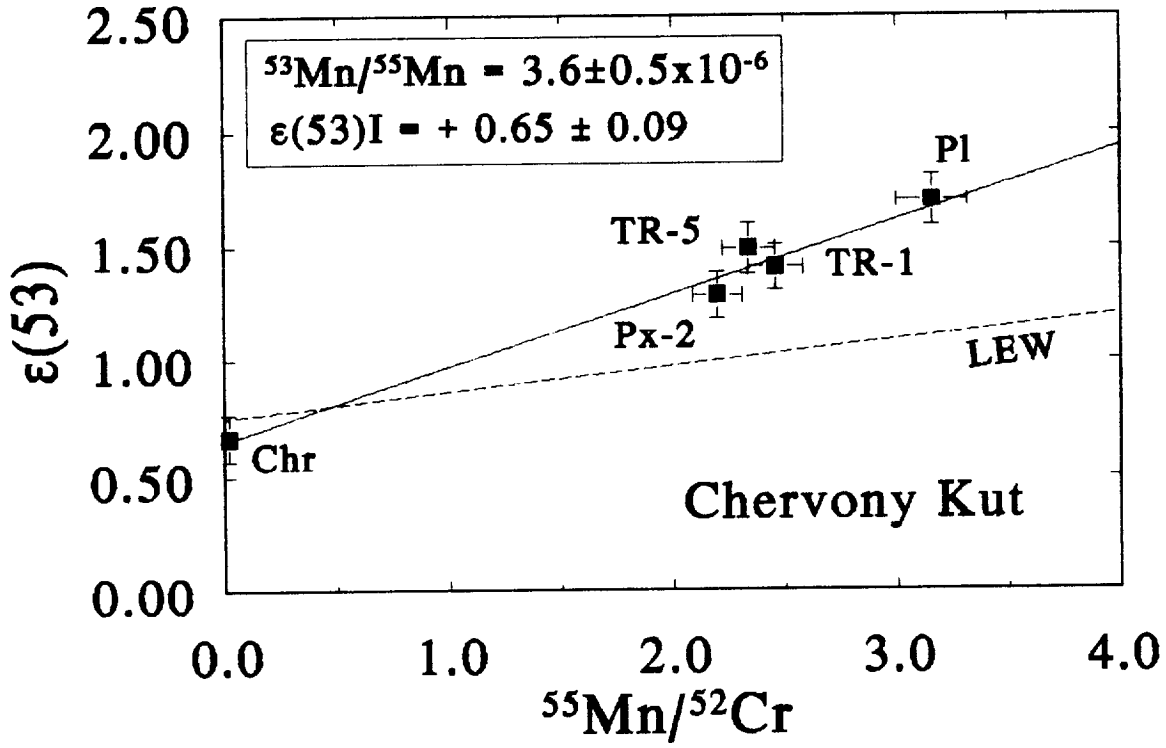

Figure: ^{53}Mn–^{53}Cr systematic in the eucrite Chervony Kut (CK). The relative deviations from the terrestrial value of $^{53}Cr/^{52}Cr$ in bulk samples and mineral separates are expressed in ε-units (1 part in 10^4). The variation of $^{53}Cr/^{52}Cr$ with $^{55}Mn/^{52}Cr$ shows that ^{53}Mn was extant when this meteorite solidified; the slope of the best fit line corresponds to a $^{53}Mn/^{55}Mn$ ratio of (3.6±0.5)x10^{-6}. The difference of this ratio in CK to that in the angrite LEW86010 (dashed line) corresponds to a ~5.5 My difference in the time of ^{53}Mn–^{53}Cr system closure.

TERRAIN SIMULATOR; W. Luo, R. Arvidson, and R. Becker, McDonnell Center for the Space Sciences, Department of Earth and Planetary Sciences, Washington University, St. Louis, MO 63130

We report initial results in the development and application of software to simulate fluvial and ground water processes. The system utilizes a cellula automata approach and includes software objects to simulate system components and a software engine to drive the overall system as a function of time. The work builds on and extends such efforts as Chase [1], Koltermann and Gorelick [2], and Howard [3]. The intent is to develop the system, to understand the interactions among system components, to calibrate it in terrestrial hyperarid terrain (e.g. Kharga plateau and escarpment in Egypt, where extensive ground water sapping has occurred), and then to utilize the system to explore the development of martian channels and related features. We intend to explore two hypotheses, one that martian landforms and deposits were produced in a climatic regime in which surface conditions were at or above the triple point of water (i.e., there was surface water), and the second that they formed under a situation in which water was frozen at the surface and most physical and chemical aqueous activity was restricted to ground water and hydrothermal systems. System-wide modeling of topography, lithology, and stratigraphy is a critical and necessary step in understanding which hypothesis is valid and what observations and measurements would be needed to further test the model.

The software system is object-oriented so that system components can be replaced by new models that are more realistic than existing objects. For example, initial experiments incorporated a precipitation model [1] in which the amount of sediment eroded at a given position is equal to an erodibility times the maximum height difference in the local area. This object can be changed with the 2-D solution to the Navier-Stokes equations as given in [2]. In addition, the system includes as many components or objects as necessary in order to simulate the terrain realistically. Fickean diffusion is included as one system component to model the effects of landslides and soil creep. The Dupuit approximation is used to model ground water flow and sapping processes with erosion in proportion to discharge [3]. Flexure in response to the sediment load distribution is modeled as another system component using thin plate flexure theory [4] solved by Fast Fourier Transform techniques [5]. We are also exploring other components, such as dissolution kinematics of carbonate rocks and the formation of karst terrains.

We report on three experiments aimed at understanding interactions among different system components. First, the basic precipitation model [1] was coupled with the parameterized climate and flexure models to simulate the effects of wetter climatic conditions on landforms in

mountainous areas on Earth. The simulations showed that a shift to more humid climatic conditions will lead to increased peak elevations, even without tectonic uplift. The reason, as intuited by Molnar and England [6], is that increased erosion produces deep valleys, whereas isostatic readjustment occurs over a finite flexural length scale. Thus, whereas mean elevation decreases, peak elevations actually increase. We also employed the basic precipitation model [1] in simulations in which eustatic sea level fluctuations were used to simulate the alluvial pediments and fluvial terraces along the Red Sea coast [7]. Eustatic controls on coastal landform evolutions are clearly manifested by the simulations. Third, a ground water sapping model for an unconfined aquifer using Dupuit assumption was applied to a structurally heterogeneous volume to simulate the landforms in Kharga region of Egypt. The model is primarily after [3], with the addition of erosion direction controlled by the direction of water table slope, and amount of erosion determined by lithology and structure. The experiments showed that ground water sapping was important in forming the scalloped escarpments observed along the escarpments north of Kharga. We are also incorporating explicit chemical dissolution of carbonate rocks as another system component, since limestones are wide-spread in Kharga region [8] and have been hypothesized for Mars.

The Kharga escarpment is particularly germane to Mars in that the scalloped escarpments look similar (visually and fractally) to parts of the Valles Marineris escarpments. From our simulations, we believe that the scalloped appearance of the Kharga escarpments is caused by dissolution that occurs preferentially along fractures where there are high discharge rates. These high flow zones lead to preferential collapse of escarpment rocks and scalloped topography. We are currently pursuing extrapolation of ground water flow to martian conditions, to simulate sapping in silicate and carbonate rocks, and the scalloped escarpment landform of Mars, and to test the two hypotheses about martian surface conditions.

References: [1] Chase, C.D., 1992, *Geomorph.*, 5, 39-57. [2] Koltermann, C.E. and Gorelick, S.M., 1992, *Science*, 256, 1775-1782. [3] Howard, A.D., 1988, *NASA Spec. Pub.* 491, 71-83. [4] Turcotte, D.L., and Schubert, G., 1982, *Geodynamics,* 121-122. [5] Gilchrist, A.R. and Summerfield, M.A., 1990, *Nature*, 346, 739-742. [6] Molnar, P. and England, P., 1990, *Nature*, 346, 29-34. [7] Arvidson, R.E., et al., accepted by *J. G. R.* [8] Said, R., 1962, *Geol. of Egypt,* 71-76.

DRY DEFORMATION OF DIABASE: IMPLICATIONS FOR TECTONICS ON VENUS

S. J. Mackwell, Department of Geosciences, Penn State University
M. E. Zimmerman, D. L. Kohlstedt, D. S. Scherber, Department of Geology and Geophysics, University of Minnesota

Chemical analyses of the rocks on the surface of Venus and observations of the topography of that planet indicate that the Venusian crust is composed predominantly of rock with a basaltic composition. The high surface temperatures of this planet suggest that degassing of magma during eruption and the lack of a return path for water to the planetary interior have probably resulted in anhydrous conditions in the crust and upper mantle of Venus. Thus the tectonics of the crust of Venus is likely to be dominated by the mechanical behavior of coarsely crystalline basalt under anhydrous conditions. On Earth, rocks of the appropriate composition and microstructure can be located in the Triassic sills and dikes in the northeast portion of the United States.

We have performed an experimental study to determine the high-temperature creep behavior of natural diabase rock from near Columbia, North Carolina, and near Frederick, Maryland, under dry deformation conditions to measure the effects of temperature, oxygen fugacity, variation in grain size, and ratio of plagioclase to pyroxene on the creep strength. The Columbia diabase has the coarser grain size ($\sim 100 \times 600$ μm plagioclase, ~ 200 μm pyroxene) and contains about 70 mol% plagioclase ($Ab_{30}An_{70}$) and about 25 mol% pyroxene (mostly hypersthene $En_{67}Fs_{33}$). The Maryland diabase has the finer grain size ($\sim 30 \times 100$ μm plagioclase, ~ 50 μm pyroxene) and contains about 56 mol% plagioclase ($Ab_{30}An_{70}$) and about 43 mol% pyroxene (mostly augite $Wo_{35}En_{53}Fs_{12}$). Samples were predried at 900°C for at least 24 h under controlled oxygen fugacity conditions prior to deformation, in order to remove any water and dehydrate any hydrous minerals that were present in the rock.

The deformation experiments were performed in a gas-medium high-pressure, high-temperature deformation apparatus at confining pressures of 300-400 MPa, temperatures from 900° to 1100°C, and strain rates from 10^{-7} to 10^{-5} s^{-1}, with the samples buffered against either Fe-FeO or Ni-NiO. The dry creep strength of both rocks is significantly greater than that measured under "as-received" or wet conditions [1,2]. In addition, the Maryland diabase is stronger by about a factor of 3 than the Columbia diabase, probably resulting from the lower modal abundance of plagioclase. Previous experimental studies [2,3] have demonstrated that the plagioclase component in the rock is likely to be the weaker phase at temperatures over 800°C, although these experiments were not performed on predried samples. In addition, research on the deformation of clinopyroxenite [4] yield strengths that are higher than those measured for the diabase under similar conditions.

Flow laws were determined for the deformation of the Columbia diabase,

$\dot{\epsilon} = 1050\ \sigma^{4.9}\ e^{-509/RT}$, when the samples were buffered against Fe-FeO, and

$\dot{\epsilon} = 1150\ \sigma^{4.3}\ e^{-482/RT}$, when the sample were buffered against Ni-NiO,

where the stress is in MPa and the activation energy is in kJ/mol.
For the Maryland diabase,

$\dot{\epsilon} = 4.2\ \sigma^{5.1}\ e^{-505/RT}$, when the sample were buffered against Fe-FeO.

Both rocks deformed by dislocation creep and are slightly weaker when deformed under more reducing conditions.

DRY DEFORMATION OF DIABASE: Mackwell, S. J. et al.

Application of these results to the tectonics of the lithosphere on Venus, assuming a temperature gradient of 25 K/km and a strain rate of 10^{-14} s^{-1}, predicts a relatively deep brittle-ductile transition (~ 8 km depth) and a strong lithosphere, dominated by the strength of the rocks in the mid- and upper crust, with no weak lower crustal zone. As the contrast in rheology between these diabase rocks and dry dunite is small at depths greater than 15 km, strong coupling between the crust and mantle seems likely.

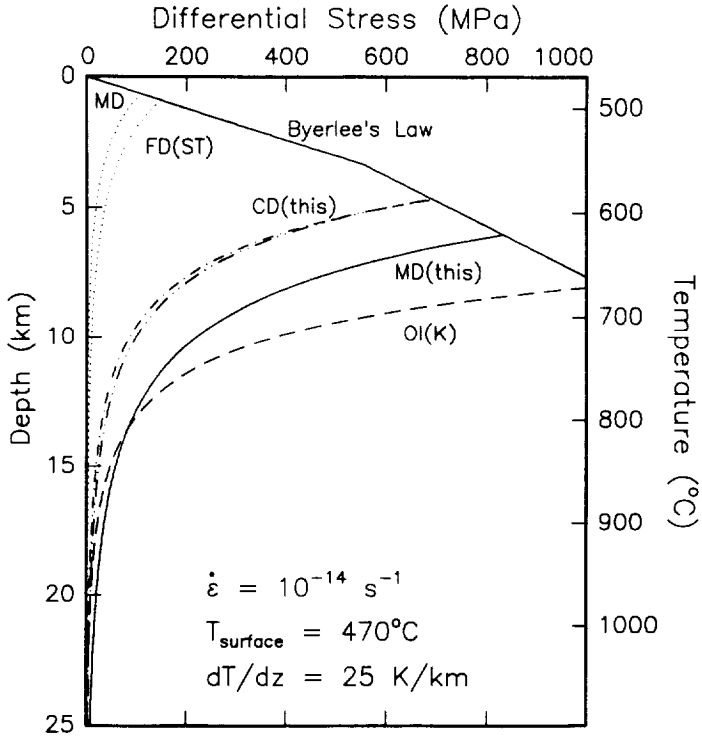

Plot of rock strength versus depth for Earth-type strain rate and thermal gradient conditions, but with a surface temperature appropriate to Venus. CD(this) and MD(this) refer to the measurements on Columbia and Maryland diabase in this study; Ol(K) refers to Karato's dunite flow law [5]; MD is from Caristan [2] and FD(ST) is from Shelton and Tullis [1] for unannealed Maryland diabase.

[1] Shelton G. L. and Tullis J. (1981) *EOS Trans AGU, 62,* 396.
[2] Caristan Y. (1982) *JGR, 87,* 6781.
[3] Kronenberg A. K. and Shelton G. L. (1980) *J Struct Geol, 2,* 341.
[4] Kirby S. H. and Kronenberg A. K. (1984) *JGR, 89,* 3177.
[5] Karato S. I. et al. (1986) *JGR, 91,* 8151.

MAGNETIC PROPERTIES EXPERIMENTS DESIGNED FOR USE WITH A MÖSSBAUER SPECTROMETER AND AN APX SPECTROMETER ON MARS;

M.B. Madsen, J.M. Knudsen, S. Faurschou Hviid, H.P. Gunnlaugsson, D.P. Agerkvist, L. Vistisen, J. Madsen, Niels Bohr Institute for Astronomy, Physics and Geophysics, DK-2100 Copenhagen Ø, Denmark; G. Klingelhöfer, E. Kankeleit, Institut für Kernphysik, Technical University of Darmstadt, 64289 Darmstadt, Germany; V.N. Khromov, E. Evlanov, O. Prilutski, B. Zubkov, Space Research Institute, Russian Academy of Sciences, Moscow, Russia.

Experiments have shown that some Mars Sample Analogues may spontaneously separate into more and less magnetic fractions when attracted by a Magnet Array. It is suggested that this effect is used for experiments on the Russian Mars-96 and the MESUR Pathfinder missions. This will give information on the magnetic properties and microscopic structure of the dust grains (multiphase/single phase grains).

Part of the scientific payload of the Russian Mars-96 mission is a ^{57}Fe-Mössbauer spectrometer [1]. Mössbauer spectroscopy will determine the oxidation state of iron as well as the dominant iron-mineralogy in the Martian soil. From the Viking missions we know that there is a magnetic mineral in the Martian soil and dust, the identity of which is not known. Detailed knowledge about the identity of this magnetic phase is important for the understanding of the evolution of the Martian surface. It has therefore been suggested to repeat the Viking Magnetic Properties Experiment with an instrument that includes also weaker magnets [2]. Such an experiment is now in the payload of the MESUR Pathfinder and the instrument (a so called Magnet Array) will provide (semi-)quantitative information on the effective magnetization of the soil. Below we show how the Mössbauer spectrometer on Mars-96 supplemented with a permanent magnet can do three experiments specifically designed to characterize the magnetic phase in the Martian dust and soil.

1. Magnetic separation experiment (concentration of the magnetic phase). Experiments, in which Mars Sample Analogues are blown onto a tilted Magnet Array (a plane containing permanent magnets similar to the ones used in the Viking Magnetic Properties Experiment), have shown that for certain Analogues particularly the weaker magnets are able to attract the most strongly magnetic grains, gravity (tilt) preventing weaker magnetic grains from being held. This effect gives rise to distinct differences between the color of the material adhering to the strongest magnet and that adhering to the weaker magnets. The observed differences show that a (partial) magnetic fractionation takes place. To optimize the separation effect a type of magnet is chosen that is weak enough *not* to attract hematite and paramagnetic material and strong enough to attract material with an effective magnetization of approximately 15 Am^2kg^{-1}.

Figure 1. a) Arrangement of permanent magnets in Magnetic Separator for investigation of Martian dust with the Mössbauer spectrometer and APX-spectrometer b) Spontaneous arrangement of strongly magnetic grains on the surface of the Magnetic Separator.

MÖSSBAUER MAGNETIC PROPERTIES EXPERIMENTS ON MARS-96: **M.B. Madsen et al.**

The magnet arrangement should not be circular as in the Magnet Array designed for using a camera to detect the circular pattern of adhering magnetic material. Instead the Array is composed of linear pieces of magnetic material - in principle arranged as indicated in Figure 1.a. With this arrangement of magnets the magnetic material adhering to the surface of the Magnetic Separator will essentially form a blanket of material, which is well suited for investigation with the Mössbauer spectrometer and the APX-spectrometer.

If there is a significant difference in optical-, APX- and Mössbauer spectra we will have two sets of spectra (from each technique) corresponding to more and less magnetic fractions. These pairs of spectra contain more information than the individual single spectra. From such pairs more detailed information on the spectral components can be extracted. If fractionation is negligible we will have learned that the different mineral phases in the dust/soil are intimately intergrown - and this is an important characteristic of the material. We know that titanomagnetites are present in the SNC-meteorites (~ Martian rocks). An important question is therefore if a connection between the magnetic phase in the soil/dust and that in the rocks can be established. Differences between the X-ray fluorescence spectrum of the material adhering to the magnet and that of the soil are important in this context: *e.g.* Does Ti follow the magnetic phase?

2. Polarization experiment (determination of the type of magnetic order). The blanket of (magnetic) material formed on the surface of the Magnetic Separator described above is not isotropic; magnetic grains will have a tendency to form chains along the field lines on the surface of the instrument as illustrated in Figure 1.b. Hence also the magnetization directions (and thereby the magnetic hyperfine fields of the magnetic components of the grains) will be essentially parallel to the field lines. If the magnetic phase constitutes a sufficient fraction of the material it may be possible to distinguish a *ferrimagnetic* from an *antiferromagnetic* material by a comparison of the signals obtained from two sets of (~ perpendicularly oriented) Mössbauer photon detectors. The experiment is done with exactly the same experimental setup, *i.e.* a tilted Magnetic Separator, as used for experiment 1, described above. The feasibility of this experiment has been demonstrated by detecting the (partial) magnetic polarization of a sample of pure maghemite using Mössbauer spectra obtained from two (almost) perpendicular scattering directions. The polarization is detected by the differences in the relative areas of the $\Delta m=0$ lines (lines 2 and 5) in the Mössbauer spectra. The polarization experiment does not depend (directly) on the possibility of magnetic separation, but of course the quality of the spectra will be better the higher the concentration of magnetically ordered phases.

3. Superparamagnetic Relaxation experiment It will be demonstrated that it may be possible *directly to detect* superparamagnetic behaviour of a superparamagnetic (ferrimagnetic) material present in the soil. This has been demonstrated in the laboratory using two identical samples (of a Mars Sample Analogue exhibiting superparamagnetic relaxation) placed on two horizontally oriented locations and investigated by a Mössbauer spectrometer. One of these locations contained permanent magnets, strong enough to substantially suppress superparamagnetic fluctuations, and the measurement on the other location served as a reference. The experiment shows that a weak external magnetic field (about 50 mT) at the site of the sample induces substantial magnetic splitting in the Mössbauer spectrum, *i.e.* the effect of the field is to move spectral area from a doublet component into a magnetically split component. In this way superparamagnetic relaxation is *directly detected.*

Acknowledgements: The Novo Nordisk Foundation is gratefully acknowledged for supporting the project with a strong Mössbauer source and so is the Danish Natural Science Research Council for financial support.
References: [1] G. Klingelhöfer et.al., *Mössbauer spectrometer for mineralogical analysis of the Mars surface for the Mars-96 mission*, LPSC XXIII (1992) 695-696. [2] M.B. Madsen et.al., *Suggestion for extended Viking Magnetic Properties Experiment on future Mars missions*, LPSC XXIV (1993) 917-918.

A MODEL FOR THE ORIGIN OF FLOOD VOLCANISM AND "PASSIVE" RIFTING IN THE LADA TERRA-LAVINIA PLANITIA REGION ON VENUS; Kari P. Magee and James W. Head, Dept. of Geological Sciences, Brown University, Providence, RI 02912

Lava flows similar in scale to terrestrial flood basalts have been observed on Venus in Earth-based Arecibo and orbiting Magellan radar image data.[1-3] The detailed morphology, source characteristics and stratigraphic relationships of many of these flow units have been analyzed.[2-4] Because of their similarity in scale to terrestrial flood basalts, the origin of these large-scale flow fields has been linked to processes of mantle upwelling, lithospheric thinning and extension, and pressure-release melting.[2,4] Current debate over the formation of terrestrial flood basalts centers on the necessity of pre-existing extension and stretched and thinned lithosphere to produce enhanced decompression melting within a large plume head or mantle thermal anomaly.[5] Our study of volcanism associated with coronae on Venus revealed that large-scale flow fields are preferentially associated with coronae located within zones of extension[4], suggesting that pre-existing conditions of lithospheric thinning and extension are necessary for the formation of large flow fields associated with coronae on Venus. In this study, we further our analysis of large-scale flow units on Venus by examining the link between extension and volcanism in the Lada Terra - Lavinia Planitia region of Venus where multiple volcanic centers with large-scale flow fields are associated with a zone of extension (the Lada rift) that we interpret to be due to passive rifting.[6]

The Lada rift is a zone of extension over 6000 km long that runs along the border of Lada Terra, a highland in the southern hemisphere of Venus, and Lavinia Planitia, an adjacent lowland basin (see Figure 1 in [7]). It is characterized by a series of discontinuous topographic lows 0.5-4.2 km deep and broad, flanking zones of relatively intense to more diffuse fracturing 115-630 km wide. Approximately 11-13 volcanic centers, including large coronae, radially fractured edifices known as novae, and large flow fields, such as Kaiwan and Mylitta Fluctus that are similar in scale to terrestrial flood basalts, are located along the rift with an average spacing of ~600 km. Volcanism post-dates the onset of significant extension, although continued rifting has deformed many of the volcanic centers along the rift.[6,7]

In contrast to other rifts on Venus, such as Devana Chasma at Beta Regio[8], deformation within the Lada rift is not restricted to a single trough bound by steep scarps, nor do multiple rift arms radiate from a large domal uplift and a major central volcanic edifice. The Lada rift is characterized by much shallower troughs and scarps than other rifts or corona chains on Venus. It is similar to corona chains such as Parga and Hecate Chasmata in that it is associated with multiple volcanic centers. However, corona chains typically contain much larger numbers of volcanic centers that are often contiguous[9], with smaller average center-to-center spacings of ~400-450 km.

On the basis of these characteristics, the origin of the Lada rift does not appear to be related to uplift and extension associated with the presence of a large mantle plume as has been proposed for other rifts on Venus.[10] If not "active" rifting, then "passive" rifting must account for the observed extension along the Lada-Lavinia border. Such rifting may be related to peripheral deformation created by mantle downwelling within Lavinia Planitia.[11] In its early stages, mantle downwelling, as modeled for Venus conditions, results in subsidence, compressional hoop strains and peripheral extensional radial strains.[12] Thus, early-stage cylindrical mantle downwelling has been proposed to account for the basin topography of Lavinia, the presence of interior compressional ridge and fracture belts, and a -30 mgal gravity anomaly centered in the eastern portion of the basin.[11] We propose that the peripheral extensional strains associated with downwelling within Lavinia may also account for the formation of the rift along the adjacent margin of Lada Terra[6] (Figure 1).

The following sequence of events is based on this model and is an interpretation of the possible evolution of the Lavinia Planitia - Lada Terra region.[6] (1) The development of a sustained region of mantle downwelling resulted in flexure and basin subsidence[11] and the formation of the Lavinia basin. Downward flexure[13] and the onset of crustal shortening[11] related to downwelling initiated compressional deformation within the interior of the basin. (2) In addition, the onset of downwelling produced tensional radial stresses about the periphery of the basin. These stresses may have been sufficient to produce the extension observed along the Lada rift or may have been enhanced by the subsequent emplacement of dikes along the trend of the rift. The extension was most developed to the east along the highland border of Lada due possibly to its closer proximity to the center of downwelling (based on the location of center of the gravity anomaly) and/or to the lower strength of the thicker highland crust. In addition, downwelling-related extension along the western border of Lavinia may have been overprinted by tectonic activity associated with the formation of Dione Regio and Themis Regio.[6] (3) Upwelling mantle, perhaps in some form of axisymmetric return flow associated with the downwelling beneath Lavinia, or upwelling related to peripheral rifting about the basin, brought hotter material up from depth that subsequently underwent substantial amounts of pressure-release melting along the rift. This resulted in the formation of multiple volcanic centers along the rift axis and large floods of lava that poured downslope into Lavinia.[6] (4) Continued extension deformed

most of the volcanic centers along the rift, except Mylitta Fluctus which remains relatively undeformed. Continued downwelling and crustal shortening produced linear ridge and fracture belts within Lavinia.

According to the model developed here, large-scale volcanism observed along the boundary of Lavinia Planitia and Lada Terra is the result of mantle upwelling related to passive rifting of the crust and lithosphere of Lada Terra. In contrast, the origin of terrestrial flood basalts is thought to require the upwelling of anomalously hot mantle within the head of a mantle plume.[5] Upper mantle temperatures on Venus are thought to be at least 200°C hotter than in Earth[14], such that melting in a hypothetical Venus spreading center environment may produce a crust 2-3 times thicker than in a typical terrestrial mid-ocean ridge.[15] Greater amounts of melting have also been predicted for smaller-scale mantle upwellings on Venus than on Earth, due to higher lithospheric temperatures on Venus.[16] Therefore, it is plausible that passive upwelling of normal Venus mantle might be sufficient to produce flood-scale volcanism as observed along the Lada rift.

It is unclear whether or not the formation of terrestrial flood basalts is dependent on the presence of stretched and thinned lithosphere to produce enhanced decompression melting within a large plume head or mantle upwelling. Although it is not yet known whether pre-existing extension is required for the formation of all large-scale flow units on Venus, limited extension (or a tensional stress regime) appears to have been active prior to the eruption of large flow fields along the Lada rift. Pre-existing conditions of lithospheric extension were also shown to be associated with the eruption of large-scale flow units at coronae on Venus.[4] Perhaps higher mantle temperatures and possibly thinner lithospheric thicknesses[14,17] on Venus cause regions of mantle upwelling or plume activity to undergo rapid thinning and extension, prior to the formation of large-scale flow units as has been described for the Earth.[18] Or, perhaps, greater lithospheric thicknesses[19] on Venus inhibit the formation of flood-type eruptions except where mantle upwellings happen to intersect (or are associated with) regions of rifted and thinned lithosphere. Continued analysis of large-scale flow units on Venus is required to answer questions regarding the formation of these possible analogs to terrestrial flood basalts and their association with zones of extension.

REFERENCES: **1)** Senske, D. A. et al., *Earth, Moon, and Planets, 55*, 97-161, 1991; **2)** Magee Roberts, K. et al., *J. Geophys. Res., 97, E10*, 15,991-16,015, 1992; **3)** Lancaster, M. G. et al., *Lunar Planet. Sci., XXIII*, 753-754, 1992; **4)** Magee Roberts, K. and J. W. Head, *Geophys. Res. Lett., 20*, 1111-1114, 1993; **5)** Richards, M. A. et al.,*Science, 246*, 103-107, 1989; White, R. and D. McKenzie, *J. Geophys. Res., 94, B6*, 7685-7729, 1989; Campbell, I. H. and R. W. Griffiths, *Earth Planet. Sci. Lett., 99*, 79-83, 1990; Hooper, P. R., *Nature, 345*, 246-249, 1990; **6)** Magee, K. and J. W. Head, *J. Geophys. Res.* (in review), 1993; **7)** Roberts, K. M. et al., *Lunar Planet. Sci., XXIII*, 1157-1158, 1992; **8)** Senske, D. A., Ph.D. thesis, Brown University, pp. 304-351, 1992; Senske, D. A. and J. W. Head, *Lunar Planet. Sci., XXIII*, 1269-1270, 1992; Senske, D. A. et al., *J. Geophys. Res., 97, E8*, 13,395-13,420, 1992; **9)** Hamilton, V. E. and E. R. Stofan, *Lunar Planet. Sci., XXIV*, 597-598, 1993; Stofan, E. R. et al., *Lunar Planet. Sci., XXIV*, 1361-1362, 1993; **10)** Grimm, R. E. and R. J. Phillips, *J. Geophys. Res., 97, E10*, 16,035-16,054, 1992; Senske, D. A. et al., *J. Geophys. Res., 97, E8*, 13,395-13,420, 1992; Solomon, S. C. et al., *J. Geophys. Res., 97, E8*, 13,199-13,255, 1992; **11)** Bindschadler, D. L.et al., *J. Geophys. Res., 97, E8*, 13,495-13,532, 1992; **12)** Bindschadler, D. L. and E. M. Parmentier, *J. Geophys. Res., 95, B13*, 21,329-21,344, 1990; **13)** Solomon, S. C. and J. W. Head, *Reviews of Geophys. and Space Phys., 18*, 107-141, 1980; **14)** Stevenson, D. J. et al., *Icarus, 54*, 466-487, 1983; **15)** Sotin, C. et al., *Earth Planet. Sci. Lett., 95*, 321-333, 1989; **16)** Erickson, S. G. and J. Arkani-Hamed, *Geophys. Res. Lett., 19*, 885-888, 1992; **17)** Solomon, S. C. and J. W. Head, *Science, 252*, 252-260, 1991; **18)** Hill, R. I., *Earth Planet. Sci. Lett., 104*, 398-416, 1991; **19)** Turcotte, D., *J. Geophys. Res., 98, E9*, 17,061-17,068, 1993.

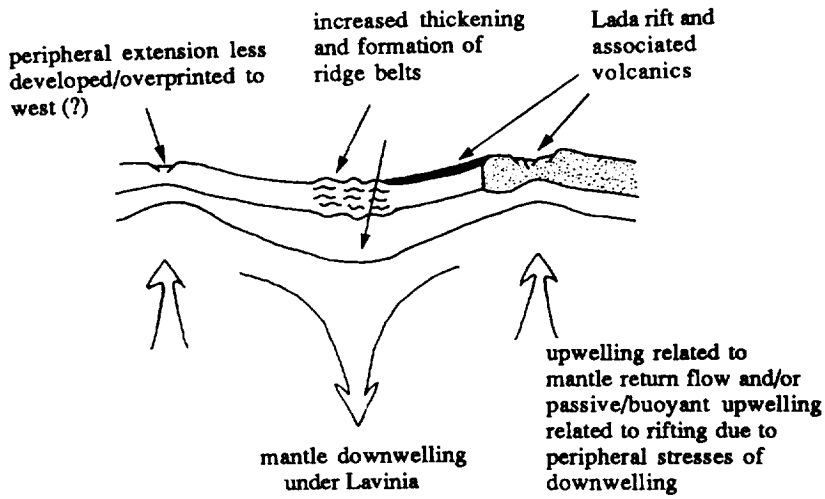

Figure 1. Sketch illustrating possible "passive" rifting origin of extension and volcanism along the Lada Terra-Lavinia Planitia boundary. Rifting is linked to mantle downwelling as described in the text. Cross-section is not drawn to scale. West is to left.

VENUS: MORPHOLOGY AND MORPHOMETRY OF VOLCANISM IN RIFTING ENVIRONMENTS, Kari P. Magee and James W. Head, Dept. of Geological Sciences, Brown University, Providence, RI 02912

As revealed by Magellan image data, over 80% of the surface of Venus is comprised of various types of volcanic plains, deposits and constructs.[1] Further analysis of the Magellan data has revealed that a major concentration of volcanic centers occurs between Beta, Atla, and Themis Regiones ("BAT"); these areas are associated with structures interpreted as major rifts and zones of large-scale mantle upwelling.[2] Associations of volcanic centers with large-scale rifts and fracture belts also occur along the margins of Aphrodite Terra and Lada Terra.[3-5] By examining the character of volcanism (abundance, spacing, style) associated with the major rifts on Venus, it should be possible to gain insight into the actual process and timing of rifting as well as the thermal structure of the crust and lithosphere during extension. In addition, an examination of volcanic centers in a particular type of tectonic environment (in this case, extensional), should provide some control on the analysis of different factors that contribute to the formation of the various types of volcanic centers (i.e., coronae vs. novae vs. shields vs. large flow fields). We continue to explore the relationship between rifting and volcanism in a series of analyses[3-7] focusing in this study on the morphology and morphometry of volcanism associated with major rift systems on Venus.

Three broad categories of rifts have been recognized on Venus.[8] Simple rifts, such as Devana Chasma in Beta Regio, are characterized by single, continuous linear troughs that reach depths of 1-5 km. They are thousands of kilometers long, 60-200 km wide and bounded by steep scarps.[8] Fracturing within a simple rift is confined to a well-defined trough. The rift flanks show little deformation and may be elevated as much as 3 km above the surrounding plains. Simple rifts are linked to volcanic rises and often radiate from a large central edifice such as Theia Mons in Beta Regio and Ozza Mons in Atla Regio. Volcanism is concentrated primarily at the central edifice. Extension associated with simple rifts is thought to be the result of regional uplift due to the upwelling of a mantle plume.[8,9]

Corona chains are characterized by multiple, often contiguous, coronae and other volcanic centers connected by zones of intense fracturing 500 to over 1000 km wide.[8,9] Corona chains are typically many thousands of km in length and found almost exclusively in plains regions, often extending from a major volcanic rise.[8,10] They are generally surrounded by arcuate troughs and steep scarps with slopes ranging up to 10° to greater than 30°.[8,11] Zones of most intense fracturing are restricted to the topographic lows along the rift. More diffuse zones of fracturing occur within 300 km of the main trough.[10,12] In contrast to simple rifts like Devana Chasma, corona chains are complex, branching networks with several discontinuous offsets along strike.[10] Corona chains have been interpreted to represent zones of extension along which mantle diapirs have risen to form coronae.[10] A "passive" rifting model for the origin of these features is presented elsewhere.[7]

Fracture belts, such as the Lada rift and those observed along the southern margin of Aphrodite Terra and within Aino and Sedna Planitiae, are characterized by a discontinuous chain of topographic lows and relatively broad zones of fracturing.[8] The Lada rift is located at the margin of a large highland, along the border of a relatively circular basin.[4,5] It does not branch in any complex fashion, nor is it one of several rift arms radiating from a major volcanic edifice atop a regional rise. Its structure is characterized by discontinuous topographic lows and relatively broad zones of fracturing not confined within a trough bound by steep scarps. It has an average depth of ~1 km, much shallower than simple rifts like Devana Chasma, where 3-5 km depths are common and it has an average slope (2.7°) much lower than that typical for either simple rifts or corona chains. Like corona chains, the Lada rift is associated with multiple volcanic centers. However, these are much fewer in number and spaced farther apart (see below). As for the case of corona chains, passive rifting may account for the number, spacing, and character of volcanic centers along fracture belts; such a model has been proposed for the origin of the Lada rift.[4,5]

To analyze the detailed volcanic characteristics of these three rift types, we collected data from Magellan C1-MIDRs on the number of volcanic centers, average center diameter, the center-to-center spacings, type of volcanic center and the presence of flow fields for the following rifts: Devana, Ganis, Juno, Atla-Ulfrun (simple rifts[8]), Dali, Hecate, Parga (corona chains[8]), Lada and Southern Aphrodite (fracture belts[8]) (Table 1). Detailed analyses of the topography of the Lada rift and Parga Chasma were also conducted, the results of which are presented elsewhere.[4,7]

Initial observations indicate that *corona chains* are the most volcanically productive along the entire rift length of the three rift types, possessing the greatest number of volcanic centers at the smallest spacings, and a high percentage of distinctive flow fields. Corona chains are also distinguished from the other rifts by relatively small diameters of volcanic centers and great overall rift lengths. The dominant type of volcanic center along corona chains are coronae (>60%) (with and without interior novae or radial structures) and volcanic shields (~20%).

RIFT-RELATED VOLCANISM ON VENUS: Magee, K.P. and Head, J.W.

Simple rifts are characterized by very few distributed volcanic centers. However, these centers are dominated by very large shield edifices (e.g., Theia Mons, Ozza Mons) that represent extremely large amounts of volcanism. Volumetrically, corona chains and simple rifts may have very similar volcanic outputs. Note that Juno Chasma is more similar to corona chains in terms of its volcanic characteristics, than to other simple rifts, as it was originally classified.[8] *Fracture belts* are most similar to corona chains, but characterized by fewer individual centers and greater average spacings. The smaller number of volcanic centers and the relatively low percentage of centers with distinctive flow fields may be related to the fact that they are located along the edges of highlands that are likely to be areas of tessera and thickened crust. In these regions, magma stalling may be enhanced, resulting in greater intrusive, plutonic activity than surface volcanic eruptions. This is consistent with the fact that a greater percentage of novae (associated and unassociated with coronae) comprise the total number of volcanic centers than along the other rifts (except for Juno Chasma). However, it should also be noted that some of the largest volcanic flow fields (e.g., Mylitta Fluctus) are observed along fracture belts.[3,4] Variations in the scale of upwelling and depth of melting along a rift may account for variations in flow field scale, as suggested for variations in volcanic output for the Lada rift.[4]

The most common type of volcanic center among the rifts considered in this analysis are coronae and coronae-like structures, which comprise up to 63% of all rift-related volcanic centers. Intermediate and large-scale volcanoes are the second most abundant feature type (~15%), followed by large flow fields (~10%) and novae (~8%). Arachnoids, rilles, and shield fields unassociated with other centers are the least abundant.

The origins of the different rifts appear to vary. "Active" rifting related to regional uplift and extension due to the upwelling of a large mantle plume is consistent with the features of simple rifts at Beta and Atla Regiones.[8-9] Our recent analyses[4-5,7] indicate that "passive" rifting may be a significant process in the formation of most corona chains and fracture belts. We also observe along-strike transitions in rift morphology. For example, several simple rifts radiating from Atla and Beta Regiones become corona chains beyond the perimeter of the central rise. In addition, the rift along Dali Chasma changes character from a corona chain east of Artemis to a fracture belt west of Artemis. This may reflect changes in crustal and lithospheric thickness and thermal structure related to the presence of thickened tessera blocks in western Aphrodite (Ovda and Thetis) and distance from the central uplift of Atla. Variations in the processes of rifting and related volcanism are the subjects of our continued investigation.

REFERENCES: **1)** Head, J. W. et al., *J. Geophys. Res., 97, E8,* 13153-13197, 1992; **2)** Crumpler, L. S. et al., *Science, 261,* 591-595, 1993; 3) **3)** Roberts, K. M. et al., *Lunar Planet. Sci., XXIII,* 1157-1158, 1992; **4)** Magee, K. and J. W. Head, *J. Geophys. Res.* (in review), 1993; **5)** Magee, K. and J. W. Head, *Lunar Planet Sci. XXV* (this volume), 1994; **6)** Magee Roberts, K. and J. W. Head, *Geophys. Res. Lett., 20,* 1111-1114, 1993; **7)** Jha, K. and E. M. Parmentier, *Lunar Planet Sci. XXV* (this volume), 1994; Jha, K./ K. Magee et al., *Lunar Planet Sci. XXV* (this volume), 1994; **8)** Senske, D. A., Ph.D. thesis, Brown University, pp. 304-351, 1992; Senske, D. A. and J. W. Head, *Lunar Planet. Sci., XXIII,* 1269-1270, 1992; **9)** Senske, D. A. et al., *J. Geophys. Res., 97, E8,* 13,395-13,420, 1992; **10)** Stofan, E. R. et al., *Lunar Planet. Sci., XXIV,* 1361-1362, 1993; **11)** Ford, P. and G. H. Pettengill, *J. Geophys. Res., 97, E8,* 13103-13114, 1992; **12)** Hamilton, V. E. and E. R. Stofan, *Lunar Planet. Sci., XXIV,* 597-598, 1993.

Table 1. Volcanic characteristic of Venus rifts*

rift type	# of volcanic centers	mean diameter (km)	mean spacing (km)	% with flow fields	rift length (km)
simple rift	*7*	*567*	*1044*	*88*	*4700*
Ganis	2	755	1585	100	3500
Juno	5	363	875	60	4000
Devana	6	643	1091	100	6700
Atla-Ulfrun	13	508	626	92	4700
corona chain	*25*	*431*	*560*	*83*	*7200*
Dali	15	615	765	80	6700
Parga	47	313	405	79	12,000
Hecate	25	289	442	80	5200
Atla-Ulfrun	13	508	626	92	4700
fracture belt	*10*	*263*	*812*	*66*	*7900*
Lada	11	280	597	64	8000-6800
S. Aphrodite	9	246	1027	67	8400

*average values for rift type given in italics; Atla-Ulfrun is considered as both a simple rift and corona chain, based on original mapping by [8]

ALTERNATIVE THERMAL HISTORIES FOR TYPE B CA-AL-RICH INCLUSIONS. *Susan V. Maharaj* and *Roger H. Hewins*, Dept. of Geological Sciences, Rutgers University, New Brunswick, NJ 08903, U.S.A.

Introduction: Chondrules and Ca-Al-rich inclusions (CAIs) were both melted in the solar nebular, but appear to have had different thermal histories (1-4) which would require different locations and/or origins. CAIs apparently experienced lower initial temperatures (~1400°C) and lower cooling rates (at most tens of degrees per hour) than many chondrules (2). Recent studies (5, 6) have shown that a variety of thermal histories can produce spherules similar to chondrules. New experiments have therefore been conducted in order to determine the effects of cooling history on the textures of CAIs. Dynamic crystallization experiments were performed on an average Type B CAI composition (1) at 1 atm in air; maximum temperatures ranged from 1420 to 1580°C and cooling rates varied from 2 to 3000°C/hr. Control experiments after (2) were followed by flash melting and dust seeding experiments which reproduced CAI textures with faster cooling rates and higher initial temperatures than in (2).

Results: Experimental results of the conditions under which different melilite textures were observed by (2) have been reproduced with good agreement (Fig. 1). Euhedral melilite textures are produced at 1420°C (T. max.; soak 3 hrs.) with cooling rates of ≤ 20°C/hr. At 1450°C (T. max.; soak 3 hrs.) cooling rates of ≤ 5°C/hr. produce euhedral melilites. Higher initial temperatures and faster cooling rates result in lattice/euhedral, lattice, lattice/dendritic, dendritic or glassy textured charges, as also seen by (2).

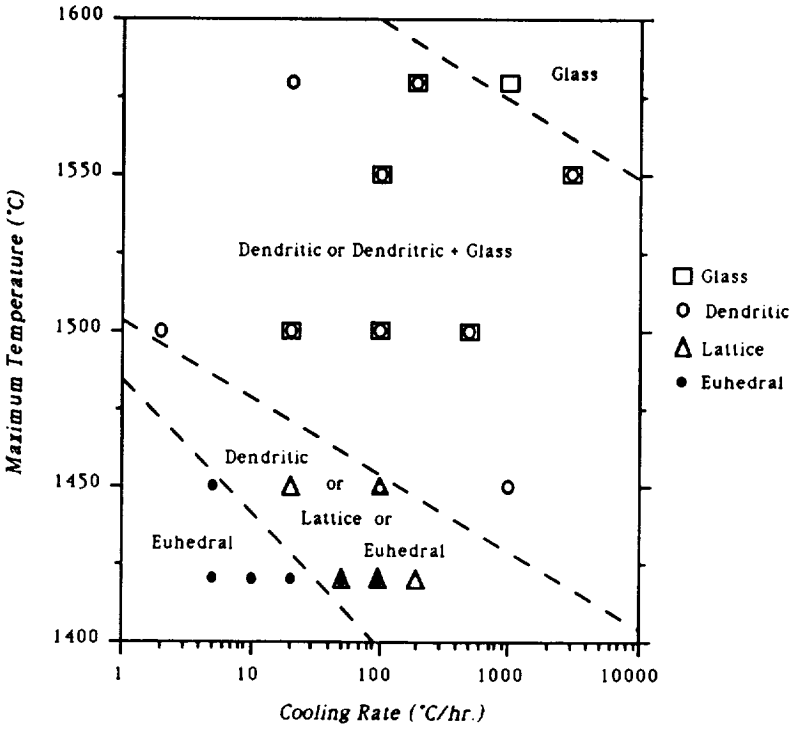

Figure 1. Melilite texture as a function of maximum temperature and cooling rate in control experiments (long melt time).

Alternate heating and cooling histories were employed in an attempt to crystallize euhedral melilite at chondrule cooling rates. Our preliminary results show that normally zoned euhedral melilites are formed in charges flash heated (1450°C for 1 minute) followed by rapid cooling at 1000°C/hr. (Fig. 2), whereas equivalent samples not flash heated (i.e. soaked for 3 hrs.) contain reversely zoned dendritic-textured melilites (Fig. 1). Hence, high cooling rates may be possible for some CAIs.

Additional experiments involved total melting followed by seeding charges by puffing anorthite, corundum, spinel or the Type B CAI starting composition dust into the furnace.

ALTERNATIVE HISTORIES FOR TYPE B CAIs

S. V. Maharaj & R. H. Hewins

All seeding compositions nucleated melilite. In this way, charges which would have been glassy became crystalline and therefore initial temperature could have been higher than previously assumed.

Figure 2: Sample Ca-Al-32 showing euhedral melilite crystals formed by rapid cooling at 1000°C/hr.

Conclusion: Moderate heating temperatures and low cooling rates for CAIs (2, 7) are not ruled out, but higher temperatures and faster cooling rates are also possible, based on textural criteria.

References: (1) Stolper, E. M. (1982) *Geochim. Cosmochim. Acta* **46,** 2159-2180.
(2) Stolper, E. M. and Paque, J. M. (1986) *Geochim. Cosmochim. Acta* **50,** 1785-1806.
(3) Tsuchiyama, A. et. al. (1980) *Earth Planet. Sci. Lett.* **48,** 155-165.
(4) Hewins, R. H. (1988) Meteorites and the Early Solar System, 660-679.
(5) Connolly, H. C. et al. (1991) *Meteoritics* **26,** 329 (abstr.).
(6) Connolly, H. C. and Hewins, R. H. (1990) *Meteoritics* **25,** 354-355 (abstr.).
(7) Wark, D. A. and Lovering, J. F. (1982) *Geochim. Cosmochim. Acta* **46,** 2581-2594.

RADIAL COMPACTION OF THE DUST SUBDISK IN A PROTOPLANETARY DISK AS A POSSIBLE WAY TO GRAVITATIONAL INSTABILITY;
A.B. Makalkin, United Institute of Physics of the Earth, Russian Academy of Sciences, B. Gruzinskaya 10, 123810 Moscow, Russia.

In the gravity-controlled process of planet accumulation, initial building blocks are the smallest gravitationally bound bodies of 0.1-1 km in size. But the way of formation of these bodies is still unclear. They could form either via gravitation instability in the dense dust-rich subdisk of the protoplanetary disk or by direct growth of particles sticking at collisions. Both mechanisms meet with difficulties: gravitation instability seems to be unattainable, because necessary severe vertical (z) contraction of the dust subdisk would be prevented by shear -driven turbulence of the gas in the subdisk [1]; the direct growth is also highly doubtful for reasons of tending to zero sticking probability for particles of size larger than 1 cm, and even for smaller ones [2,3]. We present here a simple model for radial (r) contraction of the dust subdisk. We find a necessary condition for a rise of its density without further vertical contraction and estimate the rate of this rise. The compaction of the subdisk through its r-contraction, in contrast to that through z-contraction, cannot be inhibited by turbulence and can lead to gravitation instability of the dust subdisk.

Consider the dust-rich subdisk formed by settling of dust particles to the midplane of a protoplanetary disk, the particle spatial density in the subdisk being much higher than the initial value before settling. The rotation velocity of the gas in the disk v_O is lower than the Keplerian velocity v_K owing to the partial support of the gas by radial pressure gradient $\frac{\partial P}{\partial r}$. But inside the subdisk, the gas rotation velocity v_g increases due to a coupling of the gas with the abundant particles by drag forces. In the case that particle-to-gas space density ratio $\varepsilon = \rho_p/\rho_g$ is high, the value of v_g approaches v_K. The velocity difference between the gas inside and outside the subdisk ΔV_g is $\Delta V_g = v_g - v_O = \frac{\varepsilon}{\varepsilon+1}(v_K - v_O) = -\frac{\varepsilon}{\varepsilon+1}\frac{r}{2\rho_g v_K}\frac{\partial P}{\partial r}$. This difference generates a turbulent shear zone (the Ekman layer) and a shear stress S on each face of the dust-rich subdisk $S = \rho_g \Delta V_g^2/Re^*$, where Re^* is the critical Reinolds number [4]. $Re^* \simeq 50\text{-}200$ [1].

We solve the angular momentum conservation equation for a concentric zone of the subdisk. The zone of mass $\delta m = \sigma\, 2\pi\, r\, \delta r$, where σ is the surface density of the subdisk at radius r, is subjected to the torque (per unit area) $2rS$. In the absense of accretion of the dust onto the surfaces of subdisk($d\delta m/dt=0$), we get the r-dependent radial velocity of the subdisk $u_r = -4Sr/\sigma v_K$. The flux of material through radius r is $2\pi r\, \sigma\, v_r$ and depends on radial distribution of the shear stress S. Insert this flux into the continuity equation for σ and use a power approximation for

RADIAL COMPACTION OF THE DUST SUBDISK: Makalkin A.B.

distribution of the gas surface density Σ and temperature T in the gas-dust protoplanetary disk: $\Sigma(r) = \Sigma_1 (r/r_1)^{-p}$ and $T(r) = T_1 (r/r_1)^{-q}$, where subscript 1 refers to the radial distance of 1 AU. In accordance with results of the paper [1], we suggest that the thickness of the particle subdisk H_p is determined by steady shear turbulence and is constant in time. It can also be expressed by the power function: $H_p = H_{p1} (r/r_1)^n$. Denote the initial values of σ and ε at r=1 AU by σ_{01} and ε_{01}. We come to the following equation (for the dimensionless values $\sigma \leftrightarrow \sigma/\sigma_{01}$, $t \leftrightarrow t\, v_{K1}/r_1$, $r \leftrightarrow r/r_1$), descriptive of the evolution of the subdisk surface density σ :

$$\frac{\partial \sigma}{\partial t} = K \frac{1}{r} \frac{\partial}{\partial r} \left[r^b \left(\frac{\varepsilon_{01} r^d \sigma}{1 + \varepsilon_{01} r^d \sigma} \right)^2 \right];$$

where $b = 2 - p - \frac{3}{2} q$;

$d = p - \frac{1}{2} q - n + \frac{3}{2}$;

$$K = \frac{2\,(p + q/2 + 3/2)^2}{\gamma^{1/2}\, Re^*} \frac{\Sigma_1}{\sigma_{01}} \frac{c_{s1}^3}{v_{K1}^3} ;$$

$\gamma = C_P / C_V \approx 1.4$;

$v_{K1} = v_K$ at $r = 1$ AU ;

c_s is the isothermal sound speed of the gas, $c_{s1} = c_s(T_1(r_1))$. After segregation of the dust particles into the subdisk, the exponent q should be near 0.5 for the gas disk; the exponent p is inherited from the global turbulence stage and can be in the range 0.5 - 1.5. According to results of the modeling [1], the exponent n is near 0.2 - 0.5 for the steady particle subdisk supported by shear turbulense [1], and the value ε_{01} is in the range 3-10. If H_p is proportional (or equal) to the thickness of the turbulent Ekman boundary layer, with [4] we find n = 1.75.

For the case, when $\varepsilon_{01} r^d \sigma \gg 1$, the equation for σ can be simplified: $\frac{\partial \sigma}{\partial t} \propto K\, b\, r^{b-2}$. The condition for compaction of the subdisk is b > 0. For the disk with p=0.5-1 and q=0.5, we have b=0.75-0.25, and the time scale for the tenfold increase of σ is $t \propto 9 r^{-b+1/2} \tau/(2\pi K b) \approx 2 \cdot 10^3 \tau$, where $\tau = \tau(r)$ is the Keplerian period. We also have $\rho_p = \sigma/H_p \propto r^{b-n-2}$, and the critical density for gravitational instability is $\rho_{cr} \propto r^{-3}$, hence $\rho_p / \rho_{cr} \propto r^{b-n+1}$. The exponent sign depends on n value, therefore the instability can first be reached near the outer or inner edge of the subdisk.

References: [1] Cuzzi,J.N, A.R.Dobrovolskis & J.M.Champney(1993) Particle-gas dynamics in the midplane of a protoplanetary nebula. Icarus Special Issue on Planet Formation. [2] Blum,L., & M.Munch (1993) Experimental investigations on aggregate-aggregate collisions in the Early Solar Nebula. - Ibid. [3] Chokshi,A., A.G.G. M. Tielens, & D. Hollenbach (1993) *Astrophys. J., 407*, 806-819. [4] Goldreich,P.,& W.R.Ward (1973). *Astrophys.J., 183*, 1051-1061.

NUMERICAL SIMULATION OF TIDAL CAPTURE OF A LUNAR-MASS PLANETOID BY AN EARTH-LIKE PLANET: TWO-DIMENSIONAL LIMITS OF A PROGRADE STABLE CAPTURE ZONE; Robert J. Malcuit, Dept. of Geology and Geog., Ronald R. Winters, Dept. of Physics and Astron., Denison Univ., Granville, Ohio 43023.

Over the past few years we have been doing co-planar, three-body (sun, planet, planetoid) numerical simulations assessing the capture potential of planets for planetoids by tidal energy dissipation processes. Most of our work has been concentrated on the neptune-triton system [1] and the earth-moon system [2,3]. In general we have found (1) that the deformational properties of the planet are not important for tidal capture, (2) that only planetoids (whether icy or rocky) characterized by a low Q (specific dissipation factor) and a moderate h (displacement Love number) can dissipate sufficient energy within their bodies to cause tidal capture, and (3) that the orientation of the encounter relative to the planet's orbit is critical for attaining a stable post-capture orbit if sufficient energy is dissipated for capture. Here we report the results of a set of simulations for placing limits on a Stable Capture Zone (SCZ) for the case of lunar-like planetoid encountering an earth-like planet.

The computer program uses a 4th-order Runge-Kutta integration scheme and has an energy dissipation subroutine which operates within 20 earth radii (R_e) using equations for energy dissipation from [4,2]. The major variables in the calculation are (1) the displacement Love number (h) for each body, (2) the specific dissipation factor (Q) for each body, (3) the perihelion radius of the planet's orbit, (4) the perihelion radius of the planetoid's orbit, (5) the eccentricity of the planetoid's orbit, (6) the eccentricity of the planet's orbit, (7) the planet anomaly (the initial position of the planet in its orbit), (8) the planetoid anomaly (the initial position of the planetoid relative to the planet), and (9) the initial distance of separation between the planet and planetoid. In order to limit this set of variables we use (1) a circular planet orbit, (2) a constant set of Q values for the planetoid ($Q=1$ for the initial close encounter and $Q=10$ for all subsequent encounters), (3) a constant set of h and Q values for the planet ($h=0.7$ and $Q=100$), (4) a constant perigee radius (r_p) of 1.43 R_e for all initial encounters of encounter sequences (a distance well beyond the grazing encounter distance), and (5) an initial distance of separation of 600 R_e [which is well beyond the limits of the Hill sphere for planet earth (about 235 R_e)]. The major variables that were systematically varied for generation of this data set are the eccentricity of the planetoid's orbit, the planet anomaly, the planetoid anomaly, and the h of the planetoid.

A Stable Capture Zone (Figure 1) is defined as a zone of phase space (defined here in terms of planet anomaly and planetoid orbital eccentricity) in which any prograde encounter within $r_p=1.43$ R_e (with specified planetoid anomaly) will attain a stable capture orientation if the h of the planetoid is sufficiently high to dissipate the energy for capture. In general, capture of a lunar-like planetoid can take place with an h of 0.20 or higher depending on the position of the encounter within the SCZ. A higher h for the planetoid at the time of capture results in a smaller capture orbit and in a more stable orbit relative to subsequent solar gravitational perturbations. We have found that for stable prograde capture, the major axis of the initial geocentric orbit must be nearly perpendicular (+ or -5°) to the tangent of the planet's orbit. In contrast, for stable retrograde capture the major axis of the initial geocentric orbit must be nearly parallel (+ or -5°) to the tangent of the planet's orbit. Thus, all encounters within an SCZ must fulfill this orientation requirement.

2-D STABLE CAPTURE ZONE FOR MOON; MALCUIT, R., AND WINTERS, R.

Because of the dynamics of the 3-body calculation there is a gradient in the value of the total orbital energy at the initial close encounter. The higher the negative total orbital energy is at the time of the initial close encounter, the lower the energy dissipation requirements are for stable capture. These values range from about -1.9 X 10^{28} joules in the upper right of the diagram (planet anomaly=320°, planetoid ecc.= 1.5%) to zero in the upper left part of the diagram (dashed line). h values necessary for capture vary from 0.2 (0.8 X 10^{28} joules to dissipate for capture) in the upper right to 0.7 (2.80 X 10^{28} joules to dissipate for capture) in the upper left along the dashed line. Thus the most favorable area in the SCZ for stable capture lies to the right of earth anomaly 240° because of the lower energy dissipation necessary for capture.

In addition to the SCZ described in Figure 1, we have identified two others that extend over several degrees of AN(E) (earth anomaly). A retrograde SCZ extends from AN(E)=225° to 245° (planetoid ecc.=0.75%) and another prograde SCZ extends from AN(E) 70° to 120° (planetoid ecc.=0.75%). Two-dimensional mapping of these SCZ's is in progress.

In summary, we have demonstrated (1) that tidal capture is physically possible within a certain range of conditions and (2) that Stable Capture Zones of significant two-dimensional extent exist for the Earth-Moon pair.

REFERENCES: [1] Malcuit, R. J., et al. (1992) Abstracts, LPSC XXIII, Lunar and Planet. Inst., 827-828; [2] Malcuit, R. J., et al. (1989) Proc., 19th LPSC, Cambridge Univ. Press and Lunar and Planet. Inst., 581-591; [3] Malcuit, R. J., et al. (1992) Proc. Vol., 3rd Int. Archaean Symp., Geol. Dept. & Univ. Ext., Univ. of Western Australia, Pub. 22, 223-235; [4] Peale, S. J., and Cassen, P. (1978) Icarus, 36, 245-269.

Figure 1. Plot of a prograde Stable Capture Zone for an earth-like planet and a lunar-like planetoid to the nearest 10° of planet anomaly and 0.25% of planetoid eccentricity. The dashed line on the upper left of the diagram is where the total orbital energy at the initial perigee passage is 0. Negative total orbital energy values increase to the right on the plot to -1.90 X 10^{28} joules in the upper right portion of the plot.

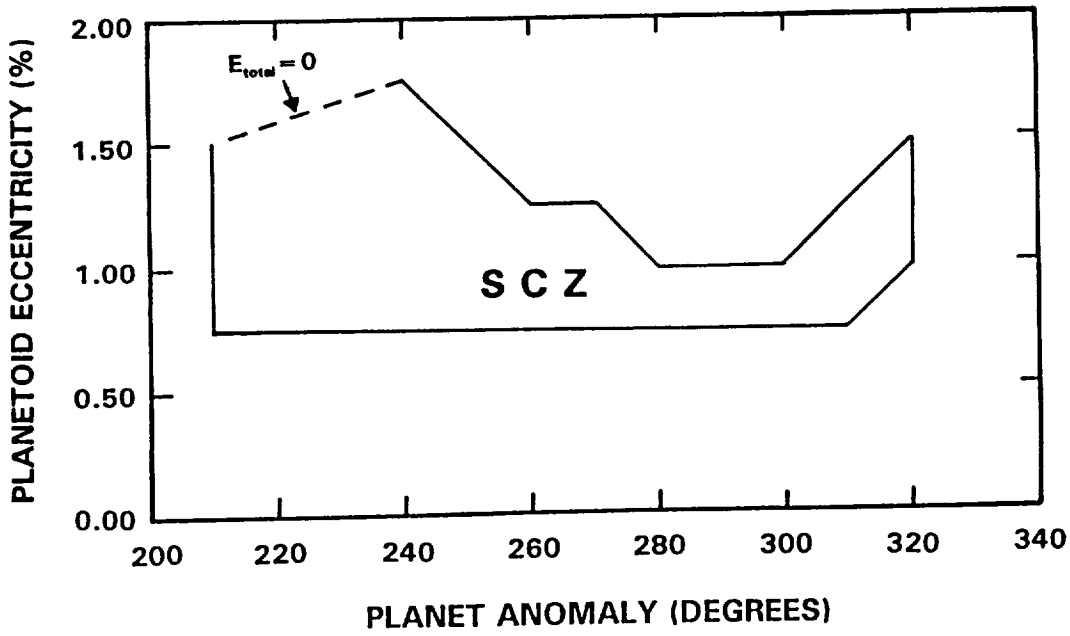

Extreme Potassium Enrichment in plagioclase from lithic clasts in the Lewis Cliff 86001 Monomict Eucrite.

MANN, Jacqueline L. and **DELANEY,** Jeremy S.: Dept. of Geological Sciences, Rutgers University, New Brunswick, NJ 08903.

ABSTRACT: Petrographic study was performed on 5 lithic clasts in the Lewis Cliffs 86001 monomict eucrite. K-rich areas in plagioclase indicate significant shock processing of these clasts. Other clasts with no K-rich areas are probably less shocked. Coexistence of heavily shocked and unshocked clasts in the same breccia indicates either mixing of clasts with different regolith histories or mixing of clasts from different parts of the same impact crater. General similarities between the 5 clasts suggests that they were from a single crater.

INTRODUCTION: Five lithic clasts in Lewis Cliff 86001,15, a monomict eucrite, have been examined both petrographically and by electron microprobe. Of the five clasts, two (LC*i* & LC*iii*) contain small (10μm - 50μm wide) chain-like regions with large K-enrichment within plagioclase hosts (Figure 1). The remaining basaltic clasts (LC*iv*, LC*v*, LC*vi*) have no potassium enrichment.

CLAST PETROGRAPHY : Clasts LC*i* and LC*iii* with K-rich regions in a plagioclase host have similar textures and compositions. A subophitic texture typical of basalt textured eucrites dominates, and consists of lathy plagioclase in subhedral pyroxene. LC*i* is very fine to fine grained, while clast LC*iii* is fine to medium grained. LC*i* contains abundant pyroxene while LCiii contains more plagioclase. The pyroxene and plagioclase in both clasts contains abundant inclusions (clouding). Pyroxene is exsolved in both clasts with augite lamellae up to 5μm present. Both have silica polymorphs, ilmenite, and chromite, and LC*iii* also contains Ti-chromite, iron-metal (+/- troilite) and a phosphate, (probably F-apatite rather than merrillite as no REE were detected). The apatites are common as inclusions in pyroxene. Both clasts are extensively cracked. Iron staining is very abundant in LC*iii*. "Normal" clasts LC*iv*, LC*v* and LC*vi* have similar textures to LC*i* and LC*iii*. The subophitic texture dominates, and grain size varies from very fine to fine. The pyroxene is finely exsolved, and the minor phases are silica polymorphs, ilmenite, and chromite. LC*iv* is almost identical to LC*iii* in texture and composition, and contains apatite, troilite, and iron-metal. LC*i* and LC*iii* have similar mineral compositions: pyroxene varies from $En_{38}Wo_{1.7}$ to $En_{30}Wo_{44}$; plagioclase in LCi is $An_{94}Or_{0.1}$ to $An_{82}Or_{9}$. In LC*iii*, feldspar varies up to $An_{61}Or_{34}$.

DISCUSSION: Although the textures and compositions in all of the clasts are very similar, the distinctive K-rich areas in two of the clasts separate them from the others. The K-rich areas probably developed because of a shock event that modified those clasts. Shock disruption of these clasts, or the source basalt from which they were derived, produced crack networks through the plagioclase grains. Since K diffuses faster than Na in shocked feldspar when heated, the decoupling of K and Na has resulted in K migration into the crack zones (c.f. 1). Subsequent annealing of the clasts preserved this metastable variation of K, Ca and Na (1) and closed the original cracks (Figure 1). These plagioclase grains apparently did not get transformed into diaplectic glass as they show no evidence of the devitrification seen in other clasts from Lewis Cliff achondrites. Clasts LC*i* and LC*iii* were probably shocked to pressures in excess of 20 GPa but below 27 GPa. In contrast, feldspar in clasts LC*iv*, LC*v*, LC*vi* have no comparable K variation. These clasts do not preserve evidence of equivalent shock. The coexistence of clasts that have undergone a powerful shock event with others that apparently have not in a single breccia, may be caused by mixing of lithologies with different petrogeneses into the same crater or the clasts represent different shock zones within a single crater. Mixing of material in the crater itself will result in shocked and unshocked material occurring in one breccia. Clasts derived from different lithologies may vary compositionally and texturally, in which case, the breccia would be classified as polymict. Strong similarities between pyroxenes

K-enrichment in eucritic feldspar: Mann & Delaney.

and minor phases in these clasts suggest that they may sample a single original lithology. Minor minerals and oxides need to be studied to see if variations exist.

CONCLUSION: The K in LC*i* and LC*iii* provides evidence for differences in shock signatures and is a relict of shock processing between 20 GPa and 27 GPa. Mixing within the crater is a plausible model for the mixture of clasts in this breccia because of the similarities between the clasts. The differences in K-distribution in plagioclase from the clasts in LEW86001 probably reflect variations in the shock intensity within a single crater. Thus, this eucrite has evidence of variable shock history despite its mineralogical uniformity which suggest that it is monomict.

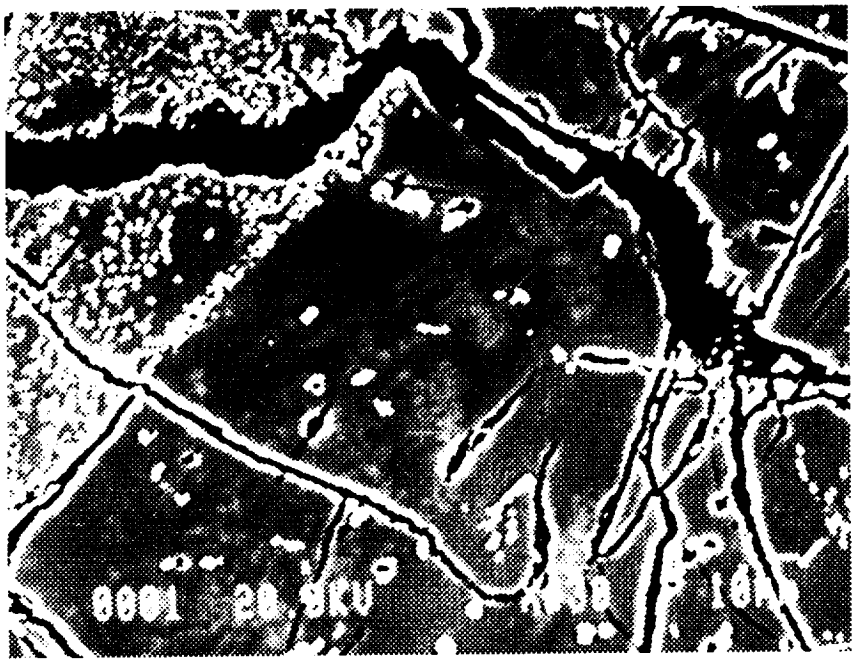

Figure 1: Enhanced contrast, backscattered electron image of plagioclase from LC*iii*. K-rich feldspar stringers appear as lighter patches within central mid-gray area. Bright grains are pyroxene and oxide mineral inclusions.

References:
(1)Ostertag and Stöffler (1982) PLPSC 13, A457;
Acknowledgment:
NASA grant NAG9-304.

GEOLOGIC MAPPING OF THE SIF MONS SOUTHERN FLANK, VENUS (PRELIMINARY RESULTS),
A.G.Marchenko, 119899, GSP, Moscow State University, Moscow, Russia

Mapping of the southern flank of Sif Mons revealed seven distinctive geological units with proper stratigraphic position each. Set of the units demonstrates discontinuity of the geologic history of the mapped region when either tectonism or volcanism was the predominant factors of the region evolution. Probable consequence of events within the area under study (F-MIDRP.20N351) is described

Introduction. Sif Mons is a large shield volcano which is about 300 km across [1]. The volcano caldera is at 20°N,352°E and about 3.5 km above the mean planetary radius. Sif Mons and Gula Mons represent two main volcanic centers of western Eistla Regio and characterized by the complex history of volcanism [1,2,3,4]. To decipher geologic history in the area at southern slopes of Sif Mons I used Magellan images of the Cycles I and III, giving the real stereo image, to map geological units within the frame F-MIDRP.20N351 (Fig.).

Unit Description. There are seven units within the area under study. From the oldest to youngest they are as follows. **(1)** *Densely Fractured Plains (Dfp).* The unit consists of several isolated local heights heavily disrupted by furrows and located at the central, NW, and E part of the studied area. The heights are embayed by the other units and due to this is considered as outcrops of the oldest terrain. The central and NW occurrences of the unit are characterized by a large amount of closely spaced linear grows with length from a few up to 150 km. Relics of preexisting plains-forming material are visible between the grooves. The eastern occurrences resemble a remnant of a double rimmed corona with the set of features typical of coronae [5]. **(2)** *Dark Plains (Dkp)* The uniform radar albedo is typical of the unit's surface. Within the area of mapping the dark plains located to the South, SW, and W from Sif Mons and at the volcano base by the altitude position. Material of the dark plains embay the remnant of the corona-like feature and due to this is considered as relatively young. The surface of the plains disturbed by spaced set wrinkle ridges and a few linear grooves. **(3)** *Domed Plains (Dmp).* The unit has mottled albedo pattern which is brighter than surface of the dark plains and consists of large amount of densely spaced small domes encircled by bright or dark haloes several km across. Clusters of the domes located to the SE and W from Sif Mons. At the western flank of the SE occurrence one can see a set of radial elongated spots several km wide and up to hundred km long. Obviously the spots are lava flows which look undisturbed at contacts with the material of the dark plains but overlapped by lava flows from the Sif volcano. Radial pattern of the flows suggest that the cluster occupies an area elevated above the surface of the dark plains. **(4)** *Lava Complexes of the Sif Mons Slopes.* Materials of the complexes overlay all above units and could be subdivided into three units: **(4.1)** *Slope Digitate Plains (Sdgp).* This is the most widespread unit within the mapped area. The unit consists of a huge number of elongated (up to 400 km long) sinuous radar bright and dark spots which often overlay each other. The spots form the radial pattern around the volcano center and extend from the volcano caldera becoming wider downslope. From morphology of the spots they interpreted as lava flows. The flows either bury or embay all above units. Variegated albedo pattern of the flows and their overlapping each other suggest that formation of the main unit of the Sif Mons was multistage. **(4.2)** *Slope Bright Plains (Sbp).* This unit occurs at the east side of the Sif slopes and consists of a set of radar bright, sinuous, narrow (a few km wide), and elongated (25-75 km long) spots which are interpreted as lava flows. The flows begin at the base of arc-like east-facing scarps disturbing the surface of the digitate plains. This suggests that the bright plains are younger. **(4.3)** *Slope Dark Plains (Sdp).* The plains surface is radar dark and featureless. The plains are located at 25-100 km from the Sif caldera due N, W, and S and fill a moat which semicircles the caldera. This suggests that the slope dark plains are younger than the main unit. However, the relationships with the slope bright plains are unclear. **(5)** *Impact Crater Material (Icm).* Within the area under study there is only one impact crater at 20.4°N, 350.1°E. The crater is of type M according to [6] and consist of two closed bowl-shaped ones. Diameter of the bigger crater is 5.0 km. Radar bright ejecta blankets from the crater as well as its dark halo overlap surface of the digitate plains and look undisturbed by lava flows.

Probable Geologic History of the Region. The oldest unit recognizable within the area of mapping is the densely fractured plains. Its grooves or fractures disturb some preexisting terrain presumably of volcanic origin. Because of the most common features of the densely fractured plains are grooves, the plains could be result of extension of older volcanic plains. Intensive tectonic deformation typical of the densely fractured plains almost do not traced within the younger units. It suggests that since the beginning of the dark plains emplacement extensional tectonic activity in the region either ceased or was less intensive than volcanism. Surface of the dark plains is characterized by uniform albedo and absence of visible lava sources. This could mean that there was no

single source of the material to form vast dark plains. In contrast, on the surface of restricted areas of the next unit, the domed plains, numerous small domes are seen. The clustered are sources for the material making up the plains. Flows from the center of the domed plains area have no visible relief in the stereo images. It may mean that the material of the plains is a veneer of brighter lava on the surface of the dark plains. Relative small area occupied by the domed plains, clustered domes, and probably very small thickness if the plains material suggests that volcanic activity by the beginning of the domed plains formation became more concentrated but less intensive in comparison with the conditions of the dark plains formation. Surface of both dark and domed plains disturbed by spaced net of low wrinkle ridges which are presumably features of compressional stresses. Thus, tectonism, even not too much intensive, became the main factor again in the history of the region. Volcanism played the main role during the next episode of the region's geologic history when lava complexes of the Sif slopes formed. The main phase of the activity was the formation of the slope digitate plains. Their surface consisting of a great number of very long lava flows that could imply large eruption rate. The flows are of different albedo and usually overlap each other. This could mean that formation of the slope digitate plains was multistage but amount of erupted material at each stage probably was approximately the same. Almost all lava flows of the digitate plains are radial relatively the Sif caldera. This suggests that during the main phase of the Sif volcanism there was the single source of the material. Only at later stages of activity new sources of lava appeared on the Sif slopes: the slope bright plains was formed on the east side of the volcano and the slope dark plains at the volcano caldera. Both types of the plains have very small areas and probably small thickness so amount of the material outpouring at the last stages of Sif development was also insignificant.

References:
[1] Senske, D.A. at al., *JGR*, 97, 13,395 1992; [2] Head, J.W. et. al., *Sciense*, 252, 276 1991; [3] Head, J.W. et al., *JGR*, 97, 13,153 1992; [4] Grimm, R.E. and R.J.Phillips. *JGR*, 97, 16,035 1992; [5] Stofan, E.R. at al., *JGR*, 97, 13,347 [6] Schsber, G.G. et al., *JGR*, 97, 13,257

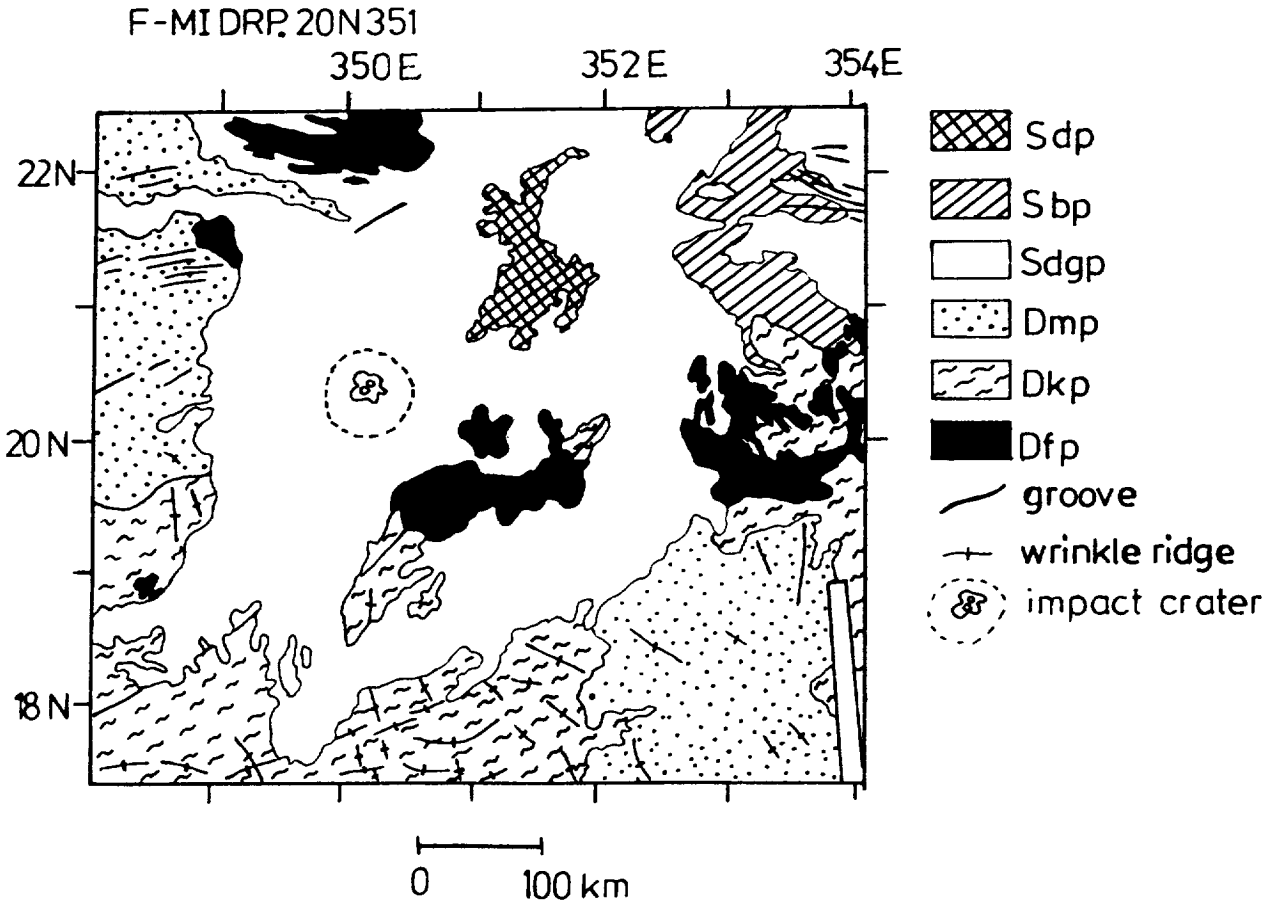

APOLLO–THE NEXT GENERATION: ACTIVITIES TO ACCOMPANY THE LUNAR SAMPLE DISK; Linda Martel and G. Jeffrey Taylor, Hawai'i Space Grant College, University of Hawai'i at Manoa, Honolulu, HI 96822

Since its inception in 1978, the Lunar Sample Loan Program has helped stimulate interest in science and space exploration for thousands of students and educators nationwide. In the summer of 1993, we began work on a new document to supplement and enrich the use of the Lunar Sample Disk in the classroom. This new teacher's guide with activities, titled *Apollo- The Next Generation*, was co-written with ten local educators representing grades K -- 12. These educators are known for their excellence in science instruction. The activities in the new document promote problem-solving and communication skills as well as teamwork using hands-on and debate formats. Each activity consists of specific background information for the teacher as well as reproducible student sheets. During the formal testing phase from mid-October to mid-December 1993, thirty teachers at twenty-one schools across the state, used all or parts of the new document along with the Lunar Sample Disk. Testing sites included: ten elementary schools, five intermediate schools, and six high schools. Educators reported that the background material was easy to use even for the non-science specialist. They found that the activities were adaptable to all the grade levels and were easily integrated into other units such as math, social studies, geography, history, language arts, and art. This lunar disk project parallels a similar one headed by Marilyn Lindstrom for the Antarctic Meteorite Disk.

The activities in *Apollo - The Next Generation* divide into three units: Pre-Apollo, the Apollo Era, and the Future. These correspond, at least roughly, to studies that can be done before the Lunar Sample Disk arrives at a school (Pre-Apollo), while it is in the classroom (Apollo Era), and after the disk has returned to NASA (Future). The Pre-Apollo activities challenge the students' current knowledge of the Moon's geology and exploration. They are asked to choose suitable landing sites based on this knowledge. Students are also given the opportunity to collect rocks to compare to the lunar samples. Careful observations of their own rocks and minerals and interpretations of the rock origins set the stage for the Lunar Disk itself. The Apollo Era activities focus on the rock and soil samples contained in the disk, and the processes that formed them. The lunar surface is examined more closely as are the actual Apollo landing sites and the astronauts' lunar roving vehicle. For more in-depth study, four anomalies are presented to the students for their investigation and interpretation: Why does the Moon have fewer quakes than does the Earth? Why are there no obvious volcanoes on the Moon? Why are almost all the maria on the nearside of the Moon? Why does the Moon currently have such a weak magnetic field? The Future activities spark students' interest in how to sustain life on the Moon. Discussions of land use and balanced life support systems lead to actual construction of models. Students are asked to develop plans for lunar transportation and recreation systems, air and water supplies, temperature control systems, and waste management.

During the testing phase, educators supplemented this curriculum with videos, guest speakers, and family-oriented, telescope-viewing parties. The children were so captivated by the Lunar Sample Disk and related projects that many parents even made special visits to the schools. Teachers have been asked to fill out evaluations and their comments will be incorporated when we revise the materials. *Apollo - The Next Generation* helps educators supplement their science and math curriculum with the excitement and adventure of space exploration. The Lunar Sample Disk is an invaluable tool. We've seen how the study of the Moon comes alive for a new generation of students, many with parents not even old enough to have personal recollections of Neil Armstrong's historic step. The history lesson of our manned space program is intricately tied to the Lunar Sample Disk. Not only can we share this history, but involve the students of today in the dreams of space exploration for tomorrow.

EVIDENCE FOR A MINERALOGICAL CHANGE IN RELATION WITH THE MARTIAN GLOBAL GEOMORPHIC DICHOTOMY IN THE THARSIS-MARE SIRENUM REGION .

P. Martin (1), P.C. Pinet (1), R. Bacon (2), A. Rousset (2).
1 UPR 234/CNRS, Groupe de Recherche de Géodésie Spatiale, Observatoire Midi-Pyrénées, Toulouse, France. 2 Observatoire de Lyon, France.

The martian surface displays low and high albedo terrains, whose spectrophotometrical features have shown a spectral variability strongly dependent on the surface mineralogy in the 0.8-1.1 μm domain (1). However, the reflectance measurements acquired by slit spectrometry have presented low spectral (R=20-80) and spatial (300-1000 km) resolutions, and did not allow for an accurate identification of the studied region of the martian disc. At the time of the 1988 opposition, the telescopic observations performed on the eastern hemisphere by multispectral imaging and near-infrared spectroscopy (R=120, spatial resolution: 80-150 km) (2,3) have proven the existence of spectral variations correlated with regional morphological units. These variations are related to the presence of Fe^{2+} and Fe^{3+} -bearing minerals and/or to the soil alteration, low albedo regions having a higher spectral variability than the bright areas. These results have been confirmed by orbital data obtained in the martian equatorial zone by the ISM/Phobos-2 spectrometer (4,5).

In order to assess the variability of the martian surface in the 0.8-1.1 μm domain, high spectral resolution (R=600) telescopic observations of the western hemisphere of Mars were obtained during the 1990 opposition with the CFH 3.6m telescope at Mauna Kea (Hawaii), using the TIGER integral field spectrograph. Acquired under excellent observational conditions (seeing 0.65", hygrometry 15 %, airmass 1.0), these data cover at high spatial resolution (250-300 km), the Tharsis dome region, including the transition zone toward the southern dark terrains in Mare Sirenum. On the basis of over 800 relative reflectance spectra obtained in the near-infrared (0.84-1.03 μm), scaled at 0.85 μm, and normalized to an homogeneous standard region located across the Tharsis area, a two-endmembers spectral mixing analysis is performed. The global analysis reveals that a mixing of two endmembers respectively taken in bright and dark terrains can account for nearly all the total spectral variability of the spectra population, in agreement with (6). Figure 1 shows the TIGER spectroscopic mapping over the Tharsis-Mare Sirenum region, where • and + symbols correspond to the respective locations of the selected bright and dark endmembers. Figure 2 displays the dark-terrain endmember fraction image, overlying the regional albedo map.

When crossing the transition zone, the results show a modification of the spectra morphology in the 0.8-1.1 μm domain, consistent with a relative variable contribution of Fe^{2+} and Fe^{3+} absorption features in the mineralogical properties of the studied area. According to previous work (5), the maximum of differential absorption, detected between 0.96 and 0.99 μm in the dark terrains, suggests the existence of a dominant Fe^{2+} contribution, related to the presence of clinopyroxene.

Overall, a possible interpretation is that the bright and dark-region spectra might be matched by basalts with varied degrees of oxidation (1). On the basis of extended laboratory works (7,8) searching for terrestrial mineralogical samples having the same spectroscopic characteristics as the remotely studied martian terrains, it is found that the Hawaiian palagonites (amorphous ferric-iron silica gel, resulting of weathering of mafic volcanic

PRECEDING PAGE BLANK NOT FILMED

basaltic glass in semi-arid environments) constitute an excellent analog for the bulk composition of martian bright soils. This bright material might be derived through alteration processes from the basaltic material, distributed over the dark terrains, for which the observed spectroscopic characteristics are consistent with an augite-bearing basalt, displaying little ferric oxidation (9,5).

References:
1. Singer, R.B., McCord, T.B., Clark, R.N., Adams, J.B., and Huguenin, R.L., (1979) JGR, 84, 8415-8426. **2**. Pinet, P.C., Chevrel, S., (1990) JGR, vol. 95, n°89, 14435-14446. **3**. Bell III, J.F., McCord, T.B., and P.G. Lucey, (1990) Proc. of L.P.S.C. 20th, 479-486. **4**. Erard, S., Bibring, J.P., Mustard, J., Forni, O., Head, J.W., Hurtrez, S., Langevin, Y., Pieters, C.M., Rosenqvist, J., Sotin, C., (1991) Proc. of L.P.S.C. 21st, Houston, 437-455. **5**. Mustard, J., Erard, S., Bibring, J.P., Head, J.W., Hurtrez, S., Langevin, Y., Pieters, C.M., Sotin, C., (1993) JGR, vol. 98, NO. E2, 3387-3400. **6**. Bell III, J.F., (1992) Icarus 100, 575-597. **7**. Singer, R.B., (1982) JGR, vol. 87, NO. B12, 10159-10168. **8**. Morris, R.V., Gooding, J.L., Lauer, H.V., Jr., Singer, R.B., (1990) JGR, vol. 95, 14427-14434. **9**. Singer, R.B., (1980) Lunar Planet. Sci., XI, 1048-1050.

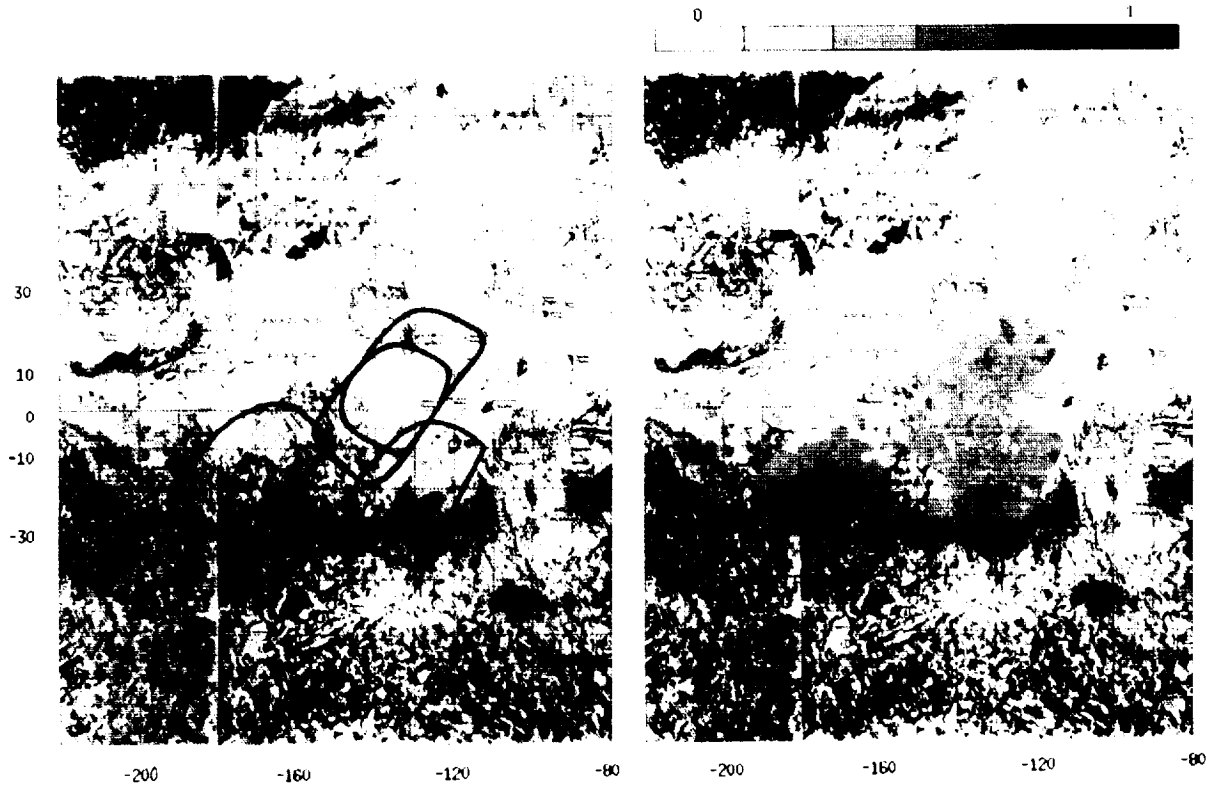

Figure 1.

Figure 2. Grey tones show the degree of spectroscopic similarity, ranging from zero to one.

EXPERIMENTAL AND THEORETICAL INVESTIGATION OF SHOCK INDUCED OUTGASSING OF DOLOMITE; I. Martinez, U. Schärer and F. Guyot, Univ. Paris 7 and IPG-Paris, 2 place Jussieu, F-75251 Paris cedex 05, France
A. Deutsch and U. Hornemann, Inst. für Planetologie, Univ. Münster, Wilh. Klemm Str. 10, D-4400 Münster, Germany.

Although carbonates are common target rocks for meteoritic impacts on Earth [1], degrees of shock-induced decarbonatation remain uncertain, and characteristic shock features in calcite and dolomite are poorly known. Quantifying CO_2 production is of great importance to evaluate the consequences of impact events on the terrestrial atmosphere. In a previous study of the impactites from the the Haughton crater (Canada) [2,3], we have shown that significant fractions of impact-released CO_2 are recombined with residual oxides (CaO and MgO). Such backreaction has rarely been considered in attempts to quantify CO_2 production from terrestrial craters. Concerning the general aspect of shock metamorphism in carbonates, characterization of shock effects would also be usefull to recognize and classify naturally shocked carbonates, and eventually to calibrate shock stages. So far, several experimental shock studies have been performed on carbonates, leading to contrasting results concerning the CO_2 outgassing rates of carbonates. In shock recovery experiments reaching 18 GPa, 0.03-0.3 mole% of the initial calcite was devolatilised [4], whereas in other experiments [5,6], 30-40% CO_2 loss was observed at 20 GPa, and incipient volatilisation occured at pressures of less than 10 GPa. Lange and Ahrens [6] report a simple relationship between shock-induced CO_2 loss and peak shock pressure, in which more than 50 wt% of CO_2 loss was observed for a peak shock pressure of 30 GPa. In all of these studies, shock pressures required for incipient volatilisation of carbonates are lower than those estimated by equilibrium thermodynamic calculations, e.g. a pressure of 45 GPa such as calculated by Kieffer and Simonds [7]. Generally, such discrepancies are attributed to the formation of localized hot spots during the shock experiments [4,8], which are most likely caused by inhomogeneities in the distribution of shock energy [9,10]. In another shock recovery study however, only 5-10% devolatilisation of calcite occured at 50-60 GPa [11]. Such low degrees of outgassing were ascribed to higher partial pressures of CO_2 than in the other experiments [8]. All these studies were performed mainly by measuring quantities of CO_2 released; in contrast, the present work reports results obtained by the detailed investigation of residual shocked material. Dolomite, experimentally shocked up to 60 GPa, was studied by Scanning Electron Microscopy (SEM), Analytical Transmission Electron Microscopy (ATEM) and X-Ray Diffractometry (XRD) with Rietveld refinement. Additionally, the same samples were analysed for C and O isotopic compositions. Shock recovery experiments were performed at the Ernst-Mach-Institut (Weil am Rhein, Germany), using steel containers impacted by explosively accelerated steel flyer plates [12]. The peak pressure of 60 GPa in the sample is reached after multiple reverberations of the shock wave and the sample thicknesses were adjusted to allow a sufficient number of reflections to occur. Additionnaly, some experimental assemblies were preheated at 350°C before the detonation, leading in that case to post-shock temperatures elevated of roughly the pre-heating temperature.

Initially cold samples:

Very limited traces of outgassing were observed in dolomites shocked at 60 GPa. The only areas having undergone volatilisation, evidenced by the presence of nm-sized MgO crystals, are zones where molten metal from the steel container invaded the carbonate. In all other areas, highly fracturated dolomites and calcites have been recovered. In TEM, the crystals show a cold-work type microstructure with highly disorientated crystalline domains with a typical size of less than 200 nm. The electron diffraction patterns of calcite and dolomite crystals show important arcing of the spots due either to the small size of diffracting domains or to internal strain. The shocked samples have experienced a strong pulverisation, previously observed in naturally shocked carbonates from the Ries crater [13].The Rietveld refinement of the XRD data confirms these observations, and allows separation and quantification of the effects of grain sizes and lattice strains.

Grain sizes were reduced by 26% and 16%, and lattice strain increased by factors of 3.5 and 3.8 in dolomite and calcite, respectively. These two parameters could probably be used for shock barometry in carbonates. In agreement with the quasi-absence of outgassing, $\delta^{13}C$ and $\delta^{18}O$ in these shocked carbonates are identical to those measured in the unshocked reference material.

Preheated samples:

Contrasting with the previous samples, the preheated material shows abundant evidences for outgassing at 60 GPa. So far, we have documented the volatilisation by the presence of numerous and very small MgO crystals (typical grain size: 20 nm), identified by their electron diffraction patterns and in situ Energy Dispersive System chemical analyses. Decarbonation is clearly an effect of the shock experiment since the 350°C preheating temperature lies well below the temperature of incipient volatilisation of calcite and dolomite. Shock-induced dissociation reactions of dolomite have thus occured in these samples, on a very small spatial scale.

Thermodynamic calculations:

Using the Hugoniot data available from previous studies (compiled in [14]), we have calculated the peak shock and post-shock temperatures reached for calcite and dolomite in our experiments by two methods: (i) estimation of the post-shock residual energy, and (ii) direct integration along the Hugoniot curve. The latter method is sensitive to the large uncertainty existing on the Grüneisen parameter at high pressure and temperature, whereas the first method suffers from the assumption that the Hugoniot and release adiabat are equal. Despite such restrictions, the following ranges of shock pressures required to produce incipient devolatilisation of carbonates during the high temperature regime following decompression can be proposed: 55-60 GPa and 40-45 GPa for non-porous dolomite and calcite, respectively, if direct shock is considered. The result for calcite is in reasonable agreement with the calculation of Kieffer and Simonds [7]. The effect of the initial porosity of the sample can be taken into account by assuming a larger initial volume for the starting material. If we assume an initial porosity of 4% for dolomite and calcite, peak pressures required to produce incipient devolatilisation are 40-45 GPa and 30-35 GPa, respectively. However, it is important to note that the experimental technique used is fundamental for the evaluation of shock temperatures. It is well known that reverberated shocks yield to lower post-shock temperatures than in direct shocks (impedance matching) carried out at identical pressures [15]. Preheating of the samples allows to compensate for the post-shock lowering. If the effects of the reverberation technique are included in the calculations, a shock pressure of 60 GPa, without preheating, is just sufficient to produce the onset of outgassing of a 4% porosity dolomite. This result is consistent with the observations that important outgassing in a 60 GPa reverberated shock occurs only in the preheated samples. The agreement observed between the experiments and the calculations strengthens the validity of our calculation of shock pressures necessary to induce calcite and dolomite volatilisation.

[1] Grieve R.A.F. and Robertson P.B. (1979) *Icarus*, 83, 212. [2] Martinez I. et al (1993) *Earth Planet. Sci. Lett.*, 119, 207. [3] Martinez I. et al., (1993), *Earth Planet. Sci. Lett.*, in press. [4] Boslough M.B. et al. (1982) *Earth Planet. Sci. Lett.*, 61, 166. [5] Lange M.A. and Ahrens T.J. (1983), *Lunar Planet. Sci.*, 14, 419. [6] Lange M.A. and Ahrens T.J. (1986) *Earth Planet. Sci. Lett.*, 77, 409. [7] Kieffer S.W. and Simonds C.H. (1980) *Rev. Geophys. Space Phys.*, 18, 143. [8] Tyburczy J.A. and Ahrens T.J. (1986) *J. Geophys. Res.*, 91, 4730. [9] Grady D.E. [1980] *J. Geophys. Res.*, 85, 913. [10] Horie Y. [1980] *Phys. Rev. Condens. Matter.*, 21, 5549. [11] Kotra R.K. et al. (1983) *Lunar Planet. Sci.*, 14, 401-402. [12] Müller W.F. and Hornemann U. (1969), *Earth Planet. Sci. Lett.*, 7, 251. [13] Barber D.J. and Wenk H.R. (1979) *Tectonophysics*, 54, 45. [14] Stöffler D. (1982) *Numerical data and functional relationships in science and technology. vol 1:Physical properties of rocks*, 129. [15] Gibbons R.V. and Ahrens T.J. (1971) *J. Geophys. Res.*, 76, 5489.

TROJAN COLLISIONAL FAMILIES AS A SOURCE FOR SHORT-PERIOD COMETS

F. Marzari, V. Vanzani, Dipartimento di Fisica "G. Galilei", Università, 35131 Padova, Italy;
P. Farinella, Observatoire de la Côte d'Azur, Nice, France

We have investigated the dynamical evolution of fragments generated by the collisional breakup of Trojan asteroids, in order to study the formation of collisional families in the Trojan clouds and to identify a possible connection between these fragments and the population of Jupiter-family comets.

A relationship between Trojan asteroids and short-period comets is suggested by the spectrophotometric similarity of the D class asteroids, which are predominant among the Trojan asteroids, and inactive comet nuclei. Shoemaker et al. [1], on the basis of this similarity, argued that a mechanism for capturing Jupiter family comets in Trojan-type orbits could be effective. Encounters with Jupiter could drive a small percentage of short period comets into temporary 1:1 libration and subsequently into Trojan-type orbits. Here we show how this process can work also in the reverse direction. The collisional breakup of a Trojan asteroid can inject some fragments into comet-like orbits.

The fact that the Trojan belt is collisionally evolved has been confirmed by the computations of proper elements in the 1:1 resonance with Jupiter by Milani [2,3]. He has proven the existence of small groups of Trojans with very close proper elements which could possibly be the results of collisional events in the Trojan belt. In particular, in the L4 region the Menelaus and Teucer groups have been confirmed as strong candidate collisional families. We intend to prove that the spreading in the orbital element space of the fragments following the breakup of the parent body, can force some of them to escape from the L4 or L5 regions. Repeated close encounters with Jupiter can drive a significant percentage of these fragments into comet-type orbits.

To model the collisional event which generates a Trojan family, we combine in a computer algorithm the semiempirical model of Davis et al. [4], which predicts the size distribution of fragments generated in an individual breakup event, with a mass-velocity distribution for the fragments derived by the experimental work of Nakamura and Fujiwara [5]. Assuming an isotropic distribution of the ejecta velocities, we compute a complete set of post-impact osculating orbital elements for each single fragment. The orbits of the fragments and of the four Jovian planets are then integrated as an N-body system using the Everhart [6] numerical integrator. The integration time span is of the order of 10^5 yr, longer than the periodicity of the variations of Jupiter's eccentricity.

In Fig. 1 we show in the a-e plane a simulated Menelaus family generated by the breakup of a parent body 200 km in diameter as it appears after the breakup (only fragments larger than 20 km are considered). The fragments represented by open circles are in Trojan-type orbits even after $4 \cdot 10^5$ yr. The filled triangles represent fragments escaping from the 1:1 resonance. The distribution in the a-e plane at $t=10^5$ yr is shown in Fig. 2, where the dashed line corresponds to a Tisserand invariant of 3.0, the usual dividing line between comets and asteroids (see Fig. 1 in Weissman et al. [7]). Note that a significant fraction ($\sim$ 17%) of fragments end-up into orbits resembling those of Jupiter-family comets, or of objects such as 944 Hidalgo, 2060 Chiron and 5145 Pholus. Some fragments even end up on hyperbolic orbits, and are ejected from the solar system. Other ones may undergo episodic temporary capture into Jupiter-bound orbits, giving raise to objects such as P/Shoemaker-Levy 9.

Figs. 3 and 4 show the corresponding plots for the Teucer family (parent body 260 km in diameter). In this case 22% of the fragments end up in comet-type orbits, including one 70 km across. The orbital evolution of this body (perihelion distance (full line) and eccentricity (dashed line) vs. time) is displayed in Fig. 5, showing that the orbit is strongly chaotic, and that after some 70,000 yr since the breakup the eccentricity is pumped up to values approaching unity.

A quantitative estimate of the flux of Trojan fragments into comet-type orbits would require a better knowledge of the Trojan size distribution, and a more detailed model for the collisional evolution of the whole Trojan clouds. However, the possibility that at least some objects with cometary dynamics are generated as collisional fragments from asteroidal parent bodies appears well established.

TROJAN COLLISIONAL FAMILIES: F. Marzari, V. Vanzani & P. Farinella

REFERENCES: [1] Shoemaker E. M., Shoemaker C. and Wolfe R. F., in *Asteroids II*, (Univ. of Arizona Press, Tucson, 1989), p. 487; [2] Milani A. (1993) *Cel. Mech. 57*, 59; [3] Milani A., Proc. IAU Symp. 160 (Belgirate, Italy, June 1993), in press; [4] Davis D. R., Weidenschilling S. J., Farinella P., Paolicchi P. and Binzel R. P., in *Asteroids II*, (Univ. of Arizona Press, Tucson, 1989), p. 805; [5] Nakamura A. and Fujiwara A. (1991) *Icarus 92*, 132; [6] E. Everhart, in *Dynamics of Comets: Their Origin and Evolution* (Reidel, Dordrecth, 1985), p. 185; [7] Weissman P. R., A'Hearn M. F., Mc Fadden L. A. and Rickman H, in *Asteroids II*, (Univ. of Arizona Press, Tucson, 1989), p. 880;

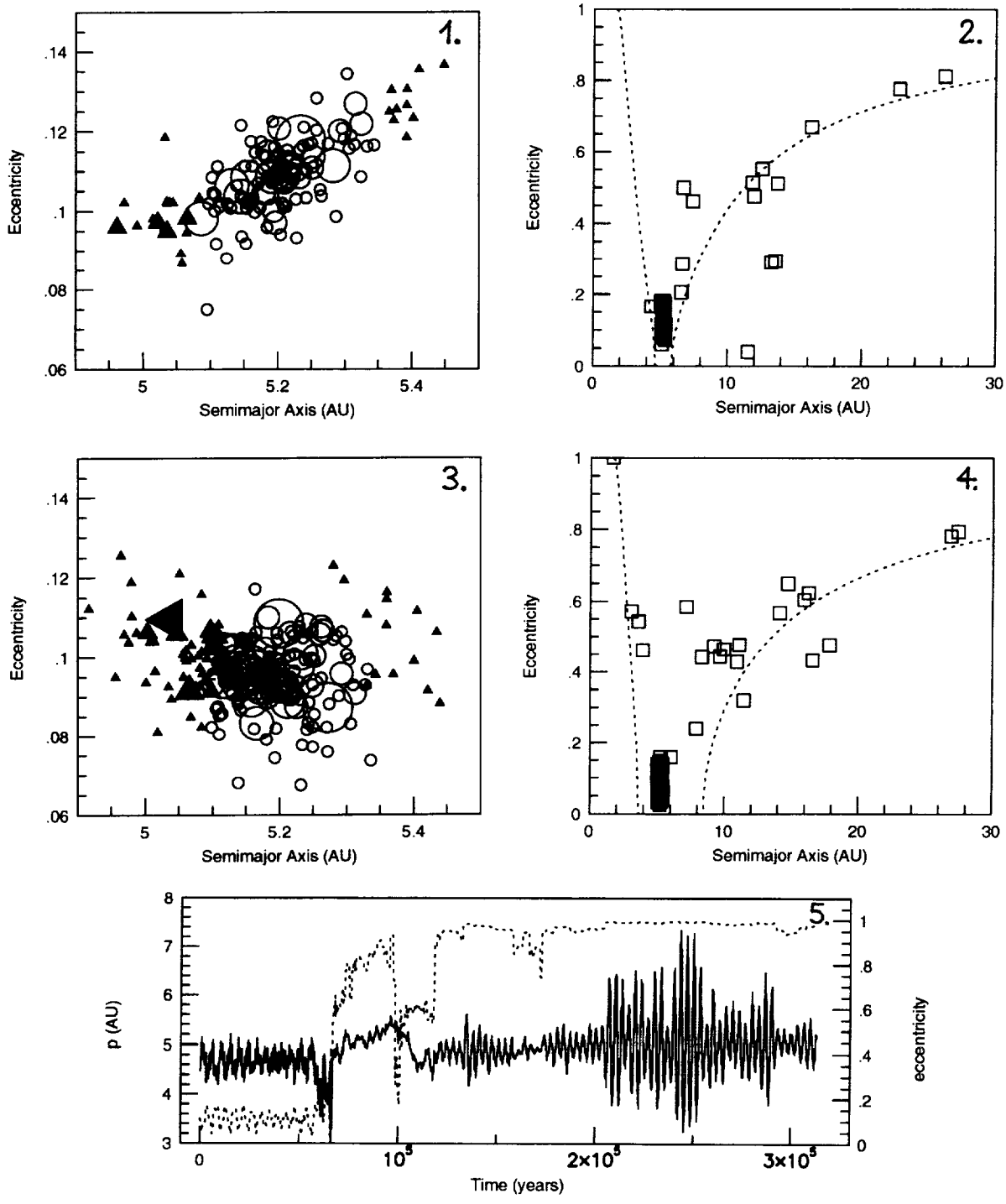

EFFECTS OF METEOROID SHAPE ON COSMOGENIC-NUCLIDE PRODUCTION RATES*; J. Masarik and R. C. Reedy, Astrophysics and Radiation Measurement Group, Mail Stop D436, Los Alamos National Laboratory, Los Alamos, NM 87545, USA.

The shape of the meteoroid irradiated in space can be one of the factors influencing cosmogenic-nuclide production. Numerical simulations with Los Alamos 3-D Monte Carlo codes for particle production and transport were done for spherical and ellipsoidal meteoroid geometries. There are statistically important differences in particle fluxes that depend on the irradiated-object's shape and the sample's location. Comparisons of our production-rate calculations with experimental cosmogenic-nuclide data for St. Séverin, which was ellipsoidal in the space, show better agreement for modeling the parent-body's geometry with an ellipsoid than with a sphere.

Nuclides produced by the interaction of cosmic-ray particles with a meteoroid are sources of valuable information about both the meteorite and the cosmic rays. The accurate modeling of the production processes is prerequisite for the interpretation of measurements. The incident particle fluxes, the meteoroid's preatmospheric shape and size, and its bulk chemical composition all determine the production rates of nuclides. As much work have been done on size effects and some done on bulk chemical composition effects [1,2], we concentrated on effects of the shape of the parent body on the production of cosmogenic nuclides.

The production depth profiles are calculated in the framework of a pure physical model [1] that describes, without free parameters, the interaction of cosmic-ray particles with a meteoroid and the subsequent production and transport of secondary particles. In this model, the nucleon spectra are calculated by Monte Carlo simulations using the LAHET Code System (LCS). Having calculated neutron and proton fluxes, the production rates of cosmogenic nuclides are calculated by integrating over energy the product of these fluxes with experimental and theoretical cross sections for the nuclear reactions producing each nuclide [1]. Similar calculations were done by [3,4].

LCS has a very powerful generalized-geometry input module based on the MCNP code [5] that can model different shapes of irradiated objects with a mesh-like geometry structure suitable for the simulation of the energy and spatial distribution of particle fluxes inside the object. The two geometries investigated in this work were an ellipsoid with semiaxes of 40, 20, and 25 cm (the preatmospheric shape of the St. Séverin LL6 chondrite inferred by [6,7]) and a sphere with radius 27 cm, which has the same volume as the ellipsoid. We used a density of 3.55 g/cm^3. As the particle production spectra and fluxes are strongly depth dependent, our model objects were divided into concentric shells with thickness 2.5 cm. In all shells, proton and neutron fluxes were calculated. For the sphere, particle fluxes were averaged over the whole volume of the shell. In the case of the ellipsoid, the fluxes were calculated in two ways: by averaging over the whole ellipsoidal shell and by averaging only over the shaded volume elements in Fig. 1. The last division of the ellipsoid was motivated by the actual location of measured samples [8–10]. Both objects were irradiated by an isotropic galactic-cosmic-ray (GCR) flux of 4.8 protons/cm^2/s, corresponding to the GCR primary particle spectrum averaged over a typical solar cycle. Our model with this GCR flux reproduced very well cosmogenic-nuclide profiles in the Knyahinya L5 chondrite [11]. Statistical uncertainties using our geometrical models and running 100,000 incident GCR particles were ~3–4%.

Our simulations confirm the importance of effects caused by parent-body shape on nucleon fluxes within the meteorite and consequently on production rates of cosmogenic nuclides. At first, we compared particle fluxes inside sphere and ellipsoid averaged over whole concentric shells. No differences in these fluxes were found. The explanation of this fact can be given in the framework of simple geometric considerations. It has been shown [e.g., 3,4] that even in small objects, the substantial contribution to the cosmogenic nuclide production comes from secondary particles. The shape of the irradiated body influences the number of particles (primary and secondary) escaping from the investigated body without participating in particle cascade development. This can lead to a change in the absolute value and the shape of the differential particle fluxes. This effect contributes to increased production rates in larger spheres up to a given radius. For the ellipsoid, there are some regions with larger and smaller curvature than the curvature of the equivalent sphere, and there are also different numbers of escaping particles in these regions. After averaging the fluxes over the whole volume of each shell, the effects caused by differences in the escape of particles are compensated and this leads to the equivalence of observed fluxes.

Many samples measured in St. Séverin were taken from core AIII going through the geometric center of the chondrite in the direction of the minor semiaxes. This is the region of the meteorite where the smallest number of escaping particles is expected, as in a larger sphere. and therefore

METEOROID SHAPES, COSMOGENIC NUCLIDES Masarik J. and Reedy R.C.

an increase in particle fluxes and production rates in comparison with those in sphere is natural consequence. The depth-profile shape for all investigated nuclides remained unchanged. An increase of about 5–10% has been found for our calculated ^{53}Mn, ^{10}Be, and ^{21}Ne production rates (Figs. 2–4), which agree well with the measurements for neon [8] and ^{53}Mn [9] (corrected to saturation) but not as well with the shape of the ^{10}Be profile measured by [10].

References [1] Masarik J. and Reedy R.C. (1994) *Geochim. Cosmochim. Acta*, submitted. [2] Michlovich E.S. *et al.* (1994) *J. Geophys. Res.*, submitted. [3] Michel R. *et al.* (1991) *Meteoritics* **26**, 221. [4] Bhandari N. *et al.* (1993) *Geochim. Cosmochim. Acta* **57**, 2361 [5] Briesmeister J.F. (1986), Los Alamos National Laboratory report LA-7396-MS, Revision 2. [6] Cantelaube Y. *et al.* (1969) in: *Meteorite Research*, Reidel, p. 705. [7] Graf Th., Baur H. and Signer P. (1990) *Geochim. Cosmochim. Acta* **54**, 2521. [8] Schultz L. and Signer P. (1976) *Earth Planet. Sci. Lett.* **30**, 191. [9] Englert P. and Herr W. (1980) *Earth Planet. Sci. Lett.* **47**, 361. [10] Tuniz C. *et al.* (1984) *Geochim. Cosmochim. Acta* **48**, 1867. [11] Reedy R.C. *et al.* (1993) *LPS-XXIV*, p. 1195. * Work supported by NASA and done under the auspices of the US DOE.

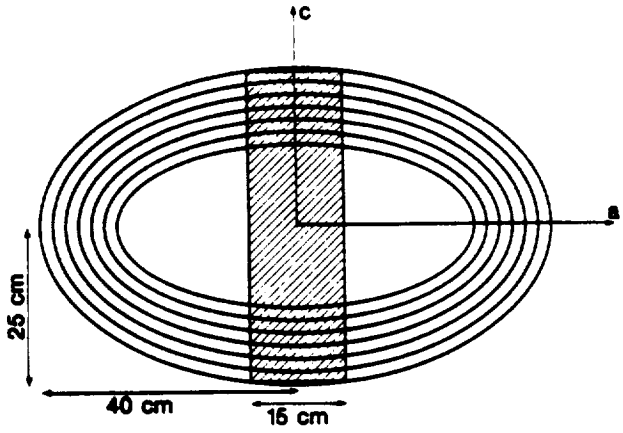

Fig. 1. The geometry used for the St. Séverin ellipsoid in these calculations. The shaded area is 15-cm×15-cm in the *ab* plane and is the region shown for the ellipsoid curves in Figs. 2–4, corresponding to core AIII.

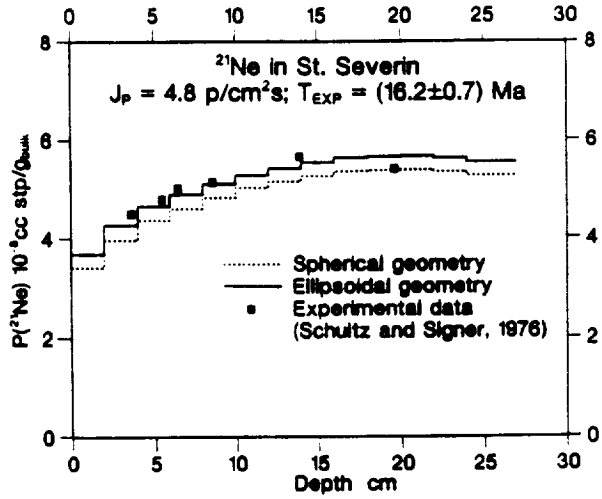

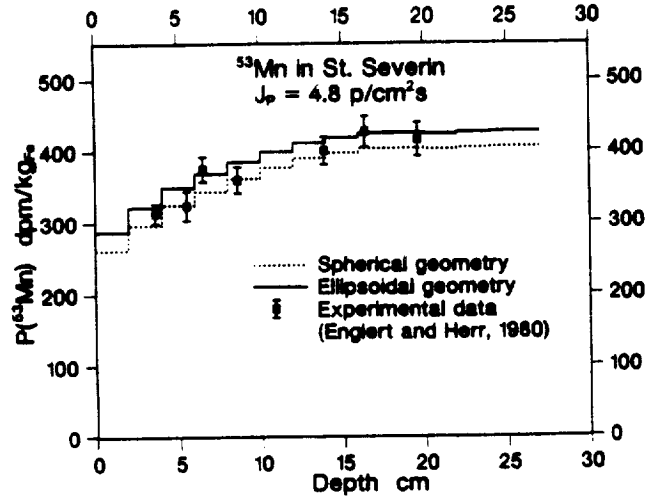

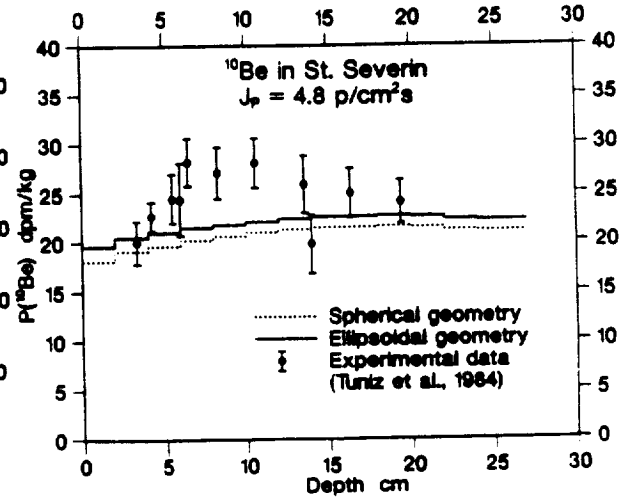

Figs. 2–4. Calculated (sphere and the 25-cm minor semiaxis of ellipsoid) and measured nuclide concentrations of ^{21}Ne (top right), ^{53}Mn (lower left), and ^{10}Be (lower right) in St. Séverin.

NUMERICAL SIMULATIONS OF GAMMA-RAY EMISSION FROM THE MARTIAN SURFACE*; J. Masarik and R. C. Reedy, Astrophysics and Radiation Measurement Group, Mail Stop D436, Los Alamos National Laboratory, Los Alamos, NM 87545, USA.

The fluxes of natural and cosmic-ray-produced gamma rays escaping from Mars were calculated for 8 water contents of the surface and 6 thicknesses of the atmosphere. The water content and atmospheric thickness both strongly affect the fluxes of gamma-ray escaping from Mars.

The γ rays escaping from planetary bodies such as the Moon, Mars, asteroids, and comets can be used for mapping the elemental composition of the surface's top few tens of centimeters [1]. Low-resolution spectrometers measured γ rays at the Moon on Apollos 15 and 16 and at Mars on Mars 5 and Phobos 2. A high-resolution γ-ray spectrometer was on Mars Observer [2], and the martian γ-ray fluxes reported here were calculated for the inversion of measured martian γ-ray fluxes to elemental compositions. Although Mars Observer is lost, γ-ray spectrometers are scheduled to be flown on Mars-94 and possibly other orbital and surface missions to Mars.

Elements that can be mapped using γ-ray spectroscopy include all major ones, many minor ones, and some trace ones [1]. Gamma-ray emission from planetary surfaces results from several processes, the most important being γ rays from the decay of the major natural radioactive elements and by nuclear reactions of primary and secondary cosmic-ray particles. Gamma rays used for most elemental studies are made by inelastic-scattering reactions of neutrons with a few MeV of energy or by neutron-capture reactions near thermal energies. Other γ-ray sources can create backgrounds or interferences. Some relative martian γ-ray fluxes calculated with a neutron-transport code by [3] examined the effects of hydrogen on γ-ray fluxes.

We calculated the fluxes of 80 γ rays made by the decay of naturally-occurring Th, U, and ^{40}K for 6 atmospheric thicknesses. Around the average martian atmospheric thickness of 15 g/cm^2, a thickness increase of $\sim$8 g/cm^2 reduces escaping γ-ray fluxes by a factor of about 2, with greater reduction for γ-ray energies below $\sim$0.5 MeV. Measurements of γ rays with both low and high energies (e.g., 238 and 2614 keV ones of Th) can be used to infer atmospheric thickness.

Using the LAHET Code System (LCS) for the simulation of galactic-cosmic-ray (GCR) interactions with Mars, we calculated the intensities of 243 γ-ray lines produced in the martian soil via nonelastic scattering reactions and 74 lines made by neutron-capture reactions. LCS is a system of general-purpose, continuous-energy, generalized-geometry, time-dependent, off-line coupled Monte Carlo computer codes that treat the relevant physical processes of particle production and transport. This code system and its successful application to meteorites are discussed in [4]. A similar code system was used by [5] to calculate fluxes of several lunar and martian γ rays. Our calculated lunar γ-ray fluxes were slightly higher than those of [6] because of higher LCS-calculated neutron fluxes below a few MeV.

An isotropic GCR irradiation by 4.56 protons/cm^2/s, corresponding to the GCR primary particle spectrum averaged over a solar cycle, of a sphere with the average radius of Mars (3390 km) was simulated. In the assumed bulk chemical composition [2], the water content was varied from zero to 90%. The elemental weight fractions used for the martian atmosphere were C=0.2639, N=0.0174, O=0.7040, and Ar=0.0147, based on the mole (volume) abundances of [7]. The thickness of the atmosphere was varied from 0 to 25 g/cm^2. The decrease of the atmospheric density with increasing altitude for the LCS calculations used a scale height of 10.8 km [8], although our γ-ray fluxes are not sensitive to details of the atmospheric height-thickness distribution. Using a density of 1 g/cm^3 for the atmosphere in the LCS calculations, the γ-ray fluxes increased by $\sim$10% compared to those calculated with the observed scale height.

Both atmosphere and soil were divided into concentric shells, with many shells near surface and fewer shells at greater depths. Neutron and proton fluxes were calculated for each shell. Production rates for neutron-capture reactions were calculated by LCS. Production rates of nonelastic γ rays were calculated using LCS-calculated particle fluxes and the cross sections of [6], analogous to that done for nuclides [4]. We are not concerned with scattered γ rays, which only contribute to the continuum, but only with the γ rays that undergo no interactions before escaping from Mars. Thus, having calculated the production rates of a γ ray at various depths, we used exponential mass attenuation coefficients for that γ ray to calculate the flux escaping from Mars and reaching a 400-km spacecraft altitude without changing energy. This integral over depth was done down to 400 g/cm^2, a depth below which very few γ rays escape. Our γ-ray fluxes agree well with those of L. Evans [priv. comm., 1993] but are only in fair agreement with those of [5] for natural and capture γ rays and, if our incident GCR flux is used, for inelastic γ rays.

Our simulations for martian γ ray fluxes span several likely martian situations. Particle fluxes in Mars are affected by the particle-transport properties of martian soil, especially to the soil's H content, and the martian atmosphere [9]. As H is added to the martian soil, its properties for neutron transport are changed, with fast and epithermal neutrons more rapidly slowed to thermal energies. This results in an enhanced thermal flux and a shallower peaking of that flux for soils with higher H contents [1]. Hydrogen and certain other elements like iron strongly absorb thermal neutrons, and increases in their concentrations depress thermal-neutron fluxes. Shifts of neutron fluxes in the martian surface are also calculated for increased atmosphere thickness [9].

The influence of hydrogen and atmospheric thickness on fluxes of γ rays made by neutron-capture reactions is demonstrated in Fig. 1 for the 4934-keV γ ray made by the $^{28}Si(n,\gamma)^{29}Si$ reaction. The trends in Fig. 1 are representative for all γ-ray lines produced by neutron-capture reactions. With the increase of hydrogen content in martian soil, the flux gradually increases, until some critical value (~30% water), where the influence of thermal-neutron absorption begins to play a substantial role leading to the decrease of γ-ray flux. An increase of γ-ray flux with the increase of atmosphere thickness is also visible up to thicknesses of 15 g/cm^2. Fluxes of this γ ray at the martian surface increase up to an atmospheric thickness of ~25 g/cm^2 and tend to decrease with increasing water content.

Fig. 2 shows the 1779-keV γ ray from ^{28}Si produced by inelastic-scattering reactions. The flux monotonically decreases with increasing atmospheric thickness and with the increase of hydrogen in martian soil because increased thermalization rates are depleting the fast neutron flux that produces these γ rays. Fluxes of this γ ray at the surface decreases with increasing water content but increase from the case of no atmosphere to peak fluxes for ~5–15 g/cm^2-thick atmospheres but then begins to decrease.

Our simulations of the intensities of martian γ-rays produced by the interactions of galactic cosmic rays with the Mars indicate that the analyses of martian γ-ray spectra require a knowledge of the hydrogen content of the soil and the atmospheric thickness, although certain γ rays can be used to infer these quantities. Gamma-ray fluxes at the martian surface are higher than those above the atmosphere and those for no atmosphere. The relations between γ-ray fluxes at the surface and at orbit can be complicated, especially for neutron-capture.

References: [1] Evans L.G *et al.* (1993) in: *Remote Geochemical Analysis*, Cambridge Press, p. 167. [2] Boynton W.V. *et al.* (1992) *JGR* **97**, 7681. [3] Evans L.G. and Squyres S.W. (1987) *JGR* **92**, 9153. [4] Masarik J. and Reedy R.C. (1994) *GCA* (submitted). [5] Dagge G. *et al.* (1991) *PLPSC-21*, p. 425. [6] Reedy R.C. (1978) *PLPSC-9*, p. 2961. [7] Owen T. *et al.* (1977) *JGR* **82**, 4635. [8] Zurek R.W. *et al.* (1992) in: *Mars*, Univ. Arizona Press, p. 835. [9] Feldman W.C. *et al.* (1989) *JGR* **94**, 513. * Work supported by NASA and done under the auspices of the US DOE.

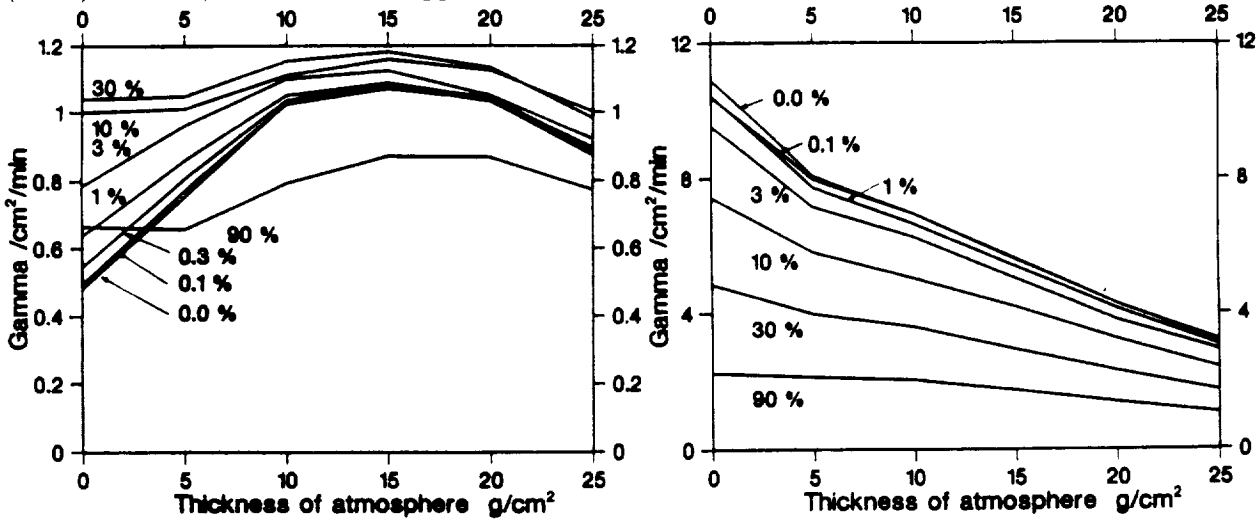

Figs. 1–2. Fluxes at a 400-km altitude above Mars of the 4934-keV γ ray made by the $^{28}Si(n,\gamma)^{29}Si$ neutron-capture reaction (left) and the 1779-keV γ ray made by the $^{28}Si(n,n\gamma)^{28}Si$ inelastic-scattering reaction (right) as a function of atmospheric thickness. Curves are for different water contents of the martian surface.

THE HIGHBURY STRUCTURE, A NEW IMPACT CRATER IN N. W. ZIMBABWE. S. Master[1], W.U. Reimold[2*], D. Brandt[2], C. Koeberl[3], D. Robertson[4] & L.A.G. Antoine[5]. [1]Lomagundi Smelting and Mining Ltd., Alaska, Zimbabwe; [2]EGRU, Dept. of Geology, Univ. of the Witwatersrand, P.O.Wits 2050, Johannesburg, RSA; [3]Inst. of Geochemistry, Univ. of Vienna, Dr-Karl-Lueger-Ring 1, A-1010, Vienna, Austria; [4]Dept. of Physics, Univ. of Zimbabwe, P. Bag MP167, Harare, Zimbabwe; [5]Dept. of Geophysics, Univ. of the Witwatersrand, P.O.Wits 2050, Johannesburg, RSA. * Corresponding Author.

INTRODUCTION: The Highbury Structure (Figs. 1,2), a circular feature at least 15 km in diameter, centred on 30°09'E and 17°05'S around Highbury Farm (between Chinhoyi and Mhangura) in the Makonde District of NW Zimbabwe, was first recognised by German (BGR) geologists in 1985 from Landsat imagery. We report here the results of the first field and petrographic investigations of this structure, which is situated within early Proterozoic metasedimentary rocks of the Magondi Mobile Belt. The presence of breccias, in an area that could represent the remnants of a central uplift, containing shocked quartz grains with planar deformation features (PDFs), and glass, provides strong evidence for an impact origin for the structure.

PREVIOUS WORK: The area around the structure was originally mapped in the early 1960's [1,2]. Jacobsen [2] found abundant tremolite and minor wollastonite in metamorphosed carbonate rocks in the Highbury area, and he also mapped a small outcrop of a granophyre in the Munwa River, which he regarded as part of a larger concealed post-tectonic intrusion which was responsible for the "skarning" of the carbonates. Microscopic brecciation and cataclastic features, as well as undulose extinction and deformation lamellae in quartz and plagioclase, were described [3] from Two Tree Hill farm to the NW of the Highbury Structure.

THIS STUDY: The country rocks in the Highbury area are arkoses and metadolomites of the Deweras Group, which are flanked to the east and west by the Striped Slates and Mountain Sandstone members of the Nyagari Formation of the Lomagundi Group [4,5]. A NE-trending belt of dolomite previously mapped [1,2] as Lomagundi Dolomite, is here reassigned to the Deweras Group on sedimentological grounds [5]. The Deweras and Lomagundi Groups form part of the Early Proterozoic (ca. 2 Ga) Magondi Supergroup, which was deformed and metamorphosed during the ca. 2.0-1.8 Ga Magondi Orogeny [4,5]. The ring structure stands out on false-color Landsat images (Fig. 2) as a circular region which contrasts strongly with the highly vegetated Striped Slates of the Lomagundi Group to East and West of the structure. An outer ring is outlined by alluvium around the west-flowing Munwa River, which forms a broad arc on the western side of the structure, and a tributary defines the southern arc of the ring structure. A broad band of alluvium is banked up against the southern part of the structure (Fig. 1). In the NE, there is an arc formed by alluvium around the Nyawenje River which joins the Munwa farther north. The ring structure is bounded on the east by an arcuate curve of hills composed of Mountain Sandstones interbedded with Striped Slates of the Nyagari Formation. The structure, as apparent on the 1:100 000 Geological Map [1], and 1:50 000 Topo Sheet, is slightly pear- shaped, and is elongate and narrows to the northwest. The Highbury Structure as defined is about 15 km in diameter. However, to the NW and W, abrupt terminations of the Mountain Sandstones (Fig. 1), coupled with indications from satellite imagery (Fig. 2), suggest that the structure is possibly even larger, with a diameter of ca. 25 km. There appears to be a central uplift almost exactly in the centre of the 15 km-diameter Highbury Structure. The uplift stands 1206m above sea level, while the surrounding areas are between 1130 and 1160m ASL. A 1: 25 000 Aeromagnetic Contour Map [6] shows that the "central uplift" is close to a NE-SW linear magnetic anomaly, interpreted as a mafic dyke occupying one of a set of NE-SW faults. There is a complex NE-SW trend of magnetic anomalies which correspond to the regional strike and structural grain. However, the aeromagnetic contour map does not show anything resembling a circular feature [6]. The structure postdates N-S trending thrust faults of Magondi (ca. 1.8 Ga) age, but is apparently offset in the southeastern sector by NE-SW trending dextral wrench faults which are thought to be of late Irumide (c.1 Ga) age [5].

Thirty-nine samples, collected at the twelve localities marked in Fig. 1, were studied for evidence of impact-characteristic shock metamorphism. A first-order observation was that quartz from several sandstone and arkose samples from the possible central uplift area (esp. sites H5 and 7), but also from H3 in the NW (in the vicinity of Two Tree Farm), contained abundant planar (!) fluid inclusion trails and bands (Fig. 3) that are strongly reminiscent of microdeformation in Vredefort quartz. Other grains show remarkably sharply defined deformation bands or undulatory, sometimes even mosaic, extinction. As in the case of Vredefort, some samples are at least partially annealed. But it was only when sample H7/2, a goethite-rich breccia, was studied in detail, that bona fide PDFs (Fig. 4) were discovered. This sample also contains pockets of unaltered, barely devitrified glass, and some of the goethite patches show relics of schlieren and perlitic cracking. These features suggest that these Fe-rich areas probably represent altered glass as well. This glass occurence is of extreme value, as it is likely to represent the only possibility to date the Highbury impact event, by application of the laser argon technique. Current work focuses on geological analysis of the central uplift area and on studies of the granophyric rock exposed at locality H4 (Fig. 1).

REFERENCES: [1] Stagman,J.G. (1961). Bull. geol. Surv. S. Rhod., 49, 107pp. [2] Jacobsen,J.B.E. (1962). M.Sc. thesis (unpubl.), Univ. Witwatersrand, Johannesburg, 127pp. [3] de Wet,J. (1976). Unpubl. Rept., MTD Ltd. Research Centre, Johannesburg, 6pp. [4] Master,S. (1991). Econ. Geol. Res. Unit Information Circular No. 238, Dept. of Geology, Univ. of the Witwatersrand, Johannesburg, 75pp. [5] Master,S. (1991). Ph.D. thesis (unpubl.), Univ. Witwatersrand, Johannesburg, 385pp. [6] Messina Rhod. Dev. Co., EPO 414, Final Report (1976).

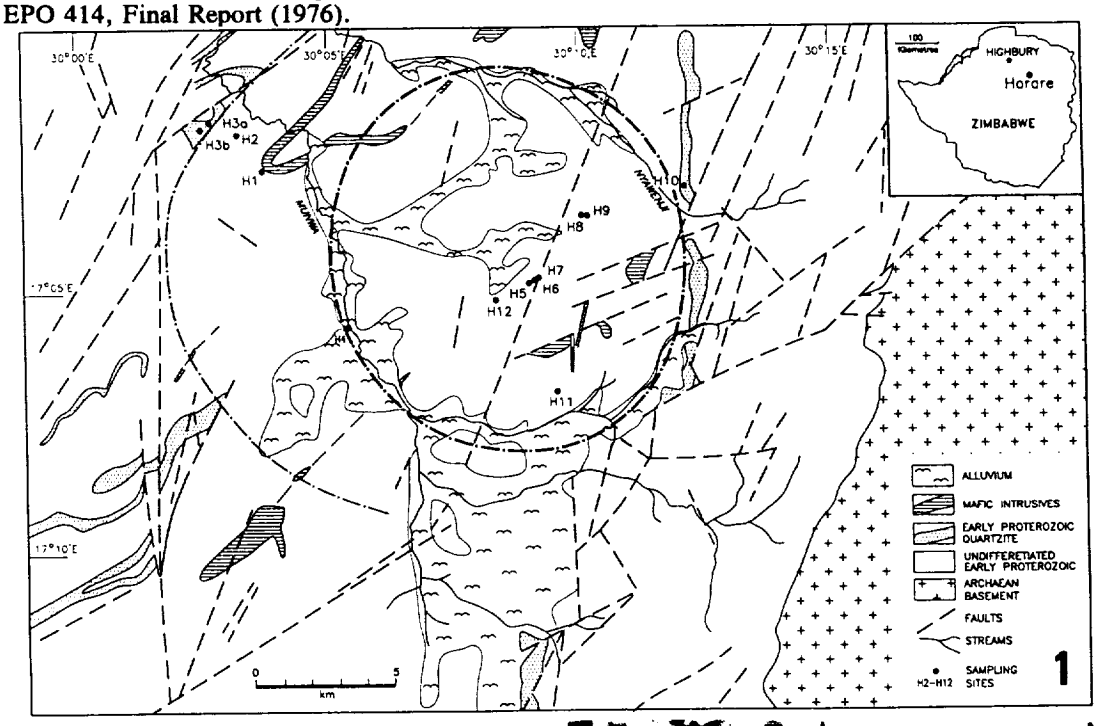

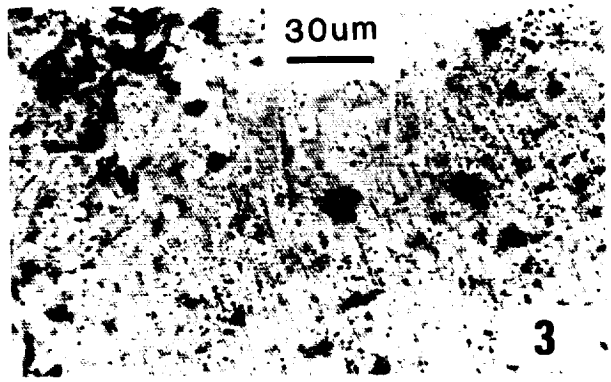

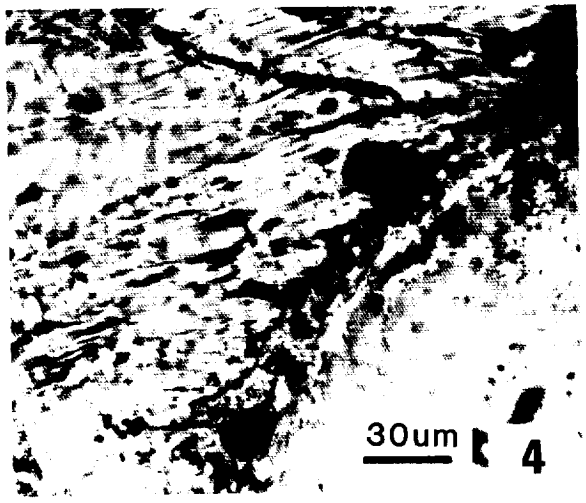

I - Xe DATING OF EL TACO INCLUSIONS.

K.J. Mathew and F. Begemann, Max Planck Institut für Chemie, 55128 Mainz, Germany.

Most iron meteorites are considered as residues from primordial melting and differentiation that occured near the core of a parent body when chondrite-like primordial material melted and separated into a heavy iron fraction (iron meteorites plus residual silicates) and a light silicate fraction (achondrite type meteorites). Other models have been proposed to explain the origin of group IAB and IIICD iron meteorites [1] which contain silicate inclusions, nearly of the unequilibrated chondritic type. The Rb-Sr, K-Ar and I-Xe ages of the IAB silicates are, within experimental uncertainties, equal to the 4.52 Gy age of the solar system. Also, there have been reports of anomalous isotopic signatures in acid residues of IAB iron meteorites Canyon Diablo, Campo del Cielo and that of Shikhote Alin for the elements N, Os, Kr and Xe [2, 3, 4]. We analysed the meteorites El Taco (Campo del Cielo) and Shikhote Alin. The results from the measurement of El Taco are discussed here.

Experimental Techniques. About 12 to 15 gms of meteorite shavings which also contained parts of several mm- to cm- sized macroinclusions were dissolved in 9M HNO_3 and the residues separated into magnetic and non-magnetic parts by a hand magnet. The magnetic part was mostly schreibersite as was verified by SEM analysis later. The non-magnetic part was further separated into four density fractions ($\leq$ 2.3 g/cm^3, 2.3 to 2.8 g/cm^3, 2.8 to 3.4 g/cm^3 and $\geq$ 3.4 g/cm^3). These residues were then wrapped in Ni foil and heated at 150°C for 36 hours in the sample fingers of the extraction system for releasing the atmospheric adsorbed noble gases.

Results and Discussion. Noble gases were extracted in 4 - 7 temperature steps and analysed following standard procedures. Results of the Kr and Xe isotopic measurements of the three heavy-density fractions will be discussed below.

The isotopic composition of Kr and Xe released at extraction temperatures higher than 900°C are identical to AVCC values within error limits. In the case of Kr isotopes in addition to the trapped/adsorbed gases there is correlated excess at ^{80}Kr and ^{82}Kr, as becomes evident from figure (a). Correlated excesses at ^{80}Kr and ^{82}Kr can be produced by (n,γ) capture reactions on ^{79}Br and ^{81}Br with characteristic ^{80}Kr/^{82}Kr ratios of 2.5 for thermal neutrons and of 3.3 for epithermal neutrons [5]. The ^{78}Kr/^{84}Kr ratio indicates that the spallation correction at Kr isotopes are negligible. The excesses at ^{80}Kr and the corresponding excesses at ^{82}Kr are estimated for each sample separately. The average value of ^{80}Kr/^{82}Kr ratio is found to be 2.85 in close agreement with the value of 2.82 deduced by [6] for silicate inclusions in iron meteorites.

The measured isotopic composition shows that xenon is predominantly trapped/ adsorbed and that the spallation and fission contributions are negligibly small. There are excesses, however, at ^{128}Xe and ^{129}Xe, mostly in the temperature steps above 900°C, Fig(b) shows them again to be correlated. Excesses at ^{128}Xe are produced by (n,γ) capture reactions on ^{127}I and ^{129}Xe excesses are produced by decay of extinct ^{129}I. A correlation between the two will mean that the ^{129}Xe is produced by in situ decay of ^{129}I since it is released from the same sites as the I sites, that is ^{129}I was live when the inclusions started to retain xenon. Rather than irradiating the samples we have relied on the natural radiation received by the samples, in an approach similar to [7] to show that the decay of ^{129}I took place in situ.

From the correlated high-temperature excesses at ^{128}Xe and ^{129}Xe we calculate the neutron fluence using the following relation

$$\Phi T = (^{128}Xe/^{129}Xe)^{*} \times (^{129}I/^{127}I)_{o}/\sigma_{127}$$

and assuming that $(^{129}I/^{127}I)_o$ was 1.0 x 10^{-4} when El Taco inclusions started to quantitatively retain radiogenic $^{129}Xe^*$. The effective σ_{127} and correlated $^{128}Xe^*$ and $^{129}Xe^*$ are used to calculate the neutron fluences in the case of each sample separately. The results thus calculated yield a mean value of 1.93 $\pm$0.48 x 10^{15} neutrons/cm^2 for the fluence in the eight samples considered here. The exposure age of El Taco is 14 Ma [8]. Hence the above fluence translates to a neutron flux of 4.3 neutrons/cm^2/s.

Conclusions. The parent body that provided El Taco with its present inclusions was formed early in the history of the solar system and had incorporated live ^{129}I in these inclusions. The inclusions had not undergone prolonged heating at very high temperatures since then. However, they might have been heated to relatively high temperatures as most of the radiogenic ^{129}Xe is released at temperatures $\geq$900°C. This heating most probably accompanied the same event that brought the metal and silicates together.

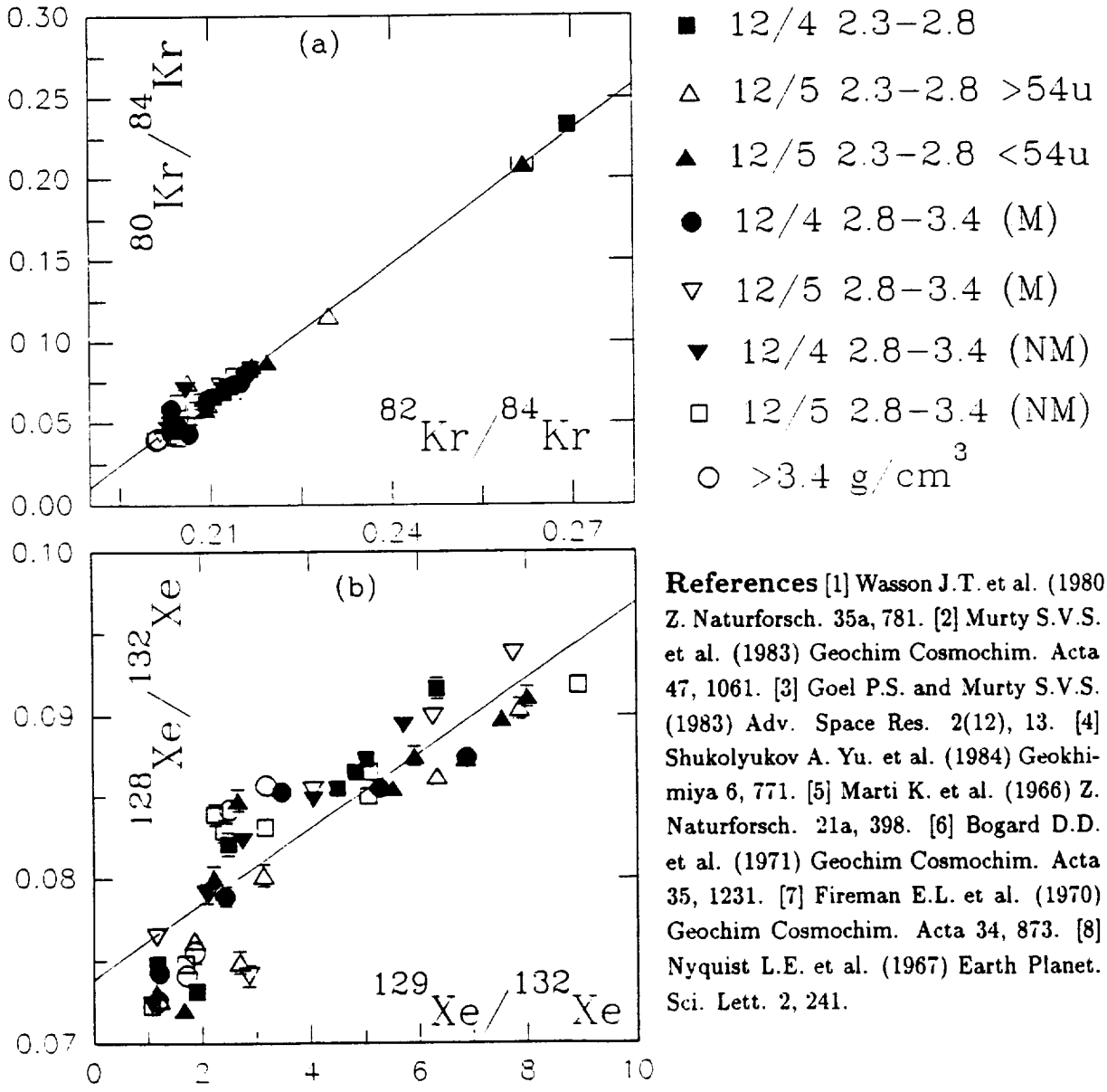

References [1] Wasson J.T. et al. (1980) Z. Naturforsch. 35a, 781. [2] Murty S.V.S. et al. (1983) Geochim Cosmochim. Acta 47, 1061. [3] Goel P.S. and Murty S.V.S. (1983) Adv. Space Res. 2(12), 13. [4] Shukolyukov A. Yu. et al. (1984) Geokhimiya 6, 771. [5] Marti K. et al. (1966) Z. Naturforsch. 21a, 398. [6] Bogard D.D. et al. (1971) Geochim Cosmochim. Acta 35, 1231. [7] Fireman E.L. et al. (1970) Geochim Cosmochim. Acta 34, 873. [8] Nyquist L.E. et al. (1967) Earth Planet. Sci. Lett. 2, 241.

PRODUCTION RATE OF NITROGEN IN MOON AND METEORITES.

K.J. Mathew[1] and S.V.S.Murty[2] 1. Max Planck Institut für Chemie, 55128 Mainz, Germany 2. Physical Research Laboratory, Navrangpura, Ahmedabad, India.

Introduction. Oxygen is the principal target element for cosmogenic nitrogen. All silicate minerals have ≈45% oxygen and hence profusely produce ^{15}N, when exposed to cosmic rays. The $\delta^{15}N$ of any extraterrestrial sample is modified by the cosmogenic nitrogen and any effort to derive the indegeneous $\delta^{15}N$ of trapped N necessitates a correction for the cosmogenic component [1, 2].

Cosmogenic nitrogen in a sample can be obtained either by direct experimental measurement or can be calculated from other cosmogenic nuclides (^{21}Ne, ^{38}Ar) if relation between the production rates of ^{15}N and ^{21}Ne or ^{38}Ar (which are easily measurable) can be established. The experimental approach is at times beset with unrecognized artifacts [3 - 5] and accurate determinations of cosmogenic nitrogen amounts are feasible only in special cases [6]. For establishing a relation between the production rates of ^{15}N and ^{21}Ne the production systematics of [7] that are based on limitted cross section data [8] have been used in the past [1, 2]. With the recent availability of new cross section measurements [9 - 12] particularly for the reaction $^{16}O(p,2p)^{15}N$ a reevaluation of ^{15}N production rates has become imperative.

Methodology. In the earlier production rate calculations [7] only ^{15}N production through the reaction channel $^{16}O(p,pn)^{15}O$ was evaluated and the contribution of the direct reaction $^{16}O(p,2p)^{15}N$ was estimated by comparing the ^{15}O production rate with ^{15}N production rates deduced from lunar sample measurements [13]. The present calculations consider these two reaction channels separately. We have constructed the excitation functions for the above two reactions using published cross section data and, in the limited energy region where experimental data are not available, using the analogous reaction $^{12}C(p,2p)^{11}B$ and the isobaric yield at mass 15 from oxygen target [11]. The production rate calculations discussed here were carried out using models described by [14] for the galactic cosmic rays (GCR) and by [15] for the solar cosmic rays (SCR). For the SCR spectrum, a (R_o, J_o) combination of 100 MV and 100 p/cm^2/s of the contemporary sun [16] has been used. For GCR calculations we used $J_{(\geq GeV)}$ = 1.8 p/cm^2/s for the case of the moon and 2.3 p/cm^2/s for meteorites [17]. An oxygen abundance of 45% is assumed for the moon and for H- and L-chondrites the composition given by [18] is employed.

Results and Discussion. Both ^{15}O and ^{15}N production rates increase with shielding depth in a large body like the moon, reaching a maximum at a depth of ≈40 g/cm^2, followed by a decrease thereafter. In fig 1 we compare the GCR- and SCR-induced total ^{15}N production rates calculated in the present work with earlier ones by [7]. Even though the depth profiles look similar, our production rates are systematically higher than the estimates by [7] by about 30%. This is mainly due to an underestimation of the contribution from $^{16}O(p,2p)^{15}N$ in [7]. The differences between the two calculations are manifest at all shielding depths including the suface.

Table 1 shows the production rates of both ^{15}N and ^{21}Ne as a function of depth in H- and L-chondrites of a radius equivalent to 108 g/cm^2. By knowing the ^{21}Ne in the meteorite one can deduce the cosmogenic ^{15}N using the above derived $^{15}N/^{21}Ne$ ratios. In view of the present production rates, the recent estimates of cosmogenic ^{15}N in the atmosphere and regolith of Mars [19] need an upward revision. For example the surface production rate estimates in the Martian regolith become 320 atoms/min/kg matrix compared to 208 estimated by [19].

We further observed [20] that the ratio $^{15}N/^{21}Ne$ is composition dependent and is different for different silicate minerals. Considering the GCR induced production in the moon and in meteorites the $^{15}N/^{21}Ne$ ratio changes with depth and the variation in this ratio is by as much as 40 to 70% for different minerals

(between the surface and a shielding depth of 500 g/cm^2). The SCR induced $^{15}N/^{21}Ne$ ratio also shows variations which, however, are much larger and are confined to the top 15 to 20 g/cm^2 of the lunar regolith [20]. Also for a given mineral the ratio $^{15}N/^{21}Ne$ is sensitive to the energy spectrum of the cosmic rays, the ^{15}N being more responsive to production by low energy particles as compared to ^{21}Ne. An experimental determination of $^{15}N/^{21}Ne$ in separated minerals, in particular feldspar, will be very diagnostic in recognizing SCR effects.

Shielding depth g/cm^2	^{15}N atoms/min/kg		$^{14}N/^{15}N$		^{21}Ne atoms/min/kg		$^{15}N/^{21}Ne$	
	H	L	H	L	H	L	H	L
0.0	547	580	0.53	0.53	100	108	5.5	5.4
3.6	552	582	0.53	0.53	104	112	5.2	5.2
10.8	564	596	0.53	0.53	110	119	5.1	5.0
18.0	582	614	0.53	0.53	120	129	4.9	4.8
28.8	612	646	0.53	0.53	129	138	4.8	4.7
36.0	646	681	0.53	0.54	138	147	4.7	4.6
45.0	683	722	0.54	0.54	147	159	4.6	4.6
64.8	764	805	0.54	0.54	170	182	4.5	4.4
72.0	794	837	0.54	0.54	177	191	4.5	4.4
108.0	863	909	0.54	0.57	198	212	4.4	4.3

Table 1

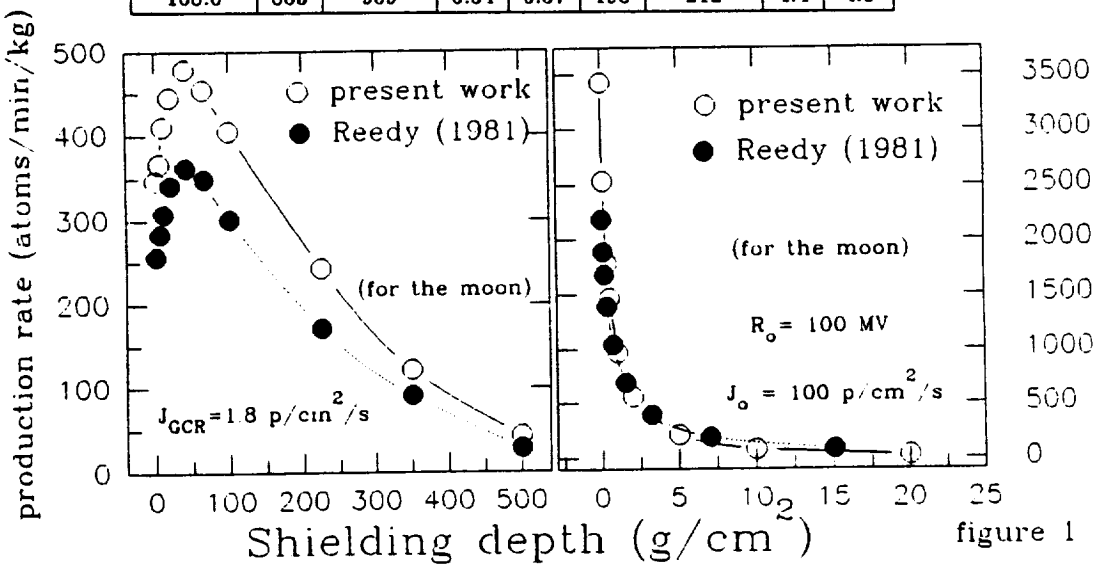

figure 1

References. [1] Murty S.V.S. and Marti K. (1990) Meteoritics 25, 227. [2] Murty S.V.S. and Goswami J.N. (1992) Proc. Lunar Planet. Sci. 22, 225. [3] Hashizume K. and Sugiura N. (1992) Geochim Cosmochim. Acta 56, 1625. [4] Murty S.V.S (1993) Geochim Cosmochim. Acta 57, 1357. [5] Kim J.S. and Marti K. (1993) Meteoritics 28, 380. [6] Murty S.V.S. and Varun Sheel (1991) Meteoritics 26, 375. [7] Reedy R.C. (1981) Proc. Lunar Planet. Sci. B12, 1809. [8] Audouze J. et al. (1967) In: High Energy Reactions in Astrophysics (ed) B.S.P Shen 225. [9] Webber W.R. et al. (1990) Phys. Rev. C41, 566. [10] Olson D.L. et al. (1983) Phys. Rev. C28. 1602. [11] Guzik T.G. et al. (1985) Proc. 19th Int. Cosmic Ray Conf. 2, 80. [12] Sisterson J.M. et al. (1991) Meteoritics 26, 395. [13] Becker R.H. et al. (1976) Proc. Lunar Sci. Conf. 7, 441. [14] Bhandari N. (1988) Proc. Indian Acad. Sci. Earth Planet. Sci 97, 117 [15] Bhattacharya S.K. et al. (1973) Moon 8, 253. [16] Rao M.N. et al. (1993) J. Geophys. Res. 98, 7827. [17] Michel R. et al. (1991) Meteoritics 26, 221. [18] Mason B. (1979) Geol. Surv. Prof. Paper 440. [19] Lal D. (1993) Geochim Cosmochim. Acta 57, 4627. [20] Mathew K.J. and Murty S.V.S. (1993) Proc. Indian Acad. Sci. Earth Planet. Sci. 102, 415.

COSMOGENIC ^{26}Al IN DEEP-SEA STONY SPHERULES

H. Matsuzaki and K. Yamakoshi
Institute for Cosmic Ray Research, University of Tokyo, Tanashi, Tokyo 188, Japan

Size dependence of averaged cosmogenic ^{26}Al activity in deep-sea stony spherules were estimated considering the effects of orbital evolutions by the Poynting-Robertson effect in the interplanetary space and the atmospheric entry. It is found that the contribution of the dust particles with high eccentricity in interplanetary motion can be ignored practically because such particles would have so high atmospheric entry velocities that they would disappear in the upper atmosphere besides the probabilities of capturing by the earth are low. To examine the results by measurering ^{26}Al activities in the spherules, we expect, the Poyinting-Robertson effect can be verified.

Radionuclides ^{26}Al is produced in the interplanetary dust particles through irradiation of the solar cosmic rays. The amounts of such nuclide production would have been determined by the motion of the dust particles and the spatial intensity of the solar cosmic rays. The Poynting-Robertson effect which has been thought to be decisive for the motion of the interplanetary dust particles has been not yet proved observationally and also experimentally. In reality, the interplanetary dust particles have various origins and are experienced complex processes of evolution. For example, comets scatter the dust near the sun which are thought to be main source of the dust around the earth's orbit. And the collisional process of the dust particles is also important. Then, it is not so clear whether the dust particles which have been affected mainly the Poynting-Robertson effect only are present or not. We think that the deep-sea spherules are the candidates of that,which would be proved by measuring the long-lived cosmogenic radionuclides in them.

In the following calculations, changes of the orbital elements a (semimajor axis) and e (eccentricity) of the paticle on an elliptical orbit according to the Poynting-Robertson effect[1] are taken into account. The energy spectrum of the solar cosmic rays, cross sections of ^{26}Al producing reactions, and p/α ratio were to be followed Lal and Venkatavaradan[2]. And the spatial distribution of the solar cosmic ray intensity is to be inversely proportional to r (heliocentric distance). The starting point was set to a = 2.8 AU which is the average heliocentric distance of asteroids. The results would be not so differed in the case of the more distant starting points due to the character of the spatial distribution of the solar cosmic ray intensity.

Fig. 1 shows ^{26}Al cumulation with time in the particle of 100μm in diameter moving from a = 2.8 AU to a = 1.0 AU according to the Poynting-Robertson effect with each initial eccentricity e_0. In the case of $e_0 < 0.3$, ^{26}Al production is almost equal to that in the case of circular orbit. In the case of higher eccentricity, however, ^{26}Al production decreases.

A particle having low eccentricity will be trapped by the earth when the semimajor axis a is nearly equal to 1 AU Hence, we expect for ^{26}Al production in such particle the value of the top point of the curve drawn in Fig. 1. But in the case of high eccentricity, a particle would cross the earth's orbit even when it's semimajor axis had not yet approached 1 AU. So we must calculate the probability for the particle to be captured by the earth in each stage of orbital evolution to estimate the average nuclide production, and the atmospheric entry velocity in each case to take the effect of the atmospheric entry into account.

Fig. 2 shows the expected atmospheric entry velocity of particles in the case of the initial eccentricity e_0 = 0.1, 0.3, 0.5, 0.7 and 0.9 with 0.1 *rad.* of the inclination of the orbial

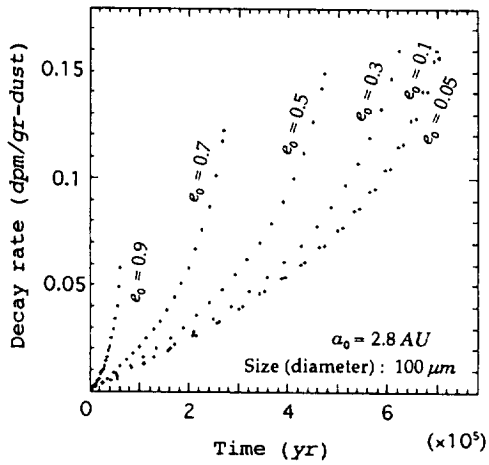

Fig. 1. ^{26}Al cumulation with time in the particle moved from a = 2.8 AU to a = 1.0 AU according to the Poynting-Robertson effect with each initial eccentricity.

COSMOGENIC ^{26}Al: H.Matsuzaki and K.Yamakoshi

plane. In the low eccentricity case, the particle captrue probability is high and the entry velocity is low. In the high eccentricity case, particularly $e_0 > 0.7$, the particle would rarely be captured by the earth and if captured, the entry velocity would be very high. By performing the atmospheric entry calculations[3][4], we can see that the process make the final sizes of particles be very small regardless of the initial sizes when the entry velocity is high. Fig. 3 shows the average ^{26}Al production in each entry velocity. In the high eccentricity cases, ^{26}Al productions are fairly low as compared with the low eccentricity cases, however, which would not make serious influences on the whole average of ^{26}Al. Moreover, the atmospheric entry process would further weaken the influences because of their high entry velocities.

Similar calculations were performed in various sizes, then atmospheric entry processes were calculated in each, and finally summed up the results to get the final size dependences of ^{26}Al productions. In this calculation, size distribution of the particles was to be of $dn \propto s^{-4}ds$ at the starting point in the interplanetary motion which agrees with the terrestrial observation and the experiments carried out on space crafts[5]. Actually, interplanetary dust particles would be the mixed ones of various eccentricities, so we must average various cases of the initial eccentricity e_0. In Fig. 4, the circles represent the average ^{26}Al productions of after-atmospheric entry of the cases of every 0.05 steps of e_0 below 0.5, and the crosses represent that of below 0.75. Fine dotted line represents the case of the circular orbit ($e_0 = 0.0$) of pre-atmospheric entry. That these two results of after-atmospheric entry are almost the same though there is some difference in pre-atmospheric ones, means that the cases of e_0 above 0.5 merely do contribute to the final results.

The influence of variation of the inclination of the orbital plane is not considered here, however high inclination cases do not contribute to the after-atmospheric entry results by the atmospheric filteration. It can be said that if the cases of various orbital elements are taken into account, the final size dependence of ^{26}Al productions does not differ seriously from the case of the circular orbit ($e_0 = 0.0$) of pre-atmospheric entry, which is easier to calculate.

References
[1] Wyatt, S. P. and F. L. Whipple (1950) Astrophys. J., 111, 134–141
[2] Lal, D. and V. S. Venkatavaradan (1967) Earth. Plan. Sci. Lett., 3, 299–310
[3] Matsuzaki H. and K. Yamakoshi (1993) Lun. Plan. Sci. (Abstracts), 24, 943-944
[4] Love, J. J. and D. E. Brownlee (1991) Icarus, 89, 26–43
[5] Grün, E. et al. (1985) Icarus, 62, 244–272

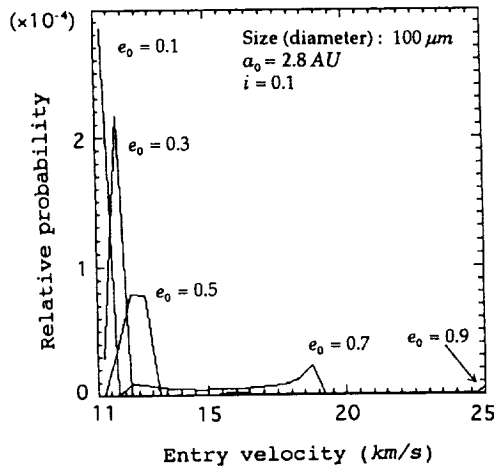

Fig. 2. Expected atmospheric entry velocity of particles in the case of the initial eccentricity e_0 = 0.1, 0.3, 0.5, 0.7 and 0.9.

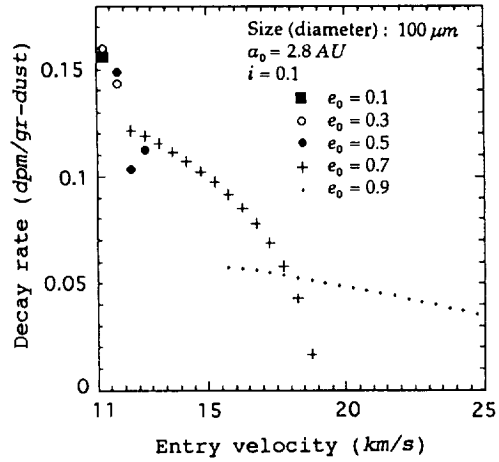

Fig. 3. Average ^{26}Al production in each entry velocity corresponding to Fig. 2.

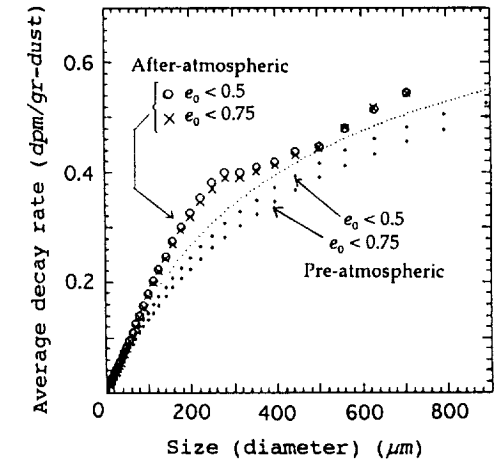

Fig. 4. ^{26}Al production of the average of each case of every 0.05 steps of e_0 below 0.5 and below 0.75. Fine dotted line represents the case of the circular orbit ($e_0 = 0.0$) of pre-atmospheric entry.

GVDR DATA PRODUCT: A SUMMARY OF ALL MAGELLAN OBSERVATIONS OF VENUS SURFACE CHARACTERISTICS; M. J. Maurer, R. A. Simpson, Stanford University.

Observations of Venus from all Magellan radar investigations have been combined into a single data product that summarizes the surface characteristics of the planet. The data set is presented in map form at approximately 20 km resolution, in several map projections. Each map pixel consists of a summary of all spacecraft measurements of that portion of the planet, indexed by the viewing geometry of each measurement. Measurements with similar viewing geometries have been averaged. This image-based presentation will make possible geologic studies based on surface statistics, especially when combined with the other map products already available from Magellan, the SAR image MIDRs and altimetry and radiometry GxDRs. The GVDR (Global Vector Data Record) will be distributed on a single CD-ROM through the Planetary Data System.

The GVDR is derived from two Magellan data products: the per-orbit altimetry and radiometry data produced by MIT (ARCDRs), and the per-orbit surface characteristics data produced by Stanford (SCVDRs). These in turn are derived from several data products created by JPL, including the SAR image strips (F-BIDRs and C-BIDRs) and the fairly raw data in the ALT-EDRs and SAR-EDRs.

The GVDR includes estimates of the near-nadir scatting law (out to 6-12 degrees, depending on geometry), best fit analytic scattering laws to the observed scattering law (including Hagfors, Exponential, and Gaussian scattering laws), and the rms slope and reflectivity parameters associated with these fits. Isolated samples of the scattering law at higher angles of incidence are also included, derived from the side-looking SAR observations of the same region; in some places up to three such samples are available due to different viewing geometries during the several mission cycles. Also included are surface properties reported in the ARCDR (derived from the altimeter by a different method) such as radius, rms slope and Fresnel reflectivity. Emissivity measurements are sorted by viewing geometry and polarization angle.

This data product can be used for geologic studies of the planet that require knowledge of the small- and medium-scale surface structure. Of particular interest is the combination of near-nadir scattering properties with those at high angles of incidence; the relationship between these measurements will give insight into the relative importance of quasi-specular and diffuse scattering mechanisms in different geologic units. Equally interesting is the separation of different viewing geometries. Several regions of the planet have appeared distinctly different when viewed from opposite directions, or have caused Doppler anomalies in the altimeter echo; both observations are most simply explained by a consistent anisotropy in the scattering behavior of the surface. Studies of these regions have been frustrated by the difficulty of comparing data from different mission cycles and data products. The GVDR puts all such observations in a single place, making comparison quite simple.

A test product has been released to a limited subset of the Magellan community. Pending their review of the data format and content, we plan to release an official version of the GVDR to the Planetary Data System in spring of 1994. That version will only contain SAR image data from Cycle 1+; we expect reprocessed data from cycles 2-3 to be available soon afterward and plan to release a final GVDR containing summaries of all available measurements.

EROSION AND DEPOSITION IN THE MARTIAN HIGHLANDS: AEOLIS AND ARABIA. Ted A. Maxwell and Robert A. Craddock, Center for Earth and Planetary Studies, National Air and Space Museum, Smithsonian Institution, Washington, D.C. 20560

In addition to runoff and outflow channels, the record of climate change on Mars is recorded in the state of preservation of the highland crater population. Prior work by us and other workers has emphasized the role of fluvial (1) and aeolian (2) processes in modifying highland craters. Based on available topography and small-scale geologic mapping we found that the age of stability represented by the fresh crater population varied with elevation such that the most elevated parts of the cratered terrain became stable first, followed by successively lower elevations. In that study, crater populations were binned by geology, latitude, and elevation, and the number of fresh impact craters per unit area was taken to represent the time at which degradation ceased and the surface became stable. In order to determine whether our regional observations based on small scale geologic mapping and available topography hold up on a local level, we have investigated three areas of the martian highlands, in some cases previously interpreted to represent drainage basins. Our results indicate that the time of stability recorded in the dissected materials (all late Hesperian in age) is not the same as that recorded by the adjacent smooth materials, which in all three cases appears to be younger. The three areas were also chosen to represent a range in elevation between 2000 and >5000 m; the age of stability does not change monotonically with age as found in our previous work. We believe that the latter result is most likely due to the small size of the individual areas counted for this study.

In each of the three areas studied, the geologic boundary between dissected and smooth highland materials was remapped on the 1:2M mosaics using the MDIM and individual frames as a guide. A binary classification of rimless and rimmed craters was applied to each area, and normal crater counting procedures were followed to determine the total age of the unit as well as the age of stability represented by the rimmed crater population. In doing this work on restricted basins, we can determine whether the ages of stability of locally eroded highland materials is equal to that of neighboring smooth materials, presumably the "sinks" of that erosion. In addition, the three areas represent different elevations, which allows us to test our previous results, albeit on a very local level.

Southwest of Isidis, the area of dissected terrain west of Huygens represents the most elevated region studied (307.5°W to 317.5°W and -7.5°N to -15°N) at elevations >5000 m. Radial drainage off the west flank of Huygens disappears into local smooth terrain, and a broad zone of northward trending dendritic drainage also debouches to the north into smooth material. In the Aeolis quadrangle (202.5°W to 212°W and -20° to -30°N), an area previously interpreted as an interior drainage basin (3), a smooth patch of material with wrinkle ridges is flanked by dendritic drainage flowing into it from both the west and the east. This area is between 4000 and 5000 m elevation. Highland materials of the Arabia quadrangle (320° to 330°W and 7.5°N to -2.5°N) between 2000 and 3000 m elevation comprise the third area. Here, several isolated patches of smooth materials are bordered by a broad zone of dendritic drainage that may be controlled by ancient, highly degraded basins.

PRECEDING PAGE BLANK NOT FILMED

MARS HIGHLAND EROSION AND DEPOSITION: T.A. Maxwell and R.A. Craddock

In each of these areas, the ages represented by the fresh crater population in the dissected terrain are late Hesperian, consistent with previous studies of martian degradation and stratigraphy (4,5). However, on a detailed level, there are variations in the timing of the age of stabilization of the surface. The age of smooth material in west of Huygens (N(5)= 170) suggests a surface younger than the time of stabilization of the adjacent dissected materials (N(5)=223). Similar relations occur in Arabia, where the smooth material has a rimmed crater population with an age of N(5)=187, and the dissected materials are N(5)=269. In Aeolis, the ridged plains have a fresh crater age of N(5)=91 and adjacent materials are N(5)=193. All three areas suggest a hiatus in time between the cessation of erosion of the dissected materials, and the cessation of resurfacing of the adjacent smooth plains. Significant modification of the plains units by aeolian processes is unlikely as the sole method, as such effects would be recorded in the adjacent highland materials as seen elsewhere on Mars (6). Throughgoing drainage (and deposition), as well as volcanic infilling of the low (?) areas remain the most likely causes of this discrepancy in ages. The ages of the dissected materials given above also do not indicate any relationship between age of surface stability and elevation. Given the relatively small size of the counting areas (~ 200,000 km^2 per area), we attribute this result to the small statistics rather than a conflict with our previous results.

(1) Craddock, R.A., and T.A. Maxwell, J. Geophys. Res., 98, 3453-3468, 1993. (2) Grant, J.A., and P.H. Schultz, Icarus, 84, 166-195, 1990. (3) Goldspiel, J.M., and S.W. Squyres, Icarus, 89, 392-410, 1991. (4) Craddock, R.A., and T.A. Maxwell, J. Geophys. Res., 95, 14,265-14,278, 1990. (5) Tanaka, K.L., Proc. Lunar Planet. Sci. Conf. 17th, Part 1, J. Geophys. Res., 91, suppl., E139-E158, 1986. (6) Grant, J.A., and P.H. Schultz, J. Geophys. Res., 98, 11025-11042, 1993.

DEPTH OF FORMATION OF LUNAR AND TERRESTRIAL ANORTHOSITES AND GABBROS FROM COMPOSITIONAL PROFILES OF EXSOLVED PYROXENES I. S. McCallum and H. E. O'Brien, Department of Geological Sciences, AJ-20, University of Washington, Seattle, WA 98195

Detailed examination of the ejecta blankets associated with large multi-ringed basins reveals that the lunar crust is heterogeneous both laterally and vertically (Davis and Spudis, 1985; Spudis and Davis, 1986). The model of lunar crustal stratigraphy that has emerged from this work shows an anorthositic upper crust (Al_2O_3 = 26-28 wt %) making up from 30 to 50% of the total crustal volume. This unit is underlain by a noritic lower crust (Al_2O_3 = 20 wt %) which extends to the crust/mantle boundary. Mg-suite rocks (troctolites, norites, gabbronorites), which are believed to occur as slightly younger intrusive bodies throughout the crust, form a minor but important part of the crust. This model is not universally accepted and we have attempted to use mineralogical data to provide some independent confirmation of the gross lunar stratigraphy.

The width, spacing, crystallographic orientation, structural state, and composition of exsolved host--lamellae pairs in pyroxenes is a function of cooling rate. Cooling rate, in turn, is primarily a function of depth of burial. To determine depth of burial at the time of formation, we have been examining in detail exsolution features in pyroxenes from lunar crustal samples. Geothermometric studies on host--lamellae pairs indicates that the closure temperature for exsolution is around 700°C (McCallum et al., 1975). Extraction of cooling rates from compositional profiles requires (1) knowledge of Ca--MgFe diffusion coefficients along various crystallographic direction (or at least along c), (2) an accurate thermodynamic model of the pyroxene solvus as a function of T, P and composition, (3) precise compositional profiles across adjacent host--lamellae pairs, (4) bulk composition of the pyroxenes. Ca-MgFe diffusion coefficients in augite and pigeonite have been measured by Fujino (personal communication) at 1200°C, 1100°C and 1000°C and we have extrapolated these to 700°C using an activation energy recommended by Fujino. This rather long extrapolation introduces an unknown uncertainty into the calculations. PTX of the pyroxene solvus has been recalculated recently by Sack and Ghiorso (1994); their solvi differ in significant ways from earlier solvi due, in large part, to the inclusion of the effects of Fe-Mg ordering. For ease of computation, a digitized version of the pigeonite--augite solvus with equilibrium tie lines was prepared. Fick's Second Law of diffusion was solved by numerical methods under the appropriate boundary conditions (Sanford, 1982). A variety of cooling models were employed from linear to asymptotic to exponential.

Translation of calculated cooling rates to depths of burial is the most difficult part of the process since this requires more information than is generally available. Measured values for thermal diffusivity vary considerably and this problem is particularly severe in the lunar case because of the presence of thick regoliths that existed early in lunar history. Material in regoliths might be expected to have significantly lower thermal diffusivities. Even though absolute depth of burial may not be known with sufficient precision, the method we use provides a useful relative scale. As a check of the cooling rate versus burial depth curve, we have measured composition profiles in similar pyroxenes from the Stillwater Complex. In this case, independent estimates of the depth of burial can be obtained by thermobarometry.

Three typical profiles are shown in Figures 1- 3. In each case, care was taken to correct for the effects of overlap at the boundary between host and lamellae (Ganguly et al., 1991). The calculated profiles are based on a linear cooling rate. In the case of the two pyroxenes from

anorthosite 67075 (Figs. 1, 2), a calculated cooling rate of 7.3 x 10^{-5} °C/year corresponds to a depth of burial of approximately 11 km (based on a thermal diffusivity of .005 cm^2/sec). Coincidentally, the best fit calculated profile for an inverted pigeonite from the Stillwater Complex (Fig. 3) gives an identical cooling rate and depth of burial. The depth to the base of the Stillwater Complex, based on olivine--orthopyroxene--quartz equilibria in iron formation just below the complex (Labotka, 1985), is 13 km and the estimated thickness of cover at the time of pigeonite formation is approximately 10 km.

References: Davis, P.A. and Spudis, P.D. (1985) PLPSC 16, D61-D74; Ganguly, J. et al. (1988) Amer. Min., 73, 901-909; Labotka, T.C (1985) Montana Bur. Mines Spec. Pub. 92, 70-76; McCallum, I.S. et al. (1975) EPSL, 26, 36-53; Sack, R.O. and Ghiorso, M.S. (1994), in press; Sanford, R.F. (1982) Computers and Geosciences, 8, 235-263; Spudis, P.D and Davis, P.A. (1986) PLPSC, 17, E84-E90.

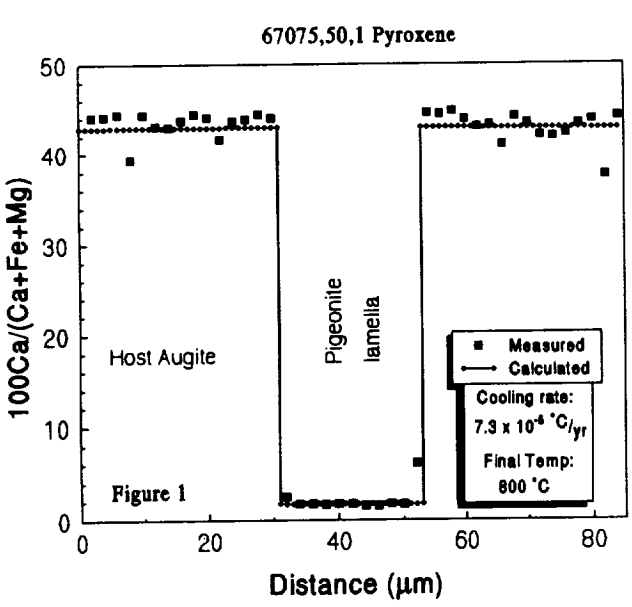

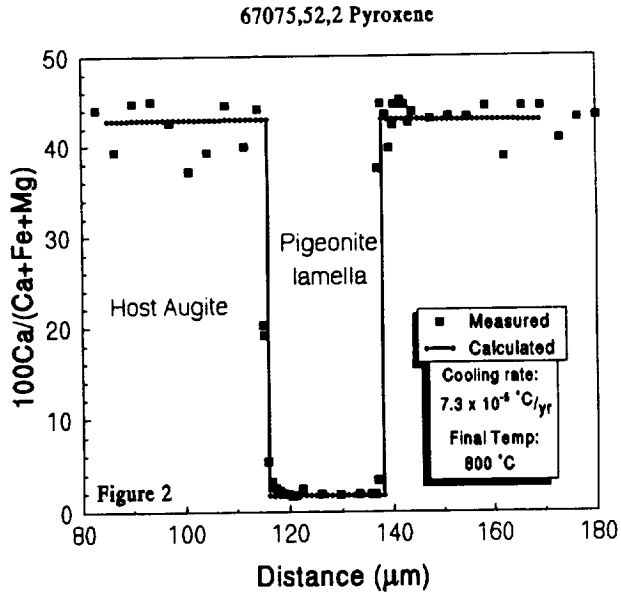

Figure 1. Quantitative step scan profile (2μm steps) across a high-Ca pyroxene from 67075,50. Calculated 100Ca/(Ca+Mg+Fe) is superimposed on measured profile.

Figure 2. Same as Fig. 1, with 1μm steps across a high-Ca pyroxene from 67075,52. Host augite in this grain contains a second set of thin (001) low-Ca lamellae.

Figure 3. Quantitative step scan profile (1μm steps) across Stillwater pigeonite. Calculated 100Ca/(Ca+Mg+Fe) is superimposed on measured profile.

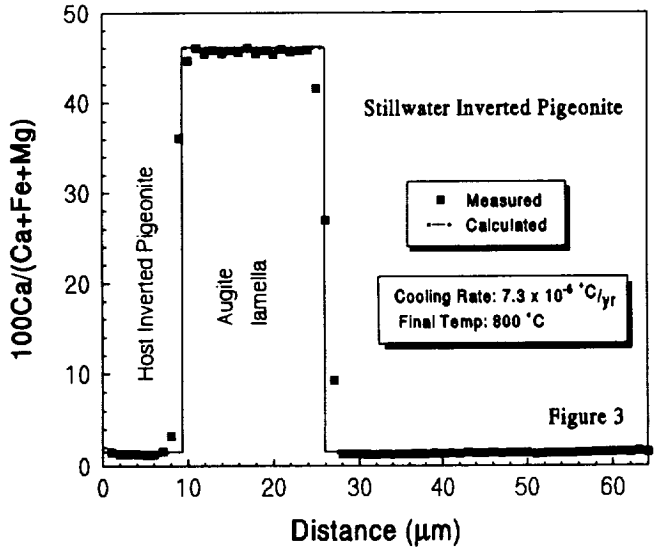

POST-IMPACT HYDROTHERMAL ALTERATION OF THE MANSON IMPACT STRUCTURE; P. McCarville and L.J. Crossey, Department of Earth and Planetary Sciences, University of New Mexico, Albuquerque, NM 87131

Core materials from the Manson Impact Structure (MIS; Manson, Iowa) are examined in order to evaluate post-impact alteration processes. Interpretation of the high temperature post-impact hydrothermal system is based on mineralogic and geochemical investigation. MIS rocks from the M1, M7, M8, and M10 cores, obtained by the continental scientific drilling project (CSDP) at the MIS in 1991 and 1992, are utilized in this study. All lithologies, including the sedimentary clast breccias (SCB), crystalline clast breccias (CCB), and central peak crystalline rocks (CPC) have been described previously [1]. Particular emphasis is placed upon cavity (vugs and pores), fracture (veins and fracture-faces), and altered clast features within these lithologies. Analyses include petrography, scanning electron microscopy, and x-ray diffraction analysis. The presence of garnet (Ga), ferro-actinolite (FA), epidote (Ep), prehnite (Pr), wollastonite (Wo), , laumontite (La), quartz (Q), adularia (Ksp), pyrite (Py), clays (Cly) including corrensite, chlorite, illite, smectite, and a chlorite/smectite mixed-layer (approximately 15% chlorite component), calcite (CC), and analcime (An) define a hydrothermal system which developed at a temperature of at least 275°C and possibly up to 360°C, and ended at approximately ambient temperatures. These minerals are grouped according to their temperatures of occurrence in modern geothermal systems. The highest temperatures in the MIS are represented by a garnet and ferro-actinolite assemblage, named assemblage I. Assemblage II contains epidote, prehnite and wollastonite, which represents slightly lower temperatures in the system. The existence of laumontite, quartz, and adularia define a third assemblage, which represents moderate to low temperatures in the system. Assemblage IV is defined by calcite and clay(s), and represents the lowest alteration temperature at the MIS.

An authigenic assemblage of garnet and ferro-actinolite (assemblage I) is found in the breccias of the M1, M8, M10, and M7 cores (Figure a). Garnet occurs primarily in the CCB-SM lithology (figure a), with the majority of the occurrences in vugs and pores. It is petrographically anisotropic and hexaoctahedral in habit (figure b). Minor amounts of grossular coexists with the more abundant andradite. Ferro-actinolite is abundant in all the CCB-type lithologies and in the CPC lithology (Figure a). It occurs in an asbestiform habit, primarily filling altered clasts and vugs/pores. According to textural associations, visible with the SEM and petrographically, garnet forms before ferro-actinolite. Garnet occurs in modern geothermal systems where measured minimum temperatures range from 275°C [2] to 360°C [5]. Ferro-actinolite, within these same systems, occurs where measured minimum temperatures range from 280°C [2] to 325°C [5]. Assemblage I represents the highest fluid temperatures in the MIS.

Prehnite, wollastonite, and epidote occur in abundance in the M7 core (Figure a). Epidote and wollastonite are preferentially found in the CPC lithology, while prehnite is found in both the CCB-SM and the CPC lithologies. They have not been observed in the CCB-MM lithology. Wollastonite occurs only in fractures of large crystalline blocks of the CPC lithology, whereas epidote and prehnite occur primarily in altered clasts. Petrographic analyses reveal that epidote occurs after ferro-actinolite, and prehnite occurs after epidote. There is no textural evidence to indicate the paragenesis of wollastonite, but x-ray diffraction shows epidote always occurring with wollastonite. Similar coeval assemblages of wollastonite, epidote, and prehnite are noted in the Larderello (Italy) [3] and Krafla (Iceland) [4] geothermal systems. Furthermore, the prehnite/epidote/wollastonite assemblage in geothermal systems around the world represents a minimum temperature of occurrence ranging from 200°C to 300°C [5]. This assemblage (assemblage II) likely represents a fluid temperature slightly cooler than the one that produced assemblage I.

Laumontite is found in all 4 cores, primarily in the altered clasts and vugs/pores of the CCB-SM and CPC lithologies, with some occurrences in these features in the CCB-MM lithology (Figure a). Textural relationships between laumontite and prehnite in core M7 exhibit laumontite growing after prehnite. Laumontite within Icelandic geothermal systems occurs over a temperature range of 100°C to 230°C [4], suggesting that the fluids forming laumontite were cooler than those that formed assemblage II. Quartz tends to be lithologically restricted to the CCB-MM of the M7 core (Figure a), while it is found in all lithologies of the M1 core, albeit in greater abundance in the CCB-MM. It is typically euhedral, granoblastic, and occasionally inclusion-rich and zoned. Adularia is a rare authigenic phase in the MIS. It is found primarily in the M1 core, where it occurs in the CCB type lithologies. The most frequent occurrence of adularia is in veins and fractures. Adularia is typically 250μm along its c-axis and euhedral. SEM-EDS analyses reveal a trace amount of iron in the structure. Although quartz and adularia have a wide temperature range over which they occur in geothermal systems [5], they appear to post-date assemblage II minerals in the MIS. The paragenetic sequence of these three minerals (assemblage III) is presently unresolved. Laumontite occurring in core M8 is interpreted to be coeval with quartz, while within cores M1 and M10 the possibility of contemporaneous formation between quartz, adularia, and laumontite exists, but is not definitive. Only in core M7 does quartz occur before laumontite, and adularia after laumontite. The fact that they all occur after the higher temperature assemblages (I,II), however, is well documented through textural relationships.

Calcite occurs in all 4 cores of the MIS. Lithologic control on the occurrence of calcite seems to be nonexistent except for in the M7 core where it is limited to the CCB-MM lithology (Figure a). Textural evidence reveals that calcite is the last mineral to form in this system (Figure b). All four cores exhibit a

combination of five authigenic clays. Corrensite and chlorite are not limited to any one lithology. They occur in major abundance in the CCB-TZ and CCB-SM, and are minor or trace in abundance in the CCB-MM. Illite and smectite are most abundant in the SCB type lithologies and are possibly of detrital origin. The mixed-layer chlorite/smectite is most abundant in the SCB-KSB and CCB-MM lithologies. A progressively more crystalline (higher percentage of chlorite component) mixed-layer clay develops as one moves down the core through the CCB-MM lithology in core M1 and M7, or through the SCB-KSB into the CCB-MSM lithology in the M10 core. Clays in the MIS are quite difficult to differentiate from one another petrographically and thus a paragenetic sequence for the five clay types is indeterminable. Paragenetic relationships between clays and the other authigenic minerals are highly varied. A consistent textural relationship, however, exists between clay and calcite. In cores M1, M10, and M8 interpretation of textural evidence suggests that calcite and clay are coeval, while clay(s) always occur before calcite in core M7. We interpret the calcite/clay assemblage (assemblage IV) to represent the lowest temperatures in the system, possibly similar to the Valles (New Mexico) geothermal system in which calcite and clays occur together at temperatures as low as 40°C [6].

The occurrence of certain minerals constrain the temperatures of the hydrothermal system that existed within the MIS. Assemblage I suggests that temperatures may have been as high as 360°C in the system. A model for the thermal history of the MIS is reported elsewhere [7]. Successively decreasing temperatures through time, approaching ambient temperatures, are suggested by the lower temperature assemblages II, III, and IV. The distribution of these minerals within the lithologies of the MIS furnish an insight into the thermal architecture and history of the MIS.

Acknowledgments: This project is supported by the Department of Energy through the Office of Basic Energy Sciences. The SEM and X-ray Diffraction Laboratories at the Department of Earth & Planetary Sciences, University of New Mexico were utilized for this research. Karen Holmes assisted with sampling. Personnel at the Iowa Department of Natural Resources and the USGS (Denver) made cores available for sampling. References: [1] Anderson, R.R. et al. (1993) *LPSC XXIV*, 35-36; [2] Gianelli, G. and Teklemariam, M. (1993) *Journal of Volcanology and Geothermal Research*, 56, 429-445; [3] Cavaretta, G. et al. (1982) *Economic Geology*, 77, 1071-1084; [4] Kristmannsdottir, H. and Tomasson, J., (1976) **Natural Zeolites: Occurrence, Properties and Use**, 277-284; [5] Bird, D.K. et al. (1984) *Economic Geology*, 79, 671-695; [6] Hulen, J.B. and Nielson, D.L., (1986) *JGR*, 91, 1867-1886. [7] Crossey et al. (1994) *LPSC XXV*, this volume.

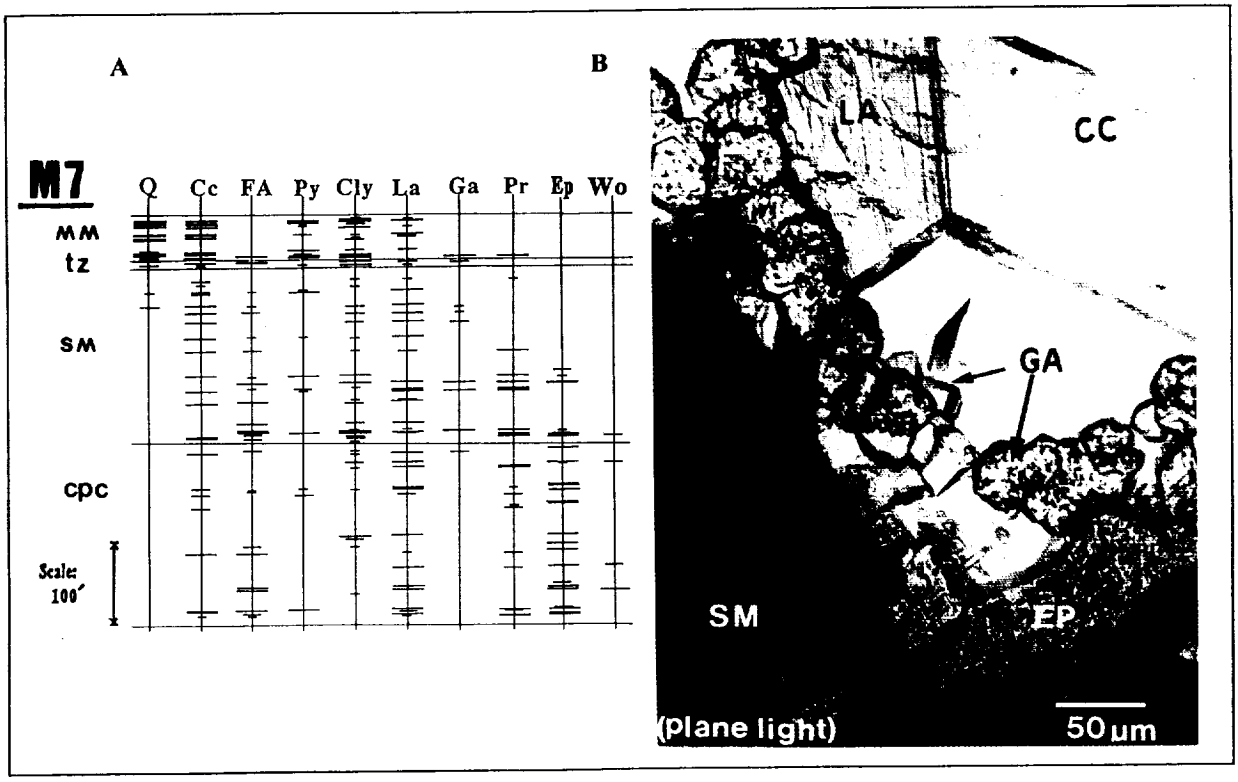

Figure a. M7 core mineral abundance chart. **Figure b.** Photomicrograph of vein minerals in CCB-SM of M7 core (411.5 ft depth). See text for mineral and lithology symbols.

THE GALILEO MISSION NEAR INFRARED MAPPING SPECTROMETER (NIMS) INVESTIGATION OF THE GALILEAN SATELLITES; T. B. McCord, Planetary Geosciences Division, School of Ocean and Earth Science and Technology, University of Hawaii, 2525 Correa Rd., Honolulu, HI 96822 and SETS Technology, Inc., 300 Kahelu Ave., Mililani, HI 96789; R. Carlson, Jet Propulsion Laboratory, MS 183-601, 4800 Oak Grove Dr., Pasadena, CA. 991109; and the NIMS team.

The Near Infrared Mapping Spectrometer (NIMS) investigation on the Galileo Mission to Jupiter will contribute a wealth of new information on the identification of the materials composing the satellites' surfaces and the spatial distribution of this material. The NIMS has already made measurements of Venus, The Moon, Earth, Gaspra and Ida, and a number of publications describing new scientific results have been produced (e.g. 1), even thought the NIMS was not designed for inner Solar System measurements. Thus, the investigation team has gained considerable familiarity with the instrument performance and the data processing and interpretation before the primary mission phase, far beyond most deep space missions. The outlook for NIMS Galilean Satellite measurements and first-order scientific results appears very promising, judging from these early serendipitous measurements. The detailed plan for NIMS measurements on the Galilean Satellites throughout the Jupiter orbital phase of the mission has been developed and is presented here in order that researchers can direct their programs to anticipate the NIMS data.

The NIMS (2) produces spectra of up to 408 contiguous spectral channels over the spectral range 0.7-5.2 μm for all pixels observed. Areal coverage for each measurement swath is usually 20 x N pixels, and overlapping swaths are used to produce mosaics of swaths. The NIMS has a multitude of measurement modes, including selection of number and placement of spectral and spatial channels, to accommodate science/measurement objectives and spacecraft resource restrictions.

The NIMS foreoptics present an image of the far-field, pointed by the spacecraft and its scan platform, to the entrance aperture of a spectrometer. The spectrometer presents a dispersed image of the aperture to a focal plane consisting of a line array of 2 silicon and 15 InSb point detectors arranged in a picket fence fashion, with spacing between each, along the dispersion. An external scan mirror sweeps a 20-pixel line across the track of the spacecraft/scan platform motion and the dispersive grating then scans in wavelength before the same 20-pixel line is scanned again. This is repeated until the spectrum for each pixel is built up, containing up to 408 spectral channels (24 grating scans; about 8.3 sec.). The scan platform/spacecraft motion than presents a contiguous 20-pixel line to be similarly measured. In this manner, an image cube of data is developed for 20 by N pixel swaths. This image cube can have a selectable number of spectral channels of, for example, 17, 51, 102, 204 and 408.

Detailed planning of the measurement objectives and of the candidate measurement sequences has been underway for nearly a year. This planning has evolved under severe restriction on downlink data rate, tape recorder volume, onboard memory, and with the usual conflicts among the various instrument investigations onboard. Nevertheless, a set of measurement scenarios is achievable which will meet science objectives and produce very exciting, first-order new knowledge about these objects and the processes operating to alter them.

The measurement strategy emphasizes obtaining broad area coverage of each

satellite at at least 51 spectral channels with spatial resolution of about 50 km and high spatial resolution observations (down to sub-1 km) of selected target areas at 204 or 408 spectral channels. Swaths of opportunity will be obtained also at 204 or 408 spectral channels within the 51-channel broad area mosaics. The objectives are to define the color/compositional units present over the entire satellites and to identify the constituent materials for representative units. Studies of thermal and photometric properties also will be conducted when possible. The NIMS and other remote sensing -- SSI (Imaging System), PPR (Photo-Polarimeter) and UVS (Ultra Violet Spectrometer) -- observations are being coordinated among these investigation teams so as to obtain as much mutually-complimentary data as possible.

The extent of the planned broad areal coverage, which will be at about 50 km per pixel and in at least 51 spectral channels, for each icy satellite is not yet fully defined but should exceed 50 % of the icy satellites surfaces and include polar areas. This coverage is limited mainly by encounter geometry, tape recorder space and down-link bandwidth. The targeted areas covered at higher spatial resolution and at more spectral channels mostly center on features which could be associated with mineralogical differences. These included palimpsests, albedo boundaries, impact features, and linear features.

Data products expected from the NIMS observations include reflectance spectra for individual pixels and spectral unit maps. These will help define the distribution of compositional units and determine the mineralogy of the units. The science topics to be addressed with this new information include thermal evolution and differentiation of the object, resurfacing and exposure of material from depth, and effects of impact and space weathering on surface material. Examples are: identify the composition of the dark material(s) on all icy satellites -- internal, external, primitive, altered; determine the cause and extent of resurfacing of Europa;

(1) Carlson, R., et al. (1991), Galileo Infrared Imaging Spectroscopy Measurements at Venus, *Science*, vol. 253, p. 1541. McCord, T.B., et al., (1993), Galileo Infrared Imaging Spectrometry Measurements at the Moon, *J. Geophys. Res.*, in press.
(2) Carlson, R., et al. (1992), Near-Infrared Mapping Spectrometer Experiment on Galileo, *Space Sci. Rev.*, vol. 60, 457-502.

LOW-FeO ORDINARY CHONDRITES: A NEBULAR ORIGIN AND NEW CHONDRITE PARENT BODY. T.J. McCoy[1], K. Keil[1], E.R.D. Scott[1], G.K. Benedix[1], A.J. Ehlmann[2], T.K. Mayeda[3] and R.N. Clayton[3], [1]Planetary Geosciences, Dept. of Geology and Geophysics, SOEST, Univ. of Hawaii, Honolulu, HI 96822, [2]Dept. of Geology, Texas Christian Univ., Fort Worth, TX 76129, [3]Enrico Fermi Inst., Univ. of Chicago, Chicago, IL 60637.

ABSTRACT - We have studied five meteorites [Wray (a), Cerro los Calvos, Willaroy, Moorabie and Suwahib (Buwah)] which differ from other chondritic meteorites and appear to form a new group. They are closely related to ordinary chondrites, but have lower FeO in the mafic silicates than H chondrites. Furthermore, their oxygen isotopic compositions are intermediate between E and H chondrites; they have highly variable metal contents, low Co concentrations in kamacite, and high troilite contents. The differences between low-FeO and H, L and LL chondrites appear to have been established in the solar nebula, not through parent body processes. Low-FeO chondrites did not originate on the H chondrite or IIE iron parent bodies, but probably represent a new ordinary chondrite parent body.

PROPERTIES - The low-FeO contents of Cerro los Calvos, Willaroy, Moorabie and Suwahib (Buwah) have been noted by several authors [e.g.,1,2] and these meteorites have been examined in detail [2]. We recently recognized the low-FeO nature of Wray (a) [3] and here report on our comparative studies.

Classification - Low-FeO chondrites are weakly metamorphosed and exhibit wide ranges of shock and weathering. Classification of petrologic types, shock stages [4] and weathering [5] are as follows: Wray (a): 4, S4, W1; Cerro los Calvos: 4, S2, W3; Willaroy: 3.8, S2, W4; Moorabie: 3.9, S4, W1; and Suwahib (Buwah): 3.8, S5, W1.

Mafic Silicate Compositions - Fa concentrations in low-FeO chondrites ($Fa_{12.8\text{-}15.3}$) are below those of H chondrites ($Fa_{16.9\text{-}20.4}$). Low-Ca pyroxene compositions are intermediate between H and E chondrites.

Metal and Troilite Abundances - Fe,Ni metal abundances in low-FeO chondrites are highly variable (11.2-19.4 wt.%, weathering corrected) and overlap with H and L chondrites. Troilite contents in the mildly weathered Moorabie (9.1 wt.%) and Suwahib (Buwah) (8.6 wt.%) are higher than found in any ordinary chondrite [6], although analyses of these meteorites by [7] suggest normal OC abundances of troilite. Sampling heterogeneity may be responsible.

Cobalt in Kamacite - The Co concentrations in kamacite of low-FeO chondrites (0.30-0.45 wt.% [2, this work]) are near or lower than those in H chondrites (0.44-0.51 wt.% [8]).

Chondrule Sizes - Low-FeO chondrites have mean chondrule diameters around 400 μm [Wray (a), Cerro los Calvos, Willaroy] and 600 μm [Moorabie, Suwahib (Buwah)]. These values are close to H (~300 μm) and L (~600-800 μm) chondrites [9]. The poorly constrained ranges of chondrule sizes in H, L and LL chondrites and large standard deviations for chondrule sizes in low-FeO chondrites suggest that this parameter is unreliable for establishing group membership.

Oxygen Isotopes - The $\Delta^{17}O$ values for low-FeO chondrites (0.32-0.87‰ [10,11]) are less than or equal to H chondrites (0.73±0.09‰,[10]). Moorabie and Suwahib (Buwah), which have slightly larger chondrules, also have higher $\Delta^{17}O$. Figure 1 plots the compositions of low-FeO chondrites, along with the fields for H, L, LL and E chondrites.

NEBULAR OR PARENT BODY ORIGIN FOR MINERALOGIC AND ISOTOPIC COMPOSITIONS?

WASSON *et al.* [2] suggested that Willaroy & Cerro los Calvos and Suwahib (Buwah) & Moorabie are H and L chondrites, respectively, that were incorporated into, and partially equilibrated with, aubritic material, primarily because their study of Cumberland Falls chondritic inclusions indicated formation by this mechanism. Low-FeO chondrites also lack the high siderophile abundances of Netschaëvo, which [12] called "HH" chondritic material based on extrapolation of H-L-LL trends. Because of the lack of definitive evidence for reduction (e.g., Fs>Fa) or a reducing host, high troilite contents, and short diffusion distances for oxygen in type 5 ordinary chondrites [10], we suggest nebular processes produced the low-FeO concentrations.

In fact, there is no reason to invoke parent body processes to produce the unusual compositions observed in low-FeO chondrites. Some properties of low-FeO chondrites do not fall on extrapolations of H-L-LL trends, owing to large variability within low-FeO chondrites. In fact, significant variability is also observed within other chondrite groups, particularly among type 3 chondrites. This variability causes overlap for some features between groups of ordinary chondrites (e.g., $\Delta^{17}O$ in L and LL chondrites). Variability of metal and troilite abundances comparable to those in low-FeO chondrites are observed in EH (17.5-23.8 wt.% Fe,Ni; 5.8-9.8 wt.% FeS; [13]) and, particularly, EL chondrites (1.6-28.0 wt.% Fe,Ni; 4.7-16.7 wt.% FeS; [13]). The variability of these properties reflects incorporation of different proportions of nebular components (e.g., matrix, type IA and II chondrules, metal), rather than parent body processes.

WHICH PARENT BODY SUPPLIED THE LOW-FeO CHONDRITES?

H Parent Body - Low-FeO chondrites have some properties identical to those in H chondrites and might have come from the H parent body. However, studies of H chondrite breccias [14,15] have not identified low-FeO chondritic clasts. A clast intermediate in chemical composition between H and E chondrites was identified [16], but this clast may have formed by shock melting. The absence of low-FeO clasts in H breccias suggests that these groups originated on different parent bodies.

Chondritic Material from the IIE Iron Parent Body - The low-FeO chondrites share many properties with highly metamorphosed, chondritic clasts in the IIE iron Netschaëvo. These clasts contain relict chondrules [17,18], have mafic silicate compositions ($Fa_{14.1}$,$Fs_{13.6}$,[17]) below H chondrites, contain abundant Fe,Ni metal (23.2 wt.%, this work) with 0.45 wt.% Co in kamacite [8] and have an oxygen isotopic composition intermediate between H and E chondrites ($\Delta^{17}O$=0.37,[19]). The major objection to a common parent body for low-FeO chondrites and IIE irons is the low petrologic types of the low-FeO chondrites. The IIE iron parent body was heated to high temperatures, as reflected by the formation of a core or metal pools, the highly metamorphosed silicates in Netschaëvo and differentiated silicates in Colomera. We question whether unequilibrated chondritic material could survive on this parent body and, thus, do not favor a common parent body for these two groups.

Another Ordinary Chondrite Parent Body - The most plausible scenario for the origin of the low-FeO chondrites is that they are samples of a separate parent body. The similarities between low-FeO and ordinary chondrites suggests that this is a new ordinary chondrite parent body, joining the H, L and LL parent bodies.

References: [1] Scott *et al.* (1985) *LPSC XVI*, 749-750. [2] Wasson *et al.* (1993) *GCA* **57**, 1867-1878. [3] Ehlmann and Keil (1994) *Meteoritics* **29**, (in press). [4] Stöffler *et al.* (1991) *GCA* **55**, 3845-3867. [5] Wlotzka (1993) *Meteoritics* **28**, 460. [6] Keil (1962) *JGR* **67**, 4055-4061. [7] Jarosewich (1990) *Meteoritics* **25**, 323-337. [8] Rubin (1990) *GCA* **54**, 1217-1232. [9] Grossman *et al.* (1988) In *Meteorites and the Early Solar System*, 619-659. [10] Clayton *et al.* (1991) *GCA* **55**, 2317-2337. [11] Clayton, pers. comm., 1993. [12] Bild and Wasson (1977) *Science* **197**, 58-62. [13] Keil (1968) *JGR* **73**, 6945-6976. [14] Keil (1982) In *Workshop on Lunar Breccias and Soils and their Meteoritic Analogs*, 65-83. [15] Wilkening (1977) In *Comets, Asteroids and Meteorites*, 389-396. [16] Leitch and Grossman (1977) *Meteoritics* **12**, 125-139. [17] Bunch *et al.* (1970) *Contrib. Min. Petrol.* **25**, 297-340. [18] Olsen and Jarosewich (1971) *Science* **174**, 583-585. [19] Clayton *et al.* (1983) *EPSL* **65**, 229-232.

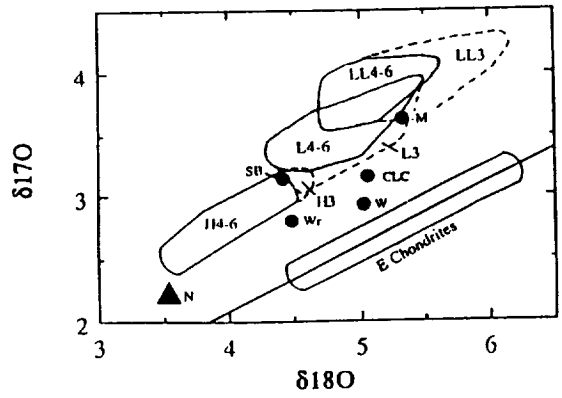

FIGURE 1. Oxygen isotopic compositions of low-FeO chondrites Wray (a) (Wr), Cerro los Calvos (CLC), Willaroy (W), Moorabie (M) and Suwahib (Buwah) (SB), as well as chondritic clasts in Netschaëvo (N), ranges for E chondrites, equilibrated H, L and LL chondrite falls (fields with solid lines) and unequilibrated H, L and LL falls and acid-washed finds (dashed fields).

EURECA'S HYPERVELOCITY IMPACT SCORE: MICROCRATER FLUX DECREASES BUT THE LARGE CRATER FLUX INCREASES IN SPECIFIC DIRECTIONS. J.A.M. McDonnell, Unit for Space Sciences, University of Kent at Canterbury, Canterbury, Kent CT2 7NR, U.K.

Eureca's 11 month space exposure in 1993-94 at a mean altitude of 508 km and orbital inclination 28.50° is very similar to both LDEF and Solar Max. From the TiCCE Capture Cell experiment aboard Eureca and other host surfaces, foil perforation distribution and crater diameter distributions have been analysed. We use for comparison the 6 point average of LDEF's records for aluminium surfaces, represents a tumbling spacecraft. Both SMM and Eureca are sun pointing and hence present over a long period a randomised exposure ('tumbling') to the orbital velocity vector.

Thus LDEF's 6 point average should therefore present a valid comparison to SMM and Eureca regarding Earth orbital components. For solar directional fluxes, however, the TICCE Eureca experiment should be more sensitive to the micron dimensioned β particles than this LDEF average.

Comparison between SMM and LDEF (exposure epochs 1980 -1984 and 1984-1990) show remarkable similarity even though on a short 10 day exposure in the middle of SMM's exposure (1982). Another perforation experiment on Space Shuttle flight 3 showed a flux a factor significantly below the average.

Eureca's exposure is, by contrast, very different from both LDEF and SMM, showing for microcraters a 10% **decrease** in the foil perforation flux. This should be compared to a 2% NASA guideline for microdebris growth rate and an assumed constant flux for natural particles.

For the "larger millicraters" (800 to 2000 μm), Eureca's flux is enhanced above LDEF by a factor of 8! If this were to be attributed to Space Debris, this flux would indeed appear to be in a runaway growth phase. But natural particulates are argued to be dominant in this increase for other reasons, namely:-

1. In size regimes where meteoroids are dominant, flux variations due to the exposure epoch and duration are evident.
2. The susceptibility of spacecraft to cometary and meteoroid sources is dependent on seasonal effects and satellite pointing direction over relatively short periods.
3. the increase of flux seen on the TICCE experiment and other faces is not apparent in the preliminary analyses of other faces. Despite the apparent randomisation of Eureca's pointing direction, the flux on different faces is not isotropic.
4. The growth of flux - and in many cases a decrease of flux - is inconsistent with the growth rate of space traffic or the accumulated manmade space population.

EVIDENCE FOR A PRE-NECTARIAN IMPACT BASIN IN NORTHWESTERN OCEANUS PROCELLARUM, Alfred McEwen, Philip Davis, and Annie Howington-Kraus, U.S. Geological Survey, Flagstaff, AZ 86001, and Merton Davies, RAND Corp., Santa Monica, CA 90407.

SUMMARY: The unified lunar control network [1,2] shows a large topographic low in the region of northwestern Oceanus Procellarum. This basin (here called the NW Procellarum basin) is almost entirely filled by mare lavas, whose surface is about 1734 km from the Moon's center of mass, 4 km below the global average. The basin has a diameter of about 700 km, comparable to that of the Serenitatis basin. Topography and partly flooded craters suggest that the mare lavas are more than 1 km deep. Craters of probable Nectarian age are superposed on the basin rim, suggesting that its age is pre-Nectarian. The Rumker and Mairan volcanic domes may be related to basin structures.

TOPOGRAPHIC DATA: Topographic and crustal-thickness lows in NW Procellarum are present in the maps of Bills and Ferrari [3]. Recently, we compiled a dataset of lunar altimetry in preparation for the Clementine mission. The data consist of Apollo 15-17 laser altimetry [4] and interpolated control points from telescopic observations [5], Mariner 10 [1,2], Apollo 15-17 metric cameras [6], and Zond-8 [7]. The dataset covers about 65% of the lunar surface. Davies et al. [2] recently updated the control net by (1) remeasuring the Mariner 10 points; (2) adding points on the far side from Lunar Orbiter [8], which were also identified in Apollo or Galileo images; and (3) recomputing the coordinates of points north of the Apollo region from Galileo images acquired during the second Earth-Moon flyby. The NW Procellarum basin is the only major topographic low in our altimetry compilation that is not within a previously postulated impact basin other than the Procellarum or Gargantuan basins. Davies et al. [2] measurements near the basin are shown on Figure 1. The basin is also apparent in the 1:2,000,000-scale nearside topographic map prepared by the Army Map Service (AMS) in 1963 [9], although the vertical and planimetric precision is suspect. We are in the process of digitizing the AMS map, so that it can be warped to match the unified control network.

DEPTH OF MARE FILL AND BASIN AGE ASSIGNMENT: Topographic data and geologic relations suggest that the mare fill in NW Procellarum is more than 1 km thick. Where topographic and mare thickness data are available for the Moon, thick lenses of basalt all occur in deep topographic lows [10]. There are no partly flooded craters in the NW Procellarum basin except near the margins. Imbrium basin materials overlie this entire region, so the basin must be pre-Imbrian. Typical Nectarian terrains contain a dozen or more craters larger than 100 km in diameter within an area the size of NW Procellarum basin. Mare lava must be more than 1.2 km thick to cover the rim of a 100-km-diameter crater with pristine depth-to-diameter dimensions [10]. Simulated floodings of impact basins suggest that actual lava thicknesses may be about twice that estimated from partially flooded craters [11]. The 125-km-diameter crater Repsold C, located near the northwest margin of the basin (latitude 48° N, longitude 73.5° W) is completely flooded in its interior, and lavas cover the southeast half of its rim. According to the technique of De Hon [10], this indicates that the southeast half is buried under at least 1.25 km of mare lava. The northwest half is near the mare-highlands boundary, so this crater probably lies on the rim of the topographic basin. Several other large craters in this region (Sinus Roris) have south and/or east rims that are partially buried; all are considered of possible Nectarian age [12], suggesting that the NW Procellarum basin is older Nectarian or pre-Nectarian. If isostatic compensation has not taken place in response to the basalt emplacement, then the original basin must have been at least 1 km deeper than the present one. Its total relief was probably at least 4 km, comparable with the relief of other lunar impact basins. There are only weak positive gravity anomalies over NW Procellarum [13], suggesting that there is either less mare fill or greater isostatic compensation than in the pronounced mascons (Imbrium, Serenitatis, Crisium, and Nectaris).

PROBABLE IMPACT ORIGIN OF NW PROCELLARUM BASIN: The NW Procellarum basin is probably of impact origin, even though rings around or within the basin are not obvious in the best available images (Lunar Orbiter IV low-sun images at 50-100 m/pixel resolution). However, impact is the only process known to create large topographic depressions on the Moon. Also, the basin is roughly circular (irregularities are probably due to Imbrium ejecta). If the basin is older Nectarian or pre-Nectarian, then many large impact craters such as those apparent on the western and northern margins would have largely obliterated the ring structure on the surface. Other pre-Nectarian basins, such as Mare Australe, also have very poorly defined

PRECEDING PAGE BLANK NOT FILMED

PAGE 868 INTENTIONALLY BLANK

rings, and even the Imbrium rings are poorly defined or absent over large sections due to burial by thick mare flows. Furthermore, some ring structures of NW Procellarum may be tentatively identified. An outer ring (Figure 1) may be marked by asymmetrical crater walls near the western margin (cf. LO IV-175-M), mare ridges and a massif west of crater Lichtenberg to the southwest, and the Mairan domes and three source craters for sinuous rilles to the east [14]. A buried inner ring may be marked by a 200-km-diameter circular pattern of wrinkle ridges and the Rumker hills (cf. LO IV-170-H2).

RUMKER HILLS AND MAIRAN DOMES: The Rumker hills and Mairan domes occur within the NW Procellarum basin (Fig. 1); they were perhaps localized by the basin structure. The Mairan domes, which may consist of more viscous lavas than typical mare basalts [15], lie near the basin's margin. The Rumker hills complex, which consists of a polygonal plateau covered by low domes [15], lies along mare ridges that form a circular pattern, perhaps over a buried inner ring. Wilhelms [12] showed an irregular (noncircular) outer Imbrium ring passing through the Rumker hills, but the ring is poorly defined over this region. The intersection of Imbrium and NW Procellarum rings could be related to the uplifted block of the Rumker hills, similar to the uplifted block at the Imbrium-Serenitatis ring intersection [16].

RELATION TO POSTULATED PROCELLARUM BASIN: The NW Procellarum basin (and indeed nearly all nearside maria) is within the hypothetical Procellarum basin [17], and several features ascribed here to the NW Procellarum basin have been attributed to the big Procellarum basin [12]. However, the big Procellarum basin is thought to have experienced significant viscous relaxation, which would account for the lack of topographic expression over most of its postulated extent. Topographic relief of up to 4 km in NW Procellarum is not consistent with significant viscous relaxation. Therefore, the identification of the NW Procellarum basin diminishes some of the evidence for the Procellarum basin.

REFERENCES: [1] Davies, M.E. et al., 1987, JGR 92, 14,177. [2] Davies, M.E. et al., 1994, in preparation. [3] Bills, B.G., and Ferrari, A.J., 1977, JGR 82, 1306. [4] Kaula, W.M. et al., 1974, LPSC 5, 3049. [5] Meyer, D.L., 1980, DMA TR 80-001. [6] Doyle, F.J. et al., 1977, NOAA Tech. Rep. NOS 70, NGS 5. [7] Aleksashin, E.P. et al., 1989, Zond-8 Selenocentric Coordinate System, Moscow, 181 pp. [8] Defense Mapping Agency, 1974, Catalog of Lunar Positions, St. Louis AFS, Missouri. [9] Army map Service, 1963, Topographic Lunar Map, 1:2,000,000, 6 sheets. [10] De Hon, R.A., 1979, PLPSC 10, 2935. [11] Head, J.W., 1982, The Moon and the Planets 26, 61. [12] Wilhelms, D.E., 1987, USGS Prof. Pap. 1348, 302 pp. [13] Muller, P.M., and Sjogren, W.L., 1968, Science 161, 680. [14] Whitford-Stark, J.L., and Head, J.W., 1980, JGR 85, 6579. [15] Scott, D.H., and Eggleton, R.E., 1973, USGS Map I-805. [16] Spudis, P.D., and Head, J.W., 1977, LSCP 8, 2785. [17] Whitaker, E.A., 1981, LPSCP 12, 105.

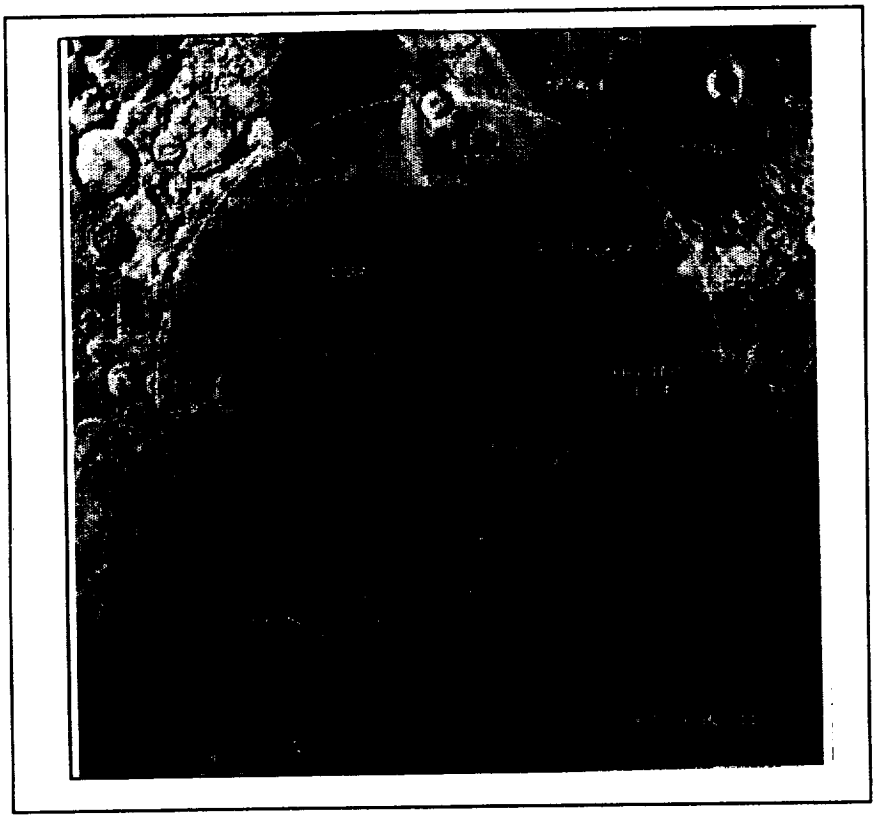

Figure 1. Lunar airbrush map reprojected to Orthographic projection, centered on latitude +42 degrees, longitude 62.5 degrees west, the approximate center of the NW Procellarum basin. Circle of 700 km diameter shows possible basin ring. Lunar radii [2] in kilometers are shown.

GLOBAL COLOR VIEWS OF MARS; A.S. McEwen, L.A. Soderblom, T.L. Becker, E.M. Lee, J.D. Swann, R. Aeschliman, and R.M. Batson, U.S. Geological Survey, Flagstaff, AZ 86001.

About 1000 Viking Orbiter red- and violet-filter images have been processed to provide global color coverage of Mars at a scale of 1 km/pixel. Individual image frames acquired during a single spacecraft revolution ("rev") were first processed through radiometric calibration, cosmetic cleanup, geometric control, reprojection, and mosaicking [1]. We have produced a total of 57 "single-rev" mosaics. Phase angles range from 13 to 85 degrees. All of the mosaics are geometrically tied to the Mars Digital Image Mosaic (MDIM), a black-and-white base map with a scale of 231 m/pixel [2].

In producing a global mosaic from Viking images with useful color and albedo information for the surface, the largest challenge has been the photometric normalization, including removal of atmospheric effects. First, we selected a subset of single-rev mosaics that provide the best global coverage (the least atmospheric obscuration and seasonal frost). A Minnaert photometric normalization was applied to normalize the variations in illumination and viewing angles. Image data acquired at illumination or emission angles larger than 77 degrees were trimmed off, as these data are strongly affected by atmospheric scattering. A model image of condensate haze was created from the violet images, consisting of 60% of the violet-filter reflectance greater than 0.05, smoothed over 20-km scales. The haze model was then subtracted from both the violet- and red-filter images. The residual polar caps were excluded from haze removal. This procedure is "conservative" in the sense that it errs on the side of undercorrecting for the haze. Finally, these normalized mosaics were combined [3] into global mosaics. Global coverage is about 98% complete in the red-filter mosaic and 95% complete in the violet-filter mosaic. A green-filter image was synthesized from an average of the red- and violet-filter data to complete a three-color set. (The Viking Orbiters acquired actual green-filter images covering about 60% of the Martian surface; we plan to mosaic these images in the near future.)

Two final datasets have been produced: "cosmetic" and "scientific" versions. For the cosmetic version, gaps were filled by interpolation, the violet-filter images were given a divide filter to remove residual atmospheric hazes, and digital airbrushing was applied to remove residual seams and other artifacts. (The divide filter consists of dividing the value of each pixel by the average value over a 200-km^2 area surrounding each pixel.) The north polar region contains the largest gaps and poorest color data, due to the typical atmospheric conditions and the geometry of the Viking orbits. For large areas near the north pole with red-only coverage, the violet-filter coverage was synthesized by using a function fit to actual Mars red- and violet-filter data. For the scientific versions, data gaps were left blank and the divide filtering and digital airbrushing were not applied. About 30% of the violet-filter data are obscured by hazes to an extent that makes the data unreliable for quantitative analyses of the surface color.

The final mosaics have been reprojected into several map projections: Sinusoidal Equal-Area (global), Lambertian Equal- Area (east- and west-hemisphere views), Polar Stereographic (half-planet views of the

northern and southern hemispheres), Mercator (equatorial region), and orthographic views centered on six different positions. The orthographic views are most like those seen by a distant observer looking through a telescope. All versions exist both with and without latitude-longitude overlays.

The color balance selected for these images was designed to be close to natural color for the bright reddish regions such as Tharsis and Arabia, but the data have been "stretched" such that the relatively dark regions are darker and less reddish than their natural appearance. This stretching allows us to better see the color and brightness variations on Mars, which are related to the composition or physical structure of the surface materials. Note that these images are also unnatural because most atmospheric effects have been removed and because we see the summertime appearance of both polar caps simultaneously.

Five major surface units can be mapped from the global mosaics: (1) bright red regions such as Tharsis, Arabia, and Hellas, which have properties consistent with surface deposits of fine-grained dust such as that carried aloft by dust storms [4]; (2) dark regions, which have properties consistent with coarse- grained sand and rock fragments [4]; (3) intermediate-brightness regions, which may have rough, indurated surfaces [5]; (4) the bright north polar residual cap, which consists of water ice mixed with dust [6]; and (5) the very bright south polar residual cap, which probably consists of carbon dioxide ice [7].

The global color mosaics have been merged with the MDIM in a set of 30 quadrangles covering Mars at a scale of 462 m/pixel. These products show both the surface morphology as seen from imaging at low sun-elevation angles and the color and albedo information best seen at high sun elevations. The datasets were merged in the following steps: (1) extracting red and violet color data (cosmetic versions) for a quadrangle and making the red/violet ratio, (2) reprojecting the red and red/violet ratio to the same map projection and scale as the MDIM quadrangle, (3) choosing match points and warping the color images to improve the geometric registration, (4) adding the red and MDIM files to create a merged red, (5) dividing the merged red by the red/violet ratio to make a merged violet, and (6) averaging the merged red and violet files to create a synthetic merged green image.

References: [1] McEwen, A.S. and Soderblom, L.A. (1993) LPS XXIV, 955-956. [2] Batson, R.M. and Edwards, K. (1990) NASA TM-4210, 573. [3] Soderblom, L.A. et al. (1978) Icarus 34, 446-464. [4] Christensen, P.R. and Moore, H.J. (1992) in Mars, Kieffer, H.H. et al., Eds, pp. 686-729. [5] Kieffer, H.H. et al. (1981) Proc. Lunar and Planet. Sci. Conf. 12, 1395-1417. [6] Kieffer, H.H. et al. (1976) Science 194, 1341-1344. [7] Kieffer, H.H. (1979) J. Geophys. Res. 84, 8263-8288.

HOW TO ACQUIRE PHOTOGRAPHIC PRODUCTS: This project was completed by many individuals at the U.S. Geological Survey in Flagstaff, Arizona, under contract to NASA. Photographic products can be purchased from Newell Color Lab, 221 N. Westmoreland Ave., Los Angeles, CA 90064, tel.: (213) 380 2980, fax: (213) 739 6984. A small number of prints or transparencies may be acquired for educational purposes from Kathy Hoyt, USGS, Flagstaff AZ 86001, tel.: (602) 556 7264, fax: (602) 556 7090. All of these datasets will be written to CD-ROMs for distribution of the digital datasets by the Planetary Data System (PDS). These should include 8-bit color versions in CompuServe GIF format.

V, CR AND MN PARTITION COEFFICIENTS BETWEEN MANTLE MINERALS AND SILICATE MELT; Elisabeth A. McFarlane*, Michael J. Drake* and David C. Rubie#. *Lunar and Planetary Laboratory, University of Arizona, Tucson, Arizona 85721, U.S.A; #Bayerisches Geoinstitut, Universität Bayreuth, D-95440 Bayreuth, GERMANY.

Introduction: The abundances of V, Cr, and Mn in the mantles of the Earth and Moon are very similar to each other, and differ from all other sampled differentiated planetary bodies (e.g. Drake *et al.*, 1989). The origin of this similarity is currently unknown, but is not attributable to metal/silicate fractionation at pressures from 1 bar to 165 kbars, or to differential volatility (Drake *et al.*, 1989; Ringwood *et al.*, 1991; Hillgren *et al.*, 1994, this volume). Mg-perovskite and magnesiowüstite are the dominant phases in the lower mantle of the Earth. The present work examines whether the V, Cr and Mn abundance pattern for the mantle of the Earth (and Moon) can be explained through high pressure and temperature fractionation of Mg-perovskite and magnesiowüstite from a silicate melt during a postulated magma ocean phase (e.g., Agee and Walker, 1988). Also investigated is the effect of fractionation of these two phases on some refractory and moderately lithophile elements (Ca/Ti, Mg/Si, Si/Ca, Si/Al) which are inferred to be approximately chondritic in the upper mantle of the Earth (e.g. Jagoutz *et al.*, 1979; see also Kato *et al.*, 1988a,b; McFarlane *et al.*, 1990,91a,91b; Drake *et al.*, 1993).

Experimental: An experiment using a mantle composition (KLB-1) was doped with V, Cr and Mn and was run using a 1200 ton multianvil apparatus at the Bayerisches Geoinstitut. A 7 mm MgO (+5 wt. % Cr_2O_3) octahedron was used together with 3 mm truncation edge lengths on the WC anvils. The sample was contained in a Re capsule, and high temperature was generated using a cylindrical $LaCrO_3$ resistance heater. Experiment UHP.723 was run at a hotspot temperature of 2650 (±100)°C and 24.5 (±0.5) GPa for 13 minutes, within the stability field of Mg-perovskite. Partition coefficients between quenched liquid and crystalline phases were measured in the vicinity of the liquidus which is estimated to have been at a temperature of 2400 (± 100)°C. Analysis was by CAMECA SX-50 electron microprobe. The structural identity of the Mg-perovskite was confirmed using X-ray microdiffractometry.

Results: Mg-perovskite/melt partition coefficients and 2 sigma uncertainty estimates are: Na=0.2(±0.1), Mg=1.0(±0.2), Al=1.3(±0.1), Si=1.18(±0.04), Ca=0.5(±0.1), Ti=1.4(±0.3), V=1.14(±0.06), Cr=1.1(±0.1), Mn=0.62(±0.08), Fe=0.6(±0.05), Ni=0.3(±0.1). Magnesiowüstite/melt partition coefficients and 2 sigma uncertainty estimates are: Na=0.8±0.2, Mg=2.3±0.1, Al=0.38±0.01, Si=0.01±0.001, Ca=0.017±0.004, V=0.45±0.01, Cr=1.27±0.03, Mn=0.77±0.06, Fe=1.43±0.05, Ni=4.1±0.4. The results of several subsequent experiments, performed at 25 GPa and 2700°C to investigate the partitioning of Ni, Co, Ga, Mo, Cr, Ge, La, Sm, Eu, Lu, Hf, Rb, Cs, Na, and K, will also be presented.

Discussion: The abundances of V, Cr and Mn in the upper mantle of the Earth decrease in the order V>Cr>Mn (Drake *et al.*, 1989). Figure 1 shows the relative abundance pattern that would result in the upper mantle of the Earth with the fractionation of Mg-perovskite from a melt. Manganese would be most abundant and V and Cr would be present in lesser and approximately equal abundances. Figure 2 shows the relative abundance pattern that would result in the upper mantle of the Earth with the fractionation of magnesiowüstite from a melt. The resulting relative abundance pattern would be V>Mn>Cr. These results show that the V, Cr and Mn abundance pattern of the mantle of the Earth (and Moon) do not result from high pressure and temperature fractionation of Mg-perovskite and/or magnesiowüstite at conditions relevant to the uppermost lower mantle of the Earth.

The ratios of partition coefficients for some refractory and moderately refractory lithophile elements deviate significantly from one. If Mg-perovskite and/or magnesiowüstite segregated from a terrestrial magma ocean, nonchondritic ratios of some refractory and moderately refractory lithophile elements (Ca/Ti, Mg/Si, Si/Ca, Si/Al) would be imparted upon the primitive upper mantle of the Earth, contrary to inference based on analyses of naturally

occurring samples. Olivine addition into the upper mantle can be invoked to eliminate this constraint for some elements (e.g., Mg/Si), but will exacerbate the problem for other elements (e.g., Si/Ca, Si/Al). There is no surviving evidence of mineral fractionation implying that either (a) the Earth was never substantially molten at the end of accretion; (b) segregation of minerals from magma was suppressed by some mechanism; (c) some other mechanism masked evidence of fractionation; or (d) partition coefficients change significantly at pressures above 25GPa.

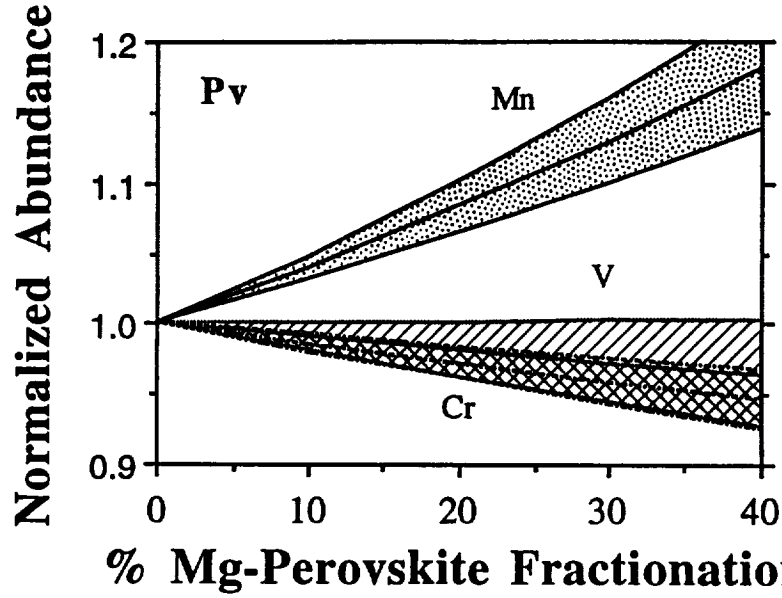

Figure 1. The pattern of V, Cr, Mn abundances that would be observed in the upper mantle of the Earth with the fractionation of Mg-perovskite from a melt, such as might have occurred during a postulated magma ocean stage. Initial abundances are defined to equal 1.0. Most likely estimates leave Cr more depleted than V, although their uncertainty envelopes overlap. Partition coefficient values used are those given in this abstract. Mg-perovskite segregation is not responsible for the pattern of V, Cr, and Mn abundances which are inferred for the primitive upper mantle of the Earth.

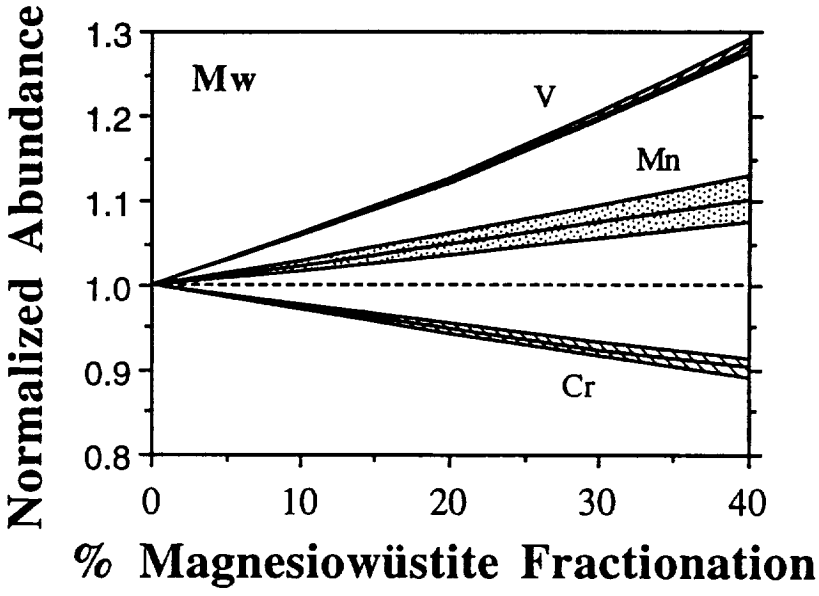

Figure 2. The pattern of V, Cr, Mn abundances that would be observed in the upper mantle of the Earth with the fractionation of magnesiowüstite from a melt, such as might have occurred during a postulated magma ocean stage. Initial abundances are defined to equal 1.0. Partition coefficient values used are those given in this abstract. Magnesiowüstite segregation is not responsible for the pattern of V, Cr, and Mn abundances which are inferred for the primitive upper mantle of the Earth.

References: Agee, C.B. and Walker, D. *Nature* **349**, 834-837. Drake, M.J. *et al.* (1989) *Geochim. Cosmochim. Acta*, **53**, 2101-2111. Drake *et al. (1993) JGR Planets* **98**, 5427-5431. Jagoutz, E. *et al. (1979) Lunar Planet. Sci. X.*, 2031-2050. Kato, T. *et al.* (1988a) *Earth. Planet. Sci. Lett.* **89**, 123-145. Kato, T. *et al.* (1988b) *Earth. Planet. Sci. Lett.* **90**, 65-68. McFarlane, E.A. *et al.* (1990) *Lunar and Planetary Science XXI*, 759-760. McFarlane, E.A. *et al.* (1991a) *Magma Oceans Workshop.* McFarlane, E.A. *et al.* (1991b) *Lunar and Planetary Science XXII*, 875-876. Ringwood, A.E. *et al.* (1991) *Icarus* **89**, 122-128.

Acknowledgements: The high pressure experiment reported above was conducted at the Bayerisches Geoinstitut. This research is supported by grant EAR 93-03676. EAM is supprted by NASA GSRP grant NGT 50612.

LUNAR FERROAN ANORTHOSITE SUBGROUPS; J. J. McGee, U. S. Geological Survey, Reston, VA 22092

Introduction: The concept that the entire suite of ferroan anorthosites was derived from a single parent magma, such as might be expected by crystallization of a magma ocean, is being evaluated by comparing internally consistent compositional data for the minerals in the ferroan anorthosite subgroups (mafic magnesian, mafic ferroan, anorthositic ferroan and, anorthositic sodic) identified by James *et al.* [1]. Data for relic igneous clasts are obtained in order to attempt to examine igneous compositional variations. These data will aid in evaluating the petrogenetic significance of the anorthosite subgroups. A previous report [2] presented extensive data for the anorthositic ferroan (or "typical") subgroup. In this report, data are reported for the following samples from the other three subgroups: 67635,8 and 67637,9 (anorthositic sodic); 15437,4 (mafic magnesian); 67915,12 (mafic ferroan).

Characteristics of 'typical' ferroan anorthosites: These rocks have < 5%, relatively ferroan, mafic minerals. In most of the typical anorthosites, low-Ca pyroxene is the dominant mafic mineral; mg' [100 x molar Mg/(Mg+Fe)] generally ranges from 52 to 67. Rocks with homogeneous pyroxenes appear to be monomict, whereas the anorthosites with heterogeneous pyroxenes are interpreted as polymict. The overall continuity of pyroxene compositions, however, suggests that all of the lithologies within the polymict rocks were derived from ferroan anorthosite-suite rocks. Concentrations of the minor elements Al, Ti, Cr, and Mn in pyroxenes show somewhat varied behavior. Cr and Ti contents of low-Ca pyroxenes are approximately constant across the entire range of mg' in the anorthosites, and there is a uniform amount of excess Al, substituting as ^{VI}Al-^{IV}Al, in the pyroxenes. The Mn contents of the pyroxenes show some variation, with the more magnesian pyroxenes having more varied Mn than the Fe-rich pyroxenes. Anorthite [100 x molar Ca/(Ca+Na+K)] contents of plagioclase in the "typical" anorthosites range from $An_{95.9}$ to $An_{98.9}$ [2]. Nearly all the anorthosites show systematic trends of decreasing magnesium and iron concentrations in plagioclase as the An content increases. Post-crystallization reequilibration and shock deformation have redistributed the minor element contents of some samples. For example, 15415 plagioclase shows little variation in either Fe or Mg and has homogeneous An content. This homogeneity appears to be a product of metamorphic recrystallization and reequilibration, as supported by this sample's annealed polygonal texture. Plagioclases in the more highly shocked anorthosites show considerable scatter in their Fe and Mg contents, presumably due to redistribution during shock. The overall variation of plagioclase An content versus low-Ca pyroxene mg' in the typical anorthosites shows no clear trend.

Anorthositic sodic subgroup: The two samples studied, 67635 and 67637, are granulated and sheared and contain abundant plagioclase fragments, as much as 0.5 mm across, and < 1% mafic minerals. Two large (~2 mm), sheared granulitic, partly disaggregated lithic clasts are present in 67635. The mafic minerals in 67635 are homogeneous high-Ca (mg' = 77.5) and low-Ca (mg' = 68.8) pyroxene. In 67637, pyroxene compositions are slightly more varied (high-Ca pyroxene mg' = 72-75; low-Ca pyroxene mg' = 60-70), and olivine (mg' = 57-63.5) is present. Plagioclase compositions (Fig. 1) have similar ranges (An_{94} -An_{98}) and averages (An_{95}-An_{96}) in both samples. Plagioclase FeO and MgO contents show regular trends as a function of An content, with somewhat more variation in FeO in 67637's plagioclase (Fig. 1).

Mafic magnesian subgroup: Anorthosite 15437 is shocked and granulated; most clasts are angular mineral fragments of twinned plagioclase, as much as 1 mm across, but matrix areas have some polygonalized texture, a remnant of annealing. Mafic minerals are locally concentrated and make up ~5-8% of the sample. Mafic-mineral compositions are homogeneous and relatively magnesian (low-Ca pyroxene mg' = 73.5; high-Ca pyroxene mg' = 81.5; olivine mg' = 67.5). Plagioclase compositions have a range of $An_{96.5}$-An_{99} and average $An_{97.3}$ (Fig. 1). Plagioclase FeO and MgO show smooth,

slightly declining trends as An increases (Fig. 1). One nicely preserved lithic clast, 1 mm across, has intergranular texture with twinned plagioclase (0.3 mm) and a large (0.1 x 0.3 mm) interstitial, high-Ca pyroxene grain; the mineral compositions are similar to those in the rest of the sample.

Mafic ferroan subgroup: Anorthosite 67915,12 is a clast from a polymict breccia. The anorthosite has been shocked, granulated and sheared, and its plagioclase has been partly converted to maskelynite. The rock contains ~5% mafic minerals, as much as 1 mm across. Olivine is the most abundant of these. Mafic mineral compositions are fairly homogeneous (low-Ca pyroxene mg' = 67.5; high-Ca pyroxene mg' = 75.5; olivine mg' = 59). Plagioclase compositions have a range of $An_{94.9}$-$An_{98.3}$ and average $An_{95.8}$ (Fig. 1). Plagioclase FeO and MgO trends are somewhat scattered, presumably due to redistribution during shock deformation .

Discussion: As in the "typical" anorthosites, in the samples of the other three subgroups the FeO and MgO contents of plagioclase decrease regularly as An content increases (Fig. 1). FeO contents of plagioclase are higher than MgO contents; in the anorthositic sodic samples, MgO is nearly undetectable in the high-An plagioclase, but increases in the low-An plagioclases, consistent with the trends observed in the other samples (Fig. 1). The mg' of plagioclase shows a weak but negative correlation with An content in 67635, 67637, and 67915. Coexisting relict low-Ca pyroxene/plagioclase pairs among the samples show no clear correlations of mg' in low-Ca pyroxene with plagioclase An content. The consistent patterns of variation of FeO and MgO in plagioclase in all the ferroan anorthosites suggest that the ferroan anorthosite subgroups are related and that crystallization conditions have been partly preserved through their disturbed history.

References: [1] James O.B., Lindstrom M.M. and Flohr M.K. (1989) PLPSC 19, 219-243. [2] McGee J.J. (1993) J. Geophysical Research-*Planets*, v. 98, 9089-9105.

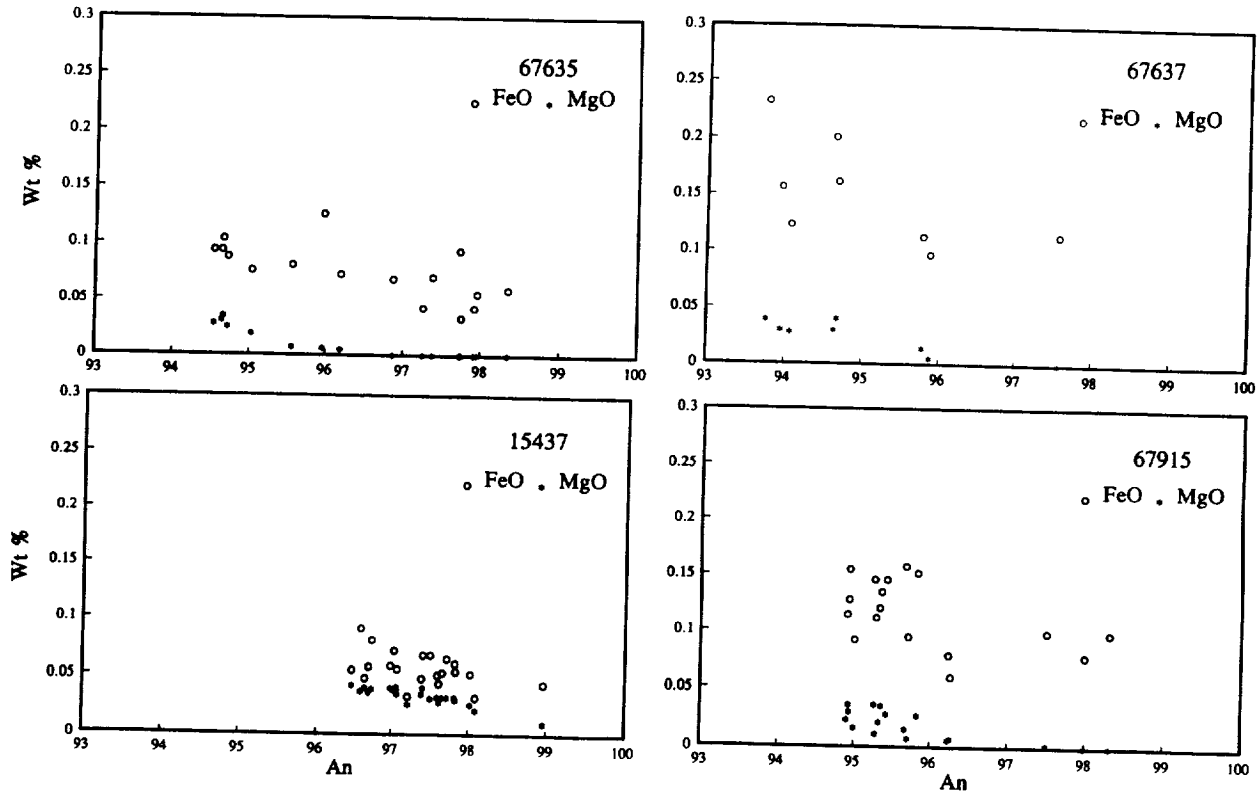

FIGURE 1. FeO and MgO contents (wt %) of plagioclase versus An content for anorthosites 67635, 67637, 15437, and 67915.

EVOLUTION OF A HOT SPOT, CENTRAL EISTLA REGIO, VENUS; George E. McGill, Department of Geology and Geography, University of Massachusetts, Amherst, MA 01003-5820.

Hot spots are believed responsible for a significant fraction of the heat lost from the interior of Venus [1,2]. Two types of features are believed to be associated with venusian hot spots: coronae and large shield volcanoes [3]. In central Eistla Regio there is a complex elevated region, referred to as "Sappho Regio" by Senske et al. [4], that includes the large shields Sappho and Anala [3,4,5]. Closely associated with these shields are several coronae and corona-like features, including Nehalennia and Sunrta. Peripheral to Sappho Regio are several more coronae and at least two moderate-sized shields. All of these features lie on or near curvilinear tectonic belts of diverse types. The close association of shields and coronae suggests that there may be a genetic link between them. Geological mapping and structural analysis of central Eistla Regio indicates that the coronae are older than the large shield volcanoes. Thus it is inferred that this hot spot evolved from producing coronae to producing large shields.

Central Eistla Regio lies entirely within the Sappho Patera (V20) 25° x 30° Quadrangle, for which I am preparing a geological map. Relative ages of major tectonic and volcanic features can be determined by traditional stratigraphic techniques such as superposition and cross-cutting relationships of associated material units, and also by abutting and offsetting relationships between structural features such as grabens, wrinkle ridges, and fracture fabrics, as previously discussed [5,6]. A greatly simplified sketch map (below) shows some of the most important structures and features.

The youngest major features are the shields Anala and Sappho. Flows from Anala (Af on the map) are superposed on fractures related to the corona Nehalennia, truncate the unnamed corona SE of Nehalennia, are diverted around the raised rim of the corona Sunrta, and are diverted by the topography of the Sappho shield. Flows from Sappho (Sf) are superposed on fractures related to the corona Nehalennia. Wrinkle ridges are extremely rare on Anala and Sappho flows, whereas they are common to abundant on most other material units. A roughly north-south fracture and graben trend (labeled 2 on the map) links Sappho and Anala, and extends on to the north (and possibly to the south), suggesting that Sappho and Anala developed in a stress regime characterized by extension oriented about east-west. The youngest wrinkle ridges (not shown) on the plains peripheral to Sappho and Anala are generally concentric to these shields and may represent gravity-driven compression of the very shallow crust, comparable to the model proposed for the Tharsis rise on Mars [7].

Most wrinkle ridges are older than Anala and Sappho, but younger than the coronae. The density of wrinkle ridges is very inhomogeneous, and locally there are distinct belts of unusually abundant wrinkle ridges (shown by wiggly lines on the map). These belts of wrinkle ridges appear to be truncated by Anala flows, and one belt clearly truncates the intense concentric structure of Nehalennia Corona. In general, wrinkle ridges of the dominant set, which varies in trend from WNW to ENE, show clear evidence that they are younger than the concentric structures of the coronae. The graben and fracture trend (Guor Linea; labeled 1) that extends from Gula Mons towards Sappho and Anala, and that may continue eastward [5] beyond Sappho and Anala to the Corona Libera (off the map), also is clearly younger than the corona Nehalennia and older than Sappho and Anala, but of uncertain age relative to the dominant wrinkle-ridge set. This graben and fracture trend implies a stress regime characterized by extension oriented roughly NNE, with evidence for limited dextral shear parallel to the trend as well. The trend of the regional wrinkle ridges implies the existence of a roughly coeval ~N-S compression in the shallow crust.

East of Anala and Sappho are two moderate-sized complexes of digitate flows emanating from low shields, one of which is on the map (Uf). These shields are characterized by a density of superposed wrinkle ridges that is much greater than for Anala and Sappho, but less than for the surrounding plains. It thus is likely that the small shields are only slightly younger than the coronae in this region. Much of the area of the V20 quadrangle is underlain by plains materials. Most of these materials appear to be relatively old, but the SAR data do not permit consistent mapping of subdivisions of these plains that can be arranged in chronological order. It is possible to define local "members" of known age relative to surrounding materials, and a small radar-dark patch (Pd) appears to be the youngest material in the area. Most of the unlabeled area on the map consists of undifferentiated plains, and both fractures related to coronae and wrinkle ridges are superposed on these plains. Isolated within these plains are small patches of even older highly deformed plains and tessera (not shown).

Thus the general sequence of materials and structures in the area shown on the map is: 1) tessera and highly deformed plains; 2) undifferentiated plains; 3) coronae; 4) regional wrinkle ridges, wrinkle-ridge belts, moderate-sized shields, Guor Linea; 5) Sappho; 6) Anala, Anala-Sappho graben system; 7) radar-dark plains, wrinkle ridges concentric to Anala and Sappho. It is generally inferred that both coronae and large shields lie above rising diapirs

or plumes in the mantle [3,4,5,8,9], the contrast between coronae and shields commonly explained as due to a difference in scale, with coronae lying above relatively small diapirs, large shields and volcanic rises above larger mantle plumes [3]. The relationships in Sappho Regio and environs suggest a more complex model in which a large plume spawns a cluster of coronae first, and large shields later. There is no obvious lateral shift of the lithosphere involved, because the shields occur among the coronae rather than to one side of them. The locus of major shield volcanism is the intersection of the two most prominent trends of grabens and fractures, similar to the relationship in the Sekmet Mons area [10]. The chronology reported here implies that the diapirs responsible for the coronae arrive at the base of the lithosphere before the main pulse of thermal energy responsible for the regional volcanic rise and the large shield volcanoes.

1. Phillips, R.J. et al., *Science, 212*, 879-887, 1981.
2. Morgan, P. and R.J. Phillips, *J. Geophys. Res., 88*, 8305-8317, 1983.
3. Stofan, E.R. et al., *J. Geophys. Res., 97*, 13,347-13,378, 1992.
4. Senske, D.A., et al., *J. Geophys. Res., 97*, 13,395-13,420, 1992.
5. Grimm, R.E., et al., *J. Geophys. Res., 97*, 16,035-16,054, 1992.
6. McGill, G.E., *Geophys. Res. Letts., 20*, 2407-2410, 1993.
7. Maxwell, T.A., *J. Geophys. Res., 87*, A97-A108, 1982.
8. Squyres, S.W., et al., *J. Geophys. Res., 97*, 13,611-13,634, 1992.
9. Janes, D.M., et al., *J. Geophys. Res., 97*, 16,055-16,067, 1992.
10. Zimbelman, J.R., *Geol. Soc. Am., Ann. Mtg. Abs.*, A221, 1993.

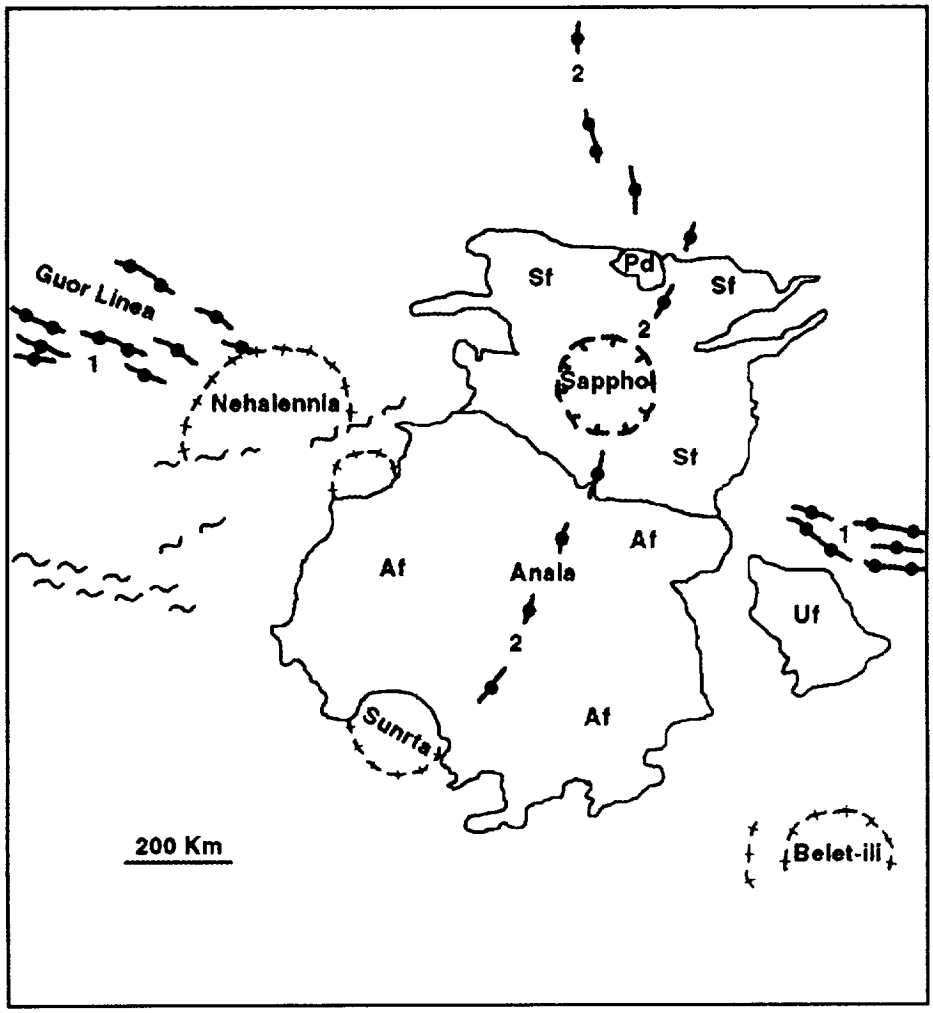

S24-10 NASA CR
3626

PRODUCTION OF FERROAN ANDESITES BY THE EXPERIMENTAL PARTIAL MELTING OF AN LL CHONDRITE; J.C. McGuire, SUNY Stony Brook, Stony Brook NY 11794; A.J.G. Jurewicz, LESC C23, 2400 NASA Rd. 1, Houston TX 77058; and J.H. Jones, SN4 NASA/JSC, Houston TX 77058.

A partial melting experiment on the St. Severin (LL) chondrite produced a melt that was andesitic, having 54-60 wt% silica, at 1200°C and an oxygen fugacity (fO_2) of IW+2, two log units above the iron-wüstite (IW) buffer *[1]*. Under these same conditions, CV, CM and L chondrites produced low-silica melts (~40 wt% silica) resembling angrites *[1,2]*. This experimental study attempts to reproduce and explain this unusual result.

INTRODUCTION: Previous studies have shown that, depending upon the oxygen fugacity, partial melts of CV, CM and H chondritic meteorites resemble either angrites or eucrites, two types of meteoric basalts *[2,3]*. The fO_2 controls the silicate phase equilibria indirectly by changing the FeO/Fe^0 ratio of the iron in system. For volatile-free CV, CM and H chondrites, partial melts produced at IW+2 (where there is no Fe^0) were low in silica (~40%), and resemble angritic meteorites. Conversely, the melts formed at IW-1 (where there is 2-7 wt% Fe^0) were higher in silica (~48-50 wt%) and resemble eucrites (Fig. 1). In sharp contrast, the partial melting experiment on the St. Severin (LL) chondrite run at 1200°C and IW+2 produced melts unlike any other. It did not resemble any known meteorite, being *much* too siliceous (~54-60 wt%). This study investigates this unusual result.

METHODS: Two starting materials were used: 1) a powder of actual St. Severin silicate (courtesy of E. Jarosewich, Smithsonian Institution) to which powders of iron and nickel metal were added to duplicate the bulk meteorite composition *[4]*, and 2) a synthetic, partially-glassed St. Severin simulant. The simulant was used in all experiments to conserve the real St. Severin; however, charges of the natural St. Severin were run with the simulant in the 1200°, 1150°, and 1120°C experiments. This duplication ensured that the simulant accurately reproduced the St. Severin phase equilibria, especially at low temperatures.

Experiments were conducted by placing pressed-pellets of starting materials in a reusable platinum basket which was then hung in a vertical, controlled-atmosphere furnace. The basket was saturated from previous use, so that negligible iron was lost from the samples *[2,3]*. The oxygen fugacity (IW+2) was controlled by a flowing mixture of CO and CO_2 *[5,6]*.The oxidation state of the mixed gas was monitored in a remote furnace using a solid electrolyte cell and oxygen as a reference gas *[6]*. It is important to note that this method of controlling fO_2 allows volatile-loss from the sample to the furnace gas.

The isothermal experiments were performed in the temperature range of 1120° to 1240°C, and lasted 4 to 7 days, with the lower-temperature experiments running for longer durations. One additional experiment, specifically designed to test the effect of sodium on the phase equilibria, ran for 2 days at IW-1 and 1300°C to volatilize Na_2O, and then ran isothermally at IW+2 and 1210°C to re-equilibrate the charge. To minimize quench effects, samples were drop-quenched into de-ionized H_2O. After sectioning, mounting and polishing, identification of phases and broad observations were made using a JEOL scanning electron microscope. A Cameca electron microprobe was used for compositional analyses at 15kV and 30 nA. Several examples of each phase were analyzed at points ~10 microns from phase boundaries to minimize fluorescence and quench effects.

RESULTS: All isothermal charges contained a high silica melt (54-60 wt% SiO_2), olivine (65-69 m% Fo), and low-calcium pyroxene (62-70 m% En; 2-10 m% Wo), as well as minor chromite and Fe-Ni sulfide. In addition, a high-calcium pyroxene (46 m% En; 44 m% Wo) was found in the 1120°C charge. Plagioclase was not observed.

Equilibrium was evaluated in several ways. For example, Fe/Mg olivine/melt distribution coefficients ($^{ol/melt}K_{DFe/Mg}$) ranged from 0.32 to 0.36, in good agreement with the values obtained for other experiments having similar phase equilibria *[2,3,7]*. Similarly, mass balances reproduced the starting compositions and calculated consistent phase abundances, suggesting that the measured compositions were representative [Fig. 2].

The extremely high silica contents and the major element ratios of the melts from the isothermal experiments differ significantly from the IW+2 melts of other meteorites, as shown by their CIPW norms [cf., Fig. 1]. Additionally, the St. Severin phase assemblages consist of a high-silica melt coexisting with equilibrium olivine, pyroxene (both with low CaO contents), and chromite; whereas other chondritic IW+2 melts coexist with olivine and pyroxene (both with higher CaO contents), and hercynitic spinel. In terms of the silica content, the volatile-rich St. Severin melts can best be compared to ferroan andesites, whereas melts from other chondritic IW+2 melts look more like angrites. In fact, the volatile-rich St. Severin melts are higher in silica than the partial melts of H, CM, and CV chondrites produced at IW-1 *[2,3,8 and Table 1]*.

PRODUCTION OF FERROAN ANDESITES: J.C. McGuire *et al.*

One experiment was performed in which a St. Severin charge was pre-processed at IW-1 in order to remove the 1-3 wt% sodium that persisted in the melts of charges from the other experiments. After sodium had been volatilized, the melt produced was ~7 wt% lower in silica [Table 1]; however, this melt was still much more siliceous than IW+2 melts from other types of chondrites. Moreover, the silica content of this melt resembled those from other chondrites run at IW-1, and the equilibrium phase assemblage contained low-calcium pyroxene and chromite rather than hercynitic spinel.

DISCUSSION: Partial melts of St. Severin differ from IW+2 melts observed in charges from other meteorites melted under the same conditions in two ways. First, at the high fO_2, it is (kinetically) difficult to devolatilize the sodium from the melt and -- as the experiment in which the charge was subjected to a pre-processing showed -- the residual Na_2O is partially responsible for the high silica content of the melts. This is consistent with the observations of *[9]* on the effect of Na_2O on the forsterite-protoenstatite boundary. A comparison of phase abundances calculated for the volatile-rich and volatile-free charges shows that there is a decrease in the percentage of pyroxene present. However, pyroxene alone would not have enough silica to account for the very high silica; plagioclase is the only solidus phase that could account for up to 60 wt% SiO_2 in the melt.

Still, even the sodium-free St. Severin charge contains a siliceous melt and a phase assemblage unlike that observed in the CV, CM, and H chondrites at IW+2, but more like that observed at IW-1 (~49 wt% SiO_2). Again, fO_2 affects the silicate phase equilibria in the H, CV, and CM chondrites indirectly: when the fO_2 is changed from IW-1 to IW+2, metal is oxidized. The FeO and NiO from the metal effects the silicate phase equilibria. If enough metal is oxidized, hercynitic spinel is stabilized, and the melts produced are silica-poor (~40 wt% SiO_2) *[2,3]*. But St. Severin has an intrinsically low Fe/Si ratio, so the melting relations don't shift even after all its iron is FeO. Therefore, the high-iron phase assemblages seen in charges of other chondrites melted at IW+2 can not be produced, and the melting relations in the bulk St. Severin resembles that of other chondrites at IW-1.

REFERENCES: *[1]* Egon Weber (1992) *LPI 8th Annual Summer Intern Conf. [abst.]* 31-33; *[2]* Jurewicz *et al.* (1991) *Sci.* **252** 695-698; *[3]* Jurewicz *et al.* (1993) *Geochim. Cosmochim. Acta* **75** 2123-2139; *[4]* Jarosewich (1990) *Meteoritics* **25** 323-337; *[5]* Deines *et al.* (1974) *Bull. Earth Mineral Sci. Exp. Sta.* **88** 129p; *[6]* Jurewicz *et al.* (1993) *NASA Tech. Memo.* **104774** 37p.; *[7]* Stolper (1977) *Geochim. Cosmochim. Acta* **41** 587-611; *[8]* Jurewicz *et al* (1994) *Lun. Planet. Sci. Conf.* XXV this volume; [9] Kushiro (1975) *Am. J. Sci.* **275** 411-431

Table 1. St. Severin (LL) partial melts produced with and without preprocessing at IW+2, and at IW-1. Melts of Lost City (H) *[1,8]* are given for comparison.

	St. Severin			Lost City	
	High Na_2O	Low Na_2O			
fO_2	IW+2	IW+2	IW-1	IW-1	IW+2
T(°C)	1200	1210	1200	1200	1200
SiO_2	57.4	50.6	50.7	50.8	40.2
TiO_2	0.31	0.38	0.47	0.40	0.50
Al_2O_3	10.2	9.96	13.0	11.1	11.9
FeO*	16.2	21.9	17.8	22.0	28.9
MnO	0.26	0.28	0.32	0.29	0.26
MgO	6.22	7.67	7.31	6.85	5.48
CaO	6.91	7.92	8.39	8.11	10.9
Na_2O	2.20	0.31	0.69	0.33	0.49
NiO	0.07	0.18	0.04	0.06	0.31
Total	100.3	99.3	99.3	100.0	99.8

* all iron as FeO.

Figure 1. Comparison of CIPW norms from St. Severin IW+2 partial melts*[this study]*, with those of CM, CV, and H chondrites at IW+2 and IW-1 *[cf., 1,2,3,8]*, as well as eucrites and angrites.

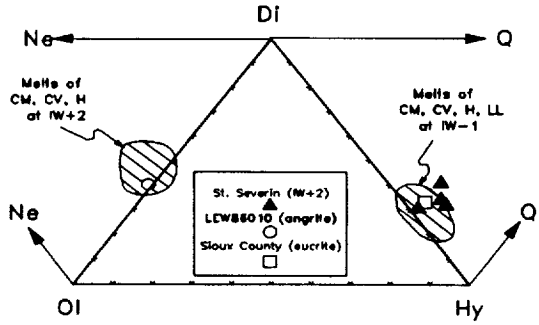

Figure 2. Abundance of silicate phases as a function of temperature. Minor chromite and sulfide are also present. Note: olivine and pyroxene define a peritectic. Symbols: Open is simulant; solid is St. Severin.

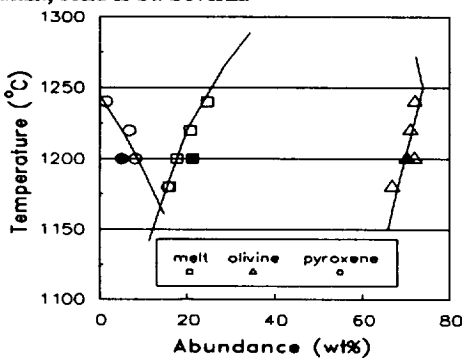

APATITE FISSION-TRACK AGE OF MARQUEZ DOME IMPACT STRUCTURE, TEXAS:

John F. McHone and Rasoul B. Sorkhabi, *Geology Dept., Arizona State University, Tempe, AZ 85287-1404*

Summary. Fission tracks in apatites from a Marquez Dome impact breccia indicate the occurrence of a strong thermal pulse at 58.3 ± 3.1 Ma., followed by a period of rapid cooling. This radiometric age for the Marquez impact event is in excellent agreement with a previously determined stratigraphic age of 58 ± 2 Ma. [2].

Background. A 15 kilometer diameter circular structure is buried by flat-lying Paleocene-to-Eocene sediments in Leon County, east central Texas [1-4]. Cretaceous marls and shales are uplifted some 1,200 meters above regional stratigraphic elevation and form a 3 kilometer wide central dome which is partially exposed near the town of Marquez. The feature is located at the western margin of the East Texas salt-diapir province and was first interpreted as a salt dome [4] but later recognition of shatter cones and shock-metamorphosed mineral grains confirmed its impact origin. A preliminary stratigraphically constrained impact age [1] between 50 and 66 Ma. temporarily identified Marquez Dome as a candidate K/T boundary event. However, further refinements [2] established a stratigraphic age of 58 ± 2 Ma or Paleocene/Eocene.

Sample Selection and Analysis. Some 766g of weakly consolidated sandy material was collected from the exposed *white breccia dikes* described by Sharpton and Gibson [2]. Clays and silts were removed by repeated ultrasonic baths and the remaining 444g of granular sample were processed by a Frantz magnetic separator and heavy liquids to isolate the apatite fraction.

Results and Discussion. In the past three decades fission track techniques have been successfully used to date numerous impact structures and products [5]. Here we present a fission-track analysis of apatites from the Marquez Dome impact structure. Two separate apatite mounts were made for polishing and etching. Each mount was irradiated separately and detailed analytical data are presented in table 1. In both mounts, single grain ages point to annealing of preexisting fission tracks by a strong thermal event at around 58 Ma. Relatively long (> 14μm) confined fission tracks in these grains indicate rapid cooling of the host rock after thermal annealing [6]. A few grains yielding much older ages (table 1) were not considered pertinent to this thermal event in view of their significantly shorter (<12μm) tracks. These grains are possibly contaminants from an older provenance. It should be noted that confined track lengths were measured on the same single grains for which ages were determined. Therefore, although we present a low number of track length measurements, they produce a more accurate representation of the thermal history of the individual grains. The figures next to table 1 are histograms showing the distribution of single grain ages (hollow columns) and confined track lengths (solid columns) for the two separate apatite mounts.

Conclusions Fission tracks in apatite grains separated from an impact breccia dike at the Marquez Dome impact structure indicate the occurrence of a strong thermal pulse at 58.3 ± 3.1 Ma (mean age for all counted grains with longer tracks) followed by rapid cooling of fission tracks as evidenced from track-length distribtion. This radiometric date supports the previously estimated stratigraphic age of 58 ± 2 Ma [2] and provides an independent evidence for the occurrence of the Marquez impact event near the Paleocene/Eocene boundary.

Acknowledgments Fieldwork and sample collection was supported by a grant from the Barringer Crater Company. We wish to thank Dr. V.L. Sharpton and Dr. Gordon Bell for able guidance and field assistance and Prof. Edmund Stump for his support of fission-track research at Arizona State University.

References. [1] Gibson J.W.Jr and Sharpton V.L. (1989) EOS, 70, no. 15, 383. [2] Sharpton, V.L. and Gibson, J.W.Jr. (1990) *Lunar & Planet. Sci. Conf. 21st*, 1136. [3] Wong A.M. et al. (1993),*Lunar & Planet. Sci. Conf. 24th*, 1533. [4] Stenzel, H.B. (1938) *Univ. Texas Publ. 3818*, 193. [5] Wagner, G. and Van Den Haute, P. (1992) *Fission Track Dating*, Kluwer Academic Publishers, pp. 217-225. [6] Gleadow et al. (1986) *Cont. Min. Pet.* 94, 405.

FISSION-TRACK AGE OF MARQUEZ ASTROBLEME, TEXAS: McHone J.F. and Sorkhabi R.B.

Table 1. Fission-track analytical data of apatite grains from sand breccia dike sample of Marquez impact structure in Texas

Grain	$\rho_s \times 10^6$ (cm^{-2})	N_s	$\rho_i \times 10^6$ (cm^{-2})	N_i	Uranium (ppm)	Age±1σ (Ma)
Mount #1 (Irradiation data: ρ_d: 1.510x10^6 cm^{-2}; N_d: 7177)						
1	0.3542	18	2.558	130	17	33.8±8.5
2	0.1102	76	0.6611	42	4	40.6±16.6
3	1.3850	88	5.194	330	34	64.9±7.9
4	0.9759	62	5.352	340	35	44.5±6.2
5	0.2274	13	1.434	82	9	38.7±11.6
6	0.4985	19	1.705	65	11	71.1±18.6
7	0.5037	32	3.022	192	20	40.6±7.8
8	1.4570	50	6.529	224	43	54.4±8.6
9	0.1259	8	0.3778	24	2.5	81.0±33.1
10	0.1574	10	0.7555	48	5	50.8±17.7
11	0.8185	52	5.068	322	33	39.4±5.9
12	0.6926	22	1.763	56	12	95.7±24.1
13	0.3463	22	1.039	66	7	81.0±20.0
14	2.066	105	6.493	330	43	77.4±8.8
15	0.1417	9	0.6611	42	4	52.2±19.2
					Mean age:	**57.7±5.1**
Old-age grains with largely shortened tracks (11.24±0.46 µm mean length for 13 tracks with standard deviation (s.d.) of distribution as 1.67 µm)						
16	0.9759	62	1.8110	115	12	130.6±20.7
17	4.596	146	4.533	144	30	243.4±28.9
Mount #2 (Irradiation data: ρd: 1.520x10^6 cm^{-2}; N_d: 9572)						
1	0.2361	15	0.7870	50	5	73.5±21.7
2	0.4093	26	2.015	128	13	49.8±10.7
3	0.0629	4	0.2883	18	2	54.5±30.1
4	0.3778	24	2.204	140	14	42.1±9.3
5	0.2361	15	1.133	72	7	51.1±14.5
6	1.511	48	7.555	240	49	49.1±7.8
7	0.2991	19	1.669	106	11	44.0±11.0
8	0.3778	24	1.574	100	10	58.8±13.4
9	0.1574	10	0.9444	60	6	40.9±14.0
10	0.2361	6	1.023	26	7	56.6±25.6
11	0.6296	40	1.637	104	11	94.0±17.6
12	0.3778	12	1.763	56	12	52.6±16.7
13	0.4250	27	1.181	75	8	88.0±19.8
14	0.5352	34	2.235	142	15	58.71±11.2
15	0.2361	15	1.055	67	7	54.9±15.7
16	0.4407	28	2.109	134	14	51.2±10.7
17	0.1574	6	0.6296	24	4	61.3±28.0
18	2.597	66	8.264	210	54	76.9±10.9
					Mean age:	**58.6±3.3**
Old-age grain with largely shortened tracks (11.87±0.70 µm mean length for 7 tracks with standard deviation (s.d.) of distribution as 1.84 µm)						
19	1.994	76	1.994	76	13	241.7±39.4

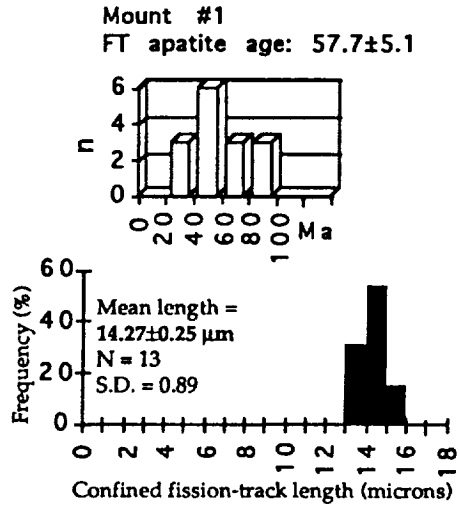

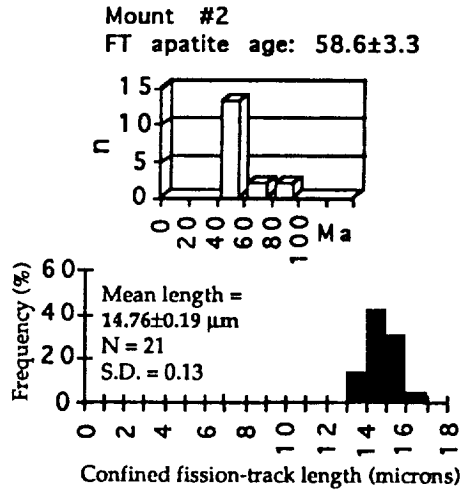

ρ_s = spontaneous fission track density; N_s= number of spontaneous fission tracks counted; ρ_i = induced fission track density; N_i = total number of induced fission tracks counted; ρ_d = induced fission track density in the dosimeter glass NBS-SRM612; N_d = total number of induced tracks counted to determine ρ_d; External detector method for fission-track dating was used. Zeta value used for calculating ages was 324±4 calibrated for the glass dosimeter NBS-SRM 612. Apatites were mounted in epoxy resin and etched with 5N HNO_3 for 20 seconds at 20°C. Muscovite detector was etched in 40% HF for 20 minutes at 20°C. Irradiation was done at the Georgia Institute of Technology Nuclear Reactor (with Cd for Au ratio of 280). The tracks were counted under dry objectctive (1250X magnification, Nikon). All experimental procedure in this study was carried out by the author RBS.

SYNTHETIC AND NATURAL NAKHLA PYROXENES: PARENT MELT COMPOSITION AND REE PARTITION COEFFICIENTS. **G. McKay (SN4, NASA-JSC, Houston, TX,77058) L. Le, and J. Wagstaff (Lockheed ESCO, 2400 NASA Rd. 1, Houston, TX 77058)**

Summary. Nakhla is one of the SNC meteorites, generally believed to be of Martian origin. It is composed mainly of cumulus augite [e.g., 1], in which primary igneous zoning is apparently preserved [2], and which thus serves as a recorder of the composition of Nakhla's parent melt and the conditions under which it crystallized. Knowledge of the composition and petrogenesis of this parent melt may help unravel Nakhla's relationship to the other SNCs, and provide clues to Martian petrogenesis in general. This abstract reports new results of an ongoing study [3 , 4 , 5] in which we are (1) comparing the major and minor element compositions of synthetic pyroxenes crystallized from various proposed parent melt compositions with those in Nakhla pyroxene to constrain the composition of the parent melt, and (2) measuring minor and trace element partition coefficients, particularly those of the REE, in order to obtain the most applicable D values with which to invert the natural pyroxene compositions to obtain the trace element composition of the parent melt. Results suggest that recent estimates of Nakhla's parent melt composition [6 , 7] are too aluminous, and that mafic or ultramafic melts are more likely candidates. REE partition coefficients for such melts are 2-4x lower than those for "normal" basaltic melts.

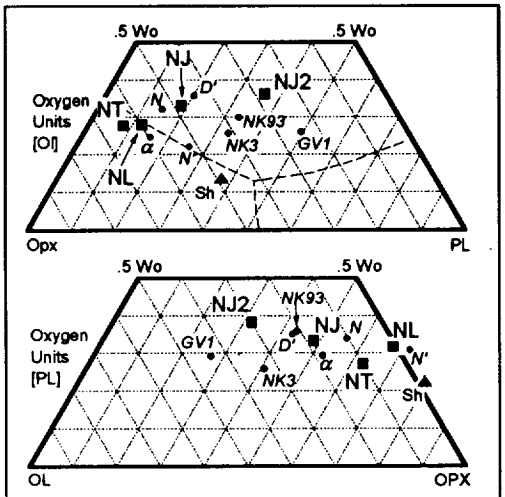

Fig. 1. Projections from Ol (top) and Pl (bottom) showing our quenched melt compositions (NT,NL,NJ,NJ2), the Shergotty analog melt for which we previously measured DREE (Sh), and proposed nakhlite parent melt compositions N [8], α [9], NK3 and GV1 [6], NK93 and N' [7], and D' [1,7.]. Olivine-saturated multiple saturation curves are after Longhi and Pan [8]. The starting compositions for our experiments are based on Longhi & Pan's composition N (our NL), an abandoned Tennessee composition α (our NT), a variation of Treiman's now-abandoned composition *D'* (our NJ), and Treiman's recent composition NK3 (our NJ2.).

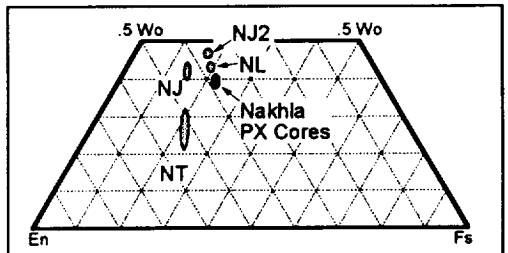

Fig. 2. Comparison of major element compositions of synthetic pyroxenes with those of natural pyroxene cores in Nakhla.

Experiments. We have studied (1) pyroxene/melt equlilbria and (2) partitioning of REE and Sr for four synthetic compositions resembling several proposed Nakhla parent melt compositions, as shown in Fig. 1. These compositions ranged from "ultramafic", with Al_2O_3 < 3 wt% and FeO + MgO > 35 wt%, to "basaltic", with Al_2O_3 ~ 8% and FeO + MgO ~ 23%. Charges were doped with 0.5-1% REE oxide or $SrCO_3$, placed on Pt wire loops, fused at 1300°C overnight in gas mixing (CO/CO_2) furnaces, quenched, and then placed back in the furnaces at temperatures just below the pyroxene liquidus (~1200°C for NL, ~1215°C for NT, ~1225°C for NJ and ~1150°C for NJ2) at fO_2 = QFM and quenched after ~4 days. Quenched charges contained glass, a small amount of Ca-rich pyroxene, and spinel. Crystals and melts were analyzed for major and trace elements with the electron microprobe. We have previously reported results for NL, NT, and NJ, and here we report new results for NJ2.

Results: Pyroxene compositions. Fig. 2 compares quadrilateral components of pyroxenes from our experiments with those of pyroxene cores in Nakhla. Each balloon contains virtually all analyzed pyroxenes from several experiments with the indicated starting composition. Except for NT pyroxenes (which have a range of Wo contents), the synthetic pyroxenes are nearly homogeneous in quadrilateral components. All are slightly less Fe-rich than Nakhla cores, suggesting the Nakhla parent melt had slightly higher *fm* values than any of our starting compositions. The NT pyroxenes are significantly lower in Wo than Nakhla cores, while NL and NJ2 pyroxenes are slightly higher. Wo content of synthetic pyroxenes appears to roughly anti-correlate with proximity to the low-Ca liquidus phase volume in Fig. 1, and thus to the degree of "over-" or "under-saturation" in low-Ca pyroxene. Our experiments appear to bracket the degree of low-Ca pyroxene "undersaturation" of the Nakhla parent melt.

A major issue for Nakhla petrogenesis is whether the parent melt was ultramafic or basaltic. As pointed out by Longhi and Pan [8], pyroxene equilibria can help constrain this issue. Fig. 3 compares

NAKHLA PYROXENES: PARENT MELT AND PARTITION COEFFICIENTS

McKay, G. *et al.*

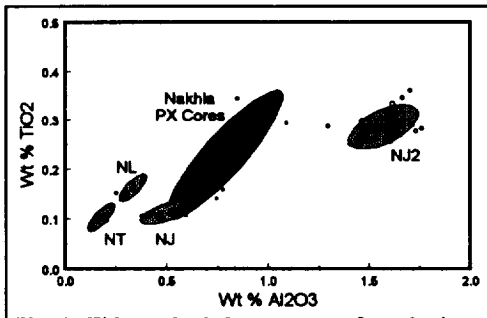

Fig. 3. TiO_2 and Al_2O_3 contents of synthetic pyroxenes and natural pyroxene cores in Nakhla. Each dot represents an individual pyroxene analysis. For synthetic pyroxenes, analyses were taken on several spots per grain, several grains per charge, and several experiments per starting composition. Nakhla analyses were taken on several spots per grain, on many grains.

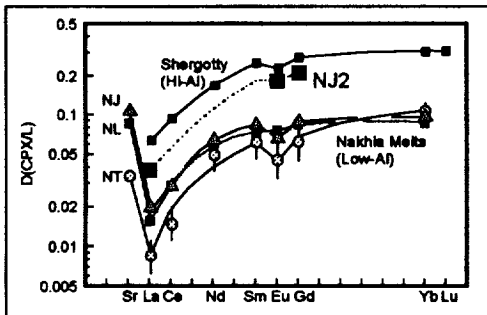

Fig. 4. REE and Sr pyroxene/liquid partition coefficients. Shergotty values are extrapolated from values observed for less calcic pyroxenes [10]. Values for low-Al Nakhla melts are from [3, 4]. Values for NJ2, our "basaltic" Nakhla parent melt composition, are new data.

Al_2O_3 and TiO_2 contents of our synthetic pyroxenes with those of Nakhla pyroxene cores. Al contents of NT and NL pyroxenes are significantly lower than those for Nakhla, while the most Al-rich pyroxenes from our NJ experiments overlap the Nakhla field. NJ2 pyroxenes contain *considerably* more Al than the Nakhla core pyroxenes. Thus, taken at face value, the data in Fig. 3 suggest that the Al content of the Nakhla parent melt is somewhat higher than that of our low-Al starting compositions (NL, NT, and NJ), but considerably lower than that of our high-Al composition (NJ2).

REE and SR partition coefficients. Fig. 4 shows partition coefficient patterns for each of our Nakhla starting compositions, together with a pattern derived from our experiments on a Shergotty parent melt [10]. We computed the latter pattern by extrapolating the partition coefficients observed for Wo_{12-25} pyroxenes in our Shergotty experiments to $Wo_{\sim 40}$ (the composition of the natural pyroxene cores in Nakhla), using equations for variation of D_{REE} with pyroxene Wo content from [10] .*

Compared with the "ultramafic" Nakhla compositions NJ, NL, and NT, the melt in the Shergotty experiments was rich in Al, and we had speculated [3, 4] that it was this difference in Al content that was largely responsible for the 3-8 fold difference in partition coefficient values. However, the Shergotty values were extrapolated, and the melts in that study differed in many compositional details from proposed Nakhla parent melts. Thus, without actual measurements for high-Al Nakhla parent melt compositions, we could not be sure that the low values might not hold even for high-Al melts.

Our new results for the NJ2 composition confirm our earlier speculation that D values from the low-Al melts are too low to be applicable if the Nakhla pyroxenes crystallized from one of the proposed high-Al melts. It is not clear whether the difference in Al content is responsible for most of the difference in D values, or whether the large difference in temperature (1150°C vs. 1200°-1230°C) is the most important factor. In either case, it is clear that use of the "wrong" set of partition coefficients for inverting the Nakhla pyroxenes to obtain the melt REE content can lead to errors of up to ~500% in estimated REE concentrations. Thus, in order to compute the trace element composition of the Nakhla parent melt with any confidence, it is important to gain a better understanding its major element composition, especially its Al content and liquidus temperature.

Sector zoning in pyroxene: A messy complication. Although Fig. 3 suggests that our experiments provide good constraints on the Al content of the Nakhla parent melt, this interpretation may be oversimplified. We previously reported a strongly bimodal distribution of Al concentrations in Nakhla pyroxene cores [5] Our early attempts at elemental mapping indicated that this distribution is not simply a result of normal core-to-rim primary zoning, but is the result of a more complex process such as sector zoning. We have not had the opportunity to collect additional mapping data on Nakhla sections, so do not yet completely understand the cause or nature of this Al zoning, or how it relates to our synthetic pyroxenes. However, a bimodal distribution of Al contents for NJ2 pyroxenes is clearly evident in Fig. 3, with one cluster of analyses around 1.5% Al_2O_3 and one around 1.7%. BSE photos and elemental mapping indicate that sector zoning is responsible for this zoning. Additional work will be required to understand the implications of this zoning for attempts to constrain the composition of the Nakhla parent melt.

References: [1] Treiman (1986) GCA 50, 1061. [2] Harvey and McSween (1992) GCA 56, 1655. [3] McKay *et al.* (1992) LPS XXIII, 643. [4] McKay *et al.* (1993) LPS XXIV, 966. [5] McKay *et al.* (1993) Meteoritics 28, 395. [6] Harvey and McSween (1992) EPSL 111, 467. [7] Treiman (1993) GCA 57, 4753. [8] Longhi and Pan (1989) PLPSC 19, 451. [9] Harvey and McSween (1991) Met. Soc. Abs., 85. [10] McKay *et al.* (1986) GCA 50, 927.

* $D^{Px/L}$ values observed for Yb and Lu for Wo_{25} pyroxenes in [10] were nearly as high as the extrapolated Wo_{40} values in Fig. 4, but the D_{La} and D_{Ce} were closer to the values in Fig. 4 for the low-Al Nakhla melts.

VENUSIAN CHANNEL GRADIENTS AS A GUIDE TO VERTICAL TECTONICS;
L.C. McLeod and R.J. Phillips, McDonnell Center for the Space Sciences and Dept. of Earth and Planetary Sciences, Washington University, St. Louis, MO 63130.

Introduction. We are investigating topographic gradients along lava channels and on lava flows to constrain vertical tectonism on a local and regional scale on Venus. It has been noted previously that there are both lava flows and channels that flow "uphill" [e.g., 1]. The gradient of the flows, during active fluid movement, must have been downslope with reference to an equipotential surface. A positive gradient along the topographic profile of a channel or lava flow implies post-flow differential surface elevation changes and provides evidence of tectonic and volcanic activity since the time of active fluid flow. It is suggested that these channels and lava flows can, therefore, be used as paleoindicators of local and regional tectonism.

Approach. We have examined the longest recognized channel for evidence of tectonism and volcanism associated with reverse topographic gradients. Hildr Fossa was first identified as a tectonic feature from Venera 15/16 data [2]; the Magellan mission enabled scientists to reclassify it as a lava channel approximately 7000 km in length. The elevation profile along Hildr Fossa was determined through the use of spherical harmonic representations of Venusian topography and geoid. The geoid-corrected topography along Hildr Fossa (Fig. 1) is not consistently downslope. When the geology is examined along the channel, it is observed that the slope changes are correlated with features such as volcanism, rifts and ridges. We conclude that the short and intermediate wavelength topography can be explained by local tectonism and volcanism that occurred after the channel formed. The long-wavelength geoid (Fig. 2) is not correlated with long-wavelength topography along the channel. This suggests that large-scale elevation variations in this region are not related at present in a direct way to mantle convection, but are instead the result of lithospheric processes.

Ongoing Efforts. Currently, we are compiling a global database of geoid-corrected elevations for all mapped channels and are using these profiles to construct maps of change in regional slope. This database will also include topographic profiles of lava flows in the regions in which the channels are found, the majority of which are located in the equatorial area of the planet and are associated with highlands, rift and fracture zones, and volcanic features [3]. We propose that the knowledge of internal processes that result in vertical tectonism can be improved by examining (i) geoid-corrected topographic gradients, (ii) relative ages of the flows and channels (determined by superposition relationships and by the weathering degradation state of the surfaces [4]), and (iii) regional variations in gravity.

References. [1]] V.R. Baker *et al.*, *J. Geophys. Res.* **97**, 13,421 (1992); [2] V.A. Kotelnikov, V.R. Yashenko, and A.F. Zolotov, *Atlas of the Surface of Venus*, Main Board of Geodesy and Cartography, Ministers of the U.S.S.R., Moscow (1989); [3] G. Komatsu *et al.*, *Icarus* **102**, 1 (1993); [4] R.E. Arvidson *et al.*, *J. Geophys. Res.* **97**, 13,303 (1992).

FIGURE 1

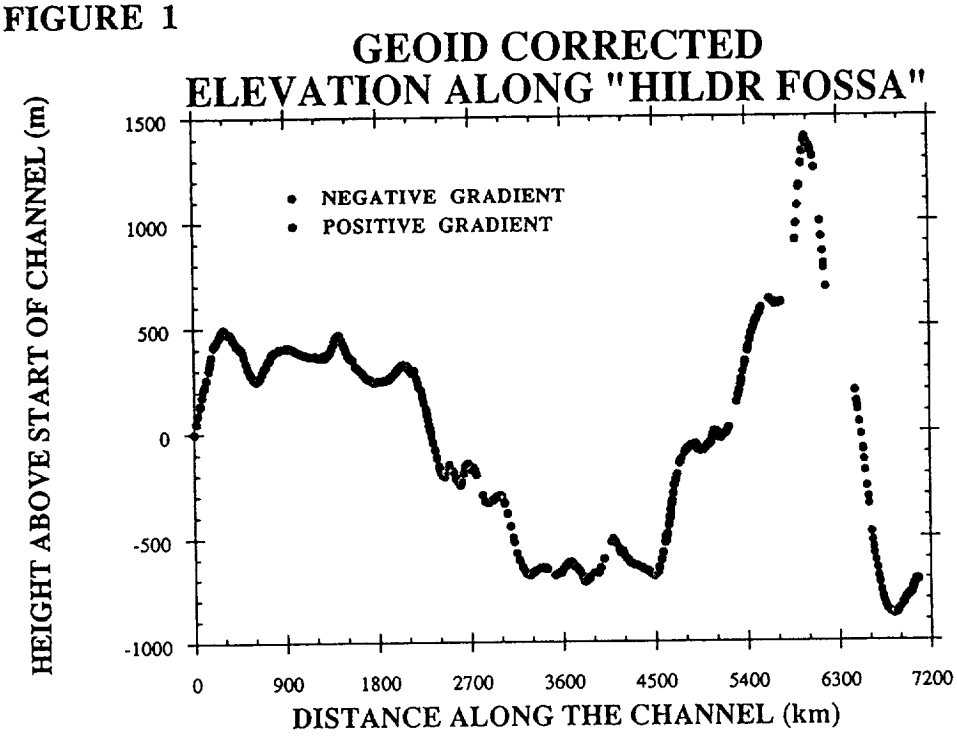

FIGURE 2

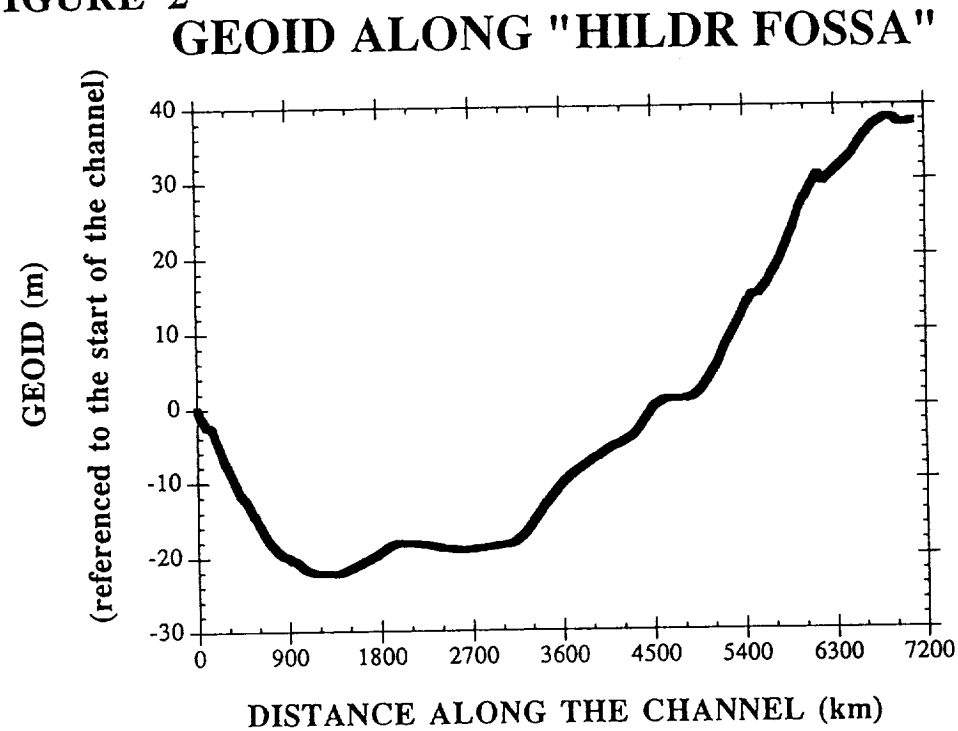

The distribution and source of Na in two type B1 CAIs

G.P. Meeker, USGS, Denver Federal Center 903, Denver CO 80225

Sodium occurs as a major element in nepheline and sodalite in the "low temperature" alteration veins, and Wark-Lovering rims of type A and B CAIs. It has been suggested that these phases record the initial condensation of Na in the solar nebula (see 1 for discussion). Sodium also occurs as a trace element in the primary phases in coarse-grained CAIs and is concentrated in melilite and anorthite. The presence of Na in the these higher temperature phases is not consistent with the predicted compositions of high-temperature condensates from a gas of solar composition (2). Higher concentrations (>0.1 wt%) of Na in melilite and anorthite in some inclusions has been shown to correlate with regions of isotopically "disturbed" Mg, suggesting that the introduction of Na might be part of a secondary process (3). It has also been demonstrated that Na concentrations in some, but not all, melilite crystals in type B CAI correlates with Akermanite (3). El Goresy et al., (4) suggested that Na in Allende inclusion 5241 was introduced by xenoliths that were captured while the inclusion was still a liquid droplet. This would mean that Na had condensed prior to the formation of the secondary alteration products in 5241.

In order to better understand how, and at what stage of the formation process Na entered type B CAIs it is necessary to know how the element is distributed on a large scale throughout the inclusions. This in not practical using normal microprobe point analysis techniques and requires detailed elemental mapping. Two well-characterized type B1 CAIs were used in this study: Allende 5241 (4,5) and USNM-3529Z (3). Digital elemental maps of several areas as large as 9 mm^2 of both inclusions were obtained by rastering the sample stage of a JEOL 8900 electron microprobe under a stationary 15keV, 20nA electron probe. The map images were collected with better than 5 μm lateral resolution using wavelength spectrometers and required approximately 9 hours to acquire. The maps clearly show the distribution of Na from the rim to the core of these inclusions. Point analyses from the regions mapped show the concentration of Na_2O to range from <0.02 to 0.2 wt% and <0.02 to1.3 wt% for 5241 and 3529Z respectively.

Digital Na distribution maps of 5241 (Fig. 1) are typical of both inclusions and show that Na is present below the EPMA detection limit in most of the melilite in the mantle (except in and near alteration veins), but is present at concentrations up to 0.2 wt% in melilite and anorthite in the core and inner mantle. The amount of Na in melilite correlates with the Ak content as seen in Figure 2. Figure 1a shows an enhanced digital Na image of a 9 mm^2 region of 5241 extending from the rim (bottom right) of the inclusion into the core (upper half). The exact same region is shown in a digital backscattered electron (BSE) image in Figure 1b. The alteration veins are seen as light lines in the Na image and as dark lines in the BSE image. The most striking observation is that alteration veins in the Ak-poor melilite mantle contain substantial Na, whereas the alteration veins in the core, containing Ak-rich melilite, do not. Instead, Na in the core is concentrated in large melilite and anorthite grains. This suggests Na that entered the inclusion during the alteration process diffused into Ak-rich melilite but not into the Ak-poor melilite in the mantle. The same pattern was found in both 5241 and 3529Z.

These results strongly support speculations that at least most of the Na in melilite and anorthite in 5241 and 3529Z entered the inclusions at the time the "low temperature" (<<1000°C) alteration products formed and diffused into anorthite and Ak-rich melilite in a compositionally controlled, subsolidus process. Such a process is compatible with Mg isotopic properties of

some CAI which show disturbed Mg in regions of higher Na concentration. It is possible that some Na was initially present in 5241 as speculated by (4) but this cannot be confirmed at present. These results do not address the environment of the process which may be nebular or planetary, but is generally considered to be nebular based on other arguments (3).

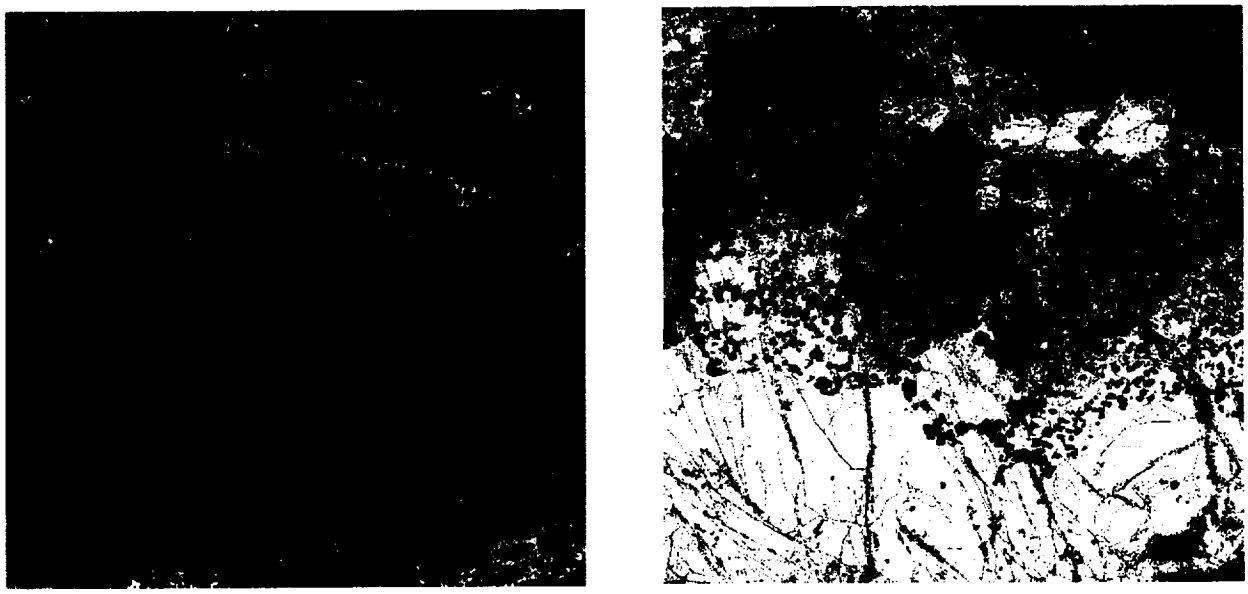

a b

Figure 1. a) Enhanced digital Na map of a 9 mm^2 area of Allende 5241. The rim of the inclusion is at the far lower right. The melilite mantle is in the lower half of the image and the core is in the upper half. Note that Na (white and gray) is concentrated in the cracks and alteration areas in the melilite mantle but is concentrated in large melilite and anorthite grains in the core. b) Digital backscattered electron image of the exact same area as shown in Fig. 2a. The phases seen are melilite (white), fassaite and anorthite (gray), and spinel (black).

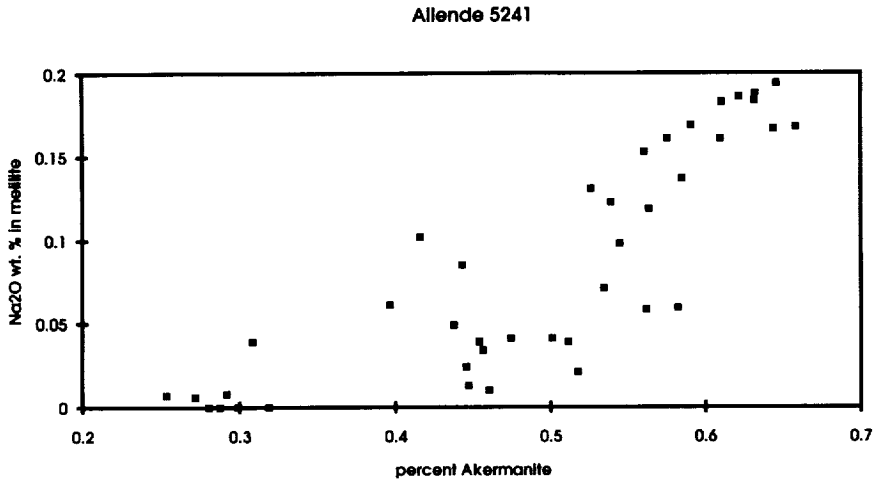

Figure 2. Na_2O concentration vs. Ak content in melilite from the mantle and core of Allende 5241. The plot shows the compositional dependence of Na concentration in type B1 melilite. The data seems to define an upper limit for Na in these melilite crystals. The lower Na concentrations in many of the analyses may reflect the distance from cracks and areas of alteration.

REFERENCES: 1) MACPHERSON G.J., et al., (1988) In *Meteorites and the Early Solar System*, eds. J.F. Kerridge and M.S. Matthews (Tucson: Univ. of Arizona Press), pp. 746-807. 2) GROSSMAN L. (1972) *Geochim. Cosmochim Acta* **36**, 597-619. 3) PODOSEK F.A. et al., *Geochim. Cosmochim. Acta* **55**, 1083-1110. 4) EL GORESY A., et al., (1985) *Geochim. Cosmochim Acta* **49**, 2433-2444. 5) MACPHERSON G.J., et al., (1989) *Geochim. Cosmochim Acta* **53**, 2413-2427.

DETERMINATION OF BULK-CARBON CONTENTS IN SEVEN IIIAB IRON METEORITES; Anders Meibom[1], Kaare L. Rasmussen[1], Ole S. Hansen[2], Poul Hornshøj[2] and Niels Rud[2]. [1] Department of Physics, University of Odense, Campusvej 55, 5230 Odense M, Denmark. [2] IFA, University of Aarhus, 8000 Aarhus C, Denmark.

Introduction Previous determinations of the carbon content in iron meteorites relied either on the method of combustion and subsequent determination of the amount of CO_2 produced (Moore et al. 1969, Lewis and Moore 1971) or estimates based on microscopy studies of the abundance of minerals rich in carbon (graphite nodules, cohenite and haxonite). Recently, accelerator techniques have been applied to measure carbon by detecting protons from nuclear reactions (Makjanic et al. 1988 and 1993). Meibom et al.(1992) used X-rays from the nuclear reaction $^{12}C(^{16}O,\alpha)^{24}Mg$ to detect carbon. Now we use detection of X-rays produced by the nuclear reaction $^{12}C(d,p)^{13}C$ with a 1.65 MeV deuteron beam to non-destructively measure the carbon content of iron meteorites. The carbon content might be of importance to the phase diagram as well as to the diffusion coefficients of several elements during the kamacite growth in the slowly cooling parent body. This will possibly have influence on metallographic cooling rate determinations. In this study we have determined the carbon content of seven IIIAB iron meteorites, and we find a weak negative correlation with bulk meteorite Ni ($k_C = 1.2$).

Experimental The tandemaccelerator at Aarhus University, Denmark, was used for bulk measurements of the carbon content of seven iron meteorites. Carbon was detected from the X-ray spectrum of the $^{12}C(d,p)^{13}C$-nuclear reaction. A carbon peak at 3090 keV and a very low background in this part of the spectrum set the detection limit to ca. 1 ppm (by weight). Absolute values of the carbon content were obtained by comparing with standards (e.g. a 0.5 wt% C).

After polishing with 1 μm diamonds and ultra sound cleaning, each meteorite was sputtered numerous times in the measurement chamber to minimize the effect of carbon surface contamination. Successive sputtering and measuring of each meteorite, showed a fast decrease in the carbon signal until a constant level was reached where practically all surface contamination had been removed. The chamber pressure during measurements was ca. 10^{-7} mbar, low enough to ensure that no significant carbon was build-up during measurements.

The size of the beam was 1-2 mm and the meteorites were scanned in one direction to record possible inhomogeneities. Such inhomogeneities have been reported (Makjanic et al. 1988), but our beam is too large to resolve these structures, indicating that our carbon values can be interpreted as the bulk meteorite carbon contents.

Results The seven IIIAB iron meteorites that have been analyzed are in order of increasing Ni-content: Henbury (7.51% Ni), Cape York (7.84% Ni), Tamarugal (8.52% Ni), El Capitan (8.68% Ni), Turtle River (8.80% Ni), Treysa (9,51% Ni) and Bella Roca (9.91% Ni). Compared to previous determinations (combustion and mineral abundance) of the carbon content, our values are systematically lower (up to 85%; Bella Roca) relative to the combustion method. This difference might be explained by our samples being less contaminated. Our beam is large enough to average out the inhomogeneities due to the different carbon solubilities in α- and γ-phase of the Widmanstätten structure, but not large enough to average out the local variations in the distribution of minerals rich in carbon, such as graphite, haxonite or cohenite. This could explain the difference between our measurements and the method of mineral mapping.

As can be seen in the figure below, the carbon contents show a tendency to decrease with increasing Ni-content.

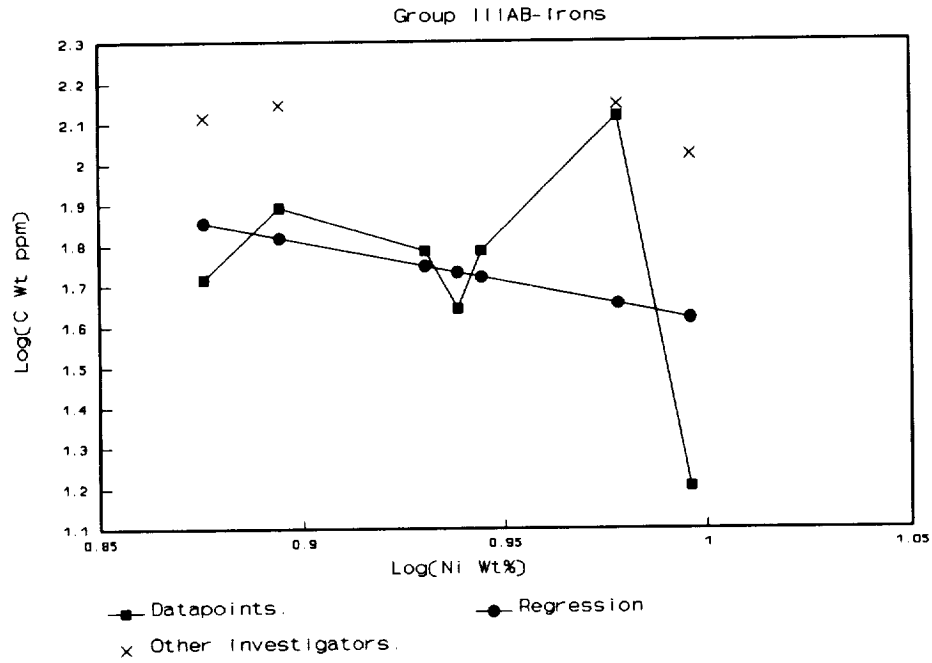

Log(Ni)-Log(C) plot of 7 IIIAB irons. Carbon correlates negatively with Ni. Slope of regression: -1.95. k_C=1.2 (k_{Ni}=0.88).

If we assume that this trend was produced by fractional crystallization described by the Rayleigh equation, a linear relationship in a log(Ni) vs log(C)-diagram can be anticipated if the distribution coefficient for carbon, k_C, is constant. The Ni-contents of the meteorites included in this study range from 7.5-9.9 wt% which spans most of group IIIAB. According to Willis and Goldstein (1982) k_{Ni} increases with increasing concentration of C, S and Ni. As a first estimate we have only taken into account the Ni-dependence using the lowest Ni-value of group IIIAB: 7 Wt%. Equations given by Willis and Goldstein (1982) then give k_{Ni}=0.88. The linear regression on the figure has a slope of -1.95. We then get k_C=1.2. Willis and Goldstein (1982) reported k_C = 0.49 based on the Fe-C phase diagram. This drastic difference might be due to the presence of Ni, S and P, but it could also indicate that processes other than fractional crystallization have been involved in the distribution of C in the core, e.g. diffusion.

Acknowledgements: This work was supported by the Carlsberg Foundation and the Danish Natural Research Council.

Moore C.B., Lewis C.F. and Nava D. (1969) in Meteorite Research (ed. P. Millman). Reidel Publishing.

Lewis C.F. and Moore C.B. (1971) Meteoritics, **6**, 195-205.

Makjanic J., Heyman D., Van der Stap C.C.A.H., Vis R.D. and Verheul H. (1988) Nuclear Instruments and Methods in Physics Research B30 466-469.

Makjanic J., Vis R.D., Hovenier J.W. and Heyman D. (1993) Meteoritics **28**, 1, 63-70.

Meibom A., Rasmussen K.L., Hornshøj P., Rud N. and Heinemeier J. (1992) Meteoritics **27**, 3, 260.

Willis J., Goldstein J. I. (1982) Proc. Lunar Planet. Sci. Conf. 13th **87**, A435-A445.

DISCOVERY DAY, INTRODUCING SPACE SCIENCE TO THE HIGH SCHOOL; R.C. Melchior and J.O. Annexstad, Bemidji State University

Bemidji State University is part of the Minnesota Space Grant Consortium. To maximize exposure of the University's space grant activities in the region, it was felt that some activity involving local high schools would be appropriate. Our location in the relatively remote northern part of the state however, makes communication and interaction with local high school students and staff, a problem. To solve this problem the idea of Discovery Day was proposed. The objectives of our Discovery Day program were multiple. They included an intent to introduce space science to a rural area of northern Minnesota, to introduce ourselves and our university programs to a range of college bound young people and to provide an opportunity for area high school teachers and university staff to exchange ideas on mutual concerns.

Discovery Day consisted of a group of high school teams competing at the University for a Space Grant scholarship. Each team consisted of 7-10 individuals selected by the high school teacher. The competition was organized around the theme -- "Life in the Universe." To allow for adequate planning, are high schools within a fifty mile radius of Bemidji were invited to participate several months before the competition. The subject matter to be addressed in the competition was announced and the ground rules for participation were briefly proposed. Comments were invited from high school teachers concerning the Discovery Day proposal and plans for its implementation. What emerged was a day long conference on Life in the Universe. Instruction on various aspects of the problem was performed by University Staff and included the following topics:

a) Evolution, presented by a distinquished mammologist
b) Cosmology, presented by a well known northern Minnesota Educator
c) Chemical basis for life, presented by the Head of the University Chemistry Dept.
d) Solar systems, presented by John Annexstad
e) Theological aspects of extraterrestrial life, presented by a local Minister
f) Legal aspects of encountering extraterrestrial cultures, presented by a local lawyer

The range of topics and presenters was organized to complement the preliminary instruction done by the high school teachers at their own schools.

The schedule for discovery day began with the arrival of the students and their instructors. Students were given a guided tour of the campus while the teachers met for coffee with University Staff. The presentations followed as a series of 25 minute talks. The theological aspects of extraterrestrial life were presented as a luncheon speech followed in the afternoon by a discussion of the legal aspects of meeting extraterrestrial cultures. These latter two talks were added to the series to emphasize the idea that life in the universe is not strictly a scientific problem.

At the conclusion of the lecture series, each high school team was given a half hour to prepare an argument for or against the possibility of life elsewhere in the cosmos. A panel of Judges consisting of Ralph Harvey, (U. of TN), Bill Garrard (Head of Aerospace Dept., U of MN) and Doug Blanchard (NASA) heard the presentations and awarded the $500 scholarship prize.

We learned a few lessons from the Discovery Day experience that are worth passing on.

- First, there is a great deal of interest in our area about Space Science. Response to our first attempt, both by the high schools and the public, was greater than we anticipated. Local media covered the event in print and on television. Several dozen adults who were otherwise unconnected to the event attended the lecture series. A number of middle school students took a day off from classes to attend.

- Second, we feel that our relations with area high schools were improved by Discovery Day. We have been approached, by students and by teachers concerning plans to have a second Discovery Day next year. The competition was very popular with the students, and the teachers appreciate the opportunity to incorporate the Discovery Day theme in their classes. Next year's theme will be "Planetary Atmospheres and Weather."
- Finally, we propose to present the idea of Discovery Day to other members of the Minnesota Space Grant Consortium for the purpose of starting a statewide consortium.

References:

1. Goldsmith, D. and T. Owen. 1980. *The Search for Life in the Universe.* Benjamin/Cummings Publishing Co., Reading, MA. 433 p.

CRATER CHAINS ON THE MOON: RECORDS OF COMETS SPLIT BY THE EARTH'S TIDES?; H. J. Melosh and E. A. Whitaker, Lunar and Planetary Lab, University of Arizona, Tucson, AZ 85721.

The recent recognition [1] that nearly a dozen crater chains on Callisto may have been created by comets disrupted during passage inside Jupiter's roche limit has prompted us to search for crater chains on the Moon that may have been created by comets similarly disrupted by passage within the Earth's roche limit. We have located at least two candidate crater chains that are not obviously secondaries from any large crater or basin. Both chains are on the lunar nearside, as expected for comets split during a close pass by the Earth, and range in length from about 50 km for the well-known Davy chain to between 200 and 250 km for a chain near the crater Abulfeda. These chain lengths are in good agreement with predictions from a tidal splitting model. The existence of two crater chains on the moon implies a cometary flux similar to that indicated by crater chains on Callisto. If this flux has been uniform over the past 4×10^9 years, it predicts a comet impact flux two orders of magnitude greater than that estimated by Shoemaker et al. [2]. This may indicate that the crater chains were formed near the end of late heavy bombardment when the impact flux was much higher than at present, or alternatively that such crater chains are also made by asteroids passing within the roche limit. This last possibility would support the rubble-pile model of asteroids. The recurrence time between these splitting events is at least 10^4 years.

Table I summarizes information about the two chains we believe may be the products of tidally-split comets. Although the Davy chain is a relatively fresh, post-Imbrian chain [3], the Abulfeda chain is more degraded and is assigned an Imbrian age [3]. The disparity in the lengths of these chains might at first suggest that they do not have similar origins. However, a simple model for tidal splitting [1] that assumes a radial breakup at perigee shows that the length of the chain is a linear function of the parent size. Since the craters in the Abulfeda chain are roughly 5 times larger than those in the Davy chain, it is not unreasonable that the Abulfeda chain is roughly 5 times longer. The Moon is roughly 60 Earth radii (R_E) from the Earth, which is relatively much more distant than Ganymede and Callisto are from Jupiter (14.9 and 26.2 Jovian radii, respectively). The length of crater chains on the Moon created by objects splitting within the Earth's roche limit is thus very sensitive to the approach velocity, as low approach velocities allow a long time for the fragments to separate. Figure 1 shows that the length of a chain of fragments produced by a 1 km radius parent comet can vary between 600 and 8 km for approach velocities at infinity ranging from 1 to 30 km/sec and a passage within 1.5 R_E. Figure 2 shows the dependence of chain length on the distance of closest approach. The length of the chain thus

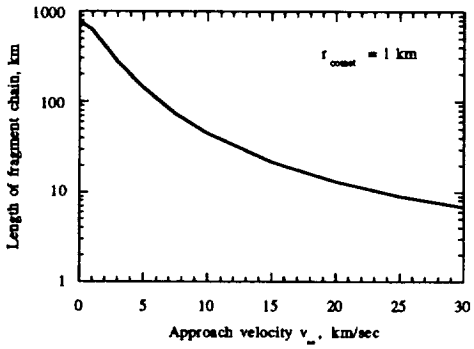

Fig. 1 Fragment chain length vs. approach velocity

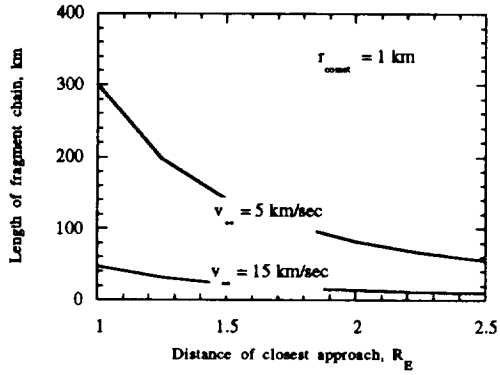

Fig. 2 Chain length vs. approach distance

CRATER CHAINS ON THE MOON: Melosh, H. J. and Whitaker, E. A.

provides very little constraint on the tidal splitting mechanism, since it is so sensitive to reasonable variations in the approach conditions.

The tidal stresses experienced by an object approaching within the Earth's roche limit are actually larger than those approaching Jupiter at a similar relative distance. Using a simple estimate of the tidal stress [4], σ_{tide} is given in terms of the comet density ρ, mass of the Earth M_E, radius of the comet r_c, and distance of approach R.

$$\sigma_{tide} \approx 0.15 \frac{\rho G M_E}{R^3} r_c^2 = 0.63 \frac{G\rho\bar{\rho}}{(R/R_E)^3} r_c^2$$

The second equation is written in terms of the planet's mean density $\bar{\rho}$, and it is clear that for approach at a given fraction of the radius of any planet, the tidal force is proportional to $\bar{\rho}$. Since the Earth's mean density is about 5 times that of Jupiter, the tidal forces on an object approaching to, say, 1.5 radii are correspondingly larger. The tidal stress on an Earth-approaching comet is thus about $\sigma_{tide} \approx 6.8 \times 10^{-4}\ r_c^2$(km), where the stress is in bars. In spite of these relative larger stresses, the inferred strength of comets is still very small (measured in millibars for comets of a few km radius) and suggests a model for comets in which a few mechanically strong chunks are held together by self gravity alone.

Supposing that the two crater chains near Davy and Abulfeda are created by tidally split comets, a few inferences on the cometary flux may be deduced. From the ratio of the areas of a sphere enclosing the Moon's orbit and the Moon's disk, the observation of two crater chains on the moon implies about 4×10^5 split comets overall, assuming that the comets approach the Earth in random directions. Over 4×10^9 years, this suggests a recurrence interval of at least 10^4 years, assuming a constant flux with time. This is about 100 times longer than the inferred recurrence time for comet splitting events about Jupiter, using the same assumptions [1]. However, the area of Jupiter's roche limit-cross section is also about 100 times larger than the Earth's, so the observation of two crater chains on the Moon thus suggests about the same flux at Earth and Jupiter. Finally, if 4×10^5 comets passed between the Earth's surface and its roche limit, then a fraction of about 0.19 of these comets should have struck the Earth itself. Over 4×10^9 years this implies a cratering rate of about 2×10^{-5} cometary impacts per year, which is much larger than Shoemaker et al.'s [2] estimate of 10^{-7} per year for comets with diameters greater than 2.5 km. There are two possible (perhaps not competing) explanations of this discrepancy. First, this computation assumes a constant cratering rate. It may be that the lunar crater chains were emplaced during the end of heavy bombardment. This is plausible for the Abulfeda chain, but perhaps less likely for the post-Imbrian Davy chain. On the other hand, Shoemaker et al. [2] estimate an impact flux of 4×10^{-6} per year of asteroids greater than 1 km in diameter, which is still smaller than the flux estimated from the crater chains, but it may be that the poor statistics on crater chains yield a spuriously high flux. In this case, however, we would have to admit that *both* asteroids and comets can be tidally disrupted to produce crater chains, a speculation tending to support the rubble-pile model for asteroids.

Table I. Crater Chains on the Moon not Secondary to Craters or Basins

Name	Latitude	Longitude	Length, km	Crater Dia. Range, km	Number of Craters	LO frame
Davy	-10°	-9°	47	1-3	~23	IV-108-H2
Abulfeda	-15	15	200-260	5-13	~24	IV-89-H2

References [1] H. J. Melosh and P. Schenk, Nature **365**, 731-733 (1993). [2] E. M. Shoemaker, R. F. Wolfe and C. S. Shoemaker, Geol. Soc. Amer. Spec. Pap. **247**, 155-170 (1990). [3] D. E. Wilhelms and J. F. McCauley, USGS Map I-703 (1971). [4] J. V. Scotti and H. J. Melosh, Nature **365**, 733-735 (1993).

GENETIC LINKS BETWEEN EQUATORIAL AND SOUTH POLAR REGIONS ON MARS?

E. Merényi[1], W.M. Calvin[2], K.S. Edgett[3], R.B. Singer[1], [1]UofA LPL, [2]USGS Flagstaff, [3]ASU

We have been reporting on the spectral and physical properties of the medium albedo equatorial region, Deucalionis Regio, in the past year and a half [1], [2], [3]. The soil in Deucalionis Regio (DR), centered at [245 ° W,15 ° S], was found different from the surface cover of the surrounding classic regions of Arabia, Sinus Meridiani, Oxia and Acidalia both spectrally and physically. Based on a high spectral resolution telescopic image of 07:21 – 08:08 UT 26 Sep 1988 [4] in the 0.4 – 1.0 μm range, this area seems to contain more pyroxene than Arabia and less than Sinus Meridiani. The crystalline hematite content appears greater than either in Arabia or Meridiani. Deucalionis cannot be modeled as a simple mixture of the nearby dark and bright units. Its physical characteristics, as derived from Viking IRTM data, indicate an immobile soil, maybe cemented by salts. However, to determine the mineralogy, information in the longer ($> 1\mu$m) range is also needed. We expected to resolve the compositional distinction with Mars Observer Thermal Emission Spectrometer data. Until MO class data become available, we take a different turn in the investigation of this soil type.

The geographic distribution of the same spectral and physical anomalies were shown to be spatially correlated over another extensive unit contained within the spectral image, part of Noachis (20 ° W – 340 ° W, 30 ° S – 50 ° S) [3]. This is suggestive of a possible genetic tie among large regions (i.e. Deucalionis and Noachis) in the southern hemisphere. We note that the spectra of DR and Noachis together form a very "tight" class, i.e. the standard deviation from the class mean is very small, smaller than for any of the other 7 spectral classes (such as Sinus Meridiani, Acidalium, Arabia type) that we mapped within the image [3]. Analysis of a second telescopic spectral image, 05:00 UT 25 Sep 1988 [4] that contains both Deucalionis and part of the South Polar (SP) region revealed an interesting relationship: spectra from a certain part of the SP region match the DR spectra except below 0.7μm, where the SP spectra are flatter (Figure 1.). As described in the next paragraph we think that soil compositionally similar to that in DR may be seen in part of SP through a thin layer of condensates. The spectra were acquired at Ls=279 or summer in the southern hemisphere. Iwasaki *et al.* [5] note the regression of the south cap was one of the slowest observed for this Ls, and that no global dust storm was observed to develop in this year.

The two spectra from DR to SP differ only in the wavelength region below 0.7 μm. There is a reasonable possibility that this is caused either by thin atmospheric hazes or increased scattering due to the increased optical depth over the south cap caused by the sublimating CO_2. Christensen and Zurek [6] have noted the appearance of polar hazes over the sublimating north cap and Jaquin *et al.* [7] and Anderson and Leovy [8] have both noted the presence of thin hazes in limb profiles. Kaufman [9] has shown that for relatively clear conditions with minimal absorption the difference in the actual surface reflectance and the upwelling remotely sensed radiance spectrum is almost exclusively in the wavelength region below 0.7 μm. Jaquin *et al.* [7] have shown that high, detached hazes, will flatten the spectral response (i.e. brighten the shortest wavelengths) in support of an atmospheric contribution to the South Polar Cap spectrum. Kahn [10] notes that clouds are found preferentially near the receding south polar cap edge in summer and that strong retrograde winds exist there as well. Exact details of the atmospheric scattering depend on surface pressures, temperatures, details of the particle phase function and single scattering albedo, all of which are relatively unconstrained. We hope to make some plausible assumptions for these parameters and run a simple scattering model testing the potential contribution of atmospheric scattering to the spectral characteristics of the SP spectrum. In addition, Viking wind speeds, though not acquired at the same time, could help to constrain the atmospheric dust loading and particle size as input to the scattering model.

GENETIC LINKS BETWEEN MARTIAN REGIONS; *E. Merényi et al.*

More, detailed work will be done to accurately map the area in SP that shows a spectral match to DR between 0.7 – 1.0 μm. Recent analysis of Viking thermal data for the South Polar region [11] will be considered to check for (dis)similar physical properties between DR and the SP area in question. If similarity is found in physical characteristics, then we would have yet another area south of the above two, Deucalionis and Noachis, with compositionally and physically very similar surface cover type. The geographic configuration of these units — a slightly zig-zagged, north-to-south chain — may thus provide a genetic relationship that spans across the southern hemisphere, linking equatorial regions to south polar regions. The present work is a step in investigating this interesting possibility.

REFERENCES

[1] Merényi, E., K.S. Edgett, R. B. Singer (1993a) *Lunar and Planetary Sci. XXIV*, 979
[2] Merényi, E., K.S. Edgett, R.B. Singer (1993b) *Bull. A.A.S.*, **25** No. 3 (1993)
[3] Merényi, E., K.S. Edgett, R.B. Singer (1993c) *Icarus* (submitted, in review)
[4] Singer, R. B., J. S. Miller, W. K. Wells, E. S. Bus, (1990), *Lunar and Planetary Sci XXI*, 1164–1165
[5] Iwasaki, K., Y. Saito, Y. Nakai, T. Akabane, E. Panjaitan, I. Radiman, and S.D. Wiramihardja, (1990) *J. Geophys. Res.*, **95**, 14751–14754
[6] Christensen, P.R., and R.W. Zurek (1984) *J. Geophys. Res.*, **89**, 4587–4596
[7] Jaquin, F., P. Gierasch, and R. Kahn (1986) *Icarus*, **68**, 442–461
[8] Anderson E., and C. Leovy, (1978) *J. Atm. Sci.*, **35**, 723–734
[9] Kaufman Y.J. (1989) Chapter 9 in *Theory and Applications of Optical Remote Sensing*, G. Asrar, Ed., John Wiley.
[10] Kahn, R. (1984) *J. Geophys. Res.*, **89**, 6671–6688.
[11] Paige, D.A., K.D. Keegan, (1994) *J. Geophys. Res.*, forthcoming

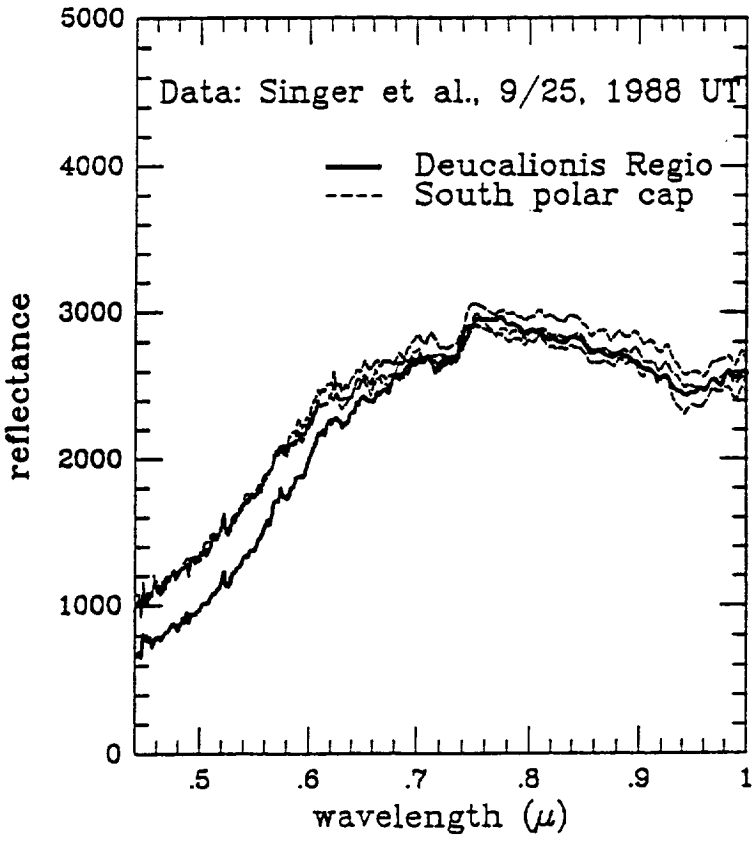

Figure 1. Comparision of the mean spectrum of Deucalionis Regio (thick solid line) and spectra from the South Polar region. The spectra match closely beyond 0.7 μm. Below 0.7 μm the South Polar spectrum shows the effect of possible scattering or atmospheric haze, as indicated by the "flattening" of the curve relative to the Deucalionis spectrum. The general shape of the two spectra is very similar even in this region which, together with the perfect match beyond 0.7 μm, may be suggestive of similar soil composition.

A SUCCESSFUL PLANETARY SCIENCE "SPACE" EDUCATION PROGRAM FOR STUDENTS IN GRADES 3-8; Jo Ann Merrell, Dick Kenealy, Doug Nash, San Juan Institute, 31872 Camino Capistrano, San Juan Capistrano, CA 92675

San Juan Institute (SJI) has developed and is successfully carrying out a new space education program for elementary school children that emphasizes planetary science. Since inception (late 1991), SJI's "SPACE" (Satellites, Planets, Asteroids, Comets, Earth) Education Program has given over 6,000 kids their first taste of planetary science and how scientists study the planets and solar system. The approach used at SJI centers around providing elementary teachers with a support program of class field trips and teacher workshops in space science that excites students to learn more about planets and the solar system.

PROGRAM OBJECTIVES:

- To train and support elementary school teachers in their role as science teachers by using planetary science as the principal topic.
- To provide a means by which students can experience planetary science in a manner that will excite them, and motivate them and their teacher to expand their experience.
- To be a continuing resource for elementary and middle schools in the area of planetary space science.

HOW SJI'S PROGRAM WORKS:

- Class field trips in a non-traditional format, using the 150-seat auditorium at SJI. Occasionally, we make presentations at schools.
- Teacher workshops at SJI associated with SJI science conferences.
- Utilizing up-to-date NASA research and public information material.
- Staffed by experienced science teachers and research scientists.

RECORD OF SUCCESS:

- In two years, a total of 6300 kids (from ~50 schools throughout southern California) have been introduced to planetary science through the SJI Field Trip Program.
- 120 teachers have participated in SJI Educators' Workshops.
- Current field trip schedule is booked solid through June '94, involving another 800 children.

PROBLEM AREAS THAT NEED TO BE ADDRESSED:

- Insufficient operating funds, limiting SJI's ability to achieve its capacity to reach more kids with planetary science field trips, hold more teacher workshops, and distribute more classroom materials.
- Diversity in cultural background of students, presenting challenges in overcoming a broad range of preconceived ideas and notions that are hurdles to learning science.
- Special needs of ESL (English as a Second Language) and Special Education children.
- Lack of planetary and general space science education on the part of most elementary school teachers.

METHODS WE HAVE FOUND SUCCESSFUL: When children become excited about learning a particular subject, good teachers will follow their lead by searching out resources and opportunities that help students to learn. San Juan Institute has found that, with modest funding (~20 K/yr.) and a

SJI "SPACE" EDUCATION PROGRAM; J. Merrell, R. Kenealy, and D. Nash

lot of volunteerism), planetary science can involve the teacher and students in several ways that have proven to be very successful.

A "Planetary Journey Through the Solar System", is SJI's first interactive program that has brought 2700 students to the Institute in the '92-'93 school year alone. We are now adding a second program, "Exploring Planets With the Electromagnetic Spectrum", and have reservations for field trip visits to our Institute from teachers that will bring over 3000 children to SJI during the '93-'94 school year.

These two field-trip programs provide an interactive visit to SJI for class groups of up to 80 children. A typical field trip involves an interactive demonstration, audio-visual-aided lecture, question-and-answer period, and a walk-through of laboratory facilities. SJI has taken its lead from the Nation Science Teachers Association and their recommendations for science inquiry at the elementary level. In attempting to be as much hands-on as possible in a laboratory/office setting, SJI has developed an interactive approach. For the demonstration and interactive parts of the field trip, the approach combines the requirement created by the institution's environment to have the children in a seated, assembly configuration; yet, maintain an atmosphere of "What If?", which young curious minds demand. This has worked quite well.

The prime elements that maintain this balance are: having demonstrators who are knowledgeable and experienced enough to handle the wide-ranging direction of children's questions; using interesting materials (such as rocks and meteorites) that are passed around to be handled for the children to make comparisons; clipboards with worksheets (which they can take home); and simple equipment (colored filters and rainbow glasses) that allow the kids to participate in the experiments being demonstrated. The assembled class talks with and ask questions of a working planetary research scientist, giving the kids an opportunity to better understand what a "scientist" actually does.

SJI provides a learning experience that is affordable. We serve a busload of children (70-80) at each presentation, which takes two hours. We have so far offered these field-trip experiences at no cost to the school. However, beginning July 94, a fee of $50 will be charged for each field trip. We have worked with the teachers to make the experience one that the children will remember, through follow-up materials given to the teacher. We have also worked with ESL and Special Ed. teachers to adjust the program to fit their needs. All this has been done with emphasis on planetary science and the solar system.

Through Educator Workshops, held in association with the many research science conferences taking place at SJI, we work to educate teachers on current findings in space and planetary science, and inform them about new technologies (such as computer visualization) that can be applied to teaching. At these workshops, teachers are given classroom materials and hands-on lessons ready to be presented to the children.

The response from teachers for both of these programs has been very positive. An ongoing evaluation program is in place: We get regular written feedback from the teachers after a field trip using a mailback questionaire. And, we are working with the University of California Irvine Social Ecology Department on a formal evaluation program. We use the feedback to adjust the program content, pace, or other needs where indicated. Based on our experience, we think SJI's SPACE program is a success, and could be a model for others to follow.

AN ABSOLUTE NORMALIZATION FOR MODELED NEUTRON FLUX DISTRIBUTIONS; A.E. Metzger, Jet Propulsion Laboratory, Pasadena, CA 91109; D. M. Drake, Max-Planck-Institut fur Chemie, Mainz, FRG; E. L. Haines, Sunrise Research Inc., Eugene, OR 97404; J. Mazarik, and R. C. Reedy, Los Alamos National Laboratory, Los Alamos, NM 87545

Reactions produced by neutrons in planetary surfaces and meteorites have been found to be important as an indicator of exposure history as well as in computing resultant yields of characteristic gamma rays. Applied to remote planetary gamma-ray spectroscopy, knowledge of the neutron flux in combination with the observation of surface gamma rays is needed to calculate surface concentrations for most elements. Where direct measurements of the neutron flux cannot be obtained, the ability to model the depth and energy distributions reliably will allow proper interpretation of the data from remote observations as well as from core and meteorite samples. We report a comparison between modeling and observation which also provides a means of estimating absolute fluxes.

Neutron transport modeling is accomplished in two steps. First, calculation by the program LAHET produces the depth and energy distributions of the high energy neutron flux due to galactic cosmic rays incident on the planetary surface. A second program, either ONEDANT or MCNP, tracks the further scattering, absorption, and leakage of the fast (15 MeV) neutrons down to thermal energies.

We have been using the combination of LAHET and ONEDANT to evaluate the effect of variations in composition and density of planetary bodies on the neutron depth distribution. ONEDANT calculates moderated fluxes as a function of energy and depth for one initial high energy (LAHET) neutron. The subsequent multiplication by the yield of neutrons per incident proton obtained from LAHET will give a good absolute flux value if both transport programs, and in particular ONEDANT, correctly represent the processes of neutron scattering, absorption, and leakage.

A measurement is available from which to derive the normalization values (and in the process to check the modeling programs) in the form of the Apollo 17 Lunar Neutron Probe Experiment, in which the absolute magnitude and the depth profile of the lunar neutron density were determined by Woolum et al. (1). To do this the ONEDANT thermal and epithermal flux values were separately converted to neutron density and summed for 22 depths from 0-500 g/cm^2. Neutron density profiles were generated by spline fitting the 22 points and the resulting profiles were least-squares fitted to the measured neutron densities over their range of 50-380 g/cm^2. Two geometries of cosmic rays incident on the lunar surface were tested, isotropic and sphere-cosine, the latter a weighting of the 2π cosmic-ray flux by the cosine to the normal. The results are shown in the Figure. Both ONEDANT profile shapes match the measured values well but a chi-square test shows the cosine profile fits the data better. Sphere-cosine geometry has also been found to give a good fit to production vs depth for cosmogenic nuclides on the Moon (2). For the cosine case, the ratio of the

NEUTRON FLUX DISTRIBUTIONS
Metzger, A. E. et al.

measured value to that derived from ONEDANT is 9.51, which is equivalent to the flux of neutrons produced by the cosmic-ray flux during the Apollo 17 mission. This provides the value needed to derive absolute neutron fluxes from the output of ONEDANT.

References:

(1) Woolum, D.S., D. S. Burnett, M. Furst, and J. R. Weiss, (1974) The Moon, 12 , pp. 231-50.
(2) Reedy, R.C., and J. Masarik, (1994) Lunar and Planetary Science XXV

Lunar neutron density, data of Woolum et al., compared with calculated profiles based on isotropic and "cosine" cosmic ray fluxes.

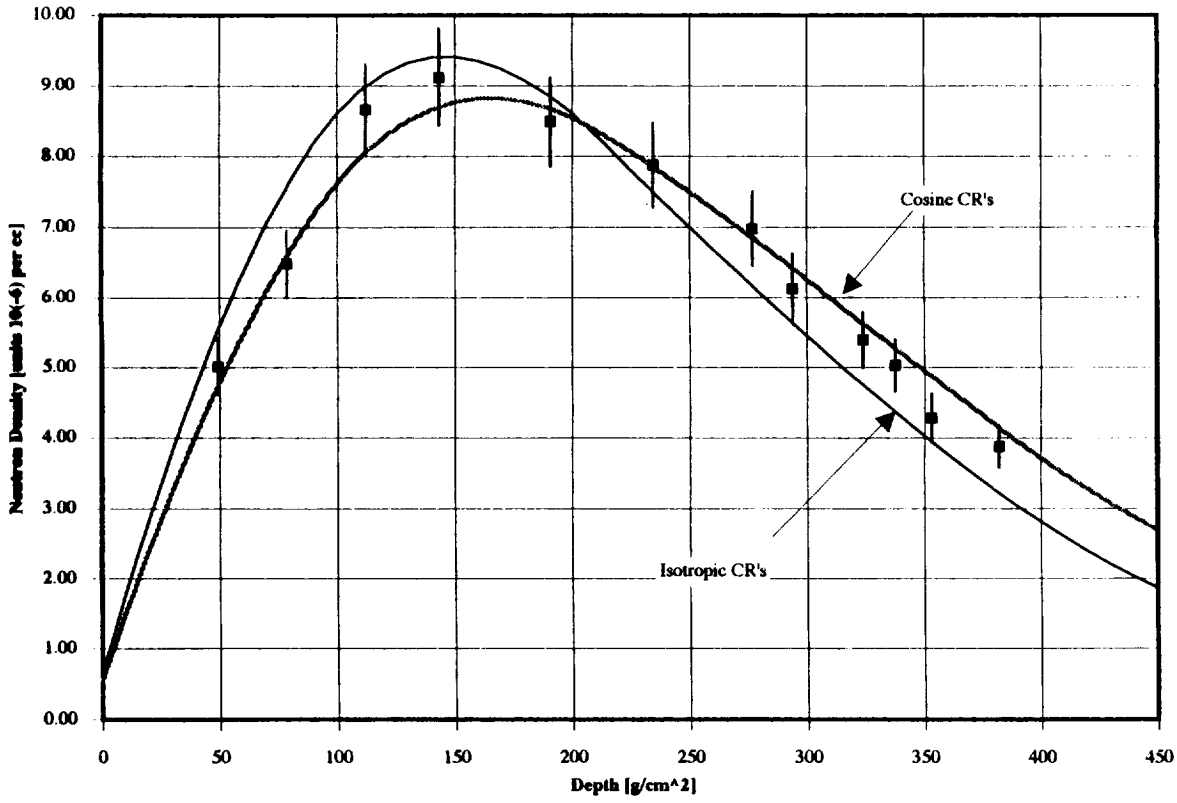

THE PASAMONTE *POLYMICT* EUCRITE - A RECLASSIFICATION

K. Metzler[1], K.-D. Bobe[2], H. Palme[3], B. Spettel[3], and D. Stöffler[1]. [1]Museum für Naturkunde der Humboldt-Universität, Invalidenstraße 43, 10115 Berlin, Germany; [2]Institut für Planetologie, Wilhelm-Klemm-Str. 10, 48149 Münster, Germany; [3]Max-Planck-Institut für Chemie, Abt. Kosmochemie, Saarstraße 23, 55122 Mainz, Germany.

The Pasamonte eucrite is usually considered as a monomict, unequilibrated eucrite [e.g.1-6] and quoted as a type meteorite [e.g. 1,2] representing a group of unequilibrated ("Pasamonte-type") lithologies. These lithologies, frequently occuring as lithic clasts and mineral fragments in polymict eucrites and howardites, contain unequilibrated pyroxenes with well-preserved igneous Fe-Mg zonings. Our petrographical, mineralogical, and chemical examination of Pasamonte revealed that this meteorite represents a polymict breccia containing pyroxene fragments of different types (equilibrated and unequilibrated) and a variety of lithic clasts (basalts, granulites, granulitic breccias, impact melt breccias). Hence, Pasamonte has to be reclassified as a *polymict eucrite*.

Samples and methods of investigation. We have investigated several thin sections prepared from a 12g sample of Pasamonte (USNM No. 897) using optical and scanning electron microscopy. Furthermore, three lithic clasts (,1/,5/,7) with weights > 50 mg were separated. Thin sections of each clast were used to determine the rock type; mineral compositions were obtained using an energy dispersive x-ray analysis system. An aliquot from each clast was analyzed by INAA (MPI Mainz); the results are summarized in Table 1.

Results. Pasamonte is a polymict breccia consisting of lithic clasts embedded in a fine-grained clastic matrix. The clastic matrix contains both **unequilibrated** (chemically zoned) **and equilibrated pyroxene** fragments. The latter are characterized by a brownish color and exsolution lamellae of augite with a maximum width of about 5 microns. The maximum grain size of these equilibrated pyroxenes is about 800 microns, indicating a relatively coarse-grained source lithology. The following clast types have been identified: **ophitic and subophitic basalts** (e.g. Pasamonte 897,1; Fig.1), **variolitic basalts** (e.g. Pasamonte 897,5; Fig.2), **granulites, granulitic breccias** (e.g. Pasamonte 897,7; Fig.3), and dark, fine-grained **impact melt breccias**. The mean chemical compositions of pyroxenes from the subophitic (,1) and the variolitic basalt (,5) are distinctly different ($En_{42}Fs_{44}Wo_{14}$ and $En_{34}Fs_{52}Wo_{14}$), although these pyroxenes are unequilibrated in both cases (Figs. 4,5). Furthermore, the mean REE enrichment in basalt ,1 is about 30xCI, whereas the basalt ,5 is enriched in these elements only by a factor of about 11xCI (Figs. 4,5). The latter is similar to *bulk* Pasamonte which shows a REE enrichment of about 12xCI [7]. The pyroxenes of the granulitic breccia ,7 are highly equilibrated (Fig. 6) with a width of augite exsolution lamellae up to 4 microns. This clast contains metallic iron and the REE concentrations show a complicated pattern (Fig.6) that could be at least partly traced back to a chondritic contamination (compare Ni, Ir, and Au in Tab.1). Nevertheless, a chondritic component cannot explain the high W concentration of about 10xCI.

Conclusions. Pasamonte has to be *reclassified as a polymict eucrite* since it contains a variety of basaltic lithologies, granulites, granulitic breccias, and impact melt breccias. Since Pasamonte contains different types of pyroxene (equilibrated and unequilibrated), terms like "unequilibrated eucrite Pasamonte" and "Pasamonte-type pyroxene" are ambigous and should be avoided in future.

REFERENCES: [1] *Basaltic Volcanism Study Project* (1981), Pergamon, New York, 1286 pp. [2] Takeda H. and Graham A.L. (1991) *Meteoritics* 26, 129. [3] Miyamoto M. et al. (1985) *PLPSC* 15th, JGR 90, Suppl., C629. [4] Batchelor J.D. (1991) *LPS* XXII, 61. [5] Buchanan P.C. and Reid A.M. (1992) *LPS* XXIII, 173. [6] Phinney W.C. et al. (1993) *LPS* XXIV, 1137. [7] Wänke H. et al. (1977) *LPSC* 8th, 2191.

Fig.1: Subophitic basalt 897,1 (BSE image)

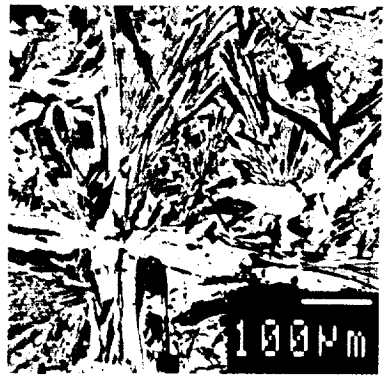

Fig.2: Variolitic basalt 897,5 (BSE image)

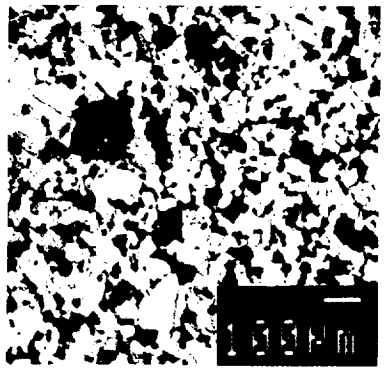

Fig.3: Granulitic breccia 897,7 (BSE image)

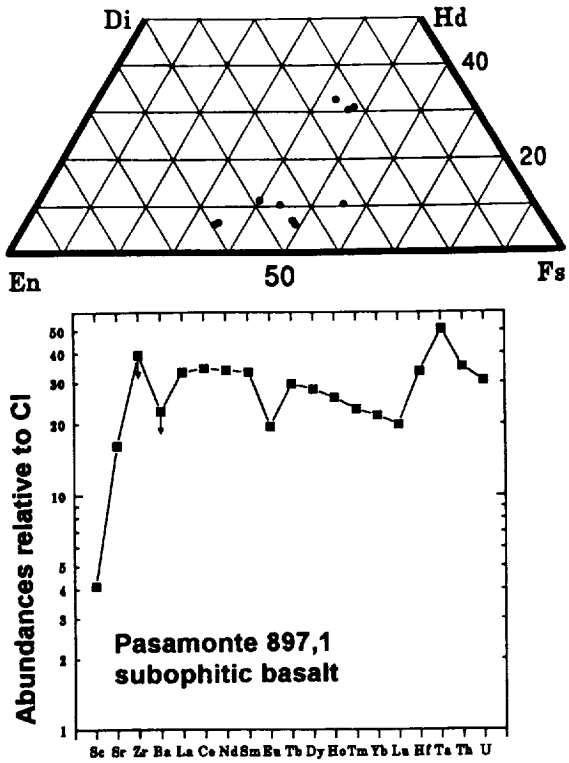

Fig.4: Pyroxen compositions and trace element concentrations of Pasamonte 897,1

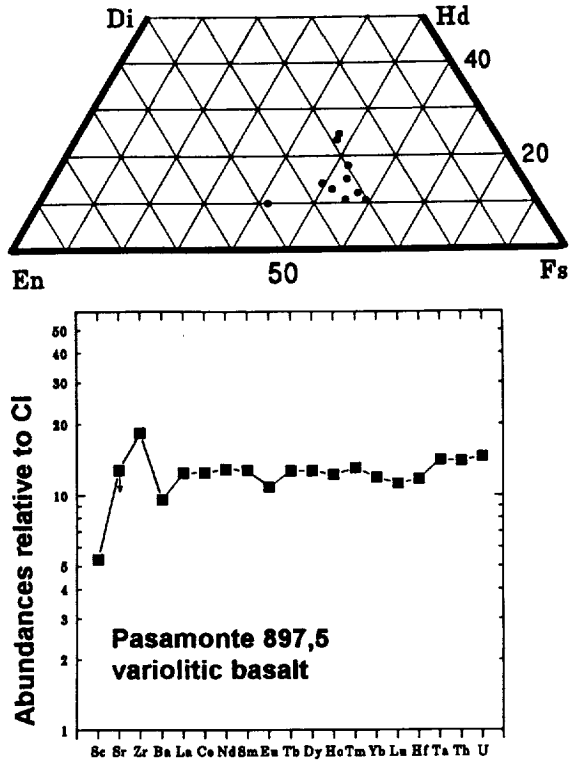

Fig.5: Pyroxen compositions and trace element concentrations of Pasamonte 897,5

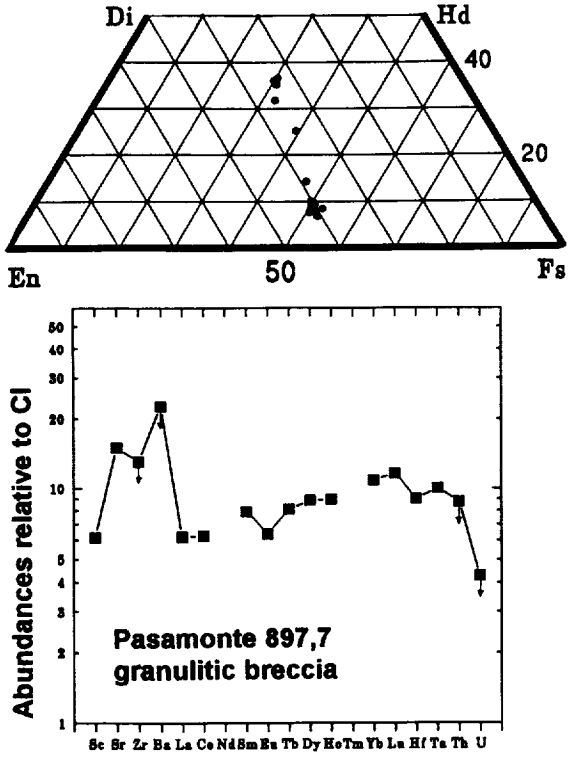

Fig.6: Pyroxen compositions and trace element concentrations of Pasamonte 897,7

Table 1: Element concentrations of Pasamonte lithologies (INAA; wt.% for Mg, Al, Ca, Ti, Fe; ppm for trace elements)

	897,1	**897,5**	**897,7**
	10 mg	28 mg	15 mg
	subophitic basalt	variolitic basalt	granulitic breccia
Mg	2.2 wt%	4.0 wt%	5.7 wt%
Al	8.3	6.5	4.4
Ca	7.4	7.1	5.5
Ti	1.2	0.5	0.4
Fe	10.5	15.0	20.3
Na	4020 ppm	5190 ppm	2435 ppm
K	450	886	180
Sc	24.2	31.4	36.2
V	29.0	73.1	82.8
Cr	793	2110	2630
Mn	2540	4150	4880
Co	28.7	6.20	140
Ni	<150	<10.0	1480
Ga	2.40	2.70	2.20
Sr	140	<110	130
Zr	<150	70.0	<50.0
Ba	<50.0	21.0	<50.0
La	8.13	3.05	1.52
Ce	21.9	7.97	4.00
Nd	16.0	6.10	
Sm	5.10	1.97	1.22
Eu	1.13	0.63	0.37
Tb	1.10	0.47	0.30
Dy	7.12	3.23	2.25
Ho	1.47	0.70	0.51
Tm	0.60	0.34	
Yb	3.58	1.97	1.78
Lu	0.50	0.28	0.29
Hf	4.01	1.41	1.08
Ta	0.71	0.20	0.14
W	<0.35	<0.15	0.90
Ir	<0.002	<0.002	0.068
Au	<0.005	<0.001	0.021
Th	1.000	0.400	<0.250
U	0.25	0.12	<0.035

ISOTOPE SOURCE TABLE FOR A 25 $M_\odot$ TYPE II SUPERNOVA

Bradley S. Meyer, Department of Physics and Astronomy, Clemson University, Clemson, SC 29634-1911.

There is a great need for a catalog of the origins of the isotopes comprising planetary materials. This catalog should provide sufficient detail of the chemical environment in which an isotope finds itself in stellar ejecta that we may evaluate theories regarding the condensation of solid particulates in stellar outflow. Such information will be invaluable to the study of presolar grains [1] and of dust alteration in the interstellar medium [2]. The present paper is a step in the construction of such a catalog. I invite any criticisms of the partial table that follows; they will help the ultimate project.

For the present work, I cataloged the origins of isotopes in the core-collapse (type II) supernova of a star about 25 times the mass of the sun (25 $M_\odot$). The particular supernova model I used was that of Weaver and Woosley [3]. These workers evolved a 25.14 $M_\odot$ star from initial core hydrogen burning to the development of a nickel-iron core. The initial composition was solar (from the compilation of [4]). A $^{12}C(\alpha,\gamma)^{16}O$ rate of 1.7 times the Caughlin and Fowler [5] rate was used, as was nominal semiconvection. A core collapse supernova was then simulated and shock- and neutrino-induced modifications to the nuclear abundances were computed. In the explosion 23.48 $M_\odot$ escaped; 1.664 $M_\odot$were left as a remnant (neutron star or black hole). This 25 $M_\odot$ type II supernova is fairly representative of the mass spectrum of type II supernovae.

For the purposes of delineating the sites of synthesis of various isotopes, I divided the presupernova star into six regions. These six regions are the outer 0.275 $M_\odot$ of nickel core that eventually escape; successive spherical shells dominated by silicon and sulphur, oxygen and neon, oxygen and carbon, helium and carbon; and a large hydrogen envelope. The different compositions of the zones reflect their different burning histories during the star's evolution. The mass of each zone (in solar masses) is given in the following table by ΔM, while the outer boundary of each zone in mass is given by $M(r)$. It is apparent that the star has narrow Si/S and O/C shells, somewhat more massive O/Ne and He/C shells, and a large hydrogen envelope that comprises more than one-half the mass of the star. The column labelled Total in the table gives the total mass of the star (25.14 $M_\odot$) and the amount of mass actually ejected (25.14 - 1.664 = 23.48 $M_\odot$).

For the present paper, I restricted my attention to the stable or longer-lived isotopes of C, N, O, Mg, and Al. The data are shown in the following table. Information for the isotopes of other elements are available upon request. For each isotope ^AZ, $\Delta M(^AZ)$ gives the mass (in solar masses) of that isotope in the given zone in the supernova ejecta. $\mathcal{O}(^AZ)$ gives the overproduction of isotope ^AZ, i.e. its mass fraction relative to its mass fraction in a solar mix, for each zone in the ejecta. Thus, for example, there are 2.465 $M_\odot$ of ^{16}O in the 5.868 $M_\odot$ of the O/Ne shell. The overproduction is 72.66, which shows that a considerable amount of ^{16}O was produced in this shell. Indeed, this shell accounts for 76% of the 3.242 $M_\odot$ of ^{16}O the star ejects into the interstellar medium. In contrast, ^{27}Al increases by only 4.7% over its initial abundance in the hydrogen envelope through the course of the star's evolution. Other points of interest: 1) nitrogen inside of the He/C shell is rare but ^{15}N rich due to neutrino spallation reactions on abundant ^{16}O during the explosion and 2) the magnesium in the He/C shell is heavy and has an isotopic pattern that seems to emulate mass fractionation with some ^{26}Mg excess.

There are some immediate applications of this catalog of isotope origins in the explosion of a 25 $M_\odot$ star. ^{16}O is largely produced monoisotopically in the inner regions of the star. This has implications for the chemical-memory interpretation of the ^{16}O enrichment in CAIs [6]. ^{17}O is strongly overproduced and $^{16,18}O$ are depleted in the hydrogen envelope. We find from the catalog that $\delta(^{17}O/^{16}O) = (\mathcal{O}(^{17}O)/\mathcal{O}(^{16}O) - 1) \times 1000 = 20250$ per mil while $\delta(^{18}O/^{16}O) = -150.2$ per mil. These numbers may have important implications for the presolar oxide grains recently found in Orgueil [7] and Murchison [8] which show strong positive anomalies in ^{17}O and negative anomalies in ^{18}O. It is also of interest to note that the ratio $^{13}C/^{12}C$ is enhanced relative to solar in the hydrogen envelope by CN burning. If microdiamonds that nucleate in the ^{12}C-rich He/C shell (where C/O>1) mix with envelope material, the $^{12}C/^{13}C$ ratio that results in these diamonds may be close to solar [9,10].

Subsequent tables in this catalog will study other astrophysical sites.

ACKNOWLEDGEMENTS I thank S. Woosley and T. Weaver for sharing detailed output of their model s25s7a with me. These authors will soon publish detailed output from over sixty supernova models [11].

ISOTOPE SOURCE TABLES: Meyer B.S.

REFERENCES [1] Anders, E. & Zinner, E. (1993) *Meteoritics*, **28**, 490; [2] Clayton, D. D., Scowen, P., & Liffman, K. (1989) *Astrophys. J.*, **346**, 191; [3] Weaver, T. A. & Woosley, S. E. (1993) *Physics Reports*, **227** 65; [4] Anders, E. & Grevesse, N. (1989) *GCA*, **53** 197; [5] Caughlin, G. A. & Fowler, W. A. (1988) *At. Data Nucl. Data Tables*, **40** 238; [6] Clayton, D. D. (1978) *Moon & Planets*, **19**, 109; [7] Huss, G. *et al.* (1993) *Meteoritics*, **28**, 369; [8] Nittler, L. R. *et al.* (1993) *LPSC*, **XXIV**, 1087; [9] Clayton, D. D., El Eid, M., & Brown, L. E. (1993) *LPSC*, **XXIV**, 307; [10] Clayton, D. D. *et al.* (1994) in preparation; [11] Woosley, S. E. & Weaver, T. A. (1994) in preparation.

Isotope Source Table for a 25 $M_\odot$ Supernova

	Ni core	Si/S shell	O/Ne shell	O/C shell	He/C shell	H envelope	Total
$M(r)$	1.939	2.330	5.868	6.662	9.260	25.14	25.14
ΔM	0.275	0.391	3.538	0.794	2.598	15.88	23.48
$\Delta M(^{12}C)$	5.351-8	1.255-5	1.029-1	1.456-1	1.277-1	2.877-2	4.050-1
$\mathcal{O}(^{12}C)$	6.418-5	1.059-2	9.599	6.051+1	1.623+1	5.979-1	5.693
$\Delta M(^{13}C)$	7.977-10	2.884-8	5.453-7	5.546-7	2.675-5	1.447-3	1.475-3
$\mathcal{O}(^{13}C)$	7.942-5	2.021-3	4.222-3	1.914-2	2.821-1	2.497	1.722
$\Delta M(^{14}C)$	2.121-12	6.349-12	2.117-7	1.064-7	2.701-6	1.771-22	3.019-6
$\mathcal{O}(^{14}C)$	7.008-9	1.476-8	5.439-5	1.218-4	9.450-4	1.014-20	1.169-4
$\Delta M(^{14}N)$	2.307-9	6.359-9	2.338-6	1.077-6	4.286-3	7.569-2	7.998-2
$\mathcal{O}(^{14}N)$	7.623-6	1.479-5	6.007-4	1.233-3	1.500	4.333	3.097
$\Delta M(^{15}N)$	3.168-8	2.241-6	7.789-5	8.092-6	5.025-6	3.092-5	1.242-4
$\mathcal{O}(^{15}N)$	2.641-4	1.315-2	5.050-2	2.337-2	4.437-3	4.465-3	1.214-2
$\Delta M(^{16}O)$	1.830-6	7.305-2	2.465	5.693-1	2.436-2	1.100-1	3.242
$\mathcal{O}(^{16}O)$	6.933-4	1.948+1	7.266+1	7.476+1	9.779-1	7.222-1	1.440+1
$\Delta M(^{17}O)$	3.209-10	4.729-9	4.370-7	1.710-8	1.386-5	9.480-4	9.623-4
$\mathcal{O}(^{17}O)$	2.997-4	3.109-3	3.175-2	5.537-3	1.372	1.535+1	1.054+1
$\Delta M(^{18}O)$	2.975-11	1.182-11	9.579-8	1.372-5	4.150-3	2.115-4	4.375-3
$\mathcal{O}(^{18}O)$	4.982-6	1.393-6	1.248-3	7.963-1	7.360+1	6.137-1	8.587
$\Delta M(^{24}Mg)$	7.625-6	1.703-4	7.054-2	3.499-4	1.307-3	8.175-3	8.055-2
$\mathcal{O}(^{24}Mg)$	5.381-2	8.455-1	3.871+1	8.557-1	9.771-1	9.996-1	6.662
$\Delta M(^{25}Mg)$	1.251-11	1.558-7	2.279-2	4.125-3	2.189-4	7.464-4	2.788-2
$\mathcal{O}(^{25}Mg)$	6.716-7	5.886-3	9.515+1	7.674+1	1.245	6.943-1	1.754+1
$\Delta M(^{26}Mg)$	3.313-12	7.882-8	2.399-2	7.446-3	5.910-4	1.500-3	3.352-2
$\mathcal{O}(^{26}Mg)$	1.552-7	2.598-3	8.736+1	1.208+2	2.931	1.217	1.840+1
$\Delta M(^{26}Al)$	8.040-10	1.321-7	6.048-5	6.662-7	6.280-6	3.257-5	1.001-4
$\mathcal{O}(^{26}Al)$	3.765-5	4.352-3	2.203-1	1.081-2	3.115-2	2.643-2	5.497-2
$\Delta M(^{27}Al)$	6.568-7	1.211-4	2.563-2	8.317-5	2.209-4	9.639-4	2.702-2
$\mathcal{O}(^{27}Al)$	4.115-2	5.342	1.249+2	1.806	1.466	1.047	1.985+1

TEXTURAL AND MINERALOGICAL HETEROGENEITY OF SILICATE INCLUSIONS IN TSAREV CHONDRITE. L.F.Migdisova[1], A.A.Yaroshevsky[2], M.A.Nazarov[1], N.N.Kononkova[1] [1] V.I.Vernadsky Institute of Geochemistry and Analytical Chemistry, RAS; [2] Department of Geochemistry, Moscow State University, Moscow, Russia.

We carred out a petrological and mineralogical study of a light in the Tsarev (L5) chondrite. The inclusion shows a textural and mineralogical heterogeneity. It consists of Opx, Pl-Ol-Opx, and Pl-Ol-Cpx aggregates included to an Ol-Pl matrix. Composition of mineral phases in the inclusion and in the Tsarev host material are practically the same.

We found several silicate inclusions in shock-metamorphosed chondrite Tsarev (L4-5e-f). Textures and mineral assemblages vary considerably from one inclusion to other. First inclusion studied [1,2] is characterized by: a fine-graind magmatic texture; chemical composition of minerals within inclusion (pyroxene and plagioclase) is identical to chemical composition of the same phases from the chondrite, but the phase proportions are similar to an eutectic (basaltic) mixture and non-identical to the chondrite composition. It is believed the inclusion matter is some differentiation product from Tsarev Parent Body.

Inclusion No.6 (6x10 mm^2) is characterized also by a fine-graind magmatic texture indicating a melting of a precursor material and subsequent very fast cooling and crystallization. The inclusion is composed of glass of a plagioclase composition, olivine, orthopyroxene; one grain of Ca-pyroxene; chromite, rare ilmenite and metal. There is textural and mineralogical heterogeneity within inclusion, which was devided into four types of matter: (1) olivine-plagioclase matrix (~55 vol.%),(2) orthopyroxene (~2%), (3) plagioclase-olivine-orthopyroxene (~30%), (4) plagioclase-olivine-clinopyroxene (~13%). The matrix is composed of parallel barred olivine lamellae embedded in plagioclase glass. The matrix is similar to barred olivine chondrules, but it is different rom them in a higher glass content. Second, third and fourth types of thematter are represented by fine-graind aggregates which resembles mm-size chondrules.

Commonly chemical composition of minerals of the inclusion are similar to those of equilibrated L-chondrites and to those of Tsarev (Table). Variations of chemical composition of olivine (22.5-26.5 mol.% Fa) and of orthopyroxene (20-23 mol.% Fs) are not correlated with the type of the matter in the inclusion. Orthopyroxene is characterized by high contents of TiO_2 (0.46-1.28%), Al_2O_3 (0.55-1.76%), Cr_2O_3 (0.4-1.77%) and CaO (0.76-1.90%); the concentrations of Ca and Cr are similar to those in orthopyroxenes associated with chromite and Ca-mineral phases from shock-metamorphosed chondrites. The glass has the composition of sodium plagioclase (11-17 mol.% An). There are rare small

glass inclusions enriched in normative spinel and corund within the second type of the matter. Chromite has a variable composition (TiO_2 1-7%, FeO 25-34%, Al_2O_3 4.5- 7%, Cr_2O_3 47-57%) which is not correlated with identified types of the matter. A positive correlation is observed between Ti and Fe; negative correlations are observed between Ti and Al, Cr and between Fe and Cr.

Thus, chemical compositions of mineral phases of the inclusion and the Tsarev host material are practically of the same. Especially, the chromite compositions shows clearly the similarity, because chromite in the Tsarev host material are very different from those in other ordinary chondrites in high Mg and very variable Ti contents (up to Ti-rich chromite). The same features are typical for chromites from the inclusion.

Two of us (LFM and MAN) were supported by the RFFI Grant 93-05-09222.

Table. Mean chemical compositions of mineral phases from inclusion No.6 in Tsarev chondrite

	Olivine	Ortho-pyroxene	Clino-pyroxene	Glass	Chromite (a)	Chromite (b)	Chromite (c)
N	46	26	1	18	22	15	4
SiO_2	40.30	54.86	55.06	63.14	0.27	0.97	1.53
TiO_2	0.03	0.91	0.61	0.06	2.82	2.97	5.67
Al_2O_3	0.13	1.19	1.78	22.08	5.27	6.06	5.28
Cr_2O_3	0.08	0.89	0.66	0.06	54.38	53.59	49.07
V_2O_3	0.02	0.04	0.00	-	0.64	0.58	0.48
FeO	21.76	13.95	5.19	0.86	30.55	29.75	32.25
MnO	0.46	0.45	0.26	0.02	0.56	0.52	0.58
MgO	38.96	27.93	15.68	0.41	3.67	4.57	4.39
ZnO	0.04	0.04	0.00	-	0.18	0.18	0.14
CaO	0.09	1.21	21.33	2.76	0.06	0.07	0.08
Na_2O	0.07	0.11	0.90	8.78	-	-	-
K_2O	0.01	0.01	0.04	0.88	-	-	-
Sum	101.95	101.59	101.53	99.05	98.40	99.26	99.47
Fa,Fs	23.9	21.3	8.6				
Wo,An		2.4	45.2	14.0			

N - number of analyses.

References. [1] L.F.Migdisova,A.A.Yaroshevsky,N.N.Kononkova (1992). LPS XXIII, 909-910. [2] A.A.Yaroshevsky,L.F.Migdisova (1992). Doklady AN SSSR, 223, No.1, 147-150 (in Russian).

Cr, Mn and Ca Distributions for Olivine in Angritic Systems: Constraints on the Origins of Cr-rich and Ca-poor Core Olivine in Angrite LEW87051; **T. Mikouchi (Mineralogical Inst., Graduate School of Science, University of Tokyo, Hongo, Tokyo 113, JAPAN), G. McKay (SN4 NASA/JSC, Houston, TX77058, USA) and L. Le (C23-C Lockheed ESCO, Houston, TX77058, USA)**

INTRODUCTION

Angrite meteorites are a type of basaltic achondrites that are noted for their very old crystallization ages (4.55b.y.)[1] and unusual chemical and mineralogical properties[2]. In spite of great interest, only four angrites have been found yet. LEW87051 is the smallest one which weighs 0.6g. It is a porphyritic rock with coarse subhedral to euhedral olivines (~0.5mm) set in a fine-grained groundmass which clearly represents a crystallized melt[3]. The largest uncertainty about the petrogenesis of LEW87051 is the relationship between the large olivine crystals and the groundmass. Prinz *et al.*[4] suggested that olivines are xenocrysts, while McKay *et al.*[5] proposed a fractional crystallization model based on experimental studies. However, the crystals have Cr-rich and Ca-poor cores (Fig.1) which do not match experimental olivines. Although Jurewicz and McKay[6] tried to explain the zoning of the rim by diffusion, some features are not explained. There also exists a definite composition boundary of Fe# and MnO (Fig.1) between the core and the rim. To clarify the origin of these olivines, we have performed experiments using LEW87051 analogs to measure the effects of oxygen fugacity(fO_2) on distribution coefficients of various elements in angritic system.

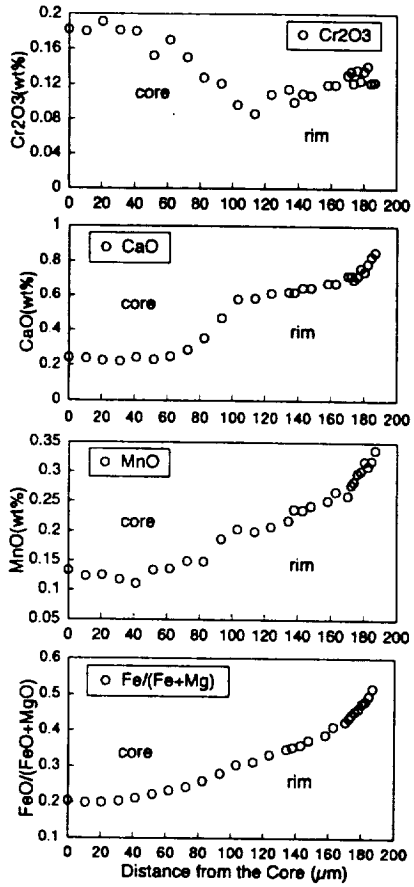

Fig.1 Observed zoning profiles of LEW87051 olivine

EXPERIMENTAL PROCEDURES

We prepared two different starting materials for the experiments. They are named L7 (bulk LEW87051) and L7A (*ca.* 10% olivine removed from L7). For each experiment, a 125mg pellet was made, placed on a $Pt_{40}Rh_{60}$ wire loop and suspended in a Deltech furnace for 96 hours at the appropriate temperature and fO_2. We ran experiments for both compositions from two log. units below the iron-wüstite buffer (I.W. -2) to four log. units above it (I.W.+4). For L7, the pellet was held in the furnace at 1430°C to melt it completely for 48 hours, then quenched to room temperature. After that, it was put back in the furnace for 48 hours at 1400°C to grow olivine crystals. For L7A, the holding times (48 hours and 48 hours) were the same, but the temperature was first 1300°C, then 1225°C. CO/CO_2 flowing gas was used for obtaining the desired fO_2 as measured by a zirconia cell[7]. We analyzed the run products by wavelength dispersive analysis (WDS) at 20 kV and 30 nA using a Cameca electron microprobe.

RESULTS

Cr Distribution: Fig.2 shows the distribution coefficient of Cr between olivine and glass ($D_{Cr}^{Ol/Gl}$) at various values of fO_2. $D_{Cr}^{Ol/Gl}$ of both L7 and L7A are almost constant against each fO_2. $D_{Cr}^{Ol/Gl}$ of L7A is higher than that of L7. The data from L7A experiments have larger error bars than those of L7. Under oxidizing conditions a lot of small spinel grains were formed with

olivine. This might be one major reason why $D_{Cr}^{Ol/Gl}$ of L7A has large error bars. Our new data are in good agreement with the previous study[5].

Mn Distribution: We also pay attention to the Mn distribution, because bulk LEW87051 has as much MnO (0.25wt%) as Cr_2O_3 (0.17wt%). Fig.3 shows the distribution coefficient of Mn vs. fO_2. Values of $D_{Mn}^{Ol/Gl}$ are constant over wide range of fO_2 and higher temperature gives lower $D_{Mn}^{Ol/Gl}$. The only difference between $D_{Cr}^{Ol/Gl}$ and $D_{Mn}^{Ol/Gl}$ is that Mn has a little higher distribution coefficient. The results of this study are in good agreement with [8].

Ca Distribution: The extremely low content of CaO in the olivine core is puzzling. Our experimental data for $D_{Ca}^{Ol/Gl}$ plotted against fO_2 show nice parabola curves. $D_{Ca}^{Ol/Gl}$ is much lower than $D_{Cr}^{Ol/Gl}$ and $D_{Mn}^{Ol/Gl}$, but shows a similar trend to lower values at higher temperature. However, our experimental olivines have much higher CaO than LEW87051 cores.

DISCUSSION

This study indicates that $D_{Cr}^{Ol/Gl}$ and $D_{Mn}^{Ol/Gl}$ are almost constant from I.W.-2 to +4 for constant temperature. This means $D_{Cr}^{Ol/Gl}$ and $D_{Mn}^{Ol/Gl}$ are little affected by fO_2, preculding changes in fO_2 as the source of the zoning in LEW87051 olivines. Assuming the profiles of Cr_2O_3 and MnO (Fig.1) are mainly a result of fractional crystallization with different distribution coefficients, there would have to exist an area of temperature where $D_{Cr}^{Ol/Gl}$ is above 1.0 and $D_{Mn}^{Ol/Gl}$ under 1.0. However, according to our data, $D_{Mn}^{Ol/Gl}$ is always a little higher than $D_{Cr}^{Ol/Gl}$ as stated before (Fig.2, 3). We can't explain the zoning profiles of the core only by the difference of the distribution coefficient. The most plausible explanation we think is that first olivine crystallized at some temperature and Cr_2O_3 and MnO zoned normally. Then, it was heated at high temperature and the rim melted. If olivine was kept at high temperature for a long time, the content of Cr_2O_3 would decrease towards the rim by diffusion because the core has higher Cr_2O_3 than that equilibrium with the bulk rock. On the other hand MnO would increase. CaO content wasn't affected very much, because the diffusion rate of Ca^{2+} will be slower than those of Cr^{3+} and Mn^{2+}. After that, the rim crystallized, producing normal zoning by fractional crystallization.

CONCLUSION

It appears inevitable that LEW87051 olivine experienced two stage crystallization. The zoning in the outer part was primary zoning from fractional crystallization, but zoning in the innner part appears compatible with diffusion. It seems likely that the core olivines are xenocrysts that once crystallized under different conditions, then mixed with the groundmass melt, whereupon the rim grew.

Fig.2 $D_{Cr}^{Ol/Gl}$ vs. log($fO2$/I.W.)

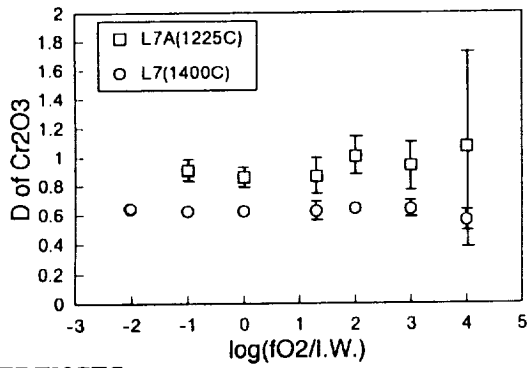

Fig.3 $D_{Mn}^{Ol/Gl}$ vs. log($fO2$/I.W.)

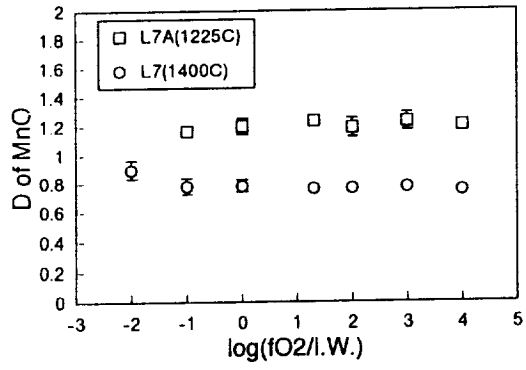

REFERENCES

[1]Lugmair G.W. and Galer S.J.G. (1992) *GCA 56*, 1673-1694 [2]Mittlefehldt D.W. and Lindstrom M.M. (1990) *GCA 54*, 3209-3218 [3]McKay G. *et al.* (1990) *LPSC XXI*, 771-772 [4]Prinz M. *et al.* (1990) *LPSC XXI*, 979-980 [5]McKay G. *et al.* (1990) *Meteoritics 26*, 370 [6]Jurewicz A.J.G. and McKay G. (1993) *LPSC XXIV*, 737-738 [7]Williams R.J. and Mullins O. (1981) *NASA Technical Memorandum 58234* [8]Miyamoto M. *et al.* (1993) *JGR 98*, No. E3, 5301-5307

OMIT TO P 923

MINERAL PARAGENESIS OF THE UREILITES: EVIDENCE FOR HIGH PRESSURE IN A LARGE PARENT BODY; O.B.Mitreikina., O.V.Chryukina, N.G.Zinovieva and L.B.Granovsky, Department of Petrology, Faculty of Geology, Moscow State University, Lenin Gory, Moscow 119899, Russia.

The research on mineral paragenesises of ureilites showed that an interstitial material formed by isochemical re-crystallization and partial melting of rock-forming minerals: olivine and pyroxene. The existence of pyrope in the re-crystallized areas and the assemblage of new-formed Mg-rich minerals + Fe-metal + Cr-Fe - sulphides + Cr-spinellid + carbon material + diamonds let us make a conclusion that the re-crystallization of ureilites happened in high pressure conditions by the reducing carbon-rich fluids.

Ureilites are very interesting because of the different formation conditions of rock-forming minerals and an interstitial material. It's well known that main minerals of ureilites are olivine and pyroxene. They have zonal-structure: Mg-content of these minerals increases to the border of the grains. The most interesting is a problem of the genesis of the interstitial fine-grained material. It was shown [1; et al.] that its bulk chemical composition is pyroxene-like and is rich in Al_2O_3, CaO and siderophile elements in comparison with centers of the grains of rock-forming minerals.

Detailed petrological research on a zonal composition of the rock-forming minerals and the interstitial material of meteorites Novo-Urei, Dyalpur, Havero and Kenna carried out by the scanning electron microscope CamScan-4DV with energy-despersive analyzer AN 10000, let us make the following conclusions.

The zonal structure of the olivine and pyroxene grains has metamorphic nature. The grains of olivine and pyroxene consist of the central parts of the grains and thin interrupted rims around them or sometimes along thin fractures inside the grains. Fractures between olivine and pyroxene grains and fractures crossing these grains are filled with carbon material, Fe-Ni metal, sulfides rich or poor in Cr, cohenite and perryite. There are fine (up to 1 mkm) crystals of diamonds in these fractures. The thickness of the rim of alteration is much more in the olivine grains (up to 150 - 300 μm) than in the pyroxene (up to 30 - 50 μm) grains (Fig. 1).

The outer parts of the olivine grains (rims) are re-crystallized nearby the fractures and are formed by the aggregate of olivine (Fa 2-3), enstatite and Fe-metal. We found that this rim has a zonal structure. There are the following zones from the fracture to the center of the olivine grains: a - enstatite + sulphide of Fe and Cr + Cr-spinellid; b - enstatite + olivine (Fa 2-3) + Fe-metal (with fine chromite grains); c - olivine (Fa 5-10) + fine Fe-metal grains. Fe-content of the olivine grains sharply increases from the rim to the center and the centers of the grains have a constant (Fa 17-20) composition without fine grains of Fe-metal. It's necessary to note that olivine (with fine grains of Fe-metal) has the deficiency of ferrous iron as the result of reducing $Fe^{2+}$to Fe^0 and forming Fe-metal. Bulk composition of completely re-crystallized parts of the rim is nearly equal to the composition of olivine with deficiency of ferrous iron. The re-crystallized phases are poor in Fe, and rich in Cr and have a good stehiometry. Small grains of primary olivine are completely re-crystallized.

Thus, the zonal structure of olivine grains is formed by the reduction of ferrous iron and by the re-crystallization of olivine. Change of paragenesises of re-crystallized aggregate shows the increasing of the reduction conditions from the centers of the olivine grains to the fractures, highly reducing carbon-rich fluids followed.

The outer parts of the pigeonite grains (rims) are re-crystallized nearby the fractures, but these rims are very thin and interrupted. The re-crystallization of pigeonite has a zonal structure as well. There are the fine grains of Fe-metal in the rim as the result of reducing Fe^{2+} to Fe^0. The rim is poor in Ca and lost Al in comparison with pigeonite core. The thin rim of low-Ca enstatite formed as a result of this process. Ca and Al are concentrated in the central part of the alterated area. The bulk composition of the re-crystallized areas of pigeonite is equal to the composition of the primary pigeonite, but is rich in Al and Si in comparison with pigeonite cores.

The mineral composition of the active re-crystallized zones of pyroxene consist of relict grains of low-Ca enstatite, augite and quartz-like phase with variable content of Al_2O_3 (up to 8 weight. %),

C-6.

Na_2O (up to 3 weight. %) and K_2O (up to 0.7 weight. %). These zones have a magmatic texture: small (up to 2-3 μm) idiomorphic augite grains grow on the surface of the low-Ca enstatite crystals. These grains together with small grains of Fe-metal are cemented by an interstitial quartz-like phase. Sometimes this melt intrudes (by the fractures) into the unchanged zones of pigeonite (Fig. 2) and even into partially re-crystallized grains of olivine. We can explain the heterogeneous composition of quartz-like phase by it small size and because of it dirty analysis. When the quartz-like phase forms larger grains it has the quartz composition. It's known that there is difference (from first to 14-15 weight %) in Al_2O_3-content of quartz-like phase. We have made analyses of Al_2O_3-rich areas and have found small (<1.5 μm) grains of pyrope surrounded by the quartz-like phase containing lesser 2 weight % of Al_2O_3. The analyses of pyrope are dirty with SiO_2 because of the small size of the pyrope grains. However, the correlation of the others components (deducted 8 % of SiO_2) shows the good stehiometry of almost pure pyrope: Pyr-82.0, Alm-7.4, Andr-5.0, Uwar-2.3, Gros-3.3 - $(Mg_{2.46}Fe^{2+}_{0.22}Ca_{0.32})(Al_{1.85}Cr_{0.04}Fe^{3+}_{0.1})[Si_{3.04}O_{12}]$. The existence of paragenesis of Pyr + low-Al Opx + Mg-Ol + Cpx testify to the high pressure formation condition of the re crystallization of ureilites.

Comparing the paragenesises of new-formed minerals replacing olivine and pyroxene, we see that they formed in the equilibrium conditions. It's well known [2; 3] that there is the heterogeneous distribution of Si, Ca, Al and Cr in the interstitial material of ureilites but this heterogeneous distribution is connected with the different compositions of the primary olivine and pyroxene, and it's not necessary to have the residual, interstitial melt of the ureilites. The re-crystallization of the ureilites has isochemical nature and doesn't need transport of the petrogenic elements. The comparison of ureilites which had been undergone the different level of impact metamorphism showed the independence of the processes of the re-crystallization and impact metamorphism.

The presence of pyrope in the melted zones of the ureilites let us to suppose that the re-crystallization of the ureilites with their partial melting was caused by the subsidence of the ureilites into the rather large parent body where ureilites were metamorphosed by the highly reducing carbon-rich fluids.

REFERENCES: [1] Goodrich C.A. (1992) *Meteoritics 27,* 327-352; [2] Ogata H. et al. (1991) *Meteoritics 26,* 195-200; [3] Scott E.R.D. et al. (1992) *LPS XXIII,* 1253-1254.

FIGURE CAPTIONS: Fig. 1. Meteorite Novo Urei. Active re-crystallization of olivine (from the left) and poorly re-crystallization and partial melting of pigeonite (from the right); Fig. 2. Meteorite Novo Urei. Melted jets in pigeonite.

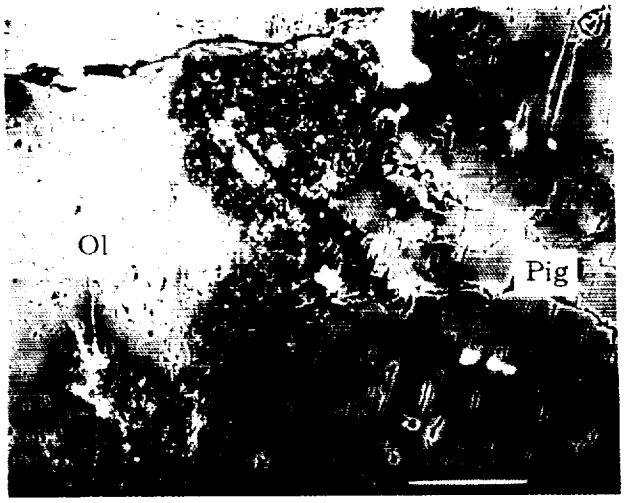

Fig. 1

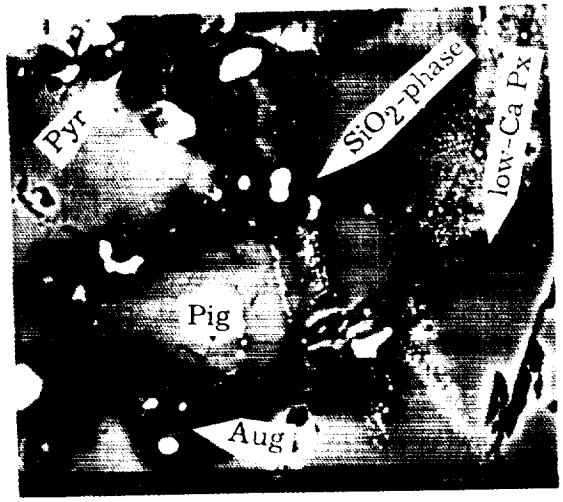

Fig. 2

ALH84001 CUMULATE ORTHOPYROXENITE: A PREVIOUSLY UNAPPRECIATED MARTIAN METEORITE

David W. Mittlefehldt, *C23, Lockheed Engineering and Sciences Co., 2400 Nasa Rd 1, Houston, TX 77058*

The shergottites, nakhlites and Chassigny are igneous rocks widely thought to be samples of the martian crust [*e.g.* 1]. Discovery of new martian meteorites always generates interest in the meteoritic community. Interest is heightened if the meteorites are petrologically unusual, because increased diversity holds promise for increased understanding of martian petrologic evolution. ALH84001, originally classified as a diogenite, has recently been properly classified as a unique orthopyroxenite martian meteorite [2,3]. Here I report on petrologic and geochemical study of ALH84001.

Petrography. ALH84001 is a coarse-grained, cataclastic orthopyroxenite with much of the original magmatic or metamorphic texture preserved. Generally anhedral orthopyroxene grains up to 6 mm across exhibit patchy extinction, and contain fractures and transecting crushed zones of fine-grained anhedral orthopyroxene and chromite produced by shock. Euhedral to subhedral chromite grains up to 0.5 mm in size are enclosed in, or are interstitial to, orthopyroxene. Maskelynite, typically a few hundred μm in size, occurs interstitial to coarse orthopyroxene and in the crushed zones. Accessory phases are augite, apatite, pyrite and Mg-Ca-Mn-Fe carbonate. Augite (~10 μm) and apatite (up to ~300 μm) are interstitial phases. Pyrite (~10 μm) is associated with interstitial chromite, maskelynite and carbonate, and in the crushed zones associated with anhedral chromite. Interstitial carbonates (~100 μm), showing fine-scale compositional zoning from Ca-Mn-Fe-rich cores to Mg-rich rims, are associated with maskelynite and pyrite. Shock damage in these carbonates demonstrates that they are pre-terrestrial. Small (~10 μm), homogeneous carbonates are found in the crushed zones and in fractures, and are post-shock. The orthopyroxene and chromite grains are relatively homogeneous in composition. Average mineral compositions are; orthopyroxene - $Wo_3En_{69}Fs_{27}$, maskelynite - $An_{31}Ab_{63}Or_6$, augite - $Wo_{42}En_{45}Fs_{13}$, carbonate - $Cc_{12}Mg_{58}Sd_{29}Rd_1$.

Geochemistry. The REE pattern for a bulk interior sample of ALH84001 exhibits a depletion in LREE relative to HREE, as would be expected for a cumulate orthopyroxenite, and a negative Eu anomaly (Fig. 1). However, the depletion in LREE is not as great as expected for a cumulate from a melt with chondritic REE ratios, as shown by a mean of orthopyroxene clasts from the Johnstown diogenite [4]. The chondritic normalized La/Lu ratio of ALH84001 is 0.36, compared to ~0.007 expected for a cumulate based on opx/melt partition coefficients.

Petrogenesis of ALH84001. The original protolith had a coarse-grained, equigranular texture with common 120° triple junctures, indicating slow cooling. The uniform compositions of orthopyroxenes and chromites similarly indicate slow cooling. Because ALH84001 is nearly monomineralic, and texture and mineral compositions indicate slow cooling, it is likely that ALH84001 is a cumulate. The interstitial maskelynite suggests that a trapped melt component is present. Many of the maskelynites are not stoichiometric plagioclases. Rather, they contain excesses of SiO_2 over that required for stoichiometry. This suggests that the interstitial regions were composed of feldspar plus silica prior to shock.

The bulk sample contains about 1% maskelynite. Because the trapped melt was likely basaltic, the amounts of normative plagioclase and pyroxene in this melt were probably subequal, and therefore the amount of trapped melt likely is ~2%. The REE pattern of ALH84001 is consistent with the presence of trapped melt. The higher than expected La/Lu ratio can be explained by inclusion of ~2% of a LREE-enriched melt with a La/Lu ratio ~4 times CI, roughly half that inferred for the nakhlite parent magma [5]. This calculated parent melt also has a negative Eu anomaly, with Eu/Sm ~0.6 times CI.

It is possible that the REE pattern of ALH84001 was affected by infiltration metasomatism, a process invoked for the nakhlites [6]. The early, zoned carbonates provide petrographic evidence for fluid fluxes in ALH84001, and their compositions suggest that they were formed at ~700°C [7]. This might be taken as evidence for infiltration metasomatism. However, the early carbonates appear to be discrete grains and not metasomatic replacements of earlier phases. Regardless, an infiltrating fluid phase, rich in REE, could cause preferential enrichment in LREE in the cumulate. The parent melt REE pattern could not then be inferred from bulk REE analyses.

Relationship to Other Martian Meteorites. ALH84001 has several mineralogic and petrographic features in common with the nakhlites and Chassigny. The latter are cumulates with minor interstitial melt [8,9], as is ALH84001. The nakhlites and Chassigny contain generally homogeneous pyroxenes

[9,10], indicating slow cooling, as inferred for ALH84001. The maskelynite compositions of ALH84001 are within the range of feldspar compositions in nakhlites and Chassigny [8,9], but more sodic than those in the shergottites [11-13]. However, many maskelynites in ALH84001 are similar to some of the mesostasis compositions of Shergotty and Zagami [12], but with less SiO_2. The parent melt inferred above for ALH84001 (assuming no infiltration metasomatism) is LREE-enriched, as were those for the nakhlites and Chassigny [5]. Pyrite is present in ALH84001, nakhlites and Chassigny, but not in the shergottites. However, petrogenetic models for the nakhlites and Chassigny are not compatible with the petrology of ALH84001. Estimated parent melts for nakhlites and Chassigny are saturated in olivine and augite, not orthopyroxene [e.g. 14], and therefore it does not seem likely that ALH84001 is directly related to the nakhlites or Chassigny.

Although shergottites contain strongly zoned minerals and textures indicative of rapid crystallization, ALH84001 does show several petrologic affinities to the shergottites. Orthopyroxenes and chromites in ALH84001 are similar in composition to those of the megacrysts from EETA79001 lithology A [11,15] (Fig. 2). Hence, a parent melt with major element composition like that which formed the megacrysts might be a suitable parent for ALH84001. The ALH84001 orthopyroxene compositions suggest its parent was slightly more ferroan (Fig. 2). The EETA79001 megacrysts contain olivine [11], which is absent in ALH84001. Olivine is in reaction relation with a megacryst parent melt composition [16], and therefore, fractional crystallization processes could form an olivine-free orthopyroxenite from this parent melt. Plagioclase compositions are a severe problem as the most calcic maskelynite in ALH84001 (An_{39}) is much more sodic than those in shergottites [11-13] or than experimental plagioclases [16]. Finally, the calculated shergottite parent melts are LREE-depleted [5], which is incompatible with the trace element composition of ALH84001, unless infiltration metasomatism affected the REE pattern of the protolith.

Thus, ALH84001 exhibits petrologic affinities to both the nakhlites-Chassigny on one hand, and the shergottites on the other, as well as differences. The parent melt of ALH84001 likely was compositionally distinct from those of the other martian meteorites.

References. [1] McSween (1985) *Rev. Geophys.* **23**, 391. [2] *Ant. Met. Newsletter* **16**(3). [3] Mittlefehldt (1994) *Meteoritics*, in press. [4] Mittlefehldt (1994) *GCA*, in press. [5] Longhi (1991) *PLPSC* **21**, 695. [6] Berkley *et al.* (1980) *PLPSC* **11**, 1089. [7] Anovitz and Essene (1987) *J. Petrol.* **28**, 389. [8] Bunch and Reid (1975) *Meteoritics* **10**, 303. [9] Floran *et al.* (1978) *GCA* **42**, 539. [10] Harvey and McSween (1992) *GCA* **56**, 1655. [11] McSween and Jarosewich (1983) *GCA* **47**, 1501. [12] Stolper and McSween (1979) *GCA* **43**, 1475. [13] Treiman *et al.* (1993) *Meteoritics*, submitted. [14] Treiman (1993) *GCA* **57**, 4753. [15] Steele and Smith (1982) *PLPSC* **13**, *JGR* **87**, A375. [16] Wasylenki *et al.* (1993) *LPS* XXIV, 1491.

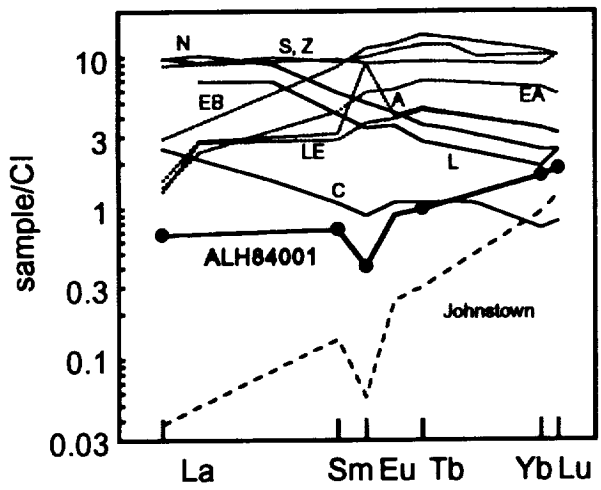

Figure 1. Rare earth element diagram for ALH84001 compared to other martian meteorites and to mean Johnstown diogenite orthopyroxene clasts [4]. REE data are from [1] - Chassigny (C), Lafayette (L), Nakhla (N), Shergotty (S); from [12] - Zagami (Z); and from [13] - ALHA77005 (A), EETA79001 lithologies A (EA) and B (EB) and LEW88516 (LE).

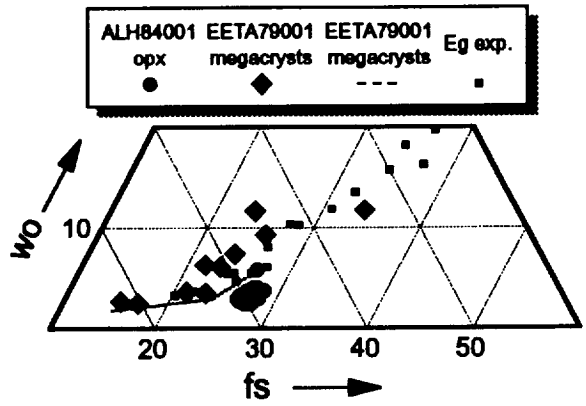

Figure 2. Molar compositions of individual pyroxene analyses for ALH84001. EETA79001 megacryst pyroxene compositions from [15] (diamonds) and [11] (line); Eg exp. - experimental pyroxenes from synthetic EETA79001 groundmass melt composition from [16].

TWO TYPES OF SHOCKED QUARTZ AND GRAPHITE AT BARRINGER IMPACT CRATER. Y. MIURA; Faculty of Science, Yamaguchi University, Yoshida, Yamaguchi 753, Japan.

Material evidences of shocked silica and carbon have been considered to be difficult to obtain at impact craters and experiments. This is mainly because high-pressure type minerals and impact materials are difficult to find at impact crater and speedy impact experiment, respectively. However, two types of shocked silica and carbon materials [1,2,3,4] are considered to be formed at different stages of dynamic impact process. The purpose of this study is to describe the detailed compression stages of formation of shocked silica and carbon found at the Barringer meteorite crater.

I. New shocked graphite and quartz aggregates from the Barringer crater

Diamond has been reported from the Barringer crater as cliftonite [5] and hexagonal diamond (lonsdaleite [6]), though these data are based mainly on optical or powder (camera) data. Recently shocked quartz and shocked graphite (with fine size, high density, and mixture with fine amorphous glasses) are reported from the Barringer crater[7,8] as follows.

I-1. Samples: Graphite block sample of the Barringer crater used in this study was one of the evaporated impact sample including silica and carbon materials collected at 4km west from rim of the crater. Pure silica samples with various shock features were collected inside or on the rim of the crater.

I-2. Compositions and textures of two types of two shocked materials : Optical, X-ray and analytical electron microscopic data reveal four major different shocked aggregates as follows [7,8] (Table 1):

a) Shocked graphite-1 in the matrix: Black fine-grained shocked graphites contain uniformly fine-grained Fe (from kamacite) and trace of Ca (from Kaibab limestone) which were formed under mixed gas state of impact.

b) Shocked graphite-2 in vein metal: Crystallized shocked graphites and shocked hexagonal chaoite-like carbon are surrounded by kamacite-rich metal under gas states of various compositions mixed from iron meteorite, sandstones and limestone.

c) Shocked quartz-1 in the rim: Kamacite-rich metal contains shocked quartz (mainly from Coconino sandstone). Shocked quartz-1 grains with high density contain Fe and Ca.

d) Shocked quartz-2: Clear shocked quartz -2 (and stishovite, and coesite) with pure silica formed from the Coconino sandstone [1].

II. Dynamic formation process of shocked graphites

Two kinds of two different shocked carbon and quartz can be explained by the dynamic impact process [9,10] as follows (Table 1).

a) First explosion by super-heating: The first shocked graphite-1 aggregates were formed from gas-state of Fe (from iron meteorite), C (from Kaibab limestone), and Ca (from sandstone) under ultra-high temperature condition from meteoritic kinetic energy to chemical heat energy.

b) Secondary destruction by shock waves: The secondary shocked graphite-2 aggregates or shocked quartz-1 were formed from huge destruction by shock waves which makes gas-melt states of Fe, Ni, Ca, C and Si elements. After evaporating and ejecting iron, compression with jetting on the Coconino sandstone makes shocked quartz-2 aggregates.

Origin of carbon of shocked graphites is considered to be from Kaibab limestone. This is mainly because shocked graphites contain chemical inclusions from the target rocks of Kaibab limestone and Coconino sandstone, which cannot be obtained in fine graphite of original meteorite [2].

Table 1. Formation stages with shocked carbon and silica in the Barringer crater [8].

Shock stage	Impact condition	Mineral assemblages
1) Compression	High pressure and temperature	Fine mixture (disappeared to gas)
2) Compression-1 (with jetting)	Vapor state (vapor plume)	Fine **shocked graphite-1** (+Fe,Ca) (in the major C matrix)
3) Compression-2 (with jetting)	Melt-solid state (mixed)	**Shocked graphite-2** (+Fe) and Chaoite-like carbon in the vein
4) Compression-1 (with jetting)	Melt-solid state (mixed)	**Shocked quartz-1** (+Fe) in the rim
5) Compression-2 (with jetting)	Solid-melt state (mixed)	**Shocked quartz-2** (+stishovite, coesite)

III. Formation processes of shocked aggregates

By applying two major impact formation-processes of two shocked graphite and quartz at the Barringer crater, two shocked features of the aggregates can be explained as two impact stages: (1) vapor plume stage, induced by initial compression and vaporization (found as dendritic or wormy texture), and (2) the second compression stage [7,8] (observed as planar feature), as listed in Table 2.

Table 2. Two major shocked materials of impact craters [7,8].

Stage of formation	Type of shocked materials	Example
1) Initial compression (with wormy glass)	Shocked quartz-1 (fine)	Barringer crater
	Shocked graphite-1	Artificial impact
2) Second compression (with lamellae)	Shocked graphite-2	Barringer crater
	Shocked quartz-2	K/T boundary
	Shocked stishovite (coesite)	Artificial impact

IV. Conclusion

The present results are summarized as follows:

a) Graphite block of the Barringer crater consists of two types of carbon materials, shocked graphite-1 and graphite-2 (chaoite-like carbon), and a silica material, shocked quartz-1 with fine grained aggregates and high density. Shocked quartz-2 without iron contamination is found at the rim of the crater.

b) The two types 1 and 2, shocked carbons and silica materials, are considered to be formed at compression-1 (by vapor-melt reaction) and compression-2 (by solid-melt reaction) with jetting stages of impact.

c) High pressure-type materials of silica and carbon are formed by solid-melt conditions at the final compression stage of impact

References:

[1] Miura Y. (1991) LPSC XXII (LPI, USA),22, 905-908. [2] Miura Y.(1991) Shock Waves, 1 35-41. [3] Miura Y. et al.(1992) Shock Waves (Springer-Verlag), 18, 403-408. [4] Miura Y. et al. (1992) Celestial Mechanics and Dynamical Astronomy, 54, 249-253. [5] Foote A. E. (1891) Am. J. Sci., 42, 413-417. [6] Hannemann R.E. et al.(1967) Science, 155, 995-997. [7] Miura Y. et al.(1993) Meteoritics, 28(3), 402. [8] Miura Y. (1993) Proc. ISAS Lunar and Planet. Symp.(ISAS), 26, 98-101. [9] Gault D.E. et al. (1968) Shock Metamorphism of Natural Materials (ed. by French and Short), p.87-100. [10] Melosh H.(1989) Impact cratering (Oxford University Press), 245pp.

LUNAR LANDING SITE AND EXPLORATION BY JAPANESE LUNAR PROJECT: Miura Y.[1,2] and Lunar Working Group of Japan[3], [1]Fac. of Sci., Yamaguchi University, Yamaguchi 753, Japan, Tsukuba Space center, NASDA of Japan, Tsukuba 305, Japan, and [3]RESTEC, Roppongi 7-15-17, Minato-ku, Tokyo 106, Japan.

Japan is planning to select landing site and exploration on the Moon. The scientific significance of the project is now in progress to summarize. The main purpose of the paper is to discuss briefly the significance of characterization of lunar materials, especially about lunar materials on surfaces and deeper places from lunar resources and shocked materials [1].

1. Main purposes of lunar exploration

The Main purposes of lunar exploration are summarized as follows [1,2]:

1) Development of space resource: Space energy is developed on 'solar energy' from the Sun, including the solar components or metals reducted by the solar beam bombardments, and on synthesis of free oxygen and water in space.
2) Development of space and planetary sciences: From collecting the lunar samples, it can be discussed unsolved problems: origin of the Earth-Moon planetary bodies, unique impact samples originated from terrestrial ring fragments, origin of lunar meteorites on Antarctica and Australia. Lunar history of magma ocean activity and impact can be developed by mare basalts, pristine anothosites, KREEPy rock, Mg-suite, lunar granite, lunar crust-mantle materials, and extra-lunar materials remained by impact. Earth history can be discussed from the origin of the Earth, giant ocean impact, and Earth interior evolution. Moon observatory on impact craters are searching on the nearside by using covering system.
3) Development of material science: New types analytical methods should be developed on X/ray and mass analyses, and finding the shocked materials of high-density and high pressure type minerals.
4) Maintenance of Earth's environment: To avoid the Earth's environmental changes (including life circulation system) by using terrestrial fossil energy, space resources can be utilized for development in space.

2. New foundings of shocked materials on the Moon

The following two types of shocked materials exist on the Moon [3,4]:

1) Shocked materials by impact on the Moon. Impact brecciated rocks are mainly formed on the lunar primordial crust. Shocked aggregates which include high-density and high-pressure grains are formed by impact (with and without atmosphere) [4], though original silica and carbon components are trace amounts on the Moon.
2) Moon-Earth unique brecciated rock: If lunar cataclysm which was perceived as a late spike in the cratering flux on about 3850 to 4000 m.y. was due to debris from the breakup of a large planetary bodies [5], the debris from the ring of primordial Earth and Mars-like can be collected on the surface or deeper place on nearside of the Moon.

3. Lunar landing site and exploration route

We are selected nine candidates for lunar landing site and exploration:

Mare Imbrium, Mare Humorum, Hevelius, Oceanus Procellarum, Mare Tranquillitatis, Mare Crisium, Mare Smythii, Mare Nectaris and Mare Serenitatis (Apollo-17 site).

One of the best candidates for lunar landing site is Mare Imbrium region because the typical impact craters, ejecta, regolith and resources can be found at the long distance exploration from Apennine Mts, Archimedes, Eratosthenes, to Copernicus craters by lunar roving vehicle. The main visiting route and lunar exploration are summarized in Table 1.

Table 1. Lunar driving route and exploration on Mare Imbrium region [3].

Visiting place	Main research project	Remarks
1) Eastern Mare Imbrium:		
	Landing site-1	Near Apollo-15 site
	Impact cratering	Pre-Imbrian and
	Stratigraphy (Imbrian)	Imbrian sediments
	Volcanism (lava, basalt)	
	Solar and metallic energy	H and He ions
	Habitation development	Water synthesis
	Weathering and erosion	Cliff outcrop
	Unique lunar materials	Debris
2) Archimedes crater:		
	Impact and volcanic materials	Imbrian crater
	Resource materials	Impact ejecta
3) Apennine Mts:		
	Various sediments	Crater rim
	Stratigraphy	Cliff & deeper place
	Resource materials	Older igneous rocks
	Mixing of lunar highland	
	Lunar dark mantle materials	
4) Eratosthenes crater:		
	Sediments (Eratosthenian)	Impact crater
	Impact & resource materials	Impact ejecta
5) Copernicus crater:		
	Stratigraphy (Copernican)	Impact crater
	Impact & resource materials	Younger lava

Acknowlegements

The present research is supported in part by the NASDA in Japan and the Monbusho of senior author.

References

[1] Moon and Planets Remote-Sensing Investigation Committee (RESTEC) (1993) NASDA Investigation Report (NASDA, Tokyo), 5, 199 pp.
[2] McKay M. et al. (1992) Space Resources (NASA), I-V. 316 pp. (III).
[3] Miura Y. et al. (1989) LPSC XX, 705-706.
[4] Miura Y. (1991) LPSC XXII, 905-908.
[5] Ryder G. (1990) EOS Trans. AGU, 71, 313.

JAPANESE FOUND METEORITES SIMILAR TO ANTARCTIC METEORITE COLLECTION: Y. MIURA[1], K. YANAI[2], and O.G.IANCU[1], [1]Faculty of Science, Yamaguchi University, Yamaguchi 753, Japan, [2]Department of Antarctic Meteorites, National Institute of Polar Research, Kaga, Itabashi-ku, Tokyo, 173, Japan.

The postulated mechanism of meteoritic concentration was reported in Antarctica, where meteorites fallen on separated snowfields are classified as type (1) of concentration in certain locations ablated near obstacles and type (2) of concentration into Antarctic Sea by iceflow [1] as listed in Table 1. Main purpose of this paper is to find similar accumulation mechanisms of found meteorites in the non-Antarctica of Japan. Two Japanese meteorites, Tahara and Mihonoseki, are considered to be of type (1) mechanism, whereas two iron meteorites of Shirahagi and Saotome might be of type (2) mechanism.

1. Two found chondritic meteorites

Two chondrites, Tahara (0.98kg) and Mihonoseki (6.49kg), were found in Shimane-ken, Japan on December, 1992 as follows [2,3,4,5].

1) Falling time and place: Mihonoseki chondrite fell into Mr. Matsumote's house without any witness near the falling place, on 10th December, 1992 and was found after two days in public and identified as chondrite (L) firstly from the tiny fragments by electron microprobe analyzer (EPMA) on 28th December, 1992 by one (YM) of the authors [2,5]. Tahara meteorite (Tahara-1) was firstly shown by one of the crew members (Mr. H. Minao) of a car-transport ship at his "house" near Matsue-shi, Shimane-ken, Western Japan on 28th December, 1992, because he heard accidentally about the new fall of Mihonoseki chondrite at Mihonoseki, Shimane-ken (17km northeast from Matsue-shi) through the mass communications. One of the crew members (Mr. T. Ayabe) who found many meteorite-like fragments on the deck of this ship anchored in Tahara, Aichi-ken, Eastern Japan (ca.400km southeast Matsue-shi) on 26th March, 1990, was kept the small strange fragments (Tahara-2) probably to ask some insurance for the damage of ship, though there were no witness of the fall and sound in that cloudy day. The estimated total mass of the Tahara meteorite which formed an impact crater of a 40 cm diameter, is ca. 6 kg, but the main mass is missing now (probably thrown out into the sea).

The first meteorite fallen on a ship is that fell in 1648 during a voyage between Holland to Java [6], though the iron meteorite was not remained now. Tahara meteorite is the 42nd meteorite fallen in Japan, and the first remained chondritic meteorite which fell on a ship's deck.

2) Transporation: Mihonoseki meteorite remained on the ground of the basement after penetrating the house. Fragments of Tahara meteorite have been kept on the crew-members' houses, brought from the Tahara-Harbor.

3) Collection place: The two chondrites, Mihonoseki and Tahara-1, were found at Eastern Shimane-ken on December, 1992.

4) Chemical group: Mihonoseki meteorite is L chondrite from the Fa-Fs diagram obtained by the EPMA [2,3]. Tahara meteorite is H chondrite from Iron diagram obtained finally by a bulk wet chemical analysis of the Tahara-2D (1.134 g for analysis); that is, Fe (in metallic form)/Si and Fe (in oxide and sulfide forms)/Si which are 0.44 and 0.36, respectively [5,7]. The EPMA data of 77 olivine and 36 pyroxene grains of Tahara

Table 1. Two types of the meteoritic transportation mechanism on the Antarctica.

Type	Falling place	Transportation	Concentration location	Found meteorites
(1) Obstacle	Snowfields	Iceflow	Obstacle	Many
(2) Sea	Snowfields	Iceflow	Sea	None

chondrite reveal Fa 18.6 (PMD 1.5 %) and Fs 16.3 in average (PMD 1.8%). Based on the petrographic data, the Tahara meteorite is classified as petrologic type 4~5 (or 4.6 in total average).

2. Two found iron meteorites

Two Japanese iron meteorites, Shirahagi (22.7kg) and Saotome (10.9kg), were found in rivers originated from a snowed mountain in the Japan Alps.

1) Falling place: The two irons were found on the bed of the Kamiichi-kawa river and into the waterfall of the river originated from Saotome-Dake mountain (2019m) on 1890.

2) Transportation: Two iron meteorites might be transported by snowflow and rivers.

3) Collection place: Two irons were found in obstacles of the bed or waterfall of the river.

4) Chemical group: Shirahagi iron is classified as IVA octahedrite [8]. Saotome iron is considered to be the same octahedrite, though it is missing now.

3. Relation with Antarctic Meteorite Concentration Mechanism

All meteorites of single or different falls can be found as belonging to the type (1) mechanism on the Antarctica. But almost all meteorites of non-Antarctica can be found only on hitting places. Major transportation on non-Antarctica is done by sandy wind on deserts [9], snowflow, or river as listed in Table 2. Two found meteorites, Tahara-1 and Mihonoseki, show different falling-place, -time and classification, where Tahara-1 was accidentally brought by people to the same founding place of Shimane-ken.

The two iron meteorites, Shirahagi and Saotome, are similar to type (2) mechanism of transportation by snowflow into the water (river in this case), though this kind of meteorites cannot be easily found in the deeper places: glacial lakes and seas (Table 3). If this hypothesis is correct, more meteorite could be found in water falls or at the bed of the rivers originated the snowed mountains.

Table 2. The probable meteoritic concentration mechanism.

Type	Falling place	Transportation	Concentration place	Example
(1)	a) Antarctica	Iceflow	Obstacle (Mountains)	Antarctica
	b) Desert	Sandy wind	Obstacle	Libya [9]
	c) House	People	House	Tahara & Mihonoseki
(2)	a) Antarctica	Iceflow	Antarctic Sea	None
	b) Snowfield	Iceflow	River, lake or waterfall	Shirahagi & Saotome(?)

4. Conclusions

The results of this study are summarized as follows:

1) The meteoritic accumulation mechanisms on Antarctica are divided into type (1) stopping by the obstacles and type (2) going into the sea. Tahara and Mihonoseki are modified type (1) mechanism of transportation by people, whereas found iron meteorites Shirahagi and Saotome belong to type (2) mechanism.

2) Tahara meteorite is the first remained chondrite in the world which fell on a ship's deck.

3) Meteorites originated from the snowed mountains could be found on the rivers.

References: [1] Cassidy W. et al. (1992) Meteoritics, 27, 490-525. [2] Miura Y. and Noma Y. (1993) LPSC, 24, 997-998. [3] Shima M. et al. (1993a) LPSC, 24, 1297- 1298. [4] Shima M. et al. (1993) Meteoritics, 28, 436. [5] Miura Y. et al. (1994) Proc. NIPR Ant. Meteorite (in press). [6] Willman O. (1992) En kort beskrivning pa en resa till Ostindien och Japan (in Swedish, Stockholm). 110pp. [7] Sears D.W.G. and Dodd R.T. (1988) Meteorites and the Early Solar System (Arizona Univ. Press), 3-31. [8] Shima M. (1979) Bul. Natl Sci Museum, E2, 1-16. [9] Jull A.J.T. et al. (1990) GCA, 54, 2985-2898.

NEW SNC METEORITE ALH84001: EVIDENCE FOR SNC METEORITE FROM NOBLE GASES;

Yayoi N. Miura[1], N. Sugiura[1] and K. Nagao[2], [1]Dept. of Earth and Planetary Physics, Univ. of Tokyo, [2]Inst. for Study of the Earth's Interior, Okayama University

ALH84001 was originally classified as diogenite [1]. Small chips of this meteorite were allocated to us under the guise of a diogenite. However, ALH84001 was recently re-classified as a new type of SNC meteorite according to mineralogical and oxygen isotopic features [2]. We measured noble gases in ALH84001, which show some characteristic elemental and isotopic compositions similar to those of other SNC meteorites and of the Martian atmosphere.

Experiment and results: Noble gas analyses were performed twice using bulk samples weighting 0.513g (#1) and 0.448g (#2), respectively. Noble gases were extracted from the samples stepwisely, and isotopic and elemental compositions of He, Ne, Ar, Kr and Xe were determined. The extraction temperatures are 700°C and 1750°C for #1, and 700°C, 1000°C, 1300°C and 1750°C for #2, respectively. Apparatus and procedure of the measurements are about the same as those described in [3] except for some improvements, *e.g.*, installation of an ion counting system.

Isotopic compositions of Ne obtained by all extraction steps show that they are mostly cosmogenic components. We assumed 1)measured Kr is mostly trapped and 2)Ne and Kr are trapped with a ratio similar to a literature value of the Martian atmospheric Ne/Kr ratio [4]. Then, trapped ^{20}Ne concentration is only 5% in the measured total ^{20}Ne concentration. On the other hand, Ar consists of cosmogenic, radiogenic and trapped components. $^{40}Ar/^{36}Ar$ ratio extracted from 1000°C fraction of measurement #2 is about 8000, which is much higher than the Martian atmospheric value and also terrestrial atmospheric value. In this fraction, radiogenic ^{40}Ar originated from in situ decay of ^{40}K seems to be released. Although the measured bulk $^{40}Ar/^{36}Ar$ ratios are as low as 1940 and 2220, the $^{40}Ar/^{36}Ar$ corrected for cosmogenic contribution are 6200 and 6500. They are much higher than the Martian and terrestrial atmospheric ratios. The meteorite may contain radiogenic ^{40}Ar. The $^{129}Xe/^{132}Xe$ ratios except for the lowest temperature fractions of 700°C show constant ratio of 2.0-2.2, which is close to those obtained from a shergottite EETA79001 glass sample [5] and from the Viking lander [6]. It seems to contain a large amount of the Martian atmospheric Xe. This is one of the strong evidence that ALH84001 belongs to SNC meteorite group.

Cosmic-ray exposure ages: Concentrations of cosmogenic ^{3}He, ^{21}Ne and ^{38}Ar and the preliminary calculation of cosmic-ray exposure ages are summarized in Table 1. The concentrations of cosmogenic light noble gases are close to those in Chassigny. The cosmogenic $^{21}Ne/^{38}Ar$ ratios of these meteorites are about 10, which suggest their higher Mg/Fe ratios than those of L-chondrites and the other SNC meteorites. In fact, 100 $Mg/(Mg+Fe^{2+})$ of orthopyroxene in ALH84001 is as high as 19 [2]. In order to calculate the production rates for ALH84001, equations as a function of chemical compositions presented by [7] and the ordinary production rates for L-chondrite [8] were used. Since bulk chemical compositions of ALH84001 are unknown, the chemical compositions of orthopyroxene reported by [9] were adopted as bulk compositions here. The mean value of cosmic-ray exposure age of T_3, T_{21} and T_{38} is calculated to be 14+/-2 Ma. Although this exposure age is slightly longer than those of Chassigny and nakhlites, they are within error limits considering uncertainties in chemical compositions and shielding effect. The exposure age of ALH84001 belongs to one of the three clusters for SNC group.

Trapped noble gases: A High $^{129}Xe/^{132}Xe$ ratio of ALH84001 suggests that this meteorite contained abundant Martian atmospheric Xe and also other noble gases. In previous works on SNC meteorites, it has been suggested that there are at least two components for SNC's trapped noble gases, which are a)Martian mantle and b)Martian atmosphere in origin (e.g., [10]). Their compositions are characterized by a)low $^{84}Kr/^{132}Xe$, low $^{129}Xe/^{132}Xe$ and low $^{40}Ar/^{36}Ar$, and b)high $^{84}Kr/^{132}Xe$, high $^{129}Xe/^{132}Xe$ and high $^{40}Ar/^{36}Ar$, respectively. Fig. 1 shows $^{129}Xe/^{132}Xe$ versus $^{84}Kr/^{132}Xe$ ratios. The data of most shergottites lie on a mixing line between them [10]. However, ALH84001 are plotted far above the line. Those of Nakhlites are also plotted above the line. Drake *et al.* [11] proposed an explanation for the high $^{129}Xe/^{132}Xe$ ratio with

relatively lower $^{84}Kr/^{132}Xe$ ratio for Nakhla that the meteorite interacted with an aqueous fluid after its crystallization, that is, atmospheric Xe was introduced into the meteorite as a sedimentary weathering product on the Mars. Our data for ALH84001 can be also explained by such a process, but there is now no other strong evidence for supporting it.

The plot for elemental ratios between $^{36}Ar/^{132}Xe$ and $^{84}Kr/^{132}Xe$ are presented in Fig. 2. The concentration of trapped ^{36}Ar is calculated assuming 0.188 and 1.55 as trapped and cosmogenic $^{38}Ar/^{36}Ar$ ratios, respectively, and those of trapped ^{84}Kr and ^{132}Xe are the measured concentrations. In this plot, elemental ratios of trapped Ar, Kr and Xe for ALH84001 do not fall on a trend between Chassigny and shergottites. The concentration of trapped Kr in ALH84001 is depleted compared with the trend of shergottite and Chassigny (Fig. 1), and that of trapped Ar is also depleted (Fig. 2). The fractionated elemental patterns can be attributed to the above process suggested by [11] or other physical processes such as shock implantation or adsorption.

Acknowledgement: We thank the Meteorite Working Group for providing the sample. This work is supported by Fellowships of the Japan Society for the Promotion of Science for Japanese Junior Scientists.

References: [1]*Antarctic Meteorite Newsletter* 8(2). [2]*Antarctic Meteorite Newsletter* 16(3). [3]Miura Y. *et al.* (1993) *GCA* **57**, 1857. [4]Hunten D.M. *et al.* (1987) *Icarus* **69**, 532. [5]Becker R.H. and Pepin R.O. (1984) *EPSL* **69**, 225. [6]Owen T. *et al.* (1977) *JGR* **82**, 4635. [7]Eugster O. and Michel Th. (1993) submitted to *GCA*. .[8]Marti K. and Graf T. (1992) *Annu. Rev. Earth Planet. Sci.* **20**, 221. [9]Berkley J. and Boynton N.J. (1992) *Meteoritics* **27**, 387. [10]Ott U. (1988) *GCA* **52**, 1937. [11]Drake M.J. *et al.* (1993) *LPSC XXIV*, 431. [12]Ott U. and Lohr H.P. (1991) *Meteoritics* **27**, 271. [13]compiled in Ozima M. and Podosek F.A. (1983) *Noble gas geochemistry*. [14]Bogard D.D. *et al.* (1984) *GCA* **48**, 1723.

Table 1. Cosmogenic noble gases and cosmic-ray exposure ages

	^{3}He	^{21}Ne	^{38}Ar	T_3	T_{21}	T_{38}	T_{mean}
ALH84001 #1	24.9	4.02	0.428	15.0	11.6	14.2	13.6+/-1.8
ALH84001 #2	24.8	3.51	0.481	14.9	10.1	16.0	13.7+/-3.1

Concentrations are given in unit of $10^{-8}cm^3STP/g$, and ages in m.y.

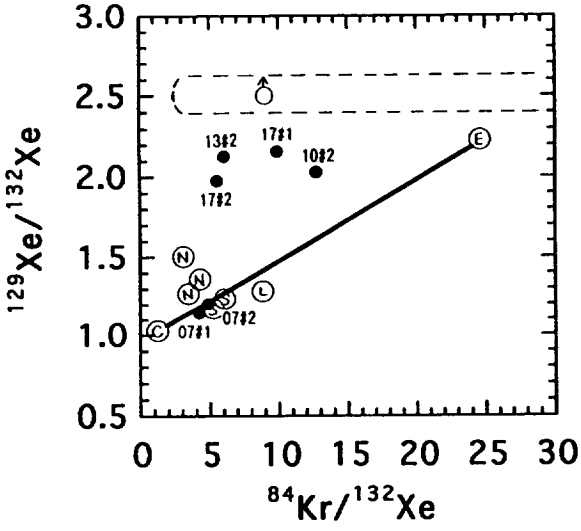

Fig 1. $^{129}Xe/^{132}Xe$ versus $^{84}Kr/^{132}Xe$.
●:This work (The numerical figures represent the extraction temperatures in 100°C) ⓔ:EETA79001 glass[5], ⓛ:LEW88516[12], ⓢ:Shergotty[10], ⓝ:Nakhla[10], ⓒ:Chassigny[10], ♁:Mars's atmosphere (large uncertainty is included) [6],[13]

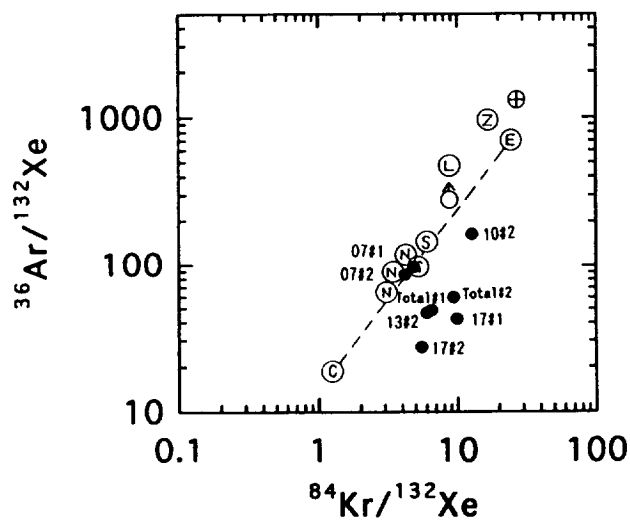

Fig 2. $^{36}Ar/^{132}Xe$ versus $^{84}Kr/^{132}Xe$.
⊕:Earth's atmosphere[13], the other symbols are the same as those in Fig. 1. ⓩ:Datum given by [14] for Zagami , for which cosmigenic ^{36}Ar is removed using the same procedure noted in the text, are added.

CHEMICAL ZONING OF OLIVINE IN SEVERAL PALLASITES SUGGESTIVE OF FASTER COOLING; M. Miyamoto and H. Takeda, Mineralogical Institute, Graduate School of Science, University of Tokyo, Hongo, Tokyo 113, Japan.

Although the origin of pallasites is still controversial [e.g., 1], discovery of many lodranites among the Antarctic meteorite collection has thrown light on the genesis of pallasites, because similar chemical zoning of mafic silicates was found in these groups [2]. We measured chemical zoning of pallasites, Yamato (Y) 8451 [3], Esquel, and Imilac with an electron microprobe and estimated cooling rates by applying the diffusion calculation similar to that used in our previous studies [4] to obtain some constraints on the formation and structure of their parent bodies. The results were compared with those of primitive achondrites (acapulcoites-lodranites). A cooling rate of 150 °C/yr from 1100 °C to 600 °C gives the best fit for the reverse zoning of Fe-Mg, which is probably related to reduction, of olivine in Esquel. The calculated cooling rates of Esquel and Y8451 are about 2 orders of magnitude faster than those of lodranites, which are a few °C/yr. Pallasite olivine records a rapid cooling history during the formation. Decreases in the CaO, Al_2O_3, and Cr_2O_3 contents toward rims of olivines in pallasites imply the presence of liquid rich in these elements at a late stage of the formation of pallasite.

Chemical zoning Y8451 olivine: The chemical zoning of Fe-Mg, CaO, Al_2O_3, Cr_2O_3, and MnO has been detected within a few hundreds of micrometers from the rim. The reverse zoning of Fe-Mg (Mg enrichment) toward the rim ranges from $Fa_{10.5}$ to $Fa_{9.9}$. CaO decreases toward the rim from about 0.1 to 0.01 wt% and Cr_2O_3 from about 0.15 to 0.03 wt%. Al_2O_3 slightly decreases toward the rim. MnO increases toward the rim from 0.32 to 0.45 wt%.

Esquel olivine: The chemical zoning of Fe-Mg, CaO, Al_2O_3, and Cr_2O_3 has been detected within a few hundreds of micrometers from the rim (Figs. 1, 2). The reverse zoning of Fe-Mg toward the rim ranges from $Fa_{11.2}$ to $Fa_{10.4}$. CaO decreases toward the rim from about 0.04 to 0.0 wt%, Al_2O_3 from about 0.04 to 0.01 wt%, and Cr_2O_3 from about 0.08 to 0.01 wt%. MnO does not show detectable zoning.

Imilac olivine: Slight zoning of CaO, Al_2O_3, and Cr_2O_3 has been detected within a few hundreds of micrometers from the rim. CaO slightly decreases toward the rim from about 0.02 to 0.0 wt%, Cr_2O_3 from about 0.08 to 0.0 wt%, and Al_2O_3 from about 0.04 to 0.01 wt%. Some olivines show increases in FeO toward the rim within a few tens of micrometers.

TiO_2 and NiO show no zoning for the Y8451, Esquel, and Imilac olivines.

Cooling rate A cooling rate of 150 °C/yr, from 1100 °C to 600 °C, gives the best fit for the observed Fe-Mg profile of olivine in Esquel (Fig. 1a). This cooling rate corresponds to a burial depth of about 12 m under a solid rock, if a thermal diffusivity of 0.01 cm^2/s is assumed. The initial temperature of cooling was estimated to be 1100 °C based on pyroxene data in Y8451 [5]. Oxygen fugacity of pallasite measured by Brett and Sato [6] was used. Fig. 3 shows the changes in the cooling rate with initial temperature of cooling for the Fe-Mg profile. The best-fit cooling rate of about 500 °C/yr from 1100 °C to 600 °C was obtained by the Fe-Mg profile of olivine in the Y8451 pallasite [2].

A cooling rate of 50 °C/yr, from 1100 to 600 °C, gives the best fit for the observed CaO profile of olivine in Esquel, obtained by using the Ca diffusion coefficient of olivine by Jurewicz and Watson [7] (Fig. 1b). The best-fit cooling rate of 0.5 °C/yr is obtained by using the Ca diffusion coefficient of olivine by Morioka [8] which is about 2 orders of magnitude smaller than that by Jurewicz and Watson [7]. Activation energy of 25 kcal/mol for Ca diffusion in olivine was assumed below 1100 °C. The best-fit rate from the Ca diffusion coefficient by Jurewicz and Watson [7] is broadly consistent with that obtained by the Fe-Mg profile of olivine in Esquel.

Discussion The reverse zoning of Fe-Mg (Mg enrichment) in olivine found in the pallasites looks like the reduced rims of olivines in ureilites [9] and is probably related to reduction. The increase in the MnO content at the rim of the Y8451 olivine also supports the idea. Decreases in the CaO, Al_2O_3, and Cr_2O_3 contents toward rims of olivines in pallasites [10] imply the presence of liquid rich in these elements at a late stage of the formation of pallasite, because these elements

CHEMICAL ZONING OF OLIVINE IN PALLASITES: Miyamoto M. and Takeda H.

tend to concentrate in the liquid compared with olivine, judging from the partition coefficients between olivine and liquid [11]. Lodranites also show decreases in the amount of these elements at pyroxene rims [e.g., 2].

The calculated cooling rates of Esquel and Y8451 are about 2 orders of magnitude faster than those of lodranites, which are a few °C/yr [e.g., 2]. Pallasite olivine records a rapid cooling history during the formation.

References: [1] Dodd R. T. (1981) *Meteorites: A petrologic-chemical synthesis*, Cambridge Univ. Press. [2] Miyamoto M. and Takeda H. (1993) *Meteoritics, 28*, 404-405. [3] Yanai K. and Kojima H. (1987) *Photographic Catalog of Antarct. Meteorites.* Natl. Inst. Polar Res., Tokyo. [4] Miyamoto M. et al. (1986) *JGR, 91*, 12804-12816. [5] Hiroi T. et al. (1993) *Proc. NIPR Symp. Antarct. Meteorites, 6*, 234-245. [6] Brett R. and Sato M. (1984) *GCA, 48*, 111-120. [7] Jurewicz A. J. G. and Watson E. B. (1988) *Contrib. Mineral Petrol., 99*, 186-201. [8] Morioka M. (1981) *GCA, 45*, 1573-1580. [9] Miyamoto M. et al. (1985) *JGR, 90*, D116-D122. [10] Zhou Y. and Steel I M. (1993) *Lunar Planet. Sci. XXIV*, 1573-1574. [11] Miyamoto M. et al. (1994) This volume.

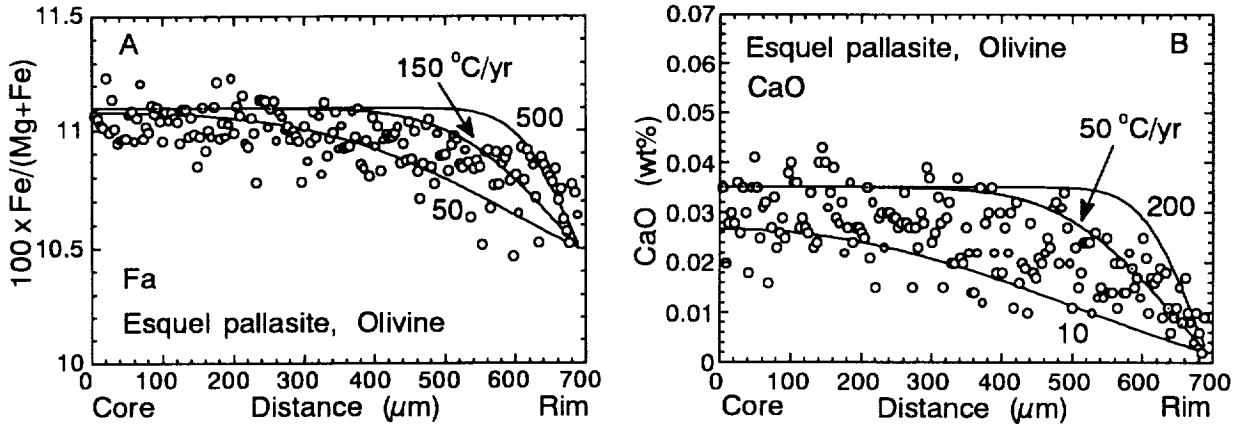

Fig. 1. Fe-Mg (a) and CaO (b) profiles of olivine in the Esquel pallasite. Open circles indicate the observed profiles. Curves show calculated diffusion profiles. Numbers on curves show cooling rates in °C/year. Data are at intervals of 4 micrometers.

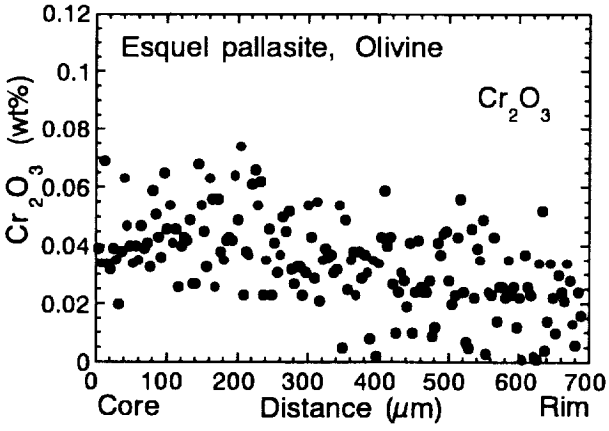

Fig. 2. Cr_2O_3 profile of the same olivine as Fig. 1. Solid circles show the observed profile.

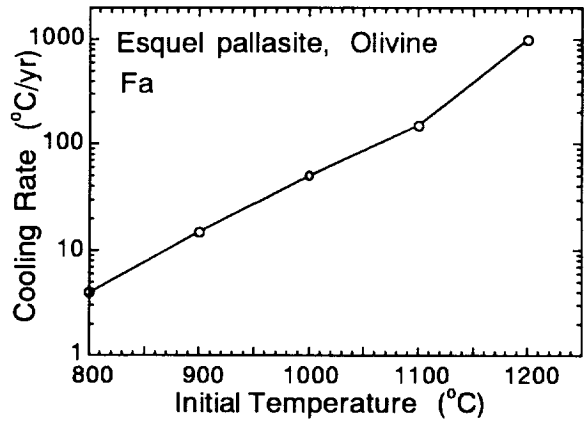

Fig. 3. Changes in the cooling rate (°C/yr) with initial temperature of cooling, obtained for the Fe-Mg zoning of the olivine shown in Fig. 1a.

PARTITION COEFFICIENTS FOR Al, Ca, Ti, Cr, AND Ni IN OLIVINE OBTAINED BY MELTING EXPERIMENT ON AN LL6 CHONDRITE;

M. Miyamoto, T. Mikouchi, Mineralogical Inst., Graduate School of Sci., University of Tokyo, Hongo, Tokyo 113, Japan and G. A. McKay, SN4, NASA-JSC, Houston, TX 77058, USA

We report the partition coefficients for Ca, Al, Ti, Cr, and Ni in olivine obtained through a series of melting experiments on an LL6 chondrite under varying conditions of temperature and oxygen fugacity. It is necessary to examine the variation of partition coefficients up to extremely reducing conditions in order to study meteoritic olivines. For Ca, Al, and Cr, the partition coefficients tend to decrease as temperature increases, but do not change as oxygen fugacity changes. The partition coefficient for Cr does not change even under extremely reducing conditions.

The starting material for the heating experiments was the PCA 82507 LL6 chondrite. The experiments were originally designed to obtain information on the magma compositions of the HED meteorites from LL chondrite-like source material [1]. In these experiments, powdered samples suspended on Pt-wire loops were heated at constant temperatures of 1050, 1125, 1200, 1275, 1350, 1425, and 1500 °C in a vertical 1-atm CO/CO_2 gas-mixing furnace at constant oxygen fugacities ranging from 3 log units below to 4 log units above the iron-wüstite (IW) buffer. Oxygen fugacity was measured by a zirconia cell, although the measured values of oxygen fugacities less than 2 log units below IW may be somewhat inaccurate. Details of these experiments are described by Lofgren [2]. Chemical analysis of experimental charges was made with an electron microprobe.

Fig.1 shows the weight ratio partition coefficients for olivine/liquid (glass) as a function of oxygen fugacity and temperature. The partition coefficient for Mn obtained by these experiments has been already reported in Miyamoto et al. [3]. The partition coefficients for Ti and Ni may be somewhat inaccurate, because the amounts in olivine are close to the detection limits. Our experiments cover relatively reducing conditions. The ranges of the partition coefficients we obtained are consistent with those previously reported by several investigators [e.g., 4]. Our results for Ca, Mn, and Cr are in good agreement with those obtained by melting experiments on angrite compositions [5].

For Ca, Al, and Cr, the partition coefficients tend to decrease as temperature increases, but do not change as oxygen fugacity changes. The partition coefficient for Cr does not change even under extremely reducing conditions and is below 1.0 for the charges heated over 1200 °C except for the 1350 °C one at log fO_2=-13. The partition coefficient for Ti tends to increase under extremely reducing conditions. The partition coefficient for Ni drastically changes and is very low under the reducing conditions. Temperature dependency of the partition coefficients for both Ti and Ni is unclear.

These data can provide a clue to explain zoning profiles of meteoritic olivines.

References:

[1] Miyamoto M. et al. (1986) *Lunar Planet. Sci. XVII*, 563-564. [2] Lofgren G. E. (1983) *J. Petrol., 24*, 229-255. [3] Miyamoto M. et al. (1993) *JGR, 98*, 5301-5307. [4] Irving A. J. (1978) *GCA, 42*, 743-770. [5] Mikouchi T. et al. (1994) This volume.

PARTITION COEFFICIENTS FOR OLIVINE: Miyamoto M. et al.

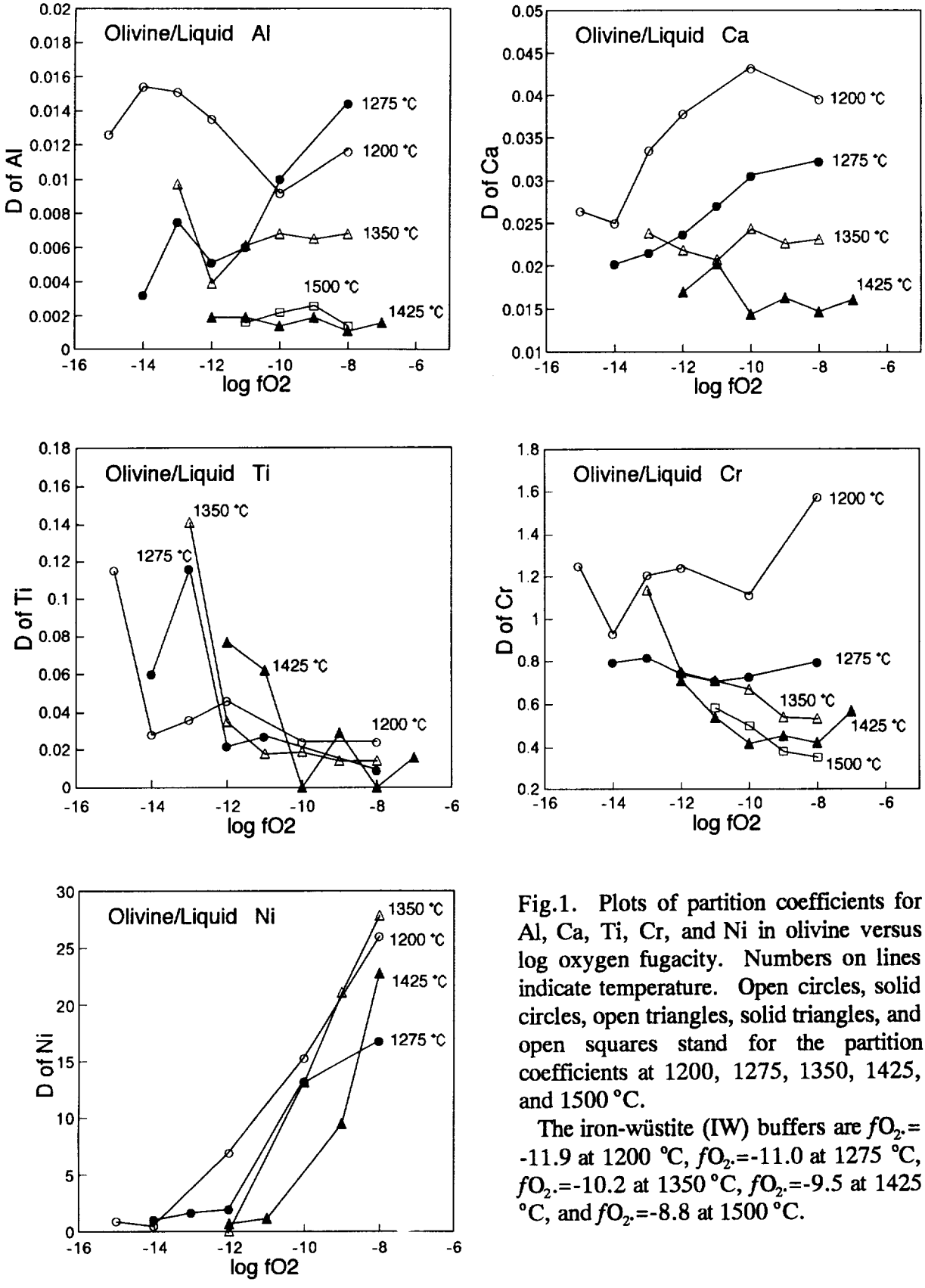

Fig.1. Plots of partition coefficients for Al, Ca, Ti, Cr, and Ni in olivine versus log oxygen fugacity. Numbers on lines indicate temperature. Open circles, solid circles, open triangles, solid triangles, and open squares stand for the partition coefficients at 1200, 1275, 1350, 1425, and 1500 °C.

The iron-wüstite (IW) buffers are fO_2.= -11.9 at 1200 °C, fO_2.=-11.0 at 1275 °C, fO_2.=-10.2 at 1350 °C, fO_2.=-9.5 at 1425 °C, and fO_2.=-8.8 at 1500 °C.

THERMAL INFRARED OBSERVATIONS OF MARS FROM PALOMAR MOUNTAIN

J. Moersch, T. Hayward, J. Houck, P. Lee, J. Miles,
P. Nicholson, M. Smith, S. Squyres, and J. Van Cleve

Center for Radiophysics and Space Research,
Cornell University,
Ithaca, NY 14853

During the opposition of 1993, we obtained imaging and spectrographic observations of Mars in the thermal infrared. We have analyzed this data using a thermal model for the planet to remove contrast caused by diurnal temperature variations. Ratio spectra show that while most locations on the disk appear to behave as blackbodies, a few locations (notably Acidalia) show definite absorption features. We are currently in the process of determining whether the spectral features seen in Acidalia are caused by dust in the atmosphere or by non-unit emissivity of surface materials and will report our findings.

Images and spectra were obtained using the newly-developed SpectroCam-10 instrument on the Hale 200" telescope at Palomar Observatory. Images were taken using a set of six wide band filters centered at 7.9, 8.8, 9.8, 10.3, 11.7 and 12.5 microns at three times over the course of the night of 11 January, 1993. Spatially resolved slit spectra with a wavelength resolution of 100 between 7.5 and 13.5 microns were also obtained covering the entire disk. Seeing on the night of the observations in this spectral region was about 0.75", corresponding to a resolution of 350 km on the surface of Mars at the sub-Earth point.

To analyze the data, we have developed a thermal model that uses finite difference techniques to solve the time-dependent one-dimensional heat diffusion equation for surface temperatures and then blackbody radiances over the entire planet on a 2 x 2 degree grid. The inputs to the model are thermal inertia, albedo, and geometry of insolation at each grid point. Running the model with a spatially uniform thermal inertia of 6.5 E-3 cal cm^(-2) s^(-1/2) K^(-1) and an average albedo of 0.21, we produced synthetic "average" Mars images. The actual images were then divided by the "average" images to remove most of the center-to-limb brightness gradient and reveal more subtle surface features. Many well-known features are readily apparent in such ratioed images, including Syrtis Major, Hellas, Sinus Meridiani, Argyre, and Acidalia. Using the Viking-derived thermal inertias and albedos as inputs to the model, a second set of spatially inhomogeneous synthetic Mars images was created. When the observed images are divided by these inhomogeneous images, the results are mostly flat, but a few significant features remain.

In at least one case, we have identified the cause of one of these features to be a change in the albedo of the surface since Viking. However, other features may be related to absorption in the Martian atmosphere, or to non-unit emissivity of materials on the planet's surface. In particular, a spatially confined feature in the location of Acidalia shows a strong absorption at 9 microns and a weaker absorption at 11.5 microns. Qualitatively, this spectrum closely matches a spectrum taken by the Mariner 9 IRIS instrument during the height of the '71-'72 global dust storm. However, optical observations taken by others during the '93 opposition indicate that the skies on Mars appeared clear at this time (D. Parker, personal communication).

In order to understand this apparent contradiction, we are currently pursuing three avenues: 1) We calculate the amount of dust that would need to be in the atmosphere in order to produce features of the depths seen in the spectrum of Acidalia, convert this dust load to a visible wavelength optical depth, and compare that to the lower limit of detectability for localized atmospheric dust in optical images. 2) Disk-resolved polarization meaurements were acquired during the '93 opposition from Tokyo by S. Ebisawa. Using these measurements, it may be posible to distinguish between surface materials and dust in the atmosphere (A. Dollfus, personal communication). 3) We hope to observe Mars again in the summer of 1994. The feature in Acidalia is spatially large enough that it should be visible then if it is still there, despite the smaller apparent size of Mars. A permanent spectral feature in this location would indicate surface origin, while a transient feature would likely be due to dust in the atmosphere. We will discuss results from 1) and 2) above, as well as plans for 3).

GEOLOGY OF THE MAHUEA THOLUS QUADRANGLE, VENUS; H.J. Moore and S.T. Arriola, U.S. Geological Survey, Menlo Park, CA 94025, and E.J. Israel, Northwestern University, Evanston, IL 60208.

Preliminary geologic mapping of the (provisionally named) Mahuea Tholus quadrangle (V49) indicates the following generalized history. A period of intense deformation was followed by vast outpourings of mafic lava that produced the extensive plains of the region. Uplift in the northern and northwestern parts of the quadrangle and compression produced northeast-trending wrinkle ridges. Extrusions from local vents produced thick sialic flows from Mahuea Tholus [1] and a variety of non-contiguous mottled, domed, and smooth plains. Subsequently, at least seven coronae [2] formed, and extensional deformation [3] produced rifts in the northern parts of the quadrangle; local extrusions of lavas accompanied the formation of the coronae and the extensional deformation. The most recent events were impacts of bolides on the surface to produce craters and on the atmosphere to produce shock waves and splotches [4].

Distributions of backscatter, moderate-scale topography, and landforms portrayed by the Magellan synthetic aperture radar images are the principal sources of information for the definition, interpretation, and determination of relative ages of map units. Data on coarse-scale topography (altimetry) [5] and physical/electrical properties (emissivity, reflectivity, root-mean-square slope, and backscatter coefficient) [6,7] provide additional information on the map units. Coarse-scale topography is of particular importance because it reveals the locations of subtle circular structures (crests of annuli and moats of some coronae) and the net effect of complex deformation in areas with myriad faults and fissures.

Of twenty-seven map units recognized, four have a combination of physical/electrical property signatures (beyond $\pm 1\sigma$; Table 1) that clearly separate them from the other units. These four are the lobate, smooth, and ridged mesa units of Mahuea Tholus (thick lava flows) and the highly fractured terrain unit; the four units have (1) average emissivities between 0.884 and 0.902, (2) average rms slopes between 3.0° and 4.6°, (3) average reflectivities between 0.062 and 0.099, and (4) average backscatter coefficients between -8.8 and -5.2 dB (θ_i ~23-35°). The areal distributions of high emissivities, low reflectivities, and large rms slopes of Mahuea Tholus mimic those of the area of its mesa units. Among the crater units, the central-peak, wall, and rim materials have large backscatter coefficients (-7 to -6 dB), while some crater halos and splotches have small backscatter coefficients (-16.5 to -15.0 dB).

Table 1. Average physical/electrical properties of materials in quadrangle.

PROPERTY	MEAN	STD DEV (1σ)	MODE	RANGE
Topography (km)	6051.7	0.52	-	6048.6 - 6053.9
Rms slope (degrees)	2.11	0.81	1.9	0.4 - 9.7
Reflectivity (fraction)	0.118	0.019	0.115	0.045 - 0.425
Emissivity (fraction)	0.854	0.015	0.849	0.803 - 0.928
Backscatter Coefficient (dB) (θ_i ~25-26°)	-9.5 [8]	-	-	- -

Nominal bulk densities inferred for the map units [9] (assuming no

electrical conductors [10]) from reflectivities and emissivities range from 1,500 to 2,400 kg/m^3 and 2,000 to 2,600 kg/m^3, respectively; the densities are higher than that of loose terrestrial soils (1,200 kg/m^3), lower than that of dense lunar rocks (3,300 kg/m^3), and consistent with those of moderately dense regoliths, porous to non-porous rocks, and mixtures of regoliths and rocks.

The relief of landforms was estimated by using parallax measurements on computer images of left- and right-looking (for craters, volcanic edifices, and a wrinkle ridge) and left- and left-looking pair (for flow lobes). The relief of a canyon was estimated by using hard copy left- and left-looking pairs. Results are shown in Table 2 (see also [11]). The consistent large thicknesses of three separate locations on the northwest flow lobe of Mahuea Tholus are compatible with north-south altimetry profiles [5] of Mahuea Tholus (relief ~0.515 km) and suggest the flow lobe is from an evolved magma [1].

Table 2. Dimensions of landforms in and near the Mahuea Tholus quadrangle.

FEATURE	LOCATION (degrees S.; E.)	RELIEF (km)	DIAMETER (km)	NOTES
Crater	20.0; 169.0	0.970*	11.1*	Floor-E. rim
		0.748*	-	Floor-N.W. rim
		1.053*	10.7*	Floor-E. rim
		0.716*	-	Floor-N.W. rim
		0.400	-	Floor-central peak
Crater	20.5; 183.1	1.602	16.4	Floor-rim; average
Crater	25.0; 168.4	1.287	52.3	Floor-rim; average
Crater	21.6; 176.4	0.193	5.6	Floor-rim; average
Edifice	40.0; 135.0	0.300*	2.7	Base-top
		0.347*	-	Base-top
Edifice	38.5; 136.0	0.779	11.2	Base-top; average
Edifice	40.2; 134.4	0.272	3.4	Base-top; average
Wrinkle ridge	21.6; 176.2	0.167	-	Flanks-crest; ave.
Flow lobe	37.5; 163.6	0.533*	-	Left-, left-look
		0.410*	-	Left-, right-look [1]
Flow lobe	37.5; 163.7	0.682*	-	Left-, left-look
		0.647*	-	Left-, right-look [1]
Flow lobe	37.4; 163.6	0.449*	-	Left-, left-look
		0.438*	-	Left-, right-look [1]
Canyon	25.7; 166.0	2.632	-	Parallax bar

* Independent measurements of same crater, edifice, or same pairs of conjugate image points on and near the northwest flow lobe of Mahuea Tholus.

[1] Moore, H.J. et al., 1992, JGR, 97, 13,479. [2] Stofan, E.R. et al., 1992, JGR, 97, 13,347. [3] Schaber, G.G., 1992, Geophys. Res. Lttrs., 1982, 9, 499. [4] Schaber, G.G. et al., 1992, JGR, 97, 13,257. [5] Ford, P.G. and Pettengill, G.H., 1992, JGR, 97, 13,103. [6] Pettengill, G.H. et al., 1992, JGR, 97, 13,096. [7] Tyler, G.L. et al., 1991, Science, 252, 265. [8] Muhleman, D.O., 1964, Astron. J., 69, 34. [9] Olhoeft, G.R. and Strangway, D.W., 1975, Earth Planet. Sci. Lett., 24, 394. [10] Pettengill, G.H. et al., 1988, JGR, 93, 14,881-14,892. [11] Moore, H.J. et al., 1993, LPS XXIV, 1003.

RHENIUM-OSMIUM ISOTOPE SYSTEMATICS IN IIAB and IIIAB IRON METEORITES.

J.W. Morgan[1], M.F. Horan[1], R.J. Walker[2], M.I. Smoliar[2] and J.N. Grossman[1], [1]U.S. Geological Survey, Reston, VA 22092, [2]Dept. of Geology, Univ. MD, College Park, MD 20742,

Using negative thermal ionization mass spectrometry, Re and Os abundances were determined by isotope dilution and $^{187}Os/^{188}Os$ isotopic ratios were measured in 16 samples of eight irons from each of the IIB and IIIB subgroups, and in one sample of Treysa IIIB (anomalous) meteorite. Also analyzed were two IIA and 12 samples of seven IIIA iron meteorites, in addition to those reported previously [1]. The purpose of this work is to examine the behavior of Re and Os during asteroid core formation, and where possible, constrain the relative ages of the various irons.

For this study, meteorites were dissolved by a combined acid dissolution - alkaline fusion technique which yielded Re blanks for each set of B sub-group analyses, of 50.7 ± 9.4 pg Re (2-σ). These values represent a considerable improvement over blanks reported in our previous iron meteorite papers; 100 pg Re [1] and 250 pg [2]. Nevertheless, for B subgroup irons with 1 ppb Re or less, the uncertainty in the blank correction introduced errors of 1 to 2 % in the abundance determination. Osmium blanks for the B subgroup runs were approximately 3 pg, with *ca.* chondritic $^{187}Os/^{188}Os$. This blank introduced insignificant error even for the lowest Os abundance samples.

IIAB Iron Meteorites.

Log plots of Re versus Os data for IIA and IIB irons describe straight lines that converge on Lombard, a IIA iron with the lowest Re and Os abundances and highest $^{187}Re/^{188}Os$ measured to date. The precisely linear IIA trend (slope = 0.776 ± 0.013) is most simply (and exactly) explained by fractional crystallization with constant k_D, even though laboratory experiments may argue otherwise [3-4](Figure 1). Thus, although we now have a larger and more precise database, the interpretation of the chemical evolution of the IIA irons has not changed since our earlier work [2]. The IIB iron trend cannot be explained via simple fractional crystallization with a constant k_D. One possibility is that small amounts of Re and Os were added to the asteroid core during the final stages of crystallization [5]. In addition, some of the chemical and isotopic (see below) variability observed in the IIB irons may be due late stage crystallization occurring in isolated pockets at different times, perhaps as dendrites [6].

The combined isotopic data for IIA irons from Horan *et al.* [1] and the present work (new samples of Negrillos and Bennett County) are plotted on a $^{187}Os/^{188}Os$ *vs.* $^{187}Re/^{188}Os$ isochron (Fig. 2), giving the following results: slope = 0.07811 ± 0.00082; intercept = 0.09602 ± 0.00051; age = 4589 ± 47 Ma (neglecting the error in the decay constant of *ca.* 3 % [7]). Comparable quality Re-Os data were obtained for four IIB iron meteorites (Navajo, Sandia Mountain, Mount Joy, Smithsonian Iron) which have Ni contents lower than 6 % and correspondingly high Re and Os abundances. Of these, only Mount Joy lies within uncertainty of the IIA isochron. The three remaining low-Ni IIB irons lie an average of 0.9 ± 0.2 % above the IIA iron isochron, well beyond analytical uncertainty (Fig. 2). These meteorites cover a limited range of $^{187}Re/^{188}Os$ (0.60 to 0.76) and define an imprecise isochron with: slope = 0.07916 ± 0.00496, intercept = 0.09669 ± 0.00348, age = 4648 ± 280 Ma. This age is insufficiently precise to distinguish an age difference from the IIA (± Mount Joy) isochron. We speculate that these three irons crystallized significantly after the IIA irons and Mount Joy, perhaps in an isolated melt pocket that remained hot for several tens of millions of years following initial core crystallization. This is plausible only if the Re/Os of the melt was sufficiently high. In the case of the IIAB parent body, the time available to develop a radiogenic signature was likely restricted to less than about 50 Ma, thus requiring an enviroment with $^{187}Re/^{188}Os \geq 1.2$. Indeed, for reasonable choices of k_D, the liquid in equilibrium with Lombard likely had a $^{187}Re/^{188}Os$ of approximately 1.2.

Four IIB iron meteorites with greater than 6 % Ni (Central Missouri, DRPA, Sao Juliao de Moriera, Santa Luzia) have relatively low Re and Os abundances (*ca.* 1 ppb Re and 10 ppb Os). Because of the uncertainty in the Re blank, the error in $^{187}Re/^{188}Os$ range from 1 to 3%. Triplicate analyses of Sao Juliao de Moreira all plot above the IIA isochron, suggesting that it may be related to the Navajo (late crystallization) subgroup. The remaining IIB iron meteorites plot on or below the IIA isochron and all points fall within error of the line. This is consistent with crystallization soon after the IIA irons crystallized. When these data are added to the IIA isochron, there is little change except for a slight improvement in the uncertainty: slope = 0.07802 ± 0.00063, intercept = 0.09604 ± 0.00035, age = 4584 ± 36 Ma. One of these IIB irons, DRPA 78009, incorporated excess ^{107}Ag at the time of its formation [8]. As a result of the Re-Os isotopic differences, we predict that the Navajo IIB subgroup, with elevated Os isotopic compositions, should contain little or no excess ^{107}Ag.

IIIAB Iron Meteorites.

The IIIAB system is chemically much more complicated than the IIAB system [6]. Rhenium and Os abundances for IIIA irons with the highest concentrations (Henbury, Costilla Peak, Casas Grandes) do not replicate as well as the IIA data, but IIIA irons with lower abundances do (Loreto, Trenton, Charcas, Tamaragul). The IIA hexahedrites are essentially single crystals and are clearly more homogeneous than IIIA medium octahedrites, particularly at the 0.15 to 0.25 g sampling size used for Costilla Peak and Henbury. Poor replication of concentrations, therefore, is most likely a function of meteorite heterogeneity. The IIIA irons are also not isochronous, unlike the IIA irons. A regression fit of 15 IIIA iron data yield: slope = 0.08071 ± 0.00241, intercept = 0.09537 ± 0.00128; age = 4736 ± 140 Ma.

Abundances of Re and Os in the IIIB iron meteorites examined (Grant, Campbellsville, Tieraco Creek, Narraburra, Chupaderos, Wonyulgunna, Thurlow, Mount Edith) are much lower than those for the IIIA irons; 0.7 to 4 ppb Re and 4 to 27 ppb Os. As with the IIB irons, error in the Re determination is 1 to 3% for the samples with the lowest abundances of Re because of the uncertainty in the Re blank. Two of the IIIB irons, Grant and Campbellsville, fall squarely on the IIIA isochron giving a combined isochron with: slope = 0.08108 ± 0.00152, intercept = 0.09523 ± 0.00087, age = 4756 ± 86 Ma. This age is too old, even given the 3% uncertainty in the ^{187}Re decay constant. It is probably the result of several factors including the crystallization of IIIAB irons over several tens of millions of years and perhaps some post crystallization disturbances to the Re-Os system. These possibilities are currently under investigation.

References. [1] M.F. Horan *et al.*, *Science* 255, 1118, 1992. [2] J.W. Morgan *et al.*, *EPSL* 108, 191. [3] J.H. Jones and M.J. Drake, *GCA* 47, 1199, 1983. [4] J.H. Jones and D.J. Malvin, *Metall. Trans.* B 21B, 697, 1990. [5] E. Pernicka and J.T. Wasson, *GCA* 51, 1717, 1987. [6] H. Haack and E.R.D. Scott, *GCA* 57, 3457, 1993. [7] Lindner *et al.*, *GCA* 53, 1597, 1989. [8] J.H. Chen and G.J. Wasserburg, *GCA* 54, 1729, 1990.

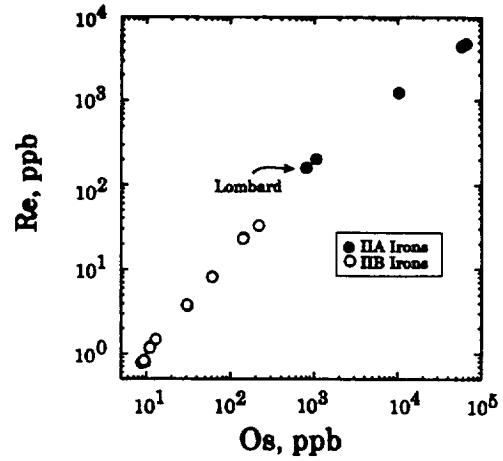

Figure 1. Re and Os abundances in IIA and IIB iron meteorites are plotted on a log-log scale. Lombard, shown with an arrow, has the largest Re/Os ratios and occurs at the break in abundances between IIA and IIB irons.

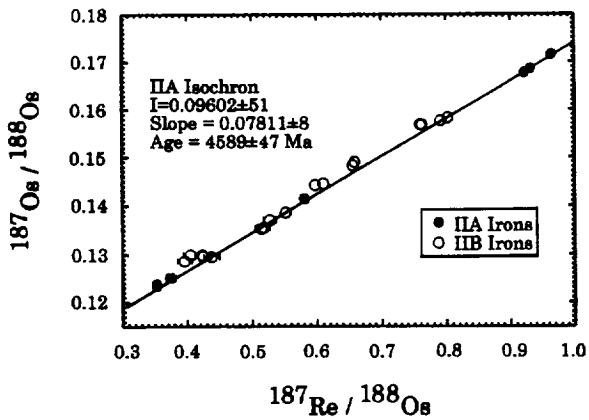

Figure 2. IIAB iron meteorite isochron. The IIA irons form a well-defined isochron. Most IIB iron meteorites fall within uncertainty of the isochron. However, Navajo, Sandia Mountain Smithsonian and Sao Juliao del Moriera lie *ca.* 0.9 % above the IIA isochron.

THERMAL CONDUCTIVITY OF PLANETARY LITHOSPHERES: NEW ESTIMATES FROM MEASUREMENTS ON MANTLE XENOLITH SAMPLES; Paul Morgan, Department of Geology, Box 4099, Northern Arizona University, Flagstaff, AZ 86011-4099, USA, and Suzanne Y. O'Reilly, School of Earth Sciences, Macquarie University, North Ryde, NSW 2109, Australia.

INTRODUCTION: During the past three decades or so, great advances have been made in the use of thermal models to understand the evolution the terrestrial lithosphere (*e.g.*, [1-4]). Similar advances related to the thermal histories of the terrestrial planets and their lithospheres have been reviewed and discussed by Solomon *et al.* [in 5]. In all conductive heat flow problems, the thermal gradient is inversely proportional to thermal conductivity. Thus, uncertainties in thermal conductivity directly result in uncertainties in temperatures calculated at depth. For terrestrial rocks with relatively low thermal conductivity at room temperature (2 W m^{-1} K^{-1}), the temperature dependence of thermal conductivity generally appears to be minor, although it may still be significant for individual heat flow determinations [6]. For rocks with room temperature thermal conductivities above 3 W m^{-1} K^{-1}, however, a significant decrease in thermal conductivity with increasing temperature is indicated by several experimental studies as temperature rise to 400 to 500 °C, above which temperature conductivities increase as radiative heat transport appears to become significant [7,8]. Rocks which are likely to contribute significantly to the bulk thermal conductivity of the terrestrial crust typically have thermal conductivities in the range 2.0 to 2.5 W m^{-1} K^{-1} [9,10], for which the temperature dependence of thermal conductivity is possibly of importance, but this dependence is almost always ignored in thermal models. Terrestrial lithospheric mantle rocks are generally assumed to have thermal conductivities >3 W m^{-1} K^{-1}, and although published experimental studies indicate strong temperature dependence of thermal conductivity in the temperature range 0 to 900°C, these effects are commonly also ignored, or applied inconsistently. For example, for a widely quoted set of geotherms, Pollack and Chapman [11] used a temperature-dependent thermal conductivity model to compute geotherms in the continental mantle, but a constant conductivity (diffusivity) cooling model to compute oceanic mantle geotherms. Many workers [*e.g., 3,7,12*] have used a constant thermal conductivity based upon an average of a temperature-dependent conductivity model. The greatest uncertainty in this parameter is the significant of radiative heat transport at elevated temperatures.

Although the probable effects of radiative heat transport on mantle temperatures have been discussed [13], and a number of studies have demonstrated the significance of radiative heat transport at lithospheric temperatures in olivine and other minerals likely to be importance in the upper mantle [*e.g.*, 7,8,14-17], these studies have not demonstrated the efficiency of radiative heat transport in multi-grain rocks. The reduction in the efficiency of radiative heat transport in multi-grain rocks as a result of photon scattering at grain boundaries is poorly constrained, but is commonly assumed to significantly reduce the effects of radiative heat transport [*e.g.*, 18]. However, in a semi-quantitative study, we have demonstrated that radiative heat transport is clearly significant in multi-grain peridotitic mantle xenolith samples.

TECHNIQUES AND RESULTS: For preliminary experiments we decided not to attempt to make thermal conductivity determinations under conditions of isotropic confining pressure because of the logistical problems of performing such experiments at high temperatures. We reasoned that if we could demonstrate that radiative heat transfer was significant at elevated temperatures under conditions of uniaxial pressure, then significant radiative heat transfer would also be expected under conditions of isotropic pressure. However, if we were unable to demonstrate the significance of radiative heat transfer under conditions of uniaxial pressure, then the additional expense of performing experiments under conditions of isotropic pressure may not be justified. We also reasoned that uniaxial pressure may be a sufficient condition for thermal conductivity determinations as long as the pressure was applied along the same axis as the heat transport.

For our preliminary experiments we adopted a modification of the steady-state divided-bar apparatus using an electrical resistance heater [19]. In order to keep this apparatus as simple as possible, the same heater was used to raise the temperature of the sample to the ambient measurement temperature and to provide the bi-directional heat flow through the stack of standards and the sample from which the thermal conductivity was determined. The system was used as a thermal comparitor, using fused silica as a calibration standard [20,21] and deducing the thermal conductivities of samples from the relative temperature drops across the calibration standards and the samples and from the relative geometries of the standards and sample.

This system was tested extensively with various experimental modifications and was found to produce semi-quantitatively reproducible results under a variety of different confining pressures and stack configurations. As many of the experimental runs above 500°C resulted in fractured standards in the stack, we are only confident in the results

from these runs as semi-quantitative. However, within individual runs before standards were fractured, or between runs with similar stack configurations, the results are considered to be significant. A sample of New England (Australia) granite was also measured as a sample for which radiative heat transport was not expected to have a major effect on the high temperature thermal conductivity to confirm that trends observed in the mantle xenolith thermal conductivities were not an artifact of the experimental technique. Distinctly different temperature-dependent behavior of thermal conductivity was demonstrated for the granite sample and four different peridotitic mantle xenolith samples, the results for which are summarized in Figure 1. Data are shown in Figure 1 for two different mantle xenolith samples (see figure caption for descriptions) with different uniaxial confining pressures of approximately 50 MPa (0.5 kbar) and approximately 150 MPa (1.5 kbar). Similar trends are seen in the thermal conductivities of both samples as a function of temperature. By comparison with the single crystal olivine thermal conductivity study of Schatz and Simmons (1972), these results clearly demonstrate the significance of radiative heat transport in actual mantle samples, and thus the project has succeeded in its primary goal. Our preliminary results indicate that radiative heat transport is significant in mantle xenolith samples above temperatures of about 400°C. There is therefore a strong need for further investigation of the effects of radiative heat transport in planetary lithospheres.

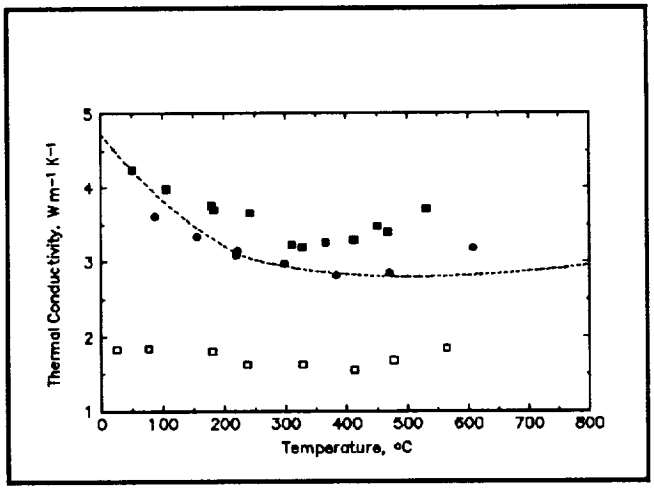

Figure 1. Preliminary high-temperature thermal conductivity data for two mantle xenolith samples and a check sample of granite. Solid square and circle symbols show data collected at uniaxial pressures of about 50 MPa (0.5 kbar) and about 150 MPa (1.5 kbar), respectively, on spinel lherzolite xenolith samples from a Quaternary maar, Lake Bullenmerri, western Victoria, Australia [22-24]. The predominant mineral in this xenolith is olivine with a composition of Fo92. These data were collected during both the heating and cooling cycles of two heating runs to a mean sample temperature of approximately 530°C, and no consistent hysteresis in the results was observed.The dashed line shows the predicted olivine conductivity of Schatz and Simmons [7]. Open square symbols show data collected on a sample of I-type granite from the Lachlan Fold Belt, New South Wales, Australia [25].

ACKNOWLEDGEMENTS: Drs. Trevor Green, Norm Pearson, and Stirling Shaw, are thanked for assistance with the experimental studies. This work was funded by grants from the Fulbright Foundation, the National Science Foundation, the Australian Research Council, and the NASA/JOVE program.

REFERENCES: [1] Sclater, J. G., C. Jaupart and D. Galson (1980) *Rev. Geophysics, 77,* 26. [2] Pollack, H. N. (1982) *Ann. Rev. Earth Planet. Sci., 10,* 45. [3] Morgan, P. (1984) *Phys. Chem. Earth, 15*, 107. [3] Haenel, R, L. Rybach and L. Stegena, eds. (1988) *Handbook of Terrestrial Heat-Flow Density Determinations*, Kluwer Academic Publishers, Dordrecht, 486 pp. [5] Basaltic Volcanism Study Project (1981) *Basaltic Volcanism on the Terrestrial Planets*, Pergamon Press, Inc., New York, 1286 pp. [6] Sass, J. H. and P. Morgan (1988) *JGR, 93,* 6027. [7] Schatz, J. and G. Simmons (1972) *JGR, 77,* 6966. [8] Roy, R. F., A. E. Beck and Y. S. Touloukian (1981) in Y. S. Touloukian, W. R. Judd and R. F. Roy, eds.,*Physical Properties of Rocks and Minerals*, McGraw-Hill, New York, p. 409. [9] Decker, E. R. and S. B. Smithson (1975) *JGR, 85,* 311. [10] Morgan, P. and W. D. Gosnold (1989) in L. C. Pakiser and W. D. Mooney, eds., *Geophysical Framework of the Continental United States, GSA Mem. 172,* Boulder Colorado, p. 493. [12] Morgan, P. and J. H. Sass (1984) *J. Geodynamics, 1,* 137. [13] Clark, S. P. (1957) *Eos, Trans. Am. Geophys. Un., 38,* 931. [14] Fujisawa, H., *et al.* (1968) *JGR, 73,* 4727. [15] Fukao, Y. H., H. Mizutani and S. Uyeda (1968) *Phys. Earth Planet. Int., 1,* 57. [16] Kanamori, H., N. Fujii and H. Mizutani (1968) *JGR, 73,* 595. [17] MacPherson, W. R. and H. H. Schloessin (1982) *Phys. Earth Planet. Int., 29,* 58. [18] Clauser, C. (1988) in [3], p. 143. [19] Beck, A. E. (1988) in [3], p. 87. [20] Ratcliffe, E. H. (1959) *British J. Appl. Phys., 10,* 22. [21] Powell, R. W., C. Y. Ho and P. E. Liley (1966) *Thermal Conductivity of Selected Materials*, National Standard Reference Data Series, National Bureau of Standards - 8, U.S. Govt. Printing Office, Washington, D.C. [22] Griffin, W. L., S. Y. O'Reilly and A. Stabel (1988) *Geochim. Cosmochim. Acta, 52,* 449. [23] O'Reilly, S. Y. and W. L. Griffin (1988) *Geochim. Cosmochim. Acta, 52,* 433. [24] Chen, Y. D., *et al.* (1991) *J. Petrology, Special Lherzolite Issue*, 291. [25] Sawka, W. N. and B. W. Chappell (1986) *Australian J. Earth Sci., 33,* 107.

USE OF MARS CLIMATE HISTORY TO DEMONSTRATE CAUSES AND CONSEQUENCES OF GLOBAL CHANGE ON EARTH: A TEACHING MODULE FOR MIDDLE SCHOOL STUDENTS;

Paul Morgan, Department of Geology, Box 4099, Raymond A. Lynch, NAU/AZ Space Grant Program, Box 6010, and Gordon P. Johnson, Box 6010, Northern Arizona University, Flagstaff, AZ 86011, USA.

THE MARTIAN RECORD OF GLOBAL CHANGE

The geologic record of Mars presents a dramatic history of climatic changes. Martian surface features have been divided into three basic geologic periods corresponding to different morphologies of modification of the surface by atmospheric processes. The oldest stage, the Noachian System, is characterized by a densely cratered surface, modified by widespread lava flooding and dendritic drainage channels suggesting significant rainfall and flooding by liquid surface water (Figure 1). The next stage, the Hesperian System, is less heavily cratered, is modified by volcanic and tectonic activity, and is cut by outflow channels which appear to have originated from underground rather than atmospheric water reservoirs, suggesting a lack of active rainfall (Figure 2). The youngest stage, the Amazonian System, is the least cratered system, and the effects of surface water are subordinate to eolian, volcanic, tectonic, and glacial processes (Figure 3). These three systems are interpreted to record evolution in the martian atmosphere from an ancient climate which included significant rainfall to the modern conditions which do not permit the persistence of liquid water on the martian surface. As a scientific teaching resource, this record presents clear evidence for young students to identify and interpret different terrains, to speculate upon the causes of the climatic changes which modified these different terrains, and through the use of inexpensive, commercially available software (*SimEarth* [1]), to experiment with the possible causes and effects of climatic change on Mars and to investigate the implications of these result to global change on Earth.

Figure 1. Example of dendritic valley networks which are common in the southern highlands of Mars. A temperate climate with active rainfall is implied. Many impact craters are also visible. This area is approximately 250 km across.

PEDAGOGY OF TEACHING INTRODUCTORY-LEVEL SCIENCE THROUGH PLANETARY STUDIES

The roots of western science are firmly planted in the ancient human desire to understand, and to develop for our own use, our natural environment. There are clear examples of the development of mathematical, physical, and chemical principles in order to attempt to quantify, predict, or exploit natural phenomena. From these attempts many *natural laws* have been recognized, the introduction and application of which forms the basis for much introductory science teaching. Many students appear to be alienated by this traditional science-teaching approach, however, and fail to grasp the principles of scientific methodology. Experience with non-science undergraduate students has shown that these students are much more receptive to scientific principles and even the accompanying mathematics if they are introduced in the context of observational discovery, for which planetary studies present an excellent and topical resource [2]. From this experience, a specific teaching module on global climatic change is being

developed and tested based upon the history of climate change indicated in the martian geologic record.

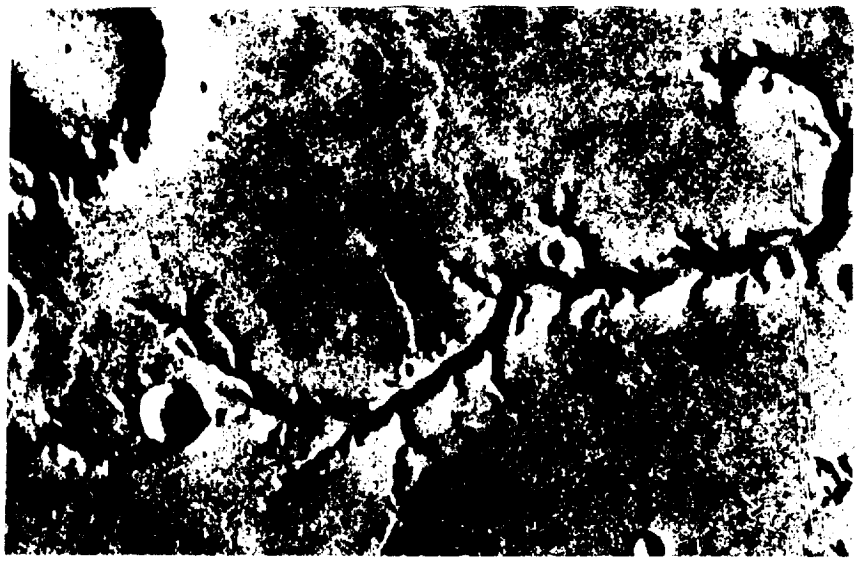

Figure 2. Example of channels probably formed by ground water sapping rather than by surface runoff (Nirgal Valles). No active rainfall is indicated, but more temperate climatic conditions than those which presently prevail are implied. This area is approximately 80 km across and is less heavily cratered than Figure 1.

TEACHING MODULE

The teaching module includes all materials for an upper level elementary or a middle school teacher to develop a hands-on project on climate change. No prior scientific knowledge is assumed, and the teacher is encouraged to lead the students to "discover" some of the *natural laws of science* for themselves. Mars images and maps are provided to allow the students to develop their own interpretations of the causes of different terrain types from their observations and experiences of terrestrial water and wind erosion. The students are encouraged to develop methods of inferring the relative ages of different terrains (crater counting, superposition, cross-cutting relations), and to deduce the basic climatic history of Mars. Simple experiments are used to demonstrate the dependance of the physical state of water upon atmospheric temperature and pressure, and the students are led to reconstruct the implied evolution of the martian atmosphere. Through the use of inexpensive, commercially available software (*SimEarth* [1]), students then explore the possible causes of changes in the atmosphere and their effects on climate, and investigate the implications of these results for terrestrial climate change. The final activity of the project is a choice of "what if?" exercises to investigate possible terrestrial and martian global change scenarios.

Figure 3. Examples of wind features which are especially common around the edge of the relative young volcano Olympus Mons. The area shown is approximately 20 km across.

REFERENCES: [1] SimEarth, The Living Planet™ Maxis and Will Wright (© 1990, 1991) IBM Version ISBN# 0-929750-32-2; Macintosh Version ISBN# 0-929750-33-0; Windows Version ISBN# 0-929750-46-2. [2] Morgan. P. (1993) *JOVE Newsletter, 4(2),* NASA/ Huntsville, Alabama, 6.

REE CHARACTERISTICS OF AN IGNEOUS INCLUSION IN THE YAMATO-75097 L6 CHONDRITE: Noritoshi Morikawa[1], Keiji Misawa[1], Noboru Nakamura[1] and Keizo Yanai[2], [1]Deparment of Earth and Planetary Sciences, Kobe University, Nada, Kobe 657, [2]National Institute of Polar Research, 9-10, Kaga, Itabashi, Tokyo 173, Japan.

As a part of consortium studies of large igneous inclusions (a few cm in size) in three YAMATO ordinary chondrites (Y-75097 L6, Y-793241 L6 and Y-794046 H5)[1,2], we report here results of REE analyses for the troctolitic inclusion (olivine + plagioclase + chromite + chlor-apatite/merrillite) in Y-75097. The inclusion and host of Y-75097 were severely shocked and the Rb-Sr systematics was perturbed by a 460 Ma event which was defined by the K-Ar age [3,4, 5]. Olivines (Fa_{25}) in both host and inclusion are equilibrated but plagioclase of the inclusion (An_{12-19}) is partially equili-brated with that of the host (An_{12}). The inclusion has the oxygen isotopic composition close to H-group while the host has that of L-group [6]. The REE abundances in the inclusion mantle are highly fractionated [7,8]. In this work, in order to investigate detailed REE distributions in the different parts of inclusion, precise isotope dilution analyses were carried out for specimens (#105) cut through the host/inclusion boundary to the inclusion core.

In Fig. 1, the specimen A sampled from the merrillite-rich core shows the highest and slightly light-REE enriched pattern (~20xO-chondrite) and a large negative Eu anomaly. This pattern reflects REE partitioning of phosphates and is complimentary to that of the merrillite-poor mantle which has a remarkable REE fractionation with middle REE depletion and a large positive Eu anomaly. The specimens B and C taken from middle parts of the inclusion show less fractionated but have the complimentary nature each other. Such REE features have been expected from the calculation of equilibrium REE partitioning between phosphate and other minerals (olivine and plagioclase) for the unfractionated REE in bulk inclusion [7]. However, it is worth noting that all specimens indicate light-REE enrichment relative to the middle REEs. Hence, the weighted mean REE abundances calculated for the bulk inclusion are slightly light-REE enriched (La=~2.8 and Lu=~1.5xO-chondritic). The REE model calculations of partial melting and fractional crystallization show that the REE patterns estimated for the melting residue or the crystallized solid with the mineral assemblage of 90% olivine + 9% plagioclase + 1% Phoshate are light-REE depleted and is different from the calculated bulk REE pattern (Fig. 1). This implies that the inclusion formed without solid/liquid separation resulting in REE fractionation. It is suggested that equilibrium REE partitioning was established during the early thermal metamorphism after the igneous formation. We suggest that the inclusion formed by melting and segregation of metal-sulfides from H-chondritic material with troctolitic composition but with grossly unfractionated REE abundances, and was then incorporated into the L-chondritic parent body and subjected to the early thermal metamorphism which eventually fractionated the REE significantly by solid/solid

equilibrium partitioning and to a late impact event.

References: [1] Yanai K. et al. (1983), Mem. Natl. Inst. Polar Res. Spec. Issue No. 30, 29-35; [2] Nakamura N. et al. (1993), Papers 18th Symp. Antarct. Meteorites 234-235; [3] Nakamura N. et al. (1993), Proc. NIPR Symp. Antarct. Meteorites (submitted). [4] Nagao K. (1993), Proc. NIPR Symp. Antarct. Meteorites (submitted); [5] Kaneoka I. et al. (1988), Proc. NIPR Symp. Antarct. Meteorites 1, 206-214; [6] Mayeda T. K. et al. (1987), Mem. Natl. Inst. Polar Res., Spec. Issue 46, 144-150; [7] Nakamura N. et al. (1984) Meteoritics 19, 278-279; [8] Warren P. H. and Kallemeyn G. W. (1989) Poc. Lunar Planet Sci. Conf. 19th 475-486; [9] Prinz M. et al. (1984), Meteoritics 19, 292-293.

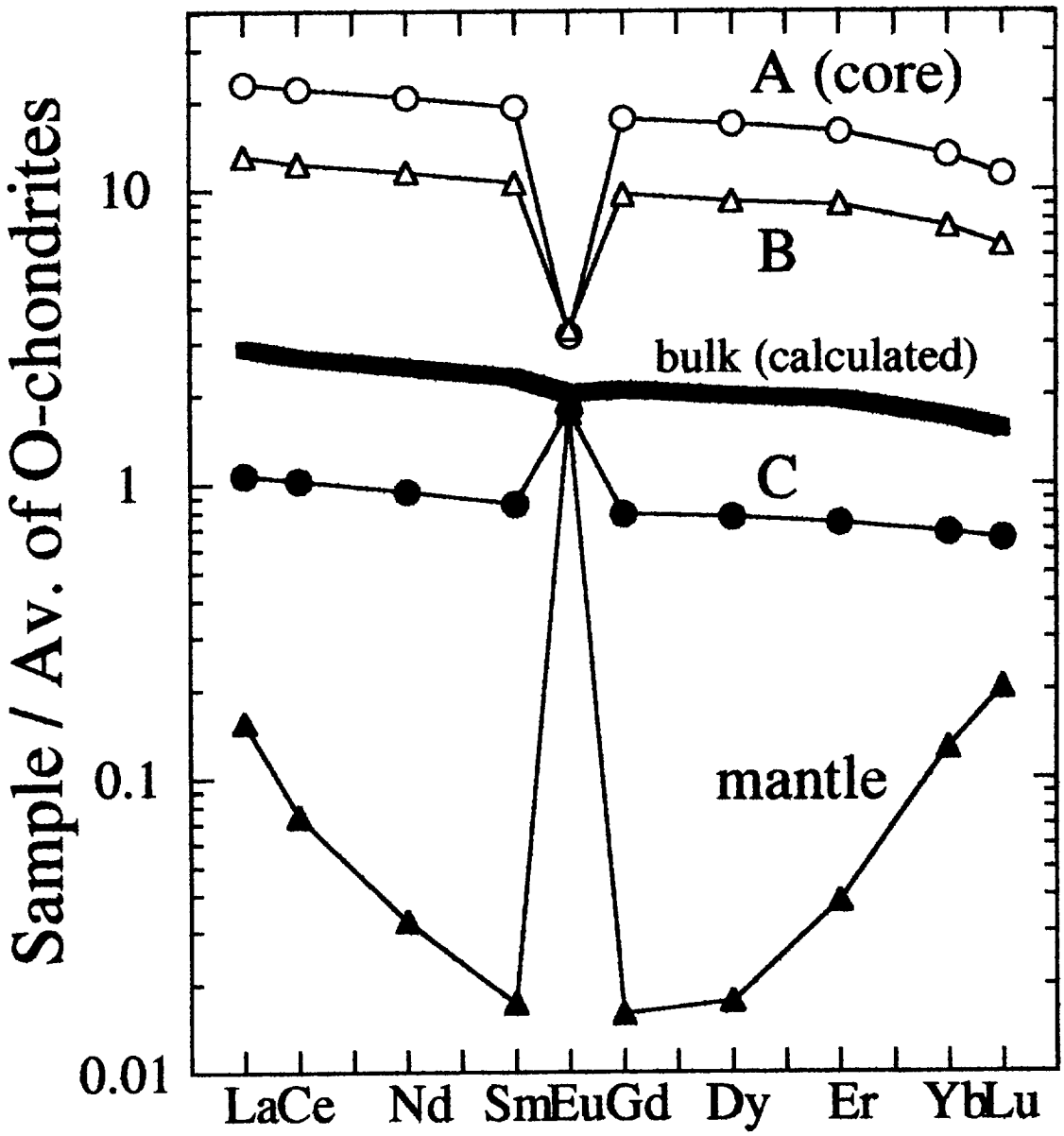

Fig. 1 Ordinary chondrite-normalized REE patterns for different parts of the troctolitic inclusion in the Y-75097 L6 chondrite.

FERROMAGNETIC RESONANCE SPECTRA OF H_2-REDUCED MINERALS AND GLASSES;

Richard V. Morris[1] and Carlton C. Allen[2]. [1]NASA Johnson Space Center, Houston, TX 77058; [2]Lockheed Engineering & Sciences Co., Houston, TX 77058.

INTRODUCTION AND BACKGROUND

In an earlier paper [1], we reported that H_2 reduction of basaltic glass, olivine, pyroxene, and plagioclase resulted in the formation of metallic iron, in the darkening and reddening of the reflectance spectra, and the masking of individual spectral features in the visible and near-IR. Such changes in the reflectance spectra of lunar soils are attributed to increasing maturation (i.e., increasing residence time of a soil in the upper ~1 mm of lunar regolith) [2]. Submicroscopic metallic iron particles disseminated in agglutinitic glass are thought to be responsible for the changes in reflectance spectra associated with maturation [2]. This metal is produced by reduction of ferrous iron and is associated with the impact-melt glass formed by micrometeorite impact at the very surface of the Moon [3,4].

As discussed by [5], submicroscopic (or nanophase) metallic iron (np-Fe^0) particles contribute to the relatively narrow resonance (linewidth ΔH = 530-800 G; [6]) observed in the FMR spectra of all lunar soils. The FMR experiment constrains these np-Fe^0 particles to have diameters in the range 4-33 nm [5]. Relative concentrations of np-Fe^0 have been measured for virtually all lunar soils using ferromagnetic resonance (FMR). The relative concentration of np-Fe^0 (I_s) normalized to total iron concentration (I_s/FeO) is used as a maturity index for lunar soils [6]. Absolute concentrations are reported by [7].

We report here FMR spectra for H_2-reduced minerals and glasses that include the samples studied by [1]. The FMR spectra were recorded at room temperature at a nominal frequency of 9.5 GHz. Sample saturation magnetization reported as Fe^0 was measured with a vibrating sample magnetometer.

RESULTS AND DISCUSSION

The FMR spectra are shown in Figure 1. The samples are ordered in increasing linewidth (ΔH = 790 to 5820 G) of the resonance centered near 3300 G. The linewidth expected for chemically-pure, spherical (only crystalline anisotropy energy), non-interacting, nanophase metallic iron particles embedded in a nonmagnetic matrix at room temperature is ~1000 G [8,9]. It is reasonable to attribute the lunar-like resonances having linewidths between 790 and 1250 to np-Fe^0. The FMR spectrum of reduced ilmenite is reasonably attributed to large metallic iron particles. This is consistent with its high concentration of Fe^0 (39 wt. %) and SEM observations of Fe^0 particles in the 1-10 μm range [10]. The samples with np-Fe^0 also contain, to variable extents, coarser-grained metal because their spectra are superpositions of narrow (np-Fe^0) and broad (coarse metal) components. This superposition is most evident in the spectrum for the reduced A11 glass. Reduced diopside has the highest relative proportion of np-Fe^0.

There are several possible reasons for the range in np-Fe^0 linewidths (790-1250 G). The SEM studies of [1,10] show that for Fe^0 particles larger than the detection limit (~0.1 μm), the average particle diameter increases through the samples series in the same order as the np-Fe^0 linewidth. It seem reasonable that np-Fe^0 particles would do the same, and that this is responsible for the linewidth variation. It is also possible that particle-particle interactions also increase through the series because total metal content generally increases with linewidth. Reduction experiments at lower temperatures for shorter times, which would give less reduction and lower diffusion rates for particle growth, might produce np-Fe^0 with smaller linewidths. If only the factors discussed above are important, the intrinsic linewidth for np-Fe^0 should be less than or equal to the lowest value we observe, which was 790 G for reduced diopside. The observation that this value is lower than the theoretical linewidth of ~1000 G implies that other interactions are important. The linewidths observed for lunar soils (530-800 G [6]) are also less than the theoretical value.

References: [1] Allen et al., *Icarus*, **104**, 291, 1993; [2] Adams and McMord, *PLPSC4*, 163, 1973; [3] Housley et al., *PLPSC4*, 2737, 1973; [4] Housley et al., *PLPSC5*, 2623, 1974; [5] Housley et al., *PLPSC7*, 13, 1976; [6] Morris, *PLPSC9*, 2287, 1978; [7] Morris, *PLPSC11*, 1697, 1980; [8] Weeks and Prestel, *PLPSC5*, 2709, 1974; [9] Griscom et al., *J. App. Phys.*, **50**, 2402 1979; [10] Gibson et al., *JGR*, submitted, 1994.

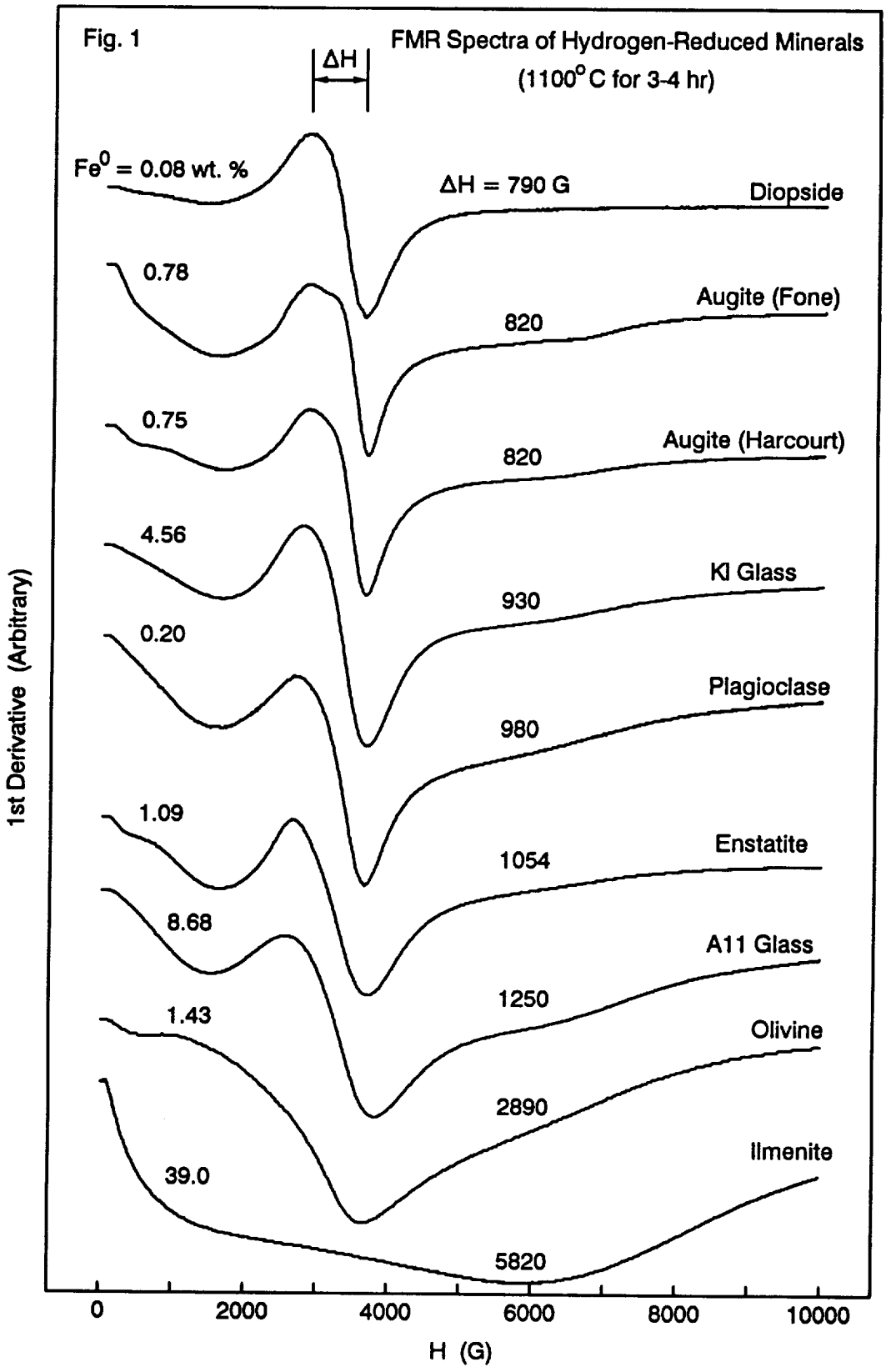
Fig. 1
FMR Spectra of Hydrogen-Reduced Minerals
(1100° C for 3-4 hr)
ΔH
Fe⁰ = 0.08 wt. %
ΔH = 790 G
Diopside
0.78
820
Augite (Fone)
0.75
820
Augite (Harcourt)
4.56
930
KI Glass
0.20
980
Plagioclase
1.09
1054
Enstatite
8.68
1250
A11 Glass
1.43
2890
Olivine
39.0
5820
Ilmenite
1st Derivative (Arbitrary)
0
2000
4000
6000
8000
10000
H (G)

HEMATITE FORMED FROM PYROXENE ON MARS BY METEORITIC IMPACT;

Richard V. Morris[1], J. F. Bell III[2], and H. V. Lauer Jr.[3]. [1]NASA Johnson Space Center, Houston, TX 77058, [2]NASA Ames Research Center, Moffett Field CA, [3]LESC, Houston, TX 77058.

INTRODUCTION

In earlier work [1,2], we showed using Mössbauer data that the mineralogy of iron-bearing phases in impact melt rocks from Manicouagan Crater (Quebec, Canada) is to a to a first approximation hematite and pyroxene. The visible and near-IR reflectivity data for these impact melt rocks show a continuous trend in band position from ~850 to ~1000 nm, which corresponds to the positions for the hematite and pyroxene endmembers, respectively. The oxidation is thought to occur shortly after the impact when oxidizing vapors and/or solutions reacted with the impact melt which was below its solidus temperature but still relatively hot [3]. The reflectance data have important implications for Mars because band positions which occur between the ~850 and 1000 nm bands observed for Mars [e.g., 4] can be attributed to hematite-pyroxene assemblages and not necessarily to a different ferric mineralogy.

Because oxidation of impact melt rocks at Manicouagan is thought to occur subsolidus, precursors for the hematite include oxides such as magnetite and ilmenite and silicates such as pyroxene and olivine. To determine if the Manicouagan impact-melt rocks are related to each other by simple thermal subsolidus oxidation, we calcined in air a relatively unoxidized Manicouagan impact-melt rock (MAN-74-608A). Previous work has shown that np-Hm (nanophase hematite) particles can be derived by calcination of iron-bearing silicates [e.g., 5].

RESULTS AND DISCUSSION

Reflectivity spectra for unheated and heated impact-melt samples are shown in Figure 1. The original, unheated impact-melt rock shows absorption features centered near 970 and 1900 nm which result from ferrous iron and are diagnostic of pyroxene. No features diagnostic of ferric iron, except perhaps for a very weak feature near 500 nm, are seen in the spectrum. Upon heating, the spectrum of this sample shows a remarkable evolution from ferrous- to ferric-dominated character. At 400°C, the 970 and 1900 nm features are essentially unchanged, but the visible color of the sample is substantially reddened. This reddening is caused by ferrous to ferric conversion in the sample and the resulting spectral effects of the very strong ferric absorption edge near 550 nm. By 500°C, there has been enough ferrous to ferric conversion to begin to see evidence for the Fe^{3+} crystal field transition bands near 660 nm and 860 nm and the distinct absorption edge at 550 nm. These spectral features are characteristic of crystalline hematite [6]. At 800°C, the ferric features are even stronger and the entire spectrum short of 1600 nm appears reddened because of an increase in reflectivity at the longest wavelengths. Evidence for the 1900 nm pyroxene feature has vanished but there is still a strong indication of pyroxene near 970 nm. Finally, at 1000°C all evidence for Fe^{2+} absorption features is gone and the spectrum looks like that of a typical hematite. As shown in Figure 2, the changes in iron mineralogy with calcination from a ferrous, pyroxene dominated assemblage to a ferric, hematite dominated assemblage are also observed in the Mössbauer spectra.

Figure 3 shows reflectivity spectra for two highly oxidized samples of impact-melt rock from Manicouagan. They are very similar to the 800 and 1000°C samples, and demonstrate that the oxidized Manicouagan rocks can be derived from the relatively unoxidized ones by simple thermal oxidation.

The calcination experiments have important implications for the interpretation of Mars reflectance spectra. Recent analyses of Phobos-2 ISM spectra of Mars [4] have revealed a class of surface materials exhibiting spectra with absorption band centers transitional between the 860 nm and 980 nm endmember wavelengths observed for most classical bright and dark regions, respectively. [4] favor the interpretation of these spectra as indicating the presence of an additional ferric oxyhydroxide phase (such as goethite or ferrihydrite). We advocate here and previously [1,2] an alternate hypothesis: that the band center wavelengths may be transitional because the spectra represent intimate assemblages of hematite and pyroxene analogous to the Manicouagan impact-melt rocks. Impacts have obviously been an important surface modification and alteration

process throughout Martian history. For example, [7] has calculated an equivalent global impact-melt layer of 521 m.

An additional likely mechanism for producing mixed hematite-pyroxene spectral signatures from Mars comes from spectroscopic evidence for both hematite and pyroxene occurring alone in specific regions of the Martian surface [4,8]. At the ISM spatial resolution of ~22 km, it is not unreasonable to expect some degree of sub-pixel areal mixing of hematite-dominated and pyroxene-dominate regions on the surface. The Manicouagan samples and our calcination experiments show that these two mineralogies can both be present as a mineral assemblage in oxidized impact-melt rocks. Both the areal mixing and oxidation mechanisms probably take place, although only the latter provides a way (meteoritic impact in an oxidizing environment) of producing hematite from initially unweathered basaltic materials.

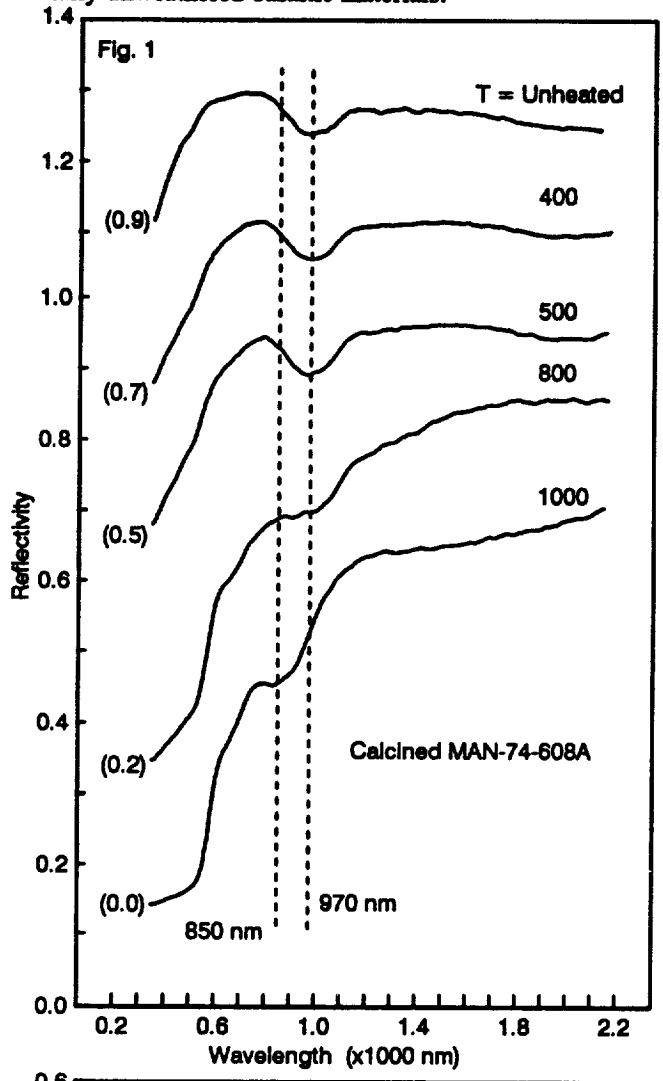

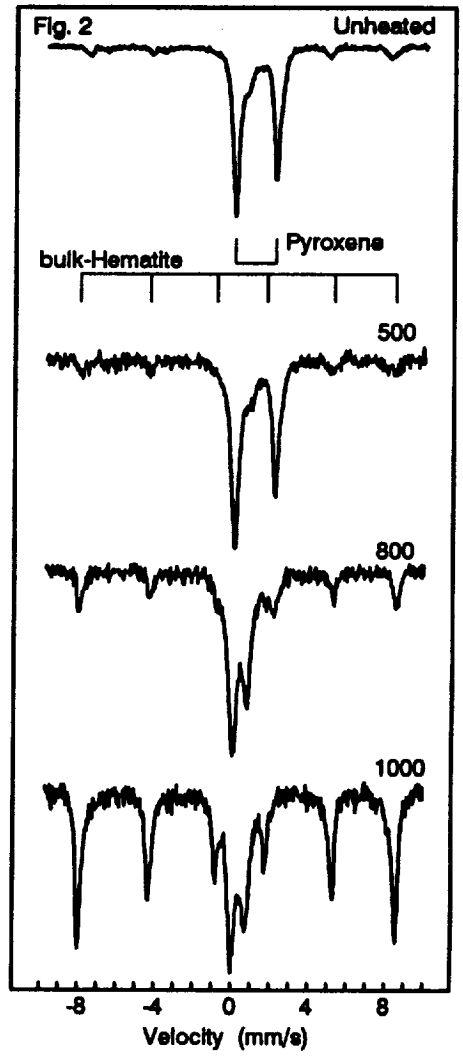

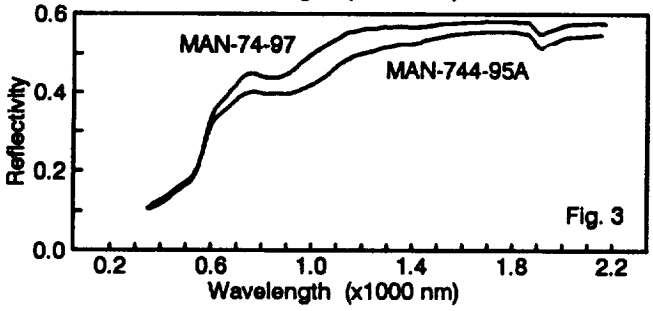

References: [1] Morris *et al.*, *LPSC24*, 1015, 1993; [2] Morris *et al.*, *MSATT*, LPI Tech. Rept. 93-06, 30-32, 1993; [3] Floran *et al.*, *JGR*, *83*, 2737, 1978; [4] Murchie *et al.*, *Icarus*, *105*, 454, 1993; [5] Straub *et al.*, *JGR*, *96*, 18830, 1991; [6] Morris *et al.*, *JGR*, *90*, 3126, 1985; [7] Clifford, *JGR*, *98*, 10973, 1993 [8] Mustard *et al.*, *JGR*, *98*, 3387, 1993.

MÖSSBAUER MINERALOGY OF CALCINED MURCHISON METEORITE:

Richard V. Morris[1], M. E. Zolensky[1], T. Hiroi[1], and M. E. Lipschutz[2]. [1]NASA Johnson Space Center, Houston, TX 77058; [2]Dept. of Chemistry, Purdue University, West Lafayette, IN 47907.

INTRODUCTION

The three Antarctic meteorites B7904, Y82162, and Y86720 are unusual because they have characteristics in common with both CI and CM groups and because they apparently underwent thermal alteration after hydrous alteration on their parent body [e.g., 1,2]. They are also spectrally similar (visible and near-IR) to C, G, B, and F asteroids, which may imply that the surface materials on those asteroids may have undergone thermal alteration [3]. Based on the reflectance spectra of samples of Murchison (CM2 carbonaceous chondrite) that were thermally altered in the laboratory (cryopumped and initial 10^{-5} atm H_2), [3] concluded that putative thermal alteration occurred at temperatures of 600 to 1000°C. [4] have done similar experiments on Murchison and reported mineralogical changes based on data from transmission electron diffraction microscopy, electron diffraction, and analytical electron microscopy. We report here the Mössbauer mineralogy of the same samples of thermally-altered Murchison analyzed by [1,3]. Mössbauer mineralogy gives the molar distribution of Fe among its oxidation states and iron-bearing mineralogies.

RESULTS AND DISCUSSION

The Mössbauer spectra of the Murchison samples are shown in Figure 1. Mössbauer parameters of spectral components used to do spectral fits are given in Table 1. Relative areas of these components as a function of calcination temperature are summarized in Table 2. Three major changes occur in iron oxidation state and/or mineralogy between unheated and 400°C samples, 500 and 600°C samples, and 900 and 1000°C samples.

The RT-400 change results from thermal decomposition of phyllosilicates, which are the dominant iron-bearing phases in Murchison. Oxidation also occurred (Figure 2), and some magnetite formed. The D3 doublet in Murchison is associated with tochilinite [4], which is a sulfide-hydroxide. There is no obvious evidence for a phase with iron chemically bound to sulfur in either the 400 or 500°C samples, unless a low-spin Fe^{2+} phase contributes to D7; in this case the fraction of Fe^{3+} is overestimated in Figure 2 for the 400 and 500°C samples. The 500-600 change is marked by a dramatic increase in the proportion of Fe^{2+}; all samples calcined at temperatures are more reduced than unheated Murchison. The most obvious mineralogic change associated with this transition is the high proportion of iron associated with olivine (40 and 60% at 600 and 700°C, respectively). Troilite (FeS) and pyroxene are also present; magnetite is not present. The unidentified phase associated with D9 has Mössbauer parameters similar to those for tochilinite (D4) in Murchison and may thus may be a Fe^{2+}-Fe^{3+} phase where iron is chemically bound to sulfur. The proportion of the D9 phase decreases in the interval 600-900°C, and is not present after the 900-1000 change. The 900-1000 change is also characterized by the appearance of Fe^0. The 34.0 T value of B_{hf} for Fe^0 implies that it is alloyed with Ni^0 and/or Co^0 [6].

When using these results to constrain the temperature of metamorphism in meteorites and asteroids, it is important to consider whether kinetic effects are important. In particular, does the 500-600 change, where the iron mineralogy changes from relatively oxidized to relatively reduced (Figure 2), just reflect the temperature at which the H_2 gas and/or carbon (intrinsic to Murchison) become reactive on the time-scale of our experiments (~1 wk), imposing reducing conditions? Longer experiment times might to lower the temperature for the 500-600 change, which would lower the temperature below 600°C required for the putative metamorphism of B7904, Y82162, Y86720, and C, G, B, and F asteroids [3] under reducing conditions.

References: [1] Paul and Lipschutz, *Z. Naturf.*, **44A**, 979, 1989; [2] Ikeda, *NIPR Symp.*, **5**, 49, 1992; [3] Hiroi et al., *Science*, **261**, 1016, 1993; [4] Akai, *NIPR Symp.*, **5**, 120, 1992; [5] Fisher and Burns, *LPSC24*, 489, 1993; [6] Greenwood and Gibb, *Mössbauer Spectroscopy*, 1971.

Table 1. Preliminary Mössbauer parameters (293K; relative to Fe metal) and phase assignments for spectral components.

	IS (mm/s)	QS (mm/s)	B_{hf} (T)	Oxidation State: Mineralogy
Doublet Components				
D1	1.11	2.58		Fe^{2+}: Phyllosilicate
D2	1.03	1.83		Fe^{2+}: Phyllosilicate
D3	0.33	0.99		Fe^{3+}: Phyllosilicate
D4	0.58	0.72		$Fe^{2+,3+}$: Tochilinite
D5	1.16	3.00		Fe^{2+}: Olivine
D6	1.16	1.80		Fe^{2+}: Unknown
D7	0.38	0.98		Fe^{3+}, low-spin Fe^{2+} (?): Unknown
D8	1.16-1.20	2.26-2.40		Fe^{2+}: Pyroxene
D9	0.53-0.66	0.68-0.49		$Fe^{2+,3+}$: Unknown
Sextet Components				
S1	0.75	-0.17	31.2	Fe^{2+}: Troilite
S2				Fe^{3+}: Magnetite-tet
S3				$Fe^{2+,3+}$: Magnetite-oct
S4	0.02	-0.01	34.0	Fe^{0}: Fe-Ni metal alloy

Table 2. Mössbauer mineralogy (% relative spectral area of iron in iron-bearing phases). There is also evidence for some pyrrhotite in the 600, 700, and 800°C samples.

Temp.	D1	D2	D3	D4	D5	D6	D7	D8	D9	S1	S2 +S3	S4
RT	32	10	33	23	2							
400					4	13	76			1	5	
500					4	20	66			1	9	
600					41			20	28	4	7	
700					61			16	12	11		
800					62			13	8	18		
900					62			15	5	17		
1000					42			19		17		22

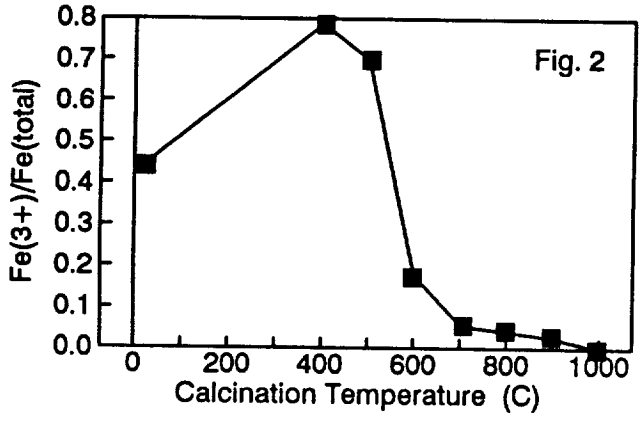

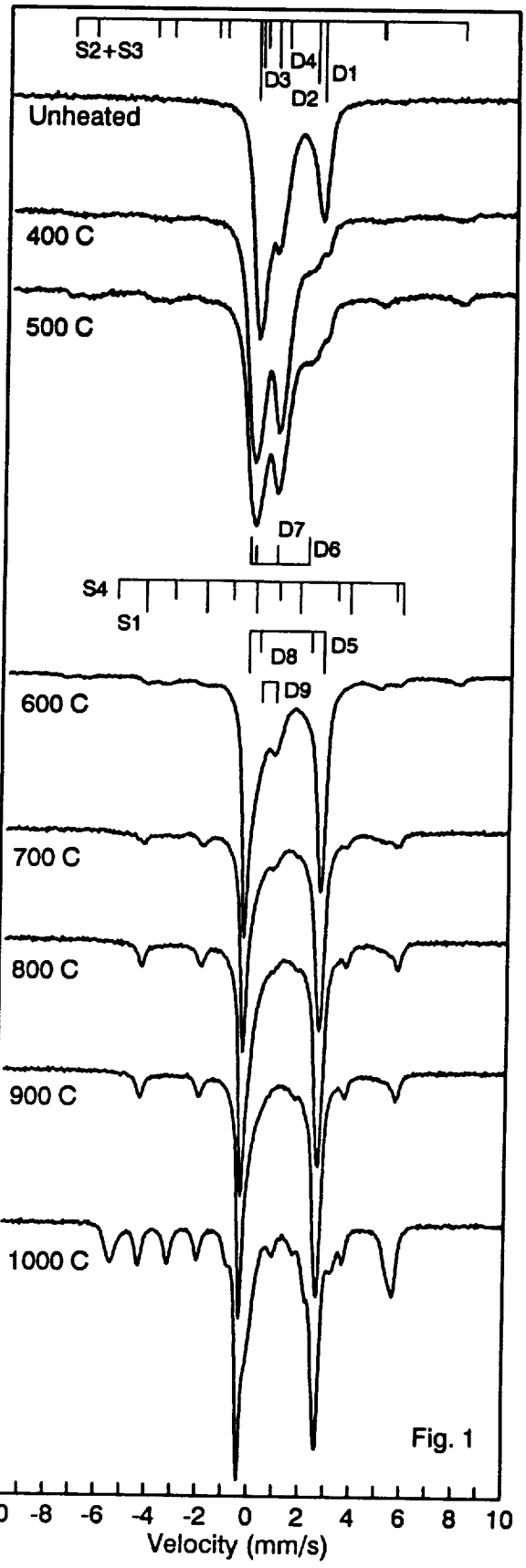

TOWARD SYSTEMATIC ESTIMATION OF THE ORIGINS OF REGOLITH MATERIALS THAT MIGHT BE SAMPLED DURING A LUNAR HIGHLAND GEOLOGIC TRAVERSE. Billy E. Moss and Larry A. Haskin, Dept. of Earth & Planetary Sciences and McDonnell Center for the Space Sciences, One Brookings Drive, Washington Univ., St. Louis, MO 63130

What is the probable origin of the materials in the regolith we sample during a highland traverse? Photogeologic interpretation, which reveals late large events, will surely be the main basis for selecting a site and planning its traverse. Suppose our interest is in the original igneous materials produced directly beneath the location of our traverse. What fraction of the regolith consists of materials indigenous to that site and what fraction consists of basin ejecta? We have developed a spreadsheet based on cratering theory to estimate systematically the proportions of basin ejecta at arbitrarily chosen, *typical* highland sites (more or less, the statistically most common locations expected at a given location). Applying it to the Apollo 16 region, we find that most of the material in the regolith is of local origin (or Procellarum- + local material if there is a Procellarum basin). The proportion of melt from Unnamed B (if primary) exceeds that of Nectaris material if the radius of the Nectaris transient crater was ~200 km. Even at 300 km rad., the proportion of Nectaris material is <30%.

A major feature of the Moon is the earliest igneous crust that formed as the interior differentiated and cooled; what was that crust like? What further igneous processes modified that crust through re-working of its materials and later additions? These questions, easily approached by theory, are hard to approach by observation. On Earth, we would undertake geologic traverses, preferring to observe changes in igneous outcrops, and sampling along the route or, under sediment blankets, by drilling. Traverses are essential to map the Moon's geology; there, we will sample and analyze regolith. But how are formerly igneous crustal materials distributed and changed, now that the accessible highlands consist of regolith and mega-regolith? If we explore and sample a patch of highland surface, where did the materials making up the bulk of the soils and breccias originate? What fraction of the accessible regolith consists of materials deposited from individual basin-forming and other large impacts, and what fraction is reworked material of local igneous origin?

Whereas sites will be chosen for special, photogeologically observable features, we must also concern ourselves with *typical* regions. Here, we apply results of cratering studies in a systematic way to estimate proportions of basin ejecta in *typical* highland regolith as a function of location on the lunar surface. We use for illustration a traverse area of 100 × 100 km (Square of Interest, SOI) in the vicinity of the Apollo 16 site, 1600 km from the center of the Imbrium basin and 610 km from the center of Nectaris, and estimate the proportions of Imbrium and Nectaris materials that fell there and the depths to which they became mixed with pre-existing regolith as a result of the Imbrium event alone. Our intent is to produce a readily programmed, convenient tool to provide background information for traverse planning.

We begin with the average mass of primary ejecta fragments (PRIFRAG) falling onto a statistically *typical* SOI in the vicinity of the Apollo 16 site [derived from 1], a distribution of PRIFRAG sizes that matches that of the entire primary event [from 2]. We distribute the mass reaching the average SOI into PRIFRAGs meeting those constraints (Fig. 1). We assumed 335 km for the diameter of the Imbrium transient crater [1] and 200 km for the smaller proposed Nectaris transient crater [1] and 300 for the larger [1]. We used a depth-to diameter ratio of 1:5. Initial results are for ejection angles of 45° with a launch point halfway between the center and edge of the transient crater. Despite the greater size of the Imbrium basin, the number of PRIFRAGs from Nectaris [Fig. 2] is greater than that from Imbrium because Nectaris is closer to the site. A larger Nectaris crater ejects more material, increasing the intensity of the bombardment of the site. The bulk of the PRIFRAGs' mass is contained in the relatively few, larger PRIFRAGs. The largest possible PRIFRAGs hit few possible SOIs. The average mass of the largest Imbrium PRIFRAGS to hit a typical square contains ~70% of the total PRIFRAG mass; this average PRIFRAG craters <5% of the SOI. The largest 100 Imbrium PRIFRAGs contain ~91% of the total PRIFRAG mass and crater <15% of the SOI. Corresponding values for Nectaris small are 60%, 5%, 85%, and 25%, and for Nectaris large are 35%, 10%, 80%, and 65%. As the distance between the SOI site and the rim of the basin's transient crater increases, the effects of the largest PRIFRAGs are relatively greater and more localized. As the quantity of material reaching the SOI increases, the mixing depth increases and the proportion of basin ejecta across the SOI varies less. Locations of the largest event(s) in any SOI should be photogeologically observable. We designate such regions as *atypical* and note that they contain most of the PRIFRAG mass. *Atypical* does not imply uninteresting; such areas might be chosen for a traverse because of photogeologically observable secondary craters.

ORIGINS OF REGOLITH MATERIALS: Moss and Haskin

In our preliminary analysis, we ignore effects such as pre-existing topography. There will be a distribution of mixing depths [Fig. 3], but over most of the SOI, the depth will be much less than that where the largest PRIFRAGs struck. To obtain the proportions of primary material, we used the following approximation: We presume that mixing at any location occurs to the depth cratered by the largest PRIFRAG to strike that location; all overlapping events are thus smaller. We mix the mass of excavated substrate with those of 1) the PRIFRAG, and 2) the average mass of infalling PRIFRAGs of each smaller size that would fall on the same area. (In this approximation, we ignore the difference between the area actually covered by ejecta and the transient crater cavity.) The resulting distributions of depths of excavation and of fractions of Imbrium material in surface regolith as a function of surface area are shown in Fig. 4.

Each traverse site is likely to be chosen for its *atypical* features. These features, however, are likely to be *atypical* only with respect to one basin. Estimates of the type just made will be appropriate in considering the proportions of materials from other basins and local sources, even if they do not apply to the 'basin of immediate interest,' whose ejecta make the site an *atypical* one. Little regolith is *typical*, in the sense that we could find it. *Typical* regolith is nevertheless far more probable than any specific situation. Our preliminary results show that *typical* regolith (~80% of a *typical* SOI) in the vicinity of Apollo 16 would contain <10% Imbrium material, less than the 13 - 18% estimated by [3] and <15% Nectaris material (small) or <30% (large).

Systematic analysis of a *typical* SOI located at the Apollo 16 site shows that material of local origin dominates the surface regolith after every basin event. Unnamed B [4] (if primary) should have a melt sheet ~30 m thick [5]. Melt rock from Unnamed B makes up ~15% of the post-Nectarian regolith and is at least as abundant as total Nectaris material (12%) for Nectaris small. Pre-Unnamed B substrate (63%) predominates over total Nectaris material (<30%) for Nectaris large. Unnamed A would have penetrated to local igneous rock in the absence of a major Procellarum basin but only into upper Procellarum strata otherwise.

Acknowledgments: This work was supported in part through NASA grant NAGW-3343. Thanks to Bill McKinnon for helpful discussions.

References: 1. McGetchen et al., 1973, EPSL 20, 226-236. 2. Melosh, Impact Cratering, a Geologic Process, 1989. 3. Morrison and Oberbeck, PLSC 6, 2503-2530. 4. Head, 1974, Moon, 11, 77-99. 5. Lange and Ahrens, 1979, PLPSC 10, 2707-2725.

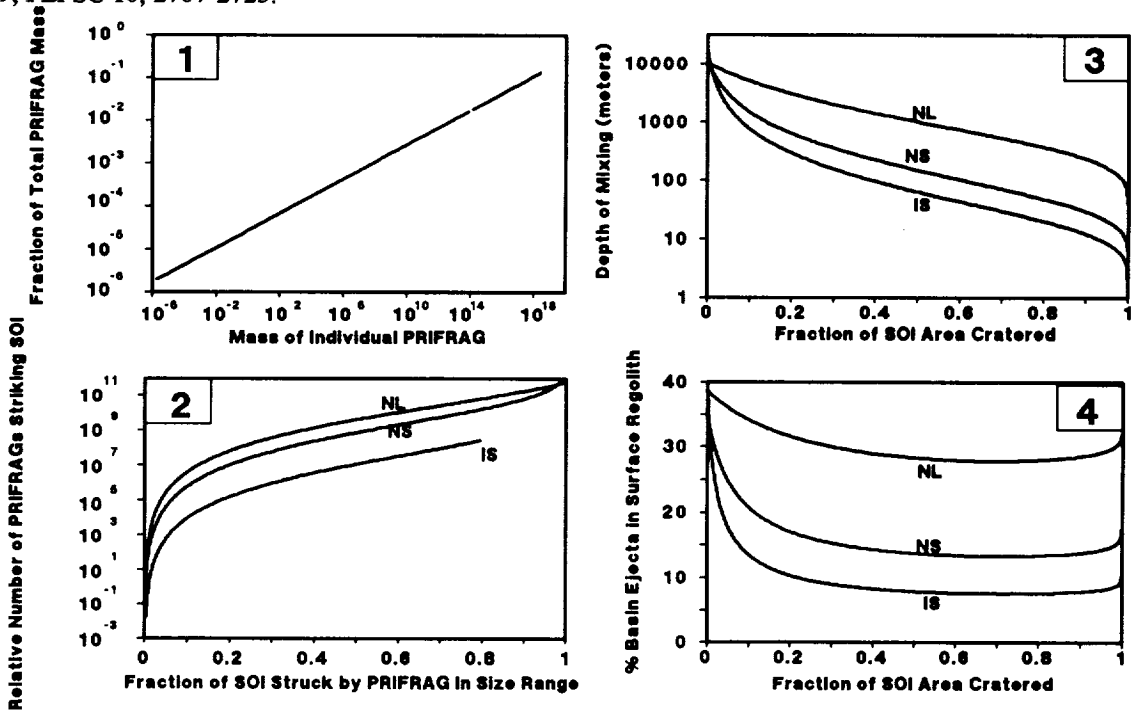

Figure Captions: 1. Relationship between masses of PRIFRAGs in a given size range and total primary fragment mass. 2. The number of PRIFRAGs of each size range and the proportion of the SOI area they strike. IS is Imbrium, NS is Nectaris Small, NL is Nectaris Large. 3. Approximate depth of mixing as a function of the total fraction of the SOI cratered. 4. Proportion of primary ejecta material in the surface regolith as a function of the fraction of the SOI cratered.

CARBON IN THE METAL OF BISHUNPUR AND OTHER ORDINARY CHONDRITES; S. Mostefaoui and C. Perron, Muséum National d'Histoire Naturelle, 75005 Paris, and Institut d'Astrophysique Spatiale, Orsay, France.

In the course of a study of Fe-Ni metal composition and inclusion content in primitive chondrites [1], we have found that graphite inclusions are common in the metal of Bishunpur (L3.1). The identification of the inclusions was made by optical microscopy, and confirmed by SEM-EDS and/or Raman microprobe. This carbon may have played a role in redox processes during chondrule formation. A preliminary survey of a number of H, L and LL chondrites of all petrologic types revealed similar inclusions in several other chondrites, although apparently not quite as abundant as in Bishunpur.

Although the association of carbon with metal has been noted in OCs [2,3], the occurence of graphite in metal was thought to be restricted to very reduced meteorites [4,5]. However, in Bishunpur, we find graphite in a large proportion (roughly one half) of the large metal grains outside chondrules (fig.1). Some of these grains contain silicates looking very much like chondrule fragments (e.g. pyroxene in mesostasis), supporting the idea that they went through the chondrule-forming process (i.e. they were expelled from molten chondrules or directly made as silicate-poor, metal-rich chondrules). The graphite inclusions usually are of irregular shape, 1 or a few μm across, but inclusions up to ~25 μm have been observed (fig. 2). Apart from rare exceptions not described here, C-containing grains do not contain Cr, i.e. no tiny chromites are seen in the metal and no Cr is detected with the electron microprobe, contrary to most metal grains in chondrules and many outside chondrules [1,6]. SEM-EDS analyses of the graphite show it is essentially pure carbon, although the Fe and Ni X-ray lines from the surrounding metal are also seen for small inclusions, and a small oxygen line is usually also present. The Raman spectra only show the graphite bands (fig. 3). Taken at face value, the ratio of the intensities at 1581 and 1355 cm^{-1} in the spectrum of fig. 3 would indicate a crystallite size of about 60 Å [7]. However, the measurements have been made on polished sections and it is well known that polishing can have important effects on graphite Raman spectra [e.g. 8]. We checked this by taking spectra of graphite from the Canyon Diablo meteorite both with and without polishing. This confirmed that polishing strongly increases the bands at 1355 and 1620 cm^{-1}. Graphite in Bishunpur metal is thus probably much more "ordered" than it appears from the spectra.

What is the origin of the C inclusions? It has been shown that Si, P or Cr in the metal of primitive OCs are in tiny inclusions, which precipitated from solid solutions during metamorphism [1]. Graphite inclusions may have formed the same way, either directly or through formation of metastable cohenite. The much larger sizes reached by C inclusions are likely due to its much larger diffusion coefficient in Fe-Ni. Although incorporation of Si, P, Cr in metal is widely accepted as resulting from condensation in the nebula [e.g. 6], it has been argued that it may have occurred during chondrule formation [1]. In this latter case, carbon may be the reducing agent. Depending on its abundance in the chondrule precursor material, substantial reduction leading to measurable amounts of P, Cr or Si in Fe-Ni may use up all the carbon, leaving no graphite inclusions in metal now containing chromite inclusions (i.e. metal now seen inside chondrules, and some metal grains outside chondrules). On the other hand, the graphite-bearing grains could have been expelled from molten chondrules too early for substantial reduction to take place, explaining why these grains usually contain no Cr. This

CARBON IN BISHUNPUR METAL: Mostefaoui S and Perron C.

would imply that dissolution of C from a C-bearing precursor material into metal was much faster than Cr reduction and dissolution, or C was already in metal before chondrule formation.

We looked for graphite in the metal of other chondrites. Polished sections of 20 Ocs were surveyed. Graphite inclusions in metal were found in 6 of them: Khohar, Inman, Mezö-Madaras (all L3), Tieschitz (H3, and in this case, one inclusion was found in troilite), Massenya (H5?) and Manych (LL3), and also, in agreement with [9], Acapulco. Raman spectra of graphite taken from these chondrites and from enstatite chondrites vary somewhat but show no clear systematic effect of the petrologic type. Again, however, the effects of polishing may mask real effects.

References: [1] Perron C. et al. (1992) Meteoritics 28, 275; Zanda B. et al. submitted. [2] Brearley A.J. (1990) GCA 54, 831. [3] Makjanic J. et al. (1993) Meteoritics 28, 63. [4] Keil K. (1968) JGR 73, 6945. [5] Ramdohr P. (1973) The Opaque Minerals in Stony Meteorites, Elsevier. [6] Rambaldi E. R. and Wasson J.T. (1981) GCA 45, 1001. [7] Tuinstra F. and Koenig J.L. (1970) J. Chem. Phys. 53, 1126. [8] Pasteris J.D. (1989) Appl. Spectrosc. 43, 567. [9] Palme H. et al. (1981) GCA 45, 727.

Fig. 2: The largest graphite inclusion (black) in metal (kamacite) found in our bishunpur polished sections (backscattered electron image).

Fig. 1: Backscattered electron image of a graphite-bearing metal grain in Bishunpur. Kamacite is light grey, taenite is white, troilite dark grey. The 5 large black patches are pyroxene, peppered with sub-µm metal blebs, like the dusty olivines commonly found in chondrules. The graphite inclusions are small black dots, the largest one is indicated by C.

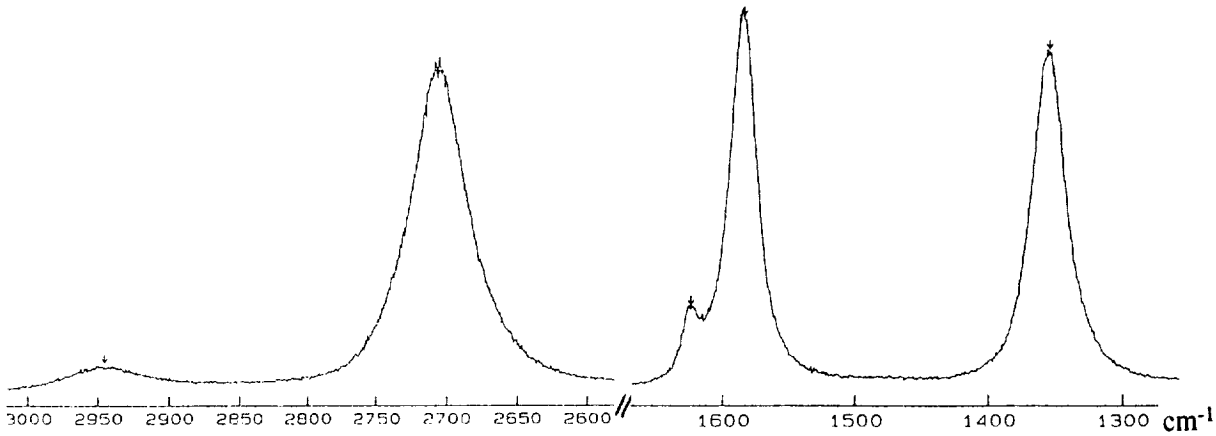

Fig. 3: Raman spectrum from the graphite inclusion of fig. 2. Spectra from other inclusions are very similar.

IMPACT CRATERS ON MARTIAN VOLCANOES. P. J. Mouginis-Mark, Planetary Geosciences, Geology and Geophysics Dept., SOEST, Univ. Hawaii, Honolulu, Hawaii, 96822.

Introduction

The style(s) of eruption of Martian volcanoes has been a topic of general interest for a number of years, not only because an understanding of the process aids in the interpretation of the landscapes seen in Viking Orbiter images (1), but also because it is likely that volcanism had a major influence on the short-term (<1,000 years) atmosphere and climate of Mars (2 - 4). In particular, the debate over whether Martian volcanoes experienced explosive or effusive eruptions, and had high or low effusion rate eruptions has been the focus of several recent studies. In many cases, it is the morphology of the volcano flanks that has been used to distinguish between explosive and effusive activity. The presence of lobate flows is used as a diagnostic attribute associated with effusive activity (e.g., 1, 5). Absence of lobate flows and the occurrence of valley networks on the flanks (6, 7), or the occurrence of subdued or mantled areas close to the summit (8), are interpreted as signs of explosive eruptions.

These observations typically relate on to the surface of the volcano, although the morphology of deeply incised valleys on the flanks of volcanoes such as Tyrrhena Patera (9, 10) can also be used to infer the 3-D characteristics of the volcano. With the realization that Alba Patera (11) and Apollinaris Patera (12) may have had different types of eruptions during their lifetime, it is relevant to consider whether other volcanoes also experienced an evolution in their activity during their growth. One way that such a hypothesis may be addressed is to use the morphology of impact craters on the flanks of the volcano to search for differences in the physical properties of the target. Also, because the crater rim and ejecta blanket of each crater form topographic obstacles when the craters are fresh, it may also be possible to constrain the origin or emplacement process of features and deposits on the volcanoes. This might be particularly useful when considering the formation of the valley networks either as density currents (6) or as valley networks formed by sapping (11, 13).

This analysis includes the study of many of the Martian volcanoes. Following the recent analysis by Robinson (14) the volcanoes included in the category of effusive volcanoes (ones with lava flows) are Biblis, Uranius, and Ulysses Paterae, and Tharsis and Albor Tholi. Volcanoes that probably experienced explosive eruptions include Ceraunius, Uranius and Hecates Tholi, and Apollinaris, Tyrrhena, Hadriaca Paterae. Alba Patera and Elysium Mons are also included in the "effusive" category.

Impact Craters on Lava Flows:

It is likely that altitude affects the morphology of impact craters (15), so that parts of very high Martian volcanoes such as Olympus Mons may possess craters with a different morphology at elevations of a few kilometers compared to those craters near the summit area at >~15 km above Mars datum. However, even at elevations of 3 - 8 km above Mars datum (i.e., comparable to the heights of the volcanoes that lack lava flows), the impact craters formed in lava flows display subtle differences in morphology. Central structures (pits, swirls, terraces) are more common on lava flows than other materials for a given crater diameter, and the ejecta lobes have a more complicated, multi-layer appearance. The numerous impact craters that are found on the mid-level flanks of Elysium Mons (16) provide fine examples of this type of crater morphology.

Impact Craters on Explosive Volcanoes:

Numerous moderately fresh impact craters in the diameter range 3 - 10 km are found on the flanks of Hecates Tholus (8). The most prominent characteristics of these craters is that their interiors lack terraces or central peaks, and that many are relatively shallow with flat floors compared to comparable diameter craters on ridged plains materials (17), which are believed to be lava plains. Exterior deposits for impact craters on Hecates and Ceraunius Tholi are typically single, continuous lobate deposits with a low distal rampart.

CRATERED MARTIAN VOLCANOES: P.J. Mouginis-Mark

Impact Craters as Obstacles:

Ceraunius Tholus and Hecates Tholus have some of the best examples of craters that have influenced valley network formation on Martian volcanoes. Both Mariner 9 (B-frame MTC 4271-51) and Viking Orbiter (516A24; 200 m/pixel) images of the northern flank of Ceraunius Tholus show the relationship between relatively young valleys and an older, elongate (34 x 18 km) impact crater. Ejecta lobes from the crater rise >14 km up the flanks of the volcano. These ejecta lobes have distal ramparts, and so should have been sufficient obstacles to divert water flowing on the surface. In two places, these lobes are cut by valleys 1.1 and 1.8 km in width. Surprisingly, the distal portions of these valleys have very small "delta deposits", implying that the total discharge volume was very small. Higher resolution images (662A54 - 61; 35 m/pixel) of Ceraunius Tholus and Hecates Tholus (86A39 - 43; 40 m/pixel) show that valleys on these volcanoes often cut crater rims and ejecta blankets. Very high resolution images (445B17/18; 9 m/pixel) of the flanks of Alba Patera show only one example of a crater that may have diverted a valley during its formation.

Conclusions

Impact craters on Mars probably excavated to depths of 0.05 - 0.2 of their diameter, based on laboratory experiments and terrestrial field data (18, 19). Thus, many impact craters on Martian volcanoes excavated material to depths of several hundred meters to perhaps more than a kilometer. It would therefore be expected that any layers with markedly different properties (e.g., ash layers buried beneath younger lava flows) would produce unusual ejecta morphologies or interior features. From this preliminary investigation, no such differences can be found that can be confidently attributed to such layers on the volcano flanks. It therefore seems likely that the surficial materials, either lava flows or ash deposits, characterize much of the recent (but buried) activity at each volcano.

The role of craters as topographic obstacles raises more questions than answers. For example, the elongate crater north of Ceraunius Tholus has had both its ejecta blanket and rim crest over-run by material that carved the valleys on the north flank of the volcano. This implies a fast moving, large volume, flow; and yet only very small distal deposits are found within the crater. A few craters on Hecates and Ceraunius Tholi have had their down-slope rim crests eroded by valleys, suggesting that valley formation took place a significantly long time after the formation of the flanks. However, because all of the distal portions of the valleys on Hecates Tholus are buried beneath the adjacent plains materials (8), this episode of valley formation must have been soon after the formation of the flanks. A few lobate deposits downslope of the valleys on Ceraunius Tholus can seen (e.g., frame 662A58), suggesting a more protracted period of valley formation on this volcano. Further analysis of these impact craters and valleys, as well as comparable studies for other Martian volcanoes (e.g., Uranius Tholus), may help resolve the process by which the valleys were carved.

References: 1) Carr, M.H. et al. (1977). *J. Geophys. Res.*, **82**, 4055 - 4065. 2) Settle, M. (1979). *J. Geophys. Res.*, **84**, 8343 - 8354. 3) Postawko, S. et al. (1988). *MEVTV Workshop Nature Comp. Surface Units on Mars*, 103 - 104. 4) Plescia, J.B. (1993) *Icarus*, **104**, 20 - 32. 5) Zimbelman, J.R. (1985). *Proc. LPSC 16th, JGR* **90**, D157 - D162. 6) Reimers, C.E. & P.D. Komar (1979). *Icarus*, **39**, 88 - 110. 7) Mouginis-Mark, P.J. et al. (1992). In: *MARS*, Univ. Arizona Press, Tucson, AZ, pp. 424 - 452. 8) Mouginis-Mark, P.J. et al. (1982). *J. Geophys. Res.*, **87**, 9890 - 9904. 9) Greeley, R. & D.A. Crown (1990). *J. Geophys. Res.*, **95**, 7133 - 7149. 10) Zisk, S.H. et al. (1992). *Icarus*, **96**, 226 - 233. 11) Mouginis-Mark, P.J. et al., (1988). *Bull. Volc.*, **50**, 361 - 379. 12) Robinson, M.S. et al. (1993). *Icarus*, **104**, 301 - 323. 13) Gulick, V.C. & V.R. Baker (1990). *J. Geophys. Res.*, **95**, 14325 - 14,344. 14) Robinson, M.S. (1993). Unpub. Ph.D. Thesis, Univ. Hawaii, Honolulu, HI. 15) Mouginis-Mark, P.J. (1979). *J. Geophys. Res.*, **84**, 8011 - 8022. 16) Mouginis-Mark, P.J. et al. (1984). *Earth, Moon & Planets*, **30**, 149 - 173. 17) Mouginis-Mark, P.J. and J.N. Hayashi (1993). *Earth, Moon & Planets*, **61**, 1 - 20. 18) Stoffler, D. et al. (1975). *J. Geophys. Res.*, **80**, 4062 - 4077. 19) Hortz, F. et al. (1983). *Revs. Geophys. Space Phys.*, **21**, 1667 - 1725.

MORPHOLOGY OF VENUS CALDERAS: SIF AND MAAT MONTES. P. J. Mouginis-Mark, Planetary Geosciences, SOEST, Univ. Hawaii, Honolulu, Hawaii, 96822.

Head and Wilson (1) reviewed the probable internal structure of volcanoes on Venus and the factors that should control the formation of their calderas. These factors include the presence or absence of mantle plumes, less gas exsolution (than on Earth), conditions more favorable to horizontal rather than vertical dike emplacement, and increased reservoir depths with higher elevation. All factors suggest that the morphology, structure and size of Venus calderas should be different from those on Earth. In order to search for morphological evidence for the influence of "neutral buoyancy zones" (1) on the structure of volcanoes of different heights, we have been studying the Magellan imaging radar and altimetric data for Sif Mons (22°N, 352°E) and Maat Mons (1°N, 194°E). Sif Mons rises to an elevation of ~2 km above the surrounding plain (max. elevation equals planetary radius of 6054.4 km), while Maat Mons has ~8 km of relief (max. elevation equals planetary radius of 6060.5 km).

Three types of pits and depressions can be identified on Sif Mons (ref. 2; Fig. 1): a large summit caldera, smaller nested calderas at the summit, and pit chains on the flanks. The largest collapse on Sif Mons is a 40 km diameter central caldera, with two smaller nested calderas each ~10 km across, and numerous pit chains comprised of depressions <1.5 km in diameter. Scalloping along the southern caldera rim indicates multiple episodes of collapse involving progressively smaller volume changes with time. These same types of features are also seen at the summit of Maat Mons (Fig. 2); the largest caldera is ~31 x 28 km in diameter and there are at least five smaller collapse craters at the summit between 5 to 10 km diameter. Extending down the SE flank to a distance of ~40 km is a series of smaller pits which are all >~3 km diameter. At full Magellan resolution (75 m/pixel), there is no sign of any constructional features around the rim of these small pits, indicating that they were all formed by collapse. There is also no sign of radial fractures which might indicate the top of dikes (1). At least two episodes of collapse can be seen on the flanks of Maat Mons, where chains of small pits cut across larger collapse features.

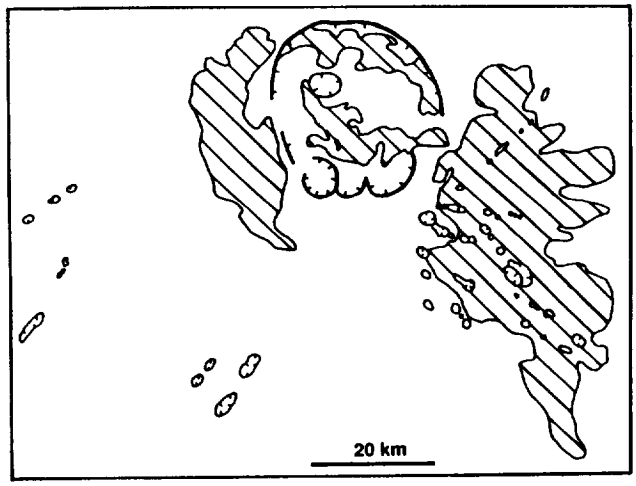

Fig. 1 (Left): Summit of Sif Mons. Fig 2. (Right): Summit of Maat Mons. Both sketch maps show the distribution of the nested calderas, pit craters and radar-dark lava flows (cross-hatch shading) in relation to the main summit caldera. North towards top for both maps.

Compared to calderas found on Mars and Earth (e.g., 3, 4), these two Venus calderas are relatively shallow. Although the Magellan altimetric data have insufficient spatial resolution to confidently determine their absolute depths, in a qualitative sense these calderas appear to be shallower based on the length of the radar shadows. No talus slopes are seen within the Venus calderas, nor are there any constructional features (e.g., cinder cones) apparent on either

volcano. Somewhat surprisingly, given the radar's ability to detect subtle topographic relief, there is little evidence that sagging or subsidence of the summits took place following the formation of the calderas. In Martian calderas such as Olympus Mons, Alba Patera, and Pavonis Mons, wrinkle ridges are prominent features and have been used to infer that subsidence occurred over areas that are tens of kilometers across once a lava lake solidified (5). This absence of wrinkle ridges within Venus calderas could either be interpreted as a lack of extensive summit lava flows (i.e., only small-volume eruptions) or the absence of deformation and subsidence after the emplacement of the flows (i.e., no deformation, or the deformation took place prior to the solidification of the lava lake).

The distribution of near-summit lava flows at Sif Mons appears to be more uniform than at Maat Mons. At Sif Mons, the flows are generally radar-bright with uniform backscatter characteristics. Radar-dark flows are found on the west and southwest flanks at 12 and 70 km from the caldera rim and correspond to vent elevations above the 6051.84 km mean planetary radius of 2.5 and 0.9 km. Within the caldera of Maat Mons, the generally radar-dark floor appears to have been partially buried by small (~10 x 15 km) flows that originated from two of the smaller pits. The most prominent of these flows is cut by the sharp boundary of the pit crater, indicating that the floor of the pit subsided after the flow was erupted. Nor are there any flows that originate from the crater chains on the flanks. This could indicate that while radial dike systems might exist within the volcano, magma transport at the higher elevations has been sub-surface, promoting collapse over the overlying material. Numerous small "fans" of radar-bright flows are particularly prominent on the eastern flank of Sif Mons (1.9 to 2.0 km elevation) and the lower southern flank of Maat Mons (at ~5.1 km elevation).

CONCLUSIONS: The above observations permit some of the theoretical predictions (1) to be compared to geomorphic observations. Interestingly, although the summit of Maat Mons is 6 km higher than Sif Mons (8 km vs. 2 km above the mean planetary radius), the two summit areas are remarkably similar. The concept of neutral buoyancy zones on Venus is therefore not supported by the landforms found on these two volcanoes.

Assuming that the volatile contents of the parental magmas were similar, it is surprising that the area of the summit affected by the primary episode of collapse is about the same on both volcanoes. Pit craters have formed on the rim of Sif Mons and within 5 km of the rim of Maat Mons, which supports the idea that there were intrusives at high elevations on these volcanoes. The process of pit chain formation seems to have worked with equal efficiency at both locations. These pit chains are approximately radial to the summit, suggesting the presence of radial dikes. However, based on the uniform distribution of fresh (radar-bright) lava flows around the volcanoes, there is no strong evidence for well developed rift zones analogous to those found in Hawaii; these rift zones should constitute topographic obstacles that diverted subsequent flows if the rift zones exist. No strong evidence for circumferential fissures (such as those identified for certain terrestrial calderas such as Fernandina; ref. 6) can be seen on either of the Venusian volcanoes described here. Several broad areas of radar-dark material close to the western summit of Sif Mons may, however, be lava flows fed by circumferential fissures that are too small to be identified in the radar images. Together with the remnant patches of radar-dark material within the caldera of Maat Mons, this suggests that low effusion rate eruptions at a range of elevations may be fed by the magma reservoir.

Acknowledgment: Harold Garbeil is thanked for his assistance in data reduction. This work was support by NASA under the VDAP Program.

References: 1) Head, J.W. & L. Wilson (1992). *J. Geophys. Res.*, **97**, 3877 - 3903. 2) Senske, D.A., G.G. Schaber, & E.R. Stofan (1992). *J. Geophys. Res.*, **97**, 13,395 - 13,420. 3) Wood, C.A. (1984). *J. Geophys. Res.*, **89**, 8391 - 8406. 4) Mouginis-Mark P.J. et al. (1994). Geomorphology of Planetary Calderas. Submitted to *Geomorphology*. 5) Mouginis-Mark, P.J. and M.S. Robinson (1992). *Bull. Volcanol.*, **54**, 347 - 360. 6) Chadwick, W.W. & K.A. Howard (1991). *Bull. Volc.*, **53**, 259 - 275.

RADAR IMAGING OF THE ICE DEPOSITS ON MERCURY'S POLES, D.O. Muhleman, B.J. Butler, Caltech, M.A. Slade, Jet Propulsion Laboratory

Anomalously strong radar echoes were detected from the north pole of Mercury and interpreted as ice deposits by Slade, Butler and Muhleman, *Science*, **258**, 635-640, 1992. Subsequently, a very similar anomaly was found on the south pole and the north pole anomaly was confirmed by Harmon and Slade, *Science*, **258**, 640-643, 1992. A full discussion of the observations and compelling arguments for the ice determination and stability on Mercury appears in Butler, Muhleman and Slade, *J. Geophys. Res.*, **98**, 15,003-15,023, 1993. At the time of this writing, our group is scheduled in Feb. 1994, to carry out synthetic aperture radar imaging of the Mercury south polar region with the Very Large Array (VLA)/Goldstone Radar. Currently, our group with others is active in the formulation of a Discovery Mission plan (called the Mercury Polar Flyby) to fly a complement of instruments, including a Synthetic Aperture Radar, over the north and south poles of Mercury and over the equatorial region.

Ice deposits in the Mercury polar regions are likely to be relatively old structures residing in the permanently shadowed regions within 100 to 200 kilometers from the poles. These structures may be unique to Mercury because of the essentially zero obliquity of that planet and the stability of that parameter. Ice on Mercury at temperatures less than, say, 120 K is stable against sublimation for millions of years. This is a time scale which, according to Butler, *et al* (1993), is sufficient for the buildup of ice from meteoritic and cometary impacts, and from the cold-trapping of water vapor outgassed from the planet to explain our observations. The measurements made at the VLA at a wavelength of 3.5 cm and those at Arecibo at 13 cm require an ice thickness of no less than a couple of meters and the deposits could very well be covered up with up to several 10's of centimeters of Mercury dust. Such dust, which must be present in some amount "protects" the ice from high-energy particles and would make the ice invisible to active probing at visible and IR wavelengths. It is obvious, of course, that the ice in permanently shadowed regions can never be visible in reflected sunlight, *e.g.*, in Mariner 10 imaging or any future passive imaging. We believe that the only remote sensing technique which could have discovered the putative ice deposits or can study them further is radar sounding. The remote possibility remains that the ice is magically clean and uncovered, and it is not impossible to image it with visible-light, laser sounding. (Radar is "laser" sounding).

The argument for the identification of the radar anomalies as ice is complex and will be reviewed in detail in the oral presentation. The essential ideas are the following: The anomalies are very tightly confined to polar regions in areas that are reasonably expected to be populated with permanently shadowed structures such as craters, cracks, *etc.* That circumstance strongly suggests that the material in the deposits is a volatile that is only stable, or condenses out in very cold regions on the planet. Planetologically, water ice is the most likely volatile. (Other ices such as CO_2, NH_3, CO, etc. could also reside there if the temperatures are very cold. These ices would have similar centimeter-wave radar signatures). Secondly, the polarization properties of the radar echoes at both wavelengths are completely consistent with those of radar echoes from the Residual South Polar Ice Cap on Mars and echoes from the icy surfaces of the Galilean satellites. At both observatories, the transmitted signals were circularly polarized in one sense and the echoes were measured in both circular

senses. The reflectivities were not only strong but the circularly polarized reflectivity ratios are the same as that from the icy surfaces listed
above. In our experience, such polarization properties of natural surfaces are limited to icy surfaces. Our theoretical understanding of the reflection phenomena is incomplete but it does seem nearly certain that a required physical characteristic of such a substance is high transparency of the material at the specific wavelength, creating relatively long path-lengths through the deposit, probably with strong forward scattering. Ice is the only likely such substance on Mercury's surface!

Results of the Feb, 1994 VLA/Goldstone Mercury south polar imaging will be presented. In addition, a brief discussion of the SAR radar experiment on the proposed Mercury Polar Flyby will be presented. The design goals are 1 kilometer imaging in both modes of circular polarization in the region within 300 km of both poles. In addition, we expect to radar image most of the planet to a resolution of order 10 km with 1-2 km resolution over a significant fraction of the equatorial region of at least one hemisphere. Mercury Polar Flyby will also have a Neutron spectrometer to certify that the polar volatiles are indeed water ice, if that be the case.

PHOTOCLINOMETRIC STUDIES OF CRATER AND GROOVE MORPHOLOGY ON PHOBOS: D. C. Munro and L. Wilson, Environmental Science Division, Institute of Environmental and Biological Sciences, Lancaster University, Lancaster, LA1 4YQ, United Kingdom.

Abstract

The surface of the larger of the two martian moons, Phobos, is peppered with impact craters and criss-crossed by a distinctive set of linear grooves [1]. Descriptions of the morphology of these features may be used to make inferences about the surface properties of Phobos and to constrain the mode of formation of the grooves. This abstract describes photoclinometric profiling of impact craters and grooves on Phobos using the Hapke photometric function [2, 3] to describe the surface reflectance. Lines of pixels from Viking Orbiter images were used to calculate topographic profiles for selected impact craters and grooves. These profiles allowed examination of the variation in width, depth and topography of individual features with the aim of formulating general descriptions of crater depth to diameter ratios, crater rim heights, groove width to depth relationships, groove rim characteristics and patterns of variation along grooves.

Methodology

Photoclinometry uses a description of the variation in surface reflectance with angles of observaton and illumination, i. e. a photometric function, to calculate the slope of individual image pixels and thereby construct topographic profiles [4, 5]. The choice of photometric function has previously been shown to be the major source of error in calculation of topographic profiles by photoclinometric methods [6]. Although simpler photometric functions such as the Minnaert or lunar-Lambert functions have been shown to be adequate for most photoclinometric applications [7], the subtle nature of topography associated with grooves on Phobos required that possible errors be minimized. For this reason the Hapke function [2, 3], with its detailed consideration of multiple scattering and the effects of unresolved macroscopic roughness provides the best possible description of the photometric properties of planetary regoliths [6] and was used in this research as a basis for the calculation of local surface tilts of pixels in Viking Orbiter images. The basis of the technique is to compare the reflectance of each pixel with that calculated for a flat surface under identical illumination and viewing geometry and thereby estimate local surface slope.

Scans of pixels were selected from the Viking Orbiter images to traverse impact craters and grooves such that; 1) the beginning and end of each scan could be estimated to be flat and at approximately the same elevation; 2) the scan was co-planar with the illumination vector; 3) the orientation of the scan was perpendicular to the strike of local topographic slope and; 4) variation in reflectance could be assumed to be due to local topographic slope and not to composition. Using the spherical harmonic expansion model of Duxbury [8] to describe the shape of Phobos and the accompanying ephemeris data from Viking Orbiter images to calculate the local viewing geometry, the incidence, emergence and phase angles for each pixel within a scan were calculated thereby removing the effects of the irregular shape of Phobos from the calculation of topography.

Two difficulties arise in the application of the Hapke photometric function to studies of topography from photoclinometry on bodies on which the detailed properties of the regolith are poorly constrained; 1) the determination of the reflectance of a flat surface; and 2) estimation of $\bar{\theta}$ which describes the rms variation in surface roughness of the surface at sub-pixel resolution and thereby influences the shadowing function. Commonly, Flat Surface Reflectance (FSR) is estimated to be the mean value of the entire scan. However, a consideration of the effects of errors in estimation of FSR [6] reveals a characteristic tilting of topography towards and away from the source of illumination in cases of under- and over-estimation of FSR, and thus the correct value for FSR can be experimentally determined by variation of FSR until profiles commence and end at the same elevation. Typically values of FSR used in this research fell

MORPHOLOGY ON PHOBOS: Munro, D. C. and Wilson, L.

within a narrow range of 101 - 104% of the mean value for the entire scan. Constancy of $\bar{\theta}$ is assumed on the basis of the absence of ejecta blankets [9] and of downslope movement of regolith within the craters. The second constraint is valid only for craters that are less than 1 km in diameter as the appearance of craters larger than this in Viking Orbiter images (e.g. Roche [10]) suggests that downslope movement of regolith within the crater may occur, implying variation in $\bar{\theta}$. The best results in this research were achieved using a narrow range of values from 36° to 38°.

Results and Discussion

The photoclinometrically produced profiles confirm earlier observations that impact craters on Phobos typically show a simple bowl shaped morphology [1]. Crater rims are typically only slightly raised with respect to the surrounding topography (2 - 3% of crater depth) but also may be markedly more prominent (5 - 7% of crater depth). This implies either variation in material properties or the effect of the variable tendency for downslope regolith movement of Phobos [11]. Depth to diameter ratios are between 0.05 and 0.143. Using the set of observations in this research (minimum depth 6.85 m - maximum depth 100 m) no marked changes in crater depth to diameter ratio were observed.

The grooves on Phobos show a complex range of morphologies that have been variously linked to the modification of fractures within the body [1], the impact of ejecta from cratering events on the body itself [12, 13], and the impact of ejecta on Phobos from the major basin forming impacts on the martian surface [14]. Measuring groove morphology via photoclinometry confirms the presence of raised rims around some grooves [14] and additionally indicates that there is a marked asymmetry of these rims that may persist along the length of a groove or may occur intermittently and vary markedly with position. The variation in rim development and rim asymmetry indicates that groove formation by the action of impact ejecta is a viable mechanism in many cases. Secondary modification of pre-existing fractures by the release of volatiles is also consistent with the observed morphology but the absence of marked albedo changes along the groove rims and the assumption of a constant $\bar{\theta}$ implicit in the approach precludes assessment of such models. Groove depth and width varies with position and shows no consistent pattern along the length of individual grooves. Where it is possible to examine grooves with a "beaded" appearance, adjacent pits may differ markedly without any consitent variation with direction. The interior of grooves with widths less than ~ 100 m are bowl shaped and show well developed symmetry. Wider grooves show irregular slopes and frequently have a stepped appearance that is similar to down-faulted blocks within tensional graben.

REFERENCES: [1] Thomas P. C. et al. (1979) *JGR*, 84, 8457. [2] Hapke B. (1984) *Icarus*, 59, 41. [3] Hapke B. (1986) *Icarus*, 67, 264. [4] Davis P. A and Soderblom L. A. (1984) *JGR*, 89, 9449. [5] Davis P. A. and McEwen A. S. (1984) *Lunar Planet. Sci XV Abstract*, 194. [6] Efford N. D. (1991) *Earth Moon, and Planets*, 54, 19. [7] McEwen A. S. (1991) *Icarus*, 92, 298. [8] Duxbury T. (1989) *Icarus*, 78, 169. [9] Thomas P. C. (1979) *Icarus*, 40, 223. [10] Veverka J. and Duxbury T. (1977) *JGR*, 82, 4213. [11] Thomas P. C. and Veverka J. (1980) *Icarus*, 42, 234. [12] Head J. and Cintala M. (1979) *NASA TM-80339*, 19. [13] Wilson L. and Head J. (1989) *J Lunar planet Sci.*, 20, 1211. [14] Murray J. B. et al. (1992) *Lunar Planet. Sci. XXIII*, 949.

SPECTRAL UNITS OF MARTIAN SOIL: POSSIBLE DISCRIMINATION OF MOBILE SEDIMENT AND SUBSTRATE Scott Murchie[1] and John Mustard[2]. [1]Lunar and Planetary Institute, Houston, TX; [2]Dept. of Geological Sciences, Brown University, Providence, RI.

Results from the ISM imaging spectrometer on Phobos 2 [1,2] indicate spatial differences in the presence and abundance of Fe-containing phases, hydroxylated minerals, and molecular H_2O in Martian soil [1-5]. We have used ISM data to characterize and map soil "units," and to determine their relationship with surficial geology. The two geographically largest groupings are "normal dark soil," which exhibits absorptions due to pyroxene and a relatively weak 3-μm H_2O absorption; and "normal bright soil" which exhibits ferric absorptions at 0.85-0.92 μm, a strong 3-μm absorption, and a weak absorption near 2.2 μm attributed to hydroxylated minerals. These groupings correspond with most areas that are "dark gray" and "bright red" at visible wavelengths, and are consistent spectrally with particulate basaltic materials and oxidized, hydrated alteration products, respectively. However their occurences cut across geologic boundaries, suggesting an origin largely as mobile sediment. The remaining ~15% of the observed surface consists of "anomalous" soils whose properties are not consistent with simple mixtures of normal bright and dark soils. Spatially, anomalous soils are correlated with areas having "dark red" visible color (Lunae Planum, western Arabia) and with specific geologic units (in Isidis and Valles Marineris). The spectral properties and geologic correlations of "anomalous" soils are consistent with exposures of the substrate underlying surficial, mobile sediment. Dark red areas are consistent with duricrust, as previously proposed, but soils covering layered materials in Valles Marineris probably represent bedrock exposures.

Analysis. We investigated three broad regions, eastern Tharsis-Valles Marineris, Arabia, and Syrtis Major-Isidis, which exhibit examples of most of the variations in visible color, thermal inertia, and geology recognized in Viking data [6-9]. The six data "windows" covering these areas were calibrated using previously described techniques [2,10]. They were registered with the digital topographic map of Mars, and reduced to a suite of "parameter" images that describe key sources of spectral variability of surface materials. These include reflectance, strength of a narrow absorption near 2.2 μm attributed to hydroxylated minerals, strength of the 3-μm H_2O absorption, depth of the broad 2-μm absorption attributed to Fe in pyroxene, and NIR spectral slope which is thought to be related to the texture and style of mixing of soil components [11,12].

The paramerized data were classified into groupings or units using principal components analysis. Three principal components were found able to account for most of the observed variance in NIR spectral properties. Spatial variations in the contributions or "loadings" of the principal components define coherent regions of soils, or units, having distinctly different spectral properties. Representative spectra were extracted from all groupings to validate their properties, and to ascertain shape and position of the 1-μm and 2-μm absorptions which are indicative of Fe mineralogy [13,14]. The map projections of these groupings or units are being compared with mapped geology and with Viking visible color and thermal inertia maps to ascertain their possible origins.

Normal Soils. About 85% of the area observed by ISM exhibits a restricted set of attributes, and we refer to such areas as "normal" soils. "Normal dark soils," which correspond with most areas having "dark gray" [cf. 7] visible color, exhibit a relatively weak 3-μm absorption. Their "1-μm" Fe absorption is centered at 0.93-0.98 μm and there is a broad, shallow absorption centered at 2.05-2.20 μm (Fig. 1). These observations are consistent with a relatively anhydrous material rich in pyroxene, inferred by several workers [e.g. 9] to occur as mobile sand. "Normal bright soils" have a "bright red" visible color, and correspond closely with low thermal intertia regions interpreted previously as accumulations of "dust" by airfall [e.g. 6-9]. They have ferric-like absorptions at 0.85-0.92 μm, a strong 3-μm absorption, and a weak, narrow 2.2-μm absorption (Fig. 1). These observations are consistent with an altered lithology containing ferric and hydroxylated minerals. Both the dark and bright soils exhibit regional variations in the shapes and positions of Fe absorptions, indicating regional-scale mineralogic differences in pyroxenes and ferric minerals [3-5]. "Transitional" soils occur mostly at borders of normal bright and dark soils. Their albedo, absorption strengths, and position of the 1-μm absorption are intermediate to normal bright and dark soils, consistent with a mixed composition. However their spectral slope is generally highly negative (Fig. 1), suggesting that the bright component coats or is intimately mixed with a darker substrate [10,12]. Most or all occurences of normal soils cut across geologic boundaries, despite their heterogeneities, consistent with an origin as regionally derived mobile sediment.

Anomalous Soils. The remaining ~15% of the observed surface is covered by "anomalous soils," with properties not consistent purely with mixtures of normal dark and bright soils. They occur in two major geologic settings, in regions with "dark red" visible color and on a restricted set of geologic units. The latter include basin-fill of Isidis and the layered materials of Valles Marineris. It is not possible to devote adequate space in this abstract to describe all of the anomalous soils, but discussion of two occurrences illustrates that they probably represent exposures of substrate underlying the surficial cover of mobile sediment.

"Dark red" areas of Lunae Planum and western Arabia (Fig. 1) exhibit an albedo, 2.2-μm band strength, and 2-μm pyroxene band strength that are generally interemediate to normal bright and dark soils. These properties are consistent with a mixed bright-dark lithology. However the dark red areas lack the negative spectral slope characteristic of "transitional" soils, suggesting a textural difference. They also have a much stronger 3-μm absorption than either normal dark or bright soils, suggesting either a textural difference or a greater H_2O content. Previous studies [e.g. 9] have suggested that dark red soils represent "duricrust." Elemental abundances at the Viking Lander sites indicate enrichment of S in the duricrust there, probably as a cementing sulfate [15]. The dominant salt in the SNC meteorites is gypsum, a water-bearing sulfate [16], and this phase is characterized spectrally by strong H_2O absorptions [17]. Thus the ISM data do not directly indicate duricrust in dark red areas, but they do support its occurrence by revealing a strong 3-μm absorption consistent with a sulfate cement.

Anomalous soils occur throughought much of Valles Marineris, and their spatial distributions are correlated with layered materials and related deposits [18]. However, soils covering different occurrences of layered material form different spectral units. Low-albedo soils on layered material in Melas and Eos Chasma (Fig. 1) have a stronger 2-μm pyroxene absorption than most other dark regions [4], yet also a stronger 3-μm absorption than most bright regions. Their flat spectral slope suggests that soil grains have minimal oxidized coatings. These properties are consistent with an unaltered pyroxene-bearing lithology, possibly with a higher water content than in most other dark areas [4]. Layered materials in the eastern and western parts of Candor Chasma (Fig. 1) have a higher albedo, a very strong 3-μm absorption, a very negative spectral slope, and a 1-μm absorption with 2 minima suggesting both ferrous and ferric components. There is no clear evidence of a 2-μm pyroxene absorption. An intervening high albedo layered deposit ("Candor Mensa"), separated by only tens of km from the above occurrences, exhibits a weaker 3-μm H_2O absorption and absorptions at 1 μm and 2 μm that are more indicative of pyroxene (Fig. 1). The properties of the high-albedo layered deposits are not diagnostic of a specific lithology, though they do suggest it is higly altered. The correlation of the "anomalous" spectral units with layered materials is consistent with exposure of the bedrock substrate, yet the differences between units indicate that layered materials are compositionally heterogeneous. This heterogeneity supports previous inferences, based on stratigraphic relations, that layered materials were emplaced under differing environmental regimes [18,19].

References. [1] J.-P. Bibring *et al., Proc. Lun. Plan. Sci. Conf. 20th*, 461, 1990. [2] S. Erard *et al., Proc Lun. Plan. Sci. Conf. 21st*, 437, 1991. [3] S. Murchie *et al., Icarus, 105*, 454, 1993. [4] J. Mustard *et al., Lun. Planet. Sci. XXIV*, 1039, 1993. [5] S. Murchie *et al., Lun. Planet. Sci. XXIV*, 1029, 1993. [6] F. Palluconi and H. Kieffer, *Icarus, 45*, 415, 1978. [7] R. Arvidson *et al., J. Geophys. Res., 87*, 10,149, 1982. [8] P. Christensen, *Icarus, 68*, 217, 1986. [9] P. Christensen and H. Moore, in *Mars*, ed. by H. Kieffer et al., p. 686,Univ. of Ariz., Tucson, 1992. [10] J. Mustard *et al., J. Geophys. Res., 98*, 3387, 1993. [11] R. Morris and S. Neely, *Lun. Planet Sci. XIII*, 548, 1982. [12] R. Singer and T. Roush, *Lun. Planet Sci. XIV*, 708, 1983. [13] R. Morris *et al., J. Geophys. Res., 90*, 3126, 1985. [14] E. Cloutis and M. Gaffey, *J. Geophys. Res., 96*, 22,809, 1991. [15] P. Toulmin *et al., J. Geophys. Res., 82*, 4625, 1977. [16] J. Gooding *et al.*, in *Mars*, ed. by H. Kieffer *et al.*, p. 626, Univ. of Ariz., Tucson, 1992. [17] G. Hunt *et al., Mod. Geol., 3*, 1, 1971. [18] N. Witbeck *et al., USGS.Misc. Inv. Ser. Map I-2010*, 1991. [19] G. Komatsu *et al., J. Geophys. Res., 98*, 11,105, 1993.

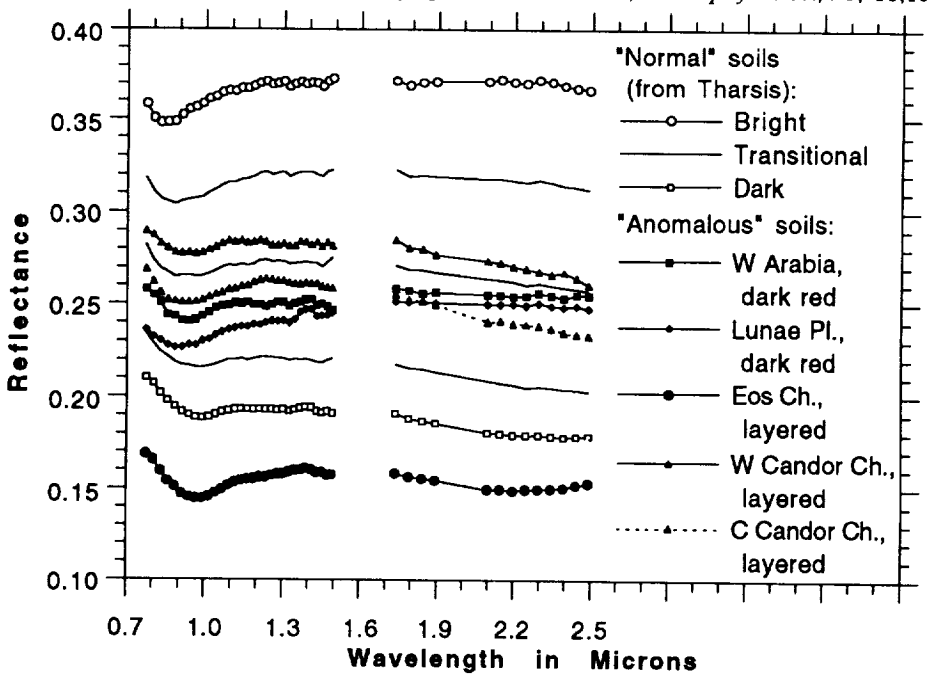

Fig. 1. Representative spectra of normal and anomalous soils. The data actually extend to 3.16 μm, but are cut off at 2.5 μm in this plot.

THE HST SPECTRUM OF PHOBOS: COMPARISON WITH MARINER 9, VIKING, AND PHOBOS 2 RESULTS AND WITH METEORITE ANALOGS Scott Murchie[1] and Ben Zellner[2]. [1]*Lunar and Planetary Institute, Houston, TX*; [2]*Astronomy Programs, Computer Sciences Corporation; Space Telescope Science Institute, Baltimore, MD.*

The Hubble Space Telescope (HST) acquired a spectrum of the leading hemisphere of Phobos [1], which we have used to evaluate previous spectral measurements from Mariner 9, Viking, and Phobos 2 and to assess spectral similarity of the satellite with proposed meteorite analogs. The HST spectrum is consistent with results from the Mariner 9 UVS spectrometer [2], and with properly calibrated measurements from Phobos 2's VSK TV cameras [3] and KRFM UV-visible spectrometer [4,5]. However the HST spectrum is much redder than the visible-NIR spectrum returned by Viking Lander 2 [6]. This discrepancy might arise from the fact that the two data sets sample different hemispheres of the satellite. The HST spectrum of Phobos is not uniquely consistent with any known meteorite analog, but it is matched most closely by high-grade carbonaceous chondrites or black chondrites. Alternatively Phobos's surface may consist of a material not represented among known meteorites.

HST Measurements. The HST Faint Object Spectrograph measured 210-900 nm spectra of the leading hemisphere of Phobos and two low-albedo C- and D-type asteroids (702 Alauda, 1144 Oda). The asteroid spectra agree well with results from the 8-color survey of Zellner *et al.* [7], indicating validity of the Phobos spectrum. Although the HST data are of some utility at wavelengths as short as 210 nm, in this analysis we use only the wavelength range 280-720 nm where the observational scatter is minimized..

Previous Measurements. Spectra of Phobos have been measured by three spacecraft in the satellite's vicinity. Mariner 9 and Viking measured disk-integrated spectra (Fig. 1). The Mariner 9 UV spectrometer acquired a 255-345 nm spectrum of the leading hemisphere [2], and the Viking Lander 2 camera measured the sub-Mars hemisphere with channels centered at 465, 669, and 880 nm [6]. Phobos 2 measured disk-resolved spectra using three instruments. The VSK camera acquired images in visible and NIR (~510-nm and ~910-nm) channels showing leading and trailing parts of the anti-Mars hemisphere and part of the sub-Mars hemisphere [3,9]. The 320-600 nm KRFM spectrometer scanned two groundtracks, also in the anti-Mars hemisphere [4,5,9]. The 760-3160 nm imaging spectrometer ISM imaged only the trailing part of the anti-Mars hemisphere [10]. The wavelength ranges of the KRFM and ISM overlap with those of VSK, so that the data sets can be joined to form composite spectra where their coverages overlap. In the leading hemisphere, observed by HST, the VSK images extend the wavelength range of KRFM. Composite spectra of that hemisphere are shown in Figs. 2 and 3.

Phobos 2 data were calibrated using parts of Mars observed by the instruments as spectral standards. Bright regions, which are stable and well-characterized spectrally, were used for KRFM so that these data are relatively reliable. Unfortunately the only suitable area observed by VSK is a dark region at 35°S,335°W, and dark areas exhibit albedo and color variations due to wind-transported dust. Initially the calibration area was modeled spectrally as purely low-albedo material [3]. This assumption produced vis/NIR color ratios for Phobos that are relatively gray (see Fig. 2). However telescopic images acquired 6 months prior to Phobos 2 data show the calibration area to have instead an intermediate albedo [11]. On this basis VSK images have been re-calibrated, by modeling the calibration area as a mixture of dark and bright components [5]. With this procedure vis/NIR color ratios of Phobos become uniformly 15% redder than reported previously [e.g. 3] (Fig. 3).

Evaluation of Previous Measurements. VSK images demonstrate significant color heterogeneity of Phobos's surface [3,5,12]. The trailing hemisphere contains a relatively redder unit, having a low vis/NIR ratio, but the leading hemisphere is covered by a relatively bluer unit with a higher vis/NIR ratio. Thus the well-controlled HST spectrum can be used to validate previous measurements covering the same wavelength range, but this comparison requires data sets that sample the same region (the leading hemisphere).

Fig. 1 compares pre-Phobos 2 observations with the HST spectrum. The Mariner 9 UVS spectrum, which like the HST spectrum samples the bluer unit in the leading hemisphere, exhibits a nearly featureless red-slope generally consistent with the HST spectrum where their wavelengths overlap. In contrast, the 3-color Viking Lander 2 spectrum of the sub-Mars hemisphere is much less red than the HST spectrum. The only independent measurements in which the sub-Mars face can be resolved separately from the rest of the leading or trailing hemisphere is VSK images. In VSK data, the only observed part of the sub-Mars hemisphere (around Stickney) has the bluest color of any part of the satellite. The most obvious explanation for the discrepancy between HST and Viking Lander 2 observations is that, on average, the sub-Mars hemisphere is intrinsically more blue than the leading hemisphere. Alternatively, there may have been calibration problems with Viking Lander 2 observations.

Figs. 2 and 3 compare Phobos 2 spectra with the HST spectrum. The HST spectrum is not significantly different from a representative KRFM spectrum of the leading hemisphere, calibrated as described by [4]. (In contrast the HST spectrum is markedly different from results of earlier attempts to process KRFM data [e.g. 13].) However the extension of the KRFM spectrum into IR wavelengths, using the NIR channel of VSK, differs

between the original and revised VSK calibrations. In Fig. 2, based on the orginal VSK calibration, NIR reflectance is too low compared to the HST spectrum. In Fig. 3, based on the revised calibration, the composite spectrum instead closely matches the HST spectrum. Thus, previous spectra of Phobos appear generally consistent with HST data, provided that account is made of proper calibration and differing viewing geometries.

Comparison with Meteorite Analogs. CI and CM carbonaceous chondrites, higher-grade anhydrous carbonaceous chondrites, and black chondrites have all been proposed as spectral and compositional analogs to Phobos's surface [10,14,15]. Representative spectra of these meteorite classes covering the wavelength range of HST are shown in Fig. 4. Spectra of CI and CM chondrites, which are the generally cited analogs, exhibit an inflection near 500 nm [16] that is absent from the Phobos spectrum. This lack of evidence for a low-grade carbonaceous chondritic composition is consistent with most interpretations of Phobos 2 data [e.g. 3-5,8-10,12]. Instead the HST spectrum exhibits a shorter-wavelength inflection consistent with that in higher-grade carbonaceous or black chondrites, and most closely matches black chondrites. However the HST data do not cover the 1-μm mafic mineral absorption whose occurrence and position are diagnostic of the two meteorite classes [cf. 16]. Therefore the HST data are equally consistent with a composition not represented among known meteorites.

Acknowledgement. This work was supported by Grant GO-3744.01-01.91A from the Space Telescope Science Institute, operated by the Association of Univeristies for Research in Astronomy, under NASA contract NAS5-26555.

References. [1] B. Zellner and E. Wells, this volume. [2] C. Barth *et al.*, *Science, 173*, 309, 1972. [3] S. Murchie *et al.*, *J. Geophys. Res., 95*, 5101, 1991. [4] S. Murchie and S. Erard, *Lunar Planet. Sci XXIV*, 1025, 1993. [5] S. Murchie *et al.*, in prep. [6] J. Pollack *et al.*, *Science, 199*, 66, 1978. [7] B. Zellner *et al.*, *Icarus, 61*, 355,1985. [8] G. Avanesov *et al.*, *Planet. Space Sci., 39*, 281, 1991. [9] L. Ksanfomality *et al.*, *Planetary and Space Science, 39*, 311, 1991. [10] J.-P. Bibring *et al.*, *Proc. Lunar Planet. Sci. Conf. 20th*, 461, 1990. [11] P. Pinet and S. Chevrel, *J. Geophys. Res., 95*, 14,435, 1990. [12] S. Murchie *et al.*, *Lunar Planet. Sci. XXII*, 943, 1991. [13] J.-P. Bibring *et al.*, *Lunar Planet. Sci. XXII*, 99, 1991. [14] K. Pang *et al.*, *Science, 199*, 64, 1978. [15] D. Britt and C. Pieters, *Astron. Vestnik, 22*, 229, 1988. [16] M. Gaffey and T. McCord, in *Asteroids*, 688, Univ. of Ariz. Tucson, 1978.

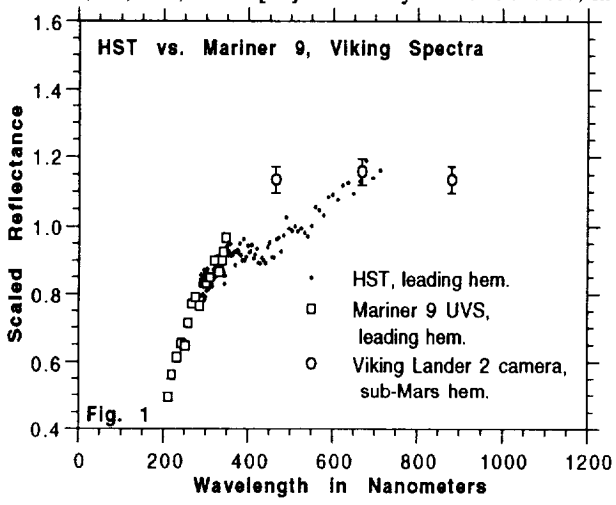

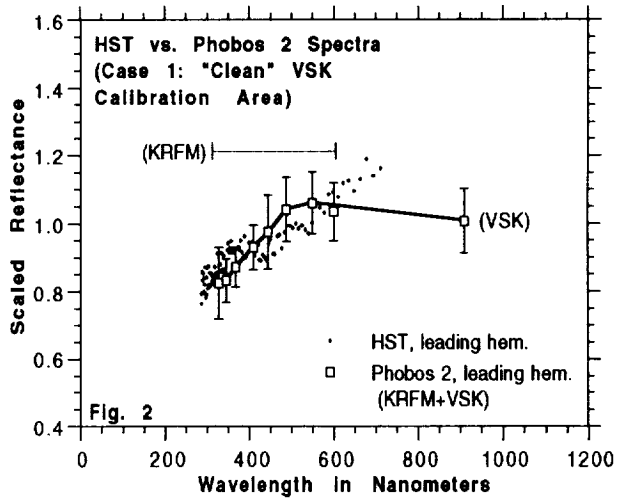

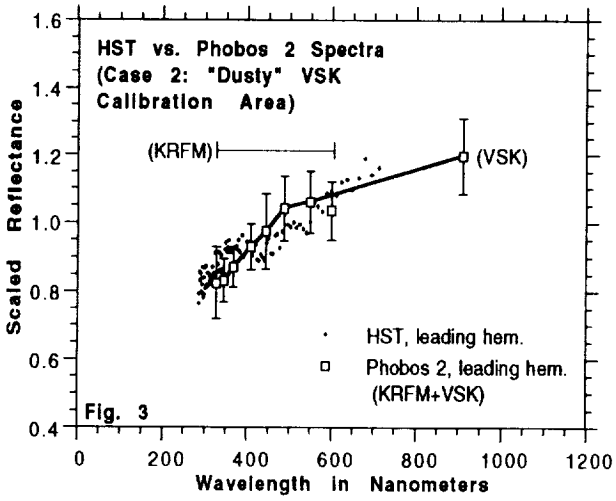

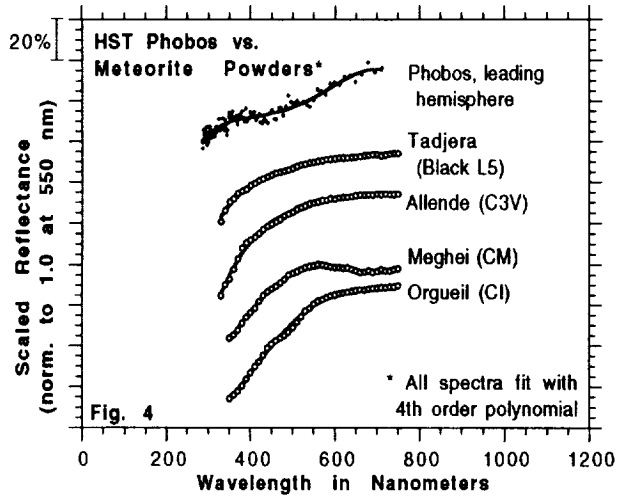

He, Ne and Ar from the solar wind and solar energetic particles in metal separates from Fayetteville and Acfer111; Ch. Murer, H. Baur, P. Signer and R. Wieler, ETH-Zürich, Isotope Geology, NO C61, CH-8092 Zürich, Switzerland.

Abstract: Solar He, Ne and Ar in Fe-Ni separates from the chondrites Fayetteville and Acfer111 were analysed by closed system stepped oxidation. He/Ar and Ne/Ar ratios are quite constant close to present day solar wind (SW) values, particularly in the first ~70% of the gas release. Thus, metal retains SW noble gases without noticeable element fractionation. In this respect, Fe-Ni differs from lunar ilmenites where He/Ar and Ne/Ar ratios in the first steps of closed system stepped etching runs are several times below SW values. Unlike the element ratios, the isotopic composition of the solar Ne shows the same pattern in ilmenite and metal: Unfractionated SW (20-Ne/22-Ne = 13.9±0.1) is released in the first steps, essentially pure SEP (20-Ne/22-Ne = 11.2±0.2) in the final steps. Nominally, SEP-Ne contributes 30-40% to the total Ne. Such a large fraction seems to require loss of SW by a non-fractionating process.

Introduction: All major minerals in lunar soils, including ilmenite, lost part of their light solar noble gases. This is manifested by the 4-He/36-Ar and 20-Ne/36-Ar ratios in the first steps of closed system stepped etching runs, which are several times below SW values (1). We have thus extended our search for elementally unfractionated solar noble gases to Fe-Ni separates from solar gas bearing chondrites (2). As in previous experiments, we separate SW noble gases from the more deeply implanted solar energetic particles (SEP) by a closed system stepped etching/oxidation technique. We studied two separates from the Fayetteville H4-6 fall and one from the slightly weathered Acfer111 H3-6 find. The samples (several hundred mg each) were oxidised with increasingly strong copper chloride solutions (2), which selectively attack metal. The first Fayetteville sample (Fayetteville90) contained about 10 vol. % of attached silicates. Presumably, later steps contain also some SW gas from the silicates. We therefore discard here the element ratios of this sample. Samples Fayetteville100 and Acfer111 contained less than 2% and 5% silicate impurities, respectively. Total trapped 36-Ar concentrations are [in 10E-8 ccSTP/g]: 15.7 (Fayetteville90); 12.9 (Fayetteville100); 3.9 (Acfer111).

Element ratios: 4-He/36-Ar and 20-Ne/36-Ar are shown in Fig. 1. Values of individual steps (given for Fayetteville100 only) scatter somewhat but the smoothed ratios are rather constant over about the first two thirds of the gas release at values close to those of the present-day solar wind (SWC, ref. 3). Pedroni (4) found similarly constant element ratios close to SWC in a stepped etch run of a metal-enriched Acfer111 sample. Thus, chondritic metal shows little or no element fractionation even in the first etch steps, contrary to lunar ilmenites. Later in the runs, the element ratios in Fig. 1 first increase above SWC and finally decrease again mostly to values below SWC. This pattern is unlike that of ilmenites and pyroxenes. Pedroni and Begemann (5) observed similar variations in 4-He/20-Ne in Acfer111 and explained this by a larger average implantation depth of Ne compared to He. This seems possible since metal grains in the SEP depth region may be attacked more "onion-shell-like" than silicate minerals, for which possibly different implantation depths may be smeared out by inhomogeneous etching. We do not believe that the SEP component is depleted in He and Ne relative to the SW composition. Very low 4-He/20-Ne ratios in the highest temperature steps of pulse heating runs of lunar ilmenites (6) result in our view from preferential diffusive release of He in lower temperature steps.

Isotope ratios: The data points of all three runs display similar patterns in the Ne three-isotope diagram (Fig. 2). Steps near the start of a run show a Ne composition close to SW values (1) determined from lunar ilmenite (except Fayetteville100, see below). Heavier Ne is released with progressive oxidation, whereby all runs show an excursion towards cosmogenic Ne in intermediate steps. The data of the last steps plot close to the SEP point deduced from lunar ilmenite (1). The somewhat low initial 20-Ne/22-Ne ratio in Fayetteville100 of 13.3 is probably due to a partial loss of SW gas caused by the harsh mechanical treatment of this sample, which was necessary to reduce silicate contamination. The steps rich in cosmogenic gas indicate the complete dissolution of one phase, presumably taenite.

In summary, the metal samples show a nearly unfractionated element abundance pattern and yet display the same two-component structure of solar Ne that was observed in all previous etch studies of solar gas bearing samples: SW-Ne is released first, followed by isotopically heavier SEP-Ne. The extreme 20-Ne/22-Ne ratios of trapped Ne measured here are close to the endmember compositions of SW-Ne and SEP-Ne, respectively, as deduced from lunar ilmenites. He and Ar also consist of the two solar components

SW (2) and SEP, but no precise compositions of SEP-He and SEP-Ar can be given.

Abundance of SEP-Ne: The relative fractions of the two solar components can be calculated if we assume both to have the same (unfractionated) isotopic composition in each step [20-Ne/22-Ne: 13.8 (SW); 11.2 (SEP)]. The nominal SEP contributions of 30-40% in our metal samples are comparable to those in Acfer111 (7) and also to those deduced for lunar ilmenites (1). SEP fractions of this order are much higher than reasonable expectations of the ratio of the flux of SW ions to that of higher energy solar particles (8). For lunar samples, this was (partly) explained by diffusive loss of SW-Ne (e. g. 1) and diffusive redistribution of SW-Ne into the grain interior (9). However, these explanations are inconsistent with the flat element ratio pattern of the metal samples. On the other hand, several processes can be invoked that would lead to a non-fractionating preferential loss of the surface sited SW gases: ion-sputtering, "micro-flaking" (10), surface abrasion and grain-boundary melting during lithification (7). SW gases may also be inefficiently trapped, either due to a low sticking probability or a very thin surface coating e. g. by small dust grains.

Acknowledgments: We thank F. Begemann for the Acfer111 sample. This work is supported by the Swiss National Science Foundation.

References: (1) Benkert J.-P. et al. (1993) *J. Geophys. Res.* **98**, 13,147. (2) Murer Ch. et al. (1993) *Lun. Planet. Sci. XXIV*, 1031. (3) Bochsler P. (1987) *Physica Scripta* **T18**, 55. (4) Pedroni A. (1993) *Lun. Planet. Sci. XXIV*, 1121. (5) Pedroni A. and Begemann F. (1992) *Meteoritics* **27**, 273. (6) Nier A.O. and Schlutter D.J. (1993) *Meteoritcs* **28**, 412. (7) Pedroni A. et al. (1992) *Lun. Planet. Sci. XXIII*, 1047. (8) Wieler R. et al. (1986) *Geochim. Cosmochim. Acta* **50**, 1997. (9) Becker R.H. and Pepin R.O. (1989) *Geochim. Cosmochim. Acta* **53**, 1135. (10) Nichols R.H. Jr. and Hohenberg C.M. (1993) *Geochim. Cosmochim. Acta* **57**, in press.

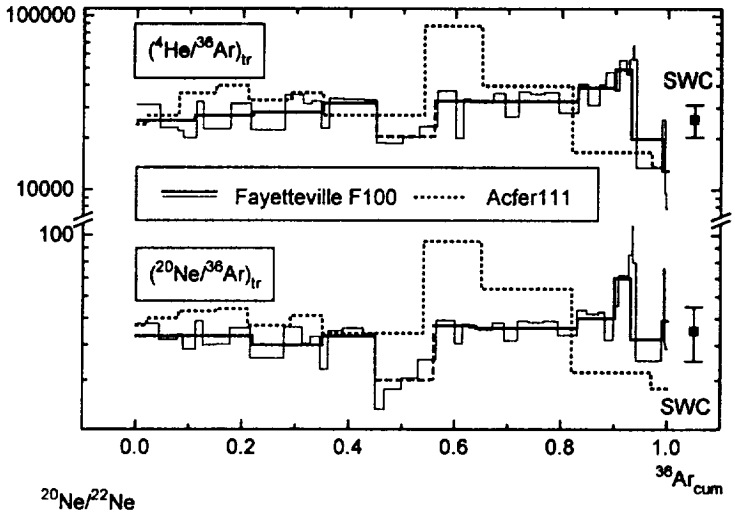

Fig. 1: Trapped 4-He/36-Ar and 20-Ne/36-Ar versus cumulative fraction of 36-Ar released. For Fayetteville100 data of individual steps (thin line) as well as smoothed values (average of 4 steps, thick solid line) are shown, dotted lines give ratios averaged over 3 steps for Acfer111. A portion of data of Fayetteville100 given by dashed line is highly uncertain due to analytical problems. In the first part of the runs, element ratios are close to those in present day solar wind (SWC, ref. 3). This indicates that SW in metal shows no element fractionation, in contrast to lunar ilmenites.

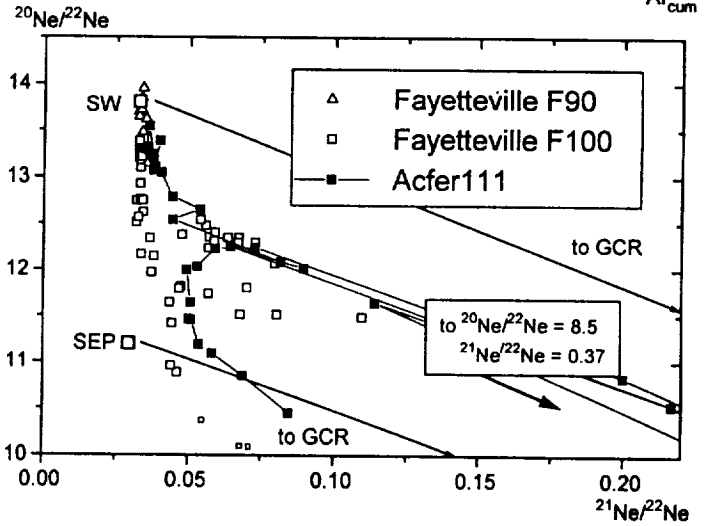

Fig. 2: Ne three-isotope diagram. For Fayetteville90 only the first ten steps are given. SW and SEP points are those determined in relatively recently irradiated lunar ilmenite 71501 (1). The most extreme trapped Ne compositions measured in metal samples of both meteorites are very close to the ilmenite endmembers. Steps with large amounts of cosmogenic Ne probably indicate complete dissolution of taenite. Small symbols represent the last three steps of Fayetteville100 which are contaminated by atmospheric Ne because they lasted very long and contained little gas.

LIMITS ON THE MAFIC MINERALOGY OF MARS THROUGH MGM ANALYSIS OF ISM SPECTRA. J. F. Mustard[1] and J. M. Sunshine[2], [1]Department of Geological Sciences, Box 1846, Brown University, Providence RI 02912, [2]SETS Technology Inc., 300 Kahelu Ave., Miliani HI 96789.

Introduction: From analysis of the ISM imaging spectrometer data, numerous areas on the surface of Mars have been identified as containing well exposed, weakly altered volcanic materials. In addition, distinct units are recognized on the basis of the position, strength, and shape of mafic mineral absorptions. The presence of pyroxenes is readily documented by their unique1 and 2 μm absorption features. Other mineral components have been inferred from qualitative comparisons of remote observations with laboratory reference spectra. However, qualitative analysis applied to subtle inflections or distortions of the "normal" pyroxene band shape to determine mineralogy is highly subjective. In this analysis we use the Modified Gaussian Model (MGM) to deconvolve the ISM reflectance spectra into constituent absorptions. The results are compared with previous MGM modeling of natural pyroxenes and pyroxene mixtures to place general limits on the composition of weakly altered martian crust.

Spectral Data: The ISM data consist of 64-channel reflectance spectra from 0.77 to 3.14 μm for each high spatial resolution pixel (22 km) in the 9 images acquired (1,2). The data windows are ≈300 km wide and 2000 km long and sample a wide variety of terrain and surface morphologies. Details of data reduction, calibration, and previous analyses are presented elsewhere (2,3). ISM spectra from surfaces that exhibit the least alteration are dominated by mafic mineral absorptions near 1 and 2 μm and are qualitatively interpreted to be volcanic materials containing augitic pyroxene of intermediate iron content (3). On the basis of these previous analyses, ISM spectra from two regions that exhibit distinct and well defined mafic mineral absorptions, Nili Patera on Syrtis Major and Eos Chasma on the floor of Valles Marineris, have been selected for detailed mineralogic modelling with the MGM.

Approach: Under the MGM, reflectance spectra are modelled as a sum of absorption bands superimposed on a baseline or continuum. The model has been used successfully to deconvolve superimposed and overlapping absorptions in mafic mineral mixtures, solid solution series, and natural lithologic samples (4,5,6,7). The parameters defining the absorption bands (center, strength, width) are quantitatively associated with mineral abundance in mixture series and composition in solid solution series. Thus, it should be possible to determine mineral abundance and composition from spectra of mafic rocks as was done for spectra of the EETA 79001 shergotite (7). The ISM data of the weakly altered terrains are dominated by pyroxene absorptions for which excellent observational (8) and modelling (4,7) bases exists. However, the strengths of mafic mineral absorptions in the ISM data are weak (5-15%) which makes derivation of unique solutions with the MGM difficult. Nevertheless, results can be critically analyzed in the context of existing data bases and experience from which we can then determine the limits on the surface compositions allowed by this approach.

Our approach to this problem was to first establish a reasonable continuum that is consistent for all model runs. Based on some initial analyses, it is determined that a negative continuum that is linear in energy provides the best approximation to the negative continuum observed for Martian dark regions. We begin with models that make the fewest assumption about consituents and proceed to more complex models. The initial model parameters for absorption band centers for the trials used in this analysis are shown in Table 1. In all trials the modified stocastic inversion was used (9,4) and model parameters were minimally constrained.

Results:

Trial 1: This model presumes that all absorptions are the result of a single pyroxene imposed on a continuum. The resulting band centers of the 1 and 2 μm bands are not consistent with laboratory studies (8), the width of the 1 μm band is atypical of known pyroxenes (4), and there is a systematic error as a function of wavelength (E(λ)) near 0.85 μm and longwards of 1.9 μm. These results indicate that addition components are required.

Trial 2: This is the same as Trial 1, but with the addition of an absorption centered near 0.85 μm to accomodate absorptions due to ferric components expected to be on Mars. The band centers

and widths are more consistent with known samples, but there is still an E(λ) longwards of 1.9 μm indicating an additional pyroxene component.
Trial 3: In this model, we assume that there are two pyroxenes present, one with absorptions typical of low calcium and one typical of high calcium pyroxene. Although there is a good fit in the 2.0 μm region, consistent with known parameters for pyroxene, the fit in the 1 μm region is inconsistent with known pyroxenes. Furthermore, it violates the coupling between 1 and 2 μm band centers and relative strength established in laboratory analyses (4,8).
Trial 4: Inclusion of a band near 0.85 to model ferric contributions provides results that are entirely consistent with known parameters for pyroxenes and for pyroxene mixtures. However, the model parameters are under-determined and specific results are highly dependent on the starting model.

Discussion It is clear from solutions using either one or two pyroxenes that a band near 0.85 μm is required. Models that do not include this band have a characteristic E(λ) between 0.77 and 1.0 μm, typical of a missing absorption. In addition, the results of some trials have band centers and widths atypical of known pyroxenes. It is not unreasonable to expect there to be a ferric component in these surfaces since ferric components are so prevelant on Mars. However the specific origins for this feature are unclear (alteration products spatially associated or ferric phases in mineral constituents (e.g. ferric pyroxenes)) and few observational and modeling bases exist for analyzing ferric absorptions (10). A negative continuum that is linear in energy adequately approximates the blue continuum for dark regions on Mars. The continuum is an important property of the MGM and can affect model parameters. The continuum used is considered at this stage to be entirely empirical and a useful approximation, but more work is needed to understand this important property of Martian surfaces. The solutions for the Trial 2 runs were extremely robust. It was possible to vary the starting conditions considerably and arrive at the same minimun solution every time. However, these solutions, assuming a single pyroxene composition, were not entirely consistent with observational data bases. Analysis of the 2.0 μm regions was together with the 1 μm region provided essential evidence for evaluating the entire fit. The solutions for the Trial 4 runs could provide band centers, widths, and strengths for both the 1 and 2 μm bands that were consistent with known low and high calcium pyroxene endmembers and pyroxene mixtures. However, these solutions were underdetermined and the specific conditions of the input model parameters strongly controlled the derived model parameters.

Conclusions: MGM analysis of ISM spectra show that the mafic mineralogy of Mars is complex. We clearly demonstrate that a ferric component and two ferrous pyroxenes are required. In addition, there is no compelling evidence for olivine within the limitations of these data. These conclusions were critically dependent on simultaneous analysis of the 1 and 2 μm regions which allowed us to examine the consistency of results with known coupling of pyroxene absorption positions and relative strengths. This argues for extended and complete wavelength coverage of any future missions that are designed to measure martian mineralogy. Further refinement of compositional estimates using visible-near infrared reflectance spectra hinges on our ability to understand and quantify ferric absorptions and the continuum of Mars.

References: (1) Bibring, J-P., *et al.*, (1989) *Nature*, 341, 591-592 (2) Erard, S. *et al.*, (1991) *Proc. Lun. Plan. Sci.* 21, 437-456 (3) Mustard, J. F., *et al*, (1993) *JGR-Planets*, 3387-340. (4) Sunshine, J. M. and C. M. Pieters,(1993) *JGR-Planets*, 9075-9087. (5) Sunshine, J.M. and C.M. Pieters, (1993) LPSCXXIV, 1379-1380. (6) Mustard, J.F., (1992) *Am. Mineral.* 345-358. (7) Sunshine, et al., (1993), *Icarus*, 105, 79-91. (8) Cloutis, E.A. and M. J. Gaffey (1991) *JGR*, 96, 22809-22826. (9) Tarantola and Valette (1982) *Rev. Geophys. Space. Phys.* 20, 219-232. (10) Straub, D.W., et al., *JGR-Planets*, 96, 18819-18830.

Table 1: Initial Band Centers for MGM Trials

Trial	0.85	0.91	1.02	1.15	1.93	2.29
1		x		x		x
2	x	x		x		x
3		x	x	x	x	x
4	x	x	x	x	x	x

MARE-HIGHLAND MIXING RELATIONSHIPS ALONG THE SOUTHWESTERN SHORES OF OCEANUS PROCELLARUM J. F. Mustard, J. W. Head, I. Antenenko, Dept. Geol. Sci., Box 1846, Brown University, Providence RI, 02912.

Introduction: The boundary between Oceanus Procellarum and the surrounding highlands contains many stratigraphic relationships important for unraveling the sequence and mode of emplacement of mare, and large crater and basin deposits. Although the record is tightly convolved because of the interaction of these processes, mixing relationships between mare and highland along the boundary provide important clues to deconvolving the record. In this paper we use multispectral observations acquired during Galileo EM-1 (1) to determine the mare-highland mixing relationships along the boundary. The region under investigation includes ≈300 km on either side of the mare-highland boundary from the crater Cavalerius (5°N, 68°W) to Mare Humorum. Mixture maps are generated and then merged with surface morphology, previous geologic mapping, and new observations to develop a detailed understanding of this important boundary.

Methods: The abundances of the three primary surface materials distinguished in the Galileo SSI 5-channel data (mare, highland, and fresh crater) were calculated using an image-based linear spectral mixture model. The endmembers are identical to those used in previous analyses of the Schiller-Schickard region (2,3) and are distinguished primarily by albedo, uv-vis slope, and strength of the 1.0 μm absorption. The calculated abundances are accurate in a relative sense and provide a useful framework for understanding the relationships between these surface constituents. The context for understanding the mixture maps is achieved by merging the mixture maps with maps of known geomorphic features (represented in digital airbrush map), geologic contacts (from the maps of 4 and 5), and analysis of Lunar Orbiter IV images.

Results: Three principal types of mixing gradients between mare and highland materials are found: narrow, moderate, and extended-complex (**Figure 1,2**). Narrow gradients (profile 1) are found adjacent to the crater Hevelius, along the western edge of Mare Humorum, and in the mare filled Grimaldi basin and crater Cruger. The geologic contact between mare and highland corresponds closely to the steep gradients, but in general the geologic contact occurs towards the low concentration side (≈20% mare abundance). These contacts are also characterized by large topographic differences between the mare and highlands either as scarps (Hevelius) or basin and crater walls (Humorum, Grimaldi, Cruger).

Moderate gradients (profile 2) are found between the craters Damoiseau and Sirsalis. The geologic contact in these areas occurs on the high side of the mare abundance gradient (>80% mare). The topography is low and rolling with numerous flooded or partially flooded craters along the contact. In addition, secondary craters, crater chains, and sculpture from the Orientale impact are common.

Extended and complex gradients (profile 3) occur from the crater Sirsalis to Mare Humorum. The principal contact between highland units and basalts of Procellarum occurs in areas of high mare abundance (>80%). The highlands geology is dominated by a hilly and furrowed unit with numerous small mare patches that decrease in frequency away from Procellarum. There are also several floor fractured (e.g. Gassendi, Hansteen) and flooded (Billy, Letronne) craters along the boundary. There is no simple pattern to the mare mixing maps. The small mare patches are identified by high abundances and are generally surrounded by zones of moderate mare abundance. Southwest of Hansteen, an extended zone of low to moderate mare abundance is mapped for ≈200 km into the hilly and furrowed unit and deposits from the Orientale basin. The ejecta blanket of Letronne is characterized by moderate mare abundances (50-60%) distributed uniformly over the region of continuous ejecta. Southwest of the continuous ejecta is a zone of low to moderate abundances (40-50%) associated with a region of plains containing dark halo craters interpreted to contain cryptomare (6,7).

Light plains deposits are thought to represent areas that are either ponded basin ejecta or maria mantled by highland crater or basin ejecta (cryptomaria). Light plains deposits in the Schiller-Schickard region are associated with elevated mare abundances that map out the regional extent of a cryptomare (2,3). Extensive light plains deposits found within the outer facies of the Hevelius

formation between the crater Cavalerius and Schickard could signal the presence of additional cryptomare. However, there are no well defined mare abundance anomalies associated with these deposits.

Conclusions: Narrow gradients in mare abundance are displaced towards the mare side of the geologic contacts, and these contacts are associated with relatively steep topography. We interpret this to indicate highland contamination of the mare surface by lateral transport facilitated by steep topography. In regions of moderate gradient mixing, the geologic contact occurs at high mare abundance with gradations extending into highland units. These highland units, therefore contain a significant component of mare. Several processes may have contributed to this including mixing of highland ejecta with mare during emplacement of Orientale basin ejecta and secondaries into pre-Procellarum volcanics, deposition of mare-rich ejecta into adjacent highlands units from impacts into Procellarum basalts, and lateral mixing through persistent small scale impacts and gardening. Given the nature of this boundary, lateral mixing seems to be the best candidate. Much of the light plains in the distal regions of the Hevelius formation in this area show no evidence for the presence of mare components. Therefore the light plains here are likely ponded ejecta deposits rather than mantled cryptomare. Within the zone of complex and extended gradients, several processes have contributed to the observed relationships. There are many small mare patches in this area and lateral mixing is likely to have contributed to the extended nature of the mare-mixing zone. As noted earlier, analysis of dark halo craters in the plains material northwest of Humorum show extensive evidence of a mare component overlain by more highland-rich material (6,7). Our mapping would imply the cryptomare covers a large part of these plains, confirming the previous analyses that this area was the site of post-Humorum basin, pre-Orientale mare-type volcanism and expanding the regional coverage. The view is further supported by ongoing dark halo crater analyses (8). We are continuing to investigate in detail stratigraphic and mixing relationships along this boundary to further refine the timing of significant geologic events in this region.

References: (1) Belton, M.J.S., et al., (1992) *Science*, 255, 570-576. (2) Mustard, J. F., *et al.*, [1992] *(abstr) Lun. Plan. Sci.* XXIV 957-958. (3) Head, J.W., et al., (1993) *JGR*, 98, 17149-17181. (4) Wilhelms, D.E., and J.F. McCauley, (1971), *U.S. Geol. Surv. Map*, I-703. (5) Scott, D.H., et al., (1977) *U.S. Geol. Surv. Map*, I-1034. (6) Lucey, P.G., et al., (1991) *Proc. Lun. Planet. Sci*, 21., 391-403. (7) Hawke, B.R., et al., (1993), *Geophys. Res. Let.*, 20, 419-422. (8) Antenenko, I., and J.W.Head, (1994), *LPSCXXV*, (this volume).

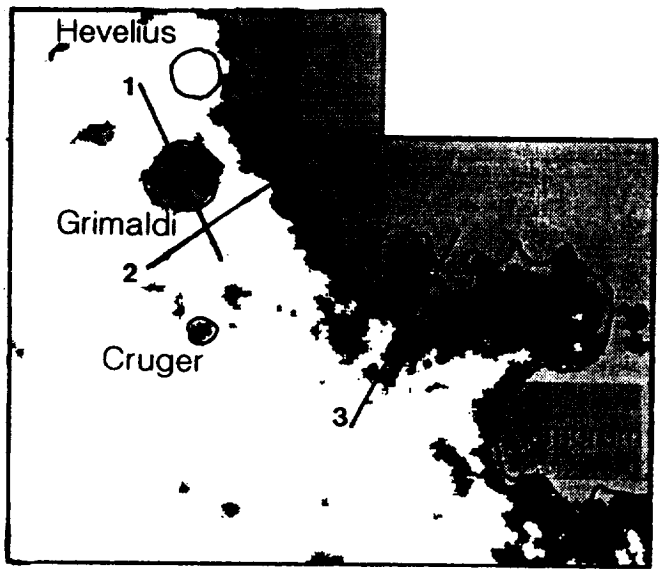

Figure 1. Generalized mixture map for the southwestern area of Procellarum. Light gray shows regions with >65% mare abundance and dark gray are between 25 and 65%. Solid lines show the contact between mare and highland units. Numbered straight lines show locations of profiles presented in Figure 2. Some major craters and the Humorum basin are labeled for reference.

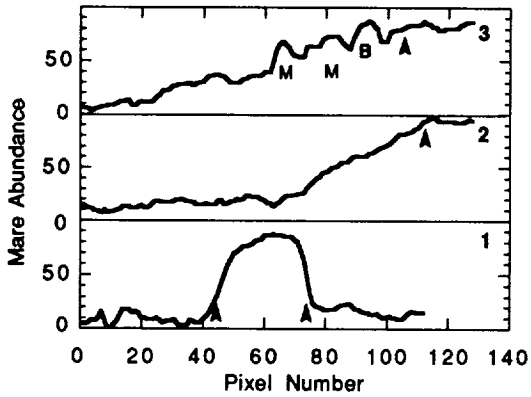

Figure 2. Profiles of mare abundance, for the areas shown in Figure 1, illustrating the three types of mixing observed at this boundary. Arrows show the mare-highland contact, M indicates a mare patch along the profile, and B indicates the crater Billy.

WHY CHONDRULES DO NOT SHOW AND SOME CAIS SHOW SIGNIFICANT ISOTOPIC FRACTIONATION ?:

Hiroko NAGAHARA, Geol. Inst., Univ. Tokyo, Hongo, Tokyo 113, Japan.

Evaporation experiments have shown that the effect of oxygen isotopic fractionation of a solid silicate in vacuum reaches several ‰ at the highest degree of evaporation but almost zero in hydrogen gas. This is because evaporation rate is small in vacuum, and silicates can isotopically fractionate when elemental diffusion in solid is large enough compared to evaporation. The results suggest that CAIs were formed in vacuum and chondrules were in hydrogen gas of the solar nebula.

Isotopic fractionation including oxygen, magnesium, silicon, calcium, and titanium has been well known for CAIs. The effects of isotopic fractionation of Mg and Si are well correlated, which suggests evaporation residue for the origin of those CAIs [1]. Isotopic fractionation for chondrules has not been established in spite of nearly the same formation conditions for chondrules and (at least type B1) CAIs. Clayton *et al.* [2] showed that silicon isotopes of Allende and Dhajala (H3) chondrules are fractionated. On the contrary, Kinsey *et al.* [3] and Esat and Taylor [4] analyzed Mg isotopes of chondrules in carbonaceous and ordinary chondrites, but did not find fractionation. They said that the degree of mass loss by evaporation during chondrule formation was less than 20%.

Recent systematic evaporation experiments have shown that isotopic fractionation should be significant if the evaporation took place in the solar nebula with the mode of Rayleigh fractionation, although it depends on dwell time of the maximum temperature. Davis *et al.* [5] experimentally showed that liquid forsterite could fractionate by several tens ‰ through evaporation in vacuum but that solid forsterite could fractionate by only one ‰ or less even with evaporation degree of 80%. Nagahara *et al.* [6], however, experimentally showed that solid SiO_2 could significantly fractionate in vacuum. They also showed that the effect of isotopic fractionation strongly depends on hydrogen gas pressure. Because silicates are oxides, evaporation in hydrogen gas is a reaction of breakdown of oxides and formation of H_2O gas. The reaction proceeds when hydrogen gas pressure is as high as maximum value of a solar nebula at 1 A.U. (10^{-5} bar) in recent physical models, and it is suppressed when the hydrogen pressure is lower than that. This is opposite to the general effect of total pressure. In general, increasing total pressure of ambient gas which is not reactive with the condensed phase, decreases the evaporation rate. However, increasing hydrogen pressure increases the evaporation rate of silicates, which should have evaporation maximum at a certain pressure.

Nagahara *et al.* [6] evaporated solid SiO_2 at 1600° and 1700°C in vacuum and in hydrogen gas, and obtained the evaporation rate. By using their results, degree of oxygen isotopic fractionation was obtained as a function of evaporation degree. The result is shown in Fig. 1. The solid curve is a calculated Rayleigh fractionation curve, and it predicts $\Delta^{18}O$ value of about 23‰ at 60% evaporation and 26‰ at 80% evaporation which corresponds to 5‰ and 6‰, respectively, relative to the original. Contrary to isotopic fractionation in vacuum, that in hydrogen gas is much smaller (broken line). The degree of isotopic fractionation is only 1‰ at 60% evaporation and smaller than 3‰ even at 90% evaporation. The small effect of isotopic fractionation is due to large evaporation rate in hydrogen. The fractionation by several ‰ from solid SiO_2 is larger than 1 to 2 ‰ from solid forsterite obtained by [5], which is due to difference in diffusion rate of oxygen in solid phase.

Elemental fractionation at the surface of solid can be effectively takes place when elemental diffusion in solid is large enough compared to evaporation rate. A similar discussion has been previously made by Wang *et al.* [7]. In the case of the present study, oxygen isotopic fractionation can take place when oxygen diffusion in SiO_2 is larger than the evaporation rate. Since SiO_2 evaporates congruently, oxygen evaporation rate is equal to that of bulk SiO_2. Evaporation rate of SiO_2 is thus compared to diffusion rate of oxygen in solid SiO_2. At the present experimental conditions, the stable phase of SiO_2 is high cristobalite. Literature data of oxygen diffusion rate in cristobalite is, however, anomalously large when compared to those in

ISOTOPIC FRACTIONATION IN CAIS AND CHONDRULES: Nagahara, H.

quartz and tridymite, and it is difficult to evaluate whether the rate is consistent with other studies [8]. Therefore, the value of oxygen diffusion rate in tridymite is tentatively used in the present study. In the calculation, the material is assumed to be infinite for one dimension, evaporation is assumed to take place at a surface, and diffusion rates of isotopes are assumed to be the same. The result is shown in Fig. 2 where evaporation rates in vacuum (free evaporation) and in hydrogen gas of 10^{-5} bar and oxygen diffusion rate in tridymite at 1600°C are compared. The figure shows that the diffusion rate and free evaporation rate cross at about 200min. Diffusion rate is larger than free evaporation rate in the beginning 200 min, where oxygen isotopic fractionation can take place according to the Rayleigh fractionation model. After 200 min, evaporation rate is larger than diffusion rate, where isotopic fractionation can not take place effectively. On the contrary in hydrogen gas of 10^{-5} bar, evaporation rate is larger than diffusion rate regardless of time. In this case, isotopic fractionation hardly takes place.

The present results give a constraint on the formation conditions for CAIs and chondrules. CAIs, which often show significant isotopic fractionation with heavier isotope enrichment, are thought to have been heated in vacuum or in a gas of very low hydrogen pressure; they have evaporated slowly enough to cause isotopic fractionation. On the other hand, chondrules, which do not show significant isotopic fractionation, are thought have been heated in nebular (hydrogen) gas, where evaporation rate of material was large and isotopic fractionation could hardly occur. Alternatively, chondrule were hardly evaporated in a highly oxidizing gas, where partial pressure of oxide components was very large. The latter possibility is, however, not preferable, because Allende chondrules show evidence for Mg isotopic fractionation [9] which suggests that significant portion of the precursor material was lost by evaporation.

REFERENCES: [1] Clayton, R. N. *et al.* (1988) *Phil. Trans. R. Soc. Lond.* **A 325** 283-501, [2] Clayton, R. N. *et al.* (1986) In Protostars and Planets II 755-771, [3] Kinsey, A. E. *et al.* (1988) *LPSC* **XIX** 603-604, [4] Esat, T. M. and Taylor, S. R. (1990) *LPSC* **XXI** 333-334, [5] Davis, A. *et al.* (1990) *Nature* **347** 655-657, [6] Nagahara, H. *et al.* (1993) *Meteoritics* **28** 406-407, [7] Wang, J. *et al.* (1991) *LPSC* **XXII** 1461-1462, [8] Fleer, R. *Contrib. Mineral. Petrol.* **76** 440-454, [9] Koga, A. *et al.* (1994) This volume.

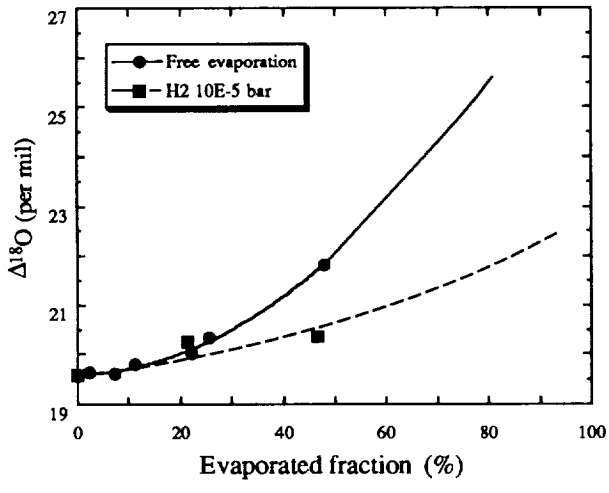

Fig. 1 Oxygen isotopic fractionation of evaporation residues in vacuum and hydrogen gas of 10^{-5} bar. The curves are regression of data, and are extrapolated to higher degree of evaporation.

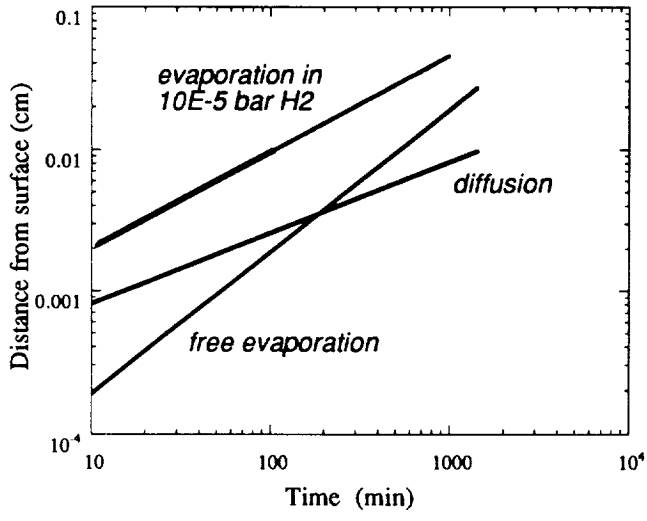

Fig. 2 Comparison of diffusion rate of oxygen in solid SiO_2 and evaporation rates in vacuum and hydrogen gas of 10^{-5} bar.

DIFFUSION MEASUREMENT ON DOUBLE-LAYERED SINGLE CRYSTALS OF OLIVINE, ORTHOPYROXENE AND ZIRCON SYNTHESIZED BY EPITAXIAL OVERGROWTH. Hiroshi Nagasawa[1], and Masana Morioka[2]. [1]Department of Chemistry, Gakushuin University, Mejiro, Toshima-ku, Tokyo 171 and [2]Radioisotope Centre, University of Tokyo, Yayoi, Bunkyo-ku, Tokyo 113, Japan.

Double-layered single crystals of olivine, orthopyroxene and zircon were synthesized for the purpose of measuring diffusivities of cations in the minerals, which are difficult to measure by the conventional pair annealing techniques (e.g., Buening and Busek [1]; Morioka [2,3]). Using the synthetic mineral crystals interdiffusivities were measured for Co-Mg and Ni-Mg in olivine and Hf-Zr in zircon. Measurement of Co-Mg interdiffusivity in orthopyroxene was also undertaken.

Method of synthesis. A large single crystal of forsterite was synthesized by CZ method, cut into mm-size rectangular pieces with each surface perpendicular to crystallographic axes and used for seed crystals. Seed crystals of hafnon($HfSiO_4$) and orthoenstatite were synthesized by using Li_2O-MoO_3(-V_2O_5) flux.

Second layers of $(Co,Mg)_2SiO_4$, $(Ni,Mg)_2SiO_4$ on forsterite, $ZrSiO_4$ on $HfSiO_4$ and $(Co,Mg)SiO_3$ on orthoenstatite were grown epitaxially on the surface of the seed crystals from Li_2O-MoO_3 (-V_2O_5) flux systems.

Evaluation of the crystals. Optical microscope observation on thin sections indicates the second layers grew continuously over the seed crystals with common optical axes. Electron microscope (SEM) observation shows that the boundaries of the two layers are sharp with diffuse areas of less than 1 μm in thickness in normal cases. Slight, gradual changes of Co-Mg and Ni-Mg ratios were observed in the second layers of olivine and pyroxene by energy dispersive X-ray analysis(EDX). However, since the observed compositional zoning is small, distribution of Co or Ni after diffusion annealing cannot be affected seriously in the high Mg region in the crystal, though the effect in the low Mg region of the crystal may be significant.

Diffusion annealing. The conditions of annealing are shown in Table 1.

Table 1. Conditions of diffusion annealing.

Mineral	Element	Temperature, °C	Duration
Olivine	Co-Mg	1050-1350	1.5-14 days
	Ni-Mg	1200-1450	25 hr-81 days
Zircon	Hf-Zr	1600	12 days
Orthopyroxene	Co-Mg	950	40 days

Diffusion measurement.

Olivine. After diffusion annealing Co-Mg or Ni-Mg concentration profiles were measured on the polished surfaces of the specimens using EDX. Diffusion coefficients (D) were calculated by using Boltzmann-Matano equation as discribed in Morioka [2].

Zircon/orthopyroxene. Because of very low diffusion rates of cations in the minerals, diffusion profiles could not be measured by EDX with spatial resolution of a few μm. Instead, scattered electron image contrast was used to determine diffusion profiles.

DIFFUSION MEASUREMENT, Nagasawa, H. and Morioka, M.

Hf-Zr concentration ratios were obtained by calibrating with synthetic zircon crystals with known Hf-Zr ratios. D in zircon was calculated by assuming a constant value over the whole range of Hf-Zr concentration ratios at a given temperature.

Results and Discussion.

Olivine. Results for olivine are plotted in Fig.1.It is shown that this method offers D values for wide range of temperature, especially those at low temperature, such as that at 1050°C for Co-Mg.

D's for both Co-Mg and Ni-Mg are smaller than those observed by Morioka(1980, 1981) by about an order of magnitude, although temperature-dependence or actication energies are similar. The observed similarity in activation energies suggests that the cations diffuse with the same mechanism in both experiments. Although the reason for the observed discrepancies of D's is undertain, the observed discrepancies may be due to the difference in seed crystals.

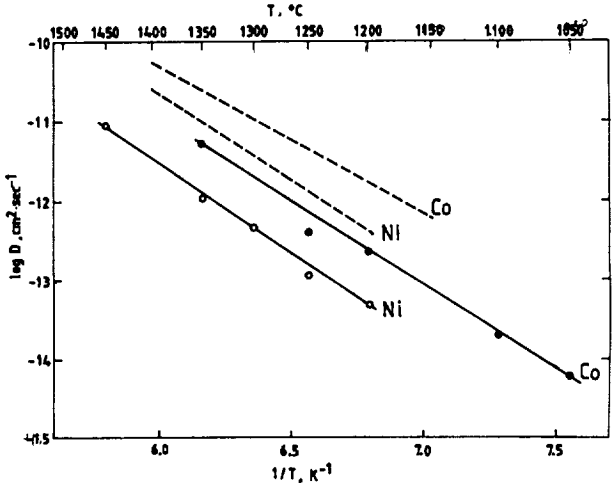

Fig.1 D's for Co-Mg and Ni-Mg in olivine. Values plotted are those obtained by extrapolating to Fo=100. ●: Co-Mg, ○: Ni-Mg, broken lines indicate those by Morioka[2,3].

Table 2. D's in zircon at 1600°C.

Axis	D, $cm^2 \cdot sec^{-1}$
⊥ c (a or b)	2×10^{-15}
// c	$\sim 2 \times 10^{-16}$

Zircon. The observed values of D in zircon are smaller by several orders of magnitude compared with those in olivine extrapolated to 1600°C. The observed higher diffusivity along a- and b-axes can be explained by the crystal structure of Zircon; i.e., vacant 6-fold coordinated sites containue along a-and b-axes. The observed low D values in zircon suggests that isotopic system in zircon is very resistant to thermal metamorphic events.

Conclusions. 1) Use of double-layered single crystal is suitable for measuring interdiffusivities of slow-moving cations which makes solid solution for a wide range of composition. It is also shown that diffusivities along two or more of the crystallographic axes can be measured for a single specimen.

2) Epitaxial overgrwoth assures of good contact between two components, thus enables a short range observation of diffusion profiles within a few um by scattered electron image which has much higher resolution compared with X-ray analysis.

3) It is most suitable for such minerals as zircon or orthopyroxene for which higher annealing temperature is unapplicable due to decomposition.

References. [1] Buening,D.K. and Busek, P.R.(1973) JGR 78,6852. [2] Morioka, M. (1980) GCA 44, 759. [3] Morioka, M. (1981) GCA 45, 1573.

HIGH-TEMPERATURE SHOCK EFFECTS ON CARBONACEOUS CHONDRITES; T. Nakamura[1], K. Tomeoka[2], T. Sekine[3] and H. Takeda[4] (1) Department of Earth and Planetary Sciences, Faculty of Science, Kyushu University, Hakozaki, Fukuoka 812, Japan, (2) Department of Earth and Planetary Sciences, Faculty of Science, Kobe University, Nada, Kobe 657, Japan, (3) National Institute for Research in Inorganic Material, Tukuba, Ibaragi 305, Japan, (4) Mineralogical Institute, Faculty of Science, University of Tokyo, Hongo, Tokyo 113, Japan.

High-temperature shock experiments on Allende and Leoville CV3 carbonaceous chondrites were carried out to see the effects of impacts on carbonaceous chondrites at high temperature using a single-stage propellent gun. The experimental conditions (peak shock pressures and pre-heated temperatures) are following; 11GPa initially at 300 °C, 21GPa at 300 °C and 21GPa at 600 °C for the experiments on Allende, and 21GPa at 660 °C and 21GPa at 800 °C for Leoville. Leoville is known to show preferred orientation of flattened chondrules [1], which was probably produced by impacts [2, 3]. We chose a direction perpendicular to the foliation for the direction of experimental shock propagation in order to observe progressive shock metamorphism on carbonaceous chondrites.

Shock loading on Allende CV3 chondrites

11GPa at 300°C: Chondrules, which were more or less spherical before shock loading, are uniformly flattened with an average ratio (long axis / short axis) 1.6 and show a recognizable preferred orientation. Olivine and low-Ca pyroxene in chondrules show irregular fractures and undulatory extinction. Mesostasis glasses in all chondrules are devitrified. Fe-Ni metal and sulfide inclusions in chondrules are fractured and partially melted; the partial melt occasionally intrudes into the fractures of silicates in chondrules. Chondrules containing many opaque inclusions tend to show higher degree of flattening. A noteworthy feature in matrix is the generation of numerous subround or irregularly-shaped grains of glassy material ranging in diameter from 10 to 30 μm. The glassy grains occupy 10 vol% of the matrix. Each grain is surrounded by relatively compacted olivine grains, suggesting that the glassy material might be produced by *in situ* melting of interstitial material between olivine grains. The glassy grains are rich in Si and Ca and have compositions close to high-Ca pyroxene.

21GPa at 300°C: Chondrules are clearly more flattened than the above product with an average aspect ratio 1.8 and display strong preferred orientation. Olivine and low-Ca pyroxene in chondrules show irregular fractures and exhibit undulatory extinction. Planar fractures are also observed in some olivine grains. Furthermore, in some chondrules, oval or rectangular grains of olivine and low-Ca pyroxene are aligned in a direction perpendicular to the compacting axis of chondrules. They appear to have rotated within chondrules during shock loading due to increase of plasticity of mesostasis glass. Like the product at 11GPa and 300 °C, Fe-Ni metal and sulfide inclusions in chondrules are deformed and partially melted. The matrix also contains numerous glassy grains which are bedded in strongly compacted olivine grains. The glassy grains are relatively larger and occupy greater volume of matrix (16 vol%) than those in the products at 11GPa. They range in diameter from 10 to 50 μm and occasionally up to 500 μm. Chemical compositions of the glassy grains are similar to those of the product at 11GPa at 300 °C. TEM observations on olivine grains in the matrix reveal the presence of high densities of cracks and dislocations.

21GPa at 600°C (the results for this condition have been already presented at the last Meteoritical Society meeting [4], but they are shown here again briefly for comparison): Chondrules are remarkably flattened with an average aspect ratio 1.8. Some olivine grains in chondrules show planar fractures. A remarkable feature that was not observed in the previous two products is that almost all chondrules show blacking. High-magnification SEM

observations reveal that optically blackened olivine and low-Ca pyroxene contain numerous cracks filled with Fe-Ni-S melt. Si- and Ca-rich glassy grains ranging typically from 10 to 50 μm and occasionally up to 500 μm in diameter occur in many places in the matrix. The glassy grains occupy 18 vol% of the matrix. Sulfide grains are apparently melted to form network-like veins in the matrix. In places, the Fe-S melt is segregated in areas ~ 400 μm across.

Shock loading on Leoville CV3 chondrite

21GPa at 660 °C: Flattening of chondrules does not appear to be enhanced by shock loading. Fe-Ni metal and sulfide inclusions in chondrules are partially melted and form many veins in chondrules, resulting in shock blackening. Notable additional shock features are not observed except those indigenous to Leoville. The glassy material that was observed in the matrix of shocked Allende at high temperatures is not observed in this matrix.

21GPa at 800 °C: Shock effects in chondrules are similar to those in shocked at 660 °C. But, shock blackening occurs in larger areas and the matrix has a smoother appearance in SEM images, being consistent that they were more compressed and sintered. In many places in the matrix, shock veins are observed with typically from 10 to 30 μm and occasionally up to 150 μm in width. Most of these veins are filled with Fe-Ni melt, and some with Fe-Ni-S melt. One large Fe-Ni-S vein contains numerous inclusions of low-Ca pyroxene, voids and Ca-Al-Si-rich melt. In the vein, kamacite occurs as fine grains less than 10 μm in diameter, suggesting that the Fe-Ni melt was rapidly cooled down from a high temperature.

The shock-loaded Allende and Leoville at high temperatures show many features different from those of shock-loaded Allende at room temperature [4]. The following are the features observed in the shocked samples at high temperatures but not in the shocked samples at room temperature [4]. (1) Shock blacking of chondrules caused by melting of Fe-Ni metal and sulfide in chondrules. (2) Generation of high-Ca pyroxene-like glassy grains in porous matrix. (3) Production of shock veins filled with Fe-S or Fe-Ni-S melt. These features can be ascribed to the shock at high temperature.

Some of the textural and mineralogical features of shock-loaded samples are different between Allende and Leoville. Deformation and elongation of chondrules are enhanced only in shocked Allende. Shock veins are produced in both shocked Allende and Leoville, but the compositions and the occurrences of the veins are different. Localized melts occur only in the matrix of shocked Allende. These differences may be due to the textural and mineralogical differences in the matrices of Allende and Leoville; the matrix of Allende is porous and contains many sulfide grains, whereas that of Leoville is much less porous and contains many Fe-Ni metal grains. Numerous pores in the matrix of Allende may have provided a room for chondrule deformation and contributed to the preferential temperature increase in the matrix. Sulfide grains in the matrix of Allende are probably responsible for the formation of Fe-S-rich shock veins. In contrast, the low abundance of pores in the matrix of Leoville restricted chondrule deformation and hindered temperature increase in the matrix. Fe-Ni metal grains in the matrix of Leoville are responsible for the formation of Fe-Ni rich shock veins.

References: [1] Kracher A. et al. (1985) *JGR, 90,* 123-135. [2] Nakamura T. et al. (1992) *EPSL, 114,* 159-170. [3] Scott E. R. D. et al. (1992) *GCA, 56,* 4281-4293. [4] Nakamura T. et al. (1993) *Meteoritics, 28,* 408.

ARGON DEGASSING AND CRUSTAL PRODUCTION RATES ON VENUS;

Noriyuki Namiki, Dept. of Earth, Atmospheric, and Planetary Sciences, Massachusetts Institute of Technology, Cambridge, MA 02139, and Sean C. Solomon, Dept. of Terrestrial Magnetism, Carnegie Institution of Washington, Washington, DC 20015.

Introduction. Radar images of Venus by the Magellan spacecraft have revealed a surface 500 My old with widespread tectonic and volcanic features but no global plate tectonics. Thus different mechanisms of heat loss and crustal production on Venus and Earth are indicated. The apparently random distribution of impact craters and the large fraction of craters little modified since formation have led to two end-member hypotheses for the history of surface renewal: episodic global resurfacing by catastrophic events [1], and essentially steady equilibrium resurfacing [2]. In this study, we attempt to constrain the rate and episodicity of magmatism and crustal production on Venus by modeling the history of degassing of ^{40}Ar.

In the absence of significant weathering and erosion on Venus, the principal mechanism of degassing of ^{40}Ar, a radioactive decay product of ^{40}K, is partial melting of mantle material and transport of magma to the surface or to near-surface reservoirs. The ^{40}Ar abundance in the present atmosphere is thus closely related to the history of magmatism and crustal production on Venus [3,4]. We have developed a new Ar degassing model from geologic observations in order to constrain the history of crustal formation and resurfacing on the planet.

Ar Degassing Model. We solve for the transfer of K and Ar among mantle, crustal, and atmospheric reservoirs under the assumption that degassing and regassing coefficients of K and Ar are constant in time [5]. Because K and ^{40}Ar in the mantle are released by partial melting of mantle material and are transported to the surface by magmatism, the degassing coefficients are governed by the crustal production process: the partition coefficients for K and ^{40}Ar between solid and melt (D^K and D^{Ar}), the fractional degree of melting (F), and the rate of crustal production. Regassing coefficients of K and ^{40}Ar represent recycling of crustal material into the mantle and vary inversely with crustal residence time (T_R).

We model the history of crustal production on Venus as repeated cycles of two different processes: episodic catastrophic resurfacing by lithospheric recycling, and steady magmatism. In a catastrophic resurfacing event, old crust is assumed to be thoroughly recycled into the mantle by transferring K and ^{40}Ar from the crust to the mantle. Accompanying recycling of old crust is the formation of an amount of new crust generated by partial melting of the mantle. K in the crust and ^{40}Ar in the atmosphere increase in proportion to this new crustal mass as K and ^{40}Ar in the mantle decrease. After cessation of a catastrophic resurfacing event, steady magmatism is assumed to transfer K and ^{40}Ar among the three reservoirs. Such magmatism is assumed to take place at a constant flux, Q_C. The importance of crustal recycling depends on the relative magnitudes of T_R and the characteristic time interval between catastrophic events.

Numerical Results. For a series of models parameterized by Q_C and the volume of crust produced during each catastrophic resurfacing event, V_C, the absolute abundances of K and ^{40}Ar in each reservoir are calculated so that the total amount of ^{40}Ar in the atmosphere, $(^{40}Ar)_A$, matches the observed value ($1.4 \pm 0.2 \times 10^{16}$ kg). The K concentration in the bulk silicate Venus and in the crust then follows from the masses of crust and mantle (Figure 1). From the measured K/U ratios in surface materials, the K concentration in the bulk silicate Venus is estimated to be between 200 and 300 ppm (dashed lines in figure). The K concentration at the Venus surface is constrained to lie between 0.14 and 0.67% from Venera and Vega lander measurements (dashed-dot lines). Models satisfying both constraints are shown by the shaded area in Figure 1.

A trade off between V_C and Q_C is clearly shown in Figure 1, i.e., we cannot distinguish the episodic catastrophic resurfacing hypothesis and the steady magmatism hypothesis from ^{40}Ar degassing alone. This is because the degassing of ^{40}Ar depends principally on the total crustal volume produced over the history of the planet and is not sensitive to the manner in which the crust forms. Contours of total crust produced divided by surface area (h_C^{total}, solid lines in Figure 1) show that h_C^{total} ranges from 70 to 120 km independent of the mode of crustal production. By the same reasoning, ^{40}Ar degassing is insensitive to the assumed interval times, i.e., the inferred crustal volume formed during each catastrophic event scales as the interval time.

ARGON DEGASSING ON VENUS: Namiki N. and Solomon S.C.

The amount of ^{40}Ar degassed from the interior is, however, dependent on F. Acceptable values for h_C^{total} are shown in Figure 2 as a function of F. The acceptable results from Figure 1 fall within the region surrounded by solid lines. Allowable models exist only if $0.03 < F < 0.22$. Two important parameters that can change h_C^{total} are D^{Ar} and $(^{40}Ar)_A$. Experimental measurements show relatively high values of D^{Ar} of 0.05 to 0.15 [6]. A high value of D^{Ar} requires a large h_C^{total} to satisfy the observed $(^{40}Ar)_A$. Therefore h_C^{total} is highest when the maximum values are assumed for D^{Ar} and $(^{40}Ar)_A$ (dashed lines in Figure 2), and lowest when the minimum values for those two parameters are assumed (dashed-dot lines). Our numerical calculations constrain h_C^{total} to be 30 to 190 km.

Discussion. The total volume of crust produced on the Earth has been estimated to be at least ~10^{11} km^3 [7]. This value corresponds to a time-integrated thickness of ~200 km, which is nearly the same as our upper bound on h_C^{total} on Venus. Because a constant crustal production rate was assumed for this estimate and that rate was likely to have been higher in the past, we may conclude that the total amount of crust produced on Venus has been less than that on Earth. In previous studies of ^{40}Ar degassing on Venus [3,4], the crustal production rate has been estimated to be no more than 10 km^3 yr^{-1}. The difference from our bounds appears to arise from different choices of parameters, especially F and D^{Ar}.

Fegley and Prinn [8] estimated the current rate of volcanism on Venus as between 0.4 and 11 km^3 yr^{-1} on the basis of the rate of reaction of atmospheric SO_2 and surface carbonates. By subtracting this rate from the average rate of crustal production, the relative importance of catastrophic resurfacing and steady magmatism could, in principle, be evaluated. However, because our results and their estimates overlap and both involve large uncertainties, neither episodic catastrophic resurfacing nor steady magmatism can be excluded. Specific scenarios, however, can be tested. In particular, the model of Parmentier and Hess [9] for the thermal and chemical evolution of Venus that included the development of a depleted mantle residuum layer predicts an integrated crustal production more than 3 times greater than our upper bound.

References. [1] G.G. Schaber et al., *JGR, 97,* 13,257, 1992; [2] R.J. Phillips et al., *JGR, 97,* 15,921, 1992; [3] E. Tajika and T. Matsui *LPSC, 22,* 863, 1991; [4] V.P. Volkov and M.Ya. Frenkel, *EMP, 62,* 117, 1993; [5] Y. Hamano and M. Ozima, in *Terrestrial Rare Gases,* Japan Sci. Soc. Press, 155, 1978; [6] H. Hiyagon and M. Ozima, *GCA, 50,* 2045, 1986; [7] R.E. Grimm and S.C. Solomon, *JGR, 93,* 11,911, 1988; [8] B. Fegley, Jr., and R.G. Prinn, *Nature, 337,* 55, 1989; [9] E.M. Parmentier and P.C. Hess, *GRL, 20,* 2015, 1992.

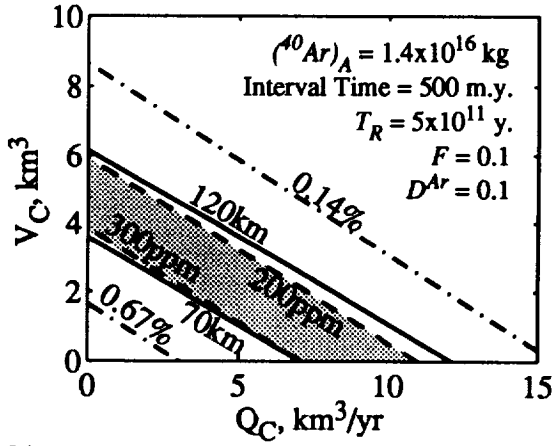

Figure 1. Contours of K concentration in the bulk silicate planet (dashed lines) and in the crust (dashed-dot lines), and contours of h_C^{total} (solid lines). The range of allowable models is shown by the shaded area.

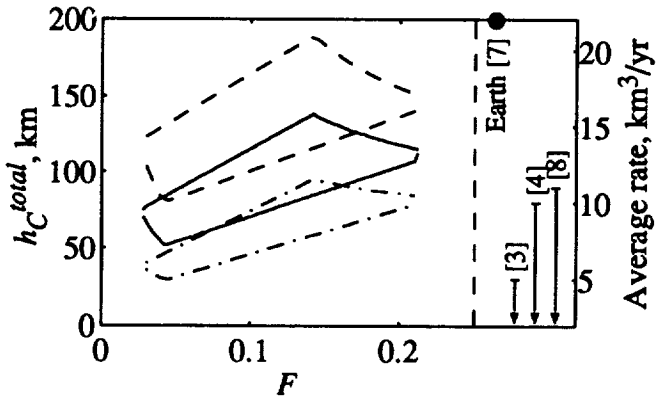

Figure 2. Limits on h_C^{total} as a function of F. The vertical axis on the right is the average crustal production rate over the age of the planet. Estimates of time-integrated crustal volume on Earth [7], other bounds on crustal production rates on Venus [3,4], and an estimate of present volcanic flux [8] are also shown.

The Impact Crater Density on Volcanoes and Coronae on Venus: Implications for Volcanism and Global Resurfacing;

Noriyuki Namiki, Department of Earth, Atmospheric, and Planetary Sciences, Massachusetts Institute of Technology, Cambridge, MA 02139, and Sean C. Solomon, Department of Terrestrial Magnetism, Carnegie Institution of Washington, Washington, DC 20015.

Introduction. Volcanic features are widely distributed over the surface on Venus [1], and their ages provide critical information on the magmatic budget of the planet. However, the generally low density of impact craters on Venus, a result of atmospheric shielding [2,3], has prevented a comparison of crater retention ages of small regions [4] and contributes to the controversy over whether a catastrophic [2] or an equilibrium model [3] better describes the global resurfacing history. The spatial diversity of the crater distribution has nonetheless been addressed by grouping areas by latitude [2], radar cross section [3] , or elevation [5]. Following this practice, we integrate the areas and cratering records on large volcanoes and also on coronae, and we assess the implications of the results for volcanism and global resurfacing.

Data Sources. We make use of a data base [5] of 838 impact craters classified according to tectonic deformation and exterior embayment. A data base for 175 volcanoes at least 100 km in diameter [6] has been compiled from Magellan images and a published map [1]. The radius and relief of the edifice and the radius of a radial flow apron are included. A data base for 362 coronae [7] includes classification by feature type and volcanic category. It should be noted that there are 44 features listed in both the volcano and corona data bases.

Crater Density on Volcanoes and Coronae. For large volcanoes, the occurrence of one or more impact craters on the edifice or flow apron is ascertained from the data bases, and the superposition relationships are verified from Magellan radar images. We include the edifice and discernible radial flows in calculating the area of each volcano. We do not count an embayed crater on the plains exterior to a volcanic edifice because it is not generally possible to determine whether the impact occurred before or during the interval of volcanic activity. Thus the crater density for large volcanoes corresponds to the average time when major eruptions ceased. The average density of impact craters on large volcanoes (total area 2.7×10^7 km^2) is $(1.0 \pm 0.2) \times 10^{-6}$ km^{-2}, significantly less than the global average of 2.0×10^{-6} km^{-2} [2]. It is unlikely that the obtained crater density is underestimated by missing a large population of old volcanoes because identification of volcanoes should not be biased by age estimation.

For coronae, we determined the crater density only within corona interiors (total area 2.7×10^7 km^2) and obtained $(1.7 \pm 0.3) \times 10^{-6}$ km^{-2}. Artemis, the largest corona on Venus, occupies nearly 15% of the total area of coronae and includes 5 craters. The crater density for coronae excluding Artemis ($1.8 \pm 0.3 \times 10^{-6}$ km^{-2}) is, however, little changed.

Rates of Volcanic Resurfacing. For a global average surface age of 500 My [2,3], the rate of resurfacing by large volcanoes is 0.05 km^2 yr^{-1}. This figure underestimates the overall volcanic resurfacing rate because many other types of volcanic landforms occur on Venus [1]. If we assume that all embayed craters can be attributed to volcanic activity and that the density of partially embayed craters is a constant for all volcanic deposits, then the area of volcanic flows capable of manifesting an embayment relationship in Magellan images is 1.0×10^8 km^2 and the global volcanic resurfacing rate is 0.2 km^2 yr^{-1}.

Thickness of Flow Units and Magmatic Flux. Large craters are more resistant to volcanic embayment than small craters, and should therefore have a higher ratio of partially embayed craters. In Figure 1 we show the fraction of embayed craters versus crater diameter [5]. The distinct increase in this fraction at a diameter near 30 km is likely because craters larger than this size tend to survive volcanic embayment. The depth of a 30-km-diameter crater on Venus is 1.3-1.8 km [5], and from scaling fresh lunar craters [8] the rim height for such a crater is 1.2 km. If 2 km is the maximum thickness of embaying flow units and the total area of such lava flows is 1.0×10^8 km^2, the maximum volume of such flow units is 2.0×10^8 km^3. For a ratio of intrusive to extrusive magmatism of 10 [9], upper bounds on the total volume of magmatic material and the magmatic flux over the last 500 My are 2.2×10^9 km^3 and 4.4 km^3 yr^{-1}, respectively. The latter

CRATERING ON VOLCANOES AND CORONAE: Namiki N. and Solomon S.C.

figure is in agreement with the current rate of volcanism on Venus (0.4 to 11 km^3 yr^{-1}) estimated from the rate of reaction of atmospheric SO_2 and surface carbonates [10].

Corona Resurfacing. Overall, the crater density on coronae is not significantly different from the global average. Coronae have been classified into five groups on the basis of morphology and postulated evolutionary stage [7,11]. The first group, radial and radial/concentric coronae, are held to correspond to the earliest stage of corona formation. The second to fourth groups (categories 1, 2, and 3 [7]) are distinguished by an increasing intensity of volcanism and are held to represent successive evolutionary stages. The last group, corona categories 2r and 3r [7], are held to be the oldest on the basis of their embayment by regional plains deposits. The crater density for each group is shown in Figure 2.

While the small numbers of craters prevent quantitative discussion with high confidence, the crater densities of category 2 and 3 coronae appear less than those of radial and category 1 coronae. If the postulated evolutionary model [7,11] is correct, this result implies that the rate of formation of coronae has not been steady over the past 500 My. If the rate were steady, crater densities in coronae at early stages (radial and category 1) would be less than those at the late stages (categories 2 and 3). The crater densities instead suggest that radial and category 1, 2r and 3r coronae represent features that for the most part ceased to evolve about 500 My ago. The lesser crater densities of category 2 and 3 coronae likely indicate volcanism that lasted until several hundred million years later. While it is possible that the deformation accompanying the formation of radial and category 1 coronae has not removed craters, the population of deformed craters in such coronae (20-25%) still argues against a young age for these features.

Implications for Global Resurfacing. In the end-member equilibrium resurfacing model, the total number of impact craters on the surface should be the result of a balance between crater production and resurfacing. Assuming that such an equilibrium also holds between the volcanic flux and global resurfacing, the crater densities on volcanoes and coronae are predicted to equal the global average density regardless of the mix of global resurfacing mechanisms or the rate of volcanic activity. This result would also hold if volcanoes and coronae formed at the time of a catastrophic global resurfacing event. Thus our results are inconsistent with the simplest end-member models for global resurfacing on Venus and suggest that large volcanoes and coronae with associated volcanic flows have been magmatically active over much of the last 500 My.

References. [1] J.W. Head et al., *JGR*, *97*, 13,153, 1992; [2] G.G. Schaber et al., *JGR*, *97*, 13,257, 1992; [3] R.J. Phillips et al., *JGR*, *97*, 15,921, 1992; [4] J.J. Plaut and R.E. Arvidson, *JGR*, *93*, 15,339, 1988; [5] R.R. Herrick and R.J. Phillips, *Icarus*, submitted, 1993; [6] P.J. McGovern et al., unpublished, 1993; [7] E.R. Stofan et al., *JGR*, *97*, 13,347, 1992; [8] R.J. Pike, in *Impact and Explosion Cratering*, Pergamon, 489, 1977; [9] J.A. Crisp, *J. Volcan. Geotherm. Res.*, *20*, 177, 1984; [10] B. Fegley, Jr., and R.G. Prinn, *Nature*, *337*, 55, 1989; [11] S.W. Squyres et al., *JGR*, *97*, 13,611, 1992.

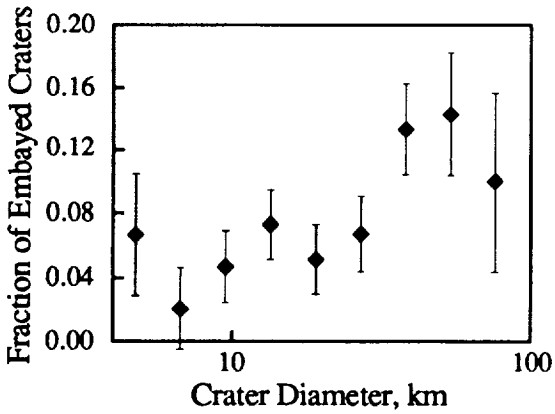

Figure 1. Fraction of embayed craters versus crater diameter. Data from [5].

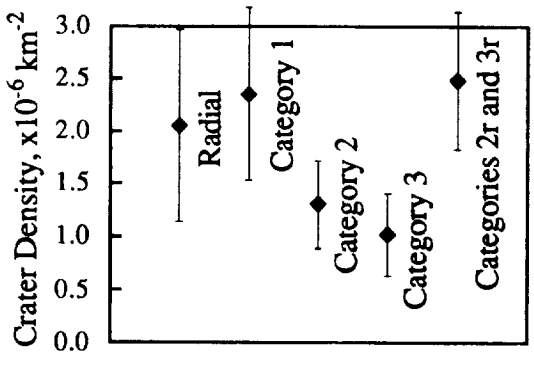

Figure 2. Crater densities on coronae by corona class [7].

MID-INFRARED SPECTRA OF CONDENSED SO_2 PHASES: LAB DATA AND APPLICATIONS TO GALILEO MAPPING OF IO; D. Nash and B. Betts, San Juan Institute, 31872 Camino Capistrano, San Juan Capistrano, CA 92675.

Introduction

SO_2 in the form of frost or ice is present on Io's surface, as originally determined based on the identification of the $\nu_1 + \nu_3$ combination band of solid SO_2 near 4 μm in Io groundbased reflectance spectra [1, 2, 3]. Although numerous papers have addressed various aspects of SO_2 on Io [e.g., 4, 5, 6], there has been no comprehensive spectral study published that presents laboratory data covering the important mid-infrared signatures (~2-25 μm) of various SO_2 phases; this spectral range contains very diagnostic band features that can be used to constrain the composition and phase state of Io's surface materials. Key portions of this spectral range (2-5 μm) will be accessible to the Near Infrared Mapping Spectrometer (NIMS) on the Galileo spacecraft. The purpose of the lab work presented here is to provide reference spectra of candidate materials for comparison with observed infrared spectra of Io's surface; identification of compositional species present on Io; and mapping of their spatial distribution with NIMS.

Experiments

Using a miniature vacuum/environmental chamber fitted to a Fourier Transform infrared (FTIR) spectrometer [7], we produced detailed laboratory reflectance spectra in the mid-infrared range, covering 2.3-23 μm (4348-435 cm^{-1}), for a variety of phase states of SO_2 as follows:

SO_2 gas -- Has characteristic doublet absorption bands centered near the following wavelengths: 4.0, 7.4, and 8.6 μm. The band near 4.0 μm has a distinct and sharp minimum at 3.981 μm that we recognize as the most diagnostic feature of a gas phase in this spectral region.

SO_2 frost -- This is probably the most relevant reflectance spectrum for comparison to Io's surface; it is characterized by a high flat continuum with strong fundamental bands near the ~530, ~1140, and ~1300 cm^{-1} regions, and sharp combination and overtone bands in the range 1600 cm^{-1} (6.25 μm) to 4000 cm^{-1} (2.50 μm). The most important band, because it is strong and relatively easily observable in Io's spectrum, is the 4.07 μm (2459.4 cm^{-1}) $\nu_1 + \nu_3$ combination band. This is produced by normal isotope SO_2 consisting of $^{32}S^{16}O_2$ [8]. The band also has three identifiable Satellite bands on its redward flank due to fractions of SO_2 molecules containing isotopes ^{34}S, ^{35}S, and ^{18}O.

SO_2 slab ice -- Absorption bands for solid SO_2 ice are essentially the same as those in thick frost, except for an additional weak band at 3.92 μm.

SO_2 liquid -- The liquid SO_2 spectrum has major absorption bands at the following wavelengths: 2.72, 2.79, 3.85, 4.36, 5.38, and 6.2 μm. Note that the 2.72 and 6.2 μm bands are unique to the liquid phase.

Adsorbed SO_2 -- A monolayer adsorbate produces a band at 4.036 μm (2478.0 cm^{-1}); as it thickens and begins to form a crystal lattice, bands appear at 4.071 μm (2456.7 cm^{-1}) and at 4.37 μm (2288 cm^{-1}). As the lattice further thickens the 4.036 μm band blends into the deepening 4.066 μm band ($\nu_1 + \nu_3$ combination), and the 4.37 μm band ($2\nu_1$ overtone) gets stronger.

Surface textures -- We found it possible to produce a wide variety of surface textures for solid SO_2, ranging from frosts of many peculiar textures, to solid slab or glaze ice.

Applications to Io

Previously reported IR spectra of condensed SO_2 (e.g. in refs [6, 8, 9, 10, 11, 15]) have usually been produced as transmission spectra obtained on thin (or thick) films of ice, not as reflectance spectra of a free frost surface as reported here (or by [1, 2, 13, 14]). In comparing results of the two approaches, it appears that thin-film transmission spectra are not adequate to properly represent all the features present in reflectance spectra of

macroscopic frosts or ices such as may exist on Io; this is because in thin lab samples there is insufficient optical pathlength to produce detectable absorption bands at certain wavelengths in reflectance spectra of thick deposits.

These systematic lab studies of band character and variation allow one to estimate what the phase state and concentration level is for condensed SO_2 on the surface of Io. Our lab results show that the $\nu_1 + \nu_3$ band minimum position is dependent on:

1. Phase state of the SO_2.
2. Frost/Ice thickness or density (g/cm^2).
3. Instrument resolution (because the band is asymmetric).

Relative thickness of a solid SO_2 (ice or frost) deposit, on a mm scale, can be assessed by strengths of bands for thickness as follows:

Thin -- 2.54, 2.79, and 3.75 μm bands absent, no 3.95 μm shoulder, 4.07 μm band present but narrow and unsaturated, 4.37 and 5.40 μm bands absent or weak;

Medium -- 3.75 band absent, 3.95 μm shoulder high, 4.07 μm band stronger, 4.37 and 5.40 μm bands present;

Thick -- 2.54, 2.79, and 3.75 μm bands strong, 3.95 μm shoulder low, 3.56 μm band distinct; 4.07 μm band broad and nearly saturated, 4.37 and 5.40 μm bands strong.

The Galileo infrared spectrometer (NIMS) is designed to measure spectra of Io's surface in the range 0.7-5.2 μm, with spectral resolution of 0.02 μm. Because our data show clearly that spectra of thin (~ 100 μm) SO_2 frosts are distinctly different than spectra for thick (> 1 mm) frost or ice, NIMS should be able to use the 4-μm band shape and depth (plus the presence or absence of the 2.54 and 2.79 μm bands) to map the relative thickness of solid SO_2 on Io's surface. Also, we estimate that NIMS should be able to detect a 0.2 cm-atm SO_2 atmospheric column over a spectrally neutral surface (such as sulfur) on Io.

References:

[1] Smythe, W., R. Nelson, and D. Nash, 1979. Nature 280, 766. [2] Fanale, F., R.H. Brown, D. Cruikshank, and R. Clark, 1979. Nature 280, 761-763. [3] Hapke, B., 1979. Geophys. Res. Ltrs. 6, 799-802. [4] Nash, D.B., M. Carr, J. Gradie, D. Hunten, and C. Yoder, 1986. In Satellites (J. Burns, M. Matthews, EOS), U. Ariz. Press, 629-688. [5] Howell, R.R., D. Nash, T. Geballe, and D. Cruikshank, 1989. Icarus, 78, 27-37. [6] Salama, F., L. Allamandola, F. Witteborn, D. Cruikshank, S. Sandford, and J. Bregman, 1990. Icarus 83, 66-82. [7] Nash, D.B., 1986. Applied Optics 25, 2427-2433. [8] Barbe, A., A. Delahague, and P. Jouve, 1971. Spectrochimica Acta 27A, 1439-1446. [9] Anderson, A. and M. Campbell, 1977. J. Chem. Phys. 67, 4300-4302. [10] Fink, U. and G. Sill, 1982. In Comets (L. Wilkening, Editor), Univ. Ariz. Press, Tucson. [11] Giguere, P. and M. Falk, 1956. Can. J. Chem. 34, 1833-1835. [12] Wiener, R. and E. Nixon, 1956. J. Chem. Phys. 25, 175. [13] Slobodkin, L., I. Buyakov, N. Triput, R. Cess, J. Caldwell, and T. Owen, 1980. Nature 285, 211-213. [14] Slobodkin, L., I. Buyakov, N. Triput, J. Caldwell, and R. Cess, 1981. J. Quant. Spectros. Radiative Transfer, 26, 33-81. [15] Schmitt, B., C. de Bergh, E. Lellouch, J. Morgan, A. Barbe, and S.Doute, 1993. Icarus (Submitted).

SHAPE, SIZE, AND DISTRIBUTION OF MAGNETIC PARTICLES IN BJURBOLE CHONDRULES

David F. Nava, Astrochemistry Branch, Code 691, NASA Goddard Space Flight Center, Greenbelt, Maryland 20771, USA.

Chondrules from the Bjurbole chondritic meteorite (L4) exhibit saturation remanence magnetization (SIRM) values which vary over three orders of magnitude [1]. REM values (Natural Remanence Magnetization/SIRM) for Allende (C3V) and Chainpur (LL3) are <0.01 but in Bjurbole some chondrules were found to have REM values >0.1 with several >0.2. REM values >0.1 are abnormal and cannot be acquired during weak field cooling. If exposure to a strong field (whatever the source) during the chondrules' history is responsible for the high REM values, was such history associated with a different processing which might have resulted in different shape, size, and distribution of metal particles compared to chondrules having REM values of <0.01? Furthermore, magnetic hysteresis results show a broad range of magnetic hardness and other intrinsic magnetic properties. These features must be related to a) size and amount of metal, and b) properties of, and amount of, tetrataenite in the chondrules (all chondrules thus far subjected to thermomagnetic analysis show the presence of tetrataenite) [2]. A scanning electron microscopy (SEM) study is underway to determine the relationship between the shape, size, and distribution of metal particles within individual chondrules and the magnetic properties of these chondrules. Results from the SEM study in conjunction with magnetic property data may also help to discern effects from possible lightening strikes in the nebula prior to incorporation of the chondrules into the parent body.

REFERENCES:

[1] Wasilewski, P. J., et al., (1993) Lunar Planet. Sci., XXIV, 1485.
[2] Wasilewski, P. J., and O'Bryan, M. V., (1994) Lunar Planet. Sci., XXV.

SMIT 79 F 925

P-RICH SULFIDE, BARRINGERITE, AND OTHER PHASES IN CARBONACEOUS CLASTS OF THE EREVAN HOWARDITE. M. A. Nazarov, Vernadsky Institute of Geochemistry and Analytical Chemistry, Moscow 117975, Russia, F. Brandstätter and G. Kurat, Naturhistorisches Museum, Postfach 417, A-1014, Vienna, Austria

A Fe,Ni,Cr-bearing sulfide (Q-sulfide) was inferred to be the major carrier of carbonaceous chondrite fission xenon that may have originated by the decay of an extinct superheavy element [1]. The nature of the phase has not been identified but it has been suggested from mineralogical studies that pentlandite [2] or a Fe,Ni,Cr,P-sulfide [3] could be the Q-phase. Such a Fe,Ni,Cr,P-sulfide was found in Murchison, Murray, and carbonaceous clasts of the Jodzie howardite [3,4]. A similar but Cr-poor sulfide was identified by us in carbonaceous xenoliths from the Erevan howardite [5]. Here we report on a the occurrence and chemistry of this phase in the Erevan howardite. The P-rich sulfide is associated with a high-temperature lithology consisting of forsterite, barringerite and a Cr-oxide. The P-rich sulfide most likely formed by condensation from the solar nebula gas. Condensation took place after CAIs formed but before forsterite and metal condensed. Our studies indicate that the P-rich sulfide is probably the first sulfide to form in the solar nebula. This is probably why it could be the main carrier of the anomalous xenon component.

OCCURRENCE. P-rich sulfide is a characteristic accessory phase of CM carbonaceous xenoliths in the Erevan howardite. Usually the grains are very small (< 10 μm in size) and heavily altered. In reflected light the sulfide resembles troilite but it is slightly darker and probably isotropic. Commonly the P-rich sulfide is associated with high-temperature minerals and is enveloped by accretionary dust mantles [6]. Fig. 1 shows the phase relationship in one of the lithologies. The P-rich sulfide (light gray) occurs in the center of a large accretionary object where it is accompanied by barringerite (white), forsterite (dark gray), and minute grains of Cr-oxide (gray). The phyllo silicate matrix (gray) is rich in Ni and Cr. One forsterite contains a metal nugget (bright; 10% Ni; 1.7% P) and, perhaps, a silica inclusion. The whole object is surrounded by a normal accretionary dust mantle containing rare forsterite grains. There is no reaction zone between the barringerite and P-rich sulfide grains. A barringerite grain (Fig.2) found in another clast is not associated with P-rich sulfide. This grain is slightly enriched in S at the margins and rimmed by an unusual Fe,S-oxide. Occasionally, P-rich sulfide grains are present as clasts (up to 100 μm) outside of the accretionary dust aggregates in the matrix of the carbonaceous clasts. The grains are never associated with pentlandite or pyrrhotite which are characteristic sulfides of CM matrices. Commonly these grains are enveloped or completely replaced by a P-rich tochilinite-like phase.

CHEMISTRY. All phases and matrices were analyzed with an analytical scanning electron microscope (ASEM) and with an electron microprobe (EMP). The results are given in the Table. We analyzed 13 P-rich sulfide grains from 4 different clasts by ASEM. However, only 3 of them could be analyzed with the EMP (Table). The compositions of these grains are similar and comparable to that of pentlandite, except for the P content. Characteristic minor elements are Cr, Na, and K. The sulfide has a low total which suggests the presence of oxygen and hydrogen. When compared to the P-rich sulfide described by [3,4] from Murchison, Murray and the Jodzie CM clasts, the Erevan P-rich sulfide is much poorer in Cr and contains Na. The atomic proportions of the main elements are $(Fe,Ni,Co,Cr,Na,K)_{9.36}S_{7.20}P$. The alteration products of the P-rich sulfide are similar in composition to tochilinite. In contrast to ordinary tochilinite this one is always enriched in Na, Cr, Ni, and P and depleted in Fe, S, and Al (Table).

The Cr-oxide grains associated with the sulfide (Fig. 1) are too small for a precise analysis. However, they contain more than 75% Cr_2O_3, a few percents of Mn, and are Al-free. Possibly the oxide could be escolaite. The barringerite described here is the first one found in a chondrite. The rare higher phosphide was reported previously only from the Ollague pallasite [7], the lunar meteorite Y-793274 [8], and a Cu-Ni deposit in China [9]. The Erevan barringerite is similar in composition to that from the Ollague pallasite but it has a higher Ni/Fe ratio and contains S and Na (Table). The Fe,S-oxide rimming an isolated barringerite grain (Fig. 2) could be a new tochilinite-like phase with a composition of $3[(Fe,Ni)(OH)_2]$*FeS. The associated forsterite (Fa 1.2) is rich in MnO (up to 0.8 wt. %) and Cr_2O_3 and poor in CaO in contrast to isolated forsterites in matrices of the other clasts which are commonly poor in MnO and rich in CaO. The phyllo-silicate matrix enveloping the sulfide - barringerite - forsterite aggregate is exceptionally rich in Cr, S and Ni (Table) and poor in Ca.

DISCUSSION. The existence of a P-rich sulfide appears to be extraordinary from the geochemical standpoint because P is known to be either a siderophile or lithophile element without any chalcophilic

PAGE 978 INTENTIONALLY BLANK
PRECEDING PAGE BLANK NOT FILMED

SULFIDE, BARRINGERITE FROM EREVAN: Narazrov M.H. et al.

tendency. However, it is also known [10] that S can replace O in the $(PO_4)^{3-}$ ion to give phosphorothioate compounds (e.g., Na_3PS_4, Cu_3PS_4). Such compounds and other thio-salts commonly contain alkalies and Cr, similar to the P-rich sulfide from the Erevan howardite. Hence, it is possible that the sulfide contains $P(S,O)_4$ tetrahedra. On the other hand, the sulfide could also accommodate $(PH_4)^+$ ions which could replace alkalies. On the basis of the EMP data it is difficult to constrain the nature of the P-rich sulfide. Because it is probably isotropic and has a pentlandite-like chemistry with a Fe/Ni ratio closed to 1, which stabilizes the pentlandite structure [11], it is possible that the sulfide is related to pentlandite. In this case its formula could be written as $(Fe,Ni,Co)_8(Fe,Ni,PH_4,Cr,Na,K)(S,O)_8$ which is similar to Ag-pentlandite [12] with the octahedral sites occupied at least partly by $(PH_4)^+$ ions.

Thus, from the chemical standpoint the P-rich sulfide is not a forbidden compound and its existence in nature only points to certain formation conditions. The P-rich sulfide assemblage consists mainly of moderately volatile elements. This suggests that the assemblage was formed from the solar nebula gas after the refractory phases had condensed. If the accretionary texture does reflect a sequence of condensation, then we have to conclude that the sulfide was precipitated before barringerite and forsterite, and together with Cr-oxide, indicating a relatively high oxygen fugacity during sulfide precipitation. The lack of any sulfide reaction rims around barringerite excludes the possiblity of forming the P-sulfide via sulfurization of barringerite. Thus, both the P-rich sulfide and the barringerite should be considered being direct nebular condensates under certain conditions which allowed them to escape equilibrium with earliest Ca-rich silicates and the later formed metal and sulfide phases. Actually, the P-rich sulfide could be the earliest sulfide phase in the solar nebula under normal oxidizing conditions and, therefore, it could be a carrier for the anomalous xenon component [1]. It is also important that the P-Fe-Ni-Cr-S assemblage could be a certain nebular component similar to CAIs. If modified by subsequent processes, the assemblage could be a parent for chromite-rich objects in ordinary chondrites [13], pentlandite-merrilite assemlages in Allende matrix [14], and troilite-chromite-phosphate inclusions in some irons [e.g., 15].

ACKNOWLEDGEMENTS. MAN was supported by the Russian Research Foundation (Project 93-05-9222). Support by the Austrian FWF (Project P 8125-GEO) is gratefully acknowledged.

REFERENCES. [1] Lewis R. S. et al. (1975) Science, 190, 1251. [2] Kerridge J. F. et al. (1979) EPSL, 43,1. [3] Bunch T. E. and Chang S. (1980) GCA, 44, 1543. [4] Bunch T. E. et al. (1979) GCA, 43, 1727. [5] Nazarov M. A. et al.(1993) LPSC, XXIV, 1053. [6] Bunch T. E. and Chang S. (1984) LPSC, XV, 100. [7] Buseck P. R. (1969) Science, 165, 169. [8] Brandstätter F. et al. (1991) GCA, 55, 1173. [9] Chen K. et al. (1984) Mineral. Abstr., 35, 1871. [10] Wells A. F. (1962) Structural Inorganic Chemistry. 3d edition. Oxford, 1055 pp. [11] Prewitt C. T. and Rajamani V. (1974) In "Sulfide Mineralogy", V.1, PR-1-41. [12] Wuenach B. J. (1974) ibid., W-21-43. [13] Krot A. et al. (1993) EPSL, 119, 569. [14] Rubin A. E. et al.(1984) LPSC XV, 699. [15] Olsen E. and Fredriksson K. (1966) GCA, 30, 459.

Table:
Chemical compositions of some phases and matrices
(EMP analyses in wt.%)

	1	2	3	4	5	6	7	8
Na	0.92	0.71	1.42	0.32	0.15	0.40	0.06	0.09
Mg	0.16	0.12	0.12	0.15	0.05	3.3	9.1	11.5
Al	-	<0.02	-	-	-	0.34	1.10	1.07
Si	0.18	0.05	0.18	0.20	0.14	1.29	15.3	13.5
P	3.7	4.0	3.7	20.1	22.0	1.59	-	-
S	29.3	28.5	27.0	1.82	0.11	19.1	3.2	1.56
K	0.36	0.46	0.22	0.04	<0.02	0.05	<0.02	<0.02
Ca	0.08	0.09	0.30	<0.02	<0.02	0.60	0.29	1.24
Ti	-	<0.02	-	-	-	0.13	0.07	0.05
Cr	0.27	0.32	1.68	0.42	0.13	1.65	1.10	0.38
Mn	-	0.06	-	-	-	0.15	0.29	0.15
Fe	36.1	32.4	28.8	36.1	49.1	42.9	22.6	19.8
Co	0.67	1.77	2.30	0.13	0.06	0.40	-	-
Ni	24.2	28.1	30.6	39.4	29.2	10.4	3.2	1.11
Sum	95.94	96.58	96.37	98.68	100.94	82.30	56.31	50.45

1-3 - P-rich sulfide; 4,5 - barringerite; 6 - P-rich tochilinite; 7 - Cr-rich matrix; 8 - normal matrix.

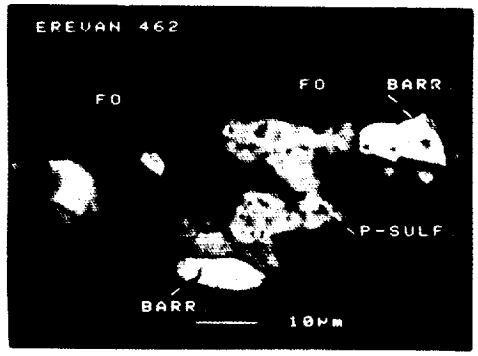

↑ Figure 1 ↓ Figure 2

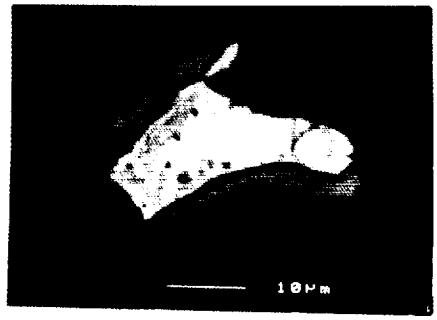

CHEMISTRY OF CARBONACEOUS XENOLITHS FROM THE EREVAN HOWARDITE; M. A. Nazarov, Vernadsky Institute of Geochemistry and Analytical Chemistry, Moscow 117975, Russia, F. Brandstätter and G. Kurat, Naturhistorisches Museum, Postfach 417, A-1014 Vienna, Austria, B. Spettel and H. Palme, Max-Plank-Institut für Chemie, Postfach 3060, D-55022 Mainz, Germany

The Erevan howardite is a polymict breccia with abundant xenoliths resembling carbonaceous chondrites [1]. Xenoliths with affinities for carbonaceous chondrites have been described from the Kapoeta, Jodzie, and Bholghati howardites [2-4], and the LEW 85300 polymict eucrite [5]. All these xenoliths have basically CM chondrite mineralogy. Apparently, the HED parent body was bombarded by a CM chondrite population in contrast to the ureilite parent body recording a CI chondrite component [6]. However, trace element data for the Bholghati and LEW 85300 xenoliths differ significantly from CM and CI chondrite patterns [5,7,8]. Our INA-bulk-analyses of clasts and EMP-analyses of matrices of Erevan carbonaceous xenoliths are compatible with CM chondrites, except for a significant Na depletion. Textural and chemical inhomogeneties identified in the clasts may be related to nebular processes.

TRACE ELEMENT PATTERN. Two carbonaceous clasts of 0.065 mg (ERW2) and 0.33 mg (ERW3) were analyzed for major and trace elements by INAA at the MPI Mainz laboratory. Both xenoliths show similar elemental abundances (Fig.1). Major differences are found in Ca, Br, and Au contents, probably related to inhomogeneous distribution. The elemental abundances match those of CM chondrites, with the larger clast ERW3 showing a better fit. When compared to CM chondrites the Erevan xenoliths are richer in refractory lithophile elements, and are characterized by a strong Na depletion (Fig.1).
The clasts consist of high-temperature components surrounded by a mantle of fine-grained material resembling accretionary dust mantles commonly observed in CM chondrites [9]. Core and mantle are embedded in a matrix rich in cronstedtite and tochilinite. High-temperature core components are forsterite (Fa 1.1-3.6), enstatite (Fs 1.0-3.6), and spinel-rich CAIs containing diopside. Some high-temperature grains are also present as isolated clasts in the Fe-rich matrix, and are not surrounded by fine-grained mantles. In addition, the matrix contains rare grains of Fe-rich olivine (Fa 30.4) and pyroxene (Fs 30.3; Wo 0.2), and Ca-carbonate. Main accessories are pentlandite, pyrrhotite, barringerite, and a P-rich sulfide described in more detail in [10].

MATRIX CHEMISTRY. The matrix of 30 carbonaceous clasts from .05 to 2 mm was analyzed by EMP techniques . The averaged data for 28 clasts are given in the Table and are shown in Figs. 2-3. Most matrix compositions are close to those of CM chondrites (Fig.2), except for a few clasts which are enriched in Si and Mg. We found only one clast that has a CI mineralogy but its matrix chemistry is closer to that of CM chondrites. Carbonaceous clasts from ureilites [6], mineralogically similar to CI-chondrites, also have a CM matrix chemistry (Fig.2). The Erevan xenolith matrices are strongly depleted in Ca, S and Na relative to CI composition (Fig.3). When compared to CM matrices they are commonly poorer in Na, and richer in K, Ti, Cr, and Mn. Therefore, the Erevan matrices are significantly different from carbonaceous chondrite matrices in their high K/Na ratio. Similar high K/Na ratios are observed only in the CI clasts from ureilites [6] and in micrometeorites [11]. Accretionary mantles are mainly composed of serpentine (high Mg and Si contents) whereas the xenolith matrix is rich in cronstedtite and tochilinite (Fig.2, Table). Both lithologies are characterized by high K/Na ratios.

DISCUSSION. In contrast to geochemical studies of the Bholghati and LEW 85300 carbonaceous clasts [5,7,8] our INAA data confirm the mineralogical identification of CM material in the Erevan howardite [1]. However, the comparison also shows that mineralogical features may be insufficient to distinguish different types of carbonaceous chondrites. In fact, the mineralogically identified CI clasts in ureilites [6] show CM matrix chemistry. The high-temperature grains (cores), accretionary mantles, and the Fe-rich matrix record a sequence of nebular processes of decreasing temperatures.

EREVAN CC XENOLITHES: Nazarov M.A. et al.

A prominent feature of the Erevan CM clasts is the strong Na depletion seen in bulk clast and clast matrix compositions. Similar Na depletions were found in bulk samples of CM and CV chondrites [12] and related to nebular processes. Other authors suggested that the Na-K fractionation in CM matrices is controlled by phyllosilicate - water ion exchange during aqueous alteration in a parent body regolith [13].

Erevan CM clasts do not show evidence for chemical and/or mineralogical impact-induced features which should have formed as a result of accretion of the material on a parent body. The presence of unaltered carbonaceous clasts in the HED parent body regolith indicates gentle accretion of the xenolithes,i.e. the small relative velocities of the HED-parent body and the exotic clasts. It could also indicate a genetic link between host and clasts [14].

ACKNOWLEDGEMENTS. MAN was supported by the Russian Research Foundation (Project 93-05-9222). Support by the Austrian FWF (Project P 8125-GEO) is gratefully acknowledged.

REFERENCES. [1] Nazarov M. A. et al. (1993) LPSC, XXIV, 1053. [2] Brearley A. J. (1993) LPSC, XXIV, 183. [3] Bunch T. E. et al. (1979) GCA, 43, 1727. [4] Reid A. M. et al. (1990) GCA, 54, 2161. [5] Zolensky M. E. et al. (1992) Meteoritics, 27, 596. [6] Brearley A. J. and Prinz M. (1992) GCA, 56, 1373. [7] Laul J. C. and Gosselin D. C. (1990) GCA, 54, 2167. [8] Wang M. S. et al. (1990) GCA, 54, 2177. [9] Metzler K. et al. (1992) GCA, 56, 2873. [10] Nazarov M. A. et al.(1994) this volume. [11] Kurat G. et al. (1992) LPSC, XXIII, 747. [12] Spettel B. et al. (1978) Meteoritics, 13, 363. [13] Bunch T. E. and Chang S. (1980) GCA, 44, 1543. [14] Kurat G. (1990) Meteoritics, 25, 377.

Table:
Chemistry of carbonaceous matrices (wt %).

	Average Erevan matrix	S.d.	Serp.-rich lithology (dust mantle)	Cronst.-rich lithology
Na	0.18	0.12	0.05	0.04
Mg	10.68	1.66	12.05	7.84
Al	1.49	0.48	1.08	1.23
Si	14.02	1.28	14.31	11.78
S	3.13	1.16	1.79	2.92
K	0.11	0.08	0.00	0.00
Ca	0.60	0.53	0.58	0.10
Ti	0.08	0.03	0.06	0.06
Cr	0.60	0.67	0.17	0.12
Mn	0.23	0.08	0.14	0.16
Fe	23.67	3.84	12.98	28.92
Co	0.06	0.02	-	-
Ni	1.33	0.32	0.75	0.62

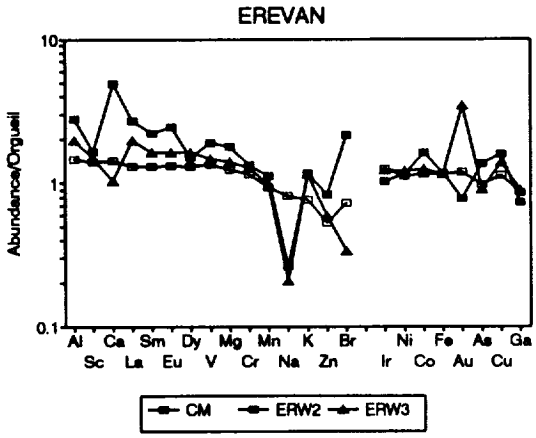

Figure 1

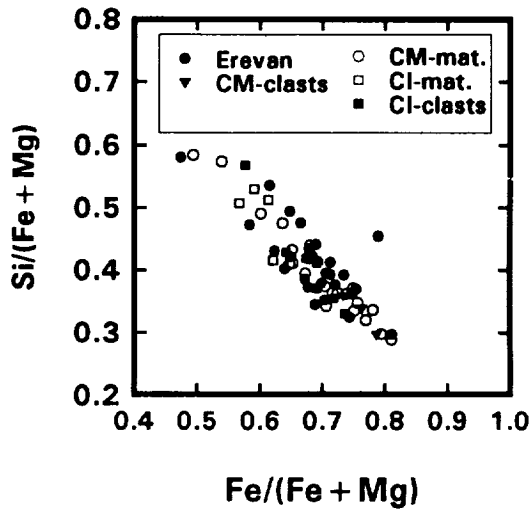

Figure 2

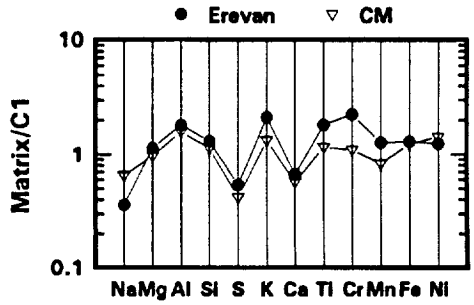

Figure 3

UTILIZATION OF ICP-MS ANALYTICAL TECHNIQUES FOR DETERMINATION OF SIDEROPHILE-ELEMENT ABUNDANCES: POTENTIAL USES FOR THE PLANETARY GEOCHEMIST.

Clive R. Neal, Dept. of Civil Engineering & Geological Sciences, University of Notre Dame, Notre Dame, IN 46556; Lawrence A. Taylor, Dept of Geological Sciences, University of Tennessee, Knoxville, TN 37996

Differentiation of the terrestrial planets into a zoned entity composed of a crust, mantle, and core requires a total re-organization of the chemical budget. The mantle will be deficient in those elements which are concentrated in the crust and the core. While the timing of such differentiation events occurred shortly after accretion [1], the exact nature and timing of the processes involved remain enigmatic [2]. On Earth, no rocks older than ≈ 3.8 Ga have survived so in order to examine the differentiation this planet, chemical signatures must used. Critical in tracing core formation are the siderophile-element abundances, which would be preferentially partitioned into the FeS/Fe-metal core. Indeed, the Earth's mantle is depleted in these elements relative to primordial CI chondrites (e.g., [3-6]). It is the magnitude of these depletions which is used to model core formation producing the following models: 1) Heterogeneous Accretion - multiple accretion and core formation stages (e.g., [7,8]); 2) Inefficient Core Formation - retention of Fe-metal + sulphides in the mantle during core formation (e.g., [9,10]). These depletions produce siderophile element abundances (W, Mo, Ru, Rh, Pd, Ir, Pt, Au, Sn, Sb) in a primitive mantle of 0.5 to 20 ppb [4,11]. Siderophile element abundances from lunar rocks indicate they are depleted by a factor of 27±20 [12] relative to the Earth's mantle. Accurate determination of these elements at such low abundances is critical for the development of the models briefly outlined above. Previously, siderophile element abundances have been determined by neutron activation techniques (e.g., [11]), nickel assay ICP-MS (e.g., [13]), and isotope dilution spark-source mass spectrometry [14]. Neutron activation requires irradiation and several weeks for completion of the counting procedures, nickel assay ICP-MS requires a pre-concentration stages prior to dissolution, and ID-SSMS requires a lot of sample preparation and can only analyze for a limited number of elements at any one time

The purpose of this paper is to report an initial study using ICP-MS analytical techniques as a fast and accurate method for siderophile element determination. The ultimate goal is to be able to accurately determine the abundances of a number of siderophile elements in silicates without pre-concentration.

ICP-MS TECHNIQUE: The initial study utilized a VG PQIISTE quadrupole ICP-MS fitted with a de Galan "V-groove" nebulizer. This was coupled with standard liquid sample introduction apparatus. The spray chamber was cooled to 5°C and the aspirated liquid sample was taken into a plasma of high purity (99.999% Ar) dry argon, where it was ionized. The machine was first tuned using a 10 ppb solution of Be, Co, In, Ce, Pb, Bi, and U. The signal was optimized at In and Pb in order to give the strongest signal over the desired mass range. The ion beam was detected in pulse counting mode and each sample was analyzed for 40 seconds in scanning mode.

Samples were prepared from a stock solution of SPEX standard containing 10 ppm Ru, Rh, Pd, Sn, Sb, Te, Hf, Ir, Pt, and Au. Samples and standards were prepared at 1 ppb, 750 ppt, 500 ppt, 250 ppt, 200 ppt, 150 ppt, 100 ppt, and 50 ppt in a matrix of 10% HCl. Three internal standards (all at 10 ppb) were used to cover the mass range and these were Sr, Sm, and Pb. One standard and five sample analyses were undertaken at each concentration.

RESULTS: Results for 50 ppt, 500 ppt and 1 ppb samples are presented in Fig. 1 along with 1 sigma error bars. These results are not directly blank subtracted and the method of standardization attempts to remove such background effects. For example, standard samples are plotted on a graph of concentration (entered by the user) against counts per second detected by the machine. At zero concentration, all standards intersect the cps axis beneath the 50 ppt standard, but above zero cps. This appears to be successful at removing blank effects at higher concentrations, but blank contributions may be raising the 50 ppt samples above the 50 ppt level (Fig. 1a). Blank levels were calculated by twice analyzing a 10% HCl solution spiked with the

internal standards. NOTE: the HCl was only single distilled and blank levels calculated using the standards from this study are as follows: 55 ppt Ru; 15 ppt Rh; 24 ppt Pd; 46 ppt Sn; 20 ppt Sb; 16 ppt Hf; 25 ppt Ir; 20 ppt Pt; and 2 ppt Au. Further interpolation of the standard data is required to totally remove the effects of blank contributions. It is envisaged that double-distilled acids will allow a further reduction of these blank levels to allow lower concentrations to be analyzed (see below).

It is evident that characterization of siderophile element concentrations down to 50 ppt is possible using the ICP-MS set-up outlined above, although analysis of the raw data indicates that the detection limit is approached at 50 ppt. There are many factors which can account for the error bars associated with some of these analyses (i.e., Pd and Sn), such as high ionization potential, blank levels (see above), machine stability, etc. Optimizing the ion beam in order to sample the area in the plasma which is most efficiently ionizing the siderophile elements can be carried out by adjustment of the torch position. Machine short-term stability is generally better than 5% across the mass range, but can be improved by use of the USN which allows increased stability and sensitivity. It is essential at such low concentrations that the aerosol is desolvated as high solvent loadings lead to high levels of interference ions [15]. Detection limits are usually improved by an order of magnitude by use of the USN [16]. The ICP-MS facility at Notre Dame is in the process of installing an USN.

PROBLEMS: The above discussion demonstrates that the ICP-MS can be used to analyze for siderophile-element abundances. Application to "real rocks" is currently underway and blank levels in HF, HNO_3, and $HClO_4$ acids (all double distilled) will be closely monitored. Problems of dissolution of refractory phases is a potential problem, but for the siderophile elements Totland et al. [17 suggested that microwave digestion is adequate to ensure that phases containing these elements are fully dissolved. Such a set-up is available at Notre Dame. Another problem is detection limit coupled with reproducibility. While we have analyzed the standard solutions five times using the somewhat crude technique outlined above, the reproducibility, especially at 50 ppt, needs to be substantiated. Furthermore, the ICP-MS requires dilution of solid samples to ≤ 2% total dissolved solids (TDS). This translates to extremely low siderophile element concentrations, especially as abundances are generally low to begin with. For example, an elemental concentration of 5 ppb translates to 100 ppt at 2% TDS. While such a concentration is within the detection limits of the technique described above, an initial concentration of 0.5 ppb will require the use of the USN.

CONCLUSIONS: The ICP-MS can analyze siderophile element abundances down to 50 ppt concentrations (after dilution to ≤ 2% TDS). Extending these detection limits to lower values requires reduction of blank levels in reagents, as well as use of an ultrasonic nebulizer to increase machine stability. Work is currently underway to fully quantify this analytical technique and its application to rock samples.

REFS: [1] Solomon et al. (1981) BVSP, 1129-1234; [2] Newsom (1990) Origin of the Earth, 273-288; [3] Chou et al. (1983) PLPSC 13th, A507-A518; [4] Wänke et al. (1984) Archean Geochemistry, 1-24; [5] Drake et al. (1989) GCA 53, 2101-2111; [6] Newsom et al. (1986) EPSL 80, 299-313; [7] Chou (1978) PLPSC 9th, 219-230; [8] Wänke (1981) Phil. Trans. Roy. Soc. London A303, 287-302; [9] Arculus and Delano (1981) GCA 45, 1331-1343; [10] Jones and Drake (1986) Nature 322, 221-228; [11] Sims et al. (1990) Origin of the Earth, 291-317; [12] Newsom (1986) Origin of the Moon, 203-229; [13] Jackson et al. (1990) Chem. Geol. 83, 119-132; [14] Jochum et al. (1988) Fresenius Z. Anal. Chem. 331, 104-110; [15] Williams (1992) Hdbk. of ICP-MS, 58-80; [16] Tingfa et al. (1990) J. Anal. Atom. Spectrom.; [17] Totland et al. (1992) Chem. Geol. 95, 35-62.

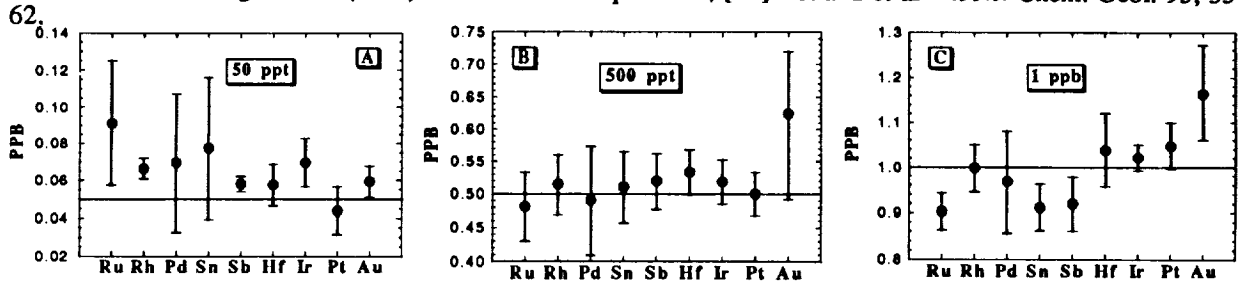

THE HERMES MERCURY ORBITER MISSION: Robert M. Nelson (1), Linda J. Horn (2), James R. Weiss (3), and William D. Smythe (4), all at Jet Propulsion Laboratory

Hermes is a Discovery class mission under study which is intended to investigate the feasibility of placing a spacecraft in orbit about the planet Mercury. It is a response to NASA's challenge to the planetary exploration community to develop missions within strict resource limits. The Hermes mission will complete the exploration of Mercury, a body whose surface is 60% unmapped. The planet has been surveyed only once by a spacecraft -- the Mariner 10 flyby mission in the 1970's. The goal of the mission is to understand Mercury's significance in planetary formation by determining the topography, composition, texture and mineralogy of the surface, searching for condensates at Mercury's poles and constraining the planet's interior structure.

The instruments on board the Hermes spacecraft will permit investigations into important scientific questions regarding Mercury including:

(1) The search for expressions of volcanism on the planet's surface.
(2) The search for iron in the crust.
(3) Identification and mapping of hypothesized water ice polar caps.
(4) The role of impact cratering in the evolution of the surface.
(5) The distribution and production and loss rates of the species comprising Mercury's tenuous atmosphere.
(6) The nature of Mercury's magnetic and gravitational fields and their relationship to the planets interior.

Hermes' highly elliptical, near polar orbit will permit mapping of the entire surface at 1 km resolution and a significant fraction (40%) will be mapped at 0.1 km resolution. These data will enable investigators to search for morphological changes that have occurred on Mercury since the Mariner 10 flyby mission. In addition to a multispectral CCD camera, the spacecraft will support a magnetometer, a ultraviolet spectrometer and a lidar.

Recent major advances in mission design, spacecraft and instrument technology, and ground system operations offer the opportunity to complete this mission at modest cost. The mission design concept calls for two flybys of Mercury followed by insertion in a 12-hour 200x15,000 km orbit. This strategy enables Hermes to use a low cost Delta II launch vehicle. The Hermes spacecraft is a TRW Lightsat that is based on spacecraft designs of recent vintage. This modification of current technology is financially attractive compared to developing a new spacecraft. The Hermes data system uses new concepts of centralized design to increase efficiency over recent decentralized data system concepts.

HERMES MERCURY ORBITER: Nelson et. al.

The temperature extremes of the Hermean environment present a challenge to spacecraft thermal design. To respond to these challenges the Hermes spacecraft will employ a variety of active and passive thermal control technologies including concepts as straightforward as sunshields to more sophisticated concepts such as heat pipes.

Hermes will utilize a ground operations system of previously proven design rather than building a new system from scratch. This will be based on the multi-mission support concept in which one ground system will maintain the personnel and equipment for several missions.

The Hermes study shows that by astute use of recent advances in space technology Discovery class missions can remain within budgetary constraints and not compromise quality science.

This work was carried out at JPL under contract with NASA.

1. Principal Investigator, Hermes Study
2. Deputy Principal Investigator, Hermes Study
3. Project Manager, Hermes Study
4. Deputy Project Manager, Hermes Study

ATMOSPHERIC OSCILLATIONS INITIATED BY THE PENETRATION OF OF A COMET OR AN ASTEROID INTO GASEOUS ENVELOPE OF A PLANET

I.V. Nemtchinov, T.V. Loseva (Institute for Dynamics of Geospheres, Russian Academy of Sciences, 38 Leninskii Prospekt, build.6, Moscow, 117979, Russia)

Lateral spreading of the body due to aerodynamic stresses leads to the disruption of a cosmic body. The simple model [1] leads to the relation $Ro/H = (\rho o^*/\rho o)^{1/2}$, where Ro is the initial radius of the body, ρo - its density, H - the characteristic scale of the atmosphere at the height Z* of the disruption, ρa^* is the density of the atmosphere at this altitude. The mass of the atmosphere Ma , entrained into motion behind the blast wave is much larger then the mass of the body Mo, and the velocity much lower then the impact velocity V. When the radius of the shock wave becomes larger then H the atmospheric gas is ejected into the rarefied layers, and the energy is converted into the kinetic energy of the plume with the velocity $Ve = V\,(Mo/Ma)^{1/2} = V(Ro/H)^{1/2}$. For the Shomaker-Levy comet [2] impacting into Jupiter with the initial velocity V = 60 km/s, assuming $\rho o = 1$ g/cm^3, spherical shape with radius Ro = 0.5 km we obtain the kinetic energy $Ek^o = 0.9\cdot10^{28}$ erg, $Mo = 0.5\ 10^{15}$ g, $\rho a^* = 3\cdot10^{-4}$ g/cm^3, H = 60 km, Z* = -70 km and Ve = 6 km/s.

The expanding fireball is changing to the conical jet with the angle of divergence of about 40-50°. The ejected mass is raised against the gravity field to the height Zm ($Zm = Ze + Ve^2/2g$, where Ze is the height of the ejection). For Ve = 6 km/s we obtain Zm-Ze = 600 km. Having reached the maximum height the ejected atmosphere with the addition of small amount of the comet's substance vapor is falling back and its velocity is close to the ejection velocity.

The flow pattern resembles a fountain. The radius Rf of this fountain at the height of the ejection is 2(Zm-Ze) and the area of the cross section $Sm = 4\pi(Zm-Ze)^2$. For Rf = 1200 km and $Sm = 4\ 10^{16}$ cm^2 we obtain the specific mass $m=Ma/S= 0.6$ g/cm^2. This falling gas compresses the atmosphere and a reflected shock wave is created. The heated gas once more is ejected into the upper rarefied layers. This is the initial substantially nonlinear stage of the acoustic gravitational waves generation. The estimates of the temperature in this shock wave and its location has been obtained by the solution of a 1D-plane nonstationary gas dynamic problem for different masses m, velocities Ve and etc. The results for m = 0.7 g/cm^2, average velocity Ve = 7.9 km/s, Ze = 240 km, the initial length of the jet l = 310 km are typical. The trajectories of different particles are given in Fig.1 (They are labeled by the initial altitudes in km). Amplitude of the oscillations increase with

ATMOSPHERIC OSCILLATIONS: Nemtchinov I.V. et al.

the height of the layer under considerations. They create a large displacement of the ionosphere layers, usually located at the heights of 500-2000 km [2]. Gas dynamic profiles as functions of the time are shown in Fig.2. The dotted curves correspond to the equilibrium characteristics of the atmosphere before the impact. At the height Z > 300 km the density is increasing by many orders of the magnitude and the temperature is very low - less then 50 K due to adiabatic cooling. The condensation of the hydrogen is even possible. But the heating of the shock wave (up to 500-100 K) will lead to its evaporation.

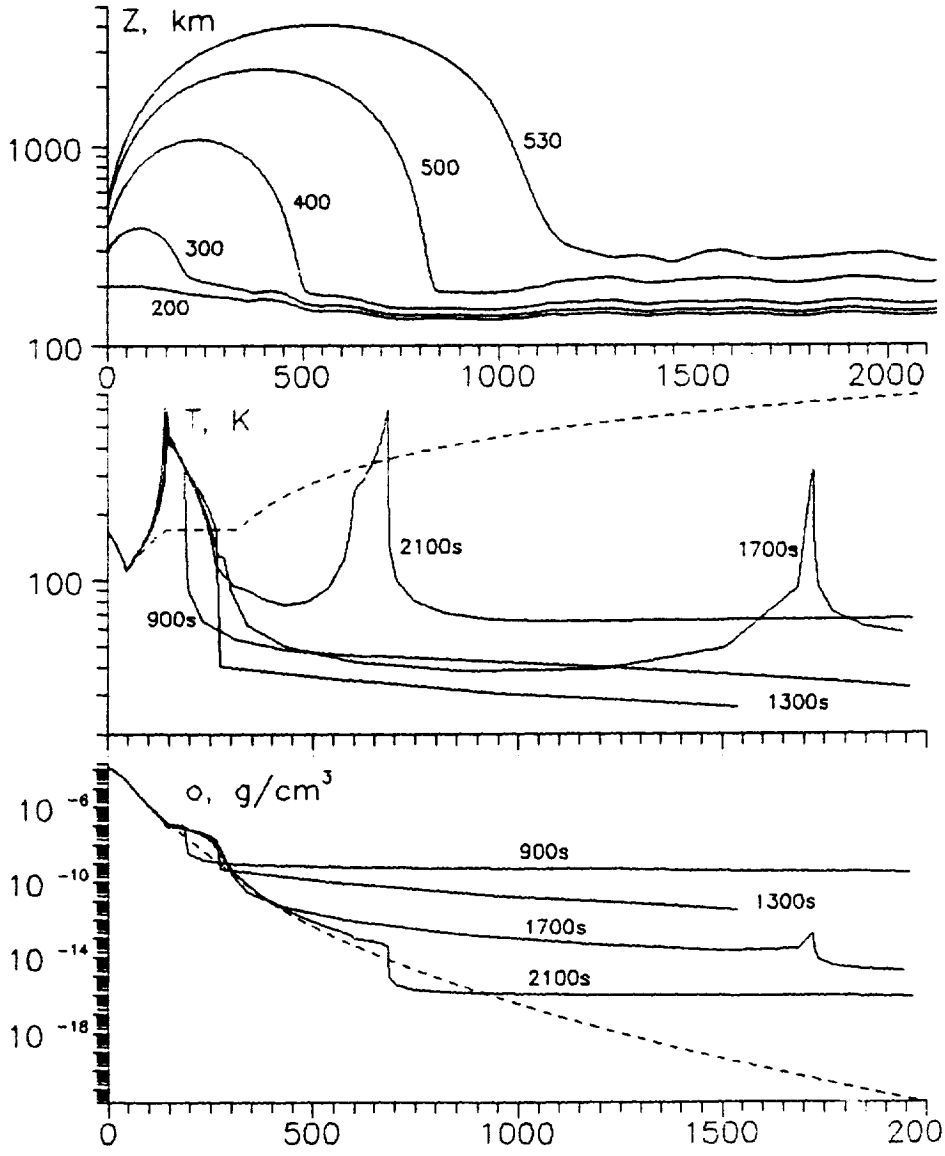

Fig.1

Fig.2(a)

Fig.2(b)

References: 1.Melosh H.J.(1989) Impact cratering: a geological process. Oxford University press, NY, Claredon press, Oxford. 2. Chapmen C.R. (1993) Comet on target for Jupiter, Nature, **363**, 492-493. 3 Gehrels T. (1976) Jupiter. The University of Arizona press, Tucson, Arizona.

WAVES CREATED BY COMET IMPACT INTO OCEAN

Nemtchinov I.V.,Teterev A.V.,Popov S.P. (Institute for Dynamics of Geospheres, Russian Academy of Sciences, 38 Leninskii Prospekt, build.6, Moscow, 117979, Russia)

Impact of large cosmic bodies into oceans and seas leads to the formation of very high waves. Numerical simulations [1,2] have given detailed picture of hydrodynamic processes caused by a vertical impact of large asteroid (modeled as a 10-km diameter stony sphere) with the velocity 20-30 km/sec. The water wave is moving ahead of the ground rim up to 120 sec.

We have carried out numerical simulations of a comet (modeled as a sphere of water) impacting into 4 km depth ocean. The velocity was assumed to be 20 km/sec. We used the same equation of state for the comet as for oceanic water. This semiempirical EOS has been calculated and given to us by G.S. Romanov's group (Heat and Mass Transfer Institute, Minsk, Belarus). We suppose that rocks of the oceanic are similar to that of the granite and used Tillotson EOS [3].

For 6-km diameter comet at 10 sec after impact the height of the dense water rim is 6 km (see Fig.1, isodensity contours labeled 1-9 correspond to the densities 0.01, 0.13, 0.26, 0.38, 0.50, 0.63, 0.75, 0.88 and 1.0 g/cm^3). Dots correspond to the oceanic bed. The ejected material is reaching the water wave at 18 km. At 25 sec the height of the wave is 4 km, depth of the transient crater is 14 km, its diameter is 24-25 km, the velocity of the water in the rim is about 1 km/sec.

For a 2-km diameter comet the height of the water is 4 km at 20 sec at 13 km and 1 km at 42 sec after the impact at the distance of 18 km from the impact point (Fig.2). The water rim is breaking away from the ground rim (it is located approximately at 15 km radius). Thus the decrease in the diameter of the impacting body changes the mechanism of water wave generation.

The impact of the huge mass of water onto the shore and near shore mountain ridges can cause the displacement of the rocks and initiate the landslips, and change the relief. It is now well established that impacts onto the planet's surface are the important geological process [3]. We see that the same may be true for the impacts onto oceans and sees.

At large distances from the impact the waves decrease their amplitude but may still be high enough. These stages of wave propagation have been simulated using the shallow water approximation. A N - type wave is formed (see Fig.3 for a 10 km body impact, the time t is in sec). The height of the wave is decreasing approximately inversely proportional to the distance. At t = 5100 sec the height of the wave is 300 m at the distance of 850 km. For a 2 km comet it is 10 m at the distance of 2000 km. The hazardous tsunamis may be the result [4].

COMET IMPACT INTO OCEAN: Nemtchinov I.V. et al.

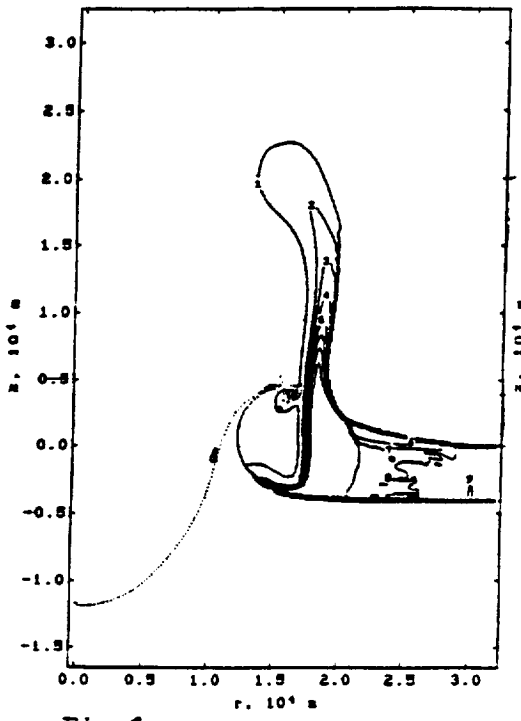

Fig.1

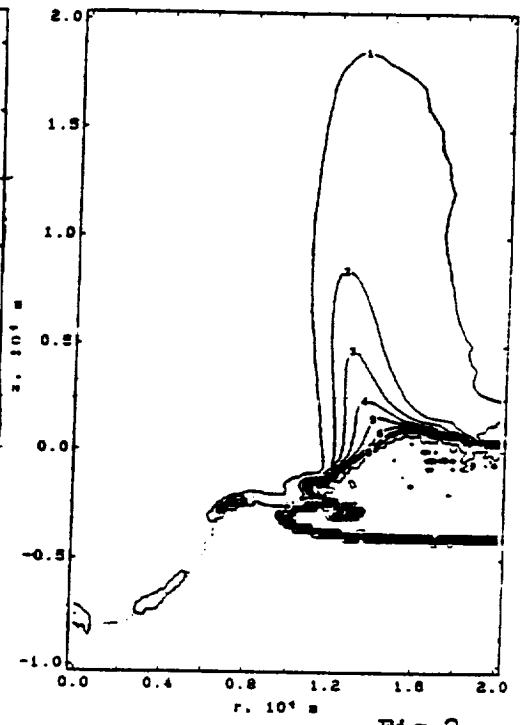

Fig.2

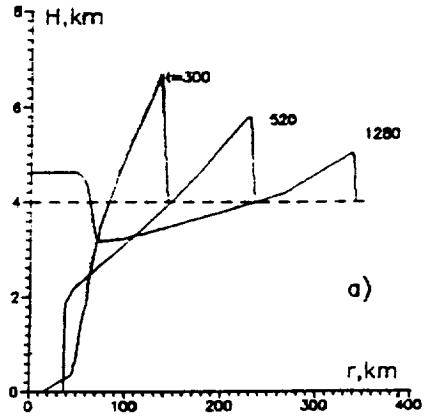

Fig.3

References: 1. Ahrens T.J. and O'Keefe J.D. (1987) Int. J. Impact Eng. 5, 13-32. 2. Roddy D.J. et al. (1987) Int J. Impact Eng. 5, 123-135. 3. Melosh H.J. (1989) Impact cratering a geological process. Oxford University Press, NY. 4. Hills J.G., Goda M.P. (1993) Astrophys. J. 105, 114-1144.

THE INNER SOLAR SYSTEM IMPACT RECORD: LUNAR, TERRESTRIAL-PLANET, AND ASTEROID SIZE-FREQUENCY DATA COMPARISON; G. Neukum, DLR, Institute for Planetary Exploration, Berlin, Germany; and B. Ivanov, Institute for Dynamics of Geospheres, Moscow, Russia

The terrestrial planets, the earth's moon, Mars, Venus, and Mercury show similarities in their production crater size-frequency distribution characteristics. The recent results from the Galileo mission flybys of the main belt asteroids Gaspra and Ida [1, 2] yield information on the crater size-frequency distribution in the source region of the bodies largely responsible for cratering the inner solar system planets. The purpose of this paper is to review the wealth of cratering data which have been gathered for the moon and for the terrestrial planets in combination with the latest results for Gaspra and Ida. This is done with a new model, taking into account major parameters controlling the cratering process: gravity and strength of a target body as well as the average velocity of impacting projectiles.

1. Production crater size-frequency distributions of the terrestrial planets:

The basis for the inter-planetary comparisons, as the best determined and most reliable data set, is the lunar production crater size-frequency distribution function termed standard or calibration distribution [3, 4, 5]. The standard distribution is a complex function with values of the distribution index, i.e. the exponent α in a power law for the cummulative crater size-frequency $N \propto D^{\alpha}$, where α varies between -1 and -4. Our modelling exercise shows that the complex form of the standard distribution curve may only partially be connected with intrinsic effects of the cratering processes. Mostly the curve reflects the complex distribution of projectile sizes.

Using the lunar curve and scaling it to the other terrestrial-planet impact conditions demonstrates the close similarity of the distributions measured on the other terrestrial planets [6, 7]. The new data from Galileo's images of Gaspra confirm the steep slope of the standard distribution for crater diameters below 1 km. The Gaspra crater size-frequency distribution is an argument against the point of view, that secondary craters make a major contribution to observed small-crater size-frequency distributions (cf. [8]).

2. Influence of cratering mechanics on the size-frequency distributions:

In order to compare crater size-frequency distributions and cratering rates on different planets in a rigorous way we take into account (i) the projectile flux variations in space and possibly in time and (ii) a number of parameters controlling the impact cratering process such as gravity, atmospheric conditions, crustal strength, density and structure, as well as projectile density and impact velocity.

For simplification we use a constant ratio of target/projectile densities. In order to avoid calculating the impact velocity distributions for each planet (still poorly defined) we use "average" or "typical" values of impact velocity for each planet. These values correspond to averaged impact parameters of planet-crossing asteroids derived from the main belt with eccentricities of e=0.6 [9]. The same procedure is used to compare gravity enhancement of cross-sections of different planets.

The scaling laws derived for the cratering processes take into account a smooth transition from strength to gravity regimes (like in [10]), and Croft's model [11] of crater gravity collapse for complex craters. The "coupling parameter" concept [12] is used to compare cratering efficiencies at different impact velocities.

The output of the model is a set of theoretical size-frequency distributions for Mercury, Venus, Earth, Mars, Gaspra and Ida, recalculated from the lunar standard curve. These theoretical

distributions are in good accordance with the terrestrial data (old cratons) for craters above 10 km diameter. A simple power law with a distribution index α=-2 as has commonly been used so far [13] fits the same data in a much cruder way only above 20 km crater diameter. For Venus, the model fits the Magellan data well above 20 to 30 km crater diameter where the atmospheric influence is not as large as for smaller craters.

Recalculation of the lunar standard distribution for Gaspra has been done provided that the observed craters are strength controlled. The fitted Gaspra crater distribution may be extrapolated to the range of hypothetical projectiles larger than 50 km in diameter, which allows direct comparison with the intrinsic probability of collision for the asteroid belt [14].

The observed crater distribution for Ida is well approximated with a recalculated lunar curve for craters larger than 2 km diameter. Craters smaller than 1 km on Ida have a shallower distribution (α=-2) than the recalculated standard distribution, indicating an equilibrium state for the small craters. The surface of Ida seems to be at least 10 times older than that of Gaspra.

Conclusions:

The overall complex shape of the lunar production crater size-frequency distribution curve cannot be made compatible with simple power-law distributions for the underlying impactor size distributions taking into account the known scaling laws for impact cratering. The lunar calibration distribution is a useful tool for approximating the size-frequency distributions on other terrestrial planets provided the appropriate scaling corrections are made. This leads to the conclusion that one and the same family of impactors is responsible for cratering the inner-solar system planets from very early times (post-accretion bombardment) until the present, that the size distribution characteristics of this impactor family have been rather constant through time, and that this impactor family is largely derived directly from the main asteroid belt.

References:

[1] Chapman, C. R. et al. (1994) LPSC **XXV** submitted
[2] Neukum, G. (1994) unpublished data, to be published as part of the reports of the GLL Imaging Team
[3] Neukum, G. et al. (1975) The Moon **12**: p. 201-229.
[4] Neukum, G. and König, B. (1976) Proc. Lunar Sci. Conf. **7th**: pp. 2867-2881.
[5] Neukum, G. (1983) Habilitation Dissertation for Faculty Membership, Ludwig-Maximilians-University of Munich, 186 pp.
[6] Neukum, G. and Hiller, K. (1981) J. Geophys. Res. **86**: p. 3097-3121.
[7] Strom, R. G. and Neukum, G. (1988) In "Mercury" (eds F.Vilas, C.R.Chapman, M.S.Matthews), University of Arizona Press, p. 336-373, Tucson
[8] Soderblom, L.A. et al. (1974) Icarus **22**: p. 239-263
[9] Horedt, G. P. and Neukum, G. (1984) J. Geophys. Res. **89**: p. 10,405-10,410
[10] Holsapple, K. A. and Schmidt, R. M. (1979) Proc. Lunar Planet. Sci. Conf. **10th**, p. 2757-2777
[11] Croft, S. K. (1985) Proc. Lunar Planet Sci. Conf. **15th**: p. C828-C842
[12] Schmidt, R. M. and Housen, K. R. (1987) Int. J. Impact. Engng. **5**: p. 543-560
[13] Grieve, R. A. F. (1984) Proc Lunar Planet Sci. Conf. **14th**: p. B403-B408
[14] Farinella, P. and Davis, D. R. (1992) Icarus **97**: 111-123

PATTERNS OF BRITTLE DEFORMATION UNDER EXTENSION ON VENUS; *G.A. Neumann*[1] and *M.T. Zuber*[1,2], [1]Department of Earth and Planetary Sciences, Johns Hopkins University, Baltimore, MD 21218, [2]Laboratory for Terrestrial Physics, NASA/Goddard Space Flight Center, Greenbelt, MD 20771.

The development of fractures at regular length scales is a widespread feature of Venusian tectonics. Models of lithospheric deformation under extension based on non-Newtonian viscous flow and brittle-plastic flow [1,2] develop localized failure at preferred wavelengths that depend on lithospheric thickness and stratification. The characteristic wavelengths seen in rift zones and tessera can therefore provide constraints on crustal and thermal structure [3]. Analytic solutions were obtained by [4] for growth rates of infinitesimal perturbations imposed on a one-dimensional, layered rheology. Brittle layers were approximated by perfectly-plastic, uniform strength, overlying ductile layers exhibiting thermally-activated power-law creep. This study investigates the formation of faults under finite amounts of extension, employing a finite-element approach. Our model incorporates non-linear viscous rheology and a Coulomb failure envelope in the manner of [5]. An initial perturbation in crustal thickness gives rise to necking instabilities. A small amount of velocity weakening [cf. 6] serves to localize deformation into planar regions of high strain rate. Such planes are analogous to normal faults seen in terrestrial rift zones. These "faults" evolve to low angle under finite extension [cf. 7]. Fault spacing, orientation and location, and the depth to the brittle-ductile transition, depend in a complex way on lateral variations in crustal thickness. In general, we find that multiple wavelengths of deformation can arise from the interaction of crustal and mantle lithosphere.

To calculate patterns of deformation, we use a finite element (FE) program for incompressible Newtonian viscous fluid flow via the penalty method [8], modified to treat non-Newtonian flow problems [9,10]. Gravitational body loads are applied to individual elements. An initial viscosity is calculated for a state of uniform extension using the power-law relation

$$\mu_{eff} = B\dot{\varepsilon}_{max}^{(1-n)/n} \exp(Q/nRT), \quad (1)$$

where $\dot{\varepsilon}_{max}$ is the maximum principal shear strain rate, n is the power-law exponent, R is the gas constant, T is temperature, Q is the material activation energy, and B is a material strength constant. An iterative procedure re-calculates the effective Newtonian viscosity $\mu(i,j)$ for each quadrilateral FE. The maximum viscosity is limited to that allowed by the Coulomb failure criterion. Before proceeding with any time-steps, we iteratively calculate the deviatoric strain rate at zero strain resulting from the brittle-plastic and velocity-weakening effects. Strain rates are locally enhanced in elements with ductile strength less than that of mantle at the base of thickened crust. Higher strain rates imply reduced effective viscosity of these elements. Strain is preferentially accomodated where viscosity is lower, leading to further reduction in strength. This feedback eventually results in highly localized rates of deformation, i.e., the material breaks and undergoes faulting. Localization of deformation is the result of non-linear dynamics and is somewhat unstable with respect to initial conditions. Generally more than 100 iterations are required to reach steady state, even with over-relaxation on strain rate. Finite deformation is then calculated by a second-order time-step integration, with dynamic topography developing at the free surface.

For the crust we use a recent experimentally obtained flow law for the rheology of diabase [11] under extremely dry conditions representative of the surface of Venus, with n=4.3 and Q=482 kJ/mol in equation (1). The stronger olivine rheology preferred by [5] is assumed for the mantle, with n=3 and Q=540 kJ/mol. The brittle-ductile transition thereby occurs at about 8-10 km in the crust and 15-20 km in the mantle. We employ a lithospheric thermal model as discussed in [3], with a surface temperature gradient of 25 °K/km. The initial strain rate is $\dot{\varepsilon}_0 = 10^{-14}$ s^{-1}. A brittle strength evelope provides an upper bound to viscosity at a given depth and strain rate, such that deviatoric stress $\tau_{max} \leq \sigma_0 + C\rho gz$. The Coulomb strength coefficient C is velocity-weakening, depending on strain rate as $C=C_0 - 0.05 \log_{10}(\dot{\varepsilon}/\dot{\varepsilon}_0)$, with $0.25<C<0.4$, $C_0 = 0.36$ and $\sigma_0 = 1$ MPa. This value of C_0 corresponds to an internal friction coefficient of about 0.71. A perturbation of crustal thickness between ±1 and ±10%, at a 50 to 100 km wavelength, is introduced.

For a range of crustal thicknesses of 8 to 18 km, preliminary results show that faulting develops at multiple scales when brittle-ductile transitions occur in both the crust and upper mantle, with the width of the shortest wavelength features being about twice the thickness of the brittle crust. Longer wavelength features occur at twice the depth to the base of the upper mantle lithosphere. The model boundary undergoes a prescribed rate of uniform extension. Integration of strain rate over time to overall strains of 10% produces conjugate patterns of faulting and rifting. Larger amounts of strain generally exceed the range of applicability of quadrilateral FE's.

BRITTLE DEFORMATION ON VENUS: Neumann, G.A. and M.T. Zuber

The pattern of normal faults and sloping terraces (Figure 1) indicates a fairly realistic simulation of the behavior of layered brittle-ductile rheology. Localized faulting develops when the initial perturbation wavelength is less than about 8 times the total thickness of the lithosphere (base of brittle mantle). Longer wavelength perturbations produce stable extension of the crust, and brittle-plastic necking of the mantle lithosphere. Perturbations at wavelengths of less than twice lithospheric thickness produce a single pair of conjugate normal faults meeting at the base of the crustal lithosphere. The growth of fault-like zones indicates a mechanism for the development of linear features at multiple scales due to extension in a Venus lithosphere with a variable-thickness crust. We plan to use this model to investigate the relationship between deformation patterns, wavelength of perturbation, and strength envelopes.

References: [1] Zuber, M.T., and E.M. Parmentier,*EPSL, 77,* 373-383, 1986. [2] Lin, J., and E.M. Parmentier, *JGR, 95,* 4909-4923, 1990. [3] Zuber, M.T., and E.M. Parmentier, *Icarus, 85,* 290-308, 1990. [4] Zuber, M.T., *JGR, 92,* E541-551, 1987. [5] Chen, Y., and J.W. Morgan, *JGR 95,* 17583-17604, 1990. [6] Scholz, C.H., *The Mechanics of Earthquakes and Faulting,* Cambridge Univ. Press, 1990. [7] Forsyth, D.W., *Geology, 20,* 27-30, 1992. [8] Bathe, K.-J., *Finite Element Procedures in Engineering Analysis,* Prentice-Hall, Inc.,1982. [9] Zuber, M.T. and E.M. Parmentier, in *Workshop on Mountain Belts on Venus and Earth,* 49-50, LPI, Houston, 49-51, 1992a. [10] Zuber, M.T. and E.M. Parmentier, *LPSC XXIII,* 1595-1596, LPI, Houston, 1992b. [11] Mackwell, S.J., and D.L. Kohlstedt, *EOS Trans. AGU, 74,* 378, 1993.

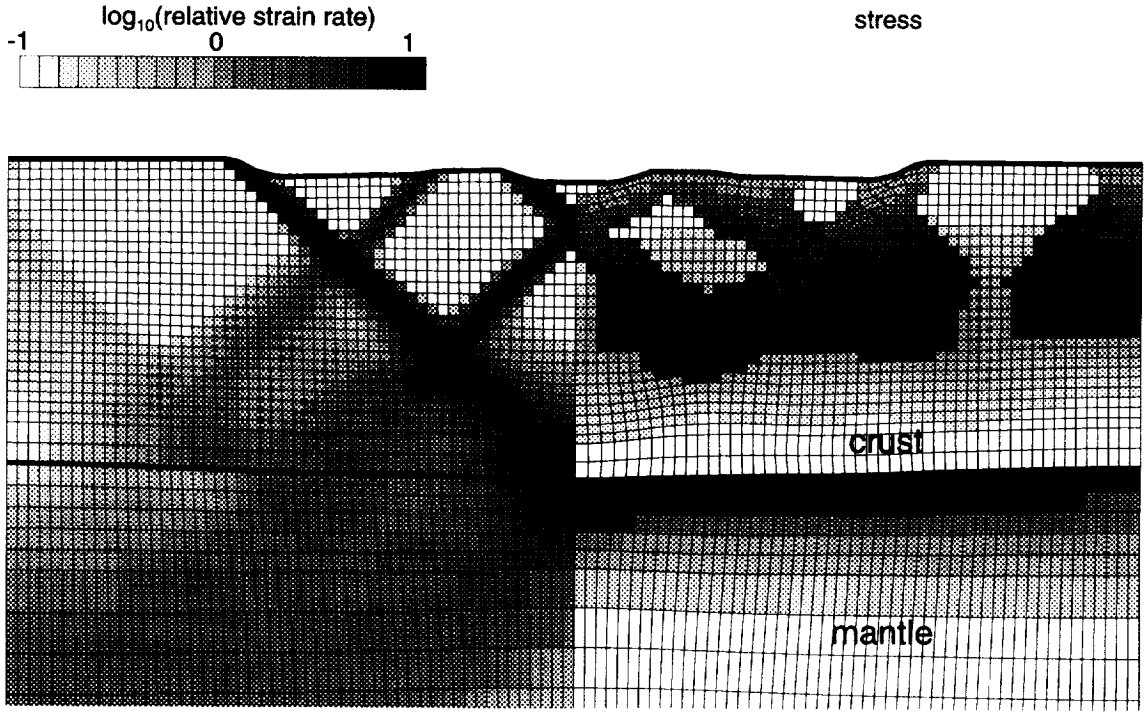

Figure 1. Finite element model with assumed flow laws and thermal structure. Original crustal structure is 50 km wide, 15 km deep, with ±5% variation in crustal thickness, greatest at the center. Density of crust is 2900 kg/m^3 and mantle is 3300 kg/m^3. The center of the grid is a symmetry axis, with periodic boundary conditions on the sides. The bottom boundary at 50 km depth has no vertical displacement, and is shear-stress free. The grid shown has undergone a total extension of 6%. Regions of high strain rate are shown on the left by the darkly shaded regions. Regions on the right are shaded where the Coulomb brittle failure envelope is locally exceeded. Dynamically produced topography at the surface reflects the perturbation wavelength as well as finer scales of faulting generated by the interaction of crustal and mantle lithosphere.

THE DEPLETION OF W IN THE EARTH'S PRIMITIVE MANTLE, A STUMBLING BLOCK FOR HIGH TEMPERATURE EQUILIBRIUM CORE FORMATION?

H.E. Newsom, P.D. Noll, Jr., and, S.A. Maehr, Institute of Meteoritics, Dept. of Earth and Planetary Sciences, University of New Mexico, Albuquerque NM 87131, K.W.W. Sims, Dept. of Geology and Geophysics, Berkeley CA.

Murthy [1], suggested that high temperature equilibrium between metal and silicate in the Earth could explain the siderophile element depletion pattern in the Earth. Although some of the detailed thermodynamic calculations have been shown to be flawed, the concept has prompted several experimental efforts to test the hypothesis [2,3]. Walker et al. [2] confirmed that some elements have decreasing metal partition coefficients with increasing temperature, but the work of Hilgren and Drake [3] has provided contrary evidence for the element W. The key question is whether the measured partition coefficient is consistent with the observed depletion of W in the Earth's primitive mantle. We have more than doubled the amount of data for terrestrial samples, with the addition of data for lower crustal xenoliths [4], island arc volcanics [5] and continental arc samples [5]. The new data confirm earlier results for the depletion of W in the Earth's primitive mantle, but provide much greater confidence in the observed depletions.

The available data for W in terrestrial samples is plotted in Figure 1, using Ba (barium) as a normalizing element. The constant ratios of W and Ba in oceanic mantle derived samples strongly suggest that these elements have the same highly incompatible geochemical behavior during igneous fractionation. The determination of the W depletion in the Earth by Newsom and Palme [6] was based only on the data for the oceanic mantle derived samples and mantle nodules. A major question remaining was the abundance of W in the continental crust, which is a major reservoir for incompatible elements. Initial work on the ancient continental crust [7], suggested that the ancient continental crust was somewhat enriched in W relative to Ba, causing us to increase estimates for the abundance of W in the primitive mantle. Our recent data on the youngest continental crust, including intracontinental volcanics, however, indicates that this reservoir is more depleted in the W/Ba ratio. We have combined this data using the following procedure: 1. The average value and the standard error in log space was determined for the W/Ba ratios in the ancient continental crust, the young continental crust, and the depleted mantle. 2. The biggest uncertainty in obtaining a total continental crust composition is the amount of ancient crust compared to the total crust, for which estimates range from 90% down to 70%. 3. The continental crust is then combined with the data for the depleted mantle, taking into account the possibility that the depleted mantle could be either the entire mantle, or just the upper mantle. Our final range for the W/Ba ratio in the Earth is from 0.00157 to 0.00268.

In order to calculate the depletion relative to chondrites we have evaluated the W/Ba ratio in chondrites. The data is quite limited, as seen in Fig. 1. The W/Ba ratios for the chondrites are normalized to the Mg/Fe ratio of the chondrites compared to CI chondrite abundance's. In addition, a correction for the Mg/Fe ratio for the Earth has been added to the chondrite W/Ba ratios to account for the slightly greater Fe content of the Earth. The resulting range of possible depletion factors for the Earth is then calculated to be from 0.032 to 0.066, or a range of depletion factors from 31 to 15. This result is in close agreement with the earlier estimate of Newsom and Palme, [6]. Therefore, the discrepancy between the trend of the experimental partition coefficients for W and the observed depletion of W in the Earth is unlikely to be explained by an error in the observed depletion.

Conclusions The depletion of W in the Earth is now well established based on data for the major reservoirs accessible to study. The depletion of W is also consistent with the stepped depletion pattern for the primitive mantle which provides evidence against a simple explanation for the siderophile element depletion pattern in the Earth by equilibrium metal-silicate partitioning [8]. Additional improvements to the depletion factors for W can be made, with more data for samples derived from the depleted mantle, and with a better understanding of the relative amounts of ancient and young continental crust. Additional data for different chondrite groups will also be desirable.

Refs. [1] Murthy (1991), *Science, 253*, 303. [2] Walker et al. (1994) *Science*, submitted. [3] Hilgren and Drake (1993) *EOS 74*, 655. [4] Newsom and Sims (1992) *Goldschmidt Abs.* A-75. [5] Noll et al. (1994), *EOS, 74*, 674. [6] Newsom and Palme (1984) *Earth Planet. Sci. Lett. 69*, 354. [7] Sims, Newsom and Gladney (1990) in *Origin of the Earth*, Newsom and Jones eds., Oxford, 291. [8] Newsom, ibid., 273.

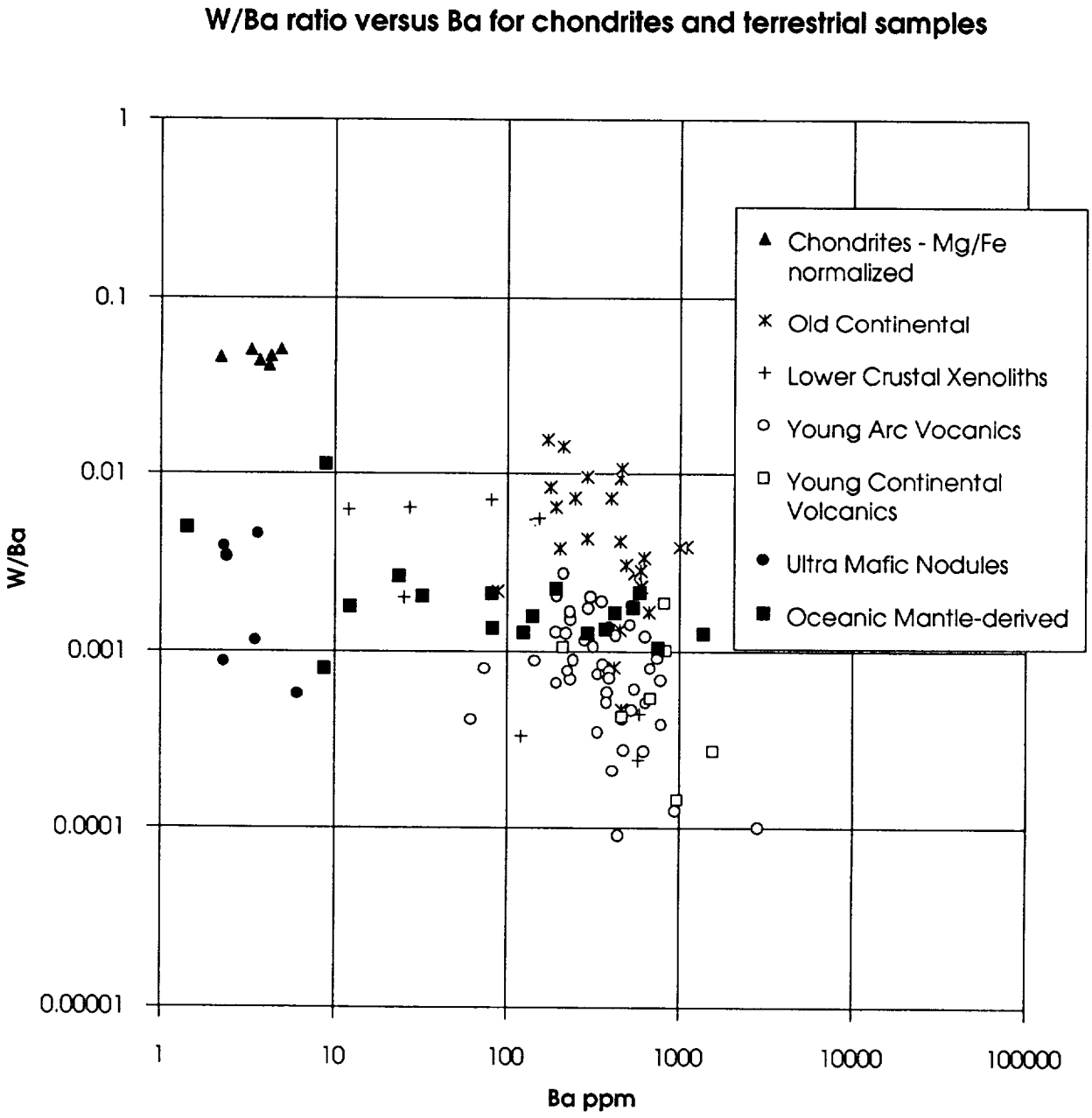
W/Ba ratio versus Ba for chondrites and terrestrial samples
W/Ba
1
0.1
0.01
0.001
0.0001
0.00001
1
10
100
1000
10000
100000
Ba ppm
Chondrites - Mg/Fe normalized
Old Continental
Lower Crustal Xenoliths
Young Arc Vocanics
Young Continental Volcanics
Ultra Mafic Nodules
Oceanic Mantle-derived

Figure 1

TRAPPED NOBLE GASES IN NATIVE GOLD; RADIOGENIC He AND FISSION Xe IN U-RICH MINERALS ACCOMPANYING PLACER GOLD; S. Niedermann[1], O. Eugster[1], Ch. Thalmann[1], R. Frei[2], J.D. Kramers[2], L. Bruno[3], and B. Hofmann[4], [1] Physikalisches Institut, University of Bern, Sidlerstrasse 5, CH-3012 Bern, Switzerland; [2] Mineralogisch-Petrographisches Institut, University of Bern, Erlachstrasse 9a, CH-3012 Bern, Switzerland; [3] ETH Zürich, Institut für Kristallographie und Petrographie, NO C 61, CH-8092 Zürich, Switzerland; [4] Naturhistorisches Museum, Bernastrasse 15, CH-3005 Bern, Switzerland

In our previous work [e.g. 1,2] we tried to find a dating method for native gold samples based on the U/Th-^{4}He and U-^{136}Xe methods. First results for Brusson (Northern Italy) vein-type gold [2] appeared to agree with those for the K-^{40}Ar age of associated muscovite (32 Ma [3]). However, these results were not very reliable since they were obtained by analyzing He, Th, and U in different splits of a sample, where concentrations often vary considerably. Moreover, for placer gold from the Napf area (Central Switzerland) we calculated ages of ~500 Ma [2], inconsistent with its supposed Tertiary origin. Here we present new U, He, and Xe data measured in the same splits of several samples [cf. 2]. These data do not confirm the U/Th-^{4}He ages for Brusson vein-type and Elvo placer gold given in [2]; instead we have gained more insight into the nature of noble gases present in native gold from their outgassing behavior in stepped heating experiments.

Fig. 1 is a plot of ^{4}He versus $^{40}Ar_r$ for various Alpine gold samples, where $^{40}Ar_r = {}^{40}Ar_{tot} - 296 \times {}^{36}Ar$. A strong correlation is evident not only for total extractions (closed symbols), but even for single temperature steps (open symbols). To explain these data by in-situ-produced radiogenic gases, a correlation between K and U would be required, but even then He should be released prior to Ar, as observed, e.g., in meteorites. In any case we know that $^{40}Ar_r$ is an inherited component, since measured K concentrations in Brusson gold can account for only ~1% of $^{40}Ar_r$ assuming an age of 30 Ma [4]. Because a correlation between in-situ-produced He and trapped Ar is very improbable, we infer that most ^{4}He in the gold samples shown in Fig. 1 is trapped as well. The similar release patterns for He and Ar indicate that both gases are concentrated in fluid inclusions and, therefore, are released simultaneously during break-up.

If ^{4}He in Alpine gold is trapped, then what has happened to the ^{4}He produced in-situ? ^{4}He production expected from U and Th decay during ~30 Ma is comparable to ^{4}He concentrations found in the samples, so in-situ-produced He would have to be largely lost. A preferential loss of radiogenic (in-situ-produced) He over trapped He is not an uncommon feature [e.g. 5]. Radioactive elements may be concentrated in accessory minerals, and radiation damages favor the loss of He atoms.

We have also analyzed a series of gold samples from the Sabie-Pilgrim's Rest gold field (Eastern Transvaal, South Africa). Temperature step extraction data for five single samples show similar correlations between ^{4}He and $^{40}Ar_r$ as observed for Alpine gold, with $^4He/^{40}Ar_r$ ratios from 0.7 to 2.6 in the different samples. In comparison, Alpine gold yields $^4He/^{40}Ar_r \approx 4$. A higher ratio for trapped gas in Tertiary than in Archean gold is expected because ^{40}K has a shorter half-life than ^{238}U, resulting in a decrease with time of crustal ^{40}Ar relative to ^{4}He.

In the above discussion, we have assumed that all ^{4}He has a radiogenic origin (although it was not produced in-situ). This assumption is supported by the observation that ^{20}Ne, ^{36}Ar, ^{84}Kr, and ^{132}Xe are present in nearly atmospheric ratios in gold, whereas $^4He/^{20}Ne$ ratios from a few hundred to $> 10^4$ are observed (air: $^4He/^{20}Ne = 0.32$). We also measured the $^3He/^4He$ ratio in Brusson gold and obtained $(0.22 \pm 0.18)\cdot10^{-6}$ (2σ error), confirming that the contribution from atmospheric He ($^3He/^4He = 1.4\cdot10^{-6}$) is small. The $^3He/^{20}Ne$ ratio of $> 10^{-4}$ is more than two orders of magnitude above the atmospheric value, indicating the presence of crustal or mantle He.

Whereas Brusson gold and most Sabie-Pilgrim's Rest samples release He and Ar at temperatures <800°C, a completely different pattern is observed for placer gold from Central Switzerland, which outgasses He mainly at ~1000°C [1]. These samples have considerably elevated, yet highly variable absolute He concentrations up to $5000\cdot10^{-8}$ cm^3 STP/g. An extreme case is a paleo-placer sample from the East Driefontain gold mine (Witwatersrand, South Africa) with $^4He = 163{,}000\cdot10^{-8}$ cm^3 STP/g. We have suspected such samples before to contain zircons or other U-rich minerals which were worked into the gold grains during transport in the river [2], therefore we have taken special care to remove such minerals in our latest experiments involving 3 large-grained splits of Grosse Fontanne (Napf area, Central Switzerland; ~1g each) and 3 splits of Elvo (south of Brusson; ~2g each). Optical inspection under ultraviolet light did not reveal the presence of any zircons. However, He abundances were clearly elevated in all six splits, and in fact after dissolution of the outgassed gold in aqua regia a few undissolved minerals – probably zircons – were observed, confirming that the high and varying He concentrations in placer gold samples are due to admixed or adjacent U-rich minerals.

Fig. 2 shows a correlation of ^{4}He and ^{136}Xe for those Elvo and Grosse Fontanne splits; included is also an earlier analysis of Krümpelgraben, another placer gold sample from the Napf area. Data points for Elvo and Napf area placer gold, respectively, lie on straight lines as expected for constant trapped gas abundances and for radiogenic He and fission Xe (Xe_f) produced in-situ from U. The slopes of the lines, corresponding to $^{136}Xe_f/^4He_r$, are $2.25 \cdot 10^{-9}$ and $2.53 \cdot 10^{-9}$, respectively, for the Napf area and Elvo samples. These values are somewhat lower than the production ratio from pure U (~$5.4 \cdot 10^{-9}$ [6]), indicating Th/U ratios of 5.9 and 4.8, respectively, in the minerals where ^{4}He and ^{136}Xe were produced.

For two of the Elvo splits, we have so far measured U abundances in gold and accompanying minerals separately. They are given in Table 1, together with U/Th-^{4}He and U-^{136}Xe ages of U-bearing minerals. It is not surprising that the minerals are much older than the gold. U/Th-^{4}He and U/^{136}Xe ages agree fairly well, however the results for EL-A24 and EL-A26 differ considerably, which may indicate variable ages of U-rich minerals.

Based on the results presented above, we conclude: (1) U/Th-^{4}He dating was not successful for the gold samples studied to date because of large concentrations of inherited ^{4}He in fluid inclusions and loss of in-situ-produced ^{4}He. (2) For placer gold, it is difficult to obtain pure samples which do not contain U-rich minerals, such as zircons. (3) For clean gold samples (particularly for vein-type gold), U-^{136}Xe or ^{39}Ar-^{40}Ar dating may be alternative methods, since unlike He, fission Xe is not expected to be lost, and ^{40}Ar loss may be recognized. However, large sample amounts as well as relatively high U concentrations and/or ages are required for the U-^{136}Xe method if accurate results are to be obtained.

Acknowledgements: We thank R. Boer and W.U. Reimold for the South African gold samples. Work supported by the Swiss NSF.

References: [1] Eugster O. et al. (1993) *LPS XXIV*, 455-456. [2] Niedermann S. et al. (1993) *Meteoritics* **28**, 411-412. [3] Diamond L.W. (1990) *Am. J. Sci.* **290**, 912-958. [4] Eugster O. et al. (1992) *Meteoritics* **27**, 219-220. [5] Kamensky I.L. et al. (1990) *Geochim. Cosmochim. Acta* **54**, 3115-3122. [6] Ragettli R. (1993) Ph. D. thesis ETH Zürich No. 10183.

Table 1 U abundances (ppm in relation to total sample weight) in gold and accompanying minerals and U/Th-^{4}He and U-^{136}Xe ages (Ma) of accompanying minerals for two splits of Elvo placer gold, Northern Italy.

Split #	U in Au	U in minerals	U/Th-^{4}He age		U-^{136}Xe age
			Th = 0	Th = 4.8 U	
EL-A24	0.200	0.076	879 ± 35	437 ± 18	940 ± 320
EL-A26	0.484	0.193	1697 ± 52	901 ± 32	1320 ± 250

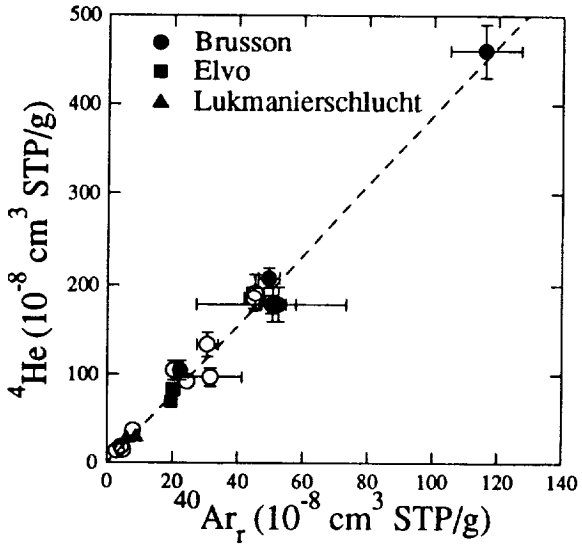

Fig. 1 Correlation of ^{4}He and $^{40}Ar_r$ (where $^{40}Ar_r = {}^{40}Ar_{tot} - 296 \times {}^{36}Ar$) for Alpine gold samples. Closed symbols represent total extractions, open symbols show single temperature steps. For Elvo, only those two splits which did not indicate contamination by U-rich minerals are included, otherwise only data with 2σ uncertainties > 50% were discarded.

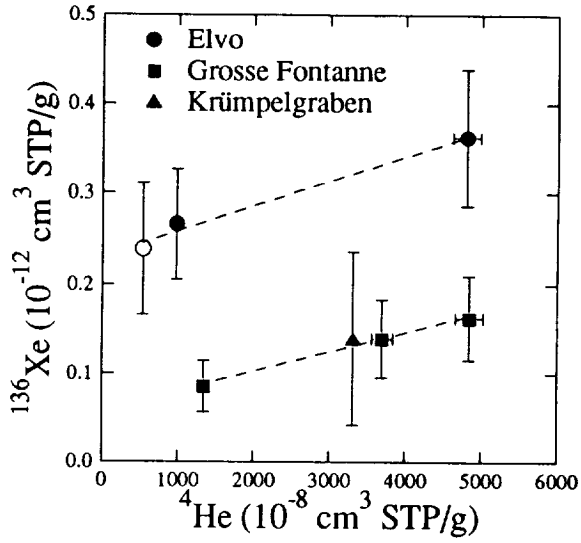

Fig. 2 Correlation of ^{136}Xe and ^{4}He for placer gold from the Napf area (Central Switzerland) and Elvo river (Northern Italy). The open symbol represents an Elvo split where Xe data had to be corrected due to technical problems during measurement. Two straight lines for Elvo and Napf area gold, respectively, are defined by the data, as expected for constant trapped gas abundances and $^{136}Xe_f$ / ^4He_r ratios within each group.

A SEARCH FOR SOLAR ENERGETIC PARTICLE HELIUM IN INTERPLANETARY DUST PARTICLES. A. O. Nier and D. J. Schlutter, School of Physics and Astronomy , University of Minnesota, Minneapolis, MN 55455, USA

Helium was extracted from individual interplanetary dust particles (IDPs) employing a stepped pulse-heating technique, which when used for gas extraction from lunar ilmenite grains confirmed the presence of two components attributable to solar wind (SW) and solar energetic particle (SEP) implantation, respectively. Although the sensitivity was adequate, the experiment was unable to detect a second component in IDPs.

During the past few years experiments have been conducted in which helium and neon have been extracted by heating individual Interplanetary Dust Particles (IDPs) and determining the amounts and isotopic composition of the gas extracted [1, 2, 3]. In our most recent investigations [3] conventional step-heating was replaced by a sequence of short pulses of increasing temperature. The technique, while developed primarily for studying the thermal history of IDPs [3, 4, 5], has the potential for distinguishing between gas released from the surfaces of individual grains and that more deeply imbedded, as from SEP implantation.

In an ingenious experiment, Wieler et al. [6] subjected bulk samples of lunar surface grains to successive chemical etchings and analyzed the gas released after each step. They concluded that the grains contained not only a shallowly implanted solar wind (SW) component but also more deeply imbedded particles called Solar Energetic Particles (SEPs), which had energies intermediate between those of the solar wind and those associated with solar flares. Further experiments confirmed and extended the results [7]. An independent study [8] of similar lunar material, employing a combination of stepwise oxidation and pyrolysis, confirmed the likely existence of a second reservoir of gas, but led to the conclusion that the effect might also be attributed to diffusion of the implanted solar wind in the grains.

In an application of our pulse-heating technique to individual ilmenite grains from lunar samples 79035 and 71501, it was found [9] that the shapes of the gas release curves not only were consistent with the existence of an SEP component, but also the helium and neon isotopic abundance ratios were similar to those deduced in the etching experiment [7]. In cases where comparisons were possible, the results also agreed with those found in total extraction experiments on individual grains of ilmenite from the same lunar material [10].

It appeared interesting to apply the pulse-heating technique to IDPs to see if the same pattern prevailed for helium released from IDPs. In a study of 12 particles (estimated diameters 10 to 20 μm, average 11 μm) seven were found to contain sufficient gas (more than 2×10^{-10} cm^3STP each), and similar enough gas release curves, to warrant combining the results to obtain an average curve. This is shown in Fig. 1. Also shown is the corresponding curve found for a composite sample of 25 IDPs (kindly provided by D.E. Brownlee), which had an average diameter of 8.8 μm. Shown, for comparison, are the curves found in the lunar ilmenite study. Neither of the IDP curves exhibits the release of any appreciable amount of helium at higher oven temperatures as seen by the lunar ilmenite curves, and attributed to the presence of SEP imbedded gas. Moreover, in the case of the 25 IDP composite sample, unlike the findings in the ilmenite study, no change in isotopic composition of helium and neon was observed as the heating progressed. On the basis of studies to date, one is forced to conclude that either the pulse-heating extraction technique, as conducted, is not applicable to IDPs, or the particles do not contain an SEP component.

In addition to the extraction experiments described above, implantation experiments were conducted in which single grains of terrestrial ilmenite, plagioclase and pyroxene were implanted with 4000 volt helium ions to simulate solar wind implantations. The implanted gases were subsequently extracted as was done in the case of the IDPs. The extraction curves exhibited the same steepness seen in the IDP curves of Fig. 1 and fell generally in the region between the two IDP curves of Fig. 1.

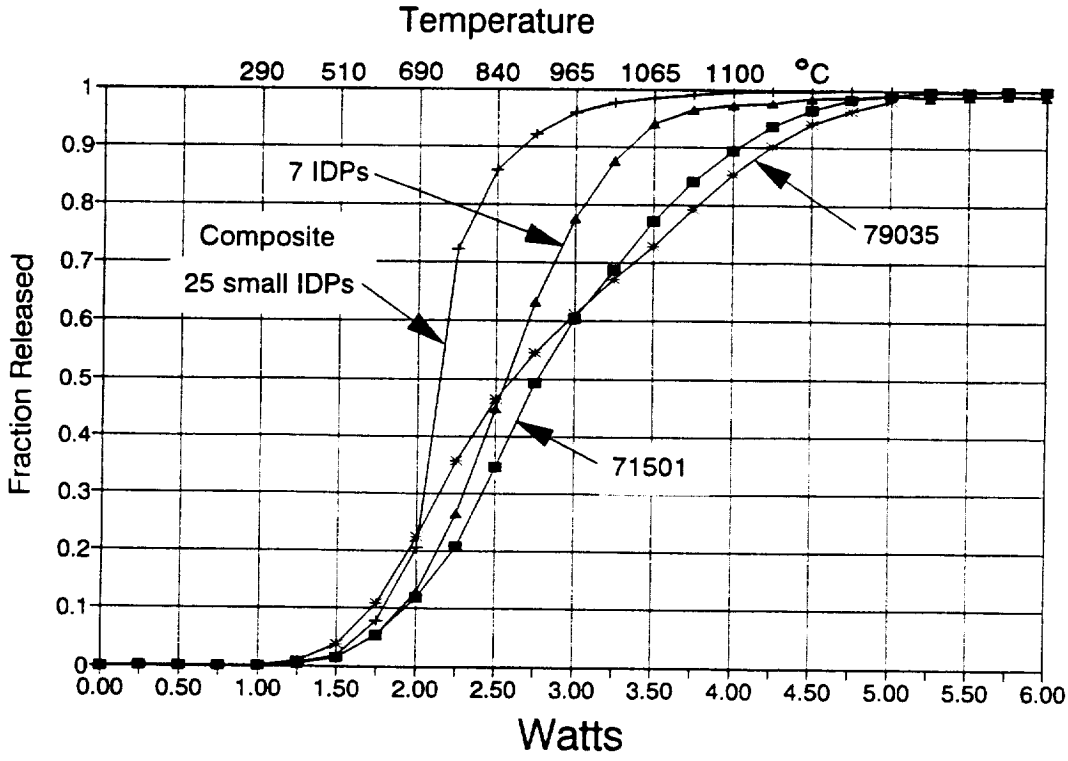

Figure 1. ^{4}He release from individual IDPs and lunar surface grains when the particles are subjected to a succession of 5-second heat pulses in an oven whose power is increased in 0.25 watt increments. The peak temperatures reached during the pulses are indicated above the figure.

REFERENCES: [1] Nier A.O. and Schlutter D.J. 1990, *Meteoritics* **25**, 263 -267. [2] Nier A.O. and Schlutter D. J. 1992, *Meteoritics* **27**, 166 - 173. [3] Nier A.O. and Schlutter D.J. 1993, *Meteoritics* **28**, 675 - 681. [4] Brownlee D. E., Joswiak D. J., Love S. G., Nier A. O., Schlutter D. J. and Bradley J. P. 1993, *LPSC* **24**th, 205 - 206. [5] Brownlee D. E. et al. 1993, *Meteoritics* **28**, 332. [6] Wieler R., Baur H., and Signer P. 1986, *GCA* **50**, 1997 - 2017. [7] Benkert J-P., Baur H., Signer P. and Wieler R. 1993. *JGR* **98**, 13,147 - 13,162. [8] Becker R. H. and Pepin R. 1989, *GCA* **53**, 1135 - 1146. [9] Nier A. O. and Schlutter D. J. 1993. *Meteoritics* **28**, 412. [10] Nichols R. H. Jr. and Hohenberg C.M. *GCA* (in press).

GEOLOGY OF AKKRUVA COLLES AREA ON VENUS: VENERA 15/16 SAR IMAGES ANALYSIS

A.M.Nikishin * , N.N.Bobina ** , G.A.Burba **
* - Moscow Lomonosov University, Geol. Dept., 119899, Moscow
** - Vernadsky Institute, Moscow, 117975, Russia

Geologic/geomorphic mapping was fulfilled for the B-14 quadrangle of Venera (BEHEPA in Russian) series 1:5,000,000 photomap. The area is located between 40 and 60 ° N, 90 and 135°E. Venera 15 and 16 1,8 km/pixel radar images were used for the mapping. Five principal terrain types were outlined: (1) tesserae, (2) hilly terrains, (3) plains, divided into five subtypes, (4) coronae, and (5) groove belts. Within some of these terrains there are volcanic, tectonic, and impact features, which are shown on the map.

TESSERAE are located at the boundaries of the quadrangle: eastern part of Tellus Tesssera is at SW corner of the area; northern part of Kutue Tessera is at the S frame; western part of Ananke Tessera is at the E frame, and unnamed tessera is at NE corner. Tessera terrains in the area are highlands reaching up to 2.5 km over 6051-km-sphere. The surfaces of the tesserae are cutted with the systems of grooves and canyons. These systems have different patterning: orthogonal - in Tellus, rhombical - in Kutue, longitudinal and diagonal to tessera outlines - in Ananke, and subparallel to the tessera outlines - in the unnamed one.

HILLY TERRAINS occupy the largest part of the quadrangle. They are elongated from NW to SE along the diagonal axis of the area. This vast belt of hills is known as Akkruva Colles. The hills have very small topographic heights over the plains. Hilly areas are changed in many places with plain ares looking as plain material embayed the hilly terrains. Individual hills are 2 - 10 km in diameter and have non-steep slopes. Typical distances between the hills are 10 to 15 km.

The hills are distributed over the area chaoticaly. There are clusters of hills at a number of locations. At the areas of hilly terrains adjacent to the plain areas the hills are more scattered, the distances between the hills are larger than in the inner parts of hilly terrains.

The whole area of hilly terrain is cutted with the net of tiny crossing lineations. There is prominently long, shallow, graben-like structure running NW to SE along the axis of the wide belt of hilly terrain - Akkruva Colles.

At the eastern part of the quadrangle the hilly terrain step-by-step joins itself into Ananke Tessera highlands. This transition looks like the hilly terrains are the result of volcanic changes of tessera through covering tessera with plain material and gradual sinking of such tessera areas. This point is supported with the presence of tessera-like areas (tens of kilometers across) located within the hilly terrains.

C-7

GEOLOGY OF AKKRUVA COLLES ON VENUS: Nikishin, A.M. et al.

PLAINS in the quadrangle are of five subtypes: (1) smooth, (2) radar-splotched, (3) banded, (4) circumvolcanic, and (5) circular-splotched. All plains are located at topographic level 1±0.5 km over the 6051-km-sphere. Age (stratigraphic) relations between the plains' subtypes were not established around the whole mapped area. Only in places one could see trasngressions of one subtype plain material into another subtype area.

CORONAE are located in the NW corner of the map sheet. There are two coronae partly located within the quadrangle: Fakahotu Corona and Vacuna Corona.

Fakahotu Corona is elongated N to S and have dimensions 300 x 450 km. This feature is located in the center of isometricaly-shaped plain area with diameter about 500 km. The corona consist of three zones: central plain, southern ridge frame, and northern ridge frame. The ridges have branches and often change their direction abruptly.

Vacuna Corona is located within the area only with its southern part. It resembles the ridge belt which could be part of the ancient corona burried with volcanic plain material.

GROOVE BELTS consist of a number of spacerly located grooves. Friagabi Fossae belt superposes the hilly terrain. The belt consists of sharp grabens 6-8 km wide located 40 km apart.

An unnamed groove belt in the NE corner of the area superposes both hilly terrain and plain. Further north (just outside the sheet frame) this belt is cutted with S boundary of Nightingale Corona. So, the grooves were formed after the hilly and plain terrains, but before the Nightingale Corona.

Volcanic centers consist of five types: (1) small cones, 2-10 km in diameter; (2) large domes, 20-50 km in diameter; (3) smooth volcanic shields, 50-100 km in diameter; (4) small calderas, around 10-30 km in diameter; (5) large calderas (or tectonic-magmatic depressions), 50-150 km in diameter.

Tectonic features on the map include large lineaments (faults), prominent scarps, individual grooves and ridges.

Impact craters are very rear within the sheet - only three small craters, 8 to 16 km in diameter, took place in hilly terrain area. Other terrain types possess no impact craters.

CONCLUSIONS. (1) Tesserae are 1-2 km higher than the plains. They are clearly embayed with plain material. So, the tessera terrains have lighter and/or thicker crust than the plain areas, and tesserae are older than the plains. (2) Hilly terrains have been formed due to volcanic modification of tessera terrains. (3) The plains are the result of areal volcanic activity. Some of them have been formed in course of lava flooding of hilly and tessera terrains. The surface morphology of plains recembles one of terrestrial basaltic plateaus. (4) Coronae were formed over the mantle hot spots. (5) Volcanoes in the centers of circumvolcanic plains were formed over small-scaled mantle hot spots.

RECENT HISTORIES OF LUNAR CORES 15009 AND 79002/1 USING COSMOGENIC RADIONUCLIDES ^{10}Be, ^{26}Al, and ^{36}Cl; K. Nishiizumi[1], R. C. Finkel[2], M. W. Caffee[2], P. Sharma[3], J. Masarik[4], R. C. Reedy[4], and J. R. Arnold[5] ; [1] Space Sciences Laboratory, University of California, Berkeley, CA 94720; [2] CAMS, Lawrence Livermore National Lab, Livermore, CA 94551; [3] NSRL, University of Rochester, Rochester, NY 14627; [4] NIS-2, Los Alamos National Lab, Los Alamos, NM 87545; [5] Department of Chemistry, University of California, San Diego, La Jolla, CA 92093.

We report here new results on the content of ^{10}Be ($t_{1/2}$ = 1.5x10^6 years), ^{26}Al (7.1x10^5 years), and ^{36}Cl (3.0x10^5 years) in bulk fines from lunar cores 15009 and 79002/1. These results allow us to deduce likely gardening and irradiation histories in the million year time scale for these two cores. The new results add to the database earlier summarized and discussed by Langevin et al [1] for lunar regolith gardening history. Although the ^{53}Mn ($t_{1/2}$ = 3.7x10^6 years) profiles for these cores have not yet been measured, we do report ^{10}Be profiles for these two cores. The ^{10}Be profile is expected to be less sensitive to surface gardening due to the lack of SCR (Solar Cosmic Ray) production of ^{10}Be as shown by measurements in lunar surface rock 68815 [2]. However, ^{10}Be is also a useful nuclide for understanding lunar surface mixing histories, as shown below.

The results reported here for ^{10}Be, ^{26}Al, and ^{36}Cl are plotted in Figure 1 and 2 along with theoretical GCR (Galactic Cosmic Ray - dashed lines in the figures) and the sum of GCR and SCR production profiles (solid lines). The GCR profiles were calculated using the Reedy-Arnold model [3] with the most recent cross section data. The SCR parameters, R_0 = 85 MV and J (>10 MeV) = 110 proton/cm^2·s·4π [2] are used for the following discussion. These theoretical profiles are based on the average chemical composition of the 13 samples in each core. All AMS measurements were performed at Lawrence Livermore National Lab except ^{36}Cl in 79002/1, which were measured at the University of Rochester. The error bars indicate only the AMS error (1σ) and do not include chemical analysis error (2-4 %). Our interpretation of the core histories is as follows:

15009: The Apollo 15 single drive core 15009 was collected from the north rim of a 12 m diameter crater at station 6. The surface into which the core was driven is littered with angular fragments on the order of 0.5 to 2 cm and smaller [4]. The bulk density of 15009 is 1.58 g/cm^3 after extrusion. The modal abundance of agglutinates in the core indicates that the core soils are submature [5]. The ^{10}Be profile is in good agreement with the Reedy-Arnold GCR profile and shows no SCR contribution, as expected. Although ^{26}Al and ^{36}Cl profiles show clear SCR effects, the activities actually decrease toward the surface above 2 cm depth. This effect, often observed in lunar cores, is not yet understood. The sum of SCR produced ^{26}Al above 5 cm (7.9 g/cm^2) is only 75 % of the predicted value from Reedy-Arnold calculation. The ^{26}Al profile is similar to that of 74002, which was collected from the rim of Shorty Crater and is reported to have lost ~2 cm from the top of the core [6]. Unfortunately, decay made it impossible to measure a ^{22}Na profile in 15009 to check for the recent loss of core-top material. It is also worth noting that a void was observed in the first dissection of core extending from the surface to nearly 9 cm (Core Synopsis-15009). Although there is legitimate concern that loss or disturbance of the upper several cm could be a problem it is nevertheless difficult to explain the detailed profiles by simple loss of surface material. The measured SCR produced ^{36}Cl is higher than the calculated profile however the Reedy-Arnold calculation underestimates production of ^{36}Cl due to the lack of low energy proton cross section data [7].

79002/1: The Apollo 17 double drive core 79002/79001 was collected at station 9, which is approximately 70 m southeast and downslope from the rim of a 90 m diameter Van Serg Crater. The upper portion of the core was predicted to represent ejecta from Van Serg Crater [8]. The bulk density of 79002 (surface - 17.4 cm depth) is 1.76 g/cm^3 and 79001 (17.4 - 46.7 cm) is 1.90 g/cm^3 after extrusion. The core has a distinct dark-light boundary inclined 25-30° from 8.5 (15) to 11 cm (19 g/cm^2) below the surface. The Is/FeO surface exposure index [9] and the agglutinate abundance [10] shows a distinct break at the light-dark boundary. The sample above the boundary (dark) indicates the most mature regolith and the sample below the boundary (light) indicates submature regolith. The upper dark sample is a mixture of highly mature soil, which is indicative of a long gardening time at the surface, and extremely coarse material which indicates a younger regolith [10]. Since ^{26}Al and ^{36}Cl profiles clearly show SCR production, the surface samples were essentially undisturbed for times on the order of a million year. Low ^{10}Be concentrations above 40 g/cm^2 are apparently due to the under saturation of this nuclide. The ^{10}Be exposure time (deposition time) is calculated to be 2.6±0.4 My for the upper dark sample and over 3.6 My for the lower light sample. If the upper sample is Van Serg Crater ejecta, the crater-forming event occurred 2.6±0.4 My ago. The ^{10}Be concentration beneath the boundary, which might be the original surface 2.6 My ago, is still under saturated compared to the Reedy-Arnold GCR profile. The soil between 20 and 50 g/cm^2 may have been deposited only a few My prior to Van Serg Crater event. However, the age estimate has a large error due to short half-life of ^{10}Be compared to the age of the event. Measurements of ^{53}Mn, in progress, will further constrain the deposition scenario. Yokoyama et al [11] estimated the Van Serg Crater event as 1.6±0.5 My based on ^{26}Al concentration in

trench soil 79221 (130±7 dpm/kg - 0-2 cm depth) [12]. This age is an underestimate due to the surface gardening effect. SCR produced ^{26}Al above 13 g/cm^2 is ~20 % in excess over the steady state profile. If we adopted a 2.6 My deposition age, the excess is ~30 %. The excess and disturbed depth are near the average of other cores [1]. After normalizing to the average chemical composition, the ^{36}Cl profile below 30 g/cm^2 smoothly decreases with increasing depth but is ~5 % higher than the Reedy-Arnold GCR profile. Again ^{36}Cl production near surface is much higher than predicted.

References: [1] Langevin Y. *et al.* (1982) *JGR, 87*, 6681; [2] Nishiizumi K. *et al.* (1988) *Proc. LPSC, 18*, 79; [3] Reedy R.C. and Arnold J.R. (1972) *JGR, 77*, 537; [4] Swann G.A. *et al.* (1971) *US Geol. Survey Interagency Rep. 36*; [5] Basu A. *et al.* (1991) *Proc. LPSC, 21*, 221; [6] Fruchter J.S. *et al.* (1978) *Proc. LPSC, 9*, 2019; [7] Nishiizumi K. *et al.* (1991) *LPSC, XXII*, 979; [8] *Apollo 17 Prelim. Sci. Rep.* (1973); [9] Morris R.V. *et al.* (1989) *Proc. LPSC, 19*, 269; [10] McKay D.S. *et al.* (1988) *LPSC, XIX*, 758; [11] Yokoyama Y. *et al.* (1975) *Proc. LSC, 6*, 1823; [12] O'Kelley G.D. *et al.* (1974) *Proc. LSC, 5*, 2139.

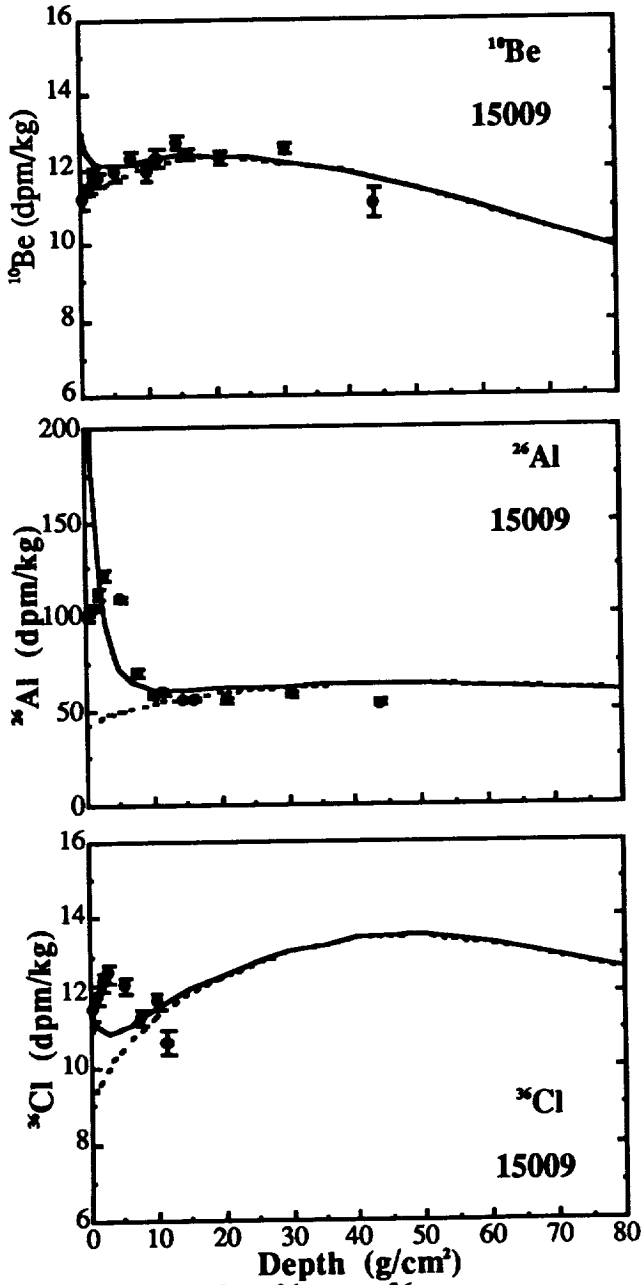

Figure 1. ^{10}Be, ^{26}Al, and ^{36}Cl in 15009

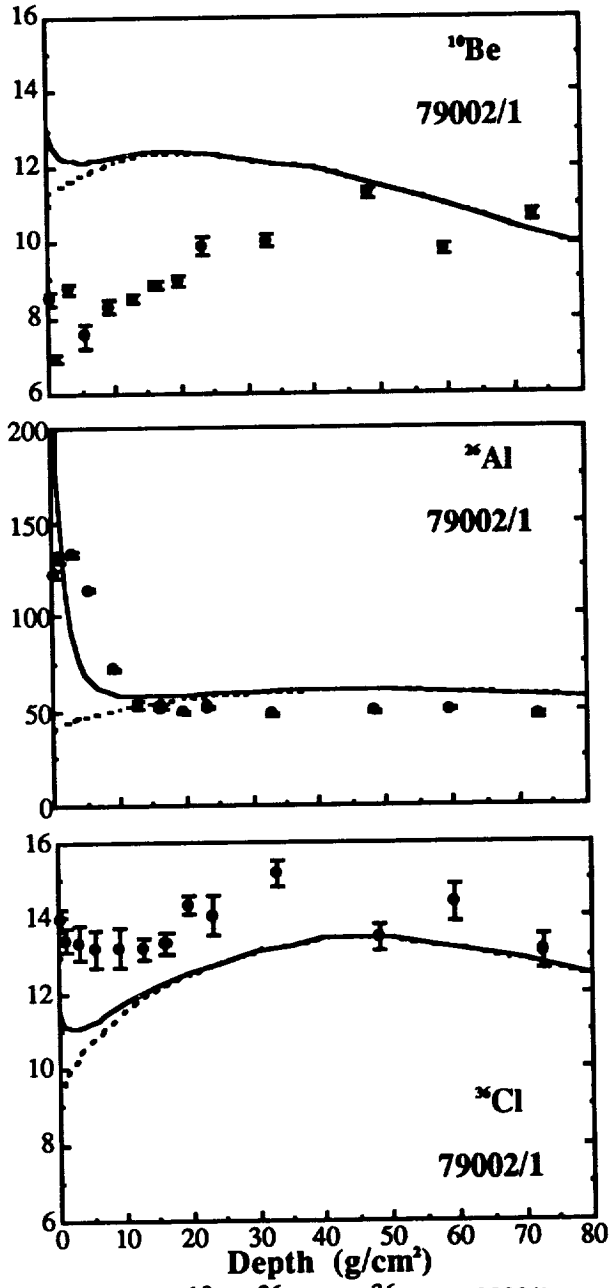

Figure 2. ^{10}Be, ^{26}Al, and ^{36}Cl in 79002/1

INTERSTELLAR CORUNDUM AND SPINEL FROM THE TIESCHITZ ORDINARY CHONDRITE; L. Nittler, C. Alexander, X. Gao, R. Walker and E. Zinner, McDonnell Center for the Space Sciences and Department of Physics, Washington University, One Brookings Drive, St. Louis, MO 63130-4899.

We have used ion imaging of O-isotopes in the ion microprobe to locate eight interstellar oxide grains in an acid residue of the Tieschitz ordinary chondrite. Seven corundums and one spinel were identified as interstellar by their highly anomalous O-isotopic compositions. In addition, four of the corundum grains have initial $^{26}Al/^{27}Al$ ratios between 2.6×10^{-3} and 7.6×10^{-3}, much higher than the canonical value of 5×10^{-5} found in the early solar system. The wide range of O-isotopic compositions observed in these grains indicates that they formed in distinct stellar sites. In Tieschitz, as in Murchison, interstellar oxide grains appear to be less abundant than interstellar SiC by at least two orders of magnitude.

A large number of pristine carbon-rich interstellar grains, including SiC, diamond and graphite have been previously isolated from primitive meteorites and identified as interstellar by their unusual isotopic compositions [1]. Tiny crystals of refractory carbides of Ti, Zr and Mo have also been found as inclusions within presolar graphite grains [2]. In contrast, only two interstellar oxide grains have been located to date. Huss *et. al.* [3,4] found one Orgueil corundum grain, out of 60 oxides studied, with a large ^{17}O excess ($\delta^{17}O$ = 1538‰) and an initial $^{26}Al/^{27}Al$ ratio of 9×10^{-4}. Nittler *et. al.* [5] found a Murchison corundum grain, out of 800 oxides studied, showing a similar $^{26}Al/^{27}Al$ ratio, a similar ^{17}O enrichment ($\delta^{17}O$ = 1072‰) and a depletion in ^{18}O ($\delta^{18}O$ = –244‰). The unusual isotopic compositions of these two grains suggest an origin in red giant stars. For this work we have extended our search for interstellar oxides to the ordinary chondrite Tieschitz (H/L 3.6).

Chemically resistant oxide grains in most primitive meteorites are dominated by material from CAIs. As the ordinary chondrite Tieschitz has few CAIs, we have conducted a search for presolar oxides in this meteorite. A new separation technique which allows more rapid production of acid residues from smaller amounts of starting material than previous methods was developed to produce Tieschitz separates enriched in interstellar dust [6]. Although these separates are less pure than the Murchison K-series [7], interstellar grain concentrations in them can be determined by a combination of weighing, SEM X-ray mapping and ion imaging. The residue analyzed here, T8, of density > 2.4 g/cm^3, has been treated with perchloric acid subsequent to colloidal and density separation [6]. According to SEM-EDX analysis, T8 contains 38% corundum, 22% spinel, 9% chromite, and 23% SiC; the remainder is made up of other phases.

For this study, we have modified our ion imaging system to automatically map the isotopic ratios of grains dispersed on gold foil. Ion images of ^{16}O and ^{18}O are digitized by a CCD camera and $^{16}O/^{18}O$ ratios in individual grains determined by image processing. To reduce possible problems encountered during the analysis of grains near the edges of the field of view, grains which show unusual isotopic ratios are moved automatically to the center of the field of view and re-imaged. Over a period of about 30 hours, we mapped approximately 2000 oxide grains from Tieschitz residue T8. For sixteen grains the images indicated large depletions in ^{18}O. Unfortunately, eight of these grains were either sputtered away during imaging or were too small for individual isotopic analysis. Subsequent high mass resolution analysis of the remaining grains, which range from 0.5-2μm in size, confirmed ^{18}O depletions and revealed a large range of $^{16}O/^{17}O$ ratios in seven corundum grains (Fig. 1). One spinel grain, 38-1, has normal ^{18}O, but is depleted in ^{17}O ($\delta^{17}O$ = –240 ‰). Magnesium isotopic measurements yielded large ^{26}Mg excesses in four of the interstellar corundum grains, corresponding to initial $^{26}Al/^{27}Al$ ratios between 2.6×10^{-3} and 7.6×10^{-3} (Fig. 2).

The oxygen isotope ratios for the ten interstellar oxide grains found to date, as well as those measured spectroscopically in the atmospheres of different types of red giant stars [8-10] are shown in Fig. 1. Three of the Tieschitz grains have oxygen isotopic compositions similar to those of Orgueil grain B and Murchison 83-5, although the deviations from solar ratios are not as extreme. Two of these grains also have high $^{26}Al/^{27}Al$ ratios. These isotopic signatures are similar

to those observed in and predicted for red giants and are consistent with the dredge-up of material having experienced H-burning via the CNO cycle into the stellar atmosphere where the grains presumably condensed [8]. Two grains, 150-1 and 120-2, have much larger ^{17}O enrichments and ^{18}O depletions than any previously observed in meteoritic material and $^{26}Al/^{27}Al$ ratios of about 4×10^{-3}, a factor of 80 higher than the canonical solar system value. These unusual isotopic compositions are similar to those expected from nucleosynthesis during CNO-cycle H-burning and could conceivably exist in the atmospheres of stars where hot-bottom burning [11] is taking place or on the surface of Wolf-Rayet stars during the WN phase. The remaining three grains, including spinel 38-1, show depletions in ^{17}O, and it is difficult to assign a definite nucleosynthetic origin for these grains. Massive stars produce large excesses of ^{16}O and ^{18}O [12], which could come to the surface during the WR stage or could be ejected in a supernova explosion. The problem is how to reproduce the ratios observed in these grains in a stellar environment where O-rich grains can form.

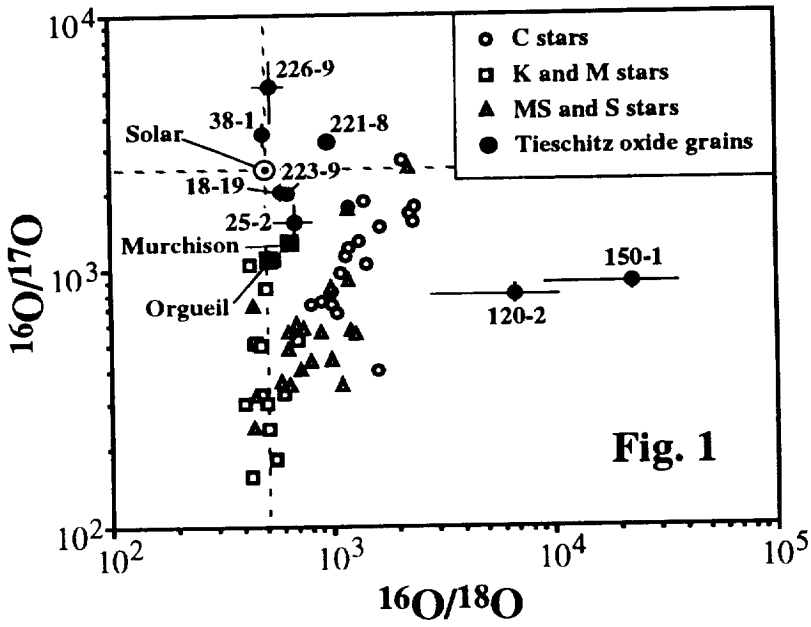

Fig. 1

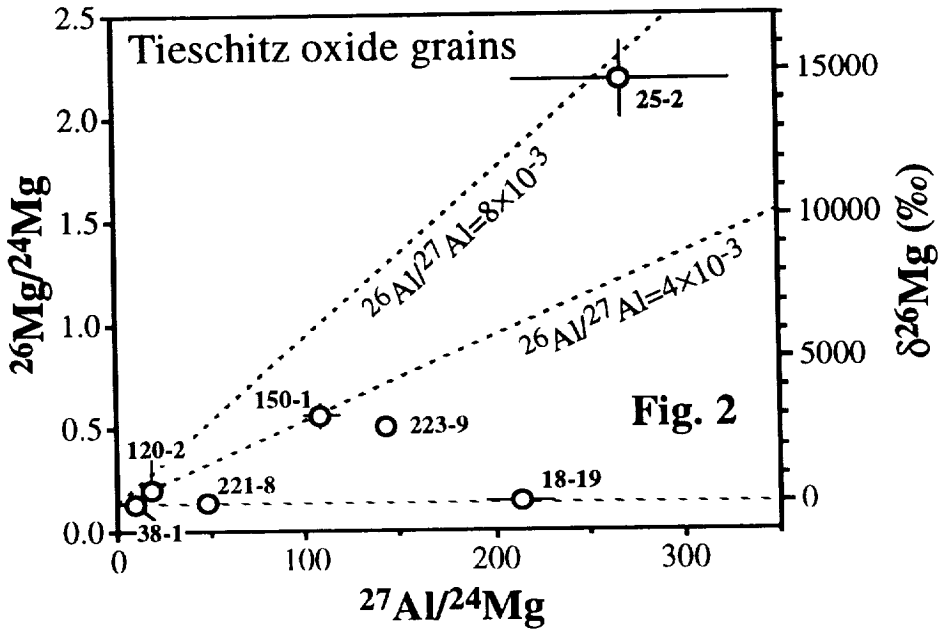

Fig. 2

References: [1] Anders E. and Zinner E. (1993) *Meteoritics* **28**, 490 [2] Bernatowicz T. *et al.* (1994) LPS XXV, this volume [3] Huss G. *et al.* (1992) LPS XXIII, 563 [4] Huss G. *et al.* (1993) *Meteoritics* **28**, 369 [5] Nittler L. *et al.* (1993) LPS XXIV, 1087 [6] Gao X. *et al.* (1994) LPS XXV, this volume [7] Amari S. *et al.* (1993) *GCA*, in press [8] Smith V. and Lambert D. (1990) *Ap. J. Suppl.* **72**, 387 [9] Harris M. *et al.* (1987) *Ap J.* **316**, 294 [10] Harris M. and Lambert D. (1984) *Ap. J.* **285**, 674 [11] Renzini A. and Voli M. (1981) *Astron. Astrophys.* **94**, 175 [12] Woosley S. E. (1986) in *Nucleosynthesis and Chemical Evolution*, Observatoire de Genève, p. 1.

SUDBURY IGNEOUS COMPLEX: EVIDENCE FAVORING ENDOGENOUS MAGMA RATHER THAN IMPACT MELT Marc D. Norman, Planetary Geosciences, Dept. of Geology and Geophysics, SOEST, University of Hawaii, Honolulu HI 96822 U.S.A.

A cornerstone of much current thought about the Moon is that development of the lunar crust can be traced through pristine highlands rocks which represent primary magmatic additions to the crust [1]. However, if cumulates similar to those of a layered intrusion can form by differentiation of a large volume of impact melt, as proposed for the Sudbury Igneous Complex (SIC) [2,3], then much of what is thought to be known about the Moon is open to question. Geochemical evidence cited as favoring an impact melt origin for the SIC is not compelling, however, because (1) similar bulk compositions can be produced by endogenous magmatic processes, (2) ultramafic xenoliths in the Contact Sublayer have compositional affinities with the SIC, and (3) PGE concentrations and Re-Os isotopic compositions in SIC ores indicate terrestrial, not meteoritic compositions. The close spatial and temporal association of Sudbury magmatism with a basin-forming impact event may nonetheless have important implications for early planetary evolution.

Based on studies of terrestrial impact craters and associated deposits, several petrographic and geochemical criteria have been developed which are thought to be useful for distinguishing primary lunar highlands cumulates from impact-generated mixtures. For example, lunar highlands rocks which have mineral compositions consistent with plutonic conditions, incompatible trace element patterns that are fractionated relative to KREEP, and very low concentrations of siderophile elements are thought to retain their endogenous magmatic composition [1]. The Sudbury Igneous Complex has mineral and chemical compositions broadly consistent with closed-system fractional crystallization [4], and a suite of lunar samples with mineralogic and geochemical characteristics analogous to those of the SIC probably would be judged as 'pristine', hence a primary igneous rock suite. However, if differentiation of a large-volume of impact melt actually produced the cumulate rocks of the SIC [2,3], then any or all of the pristine lunar highlands rocks may not necessarily represent endogenous lunar magmas but fractionated impact melts. Diverse components would still be required in the lunar crust and/or upper mantle to produce the impressive array of highlands rock types, but the connection to major geochemical reservoirs that could constrain the Moon's bulk composition and evolution would be lost. It is argued here, however, that the geochemical evidence cited as favoring an impact melt origin for the SIC is not convincing, and that endogenous magmatic processes provide a better framework for understanding the geochemical features of the SIC.

The principal geochemical feature of the SIC which has been interpreted as favoring an impact melt origin is its siliceous, crust-rich composition [2,3,6]. Bulk compositions of terrestrial impact melts typically reflect an integrated composition of the target lithologies [5]. The bulk composition of the SIC is unusually siliceous for a layered intrusion, and close to that of reasonable mixtures of upper crustal rocks near Sudbury [2]. Sr, Nd, and Os isotopic compositions of the SIC also seem to be dominated by crustal components [3,6]. Although impact melts clearly can be dominated by crustal components, open magmatic systems also can incorporate significant amounts of continental crust into mafic and intermediate composition magmas through assimilation, diffusive contamination, magma mixing, and source contamination [7]. Such processes do not require a superheated melt such as that formed during an impact event, and they can generate igneous rocks that are compositionally similar to the SIC.

The Sudbury impact event appears to have occurred near an active convergent continental margin, so the lower crust in the region probably was a mobile mixture of basaltic and older crustal components at the time of the impact. Fracturing and load-release associated with the basin-forming impact would have provided a natural locus for emplacement of locally generated magmas. Enriched or metasomatized mantle with isotopic characteristics mimicking those of continental crust is also a plausible magmatic source for the SIC in this setting, and would reduce the amount of assimilated continental crust required to account for the isotopic compositions of the SIC. Compositions of Proterozoic basalts from the Superior Province [8] are consistent with the presence of enriched mantle in the general area at the time of the impact.

SUDBURY IGNEOUS COMPLEX IS ENDOGENOUS MAGMA Norman M.D.

A significant crustal component in the SIC is a strong constraint on its origin only to the degree that impact melting produces a unique combination of ingredients relative to endogenous magmatism. Mafic and ultramafic magmatic xenoliths entrained in the Contact Sublayer of the SIC show that the processes which created the SIC were not unique because these xenoliths also had crust-rich parental magmas. If the xenoliths represent a magmatic intrusion older than the SIC but also incorporating a significant amount of remobilized continental crust, then creating a unique bulk composition for the SIC by impact melting is not necessary: endogenous processes suffice. If the Contact Sublayer is significantly younger than the Main Mass, the xenoliths may represent unexposed cumulates genetically related to the SIC. A basal mafic-ultramafic zone at depth would indicate the SIC is not contained entirely within the impact structure and would create a bulk composition for the SIC unlike that of the target stratigraphy.

Many impact melt breccias from craters on Earth show enrichments of siderophile element abundances and low Re/Ir relative to the country rock, indicating contamination of the melt by the projectile. PGE patterns in Sudbury ores are not chondritic but are highly fractionated and similar to those of terrestrial basalts. Reconstructed bulk compositions of several Sudbury ore deposits are relatively constant, with (Pt+Pd)/(Ru+Ir+Os) ratios around 10-20, representing the initial composition of the sulfide liquid parental to these deposits [9]. The correlation between (Pt+Pd)/(Ru+Ir+Os) and Re/Os in these ores allows the Re/Os of the parental sulfide to be estimated and compared with those measured in the country rocks. The inferred bulk Re/Os ratios of Sudbury ore deposits are not strongly fractionated relative to country rocks, which contrasts strongly with the record of PGE fractionation in terrestrial impact melts.

Re-Os isotopic compositions can be a sensitive tracer of meteoritic contamination in impact melts, even those with small (≤1%) meteoritic components [10]. The Os isotopic compositions of Sudbury ores place severe limits on the amount of meteoritic contamination that can be present in these ores. Mixing calculations show that ≤ 0.02% meteoritic contamination can be present in these ores, assuming a chondritic impactor (486 ppb Os, $^{187}Os/^{186}Os = 0.96$), and a model crust (0.05 ppb Os, $^{187}Os/^{186}Os = 11$ [6]). The amount of meteoritic contamination reduces to ≤0.005% for a crustal target with 0.007-0.015 ppb Os such as that preferred by [6]. The overwhelming predominance of terrestrial Os in the Sudbury ores must favor an endogenous origin for the SIC.

It may be possible that large impact events behave so differently from smaller events that the Sudbury projectile was vaporized and completely dispersed without incorporating even a trace of meteoritic material into the impact melt [12]. However, this does not seem to have happened in other large terrestrial impact structures such as Popagai and Chicxulub, which do show meteoritic contamination in their impactites and no signs of *in situ* differentiation [5, 10]. Chicxulub appears to be largest impact structure on Earth, with a diameter of 200 km, yet melt breccias recovered from cores of the structure show Ir concentrations and Re-Os isotopic compositions that are consistent with incorporation of ≤3% of a meteoritic component [10].

The SIC represents endogenous magmatism that was localized and influenced by a major impact event. The concept that pristine lunar highlands rocks are also products of endogenous magmatism is tenuously secure for the moment, but the effects of major impact events in localizing and influencing that magmatism remain obscure both for the Moon and the early Earth. Large impact events which produced regional melting may have played a crucial role in the evolution of the lunar highlands.

[1] Warren and Wasson (1977) PLPSC 8, 2215-2235; Warner and Bickle (1978) Am. Mineral 63, 1010-1015 [2] Grieve et al. (1991) JGR Planets 96, 22753-22764 [3] Faggart et al. (1985) Science 230, 436-439 [4] Naldrett and Hewins (1984) Ontario Geol. Surv. Spec. Vol. 1, 235-251 [5] Phinney and Simonds (1977) Impact and Explosion Cratering, 771-790; Grieve et al. (1977) Impact and Explosion Cratering, 791-814 [6]Walker et al. (1991) EPSL 105, 416-429 [7] Leeman and Hawkesworth (1986) JGR 91, 5901-5912; Grove et al. (1988) CMP 99, 320-343; Hergt et al. (1989) J. Petrol. 30, 841-883; Norman and Mertzman (1991) JGR 96, 13279-13295; Stewart and DePaolo (1992) Science 255, 708-711 [8] Paces and Bell (1989) GCA 53, 2023-2035 [9] Naldrett et al. (1982) Econ. Geol. 77, 1519-1534; Naldrett (1984) Ontario Geol. Surv. Spec. Vol. 1, 533-569 [10] Koeberl and Shirey (1993) Science, in press; Koeberl et al. (1993) Science, in press; Reimold et al. (1993) LPS XXIV, 1197-1198; Sharpton et al. (1992) Nature 359, 819-821 [12] R. Grieve and R. Hewins, pers. comm. (1993)

ALKALI ELEMENT CONSTRAINTS ON EARTH-MOON RELATIONS

M.D. Norman Research School of Earth Sciences, ANU, Canberra ACT 0200 Australia
M.J. Drake Lunar and Planetary Laboratory, University of Arizona, Tucson AZ 85721 USA
J.H. Jones NASA Johnson Space Center, SN4, Houston TX 77058 USA

Given their range of volatilities, alkali elements are potential tracers of temperature-dependent processes during planetary accretion and formation of the Earth-Moon system. Under the giant impact hypothesis, no direct connection between the composition of the Moon and the Earth is required, and proto-lunar material does not necessarily experience high temperatures [1]. Models calling for multiple collisions with smaller planetesimals derive proto-lunar material mainly from the Earth's mantle and explicitly invoke vaporization, shock melting and volatility-related fractionation [2]. Na/K, K/Rb, and Rb/Cs should all increase in response to thermal volatilization, so theories which derive the Moon substantially from Earth's mantle predict these ratios will be higher in the Moon than in the primitive mantle of the Earth. Despite the overall depletion of volatile elements in the Moon, its Na/K and K/Rb are equal to or less than those of Earth. A new model presented here for the composition of Earth's continental crust, a major repository of alkali elements, suggests the Rb/Cs of the Moon is also less than that of Earth. Fractionation of the alkali elements between Earth and Moon are in the opposite sense to predictions based on the relative volatilities of these elements, if the Moon formed by high-T processing of Earth's mantle. Earth, rather than the Moon, appears to carry a signature of volatility-related fractionation in the alkali elements. This may reflect an early episode of intense heating on Earth with the Moon's alkali budget accreting from cooler material.

Moon: Rb/Cs ratios of lunar rocks typically fall between 10 and 40 with mare basalts and KREEP defining a value of about 22 ± 3 [3,4]. There may to be resolvable differences in the compositions of pyroclastic glasses compared to crystalline mare basalts, with pyroclastic lunar glasses having lower Rb/Cs ratios, closer to chondritic and more similar to those of pristine lunar highlands rocks. A composite sample of Apollo 15 green glass had a Rb/Cs of about 15 [5], and individual spherules of Apollo 17 orange glass have remarkably low Rb/Cs ratios of 6-18, averaging 10 [6]. This average value is notably similar to that of CI chondrites (Rb/Cs = 12; [7]). However the database remains exceedingly small as only 5 of the spherules analyzed by [6] gave both Rb and Cs data.

Estimates of the bulk composition of the lunar crust are somewhat variable, with [9] deriving values of 1.7 ppm Rb and Rb/Cs = 24, essentially that of KREEP, compared to 0.7 ppm Rb and Rb/Cs = 35 from KREEP-free lunar meteorites [10]. It is not clear what the high Rb/Cs component is in the lunar meteorites, as pristine lunar highlands rocks tend to have Rb/Cs ratios somewhat lower than that of KREEP, typically 2-20, averaging around 15 [3,4]. The low Rb and Cs concentrations in pristine ferroan anorthosites make them an inconsequential geochemical reservoir, but Mg-suite norites have Rb contents of around 1-5 ppm and could contribute significantly to the overall bulk composition of the lunar crust [8].

The Moon probably has a Rb/Cs of between 15-25, similar to the meteoritic values of 16-24 for eucrites and howardites, and 14-17 for shergottites [11]. Portions of the Moon may have Rb/Cs ratios close to the chondritic value although these volatile-enriched reservoirs cannot be of volumetric significance. The Rb/Cs ratio of the Moon is not unique in the solar system, and an additional stage of high-temperature processing beyond the general volatile depletion observed for the eucrite parent body is not apparent in the alkali element signature of the Moon.

Earth The depleted mantle of the Earth has a Rb/Cs of 85 ± 20, as shown by fresh tholeiitic basalts from mid-ocean ridges and ocean islands [12]. Direct determination of the alkali content of the mantle via ultramafic xenoliths is difficult because of their low concentrations of alkali elements, particularly Cs, and the potentially severe effects of weathering, alteration and metasomatism, all of which tend to lower Rb/Cs ratios of xenoliths [13]. The 'most primitive' San Carlos xenolith of [14] has a Rb/Cs of 103, similar to that of fresh oceanic tholeiites. Least-metasomatized mantle xenoliths from SE Australia also have Rb/Cs values of about 100 [13].

High concentrations of alkali elements in the continental crust make it a significant repository of these elements [4]. However, alkali element compositions of the bulk continental crust are

poorly known due to the highly mobile nature of these elements during weathering and metamorphism. A Rb/Cs value of 19 ± 11 for the upper crust has been derived from sediments, sedimentary rocks, and loess [4], leading to bulk continental and primitive mantle values of 25 and 28, respectively. This bulk earth value would indicate similar compositions for the Earth and Moon. The mass balance model offered by [4] could not account for the Earth's budget of Rb and Cs from the continental crust, oceanic basalt reservoir (MORB+OIB), and oceans, and invoked a hypothetical less-depleted mantle reservoir. An alternative mass balance model by [15] that relied solely on known geochemical reservoirs determined a primitive mantle Rb/Cs of around 40, indicating a significant compositional difference between Earth and Moon.

Although sediments are especially suitable for estimating upper crustal abundances of insoluble elements (REE, Th, Sc) [16], this approach may not be appropriate for the alkalies due to the unequal selectivity of clay minerals (Cs>Rb>K>Na) [17], their orders of magnitude longer aqueous residence times compared to the REE [16], and the rapid (<1 m.y.) fractionation of these elements during subaerial weathering [18]. Alternatively, primary crystalline rocks may provide more direct constraints on the composition of continents. Despite intensive investigations of alkali element concentrations in crustal rocks, the dataset for rocks which may be considered primary continental material is surprisingly sparse. Archean felsic rocks which have K/U ratios close to the nominal crustal and bulk Earth value (10,000) have Rb/Cs ratios averaging 35 [19]. The K/U ratio of these rocks suggests their mobile elements may not have been severely modified. Coexisting sediments are consistent with this composition, but range to lower Rb/Cs and K/U [20]. Granulites typically have higher Rb/Cs and K/U [4, 19].

Phanerozoic I-type granitic batholiths and felsic eruptives provide important samples of younger primary additions to the continental crust. In the western U.S., the temporal progression from Cretaceous sodic batholiths to Tertiary potassic rhyolites is analogous to the classic pattern of crustal evolution in many Precambrian terranes, but without the complication of granulite facies metamorphism. A good example of this analogue within a coherent crustal block is the magmatic evolution recorded by the Idaho batholith and the Snake River Plain (SRP). Idaho batholith tonalites are compositionally similar to Archean sodic tonalites. SRP rhyolites are more potassic and have many geochemical characteristics in common with post-Archean upper crust (REE pattern, La/Th, K/Rb) [21]. Idaho batholith tonalites have Rb/Cs = 44-84, averaging 45, whereas least-fractionated SRP rhyolites have Rb/Cs of 55 [21 and unpub. data]. In contrast, tuffaceous sediments from the SRP have Rb/Cs = 17, suggesting significant fractionation of the alkalies during transport and sedimentation. A model for the felsic component of the continental crust based on 75% Idaho batholith tonalite (Archean analogue) and 25% SRP rhyolite (post-Archean analogue; proportions from [16]) has Rb/Cs = 50, K/Rb = 280, Th/U = 3.8 and K/U = 7530.

This model crust produces primitive mantle compositions with Rb/Cs ≥ 40. This value is significantly different from that of the Moon, and in the opposite sense to that expected if the Moon formed by thermal processing of material derived from Earth's mantle. Earth, rather than the Moon, appears to carry a signature of volatility-related fractionation in the alkali elements, possibly reflecting an early episode of intense accretionary heating. The material which accreted alkali elements to the Moon may have largely escaped similar heating.

[1] Cameron and Benz (1991) Icarus 92, 204-216; Benz et al. (1987) Icarus 71, 30-45 [2] Ringwood (1989) Z. Naturforsch. 44, 891-923 [3] Wolf et al. (1979) PLPSC 10, 2107-2130, Kreutzberger et al. (1986) GCA 50, 91-98 [4] McDonough et al. (1992) GCA 56, 1001-1012 [5] Ganapathy and Anders (1974) PLSC 5, 1181-1206 [6] Hughes et al. (1989) PLPSC 19, 175-188 [7] Anders and Grevesse (1989) GCA 53, 197-214 [8] Ryder (1979) PLPSC 10, 561-581 [9] Taylor S.R. (1982) Planetary Science: A Lunar Perspective. LPI, Houston. 481 pp [10] Palme et al. (1991) GCA 55, 3105-3122 [11] Wanke et al. (1977) PLPSC 8, 2191-2213; Palme H. et al. (1978) PLPSC 9, 25-57; Burghele et al. (1983) LPS XIV, 80-81 [12] Hofmann and White (1983) Z. Naturforsch 38, 256-266 [13] Zindler and Jagoutz (1988) GCA 52, 319-333; O'Reilly and Griffin (1988) GCA 52, 433-447; Griffin et al. (1988) GCA 52, 449-459 [14] Jagoutz et al. (1979) PLPSC 10, 2031-2050 [15] Jones and Drake (1993) GCA 57, 3785-3792 [16] Taylor and McLennan (1985) The continental crust: its composition and evolution. Blackwell, Oxford, 312 pp [17] Brouwer et al. (1983) J. Phys. Chem. 87, 1213-1219; Comans et al. (1991) GCA 55, 433-440; Sawhney (1972) Clays and Clay Minerals 20, 93-100 [18] Feigenson et al. (1983) CMP 84, 390-405 [19] Glickson (1976) GCA 40, 1261-1280; Hart et al. (1990) Chem. Geol. 82, 21-50 [20] Wronkiewicz and Condie (1987) GCA 51, 2401-2416 [21] Norman et al. (1992) Trans. R. Soc. Edinburgh 83, 71-81

FORMATION OF IRON METAL AND GRAIN COAGULATION IN THE SOLAR NEBULA, Joseph A. Nuth III and Otto Berg, Astrochemistry Branch, Code 691, NASA-Goddard Space Flight Center, Greenbelt, MD 20771

The interstellar grain population in the giant molecular cloud from which the sun formed contained little or no iron metal.[1] However, thermal processing of individual interstellar silicates in the solar nebula is likely to result in the formation of a population of very small iron metal grains.[2] If such grains are exposed to even transient magnetic fields, each will become a tiny dipole magnet capable of interacting with other such dipoles over spatial scales orders of magnitude larger than the radii of individual grains.[3] Such interactions will greatly increase the coagulation cross-section for this grain population. Furthermore, the magnetic attraction between two iron dipoles will significantly increase both the collisional sticking coefficient and the strength of the interparticle binding energy for iron aggregates. Formation of iron metal may therefore be a key step in the aggregation of planetesimals in a protoplanetary nebula. Such aggregates may have already been observed in protoplanetary systems.[4]

Experimental studies have demonstrated the enormous increase in the coagulation efficiency of magnetized iron particles[3] and have shown that the enhancement in the effective interaction distance (R) between two magnetic dipoles can be approximated by

$$R = a\left[1 + 2\left(\frac{4\pi}{3}\right)^{1/3}\frac{m_1 m_2}{M\ \mu}\left(\frac{n_o}{V_o^2}\right)^{1/3}\right]^{1/2} \qquad (1)$$

where a is the average particle radius, m_1 and m_2 are the magnetic pole strengths, M is the reduced mass of the interacting particles, μ is the magnetic permeability, n_0 is the initial number density of iron grains and V_0 is their average relative velocity. For $a = 30$ nm, $m_1 = m_2 = 5 \times 10^{-4}$ esu, $M = 7 \times 10^{-17}$ g, $\mu = 1$, $n_0 = 10^6$ cm^{-3} and $V_0 = 1$ cm/sec, equation (1) predicts an effective interaction length of ~ 2.5 cm, an enhancement over the geometric radius by a factor of nearly 10^6.

The enhancement is directly proportional to the strength of the magnetic dipoles and inversely proportional to the relative velocity. It is less sensitive to the reduced mass of the interacting particles ($\alpha\ M^{-1/2}$) and almost insensitive to the initial number density of magnetic dipoles ($\alpha\ n_0^{1/6}$). We are in the process of measuring the degree of coagulation in our condensation flow apparatus as a function of applied magnetic field and correlating these results by means of magnetic remanance acquisition measurements on our iron grains with the strength of the magnetic field to which the grains are exposed. Results of the magnetic remanance acquisition measurements and the magnetic-induced coagulation study will be presented as well as an estimate of the importance of such processes near the nebular midplane.

References 1. Cassen, P. and A. Boss (1988) in Meteorites and the Early Solar System 015=/8=/01(J0. Kerridge and M. Mathews, eds.) pp 304-328 (Univ. Ariz. Pres., Tucson). 2. Nuth, J. (1989) Earth, Moon and Planets 47, 33-50. 3. Nuth, J., O. Berg, J. Faris and P. Wasilewski (1993) Icarus (in press). 4. Beckwith, S. and A. Sargent (1991) Ap. J. 381, 250-28.

MEASUREMENT OF THE DECAY RATE OF THE SiH FEATURE AS A FUNCTION OF TEMPERATURE. Joseph A. Nuth III[1] and George F. Kraus[1,2] (1. Code 691, NASA-GSFC, Greenbelt, MD: 2, Physical Sciences Dept., Charles County Comm. Col., LaPlata, MD)

We have previously suggested that the SiH fundamental stretch could serve as a diagnostic indicator of the oxidation state of silicate surfaces exposed to the solar wind for prolonged periods.[1] We have now measured the primary decay rate of SiH in vacuo as a function of temperature and find that the primary rate constant for the decay can be characterized by the following equation: $k\ (min^{-1}) \approx 0.186 \exp(-9/RT)\ min^{-1}$, where $R = 2 \times 10^{-3}$ kcal deg^{-1} $mole^{-1}$. This means that the half-life for the decay of the SiH feature at room temperature is ~20 yrs, whereas the half-life at a peak lunar regolith temperature[2] of ~500K would be only ~20 days. At the somewhat lower temperature of ~400K the half-life for the decay is on the order of 200 days. The rate of loss of SiH as a function of temperature provides an upper limit to the quantity of H implanted by the solar wind which can be retained by a silicate grain in a planetary regolith. This will be discussed in more detail below.

Silica smokes were prepared by burning SiH_4 diluted in H_2 with O_2 in a tube furnace at ~750K.[3] The resultant product was yellowish-tan SiO_x (where $x \approx 1.5$) and exhibited a relatively strong feature near 4.4 microns attributable to the SiH stretching fundamental in an oxidized silicate. Samples were stored in a dessicator. The smoke was diluted by about a factor of 20 with KBr and placed into the sample cup of a Harrick Environmental Chamber mounted in a Mattson Polaris FTIR spectrometer equipped to yield diffuse reflectance spectra. A background spectrum of pure KBr would have already been obtained in the same apparatus. The environmental chamber was then evacuated to a pressure of less than 1 torr using a mechanical pump and the temperature of the sample cup raised to the desired temperature. Once the temperature had stabilized at the set point an initial spectrum was obtained (Ao) and the system was programmed to obtain subsequent spectra at regular intervals: the mechanical pump was on throughout the experiment. The area under the SiH stretch ratioed to the area under the SiO stretch was then measured as a function of time to obtain the SiH decay rate at a given temperature. Measurements were obtained at 650, 700, 750 and 800 K.

Plots of ln[(A(4.6)/Ao(4.6)/(A(10)/Ao(10)] versus time for the data obtained at both 650 and 800 K yield simple first order decays. Similar plots for the data obtained at 700 and 750 K show two distinct components to the decay. In each case, the slower, long-lived decay yields a rate consistent with what would be expected by interpolation of the 650 and 800 K data points on an Arrhenius Plot; e.g. a process with an activation energy of approximately 9 kcal/mole. The faster decays yield an activation energy on the order of 60 kcal/mole but are only important at the very beginning of the experiments. If the process were a unimolecular rearrangement of the silicate lattice resulting in the elimination of the SiH bond it should dominate the decay for the entire experiment.

We hypothesize that the initial, fast decay of the SiH feature in these experiments is the result of chemisorbed oxygen atoms diffusing into the lattice of the amorphous silicate and reacting to displace the H atoms. This process would stop with the depletion of the chemisorbed oxygen. The activation energy of the process is consistent with that for the diffusion of oxygen through non-stoichiometric oxides.[4] A calculation of the rate of the "fast" reaction at 650 K based on an extrapolation of the 700 and 750 K data shows that this process could account for roughly half of the initial loss of SiH before the oxygen is depleted: there is some evidence for this in the data. Unfortunately the signal to noise ratio

PRECEDING PAGE BLANK NOT FILMED

depleted: there is some evidence for this in the data. Unfortunately the signal to noise ratio is too low to definitively separate the two decay processes in this dataset. A calculation of the rate of the "fast" reaction at 800 K indicates that the reaction is probably completed during the sample warmup and before we obtained our first spectra. We are in the process of analyzing data obtained in air and therefore hope to more definitively determine the mechanism for the rapid loss of SiH in the 700 and 750 K datasets.

Thermal decomposition of SiH should be the primary decay process on planetessimals and will set a limit on the quantity of SiH which one would expect to accumulate in regolith grains. Such grains should reach an equilibrium between H-implantation from the solar wind and thermal decomposition of the SiH on a timescale equivalent to a few decay halflives. For the lunar surface this will occur within a period of from several months for the subsolar regolith to several years for cooler regolith materials. Asteroidal regoliths at temperatures of 250, 200 and 150 K will equilibrate on timescales of 350, 27 thousand, and 38 million years, respectively (based on one e-folding timescale). Even considering the inverse square decrease in the density of the solar wind as a function of heliocentric distance, the much longer timescales available for the buildup of SiH bonds in asteroidal regolith grains make such bodies ideal candidates to detect this feature.

References: 1. Nuth, J. A., Moore, M. H., Tanabe, T. and Kraus, G., Icarus 98, 207(1992). 2. Heiken, G., Vaniman, D. and French, B., The Lunar Sourcebook, (Cambridge Univ. Press, London, 1991) chap. 1. 3. Rietmeijer, F. J. M. and Nuth, J. A., Proc. Lun. Plan. Sci. Conf., 21, 591 (1991). 4. Matzke, Hj. in Non-stoichiometric Oxides (O. T. Sorensen, ed) (Acad. Press, NY, 1981) Chap. 4.

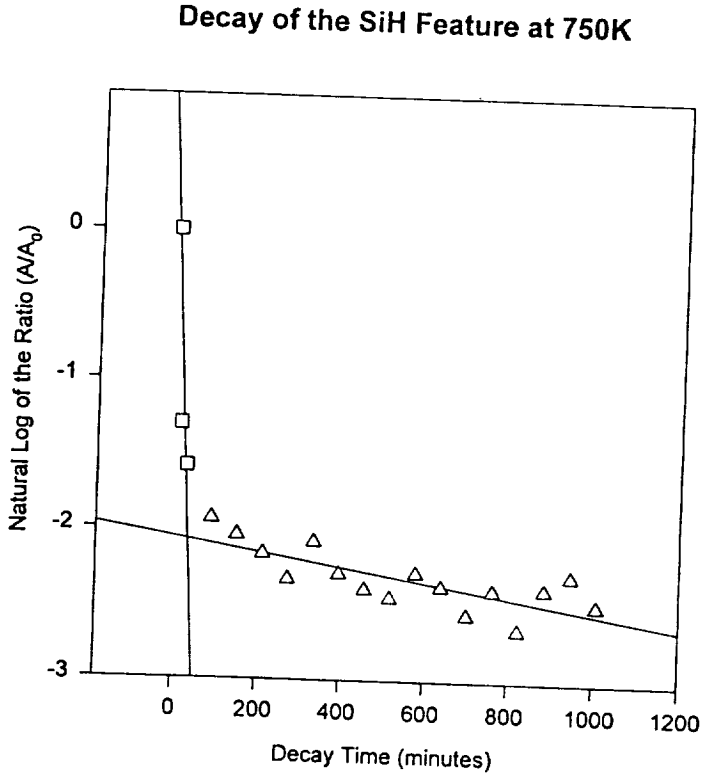

S36-90 NASA-SNG
P.2 P.3

PRE-BOMBARDMENT CRYSTALLIZATION AGES OF BASALTIC CLASTS FROM ANTARCTIC HOWARDITES EET87503 AND EET87513. L.E. Nyquist, NASA Johnson Space Center, Houston, TX 77058; C.-Y. Shih, H. Wiesmann, and B.M. Bansal, Lockheed Engineering and Science Co., 2400 NASA Road 1, Houston, TX 77258.

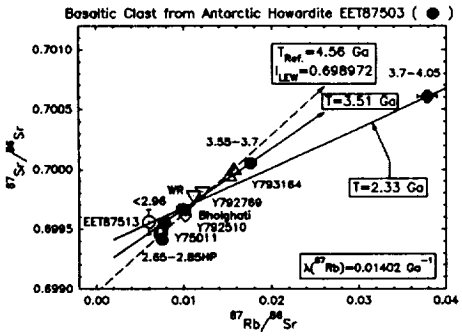

Figure 1. Rb-Sr data for whole rock and density-separated minerals of EET87503,53. Whole rock data for other eucrite clasts and matrix are shown for comparison.

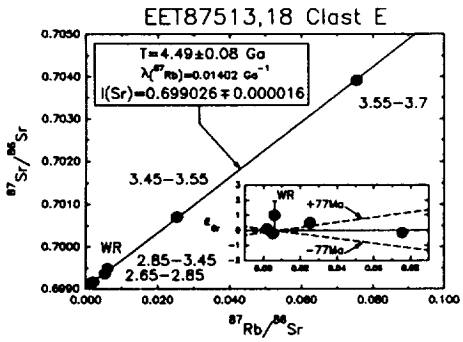

Figure 2. Rb-Sr isochron for density-separated minerals from EET87513,18 (clast E).

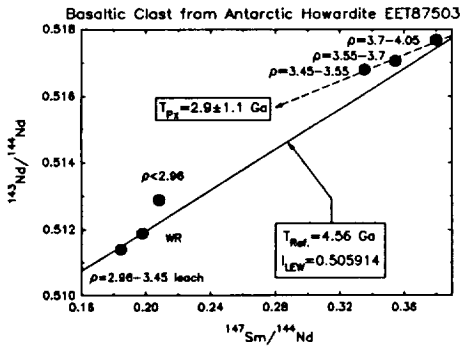

Figure 3. Sm-Nd isochron diagram for EET87503,53.

Abstract: Igneous clasts of basaltic eucrites are found in both howardites and polymict eucrites. We have studied the Rb-Sr and Sm-Nd isotopic systematics of a number of such clasts, of metamorphic grades 1-6, using the classification of Takeda and Graham [1]. Here, we report Rb-Sr, ^{147}Sm-^{143}Nd, and ^{146}Sm-^{142}Nd studies of clast ,53 from Antarctic howardite EET87503. Although there is no evidence of disturbance of trace element systematics by Antarctic weathering [2], the Rb-Sr and conventional Sm-Nd isotopic sytematics are severely disturbed, which we ascribe to thermal metamorphism. The Ar-Ar age spectrum shows ages ranging from ~3.85-3.55 Ga in an unusual "down stairstep" [3]. The ^{146}Sm-^{142}Nd systematics, however, show the presence of live ^{146}Sm ($t_{1/2}$ = 103 Ma), with $^{146}Sm/^{144}Sm = 0.0061\pm0.0007$ at the time of crystallization. This result is very similar to that previously obtained for basaltic clast ,18 from howardite EET87513 (paired with EET87503), which has concordant Rb-Sr and Sm-Nd ages of ~4.5 Ga [4]. Thus, the two clasts are nearly the same age, and we conclude further that the EET87503,53 clast crystallized within 33±19 Ma of the LEW86010 angrite by comparing initial $^{146}Sm/^{144}Sm$ to that of the angrite [8,9]. We suggest that disturbances in the isotopic systematics of EET87503,53 are consanguineous with pyroxene homogenization.

Rb-Sr Data: Rb-Sr data for EET87503,53 are shown in Fig.1. The whole rock (WR) data are typical of a number of eucrite clasts previously studied in our laboratory, and of eucrites in general. The Rb-Sr systematics of mineral phases also are similar to those of the "large" eucrite clast from the Bholghati howardite [5] except for unusually low Sr in plagioclase-enriched separates. However, they are spectacularly different from those of EET87513,18 (Fig. 2). The Rb-Sr data for EET87503,53 suggest an isotopic disturbance ~2.3-3.5 Ga ago, whereas the EET87513,18 data determine a well-fit isochron corresponding to an age of 4.49±0.08 Ga. The Rb-Sr systematics of eucritic pyroxenes are commonly disturbed [6], and when apparently well defined Rb-Sr ages near ~4.56 Ga are found, they often rely on the presence of a highly radiogenic mesostasis. The pristine clast Y75011,84B is exceptional in having undisturbed Rb-Sr systematics for both pyroxenes and mesostasis [7].

Sm-Nd Data: Figure 3 shows the Sm-Nd data in a conventional Sm-Nd isochron diagram. The WR datum plots on a 4.56 Ga reference isochron for initial $^{143}Nd/^{144}Nd$ equal to that measured for the LEW86010 angrite [8,9], consistent with the absence of weathering disturbance. However, density-separated mineral phases plot distinctly off the reference isochron. All mineral phases were leached in 1 N HCl to remove phosphates, which, if present, could dominate the Sm-Nd systematics. The leachate of mixed mineral phases of intermediate density (2.96-3.45 g/cm^3)

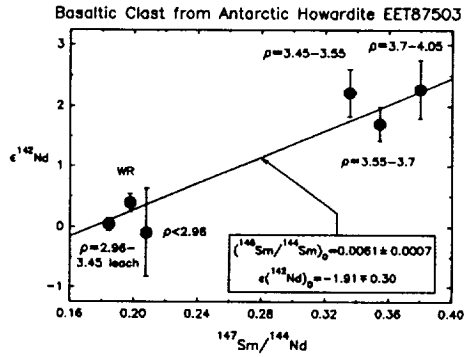

Figure 4. ^{146}Sm–^{142}Nd formation interval diagram.

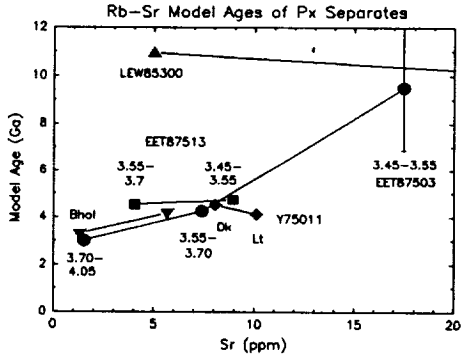

Figure 5. Rb–Sr model ages of pyroxene separates from basaltic clasts in howardites and polymict eucrites. Data from [4], [5], [7], and [10].

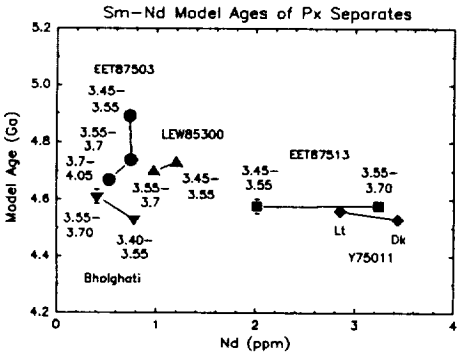

Figure 6. Sm–Nd model ages of pyroxene separates from basaltic clasts of howardites and polymict eucrites. Data from [4], [5], [7], and [10].

plots slightly below the reference isochron. The pyroxene separates progress from low to high density along a secondary isochron corresponding to an apparent age of 2.9±1.1 Ga, similar to that calculated from the Rb-Sr data of the WR and densest pyroxene (Fig. 1).

The ^{146}Sm–^{142}Nd systematics are shown in Fig. 4. In spite of disturbances in the conventional Sm-Nd systematics, these data define a line of slope corresponding to initial $^{146}Sm/^{144}Sm$ = 0.0061±0.0007, similar to 0.0066±0.0009 previously found for the EET87513,18 clast, establishing that the crystallization ages of the two basaltic clasts also are very similar.

Discussion: Why are the isotopic systematics of one howardite clast grossly disturbed, while those of another clast from a paired meteorite apparently undisturbed? We suggest the answer is linked to the differing degrees of pyroxene homogenization in the two clasts. Figure 5 summarizes Rb-Sr model ages, relative to initial $[^{87}Sr/^{86}Sr]_{LEW}$ = 0.69897 [8,9], of pyroxene separates from eucrite clasts analyzed in our laboratory; Figure 6 is an analogous summary of Sm-Nd model ages relative to initial $[^{143}Nd/^{144}Nd]_{LEW}$ =0.505914 [8,9]. Pyroxenes for each clast were separated by similar techniques, except for the Y75011 pyroxenes. The Y75011,84B clast is the least altered eucritic basalt and is classified as metamorphic grade 1 [1]. Clasts EET87513,18 and EET87503,53 are classified as grades 2-3 [11] and 5-6 [2], resp. For clasts of low metamorphic grade, the most Fe-rich, densest, pyroxene compositions are found at the rims of pyroxene grains, whereas clasts of high metamorphic grade are characterized by the presence of augite exsolution lamellae in host pigeonite or orthopyroxene of homogeneous composition [1]. Augite lamellae in EET87503,53 are ~10-20 μm wide and separated by ~60 μm [2]. Mineral separations were for material in the 44-74μm size range, thus, at least for this clast, significant fractionation of high- and low-Ca (high-and low-Sr) pyroxene should have been achieved. Both Rb-Sr and Sm-Nd model ages of the pyroxene separates from the two clasts of low metamorphic grade are ~4.5-4.6 Ga, i.e., the isotopic systematics of these clasts are undisturbed. However, the isotopic systematics of pyroxenes from clasts of high metamorphic grade in EET87503, Bholghati, and LEW85300 are disturbed, with low-density, Sr-rich, "pyroxene" separates having high Rb-Sr model ages, whereas high-density, Sr-poor "pyroxene" separates have low Rb-Sr model ages (Fig. 5). Less pronounced, but similar effects are shown by the Sm-Nd data (Fig. 6). We suggest trace element migration accompanied pyroxene exsolution and homogenization, presumably, during impact-related thermal metamorphism [1,7,12]. The ^{146}Sm–^{142}Nd systematics were little if at all affected, and preserve the pre-bombardment crystallization ages of the basalt clasts.

REFERENCES: [1] Takeda H. and Graham A.L. (1991) Meteoritics **26**, 129–134. [2] D. Mittlefehldt, p. comm. [3] D. Bogard, p. comm. [4] Nyquist L.E. et al. (1992) LPS XXIII, 1009–1010. [5] Nyquist et al. (1990) GCA **54**, 2195–2206. [6] Birck J.-L. and Allegre C.J. (1978) EPSL **39**, 37–51. [7] Nyquist et al. (1986) JGR **91**, 8137–8150. [8] Nyquist L.E. et al. (1991) LPS XXII, 989–990. [9] Nyquist L.E. et al. (1994) Meteoritics (submitted). [10] Nyquist L.E. et al. (1990) LPS XXI, 903–904. [11] P. Buchanan, p. comm. [12] Harlow G.E. and Klimentidis R. (1980) PLPSC **11**, 1131–1143.

N94-36173

NEW DATA SUPPORTING A $^{146,147}Sm$-$^{142,143}Nd$ FORMATION INTERVAL FOR THE LUNAR MANTLE.

L.E. Nyquist, NASA Johnson Space Center, Houston, TX 77058; H. Wiesmann, B.M. Bansal, and C.-Y. Shih, Lockheed Engineering and Science Co., 2400 NASA Road 1, Houston, TX 77258.

Table 1. Isotopic abundance of ^{142}Nd in ϵ-units relative to $^{142}Nd/^{144}Nd$ in the Ames standard; normalized to $^{146}Nd/^{144}Nd$ and $^{148}Nd/^{144}Nd$.

Sample	N	ϵ^{142}_{Nd}	
		146 Norm.	148 Norm.
14310	2	−0.11±0.16	−0.40±0.19
14310	6	−0.16±0.07	−0.12±0.11
14310	5	−0.18±0.15	−0.20±0.17
14078	4	−0.12±0.20	−0.16±0.18
14078	5	−0.07±0.12	−0.14±0.16
15076	4	−0.16±0.18	−0.16±0.26
15076	4	−0.19±0.09	−0.27±0.16
15555	1	−0.24±0.54	+0.18±0.21
15555	3	+0.18±0.18	+0.22±0.17
15555	3	−0.07±0.11	−0.17±0.12
74255	1	−0.03±0.22	+0.04±0.26
74255	6	+0.17±0.11	+0.16±0.15
Asuka 31	2	+0.32±0.16	+0.26±0.21
G2	3	−0.07±0.21	+0.08±0.30
BCR-1	2	−0.06±0.26	+0.03±0.30
ORB 1154	3	+0.04±0.21	+0.04±0.30

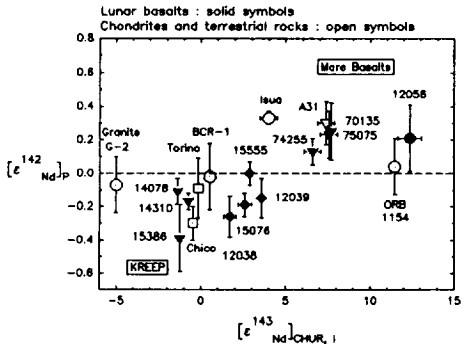

Figure 1. ϵ^{142}_{Nd} for lunar basalts, terrestrial rock standards, the Chico and Torino chondrites, and an Isua supracrustal rock [3].

Abstract: Very small variations in ^{142}Nd abundance in SNC meteorites [1] lunar basalts [1,2] and a terrestrial supracrustal rock [3] have been attributed to the decay of 103 Ma ^{146}Sm initially present in basalt source regions in varying abundances as a result of planetary differentiation. We previously interpreted variations in ^{142}Nd abundances in two Apollo 17 high-Ti basalts, three Apollo 12 low-Ti basalts, and two KREEP basalts as defining an isochron giving a formation interval of ~94 Ma for the lunar mantle [2]. Here we report new data for a third Apollo 17 high-Ti basalt, two Apollo 15 low-Ti basalts, the VLT basaltic lunar meteorite A881757 (formerly Asuka 31), basalt-like KREEP impact melt rocks 14310 and 14078, and three terrestrial rock standards. Those lunar samples which were not exposed to large lunar surface thermal neutron fluences yield a revised mantle formation interval of 237±64 Ma.

Data: Numerical data are reported in Table 1. Quoted error limits are the greater of the standard deviation of the mean ($2\sigma_m$) for N sample analyses, or $2\sigma_p/N^{1/2}$, where σ_p is the standard deviation of a much larger population of standards analyzed in the same sample series. The data were normalized to both $^{146}Nd/^{144}Nd$ and $^{148}Nd/^{144}Nd$ to avoid biases from interferences under the normalization isotope. Typical values of $2\sigma_p$ were ±0.16ϵ and ±0.18ϵ for $^{142}Nd/^{144}Nd$ normalized to $^{146}Nd/^{144}Nd$ and $^{148}Nd/^{144}Nd$, respectively. Corrections were made for interferences from ^{142}Ce and $^{144,148}Sm$ using the well-known isotopic compositions of these elements in terrestrial samples. The uncertainties in these corrections are small because the interferences are measured continuously and simultaneously with the isotopes of interest. Additionally, the mass spectrum below and above Nd was scanned at high sensitivity (electron multiplier) prior to data acquisition. The 74255 sample was twice passed through the ion exchange column to remove Ce and Sm from Nd, yielding $^{140}Ce/^{144}Nd$ ~7×10^{-6} ($^{142}Ce/^{144}Nd$ ~1×10^{-6}) and $^{154}Sm/^{148}Nd$ ~2×10^{-5} ($^{144}Sm/^{144}Nd$ ~7×10^{-7}).

Discussion: Figure 1 compares the new data to earlier measurements for lunar basalts and three terrestrial rock standards, USGS standard granite G-2, USGS standard basalt BCR-1, and ocean ridge basalt ORB-1154 [4]. Weighted averages of ϵ^{142}_{Nd} calculated with the two normalizations (Table 1) are plotted as present-day $[\epsilon^{142}_{Nd}]_P$ vs. initial $[\epsilon^{143}_{Nd}]_{CHUR,I}$ relative to a Chondritic Uniform Reservoir (CHUR, [5]) at the time of basalt crystallization. The new analyses of 14078 are preferred to those reported previously [2] because of improved instrument and run conditions. A positive correlation is evident for the lunar data, but not for the terrestrial rock standards, for which $^{142}Nd/^{144}Nd$ values are indistinguishable from the Ames shelf standard.

Figure 2 shows some possible evolutionary paths for source reservoirs formed at Δt = 100, 200, and 300 Ma after the angrite LEW86010 [6,7] for "Highly Depleted Mantle" (HDM), "Less

LUNAR MANTLE FORMATION INTERVAL: Nyquist L.E., et al.

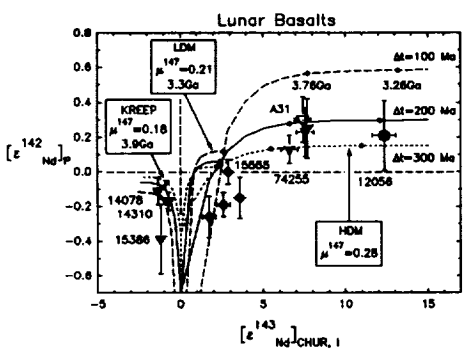

Figure 2. Evolutionary paths from $\epsilon^{142}_{Nd} = -2.69$ at 4.558 Ga ago for the Ames standard and $[^{147}Sm/^{144}Nd]_{CHUR} = 0.1967$.

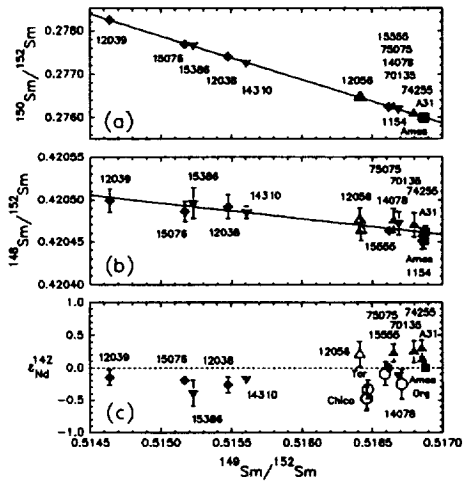

Figure 3. Correlation of (a) $^{150}Sm/^{152}Sm$ and (b) $^{148}Sm/^{152}Sm$ to $^{149}Sm/^{152}Sm$. ϵ^{142}_{Nd} vs. $^{149}Sm/^{152}Sm$ is shown in (c).

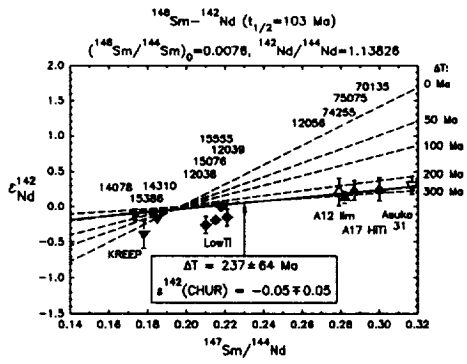

Figure 4. Lunar mantle isochron (see [2]) with updated data. Regression omits samples with high neutron fluence.

Depleted Mantle" (LDM) and the source of lunar KREEP. Values of μ^{147} ($^{147}Sm/^{144}Nd$) assumed for the KREEP, LDM, and HDM sources were 0.18, 0.21, and 0.28, respectively. The evolutionary paths were calculated with the assumptions that $^{142}Nd/^{144}Nd$ of our Ames shelf standard is appropriate for the CHUR-reservoir, which in turn is appropriate to the nascent moon. Neither assumption need be true. Points along the curve show values at basalt ages of 3.9 Ga (KREEP), 3.76 Ga (Apollo 17 high-Ti, Asuka 31 [8]), 3.3 Ga (Apollo 15 low-Ti), and 3.26 Ga (Apollo 12 ilmenite basalt 12056), respectively. The calculated curves provide a reasonable match to the data with the exception of three low-Ti basalts (12038, 15076, 12039) and an earlier analysis of KREEP basalt 15386, which plot below the curves. Nevertheless, the calculations provide at least a qualitative explanation of the rough correlation between $[\epsilon^{142}_{Nd}]_P$ and $[\epsilon^{143}_{Nd}]_{CHUR,I}$ for the lunar basalt data, and for the decoupling of these parameters with decreasing basalt age.

Discussion: Because of uncertainty in the lunar initial ϵ^{142}_{Nd}, we developed the lunar mantle isochron approach which is based on lunar ^{146}Sm-^{142}Nd systematics alone [2]. However, the possibility of non-radiogenic contributions to the variations in lunar $^{142}Nd/^{144}Nd$ ratios also must be considered. Cosmic-ray induced variations in the relative abundances of ^{149}Sm and ^{150}Sm due to thermal neutron capture by ^{149}Sm provide a sensitive monitor of lunar surface irradiation (Figure 3a). The Sm isotopic data for these samples also suggests neutron-induced variations of up to ~1 ϵ-unit in the abundance of ^{148}Sm, in spite of a thermal neutron capture cross section for ^{147}Sm which is nearly 1000-fold less than that of ^{149}Sm (Figure 3b). The thermal neutron capture cross section for ^{142}Nd is ~three-fold lower still, and no trend of ϵ^{142}_{Nd} with $^{149}Sm/^{152}Sm$ is clearly established. Nevertheless, there is a tendency among basalts of a given type for those with high neutron fluences to have low ϵ^{142}_{Nd} (12038, 12039 and 15076 vs. 15555; 15386 and 14310 vs. 14078). Omitting samples with high neutron fluence from the lunar mantle isochron regression (Figure 4) yields $\Delta t = 237\pm64$ Ma and $[\epsilon^{142}_{Nd}]_{CHUR} = -0.05\pm0.05$ (2σ from the Williamson [9] regression). These parameters differ from $\Delta t = 94\pm23$ Ma, $[\epsilon^{142}_{Nd}]_{CHUR} = -0.31$ found previously [2] primarily because of revised data for 14078 and exclusion of samples with high neutron fluence. Disregarding uncertainties in initial $[\epsilon^{142}_{Nd}]_{CHUR}$, both Figures 2 and 4 show that the HDM must have formed substantially (~100-300 Ma) after ancient meteorites such as the angrites in order not to have easily observed enhancements in ϵ^{142}_{Nd} in basalts derived from it.

REFERENCES: [1] Nyquist L.E. et al. (1991) Meteoritics **26**, 381. [2] Nyquist L.E. (1993) LPS XXIV, 1095–1096. [3] Harper C.L., Jr. and Jacobsen S.B. (1992) Nature **360**, 728–732. [4] Kay R. et al. (1970) JGR **75**, 1585–1613. [5] DePaolo D. J. and Wasserburg G.J. (1976) GRL **3**, 249–252. [6] Nyquist L.E. (1991) LPS XXII, 989–990. [7] Lugmair G.W. and Galer S.J.G. (1992) GCA **56**, 1673–1694. [8] Misawa K. et al. (1993) GCA **57**, 4687–4702. [9] Williamson J.H. (1968) Can. J. Phys. **46**, 1845–1847.

GALILEO'S NEAR INFRARED MAPPING SPECTROMETER (NIMS) SCIENCE OBSERVATION PLAN FOR EUROPA. A. Ocampo and D. Matson, (Jet Propulsion Laboratory, California Institute of Technology, Pasadena, California) and the NIMS team.

On December of 1995 Galileo's Near Infrared Mapping Spectrometer (NIMS) will observe Europa's South pole. This will be the first in a two year series of planned observations for this satellite in the 0.7 to 5.2 microns wavelengths range. NIMS's Europa observation plan will include global (27 km), medium resolution (48-57 km) and high resolution (9-12 km) mosaics. Special attention will be given to leading and trailing sides spectral differences and the Tyre Macula region.

On October 18, 1989 the Galileo spacecraft was launched on its journey to Jupiter. The Near Infrared Mapping Spectrometer (NIMS) is the first instrument of its type (0.7-5.2 microns) to be flown on a planetary mission. NIMS observations will provide unique information on the mineralogical composition and distribution of surface units and features on Europa. This objective is achieved through the collection of an optimum combination of spatial and spectral data. NIMS scientific observation strategy will be presented for the two years nominal mission.

Planned NIMS's observations of Europa are shown for the eleven orbits of the Galileo tour (92-14a) starting December, 1995 . The Jupiter approach orbit provides the only opportunity to observe Europa's South Pole region. The eleventh orbit of the tour provides an excellent, and the only, opportunity to observe the North polar region of the satellite. Both are unique opportunities for NIMS to detect frozen volatile species other than water. Each of the orbits in the tour presents unique opportunities for the NIMS observations needed to address the composition and distribution of surface materials.

Europa's "global" coverage will include all longitudes (except 0-90 degrees) at a spatial resolution of 27 kilometers or better. The "global" coverage will also address the unusually young surface of Europa, such as whether resurfacing occurred in one event or in multiple "flooding" events, and whether there is evidence that indicates these resurfacing processes are still occurring. Global tectonic issues include those of possible plate motion, compositional differences between plates, and the origin, evolution, and chemistry of the liquids that emerged from/near lineaments, craters, and, perhaps palimpsests. Mid-spatial resolution (48-57 km) observations are also planned to study resurfacing, exogenic (e.g. implantation of material from the magnetosphere) and tectonic processes.

A few opportunities are planned for high spatial resolution (9-12 km) spectroscopy of specific areas on Europa, such as Tyre Macula. These observations aim to define compositional units, characterize their boundaries and relationships to tectonic features, and identify species or minerals present in or on the ice.

NIMS has the capability to select wavelengths within the range of 0.7 to 5.2 microns. Most of the observations will be made using 51 wavelengths for discrimination of compositional differences. Higher spectral resolution (more wavelengths) will be performed for selected areas. These observations will be the first spatially resolved spectra to be obtained in this wavelength range and we expect to use them to open a new era in the study of Europa.

CALORIMETRIC THERMOBAROMETRY OF EXPERIMENTALLY SHOCKED QUARTZ. Katherine D. Ocker[1], James L. Gooding[2], and Friedrich Hörz[3]. [1]Dept. of Physics, Sam Houston State University, Huntsville, TX 77340. [2]SN2; [3]SN4, NASA/Johnson Space Center, Houston, TX 77058 USA.

Summary. Structural damage in experimentally shock-metamorphosed, granular quartz is quantitatively measurable by differential scanning calorimetry (DSC). Shock-induced loss of crystallinity is witnessed by disappearance of the α/β phase transformation and evolution of a broad endoenthalpic strain peak at 650-900 K. The strain-energy peak grows rapidly at < 10 GPa but declines with increasing shock pressure; it approaches zero at 32 GPa where vitrification is extensive. Effects of grain size and post-shock thermal history must be better understood before calorimetric thermobarometry of naturally shocked samples becomes possible.

Introduction. Shock metamorphism of quartz is a key factor in recognizing meteorite impact craters on Earth. Shock-metamorphic effects in quartz have been calibrated as "barometers" by a variety of techniques [1], including optical petrography, X-ray diffractometry, transmission electron microscopy, and infrared spectrophotometry. A possible alternative method is DSC, which measures energy flow into or outward from a sample that is heated or cooled at a controlled rate [2]. DSC directly measures polymorphic phase changes as well as more diffuse structural changes that depend on temperature. We studied artificially shocked quartz to evaluate DSC as a thermobarometric technique for shock-metamorphosed planetary samples.

Experimental Procedure. Two discrete size fractions (125-250 μm and 250-500 μm) of loose, granular quartz were shocked at pressures ranging from 9.8 GPa to 33.5 GPa [3]. Shock-recovered samples were split for DSC and for preparation of polished thin sections. For DSC, individual samples of 5-10 mg were held in aluminum oxide containers and heated (or cooled) at 10 K/min over the 300-1000 K range under continuous purge of 20 cm^3 Ar/min. Reheating experiments were run under the same conditions.

Results and Interpretations. Petrographic observations confirm the presence of deformation features that are expected for each shock pressure. With increasing stress, optical damage indicators progress from undulatory extinction, and mosaicism, to multiple sets of planar features and, finally, featureless isotropism. Optical effects are mostly the same for both grain-size fractions except that planar features are more abundant in the coarse-grained charges (250-500 μm).

DSC heat-flow curves show distinct fingerprints as a function of shock pressure (Fig. 1). As expected, shock pressure severely damages or destroys the α-quartz structure so that the normal α/β transition is pre-empted during subsequent heating. The α/β transition is replaced by a broad endoenthalpic peak at 600-950 K that represents annealing of strain in the structurally damaged quartz. Most of the strain is annealed during first heating as witnessed by the systematically smaller peaks during second heating (Fig. 2). For a given grain-size interval, replicate samples produce significant scatter in the DSC data, attesting to the heterogeneous deposition of shock energy in porous samples, in general, and their effects at the milligram scale of sampling. The steep rise in the DSC heat-flow curves near 1000 K (Fig. 1) represents the enthalpic inception of thermally induced devitrification, which is known to occur in quartz glass at 1000-1300 K [1].

Simple parameterization of the DSC data, comprising integration of the 600-950 K strain peak, confirms the thermodynamic variation of crystal damage with shock pressure (Fig. 2). The equivalent parameter for unshocked quartz, which is attributable mostly to

PRECEDING PAGE BLANK NOT FILMED

the α/β transformation, is about 10 J/g. But shock pressure as low as 10 GPa generates strain energy > 100 J/g. At shock pressures > 10 GPa, residual strain energy decreases to nearly zero at 32 GPa. Large strain-energy peaks are correlated with structural damage that is optically manifest as deformed crystals; small strain-energy peaks correlate with high degrees of vitrification. Peak deconvolution, including corrections for the heat-capacity continuum, should provide more refined parameterization of trends.

DSC appears especially sensitive to solid-state deformation at low shock pressures where optical effects imprecisely distinguish pressure. The dependence of strain energy on grain size, and possibly on post-shock thermal history, remains to be resolved.

Acknowledgments. This work was supported by the NASA Planetary Materials and Geochemistry Program (J. Gooding and F. Hörz, PIs) and by the Lunar and Planetary Institute Summer Intern Program (K. Ocker).

References. [1] Stöffler, D. (1993) *Meteoritics, 29,* 444. [2] Gooding, J.L. (1990) *Meteoritics, 25,* 367. [3] Schaal R. B. et al. (1979) *Proc. 10th Lunar Planet. Sci. Conf.,* 2547.

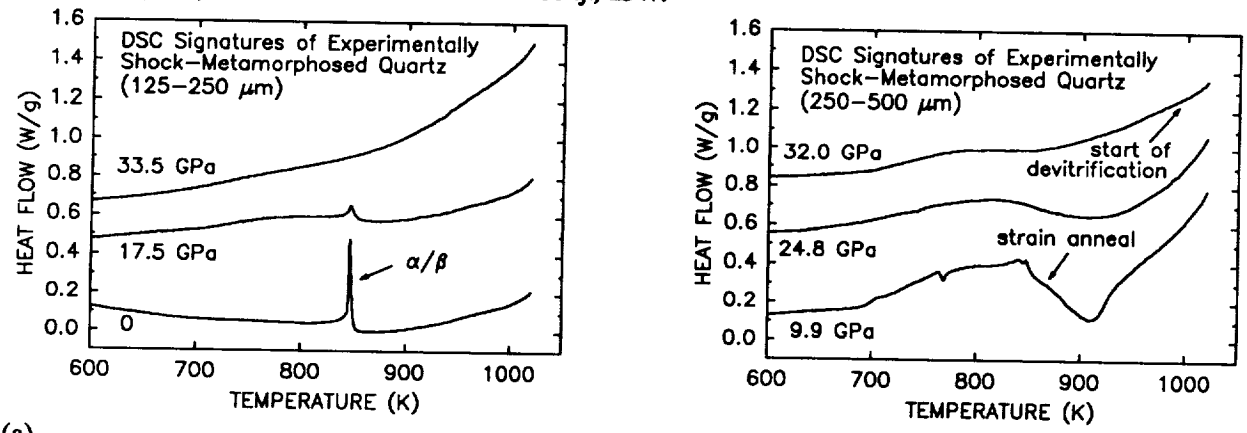

(a) (b)

Figure 1. DSC heat-flow curves (artificially staggered along y-axis for clarity) for experimentally shock-metamorphosed quartz ("0" for no shock). Each curve represents a spline drawn through approximately 1000 data points. In response to shock, the α/β peak disappears and broad "strain" peaks develop at 650-900 K. Grain-size effects probably reflect the influence of porosity on shock propagation.

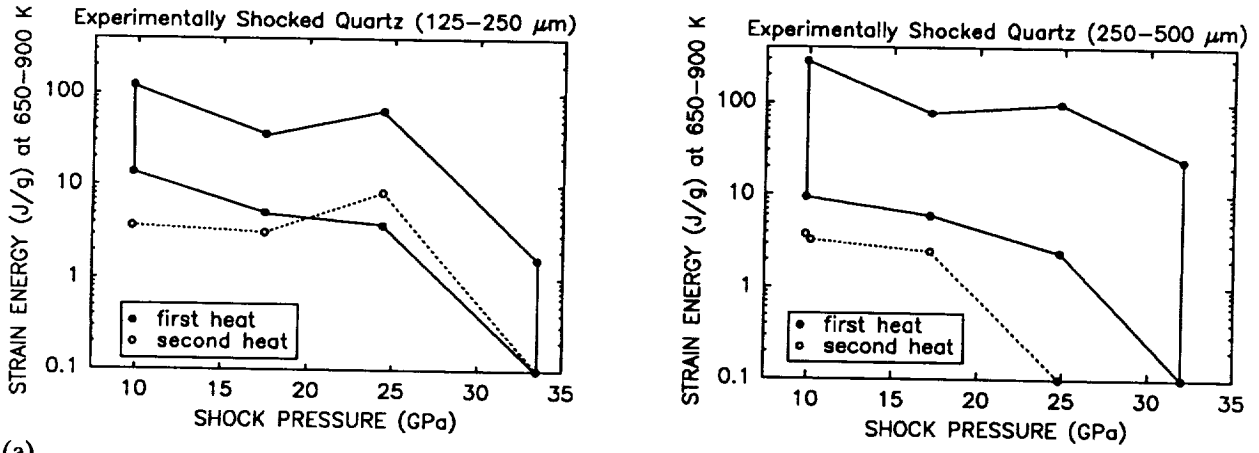

(a) (b)

Figure 2. Simple parameterization of DSC data for shocked quartz. Each data point represents integration of the endoenthalpic strain peak (Fig. 1) for a specific sample. The polygons, comprising points joined by solid lines, represent data fields defined by replicate samples. Single-string data for second heating show that most shock-induced strain is annealed during first heating.

PENETRATION OF LARGE BOLIDES INTO DENSE PLANETARY ATMOSPHERES - ROLE OF HYDRODYNAMIC INSTABILITIES; John D. O'Keefe, Toshiko Takata, and Thomas J. Ahrens, Lindhurst Laboratory of Experimental Geophysics, Seismological Laboratory 252-21, California Institute of Technology, Pasadena, CA 91125

The interaction of high velocity bolides with dense planetary atmospheres is a critical issue in planetary sciences, e.g., the depletion of small scale craters on Venus, and the atmospheric break-up upon impact of Comet Shoemaker-Levy-9 fragments onto Jupiter, Tunguska, tektites, and dispersion of spherules in the K-T event. We have examined this issue using both code calculations and analytical models and have characterized the time scales and depths for bolide: 1) deceleration, 2) deformation and spreading, 3) shedding of mass by instabilities, and 4) disintegration by instabilities and subsequent stopping or impact. We have related our results to laboratory experiments, and planetary surface observations.

The penetration of large bolides(radius = R) relative to the atmospheric scale height(ℓ) into a dense planetary atmosphere can be described in terms of three regimes: 1) initial - prior to distortion, 2) compression and distortion, and 3) disintegration and stopping.

Initial - Prior to Distortion. When the bolide enters the upper region of a planet's atmosphere it induces a high temperature shock wave in the gas in front of the bolide. The radiation and convective flow of the shocked atmosphere around the front melts and ablates material from the bolide. The high speed flow of the atmosphere tangential to the melted material drives surface-wave Kelvin-Helmholtz (K-H) instabilities that grow and shed melt droplets into the flow behind the body. These particles are micron-sized, as the fastest growing wavelengths of the K-H instabilities are microns in length. The relative mass loss for large impactors is small [1]. Wavelengths much shorter ~1 micron are suppressed by the viscosity of the melt and do not grow --this is seen in the turnover in the curves in Figure 1. The time for K-H instabilities to form was calculated using the formulation of Keith and Banks [2]. For example, the time scale for various wavelength K-H instabilities to form is shown in Figure 1.

Compression and Distortion. As the bolide penetrates further into the atmosphere, the dynamic pressure in the shock wave in front of the bolide can exceed the strength of the impactor. Besides fracturing the projectile, the pressures can be sufficient to compress and distort the bolide. The compression occurring during the passage of the fracturing wave is dependent upon R/ℓ. For large bolides impacting Venus and Jupiter the pressure rise during fracture wave propagation ($t_{fw} = 2R/U_S$) is significant and the fracturing wave evolves to a strong shock wave that propagates at a velocity(U_S), and the bolide is compressed in the region behind the shock wave(see Figure 2a). The impactor is also distorted by both the passage of the compressive-fracturing wave and by the action of the aerodynamic forces. These aerodynamic forces are greatest at the center of the fragment and give rise to the spreading and flattening of the bolide [3-6]. The relative diameter was found in SPH calculations [7] to increase from unity to maximum of ~4 for a 1 km radius impactor and ~1.7 for a 5 km radius impactor (see Figure 2b). This distortion and flattening has been observed in laboratory experiments of breakup of liquid droplets by gas streams [8], and in code calculations [7]. Hydrodynamic instabilities prevent the projectile from expanding to the effective diameters that are as large as ~20 times the undisturbed diameter predicted by models based only on inertial confinement [3].

Besides K-H instabilities, Rayleigh-Taylor (R-T) instabilities occur and these are driven by the deceleration of the bolide and by the aerodynamic forces. These instabilities occur near the center of the front of the bolide. The particles ejected in Figure 2a are believed to result from R-T instabilities. We show that the time for R-T instabilities to grow relative to the characteristic deceleration time, t_{decel}, is given by: $t_{R-T}/t_{decel} = \{[R/(2\pi\ell f)](\lambda/R)\}^{1/2}$ where $f = \ell n \{(2/(3C_d))(\rho_b R/(\rho_a \ell)\}$ and λ is the instability wavelength, C_d the drag coefficient, ρ_a and ρ_b the densities of the atmosphere and bolide. Ivanov et al. [9] observed that upon passage of impactor through the Venusian atmosphere that surface instabilities grow at the front of the projectile and limited the distortion of the projectile. Recently, Boslough et al. [10] observed similar phenomena in their calculation of Comet Shoemaker-Levy-9 impact on Jupiter.

Instabilities are driven by velocity differences between the atmosphere and the bolide surface and are most prevalent near the edge of the front face of the bolide. We show that the time for K-H

PENETRATION OF LARGE BOLIDES: O'Keefe, J. D., Takata, T., and Ahrens, T. J.

instabilities to grow relative to the bolide characteristic deceleration time is given by $t_{K-H}/t_{decel} = \left(10/(\pi\sqrt{3})\right)\left(\eta_p/\eta_a\right)^{1/2}(R/\ell)^{2/3}(\lambda/R)\,(1/f)$ where η_a and η_b are the viscosities of the atmosphere and the bolide.

Disintegration and Stopping

The final breakup of the bolide occurs when the instabilities having wavelengths on the order of the size of the bolide ($\lambda/R \sim 1$) grow to large amplitudes. Referring to Figure 1, we see that growth rates for large scale K-H instabilities are on the order of 1 s^{-1} for bolides 1 km in radius and on the order of 10^1 s^{-1} for 1 to 5 km radius impactors. The growth rates for R-T instabilities are also comparable to these values. Our SPH calculations show disintegration occurring at these time scales predicted from these growth rates (Figure 2). Shown in Figure 2c is final disintegration and the stopping of the disintegrated fragments.

REFERENCES: 1. Bronshten V. A. (1983) *Physics of Meteoric Phenomena* D. Reidel Publishing Co., Boston, 356 pp. pp. 2. Keith J. C. and Banks N. E. (1990) *Intl. J. Impact Eng.*, 10, 309-322. 3. Zahnle K. (1992) *J. Geophys. Res.* , 97, 10243. 4. Melosh H. J. (1989) *Impact Cratering, A Geologic Process* Oxford University Press, New York, 245 pp.. 5. Zahnle K. and MacLow M.-M. (1994) *Icarus* , submitted. 6. Vickery A. (1993) *EOS* , 74, 291. 7. Takata T., *et al.* (1994) *LPSC* , 25, this volume. 8. Ranger A. A. and Nichols J. A. (1970) *AIAA Journal* , 8, 1720-1722. 9. Ivanov B. A., *et al.* (1992) *J. Geophys. Res.* , 97, 16,167-16,182. 10. Boslough M. B., *et al.* (1993) *Bull. Am. Astron. Soc.* , 25, 1045.

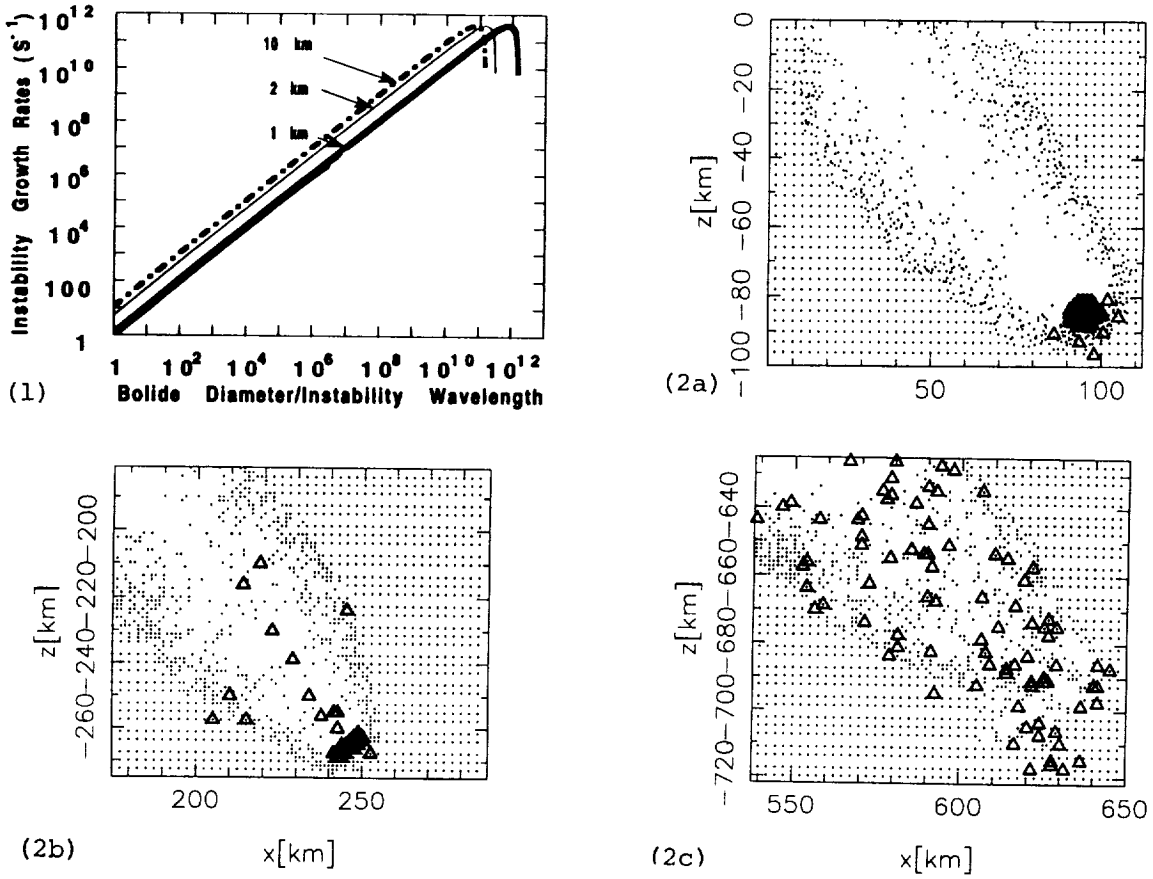

Fig 1 Growth rate of Kelvin-Helmholtz instabilities as a function of the diameter of the impactor divided by the instability wave length. The curves are for impactor diameters of 1, 2, and 10 km and the depth into the atmosphere is 300 km relative to the 1 bar level of Jupiter. Fig. 2. Smooth-Particle -Hydrodynamic (SPH) calculations of the penetration of a fragment of Comet Shoemaker-Levy-9 fragment into Jupiter's atmosphere. The diameter of the bolide is 10 km and the angle of entry is 40° from the zenith. Shown are the density fields at various times relative to the time the bolide penetrated to the 1 bar altitude. Dots indicate planetary atmosphere and triangles bolide SPH particles. The times are 2.0 , 5.0, and 21 sec., respectively .

LITHOPHILE ELEMENT DIFFUSION PROFILES IN PHOSPHATE PHASES IN IIIAB IRON METEORITES: A CLUE TO THE TRACE LITHOPHILES IN METAL DURING CORE FORMATION Edward J. Olsen and Ian M. Steele, Dept. of the Geophysical Sciences, University of Chicago, Chicago, IL, USA 60637.

From measurement of refractory siderophile trace elements in the metal of iron meteorites it has been determined that several types are magmatic and formed cores within parent bodies [1,2]. Especially interesting is the IIIAB-pallasite magmatic association because this association is further linked to mesosiderites and the HED achondrites for they share a common source of oxygen isotopes, as measured in their lithophile phases [3] — oxides, phosphates, silicates (OPS phases). Measurements of excess ^{53}Cr within phosphate phases in IIIAB irons demonstrate that core formation took place within the first 35 m.y. after parent body accretion [4, 5]. To the best of our knowledge no significant body of data exists on lithophile trace elements within bulk IIIAB irons. Our approach to this has been to study the mineralogy of minor and trace OPS phases in IIIABs to obtain some measure of the process of fractionation of lithophile elements between core and the last lithophile material the core "saw" before metal solidification. We argue that during core solidification and subsequent recrystallization into a Widmanstätten structure, oxygen and lithophile trace elements within the metal mass were occluded and concentrated within such places as troilite nodules. The partial pressure of oxygen rose locally within nodules, Fe and P in metal were partly oxidized and simple ferrous orthophosphates formed: graftonite and its polymorph sarcopside, both essentially $Fe_3(PO_4)_2$ [6]. Other lithophile trace elements reacted later to form new phosphate phases. Although terrestrial phosphates in hydrous pegmatites are notorious for their ability to form metastable assemblages, we argue that in the slow cooling regime of IIIABs the observed assemblages should be stable ones.

A few IIIABs contain OPS assemblages that are unique among them: Cape York with Na-rich buchwaldite [$NaCaPO_4$] + maricite [$NaFePO_4$] + other uncharacterized phosphates; Mount Howe with maricite + tridymite; Puente del Zacate with a fragment of a chondritic silicate rock [7], the only known occurrence of a silicate assemblage in any IIIAB. Here, however, we focus on the common OPS assemblages found in most IIIABs. These assemblages are: sarcopside ± graftonite (or beusite, if Mn≥Fe) [$(Fe,Mn)_3(PO_4)_2$] + johnsomervilleite [approx. $(Na,K)_2Ca(Fe,Mn)_7(PO_4)_6$] + a new mineral [approx.$(Na,K)_2(Fe,Mn)_8(PO_4)_6$] currently called "2:8:6-ite" until x-ray diffraction and optical data are obtained to fully characterize it. 2:8:6-ite always has Fe>Mn, however, in one occurrence is K>Na. Johnsomervilleite always occurs as enclaves within, or at the edge of sarcopside. 2:8:6-ite usually occurs with sarcopside or graftonite and never in contact with johnsomervilleite. We anticipate that 2:8:6-ite will be structurally different from johnsomervilleite in order to account for the presence of both within most of the IIIABs we have examined. All these occur near, or in contact with schreibersite and chromite and within troilite nodules (with a few rare exceptions; one of these noted later).

In order to understand the formation of these phosphates we obtained a group of electron microprobe step or beam scans across their contacts with associated phases. Mn scans were made from troilite across sarcopside. A typical scan (uncorrected for background) is shown in Fig.1 for the IIIB Mount Edith. It shows an M-shaped diffusion profile indicating that during sarcopside formation Mn diffused in from surrounding troilite. The same kind of Mn diffusion profile is seen in a high Mn graftonite in the IIIB Grant (Fig.2). A Na scan was done in Mount Edith starting (left to right, Fig.3) in troilite, across 2:8:6-ite, then into a bordering graftonite. It also shows an M-profile, albeit not as pronounced. Similarly a Ca profile in 2:8:6-ite (Fig.4) is the same, although the low count rate for such low CaO does not permit great confidence. A Ca scan across a johnsomervilleite with ≈ 4% CaO will be done in the future.

We conclude that the chemistry of these phosphates supports the model that trace lithophile elements and oxygen concentrate within troilite nodules during solidification of core metal. After Fe-phosphates form, Mn, Na, K and Ca diffuse into them forming Mn-bearing graftonite (or beusite) and sarcopside, johnsomervilleite and 2:8:6-ite. Which of these phases and how much depend on the local supply of lithophiles. We believe that graftonite with minor amounts of Na,

LITHOPHILE DIFFUSION PROFILES IN IIIAB PHOSPHATES: Olsen, E. and Steele, I.

K, Ca and Mn formed initially. With falling temperature graftonite inverted to sarcopside which could not accommodate all the minor elements. These diffused to nucleation sites within sarcopside and formed enclaves of johnsomervilleite, high Mn graftonite (or beusite), or 2:8:6-ite. As a test for this a Mn profile was measured across a graftonite in the EET 83230 iron; this phosphate is contained entirely within metal; no troilite was seen. It has no detectable Mn or any other lithophile element and appears to be the product of simple oxidation of a phosphide grain.

This raises a significant question. If traces of lithophiles were trapped in the metal core as it segregated, these trace phosphate minerals indicate that the last lithology "seen" by the separating metal contained, in order of relative abundances, Mn>Na>Ca>K. Mg and Si, however, are much more abundant lithophile elements in all the lithologies known from stone meteorites. Why is Mg absent entirely and some Si shows up only as a rarity in IIIABs: tridymite in Mount Howe and a single silica grain encountered in Grant? Volatility cannot account for this anomaly: Ca is refractory and Na is volatile; Mn and K fall between. The only solution (not entirely satisfactory) is that pallasites along the core-mantle boundary quantitatively removed Mg and Si, leaving Mn, Na, Ca and K traces in core metal. Yet one would still expect some Mg to appear in the IIIAB phosphates, for we know that a Mg-analog of johnsomervilleite, namely chladniite, can form (in the Carlton IIICD [8]). And where, among these elements, is Al? It is relatively abundant, found neither in pallasites nor among the traces of core lithophiles discussed here. Chromites coexisting with the phosphates discussed here are Al-free. It is possible that Al is less soluble in troilite than Mn, Na, Ca and K. [9]

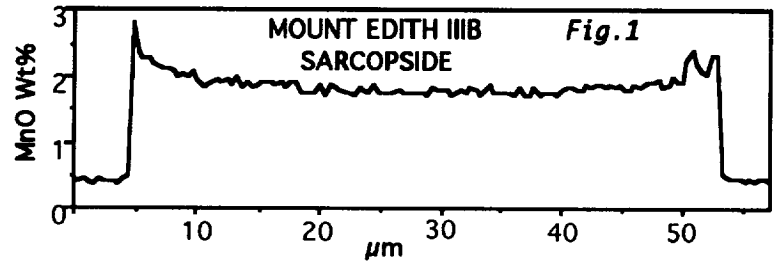

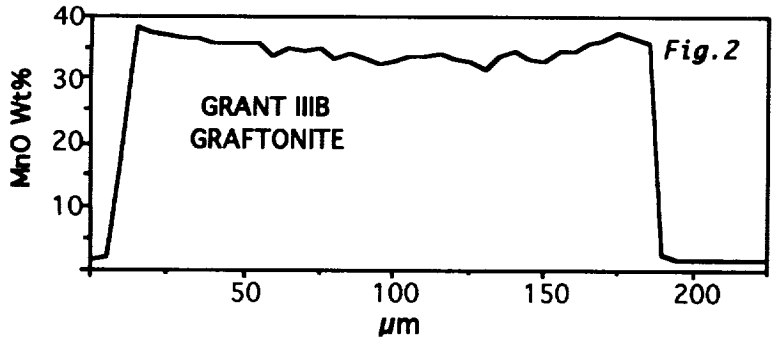

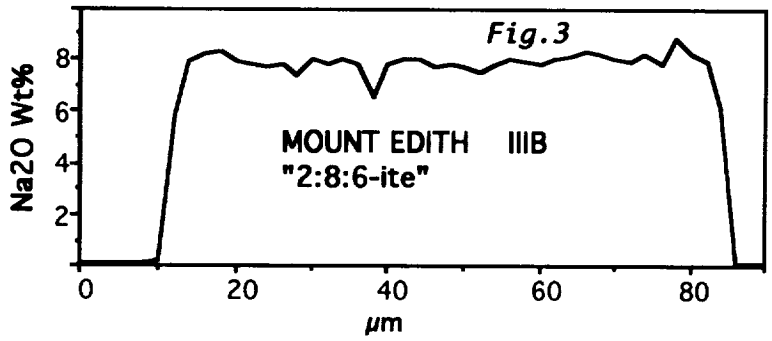

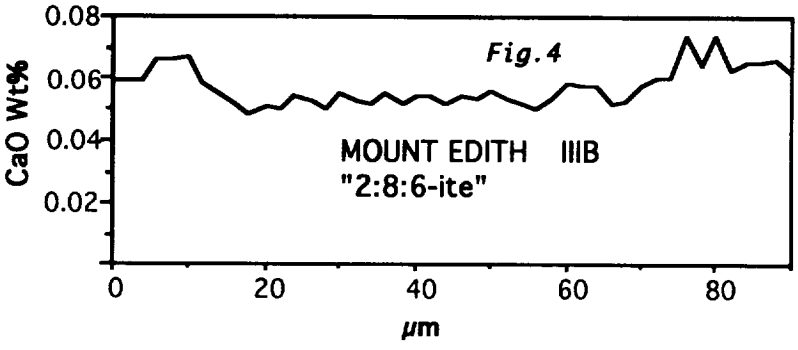

References: [1] Scott, E.R.D. (1972) *Geochim. Cosmochim. Acta* **36**, 1205. [2] Taylor G.J. (1992) *J. Geophys. Res.* **97:E9**, 14717. [3] Clayton, R.N. *et al.* (1976) *Earth Planet. Sci. Lett.* **30**, 10. [4] Davis, A.M. and Olsen, E.J. (1990) *LPSC* **XXI**, 258. [5] Hutcheon, I.D. and Olsen, E.J. (1991) *LPSC* **XXII**, 605. [6] Olsen, E.J. and Fredriksson, K. (1966) *Geochim. Cosmochim. Acta* **30**, 459. [7] Olsen, E.J. *et al.* (1992) *LPSC* **XXIII**, 1019. [8] McCoy, T.J. *et al.* (1993) *Meteoritics* **28**, 394.
[9] This work was supported by NASA grant NAGW-3569.

I DON'T BELIEVE ALL THE IRREGULARLY SHAPED SMALL BODIES IN THE SOLAR SYSTEM ARE THE RESULT OF COLLISIONS; by William A. Oran, AlliedSignal Technical Services Corp., Lanham Md., 20706, phone 301-805-3013

This synopsis discusses an alternative to the currently accepted source of irregularly shaped small bodies in the solar system. The alternative is that these shapes may be the result of solidification phenomena. This alternative was deduced based in part on a study of the shape of these small bodies ("radius" < 100-200 km) versus their size and in part on calculations of phenomena representative of the solidification of these bodies in space. Finally a suggestion is made on the use of these bodies to possibly infer some parameters associated with the early solar system.

DISCUSSION AND CONCLUSIONS

Some of the more fascinating phenomena in astronomy are associated with small bodies in the solar system. Indeed, there is a strong interest in these bodies "because they contain so much important information about the early periods of the evolution of the solar system" (ref. 1). The shape of these small bodies is also an interesting study with their morphology generally assumed to have resulted from the interplay of two basic collision phenomena: fragmentation and accretion. As part of the data for this investigation, a study was made of the smaller bodies of the solar system, including Phobos and Gaspra, for which reasonable photographs have been made(for example refs. 2-5). Although this extended abstract precludes the display of the resultant photomontage, the change in shape from a sphere as the characteristic size (radius) decreases from ~ 100 - 200 km is striking.

Several groups have investigated potential changes in the shape of these smaller bodies and noted that the self-generated gravitational force may not be enough to maintain spheriodicity below a characteristic radius of ~ 100 km. In a study of icy satellites, this may be due to the low material strength of the body assuming that the material are "mostly weakly consolidated aggregates" (ref. 6). In the case of predominantly rocky bodies, other mechanisms could force these smaller bodies into non-spherical shapes especially during the solidification process. The most likely mechanism is the shrinkage in volume as the body solidifies from a possible superheated state to a solid at the cool temperature of its local environment. Assuming a cooling by radiation into space, the outer surface of the body would initially solidify into a skin. Calculations on the solidification front (analogous to those of ref. 7), assuming a radiation into cold space, yield an initial inward velocity of ~ 0.000002 m/s which is sufficient to generally overtake and engulf particles from the skin that may break off and move inward via Stokes settling in the body's weak gravitational field (assumed ~ 0.1 m/s/s). Thus, the solidified skin should stay in place given the high viscosity of the melt (ref. 8). The slowing of the solidification front as it moves to the interior could allow Stokes settling resulting in a core and/or convective flow as the particles release their heat of fusion in the hotter interior; this could further distort the body's shape.

This is a situation not unlike the shrinkage of a plum into a prune. Based on the thermophysical properties of rock, the reduction in volume could be as much as 25% (using, in part, the values in ref. 9). Assuming the initially solidified skin remains in place (i.e. the surface area remains constant), then a 25% reduction in volume can result in a very distorted shape from an initially molten sphere. This is indicated in Fig. 1 which present the cross-sections of two extreme limits due to a 25% volume change of an initial sphere (A) resulting in a fission-like

shape (B) and/or a cylinder (C); the surface area is constant in all 3 cases. Even a 10% volume reduction during solidification can be shown to potentially result in bodies that have large shape modification from a sphere. (Note, on the other end of the scale for bodies less than a mm, while volume reduction is still present, the force of surface tension would again drive a solidifying body into a spherical shape.)

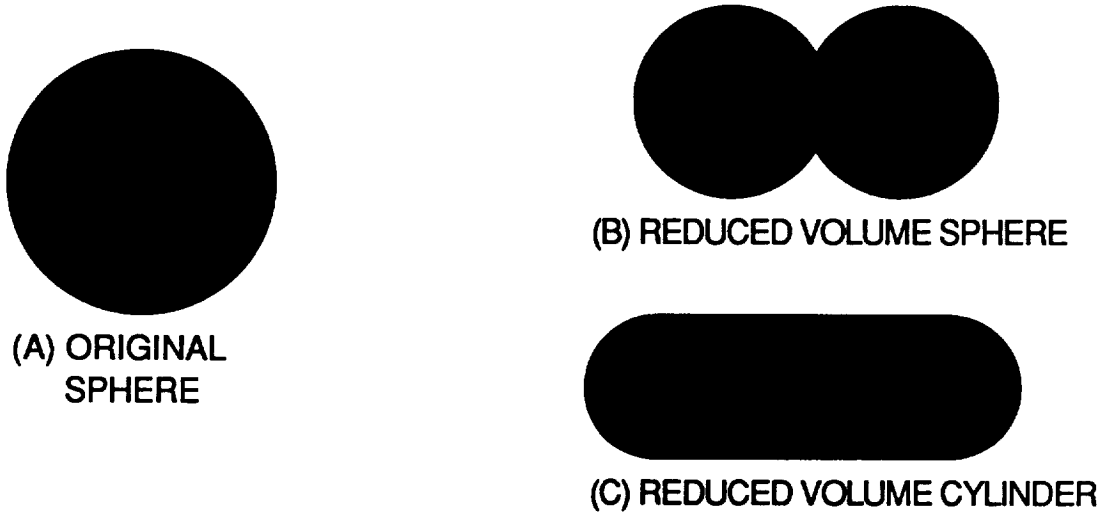

Figure 1. Cross-sections of extreme shape changes of a sphere where the surface area remains constant, but the final volumes are reduced by 25%.

In conclusion, it is assumed that the unusual shapes of small bodies of the solar system are the result of collision phenomena: fragmentation and/or accretion. An alternative explanation has been deduced in this paper that may also create these unusual shapes, namely it may be due to the basic solidification phenomena of volume shrinkage. This explanation is not being proposed as a replacement for the generally accepted theory, but rather as an alternative that may be equally valid depending upon the history of an individual body. However, if the shape of a small body in the solar system can be inferred to be caused by solidification phenomena, then it may also be possible to infer some of thermal parameters (such as peak temperature and cooling rates) of the early solar system in the general orbital location of that small body.

The author would like to thank the AlliedSignal Technical Services Corporation for its support.

REFERENCES

1. Alfred's, H. and Arrhenius, G., NASA SP-345, 1976
2. Durda, D., Astronomy, Feb. 1993
3. Frazier, K., The Solar System, Time-Life Books
4. Larson, D., Adv. in Astronautical Sciences, Vol. 31, Pt. 2, 1974
5. Avduyevsky, V., Ed., Mfg. in Space, Mir Publishers, 1985
6. Klinger, L., et. al., NATO ASI Series C: Math. and Physical Sci., Vol 156, 1984
7. Minear, J., Proc. of the 11th Lunar Planet. Sci. Conf., 1980
8. Murase, T. and McBirney, A., Geo. Soc. of America Bulletin, Nov. 1973
9. Yoder, H., Generation of Basaltic Magma, NAS, 1976

DEPOSITIONAL PATTERNS AT THE MOUTHS OF THE MARTIAN OUTFLOW CHANNELS (DAO, HARMAHKIS, MAJA, AND ARES VALLES, MARS); G.G. Ori, Dipartimento di Scienze Geologiche, Universita' di Bologna, 40127 Bologna Italy

The depositional systems at the mouths of the outflow channels on Mars must be investigated bearing in mind that the variables controlling their accumulation are rather different from those working on the Earth The deposition has been controlled by a number of factors that complicate the sedimentological interpretation. (A) The type of flooding is of paramount importance: catastrophic floods shaped the valles and filled the basins, but smaller floods occurred probably at late stages. (B) The morphology of the mouths derived by the pre-existing topography, but large-scale erosion, produced by the floods, modified the physiography of the channel mouths. (C) A major role has been played by the water level. Difficulty in recognising Earth-like deltaic structures is primarily due to the catastrophic floods that have not or little counterpart on Earth [1]. Deltaic features cannot form during the high-energy events that enter into an empty basin. Further, low-energy flows cannot form, again, delta-like structures because there is not a shelf, but the currents flow directly on the basin floor. This type of floods cannot form deltaic systems, but rather it would accumulate a laterally extensive sheet of sediment hardly recognisable from remote sensed data. Later, if a body of standing water was present, underflows or turbidity currents can occur distally from the channel mouths.

Two couples of outflow channel mouths, one from the Chryse Planitia and the other from the Hellas Basin, show contrasting morphological patterns within the same basin. The mouths of the Harmahkis and Ares Vallis exemplify the most common type [2]. They show very broad mouths gently diverging from the channel borders. The floor of the channel termini appears to be flat and merging, with not or little change in gradient, into the basin floor. These flat surfaces could represent the top of blankets of sediment deposited during the catastrophic floods. In three dimensions the bodies of sediments are sheet-like, being thin with respect to their lateral extension. These sediments seem to flood the distal part of the outflow channels suggesting onlap geometries between them and the substratum. On Earth, there are not exact equivalents of these deposits. Some analogies can be found with the turbiditic depositional systems [3]. This type of system is quite complicate and relatively poorly known. Most detritus is deposited during strong erosional episodes, when the sea-level is in a low stand position. In these stages the erosional power of the rivers is rather large and alluvial basin, as well as the exposed shelves, are deeply incised. At very high energies, the detritus is poured directly on the marine basin floors. The resulting sedimentary bodies consist of flat extensive layers of sand with lobes forming gentle relieves. The mouth of the Maja Vallis [4] is quite different from that of the Ares Vallis, which is a few hundreds kilometres apart and belong to the same basin. The hydrological history of the Maja Vallis is complicated by a set of pounding areas working as discharge buffers. The mouth in the Chryse Planitia lies downstream a gorge [5]. The related deposits show a remarkable fan shape making it extremely similar to the terrestrial alluvial fans (as can be seen from aerial view). The fan-like depositional system rests on a steep slope of the substratum and the elevation of its toe is higher than that of the basin floor. In other words, the mouth deposits of the Maja Vallis were accumulated by the stream currents with little or not direct interaction with the standing water of body filling the Chryse Planitia. This factor, along with smaller discharges (due to the pounding effects and the presence of

gorges), allowed the formation of features similar to the terrestrial alluvial fan or fan delta [5].

Harmahkis and Dao Valles, from the eastern margin of the Hellas Basin [6], display a different type of contrast. The mouth of the former feature is similar to that of the Ares Vallis whereas the Dao mouth is complicated by a topographic relief. Downstream of the enlargement of the Dao Vallis, a smaller channel is present [6]. This channel seems to be directly connected to the Dao channel, but it is different in both shape and dimension. Moreover, two narrow belts of lighter material surround on both sides this channel, suggesting the presence of natural levees. The spatial correspondence of the two channels suggests that they formed during the same stage of the depositional history. If this is true, their remarkable difference must be explained. In order to produce such a difference, two separate kinds of depositional processes must be involved. The Dao outflow channel could be formed in the usual way by mean of catastrophic floodings, whereas the smaller channel could be formed by turbidity or underflow currents when a standing body of water was present in the Hellas Basin. At this stage, the presence of an high base-level (the water level of the inundated basin) and the fact that most detritus has been already mobilised by the catastrophic floods, could lead to the formation of low-energy currents transporting small amount of sediment. These currents must be turbiditic, that is produced in a body of liquid, in order to explain the by-pass area which is present from the terminus of the outflow channel and the beginning of the smaller channel. If the system was subaerial, the head of the latter channel should be deeply incised into the relief separating the two channel types.

Summing up and putting this scattered data in a single model, the outflow channels are shaped and activated during catastrophic floods that deposits thin blankets of detritus into the basin. The base level corresponds to the basin floor. At this stage the basin is filled totally or partially by liquid water. Resedimentation, lower-energy currents (underflows or turbidity currents) form minor systems (partially similar to the Earth analogue of the channel-levee complexes in the submarine fan systems). This kind of resedimentation could be active even with the presence of ice in upper part of body of water, and, eventually, it will be inactive only when the entire mass of liquid will freeze Valles systems that do not enter directly into the standing body of liquid water could form (as in the Maja case) features similar to the alluvial fan-fan deltas of the Earth.

REFERENCES [1] De Hon R. A. (1993) *LPSC* ,XXIV, 389. [2] Mars Channel Working Group (1983) *Bull. GSA*, 94, 1035. [3] Van Wagooner et al. (1987) *AAPG Stud. Geol*, 27, 11. [4] Baker V. R & Kochel R. C. (1979) *JGR*, 84, 7961. [5] De Hon R. A. & Pani E. A. (1993) *JGR*, 98, 9129. [6] Crown A. A. et al. (1992) *Icarus*, 100, 1.

CONSTRAINTS ON THE ORIGIN OF THE OFFSET DIKES (SUDBURY IMPACT STRUCTURE, CANADA) FROM U-Pb DATA

M. Ostermann[1,2], U.Schärer[2], and A. Deutsch[1]; [1]Institut für Planetologie, Wilhelm-Klemm-Str. 10, D-48149 Münster, Germany; [2]Univ. Paris 7 and IPG, 2 place Jussieu, F-75251 Paris Cedex 05, France

The 1.85 Ga old [1] Sudbury Structure (Ontario, Canada) represents a tectonically deformed peak-ring or multi-ring impact structure with an original rim to rim diameter of up to 250 km [2-7]. Within the frame of this model, and supported by geochemical analyses [8, 9] and recent LITHOPROBE data [10], the Main Mass of the Sudbury Igneous Complex (SIC) is interpreted as the clast-free, differentiated central part of a coherent impact melt sheet, consisting of remolten crustal material only. At its base, a crystalline melt breccia, the Sublayer, forms a discontinuous thin layer.

A unique feature of the Sudbury Structure is the occurence of Offset Dikes. The term "offset" was introduced by [11] for up to 1500 m wide dikes, which radiate outward from the Main Mass of the SIC, and which are related to the SIC. Several economic important sulphide ore deposits are concentrated along these dikes [12, 13]. According to the most concise description on geological setting and petrography by [13], three types of Offsets can be distinguished: dikes occuring (*i*) perpendicular, or (*ii*) parallel to the outer margin of the SIC, or (*iii*) discontinous bodies. Dikes of type (*i*) can be traced for up to 28 km into the country rocks. The main lithology of the Offset Dikes is a quartz diorite with either hypersthene, clinopyroxene or amphibole as the dominant mafic mineral. Proximal to the contact with the SIC, the dikes show a greater compositional variety with norites, Sublayer lithologies and bodies of the Footwall Breccia. Most common are xenoliths of local country rocks as well as mafic to ultramafic clasts [14], which are probably derived from unexposed pre-Sudbury magmatic bodies. Geochemical data suggest different degrees of country rock assimilation after emplacement of the dikes. Their contacts are always sharp; they lack chilled margins, and contact metamorphic overprint in adjacent rocks is totally absent implying that country rock material was at elevated temperatures during dike intrusion.

It is generally assumed that the Sublayer and the Offset dikes are genetically related. Several models with up to four intrusion phases over an extended period of time have been proposed to explain chemical variations and complex internal contact relationships in the Sublayer [e.g., 15], as well as the origin of the Offset Dikes with their associated ore deposits [e.g., 12, 16, 17]. In all these endogenic or endogenic-exogenic models, however, age relationships between SIC, Sublayer, and Offsets remain unclear due to the lack of radiometric age data for the Offset dikes.

To bracket the age of the Offset Dikes, zircons were separated from the Foy Offset (north of the SIC), and small abraded fractions were analyzed for U and Pb. The three small to medium-grained quartz-dioritic Offset Dike samples are free of clasts and they have SiO_2 contents of 50.9, 57.3, and 58.7 wt.-%; they show various degrees of alteration. The zircons have a magmatic appearance, based on their morphology and internal structure with a total absence of inherited cores. In the concordia diagram of Figure 1, the zircon data plot slightly discordant and colinear on a trajectory intersecting the concordia line near 1850 Ma, which is the age of the SIC [1]. The U-Pb data also imply that the zircons were newly grown in the melt now forming the Offset Dikes. Moreover, on the basis of known U-Pb systematics in zircon, it can be concluded that very high temperatures were reached in this melt, causing total resetting and eventual dissolution of any older zircons present. Only impact melts can reach such high temperatures.

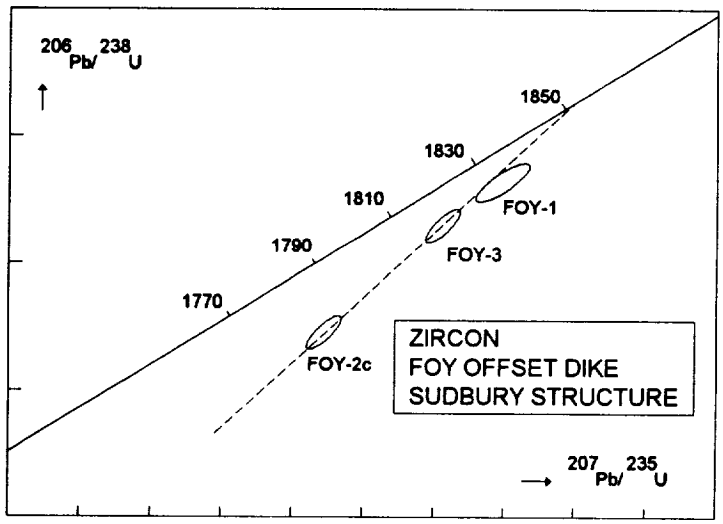

Figure 1. Concordia diagram with zircon data for the Foy Offset Dike. Sample locations: FOY 1, half distance between the outer rim of the SIC and Nickel Lake; FOY 2, Nickel Lake; FOY 3, North of Nickel Lake. 1850 ± 1 Ma (2σ) is the age of the SIC, defined by data for zircon and baddeleyite from the norite and the granophyre of the SIC [1].

On the basis of these preliminary U-Pb geochronological data, the Foy Offset Dike and the SIC show an identical age. In addition, U-Pb systematics of the zircons indicate that the Offset Dikes are also part of the impact melt system at Sudbury, consisting of re-melted crustal material. This view is supported by relatively radiogenic osmium isotope compositions in the main mass of the Cu-Ni ores and in the Offset Dikes [18, 19], which are incompatible with an mantle origin of the platinum group metals. The Cu-Ni ores must have formed by immiscibility [20] relatively early in the differentiation of the SIC. They are concentrated in the basal layer of the melt sheet, the Sublayer, and were transported along with xenoliths of basal SIC rocks into the Offset Dikes. It is proposed that the major period of their extrusion from the SIC was after the crater had formed and the ores had segregated but prior to Footwall Rock cooling. Presumably, Offset Dike emplacement was during late-stage topographic and isostatic adjustments. The spatial distribution of Offset Dikes suggests that they intruded zones of impact-induced fractures and pre-existing faults in the crater basement.

ACKNOWLEDGEMENTS. We thank Dr. B.O.Dressler (Ontario Geol. Survey) for providing the samples. Analytical work was supported by PROCOPE and by the INSU-D.B.T. grant 1991-4.17 to U.Schärer.

REFERENCES. [1] Krogh, T.E. et al. (1984) *Ontario Geological Survey, Spec. Vol.1*, 431-446; [2] Brockmeyer, P. (1990) *unpub. Ph.D. thesis* University of Münster; [3] Lakomy, R. (1990) *Meteoritics, 25*, 195-207; [4] Grieve, R.A.F.et al. (1991) *JGR, 96*, E5, .22,753-22,764; [5] Avermann, M. et al. (1994) *GRL* i.p.; [6] Stöffler, D. et al. (1994) *Geol. Soc. Am. Spec. Vol.* i.p.; [7] Grieve, R.A.F. and Deutsch, A. (1994) *this volume*; [8] Faggart, B.E. et al. (1985) *Science, 230*, 436-439; [9] Deutsch, A. (1994) *Geol. Soc. Am. Spec. Vol.* i.p.; [10] *GRL Spec. Vol.* i.p.(1994); [11] Coleman, A.P. (1905) *Ontario Bureau of Mines, 4*, Part 3, 188; [12] Souch, B.E. et al. (1969) *Economic Geology Monograph 4*, 252-261; [13] Grant, R.W. and Bite, A. (1984) *Ontario Geol. Surv., Spec. Vol.1*, 275-300; [14] Scribbins, B.T. et al. (1984) *Can. Mineral.*, 22, 67; [15] Dressler, B.O. et al. (1987) in *Research in Terrestrial Impact Structures* (Pohl, J. ed.) 39-68 (Vieweg, Braunschweig); [16] Naldrett, A.J. et al. (1972) *Intern. Geol. Congress 24th, 4*, 206-214; [17] Pattison, E.F. (1979) *Can. Mineral., 17*, 257-274; [18] Walker, R.J. et al. (1991) *EPSL, 105*, 416-429; [19] Dickin, A.P. et al. (1992) *GCA, 56*, 3531-3537; [20] Naldrett, A.J. et al. (1986) in *Metallogeny of Basic and Ultrabasic Rocks*, 75-91, Inst. of Mining Metallurgy, London, U.K.

CHROMIUM ISOTOPIC ANOMALIES IN STEPWISE DISSOLUTION OF ORGUEIL; U. Ott[1,2], F. A. Podosek[1], J. C. Brannon[1], T. J. Bernatowicz[1], and C. R. Neal[3], [1]McDonnell Center for the Space Sciences, Washington University, St. Louis, MO 63130, USA, [2]Max-Planck-Institut für Chemie, D-55020 Mainz, Germany, [3]Department of Civil Engineering and Geological Sciences, University of Notre Dame, Notre Dame, IN 46556, USA.

The Cr in carbonaceous chondrites such as Orgueil displays isotopic anomalies of both signs in a pattern which suggests that essentially all the Cr is anomalous. This suggests at least partial preservation of presolar carriers of types not yet identified. So far, however, there is no evidence for corresponding anomalies in other elements nor for the chemical/mineral identity of the putative carriers.

It is well recognized that surviving interstellar grains are preserved in primitive meteorites. Grain types thus far known are characterized by chemical inertness which allows them to be isolated by survival through extremely harsh chemical treatments; identification as interstellar grains follows primarily from observation of radical isotopic anomalies (see reviews [1,2]). It is also well recognized that some types of meteoritic material display nucleosynthetic isotopic anomalies which are more modest but still substantial and experimentally well-defined. Such effects are generally interpreted to reflect specific nucleosynthetic components carried by interstellar grains diluted by admixture of "normal" materials. In some cases such anomalies evidently represent disproportionate sampling of interstellar carriers in materials which were made in solar nebular processing; other cases may represent preserved or partially preserved interstellar grains which are diluted only by mechanical admixture. It is possible that primitive chondrite matrices contain presolar grains which have not yet been identified as such because they are too small for isotopic analysis of individual grains and because they are not so chemically resistant that they can be concentrated by dissolution of other constituents.

Here we report the first progress in a project intended to explore this latter possibility. The initial experimental focus is based on the results of Rotaru *et al.* [3], who found large (up to about 100 ε-units at ^{54}Cr) isotopic anomalies in Cr obtained in progressive dissolution of carbonaceous chondrites, mostly unaccompanied by anomalies in other iron-group elements (except for a few cases of small anomalies at ^{66}Zn). Besides isotopic analyses, our study includes SEM/EDX characterization of residues and ICP-MS analysis (currently in progress) of solutions to try to constrain the nature of anomaly-bearing phases.

Bulk Orgueil (202 mg) was sequentially dissolved in the series of steps indicated in Table 1. Steps 1-3 are the same as in the Rotaru *et al.* [3] study (these steps should account for >90% [3] of total Cr in Orgueil); the remaining steps are more elaborate, particularly the inclusion of HCl steps 4-6 before introduction of HF. We have thus far obtained Cr isotopic results for steps 2-4 and 6-8 (Figures 1, 2). Analyses were performed on a VG Sector 54 thermal ionization mass spectrometer at Washington University, using $^{50}Cr/^{52}Cr$ (≡.051859) normalization with ^{53}Cr and ^{54}Cr deviations calculated relative to the normal composition

Table 1. Steps in sequential dissolution of bulk Orgueil

1	2.5 % acetic acid, 35 min., room temperature
2	50% acetic acid, 1 day, room temperature
3	4N HNO_3, 5 days, room temperature
4	6N HCl, 3 days, room temperature
5	6N HCl, 1 day, ~36°
6	6N HCl, 1 day, ~80°C
7	HF/HCl, 1 day ~ 100°C
8	HF/HCl, 1 day, ~ 100°C (repeat)
9	CS_2 extraction
10	4N NaOH, 3 hours, ~80°C
11	conc. $HClO_4$, 2.5 hrs, ~185°C.
12	conc. H_2SO_4, 2 hrs, ~195°C

reported by Rotaru *et al.*[3]. Our normals (e.g. open symbols in Fig. 1) are somewhat lighter than the Rotaru *et al.* composition (by about 1ε at ^{53}Cr and 2 ε at ^{54}Cr) but this evident bias effect does not hamper identification of anomalies.

Our results confirm the basic features observed previously [3]. The most easily dissolved phases show negative ^{54}Cr anomalies of a few ε units, complemented by positive anomalies of several permil in subsequent steps. There is a small (1-2 ε) positive ^{53}Cr anomaly in step 2; ^{53}Cr is otherwise normal within errors. We observe that the largest positive anomaly in ^{54}Cr occurs in an HCl step (Fig. 2), before major silicate dissolution attendant on introduction of HF.

Since there are anomalies of both signs, there must be at least two carriers of anomalous Cr; the mass balance and the absence of a "preferred" normal composition suggests that nearly all the Cr in Orgueil is anomalous. The major problems to be addressed in the future are assessment of what other isotopic anomalies (if any) accompany those in Cr and identification of the anomaly-bearing phases. It is noteworthy that the phases most readily expected to dissolve in the initial steps are alteration phases, which would not be considered prime candidates to host anomalies; since (unknown) additional phases may also be dissolving in the acetic acid steps, it remains to be determined whether the alteration phases actually contain anomalous Cr.

References: [1] Ott U. (1993) *Nature* **364**, 25 [2] Anders E. and Zinner E. (1993) *Meteoritics* **28**, 490 [3] Rotaru M., Birck J-L. and Allegre C. J. (1992) *Nature* **358**, 465.

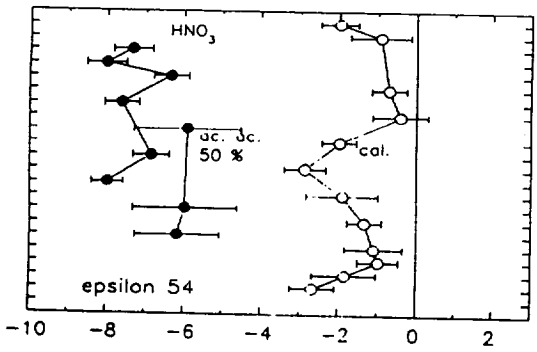

Fig. 1. ^{54}Cr data for normals (open symbols) and replicate analyses for bulk Orgueil dissolution steps 2 and 3 (solid symbols)

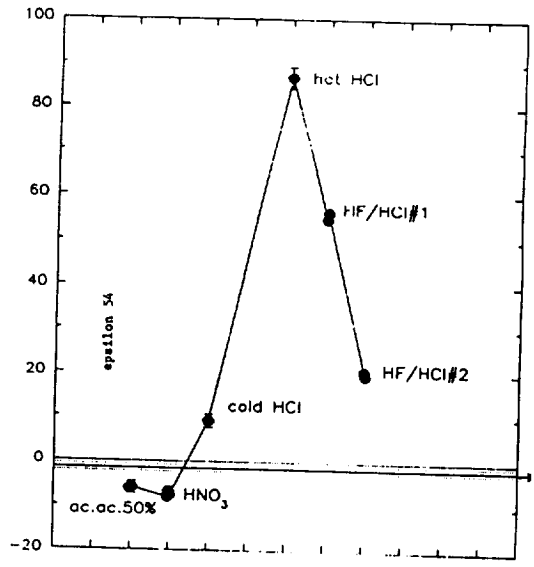

Fig. 2. ^{54}Cr anomalies in sequential dissolution (Table 1) of bulk Orgueil.

REFRACTORY SIDEROPHILES IN ANTARCTIC UNEQUILIBRATED ORDINARY CHONDRITES; H. Ozaki and M. Ebihara, Department of Chemistry, Faculty of Science, Tokyo Metropolitan University, Hachioji, Tokyo 192-03, Japan.

Introduction: Refractory siderophile elements are hard to be separated from each other in cosmo- and geochemical processes. During the condensation process, refractory siderophiles are thought to have appeared in solid phases such as metal nuggets as a group at first and later have been hosted quantitatively in Fe-Ni alloys. These elements are thought to have also been scarcely fractionated in the metal-silicate fractionation processes. After a long-standing discussion concerning the fractionation of refractory siderophiles (Re, Os, Ir) in chondrites, Anders and Grevesse [1] concluded that these elements are not fractionated in chondritic meteorites; the previously recognized variations in Re/Ir and Re/Os ratios for C1 chondrites were artificial and these ratios should be revised to be 'normal' values the other chondritic meteorites have. A possibility of the fractionation among refractory siderophiles (Re, Os, Ir, for instance) in ordinary chondrites have been discussed mainly based on the data for equilibrated ordinary chondrites (EOC) because of the scarcity of analytical data for unequilibrated ordinary chondrites (UOC). The discovery of Antarctic meteorites made it possible to study UOC intensively because a relatively large number of UOC have been collected on Antarctica. In order to characterize UOC in the light of elemental abundances, we started to analyze Antarctic UOC and a part of our results obtained by INAA were already reported [2]. In this study, we determined Re, Os, Ir as refractory siderophiles in Antarctic UOC by RNAA in order to discuss (i) whether refractory siderophiles are fractionated in UOC, (ii) whether C1 chondrite ratios of refractory siderophiles are preserved even in Antarctic UOC, and (iii) whether the weathering effect had any influence on siderophile abundances.

Experiments: The Antarctic meteorites used in this study (all UOC) were loaned by the National Institute of Polar Research, Tokyo. The samples were received in chips, which were sampled from interior portions of the individual meteorites. About a few hundred mg of each sample was ground in an agate mortar and 50 to 100 mg of the powdered sample was sealed in a synthesized quartz tube and irradiated at a neutron flux of 5.0×10^{13} $cm^{-2}sec^{-1}$ for 12 h in the JRR-4 reactor of the Japan Atomic Energy Research Institute. Reference standards were prepared from chemical reagents and were simultaneously irradiated with the meteorite samples. After irradiation , the samples were cooled for a few days and were subject to the radiochemical purification of Re, Os and Ir. The chemical procedures of Anders et al. [2] were basically used after several modifications for simplifying.

Results and Discussion: Analytical results for Re, Os and Ir are shown in Figs. 1 and 2. All the data plotted are relative values normalized to C1 values. For comparison, literature values, which are all for non-Antarctic UOC, are also plotted in these figures using filled symbols. Analytical uncertainties are estimated to be less than 10% for these three elements. As easily recognized in Fig. 1, Ir and Os are scarcely fractionated from each other in Antarctic and non-Antarctic UOC as well as in (non-Antarctic) EOC (Fig. 3). In contrast, Re and Os are largely fractionated in Antarctic UOC, whereas the literature data for non-Antarctic EOC give a better correlation between Re and Os data (Fig. 4). Figs 1 to 4 suggest that Re is fractionated from Ir and Os in Antarctic UOC. Such a deviation of Re contents compared with these of Os and Ir data is a characteristic feature for Antarctic UOC. Although we don't have sufficient data of refractory siderophiles for Antarctic EOC, an apparent fractionation of refractory siderophiles in Antarctic UOC may be extended to the line of discussion concerning the difference in genesis between Antarctic and non-Antarctic meteorite groups initially insisted by Lipschutz and coworkers [4]. Ir/Os ratios for Antarctic UOC are almost equal to a C1 value, whereas their Re/Os ratios seem to be slightly higher than the C1 ratio. The Re/Os ratios for (non-Antarctic) EOC also yield a systematic deviation from the C1 value (Fig. 4). Therefore, it is suggested that Re, Os and Ir are fractionated from each other among chondritic meteorites. As Re is the most refractory element among these elements, the condensation and/or accretion processes must be highly responsible for such a fractionation. It has been also recognized that

REFRACTORY SIDEROPHILES IN ANTACTIC UOC: Ozaki H. and Ebihara M.

Re is highly prone to aqueous weathering [5]. In the INAA work of Antarctic UOC, it was inferred that the elemental abundances of Na and Au were slightly disturbed by terrestrial weathering on Antarctica. As the sensitivity of aqueous alteration for Re seems to be smaller than that for Au [5] and the degree of deviation of Na and Au in meteorites are much smaller than those observed for refractory siderophiles in Antarctic UOC, the deviation of Re contents in Antarctic UOC must be indigenous rather than redistributed on Antarctica.

References: [1] Anders E. and Grevesse N. (1989) *GCA* **53**, 197-214. [2] Ebihara M. and Ozaki H. (1992) (submitted). [3] Anders E. et al. (1988) NAS-NS-3117, U.S. National Technical Information Service, 95 pp. [4] Dennison J. E., Lingner D. W. and Lipschutz M. E. (1986) *Nature* **319**, 390-393. Dennison J. E. and Lipschutz M. E. (1987) *GCA* **51**, 741-754. [5] Ebihara M., Wolf R. and Anders E. (1982) *GCA* **46**, 1849-1861.

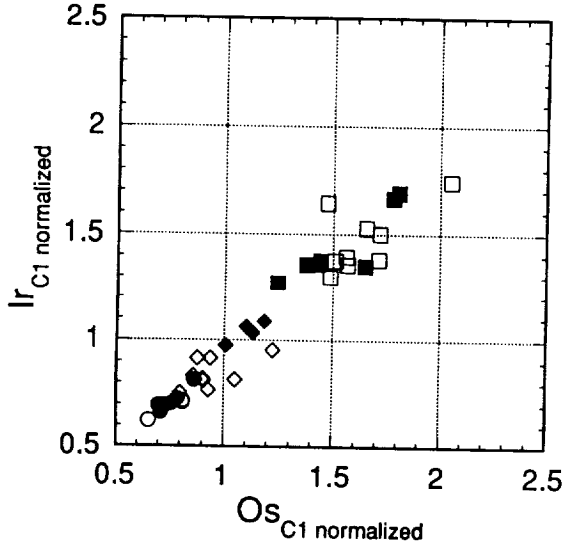

Figure 1. Ir vs. Os in Antarctic UOC (open - this work; filled - literature values).

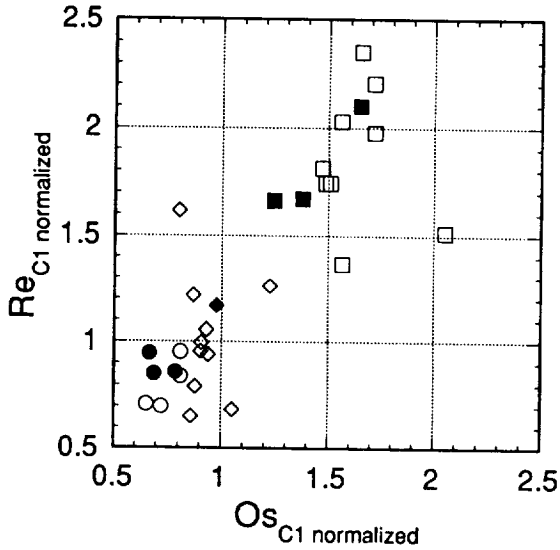

Figure 2. Re vs. Os in Antarctic UOC (open - this work; filled - literature values).

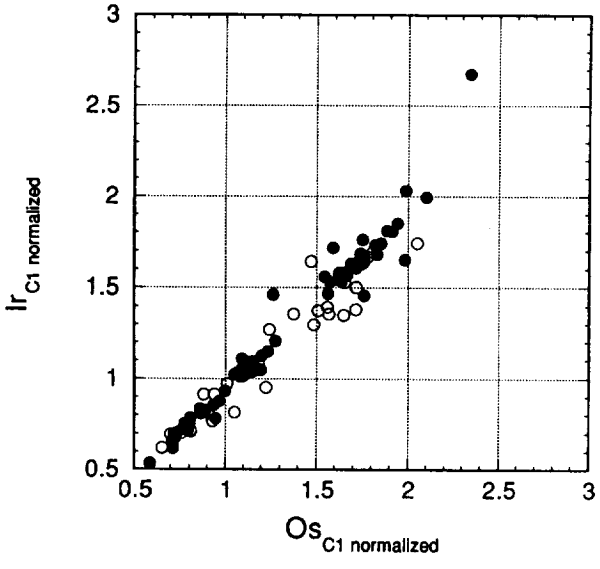

Figure 3. Ir vs. Os in ordinary chondrites (open - UOC; filled - EOC).

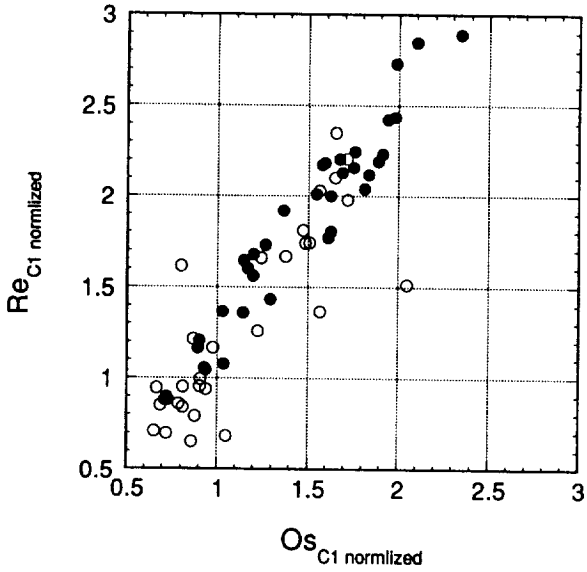

Figure 4. Re vs. Os in ordinary chondrites (open - UOC; filled - EOC).

AUTHOR INDEX*

*Page numbers refer to the first page of an abstract on which an author appears.

SAMPLE INDEX*

*Page numbers refer to the first page of an abstract in which a sample is mentioned.

METEORITE INDEX*

*Page numbers refer to the first page of an abstract in which a meteorite is mentioned.

KEYWORD INDEX*

*Page numbers refer to the first page of an abstract in which a term is mentioned.